

Lecture Notes in Mechanical Engineering

Premananda Pradhan  
Binayak Pattanayak  
Harish Chandra Das  
Pinakeswar Mahanta *Editors*


# Recent Advances in Mechanical Engineering

Select Proceedings of ICRAMERD 2021

 Springer


# Lecture Notes in Mechanical Engineering

## Series Editors

Francisco Cavas-Martínez , Departamento de Estructuras, Construcción y Expresión Gráfica Universidad Politécnica de Cartagena, Cartagena, Murcia, Spain

Fakher Chaari, National School of Engineers, University of Sfax, Sfax, Tunisia

Francesca di Mare, Institute of Energy Technology, Ruhr-Universität Bochum, Bochum, Nordrhein-Westfalen, Germany

Francesco Gherardini , Dipartimento di Ingegneria “Enzo Ferrari”, Università di Modena e Reggio Emilia, Modena, Italy

Mohamed Haddar, National School of Engineers of Sfax (ENIS), Sfax, Tunisia

Vitalii Ivanov, Department of Manufacturing Engineering, Machines and Tools, Sumy State University, Sumy, Ukraine

Young W. Kwon, Department of Manufacturing Engineering and Aerospace Engineering, Graduate School of Engineering and Applied Science, Monterey, CA, USA

Justyna Trojanowska, Poznan University of Technology, Poznan, Poland

**Lecture Notes in Mechanical Engineering (LNME)** publishes the latest developments in Mechanical Engineering—quickly, informally and with high quality. Original research reported in proceedings and post-proceedings represents the core of LNME. Volumes published in LNME embrace all aspects, subfields and new challenges of mechanical engineering. Topics in the series include:

- Engineering Design
- Machinery and Machine Elements
- Mechanical Structures and Stress Analysis
- Automotive Engineering
- Engine Technology
- Aerospace Technology and Astronautics
- Nanotechnology and Microengineering
- Control, Robotics, Mechatronics
- MEMS
- Theoretical and Applied Mechanics
- Dynamical Systems, Control
- Fluid Mechanics
- Engineering Thermodynamics, Heat and Mass Transfer
- Manufacturing
- Precision Engineering, Instrumentation, Measurement
- Materials Engineering
- Tribology and Surface Technology

To submit a proposal or request further information, please contact the Springer Editor of your location:

**China:** Ms. Ella Zhang at [ella.zhang@springer.com](mailto:ella.zhang@springer.com)

**India:** Priya Vyas at [priya.vyas@springer.com](mailto:priya.vyas@springer.com)

**Rest of Asia, Australia, New Zealand:** Swati Meherishi at [swati.meherishi@springer.com](mailto:swati.meherishi@springer.com)

**All other countries:** Dr. Leontina Di Cecco at [Leontina.dicecco@springer.com](mailto:Leontina.dicecco@springer.com)

To submit a proposal for a monograph, please check our Springer Tracts in Mechanical Engineering at <https://link.springer.com/bookseries/11693> or contact [Leontina.dicecco@springer.com](mailto:Leontina.dicecco@springer.com)

**Indexed by SCOPUS. All books published in the series are submitted for consideration in Web of Science.**

More information about this series at <https://link.springer.com/bookseries/11236>

Premananda Pradhan · Binayak Pattanayak ·  
Harish Chandra Das · Pinakeswar Mahanta  
Editors

# Recent Advances in Mechanical Engineering

Select Proceedings of ICRAMERD 2021

 Springer



*Editors*

Premananda Pradhan  
Department of Mechanical Engineering  
Siksha 'O' Anusandhan Deemed to be  
University  
Bhubaneswar, Odisha, India

Binayak Pattanayak  
Department of Mechanical Engineering  
Siksha 'O' Anusandhan Deemed to be  
University  
Bhubaneswar, Odisha, India

Harish Chandra Das  
Department of Mechanical Engineering  
National Institute of Technology Meghalaya  
Shillong, Meghalaya, India

Pinakeswar Mahanta  
Department of Mechanical Engineering  
National Institute of Technology Arunachal  
Pradesh  
Yupia, Arunachal Pradesh, India

ISSN 2195-4356

ISSN 2195-4364 (electronic)

Lecture Notes in Mechanical Engineering

ISBN 978-981-16-9056-3

ISBN 978-981-16-9057-0 (eBook)

<https://doi.org/10.1007/978-981-16-9057-0>

© The Editor(s) (if applicable) and The Author(s), under exclusive license to Springer Nature Singapore Pte Ltd. 2023

This work is subject to copyright. All rights are solely and exclusively licensed by the Publisher, whether the whole or part of the material is concerned, specifically the rights of translation, reprinting, reuse of illustrations, recitation, broadcasting, reproduction on microfilms or in any other physical way, and transmission or information storage and retrieval, electronic adaptation, computer software, or by similar or dissimilar methodology now known or hereafter developed.

The use of general descriptive names, registered names, trademarks, service marks, etc. in this publication does not imply, even in the absence of a specific statement, that such names are exempt from the relevant protective laws and regulations and therefore free for general use.

The publisher, the authors, and the editors are safe to assume that the advice and information in this book are believed to be true and accurate at the date of publication. Neither the publisher nor the authors or the editors give a warranty, expressed or implied, with respect to the material contained herein or for any errors or omissions that may have been made. The publisher remains neutral with regard to jurisdictional claims in published maps and institutional affiliations.

This Springer imprint is published by the registered company Springer Nature Singapore Pte Ltd. The registered company address is: 152 Beach Road, #21-01/04 Gateway East, Singapore 189721, Singapore

# Preface

The International Conference on “Recent Advances in Mechanical Engineering Research and Development (ICRAMERD 2021)” focused on the latest research findings and advances in the mechanical and materials engineering areas to society, specifically centered on the development of new materials and their applications, thermal engineering, design and manufacturing system engineering, industrial and system engineering, automotive engineering energy research, etc.

The proceedings received full research papers, experimental reports and review articles from different areas of mechanical engineering. All of these submissions went through a rigorous peer review process by inviting reviewers from different themes of national and international repute.

This conference received 156 papers from across the globe, and after peer review, only 79 research papers were selected and registered for presentations in 9 different parallel sessions according to the themes. Nine session chairs (9 in numbers) from various reputed institutes of our country were invited to preside over the session. The presented papers were evaluated based on their quality of work and presentations. Finally, one paper from each session was awarded as the best paper.

ICRAMERD 2021 invited a number of high-profile keynote speakers from India and abroad. Professor A. Rolstadas, Norwegian University of Science and Technology, Norway, and Prof. Jim Browne, President of Irish Academy of Engineering, jointly expressed their views on the topic “New Challenges in Manufacturing Engineering Education.” Professor David Scott Sink, Senior Advisor, Poirier Group, Adjunct Professor Virginia Tech., Canada, discussed on the topic “Large Scale Enterprise Transformation,” while Prof. Bopaya Bidanda from Pittsburgh, USA, showed light on the topic “Thriving under Uncertain and Disruptive Conditions.” Professor Md. Mamun Habib from Independent University, Bangladesh, explained about the disruption of supply chain due to COVID-19.

Professor Pinakeswar Mahanta, Director, NIT, Arunachal Pradesh and Professor, IIT, Guwahati discussed on the topic “Recent Development in Co-Gasification of Biomass with Coal”.

Eight different invited speakers from academic, research institutes and industries delivered lectures on their field of research and expertise.

We would like to thank everyone including authors, session chairs, reviewers, invited speakers, keynote speakers, organizing committee members, volunteers, students, media persons, and advisors for their contribution to make the event a success. We extend our sincere gratitude to Siksha 'O' Anusandhan, Deemed to be University as the host organization for support provided by the Institute for successfully co the event.

Bhubaneswar, India

Dr. Premananda Pradhan

# Contents

<b>Chaotic Oscillations in Axially Travelling String with Time Varying Velocity</b> .....	1
Shashendra Kumar Sahoo, Lokanath Panda, and Harish Chandra Das	
<b>Nonlinear Dynamics of Translating String with Geometric Nonlinearity</b> .....	9
Shashendra Kumar Sahoo, Lokanath Panda, and Harish Chandra Das	
<b>Quality Circle: Maximizing the Productivity in Coal Handling Plant Through Why-Why Technique</b> .....	17
Somanath Ojha, Bhatu Kumar Pal, Janender Kumar, Smita Mohanty, and Krishnan Kanny	
<b>Electrothermomechanical Responses in Smart Composite Plates</b> .....	27
S. A. Ohid and J. K. Nath	
<b>Energy and Exergy Study of a Compression Ignition Engine Running with Producer Gas</b> .....	35
Pradipta Kumar Dash, Sanjaya Kumar Mishra, Shakti Prakash Jena, and Harish Chandra Das	
<b>New Challenges in Manufacturing Engineering Education</b> .....	45
Asbjørn Rolstadås and Jim Browne	
<b>Design and Simulation of Enhanced Smart Cantilever Assembly for Active Vibration Control</b> .....	55
Biswaranjan Swain, J. Halder, N. Swain, P. P. Nayak, and S. Bhuyan	
<b>Design of Injection Mold for Manufacturing of Cup</b> .....	65
B. A. Praveena, Balachandra P. Shetty, N. Lokesh, N. Santhosh, Abdulrajak Buradi, Mahesh, Sunil, Ramesh Jalapur, and Sharanu	
<b>Accurate Computation of Transverse Shear Stresses in Smart Composite Plates</b> .....	75
T. Das and J. K. Nath	

<b>Firmware of Indigenous and Custom-Built Flexible Robots for Indoor Assistance</b> .....	85
Debanik Roy	
<b>Mechanical Properties Analysis of Kenaf–Grewia–Hair Fiber-Reinforced Composite</b> .....	101
Sampath Boopathi, G. Venkatesan, and K. Anton Savio Lewise	
<b>Co-digestion of Agricultural and Plant Wastes and Cow Dung for Biogas Production</b> .....	111
Amaresh Mohapatra, Sanjaya Kumar Mishra, Shakti Prakash Jena, and Premananda Pradhan	
<b>Prediction of Growth Percentage of Sintered Compacts Using Neural Network Technique</b> .....	123
Sujit Kumar Khuntia, Soumya Darshan Mohanty, Bibhuti Bhusan Pani, and Sankar Narayan Das	
<b>A Perceptive Approach for Multi-objective Optimization of Die-Sinking EDM Process Parameters with Utility Concept and Taguchi Method for Sustainable Machining</b> .....	133
S. D. Mohanty, S. S. Mahapatra, R. C. Mohanty, S. K. Khuntia, and J. Mohapatra	
<b>Effect of Preheat Temperature on Thermal Behavior in AlSi10Mg Powder Bed During Laser Powder Bed Fusion Process</b> .....	143
Amitav Dash and Seshadev Sahoo	
<b>The Development of Turbopumps for Low-Thrust Cryogenic Rocket Engine</b> .....	149
Sridhar Panigrahi, P. Rijish Kumar, B. Prejil Kumar, P. Unnikrishnan Nair, Paul P. George, N. Jayan, and M. S. Suresh	
<b>Effect of Partial Filling of Metal Foams on Exergy Transfer in a Vertical Channel</b> .....	157
K. Kiran Kumar, Banjara Kotresha, and Kishan Naik	
<b>Numerical Investigation of the Icing of Water Drop Striking on Solid Surface: From Hydrophilic to Superhydrophobic Surfaces</b> ....	167
Virendra Patel, Ashok Kumar Sahoo, and Rimpay Chabra	
<b>Effect of Viscous Dissipation, Soret and Uniform Heat Source on MHD Flow of a Polar Fluid Through Porous Mediums</b> .....	175
Bhabani Shankar Kamilla and Dharendra Nath Thatoi	
<b>Automation of AM Via IoT Towards Implementation of e-logistics in Supply Chain for Industry 4.0</b> .....	181
Reem Ashima, Abid Haleem, Shashi Bahl, Devaki Nandan, and Mohd Javaid	

**Parametric Studies of Dissimilar Friction Stir Welded AA2024/AA6082 Aluminium Alloys** ..... 191  
 Deepak Kumar Mohapatra and Pragyam Paramita Mohanty

**Evaluation and Optimization of Process Parameter for Surface Roughness of 3D-Printed PETG Specimens Using Taguchi Method at Constant Printing Temperature** ..... 201  
 N. Lokesh, J. Sudheer Reddy, B. A. Praveen, Y. M. Kishore Veeresh, B. Sreehari Acharya, J. Eshwar Kapse, Pramath P. Nadig, and Mahadeva Prasad

**Heat Transfer Due to Turbulent Impinging Air Jet on Flat and Concave Plate** ..... 213  
 Deepak Kumar Sethy and Pandaba Patro

**Evaluation of Preventive Activities of COVID-19 Using Multi-criteria Decision Making Method** ..... 221  
 Gnanasekaran Sasikumar, Sivasangari Ayyappan, and N. Venkatachalam

**Mechanical Characterization of Concrete with Rice Husk-Based Biochar as Sustainable Cementitious Admixture** ..... 227  
 Sourav Ghosal, P. K. Pani, R. R. Pattanaik, and M. K. Ghosal

**Ranking of Barriers for SSCM Implementation in Indian Textile Industries** ..... 235  
 Ashish Patel and T. N. Desai

**Investigation on the Influence of MQL on Machining Parameters During Hard Turning of AISI316L** ..... 253  
 P. V. Vinay and Ch. Murali

**Framework to Monitor Vehicular GHG Footprint** ..... 263  
 Soumyanath Chatterjee and S. P. Sarmah

**Accurate Prediction of Thermomechanical Stress Field in the Laminated Composite Plates** ..... 271  
 T. Das and J. K. Nath

**Solution to Real-Time Problem in Shifter Knob Assembly at Automobile Manufacturing Industry** ..... 283  
 Prabinkumar R. Jachak, Abhay Khalatkar, Nilesh M. Narkhede, and Rupesh Shelke

**Dislocation Analysis of Laser-Sintered Al Alloy Nanoparticles in Using Molecular Dynamics Simulation** ..... 291  
 Jyotirmoy Nandy, Seshadev Sahoo, and Hrushikesh Sarangi

**Design and Development of Special Purpose Vehicle for Hilly Area** ..... 299  
 Dilip S. Choudhari, Pranav Charkha, and Sumit Desai

<b>Nonlinear Free Vibration Analysis of Functionally Graded Materials Spherical Shell</b> .....	313
Pranav G. Charkha and Pradeep Khaire	
<b>Structural, Dielectric, Electrical and Optical Properties of <math>\text{Ca}_3\text{CuZr}_4\text{O}_{12}</math> Ceramics</b> .....	323
S. K. Parida, S. Senapati, S. Mishra, R. K. Bhuyan, B. Kisan, and R. N. P. Choudhary	
<b>MHD Up/Down Flow of Nanofluids with SWCNT/MWCNT Suspensions</b> .....	331
D. N. Thatoi, S. Choudhury, S. S. Mohapatra, and M. K. Nayak	
<b>Effect of GGBS and Burnt Paper Based Solid Wastes Ash in Making Sustainable Paver Blocks: An Experimental and Model Study</b> .....	341
Meyyappan Palaniappan and Ravi Tejeswar Reddy	
<b>A Prototypical Design Strategy for Soil–Cement Construction for Indian Condition</b> .....	349
Meyyappan Palaniappan and Rajha Poorna	
<b>A Numerical Study to Choose the Best Model for a Bladeless Wind Turbine</b> .....	359
Mohammed Amein Alnounou and Sikata Samantaray	
<b>Biogas Production from Dried Banana Leaves Using Cow Urine as a Biocatalyst</b> .....	371
Sanjaya K. Mishra, Premananda Pradhan, Sasanka Choudhury, and Shakti P. Jena	
<b>Effect of Tissue Properties on the Efficacy of MA on Lungs</b> .....	379
Shubhamshree Avishek and Sikata Samantaray	
<b>Multi-response Optimization of Turning Parameters for AZ91D Magnesium Alloy Using Gray-Based Taguchi Approach</b> .....	389
A. Saravanakumar, L. Rajeshkumar, G. Sisindri Reddy, K. Narashima Prasad, M. Pranava Adithya, P. Suryaprakash Reddy, P. Harsha Vardhan, and P. Bala Narasimhudu	
<b>Effect of Process Parameters and Coolant Application on Cutting Performance of Centrifugal Cast Single Point Cutting Tools</b> .....	399
Shubhashree Mohapatra, Hrushikesh Sarangi, and Upendra Kumar Mohanty	
<b>Study and Analysis of Thermal Barrier Application of Lanthanum Oxide Coated SS-304 Steel</b> .....	407
Sangita Sarangi, Santanu Mohapatra, and Ajit Kumar Mishra	

**Effect of Casting Length on Solidification of Al-33 wt% Alloy in Twin-Roll Casting** ..... 415  
 Suvam Swayam Mohapatra and Seshadev Sahoo

**Implementation of Industry 4.0 in Pharmaceutical Sector** ..... 423  
 Himanshu R. Mali, Praneet A. Chotalia, Shivangi Thakker, and Ajay K. Gangrade

**Machining of Austenitic Stainless Steel Under Various Cooling-Lubrication Strategies** ..... 435  
 Smita Padhan, Ajay Kumar Behera, and Sudhansu Ranjan Das

**In Situ Synthesis of Cobalt Oxide and Carbon Nanocomposite** ..... 443  
 Rahul Kumar, Prasanta Kumar Sahoo, and Ankur Soam

**Recovery of Iron Values from Blast Furnace Gas Cleaning Process Sludge by Medium Intensity Magnetic Separation Method** ..... 449  
 Malaya Kumar Jena, Jyotirmayee Mahanta, Manjula Manjari Mahapatra, Madhusmita Baliarsingh, and Subhabrata Mishra

**Fatigue Analysis of Rectangular Plate with a Circular Cut-Out** ..... 455  
 S. Siva Priya and P. K. Sahoo

**To Study the Implementation of Kaizen in Northern Indian Manufacturing Industries** ..... 465  
 Nitesh Verma, Simranjit Singh Sidhu, Jagjeet Singh Chatha, and Santosh Bali

**Protection of Vital Facilities from the Threat of External Explosion Using D3o Material** ..... 475  
 Mostafa Dada, Bahaa Eddin Ghrewati, and Manas Ranjan Das

**Investigation on Coefficient of Heat Transfer Through Impact of Engine Vibration** ..... 485  
 Ashwini Kumar, Aruna Kumar Behura, Gaurav Dwivedi, and D. N. Thatoi

**Measurement of Local Spray Impingement Density by Using a Novel Patternator** ..... 495  
 Santosh Kumar Nayak, Siba Prasad Behera, Purna Chandra Mishra, and Achinta Sarkar

**Performance of Chemical Route-Synthesized SnO<sub>2</sub> Nanoparticles** ..... 503  
 Harapriya Nayak, Usharani Panda, and Sushanta Kumar Kamilla

**Mechanical Behaviors of Aluminum Matrix Composite Synthesized by Stir Casting Technique** ..... 513  
 Jayashree Pati, Supriya Priyadarshinee, Pragyana Mohanty, Ranjita Mahapatra, and S. K. Kamila



<b>The Effect of Dedicated Newly Designed Dual-Axis Solar Tracking System and Cooling System on the Performance of a Commercial PV Panel</b> .....	521
Achinta Sarkar, Pragyana Borthakur, Avijit Kumar, Aiman Adhikari, Aditya Paul, Siba Prasad Behera, and Santosh Kumar Nayak	
<b>Study of Electrical Behaviors of PVDF/BiGdO<sub>3</sub> Polymer Composite</b> .....	529
Minakshi Padhy, Laxmidhar Sahoo, Ananya Rath, and P. Ganga Raju Achary	
<b>Performance Characteristics Optimization of Castor Oil Biodiesel-Powered Compression Ignition Engine Using RSM-Whale Optimization Algorithm</b> .....	537
Bibhuti Bhusan Sahoo, Prasanta Kumar Sahoo, Abhishek Barua, Dilip Kumar Bagal, Siddharth Jeet, Laxmi Narayan Rout, and Arati Rath	
<b>Stability Analysis of Rainfall Induced Unsaturated Slope by Reliability Based Optimization Using Solver</b> .....	547
Abhipsa Kar and Manas Ranjan Das	
<b>Electrical Modulus and Conductivity Study of Styrene-Butadiene Rubber/Barium Hexaferrite Flexible Polymer Dielectrics</b> .....	557
Deeptimayee Khatua, Laxmidhar Sahoo, R. N. P. Choudhary, and P. Ganga Raju Achary	
<b>Effect of Alkaline and Acrylic Acid Treatment on Improving Tensile Strength of Rattan Fibers</b> .....	565
Dolly Tiwari, Layatitdev Das, and J. R. Mohanty	
<b>A Study on Thermal Conductivity Characteristics of Waste Marble Powder/Epoxy Composites Using Different Models</b> .....	573
Subhrajit Ray, Suvam Swain, and Binayak Pattanayak	
<b>Structural, Dielectric, and Phase Shifting Characteristics of [(Pb<sub>0.5</sub>Bi<sub>0.25</sub>La<sub>0.25</sub>) (Fe<sub>0.5</sub>Ti<sub>0.5</sub>) O<sub>3</sub>] Electronic System</b> .....	581
S. K. Pradhan, S. N. Das, D. Chauhan, S. Bhuyan, and R. N. P. Chaudhary	
<b>Study on Physical and Mechanical Behavior of Bauhinia Vahlia Fiber Filled Glass-Epoxy Hybrid Composites</b> .....	587
Rashmi Ray, Sankar Narayan Das, and Abhipreet Mohapatra	
<b>A Comparative Analysis on Physical and Mechanical Properties of Aluminum Composites with Al<sub>2</sub>O<sub>3</sub> and WS<sub>2</sub> Reinforcement</b> .....	597
Sweta Rani Biswal and Seshadev Sahoo	
<b>Abrasive Jet Machining of Quartz Plates with Hot Silica Abrasives</b> .....	605
S. P. Behera, B. K. Nanda, Santosh Ku Nayak, B. C. Routara, and D. Dhupal	

**Darcy-Forchheimer Flow Over a Stretching Sheet with Heat Source Effect: A Numerical Study** ..... 615  
 S. Sahu, D. N. Thatoi, and K. Swain

**Slurry Erosion Behaviour of HVOF-Sprayed NiAl Composite Coating** ..... 623  
 Pragyan Senapati, Harekrushna Sutar, Rabiranjana Murmu, and Shubham Gupta

**Performance Analysis of DIC1-VCR Engine Fueled with Cottonseed Biodiesel and Diesel Blends** ..... 631  
 Shubham Pangavkar, Siraj Sayyed, and Kishor Kulkarni

**Fuzzy Logic Investigations on Wear Analysis of P/M-Produced Aluminum Composite Through Non-lubricated Mode** ..... 641  
 Rajesh Kumar Behera, Aezeden Mohamed, Birajendu Prasad Samal, Isham Panigrahi, and Sasanka Choudhury

**Numerical Study on Hydrodynamics Analysis of Geldart B Group of Particles in a 2D Fluidized Bed Drier** ..... 653  
 Vasujeet Singh, Pruthiviraj Nimalipuri, Vivek Vitankar, Harish Chandra Das, Malay Kumar Pradhan, and Swaroop Jena

**Simulation of Natural Gas Combustor Using CFD** ..... 667  
 Ankur Kumar, Pruthiviraj Nimalipuri, Vasujeet Singh, Vivek Vitankar, Harish Chandra Das, Malay Kumar Pradhan, and Manoj Kumar Panda

**Simulation of AlSi10Mg Powder for Temperature Profile by DMLS Method** ..... 681  
 Ashok Kumar Sahoo, Seshadev Sahoo, and Virendra Patel

**Multi-objective Optimization of EDM and Powder Mixed EDM for H-11 Steel** ..... 689  
 S. Tripathy and Deba Kumar Tripathy

**Production Optimization for a Biofuel Prepared from a High Acid Value Fuel like Nahar Oil, Its Properties and Feasibility to Use in a Four-Stroke DI Diesel Engine** ..... 699  
 Animesh Das, Manjula Das Ghatak, and Pinakeswar Mahanta

**Optimization of Power Consumption and Cost Analysis in Hard Turning Under NFMQL Condition** ..... 709  
 Lalatendu Dash, Ajay Kumar Behera, and Sudhansu Ranjan Das

**Analysis of Parametric Study on Weld Properties in TIG Welding** ..... 717  
 Shailesh Dewangan, Pavitra Singh, Manoj Kumar Agrawal, and S. Deepak Kumar

**Mechanical and Thermal Properties of Rice/Wheat Straw Fiber Reinforced Epoxy Composites: A Comparative Study** ..... 727  
Prabir Kumar Jena, Pradeep Bhoi, and Rabindra Behera

**Islanding Detection of Multi-DG-Based Microgrid Using Support Vector Machine** ..... 737  
Anasuya Roy Choudhury, Ranjan Kumar Mallick,  
Ramachandra Agrawal, Sairam Mishra, Pravati Nayak,  
and Subashish Samal

## About the Editors

**Dr. Premananda Pradhan** is the convenor of the International Conference (ICRAMERD-21) and is currently working as an associate professor at the Department of Mechanical Engineering, Institute of Technical Education and Research, affiliated to Siksha 'O' Anusandhan (Deemed to be University), Bhubaneswar, Odisha. He obtained his degree in mechanical engineering from the Institution of Engineers (Kolkata) and M.Tech. in Thermal Engineering from Siksha 'O' Anusandhan (Deemed to be University) and Ph.D. from KIIT University, Bhubaneswar, Odisha. Dr. Pradhan has got 13 years of working experience in reputed industries and 8 years of teaching and research experience. His major areas of research include thermal system design and optimization, combustion and heat transfer in porous media, bio-energy conversion, and thermal performance analysis of IC Engines and porous media combustion using both fossil and biofuels. Dr. Pradhan has published more than a dozen of research papers in reputed international journals and five conference proceedings. In addition to the above, he is engaged in several agricultural and medical equipment design projects of S'O'A (Deemed to be University). Dr. Pradhan has guided five M.Tech. scholars and several B.Tech. projects and at presently supervising two research Scholars.

**Dr. Binayak Pattanayak** is currently working as assistant professor at the Department of Mechanical Engineering, Siksha 'O' Anusandhan (Deemed to be University), Bhubaneswar. He obtained his B.Tech. (Mechanical Engineering) from Biju Patnaik University of Technology, Rourkela; M.Tech. and Ph.D. from the Siksha 'O' Anusandhan (Deemed to be University), Bhubaneswar. His major research area includes drying behavior of agricultural products, gasification of coal and biomass, dynamic modeling of solar collectors for power plant applications. He has more than 8 years of experience in teaching and research and published more than 10 papers in reputed international journals and conferences. He has guided more than 20 B.Tech. projects, five M.Tech. projects and currently two Ph.D. research scholars are enrolled under his supervision. He has also actively participated as a reviewer in peer reviewed journals as well as international/national conference proceedings.

Dr. Pattanayak has also conducted/organized academic-industrial interaction programs among the research community in the institute level.

**Prof. Harish Chandra Das** is currently working as Professor at Department of Mechanical Engineering, NIT Meghalaya. He has obtained his Ph.D. from NIT Rourkela. The research interest of Prof. Das includes vibration analysis, composite materials and explosion modeling. He has more than 30 years of teaching and research experience with more than 60 national and international publications. He has guided 12 Ph.D. scholars, 25 M.Tech. projects, and numerous B.Tech. projects. He has successfully completed more than 10 industrial consultancy projects. Currently, he holds the position of the Dean (Faculty Welfare) and Chairman (IQAC) at NIT, Meghalaya.

**Prof. Pinakeswar Mahanta** is currently the Director of National Institute of Technology Arunachal Pradesh, Yupia, Arunachal Pradesh, India. He has served as professor of mechanical engineering at IIT Guwahati. He did his Bachelors in Mechanical Engineering from Regional Engineering College, Rourkela in 1985. His areas of research include thermodynamics, heat transfer and renewable energy. He has established an international platform for research in bio-energy with the University of Nottingham, University of Birmingham, and Loughborough University, UK. He also has established collaboration in the field of clean coal technology with the University of Cranfield, UK and UCL, Belgium. He has published more than 120 papers in peer reviewed international journals, and edited four books. He has guided/mentored more than 30 B.Tech. projects, 35 M.Tech. projects, 18 PhD students and one PDF. Professor Mahanta's latest achievements include JSPS fellowship by invitation to Gifu University, Japan, Guest Lecturer at Hof University, Germany, and Indian Distinguishing visiting fellowship by the University of Nottingham, UK.

# Chaotic Oscillations in Axially Travelling String with Time Varying Velocity



Shashendra Kumar Sahoo, Lokanath Panda, and Harish Chandra Das

**Abstract** The chaotic oscillations of an axially travelling string with harmonic fluctuation in velocity are investigated. The partial differential equation of motion is discretized via Galerkin approach. Both single-mode and two-mode expansions are considered. Numerical simulations are performed to study the system behaviour with variation in control parameters. The numerical simulation indicates the existence of complex dynamical behaviours including chaos and period-doubling bifurcations for the two-mode expansion. The single-mode expansion exhibits periodic and quasiperiodic oscillations.

**Keywords** Axially travelling string · Galerkin approach · Periodic · Quasiperiodic · Period-doubling · Chaotic

## 1 Introduction

The linear and nonlinear vibration of travelling strings have been investigated for last sixty years. The harmonic fluctuation in velocity is one of the main causes of nonlinear oscillations of travelling string. The chaotic oscillations are dangerous among all the nonlinear oscillations of the string because the amplitude of vibration is larger than that of periodic and quasiperiodic vibration. Using modal analysis, Swope and Ames [1] examined the vibration behaviour of axially travelling string. Applying Floquet theory, Pakdemirli et al. [3, 4] explored the vibration behaviour of travelling string via Galerkin method. Chen et al. [5, 6] examined the bifurcation

---

S. K. Sahoo (✉)

Department of Mechanical Engineering, I.T.E.R, Siksha 'O' Anusandhan, Deemed To be University, Bhubaneswar, India

e-mail: [sashendrasahoo@soa.ac.in](mailto:sashendrasahoo@soa.ac.in)

L. Panda

Department of Mechanical Engineering, C.E.T, BPUT, Bhubaneswar, India

H. C. Das

Department of Mechanical Engineering, N.I.T, Shillong, Meghalaya, India

and chaotic behaviour for a travelling string with viscoelastic damping via Galerkin approach. Ghayesh et al. [7] studied the vibration characteristics of translating string having an elastic foundation applying multi-timescales analysis. Kesimili et al. [8] analysed the dynamic behaviour of axially moving string with number of supports applying multi-timescale analysis. Yang et al. [9] examined the nonlinear vibration behaviour of axially translating string applying gyroscopic modes of decoupling.

The paper investigates the chaotic oscillations of axially travelling string having harmonic fluctuation in velocity. The governing partial differential equation is discretized via Galerkin approach. Both single-mode and two-mode expansions are considered. The numerical simulation is performed to study the system behaviour with variation in control parameters. The numerical simulation shows a cascade of period-doubling bifurcations culminating to chaos for two-mode expansion. However, single-mode expansion exhibits periodic and quasiperiodic oscillations.

## 2 The Analytical Model

We consider a string having length  $L$ , cross-sectional area  $A$ , linear density  $\rho$  and axial tension  $P$  travelling over two pulleys as shown in Fig. 1.

The equation governing the transverse deflection of string is written as [3]

$$\rho A(\ddot{w} + \dot{v}w' + 2vw\dot{v}') + (\kappa\rho Av^2 - P)w'' = 0 \quad (1)$$

with boundary conditions

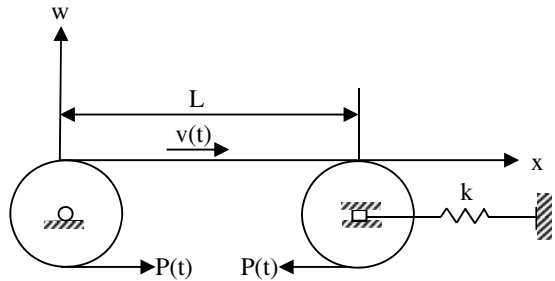
$$w(0, t) = w(L, t) = 0 \quad (2)$$

where  $w(x, t)$  is the transverse deflection of the string. The dot and prime are used to denote partial derivatives with respect to  $t$  and  $x$ , respectively.

The axial tension of the string is given as [2]

$$P = P_0 + \eta\rho Av^2 \quad (3)$$

**Fig. 1** Physical model of travelling string



where  $0 \leq \eta \leq 1$  and the axial support rigidity parameter  $\eta$  is given by

$$\eta = 1 - \kappa \quad (4)$$

Inserting Eqs. (3) and (4) in Eq. (1), we get

$$\begin{aligned} \rho A(\ddot{w} + \dot{v}w' + 2v\dot{w}') + (k\rho Av^2 - P_0)w'' &= 0 \\ w(0, t) = w(L, t) &= 0 \end{aligned} \quad (5)$$

### 3 Discretization

According to Galerkin approach, the solution to Eq. (5) may be assumed to have the form

$$w(x, t) = \sum_{n=1}^N q_n(t)\varphi_n(x) \quad (6)$$

where  $q_n(t)$  and  $\varphi_n(x)$  are the generalized coordinates and mode shapes of the stationary string, respectively.

The mode shapes of the stationary string satisfying the geometric boundary conditions is given by

$$\varphi_n(x) = \sin(n\pi x/L), \quad n = 1, 2, 3, \dots N. \quad (7)$$

Inserting Eq. (6) in Eq. (5) and using Galerkin approach and letting  $N = 1$ , we get for single-mode expansion the linear ordinary differential equation of motion as

$$\ddot{q}_1 + \left( \frac{p_0}{\rho A} - \kappa v^2 \right) \frac{\pi^2}{L^2} q_1 = 0 \quad (8)$$

Letting  $N = 2$ , we get for two-mode expansion linear ordinary differential equations which are gyroscopically coupled as

$$\ddot{q}_1 - \frac{16v}{3L}\dot{q}_2 + \left( \frac{p_0}{\rho A} - \kappa v^2 \right) \frac{\pi^2}{L^2} q_1 - \frac{8\dot{v}}{3L} q_2 = 0 \quad (9)$$

$$\ddot{q}_2 + \frac{16v}{3L}\dot{q}_1 + \frac{8\dot{v}}{3L} q_1 + \left( \frac{P_0}{\rho A} - \kappa v^2 \right) \frac{4\pi^2}{L^2} q_2 = 0 \quad (10)$$

Assuming the axial velocity of the string to vary harmonically with time



$$v(t) = V \sin \Omega t \quad (11)$$

where  $V$  and  $\Omega$  are velocity amplitude and fluctuation frequency, respectively.

## 4 Numerical Simulation

Numerical simulation is carried out to examine the system behaviour with variation in control parameters, viz. velocity amplitude and fluctuation frequency. The time trace, phase plane and frequency spectra are plotted. The physical parameters values are given in Table 1. The initial conditions chosen are  $q_1(0) = q_2(0) = 0$  and  $\dot{q}_1 = \dot{q}_2(0) = 0.001$ .

### 4.1 Single-Mode Expansion

Figure 2 shows periodic oscillations for single-mode expansion at  $V = 10$  m/s and  $\Omega = 20$  rad/s. The phase portrait is a closed trajectory, and frequency spectrum shows a sharp peak at a single frequency. Figure 3 shows quasiperiodic oscillations for  $V$

**Table 1** Physical parameters for a band-saw [2]

Physical parameter	Parameter value	Unit
$P_0$	76.22	N
$\rho$	7754.0	Kg/m <sup>3</sup>
$A$	$0.5201 \times 10^{-5}$	m <sup>2</sup>
$k$	0.22	–
$L$	0.3681	m

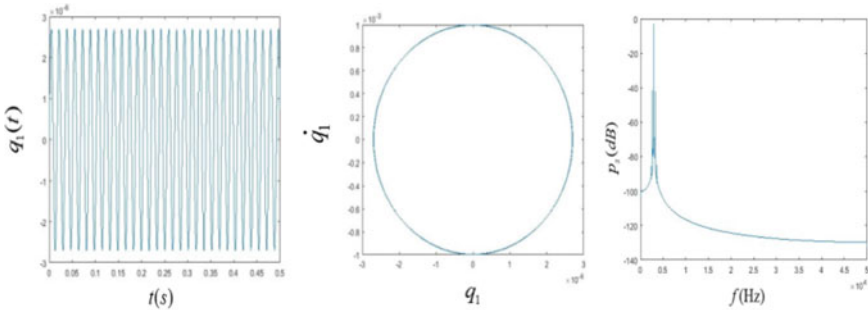


**Fig. 2** Periodic oscillations at  $V = 10$  m/s and  $\Omega = 20$  rad/s (Time trace, phase plane and frequency spectrum)

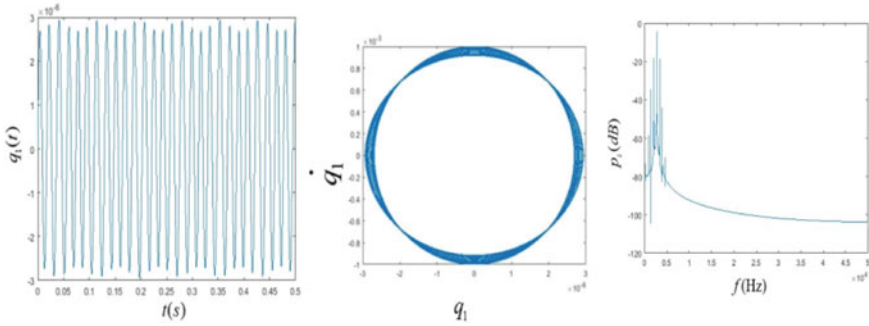


**Fig. 3** Quasiperiodic oscillations at  $V = 30$  m/s and  $\Omega = 20$  rad/s (Time trace, phase plane and frequency spectrum)

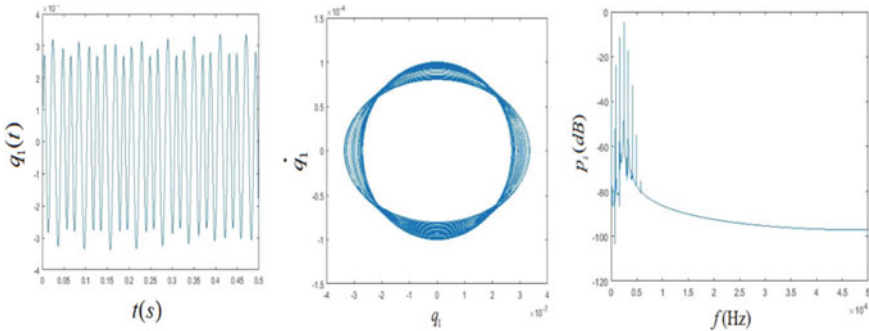


**Fig. 4** Quasiperiodic oscillations at  $V = 50$  m/s and  $\Omega = 20$  rad/s (Time trace, phase plane and frequency spectrum)

= 30 m/s and  $\Omega = 20$  rad/s. Figure 4 also shows quasiperiodic oscillations at  $V = 50$  m/s and  $\Omega = 20$  rad/s.

### 4.2 Two-Mode Expansion

Figures 5 and 6 show that both the first and second modes undergo cascade of period-doubling bifurcations at  $V = 10$  m/s and  $\Omega = 20$  rad/s. Figures 7 and 8 show chaotic oscillations for both first and second modes at  $V = 30$  m/s and  $\Omega = 20$  rad/s. The first mode shows ‘wide-band’ chaotic oscillation, whereas second mode shows ‘narrow-band’ chaotic oscillation. Figures 9 and 10 show strong chaotic oscillations for both first and second modes at  $V = 50$  m/s and  $\Omega = 20$  rad/. Again the first mode shows ‘wide-band’ chaotic oscillation, whereas the second mode shows ‘narrow-band’ chaotic oscillation.

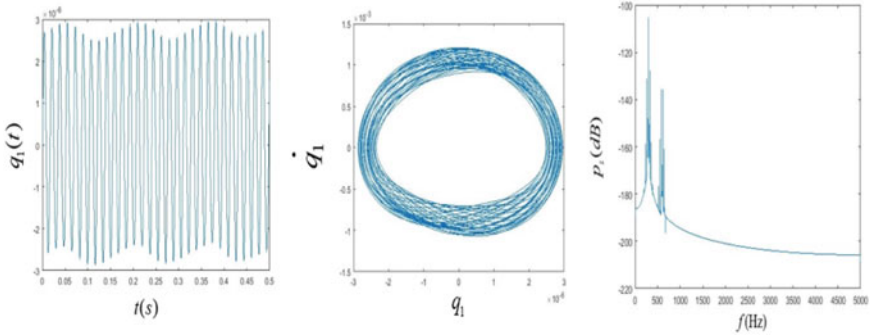


**Fig. 5** Cascade of period-doubling bifurcations at  $V = 10$  m/s and  $\Omega = 20$  rad/s for the first mode (Time trace, phase plane and frequency spectrum)

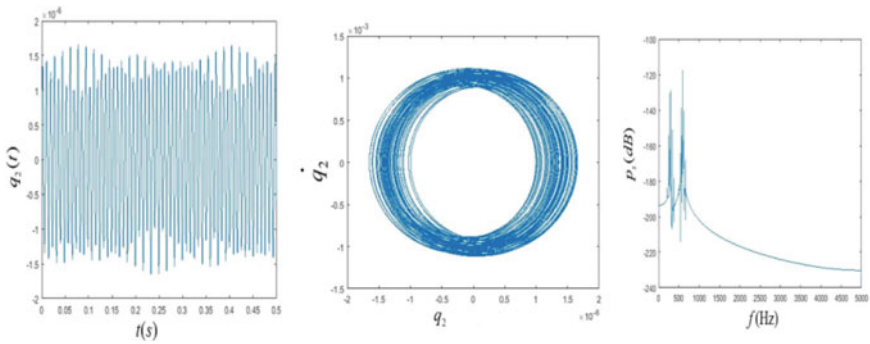


**Fig. 6** Cascade of period-doubling bifurcations at  $V = 10$  m/s and  $\Omega = 20$  rad/s for the second mode (Time trace, phase plane and frequency spectrum)

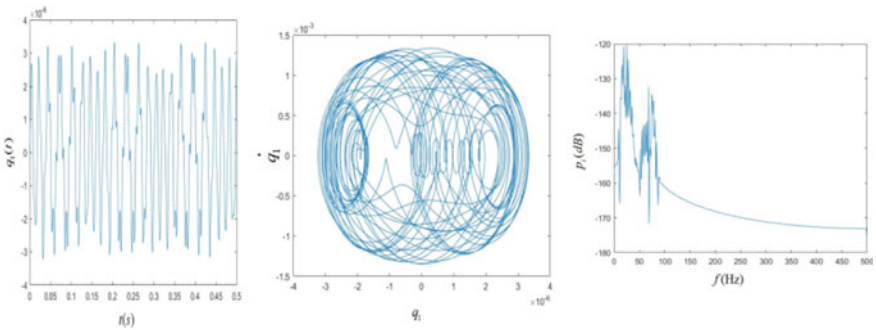


**Fig. 7** Wide-band chaotic oscillations at  $V = 30$  m/s and  $\Omega = 20$  rad/s for first mode (Time trace, phase plane and frequency spectrum)

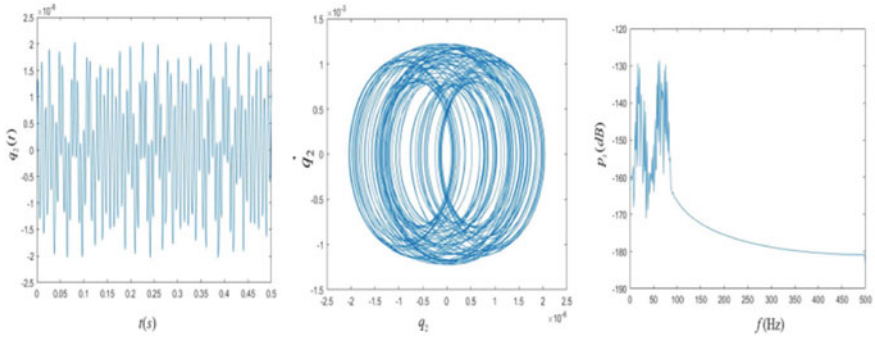


**Fig. 8** Narrow-band chaotic oscillations at  $V = 30$  m/s and  $\Omega = 20$  rad/s for the second mode (Time trace, phase plane and frequency spectrum)

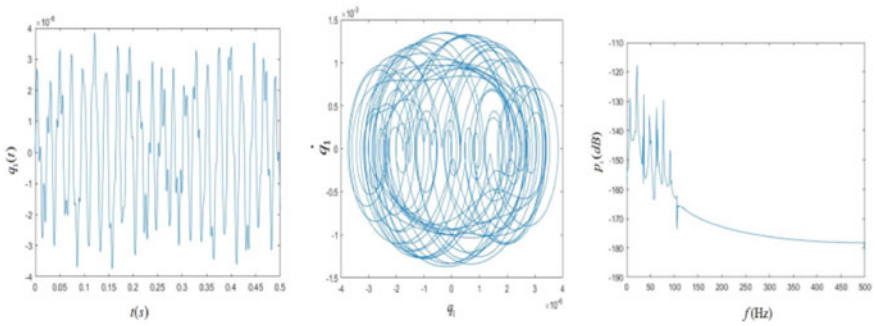


**Fig. 9** Wide-band chaotic oscillations at  $V = 50$  m/s and  $\Omega = 20$  rad/s for the first mode (Time trace, phase plane and frequency spectrum)

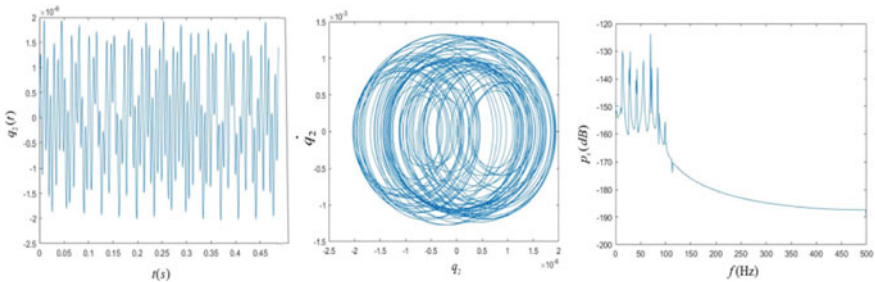


**Fig. 10** Narrow-band chaotic oscillations at  $V = 50$  m/s and  $\Omega = 20$  rad/s for the second mode (Time trace, phase plane and frequency spectrum)

## 5 Conclusion

The chaotic oscillations of travelling string having harmonic velocity fluctuations are explored. The governing equation of motion is discretized applying Galerkin approach. Numerical analysis is performed to study the system behaviour with variation in control parameters. The numerical analysis yields the following conclusions:

1. The nonlinear vibration response of the system depends on initial motion conditions.
2. The single-mode expansion exhibits periodic and quasiperiodic oscillations.
3. The two-mode expansion undergo a cascade of period-doubling bifurcations leading to chaotic oscillations. The first mode shows 'wide-band' chaotic oscillation, whereas the second mode shows 'narrow-band' chaotic oscillation.

## References

1. Swope RD, Ames WF (1963) Vibrations of a moving thread line. *J Franklin Inst* 275:36–55
2. Mote CDJ (1965) A study of band-saw vibrations. *J Franklin Inst* 279(6):431–444
3. Pakdemirli M, Ulsoy AG, Ceranoglu A (1994) Transverse vibration of an axially accelerating string. *J Sound Vib* 169(2):179–196
4. Pakdemirli M, Ulsoy AG (1997) Stability analysis of an axially accelerating string. *J Sound Vib* 203:815–832
5. Chen LQ, Zhang NH, Zu JW (2002) The regular and chaotic vibrations of an axially moving viscoelastic string based on 4-order Galerkin Truncation. *J Sound Vib* 261(4):764–773
6. Chen LQ, Zhang NH, Zu JW (2003) Bifurcation and chaos of an axially moving viscoelastic string. *Mech Res Commun* 29(2/3):81–90
7. Ghayesh MH (2009) Stability characteristics of an axially accelerating string supported by an elastic foundation. *Mechanism Mach Theory* 44:1964–1979
8. Kesimili A, Ozkaya E, Bagdatli SM (2015) Nonlinear vibrations of spring supported axially moving string. *Nonlinear Dyn* 81:1523–1534
9. Yang XD, Wu H, Qian YJ, Zhang W, Lim CW (2017) Nonlinear vibration analysis of axially moving strings based on gyroscopic modes of decoupling. *J Sound Vib* 393:308–320

# Nonlinear Dynamics of Translating String with Geometric Nonlinearity



Shashendra Kumar Sahoo, Lokanath Panda, and Harish Chandra Das

**Abstract** The dynamic response of translating string considering geometric nonlinearity is investigated. The nonlinear partial differential equation is nondimensionalized first and then discretized via Galerkin approach. Taking two mode truncation gives gyroscopically coupled nonlinear ordinary differential equations. Numerical simulation is performed applying Runge-kutta technique. Time trace, phase plane and frequency spectra are plotted to examine the influence of non-dimensional velocity on dynamic response of axially translating string. The numerical simulations indicate that the system exhibits both periodic and quasiperiodic oscillations.

**Keywords** Translating string · Geometric nonlinearity · Galerkin approach · Quasi-periodic · Periodic

## 1 Introduction

The nonlinear dynamics of axially translating string has been studied since last sixty years. The axially translating string forms the classical model for many mechanical devices such as aerial cables, power transmission belt, textile fiber, magnetic tapes, paper sheets, serpentine belts. Applying the theory of characteristics, Mote [1, 2] studied the dynamics of axially traveling string and verified that the fundamental period of vibrations is dependent on initial tension and the axial velocity. Applying the method of multi-timescales, Chen et al. [3, 4] studied the nonlinear dynamics and chaos of axially accelerating viscoelastic string via Galerkin method. Applying

---

S. K. Sahoo (✉)

Department of Mechanical Engineering, I.T.E.R, Siksha 'O' Anusandhan, Deemed To be University, Bhubaneswar, India

e-mail: [sashendrasahoo@soa.ac.in](mailto:sashendrasahoo@soa.ac.in)

L. Panda

Department of Mechanical Engineering, C.E.T, BPUT, Bhubaneswar, India

H. C. Das

Department of Mechanical Engineering, N.I.T, Shillong, Meghalaya, India

method of multi-time scales, Ghayesh [5] investigated the parametric combination resonance of an axially translating string having an elastic foundation. Applying multi-timescale analysis, Kesimili et al. [6] investigated the vibration behavior of axially translating string consisting of number of supports. Basing on gyroscopic modes of decoupling Yang et al. [7] analyzed the vibration behavior of axially traveling string. Applying assumed mode and linear superposition method, Lu et al. [8] investigated the dynamic behavior of an axially traveling string having time-varying supports.

The present work focuses on the nonlinear dynamic response of the axially translating string considering geometric nonlinearity. The nonlinear partial differential equation is nondimensionalized and then discretized via Galerkin approach. The two mode truncation results in gyroscopically coupled nonlinear ordinary differential equations. The vibration behavior is highlighted through time trace, phase plane diagram and frequency spectra for different values of nondimensional velocity.

## 2 The Analytical Model

The schematic model consists of a string of length  $L$ , linear density  $\rho$ , Young's modulus  $E$ , axial tension  $P$  traveling between two fixed eyelets with an axial velocity  $V$  as shown in Fig. 1.

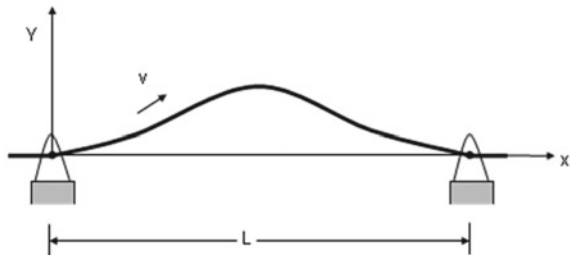
The equation of motion for transverse vibration of axially translating string considering geometric nonlinearity can be expressed as [1].

$$\rho W_{,TT} + 2\rho V W_{,XT} + (\rho V^2 - P) W_{,XX} = \frac{3}{2} E (W_{,X})^2 W_{,XX} \quad (1)$$

with boundary conditions

$$W(0, T) = W(L, T) = 0 \quad (2)$$

**Fig. 1** Physical model of an axially translating string



$W(X, T)$  being the transverse deflection of the axially translating string and comma-subscript notation represents partial differentiation with respect to coordinate  $X$  and time  $T$ . The different terms  $\rho W_{TT}$ ,  $2\rho V W_{XT}$  and  $\rho V^2 W_{XX}$  represent inertia force, coriolis force and centrifugal force respectively.

Defining nondimensional variables

$$w = \frac{W}{L}, x = \frac{X}{L}, t = T\sqrt{P/\rho L^2}, \gamma = V\sqrt{\rho/P}, \kappa = E/P \quad (3)$$

Inserting Eq. (3) into Eq. (1) yields the dimensionless governing equation

$$w_{,tt} + 2\gamma w_{,xt} + (\gamma^2 - 1)w_{,xx} = \frac{3}{2}\kappa w_{,x}^2 w_{,xx} \quad (4)$$

with dimensionless boundary conditions

$$w(0, t) = w(1, t) = 0 \quad (5)$$

### 3 Discretization

According to Galerkin's approach, the solution to partial differential equation of motion (4) may be assumed to be

$$w(x, t) = \sum_{r=1}^N q_r(t) \sin(r\pi x) \quad (6)$$

where  $q_r(t)$  and  $\sin(r\pi x)$  represent modal coordinate and the mode shapes of the stationary string respectively.

Substituting Eq. (6) into Eq. (4), and using Galerkin approach, yields a series of nonlinear ordinary differential equations

$$\begin{aligned} \ddot{q}_r + 8\gamma \sum_{r+j_{\text{odd}}}^N \frac{nr}{r^2 - j^2} \dot{q}_j + (1 - \gamma^2)(r\pi)^2 q_r \\ = 3\kappa \sum_{j=1}^N \sum_{s=1}^N \sum_{m=1}^N d_{jsmr} q_j q_s q_m \quad (r = 1, 2, \dots, N) \end{aligned} \quad (7)$$

where



$$d_{jsmr} = \begin{cases} \frac{j sm r \pi^4}{8}, & j + s = \pm(m + r), \pm(m - r) \text{ or} \\ j - s = \pm(m + r), \pm(m - r) \\ 0, & \text{otherwise} \end{cases} \quad (8)$$

Taking two mode truncations ( $N = 2$ ), yields the nonlinear ordinary differential equations that are gyroscopically coupled

$$\ddot{q}_1 - \frac{16}{3}\gamma \dot{q}_2 + (1 - \gamma^2)\pi^2 q_1 + \frac{3}{8}\kappa\pi^4 q_1^3 + 3\kappa\pi^4 q_1 q_2^2 = 0 \quad (9)$$

$$\ddot{q}_2 + \frac{16}{3}\gamma \dot{q}_1 + 4(1 - \gamma^2)\pi^2 q_2 + 3\kappa\pi^4 q_1^2 q_2 + 6\kappa\pi^4 q_2^3 = 0 \quad (10)$$

## 4 Numerical Simulation

The numerical simulation is carried out using Runge-Kutta technique. The initial conditions chosen are  $q_1(0) = q_2(0) = 0$  and  $\dot{q}_1(0) = \dot{q}_2(0) = 0.01$ . The effect of dimensionless velocity ( $\gamma$ ) on the nonlinear dynamic response is investigated through time trace, phase plane trajectory and frequency spectra. The Figs. 2 and 3 show periodic oscillations at nondimensional velocity,  $\gamma = 0$  for both first and second modes respectively. The phase plane is a closed trajectory and a dominant peak at single basic frequency is observed in the power spectrum. The Figs. 4 and 5 shows quasiperiodic oscillations at nondimensional velocity  $\gamma = 0.2$  for both first and second modes respectively. The time trace shows beating effect for both the modes. The phase plane trajectories for both the modes represents a torus. The power spectra show two sharp peaks at two different basic frequencies. The Figs. 6 and 7 show quasiperiodic oscillations at nondimensional velocity  $\gamma = 0.5$  for both the

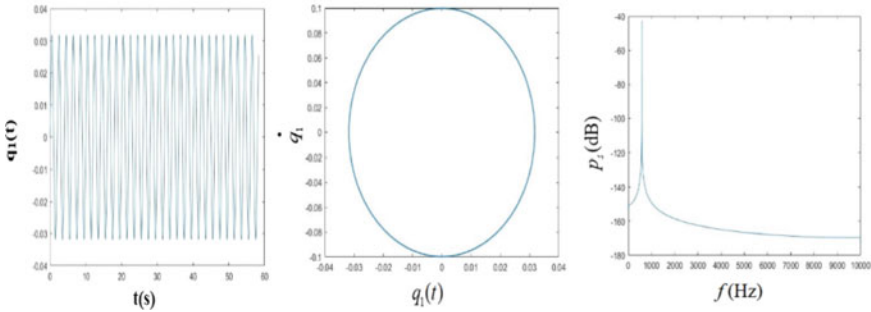


**Fig. 2** Periodic oscillations at non-dimensional velocity  $\gamma = 0$  (Time trace, phase plane and frequency spectrum of first mode)

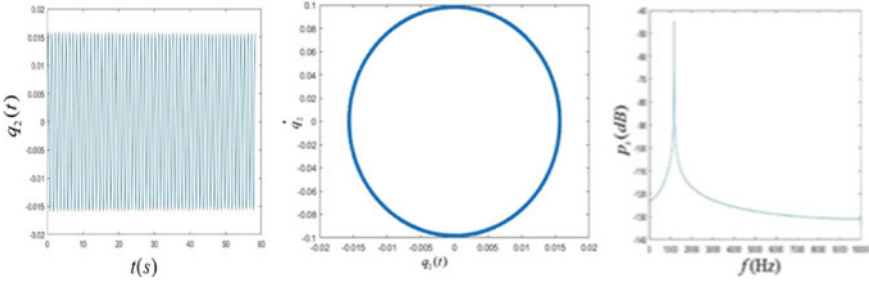


**Fig. 3** Periodic oscillations at non-dimensional velocity  $\gamma = 0$  (Time trace, phase plane and frequency spectrum of second mode)

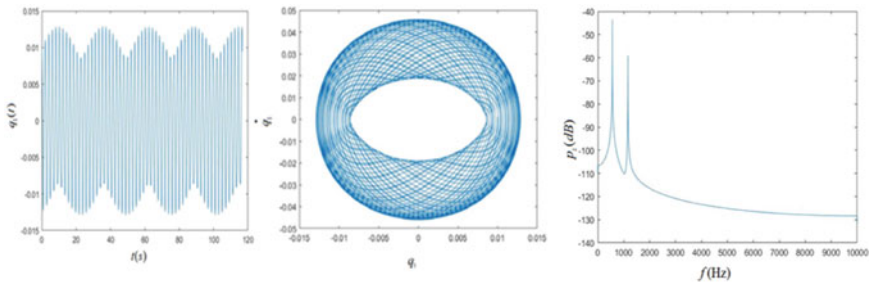


**Fig. 4** Quasiperiodic oscillations at non-dimensional velocity  $\gamma = 0.2$  (Time trace, phase plane and frequency spectrum of first mode)

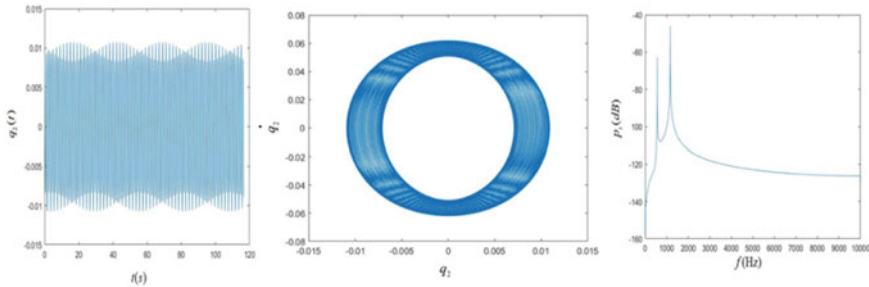


**Fig. 5** Quasiperiodic oscillations at non-dimensional velocity  $\gamma = 0.2$  (Time trace, phase plane and frequency spectrum of second mode)

modes. The phase plane trajectories of both the modes represent a torus. The power spectra show sharp peaks at two basic frequencies. The Figs. 8 and 9 show again quasiperiodic oscillations at nondimensional velocity  $\gamma = 0.7$  for both the modes. The Figs. 10 and 11 show periodic oscillations at nondimensional velocity  $\gamma = 1.0$  for both the modes. The phase plane diagram represent a closed trajectory for both the modes. The power spectra show dominant peak at single basic frequency.

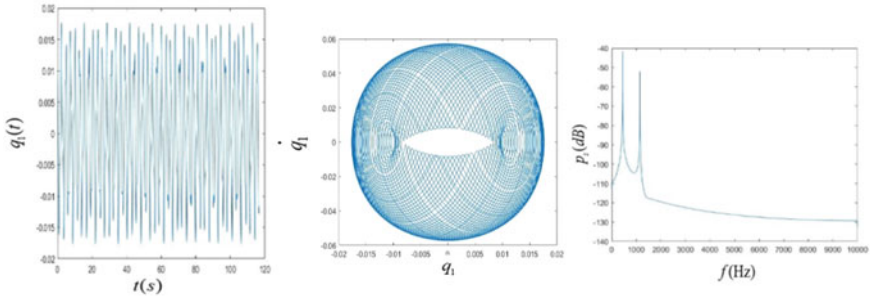


**Fig. 6** Quasiperiodic oscillations at non-dimensional velocity  $\gamma = 0.5$  (Time trace, phase plane and frequency spectrum of first mode)

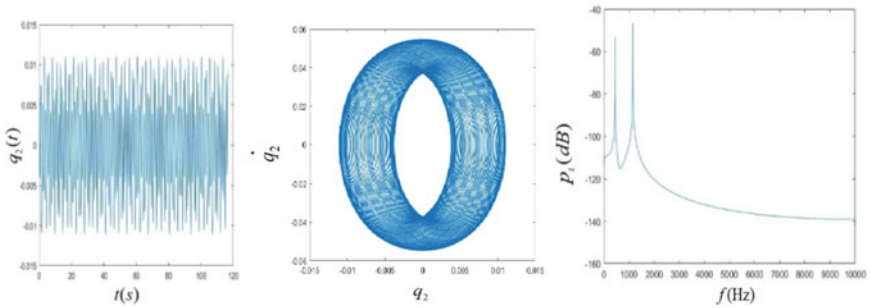


**Fig. 7** Quasiperiodic oscillations at non-dimensional velocity  $\gamma = 0.5$  (Time trace, phase plane and frequency spectrum of second mode)

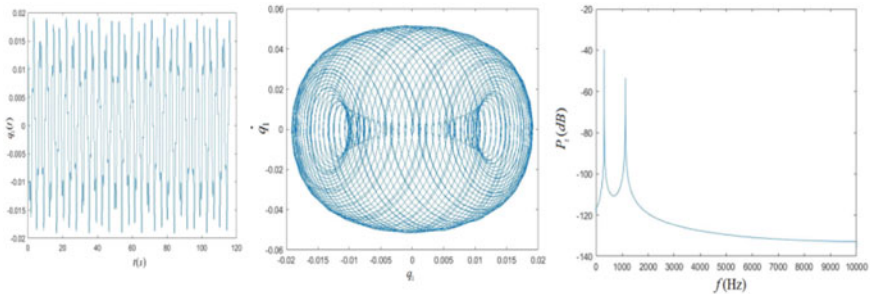


**Fig. 8** Quasiperiodic oscillations at non-dimensional velocity  $\gamma = 0.7$  (Time trace, phase plane and frequency spectrum of first mode)

## 5 Conclusion

The work explores the vibration behavior of translating string with geometric nonlinearity. The nonlinear equation of motion is nondimensionalized and then

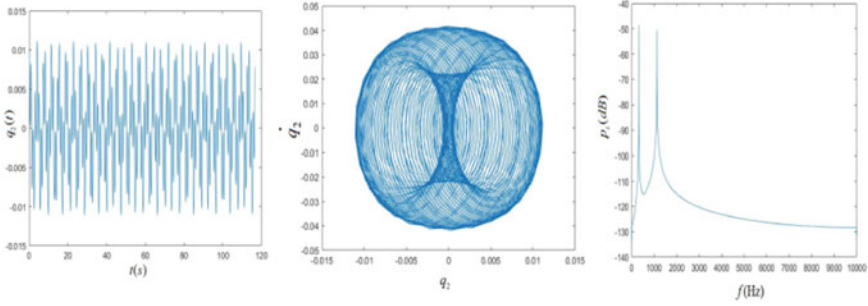


**Fig. 9** Quasiperiodic oscillations at non-dimensional velocity  $\gamma = 0.7$  (Time trace, phase plane and frequency spectrum of second mode)

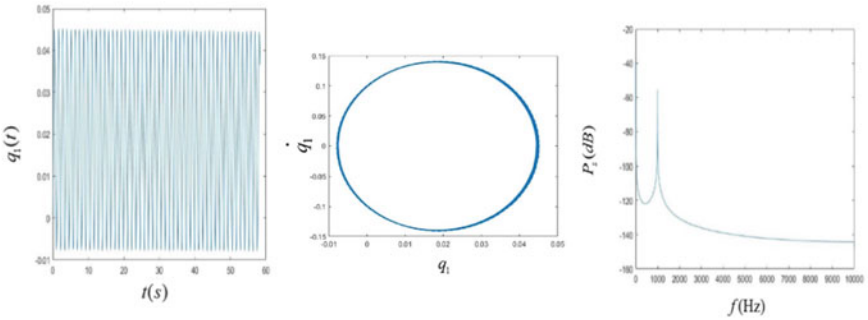


**Fig. 10** Periodic oscillations at non-dimensional velocity  $\gamma = 1$  (Time trace, phase plane and frequency spectrum of first mode)

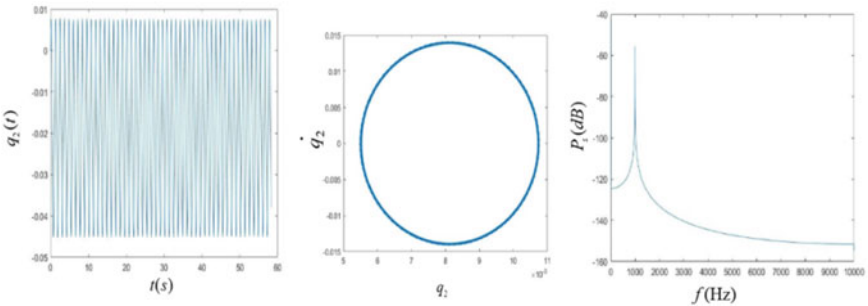


**Fig. 11** Periodic oscillations at non-dimensional velocity  $\gamma = 1$  (Time trace, phase plane and frequency spectrum of second mode)

discretized via Galerkin approach. The two mode truncation results in gyroscopically coupled ordinary differential equations. Numerical simulations are performed via Runge-kutta technique. The numerical analysis yields the following conclusions.

- (1) The nonlinear vibration characteristics are sensitive to initial motion conditions.
- (2) Both the first and second modes exhibit periodic oscillations for non-dimensional velocities  $\gamma = 1$  and  $\gamma = 1$ .
- (3) Both the first and second modes exhibit quasiperiodic oscillations for non-dimensional velocities  $\gamma = 0.2$ ,  $\gamma = 0.5$  and  $\gamma = 0.7$ .

## References

1. Mote CD Jr (1966) On the nonlinear oscillation of an axially moving string. *J Appl Mech* 33:463–464
2. Mote CDJ (1968) Parametric excitation of an axially moving string. *J Appl Mech* 35(1):171–172
3. Chen LQ, Zhang NH, Zu JW (2003) The regular and chaotic vibrations of an axially moving viscoelastic string based on 4-order Galerkin truncation. *J Sound Vib* 261(4):764–773
4. Chen LQ, Zu JW, Wu JXD (2004) Transverse vibrations of an axially accelerating viscoelastic string with geometric nonlinearity. *J Eng Math* 48(2):171–182
5. Ghayesh MH (2009) Stability characteristics of an axially accelerating string supported by an elastic foundation. *Mechanism Mach Theory* 44:1964–1979
6. Kesimili A, Ozkaya E, Bagdatli SM (2015) Nonlinear vibrations of spring supported axially moving string. *Nonlinear Dyn* 81:1523–1534
7. Yang XD, Wu H, Qian YJ, Zhang W, Lim CW (2017) Nonlinear vibration analysis of axially moving strings based on gyroscopic modes of decoupling. *J Sound Vib* 393:308–320
8. Lu L, Yang XD, Zhang W (2020) Static nodes of an axially moving string with time-varying supports. *J Vib Acoust* 142(4)

# Quality Circle: Maximizing the Productivity in Coal Handling Plant Through Why-Why Technique



Somanath Ojha , Bhatu Kumar Pal , Janender Kumar ,  
Smita Mohanty, and Krishnan Kanny

**Abstract** In the contemporary world of manufacturing due to highly competitive nature of the market, the manufacturing organizations have started to look for different approaches and practices. Every organization starting from manufacturing industry to banks, hospital, school, wants profit as much as possible with continual improvement. One of the techniques is quality circle (QC) which is most effective industrial problem-solving tool that can be aimed for customer satisfaction with zero defect. The observed data were analyzed through various problem-solving techniques like Vilfredo Pareto analysis and Ishikawa diagram. After successful implementation of quality circle, the following results were obtained: Gradually maximizes the availability of the equipment and minimizes the delay time of the industry. In this paper, why-why analysis tool is initiated for problem solving of coal handling equipment. Further, QC builds the motivation to employees ensure their finest for the firm, which not only boost the output of the firm, but also assistances in showing the potential of an individual. Finally, these assistances were emerging the intelligence of belongingness toward their work.

**Keywords** Quality circle · Quality tools · Problem-solving techniques · Why-why technique · Coal handling industry

---

S. Ojha (✉) · K. Kanny  
Durban University of Technology, Durban PO Box 1334, Durban 4000, South Africa  
e-mail: [sojha669@gmail.com](mailto:sojha669@gmail.com)

B. K. Pal  
National Institute of Technology, Rourkela 769006, India

J. Kumar  
State Institute of Engineering and Technology, Nilokheri, Karnal, Haryana 132117, India

S. Mohanty  
Laboratory for Advance Research in Polymeric Materials (LARPM), Central Institute of Petrochemical Engineering and Technology, Bhubaneswar 751024, India

## 1 Introduction

In ancient days, industries were discovered by the Japanese. The total industrial setups were ravaged of the many countries throughout second warfare. Japan was the most important suffered in this time. United Nations agency came at back foot. To tackle the challenge, the state was in hunt of quality. They were trying to develop a method that reconstructed their firm units and will recover excellence of facilities and output within the corporations [1]. After that, QC comes into the picture which is systematically implemented in Japanese industries. After a long rotation, it is implemented in India. Firstly, engineering firms were being initiated in quality circle. QC is first launched in Bharat Heavy Electricals Ltd starting from workshop to service department like personal, administrative buildings, and canteens [2]. Currently, QC is gradually spread to nationwide.

Most of the industries have completely applied this problem-solving methodology to extend their handiness, reliableness, and quality of apparatus. Mostly, quality circle may be a team of staffs of diverse connection discipline that importance on delivering chance for finding of drawback connected along with his work. Participate of each quality circle team member provides their own suggestion and thoughts for improvement of work. They may be a manager, engineer, worker, technician, or operator [1].

The teamwork helps to build belongings toward plant. The employees get motivated to do work with positive attitude.

The QC analysis work was completely different from others. Attributable to the matter was new and completely different, that is why, it did not understand throughout the literature survey. The objective of study is to solve the problem through quality circle concept which can directly enhance the productivity of the plant.

This study is organized as: Section 2 shortly introduces a literature review on varied QC studies report. Section 3 explains shortly analysis apply. Section 4 enlightens the particular event analysis to maximize the productivity with the assistance of QC tools. Finally, analysis conclusion is supplied with real suggestions.

## 2 Review of Literature

Lakshmi and Sucharitha [3] observed the influence of QC in the industry which positive efforts of workforce lead to growth of any industry. QC is a technique to solve the industrial problem of workplace. Not only it increases the morale support of employee but also gives toward company's growth which is concluded that many of the staffs are not known with this idea during survey of QC in the company. Thus, consciousness programs shall be prepared for all. Kumar et al. [4] suggested the QC methodology in manufacturing organization of small scale automobile firm where parts like shaft rocker arm, axle (front wheel and rear wheel) sprocket, etc., and all types of fasteners such as nut, bolt, screw, stud. The implementation of QC concept

in stepwise manner the production-wise defect rejection and so on was the splendid success for the firm. QC members are gained motivational skill, boosted their self-skill and become alertness for industry which are imperceptible profits. Kumar et al. [1] discussed case study of implementation of quality circle in automobile industry. Problem solving of suspension system one of the component of automobile parts results in reduction percentage was reduced drastically solved by QC team member through Why-Why analysis. Ojha et al. [5] investigated root causes of belt structure problem by taking quality control tools like fishbone diagram and Pareto analysis for cost reduction and equipment availability in coal handling plant. The author also showed the financial benefit to the company. Prasanna and Desai [6] implemented a real case of quality circle in maintenance management of petrochemical industries. In this paper, before QC, the consumption of grease was not unchanging in centrifuge which is one of the components in petro chemical industries was taken for root cause analysis. After analysis by QC team member, consumption of grease optimized leads to decrease in equipment failure. The result is moreover productivity increases and also boosting self-confidence of team leads to company's growth. Kumar et al. [2] reviewed extensively literature studied chronologically. In this paper, a real case study based upon quality circle of Kaizen approach was studied which is helpful tool for achieving improvement of an organization. This study is an evidence for product quality in small-scale industries.

### 3 Methodology: Quality Circle

In a coal handling plant of XYZ Company, the following tabular format comprise the structure of a quality circle. The name of the company is not disclosed here due to confidential reasons (Table 1).

The prosperous implementation of the QCs depends upon the staff perspective from the higher management to human resource development folks. Heads of works manager that meets once during a month to commission. For the success of the efforts in QCs activities, the coordinator plays a vital part. In 3 months, twenty-four conferences were planned and with success organized for the analysis. Facilitators from project management department were conjointly chargeable for coordinating associated leading the QC activities at intervals an organization and carrying out such functions.

### 4 Case Study

The present study was accomplished by taking a problem, which was connected with conveyor belt pulley failure in XYZ Company of coal handling plant, Kalinganagar (Odisha) by making a quality circle. The production encompasses transporting of coal with the help of conveyor belt from one place to another area. The pulley consists



**Table 1** Formation of quality circle

Sl. No.	Quality circle team description	Position in industry	Department	Work experience	Understanding the concept	Remarks
1	Somanath Ojha Team leader	Facilitator	Project management	2	Yes	
2	Rabi Das	Operation (M) Supervisor	Mechanical production	5	Yes	
3	Hari Mishra	Operation (E) Supervisor	Electrical production	4	Yes	
4	Surendra Jha	Operation (E) Supervisor	Maintenance department	3	Yes	
5	Alok Ray	Operation (E) Supervisor	Maintenance electrical department	4	Yes	
6	Som Behera	Operator	Mechanical	7	Yes	
7	Anil Parida	Technician	Electrical	8	yes	

**Table 2** Percentage contribution of conveyor pulley in belt line

Sl. No.	Root causes	% Contribution
1	Shaft shearing	52
2	Hub damage	28
3	Pipe damage	10
4	Bearing damage	07
5	Others	03

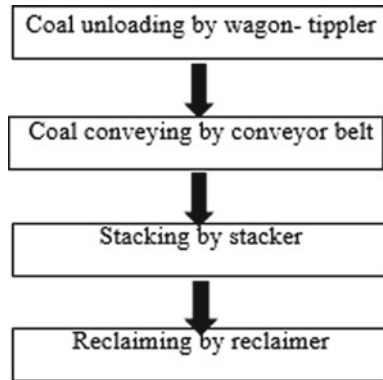
of shaft, hub, pipe and bearing for smooth rotation. During conveying of coal in production line, it caused breakdown.

The percentage-wise contribution of conveyor pulley in belt line is given below and found that shaft shearing, hub damage, pipe damage, bearing damage was main root causes. Hence, theme was selected to reduce the conveyor pulley problem as shown in Table 2.

#### 4.1 Deming Cycle

Four mantras of deming wheel are associate degree unvaried four-step management ways for completing amendment. PDCA, i.e., Plan, Do, Check, Act, could be a

**Fig. 1** Method of operations in coal handling plant



methodology for management, that is, helpful for continuous improvement of a corporation.

Minimize the delay time with maximum availability, utilization, and filling factor 80%, 85%, 90%, respectively.

### **4.2 Flowchart (Method of Operation)**

The following method was followed for transporting of coal in coal handling plant as shown in Fig. 1.

### **4.3 Fishbone Diagram**

In order to analyzing root causes of the matter, 4M was taken as shown in Fig. 2.

In order to know the root causes, the 4Ms were analyzed one by one as description is written below.

Man: Untrained, carelessly

Machine: Pulley (shaft hearing, hub damage), driving system (gearbox with motor, turbocoupling)

Method: not proper yard stock, intake capacity of destination plant

Material: scrap, boulder, big size coal.

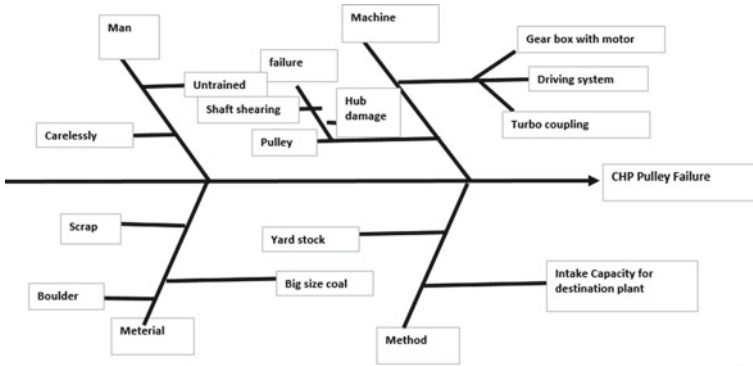


Fig. 2 Fishbone diagram for pulley failure

### 4.4 Temporary Corrective Actions

100% checkup started in conveyor pulley line for reducing failure rate and simultaneously, greasing/oiling was done by the help of maintenance people. Yet, it had been a heavy method; however, the activity was temporary.

### 4.5 Permanent Corrective Actions: Why-Why Technique

#### Problem Number 1

Conveyor pulley analysis conducted and found that due to shaft shearing, it was causing delay time then analyzed problem with the help of why-why technique. Figure 3 shows conveyor pulley in coal handling plant (Ankit Gupta 2013). Why-



Fig. 3 Conveyor pulley

Why technique is also a problem-solving method to solve problem on work-related which not only upholding the emphasis on the indications but also lead to the root cause of a problem. For that depth of analysis with brainstorming is required to reach out the root cause of the problem. For here, five questions asking answers are assumed (see Table 3).

After why-why analysis, it was observed that due to sealing and placement of plumber block together was not proper, as it is cost of maintenance was huge. The problem could be sorted out completely by replacing the pulley as the matter was discussed by top management. By the meantime, checked the proper balancing of the pulley, equal center distance from drive pulley to driven pulley, proper alignment and healthy structure for foundation which leads to reduce the downtime and maximizing the equipment availability. Thus, it leads to the productivity of improvement.

*Problem Number 2*

Failure analysis of driving system conducted. In that motor shaft is fastened with gearbox input shaft which has toothed members and transmits the facility between 2 shafts by meshing with none slip [7] as shown in Fig. 4 (Table 4).

It found that failure of conveyor pulley driving system was due to frequent off centers running of the pulley as it develops frequent jamming due to sealing system of

**Table 3** Why-why analysis for conveyor pulley failure

Sl. No.	Why-Why analysis	Answer	Action taken
1	Shaft shearing	Improper scheduled greasing	
2	Why improper scheduled greasing	Pulley casting defect	
3	Why pulley casting defect	Pulley hub and balancing not maintained properly	
4	Why Pulley hub and balancing not maintained properly	Sealing and placement of plumber block not properly	
5	Why sealing and placement of plumber block not properly	Due to heavy cost of maintenance	Finance required at management end

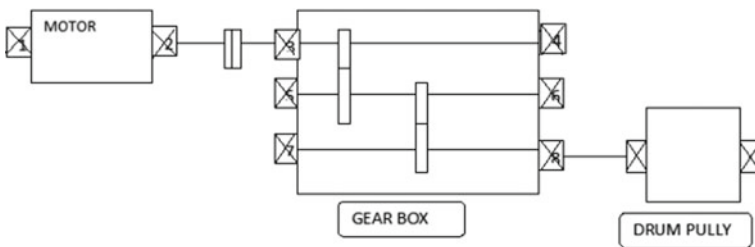


**Fig. 4** Conveyor pulley driving system [7]

**Table 4** Why-why analysis for failure of conveyor pulley driving system

Sl. No.	Why-Why analysis	Answer	Action taken
1	Why failure in driving system in conveyor pulley	Due to frequent off centers running	
2	Why frequent off-centering running	Frequent jamming due to sealing system of receiving not providing properly	
3	Why sealing system of receiving not providing properly	Due to the clearance gap between bolt and receiving chute not maintain properly	
4	Why clearance gap between bolt and receiving chute not maintain properly	Due to rubber damage frequently	
5	Why rubber damage frequently	Inspection scheduled not maintained properly	Regular inspection and maintenance

receiving chute not providing properly. The corrective measures were proper house-keeping and scheduled maintenance which includes proper lubrication which require lifeline for driving system, time-to-time oil change, breather should be clean and remove hot air mounted on the lubrication level, proper alignment of coupling, proper tightening of bolt in foundation level leads to drastic enhancement of productivity with maximize the overall equipment effectiveness.

## 5 Conclusion

Quality circle is one of the techniques for problem solving of industrial equipment. In our research work, QC team of coal handling plant was solved conveyor pulley problem through why-why analysis. Both failure of conveyor pulley and driving system are analyzed by why-why techniques. It is observed that due to heavy maintenance for sealing and placement of plumber block and the problem could be sorted out by top management by replacing of pulley. Inspection schedule is not properly maintain caused for driving system failure, regular inspection and maintenance should be carried out for avoiding such type of failure, which increases the availability and reliability of equipment and enhance in morale support of employee and thereby achieving goals by working as a team. In terms of direct benefits, maximize the overall equipment effectiveness helped the coal handling industries in reducing downtime as well as to enhance the productivity. Intangible benefit of QC is that developed morale support among the employee, working as a goal in team spirit, boosting inner quality of employee.

## References

1. Kumar J, Kataria KK, Luthra S (2020) Quality circle: methodology to enhance the plant capacity through why-why analysis. *Int J Math Eng Manage Sci* 5(3):463–472
2. Kumar SR, Duhan R, Duhan S (2015) Quality circle: a methodology to identify scope of quality improvement through kaizen approach. *Int J Modern Eng Res* 4(7):22–31
3. Lakshmi PM, Sucharitha P (2019) Motivation and satisfaction through quality circles with reference to selected organization: an empirical study. *Int J Multidiscip Res* 5(2):33–40
4. Kumar N, Mittal V (2015) Quality circle implementation in industry in India-a case study. *Int J Curr Eng Technol* 5(1):61–71
5. Ojha S, Pal BK, Biswal BB (2015) Minimising the breakdown of belt conveyor system of coal handling plant. *SSRG Int J Mech Eng* 2(9):1–4
6. Prasanna NKK, Desai TN (2011) Quality circle implementation for maintenance management in petrochemical industry. *J Eng Res Stud* 2(1):155–162
7. Ojha S, Sarangi D, Pal BK, Biswal BB (2014) Performance monitoring of vibration in belt conveyor system. *Int J Eng Res Appl* 4(7):22–31

# Electrothermomechanical Responses in Smart Composite Plates



S. A. Ohid and J. K. Nath

**Abstract** A global–local shear deformation theory is applied to laminated piezoelectric layer integrated composite plates for study of the electrothermomechanical bending responses. Double superposition based present theory has the ability of computing accurately the transverse shear stresses from the constitutive equations in addition to accurate calculation of all displacement and stress components. The principle of virtual work is used to derive the governing equations and boundary conditions for rectangular smart plates. The variationally consistent theory satisfies continuity of displacements and transverse stresses at all interfaces as well as the shear traction free boundary conditions on its lateral surfaces. From the comparisons made with the three-dimensional exact solutions and other shear deformation theories, the accuracy and versatility of the present theory is established.

**Keywords** Shear deformation theory · Piezoelectric composite plate · Transverse shear stresses · Static response

## 1 Introduction

Aerospace, marine, automotive and many other industries are using more and more laminated composite materials for weight sensitive and temperature sensitive environments, since these materials distinctly offer favorable design criteria such as low specific weight, high specific stiffness, high specific strength and good thermal resistance over the traditional metallic and non-metallic counterparts. The passive composite structures, when integrated with suitable piezoelectric material layers, do become smart structures and can be used for vibration suppression, structural health monitoring, noise reduction, and self-sensing and self-actuation applications. Extensive reviews concerning these applications of the smart structures and systems have been carried out in Refs. [1, 2]. It has been identified that the primary failure

---

S. A. Ohid (✉) · J. K. Nath

Department of Mechanical Engineering, Faculty of Engineering and Technology, Siksha ‘O’ Anusandhan Deemed to be University, Bhubaneswar, Odisha 751030, India

e-mail: [saohid@soa.ac.in](mailto:saohid@soa.ac.in)

mechanism in the smart laminated structures is due to the huge mismatch between the transverse stresses at the layer interfaces. Accurate calculations of the response entities such as the displacements and stresses under different loading conditions are required, which are highly dependent upon the accuracy of the theory or the model being used.

Among all types of shear deformation theories used for static, dynamic, buckling and transient analyses, the efficient layerwise theories [3, 4] are most accurate and efficient. Different layerwise theories differ from each other with respect to the degree of the polynomial expansions assumed and the satisfaction of different boundary conditions. Global–local theories [5] are an advanced class of such theories and provide capability to calculate accurate transverse stresses from constitutive equations in addition to accurate calculation of other entities.

In this work, the global–local theory presented by Nath and Kapuria [5] is applied to study bending responses in smart composite plates under electrothermomechanical loads. The bending responses have been analyzed and checked in comparison with the results of 3D exact piezothermoelasticity solutions [6] and a zigzag-local theory [7].

## 2 Formulation

Details of the formulation of the present global–local theory is given in Ref. [5]. For completeness, a brief discussion of the theory is given here. The smart plate of height  $h$  and  $a \times b$  consists of  $L$  orthotropic layers. A global coordinate system  $(x, y, z)$  is used to describe the deformation of the plate, whose midplane is taken as the reference  $xy$ -plane. Assuming zero transverse normal stress in the plate, the reduced constitutive equations for generalized plane stress and linear strain displacement relations have been used.

A cubically varying electric potential field is used to describe the variations of the electric potential across the thickness of the piezoelectric layers and a sub-layerwise linear function is used to describe the temperature distribution across the thickness of each layer.

The inplane and transverse components of the displacement field in the smart plate are assumed by considering the deformations induced due to the thermoelectric field, and a combination of global and local polynomials that give rise to cubic variations of inplane displacements across the plate thickness.

$$u(x, y, z) = [u_0(x, y) - zw_0 + z\psi_0(x, y) + z^2\xi(x, y) + z^3\eta(x, y)] + [\zeta_k u_1^k(x, y) + \zeta_k^2 u_2^k(x, y)] + [\zeta_k^3 u_3^k(x, y)] \quad (1)$$

$$w(x, y, z) = w_0(x, y) - \bar{\psi}_\phi^j(z)\phi^j(x, y) - \bar{\psi}_{\phi_c}^q(z)\phi_c^q(x, y) + \bar{\psi}_T^L(z)T^L(x, y) \quad (2)$$



where

$$u = \begin{bmatrix} u_x \\ u_y \end{bmatrix}, \quad u_0 = \begin{bmatrix} u_{0x} \\ u_{0y} \end{bmatrix}, \quad w_{0,d} = \begin{bmatrix} w_{0,x} \\ w_{0,y} \end{bmatrix}, \quad \psi_0 = \begin{bmatrix} \psi_{0x} \\ \psi_{0y} \end{bmatrix}, \quad \zeta = \begin{bmatrix} \zeta_x \\ \zeta_y \end{bmatrix},$$

$$\eta = \begin{bmatrix} \eta_x \\ \eta_y \end{bmatrix}$$

$$u_1^k = \begin{bmatrix} u_{1x}^k \\ u_{1y}^k \end{bmatrix}, \quad u_2^k = \begin{bmatrix} u_{2x}^k \\ u_{2y}^k \end{bmatrix}, \quad u_3^k = \begin{bmatrix} u_{3x}^k \\ u_{3y}^k \end{bmatrix},$$

$\bar{\psi}_\phi^j(z)$  represents through the thickness integration of sub-layerwise linear (i.e., each piezoelectric layer is divided into a number of sub-layers) electric potential distributions through  $j$  number of points ( $j = 1, 2, \dots, n^\phi$ ) where the electric potentials are  $\phi^j(x, y)$ . Similarly,  $\bar{\psi}_{\phi_c}^q(z)$  represents quadratic variation of the electric potential passing through the top, bottom and midpoint of each piezoelectric layer. To describe non-linear variation of the temperature field, each layer of the laminated plate is divided into a number of sublayers and sub-layerwise linear function  $\bar{\psi}_T^L(z)$  is used for representation of the temperature distribution in each layer. There are  $n^T$  such points in each layer and the temperature at those points are  $T^L(x, y)$ .

The non-linear variation of the transverse displacement is due to the effect of the thermoelectric field, and  $\zeta_k$  is a local thickness coordinate for each layer which varies between  $-1$  to  $+1$  in each layer. The layered displacement field has been made layer independent by applying the boundary conditions, i.e., (1) the displacements are continuous, (2) the transverse shear stresses are continuous and (3) transverse shear stresses are zero on the bottom and top surfaces. Thus, the final inplane displacement field is modified to

$$u(x, y, z) = u_0 - zw_{0,d} + R^k(z)\psi_0 + \bar{R}^k(z)u_1^0 + \hat{R}^k(z)u_2^0 + \tilde{R}^k(z)u_3^0 + R^{kj}(z)\phi_d^j + \bar{R}^{kl}(z)T_d^l \quad (3)$$

This final displacement field does not contain layer dependent variables. Instead, it is expressed in terms of eleven mechanical variables, one set of electric potential variables and a set of temperature variables. Using convergence study separately for electric potential and temperature, the number of variables for each of these entities can be determined.

The coefficients  $R^k(z)$ ,  $\bar{R}^k(z)$ ,  $\hat{R}^k(z)$ ,  $\tilde{R}^k(z)$ ,  $R^{kj}(z)$ ,  $\bar{R}^{kl}(z)$  are  $2 \times 2$  matrices of cubic functions of thickness coordinate, which have been obtained by utilizing the continuity of the inplane displacement field, transverse shear stress components and the stress free boundary conditions on the top and bottom surfaces of the laminated plate.

The Eq. (3) represents a cubical inplane displacement field since the coefficients appearing in it are cubic functions of the thickness coordinate.

The linear strain–displacement relations and reduced constitutive equations have been used in the formulation. To study the static response under the applied electrothermomechanical loading, virtual work principle has been used to obtain the governing equations. Under the application of electrothermomechanical loads on

the bottom and top surfaces of the laminated plate, following governing equations have been derived in terms of the stress resultants and moment resultants:

$$\begin{aligned}
 N_{x,x} + N_{xy,y} &= 0, & N_{xy,x} + N_{y,y} &= 0 \\
 M_{x,xx} + 2M_{xy,xy} + M_{y,yy} + F_5 &= 0, & P_{x,x} + P_{yx,y} - Q_x &= 0 \\
 P_{xy,x} + P_{y,y} - Q_y &= 0, & \overline{P}_{x,x} + \overline{P}_{yx,y} - \overline{Q}_x &= 0 \\
 \overline{P}_{xy,x} + \overline{P}_{y,y} - \overline{Q}_y &= 0, & \hat{P}_{x,x} + \hat{P}_{yx,y} - \hat{Q}_x &= 0 \\
 \hat{P}_{xy,x} + \hat{P}_{y,y} - \hat{Q}_y &= 0, & \tilde{P}_{x,x} + \tilde{P}_{yx,y} - \tilde{Q}_x &= 0 \\
 \tilde{P}_{xy,x} + \tilde{P}_{y,y} - \tilde{Q}_y &= 0, & \tilde{Q}_{x,x} + \tilde{Q}_{y,y} + \tilde{H}_{x,x}^q + \tilde{H}_{y,y}^q - \tilde{G}^q &= 0 \\
 S_{x,xx}^j + S_{xy,xy}^j + S_{yx,xy}^j + S_{y,yy}^j - \overline{Q}_{x,x}^j - \overline{Q}_{y,y}^j - H_{x,x}^j - H_{y,y}^j + G^j - F_6^j &= 0
 \end{aligned} \tag{4}$$

The components of the stress resultants and the moment resultants are  $N_x, N_x, N_{xy}, M_x, M_y, M_{xy}, P_x, P_y, P_{xy}, Q_x, Q_y, Q_{xy}, \overline{P}_x, \overline{P}_y, \overline{P}_{xy}, \hat{P}_x, \hat{P}_y, \hat{P}_{xy}, \tilde{P}_x, \tilde{P}_y, \tilde{P}_{xy}, \overline{Q}_x, \overline{Q}_y, \hat{Q}_x, \hat{Q}_y, \tilde{Q}_x, \tilde{Q}_y$  whose detail expressions can be found in the Ref. [5].

The obtained boundary conditions are not written here for brevity. Analytical solution has been obtained for rectangular smart laminated composite plates whose all edges are simply supported by expanding the plate variables in double Fourier series and substituting them in the above governing equations. After obtaining the reference variables, the deformation at any point in the plate has been obtained from the displacement field expressions and the stresses have been calculated from the constitutive equations.

### 3 Results and Discussion

Static responses have been obtained and analyzed in a piezoelectric bimorph and a smart composite plate. The 3D exact piezothermoelasticity solution [6] and the zigzag-local-theory (ZLT) [7] are compared with the present results.

The piezoelectric bimorph plate is made of two PZT-5H layers of equal thickness. It is subjected to a mechanical load  $-p_0 \sin(\pi x/a) \sin(\pi y/b)$  on the top surface and the plate is grounded at top, bottom and the interfaces. There exists piezoelectric poling along the thickness.

The reported results, which have been non-dimensionalized, have been plotted in graphical form in all figures. The displacements and stresses have been non-dimensionalized as

$$\overline{u} \doteq \frac{100u}{hST_0\alpha_0}, \quad \overline{w} \doteq \frac{100w}{hS^2T_0\alpha_0}, \quad (\overline{\sigma}_x, \overline{\sigma}_y, \overline{\tau}_{yx}, \overline{\tau}_{zx}) \doteq \frac{(\sigma_x, \sigma_y, S\tau_{yx}, S\tau_{zx})}{E_0T_0\alpha_0}$$

where  $h$  is height of the plate,  $S$  is aspect ratio,  $\alpha_0$  is the coefficient of thermal expansion of reference plane.  $E_0 = 10.3$  GPa,  $\alpha_0 = 22.5 \times 10^{-6} \text{ K}^{-1}$ .

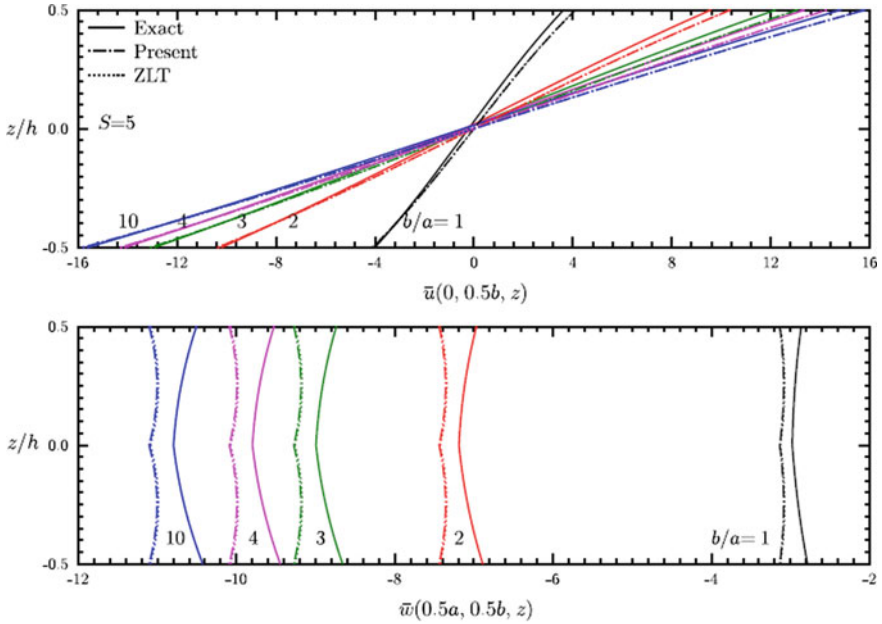


**Fig. 1** Displacement distributions in the bimorph plate under mechanical load

The non-dimensionalized displacements and stresses have been shown Fig. 1, Fig. 2 and Fig. 3 for a number of rectangular plates having length-to-width ratios  $b/a = 1, 2, 3, 4$  and  $10$  present theory responses for highly accurate solutions for the displacements, inplane stresses and transverse shear stresses. Present theory is quite accurate in calculating the transverse shear stresses by directly using the reduced constitutive equations at all locations including the laminate interface. Especially the transverse shear stresses calculated from constitutive equations are very accurately predicted at all locations including the laminate interface. The non-dimensionalized displacements are seen to increase continuously with increase in the length-to-width ratio. The inplane normal stress increases in the same fashion. However, the inplane shear stress increases, attains maximum value and then decreases with increase of the length-to-width ratio. The transverse shear stress continuously decreases with increase of the length-to-width ratio.

The five layered smart composite plate has layer thicknesses  $0.225 h/0.225 h/0.225 h/0.225 h/0.1 h$  which have orientations  $[0^\circ/90^\circ/0^\circ/90^\circ/0^\circ]$ . The four equal thickness composite layers are made of unidirectional fiber graphite-epoxy and the top piezoelectric layer is made of piezoelectric material PZT-5H. This plate is subjected to a thermal load of  $T_t = -T_b = -T_0 \sin(\pi x/a) \sin(\pi y/b)$  at its top and bottom surfaces. The piezoelectric interface and the top surface are grounded. There exists piezoelectric poling along the thickness of piezoelectric layer.

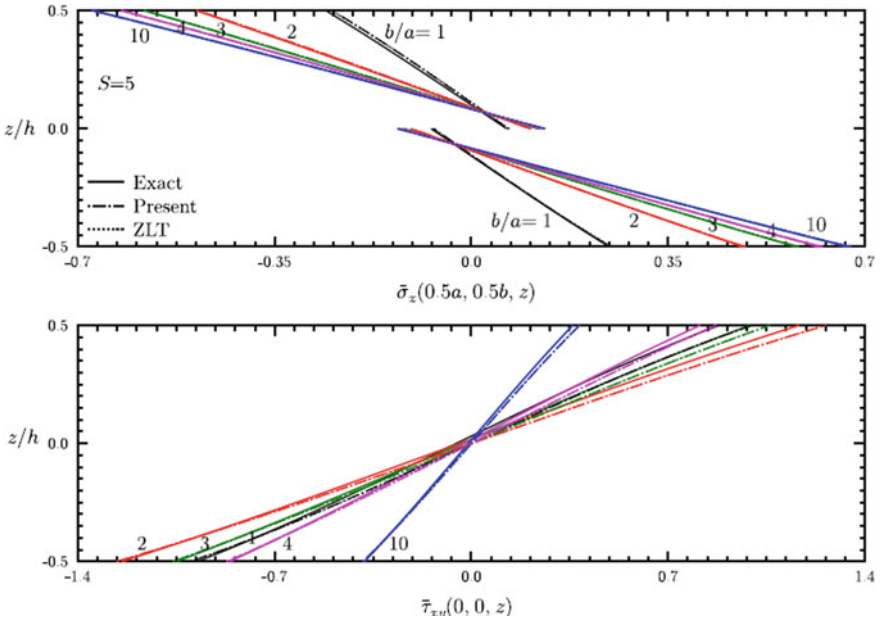


**Fig. 2** Inplane stress distributions in the bimorph plate under mechanical load

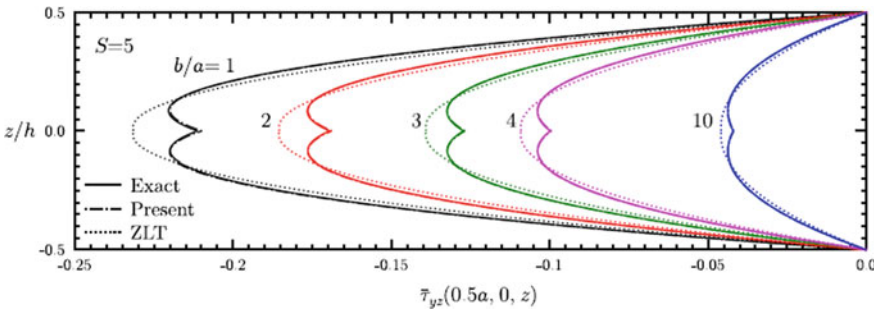


**Fig. 3** Transverse stress distributions in the bimorph plate under mechanical load

Each layer is divided into four equal sublayers to get convergence in the temperature distribution. Non-dimensionalized displacements are shown in Fig. 4, the inplane stresses are shown in Fig. 5 and the transverse shear stress is shown in Fig. 6 for square and rectangular plates having length-to-width ratios 1, 2, and 10. The displacements and stresses have been observed to be of very high accuracy. The ZLT, on the other hand, is not capable to yield similar accuracy. By the ZLT, the maximum value of the transverse shear stress as well as its distribution profile are seen to be highly erroneous.

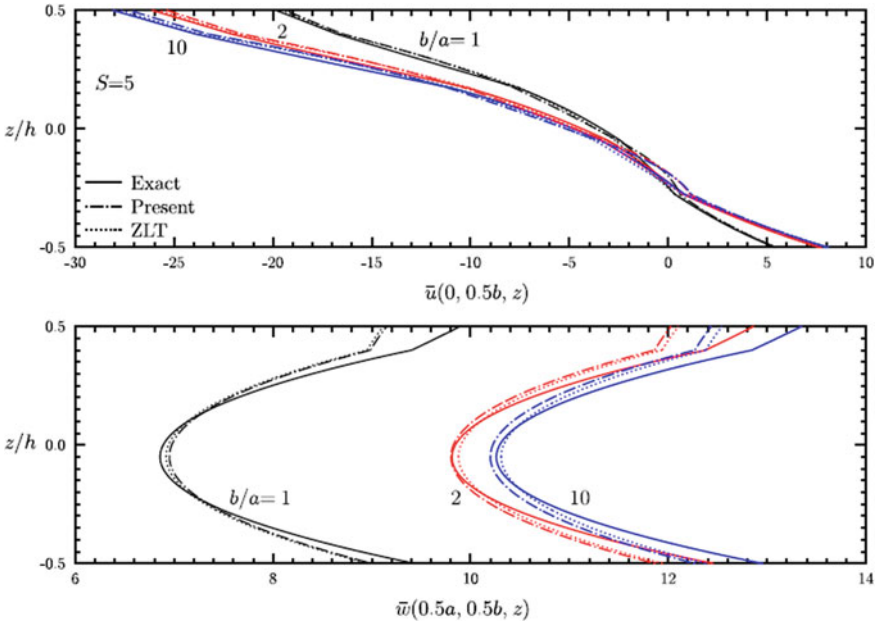


Fig. 4 Displacement distributions in the smart composite plate under thermal load

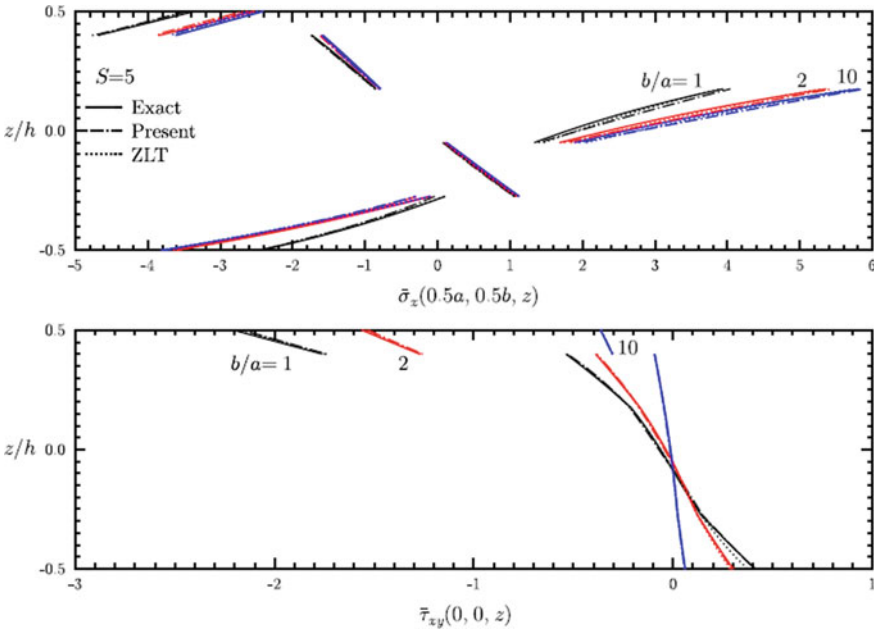
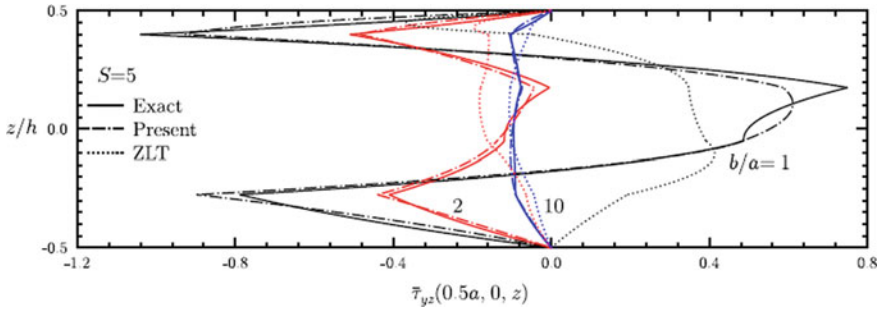


Fig. 5 Inplane stress distributions in the smart composite plate under thermal load



**Fig. 6** Transverse stress distributions in the smart composite plate under thermal load

## 4 Conclusions

The bending responses have been obtained and analyzed in smart composite plates, having square as well as rectangular, by applying the global–local theory. The theory formulated, based on the double superposition hypothesis, is variationally consistent and able to calculate the transverse shear stresses from reduced constitutive equations for smart composite plate. Its stress predictions are more accurate than a similarly developed zigzag local theory. The piezoelectric coefficient and the thermal expansion coefficients have strong influence on the non-linear profile of the transverse displacement. The results presented for a piezoelectric bimorph and a graphite-epoxy smart composite plate have distinctly established the accuracy and superiority of the present global local theory in predicting the displacements and stresses in thick smart composite plates.

## References

1. Gopinathan SV, Varadan VV, Varadan VK (2000) A review and critique of theories for piezoelectric laminates. *Smart Mater Struct* 10:229–239
2. Chopra I (2002) Review of state of art of smart structures and integrated systems. *AIAA J* 40:2145–2187
3. Tang YY, Noor AK, Xu K (1996) Assessment of computational models for thermoelectroelastic multilayered plates. *Comput Struct* 61:915–933
4. Saravanos DA, Heyliger PR, Hopkins DA (1997) Layerwise mechanics and finite element for the dynamic analysis of piezoelectric composite plates. *Int J Solids Struct* 34:359–378
5. Nath JK, Kapuria S (2013) Global-local and zigzag-local theories for direct transverse shear stress computation in piezolaminated plates under thermal loading. *Int J Mech Sci* 75:158–169
6. Kapuria S, Dumir PC, Sengupta S (1999) Three-dimensional solution for shape control of a simply supported rectangular hybrid plate. *J Therm Stresses* 22:159–176
7. Kapuria S, Nath JK (2009) Efficient laminate theory for predicting transverse shear stresses in piezoelectric composite plates. *AIAA J* 47:3022–3030

# Energy and Exergy Study of a Compression Ignition Engine Running with Producer Gas



Pradipta Kumar Dash, Sanjaya Kumar Mishra, Shakti Prakash Jena,  
and Harish Chandra Das

**Abstract** In the present investigation, the energy and exergy analysis of a dual-fuel diesel engine was performed running with producer gas (PG) to quantify the exergy characteristics under the priority to achieve the highest diesel saving. 10% volume blend of Karanja oil methyl ester with diesel (B10) was considered as pilot fuel. The results showed that the brake-specific energy consumption increased from 14.6 kJ kWh<sup>-1</sup> to 17.67 kJ kWh<sup>-1</sup> and 18.43 kJ kWh<sup>-1</sup> for dual-fuel operation with diesel and B10, respectively. It is also observed that at full-load engine operation the exergy efficiency decreases to 30.37% and 29.04% for dual-fuel operation with diesel and B10, respectively.

**Keywords** Producer gas · Exergy efficiency · Combustion · Exergy destruction

## 1 Introduction

Energy plays a significant role in the economic development of a nation. The increase in population and industrialization has resulted in an exponential hike in energy demand. The faster consumption of limited fossil fuels insists the researchers propagate their experimentation on the effective use of renewable source-based fuels to satisfy the asking rate of energy demands. The compression ignition (CI) engines were widely used in various sectors such as transport, power generation, agriculture, and construction [1]. The exhaust emission from the CI engines accounts for a detectable share of environmental pollution. It is difficult to achieve the thermal

---

P. K. Dash

Department of Mechanical Engineering, KMBB College of Engineering and Technology, Khurda 752056, India

S. K. Mishra · S. P. Jena (✉)

Department of Mechanical Engineering, SOA Deemed to be University, Bhubaneswar 751030, India

e-mail: [shaktiprakash.mech@gmail.com](mailto:shaktiprakash.mech@gmail.com)

H. C. Das

Department of Mechanical Engineering, NIT Meghalaya, Shillong 793003, India

© The Author(s), under exclusive license to Springer Nature Singapore Pte Ltd. 2023

35

P. Pradhan et al. (eds.), *Recent Advances in Mechanical Engineering*,

Lecture Notes in Mechanical Engineering,

[https://doi.org/10.1007/978-981-16-9057-0\\_5](https://doi.org/10.1007/978-981-16-9057-0_5)

efficiency of a CI engine hardly up to 45% [2]. Approximately, 22% of greenhouse gas emissions is an outcome of hasty growth in the transportation sector. Producer gas (PG) is an ignitable gas released during the gasification of different biomass can be considered as alternative fuel to run dual-fuel CI engines. Gaseous fuels are maintenance free and most convenient because of their clean-burning property and high knock resisting capacity. Researchers all around the globe are working with different alternative fuels as a substitute for diesel in CI engines. Nayak et al. experimented with PG and diesel to operate a twin-cylinder dual-fuel engine and achieved a maximum diesel saving of 83% [3]. Lal and Mohapatra carried out an experiment to observe the influence of CR on combustion and performance characteristics of a diesel engine in dual-fuel mode. With the increase in CR, they noticed a reduction in ignition delay and fuel consumption [4]. Carlucci et al. performed experimentation on a dual-fuel diesel engine by altering its injection timing to run with PG and biodiesel. They found an augmentation in combustion characteristics by advancing injection timing that results in a drop in carbon monoxide (CO) and hydrocarbon (HC) emissions [5]. Literature indicates that while running the CI engines with alternative fuels like blends of biodiesel, biogas, and producer gas, the performance of the engine slightly deteriorates from base results along with a drastic increase in engine emissions. The reason behind this drop in engine performance with the use of alternative fuels can be identified from combustion analysis. The change in trends of combustion characteristics such as rate of pressure rise, mean combustion temperature, mass fraction burnt, net heat release, and in-cylinder pressure can illustrate the scope to improve the performance of CI engines running with alternative fuels.

Further, most of the researchers focused on engines performance like thermal efficiency, fuel economy, diesel saving and emissions study, and ignored the thermal losses from the engines. Exergy analysis measures how far the actual system deviates from ideal performance. The deviation between the predicted and observed efficiency of the engine is due to the presence of internal irreversibility in the engine. To analyze the irreversibility associated with processes, 2nd law of thermodynamic need to be applied [2]. The destruction of exergy is due to poor conversion of fuel energy into productive mechanical energy under different loading conditions of a CI engine. The trimming of irreversibility can lead to improving engine performance in accordance with the 2nd law of thermodynamic [6].

The purpose of the current study is to execute a detailed energy and exergy study using standard diesel and a blend of KOMA in a dual-fuel engine with PG as inducted fuel. In the present study, emphasis is given on combustion analysis to analyze the change in trends of engine combustion to understand the influence on destruction in exergy.

## 2 Thermodynamic Analysis

The importance of energy and exergy study leads to identify the rate of energy losses and accordingly work on effective utilization of resources to boost the performance of



CI engines. The supplied fuel energy is partially transformed into useful mechanical energy, and the rest portion of the energy was lost as heat loss to a cooling medium, heat energy taken away via exhaust gas, chemical energy loss through unburned emissions, and energy destroyed unaccountably. The energy utilization efficiency may be increased through optimization of energy distribution.

The assumptions considered for current energy and exergy analysis are as follows:

- The engine operates at a steady state.
- The whole engine is considered as control volume.
- Ideal gas equations are valid for air at the inlet and gases at the exhaust manifold.
- The change in potential energy and kinetic energy was neglected.

The energy imparted ( $Q_{in}$ ) to the CI engine is stated by:

$$Q_{in} = m \times CV + m_g \times CV_g \quad (1)$$

Here,  $m$  specifies the rate of pilot fuel supply;  $CV$  is the calorific value of fuel, and  $m_g$  is the substitution rate of PG, and  $CV_g$  is the calorific value of PG.

In consequence of the 1st law of thermodynamics, we can describe:

$$Q_{in} = W_e + Q_{out} \quad (2)$$

$W_e$  Useful output in kW.

$Q_{out}$  Energy lost in kW.

The consumption of exergy may be stated as:

$$E_x = Q_{in} \left( 1 - \frac{T_L}{T_H} \right) = W_e + \delta E_x \quad (3)$$

where

$E_x$  Rate of exergy supply to the system in kW.

$\delta E_x$  Exergy destruction rate in kW.

$T_H$  Peak temperature of the cycle and

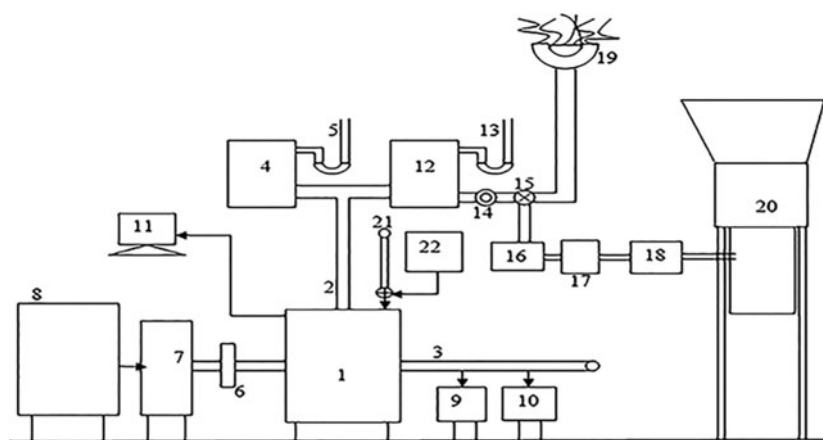
$T_L$  Ambient temperature.

Similarly, the exergy efficiency ( $\eta_{exe}$ ) was calculated as:

$$\eta_{exe} = \frac{W_e}{E_x} \quad (4)$$

### 3 Experimental Methodology

Figure 1 shows the schematic layout of the dual-fuel engine setup, chosen for experimentation with the specification of 14hp, 4-stroke, twin cylinder, CI engine (Make: Prakash Diesel Private Ltd.) with a rated speed of 1500 rpm and 16.5:1 compression ratio. A 3-phase, 415 V AC alternator was used to apply and vary the engine load. A downdraft gasifier was utilized to deliver PG, where eucalyptus wood with a moisture percentage of 10.2% was chopped into the desired size is utilized as feedstock in the gasifier. The constituents in PG drawn out of the gasifier were tested through a Gas Chromatograph-2010 (CIC, Baroda), connected with a thermal conductivity detector. The gas constituents and CV of PG are presented in Table 1. A water manometer, orifice meter, and flow control valve are attached to the gas surge tank to regulate and measure the substitution rate of PG. A producer gas injector was drilled into the inlet manifold to mix the PG with the intake air. Before mixing the PG released from the gasifier with air, a flame test was performed at the burner to check its flammability of PG. By diverting the flow of PG to the burner, when it was ignited, a blue color flame was observed at the burner. This indicates the suitability of PG to use in the dual-fuel engine. A data acquiring system (DAS) was used to collect, record, and



1. Engine, 2. Inlet manifold, 3. Exhaust manifold, 4. Air box, 5. Manometer, 6. Coupling, 7. Alternator, 8. Loading unit, 9. AVL analyzer, 10. Smoke meter, 11. DAS, 12. Gas surge tank, 13. Manometer, 14. Orifice meter, 15. Flow control valve, 16. Fine filter, 17. Passive filter, 18. Cooling unit, 19. Burner, 20. Gasifier unit, 21. Burette, 22. Fuel tank

**Fig. 1** Schematic layout of the dual-fuel engine setup

**Table 1** Constituents and CV of PG

Gas compositions	CO	CO <sub>2</sub>	H <sub>2</sub>	CH <sub>4</sub>	N <sub>2</sub>	CV (MJ Nm <sup>-3</sup> )
PG (Vol%)	20.02	10.5	19.22	2.75	46.49	5.64

**Table 2** Physical properties of pilot fuels

Properties	Diesel	B10	KOME
Specific gravity	0.8321	0.8372	0.885
Viscosity (cSt, 40 °C)	1.902	2.181	4.5
CV (MJ kg <sup>-1</sup> )	42.21	41.5	36.12

investigate the observed results. The software package “Engine Soft LV” of version 9 was used for online performance and combustion analysis. The K-type thermocouple was attached to the exhaust manifold to measure exhaust temperature. Firstly, the crude Karanja oil was collected from the crusher mill to produce biodiesel by the transesterification method. Based on the previous article documented by the author, [7] KOME blend B10 (10% volume of KOME mixed with 90% volume of diesel) and standard diesel were considered as the pilot fuel for the experimentation.

The physical properties of the pilot fuels were presented in Table 2. The flow rate of PG was gradually increased until steady combustion was observed at maximum load during the dual-fuel run.

Finally, the PG substitution rate of 21.41 kg h<sup>-1</sup> was considered for experimentation to achieve maximum possible diesel saving, as further increase in PG flow rate showed undesirable noise and vibration during engine operation.

## 4 Results and Discussion

To identify the irreversibility taking place during combustion of the selected alternative fuel, following parameters were considered for discussion.

### 4.1 Mass Fraction Burnt (MFB)

The change in MFB in line with crank angle (CA) at 100% engine load operation was showed in Fig. 2. The software package “Engine Soft LV” of version 9 was used to obtain the MFB curve based on the combustion pressure curve data. The MFB graph reveals that a late start of ignition was seen in the case of diesel + PG and B10 + PG run, where the CA50 was observed at 10° and 13° after top dead center (TDC), respectively. For standard diesel operation, the CA50 was observed at 7° after TDC. This finding can be associated with the comparatively low adiabatic flame temperature of PG and its poor burning tendency that influences the combustion process. CA50 value is shifted to the right from TDC in case of PG operation, indicating a drop in specific power yield. Thus, engine running with diesel only, the MFB attained 100% at 32° after TDC, and the same for diesel + PG and B10 + PG was noticed at 40° and 42° after TDC, respectively. This denotes that with induction of PG, the ignition delays were increased confirmed by a drop in MFB curve slope

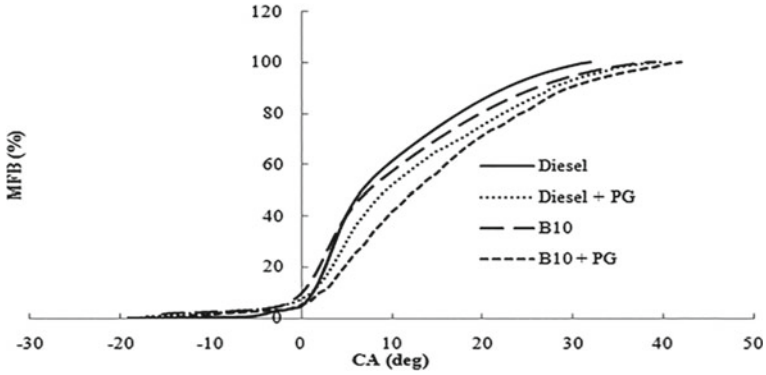


Fig. 2 Variation of MFB with respect to CA

for diesel + PG and B10 + PG, so MFB attained 100% at more crank angle after TDC as compared to diesel-alone run.

### 4.2 Neat Heat Release Rate (NHRR)

Figure 3 represents the deviation in the NHRR trend with CA at 100% engine load. At the initial stage of the cycle, a negative value of NHRR was seen for both single fuels as well as dual-fuel engine operation. The latent heat of vaporization taken by the pilot fuel (diesel/B10) reflects as the negative value of NHRR. A quick ascent in NHRR was observed nearly 5° before TDC, where the highest value of NHRR of standard diesel operation was found to be 53.23 J deg<sup>-1</sup> observed at 1° after TDC, and that for diesel + PG, the highest value of NHRR was found to be 50.26 J deg<sup>-1</sup> at 8° after TDC. While the peak value of NHRR for B10 was found to be 44.32 J deg<sup>-1</sup> located at 1° after TDC and in a similar trend for B10 + PG, the maximum value

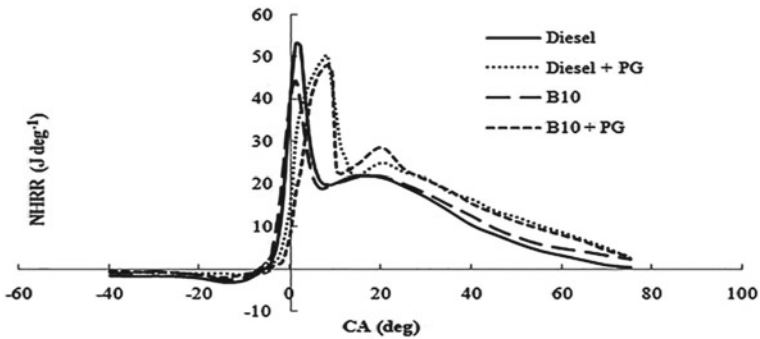


Fig. 3 Variation of NHRR with respect to CA

of NHRR was found to be  $48.03 \text{ J deg}^{-1}$  at  $8^\circ$  after TDC. The presence of B10 as pilot fuel has shown a decreased NHRR in both modes of operation as compared to diesel. The second peak of NHRR was found to be noticeable in the case of a dual-fuel operation that indicates the delayed combustion tendency of PG. This demonstrates that the heat released was higher during expansion stroke of the cycle for PG operation as compared to engine operation with standard diesel or B10 alone because of the combustion trend of PG resulting in the higher value of the second peak of NHRR as noticed for dual-fuel activity.

### 4.3 Brake-Specific Energy Consumption (BSEC)

As illustrated by Fig. 4, the change in BSEC is in line with to change in engine load (EL). A trend of reduction in BSEC was observed with a hike in EL. This can be linked to the increase in mean combustion temperature (MCT) and cylinder pressure with the rise in EL, accelerated the combustion process resulting in effective utilization of the supplied fuel. Hence, lower BSEC was observed at higher load operation than that of part-load operation. Dual-fuel operations have shown higher BSEC for both the pilot fuels.

The comparatively lower calorific value of PG requires a higher fuel supply for unit power output. Again, the poor combustion characteristics of PG also affect the thermal efficiency of the engine demanding a higher fuel supply for the same power output. At 80% EL, all the tested fuel combinations recorded their lowest value of BSECs. While with further increase in EL, the fuel-air charge becomes richer as compared to 80% EL. This results in slightly higher BSEC at full-load operation. Nayak et al. also reported similar findings of BSEC in their experimentation with

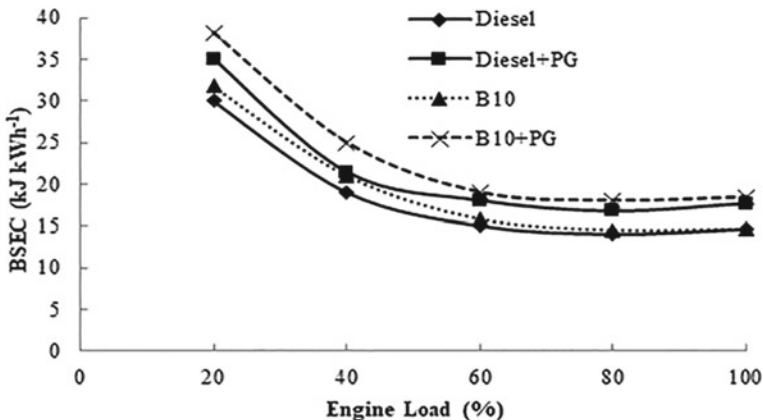


Fig. 4 Change in BSEC with respect to EL

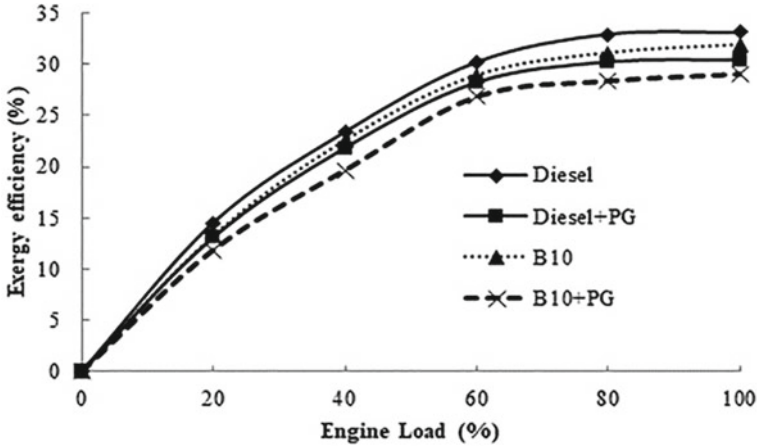


Fig. 5 Variation in exergy efficiency with respect to EL

PG [3]. Diesel-alone run showed lowest BSEC  $14.6 \text{ kJ kWh}^{-1}$  followed by B10 ( $14.65 \text{ kJ kWh}^{-1}$ ), diesel + PG ( $17.67 \text{ kJ kWh}^{-1}$ ), and B10 + PG ( $18.43 \text{ kJ kWh}^{-1}$ ).

#### 4.4 Exergy Efficiency

Figure 5 represents the variation in exergy efficiency with respect to EL. It was noticed from the figure that exergy efficiency rises proportionally with EL because of a rise in the power output and a decrease in the BSEC at higher loads. From Eqs. (3) and (4), it is clear that a higher value of peak temperature in the cycle gives higher available exergy from the system. The MCT decreases with induction of PG, as explained earlier that takes away activation energy from the system, results in a decrease in available energy from the system, which lowers exergy efficiency. As per the peak MCT value observed for different fuel combinations, diesel-alone operation showed the highest exergy efficiency, i.e., 33.1% at full engine load followed by B10 (31.86%), diesel + PG (30.37%), and B10 + PG (29.04%).

#### 4.5 Exergy Destruction

Figure 6 illustrates the variation in exergy destruction with respect to EL. The exergy destruction increases proportionally with engine load could be owing to higher fuel consumption and proportional rise in un-burnt emissions.

Exergy destruction is directly linked with the irreversibility inherently present within the system. While running the engine with alternative fuels like a blend of

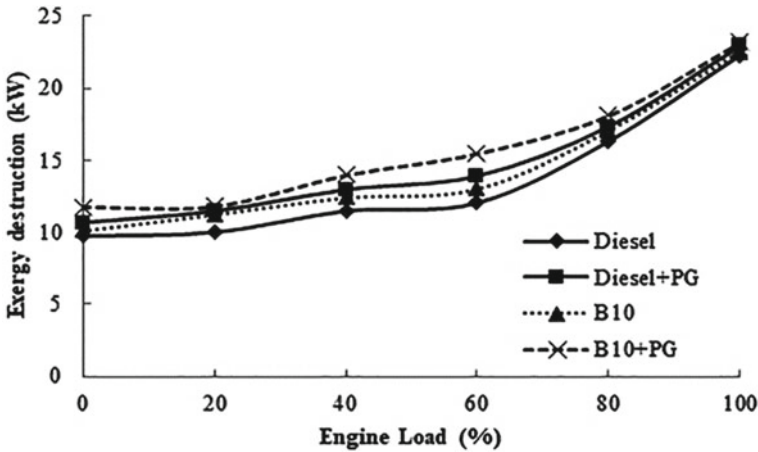


Fig. 6 Variation in exergy destruction with respect to EL

KOME and induction of PG, the irreversibility during fuel vaporization, fuel–air mixing, their trend of combustion, increase in ignition lag phase, all these factors affect the effective combustion of fuel energy into useful work. Hence, higher exergy destruction was observed in dual-fuel operations. Engine running with B10 alone showed a higher rate of exergy destruction than base results. Diesel-alone run showed lowest exergy destruction 22.25 kW followed by diesel + PG (22.49 kW), B10 (22.92 kW), and B10 + PG (23.17 kW) at full-load operation.

## 5 Conclusions

After vigorous analysis of the obtained results, the subsequent findings were strained from the experimentation.

- The highest value of NHRR somewhat pushed away from the TDC during dual-fuel operation. This indicates the increase in ignition lag while using PG as inducted fuel that needs to be taken care of to improve the performance of a dual-fuel engine.
- BSEC increased with hike in engine loading for all the tested fuel combinations as compared to the base result.
- Exergy efficiency decreases, and exergy destruction increases for dual-fuel operation with both the pilot fuels.

Hence, PG as inducted fuel can be considered to run small-scale gen-sets for power generation in rural areas while the B10 blend of KOME can be used as a partial substitution of diesel.

## References

1. Jena SP, Acharya SK (2020) Thermodynamic analysis of a thermal barrier-coated CI engine in a dual-fuel mode using biogas. *Int J Ambient Energy*:1–9
2. Jena SP, Acharya SK, Deheri C (2016) Thermodynamic analysis of a twin cylinder diesel engine in dual fuel mode with producer gas. *Biofuels* 7(1):49–55
3. Nayak C, Acharya SK, Swain RK (2015) Performance of a twin cylinder diesel engine in dual fuel mode using woody biomass producer gas. *Int J Sustain Eng* 8:341–348
4. Lal S, Mohapatra SK (2017) The effect of compression ratio on the performance and emission characteristics of a dual fuel diesel engine using biomass derived producer gas. *Appl Therm Eng* 119(5):63–72
5. Carlucci AP, Ficarella A, Laforgia D, Strafella L (2017) Improvement of dual-fuel biodiesel-producer gas engine performance acting on biodiesel injection parameters and strategy. *Fuel* 209(1):754–768
6. Rath MK, Acharya SK, Roy S (2016) Thermodynamic analysis of compression ignition engine using neat Karanja oil under varying compression ratio. *Int J Ambient Energy* 37(1):94–102
7. Jena SP, Mahapatra S, Acharya SK (2021) Optimization of performance and emission characteristics of a diesel engine fueled with Karanja biodiesel using Grey-Taguchi method. *Mater Today: Proc* 41:180–185



# New Challenges in Manufacturing Engineering Education



Asbjørn Rolstadås and Jim Browne

**Abstract** Industry 4.0, additive manufacturing, digitalization and the emergence of the circular economy are changing the face of manufacturing. New pedagogical approaches, including web-based delivery, are changing the face of teaching and learning. This paper considers these issues and offers a framework for developing a new manufacturing engineering curriculum based on a T shaped structure with five knowledge areas, and using Kolb’s learning model and the CDIO (Conceive-Design-Implement-Operate) or “teaching factory” approach.

**Keywords** Education · Manufacturing · Engineering

## 1 Introduction

Manufacturing is a key industrial sector. It is an important engine of growth for the global economy [1]. Over the last 200 years plus, manufacturing industry has undergone a number of significant changes. This is clearly demonstrated in the concept of Industry 4.0. Through the maturing and convergence of digital technologies together with the development of 5G communications systems and additive manufacturing technologies, Industry 4.0 represents a step change in terms of the digitalization of manufacturing systems and total integration across the value chain. We are thinking of developments in what might be called ubiquitous telecomputing including cloud computing, 5G, artificial intelligence, and the Internet of Things. Industry 4.0 represents *disruptive change*; it is a consequence of and an enabler of *servitization* and through the development of additive manufacturing opens the possibility of distributed and localized manufacturing, efficient small batch production and indeed one-of-a-kind products. Converging technologies are changing and

---

A. Rolstadås (✉)  
Norwegian University of Science and Technology, Trondheim, Norway  
e-mail: [asbjorn.rolstadas@ntnu.no](mailto:asbjorn.rolstadas@ntnu.no)

J. Browne  
National University of Ireland, Galway, Ireland

will continue to change the nature of business models, products, delivery of services and work.

We believe that there are four major future industry development trends that will influence future manufacturing engineering curricula: (a) circular economy and the decarbonized society, (b) digitalization and the emergence of multiple technologies which are maturing, interconnecting, and converging, (c) new manufacturing technology (in particular additive manufacturing), and (d) the shift from owning a product to buying services (servitization).

## ***1.1 Circular Economy***

Dealing with climate change, and the challenge of developing a circular economy as the 4th industrial revolution rolls out will require enormous structural change in our business models and our economy. Ultimately products will have to be redesigned with reuse and recovery in mind. Products will also have to be designed to be smart or intelligent: that is, they have to carry with them a profile of their design, constituent parts, history of use, service etc. which can then be made available to support repair, upgrading, reuse, recovery at end of life. This is all technically possible using RFID technology and embedded sensor and memory devices. The emerging Internet of Things, nano-technologies and micro sensors allow us to embed memory chips, computing and communications devices in consumer and capital good products which, combined with design for reuse, disassembly and recycling, facilitate the development of a circular economy.

The challenge is to migrate over time from a “*Design—Manufacture—Distribute—Consume—Discard*” industrial system, to a “*Design—Manufacture—Distribute—Consume—Return—Disassemble—Reuse/Recycle/Reclaim*” system. This transition requires a paradigm shift in public policy, human behaviour, economic thinking and analysis, engineering design etc. and of course the development of new industrial systems to support circularity.

## ***1.2 Digitalization***

Digitalization enables the development of “*Smart Products*” which comprise embedded technology giving them the capability to identify themselves and describe their properties, status and history. They are capable of executing computations, storing data, interacting with the environment and communicating with external devices. While early implementation was based on RFID technology, they now incorporate full sensing, computing and communicating capability. This gives them the ability to support service, maintenance and, particularly important from a circular economy perspective, *end of life* product dispositioning.

Digitalization also facilitates the development of true cyber-physical systems and the creation of *digital twins* of both products and production systems, which in turn enables the direct translation of design data into process instructions which are in turn passed directly to the production equipment. In effect the engineer can test the design of a complex component on a simulated manufacturing system before ever going to the physical production system.

Artificial Intelligence and Data Analytics systems have a wide range of applications in Industry 4.0; they facilitate the personalization of products and mass customization and facilitate smart production and circular manufacturing. They are in many cases based on statistical analysis and pattern recognition in large data bases and provide the ability to “learn” statistically from annotated “training” data, using machine learning and neural networks technologies.

At the operational level, these systems are frequently embedded in manufacturing execution systems to collect data from smart sensors on the manufacturing shop floor, diagnose or predict problems and prescribe actions in areas such as inspection and associated decisions, guiding industrial robots, managing industrial processes through component recognition systems, and real time scheduling and process selection and control, using optical character recognition, image processing, checking presence/absence of parts, feature recognition etc.

### ***1.3 Additive Manufacturing***

In recent years a new group of manufacturing technologies known as *additive manufacturing* [2] have emerged. Digital 3D design data is used to build up a component in layers by depositing material. Originally, these technologies were used to build prototypes of complex geometry components; they have now morphed into a set of production techniques capable of producing sophisticated high specification plastic and metal parts.

Additive manufacturing is now becoming established in the aerospace and med tech industries to produce small batches of very complex products efficiently and economically. Its impact can be seen in two areas; from a process point of view, it provides for “tooling free” manufacturing which considerably simplifies the supply chain, allows for the fast development of prototypes as the design emerges and reduces the lead time for production. From a production point of view, it facilitates the manufacture of parts with complex geometry in a single pass. Taking a longer-term perspective, it is likely that additive manufacturing will facilitate the greater distribution of manufacturing as locally based additive manufacturing facilities will be in a position to download part programmes over the internet and manufacture components close to market.

## 1.4 Servitization

Today for many products the customer has moved from being an *owner* to a *user* of the product; effectively the customer is paying for access to the service that the product offers. We are moving towards a *sharing economy* for products as diverse as entertainment including music and films, books, the news media, personal transport through shared bicycles and ultimately cars etc. In the business world, we see the move toward software as a service, businesses paying for the service rather than buying printers, scanners and photocopiers; hospitals paying per use for laboratory and advanced medical equipment installed in the hospital by the supplier, rather than buying the equipment. Effectively *the product has become the platform to deliver a service*, in a process known as *servitization*. The business model has been upended, the manufacturer has become a service provider, and all of this enabled by the Internet of Things, sensor technology, cloud computing, 5G and artificial intelligence working in tandem.

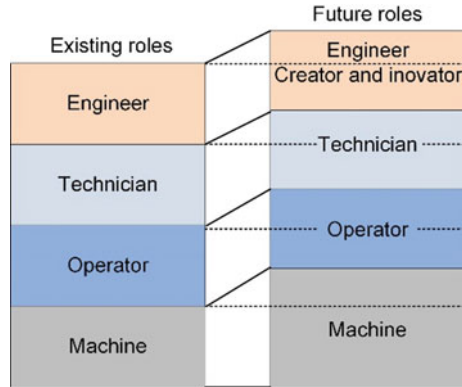
## 2 Changed Role of Manufacturing Engineers in Industry

### 4.0

Apart from the developments in circular manufacturing, digitalization and servitization, technology has already significantly changed the respective roles played by machines, operators, technicians and engineers. Consider what has happened in the traditional machine shop. In the past, skilled machinists, having served a long apprenticeship, operated the machines; technicians maintained the machines; production engineers planned the process steps, determined the tooling and machining parameters and worked with technicians to design and build any jigs and fixtures necessary to machine the part.

Today the same part is machined on a CNC machine or in a flexible manufacturing cell. The control of the machining process has passed from the operator to the CNC controller which the operator now programmes. The machine has taken over some of the tasks previously undertaken by the machinist and the machinist has upskilled to become the part programmer. Furthermore, the technician role is upgraded to undertake tasks in jig, tool and process design previously undertaken by the engineer. The engineer in turn is freed up to undertake more challenging tasks in the design of the overall process and system; tasks which require **increased creativity**, an **understanding of the products and the business** and an **ability to work in cross functional teams**. This incremental change in the respective roles of machinists, technicians and engineers illustrated in Fig. 1, has consequences for the education and training of all three.

**Fig. 1** Change in job roles



### 3 Manufacturing Engineering Education

Manufacturing engineering education follows a structure of Bachelor–Master–Doctorate (Ph.D.). Traditional manufacturing engineering curricula focus on building a solid theoretical platform so that students are well prepared to solve applications problems in industry. Graduates are trained to solve complex problems in manufacturing systems and manufacturing technologies per se, using non-routine methods.

A recent study by MIT [3] argues for socially relevant and outward-facing engineering curricula which emphasize student choice, multidisciplinary learning and societal impact, coupled with a breadth of student experience outside the classroom. “The future of education and skills 2030” [4] suggests that future-ready students need to exercise agency and a sense of responsibility to participate in the world and, in so doing, to influence people, events and circumstances for the better. The team at MIT have developed a learning framework for 2030 focusing on competences, understood as knowledge, skills, attitudes and values.

Innovation and management are as important in the curriculum as technology. Van Brussel [5] states that innovation requires creativity and multi- and transdisciplinary thinking. He sees a shift in the manufacturing engineer’s role, moving from routine tasks to solving unstructured problems. According to Moravec’s paradox manual and cognitive routine tasks are “easy” to automate while tasks requiring manipulative skills and creative thinking are much more difficult to automate.

Many employers and the professional engineering bodies emphasize the requirement for today’s young professional engineers to have deep disciplinary knowledge and broad capabilities to work across various professional, disciplinary, social and cultural boundaries. Broad skills of problem solving, creativity, team working, innovation, leadership etc. are required in order to function effectively as a design or manufacturing engineer in an Industry 4.0 environment. *Deep disciplinary skills, which were emphasized strongly in the past, are necessary but not sufficient.*

So called “T-shape” graduate professional engineers are in demand; the horizontal line of the “T” represents broad generic skills while the vertical represents deep disciplinary knowledge.

## 4 New Learning Environment

The classic model for engineering education sets the teacher to the fore imparting and transferring knowledge to students. This passive learning is far from efficient. To enhance learning outcomes, we must move to a more involved learning mode. The need for enhanced learning models arises because Industry 4.0 presents large and complex challenges (*wicked problems*) and frequent technology driven changes; manufacturing engineers must be *change agents* who seek to shape the future, understand others’ intentions, actions and feelings, and anticipate the short and long-term consequences of what they do.

This points in the direction of more *experimental learning*. Experiential learning is the process of learning through experience. Kolb [6] is one of the main contributors to the modern theory of experiential learning; see Fig. 2. During the first stage the learner is exposed to a *new experience* which at the next stage is subject to *reflective observation*. Then follows *abstract conceptualization* where the learner develops new ideas from the reflections. At the final stage ideas, effectively proposed solutions are tested through *active experimentation* in the real world.

Challenge-based learning is a similar approach. It is a framework for learning by working with real-life problems. It is organized into three phases [7]: *engage—investigate—act*. A concept using the principles of challenge-based learning is the teaching factory [8]. It aims to align manufacturing teaching and training to the needs of modern industrial practice and is based on the knowledge triangle (*research—innovation—education*). It is a two-way knowledge transfer channel as illustrated in Fig. 3. The teaching factory can also be facilitated through virtual visits for students to review manufacturing equipment and operations.

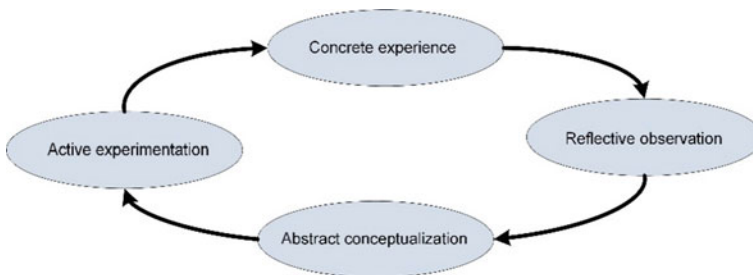


Fig. 2 Kolb’s experimental learning model

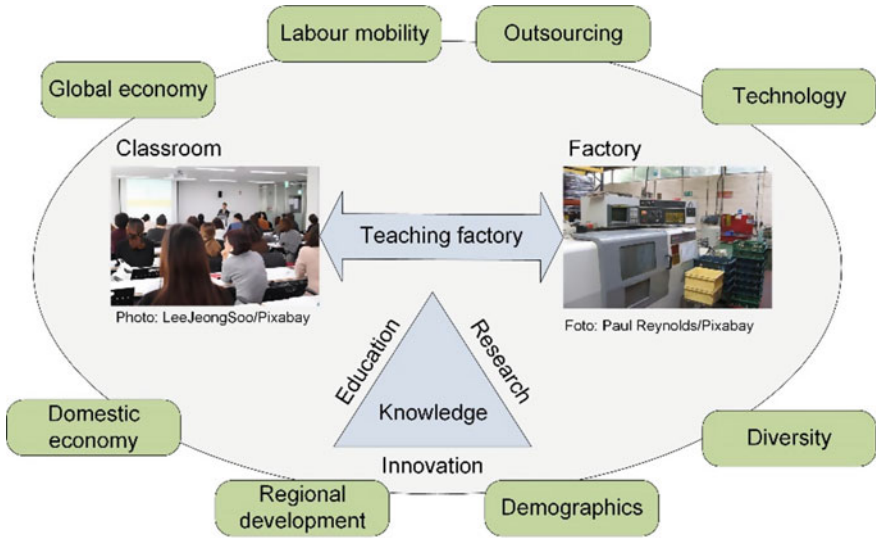


Fig. 3 The teaching factory concept

Computer games are commonly used for entertainment. Their origin however was to train people for tasks in particular roles through the development of simulated environments; well established examples include the training of pilots on simulators. By exploiting advanced simulation and visualization technology, well designed games can contextualize the learner’s experience in a realistic and challenging environment [9].

Such games add a new dimension to learning. They train the learner in decision making, but in a virtual environment where there are no consequences of a poor decision. Serious games may thus also be used in a setting with *digital twins* of the manufacturing system and the products to be manufactured.

A framework for engineering education allowing experimental learning has been launched as the CDIO initiative [10]. The framework provides the learner with an education stressing engineering fundamentals in a context of *Conceive—Design—Implement—Operate (CDIO)* real-world systems and products. The authors claim that the learners must be technically expert, socially responsible, and inclined to innovate.

In conclusion, the learning environment is rapidly changing. The future solution is based on an active learning model using experimental learning. It takes advantage of digital technology and thus creates more flexibility in the learning process with respect to time, place and progress.

## 5 Towards a New Manufacturing Engineering Education

We believe it is necessary to rethink manufacturing engineering education. In the following we will outline some thoughts on how manufacturing engineering education should be positioned in the global education system, some guiding principles for delivery of manufacturing engineering education and a framework for the design of the manufacturing engineering curriculum.

In terms of the global engineering education system, graduate engineers should be trained to the level set out in the requirements of the Washington Accord ([www.ieagreements.org](http://www.ieagreements.org)), that is to masters degree level as set out in the European Higher Education Area.

From a delivery perspective a number of principles should be followed. The programme should be delivered using the approach set out in Kolb's learning model, and therefore include significant action and project-based learning; be delivered in a research-led teaching environment; and include significant access to practice, which should include "virtual visits" to industrial sites. The programme should be delivered in a blended learning format with appropriate use of conventional "face to face" teaching and laboratory exposure and virtual learning. Given the reality of continuous change and innovation, the curriculum should be delivered in a manner which ensures that the graduate has acquired a deep knowledge of the underlying principles of manufacturing processes and systems and a capacity to continually upgrade and update his/her knowledge as technology and business processes change and develop.

Today manufacturing covers a tremendous variety of products and associated processes: from biomedical devices to biopharmaceuticals, silicon fabrication foundries to fast moving consumer goods; from aerospace and automotive to electronics and nanotechnology-based sensors; etc. Individual programmes and curricula will have to concentrate on a particular manufacturing sector, and this might reflect the industrial sector(s) which are well developed in their region, thus providing the necessary access to practice to ensure a high quality graduate.

The design of a curriculum should be based on a set of learning objectives or learning outcomes. The student should achieve competence making him or her able to:

- L1. Demonstrate fundamental knowledge of generic and enabling technologies.
- L2. Demonstrate solid knowledge in the field of product development, manufacturing processes, manufacturing systems, product and systems maintenance and operations management.
- L3. Apply relevant tools and techniques to critically analyze and solve industrial problems and develop sustainable solutions.
- L4. Effectively work in teams and in projects.
- L5. Engage in the public discussion on the impact of technology on society and environment and demonstrate a high ethical standard.
- L6. Continuously learn in a life-long learning perspective.



These learning objectives can be met by designing a curriculum using the T-shape structure discussed in Sect. 3. The “T” comprises both a breadth of knowledge and a depth of experience, and rests on a competence foundation.

The competence foundation contains subjects such as mathematics, basic natural sciences, economy, humanities and social sciences. The purpose is to serve as a basis for deeper and more specialized technological knowledge. As we define competence as a combination of knowledge, skills and attitudes, the foundation also provides the student with the necessary background to develop a positive attitude and place the technological learning in a scientific, social, and societal perspective. It contributes to learning objectives L5 and L6 above.

In the “breadth of knowledge” part of the “T”, there are basic technological subjects such as:

- Information and communication technology (ICT)
- Materials science
- Systems engineering
- Circular economy and industrial ecology
- Reliability, availability, maintainability and safety (RAMS)
- Project management.

In these fields, the candidate should develop both knowledge and skills. It contributes to learning objectives L1, L3 and L4.

The “depth of experience” part of the “T” contains the manufacturing engineering specific subjects. It falls beyond the scope of this paper to define a specific curriculum. We will provide a framework defining types of subjects to be included. We will refer to those as *knowledge areas* (KA). A knowledge area defines a number of processes with tools and techniques where the candidate should have both knowledge and skills. Following the trends of industrial and societal development discussed in the preceding, we underline the need to rethink such knowledge areas from the classic thinking towards today’s needs for sustainability and a green shift. Thus, our framework suggests the following manufacturing engineering knowledge areas:

- KA1. Servitization and new product development
- KA2. Business operation and competitive strategy
- KA3. Intelligent manufacturing processes
- KA4. Intelligent manufacturing systems and supply chains
- KA5. End-of-life engineering and management.

These knowledge areas correspond to learning objectives L2 and L3.

In conclusion we believe that this framework provides the basis for creating a detailed manufacturing engineering curriculum.

## References

1. Dusterberg T, Preeg E (2003) U.S. manufacturing—the engine for growth in a global economy. Praeger Publishers, Westport, CT
2. Rajaguru KKT, Vijayan V (2020) Additive manufacturing—state of art. *Mater Today Proc* 21:628–633
3. Graham R (2018) The global state of art in engineering education. MIT School of Engineering, Cambridge, MA
4. OECD (2018) The future of education and skills—education 2030
5. Van Brussel H (2019) Innovation, productivity, AI, robots and employment: an impossible deal. In: Euro-case annual conferences 2019. [https://www.euro-case.org/all\\_annual-conference/annual-conference-2019/](https://www.euro-case.org/all_annual-conference/annual-conference-2019/)
6. Kolb D (1984) *Experiential learning: experience as the source of learning and development*. Prentice Hall, Englewood Cliffs, NJ
7. Nichols M, Cator K, Torres M, Henderson D (2016) *Challenge based learner user guide*. Digital Promise, Redwood City, CA
8. Chryssolouris G, Mavrikios D, Rentzos L (2016) The teaching factory: a manufacturing education paradigm. *Procedia CIRP* 57:44–48
9. De Gloria A, Bellotti F, Berta R, Lavagnino E (2014) Serious games for education and training. *Int J Serious Games* 1(1)
10. Crawley EF, Malmqvist J, Östlund S, Brodeur DR (2014) *Rethinking engineering education—the CDIO approach*, 2nd edn. Springer

# Design and Simulation of Enhanced Smart Cantilever Assembly for Active Vibration Control



Biswaranjan Swain , J. Halder, N. Swain, P. P. Nayak, and S. Bhuyan

**Abstract** This article investigates ideal trembling concealment of a cantilever pillar utilizing assembled piezoelectric patch units. A rectangular aluminum salver demonstrated fit as a fiddle with one sets of piezoelectric patches as transducer has been utilized to explore the viable trembling control. A state house model for reproducing time reaction of strategies of a pillar with electricity electrical device pairs has been created. Absolute coordinated energy place away within the framework was restricted by shifting the case of piezoelectric patches of consistent length whereas keeping criticism acquires steady. COMSOL Multiphysics 5.4 variant programming has been used to determine the limited part model of the plate. As indicated by this model, the areas of ideal device are known and positive pillar is molded. A suitable recreation control methodology has been explored through MATLAB programming by which the addition of the regulator has been advanced to accomplish proficient dynamic trembling concealment with least control input.

**Keywords** Dynamic trembling concealment · Piezoelectricity · Incorporated energy

## 1 Introduction

Dynamic trembling concealment is an interaction wherein the vibration of a setup is decisively stifled by spreading counterforce to explicit design which is reasonably of inverse stage, however, equivalent in size to the first vibration. Vibration decreases of adaptable designs utilizing piezoelectric transducers has gotten impressive interest lately. This can be credited to the way that piezoelectric materials have remarkable belongings, for example, lower permittivity, fast reaction, low dielectric misfortune, simple development, plan gracefulness, minimal expense, and low influence utilization [1–3]. The exhibition of dynamic vibration control depending on the control law

---

B. Swain (✉) · J. Halder · N. Swain · P. P. Nayak · S. Bhuyan  
Department of Electronics and Communication Engineering, Siksha 'O' Anusandhan Deemed to be University, Bhubaneswar 751030, India  
e-mail: [biswaranjanswain@soa.ac.in](mailto:biswaranjanswain@soa.ac.in)

as well as on prudent position of piezoelectric transducers. From that point forward, various methodologies for ideal arrangement of piezoelectric transducers have been introduced in the writing relying on the final application [4–6].

A large part of the research for best settlement of piezoelectric transducers on a cantilever pillar discretionarily expects a static number of typical transducer pairs throughout issue detailing. This prompts an inquiry whether a similar vibration decrease execution for a specific setup can be accomplished with lesser number of properly situated transducers and changing the surroundings of the regulator. The issue of best number and arrangement of transducer sets has been considered for plates, multistore structures, and supports [7–10]. A comparative action for best number and situation of piezoelectric transducers on a basically upheld pillar has been measured herein examination. The anticipated methodology empowers to judge development in trembling concealment noninheritably by increasing range of electricity patches to urge a sense of the compromises connected with value and execution. A point-by-point examination and recreation investigation have been shown here.

## 2 System Framework

The techniques engaged with a bar model melded with piezoelectric transducers at the pinnacle floor and another piezoelectric transducers at base floor have been exhibited in Fig. 1.

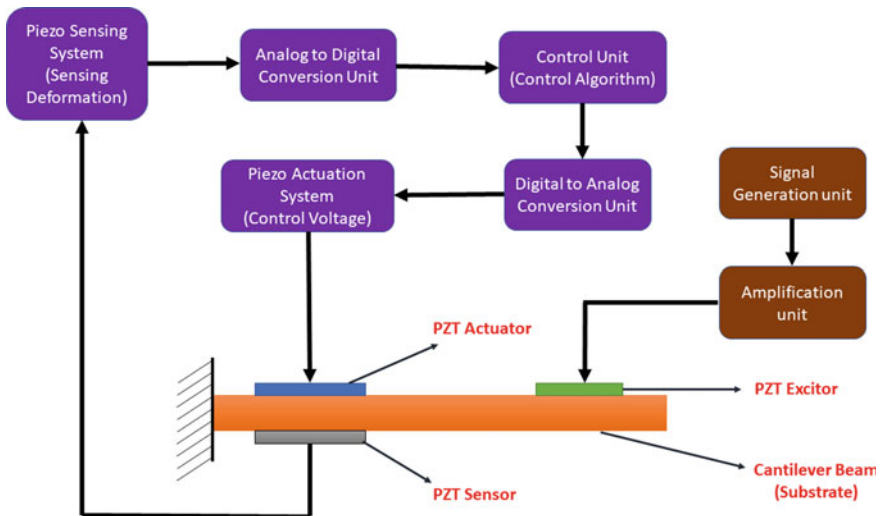


**Fig. 1** Schematic of strategies associated with a bar model intertwined with piezoelectric transducers at the pinnacle floor and sensors at the base floor

In this defined framework, the substrate is fundamentally comprised of aluminum which goes about as a cantilever shaft with measurement  $(30 \times 2.5 \times 0.5) \text{ cm}^3$ . A sensor fix is given to the static finish of the bar and is responsible for the distinguishing of the pressure shaped in the shaft and make voltage identically. Because of created strain, a piezoelectric flow is delivered. This sensor fix is by and large comprised of polyvinylidene fluoride (PVDF) material. The most elevated measure of pressure and the bowing second is created at stable side. Along these lines, for proper induction in shaft, the actuator is situated at stable side. In outlined framework, the transducers are mathematically settled with each other which provides steadiness of shut circle framework that has been refined through a PZT exciter which generates actual trembling on pillar. The mid-range return has been applied nevertheless sufficiency of data sign ought to minimum to induce any unmistakable trembling in shaft. To accomplish the objective, a speaker has been used to extend sign whose reach could be fluctuated utilizing handle of enhancer. The improved reaction esteem is not precisely the limit of exciter even as the prevalence of the trembling is corrupted due to which PZT patches might be scratched.

### 3 Beam Model Design

The transducers are mathematically placed to be organized with associate degree as this ensures solidness of the shut circle framework. There are  $m$  transducers pairs (for a combination of  $2m$  PZT patches) bolstered on outside of pillar. The patches are thought to be captivated in  $z$  bearing.

The condition of movement for the bar with once outer charges is purposeful on the electricity actuators are often delineated as

$$Y_b I_b \frac{\partial^4 w}{\partial x^4} + \rho_b A_b \frac{\partial^2 w}{\partial t^2} - b \sum_{i=1}^m \frac{\partial^2 M_i^a}{\partial x^2} = 0 \quad (1)$$

The moment on the beam by the force exerted by actuator  $i$  and is given as

$$M_i^a = r^a d_{31} Y_p \phi_i^a(x, t) \quad (2)$$

For trembling concealment of adaptable frameworks, the absolute energy put away in the framework can be considered as a portrayal of the vibration reaction. Limiting the complete incorporated energy put away in the framework has a similar impact as expansion of energy disseminated.

If input speed is taken as negative, then for actuator voltage, we may compose:

$$\phi_a = -G_s \dot{\phi}_s = GC \dot{\underline{x}} \quad (3)$$

$$\dot{\underline{x}} = A_{cl} \underline{x} \quad (4)$$

$$A_{cl} = \begin{pmatrix} 0_{n \times n} & I_{n \times n} \\ -\omega^2 & -B^*GC^* - 2\zeta\omega \end{pmatrix} \quad (5)$$

$$E = \int_0^{\infty} x^T Q x dt \quad (6)$$

where

$$Q = \begin{pmatrix} \omega^2 & 0 \\ 0 & I_{n \times n} \end{pmatrix} \quad (7)$$

From Eq. (5), we can have:

$$E = -x^T(t_0)Px(t_0) \quad (8)$$

where  $x^T(t_0)$  is the initial phase and  $P$  is final solution of

$$A_{cl}^T P + PA_{cl} = Q \quad (9)$$

where  $\rho_b$  is material density,  $Y_b$  is the Young's modulus,  $I_b$  is moment of inertia,  $r^a$  is the separation distance,  $d_{31}$  is piezoelectric strain constant,  $\emptyset_a$  is voltage applied to the actuator,  $\omega$  is natural frequency,  $E$  is the energy.

It has been seen that the absolute coordinated energy is a verifiable capacity of input acquire network. Hence, with limiting complete incorporated energy put away in the framework for a specific arrangement of improvements, we can get the ideal mathematical conveyance of the transducers.

The enhancement issue in standard structure would then be able to be composed as

Minimize  $E(\bar{x}, G)$

Subject to:

$$0 \leq x_{i1}, x_{i2} \leq L, \quad (i = 1, 2, \dots, m)$$

$$x_{i1} - x_{i2} \leq 0 \quad (i, j = 1, 2, \dots, m)$$

$$G_{ij} \leq G_u \quad (i, j = 1, 2, \dots, m)$$

$$x_{i2} - x_{(i+1)1} \leq 0 \quad (i = 1, 2, \dots, m)$$

$$G_{ij} \in G$$

where  $G_u$  is the upper limit for the individual gain elements in  $G$  matrix. Since the problem is highly non-linear, a genetic algorithm is used for solution of optimization problem.

### 4 Results and Discussion

Established on archetypal plan, ideal trembling control for beginning state reaction of a cantilever has been achieved. In reproduction investigation, we utilized COMSOL Multiphysics rendition 5.4 programming to start model of cantilever. From examination, we may decide greatest suitable incited voltage and limit redirection cantilever. As per defined model, cantilever is framed in Fig. 2a, b.

In view of the model plan and streamlining basis introduced individually, ideal vibration control for introductory condition reaction of an essentially upheld bar was performed. The particulars of piezoelectric fixes and bar used for investigation are given in Table 1 beneath. Initially, four vibration modes are taken with up to 3 transducers pairs. The original states of the state vector are selected and depicted as beneath:

$$\bar{x}(t_0) = [0 \ 0 \ 0 \ 0 \ 0.2 \ 0.4 \ 0.6 \ 0.8] \tag{10}$$

The optimization algorithm has been performed for every one of the three cases, and outcomes have been settled for perfect solution which has been appeared in Table 2.

In the wake of determining the perfect solution for each single unit of the measured part, starting state of initial four vibration modes with and without control using

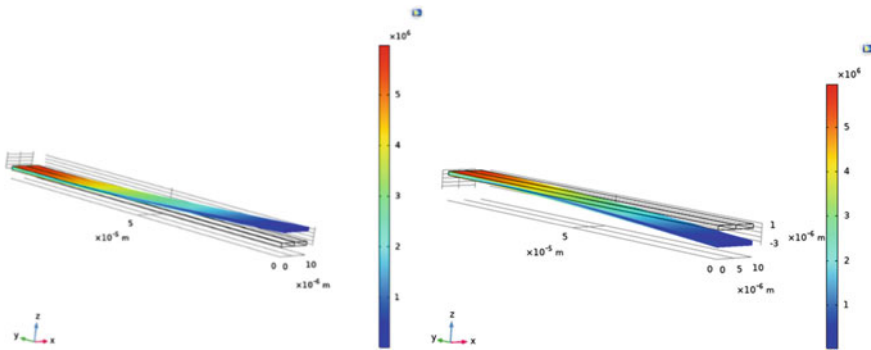


Fig. 2 Simulated result of extreme bend in beam

**Table 1** Structure and piezoelectric patch specifications

Parameter	Cantilever beam	Actuators	Sensors
Mass density ( $\text{kg/m}^3$ )	1180	1600	1600
Young's modulus (GPa)	3.2034	2	2
Poisson's ratio	0.4	0.4	0.4
Piezoelectric constant $d_{31}$ (m/V)		$2.4 \times 10^{-11}$	$2.4 \times 10^{-11}$
Piezoelectric constant $h_{31}$ (m/V)			$4.41 \times 10^8$
Thickness (m)	$1.5 \times 10^{-3}$	$4.2 \times 10^{-5}$	$4.2 \times 10^{-5}$
Length (m)	0.6		
Width (m)	0.02		
Damping ratio	0.02		

**Table 2** Optimal sensor patch location

Number of sensor patch pairs, $m$	Placement of patches	Feedback gain matrix, $G$	Objective function, $E$
1	0.0264–0.1264	[0.4]	0.1924
2	0.0268–0.1268 0.305–0.405	$\begin{bmatrix} 0.4 & 0.4 \\ 0 & 0.4 \end{bmatrix}$	0.1661
3	0.0328–0.1328 0.1408–0.2408 0.3664–0.4664	$\begin{bmatrix} 0.4 & 0 & 0 \\ 0 & 0.4 & 0.0346 \\ 0 & 0 & 0.4 \end{bmatrix}$	0.1395

around three transducer pairs has been designed and is appeared in Figs. 3, 4, 5 and 6.

## 5 Conclusion

An advanced piezoelectric shrewd construction for dynamic vibration control framework has been created. In limited component demonstrating utilizing COMSOL Multiphysics rendition 5.4, cantilever pillar has been presented to a steady power. The translations of shear pressure and dislodging at every hub have been logged through a wide scope of recurrence, in 100 sub-steps. Expanding number of piezoelectric patches brings about expanded vibration concealment for modes 1, 2, and 3. Nonetheless, for mode 4 amplitudes increment, if the quantity of fix sets is multiple. The greatest decrease in modular abundancy with three fix sets for mode 1 is just—6.12% while it is—61% for mode 2, 98.7% for mode 3, and 93.5% for mode 4.



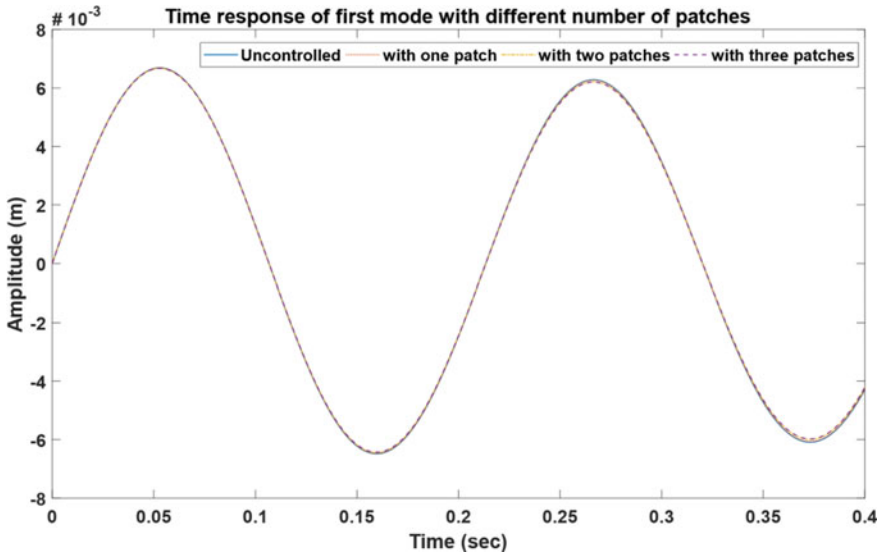


Fig. 3 Time response of first mode

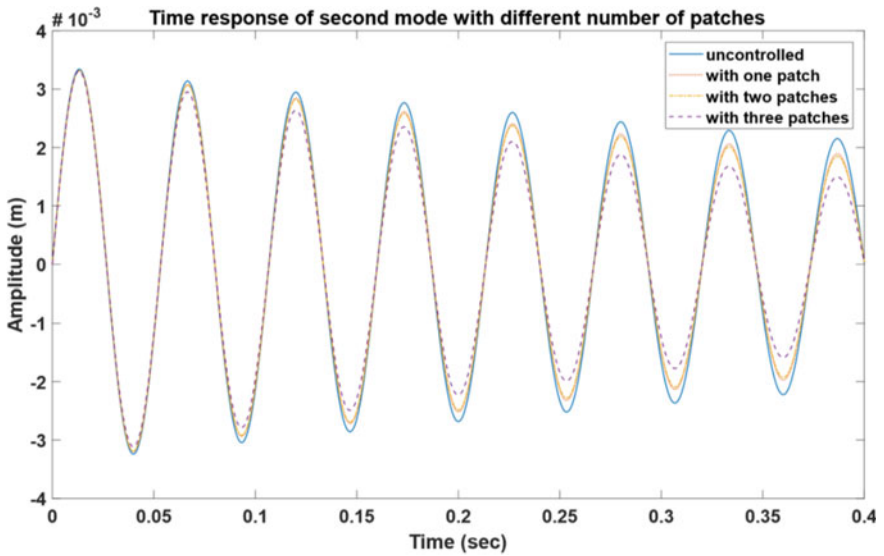


Fig. 4 Time response of second mode

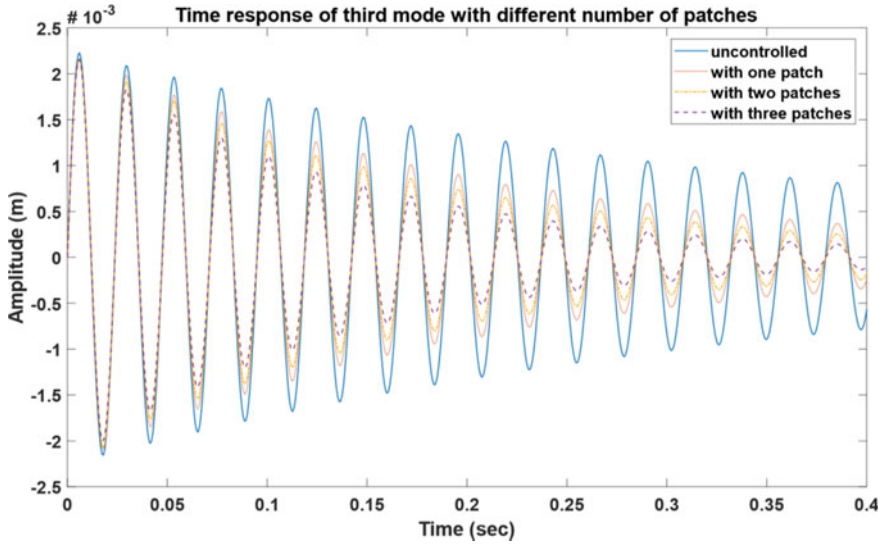


Fig. 5 Time response of third mode

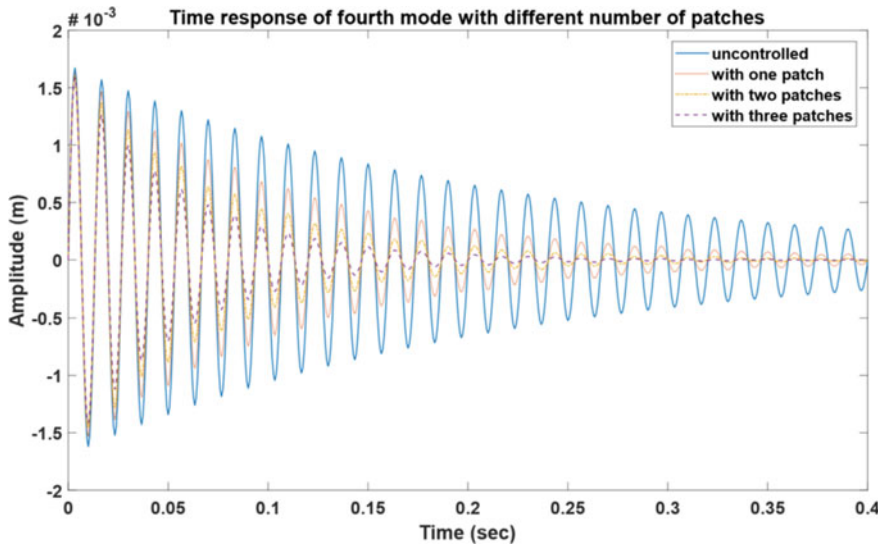


Fig. 6 Time response of fourth mode

Depending upon the level of sufficiency decrease needed for methods of interest, a choice can be made in regards to execution improvement versus cost.

## References

1. Gupta V, Sharma M, Thakur N (2010) *J Intell Mater Syst Struct* 21:1227–1243
2. Tripathi PK, Gangadharan KV (2012) *Int J Res Rev Mechatronic Des Simul* 2:92–98
3. Pourboghraat F, Pongpaiboj H, Aazhang B (2002) In: *The proceedings of the 5th biannual world automation congress*, pp 133–139
4. Crawley EF, Javier DL (1987) *AIAA J* 25:1373–1385
5. Juntao F (2005) In: *The proceedings of the 37th southeastern symposium on system theory*, pp 35–39
6. Swain B, Nayak PP, Kar DP, Bhuyan S, Mishra LP (2016) *Review of scientific instruments*. 87:074708
7. Hua NH (2004) *Eng Comput* 21:651–665
8. Yaowen Y, Jin Z, Soh CK (2005) *J Sound Vib* 282:1293–1307
9. Kumar KR, Narayanan S (2008) *Smart materials and structures*. 17:055008
10. Li QS, Liu DK, Tang J, Zhang N, Tam CM (2004) *J Sound Vib* 270:611–624

# Design of Injection Mold for Manufacturing of Cup



**B. A. Praveena, Balachandra P. Shetty, N. Lokesh, N. Santhosh, Abdulrajak Buradi, Mahesh, Sunil, Ramesh Jalapur, and Sharanu**

**Abstract** The goal of this study is to create a model, remove the core cavity, and construct an injection molding apparatus for making a plastic cup. The mold flow investigation of the part is conducted by Autodesk code in the core cavity style. The tool can be configured to produce a good-quality part while taking into account the simplicity of manufacture, assemblage, and constructive part expulsion. The device style should meet the apparatus specifications, and it may be the identical throughout the part's or products productive lifetime. While ensuring high productivity, quality must be compromised to some level. Similarly, production will be reduced when efforts are focused on improving quality. To ensure good quality and productivity, machining parameters must be optimized. The purpose of this study is to present the conditions of the plastic injection molding process. The processing conditions were suitable for the production of a high-quality product. It is one of the utmost common and versatile techniques for developed sophisticated plastics constituents with outstanding dimensional tolerances. Injection molding is most popular when good quality, high tolerance, and fast production rates are essential.

**Keywords** Injection molding process · Die · Cup and plate · Parameters · Machining · Quality Characteristics · Mold design

## 1 Introduction

Injection molding is the most widely utilized thermoplastic molding technique. The ability of thermoplastic materials to soften when heated and harden when cooled has been supported. As a result, the procedure entails softening the fabric in an extremely

---

B. A. Praveena (✉) · B. P. Shetty · N. Lokesh · A. Buradi · Mahesh · Sunil · R. Jalapur · Sharanu  
Department of Mechanical Engineering, Nitte Meenakshi Institute of Technology, Affiliated to  
Visvesvaraya Technological University, Yelahanka, Bangalore 560064, India  
e-mail: [praveena404@gmail.com](mailto:praveena404@gmail.com)

N. Santhosh  
Department of Mechanical Engineering, MVJ College of Engineering, Bangalore, Karnataka  
560067, India

hot cylinder, before pumping it stressed into the mold chamber, where it hardens as it cools [1]. Within the cyclic operation, each step is dispersed in its own zone of equivalent equipment. When the plunger is withdrawn, granular material (polymer) is fed from the hopper into the barrel [2]. The cloth is subsequently pushed into the heating zone, where it is heated and softened. The chemical substance spreads into a thin coating surrounding the sink, allowing for rapid heating.

This new material pushes the already melted chemical compound forward through the nozzle that is in direct contact with the mold [3]. The melted chemical substance pours into the mould cavity through the disorder, runner logic gate. The clamping action of the press platen forces the mold to shut tightly [4]. Before the mold is opened and the produced half is released, the fabric inside the mold should be cooled stressed below. Injection molding is a manufacturing technique that uses both thermoplastic and thermoset plastic materials to create components [5]. Melted plastic is inserted into a mold at a great pressure, creating the inverse of the products contour [6]. Molds are made from metal, sometimes aluminum or steel and accuracy machined to make the alternatives of the required half once a product is planned, sometimes by an engineer or industrial designer [7].

For thermoplastic polymers, injection molding is a primary net shaping process. The injection molding process is used to make more than 30% of all plastic parts. This is a highly preferred method in the manufacturing business because it can make complex-shape plastic goods with high dimensional precision and quick cycle times. Automobile manufacturing, exteriors, and casings of things such as mobile phones, computer monitors and further devices with a thin shell feature are typical examples [8].

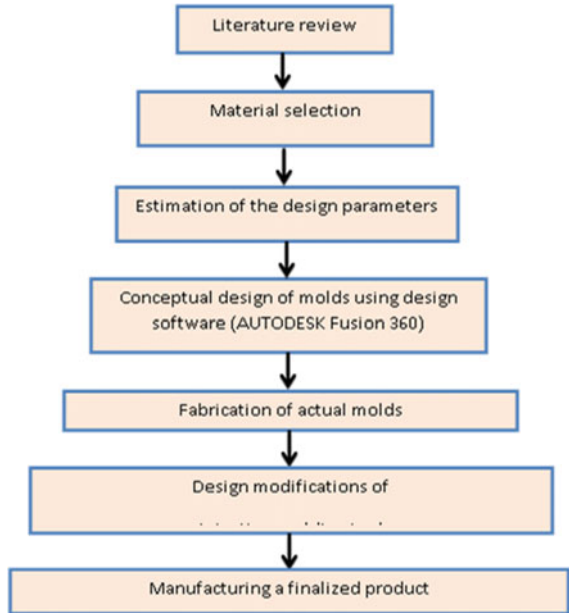
## 2 Literature Review

A lot of research is existence done to figure out what is going on, identify crucial components, and possibly mold the processes. The majority of recent research has been based on theoretical, computer-based replication prototypes, and realistic experimental judgments [9]. Some researchers attempted to investigate whether tooling elements such as mold material had a major impact on sink marks. Injection temperature and holding time are considered handling variables in mold manufacture. They discovered that allotment time was more significant than injection temperature [10].

## 3 Methods and Methodology

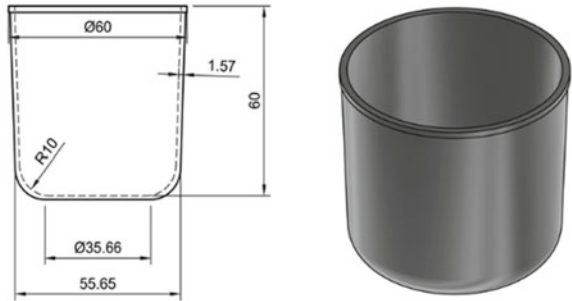
Injection molding has been difficult method for several producing associate in researches to provide product meeting requirement at an efficient means. The subsequent flow chart shows the methodology of this work. Figure 1 shows the methodology of injection molding.

Fig. 1 Methodology



The methodology adopted is achieving the said objectives can be illustrated as follows. Theoretical study about molds and their characteristics, additive manufacturing, polymer composites and various characterization techniques with appropriate standards. Obtaining the conceptual design of the cup and plate using AUTODESK Fusion 360 using final product, obtain the conceptual design of cup and plate mold using AUTODESK Fusion 360. Material Selection and Procurement. Obtain a final mold and find the analysis of various method parameters of injection molding method, calculations of different parameters [11].

Mold filling, plastication, and cooling with hardening will be separated into three independent steps in a single injection molding cycle. Plasticization: This phase is carried out within the injection component and is comparable to extrusion. The fabric method characteristics of the plastication stage determine the compound flow, a grouping of fabric physics, screw speed, back pressure, and shear, barrel temperature. The main goal is to create a uniform softening for the resulting phase of the process, regardless of where the cloth enters the mold. The back pressure, screw back temperature, and cylinder temperature are molding constraints that switch the plastication phase [12].

**Fig. 2** Cup design

### 3.1 Objectives

- To design a cup, plate and mold by AUTODESK fusion 360 software.
- To manufacture a polypropylene cup and plate by injection molding.
- To analyze properties of polypropylene material.

### 3.2 Product Design

#### 3.2.1 Cup

A cup is associate open-top instrumentation accustomed to hold liquids for running or drinking; whereas chiefly used for drinking, it can also be accustomed to store solids for running. Cups square measure used for termination thirst across a large vary of cultures and social categories and completely different kinds of cups could also be used for various liquids or in several things. Cups of various designs could also be used for various varieties of liquids or different foodstuffs, in several things, or for adornment. Cups square measure associate improvement on exploitation cupped hands or feet to carry liquids. Figure 2 shows the cup design [13].

#### 3.2.2 Mold

The phrases mold and die are commonly used to define the device used to make plastic components in molding. Molds are exclusive to produce, hence they were normally only used in fabrication where thousands of components was being made. Beryllium copper alloy, aluminium, pre-hardened steel, hardened steel, aluminium are common materials for molds [14]. The optimal of fabric to manufacture a mold out of is essentially one of economics, steel molds are normally additional expensive to concept, but their lengthier life covers the advanced original price over the next variety of components created formerly performing. Pre-hardened steel molds are fewer wear

resilient and are employed for lesser capacity needs or superior constituents, normal Rockwell-C hardness is 39–47.

### 3.2.3 Mold Structure

The injection mold, ejector plate, runner plate, and base plate are the first four components in the mold. Plastic resin goes in the mold over a gate or sprue within the injection mold, the purpose of the sprue bushing is to close warmly beside the needle of the injection barrel of the molding device and consent molten plastic to glide from the container into the mold, also identified as the hollow space. The molten plastic is directed to the hollow space photographs through channels by the sprue bushing. Because these stations consent plastic to run alongside them, they are known as runners. The melted plastic travels over the contender and into the empty area, passing through one or more specialized gates. A mold is normally built so that the precast element dependably stays on the ejector facet of the tube as it unlocks, and the sprue and runner are drawn out of the facet with the pieces. When the element is dislodged from the facet, it falls freely [15].

### 3.2.4 Mold Machining

Molds are made using dual common techniques, modern machining, and electric discharge machining. Injection molds have historically been constructed using standard machining in its traditional form. With technical advancements, CNC machining has become the primary way of producing additional intricate molds with further precise mildew information in less time than outdated procedures. The method not only allows for the creation of difficult-to-machine shapes, but it also allows for the creation of pre-hardened molds that do not require any heat treatment. Figure 3 shows the mold design and assembly [16].

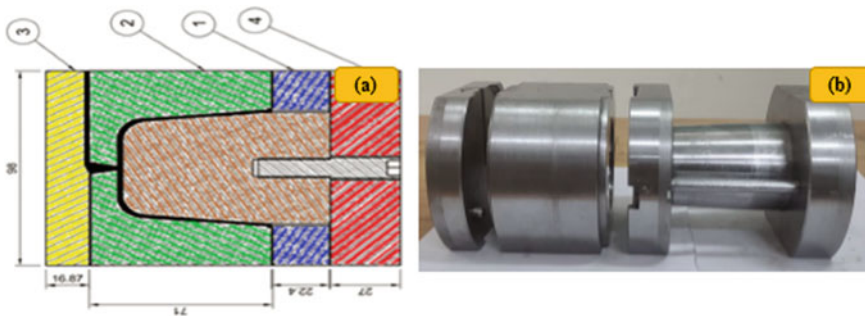


Fig. 3 a Mold design and b assembly



### 3.2.5 Base Plate

The clamp plates are used to connect the mold halves to the molding plates. Mold clamps are held in place by large bolts, while some machines employ magnets to keep mildew on the plates. The two parts of the tube must first be properly closed with the clamping device before the cloth can be injected into it. Each partial of the mildew is connected to the injection molding machine, with one half permissible to slide. The mildew splits are pushed calm by the hydraulically powered fastening unit, which uses enough pressure to keep the steel securely locked while the fabric is introduced. The quantity of period it takes to nearby and lock the gate depends on the machine, superior machineries those with more fastening services will take lengthier. The gasping cycle period of the gadget can be used to evaluate this period [17].

### 3.2.6 Ejector Plate

A series of pins or bars are used to push parts away from the core. The Ejector System is the name given to these series. After enough time has passed, the cooled section can be evacuated since the mold using the ejection apparatus, which is friendly to the rear half of the mold. When the mold is opened, a mechanism is used to force the part out of it. Because the item shrinks and adheres to the mold as it cools, it takes a lot of force to get it out. To aid in part ejection, a mold relief agent can be scattered over the outsides of the mold cavity earlier to measurable injection, after the part has been expelled, the mold can be clamped shut, permitting the subsequent shot to be injected [18].

### 3.2.7 Cavity or Mold Part

The sections of the mold where the part is molded into the required shape are known as cavities. Because molds must be balanced, only a fixed amount of cavitations are usually permitted. The cavity plate is made up of a hollow section where the object will be produced. To contest the precise dimension with the punch and cavity plate is off-centered. In direction to release the finishing product generated from the mold, the cavity plate will be separated into two sections [19].

### 3.2.8 Runner Plate

In a sprue, plastic runs via the sprue bushing, then to individual runners, which transport the material to the gates, which serve as the material's entry point into the individual cavities. It is possible to reground (chopped up) and reuse the sprue and runners. A hot runner system can be used to eliminate them [20].

## 4 Result and Discussion

Because raw materials are getting scarcer and more expensive, and energy costs are rising, the mold design approach should not only focus on cost reduction, but also on lowering source feasting and emissions over the course of its full life cycle. Injection molding presents four difficult defects like weld lines, warpage, sink marks shrinkage. In many circumstances, especially for parts with complex geometry, the development of them is unavoidable. Based on a survey of the literature, we can deduce that the majority of studies have focused on process parameters and product geometry [21]. It is simple to control faults by choosing the right geometry and settings. Process parameters can be changed at any point during the process, however other aspects such as mold design and material have cost and time constraints, whereas the use of a cooling passage can advance product quality while increasing cycle time and cost. Although the plastic injection molding process is complicated, by managing the process environment, the product can be manufactured with fewer faults [22].

Process parameters were discovered to play a significant function in the process through a literature review. Other post-process variables, such as mold/product form, size, and geometry, as well as machine setup, were not as critical as process parameters. Pneumatic injection molding for the manufacture of polymeric components in small sizes, the molding process in small scale industries is becoming increasingly important [23]. Because of its low cost and short cycle time, this technology has the potential to play a significant role in the polymeric industry in the near future. Traditional methods have a lower capacity of output. The capacity to process polymers with a variety of characteristics depend on the desired function. Several concerns must be defined as a result of this work, including the standardization of this procedure and the appropriate method to take based on component shape and polymers composite materials and additive manufacturing (3D printing) and Injection Molding can be done with a wide range of materials, such as elastomers, metals and most commonly, thermosetting and thermoplastic polymers [24–29]. However, in light of global competitiveness and the need for shorter manufacturing times, new manufacturing processes for tool production, such as Additive Manufacturing, have been investigated for injection moulding tools [30–40].

## 5 Conclusion

For the fabrication of polymeric components in small sizes, the pneumatic injection molding method in small scale productions is becoming more important. This technology has the potential to play a critical role in the polymer industry in the near future. The ability to process a wide range of polymers to accomplish the desired function. Several concerns must be defined as a result of this review, including the calibration of this procedure and the optimum method to take based on different part geometries and polymers. In this work in preference to making injection mold die for

a plastic cup, we conclude that, we are designing a product model of cup and plate by fusion 360 software, and also designing a mold for cup and plate by using CAD software AUTODESK Fusion 360. In this we are manufacturing a cup and plate products by injection molding. Many attempts are being made in this way. However, only a small percentage of them succeed, necessitating extra attention in this area. Because, according to this research, many faults emerge as a result of processing settings. As a result, processing parameter control is essential for product manufacture.

The hand injection mold component research work provided me with invaluable expertise in the design and production of a mold and cup. An actual execution of any action necessitates the cooperation of numerous departments. The tool's design begins with an abstract concept, which is subsequently translated into a full-fledged manufacturing drawing. It's also critical that the tool is made with all of the process's complexities in mind. The goal of the exercise is to obtain defect-free components that meet specifications and have built-in tool superiority in the most cost-effective manner possible. By raising the machine's holding pressure and holding time, the sink scratch start in the rib portion of the trial element was avoided. The research work was completed successfully after conducting a design exercise and selecting a plastic for the mold that had a good balance of strength and manufacturability. To improve the soundness of the gate, it's possible to engineer it. Meeting technical, financial, and delivery deadline criteria, the injection mold's design has been approved. The tool is designed and manufactured in-house.

## References

1. Datta S, Bandyopadhyay A, Kumar PP (2008) Grey-based Taguchi method for optimization of bead geometry in submerged arc bead-on-plate welding. *Int J Adv Manuf Technol* 39:1136–1143
2. Deng C-S, Chin J-H (2005) Hole roundness in deep-hole drilling as analyzed by Taguchi methods. *Int J Adv Manuf Technol* 25:420–426
3. Kim DS, Kim JS, Ko YB (2008) Experimental characterization of transcription properties of microchannel geometry fabricated by injection molding based on Taguchi method. In: *Microsystem technology*, vol 14, pp 1581–1588
4. Singh G, Sayad M (2019) Effect of injection moulding process parameter on warpage of using Taguchi method. *Int Res J Eng Technol (IRJET)* 6(11). e-ISSN: 2395-0056, p-ISSN: 2395-0072
5. Mohan Kumar T, Dhanasekar D, Chidambaram K, Anil Kumar S (2019) Optimization of process parameter in injection moulding using Taguchi method. *Int Res J Eng Technol (IRJET)* 6(5). e-ISSN: 2395-0056, p-ISSN: 2395-0072
6. Kiatcharoenpol T, Vichiraprasert T (2018) Optimizing and modeling for plastic injection molding process using Taguchi method. *IOP Conf Ser: J Phys: Conf Ser* 1026. <https://doi.org/10.1088/1742-6596/1026/1/012018>
7. Ramakrishna RK, Dr Mao K (2017) Minimization of shrinkage in injection molding process of acetal polymer gear using Taguchi DOE optimization and ANOVA method. *Int J Mech Ind Technol* 4(2):72–79. ISSN 2348-7593
8. Kale HP, Dr Hambire UV (2015) Optimization of injection molding process parameter for reducing shrinkage by using high density polyethylene (HDPE) material. *Int J Sci Res (IJSR)* 4(5). ISSN: 2319-7064

9. Tidke YP, Dhote AV, Dr Patil CR (2014) Study and optimization of process parameters in plastic injection moulding—a review. *Int J Res Appl Sci Eng Technol (IJRASET)* 2(IV). ISSN: 2321-9653
10. Jain K, Kumar D, Kumawat S (2013) Plastic injection molding with Taguchi approach—a review. *Int J Scien Res (IJSR)* 2(5). ISSN No: 2277-8179
11. Madhukumar K, Sampathkumar L, Nataraj MN, Kumarswamy R (2015) Design of plastic injection mould tool for air filter box bottom cover. *Int J Modern Trends Eng Res* 2(4)
12. Zhou J, Li L, Hu Y, Yang J, Cheng K (2011) Plastic mold design of topcover of out-shell of mouse based on CAE. *Int J Adv Control Eng Inf Sci*
13. Shinde P, Patil SS, Kulkarni SS. Design and development of plastic injection mold for auto component. *Int J Scien Res Manage Stud (IJSRMS)* 2(3)
14. Iftekhar Hussain B, Safiulla M, Ali M, Suresh G (2014) Injection mould tool design of power box side panel. *Int J Inno Res Sci Eng Technol* 3(2)
15. Praveena BA (2021) IOP Conf Ser: Mater Sci Eng 1013:012004
16. Praveena BA (2021) IOP Conf Ser: Mater Sci Eng 1013:012006
17. Yadav SPS et al (2022) Development of 3D printed electromyography controlled bionic arm. In: Srinivasa Pai P, Krishnaraj V (eds) Sustainable machining strategies for better performance. Lecture notes in mechanical engineering. Springer, Singapore. [https://doi.org/10.1007/978-981-16-2278-6\\_2](https://doi.org/10.1007/978-981-16-2278-6_2)
18. Santosh Kumar DS, Praveen BA, Kiran AS, Kempaiah UN (2015) Development of pineapple leaf fibre reinforced epoxy resin composites. *IRJET* 2(03):2190–2193
19. Patil SS, Praveen BA, Kempaiah U, Adarsha H (2017) Fabrication and characterization of Kevlar/jute reinforced epoxy. *Int Res J Eng Technol* 4(9):1441–1444
20. Praveena BA, Shetty BP, Akshay AS, Kalyan B (2020) Experimental study on mechanical properties of pineapple and banana leaf fiber reinforced hybrid composites. *AIP Conf Proc* 2274:030015. <https://doi.org/10.1063/5.0022381>
21. Praveena BA, Balachandra PS, Sachin B et al (2020) Physical and mechanical properties, morphological behaviour of pineapple leaf fibre reinforced polyester resin composites. *Adv Mater Process Technol* 2020. <https://doi.org/10.1080/2374068x.2020.1853498>
22. Singha G, Verma A (2016). A brief review on injection moulding manufacturing process. In: Proceedings of international conference of materials processing and characterization (materials today: proceedings), pp 1423–1433
23. Yi-Qi W, Jae-Gyu K, Jung-II S (2013) Optimization of plastic injection molding process parameters for manufacturing a brake booster valve body. *J Mater Des* 56:313–317
24. Dimla DE, Camilotto M, Miani F (2005) Design and optimisation of conformal cooling channels in injection moulding tools. *J Mater Process Technol* 164:1294–1300
25. Singh Yadav SP, Lakshmikanthan A, Ranganath S, Gowdru Chandrashekarappa MP, Anand PB, Shankar VK, Avvari M (2022) Effect of pin geometry and orientation on friction and wear behavior of nickel-coated EN8 steel pin and Al6061 alloy disc pair. In: advances in materials science and engineering, vol 2022, Article ID 3274672, p 16. <https://doi.org/10.1155/2022/3274672>
26. Joseph K, Jangam S, Ramesha K, Umesh V, Kumar GV, Santhosh N, Shankar G, Razak A, Afzal A, Praveena BA (2022) Design and optimization of the process parameters for fusion deposition modelling by experimental and finite element approach, *AIP Conference Proceedings* 2421, 040004. <https://doi.org/10.1063/5.0076809>
27. Praveen B, Abhishek SU, Shetty PB, Sudheer Reddy J, Praveena BA (2022) Industry 4.0 researchers computer numerical control machine tool to manufacture calligraphy board. In: Shetty NR, Patnaik LM, Nagaraj HC, Hamsavath PN, Nalini N (eds) Emerging research in computing, information, communication and applications. Lecture Notes in Electrical Engineering, vol 790. Springer, Singapore. [https://doi.org/10.1007/978-981-16-1342-5\\_15](https://doi.org/10.1007/978-981-16-1342-5_15)
28. Lokesh N, Praveena BA, Reddy JS, Vasu VK, Vijaykumar S (2021) Evaluation on effect of printing process parameter through Taguchi approach on mechanical properties of 3D printed PLA specimens using FDM at constant printing temperature. *Mater Today: Proc.* <https://doi.org/10.1016/j.matpr.2021.11.054>

29. Praveena BA, Buradi A, Santhosh N, Vasu VK, Hatgundi J, Huliya D (2021) Study on characterization of mechanical thermal properties machinability and biodegradability of natural fiber reinforced polymer composites and its applications recent developments and future potentials: a comprehensive review. *Mater Today: Proc.* <https://doi.org/10.1016/j.matpr.2021.11.049>
30. Praveena BA, Lokesh N, Buradi A, Santhosh N, Praveena BL, Vignesh R (2021) A comprehensive review of emerging additive manufacturing (3D printing technology): methods materials applications challenges trends and future potential. *Mater Today: Proc.* <https://doi.org/10.1016/j.matpr.2021.11.059>
31. Moulya HV, Vasu VK, Praveena BA, Rajesh M, Ruthuparna SA, Rahul K (2021) Study on acoustic properties of polyester—fly ash cenosphere/nanographene composites. *Mater Today: Proc.* <https://doi.org/10.1016/j.matpr.2021.11.052>
32. Nagaraja S, Kodanda R, Ansari K, Kuruniyan MS, Afzal A, Kaladgi AR, Aslfattahi N, Saleel CA, Gowda AC, Bindiganavile Anand P (2021) Influence of heat treatment and reinforcements on tensile characteristics of aluminium AA 5083/silicon carbide/fly ash composites. *Mater* 14(18):5261. <https://doi.org/10.3390/ma14185261>
33. Aftab SG, Faisal A, Hussain H, Sreedhara B, Babu NR, Praveen BA (2021) Structural analysis of human femur bone to select an alternative composite material. *Mater Today: Proc.* <https://doi.org/10.1016/j.matpr.2021.08.197>
34. Vinayaka N, Akshaya C, Praveena BA, Praveen Kumar UB, Marulasiddeshi HB (2021) Study of supercritical airfoil aerodynamics at various turbulence intensities and mach numbers in transonic regime. *High Technol Lett* 27(8):1–11
35. Praveena BA, Kumar SV, Manjunath HN, Sachin B, Yadav SP, Lochan BR, Kumar GA, Reddy JS (2021) Investigation of moisture absorption and mechanical properties of natural fibre reinforced polymer hybrid composite. *Mater Today: Proc* 45:8219–8223. <https://doi.org/10.1016/j.matpr.2021.04.254>
36. Praveena BA, Balachandra P, Vinayaka S, Srikanth N, Shiv HV, Yadav SP, Avinash L (2020) Mechanical properties and water absorption behaviour of pineapple leaf fibre reinforced polymer composites. *Adv Mater Process Technol* 1–16. <https://doi.org/10.1080/2374068X.2020.1860354>
37. Praveena BA, Mudabbir Ahmed MD, Kedambadi V, Kempaiah UN (2018) The design, optimisation and analysis of office chair base, based on the European standards. *Int J Mech Prod Eng Res Dev* 8(8)
38. Anilthota HG, Praveena BA (2017) Processing and characterization of green composites using sisal and palm fibers. *Int J Eng Sci Comput IJESC* 4262–4265
39. Harish HV, Santhosh N, Srikanth HV, Praveena BA, Patil A, Shivashankar P (2014) Optimum design of conical draft tube by analysis of flow using CFD simulation, *Ijltemas, III (Vii)*, pp 99–103
40. Santhosh N, Vinayaka N, Aswatha MU, Praveena BA (2013) Computational analysis and design for precision forging of aluminium AA 6061 connector. *Int J Comput Eng Res* 3(9):1–8

# Accurate Computation of Transverse Shear Stresses in Smart Composite Plates



T. Das and J. K. Nath

**Abstract** An efficient layerwise laminate theory is used to accurately compute the transverse shear stresses in smart composite plates. Constitutive relations have been used for their computation instead of the post processing technique involving the integration of three-dimensional equations of equilibrium. The displacement field is obtained by superposing two local expressions with a global expression. Quadratically varying layerwise function is used to express the non-linear electric potential along the thickness of each layer. The boundary conditions for continuity of displacements and transverse shear stresses at all laminar interfaces together with shear free conditions on the lateral surfaces have been satisfied by the theory. Governing equations of equilibrium do not dependent on the number of layers in the plate. Accuracy of the proposed theory has been established by comparing the bending responses with three-dimensional piezoelectricity solutions and other shear deformation theories.

**Keywords** Efficient laminate theory · Global–local theory · Smart composite plate

## 1 Introduction

Smart composite structures are made by integrating a few smart piezoelectric layers with the passive composite layers. Such structures possess the capability of offering superior characteristics such as low specific weight, high specific stiffness and high specific strength. In addition to mechanical load bearing capability, these structures can also be equipped with actuation and sensing capability through the surface bonded or embedded piezoelectric layers. Complex state of stress is produced inside these structures in response to the applied electromechanical loading. Computation of the deformation and the resulting stress field, especially the accurate computations of transverse shear stresses, requires the use of advanced and accurate shear deformation theories.

---

T. Das (✉) · J. K. Nath  
Siksha 'O' Anusandhan Deemed to be University, Bhubaneswar, Odisha 751030, India  
e-mail: [tapaswineedas@soa.ac.in](mailto:tapaswineedas@soa.ac.in)

© The Author(s), under exclusive license to Springer Nature Singapore Pte Ltd. 2023  
P. Pradhan et al. (eds.), *Recent Advances in Mechanical Engineering*,  
Lecture Notes in Mechanical Engineering,  
[https://doi.org/10.1007/978-981-16-9057-0\\_9](https://doi.org/10.1007/978-981-16-9057-0_9)

In addition to the conventional equivalent single layer theories, many advanced shear deformation theories have been developed which have been proved to be accurate, efficient and involve less computational expenses. It is seen in the three-dimensional piezoelectricity solutions [1] that there exist no discontinuity in the through-thickness profiles of displacements and transverse stresses. Moreover, the profiles are not smooth at the layer interfaces. Thus, any shear deformation theory developed for the laminated smart plates should be able to produce slope discontinuity in these entities at all interfaces. The layerwise theories (LWT) [2, 3] inherently produce slope discontinuity, since they have been formulated by the use of layered approximations for the displacement components and piecewise linear electric potential functions. These theories are, however, computationally expensive and have inability to calculate transverse stresses from constitutive equations. Zigzag theories [4–6] presented by several researchers are efficient layerwise theories and possess high accuracy as well as high efficiency.

Accurate computations of transverse shear stresses have been possible by these theories, not from constitutive equations, but from the integrations of three-dimensional equations of equilibrium. Superposition-based [7] global–local theories are capable of computing transverse shear stresses directly from constitutive equations in addition to accurate computation of all displacement and stress components. Bending responses have been obtained in the cross-ply laminated piezoelectric plates [8] by using a triangular finite element based on the global–local theory. The theory has been observed to violate the non-zero transverse shear conditions on the lateral surfaces in presence of the applied or induced inplane electric field. Moreover, the theory has no capability to address the additional transverse displacement produced due to the electric potential.

In this work, the global–local theory of Nath and Kapuria [9] is used to study the electromechanical bending responses in smart laminated plates. The responses have been compared with other shear deformation theories and analyzed by considering thick plates of different length-to-width ratios. Formulation of the theory is briefly discussed in the next section.

## 2 Formulation

As described in the Ref. [9], by grouping the stresses, strains, electric field terms and their coefficients into the inplane and transverse parts, the reduced constitutive equations for the state of generalized plane stress for any orthotropic piezoelectric laminated cross-ply plate are

$$\begin{aligned} \sigma &= \bar{Q}\varepsilon - \bar{e}_3^T E_s, \quad \tau = \hat{Q}\gamma - \hat{e}E \\ D &= \hat{e}^T \gamma + \hat{\eta}E, \quad D_s = \bar{e}_3 \varepsilon + \bar{\eta}_{33} E_s \end{aligned} \quad (1)$$

where

$$\sigma = \begin{bmatrix} \sigma_x \\ \sigma_y \\ \tau_{xy} \end{bmatrix}, \quad \varepsilon = \begin{bmatrix} \varepsilon_x \\ \varepsilon_y \\ \gamma_{xy} \end{bmatrix}, \quad \bar{Q} = \begin{bmatrix} \bar{Q}_{11} & \bar{Q}_{12} & 0 \\ \bar{Q}_{12} & \bar{Q}_{22} & 0 \\ 0 & 0 & \bar{Q}_{66} \end{bmatrix}, \quad \bar{e}_3 = [\bar{e}_{32} \ \bar{e}_{32} \ 0],$$

$$\hat{e} = \begin{bmatrix} \hat{e}_{15} & 0 \\ 0 & \hat{e}_{24} \end{bmatrix}, \quad \tau = \begin{bmatrix} \tau_{zx} \\ \tau_{yz} \end{bmatrix}, \quad \gamma = \begin{bmatrix} \gamma_{zx} \\ \gamma_{yz} \end{bmatrix}, \quad \hat{Q} = \begin{bmatrix} \bar{Q}_{55} & 0 \\ 0 & \bar{Q}_{44} \end{bmatrix}, \quad E = \begin{bmatrix} E_x \\ E_y \end{bmatrix},$$

$$D = \begin{bmatrix} D_x \\ D_y \end{bmatrix}, \quad \hat{\eta} = \begin{bmatrix} \hat{\eta}_{11} & 0 \\ 0 & \hat{\eta}_{22} \end{bmatrix}$$

$\sigma_x, \sigma_y, \tau_{xy}$  are inplane stresses;  $\varepsilon_x, \varepsilon_y, \gamma_{xy}$  are inplane strains;  $\bar{Q}_{11}, \bar{Q}_{12}, \bar{Q}_{22}, \bar{Q}_{66}, \bar{Q}_{44}, \bar{Q}_{55}$  are reduced stiffness coefficients;  $\tau_{zx}, \tau_{yz}$  are transverse shear stresses;  $\gamma_{zx}, \gamma_{yz}$  are transverse shear strains, respectively. The expressions for reduced coefficients can be found in Ref. [9]. The reduced coefficients  $\bar{Q}_{ij}, \hat{e}_{ij}$  and  $\hat{\eta}_{ij}$  are functions of thickness coordinate  $z$ . Such a stress state refers to zero transverse normal stress and non-zero transverse shear stress in the laminated plate. The laminated piezoelectric plate of thickness  $h$  is assumed to contain  $L$  orthotropic layers and its midplane is the reference  $xy$ -plane. Electromechanical load is applied on the top and bottom surfaces.

The non-linear distribution of the electric potential in each piezoelectric layer is represented by hypothetically dividing each piezoelectric layer into certain number of sublayers and using a piecewise quadratic function as given in the Ref. [9]. The assumed displacement field is

$$u = [u_0 - zw_{0d} + z\psi_0 + z^2\xi + z^3\eta] + [\zeta_k u_1^k + \zeta_k^2 u_2^k] + [\zeta_k^3 u_3^k] \quad (2)$$

$$w = w_0 - \bar{\psi}_\phi^j(z)\phi^j - \bar{\psi}_{\phi c}^q(z)\phi_c^q \quad (3)$$

The column matrices

$$u_0 = \begin{bmatrix} u_{0x} \\ u_{0y} \end{bmatrix}, \quad w_{0d} = \begin{bmatrix} w_{0,x} \\ w_{0,y} \end{bmatrix}, \quad \psi_0 = \begin{bmatrix} \psi_{0x} \\ \psi_{0y} \end{bmatrix}, \quad \xi = \begin{bmatrix} \xi_x \\ \xi_y \end{bmatrix}, \quad \eta = \begin{bmatrix} \eta_x \\ \eta_y \end{bmatrix}$$

which appear inside the expression of  $u$  are functions of plate inplane coordinates  $(x, y)$ .  $w_0$  is the midplane deflection of the laminate and  $\psi_\phi^j(z)$  is the linear interpolation function used for sublayerwise linear variation of electric potential  $\varphi^j$  at  $n_\phi$ .  $\bar{\psi}_\phi^j(z)$  is obtained using the integration  $\bar{\psi}_\phi^j(z) = \int_0^z d_{33}^j \psi_{\phi,z}^j(z) dz$ . The transverse displacement component  $w$  is non-linear due to the presence of piecewise linear and quadratic functions, and  $\zeta_k$  is the local thickness coordinate that varies from  $-1$  to  $+1$  in each layer.

The layered description of the displacement field is now made layer independent by using following boundary conditions: (1) displacements and transverse shear stresses are continuous at all interfaces, and (2) transverse shear stresses are zero on the top and bottom surfaces. The inplane displacement field comes out a polynomial of degree 3 given by



$$u = u_0 - zw_{0d} + R^k(z)\psi_0 + \overline{R}^k(z)u_1^0 + \hat{R}^k(z)u_2^0 + \tilde{R}(z)u_3^0 + R^{kj}(z)\phi_d^j \quad (4)$$

The final displacement field given in Eq. (4) is expressed in terms of reference plane variables  $u_0, w_{0d}, \psi_0, u_1^0, u_2^0, u_3^0$ , in addition to the set of electric potential variables  $\phi_d^0$  across the composite Plate. The coefficients  $R^k(z), \overline{R}^k(z), \hat{R}^k(z), \tilde{R}^k(z), \overline{R}^{kj}(z)$  are  $2 \times 2$  matrices of cubic functions of thickness coordinate.

Application of the principle of virtual work yields following governing equations

$$\begin{aligned} N_{x,x} + N_{xy,y} &= 0, & N_{xy,x} + N_{y,y} &= 0 \\ M_{x,xx} + 2M_{xy,xy} + M_{y,yy} + F_5 &= 0, & P_{x,x} + P_{yx,y} - Q_x &= 0 \\ P_{xy,x} + P_{y,y} - Q_y &= 0, & \overline{P}_{x,x} + \overline{P}_{yx,y} - \overline{Q}_x &= 0 \\ \overline{P}_{xy,x} + \overline{P}_{y,y} - \overline{Q}_y &= 0, & \hat{P}_{x,x} + \hat{P}_{yx,y} - \hat{Q}_x &= 0 \\ \tilde{P}_{xy,x} + \tilde{P}_{y,y} - \tilde{Q}_y &= 0, & \tilde{P}_{x,x} + \tilde{P}_{yx,y} - \tilde{Q}_x &= 0 \\ \tilde{P}_{xy,x} + \tilde{P}_{y,y} - \tilde{Q}_y &= 0, & \tilde{Q}_{x,x} + \tilde{Q}_{y,y} + \tilde{H}_{x,x}^q + \tilde{H}_{y,y}^q - \tilde{G}^q &= 0 \\ S_{x,xx}^j + S_{xy,xy}^j + S_{yx,xy}^j + S_{y,yy}^j - \overline{Q}_{x,x}^j - \overline{Q}_{y,y}^j - H_{x,x}^j - H_{y,y}^j + G^j - F_6^j &= 0 \end{aligned} \quad (5)$$

Governing equations for the present formulation given in Eq. (5) are a set of thirteen equations stated in terms of the stress and normal resultant

$$N_x, N_y, N_{xy}, M_x, M_y, M_{xy}, P_x, P_y, P_{xy}, Q_x, Q_y, Q_{xy}, \overline{P}_x, \overline{P}_y, \overline{P}_{xy}, \hat{P}_x, \hat{P}_y, \hat{P}_{xy}, \tilde{P}_x, \tilde{P}_y, \tilde{P}_{xy}, \overline{Q}_x, \overline{Q}_y, \hat{Q}_x, \hat{Q}_y, \tilde{Q}_x, \tilde{Q}_y$$

Details of these resultants are given in Ref. [9]. Application of the virtual work principle has also yielded the boundary conditions, but they are not given here for brevity. The governing equations are now solved for simply supported plates by using analytical Navier's technique. Stress components and electric field entities are then obtained by using the constitutive equations (Eq. 1).

### 3 Results and Discussion

A three layered plate having two PZT-5H piezoelectric layers as outer layers and the middle layer of isotropic aluminum alloy is considered. Thickness of each PZT-5H layer is  $0.1 h$  and that of the middle layer is  $0.8 h$ . Mechanical properties of aluminum alloy A12024-T3 are:  $E = 73$  GPA,  $\nu = 0.33$ . The second laminated plate has single PZT-5H layer as its top layer and four layers of fiber graphite-epoxy material as the elastic substrate. The lay-up of the elastic substrate is  $[90^\circ/0^\circ/90^\circ/0^\circ]$  from bottom to top and has thicknesses  $0.225 h/0.225 h/0.225 h/0.225 h$ . The thickness of PZT-5H layer is  $0.1 h$ . PZT-5H layer is poled in the thickness direction. The properties of fiber

graphite-epoxy material (Mat.1) and those of PZT-5H are given in Ref. [10]. The zigzag local theory (ZLT) [11] and the zigzag theory (ZIGT) [11] have been compared with the present theory. The transverse shear stresses are computed directly from the constitutive equations in all these two-dimensional theories.

Two load cases are considered. (1) Mechanical load  $-p_0 \sin(\pi x/a) \sin(\pi y/b)$  is applied on the top surface. All piezoelectric surfaces and piezoelectric interfaces are kept in electrical short circuit condition. (2) Potential load  $\phi_0 \sin(\pi x/a) \sin(\pi y/b)$  is applied on the top surface. The other piezoelectric surface and the piezoelectric layer interfaces are in short circuit condition.

The displacements and stresses have been non-dimensionalized as

$$\begin{aligned}
 (\bar{u}, \bar{w}) &= (u, w/S)1000E_0/aS^3 p_0, (\bar{\sigma}_x, \bar{\sigma}_y, \bar{\tau}_{yx}, \bar{\tau}_{zx}, \bar{\tau}_{yz}) \\
 &= (\sigma_x/S^2, \sigma_y/S^2, 10\tau_{yx}/S^2, \tau_{zx}/S, \tau_{yz}/S)/p^0
 \end{aligned}$$

where  $a$  is width of the plate and  $S$  is aspect ratio. These non-dimensionalized entities have been used in interpretation of results through all tables and figures.

Distributions obtained under mechanical and potential load cases have been plotted in the Fig. 1 for the thick square aluminum alloy smart plate. In spite of identical transverse displacement profiles, present theory is seen to predict highly

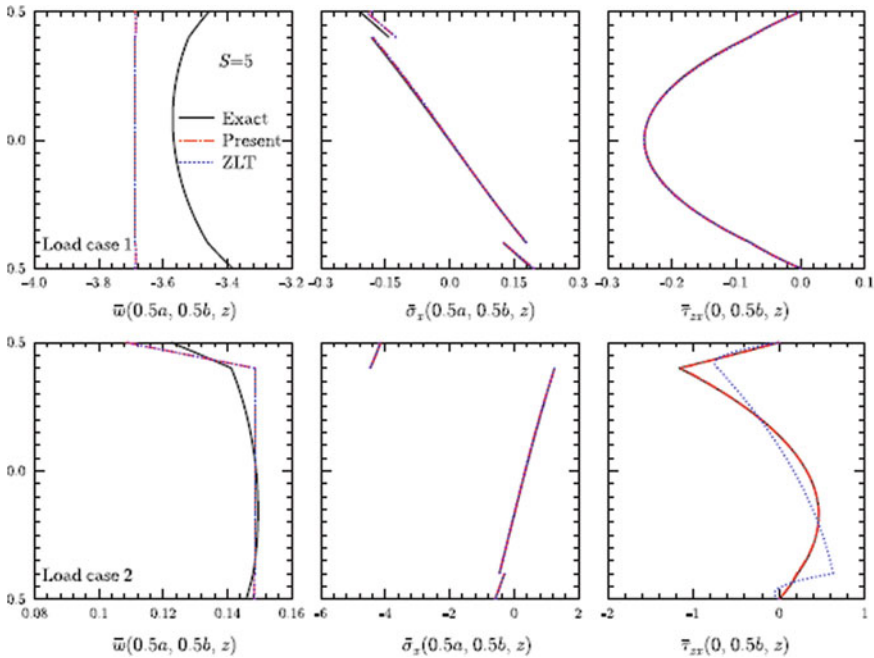


**Fig. 1** Through-thickness distributions of  $\bar{w}, \bar{\sigma}_x$  and  $\bar{\tau}_{zx}$  for metallic composite plate under mechanical and potential load

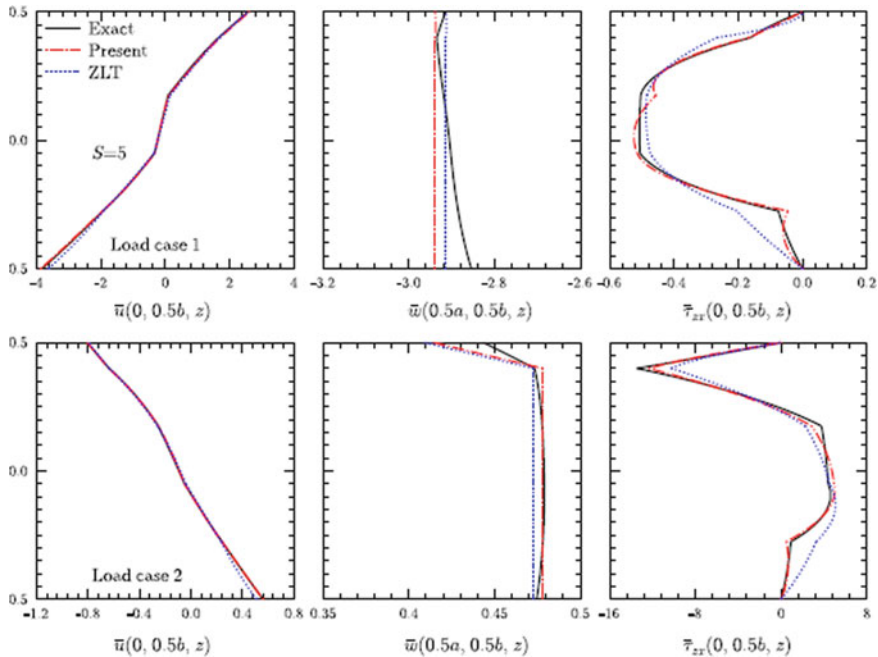


**Fig. 2** Through-thickness distributions in hybrid [90/0/90/0/p] composite plate under mechanical and potential load

accurate transverse stress profile than the ZLT under the potential load case 2 though both theories have yielded their identical profiles under mechanical load case 1.

The Fig. 2 gives the through-thickness plots in the thick square graphite-epoxy hybrid composite plate under pressure and potential load. A slight variation from the exact solution is observed for the transverse shear stress. This establishes the accuracy of the present theory.

The effect of the aspect ratio  $S$  on the response prediction in thick to thin plates is analyzed by subjecting the 3 layered smart plate to mechanical load and potential load. The responses are shown in Tables 1 and 2 for the respective loads. As the smart plate becomes thinner, the non-dimensionalized deflection decreases and hence the transverse shear stress increases under both the applied loading conditions. Both the present theory and the ZLT yield decreasing error with increasing thinness. Under potential loading, the errors produced by the ZLT for transverse shear stresses remains well above 30% even in the thin plate, whereas the errors produced by the present theory are  $\leq 1.33\%$  in the thick smart plate.

Responses in smart plates of different lengths have been analyzed by considering different length-to-width ratio  $b/a$  for the thick 3 layered smart plate. As is seen in Tables 3 and 4, with increase in the length of the plate, its mid plane deflection increases. At the same time, the transverse shear stress  $\tau_{zx}$  increases but  $\tau_{yz}$  decreases. Under the mechanical loading, the errors produced by both theories are of comparable

**Table 1** Effect of the aspect ratio  $S$  in 3 layer rectangular plate ( $b/a = 2$ ) under mechanical load

Entity	$S = 5$			$S = 10$			$S = 20$		
	3D exact	Present (% Error)	ZLT (% Error)	3D exact	Present (% Error)	ZLT (% Error)	3D exact	Present (% Error)	ZLT (% Error)
$\bar{u}(-0.5h)$	-12.290	1.41	1.41	-12.205	0.34	0.34	-12.181	0.08	0.08
$\bar{u}(0.5h)$	11.816	5.48	5.48	12.080	1.37	1.37	12.149	0.35	0.35
$\bar{w}(0)$	-8.6179	2.19	2.19	-7.9679	0.58	0.58	-7.8041	0.15	0.15
$\bar{\tau}_{yz}(0)$	-0.1948	0.13	0.13	-0.1956	0.03	-0.17	-0.1959	0.01	-0.24
$\bar{\tau}_{zx}(0)$	-0.3897	0.13	0.13	-0.3915	0.03	-0.17	-0.3919	0.01	-0.24

**Table 2** Effect of the aspect ratio  $S$  in 3 layer rectangular plate ( $b/a = 2$ ) under potential load

Entity	S = 5			S = 10			S = 20		
	3D exact	Present (% Error)	ZLT (% Error)	3D exact	Present (% Error)	ZLT (% Error)	3D exact	Present (% Error)	ZLT (% Error)
$\bar{u}(-0.5h)$	0.2325	-0.65	-1.51	0.2363	-0.19	-0.40	0.2372	-0.05	-0.10
$\bar{u}(0.5h)$	-0.5082	0.62	0.22	-0.4964	0.18	0.07	-0.4934	0.04	0.02
$\bar{w}(0)$	0.2360	-0.23	-0.23	0.2333	-0.06	-0.06	0.2326	-0.01	-0.02
$\bar{\tau}_{yz}(0.4h)$	-0.5872	-1.32	-37.93	-0.5919	-0.34	-37.15	-0.5931	-0.08	-36.95
$\bar{\tau}_{zx}(0.4h)$	-1.1743	-1.33	-37.94	-1.1838	-0.34	-37.17	-1.1861	-0.08	-36.96

**Table 3** Effect of the length-to-width ratio in 3 layer rectangular thick plate ( $S = 5$ ) under mechanical load

Entity	Theory	$b/a = 1$	$b/a = 2$	$b/a = 3$	$b/a = 5$	$b/a = 10$
$\bar{u}(-0.5h)$	3D exact	4.5402	11.816	15.001	17.149	18.194
	Present (% Error)	8.72	5.48	4.87	4.56	4.43
	ZT (% Error)	8.73	5.48	4.87	4.55	4.43
$\bar{w}(0)$	3D exact	-3.5676	-8.6179	-10.785	-12.238	-12.943
	Present (% Error)	3.36	2.19	1.96	1.84	1.79
	ZT (% Error)	3.36	2.19	1.96	1.18	1.79
$\bar{\tau}_{yz}(0)$	3D exact	-0.2426	-0.1948	-0.1461	-0.0937	-0.0482
	Present (% Error)	0.22	0.13	0.12	0.11	0.10
	ZT (% Error)	0.38	0.13	0.08	0.06	0.05
$\bar{\tau}_{zx}(0)$	3D exact	-0.2426	-0.3897	-0.4387	-0.4688	-0.4828
	Present (% Error)	0.22	0.13	0.12	0.11	0.11
	ZT (% Error)	0.38	0.13	0.09	0.06	0.05

**Table 4** Effect of the length-to-width ratio in 3 layer rectangular thick plate ( $S = 5$ ) under potential load

Entity	Theory	$b/a = 1$	$b/a = 2$	$b/a = 3$	$b/a = 5$	$b/a = 10$
$\bar{u}(-0.5h)$	3D Exact	-0.3236	-0.5082	-0.5697	-0.6076	-0.6251
	Present (% Error)	0.89	0.62	0.56	0.53	0.51
	ZT (% Error)	0.29	0.22	0.21	0.20	0.19
$\bar{w}(0)$	3D Exact	0.1489	0.2360	0.2651	0.2829	0.2912
	Present (% Error)	-0.35	-0.23	-0.20	-0.19	-0.19
	ZT (% Error)	-0.34	-0.23	-0.20	-0.19	-0.19
$\bar{\tau}_{yz}(0.4h)$	3D Exact	-1.1667	-0.5872	-0.3919	-0.2353	-0.1177
	Present (% Error)	-2.07	-1.32	-1.18	-1.10	-1.07
	ZT (% Error)	-38.53	-37.93	-37.82	-37.76	-37.73
$\bar{\tau}_{zx}(0.4h)$	3D Exact	-1.1667	-1.1743	-1.1757	-1.1764	-1.1767
	Present (% Error)	-2.07	-1.33	-1.18	-1.11	-1.07
	ZT (% Error)	-38.53	-37.94	-37.83	-37.77	-37.74

magnitudes. Under potential loading, however, the ZLT yields much higher errors in the stresses than the present theory at all length-to-width ratios.

## 4 Conclusions

Static responses in smart composite plates have been studied by using a global–local theory under the applied electromechanical loads. The governing equations have been derived using the principle of virtual work and solved for simply supported rectangular laminated smart plates. The constitutive equations have been used to obtain the stresses. The stresses have been obtained with high accuracy. The superposition principle and the cubic assumption employed for the electric potential has resulted in very accurate computations of all the response entities. Present theory has yielded much improved accuracy in the bending responses than the zigzag local theory which has been formulated over similar approximations but with two single-term local groups.

## References

1. Kapuria S, Dumir PC, Sengupta S (1999) Three-dimensional solution for shape control of a simply supported rectangular hybrid plate. *J Therm Stresses* 22:159–176
2. Tang YY, Noor AK, Xu K (1996) Assessment of computational models for thermoelectroelastic multilayered plates. *Comput Struct* 61:915–933
3. Saravanos DA, Heyliger PR, Hopkins DA (1997) Layerwise mechanics and finite element for the dynamic analysis of piezoelectric composite plates. *Int J Solids Struct* 34:359–378
4. Kapuria S (2004) A coupled zig-zag third-order theory for piezoelectric hybrid cross-ply plates. *J Appl Mech* 71:604–614
5. Kapuria S, Achary GGS (2005) A coupled zigzag theory for the dynamics of piezoelectric hybrid cross-ply plates. *Arch Appl Mech* 75:42–57
6. Kapuria S, Achary GGS (2006) Electromechanically coupled zigzag third-order theory for thermally loaded hybrid piezoelectric plates. *AIAA J* 44:160–170
7. Li X, Liu D (1997) Generalised laminate theories based on double superposition hypothesis. *Int J Numer Meth Eng* 40:1197–1212
8. Zhen W, Wanji C (2007) Refined triangular element for laminated elastic-piezoelectric plates. *Compos Struct* 78:129–139
9. Nath JK, Kapuria S (2013) Global-local and zigzag-local theories for direct transverse shear stress computation in piezolaminated plates under thermal loading. *Int J Mech Sci* 75:158–169
10. Nath JK, Kapuria S (2012) Coupled efficient layerwise and smeared third order theories for vibration of smart piezolaminated cylindrical shells. *Compos Struct* 94:1886–1899
11. Kapuria S, Nath JK (2009) Efficient laminate theory for predicting transverse shear stresses in piezoelectric composite plates. *AIAA J* 47:3022–3030

# Firmware of Indigenous and Custom-Built Flexible Robots for Indoor Assistance



Debanik Roy 

**Abstract** Customization of the design and firmware of higher-order flexible robots is highly challenging due to its inherent parameters related to real-time vibration. The field of *Flexible Robotics* is a niche ensemble of harnessing non-linearity in dynamics of the robotic system(s). The chapter delineates prime design issues for the indigenous firmware of serial-chain higher-order flexible robots having more than one link, interfaced with a miniature gripper. The chapter will bring forward hardware prototype of two such flexible robotic systems meant for indoor assistance, besides schematic designs for another two types of flexible robots.

**Keywords** Flexible robot · Vibration · Dynamics · Sensor · Hardware · Mini-gripper · Instrumentation

## 1 Introduction

The development of working prototype of flexible robotic systems (FRS) is instrumental in bringing out the issues pertaining to its ready deployment in several social and non-manufacturing sectors. However, indigenous firmware of FRS is often customized, in order to suit the requirement for indoor assistive services, e.g. patients and elderly persons. The facets of rheology (stress–strain paradigms), randomized vibration, sensory instrumentation and non-linear coupled dynamics are some of the paradigms that need extended research in a synergistic way.

It is well-known that despite having a big advantage of very low self-weight, the major bottleneck towards deployability of FRS lies with its perpetual trembling of the sub-assemblies, including the end-of-arm tooling (gripper). The origin of this inherent vibration pertains to internal stress/strain, and it is structure-independent as well as design-invariant. This very signature of natural vibration of FRS is quantitatively ascertained through two facets, viz. modal frequency and Eigen value. In fact,

---

D. Roy (✉)

Division of Remote Handling and Robotics, Bhabha Atomic Research Centre and Homi Bhabha National Institute, Department of Atomic Energy, Mumbai, India  
e-mail: [deroy@barc.gov.in](mailto:deroy@barc.gov.in)



due to multi-dimensionality of the workspace of the FRS, we do observe chronological built-up of trembling of the slender links and, at times, shaking of the link-joint interface zone.

We will present here a couple of novel design metrics for a prototype FRS towards combating the inherent vibration, without getting cluttered with sensory instrumentation. This is, indeed, a sort of paradigm shift in the design for manufacturing of multi-degrees-of-freedom FRS, as it calls for precision manufacturing aided by miniaturization at specific sub-assemblies. These design metrics are fully indigenous grassroots level onward that caters for a wide range of customization as and when assistive service is needed by the indoor inhabitant(s). These design features of the prototype FRS will be elaborated in three domains, namely: (a) improvisation in the design of revolute joints; (b) mechanical transmission of power drive and (c) counter-balancing mechanism.

The paper will present an overview on seven novel designs of FRS, conceptualized with full indigenous effort. Out of these designs, five have been realized in the form of working prototype as on date. Among the remaining two designs, one is under preliminary stage of manufacturing, while the second is at design finalization stage. We have used two forms of power transmission in the prototype FRS, viz. direct drive (where servomotors responsible for the motion of the FRS are placed at the joints directly) and loop-through drive (wherein drive gets transmitted mechanically). While the maiden working prototype was made with direct drive system, the next three of the working prototypes in chronological order had hardware via loop-through drive. The recent-most prototype of the FRS is the most compact-volume FRS that we have manufactured so far, and in order to achieve the said compactness of the workspace, the prototype has been fabricated with direct-drive system. However, the partially manufactured FRS is getting fabricated with loop-through drive in order to maintain the synergy with one of its predecessors. The finalized design of the latest of our FRS family has been conceptualized via loop-through drive as well. All of these seven prototypes have been christened with abbreviated titles so as to demarcate a particular hardware of the developed FRS with ease. Chronologically, the prototypes are titled as: (1) DDFR (Direct Drive Flexible Robot); (2) FSFR-I (Flexible Shaft-driven Flexible Robot: Type I); (3) FSFR-II (Flexible Shaft-driven Flexible Robot: Type II); (4) PAR (Patient Assistant Robot); (5) FUMoR (Flexible Universal Modular Robot); (6) SAIPAR (Sensor Augmented Intelligent Patient Assistant Robot) and (7) FlexFAR (Flexible Feeding Assistant Robot). While DDFR and FUMoR are manufactured with direct-drive transmission, the rest of the prototypes are actuated with loop-through drive mechanism, namely via flexible shaft(s).

Prior to design of multi-degrees-of-freedom FRS, we must have a fool-proof dynamic model that is commensurate to the expected work-output of the system [1, 2]. Thus, we need to consider quantitative metrics for vibration attenuation with the help of dynamic model before the onset of the design for manufacturing of a FRS [3]. Extended modelling of the spring-mass tuple has been found to be very effective in establishing new dynamic model of FRS [4]. Several other poignant methodologies have been reported for the reduction of vibration and subsequent real-time control of the FRS [5–8].

We may appreciate that non-field trials on the real-time performance of uni-link flexible manipulator (mostly without gripper) have gathered a considerable momentum in recent past. A majority of these flexible manipulators have been used extensively to validate a variety of novel control strategies [9–11]. Nonetheless, grasp-based design of the multi-link FRS having near-compliant sub-assemblies as well as miniature gripper at the free-end, remains an open research domain till date.

We have investigated interesting scenarios of control dynamics for a multi-degrees-of-freedom FRS fitted with mini-gripper [12], aided by novel spring-structural model (for vibration signature of both manipulator-links and gripper) and strain gauge-induced model (for dynamic strain signature). Firmware of a multi-link serial-chain FRS using flexible shafts for drive motion of the joints has been developed by the author's group [13]. The complete design setup with modelling for real-time vibration as well as beta version of the hardware for a slender serial-chain three degrees-of-freedom flexible robot, meant for patient assistance, is described by the author [14].

It may be stated that experiment-based case study of the performance of the FRS-gripper amidst in situ vibration demands a synergistic coupling of two metrics: (a) optimization of design parameters of the FRS-gripper and (b) joint-space redundancy of a general serial-chain slender manipulator, such as FRS. Topology optimization-based modelling and novel hypothesis towards decision matrix for robotic grasp has been delineated [15]. On the other hand, novel theory and analytical model for joint-space redundancy of the serial-chain slender manipulator are reported [16]. Based on these earlier accomplishments, a new theology on deformation and deflection for the time-specific adjudgement of natural frequency of vibration will be presented here.

The paper has been organized in six sections. An overview of the possible design variations and mechanical system of the serial-chain FRS is presented in the next section. Section 3 reports the hardware manifestation of the five flexible robot prototypes, highlighting the criticalities of fabrication of the mechanical assemblies. The finalized design facets of the rest two FRS, undergoing manufacturing, is described in Sect. 4. Section 5 addresses the generalized facets of the development of the controller of the FRS, and finally, concluding remarks have been made in Sect. 6.

## 2 Serial-Chain Flexible Robot: Design Paradigms and Overview

Design ensemble of serial-chain FRS has been refined over the years with novel research paradigms. The gamut encompasses the following ten facets: (i) cross-section of the link: {circular; rectangular; square}; (ii) design morphology of the slender link: external metrics {straight; tapered and stepped-section} and internal metrics {solid; hollow}; (iii) material of construction of the link: {type; density; Young's Modulus}; (iv) design features of the joint: {type; mating pairs; alignment:

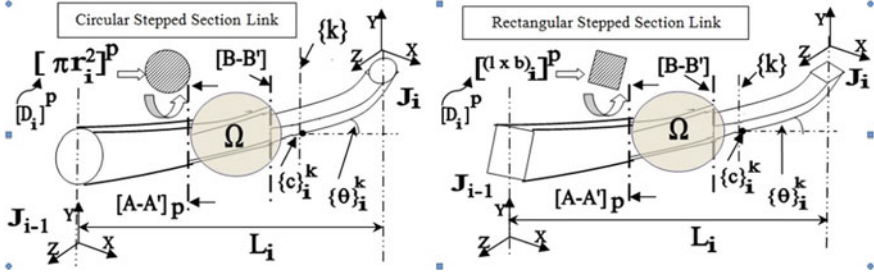


**Fig. 1** Schematics of the major design ensemble of serial-chain FRS with stepped cross-section of the links

sub-assembly}; (v) actuation of the joints: {servomotor}; (vi) drive mechanism: {direct-to-joint; via flexible shaft}; (vii) end-of-arm attachment: {tip-mass; end-effector; mini-gripper}; (viii) design features of the mini-gripper: {type; external envelope; material of manufacturing; motion of jaw; sub-assembly}; (ix) sensory layout: {type; location; interfacing; instrumentation} and (x) design of base/housing: {tripod; cuboidal; tracked support}. It is crucial to note that the vibration and/or rheological features of the FRS do alter under two situations of end-of-arm attachment, viz. end-/tip-mass vis-à-vis a mini-gripper (at the distal link of the FRS).

Figure 1 schematically depicts the relevance of major design entities of serial-FRS, as stated in (i) and (ii) above. Two types of possible cross-section of the FRS-links, namely circular and rectangular, are shown in Fig. 1 for a single-link FRS-arm having stepped section, as detailed under sections A – A' and B – B' (inclusive of the zone of stepping:  $\Omega$ ).

With reference to the design-facets of Fig. 1, the common features are: (i) variation of link cross-section at different transverse sections, e.g. section [A – A']<sub>p</sub> and (ii) variation in link inclination as 'instantaneous measure of flexibility' at different locations of the link, e.g.  $\{c_i\}^k$ . Mathematically, for N-link FRS we can state using proportionality constants  $\xi$  and  $\lambda$  where  $L_{A-A'}$  signifies the length of the link from the joint-location  $J_{i-1}$  to the location of A – A' section-plane:

$$[D_i]^p = \xi \cdot \langle L_{A-A'} \rangle_p \|i \quad \forall i \in N, \quad p \subset (J_{i-1}, J_i) \quad (1)$$

and

$$\{\theta_i\}^k = \lambda \cdot \langle L_c \rangle_k \|i \quad \forall i \in N, \quad k \subset (J_{i-1}, J_i) \quad (2)$$

where  $L_i$  is the horizontal span and  $\{\theta_i\}^k$  is the inclination of the link, which is also a measure of flexibility at the  $k$ th vertical plane. The measure of taper of the link is being indexed as  $\{c_i\}^k$  at the  $k$ th vertical plane.

Irrespective of the type of cross-section of FRS-link, we need to focus on the design morphology to factor out the effect of in situ vibration of the FRS during its

operation. Here, the sub-group, *straight* can be conceptualized as a special case of *tapered* type with uniform cross-section throughout. Likewise, the *stepped* type link is another modification of *tapered* type. The common features of these designs are: (i) variation of link cross-section at different transverse sections, e.g. section  $[A - A']_p$  (sectional area:  $[D_i]^p$ ) and (ii) variation in link inclination as ‘instantaneous measure of flexibility’ at different locations of the link, e.g.  $\{c_i\}^k$ . Besides Eqs. 1 and 2, the model will now have an additional contribution, as texted below:

$$[D_i]^{q+1} < [D_i]^q \quad \forall i \in N, \forall p = 1, 2, \dots, q, (q + 1), \dots, n \quad (3)$$

and

$$\{\theta\}_i^{s+1} \neq \{\theta\}_i^s \quad \forall i \in N, \forall k = 1, 2, \dots, s, (s + 1), \dots, n \quad (4)$$

where ‘q’ and ‘s’ denote any intermediate location on the link and interim inclination of the link, respectively.

It may be noted that Eqs. 1 and 3 are related to the variations in cross-sectional area for each link of the FRS due to tapering, in contrast to Eqs. 2 and 4 that are related to link inclination. It is important to figure out the overall inclination of the serial-chain FRS (having ‘N’ links) at a particular time-instant. The gross inclination (drooping) of N-link FRS can be modelled as:

$$\langle \theta \rangle_{FRS}^t = \max[\{\theta_i\}, \{\theta_{i+1}\}, \dots, \{\theta_{i+q}\}]^t \quad \forall i \in N, q = 1, 2, \dots, (N - i) \quad (5)$$

where  $\langle \theta \rangle_{FRS}^t$  signifies the overall drooping of the FRS at time ‘t’, which is numerically equal to the maximum of the inclinations of the individual links. This drooping of the FRS gets realized through the end-deflection of the FRS, i.e. at the end-effector/gripper. Figure 2 schematically illustrates this concept of end-drooping of the FRS, fitted with: (a) end-mass; (b) end-effector and (c) gripper. ( $W_i$ : weight of the end-mass/gripper with payload; B: object to be gripped. Rest of the nomenclatures are identical to that of Fig. 1).

The inherent trembling of the FRS-links and, subsequently, the deflection/drooping of the links and end-effector are the prime-most design factor from

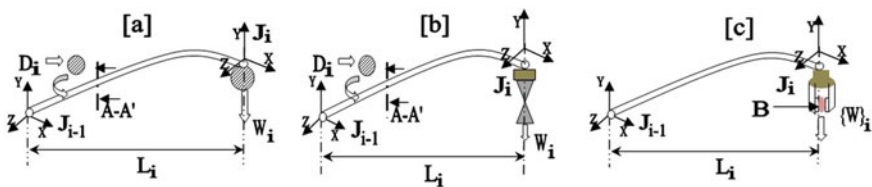
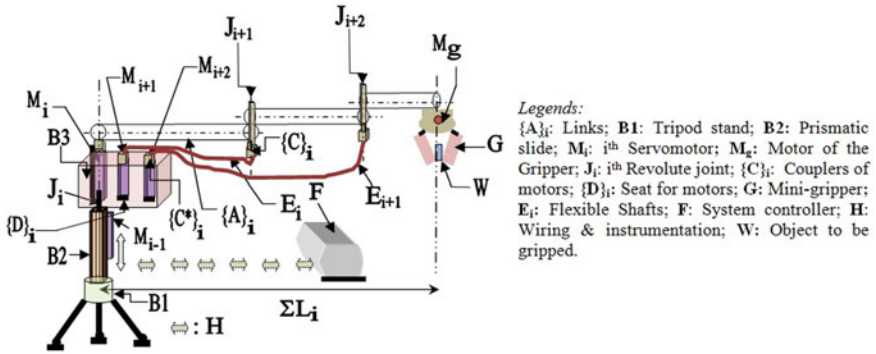


Fig. 2 Schematics of ‘end-drooping’ for a single-link FRS fitted with: a end-mass; b end-effector and c gripper



**Fig. 3** Ensemble schematic of the indigenously developed FRS hardware driven by loop-through drive mechanism

control system standpoint. As the phenomenon of ‘end-drooping’ is largely related to the transmission mechanism of the FRS, it remains as the prime-most design decision on whether to go for direct-drive type FRS or loop-through drive type. Both of the mechanisms have pros and cons, so depending upon the application scenario, we need to take a final call on the incorporation of the transmission system for the prototype FRS. Figure 3 illustrates the ensemble schematic of the indigenously developed three-link three-degrees-of-freedom FRS (with mini-gripper), actuated via loop-through drive (flexible shaft-driven mechanism). The developed prototype is manufactured and assembled through four sub-assemblies, namely: (i) base and tripod; (ii) link and joints; (iii) miniature gripper and (iv) drive system and controller. The prismatic slide, B2, was positioned on the tripod and was being actuated through re-circulating ball screw-nut mechanism having linear movements along vertical Z-axis. The motion of B2 helps the FRS to achieve the desired planar location as per the end requirement.

The design of joint plays a crucial role in the overall modelling and hardware manifestation of planar serial-chain FRS. Our prototypes of FRS have necessarily incorporated extended ‘pin’-type revolute joints, with added efficiency in some cases. These FRS-joints are assembled from elements like rotating shaft, miniature ball bearings, end-covers and housing and in few cases, a gear-train (worm-worm wheel or spur), with additional emphasis on the design of the link-joint interface.

The design models, vide Eqs. 1–5, are evaluated always with forced vibration type boundary condition. In other words, it was ensured that following two types of technical envelopes get satisfied during the process of finite element analysis (FEA)-based simulation and also the animation via computer-aided design: (i) presence of sufficient payload at the gripper (for robust force closure) and (ii) interfacing of adequate number of strain gauges over the exterior of the links of the flexible robots (for estimating deflection in real-time).

The ensemble design of the flexible manipulators and subsequent FEA of the models have been attempted by considering the following assumptions, namely: (i)

complete isotropy of the materials of manufacturing in all three axes of rotation ( $X, Y, Z$ ); (ii) ‘pin’-type rotational motion of the revolute joints of the FRS; (iii) full rigidity of the base and tripod mechanism so that the FEA-models behave in true *cantilever* mode and (iv) linear relationship between the strain gauge outcome and the deflection (in situ deformation) of the flexible links. These assumptions are essentially universal by nature for any standard FEA for real-time simulation.

### 3 Indigenous Hardware of Five Prototypes of Flexible Robot

We will describe the salient aspects of the indigenously developed hardware of five prototypes of FRS in chronological manner in this section, namely: DDFR, FSFR-I, FSFR-II, PAR and FUMoR. Although transmission mechanisms are not alike, all of these prototypes bear synergy being serial-chain FRS. The hardware development of the final prototypes was boosted up through FEA-based simulation of the design alternatives. In all of these five working prototypes, we have successfully integrated miniature gripper at the free-end with the manipulator-hardware, having three uniform cross-section links of unequal length.

#### (A) DDFR: Direct Drive Flexible Robot

The prototype DDFR was manufactured with a horizontal span of 1.5 m, assembled via three links, made of hollow carbon fibre-reinforced plastic (CFRP) tubes, having lengths of 800 mm, 400 mm and 200 mm, respectively. Being ‘direct-to-joint’ type drive, miniature servomotors (Make: Faulhaber™: integrated with gear-box and encoder) were placed at the revolute joint itself. The overrun protection of the prototype DDFR was achieved through multiple limit switches for each servomotor in both. Figure 4 shows the photographic view of the working prototype of DDFR in assembled condition (as a collage of three pieces, ‘a’, ‘b’ and ‘c’, to be seen from left to right in clockwise sense).

The design of DDFR is fool-proof, so far its basic planar layout and horizontal spanning are concerned. But, on the flip side, the hardware has not appreciable control

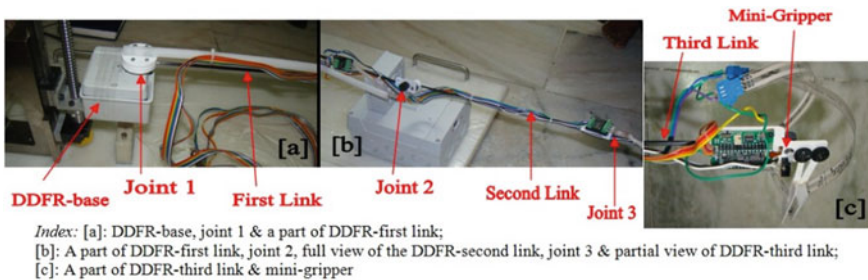


Fig. 4 Prototype of direct drive flexible robot in assembled condition

over the impending vibration. In fact, continuous shaking of the links becomes a prominent bottleneck of DDFR due to the incorporation of servomotors at the link-joint interface causing extra tare weight. As per our novel design of the FRS-base, the ensemble unit of DDFR was mounted on a tailor-made mechanism beneath the base, having translational motion to position the FRS at the desired horizontal plane (not shown in Fig. 4). The mechanism was created from two sub-assemblies, viz. tripod stand and prismatic slide (refer B1 and B2 of Fig. 3). The gripper of DDFR has a unique design for the jaws, besides size miniaturization (length: 70 mm; breadth: 20 mm; width: 12 mm.). As seen in Fig. 4c, the jaw-plates of the mini-gripper are heavily customized with non-standard dimensions and material as well. In fact, design of these jaw-plates along with two linkage mechanisms on either side of the jaw-plates is the crux of the prototyping. The controller circuitry board of the mini-gripper is attached with the adapter plate of the gripper, housing two miniature spur gears.

(B) *FSFR-I: Flexible Shaft-driven Flexible Robot—Type I*

The prototype FSFR-I was fabricated with two links and one interim revolute joint that was driven by indigenously designed and developed flexible shaft. The horizontal span of FSFR-I was limited to 1 m, in order to observe the efficacy of the transmission of drive via flexible shaft. There was no gripper attached in the prototype as our intention was to perform experiments on the dexterity and movability of the links and joints. The servo-motors were placed at the bottom (base of the robot) and those were subsumed in tripod assembly. Figure 5 presents the photographic view of the developed prototype of FSFR-I (made in two phases). It may be noted that the base was equipped with additional revolute joint (refer ‘joint 1’ of Fig. 5a).

The phase-I hardware of the prototype FSFR-I was accomplished in three functional modules, namely (a) fabrication of the links, (b) manufacturing of the revolute joint assemblies and (c) construction of the base assembly having basic tripod mechanism. In order to get an insight to the fabrication process, we decided to manufacture the links using steel as technology of machining of steel is well-known. Likewise, revolute joints were fabricated using aluminium just to ensure lightweight assembly. The base assembly was made with various ad hoc features devoid of ergonomics as

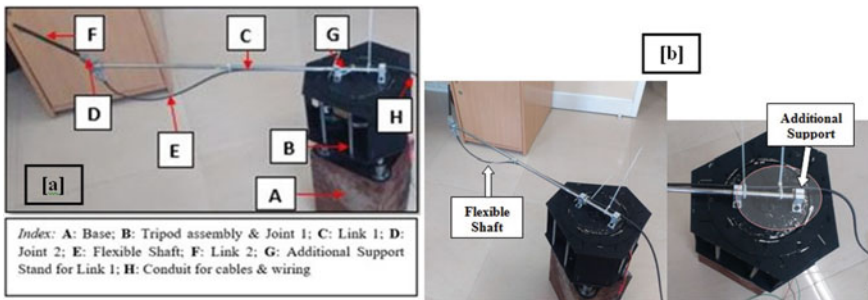
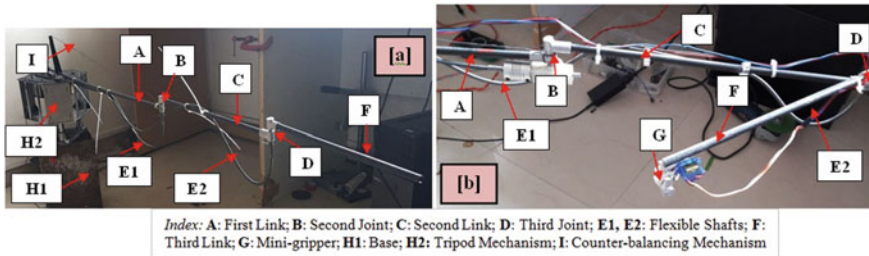


Fig. 5 Prototyping of flexible shaft-driven flexible robot—type I: a phase I; b phase II





**Fig. 6** Prototype of flexible shaft-driven flexible robot—type II: **a** overall layout; **b** zoomed view

well as aesthetics. Since the base assembly did not exist in DDFR, we decided not to make the tripod mechanism in its full form (i.e. height adjustment), as our prime intention for this phase of the hardware was to ensure smooth jerk-free planar motion of the two-link flexible manipulator with customization of the flexible shaft.

The phase-II hardware of FSFR-I was made with more design investigation on the indigenously fabricated additional support for the first link towards preventing unwarranted sagging. This phase was critical as well as decisive for an understanding of the nature of natural frequency of vibration of a flexible shaft-driven FRS. Figure 5b illustrates the partial hardware, with inset view on the disposition of two additional collar-and-boss type supports.

*(C) FSFR-II: Flexible Shaft-driven Flexible Robot—Type II*

FSFR-I was made primarily for physical validation of the performance of two-linked flexible manipulator system. The experience gathered therefrom led us to the development of the type II of FSFR, links of which were made up of CFRP tubes. FSFR-II had three links, interspaced by two revolute joints, having nearly the same dimensions of the earlier prototype, DDFR. The mini-gripper was also interfaced in this hardware in order to ensure better concentration over the real-time grasp by the FRS, besides control dynamics of the links and joints. The photographic view of FSFR-II hardware, fitted with counter-balancing mechanism, is shown in Fig. 6.

It may be noted that we have introduced the preliminary form of counter-balancing mechanism in this hardware as it was felt crucial for harnessing the in situ vibration of the slender three-link FRS. The process of improvisation from ‘collar and boss-type dual support’ (refer Fig. 5b) to ‘prop and wire-driven counter-balancing mechanism’ (refer Fig. 6a) is a big hardware leap towards combating vibration. The effect of this innovative mechanism was proven to be highly effective in the subsequent prototypes. This prototype was also instrumental in effective layouting and hardware interfacing of two long indigenously developed flexible shafts for the smooth transmission of power to the revolute joints (refer ‘B’ and ‘D’ of Fig. 6). The real-time performance of the prototype FSFR-II can be seen at: <https://youtu.be/P9-FrIKBBSM> and <https://youtu.be/4OZWxcAjlmk>.

In FSFR-II, we incorporated the following attributes, namely (a) streamlining the alignment of the flexible shafts; (b) improvisation of the second revolute joint with



worm–worm wheel pair (for improved dynamics); (c) betterment of the design of the counter-balancing mechanism and (d) physical augmentation of the mini-gripper at the end of the third link. Unlike joint designs, the base and tripod assembly (subsuming joint 1) of the FSFR-II is kept unaltered. The in situ trembling of FSFR-II was arrested to a large extent by streamlining the alignment of the flexible shafts by using re-oriented placement of the joint-servomotors. This is an important contribution of FSFR-II that has led to fine-tuning of the next prototype of our FRS.

(D) *PAR: Patient Assistant Robot*

The expertise gained through the hardware manifestation of FSFR-I and FSFR-II was instrumental in detailing out the next sojourn for building up the PAR (*beta version*), using lightweight CFRP tubes having more strength to weight ratio for the construction of the links. Besides, we could attain a successful realization of the novel design of the revolute joint with worm–worm wheel mechanism. The development of ‘PAR: beta version’ was empowered with the following attributes, namely (a) improvisation of the both second and third revolute joint with worm–worm wheel mechanism; (b) professional look for the tripod mechanism and improvement of the base assembly and (c) betterment of cable routing and allied instrumentation. Based on our finding in FSFR-II hardware, worm–worm wheel mechanism was added to both second as well as third revolute joint of prototype PAR for better control over real-time operational dynamics along with superior grasp and vibration harnessing. Figure 7 presents the photographic view of the prototype PAR. The working prototype PAR was successfully tested for a varieties of gripping actions in real-time, with objects of different dimensions (refer *youtube* video of the prototype ‘PAR’ at: <https://youtu.be/Nwbt94E8Tds>).

A substantial upgradation of the base assembly as well as ensemble tripod stand was carried out in PAR prototype, which played a crucial role in combating the vibration through the smooth and controlled functioning of the tripod stand. It may be noted here that the backbone of the prototype PAR is the tripod sub-assembly, comprising of a customized recirculating ball screw-nut mechanism, which sustains all the tare weight of the ensemble system and allows jerk-free up and down motion.

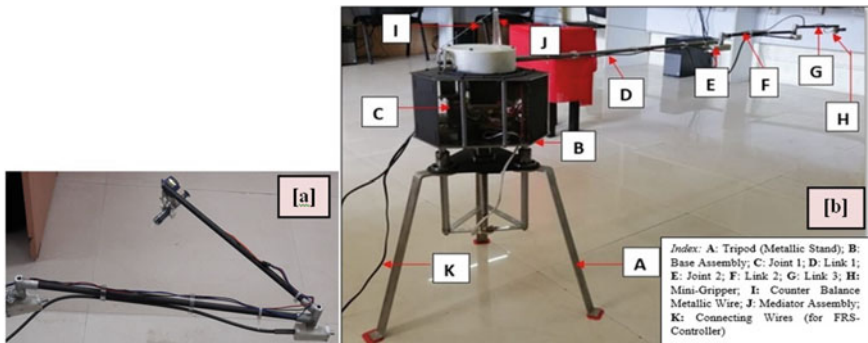
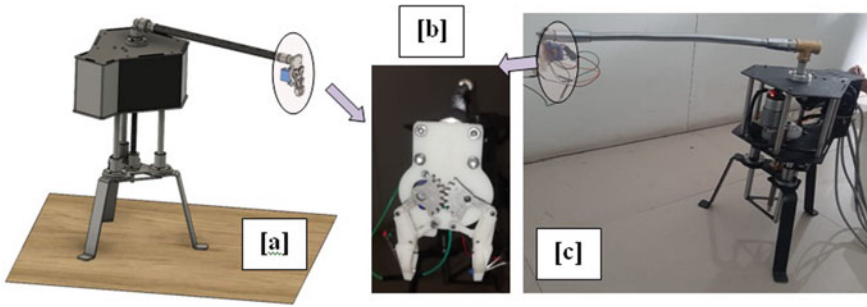


Fig. 7 Prototype of patient assistant robot: **a** zoomed view of links; **b** overall disposition



**Fig. 8** Prototype of flexible universal modular robot: **a** CAD view; **b** hardware of mini-gripper; **c** final prototype

The importance of this ball screw mechanism is envisaged in easy manoeuvrability of the entire FRS as per end-application of patient assistance in healthcare centre.

(E) *FUMoR: Flexible Universal Modular Robot*

With the advent of our expertise in prototyping multi-link FRS, we have brought in the concept of modularity in the hardware. FUMoR is the first on this kind of mono-link flexible modular robot that uses a non-standard geometry of the link, namely gooseneck-styled. The prototype FUMoR has one gooseneck link, one custom-built revolute joint, end-connectors and adapters for fitting with the tripod base at one end and miniature gripper at the other end. Figure 8 presents the computer-aided design (CAD) and the fabricated version of the prototype FUMoR, with details of the miniature gripper.

## 4 Indigenous Design Schemes of Two New Flexible Robots

(A) *SAIPAR: Sensor Augmented Intelligent Patient Assistant Robot*

Based on our accomplishments with PAR: beta version, indigenous conceptualization of SAIPAR is made so as to pick and place a variety of small objects, especially required in healthcare environment. The proposed system will be able to serve patient(s) and can grip the required object precisely by using multiple force sensors fitted on its compact miniaturized gripper. The maximum horizontal reach of SAIPAR will be 1500 mm spanned in three unequal but identical cross-sectioned tapered links in totality. The instrumentation with four different types of sensors, namely semiconductor strain gauges, flexi-force sensors, miniature load cells and infrared sensors is the prime-most contribution of SAIPAR ensemble. Rest of the components are similar to PAR, such as three revolute joints, two flexible shafts, a mini-gripper, a re-circulating ball screw, a tripod and electronics like servomotors, motion controllers and drivers. Figure 9 illustrates the design details of SAIPAR and its partial manufacturing, as completed till now (miniature gripper assembly).

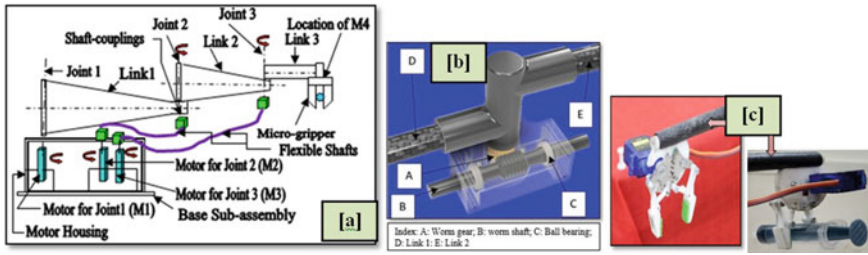


**Fig. 9** Design of SAIPAR: **a** layout; **b** zoomed view of revolute joint; **c** miniature gripper: post-manufacturing

The extreme two links of SAIPAR will be driven by worm gear-based revolute joints and powered by indigenously designed flexible shafts. These two flexible shafts will be coupled with respective motor shafts, fitted in the FRS-links.

**(B) FlexFAR: Flexible Feeding Assistant Robot**

With the advent of assistive robotics, a real need is generated to develop a custom-made semi-autonomous system that can pick daily required food stuffs and/or medicines for the senior citizens and can serve him/her on the bed/table as per the necessity. The proposed prototype of FlexFAR will be able to provide feeding assistance to the elderly person(s)/semi-patient(s)/differently-abled person(s) and can grip the required object precisely by using the sensors fitted on the compact miniaturized gripper of the robot. The prototype FlexFAR will have maximum horizontal reach of 1000 mm, spanned in three unequal but identical cross-sectioned gooseneck-style tapered links in totality. The exploded view of the proposed prototype of FlexFAR with gooseneck-styled links is presented in Fig. 10, highlighting horizontal span, ensemble link-length, three joints and three links. It also indicates the layout of the base assembly, housing the drive-motors. The decision on the designed value for the maximum horizontal reach of FlexFAR was arrived at by considering the physical space that would be available in a room as well as the relative ease of the elderly person to manoeuvre the robotic gadget in case of any eventuality or emergency.

One of the major technology hurdles in realizing multi-joint-type gooseneck-styled links with higher dexterity is the interfacing of flexible shafts. Since the inherent compliance of a gooseneck-styled link is much more than that of the standard non-metallic flexible link (e.g. made with CFRP), the proposed design of FlexFAR needs extra care for the fabrication and attachment of the revolute joint. The design of the said revolute joints of FlexFAR has been conceptualized with improvised ‘pin’-type design with a cylindrical boss around the ‘pin’.

The other salient design aspect of the prototype FlexFAR is modularity that ensures quick disassembly of the constituent members, viz. gooseneck links, joints and mini-gripper. Prototype FlexFAR will undergo substantial twist of the joints as significant part of the external load fraction will be concentrated on the revolute joints. The gripper of FlexFAR has been designed for force and form closure of grasp for a maximum payload of 800 g.

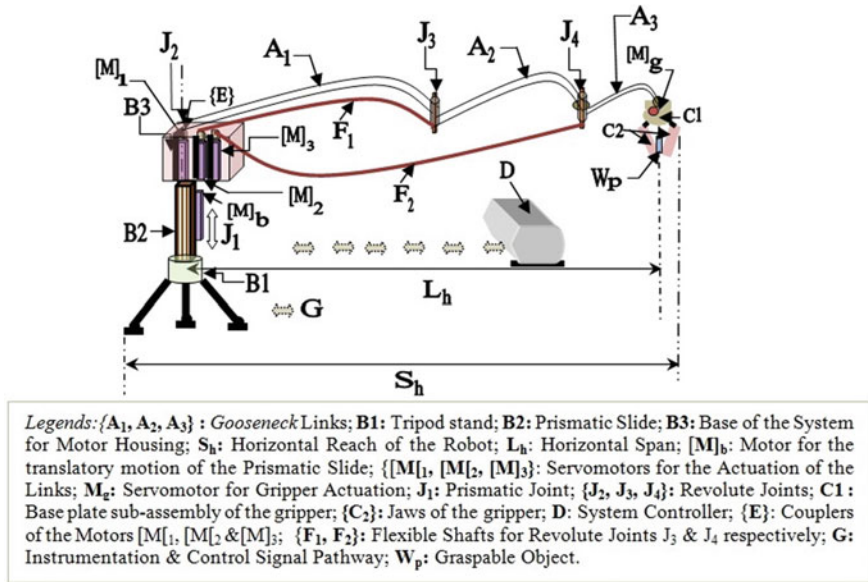


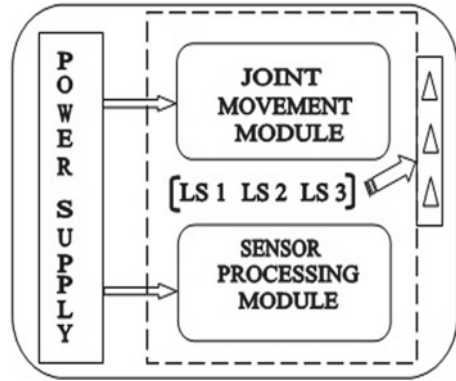
Fig. 10 Detailed schematic of the proposed prototype of flexible feeding assistant robot

## 5 Paradigms of Generalized Control System and Controller Facets of the Flexible Robots Developed

We have largely incorporated the traditional proportional-integral-derivative (PID) control as the matrix of the control system algorithm of the fabricated flexible robots. However, prototype flexible robots being tender, it felt necessary to incorporate current-based cut-offs and electronic limit switches for overrun protection of each servomotor in both directions. The generalized controller of the prototype FRS is a retrofit of Faulhaber™-make motion controllers (MCBL and MCDC series), operated through 12 V DC source. The power requirement design of the flexible robot has been made in such a manner so as to match for battery-based functioning as well, in cases of emergency. The individual motor controllers are interfaced with RS232C port of the computer, which makes the overall system user-friendly from operational stand-point. The controller is equipped with easy provision for disengagement of power supply unit as and when battery-based activation of the FRS is invoked. All controllers of the prototype FRS are designed and fabricated for indoor use, having relative humidity of the environment varying from 10 to 80%.

Although the model of the Faulhaber™ motor controllers are not all same, but the basic logic of operation is identical. All servomotors of the FRS as well as the tripod motor are controlled by Faulhaber™-Motion Manager Software. Figure 11 presents the general syntax schematic of the developed FRS-controller.

**Fig. 11** Syntax schematic of the developed controller of the prototype flexible robots



Functionally, the indigenously developed controller of the prototype flexible robots is constituted from four units, namely (I) Power Supply Unit (PSU); (II) Joint Movement Module (JMM); (III) Sensor Processing Module (SPM) and (IV) Limit Switch Unit (LSU: having a set of three units, viz. LS1, LS2 and LS3). While PSU is an integral part of the entire controller, LSU is mainly related to JMM. Except FUMoR, three limit switches of the LSU are located at the respective joint locations, i.e. those are affixed at different zones of the FRS (LS1 is being activated for joint 1 and so on). JMM consists of servomotor assemblies (motor, gear-box and encoder integrated) for all the three joints of the FRS. On the other hand, SPM takes care of strain gauges (for the joints) and flexi-force sensor (for the mini-gripper), with real-time calibration and settings. It is important to note that JMM and SPM are inter-correlated and both units are equally contributing towards smooth functioning of the FRS-controller in real-time. The PSU is made with two identical 12 V DC supplies inside the housing. Either of these two power supplies can be used to charge a 70 A-Hour battery, if needed.

The SPM is constituted of two types of sensory elements, namely (a) semiconductor-type high precision strain gauges (for the FRS-links) and (b) flexi-force sensors (for the FRS-gripper). So far as the output of SPM is concerned, strain gauges are being instrumented through Wheatstone bridge circuitries, while flexi-force sensors have got built-in bridge-balancing circuitry. Nonetheless, we need calibration of the sensor cells before final instrumentation, and it was carried out through multiple trials off-line.

The LSU of the prototype flexible robots takes care for unavoidable overrun of the joints in clockwise as well as counter-clockwise directions for protecting the servomotor of each link-joint sub-assembly. The LSU has been augmented with the FRS-controller quite effectively so that the individual limit switch gets triggered at the extreme ends of the links and mini-gripper.

## 6 Conclusions

The mechanical sub-assemblies of the prototype flexible robots were functional building blocks for the ensemble, and we could testify it too. On the other hand, ground testing of servomotors and sensor calibration and allied laboratory trials became pragmatic for the final assembly of the five prototype flexible robots towards full proofing the same. The chronology of indigenous research in flexible robotics has helped us to create a systematic procedure towards comprehending sensor data-driven modal frequencies of in situ vibration and real-time slip-free grasp of the flexible robots.

**Acknowledgements** Author gratefully acknowledges the financial assistance of Universidad Castilla La Mancha, Ciudad Real, Spain for the prototyping of DDFR. The financial support from Department of Atomic Energy, Govt. of India is acknowledged for developing flexible robot hardware of FSFR-I, FSFR-II and PAR. The research-project grant (SERB-CRG scheme) of Department of Science and Technology, Govt. of India is duly acknowledged for the fabrication of FUMoR-prototype.

## References

1. Chen W (2001) Dynamic modeling of multi-link flexible robotic manipulators. *Comput Struct* 79(2):183–195
2. Feliu V, Somolinos JA, Garcia A (2003) Inverse dynamics-based control system for a three degrees-of-freedom flexible arms. *IEEE Trans Robot Autom* 19(6):1007–1014
3. Singer NC, Seering WC (1990) Preshaping command inputs to reduce system vibration. *J Dyn Syst Meas Control Trans ASME* 112:76–82
4. Zhang J, Tian Y, Zhang M (2014) Dynamic model and simulation of flexible manipulator based on spring and rigid bodies. In: *Proceedings of the 2014 IEEE international conference on robotics and biomimetics ('ROBIO-2014')*, pp 2460–2464
5. Chen YP, Hsu HT (2001) Regulation and vibration control of an FEM-based single-link flexible arm using sliding-mode theory. *J Vibr Control* 7(5):741–752
6. Tjahyadi H, Sammut K (2006) Multi-mode vibration control of a flexible cantilever beam using adaptive resonant control. *Smart Mater Struct* 15:270–278
7. Trapero-Arenas JR, Mboup M, Pereira-Gonzalez E, Feliu V (2008) Online frequency and damping estimation in a single-link flexible manipulator based on algebraic identification. In: *Proceedings of the 16th Mediterranean conference on control and automation (IEEE)*, pp 338–343
8. Pereira E, Aphale SS, Feliu V, Moheimani SOR (2011) Integral resonant control for vibration damping and precise tip-positioning of a single-link flexible manipulator. *IEEE/ASME Trans Mech* 16(2):232–240
9. Feliu J, Feliu V, Cerrada C (1999) Load adaptive control of single-link flexible arms based on a new modeling technique. *IEEE Trans Rob Autom* 15(5):793–804
10. Canon RH, Schmitz E (1984) Initial experiments on the end-point control of a flexible robot. *Int J Rob Res* 3(3):62–75
11. Kotnick T, Yurkovich S, Ozguner U (1998) Acceleration feedback control for a flexible manipulator arm. *J Robot Syst* 5(3):181–196

12. Roy D. Control of inherent vibration of flexible robotic systems and associated dynamics. Lecture notes in mechanical engineering: recent trends in wave mechanics and vibrations, Springer, pp 201–222. ISBN: 978-981-15-0286; ISBN 978-981-15-0287-3 (eBook)
13. Warude P, Patel M, Pandit P, Patil V, Pawar H, Nate C, Gajlekar S, Atpadkar V, Roy D (2019) On the design and vibration analysis of a three-link flexible robot interfaced with a mini-gripper. Lecture notes in mechanical engineering: recent trends in wave mechanics and vibrations. Springer. ISBN: 978-981-15-0286, pp 29–46; Selected proceedings of the 8th National conference on wave mechanics and vibrations (“WMVC-2018”), Rourkela, India, Nov. 2018. <https://doi.org/10.1007/978-981-15-0287-3>
14. Roy D (2020) Design, modeling and indigenous firmware of patient assistance flexible robotic system-type i: beta version. *Adv Rob Mech Eng* 2(3):148–159
15. Bhelsaikar A, Atpadkar V, Roy D (2020) Design optimization of a curvilinear-jaw robotic gripper aided by finite element analysis. *Int J Mech Prod Eng (IJMPE)* 8(10):9–14
16. Jain T, Jain JK, Roy D (2021) Joint space redundancy resolution of serial-link manipulator: an inverse kinematics and continuum structure numerical approach. *Mater Today: Proc (Elsevier ScienceDirect)* 38(1):423–431

# Mechanical Properties Analysis of Kenaf–Grewia–Hair Fiber-Reinforced Composite



Sampath Boopathi , G. Venkatesan, and K. Anton Savio Lewis

**Abstract** In recent years, the demand for natural fiber-reinforced composite products is increasing in various industries such as automobiles, buildings, and aerospace applications. In this paper, fiber-reinforced composite material using epoxy resin matrix, kenaf, Grewia, and hair fibers has been produced by compression molding method to improve the mechanical properties such as tensile, flexural, and impact strengths. 400 g weight of composite material was made using different weights of natural fibers using Taguchi design of experiments. The weight of resin has been adjusted based on the mixing weights of three fibers. 16 specimens have been made by varying the weight of each fiber from 25 to 70 g as per the L16 orthogonal array to analyze each fiber's contributions on three mechanical properties. It was observed that the percentage of contribution of kenaf was higher than the other two fibers on flexural, tensile strength, and impact strengths of natural composite. It was also concluded that weight of hair fiber was also significantly paying to enhance both flexural and impact strengths.

**Keywords** Natural fiber · Reinforced composite · Kenaf · Hair · Grewia · Epoxy resin · Taguchi technique

---

S. Boopathi (✉)

Department of Mechanical Engineering, Muthayammal Engineering College (Autonomous), Rasipuram, Namakkal (Dt) 637408, Tamil Nadu, India  
e-mail: [boopasangee@gmail.com](mailto:boopasangee@gmail.com)

*Present Address:*

G. Venkatesan

Department of Mechanical Engineering, Haramaya Institute of Technology, Haramaya University, Diredawa, Ethiopia

*Present Address:*

K. Anton Savio Lewis

Department of Aeronautical Engineering, Noorul Islam Center for Higher Education, Thuckalay, Kumaracoil, Tamil Nadu 629180, India



## 1 Introduction

Nowadays, the industrial demands of the high strength to weight ratio of the material are improved. The use of fiber-reinforced polymer composites has been applied in aircraft, automobile, and civil construction sectors. And it was also utilized to make the protective types of equipment due to the low weight with environmental benefits. Natural fibers-reinforcement research has been increased on jute, luffa, bamboo, banana, and tree sources. It was noted that a significant development in the properties of alkali-treated EC fiber-reinforced composite while comparing with non-treated materials [1]. A study on fique-polyester mixed fiber composite was done to improve the ballistic strength. The outcomes were associated with the alignment of fiber layers with non-aligned composites [2]. The effects of the mixing percentage of Napier, hemp, and pineapple fiber with epoxy composites on the mechanical properties have been analyzed [3]. It has also revealed that the organic solutions treated kenaf fibers would improve the tensile strength compared with existing techniques [4]. The human hair and jute fibers in the resin matrix composite have been studied to decrease the absorption of moisture and to improve thermal stability [5]. The jute and human hair as a fiber have been used to make various automobile products such as seat backs, spare tire lining, door panels, cargo floor tray wood due to the high strength to weight ratio property [6]. It was investigated that the crack-free composite can be produced with significant improvement in the mechanical property by adding human and animal hair fiber-reinforcement process [7]. It was tried to use natural hair such as bird feathers and human hair as reinforcement in the composite and produced good bending and tensile strengths [8]. The twill and plain pattern of banana and kenaf fibers used in the composite had been increasing the mechanical strengths. It was also exposed that strength has been significantly improved by alkali and sodium sulfate treatments of fibers [9]. The enzyme-treated fibers (cellulose, xylanase enzyme, and pectinase) show a clear enhancement of properties of the composite related to preserved fiber [10]. The effect of sodium hydroxide-treated kenaf fiber investigated the adhesion properties of the composite materials. It was observed that the new composite will increase the flexural strength while relating with conventional epoxy-fibers composite [11]. The flexural properties of alfa fibers and polyester matrix composite are analyzed and associated with existing composites [12]. The mechanical properties of coir fiber and glass composite were studied with glass fiber composite due to the good gum connection of fibers and resin [13]. Numerous efforts have been made by researchers to study the many synthetic than natural fibers. It is observed from the aforementioned literature surveys that very few attempts tried to study the mixing effects on mechanical properties. Very few studies were conducted to observe the effect on natural, temperature, and mechanical behaviors [14]. In this study, the optimum weight of mixing Grewia, kenaf, and hair fibers had also been predicted to maximize the flexural, tensile, and impact strength for making natural composite products.

**Table 1** Mechanical properties of epoxy resin

Constituent	Viscosity (at 30 °C)	Density (at 30 °C)
Epoxy resin	10,000–12,000 mPa s	1.15–1.20 gcm <sup>-3</sup>
LY 556 (bisphenol-A)	10–20 mPa s	1.04 gcm <sup>-3</sup>

## 2 Experimental Method

### 2.1 *Materials Preparation, Treatments of Fibers, Composite Making*

The transparent resin and hardener were properly mixed with the ratio of 10:1 using the weight portion method. Its mechanical properties are shown in Table 1. The Grewia fibers are gathered from Grewia serrulata tree branches and extracted by four days immersing process. It has 60% of cellulose, 23% of hemicelluloses, and 18% Lignin. It is commercially used for making ropes, knots, bags, threads, baskets. Kenaf is a natural fiber extracted from the Hibiscus cannabinus plant which is refined in hot and sub-tropical regions. This fiber consists of 67% cellulose, 22% lignin, pectin, and other composition. The low weight and good tensile strength of hair can be collected from the local waste domain. The growing and kenaf fibers were composed and deep in water for four days. After pulling out from the stem, the fibers are drenched at room temperature by a wired brush. The fiber strands are manually spat into single strands with a length of 30 cm. At room temperature, the 2% of sodium hydroxide solutions were utilized to wash and immerse fiber into the solution in the sunlight for 4 days. The 0.8–1 cm length of natural fiber hair was prepared with good mechanical properties smoothness. Later, surface adhesive characteristics of fibers had been improved by the hot water sluicing process. The three cubic meter dimensions mold was furnished using a stainless-steel plate. The thinner solution and wax were applied to the mold cavity surface after the curing process. The hardener and resin were enthused and transferred into the mold cavity. The two layers of randomly mixed fibers were located over the resin. The curing process is initiated at 150 °C mold temperature. Later, the temperature is slowly cooled from 150 to 80 °C and constantly maintained for the next 45 min. After that, it was cooled to room temperature (30–35 °C). The 13 MPa pressure was constantly maintained during the curing process. The above-mentioned procedures were followed to make all 16 specimens.

### 2.2 *Tensile Strength, Flexural Strength, and Impact Strength Test of Composite Material*

The ASTM standard D3039 (25 cm × 1.5 cm × 0.15 cm) specimen was prepared to conduct the tensile test of composite sheets. The 100 KN load and 2 mm/min

crosshead speed rate were applied to conduct the experiments. The specimens were prepared as per the ASTM 7264 specimen (12 cm × 1.3 cm × 0.4 cm) to collect the observation results. The flexural test was done by three-point bend setup in UTM, and 10 mm length has been preserved between the two supports. The flexural strength of 16 specimens was calculated by Eq. (1).

$$\text{Flexural strength } \sigma_F = \frac{3FD}{(2bt^2)} \quad (1)$$

where  $F$ —Load in N,  $D$ —Span length in mm,  $b$ —Width in mm,  $t$ —Thickness in mm.

The specimen was prepared to conduct the impact test as ASTM-D-256 standard (6.35 cm × 1.27 cm × 1.27 cm) by the Izod impact testing machine. The impact strength of 16 specimens was calculated by Eq. (2) as follows.

$$I = \frac{E}{A} \quad (2)$$

where  $I$ —Impact strength in KJ/m<sup>2</sup>,  $E$ —Energy absorption by the material during fracture in KJ,  $A$ —Cross-sectional area for the specimen in mm<sup>2</sup>.

### 3 Design of Experiment Based on Taguchi Technique

The mechanical properties tests were conducted from 16 specimens using the L16 Taguchi orthogonal array. The L16 orthogonal array (four levels of each fiber) has been used to estimate the effects of the percentage of mixing fibers on tensile, flexural, and impact strengths [15–17]. Weight fractions of fibers and their levels are shown in Table 2. The weight of each fiber is varied from 25 to 75 g, and 25 g, 40 g, 55 g, and 70 g of each fiber are taken for conducting the experiments. The weight of each fiber is divided into 4 levels. The total weight of the composite of 400 g and resin weight have been modified based on Taguchi's design of fiber's weights. L16 orthogonal array was selected for 4 levels parameters using MiniTab® trial version software [18]. The tested results of tensile, flexural, and impact strength were shown in Table 3. Analysis of variance tests was done to estimate the null hypothesis for the results through trials [19]. For this analysis, the accepted level was elected as 95%. The

**Table 2** Weight fractions of fibers and their levels

Fibers (level)	1	2	3	4
K in grams	25	40	55	70
G in grams	25	40	55	70
H in grams	25	40	55	70

**Table 3** Taguchi L16 orthogonal array and responses

S. No.	Weight of resin (g)	Process parameters (g)				Mean		
		K	G	H	Total weight	T (MPa)	F (MPa)	I (kJ/mm <sup>2</sup> )
1	325	25	25	25	400	6.22	32.4	1.2
2	295	25	40	40	400	9.24	53.9	1.8
3	245	25	65	65	400	12.70	71.2	2.7
4	235	25	70	70	400	13.74	83.9	3.2
5	295	40	25	40	400	20.85	74.9	2.1
6	295	40	40	25	400	17.12	68.4	1.6
7	225	40	65	70	400	33.58	122.0	3.4
8	235	40	70	55	400	32.49	143.9	3.8
9	265	55	25	55	400	31.76	122.8	2.6
10	235	55	40	70	400	36.94	151.4	2.9
11	255	55	65	25	400	26.30	104.2	2.4
12	235	55	70	40	400	36.05	164.6	3.8
13	235	70	25	70	400	43.91	141.4	2.9
14	235	70	40	55	400	45.68	174.4	2.9
15	225	70	65	40	400	46.42	162.0	3.5
16	235	70	70	25	400	35.18	141.5	2.9

signal-to-noise (SN) ratio is used to forecast the optimum combinations of fiber's weight. Usually, the SN ratio is calculated to find the individual and combined effect of factors. The SN ratio is calculated from tested results based on maximizing the strengths. Hence, higher-the-better (HB) SN ratio equation has been used [19].

## 4 Taguchi Analysis

### 4.1 Analysis of Tensile Strength

From Taguchi's analysis, the tensile strength of the composite materials has been improved by adding fibers reinforcement with the resin matrix. Generally, kenaf fibers are highly composed of hemicellulose and lignin properties for sticking of fibers and matrix [20]. There are very low mixing fibers contribution, and the maximum percentage of resin was existing in the specimen. The tensile strength of trail specimen 1 is very low due to the very lower weight of fibers existing in the composite. It is increased by increasing fiber weights in the specimen. Hence, it was revealed that the weight of fiber-reinforcement increases tensile strength [21]. It was also revealed Taguchi's mean and SN graphs (Fig. 1), while the increasing weight of fibers such as kenaf, Grewia, and hair, then the tensile strength of composite materials is increased.



Fig. 1 SN ratio analysis of fiber mixing effects on tensile strength

Table 4 Analysis of variance for tensile, flexural, and impact strength

Factor	Tensile strength		Flexural strength		Impact strength	
	SS	% Contribution	SS	% Contribution	SS	% Contribution
K	2210.69	84.94	20,621.2	70.68	1.609	18.41
G	43.42	1.67	3318.1	11.37	4.152	47.50
H	278.41	10.70	4239.3	14.53	2.812	32.17
Error	70.16	2.70	995.4	3.14	0.168	1.93
Total	2602.69	–	29,174.0	–	8.742	–

It was also observed from Table 4, kenaf fiber has comparatively more contribution (84.95%) than the weight of the other two fibers. It was proved that it was improved by increasing the weight of hair fiber (10.70%). The bonding strength of hair decreases strength due to the presence of keratin cellulose and polished surfaces [20, 21]. However, the tensile strength in specimens is maximum due to improving the bonding strength of a composite by the presence of natural cellulose in the fiber [21].

### 4.2 Effect of Fibers on Flexural Strength

Generally, kenaf fibers are highly composed of lignin and hemicellulose properties which provide good bonding between fibers and matrix [22]. The strong and hard fiber’s occurrence in hair improves the elastic strength (Fig. 2). The higher flexural strength has been improved by the regaining ability of hair [22]. The presences of kenaf fibers improve the molecular strength of fiber and resin. In general, 95% of

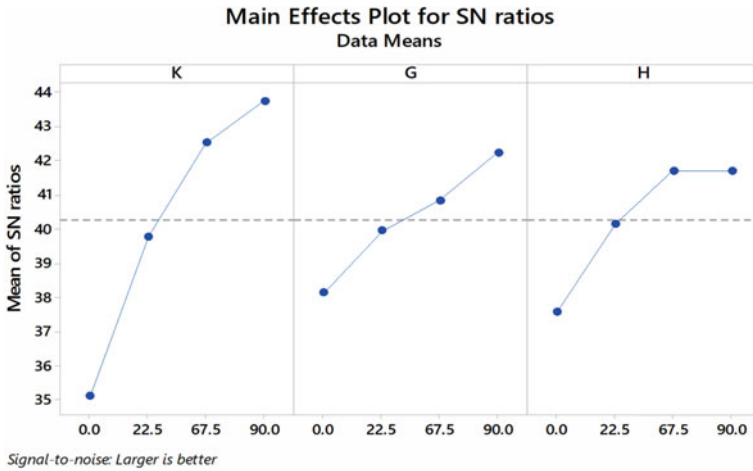


Fig. 2 SN ratio analysis of fiber mixing effects on flexural strength

hair is composed of water content with protein to improve the composite to endure maximum load [20]. The flexural strength of the first specimen is very low due to the very lower weight of fibers existing in the composite. It is increased by increasing fiber weights in the specimen [21]. Based on Taguchi mean and SN graphs, while the increasing weight of kenaf, Grewia, and hair fibers, the flexural strength of composite materials had been improved. It was also observed from Table 4, kenaf fiber has comparatively more contribution (70.68%) than the other two fibers. It was proved that while increasing the percentage of hair fiber (14.53%) in the composite parts, the tensile strength will be improved, and the Grewia serrulate is low contributing 11.37% on flexural strength.

### 4.3 Effect of Fibers on Impact Strength

Generally, the kenaf fiber molecules are shown tight connectivity within themselves. Due to the high elasticity of hair, which increases the impact strength with a low contribution on it. The impact strength of the first specimen is very low due to the very lower weight of fibers existing in the composite. It is enhanced by increasing fiber weights in the specimen. Based on Taguchi’s mean and SN graphs, while the increasing weight of fibers such as kenaf, Grewia, and hair fibers, the impact strength of composite materials is increased (Fig. 3). It was also observed from Table 4, Grewia fiber has comparatively more contribution (47.50%) than the other two fibers due to high load-carrying capacity. It was proved that the impact strength will be improved while increasing the percentage of hair fiber (32.17%) in the composite parts, and the kenaf is comparatively low contributing 11.37% on this response. The high coherence bond between fiber and resin leads to improve impact strength.

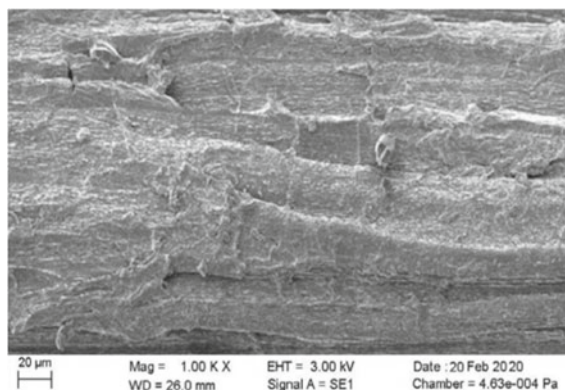


Fig. 3 SN ratio analysis of fiber mixing effects on impact strength

### 4.4 Morphological Analysis

The fiber orientation in the natural composite is shown in a microscopic SEM image. Figure 4 is the SEM picture with the best mixing condition (K4-G4-H4). The confirmation experiments to validate the best weight of fibers on composite properties were conducted and shown in Table 5. It was observed that random fiber orientation in the specimen was found in natural fiber composite. It was perceived that both broken edges and delaminated zone were viewed in the image.

Fig. 4 SEM image at Taguchi best mixing conditions (K4-G4-H4)



**Table 5** Confirmation experiments for Taguchi optimum results

Best process parameters	Tensile strength (MPa)		Flexural strength (F) (MPa)		Impact strength (I) kJ/mm <sup>2</sup>		Description
	S/N ratio	Mean	S/N ratio	Mean	S/N ratio	Mean	
K4- G4-H4	35.3284	48.184	47.143	186.384	13.5182	4.156	Prediction
	–	47.93	–	185.79	–	4.05	Confirmation tests

## 5 Conclusions

The effect of each fiber's weight (kenaf, Grewia, and hair) with epoxy matrix on the mechanical properties has been analyzed using Taguchi's L16 orthogonal array. The tensile strength is improved by hemicelluloses and lignin properties in the kenaf fiber having increased. Also, the regaining ability of hair increases flexural strength. Hence, the hair has been used to make composites for high flexural strength applications. The microscopic analysis results confirm the randomly mixed fibers in composites. It improves all three mechanical properties. The overall properties of composite have been enhanced by increasing the weight of mixing fibers. The higher weights of natural fibers improve the overall mechanical strength of the composite. The percentage of contribution of kenaf is comparatively higher on the tensile strength and flexural strengths than the other two fibers.

## References

1. Babu GD, Gudapati SPK, Prasad AVR, Babu KS (2020) Experimental investigation on mechanical and thermal properties of Esculentus Cyperus fiber reinforced polypropylene composites. *Mater Today Proc* 23:557–560. <https://doi.org/10.1016/j.matpr.2019.05.408>
2. Pereira AC, Assis FS, De Filho FDCG, Oliveira MS, Demosthenes LCDC, Lopera HAC, Monteiro SN (2019) Ballistic performance of multilayered armor with intermediate polyester composite reinforced with fique natural fabric and fibers. *J Mater Res Technol* 8:4221–4226. <https://doi.org/10.1016/j.jmrt.2019.07.031>
3. Ridzuan MJM, Abdul Majid MS, Khasri A, Gan EHD, Razlan ZM, Syahrullail S (2019) Effect of pineapple leaf (PALF), napier, and hemp fibres as filler on the scratch resistance of epoxy composites. *J Mater Res Technol* 8:5384–5395. <https://doi.org/10.1016/j.jmrt.2019.09.005>
4. Guo A, Sun Z, Satyavolu J (2019) Impact of chemical treatment on the physiochemical and mechanical properties of kenaf fibers. *Ind Crops Prod* 141: 111726. <https://doi.org/10.1016/j.indcrop.2019.111726>
5. Selvakumar K, Omkumar M (2019) Effect of fiber composition on the physical, mechanical, and thermal behavior of jute and human hair-reinforced epoxy composites. *J Test Eval* 49. <https://doi.org/10.1520/JTE20180940>
6. Selvakumar K, Meenakshisundaram O (2019) Mechanical and dynamic mechanical analysis of jute and human hair-reinforced polymer composites. *Polym Compos* 40:1132–1141. <https://doi.org/10.1002/pc.24818>



7. Butt WA, Mir BA, Jha JN (2016) Strength Behavior of Clayey Soil Reinforced with Human Hair as a Natural Fibre. *Geotech Geol Eng* 34:411–417. <https://doi.org/10.1007/s10706-015-9953-x>
8. Oladele IO, Olajide JL, Ogunbadejo AS (2015) The influence of chemical treatment on the mechanical behaviour of animal fibre-reinforced high density polyethylene composites. *Am J Eng Res* 2320–847
9. Alavudeen A, Rajini N, Karthikeyan S, Thiruchitrabalam M, Venkateshwareen N (2015) Mechanical properties of banana/kenaf fiber-reinforced hybrid polyester composites: effect of woven fabric and random orientation. *Mater Des* 66:246–257. <https://doi.org/10.1016/j.matdes.2014.10.067>
10. Karaduman Y, Gokcan D, Onal L (2013) Effect of enzymatic pretreatment on the mechanical properties of jute fiber-reinforced polyester composites. *J Compos Mater* 47:1293–1302. <https://doi.org/10.1177/0021998312446826>
11. Yousif BF, Shalwan A, Chin CW, Ming KC (2012) Flexural properties of treated and untreated kenaf/epoxy composites. *Mater Des* 40:378–385. <https://doi.org/10.1016/j.matdes.2012.04.017>
12. Rokbi M, Osmani H, Imad A, Benseddig N (2011) Effect of chemical treatment on flexure properties of natural fiber-reinforced polyester composite. *Procedia Eng*. 10:2092–2097. <https://doi.org/10.1016/j.proeng.2011.04.346>
13. Harish S, Michael DP, Bensely A, Lal DM, Rajadurai A (2009) Mechanical property evaluation of natural fiber coir composite. *Mater Charact* 60:44–49. <https://doi.org/10.1016/j.matchar.2008.07.001>
14. Mahjoub R, Yatim JM, Mohd Sam AR, Hashemi SH (2014) Tensile properties of kenaf fiber due to various conditions of chemical fiber surface modifications. *Constr Build Mater* 55:103–113. <https://doi.org/10.1016/j.conbuildmat.2014.01.036>
15. Myilsamy S, Sampath B (2021) Experimental comparison of near-dry and cryogenically cooled near-dry machining in wire-cut electrical discharge machining processes. *Surface Topography: Metrology and Properties*. 9(3):035015. <https://doi.org/10.1088/2051-672X/ac15e0>
16. Boopathi S (2019) Experimental investigation and parameter analysis of LPG refrigeration system using Taguchi method. *SN Applied Sciences*. 1:892. <https://doi.org/10.1007/s42452-019-0925-2>
17. Sampath B, Myilsamy S (2021) Experimental investigation of a cryogenically cooled oxygen-mist near-dry wire-cut electrical discharge machining process. *Strojniški vestnik J Mech Eng* 67:322–330. <https://doi.org/10.5545/sv-jme.2021.7161>
18. Sampath B, Naveenkumar N, Sampathkumar P, Silambarasan P, Venkadesh A, Sakthivel M (2021) Experimental comparative study of banana fiber composite with glass fiber composite material using Taguchi method. *Mater Today Proc* (in press). <https://doi.org/10.1016/j.matpr.2021.07.232>
19. Boopathi S, Sivakumar K (2013) Experimental investigation and parameter optimization of near-dry wire-cut electrical discharge machining using multi-objective evolutionary algorithm. *Int J Adv Manuf Technol* 67:2639–2655. <https://doi.org/10.1007/s00170-012-4680-4>
20. Paridah MT, Hafizah AWN, Zaidon A, Azmi I, Nor MYM, Yuziah MYN (2009) Bonding properties and performance of multi-layered kenaf board. *J Trop Forest Sci* 113–122
21. Lasikun, Ariawan D, Surojo E, Triyono J (2018) Effect of fiber orientation on tensile and impact properties of Zalacca Midrib fiber-HDPE composites by compression molding. *AIP Conf Proc* 1931. <https://doi.org/10.1063/1.5024119>
22. Gupta A (2014) Human hair “waste” and its utilization: gaps and possibilities. <https://doi.org/10.1155/2014/498018>

# Co-digestion of Agricultural and Plant Wastes and Cow Dung for Biogas Production



Amaresh Mohapatra, Sanjaya Kumar Mishra, Shakti Prakash Jena, and Premananda Pradhan

**Abstract** In this study, anaerobic co-digestion of different leaves such as arrow-root, cauliflower, and jackfruit collectively termed as agricultural and plant wastes (APWs) and cow dung (CD) was performed in laboratory scale. Volatile solid (VS) content of these leaves was found to be above 70%. The proportion of APW to CD for maximizing methane production rate was optimized experimentally. Sewage water in the ratio of 1:10 (w/v) was used as an inoculum for the experiment. A constant thermophilic temperature of  $55 \pm 1$  °C was maintained throughout the experiment. APW to CD mixture in the proportion 60:40 was considered as the optimum proportion for maximum yield of methane. A timespan of 17 days may be considered as the optimum hydraulic retention time (HRT) if the continuous production process is adopted instead of batch production. This method of biogas production from APW and CD will be highly suitable for rural belts in terms of maintaining cleanliness of the surroundings, economy of operation, and the preparation of nutrient rich bio-fertilizer for irrigation.

**Keywords** Biogas · Co-digestion · Anaerobic digestion · Renewable energy

## 1 Introduction

At present, India mainly depends on fossil fuels to attain the energy needs of the country. This primary dependence on fossil fuels and imports creates a lot of problems like environmental pollution, climate change, shortage of energy, an increase in oil price, and energy security. To overcome these problems and accomplish energy independence, India needs to utilize its vast renewable and sustainable energy sources [1, 2]. Open dumping, landfilling, and burning of these wastes release different particulate matter and harmful gases into the atmosphere that causes a lot of pollution [3, 4].

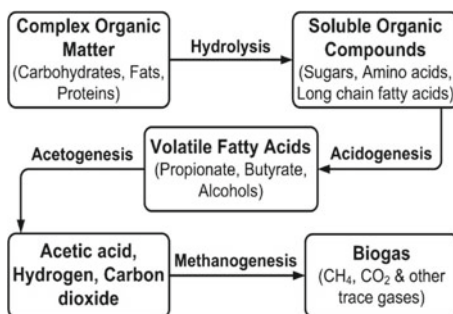
---

A. Mohapatra · S. K. Mishra · S. P. Jena · P. Pradhan (✉)  
Department of Mechanical Engineering, ITER, SOA (Deemed to be University), Bhubaneswar  
751030, India  
e-mail: [premanandapradhan@soa.ac.in](mailto:premanandapradhan@soa.ac.in)

© The Author(s), under exclusive license to Springer Nature Singapore Pte Ltd. 2023  
P. Pradhan et al. (eds.), *Recent Advances in Mechanical Engineering*,  
Lecture Notes in Mechanical Engineering,  
[https://doi.org/10.1007/978-981-16-9057-0\\_12](https://doi.org/10.1007/978-981-16-9057-0_12)

111

**Fig. 1** Different stages of the AD process



Therefore, proper management and treatment of the wastes are necessary to achieve sustainable growth.

The World Energy Council (WEC) mentioned several bioenergy conversion methods like gasification, incineration, pyrolysis, anaerobic digestion (AD), fermentation, and landfill with gas recovery that can be used to generate valuable energy from the wastes [5]. Khan and Kabir [6] studied the sustainability of various waste to energy conversion methods and found that AD, pyrolysis, and gasification methods were, respectively, 111%, 65%, and 33% more sustainable than incineration.

AD is a biological process in which different organic substances are converted into bioenergy inside a closed chamber in the absence of free oxygen. The organic substances inside the digester are degraded by the action of various micro-organisms to produce biogas. Biogas production through AD involves four processes, namely hydrolysis, acidogenesis, acetogenesis, and methanogenesis as shown in Fig. 1. Initially, the complex organic matter is converted into soluble organics in the hydrolysis stage. Further, in the acidogenesis stage, these soluble organics are converted into volatile fatty acids (VFAs) and alcohols in addition to the formation of carbon dioxide and hydrogen. Then, in the acetogenesis step, the VFAs decompose to form acetic acid, carbon dioxide, and hydrogen. In the final step, methanogens convert the products obtained from the acetogenesis phase to produce methane [7]. Biogas is a renewable source of energy and can be generated from distinct wastes and biomasses. It can be utilized for cooking, heating, and generating electricity. Moreover, the left-over bio-slurry can be used as a fertilizer in agricultural applications. There are several factors like temperature, pH value, C/N ratio, VFAs concentration, etc., that affect the AD process. Therefore, methods like pre-treatment and co-digestion of feedstocks are being adopted simultaneously by the researchers to achieve better process efficiency and enhance biogas yield.

Patowary et al. [8] observed that the co-digestion of *Ipomoea carnea* leaves with cow dung produced more amount of biogas compared to that of rice straw with cow dung. They noticed that the higher VS content in *Ipomoea carnea* leaves helped in producing more biogas than rice straw whereas higher lignin content in straw affected the biogas production. Parralejo et al. [9] performed AD of agricultural residues and animal manure mixtures and found that co-digestion stabilizes the AD process and is an appropriate method for optimizing biogas production. Ryue et al.

[10] inspected different methods to increase the stability of the thermophilic AD process and reported that co-digestion of complementary feedstocks helps to reduce the inhibitory substances by balancing the nutrients in the feedstocks and thereby provides stability to the process. Frigon et al. [11] observed an 86% increase in methane production during co-digestion of 20% wet mass fraction of switchgrass with manure compared to the mono-digestion results of manure. Giuliano et al. [12] found that co-digestion of energy crops, agricultural waste with manure is suitable for both thermophilic and mesophilic temperatures. Moreover, they also observed that replacing energy crops with a small fraction of agricultural waste enhanced the production of biogas. Salces et al. [13] also observed that mixing vegetable processing wastes with manure increased the VS removal rate and the amount of biogas yield. Potdukhe et al. [14] in their study found that co-digestion of agricultural wastes with waste activated sludge yielded more biogas as compared to mono-digestion of waste activated sludge. Almomani and Bhosale [15] examined the use of chemical pre-treatment and co-digestion techniques to improve biogas production and observed that co-digestion of agricultural waste with CD in 60:40 ratio returned the highest amount of biogas. They also noticed that the addition of  $\text{NaHCO}_3$  to the feedstock increased the methane production further by 29.7%. Muhammad and Chandra [16] investigated the biogas production using vegetable waste and leaf litters of neem plant. They found that co-digestion of vegetable waste with leaf litters of neem plant produced 87.27% more biogas in comparison with the biogas produced from mono-digestion of vegetable waste.

From the literature review, it is observed that co-digestion is the most suitable means of bioenergy conversion of different leaves with cow manure as it is a bumper complementary feedstock that controls the accumulation of VFAs, C/N concentration. The thermophilic temperature range expedites the process of VS degradation with the destruction of pathogens. Hence, in this study, the co-digestion of different leaf litters from agricultural and plant wastes (APWs) plentifully available in rural belts in India with cow dung (CD) was performed at different proportions in the thermophilic temperature range to examine their biogas potential.

## 2 Materials and Method

### 2.1 Feedstock Collection and Preparation

In this study, leaves of arrowroot, cauliflower, and jackfruit were considered with CD as the complementary feedstock for the co-digestion process. CD is one of the biggest sources of organic fertilizer on the farming land as well as biomass fuel in the form of cakes for heating and cooking in India. In addition to that these leaves are generally treated as wastes and are either dumped or burnt in the open atmosphere that causes a lot of pollution. So, use of these wastes for renewable energy generation can help in achieving the sustainable goals. Salces et al. [13] reported that the livestock

manures have a low C/N ratio as they contain a higher percentage of nitrogen and are suitable for co-digestion with plant and vegetable wastes to maintain the required C/N ratio and balance the nutrient contents during digestion. Momoh and Nwaogazie [17] reported that CD also contains methane forming micro-organisms that are helpful for biogas production. It also balances the pH required to degrade the VFAs accumulation during the initial stages VS degradation.

The various APWs used in this study and CD were collected from the villages on the outskirts of Bhubaneswar, Odisha, India and were sun-dried for 20 days. The dried APWs and CD were then crushed manually and were ground into powdered form to decrease the particle size into 1 mm. Several researchers stated that the decrease in the particle size of the feedstocks, biogas production rate increases [18, 19] due to the increased surface area of the feedstocks and the enhanced action of micro-organisms. Therefore, the particle size of the biomass samples was reduced and a fine powdered form of the APW and CD was taken for the AD process as shown in Fig. 2. Wastewater from a nearby municipality treatment plant was collected, filtered and was used as the inoculum for the AD process.

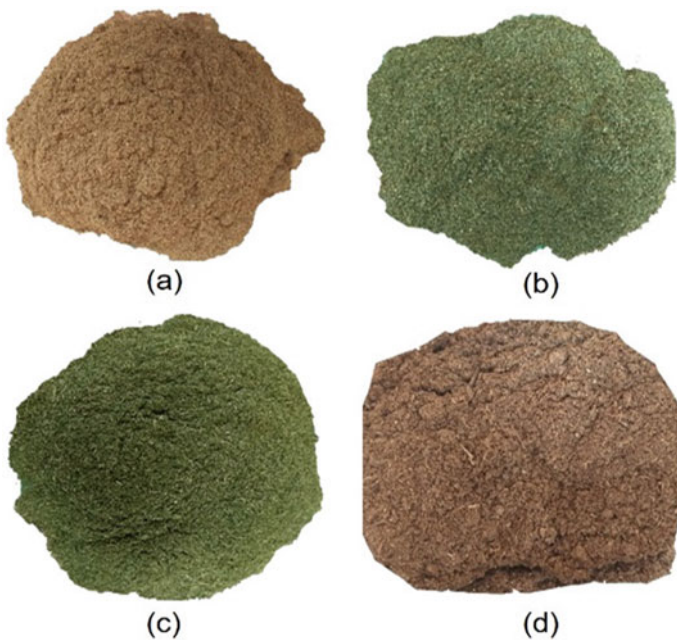


**Fig. 2** Powdered biomass samples **a** arrowroot leaves; **b** cauliflower leaves; **c** jackfruit leaves; **d** cow dung

## 2.2 Proximate Analysis of Biomass Samples

Proximate analysis of the biomass samples was conducted experimentally to determine their suitability for the process.

**Determination of Total Solid (TS) and Moisture Content:** An electronic precision balance (ECB 300, WENSAR Weighing Scales Limited) was used for weighing biomass samples separately in different crucibles. The crucibles with samples were then kept inside a hot air oven (STM-13, SATYAM) for drying at a temperature of 105 °C for 1 h. Then, the crucibles were shifted to a desiccator until they attained room temperature. The amounts of TS present in the samples were calculated using Eq. 1 [20] as follows.

$$\%TS = \frac{W_{t_2} - W_{t_1}}{W_{t_3} - W_{t_1}} \times 100 \quad (1)$$

The % of moisture content in each of the biomass sample was calculated using Eq. 2 as,

$$\%Moisture = 100 - \%TS \quad (2)$$

**Determination of Volatile Solid (VS) Content:** For VS analysis, the crucibles with the oven-dried samples were kept inside a muffle furnace (STM-99, SATYAM) at a temperature of 600 °C for 30 min and then cooled in a desiccator to attained room temperature. The weights of the residue along with crucibles were measured, and the values were recorded. Then, the weight loss and the amount of VS present in each sample were calculated using Eqs. 3 and 4, respectively, [21] as given below.

$$\%Weight\ loss = \frac{W_{t_2} - W_{t_4}}{W_{t_2} - W_{t_1}} \times 100 \quad (3)$$

$$\%VS = \%Weight\ loss - \%Moisture \quad (4)$$

**Ash and Fixed Carbon Content:** The ash content in each sample was calculated by heating the crucibles with the residue in the muffle furnace at 600 °C for 1 h and then cooling the same in a desiccator until it attained the room temperature. This process was continued until no change in weight was observed. The ash content was then calculated using Eq. 5 [22] as

$$\%Ash = \frac{W_{t_5} - W_{t_1}}{W_{t_2} - W_{t_1}} \times 100 \quad (5)$$

The fixed carbon (FC) content of each biomass samples was calculated as shown in Eq. 6 [23].

$$\%FC = 100[\%Moisture + \%VS + \%Ash] \quad (6)$$

where  $Wt_1$  = Weight of crucible,  $Wt_2$  = Weight of oven-dried sample + crucible,  $Wt_3$  = Weight of biomass sample + crucible,  $Wt_4$  = Weight of the crucible + left-over residue after ignition,  $Wt_5$  = Weight of the crucible + ash.

### 2.3 Elemental Analysis of Biomass Samples

The elemental analysis gives the carbon (C), hydrogen (H), oxygen (O), nitrogen (N) content in the biomass samples. The elemental compositions of the biomass samples were calculated theoretically from the correlations given by Shen et al. [24] using the results obtained from proximate analysis of the biomass samples as shown in Eqs. 7, 8 and 9.

$$C = 0.635FC + 0.460VS - 0.095ASH \quad (7)$$

$$H = 0.059FC + 0.060VS + 0.010ASH \quad (8)$$

$$O = 0.340FC + 0.469VS - 0.023ASH \quad (9)$$

### 2.4 Experimental Procedure for Biogas Production

Experiments were carried out to test the biogas production from five numbers of batch type anaerobic digesters with a capacity of 1 L each and are marked as  $D_1$ ,  $D_2$ ,  $D_3$ ,  $D_4$ , and  $D_5$ . The digesters were fed with 30 g of dry APW and CD mixture. Their mass proportions were shown in Table 1. Each sample was then mixed well with inoculated water collected from sewage drains in a 1:10 (w/v) ratio and was shaken manually for better mixing to form a slurry. The digesters were then closed with rubber stoppers, and the air was removed from the digesters to produce an oxygen-free environment.

**Table 1** Different proportions of APW and CD used for co-digestion

Digesters	% APW (dry weight)	% CD (dry weight)
$D_1$	80	20
$D_2$	75	25
$D_3$	70	30
$D_4$	60	40
$D_5$	50	50

The digesters were then kept inside a water bath system at a thermophilic temperature of 55 °C for 30 days. Manual shaking of the digesters was done every day for the ideal mixing of the nutrients after the collection of gas for testing. The pH values of the digestates in each digester were measured by using a digital pH meter. The gas sample was collected every day from the digester starting from the 2nd day using an airtight gas collecting syringe, and the vacuum is maintained inside the digester after the removal of the gas. The collected gas was injected into the gas chromatograph (GC-2010 TCD, CIC, Baroda) apparatus to test the composition.

### 3 Results and Discussion

#### 3.1 Composition of Biomass Samples

The results of proximate analysis for determining the TS, moisture, VS, ash, and FC content and elemental analysis for determining the C, H, O content of the biomass samples are depicted in Tables 2 and 3, respectively. VS is a key parameter that affects the production of biogas. It is the organic content present in the biomass sample that degrades under anaerobic conditions to generate biogas [8]. VS content of all the biomass samples was highly suitable for AD process except CD that had a VS content of less than 50%. Co-digestion of leaf litters with CD increases the buffering capacity, provides additional nutrients, and boosts the efficiency of the digesters, controlling the VFA production during the initial stages of reaction [13, 17]. So, CD in different proportions was taken as a potential feedstock in the experiment.

**Table 2** Proximate analysis results of arrowroot leaves

Feedstock	Moisture (%)	TS (%)	VS (%)	Ash (%)	FC (%)
Arrowroot leaves	6	94	78.04	13.82	2.14
Cauliflower leaves	14	86	69.72	15.12	1.16
Jackfruit leaves	11	89	80.01	8.98	0.00
Cow dung	23	77	44.53	32.47	0.0001
Combined	13.5	86.5	64.53	17.05	4.91

**Table 3** Elemental analysis of different feedstocks

Feedstock	C (%)	H (%)	O (%)
Arrowroot leaves	35.944	4.947	37.011
Cauliflower leaves	31.374	4.403	32.747
Jackfruit leaves	35.951	4.891	37.319
Cow dung	17.401	2.997	20.139
Combined	31.186	4.333	31.545



### 3.2 Methane Production Potential of Each Digester

The results showed that methane production increases gradually from day 2 onwards as shown in Fig. 3. It was observed that the pH values in the digesters  $D_1$  to  $D_5$  lie within the range from 6.8 to 7.1 throughout the experiment as shown in Fig. 4.

In digester  $D_1$ , the rate of methane production was slower and the percentage of maximum  $CH_4$  was around 58.11% on the 8th day. Digester  $D_2$  and  $D_3$  produced the maximum amounts of  $CH_4$  of 61.37% and 62.45% on the 7th day. While  $D_4$  and  $D_5$  gave the maximum yielding of 68.37% and 64.45% of  $CH_4$  after the end of 6 and 5 days, respectively. A higher rate of production within five to eight days might be due to better pH balance and thermophilic range of temperature within the digesters as

**Fig. 3** Methane content of the produced biogas in different digesters

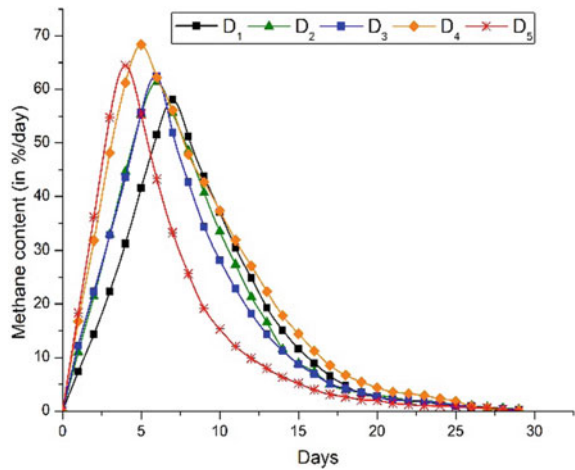
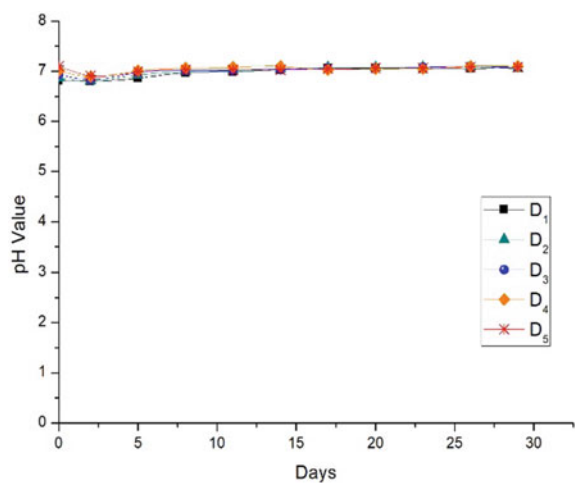


**Fig. 4** pH value of different digesters during the experiment



thermophilic temperature expedite the process of digestion destroying the pathogens present in the feedstocks and inoculated water [25]. Comparatively, slow rate and a lesser amount of  $\text{CH}_4$  production in  $D_1$  might be due to a slight imbalance in the C/N ratio [13] that controls the process of degradation as the proportion of APW to CD was 80:20. Due to the same reason,  $D_4$  might be giving the maximum  $\text{CH}_4$  yield compared to other digesters and the measured pH value at the end of each day ascertained a pH value of the digestate more than 6.8 in each digester. From the analysis of the above result, it can be concluded that the optimum composition of APW to CD is 60:40. The same can be validated with the results obtained by the other researchers [9, 10]. It was observed from all the digesters that the rate of  $\text{CH}_4$  yield decreases asymptotically from the maximum and finally approaches zero by the end of 30 days. By the end of 17 days of operation rate of  $\text{CH}_4$  yield remained below 9%. Hence, 17 days may be considered as HRT if a continuously fed digester is used instead of batch type.

## 4 Conclusion

The following conclusions were drawn from the experimental evidence obtained from the co-digestion of agricultural and plant waste (APW) leaves with cow dung (CD) for biogas production.

- The optimum proportion of APW to CD was 60:40.
- The highest production rate of  $\text{CH}_4$  per day was observed to be 68.37% at the end of the 5th day.
- The use of CD as a complimentary feedstock maintained a balance over the process controlling parameters such as pH and C/N ratio.
- With this proportion, the optimum HRT might be considered as 17 days if a continuously fed digester was used instead of batch type.
- The results were promising and suggested that different agro-leaves and plant leaves grew within a season with higher organic contents are the most suitable feedstocks for co-digestion with CD.
- The collection and utilization of these biomasses for biogas production need almost zero expenses for the AD process in rural belts. Additionally, it can provide high-value organic fertilizers and help to keep the environment clean from odor and GHG emissions by converting wastes to energy. So, it is the most suitable and economical bioenergy conversion process for both individual and community scale for the rural belt.
- AD process does not need highly skilled operators and the employability opportunity can be generated if AD plants are installed in community scales.

## References

1. Sen S, Ganguly S, Das A, Sen J, Dey S (2016) Renewable energy scenario in India: opportunities and challenges. *J Afr Earth Sci* 122:25–31
2. Tripathi L, Mishra AK, Dubey AK, Tripathi CB, Baredar P (2016) Renewable energy: an overview on its contribution in current energy scenario of India. *Renew Sustain Energy Rev* 60:226–233
3. Cremiato R, Mastellone ML, Tagliaferri C, Zaccariello L, Lettieri P (2018) Environmental impact of municipal solid waste management using life cycle assessment: the effect of anaerobic digestion, materials recovery and secondary fuels production. *Renew Energy* 124:180–188
4. Singh L, Sunderesan R, Sarin R (2014) Waste to energy generation from municipal solid waste in India. *Int J Chem Tech Res* 6(2):1228–1232
5. WEC (2016) World energy resources waste to energy. [https://www.worldenergy.org/wpcontent/uploads/2017/03/WEResources\\_Waste\\_to\\_Energy\\_2016.pdf](https://www.worldenergy.org/wpcontent/uploads/2017/03/WEResources_Waste_to_Energy_2016.pdf)
6. Khan I, Kabir Z (2020) Waste-to-energy generation technologies and the developing economies: a multi-criteria analysis for sustainability assessment. *Renew Energy* 150:320–333
7. Kainthola J, Kalamdhad AS, Goud VV (2019) A review on enhanced biogas production from anaerobic digestion of lignocellulosic biomass by different enhancement techniques. *Process Biochem* 84:81–90
8. Patowary D, West H, Clarke M, Baruah DC (2016) Biogas production from surplus plant biomass feedstock: some highlights of Indo-UK R&D initiative. *Procedia Environ Sci* 35:785–794
9. Parralejo AI, Royano L, González J, González JF (2019) Small scale biogas production with animal excrement and agricultural residues. *Ind Crops Prod* 131:307–314
10. Ryue J, Lin L, Kakar FL, Elbeshbishy E, Al-Mamun A, Dhar BR (2020) A critical review of conventional and emerging methods for improving process stability in thermophilic anaerobic digestion. *Energy Sustain Dev* 54:72–84
11. Frigon JC, Roy C, Guiot SR (2012) Anaerobic co-digestion of dairy manure with mulched switchgrass for improvement of the methane yield. *Bioprocess Biosyst Eng* 35(3):341–349
12. Giuliano A, Bolzonella D, Pavan P, Cavinato C, Cecchi F (2013) Co-digestion of livestock effluents, energy crops and agro-waste: feeding and process optimization in mesophilic and thermophilic conditions. *Biores Technol* 128:612–618
13. Salces BM, Gómez X, Morán A, García-González MC (2013) Anaerobic co-digestion of livestock and vegetable processing wastes: fibre degradation and digestate stability. *Waste Manage* 33(6):1332–1338
14. Potdukhe RM, Sahu N, Kapley A, Kumar R (2021) Co-digestion of waste activated sludge and agricultural straw waste for enhanced biogas production. *Bioresource Technol Rep* 100769
15. Almomani F, Bhosale RR (2020) Enhancing the production of biogas through anaerobic co-digestion of agricultural waste and chemical pre-treatments. *Chemosphere* 255:126805
16. Muhammad MB, Chandra R (2021) Enhancing biogas and methane production from leaf litter of neem by co-digestion with vegetable waste: focus on the effect of tannin. *Biomass Bioenergy* 147:106007
17. Momoh OIY, Nwaogazie LI (2007) Effect of waste paper on biogas production from co-digestion of cow dung and water hyacinth in batch reactors. *J Appl Sci Environ Manag* 11(4):95–98
18. Mshandete A, Björnsson L, Kivaisi AK, Rubindamayugi MS, Mattiasson B (2006) Effect of particle size on biogas yield from sisal fibre waste. *Renew Energy* 31(14):2385–2392
19. Lu H, Ip E, Scott J, Foster P, Vickers M, Baxter LL (2010) Effects of particle shape and size on devolatilization of biomass particle. *Fuel* 89(5):1156–1168
20. Sluiter A, Hames B, Hyman D, Payne C, Ruiz R, Scarlata C, Sluiter J, Templeton D, Wolfe J (2008) Determination of total solids in biomass and total dissolved solids in liquid process samples, Technical report NREL/TP-510-42621

21. Singh YD, Mahanta P, Bora U (2017) Comprehensive characterization of lignocellulosic biomass through proximate, ultimate and compositional analysis for bioenergy production. *Renew Energy* 103:490–500
22. Sluiter A, Hames B, Ruiz R, Scarlata C, Sluiter J, Templeton D (2008) Determination of Ash in Biomass, Technical Report NREL/TP-510-42622
23. Pazó JA, Granada E, Saavedra Á, Patiño D, Collazo J (2010) Heterogenic solid biofuel sampling methodology and uncertainty associated with prompt analysis. *Int J Mol Sci* 11(5):2118–2133
24. Shen J, Zhu S, Liu X, Zhang H, Tan J (2010) The prediction of elemental composition of biomass based on proximate analysis. *Energy Convers Manag* 51(5):983–987
25. Buffière P, Dooms M, Hattou S, Benbelkacem H (2018) The hydrolytic stage in high solids temperature phased anaerobic digestion improves the downstream methane production rate. *Biores Technol* 259:111–118

# Prediction of Growth Percentage of Sintered Compacts Using Neural Network Technique



Sujit Kumar Khuntia, Soumya Darshan Mohanty, Bibhuti Bhusan Pani, and Sankar Narayan Das

**Abstract** In this investigation, percentage of growth in volume of high-carbon content rapidly solidified alloyed ferrous powder sintered compacts has been found out at compaction pressures in the range of 300–700 MPa and sintering temperatures like 720, 850, and 1000 °C. It has been found that growth percentage increases with increase in sintering temperature at a constant compaction pressure and decreases with increase in compaction pressure at a particular sintering temperature. Then, an initiative has been taken to relate the compaction pressure and sintering temperature with growth percentage of the compacts. At the first stage, experimental data obtained during investigation have been used to train the network to develop mathematical models. These models have been used subsequently for prediction of growth percentage of the final products for different combinations of compaction pressures and sintering temperatures. Therefore, a new method has been developed to avoid repetition of experiments.

**Keywords** Atomization · Annealing · Ferrous powders · Green density · Sintered density · Growth percentage

## 1 Introduction

The powder metallurgy (PM) method of manufacturing follows a number of steps like powder production, physical chemical characterization, cold compaction, sintering

---

S. K. Khuntia (✉)

College of Engineering Bhubaneswar, Bhubaneswar, Odisha, India

e-mail: [sujitkhuntia72@gmail.com](mailto:sujitkhuntia72@gmail.com)

S. D. Mohanty

Radhakrishna Institute of Technology and Engineering, Khurda, Odisha, India

B. B. Pani

Veer Surendra Sai University of Technology, Sambalpur, Odisha, India

S. N. Das

Siksha O Anusandhan Deemed to be University, Bhubaneswar, Odisha, India

© The Author(s), under exclusive license to Springer Nature Singapore Pte Ltd. 2023

P. Pradhan et al. (eds.), *Recent Advances in Mechanical Engineering*,

Lecture Notes in Mechanical Engineering,

[https://doi.org/10.1007/978-981-16-9057-0\\_13](https://doi.org/10.1007/978-981-16-9057-0_13)

and post sintering operations, etc., and as such very time consuming. Unlike other manufacturing methods, the control of compaction pressure, sintering temperature, and sintering time in powder metallurgy processing to get a defect free product is quite difficult. Under such circumstances, artificial neural network (ANN) can be employed to develop mathematical models for analyzing process parameters and predict mechanical properties of powders. Again, this will help the designers to get initial data for virtual design of a product and then they can go for final design followed by manufacturing. Smith et al. [1] have employed a neural network model for identifying the relationship between input and output parameters for manufacturing copper metal. They have avoided the use of statistical method as it is found to be limited when high non-linearity exists between input and output parameters. Their study has helped to obtain materials with necessary properties. Cherian et al. [2] have developed artificial neural network methodology for selection of iron powder along with processing parameters in component manufacturing adopting powder metallurgy technology. The accuracy of the neural network has been confirmed by comparing the predicted data with experimental data for iron powder. Odhar et al. [3] have used the neural network (NN) technology to predict the sintered forged density of metal powder preform. They have observed an error, not more than 0.42%, comparing the NN predicted values with the experimental results. Amirjan et al. [4] have developed Cu–Al<sub>2</sub>O<sub>3</sub> composites adopting PM technology. They have used the Al<sub>2</sub>O<sub>3</sub> reinforcement in four different wt. percentages, and the compacts have been sintered at five different sintering temperatures ranging from 725 to 925 °C. The sintering timings have been varied from 15 to 180 min. Properties like hardness and electrical conductivity of the composites have been measured. They have related the sintering temperature, time, wt. percentage of reinforcement with the above-mentioned properties using NN model. The experimentally found properties have shown consistency with the predicted results of the neural network. Drndarevic et al. [5] have used NN technique in PM processes to predict dimensional changes. It has been found here that NN modelling is better than statistical procedure for the prediction of output characteristics. Khuntia et al. [6] have processed low-carbon content ferrous powders using powder metallurgy technique. They have added copper and carbon to it at different percentages for making structural components. Again, in 2019, Khuntia et al. [7] have prepared composites adding low-carbon content ferrous powders and high-carbon content rapidly solidified alloyed ferrous powders at different weight percentages adopting powder metallurgy technique.

However, in the present investigation, an attempt has been made to fabricate components from high-carbon content rapidly solidified alloyed ferrous powders (HCFPs) adopting powder metallurgy (PM) process. Then, neural network modelling has been developed by training some experimental data to the network. The neural network has helped to relate compaction pressure and sintering temperature with growth percentage of the sintered compacts prepared from this HCFP.

## 2 Materials and Method

### 2.1 Production, Annealing, and Characterization

High-carbon content rapidly solidified alloyed ferrous powders were produced using water atomization process. Then, the powders were annealed at two different temperatures. Here, the annealing was done at 700 °C for two hours for most of the powders. Some powders also got annealed at 900 °C for one hour in order to improve the compressibility in hydrogen atmosphere. The annealing was done by a tubular furnace manufactured by Therelek Furnaces Private Limited. The chemical as well as physical characterization of the above annealed powders were carried out and are presented in Tables 1 and 2.

From Table 1, the presence of 2.1 wt% aluminium, 1.8 wt% chromium, and 1.4 wt% silicon is found. The addition of chromium in between 1.5 and 2 wt% prohibits graphitization and allows the enhancement of the carbide volume fraction of. The presence of silicon within 2 wt% causes the A1 transformation temperature line to reach up to 900 °C. As a result, the ferrite grains escapes from decomposition, grain growth and becomes stable up to 900 °C. Grain refinement takes place because of 2–3 wt% of aluminium. From Table 2, flow rate is quite good. It is found to be 23 s/50 g. The apparent density is a very useful parameter for designing the die and punch from which the apparent height for a given dimension of a product is calculated. For the above powders, it is found to be 2.62 g/cm<sup>3</sup>, which is comparable with any quality powder of such kind.

**Table 1** Chemical analysis of high-carbon content rapidly solidified alloyed ferrous powders in wt.%

C%	Al%	Cr%	Si%	S%	P%	Fe%
3.45	2.1	1.8	1.4	0.013	0.02	Balance

**Table 2** Physical characteristics of high-carbon content rapidly solidified alloyed ferrous powders

Characteristics	Value
Apparent density (g/cm <sup>3</sup> )	2.62
Flow rate (s/50 g)	23
True density (g/cm <sup>3</sup> ) (pycnometric)	7.3
Approximate particle size range (µm)	8–100

## 2.2 Compaction Studies

Initially, the powders, which were annealed at 700 °C in hydrogen atmosphere, were compacted within the pressure range from 200 to 700 MPa. But the compressibility was very poor in all cases. Again, 900 °C annealed powders got compacted within the same pressure range. Green compacts with better strength were obtained within compaction pressure range of 300–700 MPa. This is because of the surface decarburization of the powder particles. The green density of the compacts was measured.

## 2.3 Sintering Studies and Calculation of Growth Percentage

The sintering for the above cold compacts was carried out in the same tubular furnace. The sintering was done at three different temperatures like 720, 850, and 1000 °C for one hour in hydrogen atmosphere. The sintered density of the sintered compacts was calculated. The growth percentage of the processed compacts was calculated using the following formula.

$$\alpha = (\rho_g - \rho_s) / \rho_s \quad (1)$$

where

- $\alpha$  Growth percentage
- $\rho_g$  Green density
- $\rho_s$  Sintered density.

The experimental data used here, i.e. growth percentage at different compaction pressures and sintering temperatures are presented in Table 3 to train the network. The testing data along with data predicted by NN and error percentage for validation are presented in Tables 4, 5 and 6.

**Table 3** Experimental data for training the neural network

Compaction pressure (MPa)	720 °C	850 °C	1000 °C
	Growth percentage		
300	6.20	7.17	7.44
400	5.81	6.56	7.27
500	5.62	6.42	7.06
600	5.08	6.27	6.79
700	3.76	5.65	5.88



**Table 4** Test data for validation at sintering temperature 720 °C

Compaction pressure (MPa)	Experimental growth percentage	ANN growth percentage	Error percentage
350	6.07	6.2328	0.1628
450	5.79	6.1478	0.3579
550	5.60	6.0278	0.4278
650	5.01	5.3928	0.3828

**Table 5** Test data for validation at sintering temperature 850 °C

Compaction pressure (MPa)	Experimental growth percentage	ANN growth percentage	Error percentage
350	6.71	6.9264	0.2164
450	6.53	6.6585	0.1285
550	6.39	6.6289	0.2389
650	6. 17	6.3672	0.1972

**Table 6** Test data for validation at sintering temperature 1000 °C

Compaction pressure (MPa)	Experimental growth percentage	ANN growth percentage	Error percentage
350	7.30	7.0661	0.2339
450	7.09	6.7511	0.3389
550	6.83	6.4511	0.3789
650	6.03	6.1961	0.1661

### 3 Neural Network Modelling

The neural network system was created here to get required growth percentage by selecting the process parameters of PM manufacturing method. Initially, the experimental values of growth percentage for different combinations of compaction pressures and sintering temperatures were given to train the network. In this process, mathematical models were developed for relating the parameters.

In the present investigation, a multilayered back propagation network, which is used as a gradient descent learning algorithm, was employed to create a model for indicating the growth percentage of the sintered compacts in advance. Figure 1 shows a back propagation network which consists of an input layer, two hidden layers, and an output layer. Nodes represent neurons. In this case, there are two neurons in input layer and one neuron in output layer. The neurons in hidden layer were fixed by trial and error. A value of 0.9 was selected as learning rate and  $1 \times 10^{-6}$  as tolerance. All the data got normalized before network training. Software was developed in programming language C to train the network. After each iteration, if

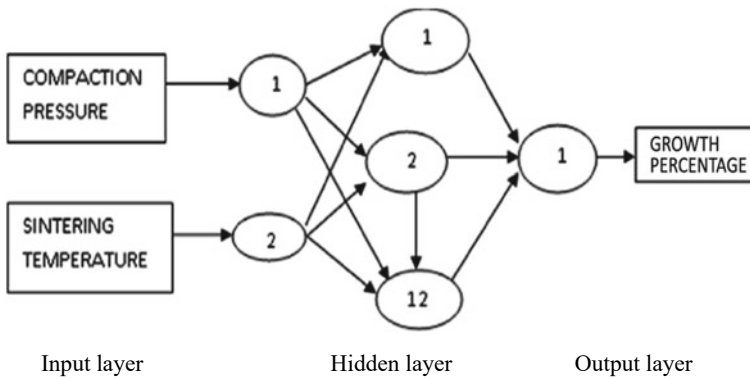


**Fig. 1** Neural network model

the network output was not matching with the desired output, the process was back propagated. Here, a number of 1000 epochs were chosen as training iteration. The training was considered to be completed when the network reached tolerable error value of  $1 \times 10^{-6}$ . Once the network training was over, it became ready to calculate the output for any arbitrarily given set of input values.

## 4 Results and Discussion

### 4.1 Training of NN and Fixing of Polynomials for Input Output Relation

The network got successfully trained with the experimental data of compaction pressure, sintering temperature, and growth percentage of high-carbon content rapidly solidified alloyed ferrous powder compacts. The computer programme got developed resulting in linear, quadratic, cubic, and fourth degree equations. Here, it is found that the residuals obtained are less for quadratic equation compared to linear equations. Again, it is found that the residuals for cubic equation are less compared to that of quadratic equation. Finally, it is observed that the residual is minimum in fourth degree equation compared to cubic equation. The cubic and fourth degree equations along with graph with residuals are shown in Fig. 2 for compacts sintered at 720 °C.

As suggested by Pratap [8] that higher degree polynomials, typically above fourth degree equations, are misleading the input output relation. So in the present case, fourth degree equation was accepted. The same tendency continues for the compacts sintered at 850, 1000 °C. The corresponding graphs are shown in Figs. 3 and 4, respectively.

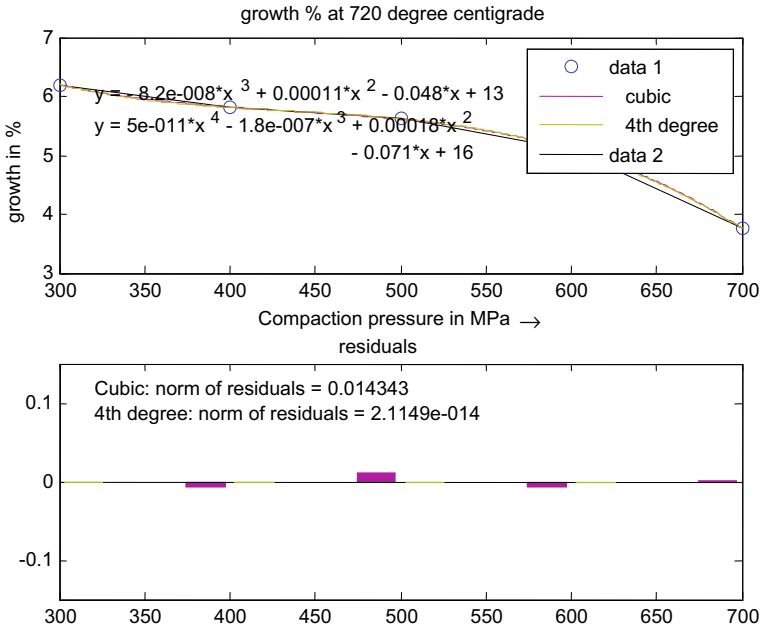


**Fig. 2** Comparison of compaction pressure versus growth percentage as well as compaction pressure versus residuals at 720 °C between cubic and fourth degree curve fittings

These equations are very powerful tools for product design as well as for manufacturing engineers working in the area of powder metallurgy for selecting particular components for a defined condition of processing from the similar kind of materials for virtual product design and manufacturing and finally going to real design and manufacturing of PM products without repetition of experiments.

### 4.2 Validation of NN Predictions with Experimental Data

To validate the neural network predictions, some output data were found out experimentally for some input values of compaction pressures, i.e. 350, 450, 550, 650 MPa and sintering temperatures, i.e. 720, 850, 1000 °C. The data predicted by the network were found out for the same set of input values. These outputs of NN predictions and experimental findings are presented in Tables 4, 5 and 6. It is found that the network predictions are in good agreement with experimental findings. Some errors are marked. At 720 °C, the maximum error percentage is 0.4278. At other two sintering temperatures, i.e. 850 and 1000 °C, the maximum error percentages are even less. Hence, these errors are negligible.

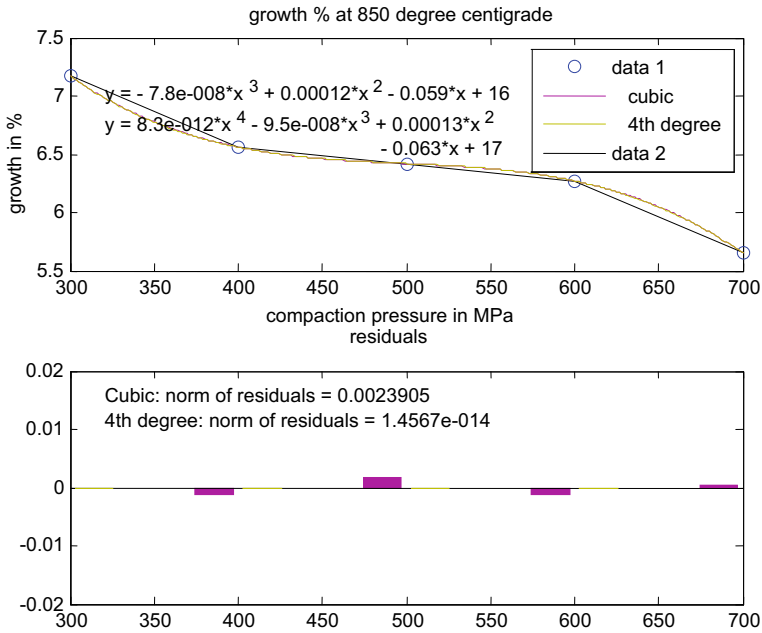


**Fig. 3** Comparison of compaction pressure versus growth percentage as well as compaction pressure versus residuals at 850 °C between cubic and fourth degree curve fittings

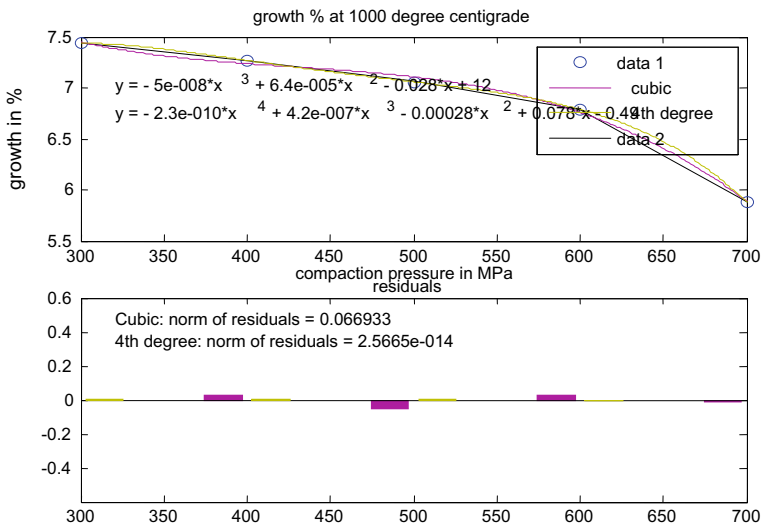


**Fig. 4** Comparison of compaction pressure versus growth percentage as well as compaction pressure versus residuals at 1000 °C between cubic and fourth degree curve fittings

## 5 Conclusions

The following conclusions are drawn.

1. The mathematical models are developed using NN programming to relate the input, i.e. compaction pressure, sintering temperature, and output, i.e. growth percentage of the HCFP sintered compacts.
2. This technique can help in reducing the requirements of the time and resources of experimentation.
3. This investigation can help the product design engineers in the analysis of similar type of materials and processes for manufacturing of powder metallurgy components.

## References

1. Smith LN, German RM, Cherian R, Midha PS, Pelletiers T (1999) A neural network for selection of powders and process setting for Cu powder metallurgy materials. In: Proceedings of the international conference of the powder metallurgy and particulate materials. Vancouver, Canada, pp 1–12
2. Cherian RP, Smith LN, Midha PS (2000) A neural network approach for selection of powder metallurgy materials and process parameters. *Artif Intell Eng* 14:39–44
3. Ohdhar RK, Pasha S (2003) Prediction of process parameters of metal powder perform forging using artificial neural network (ANN). *J Mater Process Technol* 132:227–234
4. Amirjan M, Khorsand H, Siddati MH, Farsani RE (2013) Artificial neural network prediction of Cu-Al<sub>2</sub>O<sub>3</sub> composite properties prepared by powder metallurgy method. *J Mater Res Technol* 2(4):351–355
5. Drndarevic D, Milivojevic M (2019) Neural networks in powder metallurgy. In: 11th international scientific conference on science and higher education in function of sustainable development. Mecavnik-Drvengard, Uzice, Serbia, pp 32–37
6. Khuntia SK, Pani BB (2018) Powder metallurgy processing of low carbon content ferrous powders for making structural components. *Int J Mater Sci* 13(1):7–14
7. Khuntia SK, Pani BB, Nayak S (2019) Fabrication of composites from different carbon content ferrous powders adopting thermomechanical processes. *Mater Manuf Process* 34(8):882–888
8. Pratap R (2006) *Getting started with MATLAB-7*. Oxford university Press, New Delhi

# A Perceptive Approach for Multi-objective Optimization of Die-Sinking EDM Process Parameters with Utility Concept and Taguchi Method for Sustainable Machining



S. D. Mohanty, S. S. Mahapatra, R. C. Mohanty, S. K. Khuntia,  
and J. Mohapatra

**Abstract** The present work attempts to assess the best parametric combination that satisfies multiple objectives of minimization of tool wear and surface roughness and maximization of material removal in electric discharge machining (EDM) of D2 steel. The study specifically focuses on influence of tool electrode material on machining performance. An electrode prepared by direct metal laser sintering (DMLS) has been chosen along with conventional electrodes like copper and brass to assess the feasibility of substituting the conventional electrodes with DMLS electrode which is a novel method. Very few attempts are being made to compare the performance of conventional electrodes with the electrodes prepared by non-conventional method. The study makes use of utility concept-based Taguchi method. Utility concept first finds out the overall utility index (OUI) which is a representative index of all the objectives considered in the study, and then, the problem can easily be solved by Taguchi method.

**Keywords** Multi-objective optimization · Overall utility index · Die-sinking EDM · Taguchi method

---

S. D. Mohanty (✉)  
RITE, BPUT, Rourkela, Odisha, India  
e-mail: [saumyadarsan@gmail.com](mailto:saumyadarsan@gmail.com)

S. S. Mahapatra  
NIT, Rourkela, Odisha 769008, India

R. C. Mohanty  
Centurion University of Technology and Management, R.Sitapur, Odisha, India

S. K. Khuntia · J. Mohapatra  
COEB, BPUT, Bhubaneswar, Odisha, India

## 1 Introduction

Electrical discharge machining (EDM) is a non-traditional machining process employed to remove material from any electrically conductive difficult-to-machine materials by the use of thermal energy. It can create any intricate shape irrespective of hardness of the materials. A sequence of spark generated between the tool and work helps in removing material. Simultaneous optimizations of vital performance measures like material removal rate (MRR), tool wear rate (TWR), and surface roughness ( $R_a$ ) are extremely important to make the machined parts suitable for desired applications. One of the major objectives of a manufacturing engineer is to decrease the cost of tooling and time for product development for any manufacturing operation. In order to achieve both the objectives in EDM process, rapid prototyping (RP) technology may be explored to manufacture tool electrode. Arthur et al. [1] have employed thin metal coating on stereolithography (SL) models to machine-hardened tool steel. Those electrodes found to be useful in both semi-roughing and finishing operations in EDM. Rennie et al. [2] have manufactured EDM electrodes of complex geometry by employing electroforming on a die built through rapid prototyping process and found its performance comparable with the conventional copper electrode. Durr et al. [3] have manufactured simple cylindrical metal electrodes using nickel, bronze, and copper phosphite metal powder by direct metal laser sintering. Excessive tool wear and poor surface quality were observed in comparison with conventional electrodes. Dimla et al. [4] produced complex components having sloped surfaces and deep slots by electroplating on DMLS electrodes. Czyzewski et al. [5] have prepared EDM electrodes by 3-dimensional printing technology. Amorim et al. [6] have used tools made by selective laser sintering (SLS) using different powder materials. Czelusniak et al. [7] have focused on the choice of suitable materials to manufacture EDM electrode using selective laser sintering. Mohanty et al. [8] have carried out experiments using electrodes made of Direct-Metal20 prepared by DMLS. Reddy et al. [9] have produced electroless-coated EDM electrodes by coating materials prepared earlier by fused deposition modeling. Padhi et al. [10] found the suitability of electroplated ABS plastic electrode for semi-finishing and roughing operation. Singh and Pandey [11] prepared EDM electrode by utilizing 3D printing in combination with pressure-less sintering. Singh et al. [12] have employed loose powder sintering on polymer part prepared by 3D printing to prepare copper electrode for machining of D2 steel. Peak current is observed to be the most significant parameter on the responses like MRR, TWR, and cavity dimensional deviation.

In the present study, direct metal laser sintering is employed to prepare the electrode which has been chosen along with conventional electrode like copper and brass to assess the feasibility of substituting these conventional electrodes by the RP electrode considering different machining responses like MRR, TWR, and surface roughness ( $R_a$ ).

The main objective of the present work is the multi-objective optimization of die-sinking EDM process of D2 steel using DMLS electrode. Under the *materials*

**Table 1** Process parameters along with their levels

Levels	$I_p$ (A)	$T_{on}$ ( $\mu$ s)	$T_{off}$ ( $\mu$ s)	$F_p$ (kN/m <sup>2</sup> )	TE
1	7.5	100	10	29.43	Brass
2	10	150	20	58.86	Copper
3	12.5	200	30	88.29	DMLS

*and methods* section, the materials for work piece and electrodes and the optimization method of various process parameters have been discussed. D2 steel has been selected as work piece, while brass, copper, and DMLS electrodes have been taken as tools. Utility concept-based Taguchi method has been used for optimizing various process parameters. Under the *results and discussion* section, DOE has been used to determine utility values of different quality attributes from the experimental results conforming  $L_{27}$  orthogonal array. Then, a confirmatory test has been performed to validate the experiment results. Also, a comparative study has been presented to assess the response using different electrodes. The *conclusions* section discusses the best response by optimizing various process parameters and recommendation for further work.

## 2 Materials and Methods

### 2.1 Materials

D2 steel has been chosen as work piece due to its widespread applications. Three cylindrical tools ( $20 \times 20$  mm) selected were brass electrode, copper electrode, and DMLS electrode using DirectMetal20. The selected process parameters (inputs) are peak current represented by  $I_p$ , on time represented by  $T_{on}$ , off time represented by  $T_{off}$ , flushing pressure represented by  $F_p$ , and tool electrode represented by TE. TWR, MRR, and  $R_a$  have been taken as response variables (outputs). Different process parameters along their levels while carrying out EDM are given in Table 1.

### 2.2 Methods

**Taguchi Method.** Taguchi method is an innovative method to solve single-objective optimization problems with less number of experimentation. It uses signal-to-noise ( $S/N$ ) ratio [13] as a degree of performance.  $S/N$  ratio is the ratio between signal (mean) and noise (standard deviation). The  $S/N$  ratios for greater-the-better and lesser-the-better are presented by Eqs. (1–2). The best setting corresponds to the maximum  $S/N$  ratio.



$$\text{For greater - the - better (GB), } S/N \text{ ratio} = -10 \log_{10} \left( \frac{1}{n} \sum_{i=1}^n \frac{1}{y_i} \right) \quad (1)$$

$$\text{For lesser - the - better (LB), } S/N \text{ ratio} = -10 \log_{10} \left( \frac{1}{n} \sum_{i=1}^n y_i^2 \right) \quad (2)$$

In both the cases,  $n$  represents number of repetitions and  $y_i$  represents output.

**Utility Concept-Based Taguchi Method.** As per the utility theory [14, 15], if  $Z_i$  represents degree of usefulness of a quality characteristic  $i$  and  $n$ , number of attributes are involved in assessing the result; then, the combined utility function is represented as:

$$U(Z_1, Z_2, \dots, Z_n) = f(U_1(Z_1)U_2(Z_2) \dots U_n(Z_n)) \quad (3)$$

Here,  $U_i(Z_i)$  is the utility corresponding to the  $i$ th attribute.

The overall utility function is the summation of different utilities by considering the attributes (qualities) to be independent of each other and is presented as follows:

$$U(Z_1, Z_2, \dots, Z_n) = \sum_{i=1}^n U_i(Z_i) \quad (4)$$

The attributes (qualities) may be given weightages on the basic of their significances. The overall utility function can be represented as:

$$U(Z_1, Z_2, \dots, Z_n) = \sum_{i=1}^n W_i U_i(Z_i) \quad (5)$$

Here,  $W_i$  represents the weightage allotted to the attribute  $i$ .

The summation of the weightages for all the attributes considered should be 1,

$$\text{i.e., } \sum_{i=1}^n W_i = 1 \quad (6)$$

A scale is essential to fix the utility value of each characteristic. Two numbers 0 and 9 (chosen arbitrarily) represent just satisfactory and the finest possible value of the quality attribute, respectively. Now,  $P_i$  can be represented as follows:

$$P_i = A \times \ln \left( \frac{Z_i}{Z'_i} \right) \quad (7)$$

$Z_i$  represents the value of any quality  $i$  represents  $Z'_i$  represents just acceptable value of quality  $i$ ;  $A$  is a constant that can be calculated by the circumstance.

If  $Z_i = Z^*$  ( $Z^*$  being the best value), then  $P_i = 9$ . Hence,

$$A = \frac{9}{\ln \frac{Z^*}{Z_i}} \quad (8)$$

The overall utility index (OUI) can be presented as follows:

$$U = \sum_{i=1}^n W_i P_i \quad (9)$$

where  $W_i$  is the weightage given to attribute  $i$ .

As the utility function is greater-the-better category, by maximizing this, the quality attributes chosen for its evaluation will be optimized. OUI is the mean of the utility values of individual responses as equal weightage has been given to all the responses. Then, the OUI is optimized using Taguchi method.

**DMLS Tool Preparation.** DMLS is an advanced sintering procedure, which forms 3-dimensional geometries on layer-by-layer basis. The chosen material for preparation of tool is DirectMetal20. The machine employed for the purpose is EOSINT 250 extended machine.

### 3 Results and Discussion

Experimental results conforming to  $L_{27}$  orthogonal array, DOE (presented in Table 2), have been used to determine utility values of different quality attributes by using Eqs. (7)–(8). Lesser-the-better (LB) principle has been used for TWR and  $R_a$ , and greater-the-better principle has been used for MRR.

The utility values of the individual objectives have been calculated using Eqs. (7) and (8) and are presented in Table 3. Then, OUIs for each setting are calculated using Eq. 9 and are presented in the fifth column of Table 3. While calculating the OUI, equal weightage has been given to all the three responses (attributes). S/N ratios corresponding to the OUIs for all the 27 setting have been calculated and are presented in the last column of Table 3. The OUI has then been optimized using Taguchi's HB (Higher-the-better) criterion given by Eq. (1). Ideal setting has been found to be ( $I_{p1} T_{on3} T_{off3} F_{p1} T E_1$ ) from Fig. 1. The process model for responses obtained through regression analysis is given by;

$$\begin{aligned} \text{OUI} = & 7.45052 - 0.687056I_p + 0.0379444T_{on} + 0.516T_{off} + 0.0400556F_p \\ & - 1.09428TE \text{ (Coded units)} \end{aligned}$$

The predicted value for OUI is found to be 7.371. Finally, a confirmatory test was conducted to validate the experiment.

**Table 2** Experimental results

S. N	$L_{27}$ OA					Measured responses		
	$I$	$T_{on}$	$T_{off}$	$F_p$	Tool	TWR ( $\text{mm}^3/\text{min}$ )	MRR ( $\text{mm}^3/\text{min}$ )	$R_a$ ( $\mu\text{m}$ )
1	1	1	1	1	1	10.229	9.166	2.14
2	1	1	1	1	2	5.275	9.775	2.97
3	1	1	1	1	3	6.54	5.871	3.73
4	1	2	2	2	1	8.211	12.862	1.957
5	1	2	2	2	2	4.995	13.025	3.06
6	1	2	2	2	3	7.431	6.65	4.397
7	1	3	3	3	1	7.265	11.875	1.93
8	1	3	3	3	2	3.875	11.925	2.697
9	1	3	3	3	3	5.878	6.753	3.17
10	2	1	2	3	1	7.585	12.568	2.313
11	2	1	2	3	2	5.195	12.862	3.603
12	2	1	2	3	3	4.114	2.309	4.82
13	2	2	3	1	1	9.102	17.088	2.377
14	2	2	3	1	2	5.215	17.663	3.377
15	2	2	3	1	3	5.624	9.872	5.163
16	2	3	1	2	1	11.785	12.375	2.34
17	2	3	1	2	2	7.795	12.275	3.56
18	2	3	1	2	3	8.082	5.191	4.007
19	3	1	3	2	1	11.865	18.307	2.34
20	3	1	3	2	2	9.365	19.075	3.487
21	3	1	3	2	3	10.469	12.706	5.287
22	3	2	1	3	1	13.965	17.075	2.813
23	3	2	1	3	2	10.495	15.695	3.93
24	3	2	1	3	3	11.081	9.613	5.113
25	3	3	2	1	1	15.245	19.875	2.677
26	3	3	2	1	2	10.345	20.175	3.963
27	3	3	2	1	3	11.305	12.514	4.603

The TWR, MRR, and  $R_a$  for the setting ( $I_{p1} T_{on3} T_{off3} F_{p1} T E_1$ ) have been found to be  $5.275 \text{ mm}^3/\text{min}$ ,  $12.862 \text{ mm}^3/\text{min}$ , and  $2.14 \mu\text{m}$ , respectively, and the calculated OUI is 7.394 which is greater than the predicted value of 7.371. So, the quality has improved.

The ANOVA for OUI is shown in Table 4.  $R^2$  value of 94.50% indicates the effectiveness of carrying out the experiments.  $I$  is found to be the most significant factor as found from Table 4. OUI is decreasing significantly with increase in  $I$ . OUI is in decreasing order for brass, copper, and DMLS electrodes.

**Table 3** Utility values of different responses, OUI and *SN* ratio

S. N	Utility value (TWR)	Utility value (MRR)	Utility value ( $R_a$ )	OUI	<i>SN</i> ratio
1	2.622	5.724	8.078	5.475	14.7677
2	6.973	5.991	5.15	6.038	15.6179
3	5.561	3.875	3.115	4.184	12.4318
4	4.066	7.131	8.876	6.691	16.5098
5	7.332	7.183	4.884	6.466	16.2127
6	4.722	4.392	1.646	3.587	11.0946
7	4.87	6.799	9	6.890	16.7644
8	9	6.817	6.012	7.276	17.2379
9	6.262	4.456	4.568	5.095	14.1429
10	4.587	7.035	7.383	6.335	16.0349
11	7.074	7.131	3.425	5.877	15.3831
12	8.607	0	0.826	3.144	9.9497
13	3.389	8.31	7.14	6.280	15.9592
14	7.049	8.448	4.003	6.500	16.2583
15	6.552	6.032	0.212	4.265	12.5984
16	1.691	6.971	7.28	5.314	14.5084
17	4.407	6.937	3.532	4.959	13.9079
18	4.17	3.364	2.476	3.337	10.4671
19	1.647	8.597	7.28	5.841	15.3297
20	3.202	8.767	3.717	5.229	14.3684
21	2.47	7.08	0	3.183	10.0567
22	0.576	8.307	5.635	4.839	13.6951
23	2.453	7.957	2.649	4.353	12.7758
24	2.096	5.922	0.299	2.772	8.8559
25	0	8.938	6.078	5.005	13.9881
26	2.548	9	2.574	4.707	13.4549
27	1.965	7.017	1.237	3.406	10.6449

## 4 Conclusions and Future Work

Tool electrode and peak current have been found to be the most significant factors affecting the responses which are on the expected lines and prove the efficacy of conducting the experiments. Ideal setting for best performance has been found to be ( $I_{p1} T_{on3} T_{off3} F_{p1} TE_1$ ) which has been verified by a confirmatory test. The performance of the copper electrode is found to be better than the performance of brass electrode whose performance is again found to be better than the DMLS electrode. Comparatively poor performance of DMLS electrode is owing to the higher porosity level and comparatively lower composition of copper. The future researchers should

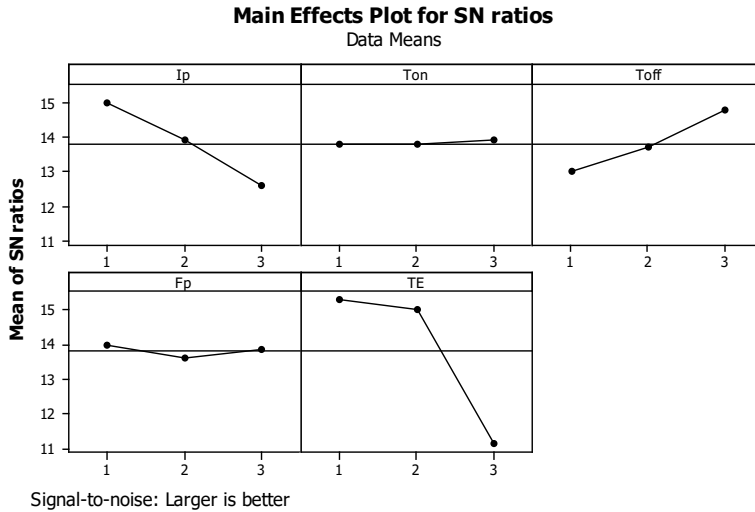


Fig. 1 Estimation of best setting

Table 4 ANOVA for OUI

Source	DF	Seq SS	Adj SS	Adj MS	F	P
<i>I</i>	2	8.5148	8.5148	4.2574	28.82	0.000
<i>T<sub>on</sub></i>	2	0.0267	0.0267	0.0134	0.09	0.914
<i>T<sub>off</sub></i>	2	4.8286	4.8286	2.4143	16.34	0.000
<i>F<sub>p</sub></i>	2	0.2217	0.2217	0.1109	0.75	0.488
TE	2	27.0115	27.0115	13.5058	91.42	0.000
Error	16	2.3637	2.3637	0.1477		
Total	26	42.9671				

$S = 0.384361$   $R^2 = 94.50\%$   $R^2$  (adj) = 91.06%

reduce porosity levels of the DMLS electrode as well as increase in the copper composition in the powder mixture (which in turn would significantly improve the electrical conductivity) to make it possible to replace conventional electrodes. Thus, DMLS tool may be recommended for semi-finishing job.

## References

1. Arthur A, Dickens PM, Cobb RC (1996) Using rapid prototyping to produce electrical discharge machining electrodes. Rapid Proto J 2(1):4–12
2. Rennie AEW, Bocking CE, Bennett GR (2001) Electroforming of rapid prototyping mandrels for electro-discharge machining electrodes. J Mater Process Technol 110:186–196

3. Durr H, Pilz R, Eleser NS (1999) Rapid tooling of EDM electrodes by means of selective laser sintering. *Comput Ind* 39:35–45
4. Dimla DE, Hopkinson N, Rothe H (2004) Investigation of complex rapid EDM electrodes for rapid tooling applications. *Int J Adv Manuf Technol* 23:249–255
5. Czyzewski J, Burzynski P, Gawel K, Meisner J (2009) Rapid prototyping of electrically conductive components using 3D printing technology. *J Mater Process Technol* 209:5281–5285
6. Amarim FL, Lohrengel A, Miller N, Schafer G, Czelusniak T (2013) Performance of sinking EDM electrodes made by selective laser sintering technique. *Int J Adv Manuf Technol* 65:1423–1428
7. Czelusniak TL, Amorim FL, Higa CF, Lohrengel A (2014) Development and application of new composite materials as EDM electrodes manufactured via selective laser sintering. *Int J Adv Manuf Technol* 72:1503–1512
8. Mohanty SD, Mahapatra SS, Mohanty RC (2017) Study on performance of EDM electrodes produced through rapid tooling route. *J Adv Manuf Sys* 16(4):357–374
9. Reddy LM, Krishna LSR, Kumar SS, Reddy PR (2018) Estimation of electrical conductivity of ABS and PLA based EDM electrode fabricated by using FDM 3D-Printing process. *Int J Mod Eng Res Technol* 5:332–338
10. Padhi SK, Mahapatra SS, Padhi R, Das HC (2018) Performance analysis of a thick copper-electroplated FDM ABS plastic rapid tool EDM electrode. *Adv Manuf* 6(4):442–456
11. Singh J, Pandey PM (2019) Process optimization for rapid manufacturing of complex geometry electrical discharge machining electrode. *Proceedings of the Institution of Mechanical Engineers, Part C: J Mech Eng Sci* 234(1):66–81
12. Singh J, Singh G, Pandey PM (2020) Electric discharge machining using rapid manufactured complex shape copper electrode: Parametric analysis and process optimization for material removal rate, electrode wear rate and cavity dimensions. *Proceedings of the institution of mechanical engineers, Part C. J Mech Eng Sci.* <https://doi.org/10.1177/0954406220906445>
13. Antony J, Antony F (2001) Teaching the Taguchi method to industrial engineers. *Work Study* 50(4):141–149
14. Kumar P, Barua PB, Gaindhar JL (2000) Quality optimization (multi-characteristics) through Taguchi's technique and utility concept. *Qual Reliabil Eng Int* 16(6):475–485
15. Walia RS, Shan HS, Kumar P (2006) Multi-response optimization of CFAAFM process through Taguchi method and utility concept. *Mater Manuf Process* 21(8):907–914

# Effect of Preheat Temperature on Thermal Behavior in AlSi10Mg Powder Bed During Laser Powder Bed Fusion Process



Amitav Dash and Seshadev Sahoo

**Abstract** The laser powder bed fusion is a kind of additive manufacturing process emerged as smart manufacturing process in the current industrial revolution. With the help of this process, the components are made with design freedom. The present work focused on to investigate the effect of preheat temperature in AlSi10Mg component through numerical analyzes. Ansys 19.2 platform is used to simulate the process with the powder bed. From the numerical analyzes, it has been seen that the temperature in the powder bed increases as the preheat temperature increases by keeping all other parameters constant.

**Keywords** Heat transfer · Powder bed · Additive manufacturing · Preheat temperature

## 1 Introduction

Laser powder bed fusion is an additive manufacturing process in which complex and integrated 3D objects are manufactured by using a precise, high-wattage laser to fuse, and melt powder material to build the first layer of the objects of defined material. This technology adopts high-laser energy to make the components from the powder materials. This process has significant characteristics like design autonomy with high efficiency by minimizing the cost [1–3]. The thermal nature of build part during this process is influenced to a great extent with the variation of operating parameters [4]. Gu et al. [5] examined the effect of laser energy and beam speed on temperature distribution and configuration of the melted zone through thermal simulation. Microstructures of components produced at varying operating environments also evaluated to validate the model. Zeng et al. [6] conducted a thermal analysis of laser processes to predict thermal stresses and microstructure of the component during processing and in a printed part. The key characteristics of temperature distribution with respect to

---

A. Dash · S. Sahoo (✉)

Department of Mechanical Engineering, Institute of Technical Education and Research, Siksha 'O' Anusandhan (Deemed to be University), Bhubaneswar, Odisha 751030, India  
e-mail: [seshadevsahoo@soa.ac.in](mailto:seshadevsahoo@soa.ac.in)

process parameters on were discussed. Convective heat and radiation were neglected in their model. Samantaray et al. [7, 8] studied the thermal nature of the multi-component powder bed in direct metal laser sintering process using finite element approach. From their investigation, the authors found that there is a rise in temperature and gradually increase in size of the melt zone by increasing the input laser energy. From the input laser energy, the authors calculated the cooling rate and predict the microstructure formation in AlSi10Mg alloy. Yuan et al. [9] explored the influences of Marangoni convection on temperature evolution and the effect of process parameters on molten pool dimensions were thoroughly investigated. A comparative study was drawn by Ojha et al. [10] to show the effect of thermal conductivity on various thermal models like the heat transfer model, enhanced thermal conductivity model, and CFD model. Most of the numerical models were developed to study the feasibility of the laser powder bed fusion process and optimize the process parameters. Limited research has been carried out to study the build parts from multicomponent powder systems in this process.

## 2 Numerical Simulation

By considering the physical model and its operation to analyze the temperature distribution in the powder bed during the fabrication process, numerical simulations are inevitable. The differential form of the heat transfer equation used to analyze the powder bed temperature during the process is

$$\nabla \cdot (k \nabla T) + Q = \rho C_p \frac{\partial T}{\partial t} \quad (1)$$

$\rho$ ,  $T$ ,  $t$ ,  $C_p$  represent density, temperature, the interaction time between the laser beam and powder, and specific heat capacity.  $Q$  is heat generation per unit volume and  $k$  represents the thermal conductivity.

### 2.1 Initial and Boundary Condition

The initial and boundary condition used for the numerical analysis of the model are given as follows:

Initially, the powder bed and the substrate are supposed to be at room temperature, i.e.,

$$T(x, y, z, t) = 300k \quad (2)$$



From each surface of the powder bed and substrate, except the bottom surface, the heat transfer is calculated by

$$-k \left( \frac{\partial T}{\partial z} \right) = \epsilon \sigma (T^4 - T_0^4) + h(T - T_a) \quad (3)$$

The laser beam is modeled using Gaussian heat source model used to calculate the input heat flux, i.e.,

$$q = \frac{0.865 \times \alpha \times P}{\pi r_b} \quad (4)$$

where  $\alpha$ ,  $P$ , and  $r_b$  are laser absorptivity, laser power, and radius of the laser beam, respectively.

## 2.2 Numerical Procedure for Simulation

Finite element approach is utilized to develop the thermal model for the laser powder bed fusion of AlSi10Mg alloy. The numerical simulations are carried out using Ansys 19.2 platform. The simulation domain is divided into two parts, i.e., substrate and powder bed. The substrate and powder bed are dimension of  $1 \times 1 \times 1$  mm and  $2 \times 2 \times 2$  mm, respectively. The laser beam focuses on the top surface of the powder bed with a diameter of 0.2 mm. The model considers the combined heat transfer phenomena, i.e., conduction, convection, and radiation in the powder bed as well as the substrate. Grid independent test is carried out to optimize the number of grids for the computational domain. After grid independent test, simulation domain has finalized with 360,937 no. of nodes, 983,152 no. of elements with hexahedral meshing type. Figure 1 represents the simulation domain used for numerical analysis.

## 3 Results and Discussion

To investigate the effect of preheating temperature on thermal behavior in the powder bed, numerical simulations are carried out at different powder bed preheat temperatures, i.e., 80, 100, 120, 140, and 160 °C by keeping other operating parameters constant. Table 1 represents the operating parameters used for the current simulations.

The temperature variation on the AlSi10Mg powder bed at different preheat temperature is shown in Fig. 2. From the simulation results, it is clearly observed that at the interaction zone of the laser beam and powder bed the temperature zone looks like elliptical profile. There is an increase in temperature with increase in powder bed preheat temperature. When the preheat temperature of the powder bed is set at

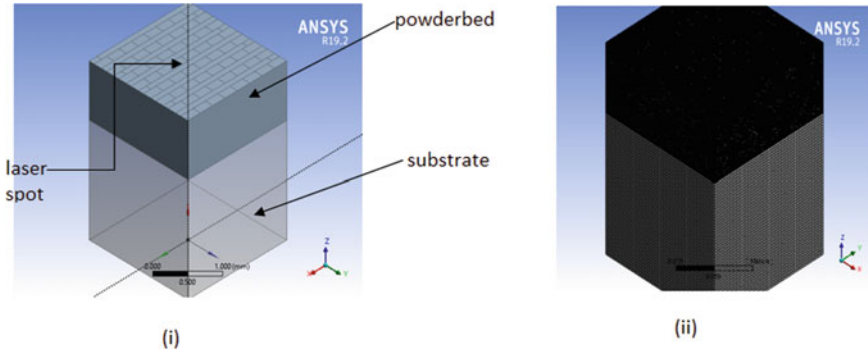


**Fig. 1** Simulation domain

**Table 1** Operating parameters used for numerical simulation

Parameters	Values
Input laser energy	100 W
Beam speed	100 mm/s
Laser beam diameter	0.2 mm
Powder layer thickness	1 mm
Powder bed preheat temperature	80, 100, 120, 140, 160 °C

80 °C and keeping all other simulation parameters fixed, the powder bed temperature increased to 120 °C, whereas for 100 °C preheat temperature, the powder bed temperature increases to 140 °C. Similarly, with an increase in preheat temperature from 120 °C to 160 °C, the temperature of the AlSi10Mg alloy powder bed rises from 160 °C to 200 °C, respectively. This is happened because of initial stored energy in the powder bed with change in preheat temperature.

When the laser beam moves over the powder layer, the elliptical profile of the temperature zone moves forward and becomes more concentrated. Behind the laser spot, it looks elongated shape due to rapid change in temperature. Due to the interaction of the laser beam with powder layer, rapid melting and solidification occur which help to make the predefined components. The simulated temperature distribution with change in preheat temperature of the powder bed helps to select the appropriate condition for making the component.

Figure 3 shows the graphical representation of the temperature variation on the scan path at different preheat temperatures during the fusion of AlSi10Mg alloy. From the figure, it is noticed that change in temperature at 100 °C preheat temperature case is slightly higher than 80 °C preheat temperature and it increases subsequently with an increase in preheat temperature. It is found that by increasing the preheat temperature of the powder bed, the temperature along the scan path increases. Due to initial heat storage with the variation of preheat temperature, the temperature increases subsequently in the powder layer as well as the solidification rate also.

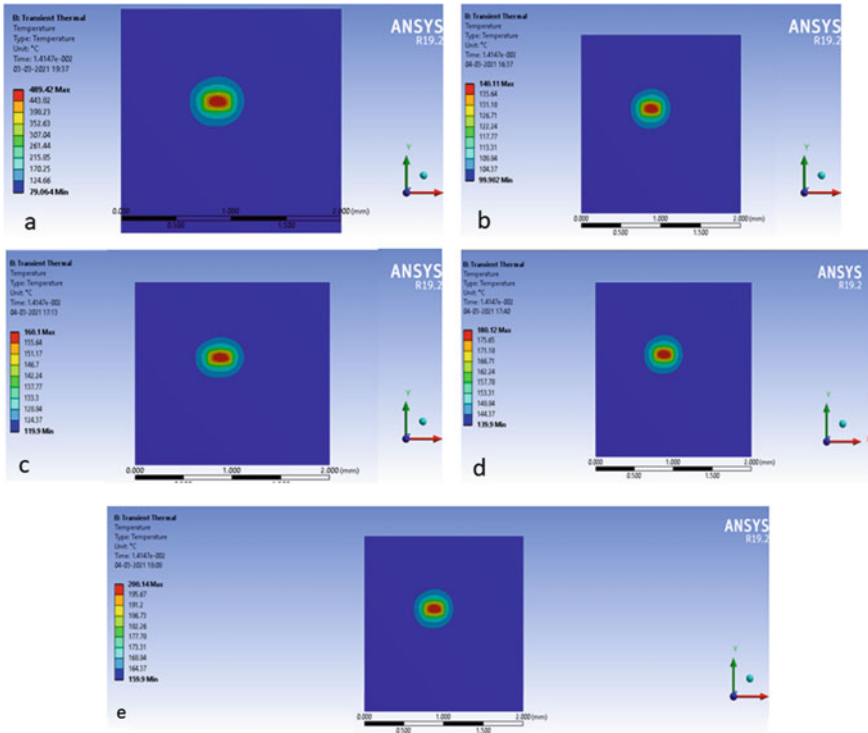


**Fig. 2** Temperature distribution in AlSi10Mg powder bed at different preheat temperature of the powder bed **a** 80 °C, **b** 100 °C, **c** 120 °C, **d** 140 °C, and **e** 160 °C

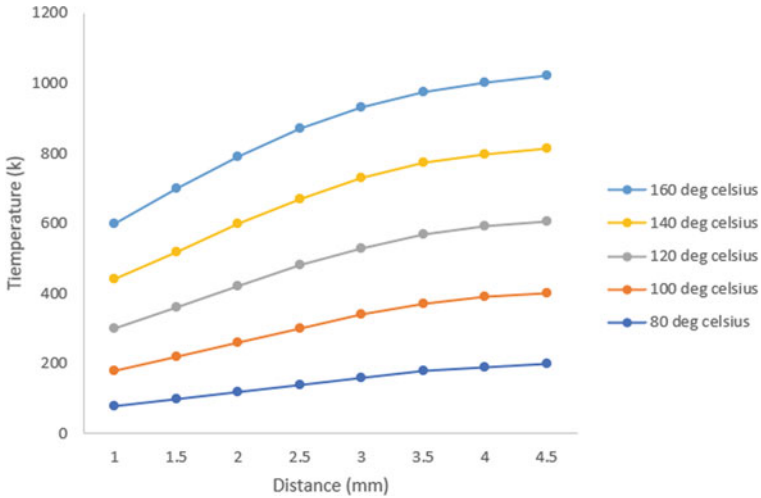


**Fig. 3** Temperature plot at different preheat temperatures along scan path

Similarly, if the temperature is much above the melting range of the alloy, it can lead to splashing caused by capillarity instability. Such circumstances can have an adverse effect and can lead to metallurgical defects like balling, accumulation of thermal stress, etc., which decreases the densification level.

## 4 Conclusions

The following conclusions were drawn from the above investigation:

- i. A numerical model was developed to understand the temperature distribution in the powder layer with variation in preheat temperature.
- ii. The powder bed temperature increases with increase in preheat temperature from 80 to 160 °C, due to initial heat storage in the powder bed as observed from the simulation results.
- iii. The simulated results gave more insight of the process feature to select the appropriate operating conditions for making the component.

## References

1. Atzeni E, Salmi A (2015) Study on unsupported overhangs of AlSi10Mg parts processed by direct metal laser sintering (DMLS). *J Manufact Process* 20:500–506
2. Kruth JP, Wang X, Laoui T, Froyen L (2003) Binding mechanisms in selective laser sintering and selective laser melting. *Assembly Autom* 23:357–371
3. Romano J, Ladani L, Sadowski M (2015) Thermal modeling of laser-based additive manufacturing processes within common materials. *Procedia Manufact* 1:238–250
4. Venuvinod PK, Ma W (2004) *Rapid prototyping—laser based and other technologies*. Kluwer Academic, London
5. Gu D, Shen Y (2009) Balling phenomena in direct laser sintering of stainless-steel powder: metallurgical mechanisms and control methods. *Mater Des* 30(8):2903–2910
6. Zeng K, Pal D, Stucker B (2012) A review of thermal analysis methods in laser sintering and selective laser melting. In: *Proceedings of solid freeform fabrication symposium Austin, TX*, vol 60, pp 796–814
7. Samantaray M, Thatoi DN, Sahoo S (2019) Modeling and optimization of process parameters for laser powder bed fusion of AlSi10Mg alloy. *J Lasers Manuf Mater Process*. <https://doi.org/10.1007/s40516-019-00099-7>
8. Samantaray M, Thatoi DN, Sahoo S (2018) An approach to numerical modeling of temperature field in direct metal laser sintering. In: *International conference on mechanical engineering, INCOM 2018: advances in materials, mechanical and industrial engineering*, pp 295–314
9. Yuan P, Gu D (2015) Molten pool behaviour and its physical mechanism during selective laser melting of TiC/AlSi10Mg nanocomposites: simulation and experiments. *J Phys D Appl Phys* 48:1–16
10. Ojha A, Samantaray M, Thatoi DN, Sahoo S (2018) Continuum simulation of heat transfer and solidification behavior of AlSi10Mg in direct metal laser sintering process. *IOP Conf Ser Mater Sci Eng* 338:1–6

# The Development of Turbopumps for Low-Thrust Cryogenic Rocket Engine



Sridhar Panigrahi, P. Rijish Kumar, B. Prejil Kumar, P. Unnikrishnan Nair, Paul P. George, N. Jayan, and M. S. Suresh

**Abstract** The Indian Space Research Organisation (ISRO) envisaged a launch vehicle to put 4 ton class satellites to Geosynchronous Transfer Orbit (GTO). GTO is Geosynchronous Transfer Orbit of 170 km perigee and 35,975 km apogee, where the satellites are injected. It is further raised to the Geostationary orbit by firing satellite thrusters. The upper stage of this launch vehicle is powered by a cryogenic engine of 200 kN nominal thrust working in gas generator cycle using liquid hydrogen (LH<sub>2</sub>) and liquid oxygen (LOX) as propellants. The engine has independent LOX and LH<sub>2</sub> turbopumps, with their turbines operating in series mode. The turbopumps were successfully developed through a series of development tests, which included subsystem level tests for pumps, turbines, bearings and seals with simulated fluids. Subsequently, tests were carried out in the turbopump level with different pump fluids like water, liquid nitrogen, liquid oxygen and liquid hydrogen. Finally, tests were carried out in closed-loop mode (boot-strap) with gas generator and turbopumps operating together. The successful completion of these tests demonstrated the design validity of these turbopumps. Subsequently, turbopumps have undergone flight duration and extended flight duration tests as part of engine. The third development engine was used in the successful flight testing of the launch vehicle in 2017. The efforts towards the development of turbopumps are detailed in this paper.

**Keywords** Launch vehicle · Cryogenic engine · Turbopumps

## 1 Introduction

A 200 kN thrust class cryogenic engine was developed by Indian Space Research Organisation (ISRO) for a launch vehicle capable of placing a 4 ton class satellite in the Geosynchronous Transfer Orbit (GTO). This engine works on gas generator (GG) cycle using liquid hydrogen (LH<sub>2</sub>) and liquid oxygen (LOX) as propellants.

---

S. Panigrahi (✉) · P. Rijish Kumar · B. Prejil Kumar · P. Unnikrishnan Nair · P. P. George · N. Jayan · M. S. Suresh  
Liquid Propulsion Systems Centre, ISRO, Trivandrum, Kerala 695547, India  
e-mail: [sridharpanigrahi@lpsc.gov.in](mailto:sridharpanigrahi@lpsc.gov.in)

The engine uses separate turbopumps to feed the propellants at high pressure into the thrust chamber. The turbines are mounted in series, with drive fluid (combustion product of LH<sub>2</sub> and LOX) after expansion in LH<sub>2</sub> turbine is fed to LOX turbine to run the respective pumps. The reference in [1] gives the details of requirements to be met by turbopump systems for liquid propulsion engines. This paper highlights the main design features of the turbopumps, development test philosophy adopted and development and qualification tests carried out.

## 2 Turbopumps—Design Features

The major design parameters for the turbopumps are given in Table 1. Due to low density of LH<sub>2</sub>, a very high speed multistage pump (two stages) is envisaged for LH<sub>2</sub> pump for meeting the high headrise requirement. This also employs a three-bladed helical pump, called inducer, which improves the suction specific speed of the pump. The LOX pump is a single-stage pump, again with an inducer for improving the suction performance. Both the turbines are two-row velocity compounded impulse turbines, with turbines directly driving their respective pumps. References given in [2–5] provide the basic design features and design requirements for liquid rocket engine centrifugal pumps, inducers and turbines.

The inducer pumps produce enough headrise to prevent cavitation in the main pump. The LH<sub>2</sub> pump impellers are made from titanium alloy, which is having high strength to weight ratio to withstand high centrifugal stresses resulting from high speed of rotation. One of the challenges faced during development was fabrication of impellers from this material. Both the impellers consist of six full vanes and six partial vanes with first stage impeller having 3D curvature vanes for better suction performance. The LOX pump impeller rotates at comparatively lower speed and doesn't have to withstand high centrifugal stresses. It is made from aluminium alloy due to low density advantage. This also consists of six full and six half vanes having 3D curvature. For the turbine, which is operating at very high temperature of the

**Table 1** Turbopump design parameters

Parameters	LH2	LOX
Pump inlet pressure (MPa)	0.23	0.22
Pump inlet temperature (K)	21	78
Pump flowrate (kg/s)	7.5	40.5
Pump outlet pressure (MPa)	9.5	8.9
Speed (rpm)	38,000	15,000
Turbine inlet pressure (MPa)	4.3	0.54
Turbine inlet temperature (K)	850	640
Turbine pressure ratio	8.1	2.03

order of 850 K, nickel-based super alloy material Inconel 718 is used since it retains its high mechanical properties at higher temperatures.

The dynamic sealing system, which is nothing but the arrangement of seals between the pump and turbine parts, is the most critical element in the turbopump. It minimises the leakage of pump side and turbine side fluids and also prevents the mixing of incompatible fluids (oxygen and hydrogen rich hot gases) in the case of LOX turbopump. To minimise the leakage from pump side, welded metal bellow seal is used, whereas on turbine side, clearance seals having 20–30  $\mu\text{m}$  clearance are used. For LOX turbopump, an additional purge seal, which is also a clearance seal, is provided between these two seals to prevent mixing of the incompatible fluids.

Angular contact ball bearing pairs are used for providing support for the rotating shaft. Angular contact ball bearings are used over deep groove ball bearings due to its higher axial load carrying capacity and due to higher DN capability. To minimise leakage in the pump from higher pressure region to lower pressure region, double-layered (with inner soft) bronze seal rings are used, which is manufactured through powder metallurgy route. In LOX turbopump, floating ring seals are used for this purpose, which help prevent any frictional rubbing during operation.

### 3 Development Tests

#### 3.1 Subsystem Level Tests

At subsystem level, tests were carried on pump and turbine elements. Pump was tested with de-mineralised (DM) water, and turbine was tested with gaseous nitrogen ( $\text{GN}_2$ ). These initial level tests were carried out for the design validation of pumps and turbines. These tests were carried out using similarity conditions to verify their performance. During pump testing, pump was driven by an electric motor, and pump flowrate was varied by adjusting the pump outlet line control valve. By measuring various parameters, pump headrise and efficiency were estimated and compared with the design value. To establish the pump net positive suction head (NPSH) requirement, cavitation test was carried out by reducing the pump inlet pressure by venting the water supply tank pressure till cavitation occurred in the pump.

During turbine testing, turbine was driven by ambient (300 K)  $\text{GN}_2$  simulating the design inlet pressure and pressure ratio across the turbine as given in Table 1. The power developed by the turbine was absorbed by a dynamometer, and by measuring the parameters like speed, torque and turbine mass flowrate, efficiency of the turbine was established. Figure 1 shows the photograph of these tests, and Fig. 2 gives the pump and turbine characteristics generated during these tests.

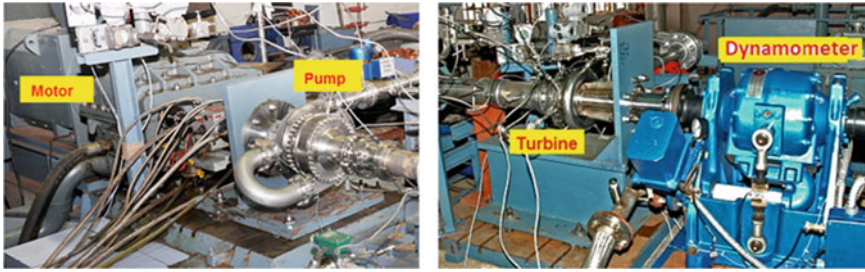


**Fig. 1** Photograph of pump and turbine testing

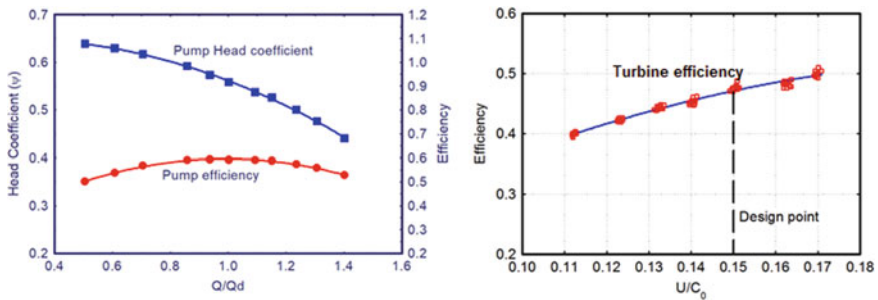


**Fig. 2** LH<sub>2</sub> pump and turbine performance curves

### 3.2 Bearings and Dynamic Seals Tests

Before incorporating the bearings and dynamic seals in the turbopumps, their design validation was carried out using a separate test rig, which simulated the turbopump operating conditions. The tests involved water level tests initially, followed by liquid nitrogen (LN<sub>2</sub>) and then actual fluids. These tests proved the capability of bearings and dynamic seals under the simulated condition of thermo-mechanical loading. These tests were carried out with enough margins on the operating condition in terms of speed, pressure, and coolant flow rates. A typical bearing and seal test parameters are shown in Fig. 3 for LH<sub>2</sub> turbopump in which bearing coolant flowrate was reduced from design value of 130 g/s to demonstrate the margin.

### 3.3 Turbopump Assembly Level Tests

The turbopump assembly level tests were carried out after completing the above tests by integrating the pump and turbine together. In these tests, pump was driven by turbine as in actual operation, instead of electric motor. Here also, different fluids for pumps and turbines were introduced in a staged manner with initial level tests



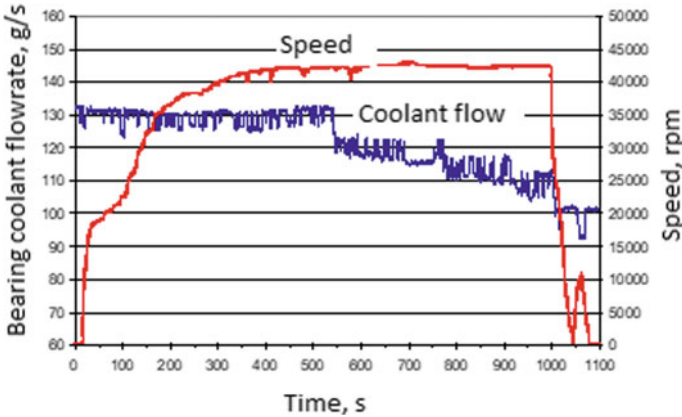


Fig. 3 LH2 bearing test parameters

with pump handling water and turbine driven by gaseous nitrogen. After completion of these tests, cryo-fluid was introduced to pump with liquid nitrogen and turbine still driven by ambient GN<sub>2</sub>. Finally, tests were carried out by introducing the actual operating fluids on pump side (LH<sub>2</sub>/LOX), and turbine driven by hot combustion products of LH<sub>2</sub> and LOX, which is produced in the test facility. The rated power level tests were carried out at this stage. Thus, as can be seen, severity of operating condition in terms of thermal and mechanical loading was introduced in a staged manner, and at each stage, problems encountered were solved, validated and moved on to the next stage. Also, due to the unique thermodynamic behaviour of cryogenic fluids under cavitating condition of the pumps, it was decided to carry out cavitation tests with actual fluids to establish their NPSH requirements. These NPSH values were used for arriving at the tank pressure required for flight operation instead of NPSH values based on water test. A total of eight tests were carried out on LH<sub>2</sub> turbopump for a cumulative duration of 900 s, whereas ten tests were carried out on LOX turbopump for a cumulative duration of 1600 s.

### 3.4 Power Head Mode Tests

One of the biggest advantages of gas generator cycle engine is that its power head including turbopumps and gas generator can be independently tested without the need for thrust chamber. So, this series of tests were carried out by mounting the turbopumps in the facility, with their turbines connected in series mode as in engine. The hot gases required for running the turbine were produced by a facility-mounted gas generator, which can work both in open-loop mode and closed-loop mode. In open-loop mode, the propellants (LH<sub>2</sub> and LOX) required for producing the hot gases are fed from facility high pressure tanks. But, in closed-loop mode, propellants are

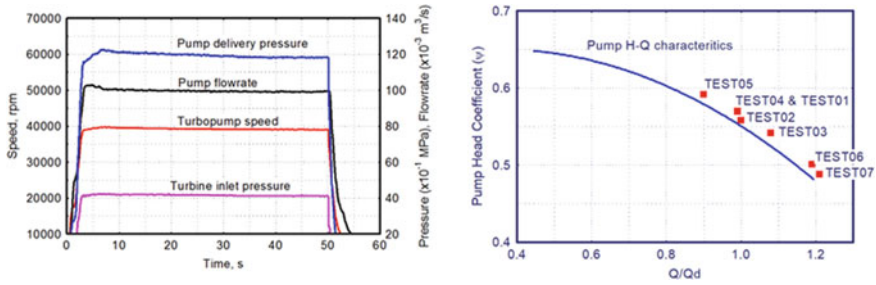


Fig. 4 LH2 turbopump test parameters and test result (boot-strap mode)

fed from pumps themselves. This is also known as boot-strap mode testing. This requires that a start-up system be used for starting the pumps initially. Hence, a high pressure, stored GH<sub>2</sub> gas start system was used for starting the turbopumps, which was subsequently used for engine tests as well as for flight testing.

A total of nine hot tests with one test in open-loop mode and eight tests in boot-strap mode were successfully completed as planned for a cumulative duration of 350 s. LH<sub>2</sub> turbopump parameters in one of these tests and test results are shown in Fig. 4. The pump performance (head rise) was close to the value obtained during pump tests with water. The successful completion of these tests marked a major milestone and paved the way for successful development of the engine. The engine start and shutdown sequences developed through these tests were successfully implemented in engine.

## 4 Engine Tests and Flight

Subsequent to the power head mode tests, the turbopumps were put to ‘real’ test by subjecting it to hot tests after integrating it as part of engine. Short-duration ignition trials were carried out initially to evolve the sequence for engine starting and shutdown. The turbopumps could meet the higher acceleration and deceleration requirement of pumps during these transients. After these tests, short, medium and long-duration hot tests were carried out. The long duration tests included the flight duration tests as well as extended duration (1.25 times the flight duration tests) tests as part of engine qualification. The first two engines were tested with sea level area ratio for the engine nozzle, whereas the third engine with full nozzle area ratio was tested inside a vacuum chamber simulating the vacuum conditions expected during flight. Besides engine tests, stage-level tests were also carried out by simulating the flight stage on ground. The cumulative duration of these tests was 3200 s, and the performance of turbopumps was as expected for meeting the flight requirements. Based on this confidence, first developmental flight testing of the new cryogenic upper stage was attempted and successfully completed in 2017.

## 5 Conclusion

LOX and LH<sub>2</sub> turbopumps for a new cryogenic upper-stage rocket engine of 200 kN thrust operating in gas generator cycle have been successfully developed after elaborate testing, overcoming many challenges on the way. The developmental testing itself was a huge effort involving many teams spread across different facilities specialised in design, manufacturing, assembly and cryogenic testing. The turbopumps were subjected to development tests in a very exhaustive manner covering all aspects of operation expected in engine. Bearings and seals were extensively qualified in a separate test rig. After the successful completion of turbopump level and power head mode tests, both the turbopumps were successfully qualified for flight duration in engine-level tests. The above efforts culminated in the first successful developmental test flight of the launch vehicle.

## References

1. NASA (1974) Turbopump systems for liquid rocket engines, NASA SP 8107
2. NASA (1973) Liquid rocket engine centrifugal flow turbopumps, NASA SP 8109
3. NASA (1971) Liquid rocket engine turbopump inducers, NASA SP 8052
4. Reynolds TW (1966) Aerodynamic design Model II turbine M-1 fuel turbopump assembly, NASA CR-54820
5. Beer R (1965) Aerodynamic design and estimated performance of a two-stage curtis turbine for the liquid oxygen for the M-1

# Effect of Partial Filling of Metal Foams on Exergy Transfer in a Vertical Channel



K. Kiran Kumar, Banjara Kotresha, and Kishan Naik

**Abstract** This paper presents the analysis of exergy transfer through metal foams partially filled in a vertical channel. The numerical model consists of a heater which is inserted between two aluminum plates and is situated at the core of the channel. To enhance heat transfer from the plate, aluminum metal foam of pore density 10 (PPI) with porosity 0.95 is located on sideways of the plate. The numerical simulations for metal foam filling rates of 25%, 50%, 75%, and 100% are carried out for fluid inlet velocity ranging from 0.1–3 m/s. The flow-through metal foam is predicted with the help of Darcy Extended Forchheimer model while heat transfer is predicted by means of local thermal non-equilibrium (LTNE) model. For validation purpose, the present work results are compared with the results available in the literature and noticed a good agreement among them. The exergy transfer and entropy generation owing to both heat transfer and flow friction are presented and discussed. It is found that the metal foam with 75% filling rate enhances the exergy transfer owing to both heat transfer and fluid flow friction compared to other filling rates.

**Keywords** Channel · Metal foams · Partially filled · Exergy ·  $WLPE_{Re}$

## 1 Introduction

Heat transfer processes are intrinsically associated with thermodynamic irreversibility, and hence, some quantity of valuable energy is ruined in the process which leads to decline in the system efficiency. Based on the second law of thermodynamics, this cost of valuable energy due to irreversibility is presented in terms of entropy generation, which can be used to estimate the performance of a system and to

---

K. Kiran Kumar · K. Naik

Department of Studies in Mechanical Engineering, University B.D.T College of Engineering, Davangere, Karnataka, India

B. Kotresha (✉)

Department of Mechanical Engineering, Government Engineering College, Haveri, Karnataka, India

e-mail: [bkotresha@gmail.com](mailto:bkotresha@gmail.com)

© The Author(s), under exclusive license to Springer Nature Singapore Pte Ltd. 2023

157

P. Pradhan et al. (eds.), *Recent Advances in Mechanical Engineering*,

Lecture Notes in Mechanical Engineering,

[https://doi.org/10.1007/978-981-16-9057-0\\_17](https://doi.org/10.1007/978-981-16-9057-0_17)

attain optimal design standards. Zhao [1] conducted a review on thermal transport in open-celled cellular high-porous metal foams, focusing mainly on effective thermal conductivity and forced convection. A few experimental and numerical studies [2–5] have been carried out to determine the hydrodynamics and thermal characteristics of porous media filled in a vertical channel. Analysis of entropy generation through nanofluids is conducted by Sarkar et al. and Pawan et al. [6, 7]. Kurtbus et al. [8] conducted an exergy transfer analysis where they presented and discussed the mean exergy transfer with respect to various factors for the porous rectangular channels.

The preceding survey of literature reveals the hydrodynamic and thermal characteristics of metal foams filled in horizontal and vertical channels. Few reported research works reveal the importance of entropy generation and exergy transfer through porous media completely filled in horizontal channels, but very few research works are observed with respect to vertical channels. Hence, this study focusses on exergy transfer analysis through metal foams filled in a vertical channel. The objective of this study is to analyze the effect of partial filling of metal foams on entropy generation and exergy transfer in a vertical channel compared to completely filled metal foams.

## 2 Methodology

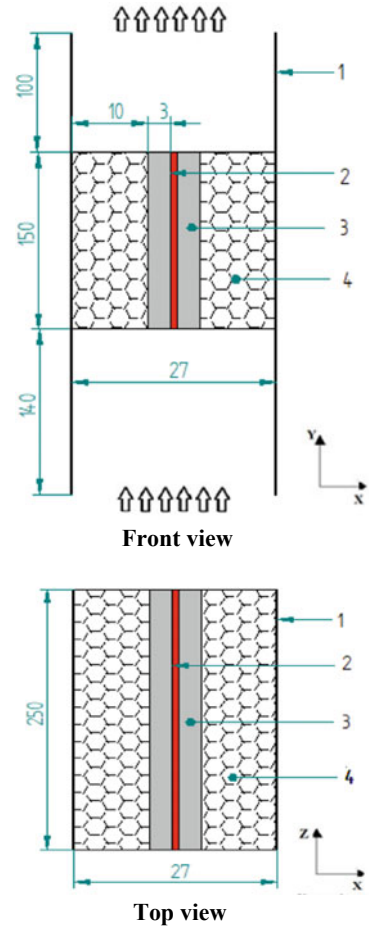
### 2.1 Geometry Configuration

The configuration of the geometry considered for the present study is shown in Fig. 1 and is similar to the geometry considered by Kotresha et al. [2]. The geometry comprises of heater, aluminum plates and metal foams assembly, in which heater is located between two aluminum plates each of which has  $250 \times 150 \times 3$  dimension (all in mm), and to augment heat transfer, aluminum metal foams having dimension of  $250 \times 150 \times 10$  (all are in mm) are attached to sideways of the aluminum plate. The aluminum metal foam of 10 PPI (pores per inch) having porosity of 0.95 is considered for 25%, 50%, 75%, and 100% filling rates in the vertical channel.

### 2.2 Computational Domain and Boundary Conditions

As the vertical channel considered in the study is symmetrical along  $Y$ -axis, only half portion of the channel has been considered for further investigation. Figure 2 shows the 2-D computational domain of the vertical channel for different metal foam filling rates, which consists of a heater specified with constant heat flux and aluminum metal foams are located on sideways of the plate along with upstream and downstream of the channel. Uniform velocity and zero pressure are presumed at the inlet and outlet

**Fig. 1** Schematic diagram of front and top view of the vertical channel filled with metal foam



of the channel, while symmetry and adiabatic wall constraints are applied at the vertical axis and channel side walls, respectively.

### 2.3 Numerical Details

In this study, ANSYS FLUENT 15.0 software is used to carry out numerical computations. In the computations, air is taken as the working fluid which enters the vertical channel through the inlet and flows in both open and metal foam regions. A variant velocity of air ( $V$ ) ranging from 0.1 to 3 m/s is used in the present analysis. For this range of air velocity, a Reynolds number based on the hydraulic diameter of the vertical channel varies from 300 to 10,000. Since the flow is taking place inside the vertical channel, Reynolds number up to 2300 is considered as laminar flow, between

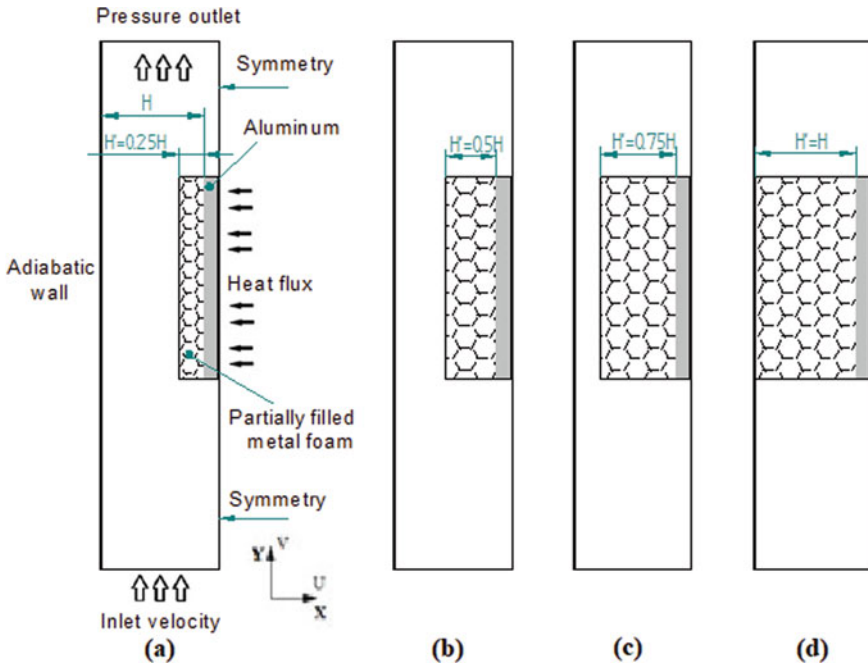


**Fig. 2** Two-dimensional computational domain for different metal foam filling rates **a** 25%, **b** 50%, **c** 75%, and **d** 100%

2300 and 6000 as transition flow and more than 6000 as turbulent flow regime. The physical properties of air and aluminum are taken at 27 °C [9], and aluminum metal foams characteristics are listed in Table 1. The flow-through metal foam porous medium is predicted with the help of Darcy Extended Forchheimer model which takes care of permeability and drag coefficient of the porous medium while heat transfer is predicted with the help of LTNE model. The calculated surface area density ( $a_{sf} = 357.02 \text{ m}^{-1}$ ) is well agreed with the literature [5] ( $a_{sf} = 360.6 \text{ m}^{-1}$ ), and Eq. (2) is used to calculate the interfacial heat transfer coefficient ( $h_{sf}$ ) [2].

Surface area density,

$$a_{sf} = \frac{3\pi d_f \left(1 - e^{-\frac{(1-\phi)}{0.04}}\right)}{(0.59d_p)^2} \tag{1}$$

**Table 1** Aluminum metal foam characteristics [4, 9]

PPI	$H$ (mm)	$\phi$	$d_p$ (mm)	$d_f$ (mm)	$K \times 10^7$ (m <sup>2</sup> )	$C$ (1/m)	$\rho$ (kg/m <sup>3</sup> )	$C_p$ (J/kg K)	$k$ (W/m K)
10	10	0.95	4.952	0.445	2.48	94.98	2790	883	168

**Table 2** Result of grid independence study for 10 PPI aluminum metal foam (Re = 3000)

Cells	Pressure drop, $\Delta P$	Temperature excess, $\Delta T$	Deviation (%)	
			$ \Delta \mathbf{P} $	$ \Delta \mathbf{T} $
31,500	27.47	7.43	0.18	1.36
57,750	27.53	7.35	0.03	0.27
98,000	27.52	7.33	Base-line	

Interfacial heat transfer coefficient,

$$h_{sf} = \frac{0.52 \text{Re}_{d_f}^{0.5} \text{Pr}^{0.37} k_f}{d_f \left(1 - e^{\frac{-(1-\phi)}{0.04}}\right)} \tag{2}$$

where  $\text{Re}_{d_f} = \frac{V d_f}{\phi \nu}$ ,  $d_f$ ,  $d_p$ ,  $\phi$ ,  $K$ ,  $C$ ,  $C_p$ ,  $k$ , and  $H$  are fiber diameter, pore diameter, porosity, permeability, form drag coefficient, specific heat, thermal conductivity, and total thickness of the metal foam, and  $V$ ,  $k_f$ ,  $\nu$  and  $\text{Pr}$  are inlet velocity, thermal conductivity, kinematic viscosity, and Prandtl number of the fluid.

### 3 Results and Discussion

#### 3.1 Grid Independence Study

To determine the optimal grids for the numerical computations, the numerical model with three different grid sizes 31,500, 57,750, and 98,000 cells were simulated for 20 W of heat input, wherein grid size of 57,750 was found to be optimum in terms of pressure drop and temperature excess which is shown in Table 2. So, further simulations were carried out with 57,750 grid cells.

#### 3.2 Validation

For validation purpose, current study results are compared with the literature where a good agreement is noticed with the literature [3, 4] that can be seen in Fig. 3. The present study result gives an average deviation of 6% and 8.5% for clear channel and completely filled channel (i.e., 100% filling rate) with respect to Kamath et al. [3], respectively. The deviation between the present numerical results and experimental results of Kamath et al. [3] is due to the following reasons. The experiments



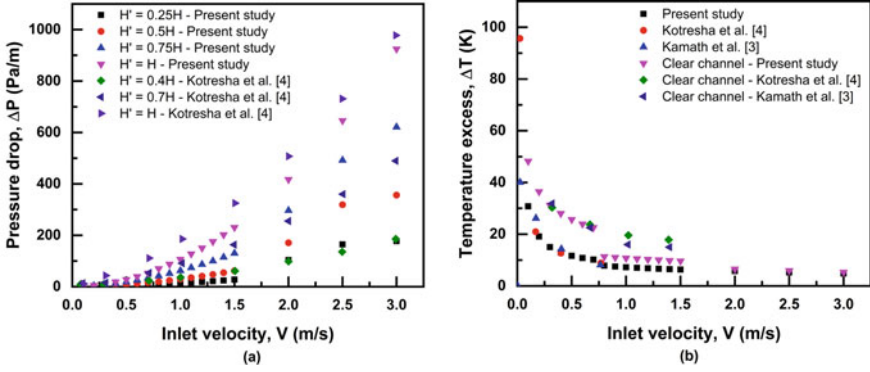


**Fig. 3** Comparison of present study results with the literature for  $H = 10$  mm: **a** pressure drop and **b** excess temperature

conducted are three dimensional, whereas numerical computation is two dimensional. The equipments used for the measurement of temperature, heat input, pressure, and velocity show uncertainties and is reported in Kamath et al. [3]. The deviation between the present results and results of Kotresha et al. [4] is because of grids used for the investigation. The velocity coupling used in the present investigation is SIMPLE scheme, whereas Kotresha et al. [4] used coupled scheme with pseudo transient.

### 3.3 Exergy Transfer and Irreversibility

Exergy is nothing but the available energy in the system. This exergy analysis evaluates the available energy at different points in the system. The mean exergy transfer Nusselt number ( $Nu_e$ ) and mean exergy transfer coefficient ( $h_{ex,m}$ ) reported by Kurtbas et al. [8] are given in Eqs. (3) and (4), respectively.

$$Nu_e = \frac{h_{ex,m} D_h}{k_f} \quad (3)$$

$$h_{ex,m} = h \left[ 1 - \frac{Re Pr}{4N_q N_{T_{in}} N_L} \left( 1 + \frac{f Re^3}{8N_{qw}} \right) \ln \left( 1 + \frac{4N_q N_L}{Re Pr} \right) \right] \quad (4)$$

where  $N_q = \frac{q D_h}{k_f T_{in}}$ ,  $N_{T_{in}} = \frac{T_{in}}{T_{\infty}}$ ,  $N_L = \frac{L}{D_h}$ ,  $N_{qw} = \frac{q \rho^2 D_h^3}{\mu^3}$ ,  $h = \frac{Q}{A \Delta T}$  [2].

$Nu_e$  is mean exergy transfer Nusselt number,  $h_{ex,m}$  is mean exergy transfer coefficient,  $D_h$  is hydraulic diameter of the channel,  $k_f$  is thermal conductivity of the fluid,  $h$  is heat transfer coefficient,  $Q$  is the heat power input (20 W),  $\Delta T$  is temperature difference between average temperature ( $T_{avg}$ ) of the aluminum plate and the environment temperature ( $T_{\infty}$ ),  $A$  is surface area of the aluminum plate exposed to

heat transfer,  $Re$  is Reynolds number based on hydraulic diameter of the channel,  $f$  is friction factor,  $q$  is heat flux ( $533.33 \text{ W/m}^2$ ),  $L$  is length of the metal foam, and  $Pr$ ,  $\rho$ ,  $\mu$ , and  $T_{in}$  are Prandtl number, density, dynamic viscosity, and inlet temperature of the fluid, respectively.

An effective heat exchanger must transfer more heat per unit area with minimum losses. With this consideration,  $Nu_e$  can also be given as [8]

$$Nu_e = Nu_{eT} - Nu_{eP} \tag{5}$$

where  $Nu_{eT}$  and  $Nu_{eP}$  are derived and lost exergy transfer Nusselt number with respect to temperature difference and fluid flow friction, and it is given by Eqs. (6) and (7), respectively.

$$Nu_{eT} = Nu \left[ 1 - \frac{Re Pr}{4N_q N_{T_{in}} N_L} \ln \left( 1 + \frac{4N_q N_L}{Re Pr} \right) \right] \tag{6}$$

$$Nu_{eP} = \frac{f Re^4 Nu Pr}{32 N_q N_{T_{in}} N_L N_{qw}} \ln \left( 1 + \frac{4N_q N_L}{Re Pr} \right) \tag{7}$$

The variation of  $Nu_e$  with  $Re$  for 10 PPI aluminum metal foam for different filling rates are shown in Fig. 4. The result shows that  $Nu_e$  reduces with increasing  $Re$  and becomes negative at higher flow rates when the non-dimensional parameters like  $Re$ ,  $Pr$ ,  $N_q$ ,  $N_L$ ,  $N_{qw}$  etc., are beyond the change range, which has no significance in engineering and gives rise to our attention to that the noteworthy parameters such as the process parameters and configuration must be within the limits permitted by exergy transfer [8]. From the plot, it is found that for the filling rates of 25%, 50%, 75%, and 100% the optimum Reynolds number ( $Nu_e = 0$ ) obtained are 6000, 5200, 5000, and 4300, respectively. This indicates that the value of Reynolds number at which  $Nu_e$  becomes zero is considered as the working limits permitted by exergy ( $WLPE_{Re}$ ), and

**Fig. 4** Mean exergy transfer Nusselt number variation for different metal foam filling rates

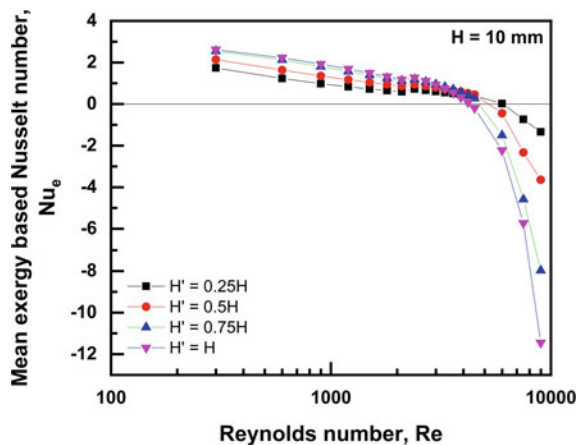
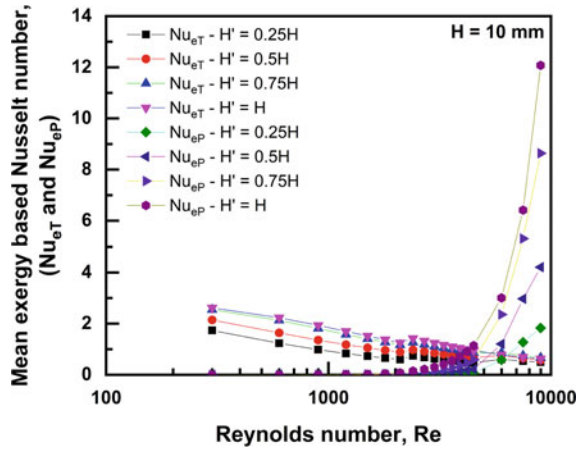


**Fig. 5** Variation of  $Nu_{eT}$  and  $Nu_{eP}$  with Reynolds number for different metal foam filling rates



above this optimum value of Reynolds number, heat transfer enhancement becomes insignificant. It is observed that  $WLPE_{Re}$  is higher for partially filled metal foams than completely filled metal foams.

From Eq. (5),  $Nu_{eT}$  becomes equals to  $Nu_{eP}$  when  $Nu_e = 0$ . This indicates that up to this optimum value, the decreasing trend of  $Nu_{eT}$  is apparent, whereas increasing trend of  $Nu_{eP}$  is negligible, i.e.,  $Nu_{eT}$  dominates the  $Nu_{eP}$ . But beyond  $WLPE_{Re}$ , increasing trend of  $Nu_{eP}$  becomes significant, whereas decreasing trend of  $Nu_{eT}$  is negligible, i.e.,  $Nu_{eP}$  dominates the  $Nu_{eT}$  which can be seen in Fig. 5 (Similar trend is noticed in Kurtbas et al. [8]). Channel filled with 100% ( $H' = H$ ) displays higher exergy heat transfer than partially filled, but this increase in exergy heat transfer with respect to 75% ( $H' = 0.75H$ ) is insignificant and it is about only 6%, but lost exergy transfer due to flow friction is 39%. Channel filled with 75% ( $H' = 0.75H$ ) enhances the exergy transfer owing to both temperature difference and fluid flow friction by 85%, 20%, and 26% more compared to 25%, 50%, and 100% filling rates, respectively.

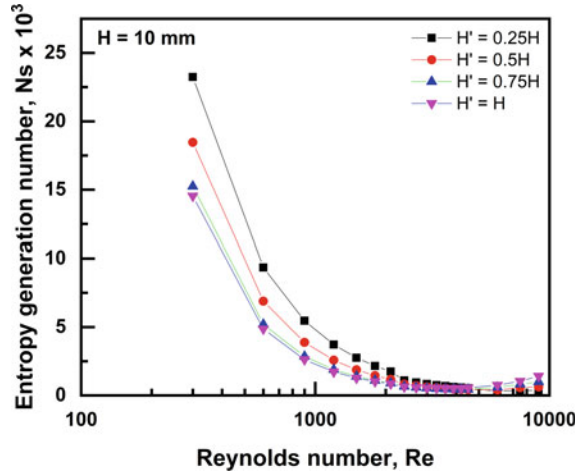
An irreversibility in the system can be explained by using entropy generation number ( $N_s$ ) which is given as [8]

$$N_s = \frac{\dot{s}_g}{\dot{m}C_p} \tag{8}$$

where  $\dot{s}_g$  is total entropy generation,  $\dot{m}$  and  $C_p$  are mass flow rate and specific heat of air.

Figure 6 shows the deviation of entropy generation number ( $N_s$ ) with Re for 10 PPI aluminum metal foam for different filling rates. The result shows that  $N_s$  decreases with increasing Re up to  $WLPE_{Re}$ , thereafter it starts to increase with increasing Re for all metal foam filling rates. For a particular Re, the channel filled with 100% ( $H' = H$ ) gives lesser  $N_s$  compared to partially filled metal foams, but this variation with respect to 75% ( $H' = 0.75H$ ) is negligible. The channel filled

**Fig. 6** Variation of entropy generation for different metal foam filling rates



with 75% ( $H' = 0.75H$ ) generates 37% and 18% less irreversibility compared to 25% ( $H' = 0.25H$ ) and 50% ( $H' = 0.5H$ ), respectively, but produces only 1.6% more irreversibility compared to completely filled metal foams ( $H' = H$ ). It also observed that irrespective of metal foam filling rates, maximum  $N_s$  is achieved at lower flow rates and minimum at optimum Reynolds number.

### 4 Conclusion

In this study, the effect of partially filled metal foams on exergy heat transfer in a vertical channel is numerically analyzed using FLUENT software for different metal foam filling rates. For the study, four different filling rates (25%, 50%, 75%, and 100%) were considered. The current work results were authenticated with the experimental and simulation results in the literature, and with that result, further investigations were conducted and then drawn the following conclusions.

- Mean exergy-based Nusselt number reduces with increasing Reynolds number ( $Re$ ) up to ( $WLPE_{Re}$ ) and beyond this, its value becomes negative. It is observed that  $WLPE_{Re}$  is higher for partially filled metal foams than completely filled.
- Entropy generation number ( $N_s$ ) used to evaluate the irreversibility in the system reduces with increasing  $Re$  and increasing metal foam filling rate up to optimum Reynolds number, and beyond this value,  $N_s$  starts to increase; this indicates the increase in total irreversibility due to both heat transfer and fluid flow friction.
- The channel filled with 75% ( $H' = 0.75H$ ) generates 37% and 18% less irreversibility compared to 25% ( $H' = 0.25H$ ) and 50% ( $H' = 0.5H$ ), respectively, but produces only 1.6% more irreversibility compared to completely filled metal

foams ( $H' = H$ ). So, the channel filled with 75% ( $H' = 0.75H$ ) is seen to give better performance compared to other filling rates.

## References

1. Zhao CY (2012) Review on thermal transport in high porosity cellular metal foams with open cells. *Int J Heat Mass Transfer* 55:3618–3632
2. Kotresha B, Gnanasekaran N, Balaji C (2019) Numerical simulations of flow-assisted mixed convection in a vertical channel filled with high porosity metal foams. *Heat Transfer Eng* 1–12
3. Kamath PM, Balaji C, Venkateshan SP (2011) Experimental investigation of flow assisted mixed convection in high porosity foams in vertical channels. *Int J Heat Mass Transfer* 54:5231–5241
4. Kotresha B, Gnanasekaran N (2018) Investigation of mixed convection heat transfer through metal foams partially filled in a vertical channel by using computational fluid dynamics. *J Heat Transfer* 140:112501
5. Kotresha B, Gnanasekaran N (2018) Effect of thickness and thermal conductivity of metal foams filled in a vertical channel—a numerical study. *Int J Num Methods Heat Fluid Flow*
6. Sarkar S, Ganguly S, Dalal A (2012) Analysis of entropy generation during mixed convective heat transfer of nanofluids past a square cylinder in vertically upward flow. *J Heat Transfer* 134:122501
7. Pawan KS, Anoop KB, Sundararajan T, Das SK (2010) Entropy generation due to flow and heat transfer in nanofluids. *Int J Heat Mass Transfer* 53:4757–4767
8. Kurtbas I, Celik N, Dincer I (2010) Exergy transfer in a porous rectangular channel. *Energy* 35:451–460
9. Kothandaraman CP, Subramanyan S. *Heat and mass transfer data hand book*. New Age International Publishers, pp 1–206

# Numerical Investigation of the Icing of Water Drop Striking on Solid Surface: From Hydrophilic to Superhydrophobic Surfaces



Virendra Patel, Ashok Kumar Sahoo, and Rimpay Chabra

**Abstract** We present the numerical modelling for simulation of solidification of water drop striking on a solid surface. Three surfaces have been used that cover from hydrophilic to superhydrophobic surfaces (advancing contact angle  $70^\circ$ ,  $90^\circ$  and  $140^\circ$ ). In this numerical method, heat transfer and transient fluid dynamics are considered. The model has been validated with experimental results from the literature. Detailed icing behaviour of water on hydrophilic and hydrophobic surfaces investigated. It has been found that the spreading and freezing of droplets on hydrophilic and superhydrophobic surfaces occurs with different time scales.

**Keywords** Water droplet · CFD model · Free surface · Solidification

## 1 Introduction

The icing of water droplets causes problems in many practical applications particularly aerodynamic wing structures and aircraft [1, 2]. In general, the study of ice sticking on solid surfaces can be split into two groups. In the first group, we can consider that water droplets are striking and solidifying on the cold solid surface. In the second group, we may consider that these water droplets are striking and freezing on the newly solidified water droplet. To advance effective de-icing or anti-icing techniques, it is very important to have in-depth knowledge of the liquid–solid phase change behaviour of droplets impacting the surface. Many experimental studies have been done to gain in-depth knowledge of freezing characteristics. LeClear et al. [3] have done an experimental study on, how water droplets spread over an inclined superhydrophobic surface while striking on it. Yeong et al. [4] have done an experimental study on spreading dynamics of different liquid droplets impacting a superhydrophobic at normal and oblique impact. Apart from these experimental studies, some computational techniques have been presented in the literature. Most

---

V. Patel (✉) · A. K. Sahoo · R. Chabra

Department of Mechanical Engineering, Institute of Technical Education and Research, Siksha O Anusandhan (Deemed To Be University), Bhubaneswar, Odisha 751030, India  
e-mail: [virendrapatel@soa.ac.in](mailto:virendrapatel@soa.ac.in)

of the numerical works are centred on solidifying characteristics of stagnant droplets [5–10]. Dash et al. [11] presented a computational model that is capable to simulate freezing and spreading striking water droplets. Blake [12] has done a numerical study to demonstrate the flow pattern of liquid drop striking on a cool superhydrophobic plane.

In spite of the fact that comprehensive ponders [3–12] have been wiped out on solidifying and outspread drops on a plane, to the most excellent of our information, simulation works on striking of drops on a plane: from hydrophilic to superhydrophobic surfaces however to come. Here we have numerically investigated the spreading and solidification characteristics of water drops striking on a surface. The presented model has been authenticated against experimental results from the literature. The present study is aimed to develop a computational technique for numerical investigation of solidification of droplet striking to surface.

## 2 Mathematical Formulation

### 2.1 Governing Equations

A finite volume approach is used in the computational procedure of the flow solver used in this analysis. For modelling the freezing of droplets, a classical principle of mixture [13–17]-based continuum solution has been used. The cell that contains only air is indicated as  $F = 0$  and a cell full of droplet material corresponds to  $F = 1$  and air–water interface corresponds as  $0 < F < 1$ . Thermal properties of the fluid in the different cells are calculated as described below:

$$c_{\text{eff}} = Fc_d + (1 - F)c_{\text{air}} \quad (1a)$$

$$k_{\text{eff}} = Fk_d + (1 - F)k_{\text{air}} \quad (1b)$$

$$\rho = F\rho_d + (1 - F)\rho_{\text{air}} \quad (1c)$$

$$\mu_{\text{eff}} = F\mu_d + (1 - F)\mu_{\text{air}} \quad (1d)$$

**Volume of fluid equation:**

$$\frac{\partial F}{\partial t} + \nabla \cdot (\mathbf{u}F) - F\nabla \cdot \mathbf{u} = 0 \quad (2)$$

**Continuity equation:**

$$\nabla \cdot \mathbf{u} = 0 \quad (3)$$

### Momentum conservation

$$\frac{\partial}{\partial t}(\rho \mathbf{u}) + \nabla \cdot (\rho \mathbf{u} \mathbf{u}) = -\nabla P + \nabla \cdot (\mu (\nabla \mathbf{u} + \nabla \mathbf{u}^T)) - \mathbf{g} \rho + \mathbf{F}_{\text{vol}} - S \mathbf{u} \quad (4)$$

where  $\mathbf{F}_{\text{vol}}$  is calculated as described in Sect. 2.3 and

$$S = \begin{cases} \left[ C \frac{(1-f_l)^2}{f_l^3 + e} \right] & \text{for } F = 1 \\ 0 & \text{for } F < 1 \end{cases} \quad (5)$$

where  $C$  is constant and its value has been taken as  $150,000 \text{ kg/m}^3 \text{ s}^1$  [15].

### Energy conservation

$$\frac{\partial}{\partial t}(\rho c_{\text{eff}} T) + \nabla \cdot (\rho u c_{\text{eff}} T) = \nabla \cdot (k_{\text{eff}} \nabla T) - S_h \quad (6)$$

where

$$S_h = \begin{cases} -L_d \frac{\partial}{\partial t}(\rho f_l) & \text{for } F = 1 \\ 0 & \text{for } F < 1 \end{cases} \quad (7)$$

## 2.2 Solidification Model

Liquid fraction ( $f_l$ ) is calculated by equilibrium solidification model as described below. It is an iterative process [17].

$$f_l = \frac{\Delta H}{L} \quad (8)$$

$$[\Delta H_p]_{n+1} = [\Delta H_p]_n + \frac{a_p}{a_p^0} \lambda_{c,d} [\{T_p\}_n - T_m] \quad (9)$$

## 2.3 Surface Tension Force Model

The continuum surface force [18] has been used to model surface tension force.



$$F_{\text{vol}} = \sigma K(\vec{x}) \frac{\rho}{\rho_{\text{air}} + \rho_{\text{d}}} \nabla F \quad (10)$$

## 2.4 Boundary Conditions: Wall Adhesion

The normal to the interface at points  $\vec{x}$  on the wall is given by [19]:

$$\mathbf{n} = \mathbf{n}_{\text{wall}} \cos \theta + \mathbf{n}_l \sin \theta \quad (11)$$

where  $\theta$  is the contact angle. Wall adhesion boundary conditions are more complicated when the contact line is in motion, but in our case, it assumes that the contact line is not moving.

## 2.5 Numerical Implementation

For this study, the freezing of water is modelled using the proposed equilibrium solidification models. The conservation equations are formulated as one domain for water and air [20]. The pressure-based finite volume method is used to solve governing equations following the SIMPLE algorithm [21]. Different grids have been used for the grid independence tests. It was observed that the  $150 \times 150$  grid has good agreement with the experimental result.

## 3 Model Validation

For model validation, simulation of water droplet striking on ice plane has been explored. Figure 1 gives clear information on the computational domain. It is a 2D axis-symmetry model, so half of the shown domain has been solved. For simplification, it has been assumed that heat from droplets is not lost to the air. The thermal properties of water have been taken as temperature-independent. For this simulation, the diameter of the spherical droplet is equal to 2.96 mm with an initial temperature of  $27^\circ$ . The impact speed is equal to 1.39 m/s. And the ice plane temperature is equal to  $-10.0^\circ \text{C}$ . These initial conditions have been taken from the literature [22].

The ice surface acts as a hydrophilic for a water droplet spreading. Figure 2 shows that the simulated spreading factor, that is, ratio of spread diameter and initial diameter of droplet, is matching to experimental results from the literature [22]. When water droplet comes in contact with ice, freezing of layer adjacent to ice surface get freeze and the recoiling mechanism is not observed.

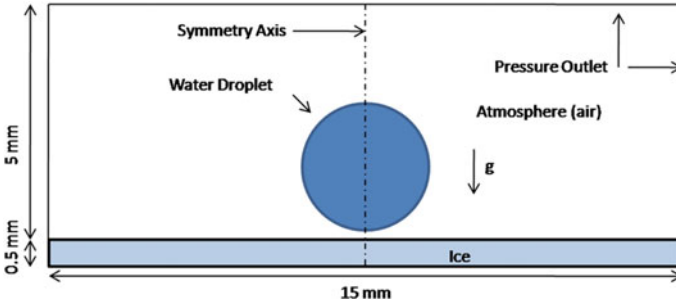
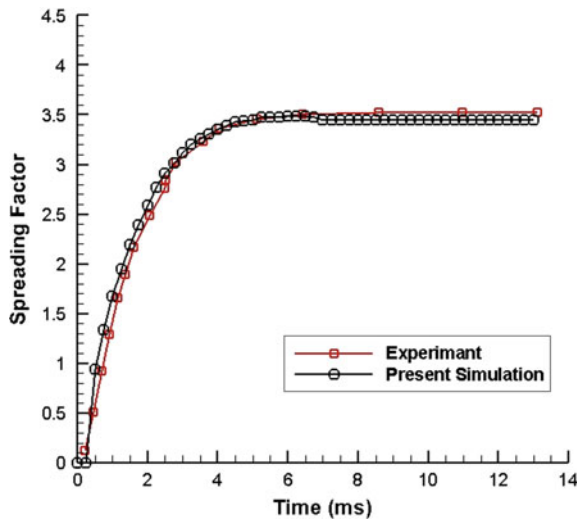


Fig. 1 Computational domain

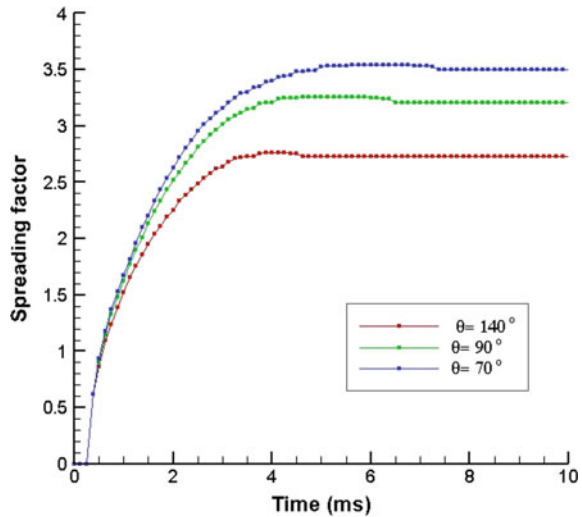
Fig. 2 Collate of the simulated spreading factor of experimental result [22] with time



### 4 Results and Discussions

Simulation of water droplet striking of alumnum surfaces having different roughness and wetting condition is done. The dynamic contact angle depends on roughness and wetting condition. In a real situation, surfaces could be hydrophilic or hydrophobic. Here we are comparing the spreading factor and freezing rate for three types of surfaces ( $\theta = 70^\circ, 90^\circ$  and  $140^\circ$ ). High contact angle ( $\theta > 90^\circ$ ) indicates that the surface is hydrophobic, and a lower contact angle ( $\theta < 90^\circ$ ) indicates that the surface is hydrophilic. In all three cases, for simulation diameter of the spherical droplet is equal to 2.96 mm with an initial temperature of  $27^\circ$ . The impact speed is equal to 1.39 m/s. And the ice surface temperature is equal to  $-10.0^\circ\text{C}$ . From Fig. 3, it can be seen that at a contact angle of  $140^\circ$  has a low spreading factor (2.6), whereas a contact angle of  $90^\circ$  has a spreading factor of value 3.2 but a contact angle of  $70^\circ$  has a more spreading factor (3.5). The surface having high contact angle causes low ice

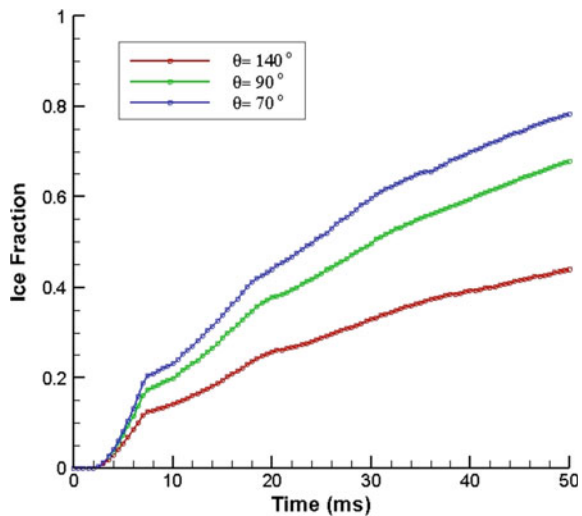
**Fig. 3** Spreading factor of the droplet at a different surface with time



formation in water droplets. From Fig. 4, it can be seen that a contact angle of  $140^\circ$  has a low ice fraction, that is, ratio of the volume of ice and total volume of water and ice, (0.4) at the time ( $t = 50$  ms) and at a contact angle of  $90^\circ$  has ice fraction (0.7) but at a contact angle of  $70^\circ$  has more ice fraction (0.8).

Figure 5 shows the spreading and freezing behaviour of water droplet impacting on surfaces for both cases. It is clear that for hydrophobic surface recoiling happens early and maximum spreading is less as compared to the case of the hydrophilic surface. And if spreading is less, then a lesser area is available for heat transfer from droplet to the substrate. It is clear from Fig. 4 that the slope of the ice fraction curve,

**Fig. 4** Variation of ice fraction of water droplet with time at different surfaces



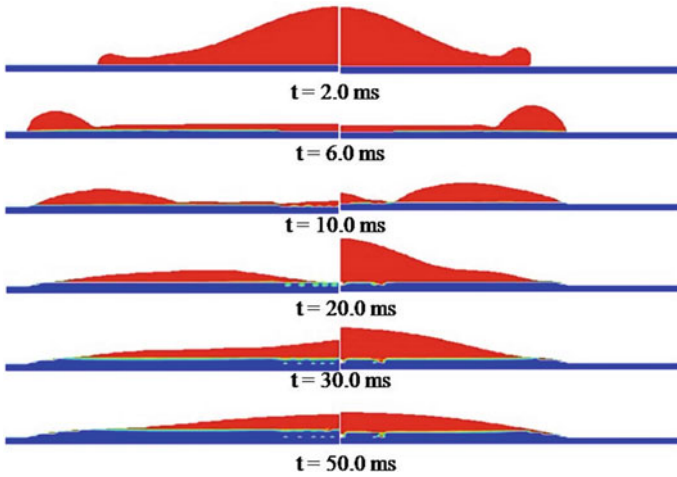


**Fig. 5** Snapshot of ice fraction of water droplet with time at different surfaces (blue colour represents solid and red colour represents liquid) (left  $\theta = 70^\circ$  and right  $\theta = 140^\circ$ )

which is a measure of the freezing rate of water droplets, is lower for the case of the hydrophobic surface. Spreading dynamics for the case of the hydrophobic surface is very different from the case of the hydrophilic surface. For a hydrophobic surface, a larger amount of liquid water recoil towards the centre. Recoiling of bulk liquid water causes a lowering in freezing rate. It is clear from Fig. 4 nature of the ice fraction curve changes after the time of maximum spreading for all three cases.

## 5 Conclusions

We have presented a computational model which helps to simulate the freezing of water droplets striking on a solid surface. We focus on the spreading and freezing characteristics of the striking water droplets. The following conclusions are drawn from this study:

- Superhydrophobic surface cause decreases in freezing rate and less spreading factor.
- Hydrophilic surfaces help in spreading and cause an increase in the freezing rate of droplet.

## References

1. Jung S, Tiwari MK, Doan NV et al (2012) Mechanism of super-cooled droplet freezing on surfaces. *Nat Commun* 3:299–306
2. Jiang XL, Jun M, Wang SH (2005) Transmission lines' ice accidents and analysis of the formative factors. *Electr Power* 38:27–30
3. LeClear S, LeClear J, Park KC et al (2016) Drop impact on inclined super-hydrophobic surfaces. *J Colloid Interface Sci* 461:114–121
4. Yeong YH, Burton J, Loth E et al (2014) Drop impact and rebound dynamics on an inclined super-hydrophobic surface. *Langmuir* 30(40):12027–12038
5. Feuillebois F et al (1995) Freezing of a subcooled liquid droplet. *J Colloid Interface Sci* 169(1):90–102
6. Hindmarsh JP, Russell AB, Chen XD (2003) Experimental and numerical analysis of the temperature transition of a suspended freezing water droplet. *Int J Heat Mass Transfer* 46(7):1199–1213
7. Tabakova S, Feuillebois F, Radev S (2010) Freezing of a super-cooled spherical droplet with mixed boundary conditions. *Proc R Soc Lond A Math Phys Eng Sci* 466(2116)
8. Karapetsas G, Chamakos NT, Papathanasiou AG (2016) Efficient modelling of droplet dynamics on complex surfaces. *J Phys Condens Matter* 28(8):085101
9. Chaudhary G, Li R (2014) Freezing of water droplets on solid surfaces: an experimental and numerical study. *Exp Therm Fluid Sci* 57(3):86–93
10. Vu TV, Tryggvason G, Homma S et al (2013) A front-tracking method for three-phase computations of solidification with volume change. *J Chem Eng Jpn* 46(11):726–731
11. Dash A, Sahoo AK, Yadav A, Patel V (2021) Computational modelling of freezing of water droplet impacting on an ice surface. *Mater Today Proc* 41:156–160
12. Blake J, Thompson D, Raps D et al (2015) Simulating the freezing of super-cooled water droplets impacting a cooled substrate. *AIAA J* 53(7):1725–1739
13. Yadav A, Ghosh A, Kumar A (2017) Modelling and experimental validation of moving tilted volumetric heat source in gas metal arc welding process. *J Mater Process Technol* 239:52–65
14. Yadav A, Ghosh A, Kumar A, Yadav (2019) Thermal transport phenomena in multi-layer deposition using arc welding process. In: *3D printing and additive manufacturing technologies*. Springer, Singapore, pp 15–27
15. Reddy P, Patel V, Yadav A, Patel S, Kumar A (2018) Modelling and simulation of equilibrium and non-equilibrium solidification in laser spot welding. In: *IOP conference series: materials science and engineering*, vol 310, no 1. IOP Publishing
16. Kamnis S, Gu S (2005) Numerical modelling of droplet impingement. *J Phys D Appl Phys* 38:3664–3673
17. Patel V, Yadav A, Sahoo S, Thatoi D, Winczek J (2020) A novel fixed-grid interfacetracking algorithm for rapid solidification of supercooled liquid metal. *Num Heat Transfer Part A Appl* 78:306–320. <https://doi.org/10.1080/10407782.2020.1791542>
18. Brackbill JU, Kothe DB, Zemach C (1992) A continuum method for modeling surface tension. *J Comput Phys* 100:335–354
19. Sussman M (2002) An adaptive mesh algorithm for free surface flows in general geometries. In: *Adaptive method of lines*, Chapman & Hall/CRC, Boca Raton
20. Liu H, Bussmann M, Mostaghimi J (2009) A comparison of hyperbolic and parabolic models of phase change of a pure metal. *Int J Heat Mass Transf* 52:1177–1184. <https://doi.org/10.1016/j.ijheatmasstransfer.2008.08.030>
21. Hirt CW, Nichols BD (1981) Volume of fluid (VOF) method for the dynamics of free boundaries. *J Comp Phy* 39:201–225
22. Jin Z, Zhang H, Yang Z (2017) Experimental investigation of the impact and freezing processes of a water droplet on an ice surface. *Int J Heat Mass Transf* 109:716–724

# Effect of Viscous Dissipation, Soret and Uniform Heat Source on MHD Flow of a Polar Fluid Through Porous Mediums



Bhabani Shankar Kamilla and Dharendra Nath Thatoi

**Abstract** Heat and mass transfer of a MHD micro polar fluid, which is flowing under electrical influence over a horizontal plate having semi infinite length with the soret effect, viscous dissipation and heat source is studied in this present work. Along with flow direction of fluid, a magnetic field has been applied uniformly. The governing equation is solved by Runge–Kutta method numerically. The variation in temperature and fluid concentration due to flow parameters has been analysed using graph results.

**Keywords** Soret effect · Micro-polar fluid · Porous medium · Viscous dissipation

## 1 Introduction

The study of micro polar fluid passing through porous medium has a vital role in practical application across various fields such as porous rocks and alloys, polymer bends and micro emulsions etc. One of the major applications of micro polar fluid is in lubrication field because the lubricant used in the clearance gap of the bearing acts is non-Newtonian fluid which acts as a heat transfer agent. The very first study of micro polar fluid having two types of effects i.e., micro rotational and inertia, both has been done by Eringen [1] which also describes the effects of micro-rotation to the product having microstructures. Eringen [2] expanded his study to the model of thermo-micro-polar fluids, which describes the thermal behaviour and microstructure of a fluid flow. Many applications in engineering areas which operates at high temperatures and radiative heat transfer such as nuclear power plants, various types of propulsion devices for aircraft and space vehicles. Most of the applications are based on micro-polar fluid, which is a non-Newtonian fluid, passing through various

---

B. S. Kamilla (✉)

Department of Mechanical Engineering, MIET, BBSR, Bhubaneswar, India

e-mail: [bhabanishankarkamilla@gmail.com](mailto:bhabanishankarkamilla@gmail.com)

D. N. Thatoi

Department of Mechanical Engineering, SOA Deemed To Be University, Bhubaneswar, India

© The Author(s), under exclusive license to Springer Nature Singapore Pte Ltd. 2023

175

P. Pradhan et al. (eds.), *Recent Advances in Mechanical Engineering*,

Lecture Notes in Mechanical Engineering,

[https://doi.org/10.1007/978-981-16-9057-0\\_19](https://doi.org/10.1007/978-981-16-9057-0_19)

types of porous medium. Vafai and Tien [3] analysed the concurrent effect of inertia force and boundary viscous resistance force on the fluid flow and the heat interaction between the fluid and porosity medium. A. Raptis [4] investigated the boundary layer profile of the flow of micro polar fluid through porous medium. Later on numerous studies were carried out by researchers [5–12] to investigate different features of such flow.

Soret effect or Thermophoresis is a fact that is observed in mixtures of mobile particles where a dissimilar type of particle possesses different responses to potency of a temperature gradient. It is the opposite incident to the dufour effect. These effects are more significant in hydrology, geothermal energy etc. Thermal diffusion or Soret effect contributes a separation process between smaller and medium molecular particle in gases. Few current studies have been done about Soret aspects which are mentioned in Refs. [15, 16]. In recent years [17–20], significant attention has been made on combined heat and mass transfer phenomenon because it has major application in engineering and industrial fields like polymer production, food processing and geothermal system etc.

Inspired by these applications, the current study finds the effect of Soret effect and viscous dissipation on heat and mass transfer through a porous medium. Here we have taken an electrically conducting MHD micro polar fluid flowing upon a horizontal plate. The applied mathematical model in this study is highly non-linear. The governing equations have been converted to ordinary partial differential equation, then solved numerically by Runge–Kutta method. The result of Eckert number, Soret effect and chemical reaction is observed on the temperature and concentration profile.

## 2 Formulation

An incompressible micro polar fluid passing over a horizontal semi-infinite plate in the existence of viscous dissipation, chemical reaction and Soret effect. The flow is along  $x$  axis. We considered a uniform magnetic field of strength  $B_0$  has been put in the transverse direction i.e., along  $y$ -axis, of the flow direction. The impact of magnetic field on the fluid flow can be neglected because of small Reynolds number.

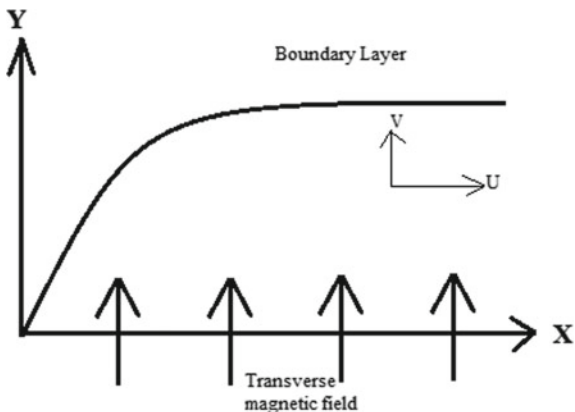
A detailed diagram of the model is shown in Fig. 1.

$$\frac{\partial u}{\partial x} + \frac{\partial u}{\partial y} = 0 \quad (1)$$

$$u \frac{\partial u}{\partial x} + v \frac{\partial u}{\partial y} = \nu \frac{\partial^2 u}{\partial y^2} + k_1 \frac{\partial N}{\partial y} + \frac{\sigma B_0^2 \varphi}{\rho} (U_0 - u) + \frac{\nu \varphi}{K_p^*} (U_0 - u) + C\varphi (U_0^2 - u^2) \quad (2)$$

$$G_1 \frac{\partial^2 N}{\partial y^2} - 2N - \frac{\partial u}{\partial y} = 0 \quad (3)$$

**Fig. 1** Schematic of the problem



$$u \frac{\partial T}{\partial x} + v \frac{\partial T}{\partial y} = \frac{k}{\rho C_p} \frac{\partial^2 T}{\partial y^2} + \frac{\mu}{\rho C_p} \left( \frac{\partial u}{\partial y} \right)^2 + \frac{S'}{\rho C_p} (T - T_\infty) + \frac{DK_T}{C_s C_p} \frac{\partial^2 C}{\partial y^2} \quad (4)$$

$$u \frac{\partial C}{\partial x} + v \frac{\partial C}{\partial y} = D \frac{\partial^2 C}{\partial y^2} + \frac{DK_T}{T_m} \frac{\partial^2 T}{\partial y^2} - \gamma (C - C_\infty) \quad (5)$$

Associated boundary conditions are:

$$\left. \begin{aligned} u = v = N = 0, T = T_w, C = C_w \quad \text{at } y \rightarrow 0 \\ u = U_0, N = 0, T = T_\infty, C = C_\infty \quad \text{at } y \rightarrow \infty \end{aligned} \right\} \quad (6)$$

Solution of the problem:

$$\left. \begin{aligned} \psi(x, y) = (2\nu U_0 x)^{\frac{1}{2}} f(\eta), N = \left( \frac{U_0}{2\nu x} \right)^{\frac{1}{2}} g(\eta), \eta = \left( \frac{U_0}{2\nu x} \right)^{\frac{1}{2}} y, \theta = \frac{T - T_\infty}{T_w - T_\infty} \\ \phi = \frac{C - C_\infty}{C_w - C_\infty}, u = \frac{\partial \psi}{\partial y}, v = -\frac{\partial \psi}{\partial x} \end{aligned} \right\} \quad (7)$$

Equations (2)–(6) convert into the dimensionless governing equations with help of Eq. (7), we get,

$$f'' + ff'' + \Delta g' + \left( M + \frac{1}{K_P} \right) (1 - f') + F(1 - f'^2) \quad (8)$$

$$Gg'' - 2(2g + f'') = 0 \quad (9)$$

$$\theta'' + \text{Pr } f\theta' + Q \text{Pr } \theta + Ec \text{Pr } f'' = 0 \quad (10)$$



$$\varphi'' + Scf\varphi' + ScSr\theta'' - KcSc\varphi = 0 \quad (11)$$

And boundary conditions are,

$$\left. \begin{aligned} f(\eta) = f'(\eta) = g(\eta) = 0, \theta(\eta) = 1, \phi(\eta) = 1 \quad \text{at } \eta = 0 \\ f'(\eta) = 1, g(\eta) = 0, \theta(\eta) = 0, \phi(\eta) = 0 \quad \text{at } \eta = \infty \end{aligned} \right\} \quad (12)$$

where,

$$\begin{aligned} Pr &= \frac{\mu C_p}{k}, \Delta = \frac{k_1}{\nu}, G = \frac{G_1 U_0}{\nu x}, F = 2cx\varphi, \\ M &= \frac{\sigma B_0^2 \varphi x}{\rho}, K_P = \frac{2\varphi \nu x}{K_p^* U_0}, Du = \frac{DK_T(C_w - C_\infty)}{\nu C_s C_p (T_w - T_\infty)} \\ K_1 &= \rho k, \nu = \frac{\mu + k}{\rho}, S = \frac{2S^* x}{\rho C_p U_0}, Ec = \frac{U_0^2}{C_p (T_w - T_\infty)}, \\ Sc &= \frac{\nu}{D}, Sr = \frac{DK_T(T_w - T_\infty)}{\nu T_m (C_w - C_\infty)}, Kr = \frac{\gamma x}{U_0} \end{aligned}$$

### 3 Result and Discussion

The solution of the governing equations along with boundary conditions has been solved by matlab using BVP4C programme. The outcome of physical parameter on temperature and concentration is examined. From Fig. 2a we noticed that Eckert number (Ec) enhances the temperature profile of the flow because as we increase the value of Eckert number, the kinetic energy of the flow increases. So with the influence of self-heating, the temperature profile of the flow field increases while Prandtl number does vice-versa in Fig. 2b. The dissimilarity of concentration profile for several values of Soret number (Sr) is shown in Fig. 2c. It is observed that Soret parameter increases the concentration profile because Soret effect is the cause behind for the mass transfer from lower solute concentration to higher due to the temperature gradient. Another fact is, velocity of the fluid flow increases with an increasing value of Soret number. Thus, fluid concentrations increase with a higher magnitude of Soret number. The chemical reaction parameter (Kr) slows down the concentration profile because some constituent in fluid reduces the depth of solute boundary layer concentration which is clear from Fig. 2d.

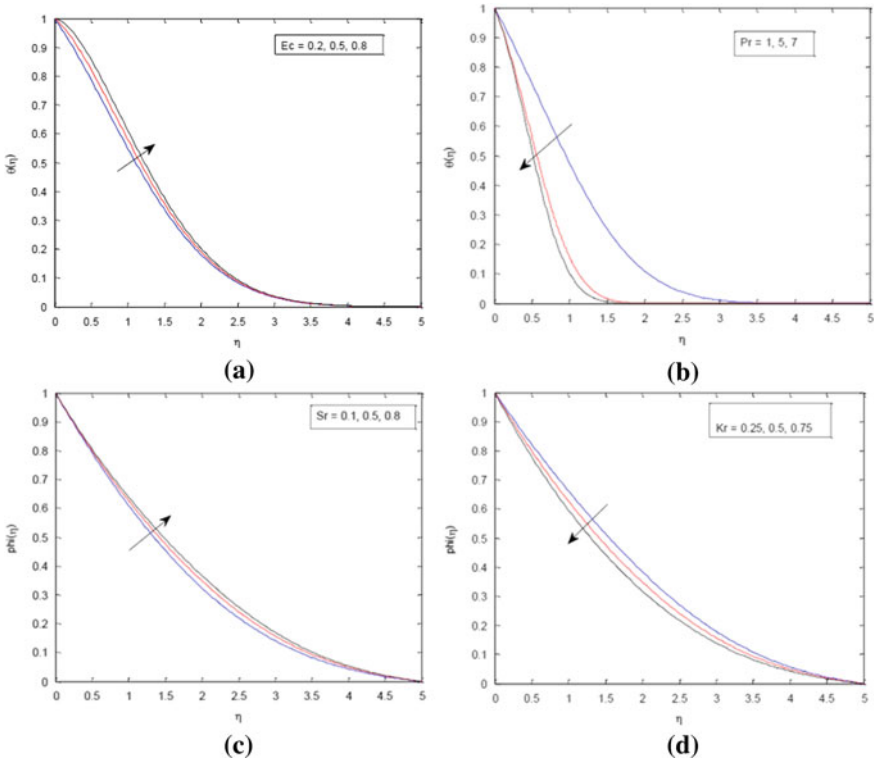


**Fig. 2** Temperature profile (a, b) for different values of Ec and Pr, Velocity profile (c, d) for different values of Sr and Kr

### 4 Conclusion

- Temperature of the fluid decreases by increasing the Prandtl number.
- The Soret parameter enhances concentration profiles.
- The chemical reaction parameter decline concentration profiles.
- For higher value of Eckert number, temperature of the profile rises.

### References

1. Eringen AC (1996) Micropolar fluids theory. J Math Mech 16
2. Eringen AC (1972) Theory of thermo-micro-polar fluids. J Math Anal 38
3. Vafai IK, Tien CL (1966) Effects of a fluid inertia force and boundary viscous resistance upon flow and heat transfer in a constant porosity porous medium. Int J Heat Mass Transfer 24
4. Raptis A (2000) Boundary layer flow of a micropolar fluid through a porous medium. J Porous Media 3(1)

5. Abo-Eldahab EM, Ghonaim AF (2005) Radiation effect on heat transfer of a micropolar fluid through a porous medium. *Appl Math Comput* 500–510
6. Khan NA, Khan S, Ara A (2017) Flow of micro-polar fluid over an off centered rotating disk with modified Darcy's Law. *Propul Power Res* 6(4):285–295
7. Khalid A, Khan I, Khan A, Shafie S (2018) Influence of wall couple stress in MHD flow of a micropolar fluid in a porous medium with energy and concentration transfer. *Results Physics* 1172–1184
8. Ibrahim H, Sirafy E (1985) Two-dimensional flow of a non-stationary micro polar fluid in the half-plane for which the shear stresses are given on the boundary. *J Comput Appl Math* 271–276
9. Nadeem S, Hussain M, Naz M (2010) MHD stagnation flow of a micro polar fluid through a porous medium. *Meccanica* 45:869–880
10. Rashidi MM, Pour SAM, Abbasbandy S (2011) Analytic approximate solutions for heat transfer of a micro polar fluid through a porous medium with radiation. *Commun Nonlinear Sci Number Simulate* 1874–1889
11. Khedr MEM, Chamkha AJ, Bayomi M (2009) MHD flow of a micro polar fluid past a stretched permeable surface with heat generation of absorption. *Nonlinear Anal Model Control* 14:27–40
12. Sajid M, Sadiq MN, Ali N, Javed T (2018) Numerical simulation for Homann flow of a micro polar fluid on a spiralling disk. *Eur J Mech B Fluids* 320–327
13. Mishra SR, Hoque MM, Mohanty B, Anika NN (2019) Heat transfer effect on MHD flow of a micro polar fluid through porous medium with uniform hear source and radiation. *Nonlinear Eng* 65–73
14. Gajjela N, Matta A, Kaladhar K (2017) The effects of Soret and Dufour, chemical reaction, Hall and ion currents on magnetized micro polar flow through co-rotating cylinders. *AIP Advances*
15. Hayat T, Nasir T, Khan MI, Alsaedi A (2018) Numerical investigation of MHD flow with Soret and Dufour effect. *Results Phys* 1017–1022
16. Khan A, Khan I, Ali F, Khalid A, Shafie S (2015) Exact solution of heat and mass transfer with MHD flow in a porous medium under time dependent shear stress and temperature. *Abstr Appl Aanl*
17. Chaudhary RC, Jain A (2007) Combined heat and mass transfer effects on MHD free convection flow past on oscillating plate embedded in porous medium. *Rom J Phys* 505–524
18. Senapati N, Dhal RK, Das TK (2012) Effects of chemical reactions on free convection MHD flow through porous medium bounded by vertical surface with slip flow region. *Am J Comput Appl Math* 35–124
19. Krishnamurty MR, Prasannakumara BC, Gireesha BJ, Gorla RSR (2015) Effect of viscous dissipation on hydro magnetic fluid flow and heat transfer of nano fluid over an exponentially stretching sheet with fluid-particle suspension. *Cogent Math*
20. Hooman K, Gurgenci H (2007) Effect of viscous dissipation and boundary conditions on forced convection in a channel occupied by a saturated porous medium. *Transp Porous Media* 301–319

# Automation of AM Via IoT Towards Implementation of e-logistics in Supply Chain for Industry 4.0



Reem Ashima, Abid Haleem , Shashi Bahl , Devaki Nandan, and Mohd Javaid 

**Abstract** The primary objective of this paper is to identify how industrial automation of additive manufacturing technology using Internet of Things (IoT) will leverage the quality of existing supply chain management processes. The importance of the implementation of e-logistics in supply chain operations is also delineated. An intensive desk-based literature survey study identifies potential advantages of incorporating IoT automated additive manufacturing to improve supply chain processes. We also discuss how the automation of logistics operations, also known as e-logistics, will help modernize supply chain management. The research paper comprises theoretical work about the application of automated additive manufacturing and e-logistics in modern supply chains. Detailed analysis on the advantages of implementing automated additive manufacturing technology and e-logistics in the supply chain is performed. Due to the novelty of the area, we have conducted this study based on available research material, and it is pretty limited. Various digital technologies introduced as a part of the fourth industrial revolution, such as artificial intelligence, machine learning, augmented reality, digital twins, and robotic process automation are being incorporated by supply chains to reduce the overall cost of production. The top-notch organizations are embracing supply chain automation for cutting down on operational costs and eliminating shortages.

**Keywords** Additive manufacturing · Automation · Global supply chains · e-logistics · Industry 4.0 · Internet of things

---

R. Ashima · A. Haleem · M. Javaid  
Department of Mechanical Engineering, Jamia Millia Islamia, New Delhi 110025, India

S. Bahl (✉)  
Department of Mechanical Engineering, I. K. Gujral Punjab Technical University Hoshiarpur  
Campus, Hoshiarpur 146001, India  
e-mail: [shashi.bahl@ptu.ac.in](mailto:shashi.bahl@ptu.ac.in)

D. Nandan  
Department of Industrial & Production Engineering, G.B. Pant, University of Agriculture &  
Technology, Pantnagar 263145, India

## 1 Introduction

The supply chain has been falling short on various facets, which eventually costs the companies. Global logistics has become costlier, and freight costs have increased as more businesses rely on traditional manufacturing processes. Most commonly employed traditional manufacturing processes are classified into two broad categories: formative and subtractive manufacturing processes. The formative manufacturing processes comprise machining processes such as injection molding, die casting, etc., and subtractive manufacturing processes include machining processes such as milling, grinding, CNC machining etc. [1, 2]. Traditional manufacturing practices add costs to processes involved in supply chain management. In addition to much unnecessary financial investment involved, conventional manufacturing technologies demand large amounts of time and human resources. The inability of the suppliers to keep up with the procurement of purchase orders in time results in poor delivery performance [3]. Inefficient transportation of delivery items also increases warehousing and storage costs. It is because of these reasons that many organizations have resorted to supplying chain management outsourcing. Companies outsource the entire supply chain, which is the essential element of an organization, to a third-party organization that specializes in the same due to economic reasons. However, outsourced supply chains have started to lose their ground due to added disadvantages about organizations' integration issues [4]. Losing control over supply chains, which forms the backbone of an organization, leads to business uncertainties that may harm the organization if not forecasted in time.

Lack of inventory and poor quality of goods further aggrandize the existing problems associated with supply chain management. The problem of supply shortage in the recent course of events, aggravated by the ongoing COVID-19 pandemic, depicts the weak nature of the supply chain logistics network [5, 6]. There has been a massive paucity of essential medical equipment such as PPE kits, testing kits, ventilators, oxygen support and vaccines at such times of need. The problem does not lie with the production of the required equipment; instead, the long and slow supply chain process is to be blamed. The majority of the Fortune 1000 companies have faced massive supply chain disruptions as COVID-19 has impacted businesses worldwide in either a negative or a strongly negative manner. The damage is so extensive that most of them have planned to downgrade their economic growth outlooks [7]. The incidence of Suez Canal blockage by Evergreen ships is another example that proves how inefficient global supply chain networks are for real. The unfortunate event resulted in the blockage of indispensable raw materials and crucial global requirements. Perhaps, the manufacturers across the globe need to learn from the lessons preached by unprecedented occurrences recently [8]. A proactive data-driven approach needs to be considered so that the companies are prepared beforehand to deal with crises that may result in large-scale disruption. It is a result of the COVID-19 pandemic that changes in consumer behavior have turned out to be a diagnostic test for companies, which may lead to consumers judging the companies based on the rapidity of mobilization of response to this painful period of disruption [7, 8].

Additive manufacturing (AM) technology allows the manufacturers to build a wide variety of products irrespective of the complexity of geometry associated with the product, thereby making rapid prototyping processes far more advantageous than conventional machining methods. The prototype services provided by additive manufacturing are somewhat economical, making it possible for small enterprises to afford this technology [9]. Additive manufacturing has found its applications in various sectors, such as the transportation industry, medical sciences, aerospace industry, consumer goods sector etc. Just-in-time production has become the new norm, and materials have become a global asset in recent times. Additive manufacturing has broadened the scope for on-demand manufacturing for customized production which is expected to have significant positive implications on logistics. How AM technology has helped in battling the shortcomings proves how 3D printing technology can positively impact global supply chains that can further enhance production processes at an overall level. Implementing AM processes for manufacturing purposes within a supply chain results in decentralized production, which helps balance excesses and surplus supplies at individual locations. Rapid prototyping processes can effortlessly 3D print digital inventories in the desired quantity, and the same can be utilized by supply chains globally to improve their efficacy [10–12]. Now that additive manufacturing capabilities are evident; organizations need to rethink their supply chain designs and exploit the crucial characteristics of 3D printing technology to the fullest to optimize their supply chain processes [13]. Customer satisfaction has become one of the most critical liabilities. Also, the environment in which supply chains operate is highly dynamic. Therefore, the supply chains must be resilient to keep up with the rapid contemporary advancements in technologies. It has become essential for organizations to respond to shortcomings in real-time so that these organizations can run successfully [14].

The concept of lean thinking is mainly applied to the manufacturing industry at present. However, lean management of other business operations is equally essential for reducing wastage and creating value. Apart from procurement of raw materials and goods manufacturing, logistics is also an essential element of a supply chain. Therefore, with the increasing dynamicity of the environment, the organizations must proceed with consistent improvements in logistics operations. The organizations are required to incorporate lean thinking culture into their logistics operation in the form of e-logistics. A continuous flow of production goods is required while paying heed to the time involved, cost investment, and material quality simultaneously. The main challenge in logistics has always been to deliver goods to customers' doorstep as quickly as possible. E-logistics, thus, enables automation of activities involved in logistics processes for providing end-to-end services to customers [15–17]. Request for Quotes (RFQ), Shipping and Tracking are processes that comprise a typical e-logistics framework. As a result of globalization, there is increased competition among organizations. For effective management of supply chain operations, e-logistics is henceforth required. It is being observed that e-logistics helps in saving costs and consequently improving customer experience. Automation of warehousing operations eliminates human involvement and reduces the complexity of the process, thus increasing the flexibility of the supply chain. Traditional logistics involves

tedious, time-taking processes that increase expenses and response time. With the help of e-logistics, it is possible to have access to a more significant number of sellers globally. The automation of logistics-related processes helps in the transformation of the business operation paradigm, which help the organizations create opportunities for themselves [18, 19].

Automation solutions are required in the form of the Internet of Things (IoT) in additive manufacturing and e-logistics to transform traditional supply chain management systems. As a part of our research study, we understand the importance of automation of supply chain management through implementing IoT enabled-3D printing and e-logistics in supply chain management and identify major automation technologies for significant industrial application areas. The primary objectives of the research study are to figure out the limitations of conventional supply chain management, explore the significance of additive manufacturing cloud and e-logistics for supply chain automation, and survey how supply chains can be optimized for growth through automation strategies.

## 2 Need for Study

Despite various conveniences that AM provides us with, certain limitations prevent its commercial viability. AM cannot be used for large-scale production due to a lack of repeatability. Also, the 3D printed parts may not have a fine surface finish compared to conventional manufacturing technologies. It forms a stair-like structure on the surface of the end product. Besides, it cannot be incorporated for manufacturing large-sized objects. Long production time is another major challenge that requires a holistic solution. The manufacturers need to effectively ensure a safer working environment to effectively utilize additive manufacturing technology for modern supply chains. Therefore, intelligent automation solutions are required for smoother 3D printing equipment production. Improvements in AM through automation would lead to the betterment of supply chain management. Automation through the implementation of the IoT improves the efficiency and reliability of manufacturing processes in general and is, therefore, a significant key to sustainability.

E-logistics also has a vital role to play in the efficient functioning of an organization's supply chain. Integration of supply chain management and e-logistics has gained popularity when organizations must reduce production costs and increase productivity. The use of the Internet as a medium of communication to provide logistics-related services obviates the requirement of the human workforce, which further reduces the chances of error. Implementing e-logistics in supply chains provides the companies with the possibility of real-time visibility, thereby enabling performance management. Successful logistics procedure forms an essential asset of an organization that acts as a deciding factor concerning the efficient operation of businesses. E-logistics has proved to be a promising technology that ensures improvement in customer experiences. Businesses can now run electronically with the incorporation of e-logistics. It also assists in the establishment of a well-defined

decentralized supply chain management system. Real-time management of the physical workflow of business operation in an entire supply chain is essential for increasing its reliability. Therefore, appropriate automation solutions are the key.

### **3 Industrial Implications of Automated Additive Manufacturing and e-logistics in Supply Chain Management**

Various technologies associated with Industry 4.0 offered promising applications during the adverse times of COVID-19 and other pandemics [20–26]. Automated additive manufacturing and e-logistics are the most disruptive technologies that can profoundly impact supply chain management shortly. The onset of the fourth industrial revolution gave rise to major game-changing digital technologies that can enhance the quality of existing supply chains. Table 1 lists Industry 4.0 technologies that can be utilized to automate 3D printing technology and logistics operation to digitize supply chains.

### **4 Limitations**

Prior research work was conducted on applying the IoT in additive manufacturing, implementing the latest information technology trends in supply chain management, additive manufacturing in supply chain management, and automation of business operations through e-logistics form the basis of the literature review of our research topic. The research work conducted is purely theoretical. The concept of e-logistics and IoT-enabled additive manufacturing in supply chain management is relatively new, and quite a few research materials are available for literature study analysis.

### **5 Conclusion**

Industry 4.0 technologies are immensely beneficial for supply chain networks. Automation is being implemented in the logistics network for efficient planning and procurement of inventory. Various computer softwares are now available for inventory control, warehouse automation, and enterprise resource planning. A more significant number of companies are expected to incorporate robotics process automation for their supply chain operation. This contributes to improved workforce efficiency since tasks requiring minimal skills are automated, which helps employees focus



**Table 1** Supply chain automation through IT technologies

Major automation technologies	Description
Predictive analytics	There are significant technological advancements taking place. Therefore, supply chains must be responsive, flexible, and resilient to cope with adverse effects that a dynamic environment may have on business operations. Supply chain analysts need up skilling in order to increase their effectiveness. Intelligent data science techniques such as forecasting and predictive maintenance are needed to digitize the supply chains. Predictive analytics would help supply chains become reliable [27, 28]
Warehouse automation	Enterprise resource planning software is used to eliminate the requirement of human assistance to keep track of inventory movement into and out of warehouses. Many other initiatives toward warehouse robotics are being taken in the form of collaborative robots. The employment of sophisticated technologies is essential for the automation of inventory operations [29, 30]
Cloud logistics	A virtual logistics network is established. Internet-based technologies support the optimized framework of logistics operation [31]
Blockchain technology	Blockchain technology enables the decentralization of the data stored, which helps the logistics network become sustainable. Authorized users in real-time can access important information about the inventory. This also helps in obtaining information about unforeseen hindrances in real-time. Since the flow of information is end-to-end encrypted, data security is ensured [32, 33]
Drones	Unmanned Aerial Vehicles (UAVs), also known as drones, helps improve the efficiency of logistics operations by cutting down on distribution costs and faster deliveries. Drones help in accessing areas that are usually difficult to access. They reduce the possibility of traffic. Besides, the drone is an eco-friendly e-logistics solution that lowers the levels of carbon emissions [34]
Deep-learning techniques for resource allocation	An intelligent deep-learning algorithm is employed in logistics that helps enhance the utility of AM cloud and meet consumers' rapidly changing demands. This helps in lowering operational costs and overall optimization of the supply chain [35]

(continued)

**Table 1** (continued)

Major automation technologies	Description
Artificial intelligence and 3D printing for humanitarian supply chains	By implementing IoT-enabled 3D printing and machine learning technologies such as artificial intelligence, the smooth flow of information and products can be assured while maintaining its quality at the same time. This makes supply chain management more transparent [36]
Economic cloud additive manufacturing paradigm	The economically robust additive manufacturing cloud provides on-demand production. This cloud AM model also helps in minimizing operational costs in case demand for any uncertain object arises [37]
Big data analytics for supply chain management	Supply chain processes can be assessed with the help of technological tracing systems. The financial performance of an organization can also be examined using big data-driven frameworks [38]
Internet of things for applications in logistics	Transparent logistics is one of the critical factors that determine the efficacy of the supply chains of an organization. Any kind of information obtained and converted into IoT data can be used for providing intelligent services. This helps in the improvement of logistics operations [39–41]

more constructively on high-value tasks. IoT-enabled additive manufacturing technology has an equally important role in the digital transformation of business operations, as e-logistics. IoT helps bring about repeatability in the 3D printing process, which further helps in increasing production volume. This would assist in the large scale production of customized goods. Therefore, IoT increases the possibility of the application of 3D printing in supply chains. Also, manufacturers can ensure that customers' demands are met at the right time, thus improving the consumer experience.

## References

1. Jimo A, Braziotis C, Rogers H, Pawar K (2019) Traditional vs additive manufacturing supply chain configurations: a comparative case study. *Procedia Manuf.* 39:765–774. <https://doi.org/10.1016/j.promfg.2020.01.432>
2. Haleem A, Javaid M (2019) Enablers, barriers, and critical success factors for effective adoption of color-jet 3D printing technology. *J Ind Integr Manag* 1950009. <https://doi.org/10.1142/S242486221950009X>.
3. Laksham N (2021) Where does the supply chain fall short? <https://www.industryweek.com/supply-chain/planning-forecasting/article/21959297/where-does-the-supply-chain-fall-short?> Last Accessed 08 Nov 2021
4. Durbin D 6 overlooked benefits of 3D printing for your supply chain

5. Javaid M, Haleem A, Vaishya R, Bahl S, Suman R, Vaish A (2020) Industry 4.0 technologies and their applications in fighting COVID-19 pandemic. *Diabetes Metab Syndr Clin Res Rev* 14:419–422. <https://doi.org/10.1016/j.dsx.2020.04.032>
6. Iyengar KP, Vaishya R, Bahl S, Vaish A (2020) Impact of the coronavirus pandemic on the supply chain in healthcare. *Br J Healthc Manag* 26:1–4. <https://doi.org/10.12968/bjhc.2020.0047>
7. Supply chain disruption. <https://www.accenture.com/in-en/insights/consulting/coronavirus-supply-chain-disruption>
8. Fretty P (2021) Forget the suez canal. Supply chains need attention. <https://www.industryweek.com/technology-and-iiot/article/21160254/forget-the-suez-canal-supply-chains-need-attention>. Last Accessed 08 Nov 2021
9. Gonzalez CM (2021) Manufacturing blog: engineering a future of sustainable manufacturing. <https://www.asme.org/topics-resources/content/manufacturing-blog-engineering-a-future-of-sustainable-manufacturing>. Last Accessed 08 Nov 2021
10. Haleem A, Javaid M (2019) Additive manufacturing applications in industry 4.0: a review. *J Ind Integr Manag*. <https://doi.org/10.1142/S2424862219300011>
11. Zijm H, Knofius N, van der Heijden M (2019) Additive manufacturing and Its impact on the supply chain BT—operations, logistics and supply chain management presented at the [https://doi.org/10.1007/978-3-319-92447-2\\_23](https://doi.org/10.1007/978-3-319-92447-2_23)
12. Molcho M (2021) Additive manufacturing's rise as an enabler of supply chain efficiencies. <https://supplychaindigital.com/supply-chain-2/additive-manufacturings-rise-enabler-supply-chain-efficiencies>. Last Accessed 08 May 2021
13. Verboeket V, Krikke H (2019) Additive manufacturing: a game changer in supply chain design. <https://doi.org/10.3390/logistics3020013>
14. Ben-Daya M, Hassini E, Bahroun Z (2019) Internet of things and supply chain management: a literature review. *Int J Prod Res* 57:4719–4742. <https://doi.org/10.1080/00207543.2017.1402140>
15. Graham D, Manikas I, Folinas DK (eds) (2013) *E-logistics and e-supply chain management: applications for evolving business*. IGI Global, Hershey, PA. <https://doi.org/10.4018/978-1-4666-3914-0>
16. Wronka A (2017) Lean logistics. *J Posit Manag* 7:55–63
17. Chung P, Chuen Yeh R, Chen Y-C (2015) Implementation of e-logistics systems for developing EC capability in small and medium-sized enterprises: a conceptual model. *Int J e-Educ e-Bus e-Manage e-Learn* 5:203–211 <https://doi.org/10.17706/ijeeec.2015.5.4.203-211>
18. Kanagavalli G, Azeez R (2019) Logistics and e-logistics management: benefits and challenges. *Int J Recent Technol Eng* 8:12804–12809. <https://doi.org/10.35940/ijrte.d7179.118419>
19. Sarkis J, Meade LM, Talluri S (2004) E-logistics and the natural environment. *Supply Chain Manag An Int J* 9:303–312. <https://doi.org/10.1108/13598540410550055>
20. Gupta N, Bahl S, Bagha AK, Vaid S, Javaid M, Haleem A (2021) Nanomedicine technology and COVID-19 outbreak: applications and challenges. *J Ind Integr Manag* 06:161–174. <https://doi.org/10.1142/S2424862221500123>
21. Softa A, Bahl S, Bagha AK, Sehgal S, Haleem A, Javaid M (2021) Tissue engineering and its significance in healthcare during COVID-19 pandemic: potential applications and perspectives. *J Ind Integr Manag* 06:221–233. <https://doi.org/10.1142/S242486222150007X>
22. Jaly I, Iyengar KP, Bahl S, Jain V, Vaishya R (2021) COVID-19 pandemic and debates on the design of operating theatre ventilation systems in healthcare facilities. *J Ind Integr Manag* 06:257–269. <https://doi.org/10.1142/S2424862221500093>
23. Bahl S, Bagha AK, Rab S, Javaid M, Haleem A, Singh RP (2021) Advancements in biosensor technologies for medical field and COVID-19 pandemic. *J Ind Integr Manag* 06:175–191. <https://doi.org/10.1142/S2424862221500081>
24. Bahl S, Iyengar KP, Bagha AK, Jaly I, Jain V, Vaishya R (2021) Bioengineering technology in context of COVID-19 pandemic: potential roles and applications. *J Ind Integr Manag* 06:193–207. <https://doi.org/10.1142/S2424862221500056>

25. Bahl S, Singh RP, Javaid M, Khan IH, Vaishya R, Suman R (2020) Telemedicine technologies for confronting COVID-19 pandemic: a review. *J Ind Integr Manag* 5:547–561. <https://doi.org/10.1142/S2424862220300057>
26. Sharma A, Bahl S, Bagha AK, Javaid M, Shukla DK, Haleem A (2020) Blockchain technology and its applications to combat COVID-19 pandemic. *Res Biomed Eng*, 1–8. <https://doi.org/10.1007/s42600-020-00106-3>
27. Lemos F, Do Nascimento T, Dalmarco G (2020) FASTEN: an IoT platform for supply chain management in a Covid-19 pandemic scenario. *Mark Glob Dev Rev* 5. <https://doi.org/10.23860/mgdr-2020-05-04-02>
28. Waller MA, Fawcett SE (2013) Data science, predictive analytics, and big data: a revolution that will transform supply chain design and management. *J Bus Logist* 34:77–84. <https://doi.org/10.1111/jbl.12010>
29. Elementum News Desk: Supply Chain Technology Roundup (2021) IoT and 3D printing. <https://www.elementum.com/chain-reaction/supply-chain-technology-roundup-iot-and-3dprinting/>. Last Accessed 08 May 2021
30. Dilmegani C (2021) Supply chain automation in 2021: in-depth guide. <https://research.aimultiple.com/supply-chain-automation/>. Last Accessed 08 May 2021
31. Bányaí Á (2014) Cloud logistics. *Adv Logist Syst* 8:11–16
32. Dobrovník M, Herold DM, Fürst E, Kummer S (2018). Blockchain for and in logistics: what to adopt and where to start. <https://doi.org/10.3390/logistics2030018>
33. Tijan E, Aksentijević S, Ivanić K, Jardas M (2019). Blockchain technology implementation in logistics. <https://doi.org/10.3390/su11041185>
34. Vlahovic N, Knezevic B, Batalic P (2016) Implementing delivery drones in logistics business process: case of pharmaceutical industry. *Int J Econ Madag Eng* 3:271–276
35. Mashhadi F, Monroy SAS (2020) Deep learning for optimal resource allocation in IoT-enabled additive manufacturing. In: 2020 IEEE 6th world forum on internet of things (WF-IoT), pp 1–6. <https://doi.org/10.1109/WF-IoT48130.2020.9221038>
36. Rodríguez-Espíndola O, Chowdhury S, Beltagui A, Albores P (2020) The potential of emergent disruptive technologies for humanitarian supply chains: the integration of blockchain, artificial intelligence and 3D printing. *Int J Prod Res* 58:4610–4630. <https://doi.org/10.1080/00207543.2020.1761565>
37. Mashhadi F, Monroy SS (2019) Economically-robust dynamic control of the additive manufacturing cloud. *IEEE Trans Serv Comput* 1. <https://doi.org/10.1109/TSC.2019.2954137>
38. Govindan K, Cheng TCE, Mishra N, Shukla N (2018) Big data analytics and application for logistics and supply chain management. *Transp Res Part E Logist Transp Rev* 114:343–349. <https://doi.org/10.1016/j.tre.2018.03.011>
39. Tran-Dang H, Krommenacker N, Charpentier P, Kim D-S (2020) The internet of things for logistics: perspectives, application review, and challenges. *IETE Tech Rev*, 1–29. <https://doi.org/10.1080/02564602.2020.1827308>
40. Sun C (2012) Application of RFID technology for logistics on internet of things. *AASRI Procedia* 1:106–111. <https://doi.org/10.1016/j.aasri.2012.06.019>
41. Tadejko P (2015) Application of internet of things in logistics—current challenges. *Appl Internet Things Logist—Curr Challeng* 7:54–64. <https://doi.org/10.12846/j.em.2015.04.07>

# Parametric Studies of Dissimilar Friction Stir Welded AA2024/AA6082 Aluminium Alloys



Deepak Kumar Mohapatra and Pragyan Paramita Mohanty

**Abstract** The work emphasizes weld quality as a measure of weld performance considering tool rotational speed as a variable parameter and investigated the effect of rotational speed on friction stir welded (FSWed) AA2024 and AA6082 alloys. Both alloys (6 mm thick) were fabricated using stir tool of shoulder and pin diameter as 20 mm, 7 mm, respectively. Specimens were welded using different rotational speeds of 1000, 1400, 2000 rpm for a given tool traverse speed of 25 mm/min. Mechanical properties of welded joint were characterized under different rotational speeds. Variation in rotational speed showed strong influence on tensile strength as well as on micro-hardness. HAZ zone was identified as low hardness zone, having hardness value close to base material. Fracture starts near HAZ, and the result is in good agreement with tensile strength value.

**Keywords** Friction stir welding · Rotational speed · Mechanical properties

## 1 Introduction

Current engineering application increases the demand of light cost-effective material with high strength and low weight [1]. Aluminium alloys are mostly utilized in automotive and aerospace industries for their lightweight, high strength, toughness, and recycling capabilities [2, 3]. Researches being carried out focussing fabrication of lightweight engineering components with good corrosion resistance [4–9]. Broad application of aluminium alloys in industries motivates many researchers to work on different metal joining processes [10, 11]. Dissimilar materials fabricated through fusion welding process are found to be unsuitable due to presence of defects and intermetallic compound at high temperature. In order to find defect free joints, friction stir welding (FSW) considered as a novel method for being carried out below melting point. FSW has certain advantages over traditional fusion welding process with minimum cracking and excellent combination of mechanical properties [12–15]. It

---

D. K. Mohapatra · P. P. Mohanty (✉)  
Department of Mechanical Engineering, VSSUT, Burla, India  
e-mail: [pragyanmohanty.design@gmail.com](mailto:pragyanmohanty.design@gmail.com)

© The Author(s), under exclusive license to Springer Nature Singapore Pte Ltd. 2023  
P. Pradhan et al. (eds.), *Recent Advances in Mechanical Engineering*,  
Lecture Notes in Mechanical Engineering,  
[https://doi.org/10.1007/978-981-16-9057-0\\_21](https://doi.org/10.1007/978-981-16-9057-0_21)

191

has been considered as one of the most widely used solid state joining processes for aluminium alloy of different grades [16–18]. Researchers have developed different models to learn the effect of different FSW parameters on weld quality of various types of aluminium, magnesium, and steel [19–26] alloys.

Alloys under 2xxx series are heat treatable/age hardenable [27, 28], possess excellent mechanical properties at high temperatures for which these are most extensively used in automotive, aerospace, and in military transport vehicles [26, 29, 30]. On the other hand 6xxx series aluminium alloys are heat treatable having low strength as compared to 2xxx series [31]. Here, an attempt has been made to join AA2024–AA6082 using FSW process and monitor the influence of process parameter in terms of tool rpm on weld qualities keeping welding speed as constant.

The procedure is demonstrated with two sections, namely experiment and characterization. Experiment carried out by considering AA2024 and AA6082 alloys as work materials and high-carbon high chromium as tool material. The process accomplished with three different rotational speed and constant welding speed. Upon completion of experiment, the samples are prepared for tensile and hardness test. Joints also characterized by visual inspection.

## 2 Experimental Procedure

### 2.1 Machine Setup

The experiment was carried out on a FSW setup with modified vertical milling machine as shown in Fig. 1. The machine runs at a highest spindle speed of 3000 rpm with unlimited variables. The joint of two work materials is found to be matched exactly with the centre of the tool pin. The tool was rotated clockwise to force the materials towards the root of weld. After plunging, complete contact of tool shoulder with the work surface was ensured. In order to generate pre-frictional heat, the shoulder of rotating tool was held under dwelling period for few seconds. Then, the horizontal movement was continued till the total length of work piece being welded.

### 2.2 Material and Tool

The base materials considered for the study were AA2024 and AA6082 alloys with 6 mm thickness. Chemical composition of AA2024 and AA6082 is shown in Table 1. All plates were cut to the required length of 100 mm and width of 100 mm. Before welding, the samples were polished to get rid of any surface contamination. The welding was performed on a 3-axis vertical milling machine. Mechanical clamps were used for positioning the initial joint configuration of two dissimilar materials.

**Fig. 1** Vertical milling machine



**Table 1** Chemical composition

Element	Si	Fe	Cu	Mn	Mg	Zn	Ti
AA2024 in %	0.5	0.5	4.9	0.9	1.8	0.25	0.15
AA6082 in %	1.3	0.5	0.1	1.2	1.0	0.2	0.1

It was clamped to the machine bed avoiding root gap in order to restrict the movement in all degree of freedom and withstand sufficient plunging and translational force. Keeping in view on high-wear resistance, non-consumable tool made of high-carbon and high-chromium steel was considered to cast the joint. The cylindrical threaded profile tool having shoulder diameter 20 mm and pin diameter as well as pin length of 7 and 5.5 mm were considered to generate the heat (as shown in Fig. 2). The welded joint that produced after welding carries three different zones is shown in the Fig. 3.

The traverse speed was kept fixed at 25 mm/min, and rotational speed was varied as 1000, 1400, 2000 rpm, respectively (shown in Table 2). After welding process, specimens cut into several sections, perpendicular to the welding directions. First of all specimens were polished with 800, 1000, and 1500 grit silicon carbide paper and then in a variable disc polisher with 3  $\mu\text{m}$  of diamond paste. After polishing, specimens were etched in methanol solution and were prepared for optical microscope and also SEM micrographs, shown in Fig. 4.

**Fig. 2** Tool pin profile



**Fig. 3** Cross section of a FSW joint

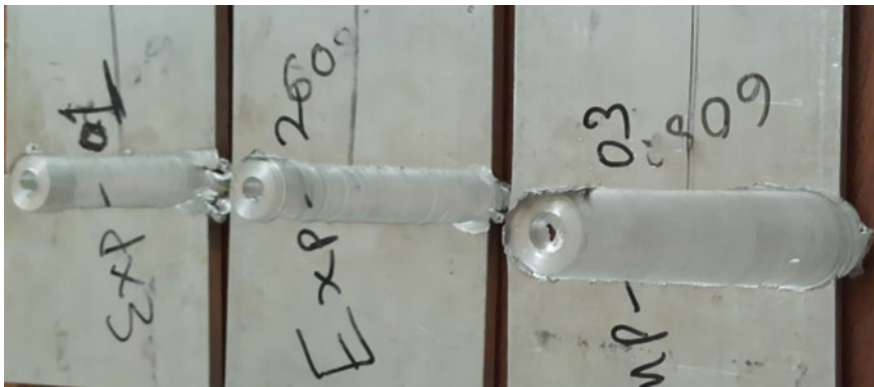
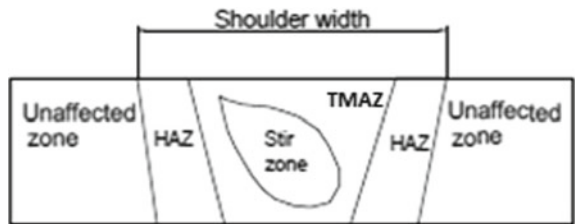


**Fig. 4** Visual inspection

**Table 2** Welding parameter chosen

Sl.no	Tool pin profile	Speed (rpm)	Feed rate (mm/min)
1	Cylindrical	1000	25
2	Cylindrical	1400	25
3	Cylindrical	2000	25





**Fig. 5** Micro-hardness testing machine

### **2.3 Mechanical Testing**

Welded joints considered for mechanical testing are sectioned transverse to the welding direction. Samples were performed micro-hardness test in order to characterize the hardness in the vicinity of the weld affected area. The test has been carried out on a Vickers hardness testing machine as shown in Fig. 5. Vickers micro-hardness measurement has been done using a load of 500 gf and 10 s of dwell time. The hardness at different zones of weldment such as base metal (BM), heat affected zone (HAZ), thermomechanical affected zone (TMAZ), and stirring zone (SZ) was measured. Measurement was taken along the cross sections perpendicular to the welding direction.

Tensile strength is another most essential property for determining the weld quality of dissimilar alloys. The welded specimens for tensile test were machined, shown in Fig. 7. Test was conducted at room temperature by using servo hydraulic testing machine (1000 KN) (Fig. 6).

## **3 Results and Discussion**

### **3.1 Micro-hardness**

Hardness values across transverse section of weld joints are given in Table 3. Peak/maximum hardness values have been observed at weld centres of AA2024-T3/AA6082 when the rotational speed is 1400 rpm and feed 25 mm/min, respectively. A decrease in the hardness was observed on moving away from the NZ towards HAZ. There is sharp drop in the value of micro-hardness on moving from TMAZ to HAZ. However, increase of rotational speed increases micro-hardness initially and then decreases. On other hand, there is decline in hardness of HAZ as compared to the

**Fig. 6** Tensile test



**Fig. 7** Dimension of tensile test specimen

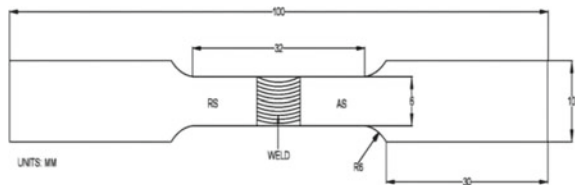


**Table 3** Hardness results

Sl. No	Base metal	HAZ	TMAZ	SZ
Exp1	49HV	41HV	70HV	72HV
Exp2	49HV	40HV	59HV	84HV
Exp3	49HV	43HV	52HV	49HV

base metal. A good joint strength with maximum micro-hardness can be observed in Exp. 2 where tool rotation speed was 1400 rpm. A low hardness value is observed when maximum rotational speed was 2000 rpm and was close to hardness of base material. This is because of the fact that at high rotational speed temperature rises rapidly and hence strengthening precipitates undergoes coarsening due to thermal

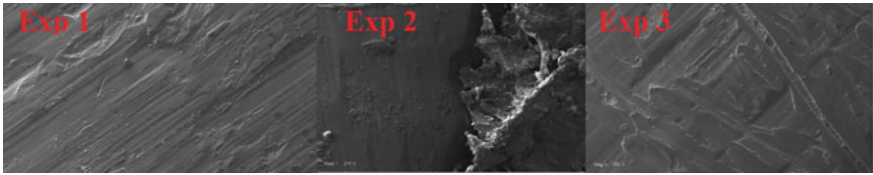


**Fig. 8** SEM micrographs

cycle causing decrease in hardness. Severe plastic deformation results higher hardness in stirring zone and TMAZ. However, the heat transfer gradually decreases towards HAZ zone.

The magnified images of SEM of weld interface are presented in Fig. 8. The figure shows clear difference with cracks and voids. Experiment conducting with tool rotational speed 1400 rpm could led to more cracks and voids in stirring zone in comparison with lower and higher rpm. However, ruptured surface is found to have higher weld quality in the form of hardness and tensile strength.

### 3.2 Tensile Test

Fracture location in all test samples is found to be nearly HAZ zone as shown in Fig. 9 which is close to centre of weld. The tensile and yield strength results are given in Table 4. Maximum tensile strength obtained is 173.8 MPa when AA2024 held on advancing and AA6082 on retreating side. Tensile strength initially increases with rotational speed and then decreases for a given constant traverse speed, 25 mm/min. Surface appearance of the welded joint under microscope for experiment 2 is shown in Fig. 10. It has been found that increase in the rotational speed will develop more frictional heating and hence increases the plastic deformation rate that helps in softening of material. Adequate plastic deformation enhances the strengthening effect

**Fig. 9** Welded specimen after failure



**Table 4** Tensile test results

Sl. No	Tensile strength (N/mm <sup>2</sup> )	Yield stress (N/mm <sup>2</sup> )	% of elongation
Exp. 1	90.88	72.5	6.88
Exp. 2	173.8	137.9	7.19
Exp. 3	162.35	129.31	6.88

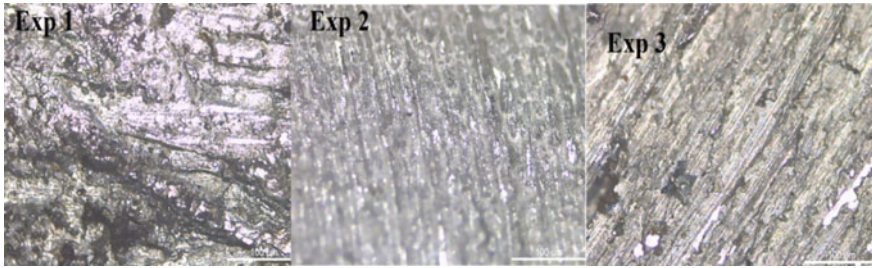


**Fig. 10** Surface appearance of friction stir welding at stirring zones

and improves joint strength. On the other hand, at very high rotational speed, excess heat generated resulting melting and deterioration of weld material. Highest tensile strength of welded joint can be achieved at 1400 rpm and is 173.8 MPa. The result also in agreement with the hardness region.

## 4 Conclusion

FSW was performed on AA2014-AA6082 alloy with a cylindrical threaded tool and joint performances were compared under different rotational speed keeping feed as constant. The study established following conclusions.

- a. The results indicate that the tool rotational speed has effect both on the tensile strength and micro-hardness.
- b. Micro-hardness as well as tensile strength of FSW joint of AA2024-AA6082 are poor at low and very high rotational speed (1000 and 2000 rpm) in comparison with 1400 rpm whilst welding speed is kept constant at 25 mm/min.
- c. The cylindrical threaded pin with a rotational speed of 1400 rpm exhibits better tensile strength, 173.8 N/mm<sup>2</sup>.
- d. The maximum hardness obtained in the stir zone (84HV) of this welded joint and the lowest one obtained in its HAZ (40HV) that led to more cracks and voids in stirring zone at 1400 rpm in comparison with lower and higher rpm where as the result is in good agreement with strength value.

## 5 Future Works

- a. Attempts have been made on preliminary study of the welded joints of AA2024-AA6082 with a variation in rotational speed.
- b. However, in order to ensure the quality of welded joint, number of experiments to be conducted and numerical study could be carried out for the prediction of material flow of welded joints under various welding conditions or parameters.

- c. Future work will be performed considering micro-structural characterization to understand the material flow in the SZ.
- d. Corrosion and fatigue behaviour studies of various combinations of dissimilar AA2024-AA6082 alloy joints will be performed to expand its industrial use.

## References

1. Bodunrin MO, Alaneme KK, Chown LH (2015) Aluminium matrix hybrid composites: a review of reinforcement philosophies; mechanical, corrosion and tribological characteristics. *J Market Res* 4(4):434–445
2. Thirumoorthy A, Arjunan TV, Kumar KS (2018) Latest research development in aluminum matrix with particulate reinforcement composites—a review. *Mater Today: Proc* 5(1):1657–1665
3. Abioye TE, Zuhailawati H, Aizad S, Anasyida AS (2019) Geometrical, microstructural and mechanical characterization of pulse laser welded thin sheet 5052–H32 aluminium alloy for aerospace applications. *Trans Nonferrous Metals Soc China* 29(4):667–679
4. Singh T, Tiwari SK, Shukla DK (2019) Friction-stir welding of AA6061-T6: the effects of Al<sub>2</sub>O<sub>3</sub> nano-particles addition. *Results Mater* 1:100005
5. Vysotskiy I, Malopheyev S, Mironov S, Kaibyshev R (2019) Effect of pre-strain path on suppression of abnormal grain growth in friction-stir welded 6061 aluminum alloy. *Mater Sci Eng, A* 760:206–213
6. Singh VP, Patel SK, Ranjan A, Kuriachen B (2020) Recent research progress in solid state friction-stir welding of aluminium–magnesium alloys: a critical review. *J Market Res* 9(3):6217–6256
7. Chandran R, Ramaiyan S, Shanbhag AG, Santhanam SKV (2018) Optimization of welding parameters for friction stir lap welding of AA6061-T6 alloy. *Mod Mech Eng* 8(1):31–41
8. Wang T, Zou Y, Matsuda K (2016) Micro-structure and micro-textural studies of friction stir welded AA6061-T6 subjected to different rotation speeds. *Mater Des* 90:13–21
9. Shamin MK (2017) Morphological and structural study of friction stir welded thin AA6061-T6 sheets. *Int J Mech Eng* 6(5):19–24
10. Çam G, İpekoğlu G (2017) Recent developments in joining of aluminum alloys. *Int J Adv Manuf Technol* 91(5):1851–1866
11. Gite RA, Loharkar PK, Shimpi R (2019) Friction stir welding parameters and application: a review. *Mater Today: Proc* 19:361–365
12. Çam G, Ventzke V, Dos Santos JF, Koçak M, Jennequin G, Gonthier-Maurin P (1999) Characterisation of electron beam welded aluminium alloys. *Sci Technol Weld Joining* 4(5):317–323
13. Von Strombeck A, Çam G, Dos Santos JF, Ventzke V, Koçak M (2001) A comparison between microstructure, properties, and toughness behavior of power beam and friction stir welds in Al-alloys. In: *Proceedings of the TMS 2001 annual meeting aluminum, automotive and joining*, Feb 2001, pp 249–264
14. Zhang C, Huang G, Cao Y, Zhu Y, Li W, Wang X, Liu Q (2019) Microstructure and mechanical properties of dissimilar friction stir welded AA2024-7075 joints: influence of joining material direction. *Mater Sci Eng: A* 766:138368
15. Pang Q, Zhang JH, Huq MJ, Hu ZL (2019) Characterization of microstructure, mechanical properties and formability for thermomechanical treatment of friction stir welded 2024-O alloys. *Mater Sci Eng: A* 765:138303
16. Mohammadi J, Behnamian Y, Mostafaei A, Gerlich AP (2015) Tool geometry, rotation and travel speeds effects on the properties of dissimilar magnesium/aluminum friction stir welded lap joints. *Mater Des* 75:95–112

17. Thomas W, Nicholas ED, Staines D, Tubby PJ, Gittos MF (2005) FSW process variants and mechanical properties. *Weld World* 49(3):4–11
18. Zhao H, Pan Q, Qin Q, Wu Y, Su X (2019) Effect of the processing parameters of friction stir processing on the microstructure and mechanical properties of 6063 aluminum alloy. *Mater Sci Eng, A* 751:70–79
19. Sato YS, Park SHC, Michiuchi M, Kokawa H (2004) Constitutional liquation during dissimilar friction stir welding of Al and Mg alloys. *Scripta Mater* 50(9):1233–1236
20. Venkateswaran P, Reynolds AP (2012) Factors affecting the properties of friction stir welds between aluminum and magnesium alloys. *Mater Sci Eng, A* 545:26–37
21. D’Urso G, Giardini C, Lorenzi S, Cabrini M, Pastore T (2017) The Effects of process parameters on mechanical properties and corrosion behavior in friction stir welding of aluminum alloys. *Proc Eng* 183:270–276
22. Abolusoro OP, Akinlabi ET (2020) Effects of processing parameters on mechanical, material flow and wear behaviour of friction stir welded 6101-T6 and 7075-T651 aluminium alloys. *Manuf Rev* 7:1
23. Ericsson M, Sandström R (2003) Influence of welding speed on the fatigue of friction stir welds, and comparison with MIG and TIG. *Int J Fatigue* 25(12):1379–1387
24. Abioye TE, Olugbade TO, Ogedengbe TI (2017) Welding of dissimilar metals using gas metal arc and laser welding techniques: a review. *J Emerg Trends Eng Appl Sci* 8(6):225–228
25. Garg A, Bhattacharya A (2019) Influence of Cu powder on strength, failure and metallurgical characterization of single, double pass friction stir welded AA6061-AA7075 joints. *Mater Sci Eng, A* 759:661–679
26. Park JC, Kim SJ (2010) The effect of traveling and rotation speeds on mechanical properties during friction stir welding of dissimilar Al alloys. In: *Defect and diffusion forum*, vol 297, pp 590–595. Trans Tech Publications Ltd
27. Wang G, Zhao Y, Hao Y (2018) Friction stir welding of high-strength aerospace aluminum alloy and application in rocket tank manufacturing. *J Mater Sci Technol* 34(1):73–91
28. Azarniya A, Taheri AK, Taheri KK (2019) Recent advances in ageing of 7xxx series aluminum alloys: a physical metallurgy perspective. *J Alloy Compd* 781:945–983
29. Cam G, Mistikoglu S (2014) Recent developments in friction stir welding of Al-alloys. *J Mater Eng Perform* 23(6):1936–1953
30. Zhang C, Huang G, Cao Y, Li Q, Niu L, Liu Q (2020) Characterizations of microstructure, crystallographic texture and mechanical properties of dissimilar friction stir welding joints for AA2024 and AA7075 under different tool shoulder end profiles. *Mater Today Commun* 25:101435
31. Gharavi F, Matori KA, Yunus R, Othman NK, Fadaeifard F (2015) Corrosion behavior of Al6061 alloy weldment produced by friction stir welding process. *J Market Res* 4(3):314–322

# Evaluation and Optimization of Process Parameter for Surface Roughness of 3D-Printed PETG Specimens Using Taguchi Method at Constant Printing Temperature



**N. Lokesh, J. Sudheer Reddy, B. A. Praveen, Y. M. Kishore Veeresh, B. Sreehari Acharya, J. Eshwar Kapse, Pramath P. Nadig, and Mahadeva Prasad**

**Abstract** 3D printing technology is also known as additive manufacturing technology where the products are manufactured layer by layer. In recent years, huge research is taking place in this field to increase the strength of products by varying the printing process parameters with respect to different materials for various applications. In this research, efforts have been made to decrease the surface roughness for PETG-printed specimen using fused deposition modeling (FDM) process through Taguchi method. The process parameter chosen for the current research is raster angle (RA), infill density (ID), and layer thickness (LT) by keeping other process parameter constant. For the surface texture (roughness) of FDM-printed specimens, three level of values is considered for each process parameter, and correlations between these process parameters were examined which is not found in the literature for PETG specimens. Using design of experiment (DOE) via L27 orthogonal array study has been started. The obtained experimental data were analyzed to examine the impact of each process parameter on the top surface roughness. To assess if process variables have any significant features, the analysis of variance (ANOVA) is performed. The layer thickness has greater than 73% influence on surface roughness, followed by infill density and raster angle, according to the ANOVA results. The results from investigation of Taguchi methods showed that from the selected process parameter 0.1-mm layer thickness, 90% infill density and 60° raster angle are found to be the optimum for better surface finish at 245 °C and at 45 mm/s print speed. The research

---

N. Lokesh (✉) · J. S. Reddy · B. A. Praveen · M. Prasad  
Department of Mechanical Engineering, Nitte Meenakshi Institute of Technology, Yelahanka,  
Bangalore 560064, India  
e-mail: [n.lokesh1234@gmail.com](mailto:n.lokesh1234@gmail.com)

Visvesvaraya Technological University, Belagavi, Karnataka 590018, India

Y. M. K. Veeresh · B. Sreehari Acharya · J. E. Kapse · P. P. Nadig  
Department of Mechanical Engineering, Nitte Meenakshi Institute of Technology, Bangalore,  
Karnataka 560064, India

is focused on a simple yet effective method for estimating surface roughness over various surfaces of FDM specimens using PETG material.

**Keywords** Fused deposition modeling · Raster angle · Infill density · Layer thickness PETG · ANOVA

## 1 Introduction

Additive manufacturing is an advanced manufacturing method used to fabricate prototypes, tooling as well as functional prototypes. There are various types of additive manufacturing technologies, including Binder jetting, selective laser melting, fused deposition modeling, and powder bed fusion. All these works by depositing materials layer by layer to produce three-dimensional (3D) objects, where it is directly built from a 3D computer-aided-design model of the object [1]. Many research works are being carried out in the recent years, on both 3D printing technology and the applications in smart materials and in tribology [2]. The FDM techniques as an end application product or prototype are dependent on process parameters in the manufacturing industries [3]. Surface roughness plays an important role in determining how an object interacts with its surroundings because of the frictional force opposing it, affecting tribological behavior of surfaces [4–6].

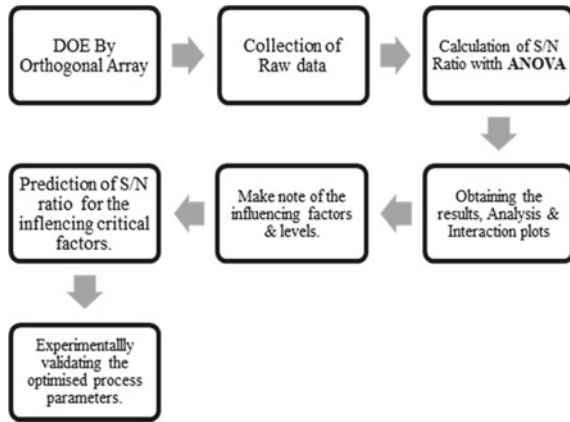
The vital process parameters in the fused deposition modeling (FDM) include mainly raster angle, layer thickness, and infill density. Surface roughness of the part product being printed by FDM mainly depends on process parameter for the thermoplastic polymer, polyethylene terephthalate glycol (PETG). The part characteristics of the final product depend on many factors including raw material used, process parameters, and operational environment. Thermoplastic polymers used in rapid prototyping techniques can be used to produce durable parts subjected to static and dynamic loading conditions [7].

FDM enables great diversity of the filament materials available in the market. The low cost and abundance of the thermoplastic polymers PETG and need for the hydrophobicity enabled the selection of PETG material [8]. The experimental investigation on the individual effect of different process parameters such as layer thickness, infill density, and infill pattern is carried out on PETG material to see if any considerable differences in surface roughness is being found [9]. Taguchi techniques of optimization are best suited as it reduces the substantial number of experimental runs.

The technique used in the current study is depicted in Fig. 1. The specimens were printed using FDM [10] in accordance with the DOE by L27 orthogonal array, and raw data for surface roughness were obtained on the top, side, and bottom surfaces. Smaller the optimum value for signal-to-noise ratio (SNR) was determined using ANOVA for each response [11]. Furthermore, the parameters' rankings are established, and an interaction plot is produced to investigate the significance of



**Fig. 1** Detailed flowchart of the research work



influencing parameter and to decide its level. The regression equation is used to find the essential factors for achieving the best surface finish, which is then confirmed by experimentation. Hence, the current work in this paper highlights on enhancing and controlling the influencing process parameters which ultimately impacts the surface finish of 3D-printed parts.

## 2 Materials

The material used in this work is the polyethylene terephthalate glycol, commonly known as PETG WHITE filament. Properties of PETG is represented in Table 1. This material is extensively used in the field of additive manufacturing for some of its unique properties [12]. It offers good impact resistance, resistance to heat, and chemicals compared to other materials like PLA and ABS. It has an excellent feature definition and an appreciable surface finish. When compared to acrylic or polycarbonate, it is considerably stronger and lasting longer. Because of its distinct properties, it is ideal for impact-resistance testing and high-strength display devices [13]. It is better suited to be worked at high temperatures and is considerably brittle than the other materials. Its rigid structure is one of the significant reasons behind

**Table 1** Material property of PETG

Mechanical properties	Standard	Units	Typical value
Tensile toughness	ASTM (D-638)	MPa	50
Young's modulus	ASTM (D-638)	MPa	2100
Tensile length extension	ASTM (D-638)	%	130
Flexibility/Elasticity	ISO 178	MPa	68

finding its wide range of applications. It finds its uses in the biomedical field, for medical implants, pharmaceutical, and medical device packaging [14]. The material which is available in the filament form is used and is fed into the 3D printer, and the testing specimens are obtained by using the concept of fused deposition modeling (FDM). Later, these specimens are tested for their surface roughness, and the consequent values are determined.

### 3 Objectives and Methodology

The present study focuses on evaluating the influence of the selected process criteria on the surface texture of the 3D-printed PETG specimens. Surface roughness is measured on the basis of deviations from the existent surface texture to its absolute one. Taguchi analysis is used to discover and identify the significant process parameters influencing the surface roughness for all three faces of the printed components, using portable Mitutoyo SJ-210 surface roughness tester thereby generating the empirical relationships via regression equation for the reduced surface roughness between the FDM and MPI operating parameters.

The methodological flow followed for the present project is depicted in Fig. 1. It begins with the design of an experiment using an outer array or an orthogonal array L27 shown in Table 2. Multiple emulations of the tested surface roughness specimens are used to gather raw data for the top, side, and bottom faces. The variance is decreased by increasing the signal-to-noise ratio (SNR) for each individual answer, which is done using ANOVA. Individual plots are then produced once the replies have been evaluated to establish the rankings. The important influencing elements for multi-replies are determined once the processing model has been improved. For the optimal values of parameters, the SNR ratio is projected, and raw data for important variables are computed, resulting in a reduced surface roughness.

### 4 Experimental Work

Primarily, the specimens were designed as per the ASTM standard D256 using CATIA V5 converted to STL file which is imported to Ultimaker CURA 4.0 for slicing. Raster angle, layer thickness, and infill density were chosen as the process parameters in this project since they play vital role in 3D orienting process and have not been utilized before in the literature. The printed specimens were tested for Ra on top, side, and bottom surfaces using Mitutoyo MJ 190 (Fig. 2).

**Table 2.** Shows the orthogonal array (or outer array) with the measured Ra surface roughness value and SNR ratio

Specimen	Raster angle	Infill density	Layer thickness	Ra (Top)	Ra (Bottom)	Ra (Side)	SNRA (Top)	SNRA (Bottom)	SNRA (Side)	SNRA (Combined)
RIL-01	30	30	0.1	0.38	1.2	0.68	8.404328	-1.58362	3.349822	1.660458464
RIL-02	30	30	0.15	1.17	1.25	1.25	-1.36372	-1.9382	-1.9382	-1.755021494
RIL-03	30	30	0.2	1.21	1.77	1.39	-1.65571	-4.95947	-2.8603	-3.377320656
RIL-04	30	60	0.1	1.12	1.72	0.54	-0.98436	-4.71057	5.352125	-1.765156951
RIL-05	30	60	0.15	1.41	1.77	0.95	-2.98438	-4.95947	0.445528	-3.0272766
RIL-06	30	60	0.2	1.74	1.59	1.33	-4.81098	-4.02794	-2.47703	-3.876626579
RIL-07	30	90	0.1	0.29	1.27	0.38	10.75204	-2.07607	8.404328	2.119731159
RIL-08	30	90	0.15	1.12	1.43	0.89	-0.98436	-3.10672	1.0122	-1.347506861
RIL-09	30	90	0.2	1.98	1.95	0.84	-5.9333	-5.80069	1.514414	-4.486290364
RIL-10	45	30	0.1	0.57	1.23	0.86	4.882503	-1.7981	1.310031	0.659394305
RIL-11	45	30	0.15	1.06	1.44	0.79	-0.50612	-3.16725	2.047458	-1.050898796
RIL-12	45	30	0.2	1.82	1.38	1.64	-5.20143	-2.79758	-4.29688	-4.208575276
RIL-13	45	60	0.1	0.61	1.31	0.54	4.293403	-2.34543	5.352125	1.005807945
RIL-14	45	60	0.15	1.32	1.97	0.9	-2.41148	-5.88932	0.91515	-3.313125493
RIL-15	45	60	0.2	1.8	2.04	1.41	-5.10545	-6.1926	-2.98438	-4.955304621
RIL-16	45	90	0.1	0.74	2.38	0.61	2.615366	-7.53154	4.293403	-3.413751636
RIL-17	45	90	0.15	1.51	2.06	0.83	-3.57954	-6.27734	1.618438	-3.809705928
RIL-18	45	90	0.2	2.03	2.24	1.26	-6.14992	-7.00496	-2.00741	-5.533205869
RIL-19	60	30	0.1	0.62	2.19	0.91	4.152166	-6.80888	0.819172	-3.016520387
RIL-20	60	30	0.15	1.62	1.02	1.5	-4.1903	-0.172	-3.52183	-2.948188095
RIL-21	60	30	0.2	1.74	3.84	1.88	-4.81098	-11.6866	-5.48316	-8.514132806

(continued)

Table 2 (continued)

Specimen	Raster angle	Infill density	Layer thickness	Ra (Top)	Ra (Bottom)	Ra (Side)	SNRA (Top)	SNRA (Bottom)	SNRA (Side)	SNRA (Combined)
RIL-22	60	60	0.1	0.85	1.56	0.89	1.411621	-3.86249	1.0122	-1.192778895
RIL-23	60	60	0.15	1.3	0.83	1.06	-2.27887	1.618438	-0.50612	-0.672568892
RIL-24	60	60	0.2	1.45	2.17	1.6	-3.22736	-6.72919	-4.0824	-4.946832206
RIL-25	60	90	0.1	0.96	1.48	0.69	0.354575	-3.40523	3.223018	-0.777432836
RIL-26	60	90	0.15	1.86	1.46	0.98	-5.39026	-3.28706	0.175478	-3.392261195
RIL-27	60	90	0.2	2.17	1.28	1.44	-6.72919	-2.1442	-3.16725	-4.482372553

**Fig. 2** 3D-printed test sample



### 4.1 Data Collection and SNR Ratio

For the functionality of the product, surface behavior is as much important as the mechanical properties. For a better surface finish, the measured Ra values should be low; thus, the “smaller the better” quality characteristic is used in this study and is given in Eq. (1)

$$\eta = -10 \log_{10} \left[ \frac{1}{n} \sum_{i=1}^n Y_i^2 \right] \tag{1}$$

In comparison to the top and bottom faces, the side face has a flat surface finish, according to the raw data. This difference in the bottom surface is due to the temperature of the printing platform, which is regulated at 80 °C throughout the process to prevent warpage by anchoring the beneath layers. Because of the larger nozzle size, the top surface roughness can be attributed to reduce surface detailing. The SNR data obtained are shown in Table 2.

### 4.2 Analysis of Variance

ANOVA was used to calculate the relative effect of the components and interactions using MINITAB at 95% CI. The total DOF for three components with three levels each and an interaction parameter is 27, which matches the observed DOF exactly. The *P*-value from the test was used to assess the factor’s significance. By comparing the phrase’s sum of squares (Adj SS) to the entire sum of squares, the percentage contribution was calculated. Minor factors were removed from the ANOVA table because they were judged insignificant. The ANOVA findings for the Ra responses value of the top face is shown in Table 3. The DOF of unnecessary components with

**Table 3** ANOVA for the top surface Ra value

Source	DF	Adj SS	Adj MS	F-value	P-value	Contribution (%)
Raster angle (R)	2	0.03899	0.038989	0.64	0.433	3.54
Infill density (I)	2	0.09830	0.098298	1.62	0.219	4.67
Layer thickness (L)	2	0.00376	0.003757	0.06	0.048	73.53
Raster angle * Infill density	4	0.08497	0.084966	1.40	0.251	8.17
Raster angle * Layer thickness	4	0.05250	0.052500	0.86	0.364	0.05
Infill density * Layer thickness	4	0.11406	0.114063	1.88	0.186	1.13
R * I * L	6	0.07411	0.074113	1.22	0.283	1.02
Error	2					7.89
Total	26					100

tiny percentage contributions was used to modify the ANOVA error function. The difference between the total DOF and the sum of all the DOF of minor variables was used to calculate the goal function. The correlation between various parameters was also investigated in order to evaluate the ANOVA experimentally measured Ra levels for the relevant objective.

### 4.3 Response to Signal-To-Noise Ratio

The responses and relative contributions of the different components were then studied further using the SNR ratio data. This research helped to determine the relative importance of several components in reaching the aim. The delta values of the various criteria were used to establish the ranking. The response tables for each response may be found in Table 4.

**Table 4** SNR response for top Ra values

Level	1	2	3	Delta	Rank
Raster angle	0.04884	-1.2403	-2.30096	2.34979	2
Infill density	-0.03214	-1.78865	-1.67162	1.75651	3
Layer thickness	3.98685	-2.63211	-4.84715	8.834	1

## 5 Analysis and Discussion of the Results

The effect of the process parameters such as raster orientation, infill component density, and the layer thickness on the surface finish of the FDM-printed part’s top, side, and bottom faces was investigated. For two replications, the values of raw data and SNR were determined considering their average values and were shown in Table 2. To assess the parametric effect on response characteristics, SNR response curves were utilized for Ra values measured on the top, side, and bottom faces. The effect of the process variables and their levels on the response characteristics was determined using the analysis of variance for SNR. The best process variable settings were determined by evaluating the response curves as well as the ANOVA table in terms of mean performance parameters.

### 5.1 Effect on the Surface Finish of the Top Face

Main effect plot for SN ratio of top surface with different process parameter is shown in Fig. 3. Surface roughness reduces with increasing raster angle and infill density, but rises with increasing layer thickness, as seen in the graph. From the response table for SN ratio for top surface (Table 4), it can be noted that the thickness of the layer is having high influence on surface roughness compare to other two process parameter. ANOVA data from Table 3 gives the significant influencing factor. It is further perceived that layer thickness and infill component density have a significant impact on the surface roughness than any other individual or interaction factor for the confidence interval of 95% since their p values are less than 0.05. The surface

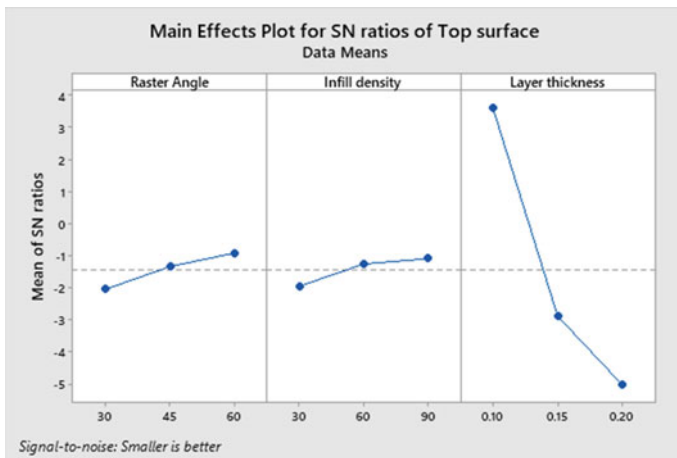


Fig. 3 Main effect plot

roughness decreases as the infill density increases because the space between the lines decreases. Surface roughness is reduced along the top surface of the specimen with 90% infill density. It is observed that with decrease in layer thickness the surface roughness decreases since the width of each line decreases. It is also noted that with increase in raster angle surface roughness decreases in this work 60° raster angle is giving the optimum value and will be chosen for further analysis. From the ANOVA Table 3, it is witnessed that raster angle has minimum significant compared to other process parameter with a contribution less than 4% on surface roughness for PETG specimen.

It is observed from that printing temperature places vital role in filling the gap between each layer [15], and printing with high temperature results in warpage; printing with low temperature results in improper adhesion between layers [15]. In this research, optimum printing temperature 245 °C has been chosen because beyond this temperature, the material might slowly melt leading to a distorted material surface. The printing speed is 40 mm/s, and infill pattern chosen is line pattern. Because the deposited layer contracts when the temperature of the material equals the room temperature, hence, 100% infill density is not considered in this study. From the ANOVA result Table 3, it is observed that interaction between raster angle and infill density is more significant than any other process parameter interaction. The interaction plots are shown in Fig. 4. To analyze the data for non-normality, non-random variation residual plots were used. All the residuals were extremely evenly distributed on the straight line in the normal probability plot. Results obtained were similar to the discussion made by other researchers [15] for other material. From

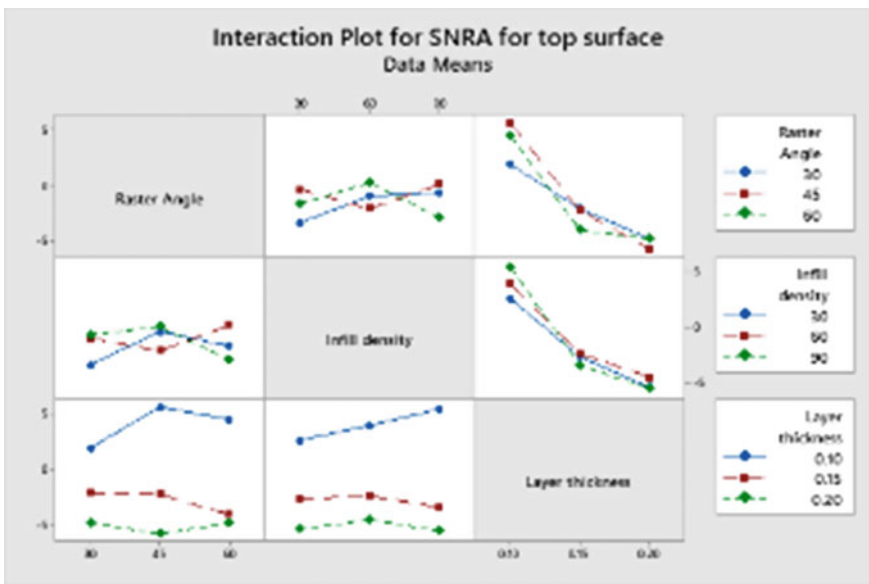


Fig. 4 Interaction plot



the AVOVA Table 3, it can be noted that interaction between the process parameter raster angle and infill density is slightly significant compared to other interactions. Similar procedure may be employed to analyze the surface roughness of other two faces.

## 6 Conclusion

To determine the best factor values, significant factors, and interactions, the Taguchi DOE was employed. The analysis revealed that the factor ideal settings were the same for all response characteristics. The Taguchi approach revealed that a layer thickness of 0.1 mm, raster angle of 60, and 90% infill part density were the optimum values for linear infill pattern style at 245 °C nozzle temperature and 40 mm/s printing speed to obtain fine surface finish. Further, increase in raster angle may increase the surface finish in minor range since contribution of raster angle is very less compared to other two process parameter. From the ANOVA response, it is noticed that thickness of the layer is having higher influence than any other factor, and its contribution is 75.34%. The Ra values for the component printed with optimal process parameters on the top, side, and bottom faces were 0.95, 2.145, and 1.212, respectively. Because both layer thickness and infill density have a higher impact on build time, further, build time optimization is required without losing the printed object's strength. However, the proposed settings have a 90% infill component density, which increases the part's weight and, if increased to 100% for bigger volume models, may cause thermal warpage. As a result, the replies must be chosen with great care. Further, the work may be extended to find out the influence printing speed on surface roughness at different temperature.

## References

1. Jin Y, Ji S, Li X, Yu J (2017) *J Manuf Technol Manage* 1741–038X
2. Bogue R (2012) *Assembly automation* 0144–5154
3. Anitha R, Arunachalam S, Radhakrishnan P (2001) *J Mater Process Technol* 118(1–3):385–388
4. Nancharaiah T, Raju DR, Raju VR (2010) *Int J Emerg Technol* 1(2):106–111
5. Thrimurthulu K, Pandey PM, Reddy NV (2004) *Int J Mach Tools Manuf* 44(6):585–594
6. Horvath D, Noorani R, Mendelson M (2007) *Mater Sci Forum* 561:2389–2392
7. Nagendra J (2016) *Int J Res Aeronautical Mech Eng* 4(1):110–119
8. Barrios JM, Romero PE (2019) *Industrial additive manufacturing process planning: process evaluation, metrology, and post-processing techniques* 12(15)
9. Srinivasan R, Prathap P, Raj A, Aswirth Kannan S, Deepak V (2020) part 2 vol 27
10. Praveena BA, Lokesh N, Buradi A, Santhosh N, Praveena BL, Vignesh R (2021) A comprehensive review of emerging additive manufacturing (3D printing technology): Methods materials applications challenges trends and future potential. *Mater Today: Proc.* <https://doi.org/10.1016/j.matpr.2021.11.059>
11. Lokesh N, Praveena BA, Reddy JS, Vasu VK, Vijaykumar S (2021) Evaluation on effect of printing process parameter through Taguchi approach on mechanical properties of 3D printed

- PLA specimens using FDM at constant printing temperature. *Mater Today: Proc* <https://doi.org/10.1016/j.matpr.2021.11.054>
12. Szykiedans K, Credo W, Osiński D (2017) XXI International Polish-Slovak conference "Machine modeling and simulations 2016. *Procedia Eng* 177:455–461
  13. Subbarao Ch.V, Srinivasa Reddy Y, Inturi V, Indra Reddy M (2021) *IOP Conf Ser Mater Sci Eng* 1057:012031
  14. Vishal G, Vempati SR, Srinivasulu R (2020) *Int Res J Eng Technol (IRJET)* 07(10)
  15. Nagendra J, Ganesha Prasad MS, Shashank S, Vijay N, Ali S.Md (2019) *AIP Conf Proc* 2057(1):020047
  16. Sood AK, Ohdar R, Mahapatra S (2009) *Mater Des* 30(10):4243–4252
  17. Zhang JW, Peng AH (2012) *Adv Mater Res* 538:444–447
  18. Laeng J, Khan ZA, Khu SY (2006) *J Appl Sci* 6:622–630

# Heat Transfer Due to Turbulent Impinging Air Jet on Flat and Concave Plate



Deepak Kumar Sethy and Pandaba Patro

**Abstract** Heat transfer characteristics for an unconfined, axially symmetric impinging air jet on a curved surface as well as a flat surface have been studied numerically for a range of impingement parameters, i.e. Reynolds number and radius of curvature. Impinging fluid is air, which is considered incompressible and turbulent. SST  $k - w$  turbulence model was used for closure of the governing equations. Nozzle exit Reynolds number (Re) was varied from 10,000 to 30,000, and jet spacing (H/D) was varied from 2 to 6. Heat transfer was predicted from the numerical simulations for different Reynolds number and curvature ratio for the concave surface and compared with the heat transfer from the flat surface due to air impingement.

**Keywords** Jet impingement · Heat transfer · Concave surface · CFD

## 1 Introduction

In jet impingement, cold or hot fluid impinges on a hot or cold surface for the heat transfer either from the hot surface or cold fluid. It provides an effective and enhanced way of heat transfer in industrial applications like cooling of hot metals, heat treatment process, electronics cooling, heating of optical surfaces for defogging and many others. Jet impingement heat transfer has numerous advantages over other type of cooling or heating process as it fits well with space limitation problem, heat transfer efficiency is more and heat removal from specific location can be done easily. A lot of research has been done in the area of jet impingement experimentally as well as numerically [1–5]. In the present study, numerical simulations are performed using computational fluid dynamics (CFD) for an air jet impingement problem flat plate and concave plate are chosen with same surface area. Comparison of heat transfer characteristics was investigated for different Reynolds number and radius of curvature. Hofmann et al. [6] performed an extensive study of different turbulence models for jet impingement. They studied 13 turbulence models for heat transfer prediction

---

D. K. Sethy · P. Patro (✉)

Department of Mechanical Engineering, VSSUT, Burla, Sambalpur, Odisha 768018, India  
e-mail: [ppatro\\_me@vssut.ac.in](mailto:ppatro_me@vssut.ac.in)

© The Author(s), under exclusive license to Springer Nature Singapore Pte Ltd. 2023  
P. Pradhan et al. (eds.), *Recent Advances in Mechanical Engineering*,  
Lecture Notes in Mechanical Engineering,  
[https://doi.org/10.1007/978-981-16-9057-0\\_23](https://doi.org/10.1007/978-981-16-9057-0_23)

213

in numerical simulations using Ansys Fluent. They found that SST  $k - w$  model provided satisfactory results for jet impingement. Xing et al. [7] investigated the numerical modelling of inline and staggered array of jets. They also found that SST  $k - w$  turbulence model predicted results which are in good agreement with experimental data. Hence, in the present study, we also used shear stress transport turbulent model for the numerical simulations of turbulent jet impingement on flat surface and concave surface.

## 2 Mathematical Modelling

### 2.1 Physical Setup

The fluid taken is air and impingement of hot air at 338 K from a circular nozzle takes place on a round flat plate as well as a curved (concave). The surface plate is taken as aluminium with thermal conductivity 202.4 W/m.k.

Mass, momentum and energy equation can be written in Cartesian tensor notation as follows:

$$\frac{\partial \rho}{\partial t} + \frac{\partial U_i}{\partial x_i} = 0 \quad (1)$$

$$\rho U_j \frac{\partial U_i}{\partial x_j} = -\frac{\partial P}{\partial x_j} + \frac{\partial}{\partial x_j} \left( \mu \left( \frac{\partial U_i}{\partial x_j} + \frac{\partial U_j}{\partial x_i} \right) \right) - \rho \overline{U'_i U'_j} \quad (2)$$

$$\rho U_j \frac{\partial T}{\partial x_j} = \frac{\partial}{\partial x_j} \left( \frac{\mu}{Pr} \frac{\partial T}{\partial x_j} - \rho \overline{T' U'_j} \right) \quad (3)$$

where  $P$  is the mean pressure,  $T$  is the temperature and  $U$  is the velocity.  $T'$  and  $U'$  are the fluctuating temperature and velocity in  $x$ - and  $y$ -direction, respectively. The turbulence Reynolds stress  $-\rho \overline{U'_i U'_j}$  is calculated by using the SST  $k - w$  turbulence model. In the eddy viscosity turbulent models, Boussinesq approximation was used, i.e. turbulent stresses are assumed to be linearly proportional to the strain rate.

$$-\rho \overline{U'_i U'_j} = \mu_t \left( \frac{\partial U_i}{\partial x_j} + \frac{\partial U_j}{\partial x_i} \right) - \frac{2}{3} \rho k \delta_{ij} \quad (4)$$

For the numerical simulation, SST  $k - w$  model is chosen because it more accurate and reliable for jet impingement problems as reported in literature.

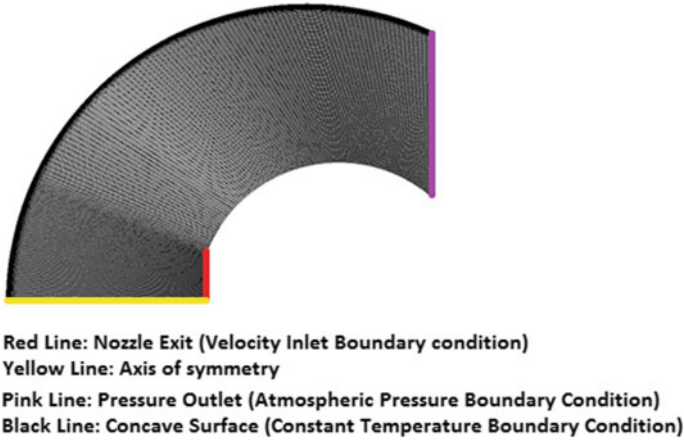


**Fig. 1** Computational domain with meshing

## 2.2 Numerical Solution Using Ansys Fluent Software

Ansys Fluent is based on control volume method. Three-dimensional analysis of jet impingement has been done using Ansys Fluent 19 software using pressure-based solver. SIMPLE algorithm was used for the pressure-velocity coupling. The discrete schemes of pressure are taken as second order, momentum, turbulent kinetic energy, specific dissipation rate and energy are second order upwind implicit schemes. Because of symmetry nature of physical model about the pipe axis, 3D analysis can be done by considering 2D axisymmetric model by taking symmetry axis as  $X$ -axis in geometrical modelling. The computational domain employed as shown in Fig. 1 was prepared using ICEM CFD 16.0. The material of plate is aluminium with conductivity 202.4 W/m.k.

Fully developed velocity was imposed at nozzle exit. Temperature of hot air at nozzle exit is 338 K. The plate is maintained at 277 K. Other boundaries of the computational domain are pressure outlet, i.e. atmospheric pressure. No slip boundary condition was used for the plate. Turbulent intensity for jet flow is considered to be 4%.

## 2.3 Grid Independence Test and Validation

Before starting CFD simulation runs, a study of grid is required to determine the minimum number of cells for the computational domain. Here, variation of local Nusselt number along the flat plate has been chosen both for grid independence and validation with experimental work of Sagot et al. [5].

**Table 1** Percentage error calculation for average Nusselt number

H/D	Nu_Exp	Nu_Num			% error		
		SST $k - \omega$ Model (A)	RNG $k - \epsilon$ Model (B)	Realizable $k - \epsilon$ Model (C)	A	B	C
2	52.14	47.9375	43.5169	41.1429	8	16.5	21.09
4	51.59	46.3185	41.7889	38.19262	10.21	18.9	25.96
6	49.95	42.6595	38.4339	34.8119	14	23	30.30

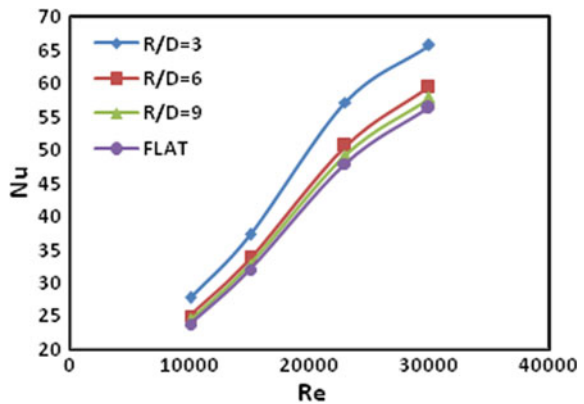
Initially, the computational domain was meshed with 22,000 cells and heat transfer was predicted. Then, grid size was increased to 55,000 cells and 65,000 cells to see whether any change in heat transfer occurred. It is found that after 55,000 cells, the heat transfer did not change significantly and the change was observed less than 1%. So, to save computational time, 55,000 grid size mesh was selected for this study.

Three turbulence models, i.e. SST  $k - \omega$ , RNG  $k - \epsilon$ , realizable  $k - \epsilon$  were tested to find the most appropriate one for the present case. It was found that SST  $k - \omega$  model predict well with the experimental data of Sagot et al. [5] with maximum variation of 14% as depicted in Table 1 for different values of H/D ratio. The error between simulation and experimental results is less than 15% in case of SST  $k - \omega$  model, which is within acceptable limit.

### 3 Results and Discussion

Figure 2 shows the effect of Reynolds number on heat transfer. Heat transfer is predicted in the form of non-dimensional number known as Nusselt number (Nu). This is observed that increment in Reynolds number increases the turbulence level and convection strength which is the cause for enhancement of heat transfer. Viscous effect is more dominant at low Reynolds number, which results in thicker boundary

**Fig. 2** Average Nusselt number versus Reynolds number at  $H/D = 2$



layer. As Reynolds number increases, this effect is less dominant. So, thinner the boundary layer enhances the heat transfer. Heat transfer is more in a concave surface compared to a flat surface of same surface area.

Figure 3 is plotted between Nusslet number and position along the flat plate. A flat is positioned in vertical direction and hence can be represented by different  $Y/D$  values.  $Y/D = 0$  refers to the centre of the plate, which is the stagnation point, where the axis of the jet strikes the plate. A peak occurs at a distance from the stagnation point, i.e.  $Y/D = 0.625$ . Secondary peak occurs at  $Y/D = 2.05$ . Primary peak in Nusselt number distribution is due to turbulence in jet and thin thermal boundary layer created in that region. So, heat transfer is maximum.

Figures 4 and 5 are plotted for concave surface at  $H/D = 3$  and  $H/D = 6$ , respectively. Here also, primary peak is obtained at  $R/D = 0.625$  and secondary peak is obtained at  $R/D = 2.049$  for all cases. The reason for primary peak is already explained for flat surface and the same cause here also. A secondary peak is obtained due to mixing of primary vortices with the counter rotating secondary vortices which causes more turbulence. Hence, it is enhancing the heat transfer. Primary vortex

**Fig. 3** Local Nu along the length of flat plate at  $H/D = 2$  at different Re

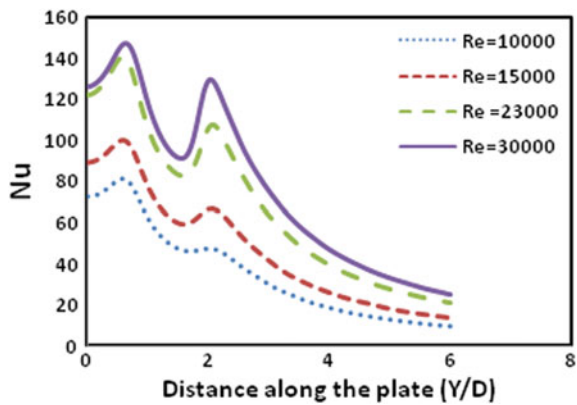


**Fig. 4** Local Nu along the length of concave plate of  $R_C/D = 3, H/D = 2$  (Position 0 refers to the centre of concave surface)

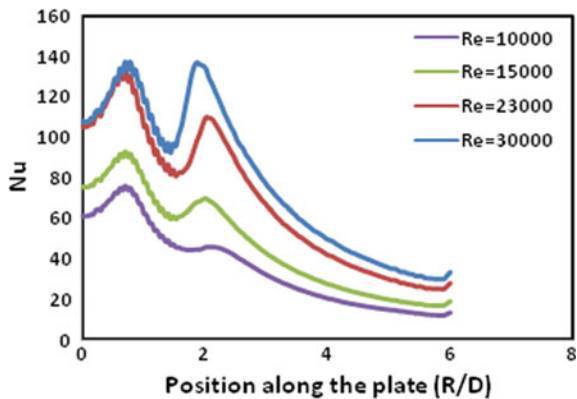
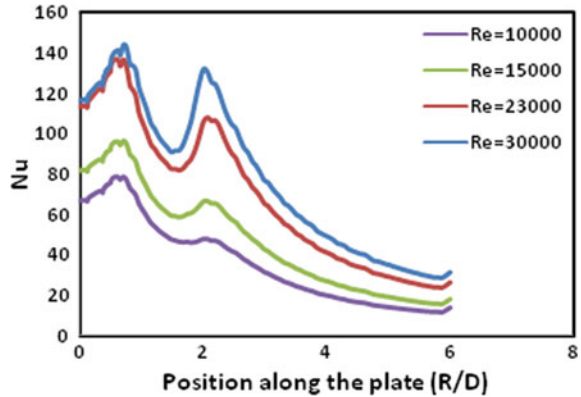


**Fig. 5** Local Nu along the length of concave plate of  $R_C/D = 6$ ,  $H/D = 2$  (Position 0 refers to the centre of concave surface)



generation is due to turbulence in free jet, and secondary is due to unsteady separation of boundary layer along the plate. Secondary maxima appear when turbulent kinetic energy, turbulent dissipation rate and turbulence intensity are maximum.

The primary maxima are almost same for all above three different shaped surfaces. But, magnitude of secondary maxima is increased as the curvature decreased. This is due to the fact that more curvature means more centripetal force, which causes the flow to be unstable leading to more enhancements in heat transfer.

## 4 Conclusions

Numerical simulation was performed for jet impingement on a flat surface as well as concave surface of different radius of curvature. Ansys Fluent software was used for the numerical simulation, which is based on control volume approach. Different turbulence models are available for such flows and when compared to experimental data, SST  $k - w$  model is found to be better compared to other turbulence models for jet impingement problems. It was found that an increase in Reynolds number increases heat transfer in all cases. Heat transfer is maximum near the stagnation point at a distance of 0.625 from the centre of the plate for both flat as well as curved surface and decreases towards the periphery. A secondary peak is obtained at a distance of 2.05 from the centre of the plate, which increases by the decrease of curvature. Heat transfer is more in a curved surface than a flat surface at same Reynolds number.



## References

1. Thomson H (1968) Effect of streamwise wall curvature on heat transfer in a turbulent boundary layer. *J Fluid Mech* 33(2):283–292
2. Cornaro C, Fleischer AS, Goldstein RJ (1999) Flow visualization of a round jet impinging on cylindrical surfaces. *Exp Thermal Fluid Sci* 20(2):66–78
3. Sharif MAR, Mothe KK (2009) Evaluation of turbulence models in the prediction of heat transfer due to slot jet impingement on plane and concave surfaces. *Numer Heat Transf Part B Fundam* 55(4):273–294
4. Al Ali AR, Janajreh I (2015) Numerical simulation of turbine blade cooling via jet impingement. *Energy Procedia* 75:3220–3229
5. Sagot B, Antonini G, Christgen A, Buron F (2008) Jet impingement heat transfer on a flat plate at a constant wall temperature. *Int J Therm Sci* 47(12):1610–1619
6. Hofmann HM, Kaiser R, Kind M, Martin H (2007) Calculations of steady and pulsating impinging jets—an assessment of 13 widely used turbulence models. *Numer Heat Transf Part B Fundam* 51(6):565–583
7. Xing Y, Spring S, Weigand B (2010) Experimental and numerical investigation of heat transfer characteristics of inline and staggered arrays of impinging jets. *J Heat Transf* 132(9):092201

# Evaluation of Preventive Activities of COVID-19 Using Multi-criteria Decision Making Method



Gnanasekaran Sasikumar, Sivasangari Ayyappan, and N. Venkatachalam

**Abstract** In this paper, a Multi-Criteria Decision Making (MCDM) process based on Analytical Hierarchy Process (AHP) method is presented with an objective of helping decision makers (DMs) to evaluate the important activities that cause the spread of COVID-19 disease. In this study, seven important activities have been identified and a decision hierarchy is constructed based on these criteria. The criteria weights are calculated using the additive normalization method. The consistency of pairwise comparison matrix is calculated and found within the allowable limit. Based on the AHP method, a user friendly decision support system was developed in order to perform the calculations quickly and accurately. It is found that the proposed AHP method deals with evaluation of preventive activities of COVID-19 efficiently.

**Keywords** COVID-19 · MCDM · Analytical hierarchy process · Pairwise comparison · Criteria

## 1 Introduction

The novel coronavirus known as SARS-CoV-2 and called as COVID-19 was first identified in Wuhan [3]. Globally, as on 18 May 2021, there have been 16,33,12,429 confirmed cases of COVID-19, including 33,86,825 deaths, thus it becomes a major global health challenge. The spread of COVID-19 happens mainly due to transmission of saliva from an infected patient to others. The COVID-19 infection initiated

---

G. Sasikumar (✉)

Department of Mechanical Engineering, GMR Institute of Technology, Srikakulam, Andhra Pradesh 532127, India

e-mail: [sasikumar.g@gmrit.edu.in](mailto:sasikumar.g@gmrit.edu.in)

S. Ayyappan

Department of Electronics and Communication Engineering, GMR Institute of Technology, Srikakulam, Andhra Pradesh 532127, India

N. Venkatachalam

Department of Mechanical Engineering, Excel Engineering College, Komarapalayam, Tamil Nadu 637303, India

© The Author(s), under exclusive license to Springer Nature Singapore Pte Ltd. 2023

221

P. Pradhan et al. (eds.), *Recent Advances in Mechanical Engineering*,

Lecture Notes in Mechanical Engineering,

[https://doi.org/10.1007/978-981-16-9057-0\\_24](https://doi.org/10.1007/978-981-16-9057-0_24)

with respiratory disease leading to an increase in death rate [5]. The infected people will have minor to medium respiratory disease. People of old age and those who are suffering from heart disease, diabetes, prolonged respiratory disease, cancer etc. are more vulnerable to develop severe illness [6]. A hesitant Fuzzy AHP is used to make pairwise comparison of COVID-19 country-level intervention strategies for various countries to decide relative importance scores [7].

The number of infected persons and casualties are increasing steadily on a daily basis and present condition is viewed as medical emergence all over the globe. The WHO advised the preventive measures against COVID-19 infection such as, frequent hand washing, maintaining social distancing, avoiding gathering, coughing or sneezing etiquette and staying home [14]. The major symptoms of COVID-19 are high fever, dry cough and body pain, prolonged tiredness. If proper treatment is not taken at the initial stage of symptoms, problems leading to death that consists of breathing failure, ARDS, sepsis and septic shock and multi-organ failures [1, 6 and 9]. Due to the second wave of COVID-19, children are also affected with above said serious problems.

Many professional bodies across the world have advised on preventing further spread of COVID-19 and scientists are working continuously with medical professional to curb the casualties of COVID-19. In spite of several strict measures, the numbers of COVID-19 cases continue to increase. While many countries have come up with vaccines and medications for COVID-19, still social awareness and civic intelligence are to be improved for curtailing the spread of COVID-19 through which reduction of the number of infections and fatalities are possible. The measures such as social distancing, continuous usage of face mask, avoiding needless travel, appropriate food, maintaining elementary hygiene, etc. have been suggested for preventing the COVID-19 disease [12]. It is essential to develop a model to identify the critical preventive activities which have high impact on the number of COVID-19 affected people. In this paper, AHP method is developed to find out the critical preventive activities by calculating their weights.

## 2 Model Development Using AHP Method

The AHP is one of the Multiple Criteria Decision Making (MCDM) techniques for evaluating alternatives which was introduced by Saaty [10]. AHP is used to evaluate the competitive priorities of the criteria for improving the effectiveness of green supply chain management implementation of mining industries [8].

In AHP, quantitative and qualitative performances of alternatives are evaluated through a simple hierarchy structure and application of numerical scale [2]. This AHP model involves following six steps:

**Step 1:** Identifying the criteria for COVID-19 preventive activities.

**Step 2:** Constructing a decision structure by dividing problem into different level consisting of criteria and alternatives.

**Table 1** Random index values based on  $n$  value

$n$	1	2	3	4	5	6	7	8	9	10
RI	0	0	0.58	0.9	1.12	1.24	1.3	1.4	1.45	1.49

**Step 3:** Developing pairwise comparison matrix ‘A’ using Eq. 1:

$$\begin{matrix} & C_1 & C_2 & \dots & C_n \\ C_1 & \begin{bmatrix} 1 & a_{12} & \dots & a_{1n} \\ 1/a_{12} & 1 & \dots & a_{2n} \\ \vdots & \vdots & \ddots & \vdots \\ 1/a_{1n} & 1/a_{2n} & \dots & 1 \end{bmatrix} \\ C_2 & & & & \\ \vdots & & & & \\ C_n & & & & \end{matrix} \tag{1}$$

where  $a_{ij} = 1$  and  $a_{ji} = 1/a_{ij}$ ,  $i, j = 1, 2, \dots$ ,

$C_{1,2}, \dots, C_n$  signifies criteria involved in the problem, while  $a_{ij}$  shows decision between criteria  $C_i$  and  $C_j$ .

The comparative position of two features is evaluated by values 1, 3, 5, 7 and 9. 1 means “same importance”, 3 indicates “slight importance”, 5 shows “significantly important”, 7 signifies “strongly important” and 9 means “extremely important” [11].

**Step 4:** Computing the weight of pairwise comparison matrix by additive normalization technique.

**Step 5:** : Checking the consistency of each comparison matrix to ascertain consistency of expert judgment by computing the consistency index and consistency ratio by Eqs. 2, 3:

$$CI = \frac{(\lambda_{\max} - n)}{(n - 1)} \tag{2}$$

$$CR = CI/RI \tag{3}$$

where  $n$  and  $\lambda_{\max}$  denotes the size of matrix and eigen value. The judgment consistency is tested by calculating consistency ratio (CR) by dividing CI with Random index (RI) based on the relevant value in Table 1. The CR is satisfactory, if it is below 0.10 [11].

### 3 Empirical Study

Analytic Hierarchy Process includes determination of criteria weights through AHP method by proper incorporation of judgments from different experts.

### 3.1 Defining the Criteria

This case study involves seven potential COVID-19 preventive measures like social distancing ( $P_1$ ), wearing mask ( $P_2$ ), frequent hand washing ( $P_3$ ), avoiding unnecessary touching ( $P_4$ ), maintain fitness ( $P_5$ ), avoiding outside food ( $P_6$ ) and consuming healthy food items ( $P_7$ ) as selection criteria.

### 3.2 Determining Weights of Criteria by AHP

The AHP method was accomplished by consulting health experts and in order to simplify the calculation procedure, a program is developed using EXCEL to consolidate evaluators' judgments and calculate the criteria weights. The decision matrix for COVID-19 preventive measures based on seven criteria are gathered and shown in Table 2.

The judgment matrix size is  $7 \times 7$ . The weights of the evaluative criteria are calculated by adopting the procedure explained in Sect. 3 and the same is presented in Table 3.

From the Table 3, it can be understood that maintaining social distancing, frequent hand washing and wearing mask were considered to be the most important activities in the prevention of COVID-19. The consistency ratio of above matrix was calculated as 0.05 which specified that the judgment matrix had acceptable consistency.

**Table 2** Decision matrix for COVID-19 preventive measures evaluation

Preventive activities	$P_1$	$P_2$	$P_3$	$P_4$	$P_5$	$P_6$	$P_7$
$P_1$	1	9	7	5	3	3	3
$P_2$	0.111	1	5	3	3	1	1
$P_3$	0.1428	0.2	1	3	7	3	3
$P_4$	0.2	0.333	0.333	1	3	1	7
$P_5$	0.333	0.333	0.1428	0.333	1	3	3
$P_6$	0.333	1	0.333	1	0.333	1	5
$P_7$	0.333	1	0.333	0.1428	0.333	0.2	1

**Table 3** Weights of COVID-19 preventive measures

Criteria	$P_1$	$P_2$	$P_3$	$P_4$	$P_5$	$P_6$	$P_7$
Weight	0.36	0.142	0.16	0.1087	0.089	0.089	0.0465

## 4 Result and Discussion

The AHP method was applied to evaluate the preventive activities and rank the criteria according to the criteria weights. Seven preventive activities of COVID-19 were considered in the case study and hence the judgment matrix size is  $7 \times 7$ . The criteria weights are calculated using the additive normalization method. The weights of the seven criteria are 0.36, 0.142, 0.16, 0.108, 0.089, 0.089 and 0.0465. Out of the seven criteria, maintaining social distancing, frequent hand washing and wearing mask were considered to be the most critical activities. The computational procedure of the proposed model is simplified using EXCEL program. It is observed that the finding of the proposed model coincide with the recommendations of WHO for preventing COVID-19.

## 5 Conclusion

The COVID-19 pandemic has resulted with huge loss of human life across all countries and leads to an unprecedented challenge in the sector of public health, socio-economic status, employment, medical eco system and food systems. The economic and social interruption caused by this is distressing. Though there are lot of measures taken to curb the number of affected people, still it continues as a challenge to arrest the spread of disease. In this paper, the preventive activities of COVID-19 as suggested by WHO and other health bodies are taken in to account to design the AHP methodology. After consulting with experts and doctors, the vital preventive activities such as are considered for developing the AHP model. The priority vectors are calculated by additive normalization technique and the consistency ratio 0.05 was found to be well within the acceptable value. Based on the application of AHP, maintaining social distancing, frequent hand washing and wearing mask were considered to be the most critical activities in the prevention of COVID-19. This model will help the government agencies and general public to focus more on the preventive measures of COVID-19 and based on which strategies shall be formulated to control the COVID-19 spread.

Advantages of the proposed model:

- The AHP method is very accurate and transparent to the users. The hierarchical structure adopted in AHP is easy to construct.
- The number of criteria and alternatives shall be changed according to the problem.
- AHP allows to quantify the qualitative criteria and gives flexibility to validate the subjectivity of factors.
- It is easy to incorporate sensitivity analysis in the AHP framework.

**Acknowledgements** The authors are grateful to their management for allowing them to perform this research and thankful to the esteemed reviewers for their valuable observations to improve the quality of the manuscript.

## References

1. Huang C, Wang Y, Li X (2020) Clinical features of patients infected with 2019 novel coronavirus in Wuhan, China. *Lancet* 395:497–506
2. Lee WB, Lau H, Liu ZZ, Tam S (2001) Fuzzy analytic hierarchy process approach in modular product design. *Exp Syst* 18:32–42
3. Li Q, Guan X, Wu P (2020) Early transmission dynamics in Wuhan, China, of novel coronavirus-infected pneumonia. *N Engl J Med* 382:1199–1207. <https://doi.org/10.1056/NEJMoa2001316>
4. Haleem A, Javaid M, Vaishya R (2020) Areas of academic research with the impact of COVID-19. *Am J Emerg Med* (2020). <https://doi.org/10.1016/j.ajem.2020.04.022>
5. Chen N, Zhou M, Dong X (2020) Epidemiological and clinical characteristics of 99 cases of 2019 novel coronavirus pneumonia in Wuhan, China: a descriptive study. *Lancet*. [https://doi.org/10.1016/S0140-6736\(20\)30211-7](https://doi.org/10.1016/S0140-6736(20)30211-7)
6. Wang D, Hu B, Hu C (2020) Clinical characteristics of 138 hospitalized patients with 2019 novel coronavirus–infected pneumonia in Wuhan, China. *J Am Med Assoc*. <https://doi.org/10.1001/jama.2020.1585>
7. Samanlioglu F, Kaya BE (2020) Evaluation of the COVID-19 pandemic intervention strategies with hesitant F-AHP. *J Healthcare Eng*. <https://doi.org/10.1155/2020/8835258>
8. Shen L, Muduli K, Barve A (2015) Developing a sustainable development framework in the context of Indian mining industries: AHP approach. *Resour Policy* 46(1), 15–26
9. Madhav N, Oppenheim B, Gallivan M, Mulembakani P, Rubin E, Wolfe N (2017) Pandemics: risks, impacts, and mitigation. *Dis Control Priorities Improv Heal Reducing Poverty*. <https://doi.org/10.1596/978-1-4648-0527-1/pt5.ch17>
10. Saaty TL (1980) *The analytic hierarchy process*. McGraw-Hill, New York
11. Saaty TL (2000) *Fundamentals of decision making and priority theory with AHP*. RWS Publications, Pitsburg
12. Sohrabi C, Alsafi Z, Neill N (2020) World health organization declares global emergency: a review of the 2019 novel coronavirus (COVID-19). *Int J Surg* 76:71–760. <https://doi.org/10.1016/j.ijssu.2020.02.034>
13. World Health Organization Coronavirus Disease (2019a) (COVID-19) situation report—72 (2020)
14. World Health Organization Coronavirus Disease (2019b) (COVID-19) situation report—43 (2020)

# Mechanical Characterization of Concrete with Rice Husk-Based Biochar as Sustainable Cementitious Admixture



Sourav Ghosal, P. K. Pani, R. R. Pattanaik, and M. K. Ghosal

**Abstract** Cement being a vital component in the concrete technology produces huge quantity of CO<sub>2</sub> during its production. There is therefore the need of searching a suitable and environment friendly alternative for partial replacement of cement as the cementitious **material**, may be the smaller percentage, without affecting much the strength and durability compared to the conventional concrete. The present work thus focusses on the feasibility of using biochar from agricultural residues, as cementitious admixture in the partial replacement of cement for studying the mechanical properties (compressive, tensile and flexural strengths) of concrete. The biochar from one abundantly available source, i.e. rice husk was considered in this study and prepared through microwave-assisted pyrolysis powered by solar photovoltaic electricity. Experimental investigations were carried out both for concrete and mortar by replacing 1.0, 1.5, 2.0, 2.5 and 3.0% of cement with the biochar. The average values of compressive, tensile and flexural strength were found to be better for 1% replacement of cement with the biochar compared to the other percentage replacements in this study. The percentages increase of compressive, tensile and flexural strength at 1% replacement were calculated to be 1.89, 2.85 and 7.34, respectively, at 28 age days compared to the control samples. Further researches are also needed to improve the quality of biochar by optimizing the pyrolysis process conditions and using other locally available biomass feedstock for enhancing the strengths and durability of concrete compared to the conventional one.

**Keywords** Cement-Based composites · Concrete · Rice husk · Biochar · Microwave pyrolysis

---

S. Ghosal  
Indira Gandhi Institute of Technology (IGIT), Sarang, Dhenkanal, Odisha, India

P. K. Pani  
IGIT, Sarang, Dhenkanal, Odisha, India

R. R. Pattanaik · M. K. Ghosal (✉)  
Odisha University of Agriculture and Technology, Bhubaneswar, Odisha, India  
e-mail: [mkgghosal1@rediffmail.com](mailto:mkgghosal1@rediffmail.com)



## 1 Introduction

Cement is a key component in the construction industry. The production of cement is increasing at a faster rate due to the growing demands of infrastructure development for the rising human population in the world. However, production of cement contributes the third largest source of man-made carbon dioxide emission next to deforestation as well as other land use changes and burning of fossil fuels [1]. Scientific data reveal that about 0.5 tonne of CO<sub>2</sub> is emitted from the production of 1 tonne of cement [2]. At present, cement industry contributes about 7% of the total global emission of CO<sub>2</sub> [3]. Hence, to mitigate the emission of CO<sub>2</sub> from the cement factories, more and more researches are being focussed to explore the suitable cementitious materials to supplement cement in a cost effective and environmentally sustainable manner. In recent years, one such material, i.e. biochar from the pyrolysis process of biomass is gaining importance amongst the researchers as a supplementary material in cement composites [4]. Earlier efforts on the applications of industrial wastes such as fly ash, silica fume, ground granulated blast-furnace slag and lime stone powder as the supplementary cementitious materials have established the fact that their uses are not a sustainable solution for the partial replacement of cement in concrete/mortar mix because of inadequate availability, higher cost involvement in transportation to the points of applications and requiring further processing before use [5]. Biochar, therefore, offers a sustainable source due to its production from naturally, cheaply and adequately available sources like crop residues, agro-processing residues, municipality solid wastes, food wastes, forest-based biomass residues, etc. This would ultimately solve the disposal problem and prevent the current rising issue of on-farm crop residues burning to reduce the emissions of hazardous particulate matter to the environment. Rice, being the principal food grain crop in India, produces a considerable quantity of straw, husk and bran which can therefore be considered as the sustainable sources of bioenergy for producing biofuels.

Biochar is a carbon rich solid product obtained from the thermochemical conversion of biomass in the absence of air at the temperatures ranging from 400–550 °C [6]. The yield and quality of biochar depend on the operating conditions, i.e. temperature, heating rate, reaction time and use of catalyst in the pyrolysis process. One such novel technology to control the pyrolysis process to get the desired yield and quality of pyrolytic products (biochar, bio-oil and syngas) is the microwave-assisted pyrolysis [7]. Biochar has been proved to be a potential material for soil amendment for agricultural lands [8] and in other applications such as for horticultural crops [9], waste water treatment [10] and carbon sequestration [11]. However, to date, very limited works have been undertaken to investigate the use of biochar as an additive in concrete/mortar making. Therefore, the objectives of this work are to study the effects of rice husk-based biochar as a cementitious material in concrete/mortar for assessing mechanical properties and to determine its optimal use in conventional concrete applications.

## 2 Materials and Method

The work was undertaken during 2020–21 in the Department of Agricultural Structures, Civil and Environmental Engineering, Odisha University of Agriculture and Technology, Bhubaneswar, Odisha. The feedstock (rice husk) for the production of biochar was collected locally, sun-dried, cut into small pieces and sieved to get the particle size of about 10 mm. The processed feedstock was kept in hot air oven for 24 h at the temperature of  $105 \pm 2$  °C to determine the moisture content. The ranges of moisture content of the feedstock for use in microwave reactor were 8–12%. The prepared rice husk was pyrolyzed in microwave reactor, powered by solar photovoltaic electricity. The operating conditions of pyrolysis (3 levels of input power, i.e. 500, 700 and 900 W; 3 levels of reaction time, i.e. 10, 15 and 20 min and 3 levels percentages of additive, i.e. 0, 5, 10 and 15% to the weight of feedstock) were investigated with activated carbon as additive to optimize the higher yield and quality of biochar. Each condition of experiment was conducted 3 times, and the optimized conditions were found to be 500 W input power, 20 min reaction time and 10% of additive for better yield of biochar. The optimized yield of biochar was measured to be about 37%. The experimental investigations were carried out both for cement mortar and concrete by using ordinary portland cement (OPC). Mixture was prepared with tap water, biochar and cement. Six different percentages (0, 1.0, 1.5, 2.0, 2.5 and 3.0%.) of biochar with respect to the weight of cement were used with a water to cement (w/c) ratio equal to 0.35. A proper mixing procedure was followed to prepare concrete and mortar samples. The mechanical properties such as compressive strength, split tensile strength and flexural strength of the concrete and mortar samples mixed with biochar were measured at 7 and 28 days of curing and compared with the control specimens to assess the effects of rice husk-based biochar in concrete making. The photographs showing raw rice husk and rice husk char are shown in Fig. 1. The composition of materials used in preparing concrete and mortar is as follows.



**Fig. 1** Photographs of raw rice husk and rice husk biochar

For concrete → Cement: sand: coarse aggregates = 1: 1.5:3 by volume and water to cement ratio = 0.35

For mortar → Cement: sand = 1: 3 by volume and water to cement ratio = 0.35

The photographs of rice husk and its biochar used in this study are shown below.

### 3 Results and Discussion

A total of 72 concrete cubes (100 mm) were produced for all mixes: CS-0 (no addition of biochar and control specimen), RHB-1 (1% addition of biochar), RHB-1.5 (1.5% addition of biochar), RHB-2 (2.0% addition of biochar), RHB-2.5 (2.5% addition of biochar) and RHB-3 (3.0% addition of biochar), following ASTM C109. The strength of concrete cubes was determined for three replicates for each mix at 7 and 28 age days, and the average value was reported for analysis. The results of compressive strength of concrete are presented in Table 1. In all cases, the compressive strengths were found to be higher at 28 age days compared to 7 age day. Also, it was found that with the increase in the percentage of biochar in the concrete mix, the strength, exhibited the decreasing trends. The strength was found to be better at 1% replacement of cement with biochar. The decreasing strength due to higher percentage replacement of cement with biochar can be attributed to the porous nature of biochar and its high-water absorption capacity which becomes detrimental to the strength properties. Similar trends were also observed in case of tensile strength. However, the tensile strength was found to be highest at 1.5% replacement of cement with biochar. The flexural strengths were found to be increased with the increase in the content of biochar in the concrete mixture. This can be explained with the pore filling effect of biochar which makes links with the components of concrete and increases the flexibility of the composites. The compressive strengths of mortar are presented in Table 2. For the mortar, 18 nos. of concrete cubes (100 mm) were produced and the compressive strengths were found to be in the decreasing trend with the increase in the biochar content in the cementitious matrix. At 1% replacement of cement with biochar, the compressive strength was found to be better; however, for 1.5%, there was only slight increase and after that the compressive strengths exhibited the decreasing trends.

### 4 Conclusions

Replacement of concrete with a suitable and green material is the need of hour due to higher environmental impacts in the production of cement in the construction sector. The present research work is based on the feasibility of using biochar especially from the agricultural residues for its application in cementitious composites with different percentages of addition with respect to the weight of the cement, in order to improve the mechanical properties and reduce the carbon footprint of cementitious materials.

**Table 1** Test results for concrete

Specimen control specimen (CS) Rice husk biochar (RHB)	Average compressive strength (Mpa)		% increase (+) and decrease (-) compared to CS		Average tensile strength (MPa)		% increase (+) and decrease (-) compared to CS		Average flexural strength (MPa)		% increase (+) and decrease (-) compared to CS	
	7 days	28 days	7 days	28 days	7 days	28 days	7 days	28 days	7 days	28 days	7 days	28 days
CS-0	27.54	43.85	0.00	0.00	3.54	4.55	0.00	0.00	4.69	6.4	0.00	0.00
RHB-1	<b>32.38</b>	<b>44.68</b>	<b>+17.57</b>	<b>+1.89</b>	3.57	4.68	+0.8	+2.85	4.45	6.87	-5.11	+7.34
RHB-1.5	26.91	42.85	-2.34	-2.28	<b>3.59</b>	<b>5.08</b>	<b>+1.4</b>	<b>+11.64</b>	4.67	6.23	-0.43	-2.65
RHB-2	22.59	42.4	-17.97	-0.3	3.45	4.89	-2.54	+7.47	<b>5.62</b>	<b>7.12</b>	<b>+19.8</b>	<b>+11.25</b>
RHB-2.5	25.94	38.85	-5.80	-11.3	3.12	4.08	-11.9	+10.32	4.08	5.88	-13.0	-8.12
RHB-3	25.56	31.59	-7.18	-27.95	2.88	3.25	-18.6	-28.57	3.38	4.85	-27.9	-24.21

**Table 2** Test results for mortar

Specimen control specimen (CS) rice husk biochar (RHB)	Average compressive strength (MPa)		% increase (+) or decrease (-)	
	7 days	28 days	7 days	28 days
CS-0	23.13	41.37	0.00	0.00
RHB-1	31.19	42.35	+34.85	2.36
RHB-1.5	16.54	42.9	-28.49	+3.70
RHB-2	16.52	33.57	-28.58	-18.85
RHB-2.5	14.45	24.27	-37.53	-41.33
RHB-3	12.58	21.44	-45.61	-48.18

The biochar used in this study was produced from the microwave-assisted pyrolysis of rice husk which is available plentifully in an agricultural based country like India. Based on the experimental findings of the study, the following conclusions have been drawn.

- i. Biochar from the agricultural residues can be considered a potential candidate for replacement of cement as a green admixture
- ii. Microwave-assisted pyrolysis is a novel technology and an efficient practice for controlling pyrolysis conditions for better yield and quality of pyrolytic products.
- iii. The optimized operating conditions for higher yield biochar from the rice husk are 500 W input power, 20 min' reaction time and 10% activated carbon additive with the feedstock
- iv. Mechanical strengths such as average compressive, tensile and flexural strength of concrete with 1% addition of biochar with respect to weight of cement were found to be 2.0, 2.85 and 7.5% higher at 28-day age compared to control concrete specimen.
- v. Average compressive strength of mortar with 1% addition of biochar with respect to weight of cement was found to be 2.4% higher at 28-day age compared to control concrete specimen.

## References

1. Andrew RM (2018) Global CO<sub>2</sub> emissions from cement production. *Earth Syst Sci Data* 10:195–217
2. Klee H (2009) The cement sustainability initiative. *Eng Stab* <https://doi.org/10.1680/ensu.2004.157.1.9>
3. Akhtar A, Sarmah, AK (2018) Novel biochar-concrete composites: manufacturing, characterization and evaluation of the mechanical properties
4. Rayane M, Chehab G (2019) Mechanical and microstructure properties of biochar-based mortar. An internal curing agent for PCC. *Sustainability* 11:2491. <https://doi.org/10.3390/su11092491>

5. Anjaneya D, Gupta S, Dai Pang, Kua H (2019) Waste Valorisation using biochar for cement replacement and internal curing in ultra-high Wei. Performance concrete. *J Cleaner Prod* 238:117876
6. Khalid A, Khushnood RA, Mahmood A, Ferro GA, Ahmad S (2018) Synthesis, characterization and applications of nano/micro carbonaceous inerts: a review. *Procedia Struct Integrity* 9:116–125
7. Fodah AEM, Ghosal MK, Behera D (2021) Microwave assisted pyrolysis of agricultural residues: current scenario, challenges and future direction. *Int J Environ Sci Technol*. <https://doi.org/10.1007/s13762-020-03099-9>
8. Zhu X, Chen B, Zhu L, Xing B (2017) Effects and mechanisms of biochar-microbe interactions in soil improvement and pollution remediation: a review. *Environ Pollut* 227:98–115. <https://doi.org/10.1016/j.envpol.2017.04.032>
9. Vaughn SF, Kenar JA, Tisserat B, Jackson MA, Joshee N, Vaidya BN, Peterson SC (2017) Chemical and physical properties of Paulownia elongata biochar modified with oxidants for horticultural applications. *Ind Crop Prod* 97(260–267):2017. <https://doi.org/10.1016/j.indcrop.2016.12.017>
10. Lee S, Gupta P, Ann T, Lee S (2016) Use of biochar to enhance constructed wetland performance in wastewater reclamation. <https://doi.org/10.4491/eer.2015.067>
11. Woolf D, Amonette JE, Street-Perrott FA, Lehmann J, Joseph S (2010) Sustainable biochar to mitigate global climate change. *Nat Commun* 1:56. <https://doi.org/10.1038/ncomms1053>

# Ranking of Barriers for SSCM Implementation in Indian Textile Industries



Ashish Patel and T. N. Desai

**Abstract** In present situation of globalization, sustainable supply chain management (SSCM) of manufacturing system is very imperative. Numerous of the organizations are in front of a lot of problems in supply chain management. Thus, rationale of manuscript is toward classifying the most barriers in SSCM and to rank them in favor of effective SSCM strategy. To categorize the main barriers in SSCM, fuzzy analytical hierarchy process (FAHP) is used. Used for giving keep score to completely different issue, a team of three consultants was completed. All consultants have quite 10 years of information in space of supply chain management. Requirement of top management support, lack of SSCM project coaching, and learning and lack of tactical designing and implementation have emerged as prime three barriers in implementation of systems in textile industries. Findings imply that for successful SSCM, top management ought to be terribly ancillary for taking completely different initiatives, coaching programs, etc. Organizations ought to try and improve overall performance of textile business productivity. These findings are extremely helpful for professionals from textile producing sector in implementing effective SSCM system.

**Keywords** Sustainable supply chain management · Fuzzy SET · FAHP · MCDM

## 1 Introduction

It is very important for any organization to spot barriers before the execution of any quality upgrading method. Throughout the literature search allotted over the property provides sustainable supply chain management (SSCM) barriers; it is ascertained that many authors contribute valuable works to speck the position of the

---

A. Patel (✉)

Department of Mechanical Engineering, Laxmi Institute of Technology, Sarigam, Gujarat, India  
e-mail: [ashish.lit@laxmi.edu.in](mailto:ashish.lit@laxmi.edu.in)

T. N. Desai

Department of Mechanical Engineering, Sardar Vallabhbhai National Institute of Technology, Surat, India

SSCM barriers. Table 1 presents the SSCM barriers accordingly by varied authors in literature.

Several researchers in literature have argued that though corporations have with success deployed several logistics-related improvement initiatives like supply chain management, inexperienced supply chain management, and SSCM, still a major range of corporations have didn't gain any advantages from their preparation, and different corporations didn't succeed the expected results [34, 71]. Lee et al. [42], argued that each supply chain improvement initiative comes tend to fail to achieve the expected results because of lack of attention toward barriers and failure factors. Micmac [48], according that up to forty % of the businesses implementing, SSCM has been failing. One among the study conducted in UK organizations showed that fewer than twenty % of the organizations had enforced SSCM with success [31]. Several authors like Lin and Tseng [46] and Zhu et al. [71] have conducted a survey of corporations, and according to their results that respondents' satisfaction with SSCM, results were below 50%. Management's angle concerning the configuration of policies and designing for method execution is essential [2, 9].

The main objectives of the study are as follows:

- To explore a comprehensive list of barriers for SSCM success.
- To test the validity of these barriers.
- To evaluate the priority weight of barriers with respect to objective using FAHP.

## 2 Literature Review

Carter and Jennings [13] examined the processes related to purchasing, transportation, packaging, warehousing, and reverse logistics in their research on logistics social responsibility (LSR), and defined six topics to classify LSR environment, ethics, diversity, working conditions and human rights, safety, philanthropy, and community involvement. Other studies in the context of sustainable supply chain techniques, such as environmental purchasing, have since connected traditional purchasing with the environmental management component [70]. According to Lee and Wu [43], every supply chain improvement initiative project in general fails to achieve the desired results because barriers and failure factors are not addressed. Furthermore, Pepper and Spedding [54] reported that up to 40% of companies attempting to implement SSCM failed. In 2005, research conducted in UK organizations attempting to implement SSCM initiatives revealed that only about 20% of them succeeded [31]. Several authors, including Cheng et al. [16], Metta and Badurdeen [47], and Zhu et al. 71, conducted surveys.

Hence, it becomes necessary for industry practitioners to deeply investigate the root causes and identify the hurdles that hinder the successful implementation of SSCM. Very few articles in the literature discussed the set of hurdles that acts as the obstacle while SSCM implementation. Table 1 represents the set of hurdles



**Table 1** Barriers of SSCM report in the literature

S.No	Barriers of SSCM	Literature support
1	Lack of top organization attitude, assurance, and involvement	Turker and Altuntas [63], Zhu et al. [71], Kumar and Rahman [40]
2	Requirement of preparation and learning	Wu and Pagell [68], Lee et al. [42]
3	The increased cost of adoption	Parlak et al. [51], Wong et al. [67], Chung et al. [17]
4	Need of resources (economic, technological, human, etc.)	Gupta et al. [30], Arumugam et al. [5]
5	Weak linkage sandwiched between the CI project and the tactical objectives of the association	Li et al. [44], Walker and Jones [64], Ageron et al. [2]
6	The resistance of culture change	Zhuang et al. [72], Cochran and Roche [20]
7	Poor communication	Jeyaraman and Teo [36], Hilton and Sohal [32]
8	Leadership skills are lacking, as is visionary and compassionate leadership	Sengupta et al. [58], Wong et al. [67], Bai et al. [8]
9	Requirement of concern of the human factor	Bastian and Zentes [9], Pishvaei et al. [56]
10	Awareness of low financial come back	Ganguly and Guin [24], Ashby et al. [6]
11	Outdated auditing standards	Amindoust et al. [4], Zaabi et al. [69]
12	Lack of technology sharing	Nakano [50], Ageron et al. [2], Croom et al. [21]
13	Lack of consideration for various types of clients/VOC	Beske et al. [11], Wolf and Seuring [66]
14	A lack of staff engagement and contribution/a lack of team autonomy	Beske et al. [11], Arumugam et al. [5]
15	Lack of procedure philosophy and process possession	Ashby et al. [6], Wong et al. [67]
16	Unfortunate organization capability	Chung et al. [17], Parlak et al. [51]
17	High implementation cost	Jayaraman et al. [35], Pillai et al. [55]
18	Ineffective project management	Karthi et al. [37], Jayaraman et al. [35]
19	A lack of clear vision and a future roadmap	Gibbons et al. [26], Chakravorty and Shah [14]
20	There isn't a good form or roadmap in place to direct the execution	Thomas et al. [62], Gibbons et al. [26], Wolf and Seuring [66]

(continued)

**Table 1** (continued)

S.No	Barriers of SSCM	Literature support
21	Poor execution	Waterbury and Bonilla [65], Beske et al. [11]
22	Time-consuming	Snee [61], Huang et al. [33], Erol et al. [23]
23	Lack of a cost-of-operations analysis	Gremyr and Fouquet [28], Jayaraman et al. [35], Pishvaei et al. [56]
24	Scrawny infrastructure	Amindoust et al. [4], Erol et al. [23], Jayaraman et al. [35]
25	Replicating the SSCM approach of another company	Blowfield 2005, Ageron et al. [2]
26	Lack of a performance measurement system	Wu and Pagell [68], Klassen and Vachon 2003, Lee 2008, Bitzer et al. 2008
27	Algebraic theory has no meaning	Montgomery (2010)
28	Weak between to supplier	Found (2012), Habidin and Mohd Yusof (2013)

reported in literature. Every practitioner must keenly observe these hurdles while implementing SSCM.

The advancement of SSCM appropriation relies completely upon direction and instruction gave to production network the board to the execution of comes. Any unwinding on the higher than concern brings about position with reasonable undertaking fruition [60]. With the exception of training, correspondence inside the office is critical; thus, helpless specialized information correspondence inside divisions brings about deficiency of the board over the venture [27, 63].

Poor choice of property practices could be an important barrier for effective SSCM implementation [3]. Upheld the laborer viewpoint, “absence of dependable cooperation” ad “absence of specialist commitment and group self-sufficiency” influence is the chief significant boundaries for SSCM execution. Many authors (Hervani et al. [31]; Curwen [22]; Kudla and Klaas-Wissing [38]) referenced absence of an exhibition action framework, wasteful quality information, and investigation, culture adjustment, non-esteem added time utilization and absence of a decent model or guide to control the usage as some of the compulsory regions needed to be inspected before SSCM execution. While simple distinguishing proof of the obstruction isn’t sufficient, as focusing on and positioning of hindrances upheld their impact inside the usage strategy is amazingly vital. To keep up the precision of results, the fuzzy unadulterated math has consolidated to AHP. The framework of fuzzy AHP is referenced inside the following segment.

### 3 Fuzzy Analytical Hierarchy Process (FAHP)

The FAHP procedure might be a multi-trait dynamic strategy that is related with the added substance weight technique, any place various applicable boundaries territory unit offered regarding their relative significance. FAHP has AN ample vary of applications within the domain of engineering, as well as the selections associated with money, implementation and choice, etc. among numerous obtainable attributes [49]. In line with Chung et al. [18], “By applying FAHP, the importance of variety of attributes may be obtained by paired comparison method through specialists that represents the priority of every attribute over alternative attributes.” Despite grouped preferences delivered by this framework, it furthermore displays bound weaknesses. Rule and Chen and Paulraj [15], realized that most of the uses of FAHP method square measure emerged to intently fresh data calls; the FAHP strategy creates and directs with an outrageously flimsy method of dynamic; human judgment may lead the positioning to be non-exact. As a result, the chiefs’ decisions would have a significant impact on the yield obtained using the AHP process. To beat these weaknesses and to support the irregularity related with the AHP procedure, various specialists consolidated the fuzzy unadulterated math with AHP. Numerous creators led contextual investigations to demonstrate the advantages acquired by mix fuzzy AHP.

The application of fuzzy AHP in human resource management was described by Abdullah and Zulkifli [1] and Sachin K. Patil and Kant [52]. Patil and philosopher [53] used a hybrid method of fuzzy AHP-TOPSIS to rate data management acceptance strategies within the offer chain in order to address barriers. Bhosale and Kant [12] used an integrated fuzzy AHP-VIKOR model to find the simplest active information flow organization. The applications of FAHP described by various authors are listed in Table 2.

**Table 2** Applications of FAHP

Author	Area of application
Guo et al. [29]	Green supplier evaluation
Giannakis and Papadopoulos [25]	Assessment of sustainability adoption
Abdullah and Zulkifli [1]	Human source organization
Beikhhakhian et al. [10]	Set of flexible suppliers
Kumar et al. [39]	Analyzing client liking and effectiveness
Avikal et al. [7]	Line assessment
Shukla et al. [59]	Modeling supply chain management
Bhosale and Kant [12]	Choice of best information stream practicing institute
Sachin et al. [52]	Standing the barriers of information organization
Sachin et al. [52]	Ranking solution for knowledge supervision implementation to success over barriers
Lin [45]	Design plan opinion
Samvedi et al. [57]	Supply chain risk quantification

## 4 Methodology Adopted for the Study

For exact prioritization of SSCM hindrances, the entire construction is part into two stages, any place the essential segment incorporates leading a writing survey of SSCM obstructions, and along these lines, the subsequent segment incorporates utilization of fuzzy AHP for positioning the known SSCM boundaries. Inside the underlying area, the serious writing survey of SSCM hindrances is led through articles from the sole companion-assessed diaries of implied distributors like Science Direct, Taylor and Francis, Emerald full content, Inderscience, and Springerlink. The obstructions of SSCM known through writing square measure any referenced with mechanical experts for their talented assessment. For the higher than reason, a lot of about six exchange advisors and two experts from world counseled to make the most standards, produce the information structure, and make the pairwise correlation of the grouped boundaries. They got yields that can go about as associate in nursing contribution for succeeding part of fuzzy AHP application to rank the boundaries of SSCM. Figure one depicts the strategy received inside the current investigation.

## 5 SSCM Barriers Prioritization Through Fuzzy AHP Method

As discussed in the previous section, the SSCM barriers are placed using the fuzzy AHP methodology. Prioritization is accomplished through the steps mentioned below.

- (1) Build a decision-making committee.

A preference cluster panel of eight experts is organized to determine the SSCM barriers. Six experts from the Indian textile industry and two academicians from academic institutions have been assigned to assess the SSCM barriers.

- (2) Create a hierarchical structure by listing key and sub-criteria.

In the current investigation, 27 potential SSCM boundaries square measure known from a far reaching writing survey led across peer checked on diaries. Afterward, they are finished by examining with an educated board formed inside the past advance. These concluded obstructions square measure at that point ordered under a lot of rules to build up a chain of importance for the execution of the entire strategy. The most even handed of the set up progression is to go the picked SSCM obstructions that exist at the essential level.

- (3) Determine the triangular fuzzy number scale embraced for shaping the pairwise examination framework. In the current examination, the TFN scale  $\tilde{1}, \tilde{9}$  is utilized to upgrade the arrangement's precision for the chose issue. Tables 3, 4, 5, 6, 7, 8 and 9 shows the size of relative significance used in the pairwise examination grid.
- (4) Create a pairwise comparison matrix that is fuzzy (FCM)

**Table 3** Pairwise comparison of main criteria

Attributes	Strategy-oriented barriers	Technology-oriented barriers	Social-cultural barriers	System-oriented barriers	Independent barriers
Strategy-oriented barriers	1	3	7	3	9
Technology-oriented barriers	1/3	1	7	3	7
Social-cultural barriers	1/7	1/7	1	1/5	3
System-oriented barriers	1/3	1/3	5	1	5
Individual barriers	1/9	1/7	1/3	1/5	1

**Table 4** Pairwise comparison of strategic-oriented barriers (SOBs)

Attributes	SOB1	SOB 2	SOB 3	SOB 4	SOB 5	SOB 6	SOB 7
SOB 1	1	5	3	7	1/3	9	3
SOB 2	1/5	1	1/3	3	1/7	5	1/3
SOB 3	1/3	3	1	5	1/3	9	3
SOB 4	1/7	1/3	1/5	1	1/9	3	1/5
SOB 5	3	7	3	9	1	9	5
SOB 6	1/9	1/5	1/9	1/3	1/9	1	1/7
SOB 7	1/3	3	1/3	5	1/5	7	1

**Table 5** Pairwise comparison of technology-oriented barriers (TOBs)

Attributes	TOB1	TOB2	TOB3	TOB4	TOB5
TOB1	1	1/9	1/3	1/3	1/7
TOB2	9	1	7	7	3
TOB3	3	1/7	1	1/3	1/5
TOB4	3	1/7	3	1	1/3
TOB5	7	1/3	5	3	1

**Table 6** Pairwise comparison of social-cultural barriers (SCBs)

Attributes	SCB1	SCB2	SCB3	SCB4
SCB1	1	3	1/5	1/5
SCB2	1/3	1	1/9	1/9
SCB3	5	9	1	1/5
SCB4	5	9	5	1

**Table 7** Pairwise comparison of system-oriented barriers (SOBC)

Attributes	SOBC1	SOBC2	SOBC3	SOBC4	SOB5	SOBC6
SOBC1	1	7	5	3	3	1/3
SOBC2	1/7	1	1/3	1/5	1/7	1/9
SOBC3	1/5	3	1	1/3	1/5	1/7
SOBC4	1/3	5	3	1	1/3	1/5
SOBC5	1/3	7	5	3	1	1/3
SOBC6	3	9	7	5	3	1

By the guide of etymological factors included, the choice gathering board is approached to fabricate the pairwise correlation lattice for the primary standards just as sub-rules, as referenced in the progressive system.

**Table 8** Pairwise comparison of individual barriers (IBs)

Attributes	IB1	IB2	IB3	IB4	IB5
IB1	1	3	1/5	1/7	1/3
IB2	1/3	1	1/7	1/7	1/5
IB3	5	7	1	1/3	3
IB4	7	7	3	1	5
IB5	3	5	1/3	1/5	1

**Table 9** Final prioritization of SSCM barriers

Main criteria	Main criteria Wt	Sub-criteria	CR value	Local Wt	Global Wt	Rank
Strategy-oriented barriers	0.449	SOB1	0.088	0.236	0.106	3
		SOB2		0.063	0.028	12
		SOB3		0.159	0.071	5
		SOB4		0.034	0.015	16
		SOB5		0.375	0.169	1
		SOB6		0.020	0.009	20
		SOB7		0.109	0.049	7
Technology-oriented barriers	0.285	TOB1	0.083	0.038	0.011	18
		TOB2		0.522	0.149	2
		TOB3		0.069	0.019	13
		TOB4		0.111	0.031	10
		TOB5		0.257	0.073	4
Social-cultural barriers	0.060	SCB1	0.049	0.110	0.006	22
		SCB2		0.047	0.002	25
		SCB3		0.250	0.015	17
		SCB4		0.591	0.035	9
System-oriented barriers	0.169	SOBC1	0.085	0.240	0.040	8
		SOBC2		0.027	0.004	24
		SOBC3		0.050	0.008	21
		SOBC4		0.098	0.016	15
		SOBC5		0.177	0.030	11
		SOBC6		0.405	0.068	6
Independent barriers	0.034	IB1	0.089	0.070	0.002	26
		IB2		0.039	0.001	27
		IB3		0.266	0.009	19
		IB4		0.484	0.016	14
		IB5		0.139	0.004	23

(5) The transition of FCM into crisp comparison matrix (CCM)

Condition (5) is used by  $\alpha$ -cut to allow for the lower and upper restriction of fuzzy numbers. The condition (5) is then added to each part of the illustrated lattice. The motivation for  $\alpha = 0.5$  is used here for the sake of health and to obtain precise results. As a result, the FCM is changed into addressing the crisp comparison matrix (CCM), by assigning the estimate of in the specified condition.

$$\tilde{X}^\alpha = \begin{bmatrix} 1 & 2, 4 & 6, 8 & 2, 4 & 8, 10 \\ 0.25, 0.50 & 1 & 6, 8 & 2, 4 & 6, 8 \\ 0.13, 0.17 & 0.13, 0.17 & 1 & 0.17, 0.25 & 2, 4 \\ 0.25, 0.50 & 0.25, 0.50 & 4, 6 & 1 & 4, 6 \\ 0.10, 0.13 & 0.13, 0.17 & 0.25, 0.50 & 0.17, 0.25 & 1 \end{bmatrix} \quad (1)$$

For the computation reason, the estimation of  $\mu$  (level of confidence) is taken as 0.5, which infers that the appraisals settled on by choice gathering board are adjusted in the event that hopefulness. Subsequently, by supplanting the estimation of  $\mu$  in condition (2) of the  $\alpha$ -slice, correlation grid is changed over to CCM X.

$$X = \begin{bmatrix} 1 & 3 & 7 & 3 & 9 \\ 0.375 & 1 & 7 & 3 & 7 \\ 0.145 & 0.145 & 1 & 0.208 & 3 \\ 0.375 & 0.375 & 5 & 1 & 5 \\ 0.115 & 0.145 & 0.375 & 0.208 & 1 \end{bmatrix} \quad (2)$$

(6) Carry out the check for consistency

The following big parameters have eigenvalues estimated for them:

$$\begin{aligned} \lambda_1 &= 5.439, 2 = 0.036 + 1.235i, 3 = 0.036 - 1.235i, \\ 4 &= -0.254 + 0.404i, 5 = -0.254 - 0.404i; \\ 1 &= 5.439; 2 = 0.036 + 1.235i; 3 = 0.036 - 1.235i; \\ 4 &= -0.254 + 0.404i; 5 = -0.254 - 0.404i; 5 = -0.254 - 0.404i; \end{aligned}$$

Hence consistency index (CI):

$$CI = \frac{\lambda_{\max} - n}{n - 1} = \frac{5.437 - 5}{5 - 1} = 0.10925$$

From standardize RI = 1.11 corresponding to  $n = 5$ ,

$$CR = \frac{CI}{RI} = \frac{0.10925}{1.11} = 0.09842$$



Since the CR estimate is less than 0.1, the CCM for the calculated significant measures is now agreeable and significant. If the CCM for X is stable, the FCM is as well. All of the determined frameworks have a CR value of less than 0.1. As a result, all is appropriate. Table 9 shows the individual CR estimations for all of the frameworks.

(7) Determine the weight criteria of the selected matrix

After obtaining the CR values for all of the grids, the next step is to determine the weight models for each factor. The following are a number of the most important rules:

- a. The column sum is calculated for all elements of each column.

$$[ 2.01 \ 4.665 \ 20.375 \ 7.416 \ 25 ]$$

- b. Now, the column sum of each column is used to divide their respective element of CCM.

$$X = \begin{bmatrix} 0.4975 & 0.6430 & 0.3435 & 0.4045 & 0.36 \\ 0.1865 & 0.2143 & 0.3435 & 0.4045 & 0.28 \\ 0.0721 & 0.0310 & 0.0490 & 0.0280 & 0.12 \\ 0.1865 & 0.0803 & 0.2453 & 0.1348 & 0.2 \\ 0.0572 & 0.0310 & 0.0184 & 0.0280 & 0.04 \end{bmatrix} \tag{4}$$

- c. Finally, compute the row total for each row of the matrix and divide each row total by the array order (i.e., the criteria contained inside the chosen matrix); the weight of the standards is reflected.

$$X = \begin{bmatrix} 0.4497 \\ 0.2858 \\ 0.0600 \\ 0.1694 \\ 0.0349 \end{bmatrix} \tag{5}$$

(8) Prioritize each criterion according to final weight obtained

Finally, a definitive loads for each model square measure acquired by duplicating the premier standards weight with sub-rules weight to get a definitive load of the relating rules. A definitive loads of the multitude of guidelines square measure got, and each one the rules' square measure focused on that square measure is appeared in Table 9

## 6 Result and Discussions

In the current examination, the total writing look and educated assessment from the decision bunch board settled 27 SSCM boundaries for the Indian material ventures. The picked obstructions are arranged under five essential illustrated models, explicitly essential bound boundaries, innovation situated hindrances, social-social boundaries, and framework bound hindrances and independent obstructions. Consequently, to put the picked SSCM hindrances, the fuzzy AHP method is utilized. The consequences of the applied technique are appeared in Table 11. Among all the most measures, procedure-bound boundaries set out to be generally crucial with the weight of 0.449. It conjectures that around 45% of hindrances for SSCM usage is because of the essential obstructions. Consequently, the Indian material ventures should take past consideration regarding conquer of these hindrances. The excellent utilization of innovation and correspondence leads toward the agile execution of SSCM, as innovation situated hindrances conjointly aggregate to be a great deal of prominent regarding weight 0.285, trailed by framework bound obstructions with a load of 0.169. Beating the design boundaries could be an all-encompassing method; accordingly, imperative advances should be started inside the deciding to achieve the normal outcomes.

Among the technique-based boundaries, “Absence of high administration point, responsibility and contribution” (SOB 5) holds the absolute best weight among all the sub-models obstructions, as demonstrated in Table 9 High administration point is principally amiable to choose the essential arrangements, planning the vision. Responsibility and inclusion construct a sound working setting and improve the laborer execution to achieve the design objectives. Thus, it is fundamental that high administration comprehends the significance of SSCM and executes it adequately to fortify construction profitability. Relate SSCM project solidly; it is basic to supply instructing to the workers, as crude hands bring about the disappointment of SSCM execution. Poor key planning (SOB 1) underneath system essentially based boundaries is that the third sub-hindrances. Unclear objectives and dispersed vision ne’er show the guide toward profitability improvement. Consequently, it is imperative to possess clear goals for higher vital planning.

## 7 Conclusion

Extensive literature searches and expert advice from the decision group panel were used in this study to resolve 27 SSCM hurdles for the Indian textile industries. Strategically oriented barriers, technology-focused barriers, social-cultural barriers, system-oriented barriers, and independent barriers are the five key defined criteria for the selected barriers. As a result, the fuzzy AHP approach is employed to prioritize the selected SSCM barriers. With a weight of 0.449, strategy-oriented barriers emerge as the most significant of all the main criteria. It is estimated that strategic hurdles

account for about 45 percent of the challenges to SSCM adoption. As a result, the Indian textile industry must prioritize overcoming these obstacles. As technology-oriented barriers accumulate to be more notable in terms of weight 0.285, followed by system-oriented barriers with a weight of 0.169, the primary usage of technology and communication leads to the easy implementation of SSCM. Because overcoming organizational barriers is a lengthy process, major actions need be taken early on to obtain the desired outcomes.

“Lack of technology sharing” is the fourth essential SSCM barrier established from the investigation and falls under the technology standpoint (TOB 4). The availability of technology-based resources is critical to the successful execution of the SSCM. These tools aid in the tracking of diverse activities, the monitoring of fluctuations, and the analysis of data. Under the independent barrier, “Lack of resources” (SOB 3) is rated fifth, followed by “Misalignment between organizational goals, (IB 4) project target, and customer demand” (IB3) at sixth. Synchronizing an organization’s major aim, sub-goal, and customer needs is critical, as any misalignment has a direct impact on the success of the Indian textile sector. The seventh item on the list is “lack of clear vision and plan” (SOB7), indicating the necessity of a corporate vision that is tied to future operations. Following that the rest of the SSCM obstacles are ranked using the final weights.

The attitude of top management is significantly amenable in determining strategic policies and mapping the vision. Commitment and involvement foster a positive work environment and boost employee performance in order to achieve corporate objectives. “Lack of training and education toward sustainability adoption” (TOB 2) is the second-highest weight 0.149 among all other criterion. It is critical to provide training to staff in order to effectively identify with the SSCM project, as untrained hands contribute to SSCM implementation failure. The third sub-barrier under strategy-based barriers is poor strategic planning (SOB 1), which has a weight of 0.106. Undefined objectives and a hazy vision never result in a clear path to increased production. As a result, having clear objectives is critical for better strategic planning. As a result, the fuzzy AHP approach is employed to prioritize the selected SSCM barriers. According to the final weights collected, the SSCM obstacles are ranked.

## References

- Abdullah L, Zulkifli N (2015) Integration of fuzzy AHP and interval type-2 fuzzy DEMATEL: an application to human resource management. *Exp Sys App (Elsevier Ltd)* 42(9):4397–4409. <https://doi.org/10.1016/j.eswa.2015.01.021>
- Ageron B, Gunasekaran A, Spalanzani A (2012) Sustainable supply management: an empirical study. *Int J Prod Econ (Elsevier)* 140(1):168–182. <https://doi.org/10.1016/j.ijpe.2011.04.007>
- Ahi P, Searcy C (2013) A comparative literature analysis of definitions for green and sustainable supply chain management. *J Clean Prod (Elsevier Ltd)* 52:329–341. <https://doi.org/10.1016/j.jclepro.2013.02.018>

- Amindoust A et al (2012) Sustainable supplier selection: a ranking model based on fuzzy inference system. *Appl Soft Comput J* 12(6):1668–1677 (Elsevier B.V.). <https://doi.org/10.1016/j.asoc.2012.01.023>
- Arumugam V, Antony J, Douglas A (2012) Observation: a Lean tool for improving the effectiveness of Lean Six Sigma. *TQM J* 24(3):275–287. <https://doi.org/10.1108/17542731211226781>
- Ashby A, Leat M, Hudson-Smith M (2012) Making connections: a review of supply chain management and sustainability literature. *Supply Chain Manag* 17(5):497–516. <https://doi.org/10.1108/13598541211258573>
- Avikal S, Mishra PK, Jain R (2014) A Fuzzy AHP and PROMETHEE method-based heuristic for disassembly line balancing problems. *Int J Prod Res* 52(5):1306–1317. <https://doi.org/10.1080/00207543.2013.831999>
- Bai C, Sarkis J, Wei X (2010) Addressing key sustainable supply chain management issues using rough set methodology. *Manag Res Rev* 33(12):1113–1127. <https://doi.org/10.1108/01409171011092176>
- Bastian J, Zentes J (2013) Supply chain transparency as a key prerequisite for sustainable agri-food supply chain management. *Int Rev Retail Distrib Consum Res* 23(5):553–570. <https://doi.org/10.1080/09593969.2013.834836>
- Beikhhakhian Y et al (2015) The application of ISM model in evaluating agile suppliers selection criteria and ranking suppliers using fuzzy TOPSIS-AHP methods. *Expert Syst Appl* (Elsevier Ltd) 42(15–16):6224–6236. <https://doi.org/10.1016/j.eswa.2015.02.035>
- Beske P, Koplin J, Seuring S (2008) The use of environmental and social standards by German first-tier suppliers of the volkswagen AG. *Corp Soc Responsib Environ Manag* 15(2):63–75. <https://doi.org/10.1002/csr.136>
- Bhosale VA, Kant R (2014) Selection of best knowledge flow practicing organisation using hybrid fuzzy AHP-VIKOR method. *Int J Decis Sci Risk Manag* 5(3):234–262
- Carter CR, Jennings MM (2002) Social responsibility and supply chain relationships. *Trans Res Part E: Log Trans Rev* 38(1):37–52. [https://doi.org/10.1016/S1366-5545\(01\)00008-4](https://doi.org/10.1016/S1366-5545(01)00008-4)
- Chakravorty SS, Shah AD (2012) Lean Six Sigma (LSS): an implementation experience. *Eur J Ind Eng* 6(1):118. <https://doi.org/10.1504/EJIE.2012.044813>
- Chen JJ, Paulraj A (2004) Towards a theory of supply chain management: the constructs and measurements. *J Oper Manag* 22(2):119–150. <https://doi.org/10.1016/j.jom.2003.12.007>
- Cheng LTCE et al (2015) Management of environmental quality: an international journal article information. *Manag Dec* 39(3):233–243. <https://doi.org/10.1108/EUM000000005454>
- Chung KJ, Lin TY, Srivastava HM (2015) An alternative solution technique of the JIT lot-splitting model for supply chain management. *Appl Math Inf Sci* 9(2):583–591. <https://doi.org/10.12785/amis/090205>
- Chung SH, Weaver RD, Friesz TL (2013) Strategic response to pollution taxes in supply chain networks: dynamic, spatial, and organizational dimensions. *Eur J Oper Res.* (Elsevier B.V.). 231(2):314–327. <https://doi.org/10.1016/j.ejor.2013.05.036>
- Clemens B, Thomas JD (2003) Stakeholders for environmental strategies. In: Andriof J, Waddock S, Husten B, Rahman SS (eds) *Unfolding stakeholder thinking*. Sheffield, UK Greenleaf Publishing Limited, p 128–144
- Cochran JK, Roche KT (2009) A multi-class queuing network analysis methodology for improving hospital emergency department performance. *Comput Oper Res* 36(5):1497–1512. <https://doi.org/10.1016/j.cor.2008.02.004>
- Croom S, Romano P, Giannakis M (2000) Supply chain management: an analytical framework for critical literature review. *Eur J Purch Supply Manag* 6(1):67–83. [https://doi.org/10.1016/S0969-7012\(99\)00030-1](https://doi.org/10.1016/S0969-7012(99)00030-1)
- Curwen LG (2012) Challenges and solutions sustainable apparel product development: a case study of Eileen Fisher. pp 1–82.
- Erol I, Sencer S, Sari R (2011) A new fuzzy multi-criteria framework for measuring sustainability performance of a supply chain. *Ecol Econ* 70(6):1088–1100. <https://doi.org/10.1016/j.ecolecon.2011.01.001>

- Ganguly KK, Guin KK (2013) A fuzzy AHP approach for inbound supply risk assessment. *Benchmarking: An International Journal* 20(1):129–146. <https://doi.org/10.1108/14635771311299524>
- Giannakis M, Papadopoulos T (2016) Supply chain sustainability: a risk management approach. *Int J Prod Eco (Elsevier)* 171:455–470. <https://doi.org/10.1016/j.ijpe.2015.06.032>
- Gibbons PM et al (2012) The development of a value improvement model for repetitive processes (VIM): combining Lean, Six Sigma and systems thinking. *Int J Lean Six Sigma* 3(4):315–338. <https://doi.org/10.1108/20401461211284770>
- Gold S, Seuring S, Beske P (2010) Sustainable supply chain management and inter-organizational resources: a literature review. *Corp Soc Respons Environ Manag* 17(4):230–245. <https://doi.org/10.1002/csr.207>
- Gremyr I, Fouquet J-B (2012) Design for Six Sigma and lean product development. *Int J Lean Six Sigma* 3(1):45–58. <https://doi.org/10.1108/20401461211223722>
- Guo Z et al (2017) Green supplier evaluation and selection in apparel manufacturing using a fuzzy multi-criteria decision-making approach. *Sustain* 9(4):650. <https://doi.org/10.3390/su9040650>
- Gupta V, Acharya P, Patwardhan M (2012) Monitoring quality goals through lean Six-Sigma insures competitiveness. *Int J Prod Perf Manag* pp 194–203. <https://doi.org/10.1108/17410401211194680>
- Hervani AA, Helms MM, Sarkis J (2005) Performance measurement for green supply chain management. *Benchmarking: Int J* 12(4):330–353. <https://doi.org/10.1108/14635770510609015>
- Hilton RJ, Sohal A (2012) A conceptual model for the successful deployment of Lean Six Sigma. *Int J Qual Reliab Manag* 29(1):54–70. <https://doi.org/10.1108/02656711211190873>
- Huang C-T et al (2009) A fuzzy AHP-based performance evaluation model for implementing SPC in the Taiwanese LCD industry. *Int J Prod Res* 47(18):5163–5183. <https://doi.org/10.1080/00207540801935608>
- Inoue HB, Yamada S (2013) Critical factors for process improvement in pharmaceutical research. *TQM J* 25(2):141–152. <https://doi.org/10.1108/17542731311299582>
- Jayaraman K, Kee TL, Soh KL (2012) The perceptions and perspectives of Lean Six Sigma (LSS) practitioners: an empirical study in Malaysia. *TQM J* 24(5):433–446. <https://doi.org/10.1108/17542731211261584>
- Jeyaraman K, Teo LK (2010) A conceptual framework for critical success factors of lean Six Sigma: implementation on the performance of electronic manufacturing service industry. *Int J Lean Six Sigma* 1(3):191–215. <https://doi.org/10.1108/20401461011075008>
- Karathi S, Devadasan SR, Muruges R (2011) Integration of Lean Six-Sigma with ISO 9001:2008 standard. *Int J Lean Six Sigma* 2(4):309–331. <https://doi.org/10.1108/20401461111189416>
- Kudla NL, Klaas-Wissing T (2012) Sustainability in shipper-logistics service provider relationships: a tentative taxonomy based on agency theory and stimulus-response analysis. *J Purchas Supp Manag (Elsevier)* 18(4):218–231. <https://doi.org/10.1016/j.pursup.2012.04.001>
- Kumar A, Shankar R, Debnath RM (2015) Analyzing customer preference and measuring relative efficiency in telecom sector: a hybrid fuzzy AHP/DEA study. *Telemat Infor (Elsevier Ltd)* 32(3):447–462. <https://doi.org/10.1016/j.tele.2014.10.003>
- Kumar Z, Rahman Z (2017) Analyzing enablers of sustainable supply chain: ISM and fuzzy 358 AHP approach. *J Model Manag* 12(3):498–524. <https://doi.org/10.1108/JM2-02-2016-0013>
- Kumar M, Antony J (2008) Comparing the quality management practices in UK SMEs. *Ind Manag Data Sys* 108(9):1153–1166. <https://doi.org/10.1108/02635570810914865>
- Lee C, Realf M, Ammons J (2011) Integration of channel decisions in a decentralized reverse production system with retailer collection under deterministic non-stationary demands. *Adv Eng Inf (Elsevier Ltd)* 25(1):88–102. <https://doi.org/10.1016/j.aei.2010.04.001>
- Lee KH, Wu Y (2014) Integrating sustainability performance measurement into logistics and supply networks: a multi-methodological approach. *British Account Rev (Elsevier Ltd)* 46(4):361–378. <https://doi.org/10.1016/j.bar.2014.10.005>

- Li S et al (2006) The impact of supply chain management practices on competitive advantage and organizational performance. *Omega* 34(2):107–124. <https://doi.org/10.1016/j.omega.2004.08.002>
- Lin C (2013) Application of fuzzy Delphi method (FDM) and fuzzy analytic hierarchy process (FAHP) to criteria weights for fashion design scheme evaluation. *Int J Cloth Sci Technol* 25(3):171–183. <https://doi.org/10.1108/09556221311300192>
- Lin Y-H, Tseng M-L (2016) Assessing the competitive priorities within sustainable supply chain management under uncertainty. *J Clean Prod (Elsevier Ltd)* 112:2133–2144. <https://doi.org/10.1016/j.jclepro.2014.07.012>
- Metta H, Badurdeen F (2013) Integrating sustainable product and supply chain design: modeling issues and challenges. *IEEE Trans Eng Manag* 60(2):438–446. <https://doi.org/10.1109/TEM.2012.2206392>
- Micmac I (2010) Improvement of a structural framework to improve sustainable supply chain acceptance: an ISM-fuzzy MICMAC approach abstract
- Moore SB, Manring SL (2009) Strategy development in small and medium sized enterprises for sustainability and increased value creation. *J Clean Prod (Elsevier Ltd)* 17(2):383–276–282. <https://doi.org/10.1016/j.jclepro.2008.06.004>
- Nakano M (2009) Collaborative forecasting and planning in supply chains: the impact on performance in Japanese manufacturers. *Int J Phy Dist Log Manag* 39(2):84–105. <https://doi.org/10.1108/09600030910942377>
- Parlak AI et al (2012) Population behavioral scenarios influencing radiological disaster preparedness and planning. *Acc Anal Prev (Elsevier Ltd)* 48:353–362. <https://doi.org/10.1016/j.aap.2012.02.007>
- Patil SK, Kant R (2014a) A fuzzy AHP-TOPSIS framework for ranking the solutions of knowledge management adoption in supply chain to overcome its barriers. *Exp Sys Appl (Elsevier Ltd)* 41(2):679–693. <https://doi.org/10.1016/j.eswa.2013.07.093>
- Patil SK, Kant R (2014b) Ranking the barriers of knowledge management adoption in supply chain using fuzzy AHP method. *Int J Bus Inn Res* 8(1):52–75
- Pepper MPJ, Spedding TA (2010) The evolution of lean Six Sigma. *Int J Qual Reliab Manag* 27(2):138–155. <https://doi.org/10.1108/02656711011014276>
- Pillai AKR, Pundir AK, Ganapathy L (2012) Implementing Integrated lean six sigma for software development: a flexibility framework for managing the continuity: change dichotomy. *Glob J Flex Sys Manag* 13(2):107–116. <https://doi.org/10.1007/s40171-012-0009-2>
- Pishvae MS, Razmi J, Torabi SA (2014) An accelerated benders decomposition algorithm for sustainable supply chain network design under uncertainty: a case study of medical needle and syringe supply chain. *Trans Res Part E: Log Trans Rev (Elsevier Ltd)* 67:14–38. <https://doi.org/10.1016/j.tre.2014.04.001>
- Samvedi A, Jain V, Chan FTS (2013) Quantifying risks in a supply chain through integration of fuzzy AHP and fuzzy TOPSIS. *Int J Prod Res* 51(8):2433–2442. <https://doi.org/10.1080/00207543.2012.741330>
- Sengupta D, Hawkins TR, Smith RL (2015) Using national inventories for estimating environmental impacts of products from industrial sectors: a case study of ethanol and gasoline. *Int J Life Cycle Assessment* 20(5):597–607. <https://doi.org/10.1007/s11367-015-0859-x>
- Shukla RK, Garg D, Agarwal A (2014) An integrated approach of Fuzzy AHP and Fuzzy TOPSIS in modeling supply chain coordination. *Prod Manufac Res* 2(1):415–437. <https://doi.org/10.1080/21693277.2014.919886>
- Silvestre BS (2015) Sustainable supply chain management in emerging economies: environmental turbulence, institutional voids and sustainability trajectories. *Int J Prod Eco (Elsevier)* 167:156–169. <https://doi.org/10.1016/j.ijpe.2015.05.025>
- Snee RD (2010) Lean Six Sigma – getting better all the time. *Int J Lean Six Sigma* 1(1):9–29. <https://doi.org/10.1108/20401461011033130>

- Thomas A, Barton R, Chuke-Okafor C (2009) Applying lean six sigma in a small engineering company – a model for change. *J Manufac Technol Manag* 20(1):113–129. <https://doi.org/10.1108/17410380910925433>
- Turker D, Altuntas C (2014) Sustainable supply chain management in the fast fashion industry: an analysis of corporate reports. *Euro Manag J (Elsevier Ltd)* 32(5):837–849. <https://doi.org/10.1016/j.emj.2014.02.001>
- Walker H, Jones N (2012) Sustainable supply chain management across the UK private sector. *Supp Chain Manag* 17(1):15–28. <https://doi.org/10.1108/13598541211212177>
- Waterbury T, Bonilla C (2008) A Lean Six Sigma execution strategy for service sectors: what you need to know before starting the journey. *Int J Six Sigma Comp Adv* 4(4):395. <https://doi.org/10.1504/IJSSCA.2008.022951>
- Wolf C, Seuring S (2010) Environmental impacts as buying criteria for third party logistical services. *Int J Phy Dist Log Manag* 40(1–2):84–102. <https://doi.org/10.1108/09600031011020377>
- Wong WP, Jaruphongsa J, Lee LH (2008) Supply chain performance measurement system: a Monte Carlo DEA-based approach. *Int J Ind Sys Eng* 3(2):162–188. <https://doi.org/10.1504/IJISE.2008.016743>
- Wu Z, Pagell M (2011) Balancing priorities: decision-making in sustainable supply chain management. *J Oper Manag (Elsevier B.V.)*. 29(6):577–590. <https://doi.org/10.1016/j.jom.2010.10.001>
- Zaabi S. Al, Dhaheiri N. Al, Diabat A (2013) Analysis of interaction between the barriers for the implementation of sustainable supply chain management. *Int J Adv Manuf Technol* 68:895–905. <https://doi.org/10.1007/s00170-013-4951-8>
- Zachariassen F et al (2008) Article information
- Zhu Q, Sarkis J, Geng Y (2005) Green supply chain management in China: pressures, practices and performance. *Int J Oper Prod Manag* 25(5):449–468. <https://doi.org/10.1108/01443570510593148>
- Zhuang J, Xu X, Cai G (2014) Discrete dynamic gaming models in supply chain management and project management. *Disc Dyn Nat Soc* pp 2–4. <https://doi.org/10.1155/2014/960239>

# Investigation on the Influence of MQL on Machining Parameters During Hard Turning of AISI316L



P. V. Vinay and Ch. Murali

**Abstract** Turning of steels has been a long pursued method of material removal. The usage of AISI316L steels in environments having high corrosion is being used, especially in applications where there is a contact with sea water. This is more relevant for our location and a correct set machining parameters for effective machining of this steel is the driving force behind this investigation. The usage of MQL has been to reduce the environmental as well as health impacts to machinists. These parameters and accessories were so chosen to have a cost effective method of machining, and the results are compared with the outputs acquired from deform 3D software. The correlation has been very good with the results obtained in terms of temperature generated during turning. The vibrations and surface roughness are the other outputs measured while varying the input parameters of speed of the spindle, feed and depth of cut. The best input parameters in both dry and MQL regimes are medium spindle speed of 170 rpm, low feed of 0.3 mm/rev, high depth of cut of 0.15 mm for having good surface finish, lower vibration, and low temperature.

**Keywords** MQL · AISI316L · Hard turning

## 1 Introduction

The usage of coolant or lubricant to reduce the tribological impact caused due to the meshing of tool with the workpiece during turning has been through centuries. Because of the relative motion of the tool with respect to the work piece causes plastic deformation which leads to the production of heat which is due to the breakage of bonds as well as friction. This heat causes damage to not only the workpiece but to the tool also by reducing its life time. This reduction of life time is costly as the tooling cost is high due to the cost of manufacturing of tools [1, 2]. This can be countered by having a mechanism to carry away the heat generated at the tool workpiece interface

---

P. V. Vinay (✉) · Ch. Murali

Department of Mechanical Engineering, Gayatri Vidya Parishad College for Degree and PG Courses (A), Visakhapatnam, Andhra Pradesh, India  
e-mail: [vpragada@gvpcdpgc.edu.in](mailto:vpragada@gvpcdpgc.edu.in)



by the usage of an external agent like a liquid or gas being impinged on the heat generating zone. This has led to different methods of cooling being implemented by industry in case of liquids [3] called pool/flood cooling. With the advent of new technologies and search for different strategies to reduce the impact of pool cooling in terms of environmental as well as health of the operator was considered as a major factor in machining. The usage of coolant has caused more negative effects [4] along with causing health issues to the operators [5, 6], and they amount to about 16–20% of the manufacturing costs during machining. Apart from using the liquid coolants, several other techniques like cryogenics, high-pressure cooling, minimum quantity lubrication (MQL), solid lubrication, etc., have been developed for heat alleviation from the heat affected zone and are discussed by Sharma et al. [7].

Dhar et al. [4] used MQL as the cooling and lubricating mechanism during turning AISI 1040 and showed that MQL is the alternative to flood cooling. Paulo Davim et al. [8] experimented on varying levels of MQL to be used during turning of brasses and suggested that the amount of MQL plays an important role in the achievement of good surface finish. AISI 9310 alloy steel was turned using vegetable oil-based cutting fluid and MQL produced the best surface finish over a wide range of machining time when compared to the wet and dry turning [9]. Turning AISI 1040 steel using MQL reduced the friction at the tool-chip interface and effectively reduced the deterioration of rake angle due to built-up edge formation and wear at the cutting edge. A reduction in auxiliary flank wear was observed when compared to dry turning. The reduction in flank temperature by using MQL was attributed as the reason [10]. Cetin et al. [11] experimented with vegetable-based cutting fluids under pressure during turning of AISI 304L steel and suggested that sunflower and canola-based cutting fluids performed better than the others. MQL has given best surface finish during turning of AISI 4140 alloy steel when two nozzles were used to pump ester oil (RS 1642) supplied at the rate 30 ml/h and at 3 bar pressure. The forces generated when using both nozzles and MQL have reduced them as well as improved surface roughness when compared to dry as well as wet conditions. This reduction of forces has also reduced the amount of heat generated as the friction has reduced. AISI4340 steel was machined using CBN inserts in dry, wet, and MQL regimes, and a reduction of 36% in temperature was observed when using MQL. Surface finish improved by 30% when compared to dry as well as wet condition machining [12]. Optimization of the process parameters for machining AISI4340 steel was done using different carbide inserts, and usage of MQL was found to be better than dry machining and its use reduced the cutting forces up to 17.07% and tool-tip temperature up to 6.72% as compared to dry machining [13]. Haynes 25 a cobalt-based super alloy was machined using carbide inserts, the results were optimized using Taguchi-based GRA was used, and the condition of 180 ml/h flow rate of vegetable oil was found to give better results in terms of reduction of tool wear and lower surface roughness.

Hwang and Lee [14] optimized the cutting parameters while machining AISI 1045 steel under dry, wet, and MQL conditions. The MQL condition at 7 bar pressure has yielded good surface finish and lower forces at a cutting velocity of 361 m/min, 0.01 mm/rev feed rate, and 0.1 mm depth of cut with a nozzle diameter of 6 mm. Nur [15] found out the power demand for turning AISI 316L steel using coated

and uncoated carbide inserts and concluded that as the cutting speed is the most influencing factor in increasing cutting force and power consumption. Investigations on finding the optimum cutting parameters during turning AISI 316 stainless steel were performed using different cutting tools by various researchers [16–20]. The need for researching on the usage of MQL technique with the most used oil in the manufacturing industry to reduce the cost as well as improve the machinability and also to provide a good quality product has been the driving force to experiment on the AISI 316L austenitic stainless steel. This steel also has good corrosion resistance properties and hence is being used in applications where there is an exposure to highly corrosive environments like sea water.

## 2 Experimentation

Experimentation is performed on a two axes manually operated lathe machine connected to a force dynamometer. The input parameters considered for turning operation are spindle speed, feed rate, and depth of cut. Mitutoyo surface roughness tester SJ201 is used for measuring the surface roughness. Infrared thermometer fluke 59 max is used to measure the temperature and a force dynamometer connected to a computer for recording the incoming force values at the rate of 10 readings per second is used during turning operation. A spray gun having an attachment to supply the coolant as shown in Fig. 1 is used to supply the oil-air mixture during the turning operation. The required air was supplied through air compressor at a constant pressure of 3 bar. Coolant oil used is veedol amulkut 4C metal working mineral oil mixed in the ratio of 50:50 with water is supplied at a constant flow rate of 8 ml/min. The equipment is set up as shown in Fig. 1 in such a way to supply the lubricant mixture effectively to the heat affected zone to reduce the temperature rise and also to assist in lubrication of the cutting zone.

**Fig. 1** Experimental setup



**Table 1** Input parameters with their levels

Input parameter	Levels
Speed (RPM)	75, 170, 268
Feed (mm/rev)	0.3, 0.4, 0.5
Depth of cut (mm)	0.05, 0.1, 0.15

The experimentation is carried out by plain turning on AISI 316L stainless steel in both dry and MQL state to determine the effect of using MQL on the forces developed, surface roughness, temperature, and power requirement compared to the dry machining. Surface roughness was measured at three separate locations on the surface after machining, and an average roughness value is considered. The outputs chosen to be analyzed are forces developed, surface roughness, temperature, displacement, and power as they are the main parameters to know the effect of MQL during turning. The input parameters with the levels chosen are given in Table 1.

The composition of the workpiece AISI 316L is given in Table 2.

For performing the experimentation, Box-Behnken design matrix is developed using Minitab 16.0 software with the three input parameters. Table 3 shows the design matrix consisting of total 15 experiments to be performed.

**Table 2** Chemical composition of AISI 316L stainless steel

C	Si	Mn	Cr	S	P	Ni	N	Fe
0.03	0.75	2.0	18.0	0.03	0.045	14.0	0.10	Balance

**Table 3** Box-Behnken design matrix

Experiment No.	Speed (RPM)	Feed (mm/rev)	Depth of cut (mm)
1	75	0.3	0.10
2	268	0.3	0.10
3	75	0.5	0.10
4	268	0.5	0.10
5	75	0.4	0.05
6	268	0.4	0.05
7	75	0.4	0.15
8	268	0.4	0.15
9	170	0.3	0.05
10	170	0.5	0.05
11	170	0.3	0.15
12	170	0.5	0.15
13	170	0.4	0.10
14	170	0.4	0.10
15	170	0.4	0.10

### 3 Results and Discussion

To analyze the output parameters and to determine the effect of using MQL on the surface roughness, temperature, and power requirement, when compared to dry machining, response surface methodology (RSM) is used. The results after performing the experimentation are tabulated for both dry as well as MQL regime are shown in Tables 4 and 5.

From Fig. 2a and b, it is evident that the usage of MQL has reduced the temperatures generated during machining when compared to the dry regime. The temperatures generated are during the all high parameter inputs of 268 rpm speed of the spindle, feed of 0.5 mm/rev, and depth of cut of 0.15 mm. The MQL regime shows a variation in the recording of higher temperatures which are in the range of depth of cuts from 0.1 to 0.15. The difference of temperatures between dry and MQL regimes is about 25 °C.

The surface roughness values shown in Fig. 3a and b are better for higher speeds medium feed and low depth of cut in dry, and the same trend is holding good for MQL regime also. There is a considerable reduction in surface roughness values in the case MQL in the range of 6–20%. Lower values of speed and depth of cut along with high feed yields higher surface roughness and this setting should be avoided in even MQL regime. High speed along with low feed and low depth shows good surface finish in MQL.

**Table 4** Data after machining in dry regime

S. No.	Speed (RPM)	Feed (mm/rev)	Depth of cut (mm)	Temp. (°C)	Surface roughness (microns)	Displacement (mm)
1	268	0.5	0.10	85	10.54	9
2	75	0.5	0.10	48	7.95	9
3	268	0.3	0.10	66	8.47	9
4	75	0.3	0.10	45	11.5	9
5	268	0.4	0.15	71	9.56	9
6	75	0.4	0.15	45	10.58	8
7	268	0.4	0.05	39	7.44	9
8	75	0.4	0.05	78.5	10.85	8
9	170	0.5	0.15	75.4	10.2	9
10	170	0.3	0.15	35	10.4	8
11	170	0.5	0.05	50.5	11.28	8
12	170	0.3	0.05	31.2	11.48	9
13	170	0.4	0.10	51	10.96	9
14	170	0.4	0.10	49	10.52	9
15	170	0.4	0.10	58	10.87	9

**Table 5** Data after machining in MQL regime

S. No.	Speed (RPM)	Feed (mm/rev)	Depth of cut (mm)	Temp. (°C)	Surface roughness (μm)	Displacement (mm)
1	268	0.5	0.10	63	9.46	11
2	75	0.5	0.10	45	10.33	9
3	268	0.3	0.10	41	5.3	15
4	75	0.3	0.10	28	9.86	10
5	268	0.4	0.15	43	7.33	13
6	75	0.4	0.15	30.9	8.12	10
7	268	0.4	0.05	28	6.99	20
8	75	0.4	0.05	60	9.82	10
9	170	0.5	0.15	47.1	8.45	12
10	170	0.3	0.15	28	8.02	10
11	170	0.5	0.05	40.6	10.4	9
12	170	0.3	0.05	23	9.82	12
13	170	0.4	0.10	39	9.66	10
14	170	0.4	0.10	35.6	7.43	11
15	170	0.4	0.10	42	8.64	10

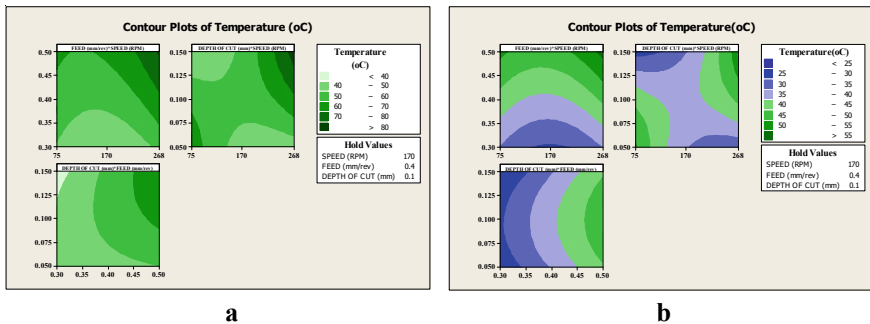


**Fig. 2** a Temperature variation with input parameters in dry regime. b Temperature variation with input parameters in MQL regime

There is a marked reduction in the vibration caused due to machining AISI 316L in dry regime to that of MQL regime as can be seen from Fig. 4a and b. The values have reduced due to the introduction of oil which has caused enough lubrication to reduce the vibration being experienced during machining, and this has in turn reduced the temperatures generated due to the higher removal of heat and also assisted in the reduction of chip length which helps in reducing erosion of tool surface and assists in increasing the tool life. The displacement produced at high feed, low speed, and in the range of depth of cuts shows reasonably low displacements.

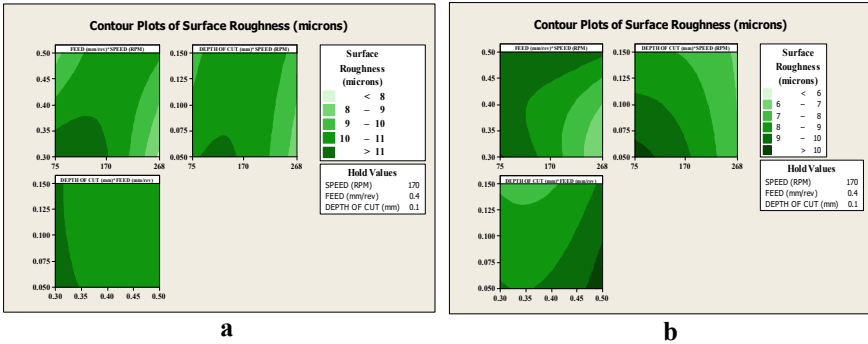


Fig. 3 a Surface roughness variation with input parameters in dry regime. b Surface roughness variation with input parameters in MQL regime

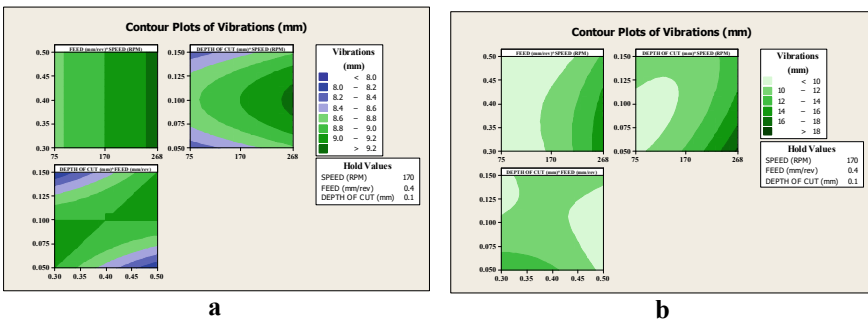


Fig. 4 a Variation in displacement with input parameters in dry regime. b Variation in displacement with input parameters in MQL regime

The change from dry to MQL condition is due to the introduction of lubricant in the MQL mode, and it shows that the reduction is credible enough and is suggestible to be used during machining of hard to machine materials if lower temperatures are to be realized as well as better surface finish.

The usage of available cutting fluid mixed in equal proportions with water and sprayed onto the cutting zone has yielded good results in terms of reduction of temperature generated as well as reduction of cutting forces.

### 4 Results Validation Using Deform 3D Software

Deform 3D software was used to validate the experimental results. Simulations were performed for three random runs according to design matrix. Both the experimental and analytical values obtained from the software are correlating. MQL conditions

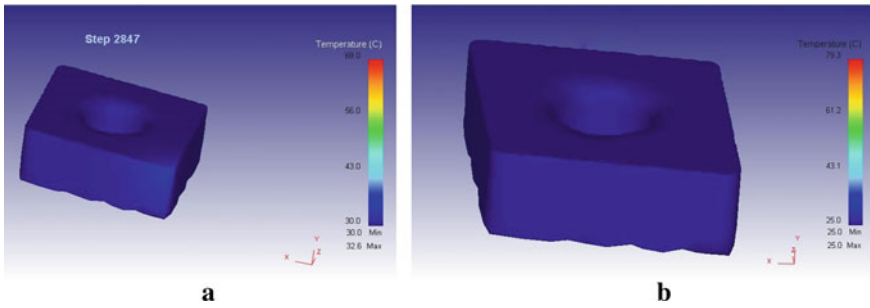


**Fig. 5** **a** Temperature variation with input parameters speed = 75 RPM, feed = 0.3 mm/rev, depth of cut = 0.1 mm in dry regime. **b** Temperature variation with input parameters speed = 75 RPM, feed = 0.3 mm/rev, depth of cut = 0.1 mm in MQL regime

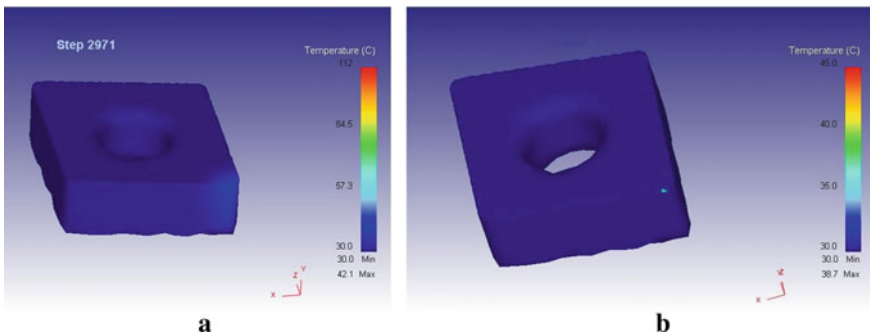


**Fig. 6** **a** Temperature variation with input parameters speed = 170 RPM, feed = 0.4 mm/rev, depth of Cut = 0.1 mm in dry regime. **b** Temperature variation with input parameters speed = 170 RPM, feed = 0.4 mm/rev, depth of Cut = 0.1 mm in MQL regime

were also mimicked in the software by changing the heat transfer coefficient as proposed by Kurgin et al. [21] who proposed that the dry regime heat transfer coefficient to be  $22 \text{ W/m}^2 \text{ C}$ , and the MQL regime heat transfer is chosen to be  $125 \text{ W/m}^2 \text{ C}$ . Figures 5a, 6a and 7a show the temperature profile generated in the HSS tool when machining in dry regime, and Figs. 5b, 6b and 7b show the temperature profiles generated in a HSS tool when machining in MQL regime. The results from the software are correlating with the experimental results from machining.

## 5 Conclusions

The usage of 50–50 mixture of mineral oil and water pumped under 3 bar pressure in MQL condition onto the heat generated zone and comparison with the dry regime

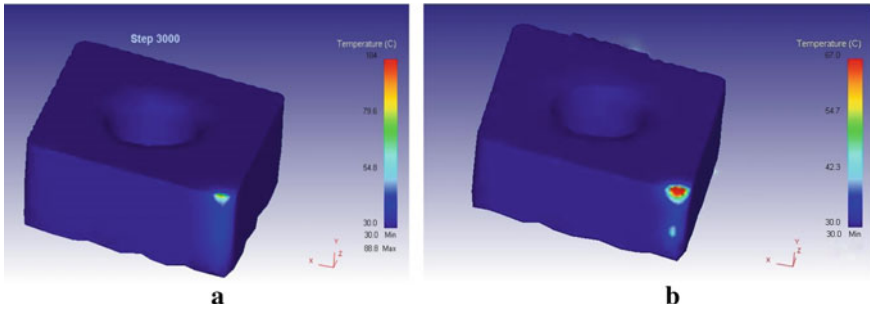


**Fig. 7** **a** Temperature variation with input parameters speed = 268 RPM, feed = 0.5 mm/rev, depth of cut = 0.1 mm in dry regime. **b** Temperature variation with input parameters speed = 268 RPM, feed = 0.5 mm/rev, depth of cut = 0.1 mm in MQL regime

of machining has good yielded results that can be categorized under different output parameters below:

The temperature generated during machining has reduced by a percentage of 27 in MQL conditions than under dry machining. This will lead to good tool life and better machining conditions as well as better surface quality.

The usage of deform 3D software for evaluating the temperatures generated in both dry and MQL conditions is correlating with the experimental results obtained during machining.

The displacement measured while machining in dry and MQL regimes have shown a variation, when using MQL, this might primarily be due to the influx of lubricant into the cutting zone.

The surface roughness has shown a 20% decrease when using MQL over dry turning of AISI 316L steel.

The best cutting condition is 170 rpm spindle speed, 0.3 mm/rev feed, and 0.15 mm depth of cut, and the usage of MQL has shown that the surface roughness is better and hence the machined component can be directly put to use without any further finishing operations.

**Acknowledgements** This research has been supported by the seed money granted by Gayatri Vidya Parishad College for Degree and PG Courses (A).

## References

1. Silva LE, Bianchi EC, Fusse RY, Catai RE, França TV, Aguiar PR (2007) Analysis of surface integrity for minimum quantity lubricant—MQL in grinding. *Int J Mach Tool Manuf* 47:412–418
2. Bruni C, Gabrielli FF, Simoncini M (2006) Effect of the lubrication-cooling technique, insert technology and machine bed material on the workpart surface finish and tool wear in finish turning of AISI 420B. *Int J Mach Tools Manuf* 46:1547–1554



3. Baradie MAE (1996) Cutting fluid: Part-I characterization. *J Mater Process Technol* 56:786–797
4. Dhar NR, Islam MW, Islam S, Mithu MAH (2006) The influence of minimum quantity of lubrication (MQL) on cutting temperature, chip and dimensional accuracy in turning AISI-1040 steel. *J Mater Process Technol* 171:93–99
5. Sokovic M, Mijanovic K (2001) Ecological aspects of the cutting fluids and its influence on quantifiable parameters of the cutting processes. *J Mater Process Technol* 109:181–189
6. Weinert K, Inasaki I, Sutherland JW, Wakabayashi T (2005) Dry machining and minimum quantity lubrication. *CIRP Annu Manuf Technol* 53(2):511–537
7. Sharma VS, Dogra M, Suri NM (2009) Cooling techniques for improved productivity in turning. *Int J Mach Tools Manuf* 49:435–453
8. Paulo Davim J, Sreejith PS, Silva J (2007) Turning of brasses using minimum quantity of lubricant (MQL) and flooded lubricant conditions. *Mater Manuf Process* 22:45–50
9. Khan MMA, Mithu MAH, Dhar NR (2009) Effects of minimum quantity lubrication on turning AISI 9310 alloy steel using vegetable-oil based cutting fluid. *J Mater Process Technol* 209:5573–5583
10. Dhar NR, Ahmed MT, Islam S (2007) An experimental investigation on effect of minimum quantity lubrication in machining AISI 1040 steel. *Int J Mach Tools Manuf* 47:748–753
11. Cetin MH, Ozcelik B, Kuram E, Demirbas E (2011) Evaluation of vegetable based cutting fluids with extreme pressure and cutting parameters in turning of AISI 304L by Taguchi method. *J Clean Prod* 19:2049–2056
12. Lohar DV, Nanavaty CR (2013) Performance evaluation of minimum quantity lubrication (MQL) using CBN during hard turning of AISI 4340 and its comparison with dry and wet turning. *Bonfring Int J Ind Eng Manag Sci* 3(3):102–106
13. Saini A, Dhiman S, Sharma R, Setia S (2014) Experimental estimation and optimization of process parameters under minimum quantity lubrication and dry turning of AISI-4340 with different carbide inserts. *J Mech Sci Technol* 28(6):2307–2318
14. Hwang YK, Lee CM (2010) Surface roughness and cutting force prediction in MQL and wet turning process of AISI 1045 using design of experiments. *J Mech Sci Technol* 24(8):1669–1677
15. Nur R (2016) Calculating the power demand in turning of AISI 316L stainless steel through the cutting forces data. *J INTEK* 3(1):43–49
16. Ali Khan A, Salama Hajjaj S (2006) Capabilities of cermets tools for high speed machining of AISI 316. *J Appl Sci* 6(4):779–784
17. Bonnet C, Valiorgue F, Rech J, Bergheau JM, Gilles P, Claudin C (2008) Development of a friction modeling method in dry cutting of AISI 316L austenitic stainless steel. *Int J Master Form Suppl* 1(1):1211–1214
18. Kaladhar M, Venkata Subbaiah K, Srinivasa Rao C (2011) Performance evaluation of coating materials and process parameters optimization for surface quality during turning of AISI 316. *Int J Eng Sci Technol* 3(4):89–102
19. Lin WS (2008) The study of high speed fine turning of austenitic stainless steel. *J Achiev Mater Manuf Eng* 27(2):191–194
20. Nikolaos I, Galanis D, Maolakos E (2010) Surface roughness prediction in turning of femoral head. *Int J Adv Manuf Technol* 51:79–86
21. Kurgin S, Dasch JM, Simon DL, Barber GC, Zou Q (2012) Evaluation of the convective heat transfer coefficient for minimum quantity lubrication (MQL). *Ind Lubr Tribol* 64(6):376–386

# Framework to Monitor Vehicular GHG Footprint



Soumyanath Chatterjee and S. P. Sarmah

**Abstract** Vehicular movement is one of the major contributors to CO<sub>2</sub> emission. Poor vehicle maintenance and driving habits are the key reasons for such low fuel efficiency. Current method of indirect estimation of carbon footprint do not give actionable information to address the emission at its source. In this paper an IoT based methodology is proposed to collect the emission data during vehicle movements and provide information to various stakeholders to address the problem directly.

**Keywords** Carbon footprint · Internet of things · Transport industry · Cloud computing

## 1 Introduction

India is a signatory of UN Framework Convention on Climate Change (UNFCCC 1992). After Paris Agreement (2015), India has a commitment to participate in multi-lateral negotiations under United Nations Framework Convention on Climate Change (UNFCCC) and have committed to reduce Green-House Gas (GHG) emission intensity per unit GDP by 33 to 35% below the 2005 level by 203 [14]. India has always shown leadership in taking action for controlling climate change. India has been in at the forefront in implementing world standard emission norms [1] and implemented the latest world standards. However, implementation of emission norms has not resulted in reduction of carbon emission from heavy-duty vehicles [19]. Further research of Gota and Schipper [9] shows that truck and buses that travel the highest distance have the lowest fuel efficiency. Various studies have also showed that trucks consume the highest percentage of diesel fuels in India [3, 6, 15]. Poor vehicle maintenance and driving habits are the important reasons for such low fuel efficiency. As

---

S. Chatterjee (✉) · S. P. Sarmah  
ISE Department, IIT Kharagpur, Kharagpur, India  
e-mail: [soumyanath.c@gmail.com](mailto:soumyanath.c@gmail.com)

S. Chatterjee  
Siksha O Anusandhan (Deemed to be) University, Bhubaneswar, India

carbon emission estimates are calculated indirectly by fuel consumption approach, it is very difficult to get actual value of carbon emission [15]. Moreover, such indirect estimation does not provide information for proper remedial measure to be taken.

Application of digital technology like IoT, Cloud computing, Spatial Analysis etc. opens up new avenue to capture vehicle level accurate data on carbon emission. These data can be correlated with vehicle location, vehicle types, and driving habits to come up with (a) Direct feedback to driver for better driving, and (b) formulation of effective strategies for reducing carbon emission [10, 11, 13].

Reduction of carbon emission and improvement in fuel efficiency will help both transporter and nation to save on fuel cost, improve environment and reduce health care cost [5]. There have been lots of interest in ecodriving that mainly focus on driver training, but only driver training is not sufficient to reduce GHG foot-print. Access to correct information to the correct agency at the right time is essential to bring change in the current situation. Our research is aimed to propose such an infrastructure.

## 2 Literature Survey

The subject of IoT based vehicular emission control spans across many disciplines; namely, vehicle emission, driving habits, mobile data collection and big data computing. Latest information of these different aspects is often available only in technical bulletin. To get this information we have first looked into the published research and patent. In addition, where appropriate, we have also included technical bulletin and manuals.

Effect of GHG emission/fuel consumption have been studied by Carrese et al. [4], Gao et al. [8], and Fontaras et al. [7]. They observe for similar vehicles, the key drivers for the GHG emission/fuel consumption are: driving style (27%) and road condition (7% 26%). They also note that there is an optimum speed at which fuel efficiency is at its peak. In situation where vehicle needs to stop frequently, fuel consumption may rise by 14%, but GHG emission in such situation may rise by 40%. Congestion increases fuel consumption by 53% and increase in GHG emission by 63–170%.

Ng et al. [12], Strömberg et al. [18] and Xu et al. [20] suggested, ecodriving training should be made a mandatory requirement for drivers. Ng et al. [12] proposed a device to provide feedback to the driver. Smit et al. [16] have conducted experiments of ecodriving in Australian traffic. These experiments show ecodriving can reduce CO<sub>2</sub> emission by 10% and NO<sub>x</sub> emission by 14%. A similar study conducted for bus operation in USA by Xu et al. [20] shows fuel consumption can be reduced by 7% even in environment friendly CNG buses by adapting algorithm based ecodriving.

Bandeira et al. [2] suggested GPS based real-time data collection and analysis to plan transport routes for reduction of GHG emission. Kanarachos et al. [11] proposed use of smartphones to capture location, speed, and acceleration data from the smartphone to estimate fuel consumption and emission data. Kan et al. [10] suggests using big-data-analytics on GPS data to estimate pollution.

### 3 Research Gap and Objectives

Literature survey identified road condition, driving habit, and terrain as important factors for pollution. Various data collection, analysis, and training methods have been discussed but the diversity of stake-holders for different types of action remains needs more attention.

The proposal is aimed to create an information technology facility that will collect operating data from onboard sensors in vehicle and share actionable information to different stakeholders like driver, transport fleet owner, highway authority/municipalities and vehicle manufacturers to enable each of them to reduce emission.

### 4 Proposed Methodology

In the whole system of vehicular operation there are four stakeholders:

1. Transport owner: They decide type of vehicles to buy, routes to operate, and maintenance of the vehicle
2. Driver: Who will drive the vehicle and is the last person who can influence fuel consumption
3. Road owner: Generally, government agency or the lease owner of toll road. They are the final decision maker on the road conditions and party to decision-making process of multi-lane the road to reduce congestion
4. Vehicle manufacturer: Who design the vehicle and decides power, drivetrain characteristics and physical characteristics of the vehicle

Currently, transport owners have somewhat inaccurate information on performance of different vehicles in the route they plan to operate. Availability of accurate information with saving potential will help them decide on correct vehicle selection, route planning and driver training. Government agencies currently have no indication on the economic cost of their various measures or inaction. Benchmarking and Measurement of these economic and environmental costs due to bad roads, congested roads, speed breakers, speed limits will help the decision makers assign correct priorities. Lastly, vehicle manufacturer has imperfect information on how their vehicles are used. During design and development, they spend considerable money in collecting terrain and usage data but accuracy of these data differs from reality. Access to real-life data will help the manufacturers design correct drive train and achieve better fuel efficiency and lesser GHG emission.

Most modern vehicles already have sensors to monitor engine speed and vehicle speed. Many of them also have sensors to measure fuel consumption. In case fuel flow meter is missing, a generic ultrasonic in-line fuel flow-meter can be easily fitted in the fuel line to give accurate fuel consumption data.

The proposal calls for augmenting these existing data with geolocation and share it with central servers at near real-time using a GPS module and mobile data network.

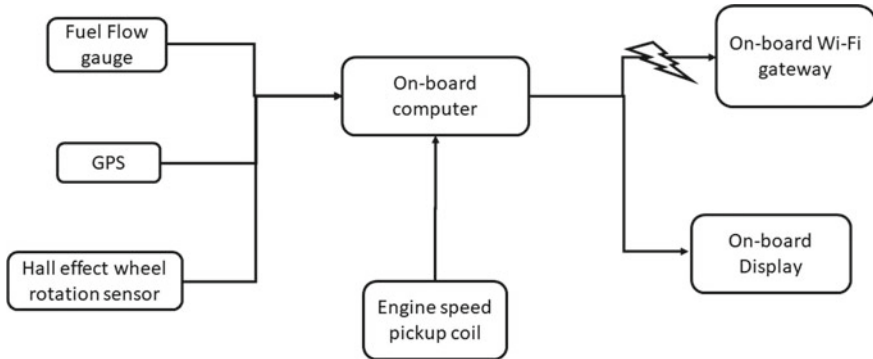


**Fig. 1** On-board IoT ecodrive system

In places where mobile data connectivity is not available the data can be stored temporarily and shared with the servers at the next opportunity.

Apart from data acquisition, the on-board device will also provide ecodrive feedback to the driver. Optimal parameters for ecodrive will be supplied from central server that have information of traffic condition ahead of the road, operating characteristic of the vehicle and benchmark performance of similar other vehicles.

Schematic diagram of the onboard data acquisition and ecodrive guidance (ODAGE) system is given in Fig. 1. At core of the system, there is a single board computer (SBC) with Wi-Fi. This SBC gets input from fuel consumption data from fuel flow meter, real time location data from a GPS module. A small magnet is fixed on a wheel hub and hall-effect sensor is used to pick up wheel rotations. Time interval between two signals from the hall-effect sensor gives indication of wheel speed and number of rotation indicates distance traveled. For the test vehicle, a petrol engine is used. An electrical pick-up coil was used to get engine speed data. For diesel engines, hall-effect sensors can be used to get engine speed from flywheel.

Inputs from these sensors is processed by the SBC. It calculates gear ratio by finding the speed ratio of engine and wheel. The SBC has optimal engine speed table for the terrain. It gives continuous feedback to driver on correct speed and gear. At every kilometer of travel SBC sends out JSON encoded data through on-board mobile Wi-Fi gateway to a cloud-based server and receives the updated speed and gear setting data for the location it is traveling from the central cloud server.

Architecture of the overall system is given in Fig. 2. Onboard data acquisition and ecodrive guidance (ODAGE) devices will exchange data using mobile data or Wi-Fi in dedicated stations to an array of cloud servers. Operation level data from the cloud server will be analyzed by big-data servers and recommended operation characteristic for specific location and vehicle model will be shared back to cloud servers. Other performance reports will be shared with respective stakeholders.

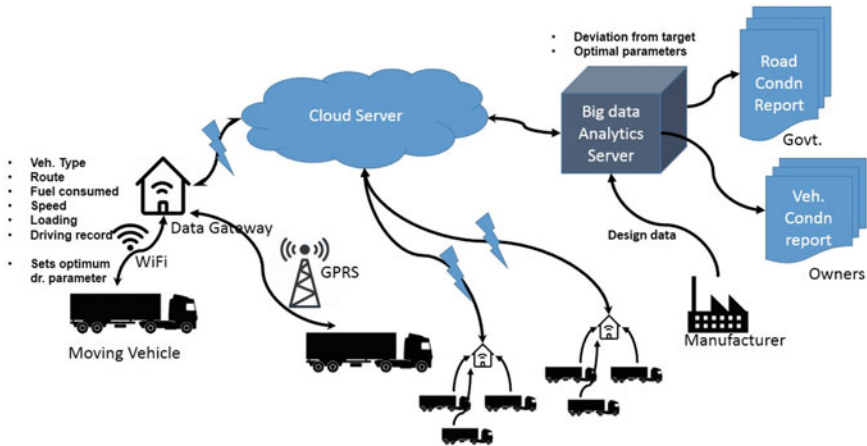


Fig. 2 Monitoring system

### 5 Proposed Analysis Framework

India alone had 295.77 million registered vehicles in 2019 [17]. Initially only a few vehicles will use the facility, but the system design needs to be scalable to handle data from most of the operating vehicles. Real time monitoring of such massive number of devices calls for distributed computing framework. There are opportunities to reduce analysis load by summarizing the collected data in regional and vehicle model levels. Performance data of individual vehicle can be stored in the ODAGE device itself and transmitted to fleet owner at a predetermined frequency. This data can also indicate when a maintenance is due or there is any deterioration of the vehicle performance.

The aggregated statistical analysis from various geographical locations will be mined periodically for:

1. Generating renewed best practice recommendations for vehicle make and model
2. Sending road condition report and generating any alert on adverse road condition
3. Providing a database for vehicle manufacturers on route, terrain and driving habit data

### 6 Concluding Remarks

The proposed framework of ODAGE builds upon ecodrive concept and further optimize driving parameters by machine learning approach. Integrated fuel consumption and route monitoring has the potential to make better improvement than ecodrive approach. Ecodrive is proven to make significant reduction (10–14%) of GHG emission and fuel consumption (7%) [16, 20]. The system is tested as proof of concept. However, any real benefit will come only when this system is adopted for large

number of vehicles and generate data for different vehicles and geographical locations. Additional investment to implement the system will be paid back by the saving in fuel as well as availability of better information that will make better planning possible. Many transport operators install vehicle tracking devices, ODAGE can replace such device.

The novel approach as proposed here will help share required information to correct agencies to address the problem of high GHG emission and also reduce fuel consumption.

There are few challenges that need to be addressed to implement the proposed solution. Any data sharing between different agencies has an element of data privacy concern. Country needs to formulate and implement data privacy laws to stop data theft and bring transparency on how data is being used. Similarly, strict control of data security to stop sharing competitor data for transport operator and for vehicle manufacturer is required for success of this integrated motoring program. Once the legal and security aspects are addressed the collaborative data sharing will improve.

## References

1. ARAI (2018) Indian emissions regulations. Automotive Research Association of India
2. Bandeira J et al (2013) Generating emissions information for route selection: experimental monitoring and routes characterization. *J Intell Transp Syst Technol Plann Oper* 17(1):3–17
3. CAA (ed) (2012) Accessing Asia: air pollution and greenhouse gas emissions indicators for road transport and electricity
4. Carrese S, Gemma A, La Spada S (2013) Impacts of driving behaviours, slope and vehicle load factor on bus fuel consumption and emissions: a real case study in the city of Rome. *Proc—Soc Behav Sci* 87:211–221
5. Eckelman MJ, Sherman JD (2018) Estimated global disease burden from US health care sector greenhouse gas emissions. *Am J Public Health* 108(Suppl 2)
6. Facanga C, Blumberg C, Miller J (2012) Global transportation energy and climate roadmap. *Int Council Clean Transp*
7. Fontaras G, Zacharof NG, Ciuffo B (2017) Fuel consumption and CO<sub>2</sub> emissions from passenger cars in Europe Laboratory versus real-world emissions. *Prog Energy Combust Sci* 60:97–131
8. Gao J et al (2020) Fuel economy and exhaust emissions of a diesel vehicle under real traffic conditions. *Energy Sci Eng* 8(5):1781–1792
9. Gota S, Schipper L (2013) Transport emissions and India's diesel mystery
10. Kan Z et al (2018) Estimating vehicle fuel consumption and emissions using GPS big data. *Int J Environ Res Public Health* 15(4):1–23
11. Kanarachos S, Mathew J, Fitzpatrick ME (2019) Instantaneous vehicle fuel consumption estimation using smartphones and recurrent neural networks. *Expert Syst Appl* 120:436–447
12. Ng ECY et al (2021) Reducing vehicle fuel consumption and exhaust emissions from the application of a green-safety device under real driving. *Sci Total Environ* 793(2):148602
13. Perrotta F, Parry T, Neves LC (2017) Application of machine learning for fuel consumption modelling of trucks. In: *Proceedings of 2017 IEEE international conference on big data, big data 2017 Jan 2018*, pp 3810–3815
14. PMMC (ed) (2015) Paris agreement to climate change, a strong call for action to transport sector. <http://www.ppmc-transport.org/parisagreement-on-climate-change-a-strong-call-to-action-forthe-transport-sector>

15. Singh N, Mishra T, Banerjee R (2019) Greenhouse gas emissions in Indias road transport sector. In: Venkataraman et al C (eds). Springer, Singapore
16. Smit R, Rose G, Symmons M (2010) Assessing the impacts of ecodriving on fuel consumption and emissions for the Australian situation. In: ATRF 2010 33rd Australasian transport research forum, Oct 2010, pp 1–15
17. Statista (ed) (2020) Number of vehicles in operation across India from financial year 1951 to 2019
18. Strömberg H, Karlsson ICMA, Rexfelt O (2015) Eco-driving: drivers' understanding of the concept and implications for future interventions. *Transp Policy* 39:48–54
19. THBL (ed) (2019) Indias energy demand outpace global growth
20. Xu Y et al (2017) Eco-driving for transit: an effective strategy to conserve fuel and emissions. *Appl Energy* 194:784–797



# Accurate Prediction of Thermomechanical Stress Field in the Laminated Composite Plates



T. Das and J. K. Nath

**Abstract** Thermomechanical stress fields in composite plates are obtained using an efficient global–local theory. All components of the stress field have been computed by direct use of the constitutive equations, not from the use of post-processing techniques. It has been possible to get accurate computations due to the double superposition-based displacement field assumption and a priori satisfaction of the boundary conditions on the displacements and stresses at all interfaces as well as the outer surfaces. Across-the-thickness nonlinearity in the distribution of the transverse displacement component has been effected by using a sub-layerwise piecewise linear function for the temperature field. The theory incurs constant computational expenses for all types of composite laminated plate structures, since the plate-governing equations contain only the reference layer variables. By comparing with the 3D exact solutions of thermoelasticity, displacements and stresses calculated by the present theory have been found to be very accurate. They have been seen to be superior to other shear deformation theories. Effects of the aspect ratio and length-to-width ratio under thermomechanical loads have been investigated.

**Keywords** Zigzag theory · Shear deformation · Global–local theory

## 1 Introduction

Beams, plates and shells made of laminated composites offer many advantages when compared with their traditional single-material counterparts. Composites have been known to provide the desired low-specific weight, high-specific stiffness, high-specific strength and easy tailorability to any complex shape. Use of the polymer composites in civil constructions has been discussed in Ref. [1]. Computationally, the most efficient shear deformation theories are the equivalent single-layer (ESL) theories that include the zero transverse shear stress producing classical laminate

---

T. Das (✉) · J. K. Nath  
Siksha 'O' Anusandhan Deemed to be University, Bhubaneswar, Odisha 751030, India  
e-mail: [tapaswineedas@soa.ac.in](mailto:tapaswineedas@soa.ac.in)

theory (CLT), constant transverse shear stress producing first-order shear deformation theory (FSDT), parabolic transverse shear stress producing third-order theory (TOT) [2], and other higher order theories (HOTs). The accuracy of a particular ESL theory depends upon the degree of the polynomial used for the displacement field description. CLT and FSDT are good for thin plates. Global level responses, such as natural frequencies and critical buckling load, are well predicted by the TOT and HOT in moderately thick to thick plates. Local level phenomena, such as the effects arising out due to the interactions between the adjacent layer properties at the interfaces, cannot be very well described by such theories.

The shear deformation theories that have been built on layerwise displacement field assumptions describe accurately the interlaminar interactions and other local responses. The greatest drawback associated with any layerwise theory is the prohibitively high computational expenses. The strive toward development of layer independent efficient layerwise theories resulted in the advanced shear deformation theories, known as zigzag theories, zigzag-local theories and global–local theories. These efficient theories have used different conditions on displacements and stresses so that the number of field variables are independent of the number of layers in the laminated plate. Cho and Parmerter [3] and Shu and Sun [4] have presented the efficient zigzag theories for elastic composite plates. Accurate computation of the transverse shear stresses in a zigzag theory has been made by integration of three-dimensional equations of equilibrium. The tedious process involving such integrations has been circumvented by the development of superposition-based shear deformation theories. Global–local theory [5] belongs to this class.

In this work, a variationally consistent global–local theory developed by Nath and Kapuria [6] has been used to study the thermomechanical bending responses in laminated composite plates with different aspect ratios and different length-to-width ratios. The constitutive equations have been used to obtain the stress profiles, and they have been compared and analyzed with respect to three-dimensional thermoelasticity solutions. Comparison has been made with another shear deformation zigzag-local theory [6] to illustrate their accuracies in obtaining static responses.

## 2 Formulation

The inplane components,  $u_x$  and  $u_y$ , and the transverse component  $w$  of the displacement field for the present global–local shear deformation theory are assumed as

$$u = u_G + \bar{u}^k + \hat{u}^k, \quad w = w_0 + \bar{\Psi}_T^l(z)T_l(x, y) \quad (1)$$

where

$$u = \begin{bmatrix} u_x \\ u_y \end{bmatrix}, u_G = \begin{bmatrix} u_{Gx} \\ u_{Gy} \end{bmatrix}, \bar{u}^k = \begin{bmatrix} \bar{u}_x^k \\ \bar{u}_y^k \end{bmatrix}, \hat{u}^k = \begin{bmatrix} \hat{u}_x^k \\ \hat{u}_y^k \end{bmatrix}$$

$u_G$  is global cubic expression along thickness coordinate  $z$ . The column matrices

$$u_0 = \begin{bmatrix} u_{0x} \\ u_{0y} \end{bmatrix}, w_{0d} = \begin{bmatrix} w_{0,x} \\ w_{0,y} \end{bmatrix}, \psi_0 = \begin{bmatrix} \psi_{0x} \\ \psi_{0y} \end{bmatrix}, \zeta = \begin{bmatrix} \zeta_x \\ \zeta_y \end{bmatrix}, \eta = \begin{bmatrix} \eta_x \\ \eta_y \end{bmatrix}$$

which appear inside the expression of  $u_G$  are functions of plate inplane coordinates  $(x, y)$ . In similar manner, the quadratic layerwise terms  $\bar{u}^k$  and  $\hat{u}^k$  are defined. The complete expressions for,

$u_G, \bar{u}^k$  and  $\hat{u}^k$  are given by

$$u_G = u_0(x, y) - zw_{0d}(x, y) + z\psi_0(x, y) + z^2\xi(x, y) + z^3\eta(x, y)$$

$$\bar{u}^k = \zeta_k u_1^k(x, y) + \zeta_k^2 u_2^k(x, y), \quad \hat{u}^k = \zeta_k^3 u_3^k(x, y) \tag{2}$$

The local coordinate  $\zeta_k$  varies from  $-1$  to  $+1$  in each layer. A piecewise continuous cubic function has been used across the plate thickness for nonlinear transverse displacement. The parts of initial displacement field and the final field are given in Fig. 1.

The laminated composite plate consists of  $L$  number of perfectly bonded orthotropic layers, and the reference  $xy$ -plane passes through its midplane, where  $z = 0$ . Bottom and top surfaces of the plate are at  $z_0 = -h/2$  and  $z_L = h/2$ . The constitutive equations with respect to the structural coordinate system  $(x, y, z)$ , neglecting the transverse normal stress (i.e.  $\sigma_z = 0$ ), are

$$\sigma = \bar{Q}\varepsilon - \bar{\beta}T, \quad \tau = \hat{Q}\gamma \tag{3}$$

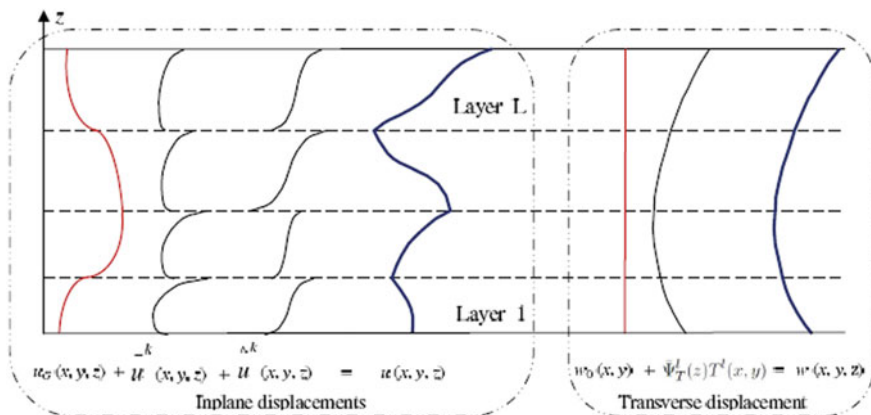


Fig. 1 Inplane and transverse displacement assumptions

where stresses, strains and coefficient matrices are

$$\begin{aligned} \sigma &= \begin{bmatrix} \sigma_x \\ \sigma_y \\ \tau_{xy} \end{bmatrix}, \quad \varepsilon = \begin{bmatrix} \varepsilon_x \\ \varepsilon_y \\ \gamma_{xy} \end{bmatrix}, \quad \bar{Q} = \begin{bmatrix} \bar{Q}_{11} & \bar{Q}_{12} & 0 \\ \bar{Q}_{12} & \bar{Q}_{22} & 0 \\ 0 & 0 & \bar{Q}_{66} \end{bmatrix}, \quad \bar{\beta} = \begin{bmatrix} \bar{\beta}_1 \\ \bar{\beta}_2 \\ 0 \end{bmatrix} \\ \tau &= \begin{bmatrix} \tau_{zx} \\ \tau_{yz} \end{bmatrix}, \quad \gamma = \begin{bmatrix} \gamma_{zx} \\ \gamma_{yz} \end{bmatrix}, \quad \hat{Q} = \begin{bmatrix} \bar{Q}_{55} & 0 \\ 0 & \bar{Q}_{44} \end{bmatrix} \end{aligned} \quad (4)$$

$\sigma_x, \sigma_y, \tau_{xy}$  are inplane stresses;  $\varepsilon_x, \varepsilon_y, \gamma_{xy}$  are inplane strains;  $\bar{Q}_{11}, \bar{Q}_{12}, \bar{Q}_{22}, \bar{Q}_{66}, \bar{Q}_{44}, \bar{Q}_{55}$  are reduced stiffness coefficients;  $\bar{\beta}_1, \bar{\beta}_2$  are reduced stress temperature coefficients;  $\tau_{zx}, \tau_{yz}$  are transverse shear stresses; and  $\gamma_{zx}, \gamma_{yz}$  are transverse shear strains, respectively. The expressions for reduced coefficients can be found in Ref. [6]. Imposition of the continuity conditions on each local term in the inplane displacement field yield

$$u_1^k + u_2^k = -u_1^{k+1} + u_2^{k+1}, \quad u_3^k = (-1)^k u_3^0 \quad (5)$$

where  $u_3^0$  is a reference layer variable. Using the displacement field expressions, the transverse shear stresses  $\tau$  are obtained. The zero boundary conditions and the interlaminar continuity conditions on  $\tau$  are imposed. The resulting sets of equations are then solved to eliminate layer-dependent terms in the displacement field, and the final expression for inplane displacement field comes out to be

$$\begin{aligned} u &= u_0 - z w_{0,d} + R^k(z) \psi_0 + \bar{R}^k(z) u_1^0 \\ &\quad + \hat{R}^k(z) u_2^0 + \tilde{R}^k(z) u_3^0 + \bar{R}^{kl}(z) T_d^l \end{aligned} \quad (6)$$

The final displacement field given in Eq. (6) is expressed in terms of reference plane variables  $u_0, w_{0,d}, \psi_0, u_1^0, u_2^0, u_3^0$ , in addition to the set of temperature variables  $T_d^0$  across the composite plate. The coefficients  $R^k(z), \bar{R}^k(z), \hat{R}^k(z), \tilde{R}^k(z), \bar{R}^{kl}(z)$  are  $2 \times 2$  matrices of cubic functions of thickness coordinate.

After defining the components of the stress and moment resultants for the laminated composite plate and then applying the virtual work principle, boundary conditions and governing equations have been obtained. Under the application of bottom and top mechanical loads  $p_z^1$  and  $p_z^2$ , the governing equations derived are

$$\begin{aligned} N_{x,x} + N_{xy,y} &= 0, \quad N_{xy,x} + N_{y,y} = 0 \\ M_{x,xx} + 2M_{xy,xy} + M_{y,yy} + p_z^1 + p_z^2 &= 0 \\ P_{x,x} + P_{xy,y} - Q_x &= 0, \quad P_{xy,x} + P_{y,y} - Q_y = 0 \\ \bar{P}_{x,x} + \bar{P}_{xy,y} - \bar{Q}_x &= 0, \quad \bar{P}_{xy,x} + \bar{P}_{y,y} - \bar{Q}_y = 0 \\ \hat{P}_{x,x} + \hat{P}_{xy,y} - \hat{Q}_x &= 0, \quad \hat{P}_{xy,x} + \hat{P}_{y,y} - \hat{Q}_y = 0 \end{aligned}$$

$$\tilde{P}_{x,x} + \tilde{P}_{xy,y} - \tilde{Q}_x = 0, \quad \tilde{P}_{xy,x} + \tilde{P}_{y,y} - \tilde{Q}_y = 0 \tag{7}$$

Governing equations for the present formulation given in Eq. (7) are a set of eleven equations stated in terms of the stress and normal resultant  $N_x, N_y, N_{xy}, M_x, M_y, M_{xy}, P_x, P_y, P_{xy}, Q_x, Q_y, Q_{xy}, \overline{P}_x, \overline{P}_y, \overline{P}_{xy}, \hat{P}_x, \hat{P}_y, \hat{P}_{xy}, \tilde{P}_x, \tilde{P}_y, \tilde{P}_{xy}, \overline{Q}_x, \overline{Q}_y, \hat{Q}_x, \hat{Q}_y, \tilde{Q}_x, \tilde{Q}_y$ .

Details of these resultants are given in Ref. [6]. The sets of boundary conditions have not written for brevity. The governing Eqs. (7) have been solved analytically for the simply supported cross-ply plates by using Fourier expansion techniques. After the solutions for the displacement variables have been obtained, the stresses have then been computed using the strain–displacement relations and the constitutive equations.

### 3 Results and Discussion

A four-layer composite plate and a sandwich plate are considered. The sandwich plate is modeled as a soft core with two face sheets on either side. The configurations of  $[0^\circ/90^\circ/90^\circ/0^\circ]$  composite plate with materials Mat1/Mat1/Mat1/Mat1 and layer thicknesses  $0.25 h/0.25 h/0.25 h/0.25 h$ , and the sandwich plate  $[0^\circ/90^\circ/0^\circ/90^\circ/0^\circ]$  with materials Face/Face/Core/Face/Face and layer thicknesses  $0.1 h/0.1 h/0.6 h/0.1 h/0.1 h$  are given in Fig. 2. The material properties of Mat 1 are:  $E_1 = 181 \text{ GPa}, E_2 = E_3 = 10.3 \text{ GPa}, G_{23} = 2.87 \text{ GPa}, G_{13} = G_{12} = 7.17 \text{ GPa}, \nu_{12} = \nu_{13} = 0.28, \nu_{23} = 0.33, \alpha_1 = 0.02 \times 10^{-6} \text{ K}^{-1}, \alpha_2 = \alpha_3 = 22.5 \times 10^{-6} \text{ K}^{-1}, k_{11} = 1.5 \text{ W/m-K}$  and  $k_{22} = k_{33} = 0.5 \text{ W/m-K}$ . The material properties of face sheet are:  $E_1 = 131.1 \text{ GPa}, E_2 = E_3 = 6.9 \text{ GPa}, G_{23} = 2.3322 \text{ GPa}, G_{13} = G_{12} = 3.588 \text{ GPa}, \nu_{12} = \nu_{13} = 0.32, \nu_{23} = 0.49, \alpha_1 = 0.0225 \times 10^{-6} \text{ K}^{-1}, \alpha_2 = \alpha_3 = 22.5 \times 10^{-6} \text{ K}^{-1}, k_{11} = 1.5 \text{ W/m-K}$  and  $k_{22} = k_{33} = 0.5 \text{ W/m-K}$ . The material properties of the core material are:  $E_1 = 0.2208 \times 10^{-3} \text{ GPa}, E_2 = 0.2001 \times 10^{-3} \text{ GPa}, E_3 = 2.76 \text{ GPa}, G_{23} = 0.4554 \text{ GPa}, G_{13} = 0.5451 \text{ GPa}, G_{12} = 0.01656 \text{ GPa}, \nu_{12} = 0.99, \nu_{13} = \nu_{23} = 0.3 \times 10^{-4}, \alpha_1 = \alpha_2 = \alpha_3 = 30.6 \times 10^{-6} \text{ K}^{-1}$  and  $k_{11} = k_{22} = k_{33} = 3.0 \text{ W/m-K}$ .

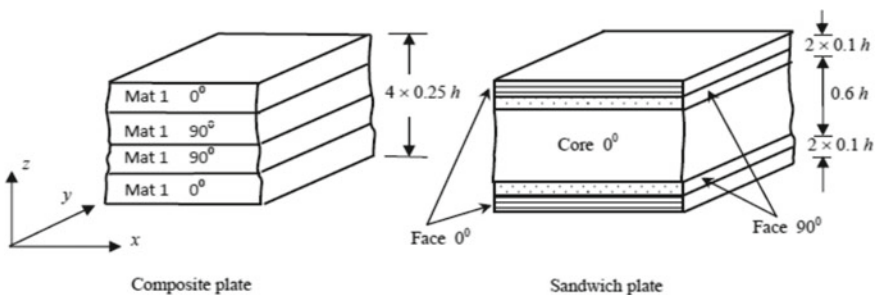


Fig. 2 Configurations of the plates

The plates are subjected to the temperature loads of  $T_t = -T_b = T_0 \sin(\pi x/a)\sin(\pi y/b)$  on the top and bottom surfaces. Through-the-thickness distribution of the resulting temperature field is obtained by solving analytically the three-dimensional equation of heat conduction after dividing each layer of the composite plate into four sublayers which are equal. Each face sheet of the sandwich plate is divided into four sublayers, while the soft core is divided into eight sublayers for discretization of the temperature.

The displacements and stresses have been non-dimensionalized as

$$\bar{u} \doteq \frac{100u}{hST_0\alpha_0}, \bar{w} \doteq \frac{100w}{hS^2T_0\alpha_0}, (\bar{\sigma}_x, \bar{\sigma}_y, \bar{\tau}_{yx}, \bar{\tau}_{zx}) \doteq \frac{(\sigma_x, \sigma_y, S\tau_{yx}, S\tau_{zx})}{E_0T_0\alpha_0}$$

where  $h$  is height of the plate,  $S$  is aspect ratio, and  $\alpha_0$  is the coefficient of thermal expansion of reference plane.  $E_0 = 10.3 \text{ GPa}$ ,  $\alpha_0 = 22.5 \times 10^{-6} \text{ K}^{-1}$ . These non-dimensionalized entities have been used in interpretation of results through all tables and figures. Non-dimensionalized displacements and stresses obtained under the applied temperature load are shown in Fig. 3 for the four-layered composite plate. Solutions have been shown for the thick square ( $b/a = 1$ ) and rectangular ( $b/a = 3$ ) plates, where  $a$  is the dimension along  $x$  axis and  $b$  is the dimension along  $y$  axis. The aspect ratio  $S = 5$  is taken for the thick plate.

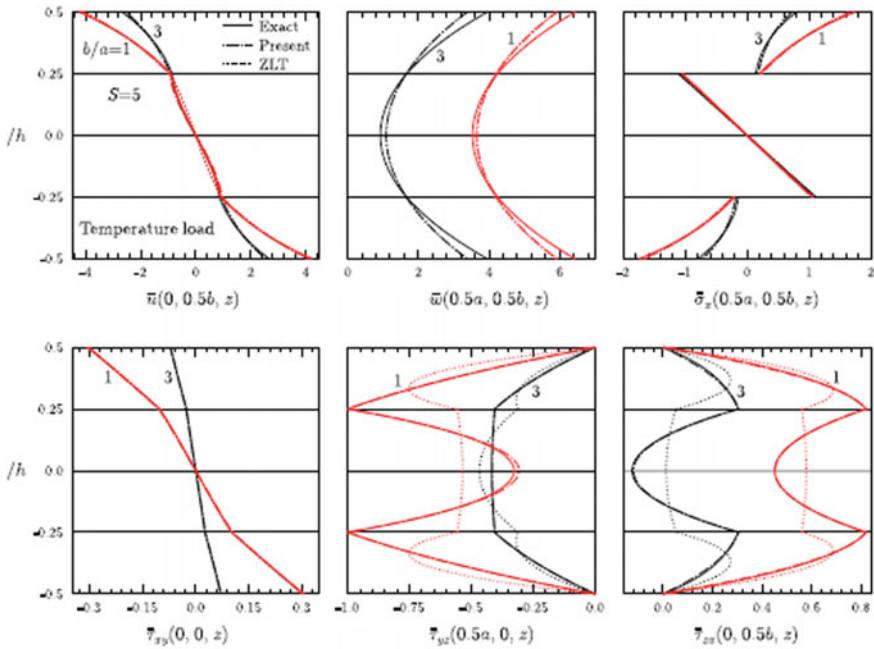


Fig. 3 Through-the-thickness distribution in composite plate under thermal load

The inplane displacement  $u$  shows zigzag nature of its distribution which is well matched with the 3D thermoelasticity response. The profile is more accurate than that yielded by the ZLT. Use of the piecewise linear function in the transverse displacement  $w$  has resulted in accurate prediction of the corresponding displacement profile. It is seen that there is almost no difference between the predictions of the present theory and the ZLT so far as the inplane stresses and transverse displacement are concerned. However, huge contrast between the two theories is observed when one delves into computing the transverse shear stresses.

Whether it is a square plate or a rectangular plate, the use of the ZLT for computation of these stresses is not at all acceptable. On the other hand, present theory is highly preferable in this aspect. It is to be borne in mind that the present theory and the ZLT have been developed on similar assumptions for the displacement field. But the two local groups in their inplane displacement components are entirely different. The difference between the two theories, in that respect, has made the distinct contrast in their transverse shear stresses computation capabilities.

The effect of aspect ratio  $S$  on the displacement and transverse stress predictions has been studied in the four-layer rectangular composite plate with length-to-width ratio  $b/a = 3$ . Whereas,  $S = 5$  defines a thick plate, the thin plate is defined by  $S = 20$ , and the moderately thick plate is defined by  $S = 10$ . In Table 1, the 3D exact solution results have been given, and the percent errors yielded by the present theory and the ZLT have been given. Specification of the percent error facilitates easy comparison of their accuracies. By comparing the percent errors predicted by the present theory, it is inferred that the percent errors decrease with increase of the aspect ratio, that is, the predictions approach the 3D exact thermoelasticity solution results as the plate becomes thinner and thinner. ZLT has shown the same trend for the displacements and inplane stresses only. The interlaminar shear stresses have been grossly mispredicted by the ZLT for thin plates also. This clearly establishes that the nature of the displacement field approximation used in the ZLT is not capable enough to correctly predict the displacement and stress fields, and hence, it needs further refinement.

In Fig. 4 are given the through-thickness variations in the response entities for the thick sandwich plate. Attention of the reader is brought to the transverse stress profiles here again. In addition to the inaccuracy in their values, their profiles are completely reversely predicted by the ZLT. Present theory is excellent in prediction of all entities. The wise selection of the terms in the local displacement groups is the only reason for the marked difference between these two theories.

Prediction accuracies in the thick and thin sandwich plates have been shown in Table 2 at  $b/a = 3$ . Accuracy predicted by the present theory has increased for the thin sandwich plate. Excepting the transverse shear stresses, the accuracy of ZLT has similarly increased for thin sandwich plate. The observations, as have been made for the present theory and ZLT while analyzing the responses of composite plate in Table 1, hold equally well for the thick and thin sandwich plates.

**Table 1** Variations in percent errors with aspect ratio  $S$  in rectangular composite plate ( $b/a = 3$ ) under temperature load

Entity	$S = 5$			$S = 10$			$S = 20$		
	3D exact	Present (% error)	ZLT (% error)	3D exact	Present (% error)	ZLT (% error)	3D exact	Present (% error)	ZLT (% error)
$\bar{u}(-0.5h)$	2.6768	- 4.60	- 5.68	2.3760	- 1.40	- 1.73	2.2936	- 0.37	- 0.45
$\bar{u}(0.5h)$	- 2.6768	- 4.60	- 5.68	- 2.3760	- 1.40	- 1.73	- 2.2936	- 0.37	- 0.45
$\bar{w}(0)$	0.9246	18.28	17.24	1.3214	3.15	2.94	1.4127	0.73	0.68
$\bar{\tau}_{yz}(-0.25h)$	- 0.4060	- 0.09	- 23.23	- 0.4277	- 0.02	- 22.46	- 0.4336	0.00	- 22.25
$\bar{\tau}_{yz}(0.25h)$	- 0.4060	- 0.09	- 23.23	- 0.4277	- 0.02	- 22.46	- 0.4336	0.00	- 22.25
$\bar{\tau}_{zx}(-0.25h)$	0.3044	0.31	- 82.71	0.3301	0.09	- 80.13	0.3371	0.02	- 79.47
$\bar{\tau}_{zx}(0.25h)$	0.3044	0.31	- 82.71	0.3301	0.09	- 80.13	0.3371	0.02	- 79.47



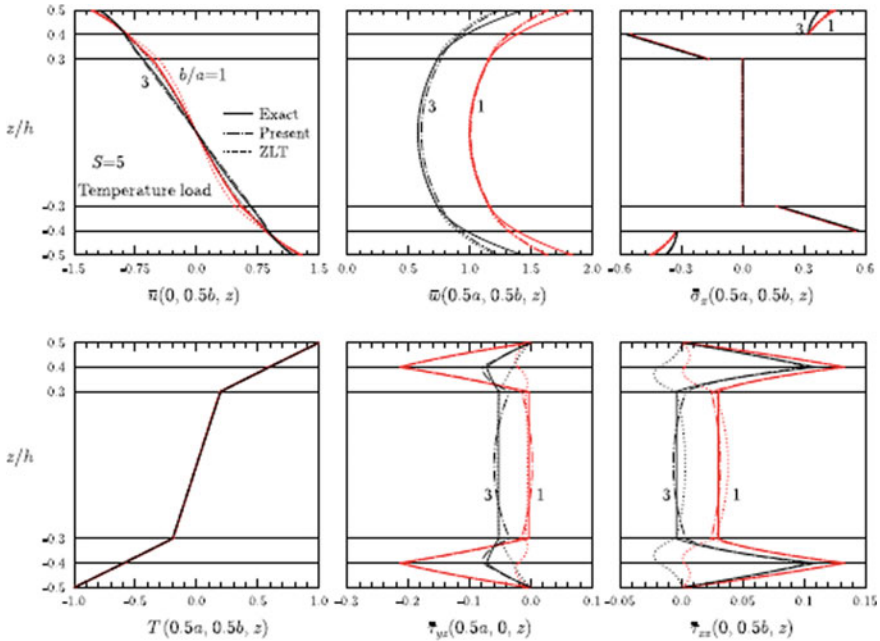


Fig. 4 Through-thickness distribution in sandwich plate under thermal load

### 4 Conclusions

The superposition employed to combine two local groups, namely a two-term quadratic local group and a one-term cubic local group, with the zigzag theory approximation to make the approximations for inplane displacements with an aim to calculate accurately the transverse shear stresses from the constitutive equations directly has been met with success. This theory has predicted the deflections and stresses in the thick and thin as well as the square and rectangular laminated composite plates much more accurately than the zigzag-local theory developed by following the similar approach, but with two single-term local groups. The results analyzed for a laminated composite plate and a sandwich plate have established the effect of the correct selection of the terms in the two local groups of the displacement field approximation. Such selection has not only yielded accurate responses but also provided the capability for calculation of the transverse shear stresses correctly from the constitutive equations.

**Table 2** Variations in percent errors with aspect ratio  $S$  in rectangular sandwich plate ( $b/a = 3$ ) under temperature load

Entity	$S = 5$			$S = 10$			$S = 20$		
	3D exact	Present (% error)	ZLT (% error)	3D exact	Present (% error)	ZLT (% error)	3D exact	Present (% error)	ZLT (% error)
$\bar{u}(-0.5h)$	1.1947	-1.80	-0.70	1.1996	-0.45	-0.18	1.2052	-0.11	-0.04
$\bar{u}(0.5h)$	-1.1947	-1.80	-0.70	-1.1996	-0.45	-0.18	1.2052	-0.11	-0.04
$\bar{w}(0)$	0.5786	4.67	-0.58	0.7316	0.88	-0.88	0.7606	0.21	-0.02
$\bar{\tau}_{yz}(-0.4h)$	-0.0725	9.36	-59.88	-0.0768	11.75	-50.97	-0.0784	12.59	-47.73
$\bar{\tau}_{yz}(0.4h)$	-0.0725	9.36	-59.88	-0.0768	11.75	-50.97	-0.0784	12.59	-47.73
$\bar{\tau}_{zx}(-0.4h)$	0.1098	-6.07	-116.94	0.1171	-5.37	-112.86	0.1199	-5.12	-111.43
$\bar{\tau}_{zx}(0.4h)$	0.1098	-6.07	-116.94	0.1171	-5.37	-112.86	0.1199	-5.12	-111.43

## References

1. Pendhari SS, Kant T, Desai YM (2008) Application of polymer composites in civil construction, a general review. *Compos Struct* 84:114–124
2. Reddy JN (1984) A simple higher-order theory for laminated composite plates. *J Appl Mech* 51:745–752
3. Cho M, Parmerter RR (1993) Efficient higher order composite plate theory for general lamination configurations. *AIAA J* 31:1299–1306
4. Shu X, Sun L (1994) An improved simple higher-order theory for laminated composite plates. *Comput Struct* 50:231–236
5. Zhen W, Wanji C (2007) A study of global-local higher-order theories for laminated composite plates. *Compos Struct* 79:44–54
6. Nath JK, Kapuria S (2013) Global-local and zigzag-local theories for direct transverse shear stress computation in piezolaminated plates under thermal loading. *Int J Mech Sci* 75:158–169

# Solution to Real-Time Problem in Shifter Knob Assembly at Automobile Manufacturing Industry



Prabinkumar R. Jachak, Abhay Khalatkar, Nilesh M. Narkhede,  
and Rupesh Shelke

**Abstract** To accomplish the desire target, various operations take place simultaneously at automobile manufacturing industries every day. As their market demand is on peak, enormous parts are being manufactured and assembled daily at the industry in a limited amount of time. Due to which confusion between similar looking parts among operator/labor gets created. This eventually leads to wrong fitment of component on automobile. Therefore, doing operations in a traditional way are not accepted nowadays. To increase overall performance, industries are embracing toward automation technologies to improve their processes, production rate, work efficiency, and so on. In this paper, we have discussed the case study which we have conducted in one of the automobile manufacturing industry to optimize the gear shifter knob selection process on assembly line for various models of the tractor. Also, we have elaborated the real-time problem of wrong fitment of shifter knob on automobile during its assembly operations and have provided solution for the same.

**Keywords** Real-time problem · Automobile industry · Knob assembly · Gear shifter knob · Range shifter knob · Tractor manufacturing industry

## 1 Introduction

Multinational companies like Mahindra and Mahindra, John Deere, Ford Motors, and so on produce many variants of automobile in short period of time [1]. All these variants have many components to assembly within this time; thus, sometimes worker/operator/labor gets confuse between similar looking parts during fitment of those components on their respective automobile. This eventually leads to wrong fitment of component on that automobile. To eliminate possibility of fitment of

---

P. R. Jachak (✉) · A. Khalatkar · R. Shelke  
G.H Raisoni College of Engineering, Nagpur, India  
e-mail: [prabinjachak8@gmail.com](mailto:prabinjachak8@gmail.com)

N. M. Narkhede  
Mahindra and Mahindra Limited, Nagpur, India

different component on different automobile from the process, we should introduce technology into the process. Automobile industries are always into developing and accepting technological innovations for maximizing their efficiency in industrial production processes, managerial effectiveness to compete with competitors, and be top in the market [2–4]. Thus nowadays, many companies are eliminating traditional manufacturing and assembly operations for product and adopting industry 4.0 to significantly improve product quality, process efficiency, international competitiveness, productivity, and great profits [5, 6]. Also, Spanish companies like Nissan, SEAT, and Renaults have already implemented it in their organizations successfully [7]. During this case study, we focused to analyze problem regarding wrong fitment of components on automobile and have implemented solution (i.e., a machine developed using concept of poka-yoke) for the same on the assembly line at one of the automobile manufacturing industry. In this paper, we have elaborated problem and provided solution for real-time problem of wrong shifter knobs fitment on automobile occurring at automobile manufacturing industry.

## 2 Literature Review

An automobile shift knob is the knob placed on top of lever which allows user to change gears in automatic-transmission vehicle [8]. Main shifter knobs which assemble on heavy duty automobile are gear shifter knobs, range shifter knobs, power take off (PTO) knobs, hand accelerator knobs. Embossing on gear shifter knobs and range shifter knobs is different as shown in Figs. 1 and 4. But if we neglect their embossing and want to choose desire knob, then it would be very difficult for us to select as their physical appearance and assembly socket are same as shown in Figs. 2, 5, and Figs. 3, 6, respectively.

During our case study, we found that assembly socket of all shifter knobs is same (as shown in Figs. 3 and 6) and these knobs can easily get assemble on any gear shifter lever of automobile. This is the common error in manual selection of gear knob shifter during it assemble on automobile.



**Fig. 1** Gear shifter knobs having same dimension with different embossing



**Fig. 2** Side view of different gear shifter knobs

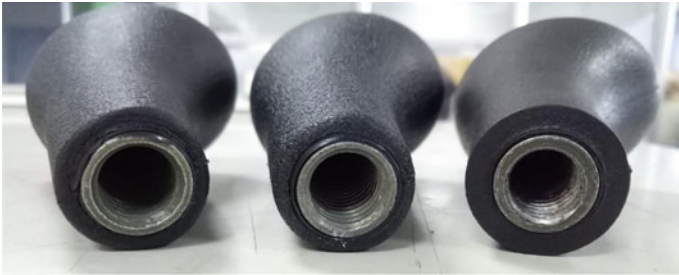


**Fig. 3** Bottom view of different gear shifter knobs



**Fig. 4** Range shifter knobs having same dimension with different embossing



**Fig. 5** Side view of range shifter knobs

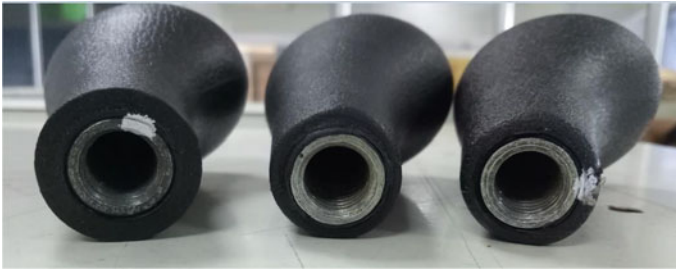


**Fig. 6** Bottom view of range shifter knobs

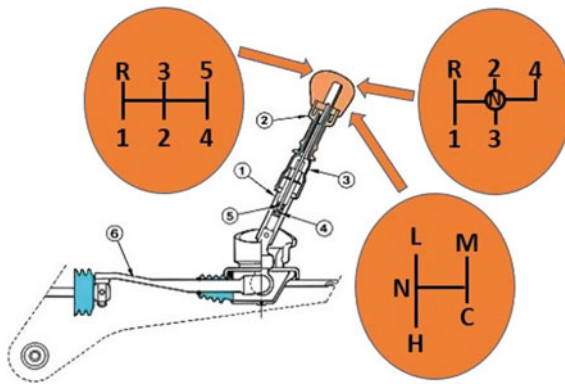


**Fig. 7** Possibilities of knob fitment on shifter lever

Since assembly socket of shifter knobs is same, above figure shows the visual possibilities that any shifter knob (i.e., gear shifter or range shifter) could be fitted on shifter lever of any tractor. As shown in Fig. 7, shifter is a complete unit and in case of failure must be completely replaced. And if mismatched fitment of shifter knobs activity happens (as shown in Fig. 7), then it could not only affect quality of product, failure of gear box but also could harm operator. Fault correction at this stage definitely increases the obstacles. Thus, to eliminate this problem, we have developed a machine which is not only providing ease in its assembly process but also eliminating chances of mismatching during its assembly on automobile.

### 3 Methodology

In this project, we have used concept of poka-yoke to build solution for the above elaborated problem [9]. Firstly, we studied the properties of knob and tried to find out property which makes it unique from rest. And after the research, we found out that embossing of shifting pattern on them makes them unique (as shown in Figs. 1 and

**Table 1** Master file

S. No.	Variants	Model	Model No.	Knob
1	605 REG	52 HP	WHBCYE, WHBCAE	Part no. 17546945B14

The master file has all information of variant, model, model number and photograph of shifter knobs along with its part number

4). As we found loop hole, we decided to make machine as a solution which cannot only help to segregate all knobs but also can eliminates chances of their mismatched fitment on automobile. At the first stage of manufacturing of automobile, each automobile get allotted with the unique serial number separately and also that number gets printed on the same. Also, it gets printed on its travel card along with its barcode (as shown below). Thus, using that unique series number, we can track/identify any automobile.

**Automobile serial number:** MBNWHBCAEKNA03305



Every alphanumeric combination in the automobile serial number behaves as an information code. In the above mentioned example, the highlighted six alphabets are known as the automobile series. Bill of material (BOM) of automobile is fetched up with its respective unique series. The programmable logic controller (PLC) system is based on comparing the recognized characters against the master file maintained in the form of excel sheet (as shown in Table 1 as an example).

Figure 8 shows the photograph of developed machine. After completing first step that is scanning a barcode present on traveler card of automobile with scanner, data which we have stored in programmable logic controller (PLC) unit in the form of master file will get triggered and will actuate the pneumatic cylinder installed in the machine which is allotted for respective input to open the door of container having knob which is to be assembled on respective automobile. After opening the door of container (with respective input), operator will pick up the knob and will assemble it on that automobile. This whole process gets completed within 1.5–2 min. Inside the container, we have installed a part sensor which gives indication to PLC if the container is about to empty. This way operator gets indications to refill the container. The whole process from loading to unloading operation for one knob gets completed with an average time of 3.21 min. This machine only requires pneumatic supply for actuating the pneumatic cylinders and power supply for PLC working. Piezoelectric elements have various application for generating electricity in an convenient way [10–12]. As we required power supply to operate PLC panel, we are also trying to develop a mechanism using piezoelectric element so that we could generate and use required amount of electricity economically.



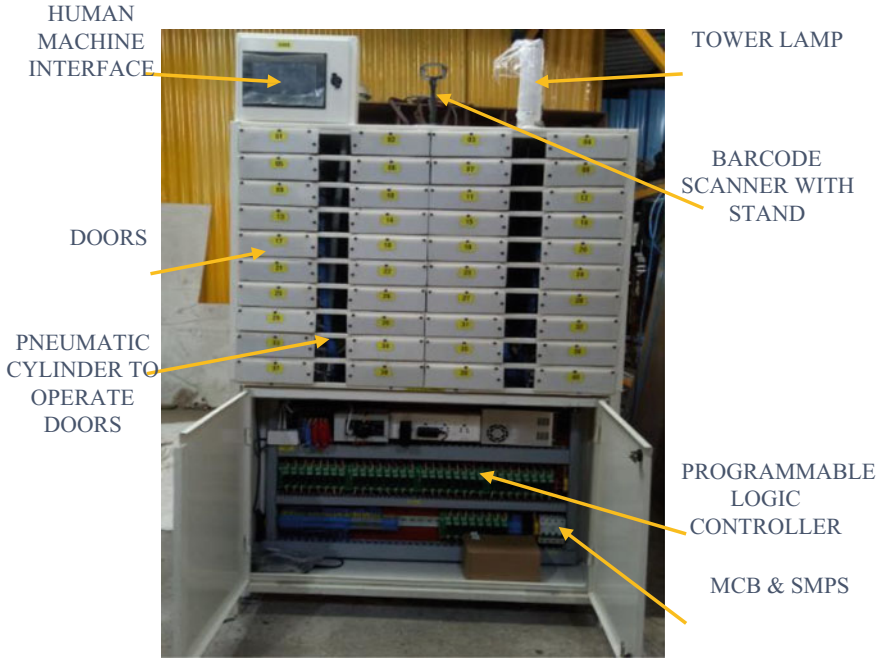


Fig. 8 Actual photograph of machine

### 4 Results and Discussion

After installing this machine on the assembly line at automobile manufacturing industry, we compared some factors of the previous process with new one and portrayed those using graphs. First entity which we have compared is time consumption for fitment of one knob on automobile in respective shifts (Fig. 9).

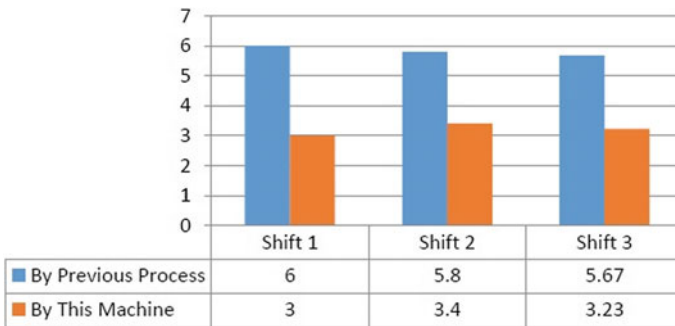
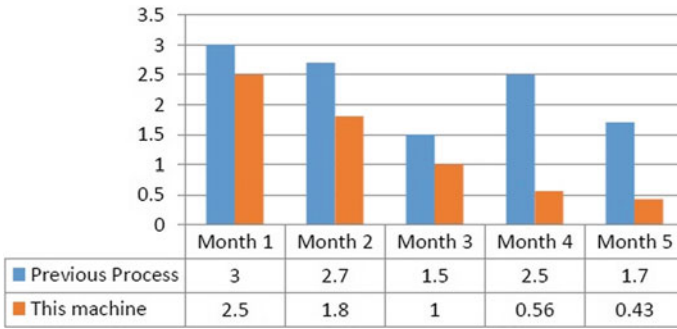


Fig. 9 Average time consumption to complete the process (in min)



**Fig. 10** Detection of mismatched fitment of knobs found on automobile (per month on scale of 10)

After analyzing, we found that our machine is not only providing accuracy and ease in process but also consuming less time than in the previous process which is eventually promotes increase in production rate. It is also providing cost saving for company by eliminating manpower requirement. We have designed and fabricated our machine by considering the concepts/factors of ergonomics and fatigue management without compromising the main factors to be consider while designing new machine that is cost of machine, operational safety, ease of assembly, and so on [13–15]. So that manpower involved in this process could work efficiently (Fig. 10).

## 5 Conclusion

We have successfully designed and developed a machine (as shown in Fig. 8) using concept of poka-yoke which is helping respective automobile manufacturing industry to resolve real-time shifter knob mismatched problem. With the help of this case study and fabricated project, we have reduced occurrence of mismatched fitment of shifter knob on automobile, increased work efficiency of manpower working in the process, accuracy in shifter knob fitment process, cost saving by eliminating excess manpower requirement, have reduced time consumption to complete whole fitment process, fatigue management, and so on. We are also working on this machine by conducting further R&D using tools like FMEA, model-based development and simulations, quality function deployment (QFD), and so on to increase reliability, system quality, durability, safety, as well as trust in the system [16, 17].

## References

1. New cars, car price, car model and variants in India—Times of India. <https://timesofindia.indiatimes.com/zigwheels.cms>. Accessed 15 May 2021
2. Peters S, Chun J-H, Lanza G (2016) Digitalization of automotive industry-scenarios for future manufacturing. <https://doi.org/10.1051/mfreview/2015030>
3. Pinto B, Silva FJG, Costa T, Campilho RDSG, Pereira MT (2019) A strategic model to take the first step towards industry 4.0 in SMEs. *Procedia Manuf* 38:637–645. <https://doi.org/10.1016/j.promfg.2020.01.082>
4. Industry 4.0: the future of productivity and growth in manufacturing industries. [https://www.bcg.com/publications/2015/engineered\\_products\\_project\\_business\\_industry\\_4\\_future\\_productivity\\_growth\\_manufacturing\\_industries](https://www.bcg.com/publications/2015/engineered_products_project_business_industry_4_future_productivity_growth_manufacturing_industries). Accessed 15 May 2021
5. Fromhold-Eisebith M, Marschall P, Peters R, Thomes P (2021) Torn between digitized future and context dependent past—how implementing ‘Industry 4.0’ production technologies could transform the German textile industry. *Technol Forecast Soc Change* 166:120620. <https://doi.org/10.1016/j.techfore.2021.120620>
6. Llopis-Albert C, Rubio F, Valero F (2021) Impact of digital transformation on the automotive industry. *Technol Forecast Soc Change* 162:120343. <https://doi.org/10.1016/j.techfore.2020.120343>
7. F. Investment and T. M. Survey, *OF*
8. Custom shift knobs: get the facts and install one yourself—Autos.com. <https://www.autos.com/aftermarket-parts/how-to-install-an-automatic-shift-knob>. Accessed 15 May 2021
9. Widjajanto S, Purba HH, Jaqin SC (2020) Novel poka-yoke approaching toward industry-4.0: a literature review. *Oper Res Eng Sci: Theory Appl* 3(3):65–83. <https://doi.org/10.31181/oresta20303065w>
10. The piezoelectric effect—Piezoelectric Motors & Motion Systems. <https://www.nanomotion.com/nanomotion-technology/piezoelectric-effect/>. Accessed 25 Aug 2021
11. Khalatkar AM, Gupta VK (2017) Piezoelectric energy harvester for low engine vibrations. *J Renew Sustain Energy* 9(2). <https://doi.org/10.1063/1.4979501>
12. Haldkar R, Gupta VK, Kumar Haldkar R, Khalatkar A, Kumar Gupta V, Sheorey T (2020) New piezoelectric actuator design for enhance the micropump flow. It was an MHRD project on development of virtual laboratories for engineering students to run experiments without having costly setup and gain full understanding. View project Injection Molding and Polymer Composites View project New piezoelectric actuator design for enhance the micropump flow. <https://doi.org/10.1016/j.matpr.2020.10.702>
13. Casilla K (2021) Factors to be considered during machine design [Online]. Available at: [https://www.academia.edu/39771745/Factors\\_to\\_be\\_considered\\_during\\_Machine\\_Design](https://www.academia.edu/39771745/Factors_to_be_considered_during_Machine_Design). Accessed 15 May 2021
14. Design Considerations | Machine Design. <https://www.machinedesign.com/fastening-joining/article/21812885/design-considerations>. Accessed 15 May 2021
15. Consulting—Specifying Engineer | 14 aspects to consider in equipment selection. <https://www.csemag.com/articles/14-aspects-to-consider-in-equipment-selection/>. Accessed 15 May 2021
16. Are these the best tools for R&D Management? | R&D Today. <https://www.rmdtoday.co.uk/latest-news/are-these-the-best-tools-for-rd-management/>. Accessed 15 May 2021
17. Mityakova OI, Chernenko AV (2018) Tools for planning research and development projects. *Econ Ind* 11(1):29–36. <https://doi.org/10.17073/2072-1633-2018-1-29-36>

# Dislocation Analysis of Laser-Sintered Al Alloy Nanoparticles in Using Molecular Dynamics Simulation



Jyotirmoy Nandy, Seshadev Sahoo, and Hrushikesh Sarangi

**Abstract** Additive manufacturing (AM) processes have proved to be the most efficient manufacturing techniques over the past decade due to the ease of manufacturing, faster production, and less wastage of raw materials. Direct metal laser sintering (DMLS) is one of the widely used AM processes in which a high-power laser is used to scan over the powder bed according to the required design. Added to this, computational modeling has allowed researchers to predict the material behavior in an efficient manner which further helps in optimizing as well as reducing the material wastage. In the present work, a molecular dynamics (MD) model has been used for studying the emergence of dislocations in the AlSi10Mg nanoparticle pairs during sintering. Dislocation analysis (DXA) and dislocation density are used to understand the effect of laser energy densities on the occurrence of different types of dislocations during the sintering process.

**Keywords** Laser sintering · Molecular dynamics · Defects · Dislocations

## 1 Introduction

The era of traditional manufacturing has reached a point where other advanced technologies are emerging to be more efficient and less time taking. Gradually, over the last decade, AM processes have established their capabilities in manufacturing intricate parts with high-quality precision [1]. Among numerous AM processes, the DMLS process has added advantages such as part weight reduction, production of strong and durable components, high accuracy in fine details, and ease of functional testing which allows for more severe testing of prototypes. Unlike in selective laser melting (SLM) where metal powders are completely melted, the DMLS process utilizes a high-power laser source for the fusion of powdered metal to produce solid parts in a layer-by-layer build technique [2–4].

---

J. Nandy (✉) · S. Sahoo · H. Sarangi

Department of Mechanical Engineering, Institute of Technical Education and Research, Siksha 'O' Anusandhan (Deemed to be University), Bhubaneswar, Odisha 751030, India  
e-mail: [jeetmusicedition@gmail.com](mailto:jeetmusicedition@gmail.com)

The variation in process parameters affects the thermo-mechanical aspects of the final products manufactured using the DMLS process. It is difficult to understand the technical aspects of manufacturing completely dense parts. As a result, the need for computational modeling has increased severely to understand and predict the evolution of microstructure and various other material properties. In the past few decades, continuum and mesoscale modeling were used extensively for the prediction of microstructural properties of materials under different manufacturing techniques [5–7]. However, when the beam radius is much larger than the particle radius, the validity of these modeling techniques is limited. Atomistic modeling, on the other hand, has been more advantageous due to its applicability at the nanoscale level which provides a deeper insight into the underlying mechanisms of the manufacturing processes. The molecular dynamics (MD) method has been an efficient tool to study the material characteristics, process mechanism, physical, and mechanical properties of materials using which many researchers have focused on the neck growth mechanisms and have studied the effect of sintering rates on the final structures. Sementa et al. [8] performed an analysis for examining melting and sintering in Si nanoparticles with the help of classical MD simulations. This study focused on the effects of the melting point on nanoparticle size. Liu et al. [9] examined the coalescence of  $\text{Fe}_2\text{O}_3$  corresponding to two different temperatures (300 and 1300 K). This study proposed the evaluation of the sintering degree using the sintering area and effective sintering volume. Yang et al. [10] investigated the sintering process of Li and Pb nanoparticles at three different temperatures (200, 250, and 400 K). The authors identified the dismantled contact region, an ensemble of atoms at a distinct thermodynamic stage, and phase formation in mixed regions as three stages of sintering for all three cases. Nandy et al. [11] performed MD simulations on AlSi10Mg nanoparticles in DMLS to study the coalescence of multi-component Al powders using two sets of particles of radii 40–40 Å and 40–20 Å. This study showed that the diffusion rate was faster in multi-component alloys than in pure metal. He et al. [12] investigated the sintering of graphene nanoplatelet (GNP) reinforced aluminum matrix composite powder using MD simulations. This study showed that particle size and coalescence temperature had vital effects on the rate of sintering. Seunghwa et al. [13] studied the coalescence kinetics and mechanical behavior of thermally sintered nanoporous Cu nanoparticles. Three different sizes (4, 5, and 6 nm) were selected to study the effect of size at temperatures 300, 500, and 700 K. Few other researchers examined the sintering phenomena in Ni and Ti particles to understand the characteristics of the sintering process [14, 15]. Hu et al. [16] performed atomistic modeling to study the thermal, kinetic, and mechanical behavior of pressure-assisted Cu nanoparticles during sintering. They found that elevation of temperature can promote atomic diffusion around the defects. Albooyeh et al. [17] used MD simulations to study the mechanical properties of boron nitride (BN) nanotubes with different numbers of doped carbon atoms. Under uniaxial tensile loading at a constant strain rate, it was found that the armchair structures appeared in higher numbers than those of zigzag structure in every type of vacancy defect. Yasbolaghi et al. [18] modeled fatigue crack propagation using molecular dynamics for single and polycrystalline structures under cyclic loading/unloading. They found that microstructural barriers decrease

crack growth significantly which leads to crack arrest. Most of the studies which were carried out by researchers have mostly been focused on the sintering behavior of different materials. Comparatively, very few findings have been reported which study the defect formation in Al alloy nanoparticles during the sintering process.

Hence, in this study, defect formation due to different types of dislocations is studied during the laser sintering of AlSi10Mg nanoparticles. The variation in dislocations is studied using the dislocation densities at varying laser energy densities.

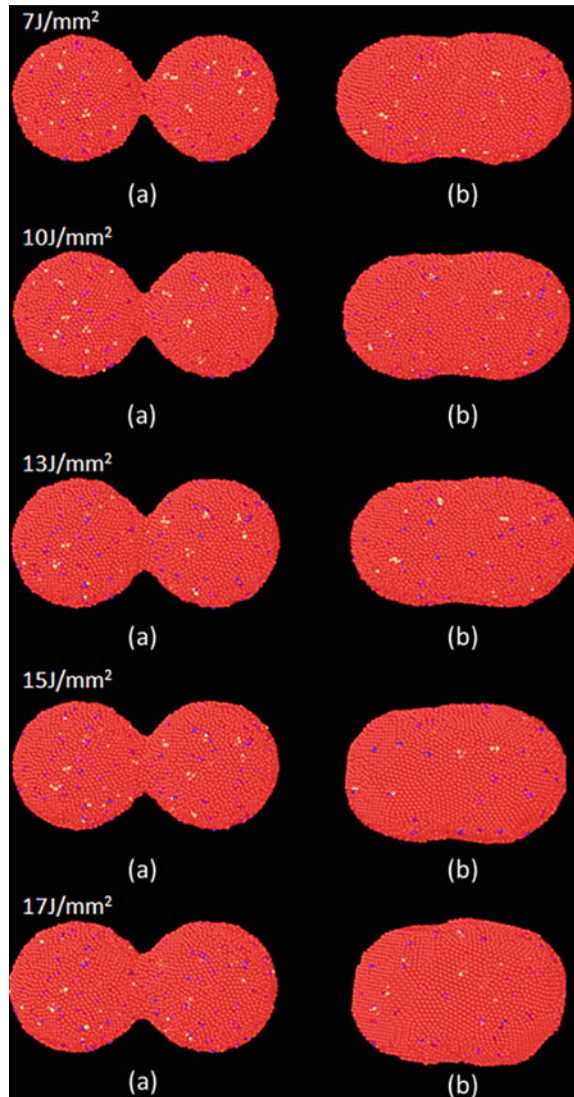
## 2 Modeling Details and Simulation Procedure

For consolidation of AlSi10Mg nanoparticles by varying laser energy density, a hybrid overlay method has been employed to model interatomic interactions between Al, Si, and Mg particles. The details of interatomic interactions can be found in the works of Nandy et al. [19]. Large-scale atomic/molecular massively parallel simulator (LAMMPS) from Sandia National Laboratories [20] is used for all sintering and tensile simulations. Open visualization tool, OVITO has been used to visualize the MD profiles and other properties. Different laser energy densities are incorporated within the simulation domain with help of the NVT ensemble. In this work, the laser energy densities are incorporated in terms of temperature. A specific range of temperatures has been extracted from the thermal model developed by Panda et al. [21]. For creating a pre-alloyed AlSi10Mg system, the simulation domain is occupied using spherical Al particles possessing a lattice constant of 4.05 Å. Si and Mg atoms have been included by swapping Al atoms at a weight fraction of 0.10 and 0.05, respectively. Similarly, another spherical nanoparticle of radius 4 nm is replicated and placed at a center-to-center distance of 8.3 nm from the first nanoparticle. The nanoparticle pair is placed in a simulation domain of length 500 Å × 500 Å × 500 Å in the X, Y, and Z-direction. A total of 32,299 numbers of atoms are placed in the system with a crystallographic orientation of <100> , <010> , and <001> in the x, y, and z directions. The shrink-wrapped boundary condition is applied in all directions. The nanoparticle pair is equilibrated at 300 K for 20 ps to stabilize the atoms. With increasing laser energy densities (7 J/mm<sup>2</sup> to 17 J/mm<sup>2</sup>), the temperatures are increased in the simulation domain. Visualization and analysis software OVITO are used to study the different types of dislocations in AlSi10Mg nanoparticle pairs formed during the sintering process. Figure 1 depicts the sintered profiles of AlSi10Mg pairs during the initial and final stages of sintering.

## 3 Results and Discussion

The microstructure of DMLS built AlSi10Mg comprises cell-like structures where the primary structures are  $\alpha$ -Al which are confined by the eutectic Si walls. Due to the microstructural behavior of AlSi10Mg, the pre-existence of dislocation networks

**Fig. 1** MD profiles of AlSi10Mg nanoparticle pairs during **a** initial stage of sintering (20 ps) and **b** final stage of sintering (450 ps)



is obvious. Figure 2 represents the final sintered profiles of DMLS built AlSi10Mg at a specific laser energy density of  $7 \text{ J/mm}^2$ . It was observed from the MD profiles that the number of pre-existing dislocations was higher during the application of higher laser energy densities.

For example, the number of dislocation segments in the case of laser energy density  $7 \text{ J/mm}^2$  was found to be 7 (Fig. 2) which increases to 28 dislocation segments after the tensile testing. Also, the freely moving dislocation segments give rise to the generation of new ones. As a result, complex networks of entangled dislocation segments



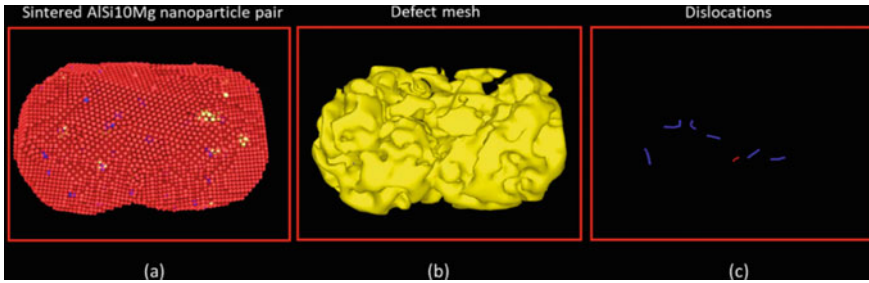


**Fig. 2** MD profiles of **a** DMLS built AlSi10Mg nanoparticles **b** defect mesh **c** dislocations

are found all over the system. Therefore, the input laser energy densities play a major role during the generation of numerous defects in the overall system. Figure 3 shows the number of dislocation segments for cubical samples of DMLS built AlSi10Mg. Table 2 shows the measured total dislocation line length and dislocation density of the deformed cuboidal samples concerning their corresponding laser energy densities. Figure 4 shows the trend of dislocation density with increasing laser energy densities. Due to increased internal stresses, the generation of dislocations increases inside the core of the nanoparticles. Hence, it was observed that the dislocation density increases with increasing laser energy density (Table 1).

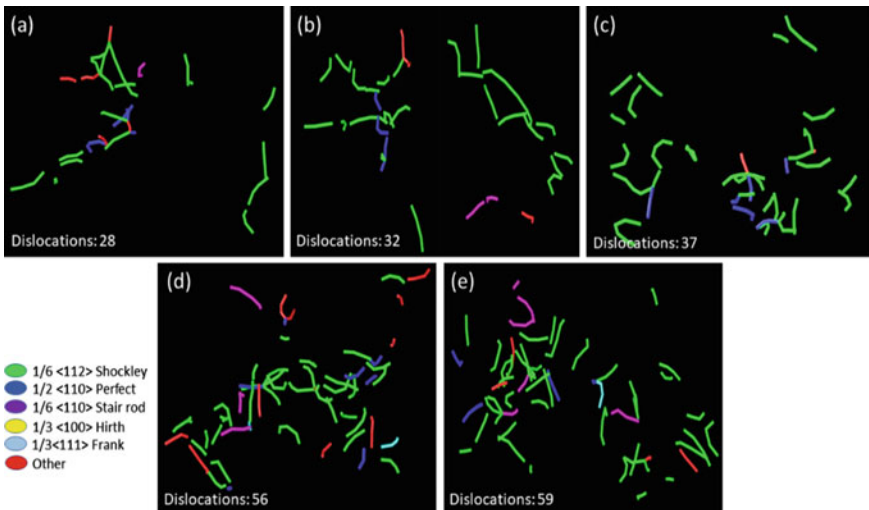


**Fig. 3** Number of dislocation segments for AlSi10Mg cuboidal tensile samples for different laser energy densities **a** 7 J/mm<sup>2</sup>, **b** 10 J/mm<sup>2</sup>, **c** 13 J/mm<sup>2</sup>, **d** 15 J/mm<sup>2</sup>, **e** 17 J/mm<sup>2</sup>



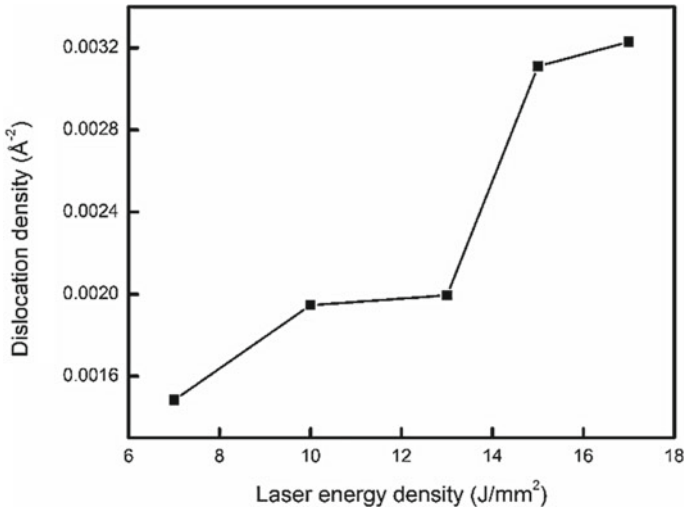


**Fig. 4** Effect of laser energy density on dislocation density of AlSi10Mg sample in DMLS

**Table 1** Different types of dislocations at varying laser energy densities

S. No.	Laser energy density (J/mm <sup>2</sup> )	Type of dislocations			
		Perfect <110>	Shockley <112>	Stair rod <110>	Other
1	7	4	18	1	5
2	10	3	24	2	3
3	13	6	29	0	2
4	15	7	35	3	12
5	17	4	41	6	4

**Table 2** Total dislocation line length and dislocation density at different laser energy densities

Laser energy density (J/mm <sup>2</sup> )	Total dislocation line length (Å)	Dislocation density (Å <sup>-2</sup> )
7	267.406	0.001485
10	350.923	0.001948
13	359.052	0.001994
15	560.971	0.003116
17	583.032	0.003234

## 4 Conclusion

MD simulations were used to examine the dislocations formed during the laser sintering of AlSi10Mg nanoparticles. A hybrid overlay method was used to model the AlSi10Mg nanoparticle pairs where sintering temperature was extracted from a

thermal model. It was found that laser energy densities play a vital role in the formation of dislocation segments during the sintering process. The increase in laser energy densities increased the dislocation segments. The dislocation density of AlSi10Mg nanoparticle pairs was measured and plotted with respect to corresponding laser energy densities. The results showed that the rising internal stresses inside the core of the nanoparticles lead to an increase in dislocation densities with respect to increasing laser energy densities.

## References

1. Attaran M (2017) The rise of 3-D printing: the advantages of additive manufacturing over traditional manufacturing. *Bus Horiz* 60(5):677–688
2. Singh S, Ramakrishna S (2017) Biomedical applications of additive manufacturing: present and future. *Curr Opin Biomed Eng* 2:105–115
3. Camacho DD, Clayton P, O'Brien WJ, Seepersad C, Juenger M, Ferron R, Salamone S (2018) Applications of additive manufacturing in the construction industry—a forward-looking review. *Autom Constr* 89:110–119
4. Liu R, Wang Z, Sparks T, Liou F, Newkirk J (2017) Aerospace applications of laser additive manufacturing. In: *Laser additive manufacturing*. Woodhead Publishing, pp 351–371
5. Zhang Y, Chen Q, Guillemot G, Gandin CA, Bellet M (2018) Numerical modelling of fluid and solid thermomechanics in additive manufacturing by powder-bed fusion: Continuum and level set formulation applied to track-and part-scale simulations. *Comptes Rendus Mécanique* 346(11):1055–1071
6. Ji Y, Chen L, Chen LQ (2018) Understanding microstructure evolution during additive manufacturing of metallic alloys using phase-field modeling. In: *Thermo-Mechanical modeling of additive manufacturing*. Butterworth-Heinemann, pp 93–116
7. Nandy J, Sarangi H, Sahoo S (2018) Microstructure evolution of Al-Si-10Mg in direct metal laser sintering using phase-field modeling. *Adv Manufact* 6(1):107–117
8. Sementa L, Barcaro G, Monti S, Carravetta V (2018) Molecular dynamics simulations of melting and sintering of Si nanoparticles: a comparison of different force fields and computational models. *Phys Chem Chem Phys* 20(3):1707–1715
9. Liu Z, Cheng Q, Li K, Wang Y, Zhang J (2020) The interaction of nanoparticulate Fe<sub>2</sub>O<sub>3</sub> in the sintering process: a molecular dynamics simulation. *Powder Technol*
10. Yang L, Gan X, Xu C, Lang L, Jian Z, Xiao S, Deng H, Li X, Tian Z, Hu W (2019) Molecular dynamics simulation of alloying during sintering of Li and Pb metallic nanoparticles. *Comput Mater Sci* 156:47–55
11. Nandy J, Yedla N, Gupta P, Sarangi H, Sahoo S (2019) Sintering of AlSi10Mg particles in direct metal laser sintering process: a molecular dynamics simulation study. *Mater Chem Phys* 236:121803
12. He H, Rong Y, Zhang L (2019) Molecular dynamics studies on the sintering and mechanical behaviors of graphene nanoplatelet reinforced aluminum matrix composites. *Model Simul Mater Sci Eng* 27(6):065006
13. Yang S, Kim W, Cho M (2018) Molecular dynamics study on the coalescence kinetics and mechanical behavior of nanoporous structure formed by thermal sintering of Cu nanoparticles. *Int J Eng Sci* 123:1–19
14. Zhang Y, Zhang J (2016) Sintering phenomena and mechanical strength of nickel based materials in direct metal laser sintering process—a molecular dynamics study. *J Mater Res* 31(15):2233–2243
15. Jeon J, Jiang S, Rahmani F, Nouranian S (2020) Molecular dynamics study of temperature and heating rate-dependent sintering of titanium nanoparticles and its influence on the sequent tension tests of the formed particle-chain products. *J Nanopart Res* 22(1):1–12

16. Hu D, Cui Z, Fan J, Fan X, Zhang G (2020) Thermal kinetic and mechanical behaviors of pressure-assisted Cu nanoparticles sintering: a molecular dynamics study. *Results Phys* 19:103486
17. Albooyeh AR, Dadrasi A, Mashhadzadeh AH (2020) Effect of point defects and low-density carbon-doped on mechanical properties of BNNTs: a molecular dynamics study. *Mater Chem Phys* 239:122107
18. Yasbolaghi R, Khoei AR (2020) Micro-structural aspects of fatigue crack propagation in atomistic-scale via the molecular dynamics analysis. *Eng Fract Mech* 226:106848
19. Nandy J, Sahoo S, Yedla N, Sarangi H (2020) Molecular dynamics simulation of coalescence kinetics and neck growth in laser additive manufacturing of aluminum alloy nanoparticles. *J Mol Model* 26(6)
20. Plimpton S, Crozier P, Thompson A (2007) LAMMPS-large-scale atomic/molecular massively parallel simulator. Sandia National Laboratories, vol 18, p 43
21. Panda, B.K. and Sahoo, S., 2018, March. Numerical simulation of residual stress in laser based additive manufacturing process. In: *IOP conference series: materials science and engineering*, vol 338, no 1. IOP Publishing, p 012030

# Design and Development of Special Purpose Vehicle for Hilly Area



Dilip S. Choudhari, Pranav Charkha, and Sumit Desai

**Abstract** Special Purpose Vehicle (SPV) for hilly area design engineering enthusiasts provides a platform to apply engineering principles and achieve proficiency in the automobile world. The challenge is to design and build a single-seat, all-terrain, sporting vehicle whose structure contains the driver. The vehicle must comply with the static and dynamic events, demonstrating the understanding and test of the vehicle's performance. Building this vehicle aims to provide the students a platform to design, fabricate, and test a durable high performance, and safe. This paper describes the design of an SPV, emphasizing the vehicle specifications, problem statements, design considerations, methodology implemented for self-designing critical components, and analysis of these components considering extreme conditions. Heavy emphasis is given on the safety of the driver and weight reduction of the buggy, for which a rigid and torsion-free chassis, well-mounted power train, and dynamically tested steering and suspension system are incorporated. The vehicle designed modeling on CATIA V5R19 software and simulated, analyzed using ANSYS workbench 19.1.

**Keywords** Special purpose vehicle · All-terrain · Design · Weight reduction · ANSYS

## Nomenclature

$\sigma_b$  Bending strength  
 $k$  Bending stiffness  
 $w$  Weight per meter

---

D. S. Choudhari (✉) · P. Charkha · S. Desai  
Department of Mechanical Engineering, Dr. D.Y. Patil Institute of Technology, Pimpri, Pune, India  
e-mail: [dilipchoudhari2009@gmail.com](mailto:dilipchoudhari2009@gmail.com)

P. Charkha  
Department of Mechanical Engineering, Nutan Maharashtra College of Engineering, Talegon,  
Pune, India

$S_{ut}$	Ultimate tensile strength
$E$	Young's modulus
$c$	Wheel track
$b$	Wheelbase
$\emptyset$	Inner wheel angle
$l$	KPI distance
$r$	Steering wheel radius
$G$	Steering ratio
$L$	Rack lock to lock travel
$P$	System pressure
$F_c$	Clamping force
$T_b$	Generated braking torque
$d$	Stopping distance

## 1 Introduction

The paper describes the design of SPV, emphasizing the objectives, problem statements, design description, vehicle specification, and methodology implemented for self-designed critical components and analyzing. More significance is given to the safety of drivers and the performance optimization of SPV. Chassis is used to relate basic engineering principles to particular requirements [1]. In the collaborative technology of mechanical and control engineering, chassis expertise has become a majority of research and development for vehicle dynamics performance [2]. The design of the vehicle suspension is specific due to the non-standard body shape and the need to adjust the camber angle, high wheelbase, damping effects, deceleration, and cornering [3]. Adjust the camber angle in transverse direction thus the problem has been solved due to the design of the suspension system [4]. In the suspension system, a quarter of the vehicle models show possible improvements in ride comfort, good traction, limited suspension travel, and drive force, while saving a significant portion of communication resource costs [5]. Quadra steering is a good option for a reduction in steering radius as well as not required a greater amount of effort on the part of the driver [6]. This paper introduces an improved FE disk brake corner that includes a wheel hub and steering knuckle. Test FE model using an experimental modal analysis of the disk brake system [7]. SPV presents the methods of testing tires outdoors with a focus on traction performance [8]. The design and development of a two-stage gearbox used of the general AGMA approach required [9]. An integrated simulation tool has been developed which applies to all listed design issues [10]. Consequently, the Taguchi method and the traditional multipurpose optimization of particle swarm methods proposed in this study improve processing quality and can be widely applied to other metal materials to improve processing efficiency [11]. Minimize power loss with a recent overview of automotive power train management, control over gasoline, and diesel engine cleaning systems [12].

## 2 Chassis System

### 2.1 Design Description

The objectives of the Chassis are to designed and provides driver safety by mounting a subsystem. The material selection for Chassis is to achieve desired bending strength and bending stiffness with minimum tube dimension and also provide good weldability for AISI 4130. Considering the overall weight of the vehicle 200 kg, velocity during collision is 56 km/H various forces on the vehicle of different conditions. Forces applied and calculated on different sides of chassis front, side, rear, impacts, and chassis to ensure driver safety. These forces are calculated by using the principle of conservation of momentum; coefficient of restitution, and impulse-momentum theorem, and for rollover, projectile motion theory is used. The calculated impact forces for the vehicle at the front, side, and rear are 5166N at each side and for rollover are 8620N. Materials specifications of AISI 4130 members for Chassis are shown in Table 1.

The materials and dimensions of AISI 4130 members are used for the Chassis shown in Fig. 1.

**Table 1** Materials specifications of AISI 4130 members for Chassis

Bending strength, $\sigma_b$ (N/mm <sup>2</sup> )	206,869.50
Bending stiffness, $k$ (N/mm)	1,170,836
Weight per meter, $w$ (Kg/m)	1.12
Ultimate tensile strength, $S_{ut}$ (MPa)	560
Carbon, $C$ (%)	0.30
Young's modulus, $E$ (GPa)	205

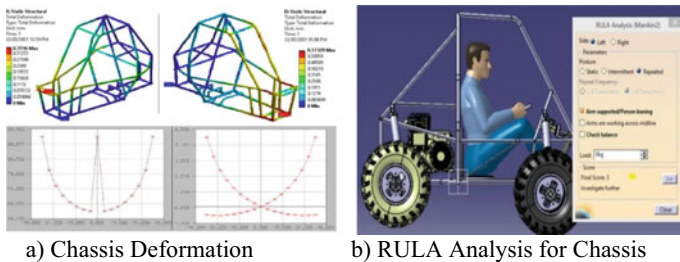


**Fig. 1** Chassis result **a** Chassis deformation, **b** RULA analysis for Chassis

**Table 2** Results analysis of different impact conditions

Impact	FOS	Stress (MPa)	Deformation (mm)
Front and rear	1.39 and 1.27	321.54 and 351.64	3.65 and 4.50
Side and roll over	1.16 and 1.14	387.37 and 392.03	3.75 and 4.21

**Table 3** Comparison of yield stresses of material

Types of member	Tested values (MPa)	Design values (MPa)
Primary member	514.94	460
Secondary member	733.11	460

## 2.2 Finite Element Modeling

CATIA V5 R21 software is used to design Chassis considering manufacturing feasibility, ergonomics, and visibility of the driver. The software was used for Chassis analysis ANSYS workbench 19.1, and it is considered by beam method and mesh size as 10 mm. The static structural analysis yielded the result of different impact conditions shown in Table 2 and the yield stresses of material, as shown in Table 3.

## 2.3 Ergonomics

The RRH is inclined at an angle of 5 degrees w.r.t vertical. RULA and REBA analysis has been done to see that driver is in a comfortable table sitting position. Figure 1a shows that chassis deformation and (b) RULA analysis for chassis.

## 3 Suspension System

The objective of a suspension system is to transfer the minimum amount of vibrations to the driver and increase the vehicle's rolling resistance by which it can perform high-speed cornering without losing contact from the ground, which in turn gives maximum ride quality.

**Table 4** Suspension considerations

Parameters	Front	Rear
Bump camber change (°)	3	3.5
Wheel travel (")	Jounce and rebound 4	Jounce and rebound 4
Bump force (N)	8000	8000
Static weight distribution (%)	43.36	56.64
Motion ratio	0.80	0.65
King-pin inclination (°)	10	No King-pin
Ground clearance (")	10.38	10.38

### 3.1 Design Description

The suspension system is designed to consider various forces on the vehicle and setting the kinematic parameters as shown in Table 4 to achieve better dynamic stability.

### 3.2 Vehicle Geometry

Double wishbone geometry has been designed in the front with an RC height of 312.57 mm and an anti-dive of 15%, while the H arm with a single control link is designed in the rear with an RC height of 329.15 mm. While the high-speed cornering rear inner tire is the one that loses the traction, so we have kept the front RC height less than the rear, so there will be a less rolling moment, and the tire will be continuously in contact with the ground, satisfying our first objective. The results of static structural stress analysis 534.1 and 114.2 MPa for arms and upright and deformation are 1.617 and 0.541 mm, respectively. Vehicle calculated the frequency and transmissibility of vehicle as shown in Table 5.

Damping properties calculated considering the damping ratio of 0.7 and velocity of 0.3 m/s, the force comes up to be 226.7 N, and the damping coefficient 1079.8 N-s/m. It gives comfortable damping, increasing ride quality. Upright has been designed in a C shape in which the steering arm and caliper mounting are integrated. It has

**Table 5** Calculated frequency

Frequency	Values (Hz)
Ride frequency	F:1.89; R:2.04
Bounce frequency	2.045
Pitch frequency	1.89



been designed for 8 KN of bump load and 4 KN lateral load. Total deformation of A-type arms as shown in Fig. 2 and equivalent stresses of the hub as shown in Fig. 3.

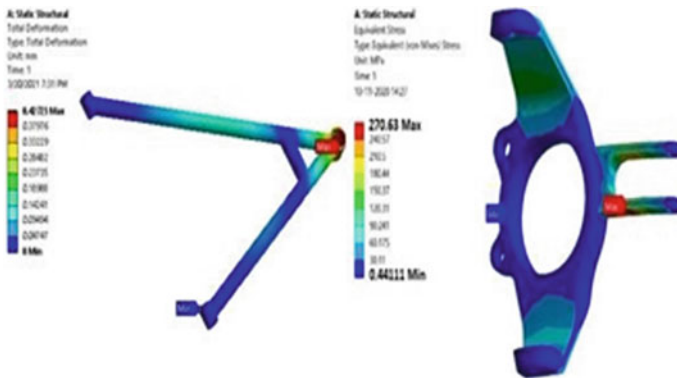


Fig. 2 Total deformation of A-type arms

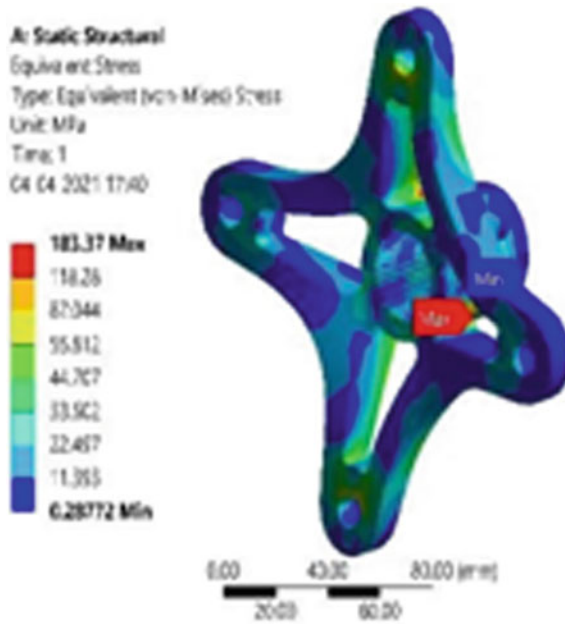


Fig. 3 Equivalent stresses of Hub

## 4 Steering System

The system’s main objective is to steer the front wheels in response to the driver’s command input and provide overall directional control to the vehicle in all terrains with maximum safety and minimum effort.

### 4.1 Design Description

The steering system is designed based on various calculated specifications of the system to maneuver the vehicle with ease. System design specifications for steering are shown in Table 6.

The Ackerman steering geometry helps the vehicle avoid side slippage during high-speed turning, while oversteer characteristics provide the driver with the ability to take sharp turns, increasing vehicle agility. The AI 7075-T6 rack and pinion gearbox have been designed due to their high strength-to-weight ratio. The gearbox is designed to get the maximum inner wheel angle of 44° while the steering wheel is turned to 90°—the gearbox dimensions are calculated by using the AGMA system. The no. of teeth on pinion and rack are 20 and 21 teeth, respectively, and PCD of pinion 50 and module is 2.5. The AI 6061-T6 steering wheel dimensions are selected to reduce the total steering effort. The butterfly shape structure also helps in gripping and effort reduction. The steering column has been given an inclination at 45° w.r.t. vertical axis as per the driver requirement and ergonomics.

The steering system’s design is done using CATIA V5R21, and the use of ANSYS workbench 19.1 did the pre-manufacturing analysis. All geometrical simulations and iterations are done on LOTUS SHARK software. The static structural analysis is shown in Table 7 and equivalent stress for pinion and tie rod in Fig. 4.

**Table 6** System design specifications for steering

Parameters	Design values	Parameters	Design values
Steering geometry and gear box	Ackermann and Rack and Pinion	St wheel radius, $r$ (mm)	140
Ackerman percentage	97.97	Critical turning speed (m/s)	4.489
Ackerman angle (°)	22.88	Steering ratio, $G$	2.01:1
Inner wheel angle (°)	44	Rack lock to lock travel, $L$ (mm)	78
Wheel track, $c$ (")	50 (F) & 48 (R)	Tire size	23 × 7–10
Wheel base, $b$ (")	52	Steering wheel turn angle	180°
Inner wheel angle, $\emptyset$ (°)	44°	KPI distance, $l$ (")	43.90

**Table 7** Results from static structural analysis

Component	FOS	Stress (MPa)	Deformation (mm)
Rack	1.1	421.67	3.889
Pinion	1.0	474.85	0.971
Clevis	4.0	117.36	0.020
Tie rod	2.3	201.86	4.166
Steering arm	1.3	362.61	0.723

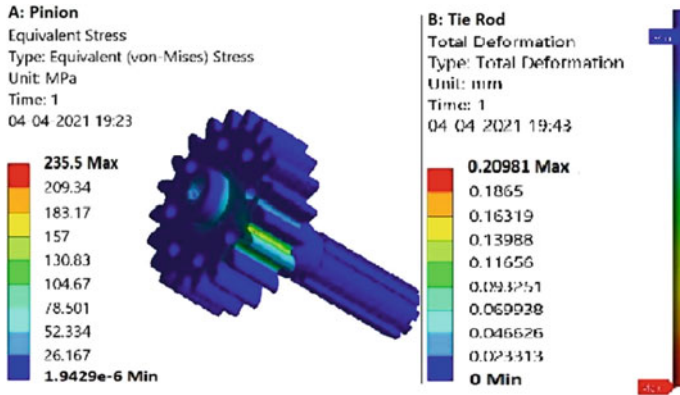


**Fig. 4** Equivalent stress for pinion and tie rod

## 5 Braking System

The ultimate objective of the braking system is to lock all the four wheels of the vehicle at the same instant and to slow or stopping the vehicle at a driver’s command.

### 5.1 Design Description

SPV brake with a parallel split hydraulic disk type braking system, where a combination of flexible and fixed hoses are used for connections. Using an Inboard braking system reduces the number of rotors and calipers. Customized calipers are used considering packaging space, and thus the compact system is designed. The brake pedal has been designed to provide maximum force with minimum driver effort. The pedal ratio is set at 7:1 with the curve design for the driver’s comfort. Two master cylinders with a bore of 15 mm and a stroke length of 18.31 mm are used considering pedal travel, driver’s effort, etc. Self-designed laser-cut SS420 rotors are used. The diameter of the rotor was chosen considering the effective radius. Design considerations as shown in Table 8 and design specifications as shown in Table 9.

**Table 8** Design considerations

Parameters	Design values	Parameters	Design values
Mass of vehicle with driver (Kg)	200	Pedal ratio	7:1
Dynamic wt. transfer (N)	533.3	Required braking torque (Nm)	283 (F); 106 (R)
COF between road and tire	0.68	Projectile force (KN)	4.21
COF between pads and rotor	0.38	Centrifugal force (KN)	13.51
Driver effort (N)	300	Bump force (KN)	5.8

**Table 9** Design specifications

Parameters	Front	Rear
System pressure, $P$ (bar)	83.9 (F)	32.8 (R)
Clamping force, $F_c$ (N)	2340.5 (F)	907.8 (R)
Generated braking torque, $T_b$ (Nm)	304.12	118
MFDD ( $m/s^2$ )	6.8	6.8
Stopping distance, $d$ (m)	9.25	9.25

## 5.2 Results and Discussion

Caliper, Rotor, and Pedal have been analyzed using the ANSYS workbench 19.1. The rotor underwent thermal analysis and torsional test to check the heat dissipation and twisting. The maximum temperature of the rotor did not exceed 70 °C. Transient structural analysis of Float Caliper assembly was done to ensure its proper actuation under peak pressure. The results of the static structural analysis are shown in Table 10 and the equivalent stress of the brake caliper, as shown in Fig. 7.

Validation of system pressure is done using pressure sensors, mounting them at the MC outlet and the pads, thus showing equivalent pressure at both the sensors. The pedal is validated using an experimental setup consisting of cable, pulley, pedal, and load. Thus, it is ensured that the pedal is safe under maximum loading.

**Table 10** Results of static structural analysis

Component	FOS	Equivalent stress (MPa)	Deformation (mm)	Life
Brake pedal	1.97	242	3.8	$10^6$
Brake caliper	1.74	275	0.25	$10^6$
Wheel hub	2.62	183	0.13	$10^7$

**Table 11** Rear drive train specifications

Parameter	Value
Engine torque (Nm)	19.2
Gaged GX-9 clutch range	3.9–0.9
Gearbox stage-1 reduction	2.7:1
Gearbox stage-2 reduction	2.9:1
Overall reduction	7.85:1
Torque on wheels (Nm)	448

## 6 Power Train System

The primary objective of the power train is to transfer the maximum possible torque or power to driving wheels with minimum losses. The entire system has been designed to target minimum rotational inertia and maximum reliability.

### 6.1 Design Descriptions

The configuration is sent from the rear to the front from a torque splitter through a propeller shaft which is then distributed to the front wheels through a custom Limited Slip Differential. The core parameter in design calculations being laden vehicle weight has been used to calculate the various resistances that inhibit the vehicle's motion rear drive train specifications as shown in Table 11.

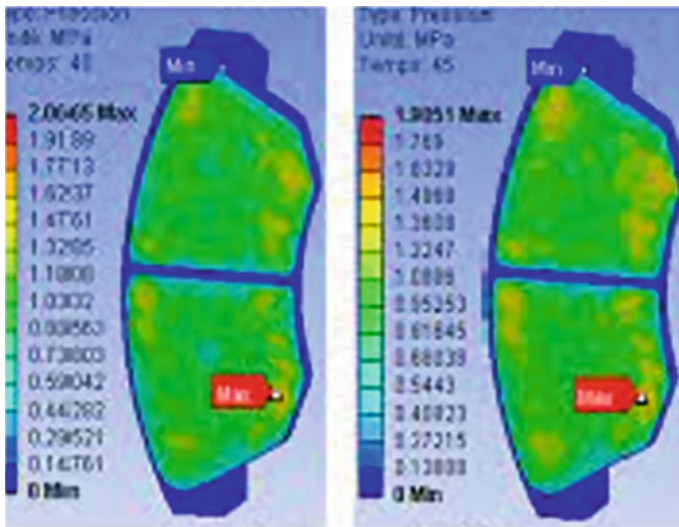
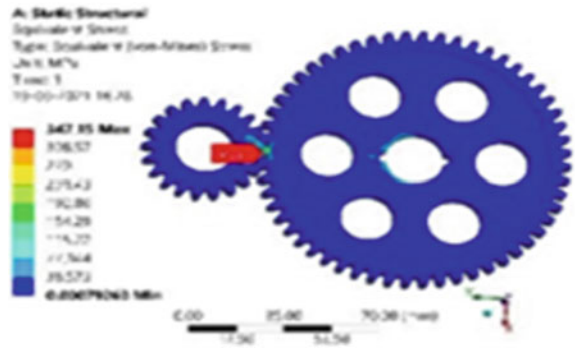
### 6.2 Results and Discussion

The Gears and shafts were subjected to torsional loads and bending loads in a static structural condition. Similarly, the drive shaft assembly was also subjected to a torsional moment. Considering the bump force of 5886 N and the axial force of 2943 N, and the braking torque of 432 N-m, the theoretical value of the safety factor for gears comes out to be 1.9, which has been validated in ANSYS workbench 19.1, giving its factor of safety as 1.7. The results of static structural analysis as shown in Table 12. Equivalent stresses for pinion and gear are shown in Fig. 5. Also in Figs. 6 and 7 shows that equal pressure distribution, and temperature of the rotor, respectively.

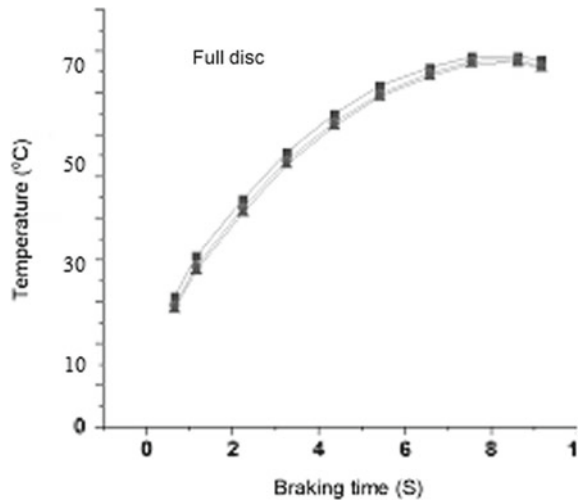
**Table 12** Results of static structural analysis

Components	FOS	Stress (MPa)	Deformation (mm)
Pinion 1, 2	1.7, 1.2	179.71, 209.28	0.0094, 0.0149
Gear 1, 2	1.2, 1.4	206.81, 179.71	0.0333, 0.0241
Bevel pinion	1.3	197.21	0.0108
Universal joint	1.9	130.29	0.0422
Driveshaft	1.3	113.21	2.1929

**Fig. 5** Equivalent stress



**Fig. 6** Equal pressure distribution

**Fig. 7** Temperature of rotor

## 7 Conclusion

The design modeling, analysis, and simulation of the SPV are on their way to justifying off-road capabilities and sporting vehicles. The Chassis design is entirely safe for the driver and ergonomically suit. The compatibility of suspension and the efficiency of transmission will make the driver forget about the power limitations of the vehicle. At the same time, the design of the steering system to provide maximum directional stability with a minimum turning radius and to reduce driver fatigue. The braking system can lock all wheels of the vehicle at the same time. The design of the power train system is to provide maximum possible torque or power with minimum friction loss to the driving wheels. Also, the entire system has been designed to target minimum rotational inertia and maximum reliability. Additionally, the whole framework has been intended to target the least rotational idleness and most extreme dependability.

## References

1. Reimpell J, Stoll J, Betzler J (2001) The automotive chassis engineering principles, 2nd edn
2. Shibahata Y (2005) Progress and future direction of Chassis control technology. *Ann Rev Control* 29(1):151–158
3. Milan B, Lubos K, Lukas S (2019) Front suspension design of the lightweight vehicle'. *Transp Res Proc* 40:623–630
4. Sundaravel S, Pakash S, Kaja Bantha Navas R, Rajasekaran T (2019) Design and analysis of camber angle adjustment using actuators by transverse motion in all-terrain vehicle. *Mater Today Proc* 16(2):1226–1232

5. Ge X, Ahmad I, Han Q-L, Wang J, Zhang X-M (2021) Dynamic event-triggered scheduling and control for vehicle active suspension over controller area network. *Mech Syst Signal Process* 152:107481
6. Choudhari DS (2014) Four wheel steering system for future. *Int J Mech Eng Robot Res* 3(4):383–387
7. Nouby N, Srinivasan K (2011) Simulation of the structural modifications of a disc brake system to reduce brake squeal. *J Automob Eng* 225(5):653–672
8. Cutini M, Brambilla M, Toscano P, Bisaglia C, Abbati G, Meloro G (2020) Evaluation of drawbar performance of winter tires for special purpose vehicles. *J Terramech* 87:29–36
9. Shigley J, Mischke C, Budynas R (2004) *Mechanical engineering design*. McGraw-Hill Companies, Inc., pp 652–711
10. Ciesla C, Keribar R, Morel T (2000) Engine/powertrain/vehicle modeling tools applicable to all stages of the design process. *SAE Technical Paper*, pp 1–13
11. Chen WJ, Hsu CC, Yang YL (2014) Improving roughness quality of end milling Al 7075–T6 alloy with Taguchi based multi-objective quantum behaved particle swarm optimization algorithm. *Mater Res Innov* 18(2):647–653
12. Cook JA, Sun J, Buckland JH, Kolmanovsky IV, Peng H, Grizzle JW (2007) Automotive powertrain control. *Asian J Control* 8(3):237–260



# Nonlinear Free Vibration Analysis of Functionally Graded Materials Spherical Shell



Pranav G. Charkha and Pradeep Khaire

**Abstract** Through the advancement of technology in various fields in today's century, we are able to come up with a wide range of solutions for the betterment of mankind. We are making strides in areas such as space exploration and nuclear power plants, but we are still confronted with certain obstacles. These applications necessitate the use of special materials designed to survive the harsh climate. Functionally graded materials (FGM) are the best alternative to traditional materials for addressing this problem. As a result, it is important to verify the properties of FGM before putting them to use in applications. This paper mainly focuses on finding nonlinear frequency of vibration of the shell of spherical shape. As material is having varying material properties, it is nonlinear in nature; hence, it becomes necessary to consider its nonlinear frequency. Also, it is necessary to find the effect of composition of material, effect of temperature on frequency response in order to avoid the failure of parts being used. This paper gives the insights into the frequency, considering the above-said parameters. This will help to decide material composition, temperature, and different boundary conditions for required application. The paper considers the FGM made from the mixture of aluminum and alumina ( $Al/Al_2O_3$ ) and stainless steel/silicon nitride ( $SUS304/Si_3N_4$ ) Nonlinear free vibration response of a spherical geometry made of FGMs in a thermal atmosphere is the subject of this article. Since some material properties change with temperature [temperature-dependent (TD)] while others remain stable [temperature-independent (TID)], it is essential to consider both for testing purposes. This study would look at not only uniform but also non-uniform temperature differences. This study enlists the help of mathematical modeling using higher-order shear deformation theory (HSDT) in combination with nonlinear strain kinematics theory given by von Karman. The finite element formulation benefits from modified  $C^0$  continuity. The proposed method is validated by comparing the outcomes in the literature.

**Keywords** Spherical shell · FGM · Nonlinear free vibration · HSDT

---

P. G. Charkha (✉) · P. Khaire

Department of Mechanical Engineering, Nutan Maharashtra Institute of Engineering and Technology, Talegaon, Pune, India

e-mail: [pgcharkha@gmail.com](mailto:pgcharkha@gmail.com)

© The Author(s), under exclusive license to Springer Nature Singapore Pte Ltd. 2023

313

P. Pradhan et al. (eds.), *Recent Advances in Mechanical Engineering*,

Lecture Notes in Mechanical Engineering,

[https://doi.org/10.1007/978-981-16-9057-0\\_33](https://doi.org/10.1007/978-981-16-9057-0_33)

## 1 Introduction

In places like space travel and nuclear power stations, we are making progress. These applications necessitate materials that can withstand a significant temperature gradient. Metals tend to melt at high temperatures, so using only metals isn't an option. Due to its delicate existence, the use of only ceramics becomes impossible. As a result, a modern material consisting of metal and ceramic may be used to solve this problem. This mixture benefits both metals' high strength and ceramics' ability to withstand high temperatures. As a result, this new material can withstand a high thermal resistance while remaining structurally stable. Metal and ceramic are blended in FGM using the power index rule.

Jagtap et al. [1, 2] used HSDT in combination with nonlinear strain kinematics theory given by von Karman and modified continuity to examine stochastic nonlinear free vibration and bending reaction of FGMs plate stabilized by nonlinear elastic base in a thermal setting. Free vibration and stability study of FGMs shallow shells were proposed by Hiroyuki Matsunaga [3]. 2-Degree HODT was used by the scientist. On the basis of HSDT, Alijani et al. [4] provided nonlinear motions of FGM spherical shells exposed to thermal variation.

From the literature survey, it can be seen that most of the work focuses on shapes as plate cylindrical shell and very few research is available on spherical shell. Also, many papers tried to find bending and buckling characteristics. So this paper will consider the spherical shape and will try to get insights into nonlinear frequency characteristics. Also, paper will consider different approaches for finding the frequency response, which is not used for spherical shell.

## 2 Formulation

Consider the spherical nature of FGMs. Let the length of shell "a", width is being "b", two radii along X- and Y-axes being "R1, R2" and thickness being "t" is made of a combination of ceramics and metal with a composition that varies from upper surface to the bottom. As seen in Fig. 1, the top layer of the spherical shell ( $z = t/2$ ) has far more ceramic material, whereas the lower part ( $z = -t/2$ ) has much more metal.

The thickness of the shell is thought to change the characteristics of the shell. Let us consider the subsequent properties of material for the shell, such as elasticity modulus is "E" and "ρ" is mass density, are expressed as [1] at every capricious point inside the shell.

$$\begin{aligned} E(z) &= E_{mm} + [E_{cc} - E_{mm}]V_{cc}(z) \\ \alpha(z) &= \alpha_{mm} + [\alpha_{cc} - \alpha_{mm}]V_{cc}(z) \\ \rho(z) &= \rho_{mm} + [\rho_{cc} - \rho_{mm}]V_{cc}(z) \end{aligned}$$

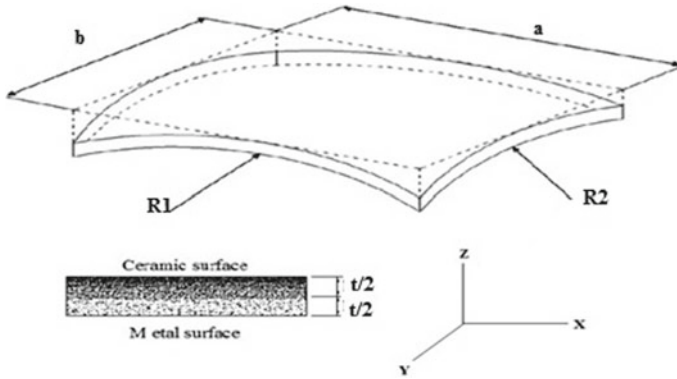


Fig. 1 Spherical shell geometry

$$k(z) = k_{mm} + [k_{cc} - k_{mm}]V_{cc}(z) \tag{1}$$

Here, cc and mm represent content of ceramic and metal present in the spherical shell.  $E, \rho, k$  and  $\alpha$  are the elasticity modulus, mass density, thermal conductivity and thermal expansion coefficient, “ $V_{cc}(z)$ ” is volume fraction for ceramic. The ceramic’s volume fraction is depending on the  $z$ -direction, as shown by the formula.

$$V_{cc}(z) = \left(0.5 + \frac{z}{t}\right)^{n_i}, \quad -\frac{t}{2} \leq z \leq \frac{t}{2}, \quad \text{Where } 0 \leq n_i < \infty \tag{2}$$

where  $n_i$  is volume fraction index and value of  $n$  is always lies between zero and infinity. When  $n_i = 0$ , the volume fraction of ceramic becomes one, indicating that the shell is entirely composed of ceramic. As the value of  $n_i$  approaches infinity, the shell becomes completely metallic.

### 2.1 Mathematical Model of a Displacement

The displacement field method was fitted using Reddy’s HSDT with C0 continuity [5]. The equation given below is giving the displacement of the point from its original position at the time of vibration.

$$\begin{aligned} \bar{u}_x &= u \left(1 + \frac{z}{R_1}\right) + f_{11}(z)\phi_{xx} + f_{22}(z)\theta_{xx} \\ \bar{v}_y &= v \left(1 + \frac{z}{R_2}\right) + f_{11}(z)\phi_{yy} + f_{22}(z)\theta_{yy} \end{aligned} \tag{3}$$

$$\overline{w_z} = w$$

where  $(\overline{u_x}, \overline{v_y}, \overline{w_z})$  represents the displacement for any random point in Cartesian  $(x, y, z)$  coordinates,  $(u, v, w)$  denotes following displacements of a mid-plane point,  $\phi_{xx}$  and  $\phi_{yy}$  being normal' the rotations at the mid-plane at  $z = 0$  in reference to  $x$ - and  $y$ -axes.

$$\{\gamma\} = [u_x \ v_y \ w_z \ \theta_{yy} \ \theta_{xx} \ \phi_{yy} \ \phi_{xx}]^T \tag{4}$$

### 2.2 Relationships of Strain and Displacement

Vector of strain corresponding to the displacement vector that contributes for the strains in form deformation of mid-plane, normal' rotation to the mid-plane is represented as

$$\{\varepsilon_T\} = \{\varepsilon_{ls}\} + \{\varepsilon_{nls}\} - \{\overline{\varepsilon}_{ts}\} \tag{5}$$

where  $\{\varepsilon_{ls}\}$  is the vector of linear strain,  $\{\varepsilon_{nls}\}$  is nonlinear strain and  $\{\overline{\varepsilon}_{ts}\}$  is thermal strain.

Utilizing nonlinear strain kinematics of von-Karman, the vector of nonlinear strain can be expressed as,

$$\varepsilon_{nls} = \frac{1}{2} [A_{nls}] \{\theta\} \tag{6}$$

$$\text{Here } A_{nls} = \frac{1}{2} \begin{bmatrix} \frac{dw_z}{dx} & 0 \\ 0 & \frac{dw_z}{dy} \\ \frac{dw_z}{dx} & \frac{dw_z}{dy} \\ 0 & 0 \\ 0 & 0 \end{bmatrix} \text{ and } \theta = \begin{Bmatrix} \frac{dw_z}{dx} \\ \frac{dw_z}{dy} \end{Bmatrix} \tag{7}$$

The vector of thermal strain given in Eq. 5 can be written as,

$$\{\overline{\varepsilon}_{ts}\} = \begin{Bmatrix} \overline{\varepsilon}_{xx} \\ \overline{\varepsilon}_{yy} \\ \overline{\varepsilon}_{xy} \\ \overline{\varepsilon}_{yz} \\ \overline{\varepsilon}_{zx} \end{Bmatrix} = \Delta T \begin{Bmatrix} \alpha_{xx} \\ \alpha_{yy} \\ \alpha_{zz} \\ 0 \\ 0 \end{Bmatrix} \tag{8}$$

where  $\alpha_{xx}, \alpha_{yy}$  and  $\alpha_{zz}$  = thermal expansion coefficient along with  $x$ -,  $y$ -, &  $z$ -axes and temperature difference that is not only uniform but also non-uniform in the spherical shell is denoted by  $\Delta T$ . This variation in temperature is as mentioned below.

For non-uniform temperature variation, the temperature distribution is represented as

$$\Delta T = T(zz) - T_0 \tag{9a}$$

The temperature shift is believed to exist only in thickness orientation in this analysis, so only a one-dimensional temperature field is assumed. The equation of steady-state heat transfer is to be used to determine temperature distribution in thickness path of the shell in this case.

$$-\frac{d}{dz} \left[ k(z) \left[ \frac{dT}{dz} \right] \right] = 0 \tag{9b}$$

After solving and rearranging, the above equation can be written as,

$$T(zz) = T_b + (T_u - T_b)\tau'(z) \tag{10}$$

where  $T(zz)$  represents distribution of temperature in the thickness ( $z$ ) direction,  $T_u$  and  $T_b$  denote the top and bottom surface temperature of spherical shell, respectively, where value of  $\tau'(z)$  is given as [6, 7].

Considering uniform change Eq. 10 is modified as

$$T(zz) = T_0 + (T_u - T_b) \tag{11}$$

Here  $T_0$  is considered as initial stage temperature.

### 2.3 Relation Between Stress–Strain

Following is the relationship between strain and stress when considering the influence of temperature on the spherical shell,

$$\{\sigma\} = \{\overline{Q}\}\{\varepsilon_T\} \quad \text{or} \quad \begin{Bmatrix} \sigma_{xx} \\ \sigma_{yy} \\ \sigma_{xy} \\ \sigma_{yz} \\ \sigma_{xz} \end{Bmatrix} \tag{12}$$

where  $\{\bar{Q}_{ij}\}, \{\varepsilon_T\}$ , and  $\{\sigma\}$  denote vectors of the matrix for stiffness for the shell, strain, and stress of shell.

### 2.4 The Spherical Shell's Strain Energy

Once relation between strain and stress is evaluated, we can find the strain energy for the FGMs spherical shell as, [8]

$$U_T = \frac{1}{2} \int_A \{\varepsilon_T\}^T \{\sigma\} dA \tag{13}$$

### 2.5 Work Done

As the temperature varies uniformly and non-uniformly, pre-buckling stresses are produced in the FGM shell, and these pre-buckling stresses per unit length cause the shell to buckle. In-plane stresses produce work ( $W$ ) that can be written as,

$$\begin{aligned} W_T &= \frac{1}{2} \int_A [N_{xx}(w_{xx})^2 + N_{yy}(w_{yy})^2 \\ &\quad + 2N_{xy}(w_{xy})^2] dA \\ &= \frac{1}{2} \int_A \begin{Bmatrix} w_{xx} \\ w_{xy} \end{Bmatrix}^T \begin{bmatrix} N_{xx} & N_{xy} \\ N_{xy} & N_{yy} \end{bmatrix} \begin{Bmatrix} w_{xx} \\ w_{yy} \end{Bmatrix} dA \end{aligned} \tag{14}$$

### 2.6 Spherical Shell's Kinetic Energy

Kinetic energy of vibration FGMs spherical shell,

$$T_s = \int_V \rho^{(k)} \{\hat{u}_j\}^T \{\dot{\hat{u}}_j\} dV \tag{15}$$

where  $\rho$  and  $\{\hat{u}_j\} = \{\dot{\hat{u}}_x \dot{\hat{v}}_y \dot{\hat{w}}_z\}$  denotes vector of density and velocity for shell, respectively; this equation might be further modified as

$$T_s = \sum_{e=1}^{NE} T_s^{(e)} = \sum_{e=1}^{NE} \{\dot{\Theta}\}^T [m] \{\dot{\Theta}\} = \{\dot{q}_v\} [M_G] \{\dot{q}_v\} \quad (16)$$

Here,  $[M_G]$  represents global mass matrix.

### 3 The Motion Equation and the Solution

When considering the influence of temperature, Lagrange's equation of motion's help is taken to obtain the shell's governing equation for nonlinear free vibration. And is given as,

$$\delta \int_{t_1}^{t_2} (U_T - W_T - T_S) dT = 0 \quad (17)$$

Considering values from Eqs. 14, 15, 17 and solving above equation and converting in generalized nonlinear eigenvalue we get,

$$[K_T] \{q_v\} + [M_G] \{\ddot{q}_v\} = 0 \quad (18)$$

$$\text{Here, } [K_T] = \{[K_{ls}] + [K_{nls}(q)] - \lambda_T [K_g]\}$$

Equation 19 represents nonlinear free vibration equation for the shell;

$$[[K_T] - \lambda [M_G]] \{q_v\} = 0 \quad (19)$$

Here  $\lambda = \omega^2$  &  $\omega$  = natural frequency. A direct iterative nonlinear finite element approach combined with  $C^0$  continuity is used to solve the nonlinear eigenvalue problem.

### 4 Result and Discussion

HSDT model is considered for the current study, here Lagrange's nine-nodded isoparametric element having 63 DOFs per element was used to discretize the FGMs casing, and a (5 \* 5) mesh was used for the analysis. The findings are linked to those found in the literature. At the spherical shell's sides, Here temperature  $T = 300$  K, for the whole analysis. Properties of (*SUS304/Si<sub>3</sub>N<sub>4</sub>*) are used for calculation [9].

Mean natural frequency in dimensionless form, for the FGMs shell is defined [9],

$$\bar{\omega} = \omega(b^2/t)\sqrt{\rho_{mm}/E_{mm}}, \tag{20}$$

Table 1 shows effect of temperature transition ( $\Delta T$ ), index of volume fraction ( $n_i$ ), ratio of amplitude ( $W_{max}/t$ ), and modes of temperature distribution with not only TD but also TID properties. Nonlinear frequency reduces as the index of volume fraction increases with the same temperature shift and amplitude ratio. This is because the amount of metal contained in FGMs spherical shell increases as the value of  $n$  increases, affecting the stability of the spherical shell. It is often observed that as temperature rises, the nonlinear fundamental frequency decreases, affecting the spherical shell's stiffness.

The effect of conditions of support with index of volume fraction ( $n_i$ ),  $W_{max}/t$ , and temperature transition with not only TID but also TD properties are presented in Table 2. The SSSS and CCC help requirements were included in the computation. The greater nonlinear frequency values can be seen in the spherical shell with all edges clamped. The SSSS shell, on the other hand, displays lower nonlinear fundamental frequency values with the same value of ( $n_i$ ) and  $W_{max}/t$ .

**Table 1** Effect of temperature transition ( $\Delta T$ ), index of volume fraction ( $n_i$ )

$\Delta T$	$n_i$	$W_{max}/t$	Uniform temperature distribution (UTD)		Non-uniform temperature Distribution (NUTD)	
			TD	TID	TD	TID
100 K	0.5	0.3	4.1897	4.2934	4.4167	4.4763
		0.6	4.6140	4.7113	4.8208	4.8784
		0.9	5.1204	5.2113	5.3074	5.3628
		1.0	5.3018 (3.8872)*	5.3908 (3.9960)	5.4827 (4.1311)	5.5374 (4.1921)
	1	0.3	3.6729	3.7633	3.8644	3.9157
		0.6	4.0383	4.1233	4.2130	4.2627
		0.9	4.4766	4.5561	4.6347	4.6825
		1.0	4.6340 (3.4150)	4.7118 (3.5094)	4.7869 (3.6204)	4.8341 (3.6726)
200 K	0.5	0.3	3.7471	4.0034	4.2601	4.3859
		0.6	4.2196	4.4488	4.6807	4.7956
		0.9	4.7718	4.9754	5.1840	5.2877
		1.0	4.9673 (3.4021)	5.1631 (3.6822)	5.3645 (3.9607)	5.4646 (4.0953)
	1	0.3	3.2770	3.5063	3.7113	3.5762
		0.6	3.6844	3.8904	4.0751	4.1801
		0.9	4.1628	4.3466	4.5122	4.6076
		1.0	4.3326 (2.9825)	4.5095 (3.2318)	4.6692 (3.4548)	4.7615 (3.8256)

\*Bracket contains linear values



**Table 2** Impact of index of volume fraction ( $n_i$ ), ratio of amplitude, and temperature distribution forms with TID as well as TD properties of material on dimensionless nonlinear frequency of FGM (SUS304/Si<sub>3</sub>N<sub>4</sub>) spherical shell at temperature difference  $\Delta T = 250$  K,  $a/t = 5$  &  $R_1/a = R_2/b = 10$

Support condition	$n_i$	$W_{max}/t$	Uniform temperature distribution		Non-uniform temperature distribution	
			TD	TID	TD	TID
SSSS	0.5	0.5	4.0417	4.1036	4.1942	4.2183
		1.0	4.7269 (3.6519)*	4.7742 (3.7232)	4.8564 (3.8218)	4.8719 (3.8505)
	1	0.5	3.5453	3.6048	3.6746	3.7007
		1.0	4.1365 (3.2148)	4.1844 (3.2811)	4.2464 (3.3584)	4.2662 (3.3874)
CCCC	0.5	0.5	6.9967	7.0139	7.0975	7.0904
		1.0	8.4361 (6.2188)	8.4353 (6.2470)	8.5194 (6.3336)	8.4986 (6.3339)
	1	0.5	6.1367	6.1584	6.2220	6.2223
		1.0	7.4024 (5.4570)	7.4086 (5.4877)	7.4729 (5.5540)	7.4615 (5.5602)

\*Bracket contains linear values

## 5 Conclusion

The study’s findings have been used to draw subsequent conclusions.

1. The ratio of amplitude of the nonlinear fundamental frequency declines as the VF index ( $n_i$ ) increases with the same temperature rise. This is because the amount of metal contained in FGMs spherical shell increases as the value of  $n$  increases, affecting the stability of the spherical shell.
2. The results also show that as ratio of amplitude increases, the dimensionless nonlinear fundamental frequency of vibration increases.
3. It can be shown that as the temperature rises, the value of the nonlinear vibration frequency decreases. The reason for this is that as the temperature rises, the stiffness of the FGM’s spherical shell decreases. This demonstrates the significance of temperature in the design process.
4. The nonlinear frequency is greatest in the spherical shell with all edges clamped. For same VF index ( $n_i$ ) and ratio of amplitude, the shell with all edges simply assisted displays the least values of nonlinear fundamental frequency. The reason for this is that CCCC boundary conditions impose additional restrictions.

## References

1. Jagtap KR, Lal A, Singh BN (2011) Stochastic nonlinear free vibration analysis of elastically supported functionally graded materials plate with system randomness in thermal environment. *Comut Struct* 93:3185–3199
2. Jagtap KR, Lal A, Singh BN (2012) Stochastic nonlinear bending response of functionally graded material plate with random system properties in thermal environment. *Int J Mech Mater Des* 8:149–167
3. Matsunaga H (2008) Free vibration and stability of functionally graded shallow shells according to a 2D higher-order deformation theory. *Comput Struct* 132–146
4. Alijani F, Ambili M, Bakhtari-Nejad F (2011) Thermal effects on nonlinear vibrations of functionally graded doubly curved shells using higher order shear deformation theory. *Compos Struct* 93:2541–2553
5. Lal A, Singh BN, Anand S (2011) Nonlinear bending response of laminated composite spherical shell panel with system randomness subjected to hygro-thermo-mechanical loadingpp. *Int J Mech Sci* 53:855–866
6. Huang X-L, Shen H-S (2004) Nonlinear vibration and dynamic response of functionally graded plates in thermal environments. *Int J Solids Struct* 41:2403–2427
7. Lal A, Jagtap KR, Singh BN (2013) Post buckling response of functionally graded materials plate subjected to mechanical and thermal loadings with random material properties. *App Math Mod* 37:2900–2920
8. Singh BN, Yadav D, Iyengar NGR (2003) A  $C^0$  element for free vibration of composite plates with uncertain material properties. *Adv Compos Mater* 11:331–350
9. Shen H-S, Wang H (2014) Nonlinear vibration of shear deformable FGM cylindrical panels resting on elastic foundations in thermal environments. *Composites* 60:167–177

# Structural, Dielectric, Electrical and Optical Properties of $\text{Ca}_3\text{CuZr}_4\text{O}_{12}$ Ceramics



S. K. Parida, S. Senapati, S. Mishra, R. K. Bhuyan, B. Kisan, and R. N. P. Choudhary

**Abstract** In this paper, the synthesis of  $\text{Ca}_3\text{CuZr}_4\text{O}_{12}$  (CCZO) ceramic by a cost-effective mixed solid-state reaction route is discussed. The analysis of XRD profile confirms a rhombohedral structure with space group R-3c. The Williamson-Hall method is used to calculate average crystallite and lattice compressive strain, which are about 38.7 nm and 0.0238%, respectively. The UV–visible spectroscopy indicates that the sample has the highest absorbance in the visible region of 650–670 nm. The electrical plots are very much helpful to evaluate the effect of microstructure on the conduction mechanism in the sample. The investigation of the dielectric properties with both frequency and temperature suggests the negative temperature coefficient of resistance (NTCR) behavior. The variation of activation energy with frequency confirms the presence of a thermally activated conduction mechanism. These materials may have potential electronic device applications.

**Keywords**  $\text{Ca}_3\text{CuZr}_4\text{O}_{12}$  · Rhombohedral · Lattice strain · Activation energy · NTCR

## 1 Introduction

To have a better understanding of the implementation of lead-free newly fabricated eco-friendly ceramic materials, one should be aware of the parameters such as dielectric, ferromagnetic, ferroelectric, pyroelectrics, and piezoelectric characteristics [1, 2]. In the present research, people focus on the electro-ceramic properties and their

---

S. K. Parida (✉) · S. Senapati · S. Mishra · R. N. P. Choudhary  
Department of Physics, ITER, Siksha ‘O’ Anusandhan Deemed to be University, Bhubaneswar  
751030, India  
e-mail: [santoshparida@soa.ac.in](mailto:santoshparida@soa.ac.in)

R. K. Bhuyan  
P.G. Department of Physics, Government (Auto) College Angul, Angul 759143, India

B. Kisan  
Department of Physics, Utkal University, Vani Vihar, Bhubaneswar 751004, India

uses in the multilayer ceramic capacitors, spintronic, sensors, and transducers in addition to optoelectronic devices [3–8]. The general formula for perovskite material is  $ABO_3$ , where A and B are two cations and O is an anion. The formation of the sample is checked by Goldschmidt's tolerance factor  $t$  in the allowed range ( $0.75 < t < 1.0$ ) [9]. In the last few years, new quadruple perovskite like  $AA_3B_4O_{12}$  grabs the research of material scientists because of elevated permittivity value and low linkage current. The first quadruple perovskite material is  $CaCu_3Ti_4O_{12}$  (CCTO). These materials catch the eye due to their high dielectric constant ( $\sim 10^3$ – $10^5$ ) over the range of 100–600 k and low tangent loss ( $\sim 0.02$  at 1 kHz) [10, 11]. The  $Cu^{2+}$  ion tenanted an A-site and  $Ti^{4+}$  accommodate at the tilted octahedral in structure [12]. The Cu atom segregates in the sintering process and puts an effort on the thickness of grain boundaries to obtain required physical properties [13]. The calcium copper zirconate ( $Ca_3CuZr_4O_{12}$ ) quadruple ceramics is one of the novel's functional ceramics for applications. Zirconia is one of the most widely used ceramic oxides because of its application in solid oxide fuel cells (SOFCs). In this paper; analysis of the structural, dielectric, electrical, and optical properties of the  $Ca_3CuZr_4O_{12}$  ceramics is reported. There is no sufficient literature available for the studied material. A decision is taken to synthesize the sample by a conventional mixed solid-state reaction method. The structural analysis predicts a rhombohedral structure; and dielectric plots predict semiconducting nature of the sample.

## 2 Experimental Details

The  $Ca_3CuZr_4O_{12}$  quadruple perovskite was prepared by a mixed solid-state reaction technique. The starting raw materials are  $BaCO_3$  (99.9%),  $ZrO_2$  (99.9%), and  $CuO$  (99.9%) and weighted as per stoichiometric ratio using digital spring balance (model: ML204/A01) which gives accuracy up to four decimal places. The chemical reaction for the synthesis of the final product can be written as  $3CaCO_3 + CuO + 4ZrO_2 \rightarrow Ca_3CuZr_4O_{12} + 3CO_2 \uparrow$ . The metal oxides were grinded together in the mortar with the help of a pestle for 2–3 h in the dry medium. Then, for better homogeneity, the powder samples were mixed in a wet medium with methanol for 2–3 h. The powder samples were taken in a high-temperature silica crucible and put inside a high-temperature furnace at 1150 °C for 10–12 h, so called calcination. The formation of the sample is confirmed from the primary recorded XRD pattern (Rigaku Mini flex, Japan). To obtain the XRD data, source energy  $CuK\alpha$  (wavelength,  $\lambda = 1.5405 \text{ \AA}$ ) has been used in a range of Bragg angles  $2\theta$  ( $20^\circ \leq 2\theta \leq 80^\circ$ ) at 0.005°/min scan rate to understand the primary structure and phase. The XRD data was analyzed using origin 8.5 software and the X'Pert High Score Plus software. Then, the calcinated sample powders were used to make cylindrical pellets. The thickness and diameter of a pellet are about 10 mm and 1–2 mm, respectively. The pellets are made using PVA binder under KBr hydraulic press of an axial pressure of  $3.5 \times 10^6 \text{ Nm}^{-2}$ . The obtained cylindrical pellets have undergone a sintering process with an optimized temperature of 1200 °C for 10–12 h in a silica

sample holder to obtain highly dense pellets in the required dimension. The surface of resulted sintered pellets was polished properly to make the surface perfect parallel and smooth by using a fine sand paper. Then, the pellet is made into the electrodes by applying silver paint of Alfa Aesar on both surfaces and gently heated for 1 h at 110 °C. Then, sample is ready to record the electrical parameters like a dielectric, impedance, conductivity, etc., using an impedance analyzer (Model; PSM 1735, N4L), at a wide range of frequency from 1 kHz to 1 MHz and along with different temperature (from 25 °C to 500 °C). The structure and optical measurements were taken by XRD and UV–visible spectroscopy that discussed in details in next section

### 3 Results and Discussion

#### 3.1 Structure Confirmation

The tolerance factor of the  $\text{Ca}_3\text{CuZr}_4\text{O}_{12}$  ceramics can be calculated by  $t = \frac{r_A + r_o}{\sqrt{2}(r_B + r_o)}$ , where  $t$  = tolerance factor,  $r_o$  = radius of oxygen,  $r_A$  = radius of A-atom Å, and  $r_B$  = radius of B-atom. The different possible values of the tolerance factor for different crystal structure are given; cubic structure;  $0.9 < t < 1.0$ , for hexagonal crystal structure;  $1.00 < t < 1.13$  and for orthorhombic/rhombohedral structure  $0.75 < t < 0.9$  [14]. The ionic radii of  $\text{Ca}^{2+}$ ,  $\text{Cu}^{+2}$  and  $\text{Zr}^{4+}$  are 1.26 Å, 0.73 Å and 0.72 Å, respectively [15]. The tolerance factor of calcium zirconate ceramics is found to be 0.79, indicating the formation of the sample.

#### 3.2 XRD Analysis

The scan of the X-ray diffractometer ( $\text{CuK}_\alpha$ ,  $\lambda = 1.5406 \text{ \AA}$ ) was taken on the sample from  $20^\circ$  to  $80^\circ$  with a step size of  $0.005^\circ$  per minute as shown in Fig. 1. The presence of the clear and distinguished peaks in the X-ray diffraction profile hint a single-phase sample.

The occurrence of the highest intense peak at scattering angle  $30.16^\circ$  is well-matched with JCPDF-00-005-0586; which suggests a rhombohedral structure. The refined lattice parameters for the rhombohedral crystal structure (#R-3c) are  $a = b = 4.989 \text{ \AA}$ ,  $c = 17.062 \text{ \AA}$ ,  $\alpha = 90^\circ$ ,  $\beta = 90^\circ$ ,  $\gamma = 120^\circ$ ,  $V = 367.38 \text{ \AA}^3$ , and density =  $2.71 \text{ g/cm}^3$ .

The indestructible atomic interaction and mechanical bond stretching provide the lattice micro-strain in the host matrix. Williamson-Hall (W–H) formulated a relation as  $\beta \cos \theta = 4\varepsilon \sin \theta + \frac{k\lambda}{D}$  where  $k = 0.89$ ,  $\lambda = 1.54 \text{ \AA}$ ,  $D$  = average crystallite,  $\varepsilon$  = lattice strain,  $\beta$  = full width half maxima, and  $\theta$  = diffraction angle [16]. Figure 1b represents a graph between  $4\sin\theta$  and  $\beta\cos\theta$ . The y-intersect provides an average

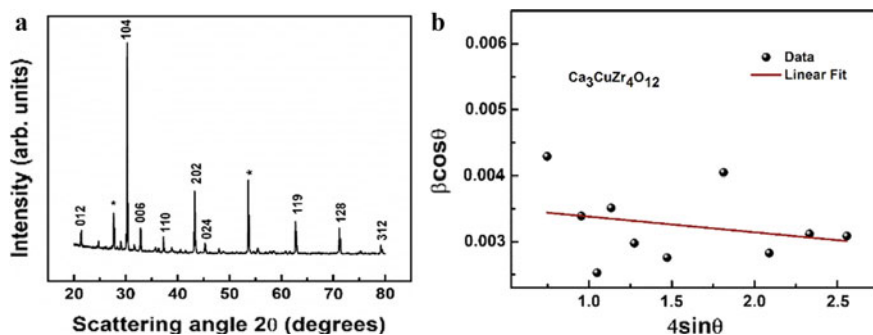


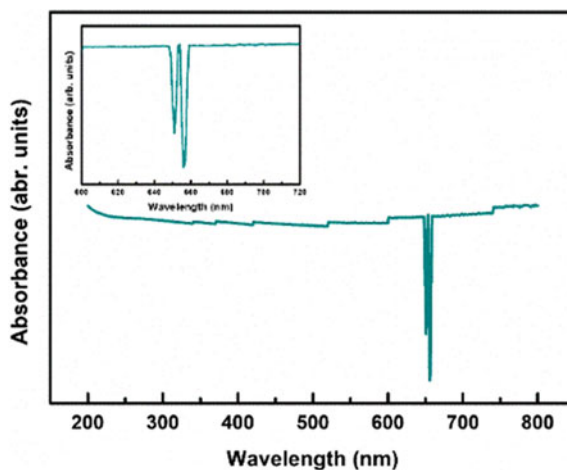
Fig. 1 a XRD pattern, b Williamson-Hall plots of the  $\text{Ca}_3\text{CuZr}_4\text{O}_{12}$  ceramic

crystallite size, which is about 38.7 nm. A linear fit to the W–H plots provides lattice compressive strain, which is about 0.0238% [17].

### 3.3 UV–Visible Spectroscopy

The absorbance coefficient versus incident wavelength is plotted in Fig. 2. The range of incident wavelength is from 200 to 800 nm. In the present study, the absorbing power of the copper and zirconate atoms is finalized from the presence of other neighboring anions. The material under study absorbs incident visible light in the wavelength range of 650–670 nm. Therefore, this material may be used for the device fabrication with response to visible light.

Fig. 2 Absorbing power versus incident wavelength



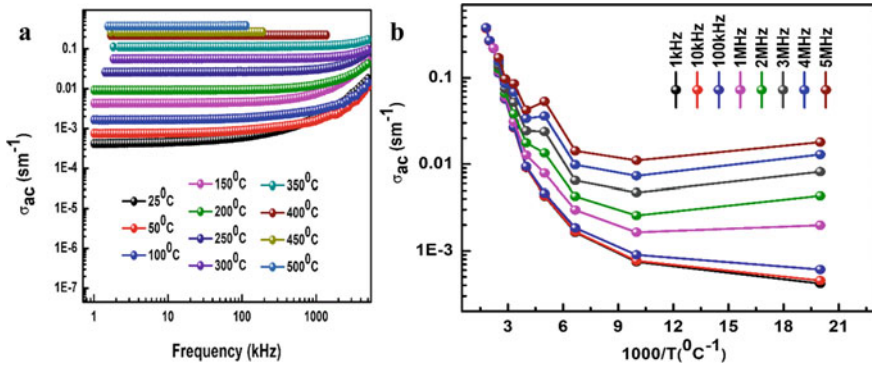


**Fig. 3** **a** ac conductivity versus frequency. **b** ac conductivity ( $\sigma_{ac}$ ) versus  $1000/T$  at some selected frequency of the  $\text{Ca}_3\text{CuZr}_4\text{O}_{12}$  ceramics

Figure 3a reveals the frequency dependency nature of ac conductivity ( $\sigma_{ac}$ ) of the  $\text{Ca}_3\text{CuZr}_4\text{O}_{12}$  ceramics. The graphical plot depicts that the ac conductance increases with temperature as well as frequency. At the lower frequency range, the  $\sigma_{ac}$  disperses with the temperature rise due to the space charge polarization effect. However, at the high-frequency region, the ac plots merge asymmetrically due to thermal agitation, oxygen vacancies/ions travel short distances and hence relax very rapidly. Figure 3b represents ac conductivity versus  $(10^3/T)$  of the  $\text{Ca}_3\text{CuZr}_4\text{O}_{12}$  ceramics. The value of the activation energy is calculated using a relation;  $\sigma_{ac} = \sigma_0 \exp(-E_a/k_B T)$ , where  $k_B$  = Boltzmann constant,  $\sigma_0$  = initial exponential factor,  $E_a$  = activation energy, and  $T$  = absolute temperature.

The calculated activation energies are 4.28 meV, 4.68 meV, 5.26 meV, 6.24 meV, 8.78 meV, 13.04 meV, 13.72 meV, and 16.31 meV at 1 kHz, 10 kHz, 100 kHz, 1 MHz, 2 MHz, 3 MHz, 4 MHz, and 5 MHz, respectively. The activation energy increases with frequency which suggests a thermally activated relaxation process [18, 19]. Figure 4a shows the change of dielectric constant ( $\epsilon_r$ ) with frequency from 25°C to 350°C. At lower frequencies, dispersed dielectric constants are observed because of the occurrence of electronic, ionic, dipolar, and space charge polarization, which may support the ferroelectric nature of the sample. However, the dielectric constant decreases in the higher range of frequency due to the space charge polarization effect [20]. Figure 4b depicts the pictorial representation of tangent loss versus the frequency of CCZO ceramic from 25°C to 350°C. It is noticed that tangent loss is maximum at low frequency and decreases smoothly approaching zero at higher frequencies, which may be due to the release of space charge polarization [21].

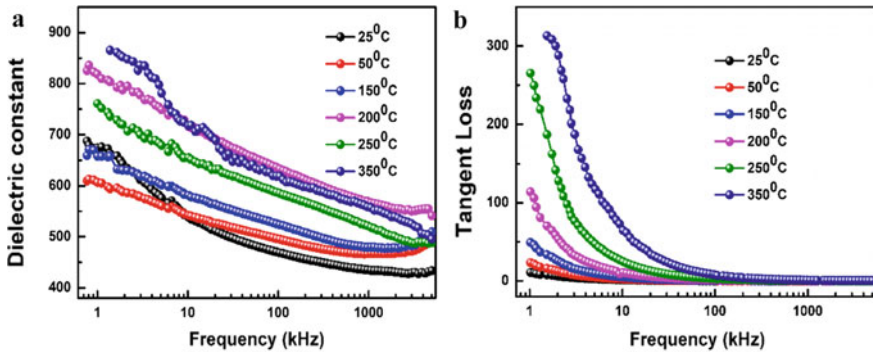


**Fig. 4** a Frequency-dependent dielectric constant ( $\epsilon_r$ ) at some selected temperatures and **b** represents the frequency-dependent dielectric loss ( $\tan \delta$ ) of the  $\text{Ca}_3\text{CuZr}_4\text{O}_{12}$  ceramics

## 4 Conclusion

The CCZO sample was prepared by conventional solid-state reaction method. The XRD profile suggests a rhombohedral structure with space group R-3c. The W–H method provides average crystallite size and lattice compressive strain; which are about 38.7 nm and 0.0238%, respectively. The UV–visible study indicates that the material has the highest absorbance in the visible region of 650–670 nm. The study on the dielectric suggests NTCR behavior, and ac conductivity confirms thermally activated conduction mechanism in the sample.

**Conflict of Interest** The authors have no *conflicts of interest* to declare.

## References:

1. Yalcin O, Cosskun R, Okutan M, Ozturk M (2013) Comparison effects and dielectric properties of different dose methylene-blue-doped hydrogels. *J Phys Chem B* 117(30):8931–8938
2. Yoo SY, Ha JY, Yoon SJ, Choi JW (2013) High-power properties of piezoelectric hard materials sintered at low temperature for multilayer ceramic actuators. *J Eur Ceram Soc* 33(10):1769–1778
3. Goyal RK, Katkade SS, Mule DM (2013) Dielectric, mechanical and thermal properties of polymer/BaTiO<sub>3</sub> composites for the embedded capacitor. *Compos: Part B* 44(1):128–132
4. Chung S-Y, Choi J-H, Choi J-K (2007) Tunable current-voltage characteristics in polycrystalline calcium copper titanate. *Appl Phys Lett* 91(9):091912–091913
5. Kim HE, Yang S, Lee J-W, Park HM, Yoo S-I, Cryst J (2014) Growth and characterization of  $\text{CaCu}_3\text{Ti}_4\text{O}_{12}$  single crystals. *J Cryst Growth* 408:60–63
6. Parida SK, Choudhary RNP, Ganga Raju Achary P (2019) Structure and ferroelectric properties of lead nickel tungsten titanate:  $\text{Pb}(\text{Ni}_{1/3} \text{T}_{1/3} \text{W}_{1/3}) \text{O}_3$  single perovskite. *Ferroelectrics* 551(1):109–121
7. Uchino K (2000) *Ferroelectric devices*. Marcel Dekker, New York



8. Achary PGR, Nayak AA, Bhuyan RK, Choudhary RNP, Parida SK (2021) Effect of cerium dopant on the structural and electrical properties of SrMnO<sub>3</sub> single perovskite. *J Mole Struct* 1226(A):129391–129399
9. Chen K, Li GL, Gao F, Liu J, Liu JM, Zhu JS (2007) Conducting grain boundaries in the high-dielectric-constant ceramic CaCu<sub>3</sub>Ti<sub>4</sub>O<sub>12</sub>. *J Appl Phys* 101(7):074101–074104
10. Parida SK (2021) Structural, electrical and optical properties of zinc and tungsten modified lead titanate ceramics. *SPIN* 11(2):2150018–2150114
11. Pansara PR, Raval PY, Vasoya NH, Dolia SN, Modi KB (2018) Intriguing structural and magnetic properties correlation study on Fe<sup>3+</sup> substituted calcium-copper-titanate. *Phys Chem Chem Phys* 20(3):1914–1922
12. Jing Liang HE, Chao LF, Jun HU, Hua LY (2011) Cu segregation and its effects on the electrical properties of calcium copper titanate. *Sci China Tech Sci* 54:2506–2510
13. Zhang L, Song F, Lin X, Wang D (2020) High-dielectric-permittivity silicone rubbers incorporated with polydopamine-modified ceramics and their potential application as dielectric elastomer generator. *Mater Chem Phys* 241:122373–122377
14. Voorhoeve RJH (1977) *Advanced materials in catalysis*. Acad Press, New York, pp 1–129
15. Dean JA (1998) *Lange's handbook of chemistry*, 15th edn. McGraw-Hill, New York
16. Cullity BD (1967) *Elements of X-ray diffraction*. Addison-Wesley, Reading MA, 388
17. Parida SK (2016) Structural behavior of Cu<sub>0.5</sub>Ag<sub>0.5</sub> and Cu<sub>0.5</sub>Al<sub>0.5</sub> alloys synthesized by co-melting technique. *Adv Sci Lett* 22(2):584–587
18. Parida SK, Choudhary RNP, Achary PGR (2020) Study of structural and electrical properties of polycrystalline Pb(Cd<sub>1/3</sub>Ti<sub>1/3</sub>W<sub>1/3</sub>)O<sub>3</sub> tungsten Perovskite. *Int J Microstruct Mater Prop* 15(2):107–121
19. Parida SK, Swain MK, Bhuyan RK, Kisan B, Choudhary RNP (2021) Effect of cerium on structural and dielectric properties of the modified BiFeO<sub>3</sub>-PbTiO<sub>3</sub> ceramics for photovoltaic applications. *J Electron Mater* 50(8):4685–4695
20. Parida RK, Parida BN, Bhuyan RK, Parida SK (2021) Structural, mechanical and electric properties of La doped BNT-BFO perovskite ceramics. *Ferroelectrics* 571(1):162–174
21. Ganga Raju Achary P, Choudhary RNP, Parida SK (2020) Investigation of structural and dielectric properties in polycrystalline PbMg<sub>1/3</sub> Ti<sub>1/3</sub>W<sub>1/3</sub>O<sub>3</sub> tungsten perovskite. *SPIN* 10(3):2050021–20500210

# MHD Up/Down Flow of Nanofluids with SWCNT/MWCNT Suspensions



D. N. Thatoi, S. Choudhury, S. S. Mohapatra, and M. K. Nayak

**Abstract** Carbon nanotubes (SWCNTs/MWCNTs) have widespread applications in micro and nano-electronics, flat panel displays, conductive plastics, gas storage, technical textiles, ultra-capacitors, sensors, biosensor and several others. The shape effects of various kinds of SWCNT/MWCNT nanoparticles share major role in the amelioration of heat transfer rate. The impact of SWCNT/MWCNT nanoparticles' shapes on the dissipative up and down MHD flow of nanofluids past thin needle subject to second order slip is investigated in the present study. Brick, Cylinder, Platelet and Blade shapes of nanoparticles are taken into consideration. Numerical solution is obtained by R-K method cum shooting technique. The important outcome of this study conveys that heat transfer rate is the lowest for Brick nanoparticles while it is the largest for Platelet nanoparticles.

**Keywords** Up/down flow · MHD · SWCNT/MWCNT

## Nomenclature

$(u, v)$	Velocity components
$(\rho_{nf}, \rho_s, \rho_f)$	Density of (nanofluid, CNTs, base fluid)
$((\rho C_p)_{nf}, (\rho C_p)_f, (\rho C_p)_{CNT})$	Are heat capacity of (nanofluid, base fluid, CNTs), respectively
$(\mu_{nf}, \mu_f)$	Dynamic viscosity of nanofluid and base fluid
$(\beta_{nf}, \beta_f, \beta_s)$	Thermal expansion of (nanofluid, base fluid, CNTs)
$(k_{nf}, k_f, k_s)$	Thermal conductivity of (nanofluid, base fluid, CNTs)
$S'_0 = \frac{4k_f(\theta_f - 1)^2}{x^2}$	Characteristic EG rate
$\nu_{nf}$	Kinematic viscosity of nanofluid

---

D. N. Thatoi · S. Choudhury · S. S. Mohapatra · M. K. Nayak (✉)  
Department of Mechanical Engineering, FET, ITER, Siksha 'O' Anusandhan University,  
Bhubaneswar 751030, India  
e-mail: [manojkumarnayak@soa.ac.in](mailto:manojkumarnayak@soa.ac.in)

$\sigma_{nf}$	Electrical conductivity of nanofluid
$\sigma_{SB}$	Stefan-Boltzmann constant
$a_R$	Mean absorption coefficient
$T$	Fluid temperature within boundary layer
$T_w$	Surface temperature
$T_\infty$	Ambient fluid temperature
$\alpha_f$	Thermal diffusivity of the base fluid
$\lambda$	Mixed convection parameter
Re	Reynolds number
$M$	Hartmann number
Pr	Prandtl number
Nr	Radiation parameter
$\varepsilon$	Velocity ratio parameter
Ec	Eckert number
Br	Brinkman number
$\lambda_m$	Molecular mean free path
Kn	Knudsen number
$\Gamma^*$	Momentum accommodation coefficient
$B_i$	Biot number

## 1 Introduction

The importance of magnetohydrodynamics (MHD) flow of nanofluids (nfs) has relevance in many engineering processes. The magnetic field imposed is utilized in controlling momentum and heat transfer (HT) in the boundary layer flow (BLF) of diverse nanoliquids [1–5]. Experimental study reveals that spherical and non-spherical shapes of nps possess higher thermal conductivity (TC) compare to conventional fluids and are therefore inevitably useful in diversified engineering and industrial processes. The investigations on the flow and HT of carbon nanotubes (CNTs) nfs with several geometries and flow characteristics are in [6–10].

Owing to the survey of literature it is visualized that Brick, Cylinder, Platelet and Blade shapes of nanoparticles (nps) are rarely utilized by researchers in different nfs in their works. However, inclusion of such shapes of SWCNT/MWCNT nps in nfs and the related research are yet to be conducted. The novelty of the present research is to investigate the influence of Brick, Cylinder, Platelet and Blade shapes of SWCNT/MWCNT nps on up and down MHD flow of nfs past a thin needle subject to second order slip.

## 2 Formulation of the Problem

We consider a steady, laminar BLF over a thin needle moving with a constant velocity  $U_w$ . Here, SWCNT and MWCNT are assumed as nps while water as bf. A schematic diagram imparting physical description of the problem is shown in Fig. 1.

The governing equations for the present problem:

$$\frac{\partial}{\partial x}(ru) + \frac{\partial}{\partial r}(rv) = 0, \tag{1}$$

$$u \frac{\partial u}{\partial x} + v \frac{\partial u}{\partial r} = \frac{\nu_{nf}}{r} \frac{\partial}{\partial r} \left( r \frac{\partial u}{\partial r} \right) \pm g \frac{(\rho\beta)_{nf}}{\rho_{nf}} (T - T_\infty) - \frac{\sigma_{nf} B_0^2 u}{\rho_{nf}} \tag{2}$$

$$u \frac{\partial T}{\partial x} + v \frac{\partial T}{\partial r} = \frac{\alpha_{nf}}{r} \frac{\partial}{\partial r} \left( r \frac{\partial T}{\partial r} \right) + \frac{1}{(\rho c_p)_{nf}} \frac{16\sigma_{SB} T_\infty^3}{3a_R} \frac{\partial^2 T}{\partial r^2} + \frac{\mu_{nf}}{(\rho C_p)_{nf}} \left( \frac{\partial u}{\partial r} \right)^2 \tag{3}$$

The BCs are:

$$\left. \begin{aligned} u = U_{slip} + U_w, \quad v = 0, \quad -k_f \frac{\partial T}{\partial r} = h_f(T_f - T), \quad \text{at } r = R(x) \\ u \rightarrow U_\infty(x), \quad T \rightarrow T_\infty \quad \text{as } r \rightarrow \infty \end{aligned} \right\} \tag{4}$$

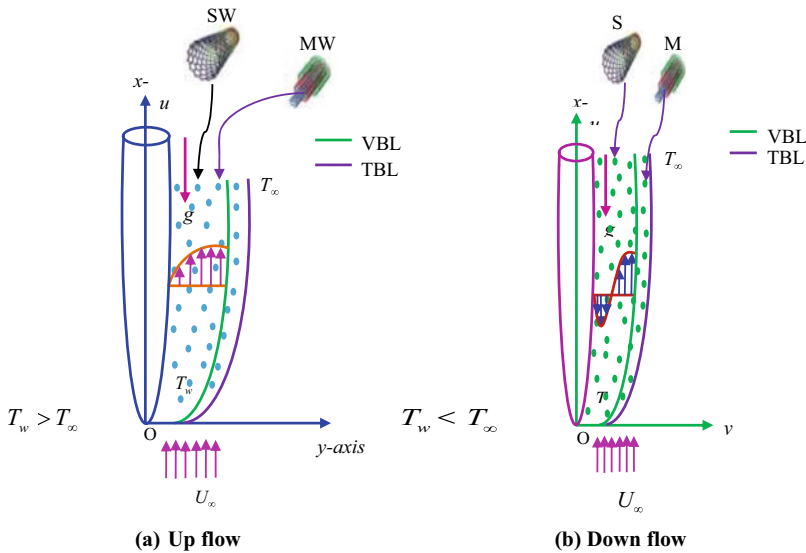


Fig. 1 Flow geometry

The second order slip is defined as

$$U_{\text{slip}} = \frac{2}{3} \left( \frac{3 - \Gamma^* l^3}{\Gamma} - \frac{3}{2} \frac{1 - l^2}{\text{Kn}} \right) \lambda_m \frac{\partial u}{\partial r} - \frac{1}{4} \left[ l^4 + \frac{2}{\text{Kn}^2} (1 - l^2) \right] \lambda_m^2 \frac{\partial^2 u}{\partial r^2} \tag{5}$$

$$\text{or } U_{\text{slip}} = L_1 \frac{\partial u}{\partial r} + L_2 \frac{\partial^2 u}{\partial r^2} \tag{6}$$

$$\text{where } L_1 = \frac{2}{3} \left( \frac{3 - \Gamma^* l^3}{\Gamma} - \frac{3}{2} \frac{1 - l^2}{\text{Kn}} \right) \lambda_m \text{ and} \tag{7}$$

$$L_2 = -\frac{1}{4} \left[ l^4 + \frac{2}{\text{Kn}^2} (1 - l^2) \right] \lambda_m^2$$

In (5) and (7),  $l = \min\left[\frac{1}{\text{Kn}}, 1\right]$ ,  $0 \leq \Gamma^* \leq 1$  and  $\text{Kn} = \frac{\lambda_m}{l}$ .

The transformations needed:

$$u = 2Uf'(\eta), \quad v = -\frac{v_f}{r} f + \eta \frac{v_f}{r} f'(\eta), \quad \theta(\eta) = \frac{T - T_\infty}{T_f - T_\infty}, \quad \eta = \frac{Ur^2}{v_f x} \tag{8}$$

Here,  $U = U_w + U_\infty \neq 0$  is the composite velocity. For  $\eta = a$  in Eq. (5),  $R(x) = (avx/U)^{1/2}$ .

The thermophysical properties of nf:

$$\left. \begin{aligned} \frac{\rho_{\text{nf}}}{\rho_f} &= (1 - \phi) + \frac{\rho_s}{\rho_f} \phi, & \frac{(\rho C_p)_{\text{nf}}}{(\rho C_p)_f} &= (1 - \phi) + \frac{(\rho C_p)_s}{(\rho C_p)_f} \phi, \\ \frac{(\rho \beta)_{\text{nf}}}{(\rho \beta)_f} &= (1 - \phi) + \frac{(\rho \beta)_s}{(\rho \beta)_f} \phi, & \frac{\sigma_{\text{nf}}}{\sigma_f} &= \left[ 1 + \frac{3(\Lambda - 1)\phi}{(\Lambda + 2) - (\Lambda - 1)\phi} \right], \\ \Lambda &= \frac{\sigma_p}{\sigma_f}, \quad \frac{k_{\text{nf}}}{k_f} = \frac{k_s + (n-1)k_f - (n-1)(k_f - k_s)\phi}{k_s + (n-1)k_f + (k_f - k_s)\phi} \end{aligned} \right\} \tag{9}$$

where  $n$  is the shape factor of the solid nps which depends on the sphericity factor  $\omega$  and related as  $n = 3/\omega$ . The value of  $\omega$  is given in Table 1.

The dynamic viscosity of the nf:

$$\mu_{\text{nf}} = \mu_f (1 + A\phi + B\phi^2) \tag{10}$$

where  $A$  and  $B$  are constants depending upon particle shape and shown in Table 2.

Using (8)–(10) in (2), (3) and (4) we get

**Table 1** Sphericity values for various nanoparticle shapes

Parameter	Brick	Cylinder	Blade	Platelet
$\omega$	0.81	0.62	0.36	0.52

**Table 2** Values of constants A and B for different shape of the nanoparticles

Parameter	Brick	Cylinder	Blade	Platelet
A	1.9	13.5	14.6	37.1
B	471.4	904.4	123.3	612.6

$$(1 + A\phi + B\phi^2)\Omega_1(f'' + \eta f') + \frac{1}{2}ff'' + \frac{1}{8}\Omega_2\lambda\theta - \frac{1}{4}\Omega_1\left(\frac{\sigma_{nf}}{\sigma_f}\right)Mf' = 0 \tag{11}$$

$$\Omega_3\left[\frac{k_{nf}}{k_f}\theta' + \eta\left(1 + \frac{1}{3Nr}\right)\theta''\right] + \frac{1}{2}\text{Pr}f\theta' + 4(1 + A\phi + B\phi^2)\eta\Omega_3\text{Br}(f'')^2 = 0 \tag{12}$$

$$\text{With } \left. \begin{aligned} f'(\eta) &= 2\Gamma_1 f''(\eta) + 2\Gamma_2 f''(\eta) + 4\Gamma_2^2 f'(\eta) + \frac{1}{2}(1 - \varepsilon) \\ f(\eta) &= \eta f'(\eta), \theta'(\eta) = -\frac{1}{2}\text{Bi}[1 - \theta(\eta)] \text{ at } \eta = a \\ f'(\eta) &\rightarrow \frac{1}{2}\varepsilon, \theta(\eta) \rightarrow 0 \text{ as } \eta \rightarrow \infty \end{aligned} \right\} \tag{13}$$

Here

$$\left. \begin{aligned} \lambda &= \frac{g\beta_f(T_f - T_\infty)x}{U^2}, M = \frac{\sigma_f B_0^2 x}{\rho_f U}, \varepsilon = \frac{U_\infty}{U}, \text{Pr} = \frac{\nu_f}{\alpha_f}, Nr = \frac{ka_R}{4\sigma_{SB}T_\infty^3}, \\ E_c &= \frac{U^2}{(T_f - T_\infty)(c_p)_f}, \text{Br} = \text{Pr} \cdot \text{Ec}, \Gamma_1 = \frac{L_1 U r}{\nu_f x}, \Gamma_2 = \frac{L_2 U^2}{\nu_f x}, \\ \text{Bi} &= h_f/k_f \left(\frac{Ur}{\nu_f x}\right) \end{aligned} \right\} \tag{14}$$

and

$$\left. \begin{aligned} \Omega_1 &= \frac{1}{\left[(1 - \phi) + \phi\left(\frac{\rho_s}{\rho_f}\right)\right]}, \Omega_2 = \frac{(1 - \phi) + \phi\left\{\frac{(\rho\beta)_s}{(\rho\beta)_f}\right\}}{\left[(1 - \phi) + \phi\left(\frac{\rho_s}{\rho_f}\right)\right]}, \\ \Omega_3 &= \frac{1}{\left[(1 - \phi) + \phi\left\{\frac{(\rho c_p)_s}{(\rho c_p)_f}\right\}\right]} \end{aligned} \right\} \tag{15}$$

The local skin friction coefficient and local Nusselt number:

$$\text{Re}_x^{0.5} C_f = 8(1 + A\phi + B\phi^2)a^{\frac{1}{2}} f''(a) \tag{16}$$

$$\text{Re}_x^{-0.5} \text{Nu} = -2a^{\frac{1}{2}} \left(\frac{k_{nf}}{k_f} + \frac{4}{3Nr}\right)\theta'(a) \tag{17}$$

### 3 Results and Discussion

The governing Eqs. (11) and (12) along with BCs (13) are solved using shooting method. Shooting method is adopted to establish the initial guess. Here, we have assumed the  $\eta_{\max}(\eta_{\infty})$  as 15. This section deals with the interpretation of numerical results exploring impact of various emerging parameters. In the present problem, we have taken the general values of the parameters as  $\lambda = 1, \varepsilon = 0.5, M = 15, \Gamma_1 = 0.1, \Gamma_2 = 0.1, a = 0.2, \beta = 0.1, Re = 1, \phi = 0.001, \phi = 0.001, Nr = 5,$

$Pr = 7, Br = 0.5, Bi = 0.4.$  Properties of the CNTs are shown in Table 3.

In the velocity field representation, Fig. 2 delineates the flow behavior for different shapes of nps such as Brick ( $A = 19, B = 471.4$ ), Cylinder ( $A = 13, B = 904.4$ ), Blade ( $A = 14.6, B = 123.3$ ) and Platelet ( $A = 37.1, B = 612.6$ ) for up flow ( $\lambda = 1$ ) and down flow ( $\lambda = -1$ ) for SWCNT/MWCNT-water nfs. For up flow ( $\lambda = 1$ ), fluid velocity  $f'(\eta)$  grows in the order Brick, Cylinder, Blade and Platelet. It seen that  $f'(\eta)$  attains the lower value when Brick shaped nps are inserted while it attains greater value with the inclusion of Platelet nps. It is noted that for down flow ( $\lambda = -1$ ),  $f'(\eta)$  shows the same behavior in the same order of the np shapes. Figure 3 narrates

**Table 3** Thermophysical properties of the base fluid and nanoparticles at  $T = 300\text{ K}$

	$\rho(\text{Kg/m}^3)$	$C_P(\text{J/KgK})$	$k(\text{W/mK})$	$\mu_f(\text{Ns/m}^2)$
Pure water	997.1	4179	0.613	0.001003
SWCNTs	2600	425	6600	
MWCNTs	1600	796	3000	

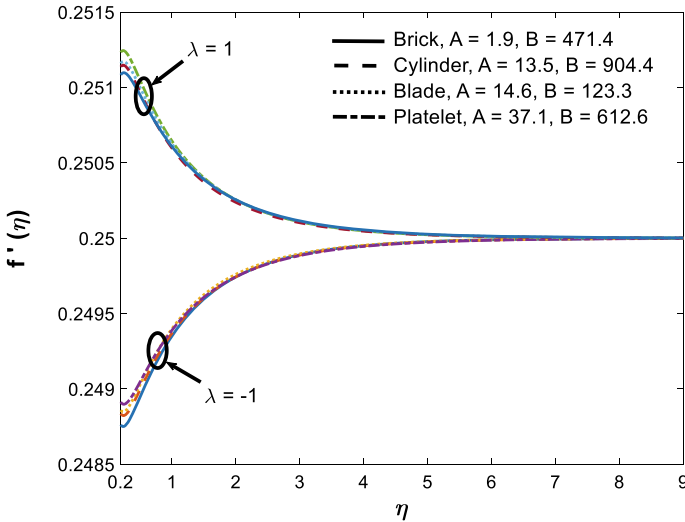


**Fig. 2**  $f'(\eta)$  for diverse shape and  $\lambda$

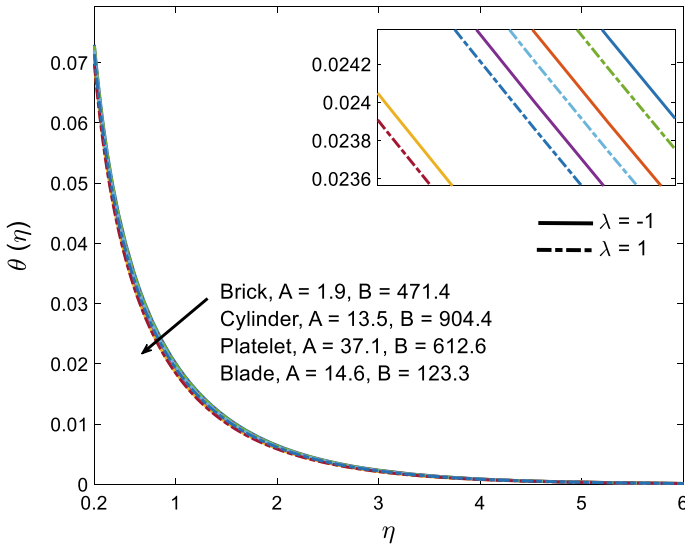


**Fig. 3**  $\theta(\eta)$  for diverse shape and  $\lambda$

that for any nature of the flow (up/down),  $\theta(\eta)$  decays in the order of Brick, Cylinder, Platelet and Blade. This implicates the rate of HT would intensify in the above order of the nps shapes.

Figure 4 illustrates the characteristics of skin friction ( $C_f$ ) for different shapes of nps subject to several flow situations. In such environment, in the down flow case,  $C_f$  for nps of different shapes are related as  $(C_f)_{Brick} > (C_f)_{Cylinder} > (C_f)_{Blade} > (C_f)_{Platelet}$  (in magnitude). It is visualized that surface viscous drag (SVD) is the largest for Brick while it is lowest for platelet under the influence of down flow ( $-1 < \lambda < 0$ ). Exactly reverse effect is attained in case of up flow ( $0 < \lambda < 1$ ). From Fig. 5 it is observed that Nusselt number (Nu) diminishes whatever the character of the flow (down/up) and nps' shapes (Brick/Cylinder/Blade/Platelet) may be. The HTR enhances in the order of shapes as Brick ( $A = 19, B = 471.4$ ), Cylinder ( $A = 13, B = 904.4$ ), Blade ( $A = 14.6, B = 123.3$ ) and Platelet ( $A = 37.1, B = 612.6$ ).

## 4 Conclusions

The major finding of the present study include that the velocity field intensifies for up flow as well as down flow in the order of nanoparticle shapes as Brick, Cylinder, Blade and Platelet. For any flow (up/down), the temperature distribution emaciates in the order of nanoparticle shapes as Brick, Cylinder, Platelet and Blade indicating intensification of heat transfer rate in the above order of nanoparticle shapes.



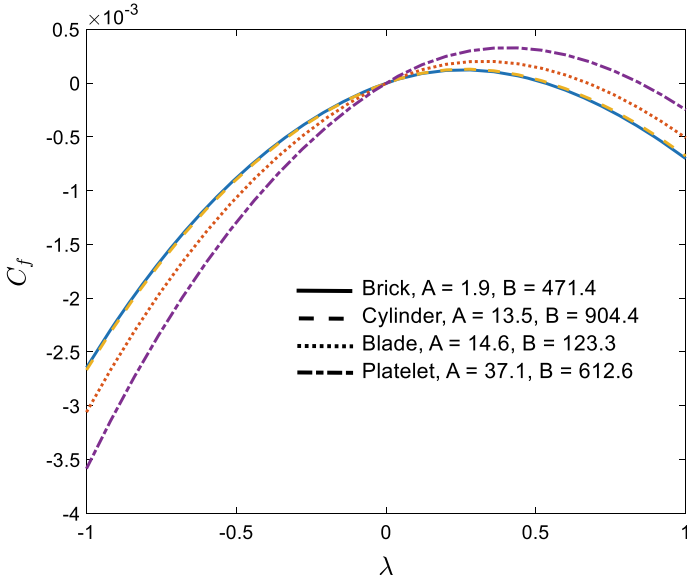


Fig. 4 Skin friction versus  $\lambda$  for diverse shape factor

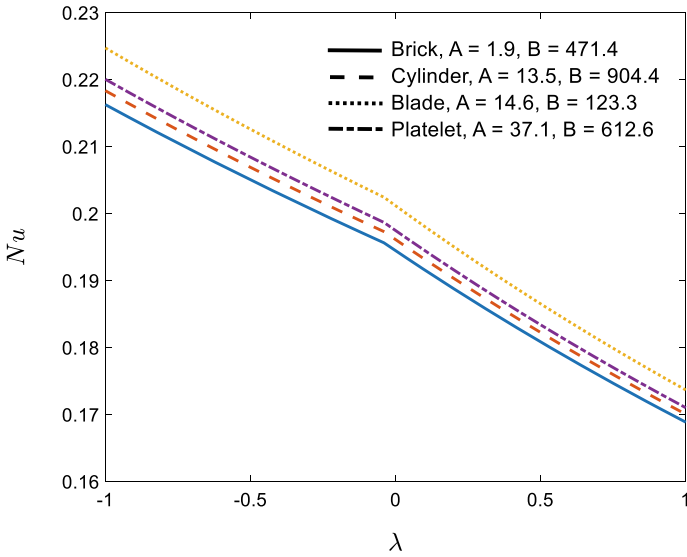


Fig. 5 Nusselt number versus  $\lambda$  for diverse shape factor

## References

1. Choi SUS, Eastman JA (1995) Enhancing thermal conductivity of fluids with nanoparticles. In: Proceedings of the 1995 ASME international mechanical engineering congress and exposition, San Francisco, USA, ASME, FED 231/MD, vol 66, pp 99–105
2. Ijaz KM, Waqas M, Hayat T, Alsaedi A (2017) A comparative study of Casson fluid with homogeneous-heterogeneous reactions. *J Colloidal Interface Sci* 498:85–90
3. Ijaz MM, Alzahrani F (2020) Nonlinear dissipative slip flow of Jeffrey nanomaterial towards a curved surface with entropy generation and activation energy. *Math Comput Simul* 185:47–61
4. Ijaz KM, Alzahrani F (2021) Dynamics of activation energy and nonlinear mixed convection in Darcy-Forchheimer radiated flow of Carreau nanofluid near stagnation point region. *J Thermal Sci Eng Appl* 11(5):051009
5. Ijaz KM, Alzahrani F (2021) Free convection and radiation effects in nanofluid (silicon dioxide and molybdenum disulfide) with second order velocity slip, entropy generation, Darcy-Forchheimer porous medium. *Int J Hydrogen Energy* 46:1362–1369
6. Yu C, Shi L, Yao Z, Li D, Majumdar A (2005) Thermal conductance and thermopower of an individual single-wall carbon nanotubes. *Nano Lett* 5:1842–1846
7. Grujicic M, Cao G, Gersten B (2004) Atomic-scale computations of the lattice contribution to thermal conductivity of single-walled carbon nanotubes. *Mater Sci Eng B* 107:204–216
8. Al-Rashed AAA, Kolsi L, Öztop HF, Aydi A, Malekshah EH, Hamdeh N, Abu BMN (2018) 3D magneto-convective heat transfer in CNT-nanofluid filled cavity under partially active magnetic field. *Physica E* 99:294–303
9. Kolsi L, Al-Rashed AAA, Al-Salem K, Öztop HF, Borjini MN (2017) Control of natural convection via inclined plate of CNT-water nanofluid in an open sided cubical enclosure under magnetic field. *Int J Heat Mass Transf* 111:1007–1018
10. Selimefendigila F, Öztop HF (2018) Numerical analysis and ANFIS modeling for mixed convection of CNT-water nanofluid filled branching channel with an annulus and a rotating inner surface at the junction. *Int J Heat Mass Transf* 127:583–599

# Effect of GGBS and Burnt Paper Based Solid Wastes Ash in Making Sustainable Paver Blocks: An Experimental and Model Study



Meyyappan Palaniappan and Ravi Tejeswar Reddy

**Abstract** In school and higher educational institutions, the paper based solid wastes are majorly generated and disposed through various solid waste management methods. Especially through incineration methods, these solid wastes are subjected to thermal treatment and wastes are converted into ashes which are left out as landfills. In reference with past researches, in the sustainable point of view, these ashes can have a possible significance to act as a partial replacement materials along with the conventional in making building materials. An attempt has made to utilize these paper-based waste burnt ashes in making pavement blocks. These ashes are used as a partial replacement material for cement in the replacement ratio of 10, 20, 30, 40 and 50% in combination of with and without GGBS material. The pavement block specimens are in the size of 70 mm (length)  $\times$  50 mm (thickness) in a hexagonal shape are considered in this study. Totally 71 specimens of various proportions in the mix ratio of 1:3 (Cement:Sand) were casted and tested to examine the compressive strength and water absorption characteristics in the curing age of 7 and 28 days. Without considering GGBS content, 10% of waste burnt ash can be optimum in producing 0.82 times of the conventional strength. In considering GGBS content, 30% of waste burnt ash can be optimum in producing 0.91 times of the conventional strength. Better result obtained in water absorption test also. Through regression analysis, model equation arrived for estimating compressive strength and volume of pores by incorporating the paper ash and GGBS content.

**Keywords** GGBS · Waste burnt paper ash · Paver blocks

## 1 Introduction

Educational institutions are generating higher amount of paper-based solid waste products such as papers, card boards and paper-based cups. These are collected and disposed on the landfills on the daily basis. Mostly, on weekly basis these dumped

---

M. Palaniappan (✉) · R. T. Reddy  
Kalasalingam Academy of Research and Education, Krishnankoil, TN 626126, India  
e-mail: [meyyappan@klu.ac.in](mailto:meyyappan@klu.ac.in)

© The Author(s), under exclusive license to Springer Nature Singapore Pte Ltd. 2023  
P. Pradhan et al. (eds.), *Recent Advances in Mechanical Engineering*,  
Lecture Notes in Mechanical Engineering,  
[https://doi.org/10.1007/978-981-16-9057-0\\_36](https://doi.org/10.1007/978-981-16-9057-0_36)

341

wastes are subjected to incineration and burnt out into ashes. This leads to severe pollution related issues to the environment [1, 2]. Many past literatures indicating the ashes which obtained from the burning of waste materials can be effectively used as a sustainable alternative material for civil engineering materials [3–6]. In the recent days, the cement is partially or fully replaced with various materials which are greatly resolving the issues related with CO<sub>2</sub> emission and green house emission [7–11]. An attempt is made to utilize the waste burnt paper ashes into manufacturing a sustainable paver blocks can address the two major issues viz., effective utilization of waste materials and optimized/regulated the usage of cement in the civil engineering applications [12–15]. This utilization of burnt ash content in different proportion definitely brings down the cost of paver blocks since this material is available in plenty throughout the year in free of cost manner. It has low density in comparing with cement materials and thereby it can able to reduce the weight of paver block to some extent. In order to enhance the strength and durability related properties of the paver blocks, 5% of GGBS materials can be introduced along with cement, aggregate and burnt ash materials in this experimental study. The following objectives are formulated in this experimental study:

- (a) To utilize the waste material ash in form of paver block.
- (b) To determine whether the ash can be used as a construction material or not.
- (c) To determine required value of compression strength and water absorption required for normal paver blocks.
- (d) To study the effect of various types of replacements (10, 20, 30, 40, 50%) of cement by ash and conventional concrete on 7 days and 28 days of compressive strength and water absorption test.

## **2 Material Used**

### **2.1 Cement**

The cement used in this experimental study is ordinary Portland cement of 53-grade conforming to standards of IS 12269. The cement's properties are found as specific gravity 3.16, initial setting time 31 min and final setting time 570 min.

### **2.2 Fine Aggregate**

The locally available good quality river sand passing through 2.36 mm sieve confirming to zone II grading is used in this study. Its specific gravity is 2.61.

**Table 1** Properties of GGBS

S. No.	Properties	Values	S. No.	Properties	Values (%)
1	Specific gravity	2.92	6	SiO <sub>2</sub> content	32–35
2	Bulk density	1250 kg/m <sup>3</sup>	7	Al <sub>2</sub> O <sub>3</sub> content	12.5–15
3	Maximum dry density	2.52 g/cc	8	MgO content	6.5–8.5
4	Fineness	370 m <sup>2</sup> /kg	9	Loss of ignition	<2.0
5	CaO content	36–41%			

### 2.3 *Burnt Paper Ash*

The waste papers are incinerated nearby our place. These ashes were collected and it is sieved by 300  $\mu$ m sieve to get uniformed fine particles. Its specific gravity is 3.56.

### 2.4 *GGBS*

GGBS is the by-product which is obtained from the blast furnace as a waste residue on the iron manufacturing process. The properties of GGBS is mentioned in Table 1.

### 2.5 *Water*

For the entire experimental study, normal potable drinking water obtained from a single source of supply is considered.

## 3 **Experimental Study**

In this experimental study, the paver block shape chosen is hexagonal due to its simplicity. For long time use, the mould for this hexagonal shape paver block fabricated from aluminium sheet material. Based on the suitability and placement of paver blocks, its dimensions are designed as 7 cm side length and 5 cm depth as shown in Fig. 1a. The materials such as cement, sand, burnt paper ash and GGBS have taken as per the proportions mentioned in Tables 2 and 3 for dry mixing and required water is allowed in gradual manner to achieve homogeneous wet mixture as shown in Fig. 1b.

Totally, 36 and 30 paver block specimens were casted for this two trials considering with and without GGBS respectively (Tables 2 and 3). For both trials each 6 paver block specimens in each proportions were casted for conducting compression and water absorption test.



**Fig. 1** a Paver block mould. b Mixing of materials

**Table 2** Mix proportions and specimen details considering without GGBS

S. No.	Sand (%)	Cement (%)	Burnt paper ash (%)	Specimen casted for	
				Compression test	Water absorption test
1	50	50	0	3	3
2	50	40	10	3	3
3	50	30	20	3	3
4	50	20	30	3	3
5	50	10	40	3	3
6	50	0	50	3	3
Total				18	18

**Table 3** Mix proportions and specimens details considering with GGBS

S. No.	Sand (%)	Cement (%)	GGBS (%)	Burnt paper ash (%)	Specimen casted for	
					Compression test	Water absorption test
1	50	45	5	0	3	3
2	50	35	5	10	3	3
3	50	25	5	20	3	3
4	50	15	5	30	3	3
5	50	5	5	40	3	3
Total					15	15

For this experimental study totally 71 paver specimens were casted for both trials with and without GGBS content. The casted specimens on size 70 mm on each sides and 50 mm depth are shown in Fig. 2a. After 24 h of casting, specimens are demoulded and placed under water curing for 7 and 28 days (Fig. 2b). Specimens are subjected to testing after respective curing days on compressive testing machine



**Fig. 2** a Casted paver block specimen. b Specimen under curing

to evaluate its compressive strength. The compression strength test of these paver block specimens were carried out in the compression testing machine which is having capacity of 1000 kN as prescribed by ASTM C 140 standards. This test was carried out at a reliable consistent stress rate of 14 N/mm<sup>2</sup>/min, once the specimen is kept in between the centric plates. The failure load is noted and compressive strength is obtained by dividing the failure load to the contact area of the Paver block. Water absorption test is carried out by finding the weight difference of the specimen before and after placing over under 70–90 °C for duration of 48 h. In water absorption test, the volume of pores is evaluated.

## 4 Results and Discussion

Table 4 shows the compressive strength and porosity test results for the burnt paper ash proportion such as 0, 10, 20, 30, 40 and 50% against 7 days curing and 28 days curing for without and with GGBS content. It is observed that the compressive strength is increased for 28 days due to the reaction of binders and fillers with water. For control specimen (0% burnt ash), the compressive strength for 7 days is

**Table 4** Test results of paver blocks with and without GGBS content

Burnt paper ash (%)	Compressive strength (N/mm <sup>2</sup> )				Porosity (%)			
	Without GGBS		With GGBS		Without GGBS		With GGBS	
	7 days	28 days	7 days	28 days	7 days	28 days	7 days	28 days
0	16.74	25.12	16.74	25.12	7.88	5.75	7.88	5.75
10	13.88	20.59	13.88	20.59	8.43	6.13	8.43	6.13
20	11.03	17.08	11.03	17.08	10.92	8.18	10.92	8.18
30	9.27	13.81	9.27	13.81	15.06	11.29	15.06	11.29
40	6.28	10.04	6.28	10.04	18.98	14.71	18.98	14.71
50	3.87	6.03	3.87	6.03	23.36	19.84	23.36	19.84

16.74 and 25.12 N/mm<sup>2</sup>. If the waste burnt ash is introduced to 10%, the compressive strength obtained is around 0.82% of the control specimen. Further if the proportions of burnt paper ash is increased to 20, 30, 40 and 50%, the compressive strength is decreased to 0.68 times, 0.55 times, 0.39 times and 0.24 times of the control specimen's compressive strength.

It reciprocates that lower proportion of burnt paper can be effective in getting minimum 80% of the strength but the increase in burnt ash proportions the strength is getting affected due to the partial reaction / improper reaction of the burnt ash with the binder cement material which is clearly seen in Fig. 3. In estimating the volume of pores, 28 days getting lesser percentage than 7 days due to the effect of increase in the curing period. This is mainly because of the completion of the maximum of the binders and fillers in increase in curing time. For control specimen, the volume of pores estimated as 5.75% in 28 days age of curing. For 10% burnt paper ash, the volume of pores is increased to 6%. In extending the proportions of burnt paper ash 20%, 30%, 40% and 50%, the volume of pores can be is getting increased to 29.71%, 49.06%, 60.91% and 71.02%, respectively. This clearly indicating the presence of 10% burnt paper is not enhancing too much pores in comparing with other proportions.

From Figs. 3 and 4, it is understood that the introduction of 5% GGBS content is giving some enhancement in the strength and durability characteristics. For 10% burnt ash proportions the strength is around 0.91 times of the control specimen. So with the presence of GGBS content, strength reduction rate has some improvement

**Fig. 3** Compressive strength versus percentage of paper burnt ash

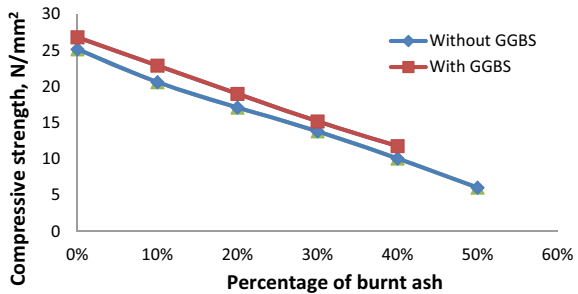
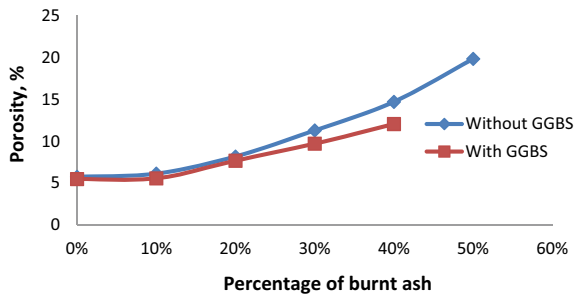


**Fig. 4** Porosity versus percentage of paper burnt ash





from 0.82 times. For waste burnt paper ash proportions 20, 30 and 40%, the strength obtained is estimated at around 0.76 times, 0.60 times and 0.47 times the compressive strength of the control specimen (without burnt ash proportions). For estimating the volume of pores, there is no much difference for 10% burnt ash as seen from Fig. 4. For burnt ash proportions 20%, 30%, 40% the volume of pores estimated is around 25.13%, 40.78%, 52.32%, respectively. In order to validate the experimental test results, the regression analysis is carried out. The compressive strength of the Paver block can be estimated through model Eq. (1) by incorporating the percentage of paper ash and GGBS. The same equation can be applicable for with and without GGBS content.

$$CS = 2.785 P_{PA}^2 - 38.64 P_{PA} + 0.52 P_G + 23.85 \quad (1)$$

where

CS = Compressive Strength, N/mm<sup>2</sup>;

P<sub>PA</sub> = Percentage of paper ash;

P<sub>G</sub> = Percentage of GGBS.

The volume of pores on the Paver block can be estimated through model Eq. (2) by incorporating the percentage of paper ash and GGBS. The same equation can be applicable for with and without GGBS content.

$$P = 50.19 P_{PA}^2 + 1.282 P_{PA} - 0.09 P_G + 5.13 \quad (2)$$

where

P = Percentage of pores;

P<sub>PA</sub> = Percentage of paper ash;

P<sub>G</sub> = Percentage of GGBS.

Both of the model equations are well correlated with the experimental test results with a minimum of 8–13% errors.

## 5 Conclusions

The compressive strength for the control specimen (without burnt paper ash) is 25.12 N/mm<sup>2</sup>. If GGBS is introduced to 5%, there is an increase of 6.12% in the compressive strength. For the same control specimen, the volume of pores is 5.75%, whereas for the presence of GGBS has a reduction of pores up to 4.52%. The increase in the proportion of burnt paper ash will result in the decrease of the compressive strength and increase in the volume of pores. If the GGBS is introduced in the various proportion of burnt paper ash, seems that there is some moderate enhancement in the strength (CS) and durability properties (Porosity) of the Paver blocks. It is found that 10% proportion of burnt paper ash and 5% GGBS content will be an optimum proportion for this Paver blocks in getting 0.91 times of the compressive strength

and almost same of the percentage of pores. Hence, the lower proportion of burnt ash will give desired strength and durability properties of the Paver blocks. In order to increase the properties to further extent, the GGBS content can be increased from 5 to 10%. Model equations are arrived for computing compressive strength and volume of pores by incorporating the percentage of paper ash and GGBS content. The model equations are well correlated with the experimental test results with a minimum of 8–13% errors.

## References

1. Mason I, Brooking A, Oberender A, Hardford J, Horsley P (2003) Implementation of a zero waste program at a university campus. *Resour Conserv Recycl* 38(1):257–269. [https://doi.org/10.1016/S0921-3449\(02\)00147-7](https://doi.org/10.1016/S0921-3449(02)00147-7)
2. Armijo de Vega C, Benítez S, Ramirez-Barreto M (2008) Solid waste characterization and recycling potential for a university campus. *Waste Manag* 28(1):21–26. <https://doi.org/10.1016/j.wasman.2008.03.022>
3. Ravikumar M, Anilkumar C, Prashanth M, Reddy Venkat S (2012) Experimental studies on iron ore tailing based interlocking paver. *Int J Earth Sci Eng* 5(3):501–504
4. Mall R, Sharma S, Patel RD (2014) Studies of the properties of paver block using fly ash. *Int J Sci Res Dev* 2(10):59–65
5. Tapkire G, Parihar S, Patil P, Kumavat HRR (2014) Recycled plastic used in concrete paver block. *Int J Res Eng Technol* 3(9) 33–35
6. Ling T, Poon C (2014) Use of recycled CRT funnel glass as fine aggregate in dry-mixed concrete paving blocks. *J Clean Prod* 68(1):209–215
7. Kashiyani BK, Pitroda J, Shah B (2013) Innovative addition of polypropylene fibre in interlocking paver block to improve compressive strength. *Int J Civ Struct Environ Infrastruct Eng Res Dev* 3(2):17–26
8. Reddy A, Gupta V, Garg D (2015) Effect of partial replacement of cement by rice husk ash using nylon fibers in concrete paver block. *Int J Sci Res Dev* 3(3):45–49
9. Revathi S, Kumutha R, Vijai K (2015) Properties of paver blocks with groundnut husk ash as fine aggregates. *Int Res J Eng Technol* 2(2):657–660
10. Meyyappan PL, Carmichael MJ (2020) A comparative investigation on the utilization of marble dust and granite dust in the cement mortar against the sulphate resistance. *Lect Notes Civ Eng* 97. [https://doi.org/10.1007/978-3-030-55115-5\\_48](https://doi.org/10.1007/978-3-030-55115-5_48)
11. Meyyappan PL, Rajasekaran MP, Soroopan RS (2020) An experimental and analytical investigation on the characteristics of light weight concrete using waste burnt ash and pumice stones. *Lect Notes Civ Eng* 97. [https://doi.org/10.1007/978-3-030-55115-5\\_50](https://doi.org/10.1007/978-3-030-55115-5_50)
12. Ganjian E, Jalull G, Sadeghi-Pouya H (2015) Using waste materials and by products to produce concrete paving blocks. *Constr Build Mater* 77(1):270–275
13. Limbachiya V, Ganjian E, Claisse P (2016) Strength, durability, and leaching properties of concrete paving blocks incorporating GGBS and SF. *Constr Build Mater* 113(1):273–279
14. Agyeman S, Obeng-Ahenkora NK, Assiamah S, Twumasi G (2019) Exploiting recycled plastic waste as an alternative binder for paving blocks production. *Case Stud Constr Mater* 11(1):1–7
15. Djamaluddin AR, Caronge MA, Tjaronge MW, Lando AT, Irmawaty R (2020) Evaluation of sustainable concrete paving blocks incorporating processed waste tea ash. *Case Stud Constr Mater* 12(1):1–7

# A Prototypical Design Strategy for Soil–Cement Construction for Indian Condition



Meyyappan Palaniappan and Rajha Poorrna

**Abstract** Soil–cement is the blended mixture of Portland cement with soil along with the required quantity of water which can be effectively used in the pavement application with adequate compaction. The major parameters such as optimum moisture content, maximum dry density, unconfined compressive strength and flexural strength are to be arrived for designing the pavements. A preliminary study is formulated to develop the linear equation model to be the best fit for to arrive those parameters through regression analysis with the past limited experimental data and proportions of with and without fly ash combinations in the soil–cement construction. The developed model equations are well correlated for the different proportions such as 1% of cement to 10% cement along with the soil and 5% of fly ash. In the soil–cement developed model, the multiplicative factor of 1.75, 0.90 and 0.85 can be introduced for the addition of 5% of fly ash on those soil–cement combinations. A prototypical design strategy can be formulated for the soil–cement construction in satisfying Indian conditions in the presence of fly ash particles.

**Keywords** Soil–cement · Fly ash · Regression analysis

## 1 Introduction

Soil–cement is the mixture of a blended Portland cement, soil and required amount of water. It could be used in the construction of pavements after achieving proper and well-graded compaction [1–3]. This combined the actions of soil and cement together to form a hardened dense mass like a conventional concrete under the hydrated performance of binding material. This is considered as one of the better pavement materials and acted as a better option for the improvements of road networks, especially developing countries like India [4, 5]. It has lot of merits like better in the compressive strength and shear strength properties, cost-effective approach with high strength and good long-life characteristics [3, 6]. It is used as a suitable construction material

---

M. Palaniappan (✉) · R. Poorrna  
Kalasalingam Academy of Research and Education, Krishnankoil, Tamil Nadu 626126, India  
e-mail: [meyyappan@klu.ac.in](mailto:meyyappan@klu.ac.in)

© The Author(s), under exclusive license to Springer Nature Singapore Pte Ltd. 2023  
P. Pradhan et al. (eds.), *Recent Advances in Mechanical Engineering*,  
Lecture Notes in Mechanical Engineering,  
[https://doi.org/10.1007/978-981-16-9057-0\\_37](https://doi.org/10.1007/978-981-16-9057-0_37)

349

in the fields of pipe bedding, slope production, sub-base layer reinforcing layer in the various pavement sectors along with various sustainable materials, fibres and polymers [7–11]. From the past researches, it is noticed that the construction of soil–cement will be a challenging aspect during execution and implementation. There are two major issues that need to be verified during construction. One is compaction issues due to the various ranges of moisture content and another one is proportion issues due to the insufficient in that blended mixture. Both of the issues does not meet the adequate design norms and requirements to achieve the strength and durability aspects of this soil–cement construction [12–15]. The previous experimental researches on soil–cement construction have not addressed the above-mentioned issues in a complete manner, and this can be fulfilled with the aid of modelling equations. So the work is planned to develop model equation based on the past research data to compute the various soil parameters such as optimum moisture content, maximum dry density, unconfined compressive strength and flexural strength for the soil–cement mix in considering with and without fly ash material. Also, it is marching towards establishing a design strategy to implement the soil–cement construction for the Indian scenario in the large extent.

## 2 Objectives of This Study

The objectives of this study are given below:

- (a) To identify the various issues to be handled in construction parameters. Such as Optimum moisture content (OMC), Maximum dry density (MDD), Unconfined compressive strength (UCS) and Flexural strength (FS).
- (b) To develop the model equation based on the previous researchers data through the regression analysis for various soil–cement mix.
- (c) To develop the model equation for arriving soil-cement parameters for soil-cement fly ash proportions.

## 3 Analytical Work

The past research works of Biju [6], P. Kumar [11] and S. Singh [4] are taken to establish the model equations for arriving the parameters like optimum moisture content, maximum dry density and unconfined compressive strength for the soil–cement mix based on the regression analysis. Based on the past research work of Raja (2018), the developed soil–cement equation models are modified with some multiplicative factor to arrive the soil parameters on the soil–cement mix in considering with and without fly ash content. The relationship of unconfined compressive strength and flexural strength in the past research of Linares (2019) is taken and used to computing flexural strength with the computed unconfined compressive strength values. Based on

this developed model equations, the values of soil parameters are arrived. A prototypical design strategy can be arrived in implementing for the soil-cement construction in considering with and without fly ash.

## 4 Results and Discussions

### 4.1 Model Equation for Soil–Cement Mix

#### (a) Optimum Moisture Content

Table 1 shows the compiled values of optimum moisture content in percentage for the various proportions of soil–cement mix for the past studies of Biju (2018), Kumar (2017) and Singh [4].

For soil with 1% cement content, the optimum moisture obtained is 6.927%, and it is increased from 1.08 times to 1.76 times for the soil with 10% cement content. The past research data shows only the limited proportions, and based on the regression analysis model, Eq. 1 is formulated to compute the optimum moisture content for the various soil–cement mix proportions.

**Table 1** Optimum moisture content values

S.No.	Content	Biju (2018) (%)	Kumar (2017) (%)	Singh [4] (%)	Based on model equation 1 (%)
1	Soil + 1% cement	–	–	–	6.927
2	Soil + 2% cement	–	–	–	7.512
3	Soil + 3% cement	6.85	6.85	6.37	8.097
4	Soil + 4% cement	–	–	–	8.682
5	Soil + 5% cement	9.9	8.45	8.52	9.267
6	Soil + 6% cement	–	–	–	9.852
7	Soil + 7% cement	8.45	9.9	9.19	10.437
8	Soil + 8% cement	–	11.11	11.26	11.022
9	Soil + 9% cement	–	11.7	11.82	11.607
10	Soil + 10% cement	–	11.9	11.96	12.192

$$OMC = (0.585 C) + 6.364 \tag{1}$$

where

‘OMC’ is optimum moisture content in %

‘C’ is cement content in that soil–cement content in %

The model equation 1 holds good, since the deviations of results can be around  $\pm 20\%$ . It is also observed that, for higher content of cement with the soil, the predicted errors will be only 8%. The equation is more suitable for higher content of cement with soil content. It is noted that the optimum moisture content is increasing with the increasing content of cement with the soil as seen from Table 1. Therefore, it denotes that the soil–cement content is proportional to the optimum moisture content.

**(b) Maximum Dry Density Values**

Table 2 shows the compiled values of maximum dry density values in percentage for the various proportions of soil–cement mix for the past studies of Biji (2018), Kumar (2017) and Singh [4]. Like optimum moisture content, the past research data shows only the limited proportions, and based on the regression analysis, the model equation 2 is formulated to compute the maximum dry density for the various soil–cement mix proportions.

**Table 2** Maximum dry density values

S.No.	Content	Biju (2018) (g/cc)	Kumar (2017) (g/cc)	Singh [4] (g/cc)	Based on model equation 1 (g/cc)
1	Soil + 1% cement	–	–	–	1.895
2	Soil + 2% cement	–	–	–	1.88
3	Soil + 3% cement	1.89	1.95	1.96	1.865
4	Soil + 4% cement	–	–	–	1.85
5	Soil + 5% cement	1.99	1.97	1.92	1.835
6	Soil + 6% cement	–	–	–	1.82
7	Soil + 7% cement	1.91	1.94	1.94	1.805
8	Soil + 8% cement	–	1.9	1.9	1.79
9	Soil + 9% cement	–	1.95	1.97	1.775
10	Soil + 10% cement		1.87	1.89	1.76

$$MDD = (-0.015 C) + 1.91 \tag{2}$$

where

‘MDD’ is maximum dry density in g/cc.

‘C’ is cement content in that soil–cement content in %

The model equation 2 holds good since the deviations of results can be around ±9% in comparison with the past research data’s. It is observed that the maximum dry density is decreasing with the increasing content of cement with the soil mix as seen from Table 2. For soil with 1% cement content, the optimum moisture obtained is 1.895 g/cc, and it was decreased to 1.07 times for the soil with 10% cement content. It is indicating that the maximum dry density is inversely proportional to the increasing content of cement with the soil.

(iii) **Unconfined compressive strength**

Table 3 shows the compiled values of unconfined compressive strength in percentage for the various proportions of soil–cement mix for the past studies of Kumar (2017) and Singh [4]. The past research data shows only the limited proportions, and based on the regression analysis, the model equation 3 is formulated to compute the unconfined compressive strength for the various soil–cement mix proportions.

**Table 3** Unconfined compressive strength values

S.No.	Content	Biju (2018) (N/mm <sup>2</sup> )	Kumar (2017) (N/mm <sup>2</sup> )	Singh [4] (N/mm <sup>2</sup> )	Based on model equation 1 (N/mm <sup>2</sup> )
1	Soil + 1% cement	–	–	–	1.598
2	Soil + 2% cement	–	–	–	1.621
3	Soil + 3% cement	–	1.659	1.562	1.644
4	Soil + 4% cement	–	–	–	1.667
5	Soil + 5% cement	–	1.674	1.575	1.69
6	Soil + 6% cement	–	–	–	1.713
7	Soil + 7% cement	–	1.722	1.592	1.736
8	Soil + 8% cement	–	1.745	1.534	1.759
9	Soil + 9% cement	–	1.765	1.671	1.782
10	Soil + 10% cement	–	1.778	1.689	1.805

$$UCS = (0.023 C) + 1.575 \tag{3}$$

where

‘UCS’ is unconfined compressive strength in N/mm<sup>2</sup>.

‘C’ is cement content in that soil–cement content in %

The model equation 3 holds good since the deviations of results can be around ±7% in comparison with the past research data. It is observed that the unconfined compressive strength is mildly increasing with the increasing content of cement with the soil mix as seen from Table 3. For soil with 1% cement content, the optimum moisture obtained is 1.895 g/cc, and it was decreased to 1.07 times for the soil with 10% cement content. The values are ranging from 1.598 g/cc to 1.805 g/cc for the soil–1% cement mix to soil–10% cement mix, respectively. It is indicating that the unconfined compressive strength is directly proportional to the increasing content of cement with the soil.

### 4.2 Model Equation for Soil–Cement–Fly Ash Mix

Based on the past research, data of Raja (2018), of soil–5% cement–5% flyash mix, is incorporated with the soil–cement equation models 1 to 3 with the multiplicative factor of 1.75, 0.90 and 0.85 can be introduced for the addition of 5% of fly ash on those soil–cement combinations. With the regression analysis, the multiplicative factor is found, and based on that, the parameters such as OMC, MDD and UCS are found, and it is shown in Table 4. The modified equations for this soil–cement–fly ash are shown in Eqs. 4–6.

$$OMC = \{(0.585 C) + 6.342\} * 1.75 \tag{4}$$

**Table 4** Parameters for soil–cement–fly ash mix

S.No.	Content	OMC	MDD	UCS	FS
1	Soil + 1% cement + 5% FA	12.12225	1.7055	1.3583	0.479
2	Soil + 2% cement + 5% FA	13.146	1.692	1.37785	0.48
3	Soil + 3% cement + 5% FA	14.16975	1.6785	1.3974	0.484
4	Soil + 4% cement + 5% FA	15.1935	1.665	1.41695	0.486
5	Soil + 5% cement + 5% FA	16.21725	1.6515	1.4365	0.4885
6	Soil + 6% cement + 5% FA	17.241	1.638	1.45605	0.49
7	Soil + 7% cement + 5% FA	18.26475	1.6245	1.4756	0.49
8	Soil + 8% cement + 5% FA	19.2885	1.611	1.49515	0.495
9	Soil + 9% cement + 5% FA	20.31225	1.5975	1.5147	0.497
10	Soil + 10% cement + 5% FA	21.336	1.584	1.53425	0.4996



$$\text{MDD} = \{(-0.015 C) + 1.91\} * 0.90 \quad (5)$$

$$\text{UCS} = \{(0.023 C) + 1.575\} * 0.85 \quad (6)$$

The relationship of unconfined compressive strength and flexural strength is expressed (in Eq. 7) in the past research of Linares (2019). That relationship is applied in this soil–cement–fly ash mix for arriving the values of flexural strength with the help of the obtained unconfined compressive strength values.

$$\text{FS} = [0.1131 * \text{UCS}] + 0.3261 \quad (7)$$

The flexural strength values are marginally getting increasing with the increase in the cement content of the soil–cement–fly ash mix. The values of flexural strength based of the computation on Eq. 7 are ranging from 0.479 N/mm<sup>2</sup> to 0.4996 N/mm<sup>2</sup> for cement content 1–10% in the soil–cement–fly ash.

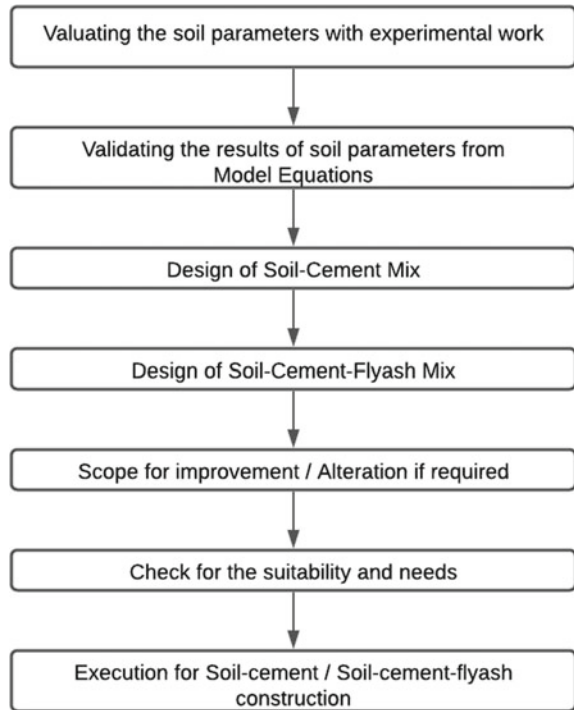
### 4.3 Design Strategy for Soil–Cement Construction

Based on the experimental and analytical work, the soil parameters such as optimum moisture content, maximum dry density, unconfined compressive strength and flexural strength are arrived based on the prediction of regression analysis. Then, design an optimum soil–cement or soil–cement–fly ash mix based on the arrived soil parameters. If there is any improvement or performance, the optimum mix can be altered. Then, it has to be checked the suitability based on the possibility of adopting soil–cement or soil–cement–fly ash. The conceptual design framework strategy for soil–cement construction is described through the following steps as mentioned in Fig. 1.

## 5 Conclusions

Based on the limited proportion of soil-cement works done by the Biju [6], P. Kumar [11] and S. Singh [4], their experimental results were taken and through regression analysis, a common best fit equation suited for soil–cement mix is arrived, and validation is done for optimum moisture content, maximum dry density and unconfined compressive strength parameters. The prediction of errors between the past research data and the suitability of are in the range of 10–20%. Based on the flexural strength prediction model form Linares (2019), flexural strength was arrived for various soil–cement proportions. Based on the incorporation of a prototypical design strategy, framework for soil-cement construction with or without fly ash is arrived for implementing purpose for the construction industry. By fitting soil–cement equation

**Fig. 1** Conceptual design framework



models 1 to 3, a multiplicative factor of 1.75, 0.90 and 0.85 can be introduced for the addition of 5% of fly ash on those soil–cement combinations based on the regression analysis.

## References

1. Linares-Unamunzaga A (2017) Flexural strength prediction models for soil–cement from unconfined compressive strength at seven days. *Materials* 12(1):387–403
2. Asadi SS, Lahari K, Sai Madhulika K (2017) Analysis of soil quality for environmental impact assessment—a model study. *Int J Civil Eng Technol* 8(3):798–805
3. Raja PS (2017) Study of stabilization for rural road sub-grade development. *Int J Innov Res Sci Eng Technol* 7(5):199–205
4. Singh S (2017) A study on design of soil–cement road. *Int J Adv Res Sci Eng* 6(12):2051–2056
5. Ravikumar T, Krishna S (2017) Design of soil–cement road. *Int J Civil Eng Technol* 8(5):199–205
6. Biju A, Anand B, Maria Baby A, Krishna S, Rahul TP, Bose S (2018) Design of soil–cement road. *Int Res J Eng Technol* 5(4):4343–4347
7. Basha EA, Hashim R, Mahmud HB, Muntohar AS (2005) Stabilization of residual soil with rice husk ash and cement. *Constr Build Mater* 19(6):448–453
8. Galán-Marín C, Rivera-Gómez C, Petric J (2010) Clay-based composite stabilized with natural polymer and fibre. *Constr Build Mater* 24(8):1462–1468

9. Hossain KMA, Mol L (2011) Some engineering properties of stabilized clayey soils incorporating natural pozzolans and industrial wastes. *Constr Build Mater* 25(8):3495–3501
10. Achenza M, Fenu L (2006) On earth stabilization with natural polymers for earth masonry construction. *Mater Struct* 39(2):21–27
11. Singh P, Kumar P (2015) Light weight cement-sand and bagasse ash bricks. *Int J Innov Res Sci Technol* 1(12):284–287
12. Walker PJ (1995) Strength, durability and shrinkage characteristics of cement stabilised soil blocks. *Cem Concr Compos* 17(4):301–310
13. Hossain KMA (2011) Stabilized soils incorporating combinations of rice husk ash and cement kiln dust. *J Mater Civil Eng* 23(9):1320–1327
14. Okafor FO, Ewa DE (2012) Predicting the compressive strength of obudu earth blocks stabilized with cement kiln dust. *Niger J Technol* 31(2):149–155
15. Onchiri R, James K, Sabuni B, Busieney C (2014) Use of sugarcane bagasse ash as a partial replacement for cement in stabilization of self-interlocking earth blocks. *Int J Civil Eng Technol* 5(10):124–130

# A Numerical Study to Choose the Best Model for a Bladeless Wind Turbine



Mohammed Amein Alnounou and Sikata Samantaray

**Abstract** A new type of wind turbine has been created called the bladeless turbine, which uses a completely new type to capture wind energy, as it works with a minimum of moving parts to generate electric current using the vibration produced by the wind. In this chapter, numerical modeling of airflow around a two-dimensional cylinder was made and compared with the reference values to ensure the correctness of the program used, and then the three-dimensional cylinder was studied and the numerical study expanded to include several cases. Where the study was conducted on five different shapes of the mast by changing the angles of inclination of the cylinder under boundary conditions  $T = 288.16$  K,  $P = 1$  atm,  $V = 0.0003$  m/s and studying the effect of model dimensions on the results of the modeling process by comparing the pressure diagrams around the studied shapes in order to ensure that the results are within the least relative error. The results also showed that with increasing the angle of inclination of the cylinder, a lower pressure drop was obtained. Numerical modeling of the airflow around the bladeless wind turbine was also made according to two cases: the first case when the same boundary conditions  $V = 0.0003$  m/s,  $T = 288.16$  K,  $P = 1$  atm, the second case at reference boundary conditions  $V = 3$  m/s,  $T = 300$  K,  $P = 1$  atm, Using a regular mesh and hexahedron, the density of the used mesh has been modeled, and then reviewing the effect of the used perturbative model on the results, choosing the perturbative model best suited to the studied case, and comparing it with the reference case.

**Keywords** Vortex-induced vibrations · Bladeless windmill · Vortex shedding · Numerical modeling

## 1 Introduction

Pipe curvatures are the most accurate and important part of increase in requirements of living life; the search for a large and stable source of energy that secures the needs

---

M. A. Alnounou (✉) · S. Samantaray  
Siksha O Anusandhan University, Bhubaneswar, Odisha, India  
e-mail: [amein.alnounou@gmail.com](mailto:amein.alnounou@gmail.com)

© The Author(s), under exclusive license to Springer Nature Singapore Pte Ltd. 2023  
P. Pradhan et al. (eds.), *Recent Advances in Mechanical Engineering*,  
Lecture Notes in Mechanical Engineering,  
[https://doi.org/10.1007/978-981-16-9057-0\\_38](https://doi.org/10.1007/978-981-16-9057-0_38)

359

of these large gatherings has become obsessed by scientists, and finally, electric energy was the best type of energies due to the ease of transferring it and converting it to other forms of energy where all countries of the world today depend entirely on electricity and its progress is measured by the amount its consumption of this energy; therefore, it was necessary to find the means and methods that lead to the production and utilization of this energy.

One of these methods was wind turbines where there are two main classes of wind turbines called the first horizontal axis while the second is called vertical axis, but these turbines were suffering from some problems, the most prominent of which is (loud noise—requiring high wind speeds)—containing mechanical parts that are exposed to wear due to friction and impact on wildlife—high operating and maintenance costs.

Therefore, a new type of profitable turbine has been devised called the blade-free turbine that uses a radical new approach to capture wind energy, as it works through the phenomenon of nonlinear resonance, which is known as vibration resulting from eddies (VIV). This phenomenon is of great importance in many branches of mechanical engineering.

For example, it can be found in marine structures or heat exchanger tubes, as well as in urban structures such as slender chimneys, tall buildings, power lines, and bridges.

During the past years, many studies have been conducted on this phenomenon; usually, this phenomenon is considered an undesirable effect because it may affect the structural integrity or reliability of performance, but now this phenomenon can be used in extracting clean energy [1].

## ***1.1 Bladeless Turbine Parts***

This turbine consists of one structural component, as it consists of the following parts:

(1) The lower section fixed to the ground: the upper section which is a hollow conical cylinder made of lightweight materials and is subject to vibration when exposed to the wind.

(2) The mast: It is a cylinder that connects the upper and lower sections, where the lower part of it is fixed in the ground, while the upper part supports the upper part of the turbine in increasing its oscillations, and it also reduces the mechanical pressure on the lower section.

(3) The magnetic generator: It consists of two rings of magnets between the upper section of the vibrating and the fixed axis fixed from the ground. Due to its simplicity to manufacture, it has distinct advantages such as transportation, storage, and assembly.

### 1.2 Turbine Working Principle

The turbine captures wind energy by means of a nonlinear resonance phenomenon known as vortex-induced vibrations (VIV). It is an aerodynamic effect experienced by engineers, when the wind exceeds the structure of the turbine, the flow changes. The air generates a periodic pattern of vortices, and as soon as these forces are strong enough, the fixed structure begins to oscillate, and this vibration causes a convergence between the rings of the two magnets, then the value of the forces of repulsion between them increases and the divergence occurs and the wind returns to affect the moving mast and thus the process of convergence and divergence between the two magnets continues and is done power generation, and research continues to determine the best way to generate power from this technology [1] (Fig. 1; Table 1).



**Fig. 1** A bladeless wind turbine

**Table 1** A comparison between bladeless wind turbines and blade wind turbines

	Bladeless wind turbine	Blades wind turbines
Blades	You don't need	You need
Wind velocity	It operates at different and relatively low wind velocity	They operate at high wind velocity
Noise	Don't make noise	Make noise
Construction and maintenance cost	Low cost	High costs
Movable rotating parts	It does not contain rotating parts	Rotating parts contain
Payoff	Relatively low payoff	Higher payoff
Size	Small size	Big size
Steering blades	No steering blades needed	Need guide blades
Its impact on wildlife	It does not affect wildlife	Affect wildlife

## 2 Literature Review

### 2.1 Phenomenon of Vibration Caused by the Vortex (VIV)

In 2012, researchers Santiago Gil Barrero Antonio Avila, Pindado Sergio were introduced A study focused on the phenomenon of vibration caused by the vortex (VIV) by considering a circular cylinder to be analyzed as a potential source for obtaining energy and determining the effect of some parameters on the energy conversion factor, such as the mass ratio  $m^*$  (the ratio of the body density to the density of the surrounding fluid) or the mechanical damping factor. The study concluded that there is an ideal value of the damping factor by which the highest energy conversion factor  $r/M$  can be obtained, and that increasing the Reynolds number can achieve higher values of the energy conversion factor [2].

In 2014, researchers Robert Correa, Eric Cremer presented a study dealing with the development of a compact device capable of harvesting wind energy and converting it into electrical energy through the phenomenon of nonlinear resonance, where a small model was constructed and tested in an air tunnel, and the results showed the possibility of vortexing, which in turn causes vibration and harvesting. Wind energy and electricity generation, but it will be difficult because of the low air density compared to other fluids such as water that have proven effective in this device, and Fig. 2 shows how to vortex-induced vibration [3].

And In 2018, the Keystone School of Engineering, Pune, Maharashtra, India, published A study focused on the phenomenon of nonlinear resonance known as vibration caused by the turbine, which is of great importance in energy extraction, and the Alya code was developed in order to simulate the problems of fluid–structure interaction, which is the phenomenon of the mutual effect between a fluid and a solid body (fluid–structure interaction) FSI and conduct several experiments for graded models of turbine and a comparison of numerical and experimental results with an error rate of less than 10% [4].

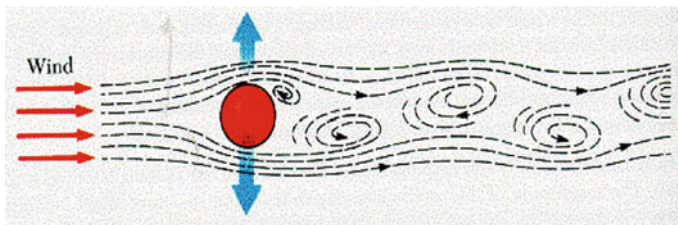


Fig. 2 Vortex-induced vibration

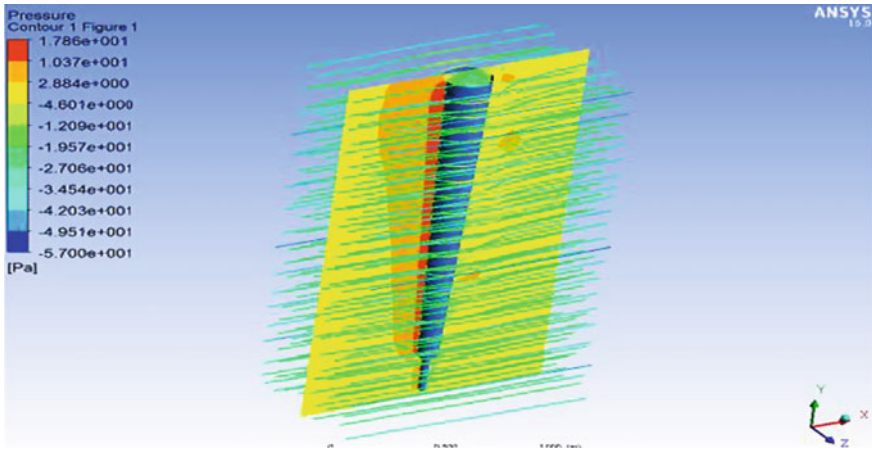


Fig. 3 Pressure field resulting from the study

### 2.2 Models of Turbines Approved in the Studies

In 2019, researchers Onkar D. Kshirsagar, Amol B. Gaikwad presented a numerical study of the shape of the turbine and reached the following conclusions:

The pressure distribution in the shape of the turbine ranges from Pa  $[-57$  to  $17.8]$ , the maximum turbine deformation was  $5.4318$  mm and minimum  $0$  mm as in Fig. 3, and the study concluded that fiberglass is the most suitable material for the manufacture of the shape because it gives maximum deformation [5]. And in 2016, researchers Saurav Jadhav Bobde, Sameer presented a study on methods of generating electricity through a linear generator (magnetic generator) instead of a linear motor, so there is no need for an arm that converts reciprocating motion into rotational motion, which had failed in this project during its experiment on a model small, well study and design of the mast and its analysis for maximum vibration [6].

In a journal study [7], several tests on tapered cylinders are carried out to investigate the effects of taper ratios. In comparison with uniform cylinders, tapered cylinders have a far wider variety of lock in ranges.

## 3 Numerical Solution Approach and Performance Parameters

### 3.1 Study of Airflow Around a Cylinder

The airflow around a two-dimensional cylinder is considered one of the simplest flows, but studying this flow here is an essential step, to compare the results with



previous studies, and thus ensure the mastery of the programs used as well as obtain some of the necessary data as initial values, which are used later when modeling the flow around the turbine. The two-dimensional and three-dimensional flux has been studied.

### 3.2 Two-Dimensional Flow Study

The studied shape is drawn with the size of the observation, as in Fig. 4, but before starting this step, the type of study must be determined 2D, given that the study is a primary study, so we choose 2D and enter the boundary conditions, which are: the entry area and the outlet area.

Based on the reference studies that were conducted on the studied form and compared with the values which resulted from our study of the same figure shows the following:  $Cd$  values for the reference study were  $Ci = 3.88$ , and for the studied model,  $Co = 3.94$  (Figs. 5 and 6).

Where the uncertainty percentage was 1.5%, thus making sure of the correct work of the program used and testing the accuracy of the results (Fig. 7).

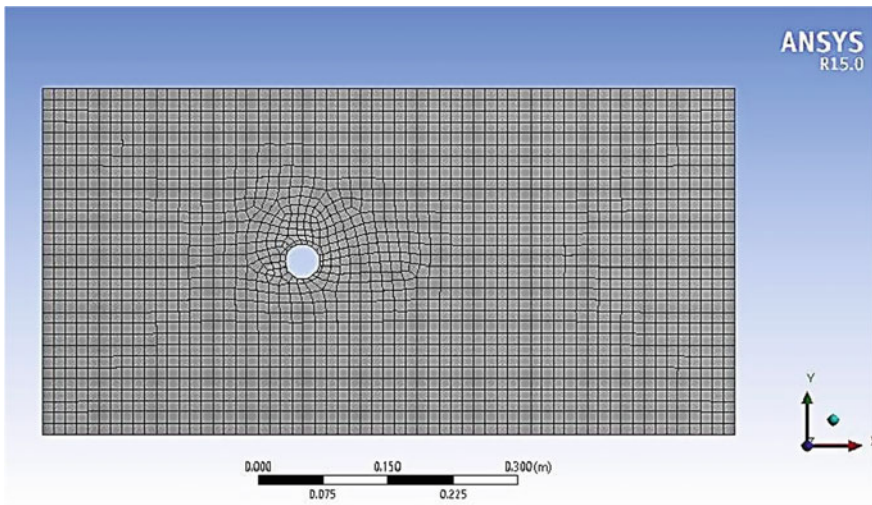


Fig. 4 Drawn shape with mesh in two-dimensional case

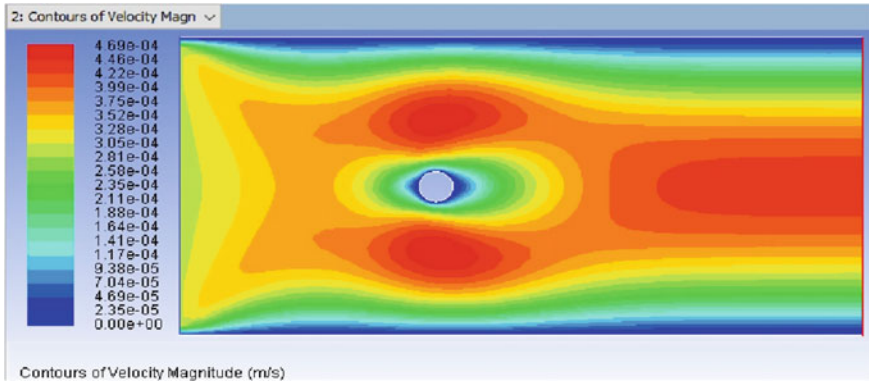


Fig. 5 Velocity distribution diagram around the studied shape

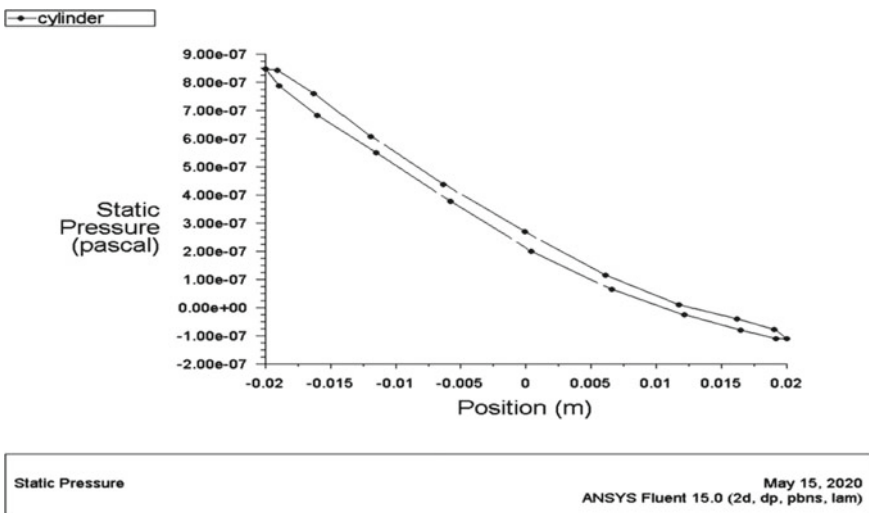


Fig. 6 Pressure distribution diagram around the first studied model is shown

### 3.3 Three-Dimensional Flux Study

A three-dimensional flow was studied around a fixed diameter cylinder having the same boundary conditions used in the case of two-dimensional flow. This study was carried out with the same boundary conditions and we reached the following results: Fig. 8 shows the pressure distribution diagram around the model (1) (Table 2).

By adopting the same previous conditions, the three-dimensional study was expanded. Several studies were conducted on different shapes by changing the angle of inclination of the cylinder until reaching the desired turbine shape as in Fig. 9.

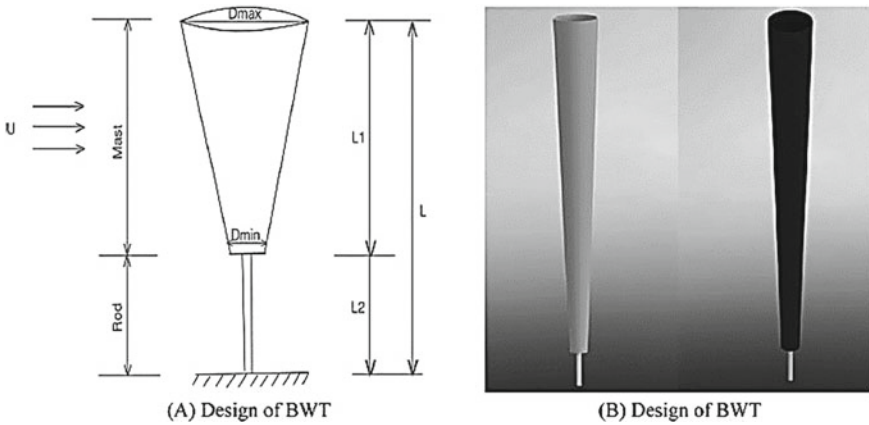


Fig. 7 a Vortex turbine size and components. b Vortex bladeless wind turbine solid model

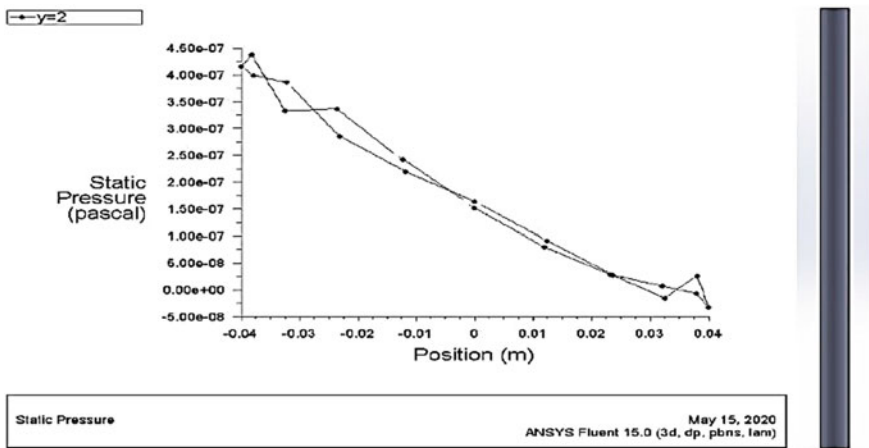


Fig. 8 A diagram of the pressure distribution around the model

Table 2 Varied dimensions of five distinct turbine types

Sl. No.	Parameters	Dimensions (mm)				
		1	2	3	4	5
1	Dmax	200	210	220	225	225
2	Dmin	175	150	150	140	125
3	d	0	0	0	0	20
4	L1	2000	2000	2000	2000	1800
5	L2	0	0	0	0	600
6	L	2000	2000	2000	2000	2400

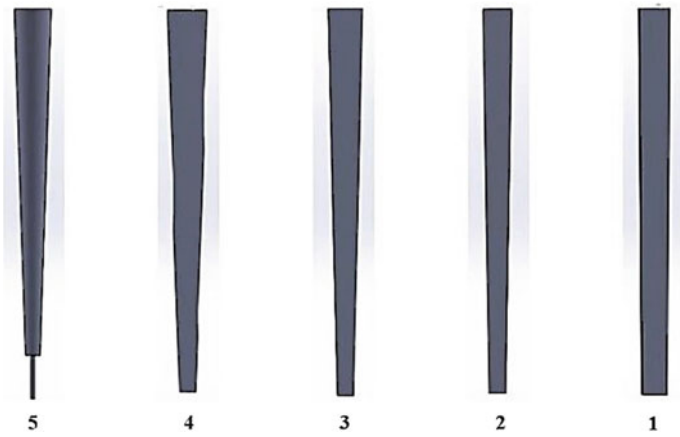


Fig. 9 Gradient of the studied shapes of the turbine shape

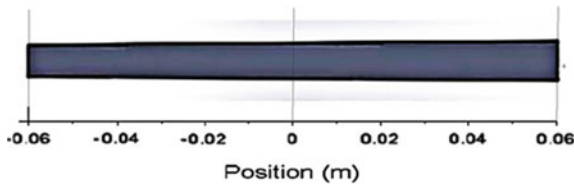


Fig. 10 Turbine position division

Figure 10 shows how the position of the turbine was divided into the study of pressure on the turbine in both directions (Figs. 11 and 12).

## 4 Conclusion

With an increase in the angle of inclination of the cylinder (mast), we notice a decrease in pressure caused by wind and vibration. In the numerical study of the airflow around the shape of the turbine chosen for the study, we note that the velocity distribution pattern is proportional to the pressure distribution pattern around the mast. Further study into optimizing VIV phenomena will be conducted in order to improve energy extraction rate dependent on cylinder geometries. Different VIV device designs would be numerically and experimentally investigated in order to induce more stringent vortex shedding operations, thus the energy production. VIV can also be combined with other clean energy technology such as solar, wind, and tidal.

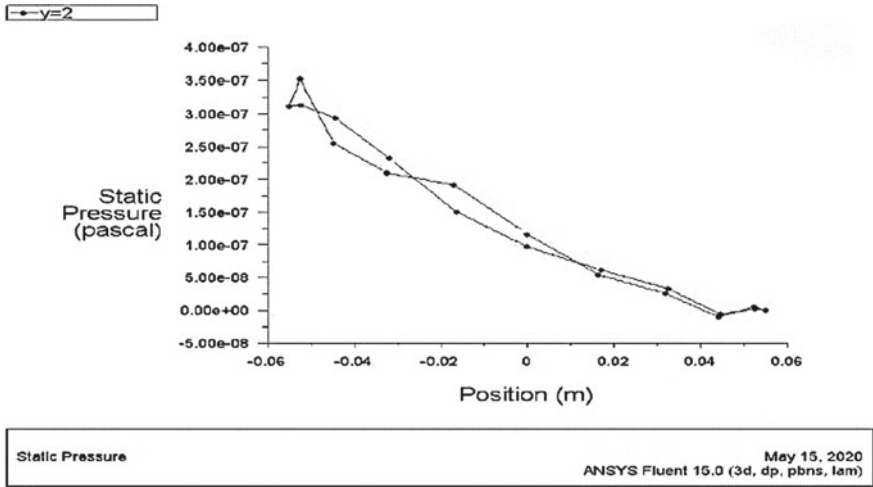


Fig. 11 Pressure distribution diagram around the model (1)

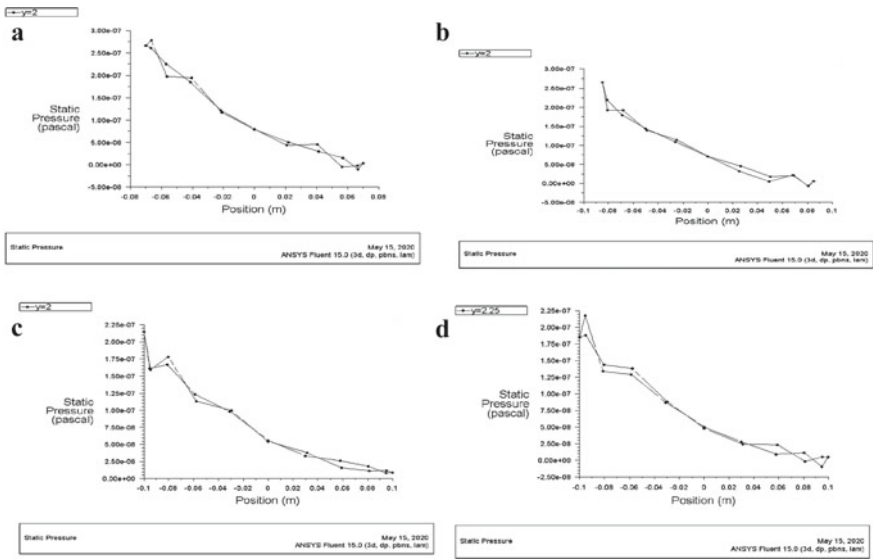


Fig. 12 Pressure distribution diagram a, b, c, d around models 2, 3, 4, 5, respectively

### References

1. Navkar P, Sable R, Satputale M, Int J Eng Sci Res Technol Vortex Bladeless Turbine Gyro E-Generator
2. Özdemir Ö, Kaya MO (2006) Flapwise bending vibration analysis of a rotating tapered cantilever Bernoulli-Euler beam by differential transform method. J Sound Vib 289(1–2):413–420

3. Barrero-Gil A, Pindado S, Avila S (2012) Extracting energy from vortex-induced vibrations: a parametric study. *Appl Math Model* 36(7):3153–3160
4. Gohate G, Bobde S, Khairkar A, Jadhav S (2016) Study of vortex induced vibrations for harvesting energy. *Int J Innov Res Sci Technol* 2(11):374–378
5. Kshirsagar OD, Gaikwad AB, Design and analysis of vortex bladeless windmill for composite material. *J Ind Mech* 4(2)
6. Mane A, Kharade M, Sonkambale P, Tapase S, Kudte SS (2017) Design and analysis of vortex bladeless turbine with gyro e-generator. In: 7th international conference on recent trends in engineering, science and management, pp 590–597
7. Monkewitz PA, Williamson CH, Miller GD (1996) Phase dynamics of K<sub>arm</sub>an vortices in cylinder wakes. *Phys Fluids* 8(1):91e96

# Biogas Production from Dried Banana Leaves Using Cow Urine as a Biocatalyst



Sanjaya K. Mishra, Premananda Pradhan, Sasanka Choudhury,  
and Shakti P. Jena

**Abstract** Alternative gaseous fuels produced from biomass can be viewed as a suitable replacement for conventional fuels. The current experimental work was focused on the anaerobic digestion (AD) process to produce biogas from dried banana leaves as the substrate and sewage water (SW) with cow urine (CU) mixture in different proportions as the inoculum in the laboratory scale. The inoculum was prepared with different blends of cow urine (0%, 5%, 10%, and 15%) on a volume basis with the sewage water. The influence of these blends on the lag phase of methane production and the composition of biogas was studied. 5% blend of CU with SW had shown the highest rise in the methane yield from 63.46% to 67.78% compared to only SW as the inoculum. At the same time, blending not only improved composition but also an improved calorific value of  $25.717 \text{ MJ Nm}^{-3}$  was obtained. So, 5% blending of cow urine with sewage water will be considered as the optimum value for maximizing  $\text{CH}_4$  production from banana leaves.

**Keywords** Banana leaves · Cow urine · Anaerobic digestion

## 1 Introduction

The use of fossil fuels has come to an alarming situation in terms of its sustainability and the adverse effects on the environment and human beings. Although stringent rules and regulations were set up to curb the issues, nothing seems to bring it to the right track. Second-generation biofuels are made from different feedstocks and therefore may require different technology to extract useful energy from them. The production and the use of biogas are the widely suggested options for rural areas due to the ease and inexpensive availability of raw materials. Biogas can be made from biomass, such as algae, garden or agricultural, food, and municipal wastes, through anaerobic digestion. Biogas can be used for cooking, lighting, generation of

---

S. K. Mishra · P. Pradhan · S. Choudhury · S. P. Jena (✉)

Department of Mechanical Engineering, SOA Deemed to be University, Bhubaneswar 751030,  
India

e-mail: [shaktijena@soa.ac.in](mailto:shaktijena@soa.ac.in)

electricity, steam, and heating purposes in rural as well as urban areas [1]. Different researchers have documented different processes of biogas production and studied the factors that influence the reaction stages during an anaerobic digestion process. Chen et al. studied the key factors in the experiments on biogas reactors and noticed that formation of methane ( $\text{CH}_4$ ) is the sensitive stage of AD that depends on temperature, pH, and characteristics of the substrate [2]. Siegrist et al. observed that the methanogenesis process during biodegradation dropped when pH reached below 6.2 [3]. However, considering the degradation of lignocellulosic biomass that are recalcitrant solid materials, the process of hydrolysis is also slowed down the rate of AD [4]. Thus, pretreatment of lignocellulosic biomass before AD is vital for reducing the compositional and structural disablements of the biomass. This facilitates the microbial breakdown of polymeric cellulose and hemicellulose chains, resulting in a faster rate of organic degradation and biogas production. In India, the banana is the second most harvested fruit. It accounts for an average yield of about 37.79 tons per hectare and is much higher than most of the countries in the world [5]. Banana tree wastes are scattered in irrigated land to decay naturally causing bad odor and release of greenhouse gases [6]. Jena et al. investigated the AD process using semi-dried banana leaves (BL). They observed that with a decrease in the sample size of the substrate, the biogas production rate was increased [7].

None of the authors so far used dried BL for biogas synthesis using cow urine. In this experiment, cow urine is considered as a charge material mixed with sewage water to prepare the inoculum for the AD process.

## 2 Materials and Method

### 2.1 Characterization of Dried and Fresh Banana Leaves

Proximate, lignocellulosic analysis of both dried and fresh BL, and their respective higher heating value (HHV) data are given in Table 1. The proximate analysis reveals the characterization of the samples in terms of ash content (A), moisture content (M), volatile matter (VM), and fixed carbon (FC).

**Table 1** Proximate, lignocellulosic analysis, and heating values of banana leaves [6]

Biomass	VM (%)	A (%)	Cellulose	Hemicellulose	Lignin	HHV ( $\text{MJ Kg}^{-1}$ )
Dried BL	78.2	6.2	$26.7 \pm 0.9$	$25.8 \pm 0.9$	$17 \pm 0.3$	$19.8 \pm 0.6$
Fresh BL	41.3	12.2	$53.5 \pm 0.9$	$28.5 \pm 0.8$	$15.4 \pm 0.4$	$5.5 \pm 0.2$



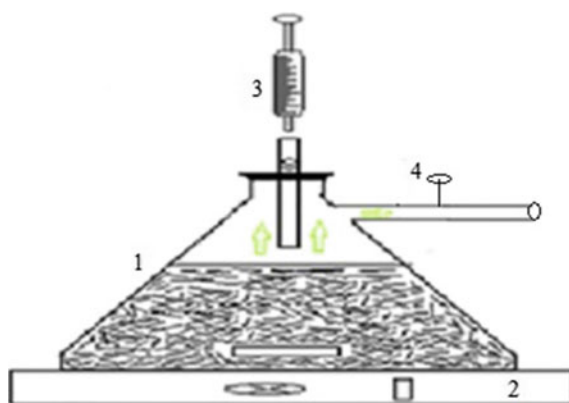
## 2.2 Procurement of the Materials

BL was fetched from a local farm, where only the leaf blades were considered for the experimental analysis. So, the leaves collected from the farms were thoroughly washed in water and the midrib was separated so that only leaf blades are available for the experimental analysis. Cleaned leaf blades were sundried to ensure complete drying. They were then cut into smaller pieces of size 2–6 mm and ground into powder form. Sewage water was collected from sewage drains from the locality and was filtered to remove sand and other solid particles. Cow urine was collected from the nearest livestock farm. It is rich in nitrogen content and was used as a biocatalyst for the experiment.

## 2.3 Experimental Setup and Procedure

Four batch type reactors with a capacity of 1L each were used to conduct the experiment. The experimental setup with the reactor, magnetic stirrer, rubber stopper, syringe, gas outlet valve, and gas collection vessel is illustrated in Fig. 1. Each reactor was fed with 50 g of ground BL powder and 500 mL of inoculum in a ratio of 1:10 (w/v). The composition of cow urine is given in Table 2 [8]. It was mixed with sewage water in different proportions and was used as an inoculum to study its effect on biogas yield and optimization of the result.

**Fig. 1** Biogas reactor



1. Reactor, 2. Magnetic stirrer, 3. Syringe, 4. Gas outlet valve

**Table 2** Composition of cow urine [8]

Compositions	H <sub>2</sub> O (%)	Urea (%)	N (%)	K (ppm)	Ca (ppm)	Mg (ppm)	Na (ppm)
Cow urine	95	2.5	1.21	156,261	32,039	21,739	12,470

**Table 3** pH value of the inoculums

Inoculum	Cow urine	B0	B5	B10	B15
pH value	7.73	7.58	7.63	7.66	7.68

The inoculums were prepared using cow urine as blends of 0, 5, 10, and 15% of the total volume, and a comparison of the results was made with sewage water as the base inoculum. The reactor that was marked as B0 signifies the absence of cow urine in the reactor. Similarly, B5 indicates 475 ml of sewage water and 25 ml of cow urine, B10 signifies 450 ml of sewage water with 50 ml of cow urine and lastly, B15 implies that 75 ml cow urine and 425 ml of base inoculum. The pH values of the inoculums were measured with the help of a digital pH meter and were shown as shown in Table 3.

After inserting the stoppers in the reactors, all the reactors were tightly sealed and were evacuated using a vacuum pump to ensure an oxygen-free environment within each reactor. Magnetic stirrers were used to continuously agitate the mixture [7]. The biogas samples were collected from each reactor every 3–4 days through an airtight gas syringe (VICI, US), and their composition was checked using a gas chromatograph-2010 (CIC, Baroda).

### 3 Results and Discussion

#### 3.1 Variation in CH<sub>4</sub> and Carbon Dioxide Content in the Reactors

The biogas reactors were held under inspection for 56 days. Every third day, the composition of the gas mixture was tested and noted down. The mean value of three consecutive readings was considered for the observation. The variation in the composition of CH<sub>4</sub> and CO<sub>2</sub> with time in days from different reactors was illustrated in Fig. 2 for a comparative study of the influence of cow urine as the catalyst for biogas production. It is observed that in the selected blends of cow urine with sewage water, the composition of CH<sub>4</sub> was very low during the initial phase of the reaction. It might be due to the slow growth of acidogenesis responsible for breaking down the hydrolyzed monomers into NH<sub>3</sub>, CO<sub>2</sub>, H<sub>2</sub>, H<sub>2</sub>S, alcohols, and volatile fatty acids because of the higher alkalinity in the solution. Acidogenesis can grow very fast and can be doubled in a time of 30 min [9], and the suitable range of the pH should be 5.5–6.5. A rise in CH<sub>4</sub> content was observed between 8–14 days in all the reactors except B0 due to the exponential growth of methanogenesis because of the enhanced buffer capacity. It reached the highest peak around 38–41 days, owing to the effective replication of methanogenic microbes accompanied by appropriate agitation that enable the faster activity of microorganisms within the reactors. While the B0 blend has shown a higher lag period of 13 days compared to others. Then, sharp rise in

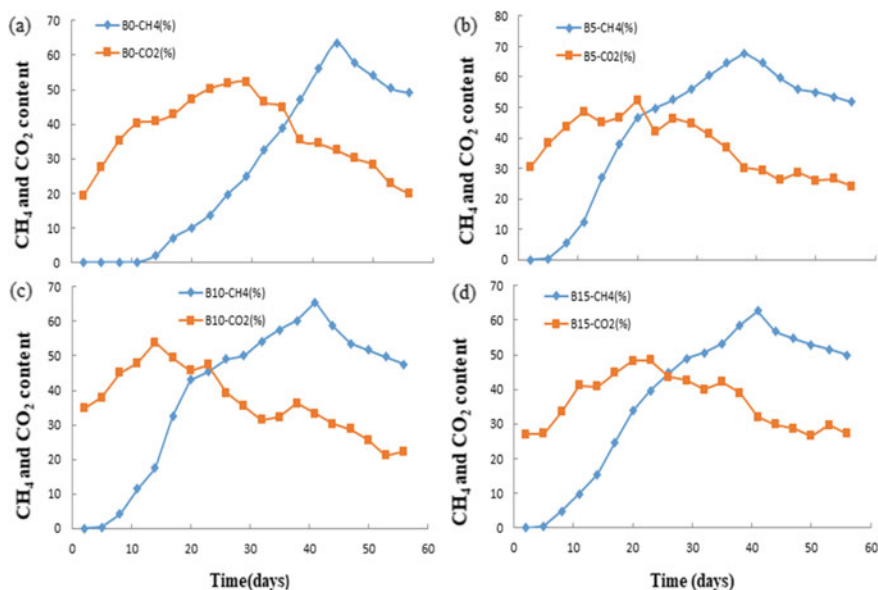


**Fig. 2** Change in CH<sub>4</sub> and CO<sub>2</sub> content in biogas with respect to time: **a** B0, **b** B5, **c** B10, **d** B15

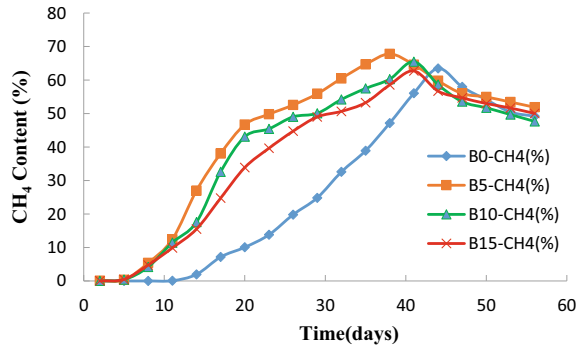
the %CH<sub>4</sub> was observed within a period of 14–17 days and reached to highest peak between 44–47 days. Then, the %CH<sub>4</sub> shown a steady decline up to 56 days, which might be due to the rise in ammonia content, decrease in C/N ratio, that inhibit the release of gas.

A rapid rise in the CO<sub>2</sub> percentage was directly attributed to the steep rise in methanogenic activity between 8–14 days of observation leading to the increased levels of CH<sub>4</sub> formation compared to CO<sub>2</sub> in later stages due to CO<sub>2</sub> and H<sub>2</sub> reaction [7]. Both CH<sub>4</sub> and CO<sub>2</sub> content began to drop steadily once CH<sub>4</sub> reached its highest peak due to the development of intermediate acidic compounds, which increased the slurry's toxicity, hindering bacterial growth, and decreased volatile content leading to the lowered fermentation rate.

### 3.2 Impact of Cow Urine Blends on Methane Concentration

Figure 3 depicted the variation in the CH<sub>4</sub> content with respect to time (days) for all the reactors to study the effect of cow urine on CH<sub>4</sub> production and helped in optimizing the urine blend for maximizing the yield. Due to the slow growth of acetogenesis, CH<sub>4</sub> generation in the primary stages was quite low and reached around 15% within 14 days. Generation of CH<sub>4</sub> from each reactor was progressively increased and reached a peak between 38 and 41 days. It was due to proper mixing

**Fig. 3** Influence of cow urine blends on CH<sub>4</sub> content



that ensured that the solution was homogeneous and got a higher exposed area for the anaerobic bacterial growth.

Periodic agitation also allows trapped gas bubbles in the medium to escape and prevents sedimentation on the leaves. B5 showed 67.78% CH<sub>4</sub> and it is the highest value among all the blends, B0, B10, and B15. It might be due to adequate buffering and pH balance compared to others. The CH<sub>4</sub> content slope of the B5 curve was also noticed to be higher than all other blends. With the increase in resident time beyond 40 days CH<sub>4</sub> content gradually decreases for all inoculums. It might be due to an increase in urea content with an increase in cow urine blend that leads to the accumulation of ammonia and inhibits bacterial growth. From the above discussion, it can be concluded that cow urine as a biocatalyst has a positive influence on CH<sub>4</sub> yield. As B15 shows comparatively lower CH<sub>4</sub> slop than B5 and B10, hence further increase in cow urine blend in the inoculum was not considered in the present work.

### 3.3 Biogas Characterization

The major contents of biogas are CH<sub>4</sub> and CO<sub>2</sub> with traces of CO, H<sub>2</sub>, N<sub>2</sub>. The heating value of any gaseous fuel is dependent on the quantity of the combustible gases present in it. The composition of biogas further depends on the reactor temperature, feeding material, and bacterial growth. The composition of collected biogas from different reactors was presented in Table 4, and the samples were also tested for their CVs. The best composition of combustible gases, CH<sub>4</sub> (67.78%), CO (0.259%), and H<sub>2</sub> (0.003%) was obtained from B5 than others with a highest calorific value of 25.717 kJ Nm<sup>-3</sup> and is validated.

**Table 4** Composition of biogas with different blend

Compositions	B0	B5	B10	B15
CH <sub>4</sub>	63.46	67.78	65.48	62.72
CO <sub>2</sub>	32.53	30.22	33.27	32.08
H <sub>2</sub>	0.002	0.003	0.002	0.002
CO	0.268	0.295	0.258	0.131
CV (MJ Nm <sup>-3</sup> )	23.634	25.717	22.889	21.153

## 4 Conclusions

The following conclusions were drawn from the experimental findings obtained from the anaerobic digestion of dried BL with cow urine as the biocatalyst for the production of biogas.

- The use of CU as 5% of the total volume of the inoculum (SW + CU) increases the methane yield from 63.46 to 67.78% compared to no CU in the inoculum.
- Further increase in the blending of cow urine in the inoculum decreases the biogas yield.
- Composition of biogas, thereby CV of the biogas generated from the reactors improves from 23.634 to 25.717 MJ Nm<sup>-3</sup> with 5% blending of cow urine in the inoculum.
- Hence, a 5% blending of cow urine with sewage water is the optimum value for maximizing CH<sub>4</sub> production from BL.
- CO<sub>2</sub> removal methodology may be adopted to improve the combustion characteristics of the produced biogas as its content lies in the range of 1/3rd of the total volume of the biogas.

Different researchers have used sodium hydroxide or calcium hydroxide solution in scrubbing units to upgrade biogas by absorbing CO<sub>2</sub> content from it. As a result, we can enrich the CH<sub>4</sub> content and combustion quality of the produced biogas.

## References

1. Jena SP, Mohanty UK, Mahapatra S (2020) Anaerobic digestion of semi-dried banana leaves in sewage water under the influence of certain additives. *Mater Today Proc* 33:4988–4992
2. Chen C, Guo W, Ngo HH, Lee D, Tung K (2016) Challenges in biogas production from anaerobic membrane bioreactors. *Renew Energy* 98:120–134
3. Siegrist H, Vogt D, Garcia-Heras JL, Gujer W (2002) Mathematical model for mesophilic and thermophilic anaerobic sewage sludge digestion. *Environ Sci Technol* 36(5):1113–1123
4. Cirne DG, Lehtomaki A, Bjornsson L, Blackall L (2007) Hydrolysis and microbial community analyses in two-stage anaerobic digestion of energy crops. *J Appl Microbiol* 103:516–527
5. National Horticulture Board (NHB) (2014) Home page Retrieved on 16th Aug 2014. <http://nbh.gov.in>

6. Fernandez ERK, Marangoni C, Souza O, Sellin N (2013) Thermochemical characterization of banana leaves as potential energy. *Energy Convers Manage* 75:603–608
7. Jena SP, Mishra S, Acharya SK, Mishra SK (2017) An experimental approach to produce biogas from semi-dried banana leaves. *Sustain Energy Technol Assess* 19:173–178
8. Akila B, Manickavasakam K, Shakila R (2014) Chemical analysis of Gomutra Silasathu Parpam. *Int J Drug Deliv* 6:88–93
9. Pham TN, Nam WJ, Joen YJ, Yoon HH (2012) Volatile fatty acids production from marine macroalgae by anaerobic fermentation. *Bioresour Technol* 124:500–503

# Effect of Tissue Properties on the Efficacy of MA on Lungs



Shubhamshree Avishek and Sikata Samataray

**Abstract** Microwave Ablation (MA) has been playing a crucial role in the field of Cancer Treatment possessing a significant advantage over Radiofrequency Ablation (RFA). Due to the possibilities of treating tumors  $>3$  cm in a shorter time with greater efficacy, MA has been proved as an alternative to RFA for treating cancerous tumors. The efficacy of MA can be determined by the output Ablation Zone generated to ablate the tumor from the targeted region. Thermal therapies highly depend on the tissue properties to successfully ablate the tumor from the targeted region. Tissue physical properties like Blood Perfusion Rate, Thermal, and Electrical Conductivity potentially affect the heat generation and the energy deposition over the tissue resulting in shorter ablation zones. Therefore, to understand the role of tissue properties like Blood Perfusion Rate, Thermal, and Electrical Conductivities, a finite element-based numerical study has been made to analyze the individual impact of these tissue properties on the Ablation Volume attained during the MA on lungs. It has been found that the higher values of Electrical Conductivity play a positive role during the treatment process as higher Electrical Conductivity results in larger ablation zones. Alternatively, the other tissue properties like the Blood Perfusion Rate (BPR), and the Thermal Conductivity have a negative correlation with the ablation volume, signifying a tissue with a higher rate of Blood Perfusion and Thermal Conductivity would make it difficult to generate an intense temperature profile, hence, leading to small ablation zones. The results obtained from the study clear out the individual impact of tissue properties during the Microwave Ablation. Understanding the effect of tissue properties would help clinical practitioners to adjust the optimal settings required for the MA to ablate the tumor in a short period without damaging the healthy tissue.

**Keywords** Microwave ablation · Hyperthermia · Computational modeling · Thermal therapy

---

S. Avishek · S. Samataray (✉)  
Department of Mechanical Engineering, ITER, SOA (Deemed to be University), Bhubaneswar  
751030, India  
e-mail: [sikatasamantaray@soa.ac.in](mailto:sikatasamantaray@soa.ac.in)

## 1 Introduction

The advancement in technology has witnessed the possibilities of diagnosing cancer at the early phase using modern imaging and treating it with Minimally Invasive Thermal Therapies. This helps the patient to overcome surgical intolerance, time management, and monetary problems. The surge in the area of Thermal Therapies for the last few decades has now evolved into a better stage with a high efficacy rate and lower reoccurrence of the tumors in the nearby region. Among all the Thermal Therapies, RFA is widely applied to treat various tumors and has been extensively studied. However, due to certain limitations of RFA resulting in poor efficacy while treating tumor  $>3$  cm and tissue having lower electrical conductivity, the need for a better alternative comes up. In this context, MA plays a vital role in treating tumors greater than 3 cm with higher efficacy in a shorter period. As the MA induces faster heating in a short period of time the attained ablation zones are quite comparatively larger and tend to be a promising treatment modality to the existing RFA [1]. The MA has been adopted to treat a variety of tumors in different organs like lungs, liver, kidney, bone, etc. [2, 3].

Several kinds of research both experimental and numerical modeling have been carried out on different organs to treat the tumors. Past researches show the significance of the MA over other thermal therapies including RFA both numerically and experimentally [2, 4]. The variation in the tip temperatures of the antenna affects the ablation volume while treating with RFA but the ablation zones with maximum temperatures above  $150^{\circ}\text{C}$  can be attained by using MA [5]. Though MA provides a larger ablation volume in comparison to other thermal therapies, the risk of damage to peripheral small vessel inducing thrombosis is quite higher [6]. Therefore, proper treatment planning with prior information is required in the planning stage to determine the optimal setting for the Microwave Thermal Ablation to ablate the tumor keeping the healthy tissue safe. The critical parameters having a significant impact on the efficacy of MA on lungs and liver have been also studied to understand the effect of the individual parameters while deriving the optimal settings required for the treatment process [7–9]. Vanni Lopresto made a study on the effects of temperature varies depending on the dielectric and thermal properties which results in the extension of the coagulated zone [10]. From the literature, it can be quantified that the design of the antenna could also help in achieving an intense temperature profile on the tissue, for example, the use of multi-slot coaxial antennae has been seen to induce a larger temperature profile than using a Single Slot Coaxial Antennae [11, 12].

In this respect, this current study is made to inspect the effect of tissue properties like Blood Perfusion Rate, Thermal, and Electrical Conductivity on the total ablation zone that is achieved throughout the treatment process of MA for 5 min. A numerical approach has been conducted using the finite element-based analysis to obtain the results for all the tissue properties taken into account for this study. This approach plays a vital role in predicting the temperature profiles, deriving the fraction of necrosed tissue, and understanding the effects of various critical parameters while



allowing the clinical practitioners to get a priori-information during the treatment planning stage.

## 2 Methods and Methodology

A single slot interstitial antenna is embedded into the geometric center of the homogenous biological tissue. Inducing heat to the geometric center of the tissue ensures uniform heat distribution throughout the tumor volume. The antenna is made up of dielectric sandwiched between the conductors where a ring-shaped slot is cut at the outer conductor from the tip. The entire interstitial antenna is housed inside a cylindrical catheter as shown in Fig. 1.

A power of 10, 25, 50 W is used to deliver the microwave power to the targeted tissue to attain the ablated volume. All the tissue properties of lungs have been derived from the literature given in Table 1 and further, for this present study the tissue properties have been divided into three levels for detecting the effects of individual factors on the efficacy of MA as shown in Table 2.

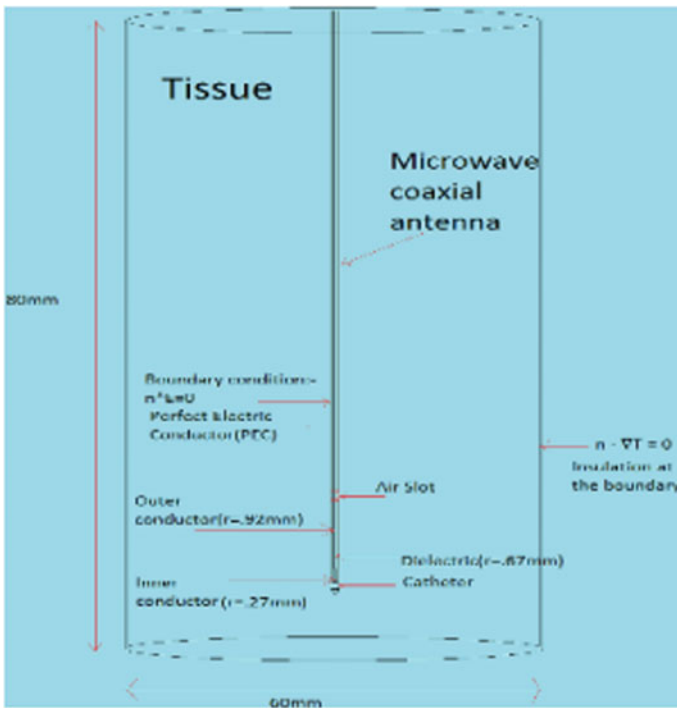


Fig. 1 Computational domain

**Table 1** Tissue properties of lungs

Parameters	Values
Relative permittivity	20.5
$\sigma$	0.804
$k$	0.39
BPR	0.00263

**Table 2** Tissue properties levels

Tissue properties	L1	L2	L3
$\sigma$	0.459	0.637	0.804
$k$	0.28	0.39	0.48
BPR	0.00263	0.005	0.0674

### 2.1 Numerical Modeling

Due to the limitations of the experimental data and the advantage of iterating numerically to detect the optimal setting, position of the applicator, and saving experimentation time the numerical approach has been accounted to determine the individual tissue properties effect. To derive the temperature profile and attain the ablation zone the 3d homogenous model tissue needs to be discretized. The coupled Electromagnetic-Heat Transfer problem can be solved and the computational domain can be discretized using the Finite Element Based COMOSOL Multiphysics. The extra-fine mesh was created near the dielectric port and finer mesh was created in the rest of the domain. A total of 363,822 tetrahedral elements were formed in the computational domain as shown in Fig. 2.

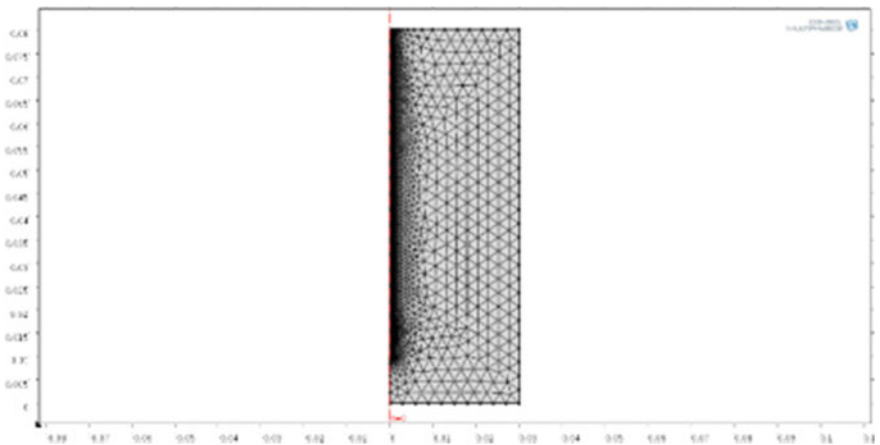


**Fig. 2** Meshed computational domain

## 2.2 Solution Methodology

The tissue temperature increases due to the accumulation of electromagnetic energy in the targeted region. The transient temperature profile and the electric field generated during the MA are required to derive the size of the ablation volume and to analyze the effect of various tissue properties like Perfusion rate, Thermal & Electrical Conductivity. The Pennes Bioheat Equation can be formed to calculate the attained temperature zones in a tissue shown in Eq. 1 [13, 14]

$$\rho c \frac{dT}{dt} = \nabla k \nabla T - \rho_b c_b (T - T_b) + \rho \cdot \text{SAR} \quad (1)$$

$$\rho \cdot \text{SAR} = \sigma |E|^2 \quad (2)$$

where  $T$  is temperature,  $t$  is time,  $k$  is thermal conductivity,  $\rho_b$  is the blood density,  $c$  is specific heat  $\rho$  is the density,  $c_b$  is the blood specific heat,  $\omega_b$  is the blood perfusion rate,  $\rho \cdot \text{SAR}$  is the Tissue's Specific Absorption Rate.

The Electric field can be discovered using the Helmholtz-wave equation given in Eq. 3,

$$\nabla \times \mu_r (\nabla \times E) - k_0^2 \left( \epsilon_r - \frac{j\sigma}{\omega\epsilon_0} \right) E = 0 \quad (3)$$

where  $\mu_r$  is relative permeability,  $E$  depicts the electric field,  $k_0$  signifies the propagation const. in free space,  $\epsilon_r$  is Relative Permittivity ratio,  $\sigma$  is Electrical Conductivity,  $\omega$  is the frequency, and  $\epsilon_0$  is the permittivity of free space.

The ablated volume is nearly equal to the temperature it receives. Now, the Arrhenius model is used to get the degree of tissue injury [14]

$$\frac{d\alpha}{dt} = A \exp\left(-\frac{dE}{RT}\right) \quad (4)$$

$$\theta_d = 1 - \exp(-\alpha) \quad (5)$$

where  $\theta_d$  signifies the degree of damaged tissue,  $d$  is the fraction of necrotic tissue.  $T$  is the temperature,  $t$  is the time, and  $R$  is the gas constant value,  $A$  and  $dE$  are the Frequency Factor and Electric Field, respectively.

## 3 Results and Discussion

Due to the low permittivity and low conductivity of the lungs, microwave energy can propagate deep inside the tissue than any other organ like the liver. As the microwave

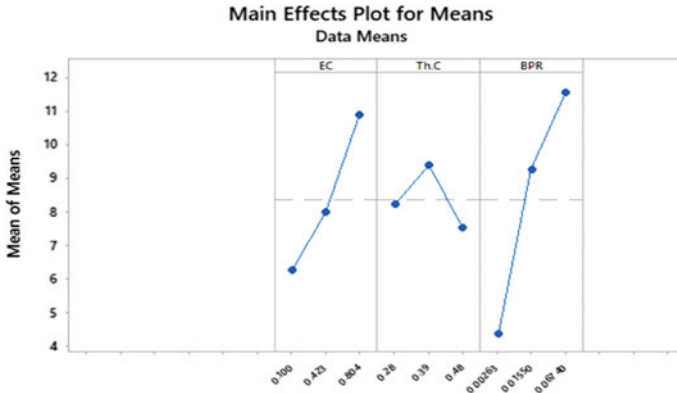


Fig. 3 Mean effects plot for S/N ratio of tissue properties

heating is independent of Electric Conductance, it doesn't get hindered by the tissue with lower Electrical Conductivity which was previously difficult to treat with RFA. Alternatively, the enhanced thermal gradient creates passive heating of the tumor margin and the maximum temperature can easily exceed 150 °C.

Using the FEM-based analysis and the governing equations with the relative boundary conditions the effect of the tissue properties has been recorded. The outcome of the different tissue properties is then plot using the Mean Effects Plot for the Signal to Noise Ratio Shown in Fig. 3. The results from the individual parameters and the mean effect plot are then analyzed to get the final conclusion. The current aim of the study is to maximize the Ablation Zone, therefore the larger-the-better category is chosen for the Signal-to-Noise ratio which can be represented by [15]

$$\frac{S}{N} = -10 \log \left[ \frac{1}{V_1^2} \right] (dB) \tag{6}$$

From Fig. 3 the Rate of Blood Perfusion and the Electrical conductivity tends to be the primary tissue properties that are affecting the output response. The individual effects of the parameters are given in the section below.

### 3.1 The Effect of Blood Perfusion Rate

Blood Perfusion Rate is a crucial Thermophysical Property that rules the result of the thermal treatments. From Fig. 4 it can be observed that a higher Blood Perfusion Rate results in shorter Ablation Volumes.

The reason for the decrease in Ablation volume is due to the hindrance in energy accumulation where the thermal energy is easily convected to the surrounding region. This heat sink effect restricts the microwave power to efficiently heat the region

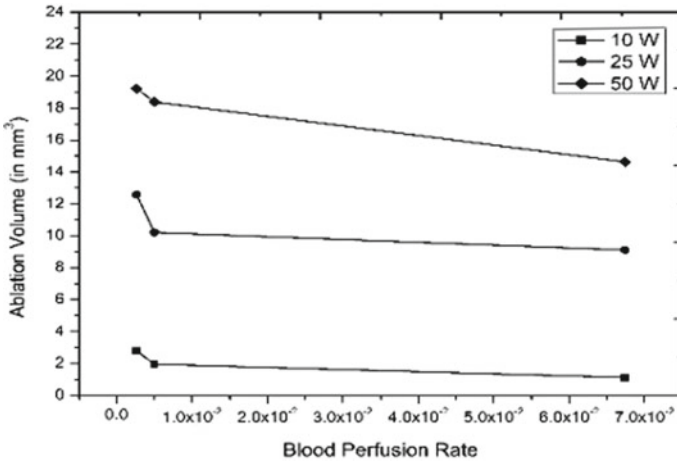


**Fig. 4** BPR versus ablation volume for 10, 25, and 50 W Power

resulting in lower ablation volumes. However, the Relative Permittivity and Blood Perfusion Rate of the lungs are quietly low, hence, making the MA easier to entertain. The Blood Perfusion Rate has a distinct remarkable influence on the output ablation zones. The organs with a higher Blood Perfusion Rate like kidneys would require larger applied power to ablate the desired volume of the tumor.

### 3.2 Effect of Electrical Conductivity

The Electrical Conductivity of tissue determines how well the tissue can allow the electric field to pass through it. As the microwave passes in the form of electromagnetic waves the Electrical Conductivity of tissue plays an essential role in allowing the propagation. Following the Blood Perfusion Rate of tissue, the Electrical Conductivity also plays a significant role in the MA technique. Figure 5 shows that it has a positive correlation with the dimensions of ablation volume, which signifies, a tissue having higher Electrical Conductivity would result in larger ablation zones. However, lungs have lower electrical conductivity, therefore treating with RFA would result in poor efficacy as it purely depends on the electric properties of the tissue. In this regard, the MA could help in attaining a larger ablation zone using higher applied power and frequency.

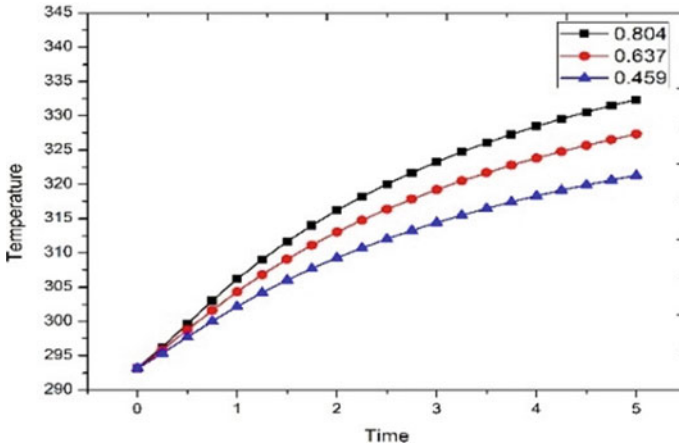


Fig. 5 Time versus temperature for different electrical conductivity of a tissue

### 3.3 Effect of Thermal Conductivity

The Thermal Conductivity of a tissue depicts the ability of a tissue to allow the transfer of heat, which means, a tissue having higher thermal ablation would allow a rate of higher heat transfer. As the rate of heat transfer is higher in the tissue, the heat generated from the microwave can be easily convected away to the surrounding tissue.

From Fig. 6, it can be observed that higher Thermal Conductivity of a tissue results in lower ablation zones due to the heat being convected away. The easy heat convection to the surrounding tissue results in the restriction of the intense thermal profile and smaller ablation zones. Due to poor thermal conduction, the creation of the ablative margins is restricted and can destroy satellite cell clusters in the lungs. Alternatively, the Thermal Conductivity of tissue has a minimum impact on the dimensions of the ablation zone achieved throughout the MA.

## 4 Conclusion

Based on the results derived from the FEM-based numerical analysis it has been found that the tissue properties like Electrical Conductivity, Blood Perfusion Rate, and Thermal Conductivity are the important factors to consider while planning the treatment process and choosing the right treatment technique. Depending on these factors the optimal settings of the Microwave Applicator need to be analyzed before the starting of the treatment process. The results show that the Blood Perfusion Rate and the Electrical Conductivity have a distinct remarkable impact on the dimensions of ablation volume. A tissue having a higher Rate of Blood Perfusion tends to

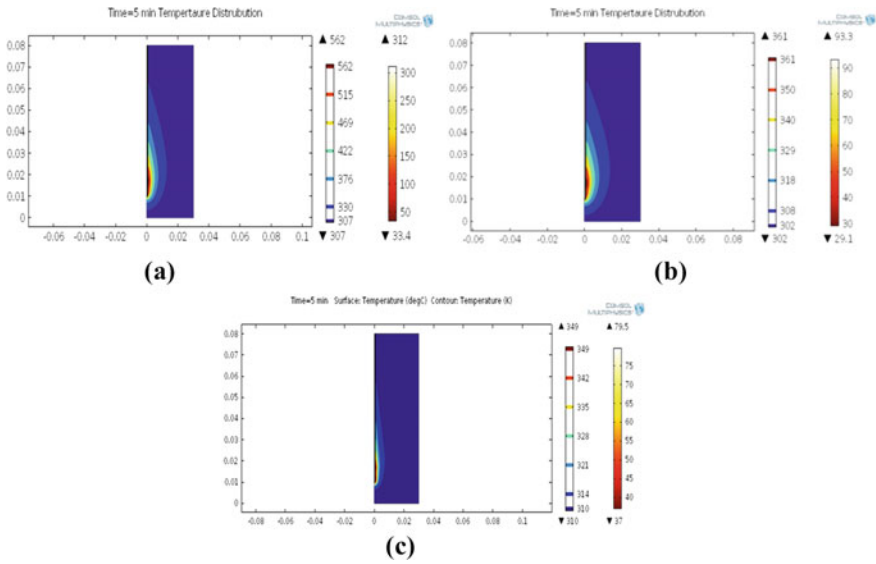


**Fig. 6** Temperature contour plot **a**  $k = 0.28$ , **b**  $k = 0.39$ , **c**  $k = 0.48$

hinder the propagation of the electric field and results in smaller temperature profiles, whereas, a tissue having larger Electrical Conductivity would potentially increase the ablation volume size, as it allows more electric fields to pass through it. On the other hand, the tissue Thermal Conductivity makes the heat convected away easily to the surrounding tissue and hence resulting in lower ablation zones. So, the higher the tissue Thermal Conductivity, the lower the ablation volumes. Lungs have less perfusion rate and conductivity which makes the MA an ideal thermal ablation technique than other thermal therapies. By understanding the individual effect of the Blood Perfusion Rate, Thermal and Electrical Conductivity on the ablation volume size, the best suiting treatment technique and the optimal setting for power and frequency can be determined before the treatment. These results would potentially help the radiologists to prioritize the treatment planning according to the variability in the tissue properties.

## References

1. Chu KF, Dupuy DE (2014) Thermal ablation of tumours: biological mechanisms and advances in therapy. *Nat Rev Cancer* 14:199–208
2. Brace CL (2009) Radiofrequency and microwave ablation of the liver, lung, kidney, and bone: what are the differences? *Curr Probl Diagn Radiol* 38:135–143
3. Wasser EJ, Dupuy DE (2008) Microwave ablation in the treatment of primary lung tumors. *Semin Respir Crit Care Med*. 29:384–394

4. Sidoff L, Dupuy DE (2017) Clinical experiences with MTA of lung malignancies. *Int J Hyperth* 33(1):25–33. <https://doi.org/10.1080/02656736.2016.1204630>
5. Wang X, Numerical evaluation of ablation zone under different tip temperatures during RFA. *Math Biosci Eng* 16(4):2514–2531. <https://doi.org/10.3934/mbe.2019126>
6. Crocetti L et al (2010) Thermal ablation of lung tissue: in vivo experimental comparison of microwave and radiofrequency. *Cardiovasc Intervent Radiol* 33:818–827
7. Avishek S, Samataray S (2021) Sensitivity analysis of critical parameters affecting the efficacy of MTA on lungs. [https://doi.org/10.1007/978-981-33-4795-3\\_28](https://doi.org/10.1007/978-981-33-4795-3_28)
8. Singh S (2019) Sensitivity analysis of critical parameters affecting the efficacy of microwave ablation using Taguchi method. *Int J RF Microw Comput Aided Eng* 29:e21581
9. Lopresto V, Pinto R, Farina L, Cavagnaro M (2017) MTA: effects of tissue properties variations on predictive models for treatment planning. *Med Eng Phys* 46:63–70
10. Lopresto V, Pinto R, Farina L, Cavagnaro M (2017) Treatment planning in MTA: clinical gaps and recent research advances. *Int J Hyperth* 33(1):83–100. <https://doi.org/10.1080/02656736.2016.1214883>
11. (2015) Piotr gas multi–frequency analysis for interstitial microwave hyperthermia using multi–slot coaxial antenna. *J Electr Eng* 66(1):26–33
12. Sawicki JF, Shea JD, Behdad N, Hagness SC (2017) The impact of frequency on the performance of microwave ablation. *Int J Hyperth* 33(1):61–68
13. Huang-Wen H, Tzyy-Leng H, Bioheat transfer and thermal heating for tumor treatment. <https://doi.org/10.1016/B978-0-12-408077-5.00001-8>
14. Yang D, Cao M (2020) Effect of changes in lung physical properties on microwave ablation zone during respiration. *Biomed Eng Lett*. <https://doi.org/10.1007/s13534-019-00145-5>
15. Singh S, Repaka R (2018) Parametric sensitivity analysis of critical factors affecting the thermal damage during RFA of breast tumor. *Int J Therm Sci* 124:366–374



# Multi-response Optimization of Turning Parameters for AZ91D Magnesium Alloy Using Gray-Based Taguchi Approach



A. Saravanakumar, L. Rajeshkumar, G. Sisindri Reddy,  
K. Narashima Prasad, M. Pranava Adithya, P. Suryaprakash Reddy,  
P. Harsha Vardhan, and P. Bala Narasimhudu

**Abstract** The current research aims to determine the optimal process parameters during the turning of AZ91D magnesium alloy using uncoated carbide insert tool under dry cutting conditions. Speed, feed rate, and depth of cut were considered as the turning process parameters in three levels each, while the design of experiments was carried out using Taguchi's L9 orthogonal array (OA). Responses for the experiments were taken as surface finish and roundness error with larger-the-better as objective function. Influence of the parameters over the responses recorded during the turning operation was statistically analyzed by analysis of variance (ANOVA) technique. Experimental results portrayed that feed followed by speed influenced the responses to a higher extent when compared with other process parameters.

**Keywords** Surface roughness · Roundness error · Taguchi method · GRA

## 1 Introduction

Magnesium alloys find their majority of applications in various key engineering fields like automotive and aerospace industries owing to their excellent specific strength relatively. Though cast and wrought magnesium alloys are comparatively expensive, their recent utilization has seen a steep growth owing to their better inherent characteristics [1–5]. Density of the magnesium alloys is yet another advantage of these alloys, and they possess almost one-fourth of the steel density and one-third of the aluminum density. Magnesium alloy components help in drastically reducing the overall assembly weight even if very fewer components of the assembly were

---

A. Saravanakumar · G. Sisindri Reddy · K. Narashima Prasad · M. Pranava Adithya ·  
P. Suryaprakash Reddy · P. Harsha Vardhan · P. Bala Narasimhudu  
Department of Mechanical Engineering, K.S.R.M. College of Engineering, Kadapa, A.P 516003,  
India

L. Rajeshkumar (✉)  
Department of Mechanical Engineering, KPR Institute of Engineering and Technology,  
Coimbatore, Tamilnadu 641407, India  
e-mail: [lrkln27@gmail.com](mailto:lrkln27@gmail.com)

made of magnesium and its alloys [6–10]. Hence, the scope of utilization of magnesium alloys has widened to a broader spectrum in fields like weapons, automotive, marine, and aerospace applications. Magnesium alloys are characterized by some inherent advantages like excellent electrical and thermal conductivity, high potential toward absorbance of shock waves, and outstanding shielding ability against electromagnetic waves [11–15]. Many manufacturing techniques like disintegrated melt deposition, stir and squeeze casting, spray deposition and powder metallurgy methods were used for the preparation of commonly used AZ91D magnesium alloys [16–19]. Many experimental researches portrayed that if the choice of manufacturing method of magnesium alloys were not suitable, then the characteristics of resulting alloys/composites would be undesirable. It was stated in most of the literatures that die casting, gravity, or permanent mold casting are the most appropriate methods for the fabrication of magnesium-based alloys and composites [15, 20–24]. Machinability of the alloys and composite materials is the most desirable attribute for the subtractive machining process. Among every other method, turning is considered to be most flexible and faster method of material removal process [25–28]. Contemporary production during the current times is very much worried about the superiority of manufactured goods in the terms of quality. They are showing more interest in increasing the yield and getting enhanced quality products are among the major purpose of the current manufacturing industries [29–33]. Owing to necessities of the contemporary industries, widespread research activities carried on all the characteristics of the turning process include finished components surface quality, dimensional accuracy of the finished part, cutting force, and tool wear [34–37]. The major idea of this experimentation is to decide the most important factors and consequently choose on the optimal turning process parameters that machine the AZ91D magnesium alloy with least roundness error and better quality in surface finish.

## 2 Materials and Methodology

Magnesium alloy (AZ91D) was used in circular billet form of 30 mm diameter. Experiment design was performed using Taguchi's L9 OA designs of experiment coupled with gray relational analysis (GRA). In turning of magnesium alloy, most significant factors were taken to be spindle speed ( $v$ ), depth of cut ( $d$ ), feed rate ( $f$ ) at three levels with consistent limits. The turning factors and its levels are specified in Table 1. The testing has been carried out according to L9 (OA) shown in Table

**Table 1** Process parameters and their levels

Levels	Spindle speed ( $v$ ) in rpm	Rate of feed ( $f$ ) in mm/rev	Depth of cut ( $d$ ) in mm
1	750	0.1	0.20
2	1000	0.15	0.40
3	1250	0.2	0.60

**Table 2** Experimental result based on Taguchi’s L9

Exp. No.	Spindle speed ( $v$ ) in rpm	Feed rate ( $f$ ) in mm/rev	Depth of cut ( $d$ ) (mm)	Surface roughness ( $\mu\text{m}$ )	Roundness error ( $\mu\text{m}$ )
1	750	0.1	0.2	2.29	4.27
2	750	0.15	0.4	2.25	4.71
3	750	0.2	0.6	2.44	7.13
4	1000	0.1	0.4	2.27	4.16
5	1000	0.15	0.6	2.42	6.14
6	1000	0.2	0.2	2.44	8.16
7	1250	0.1	0.6	2.35	5.02
8	1250	0.15	0.2	2.36	4.58
9	1250	0.2	0.4	2.47	7.37

2 so as to reduce the roundness error and surface roughness. The turning operations were performed in CNC Turning Center Sprint 16TC (Make: FANUC) under dry conditions using carbide insert cutting tools which have superior hardness at elevated temperatures [3].

Surface roughness for the machined components was calculated by means of HANDYSURFE-35B surface roughness tester shown in Fig. 1b. Coordinate measuring machine (CMM) is a 3D measuring device which can either be computer operated or manually controlled that measures the physical geometrical parameters of the object. In the current experiments, roundness error was measured using CMM as shown in Fig. 1c. Table 2 shows the experimental responses tabulated according to the design of experiments. Every reading is repeated thrice, and the average of those values was considered for further analysis.

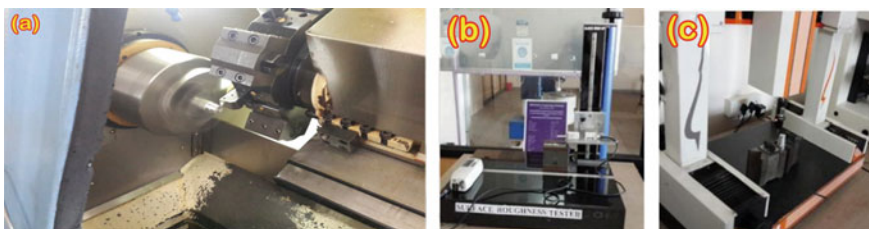


**Fig. 1** a Machine arrangement, b surface roughness testing equipment, c CMM

### 2.1 Gray Relational Analysis Technique

- The gray relational investigation is a multiple response optimization method used to discover the most optimal combination of the process parameters that reduces the error in roundness and surface roughness and can be normally utilized to translate multi-response problem into a problem of single response [5] and also to inspect the significance of each factors on the output response with the help of larger-the-better concept in Taguchi method [6]. Implementation of GRA involves the following steps where the conversion of multi-response problem to single response, and the revelation of optimal parameters takes place: Conversion of the obtained response values as  $\gamma_{ij}$  by using the appropriate equation as per the chosen objective function. Normalization of response ( $Z_{ij}$ ) data in order to minimize the variability and homogenous distribution of response values. Computation of GR coefficient ( $GC_{ij}$ ) for the normalized values of SN-ratio using the following equation where  $\lambda$  is the value of distinguishing coefficient and  $\Delta$  is the difference between normalized response values. Computation of GRG from the coefficient values is done. Using the maximum values of average  $G_i$ , optimum process parameters can be selected through ANOVA. Experimental responses, normalized values, and GRC along with GRG are enlisted in Table 3. Figure 2 shows the GRG values for various experimental trials.

$$Z_{ij} = \frac{\max(\gamma_{ij}) - \gamma_{ij}}{\max(\gamma_{ij}) - \min(\gamma_{ij})} \tag{1}$$

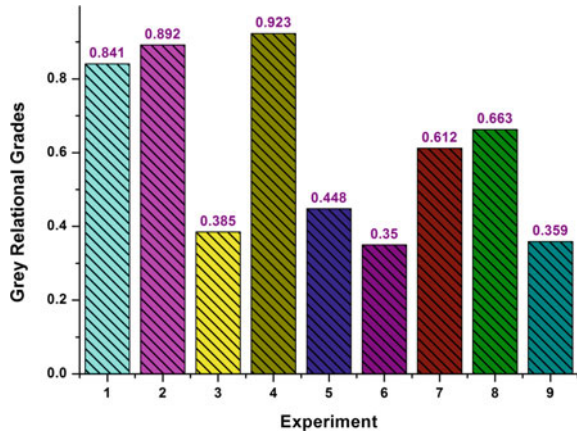
$$GC_{ij} = \frac{\Delta_{\min} + \lambda \Delta_{\max}}{\Delta_{ij} + \lambda \Delta_{\max}} \tag{2}$$

$$G_i = \frac{1}{m} \sum GC_{ij} \tag{3}$$

**Table 3** Gray relational coefficients and gray relational grades

Exp. No.	Experimental value		Normalization		Gray relational coefficients				GRG
	SR ( $\mu\text{m}$ )	Roundness ( $\mu\text{m}$ )	SR ( $\mu\text{m}$ )	R ( $\mu\text{m}$ )	$\Delta\text{SR}$	$\Delta\text{R}$	SR	R	
1	2.29	4.27	0.818	0.973	0.182	0.027	0.733	0.948	0.841
2	2.25	4.71	1.000	0.863	0.000	0.138	1.000	0.784	0.892
3	2.44	7.13	0.136	0.258	0.864	0.743	0.367	0.402	0.385
4	2.27	4.16	0.909	1.000	0.091	0.000	0.846	1.000	0.923
5	2.42	6.14	0.227	0.505	0.773	0.495	0.393	0.503	0.448
6	2.44	8.16	0.136	0.000	0.864	1.000	0.367	0.333	0.350
7	2.35	5.02	0.545	0.785	0.455	0.215	0.524	0.699	0.612
8	2.36	4.58	0.500	0.895	0.500	0.105	0.500	0.826	0.663
9	2.47	7.37	0.000	0.198	1.000	0.803	0.333	0.384	0.359

**Fig. 2** Gray relational grade value



### 3 Result and Discussion

According to the GRG values, highest value was ranked one, to infer the combination of process parameters that gave the better results. For that reason, “larger-the-better’ type for the GRG value is used to obtain best possible turning process parameters. MINITAB 16 is used to calculate S/N ratios [7]. The optimal parameters were selected based on (i) plot between main effects (ii) table of response values with ranks (iii) ANOVA. Figure 3 illustrates the main effect plot for gray relational grade value. Further, it is observed that highest values were at 750 rpm of spindle speed, 0.2 mm/rev of feed rate, and for 0.40 mm of depth of cut. The significance of turning process parameters upon roundness error and surface roughness interns of

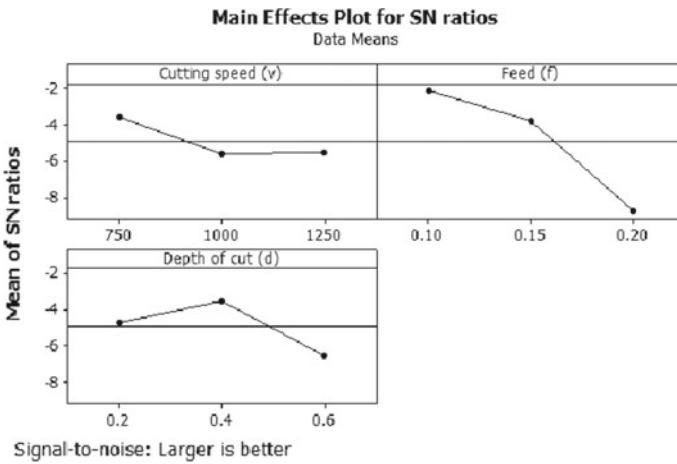


**Fig. 3** Main effect graph

**Table 4** Ranking table based on responses

Levels	$v$	$f$	$d$
1	-3.6	-2.158	-4.731
2	-5.598	-3.846	-3.531
3	-5.582	-8.776	-6.518
Delta	1.998	6.618	2.986
Rank	3	1	2

**Table 5** ANOVA

Parameters	Degree of freedom	Sequential sum of squares	Adjusted mean square	$F$ -value	$P$ -value	Contribution %
$V$	2.0	0.044340	0.08868	2.47	0.288	10.04
$F$	2.0	0.290020	0.58004	16.17	0.05	65.68
$D$	2.0	0.089280	0.17856	4.98	0.167	20.22
Residual error	2.0	0.017940	0.03588			4.06
Total	8.0	0.441580				100.00

GRG value is obtained from Table 4. This table indicates the average output values for each level of every factor considered for the design of experiments. The process parameters are ranked on basis of the delta value, and this rank specifies the effect of those processes on the responses. ANOVA table for GRG values is displayed in Table 5. Further, it could be clearly noted that feed is the high-ranked parameter due to its higher influence over the responses followed by depth of cut and spindle speed.

Variance analysis can be appropriate for representing a relationship between a response variables and process parameters. Additionally, the analysis employed to authenticate the factors is statistically not significant or significant along with  $P$ -value [7]. Higher level of significance is said to be achieved if the value of  $P$  is less than or equal to 0.05. The last column of the ANOVA illustrates the contribution percentage, wherein feed exhibits the uppermost level of contribution trailed by depth of cut and then by spindle speed.

### 3.1 Results of Optimal Experiment

Confirmation test has been carried out at optimum conditions to determine the surface roughness and roundness error. From the result, it is observed that surface roughness and roundness error are minimum compared to other conditions (Table 6).

**Table 6** Results of optimal experiment

Experiment	$v$ (rpm)	$f$ (mm/rev)	$d$ (mm)	Surface roughness ( $\mu\text{m}$ )	Roundness error ( $\mu\text{m}$ )	GRG
Initial	750	0.1	0.2	2.29	4.27	0.841
Optimal	750	0.1	0.4	2.22	3.81	0.998

## 4 Conclusion

AZ91D magnesium alloy was subjected to turning process with a combination of process parameters based on Taguchi's design, and the roundness error and surface roughness of turning parameters were optimized by using GRA. Experimental analysis rendered the following conclusions:

Optimum process parameters during turning operation for achieving lowest surface roughness value and roundness error were obtained as 750 rpm spindle speed, 0.15 mm/min of feed rate, and 0.2 mm depth of cut.

ANOVA results rendered that the responses were greatly influenced by feed rate (65.68% contribution) with first rank, trailed by depth of cut (20.22% contribution), and spindle speed (10.44% contribution) in order.

The Taguchi model coupled with GRA could be effectively utilized for getting the optimum result which shows the effectiveness of this technique, and it could be evidently seen from the confirmation experiments. From all the above discussions, it could be stated that while turning AZ91D magnesium alloy using uncoated carbide inserts, the aforesaid parameters could be adopted for begetting better surface finish.

## References

1. Duan G, Yang L, Liao S, Zhang C, Lu X, Yang Y, Zhang B, Wei Y, Zhang T, Yu B, Zhang X (2018) Designing for the chemical conversion coating with high corrosion resistance and low electrical contact resistance on AZ91D magnesium alloy. *Corros Sci* 135:197–206
2. Rajeshkumar L, Amirthagadeswaran KS (2019) Variations in the properties of copper-alumina nanocomposites synthesized by mechanical alloying. *Mater Technol* 59(1):57–63. <https://doi.org/10.17222/mit.2018.122>
3. Chen L, Zhao Y, Hou H, Zhang T, Liang J, Li M, Li J (2019) Development of AZ91D magnesium alloy-graphene nanoplatelets composites using thixomolding process. *J Alloy Compd* 778:359–374
4. Saravanakumar A, Bhuvaneshwari V, Gokul G (2020) Optimization of wear behaviour for AA2219-MoS<sub>2</sub> metal matrix composites in dry and lubricated condition. *Mater Today: Proc* 27:2645–2649
5. Xu Y, Chen C, Zhang X, Dai H, Jia J, Bai Z (2018) Dynamic recrystallization kinetics and microstructure evolution of an AZ91D magnesium alloy during hot compression. *Mater Charact* 145:39–52

6. Saravanakumar A, Sivalingam S (2018) Dry sliding wear of AA2219/Gr metal matrix composites. *Mater Today: Proc* 5(2):8321–8327
7. Woo SK, Blawert C, Yasakau KA, Yi S, Scharnagl N, Suh BC, Kim YM, You BS, Yim CD (2020) Effects of combined addition of Ca and Y on the corrosion behaviours of die-cast AZ91D magnesium alloy. *Corros Sci* 166:108451
8. Davis TA, Bichler L, D'Elia F, Hort N (2018) Effect of TiBor on the grain refinement and hot tearing susceptibility of AZ91D magnesium alloy. *J Alloy Compd* 759:70–79
9. Siddique S, Li CX, Bernussi AA, Hussain SW, Yasir M (2019) Enhanced electrochemical and tribological properties of AZ91D magnesium alloy via cold spraying of aluminum alloy. *J Therm Spray Technol* 28(7):1739–1748
10. Rajeshkumar LRK (2018) Dry sliding wear behavior of AA2219 reinforced with magnesium oxide and graphite hybrid metal matrix composites. *Int J Eng Res Technol* 6:3–8
11. Saravanakumar A, Saravanakumar R, Sivalingam S, Bhuvanewari V (2018) Prediction capabilities of mathematical models for wear behaviour of AA2219/MgO/Gr hybrid metal matrix composites. *Int J Mech Prod Eng Res Dev* 8(8):393–399
12. Zagórski I, Korpysa J (2020) Surface quality assessment after milling AZ91D magnesium alloy using PCD tool. *Materials* 13(3):617
13. Kumar A, Kumar P, Singh B (2021) Optimizing the effect of wear test parameters on the specific wear rate of AZ91D magnesium alloy. *Mater Today: Proc* 44:4885–4890
14. Shen H, Yan J, Niu X (2020) Thermo-fluid-dynamic modeling of the melt pool during selective laser melting for AZ91D magnesium alloy. *Materials* 13(18):4157
15. Niu X, Shen H, Fu J, Feng J (2021) Effective control of microstructure evolution in AZ91D magnesium alloy by SiC nanoparticles in laser powder-bed fusion. *Mater Des* 206:109787
16. Rajesh Kumar L, Sivalingam S, Prashanth K, Rajkumar K (2020) Design, analysis and optimization of steering knuckle for all terrain vehicles. *AIP Conf Proc* 2207(1):020003. <https://doi.org/10.1063/5.0000044>
17. Saravanakumar A, Rajeshkumar L, Balaji D, Karunan MJ (2020) Prediction of wear characteristics of AA2219-Gr matrix composites using GRNN and Taguchi-based approach. *Arab J Sci Eng* 45(11):9549–9557
18. Bhuvanewari V, Rajeshkumar L, Nimel Sworna Ross K (2021) Influence of bioceramic reinforcement on tribological behaviour of aluminium alloy metal matrix composites: experimental study and analysis. *J Mater Res Technol* 15:2802–2819
19. Holguin DAM, Han S, Kim NP (2018) Magnesium alloy 3D printing by wire and arc additive manufacturing (WAAM). *MRS Adv* 3(49):2959–2964
20. Kumar LR, Amirthagadeswaran KS (2020) Corrosion and wear behaviour of nano Al<sub>2</sub>O<sub>3</sub> reinforced copper metal matrix composites synthesized by high energy ball milling. *Part Sci Technol* 38(2):228–235
21. Li G, Jiang W, Guan F, Zhu J, Zhang Z, Fan Z (2021) Microstructure, mechanical properties and corrosion resistance of A356 aluminum/AZ91D magnesium bimetal prepared by a compound casting combined with a novel Ni-Cu composite interlayer. *J Mater Process Technol* 288:116874
22. Rajesh Kumar L, Saravanakumar A, Bhuvanewari V, Jithin Karunan MP, Raja NK, Karthi P (2020) Tribological behaviour of AA2219/MOS<sub>2</sub> metal matrix composites under lubrication. *AIP Conf Proc* 2207(1):020005. <https://doi.org/10.1063/5.0000042>
23. Saravanakumar A, Karthikeyan SC, Dharmotharan B (2018) Optimization of CNC turning parameters on aluminum alloy 6063 using Taguchi robust design. *Mater Today: Proc* 5(2):8290–8298
24. Rajeshkumar L, Suriyanarayanan R, Hari KS, Babu SV, Bhuvanewari V, Karunan MJ (2020) Influence of boron carbide addition on particle size of copper zinc alloys synthesized by powder metallurgy. *IOP Conf Ser: Mater Sci Eng* 954(1):012008
25. Buldum BB, Cagan SC (2017) The optimization of surface roughness of AZ91D magnesium alloy using ANOVA in ball burnishing process. *Turk J Eng* 1(1):25–31
26. Arunachalam S, Perumal S (2016) Investigation of effect of graphite particles on drillability of metal matrix composite. *Mater Sci* 22(3):390–396



27. Rajeshkumar L, Bhuvanewari V, Pradeepraj B, Palanivel C (2020) Design and optimization of static characteristics for a steering system in an ATV. *IOP Conf Ser: Mater Sci Eng* 954(1):012009
28. Mahendran R, Rajkumar P, Raj LN, Karthikeyan S, Rajeshkumar L (2021) Effect of deep cryogenic treatment on tool life of multilayer coated carbide inserts by shoulder milling of EN8 steel. *J Braz Soc Mech Sci Eng* 43(8):1–11. <https://doi.org/10.1007/s40430-021-03100-7>
29. Aldas K, Ozkul I, Akkurt A (2014) Modelling surface roughness in WEDM process using ANFIS method. *J Balkan Tribol Assoc* 20(4):548–558
30. Buldum BB, Şık A, Akdağlı A, Biçer MB, Aldas K, Özkul İ (2017) ANN surface roughness prediction of AZ91D magnesium alloys in the turning process. *Mater Test* 59(10):916–920
31. Ramesh M, Marimuthu K, Karuppusamy P, Rajeshkumar L (2021) Microstructure and properties of YSZ-Al<sub>2</sub>O<sub>3</sub> functional ceramic thermal barrier coatings for military applications. *Boletín de la Sociedad Española de Cerámica y Vidrio*. <https://doi.org/10.1016/j.bsecev.2021.06.004>
32. Saravanakumar A, Ravikanth D, Rajeshkumar L, Balaji D, Ramesh M (2021) Tribological behaviour of MoS<sub>2</sub> and graphite reinforced aluminium matrix composites. *IOP Conf Ser: Mater Sci Eng* 1059(1):012021
33. Rajesh Kumar L, Sivalingam S, Prashanth K, Rajkumar K (2020) Design, analysis and optimization of steering knuckle for all terrain vehicles. *AIP Conf Proc* 2207(1):020003
34. Saravanakumar A, Sasikumar P, Nilavusri N (2016) Optimization of machining parameters using Taguchi method for surface roughness. *J Mater Environ Sci* 7(5):1556–1561
35. Rajeshkumara L, Balajia D (2020) Study of mechanical and tribological properties of bio-ceramics reinforced aluminium alloy composites. *Solid State Technol* 63(5):4552–4560
36. Liu C, Li Z, Pei X, Yang L, Zhang Y, Wei S (2017) Microstructure and properties of AL-SI alloy cladding on AZ91D magnesium alloy by low heat input DC-PMIG welding. *Surf Coat Technol* 329:42–48
37. Saravanakumar A, Rajeshkumar L, Sanjay kumar NS, Sivakumar R, Sriramthilak S, Vignesh R (2020) Multi response optimization of aluminium alloy machining using full factorial design of experiments. *AIP Conf Proc* 2207(1):020002

# Effect of Process Parameters and Coolant Application on Cutting Performance of Centrifugal Cast Single Point Cutting Tools



Shubhashree Mohapatra, Hrushikesh Sarangi,  
and Upendra Kumar Mohanty

**Abstract** Centrifugal casting methods were employed for the production of single point cutting tools. HSS tool scraps were used for this purpose. The performance of the developed tool was analysed by turning of mild steel material. Cutting velocities were varied, keeping all other parameters constant under both dry cutting conditions and with the application of a coolant (emulsifiable water-based coolant). Analysis was based on flank surface wear, workpiece surface roughness, and main cutting force generated during machining considering both dry and wet cutting environments. The flank wear of the tool, the surface roughness of the machined surface, and the main cutting force were seemed to reduce when the coolant was used. However, the rate of reduction of main cutting force and tool flank wear was seemed to vary at cutting speeds under coolant application.

**Keywords** Centrifugal casting · Tool flank wear · Surface roughness · Cutting force

## 1 Introduction

High feed, depth of cut, and cutting velocities are essential factors to meet the increasing demand of productivity and for the reduction of machining cost. These factors cause high heat generation at the cutting zone [1]. However, a cutting zone with high temperature accounts for an increase in cutting force, wear at tool surface, workpiece surface roughness and adversely affects the dimensional tolerances. This necessitates the adoption of a suitable coolant that not only cools down the cutting zone but effectively functions as a lubricant [2]. Frictional forces are reduced. Heat dissipation is enhanced. Transportation of the chips and clearing of the cutting zone is augmented. Emulsions or straight oils can be employed as coolants. Emulsions having high water content have excellent heat transfer characteristics. Two popular

---

S. Mohapatra · H. Sarangi (✉) · U. K. Mohanty  
Department of Mechanical Engineering, ITER, SOA Deemed to be University, Bhubaneswar,  
Odisha, India  
e-mail: [hrushikeshsarangi@soa.ac.in](mailto:hrushikeshsarangi@soa.ac.in)

methods, which include flooding and minimum quantity lubrication (MQL), are popular amongst the many methods of using water-based emulsifiable coolants. Improved levels of lubrication, cooling, and chip removal are achieved with the flooding method. When this method is adopted, coupled with the adoption of low cutting speed, flank wear is minimized [3]. The effect of dry, wet, and MQCL cutting conditions during the turning of AISI 1050 steel has been examined by Sarikaya and Güllü [4]. MQL cutting conditions are seen to decrease both vibrations and surface roughness, whereas these parameters are increased under dry turning conditions. Use of coolants under high pressure, both the flank wear and rake surface wear are seen to reduce the cutting forces significantly reducing the cutting temperature [5]. Using a developed green cutting fluid [6] under dry, flood cooling and MQL environments, it is seen that cutting forces, surface roughness, and tool wear are adversely affected under a dry cutting environment as compared to other environments. Lower tool wear, power consumption, and microhardness of the machined surface are reported by Khanna et al. [7] under the cryogenic CO<sub>2</sub> cooling technique. However, when the surface roughness is concerned, machining under flood cooling conditions is seen to yield better results. The above implies the cooling environment affects the machining quality to a great extent. Dry machining and machining with coolant have their own say in influencing the machining qualities.

The paper analyses the impact of flood cooling and other cutting parameters on the machined surface quality, main cutting forces, and flank wear of the tool. The observations are compared with the same under cooling operations in a dry cutting environment when a coolant is not used. A centrifugal cast cutting tool is used, in all cases, for the study.

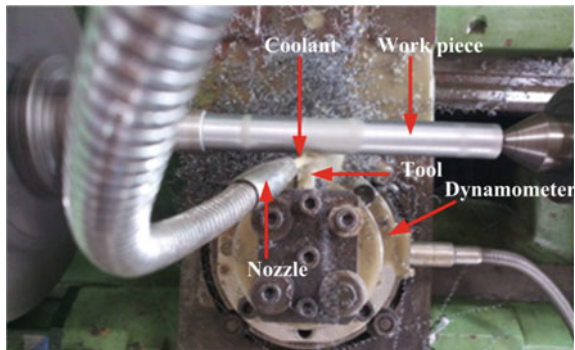
## 2 Experimental Design

The centrifugal cast tool is fabricated by taking HSS tool scraps as raw materials. The scraps were melted in an induction furnace. After slag removal, the molten HSS were poured into a rotating mould rotated at 350 rpm. After complete solidification, the centrifugal cast cylindrical blank was retrieved and processed through machining operation in order to generate single point cutting tools of standard size. The cutting tools were then subjected to heat treatment (heating of the metal to 1200 °C followed by sudden water quenching and tempering) in order to render a hardness of 54 HRC. Mild steel is used as workpiece material. The experimental details are provided in Table 1. The coolant is allowed to flow continuously throughout the cutting operations on the tool rake surface.

The turning operation is performed for 30 min in order to study the form stability of cutting tools. After successful cutting operations, the cutting force ( $F_z$ ), flank wear (VB), and surface roughness (Ra) of the tool are measured. For measurement of  $F_z$ , a piezoelectric dynamometer is attached to the lathe (Fig. 1). The  $F_z$  value for each cutting operation is calculated by taking the averages of  $F_z$  value noted in small time intervals throughout the cutting operation. At the end of the machining operation

**Table 1** Details of the experiment

Machining conditions	Details
Machine	HMT lathe
Cutting tool	Centrifugal cast single point cutting tool
Tool geometry	11°, 11°, 8°, 7°, 7°, 16°, 0.5 (mm)
Cutting condition	Dry and coolant
Coolant	Emulsifiable coolant (water-based)
Cutting velocity (m/min)	25, 35, 40, 51
Cutting time (min)	30
Other parameters	Feed = 0.16 mm/rev, depth of cut = 0.4 mm

**Fig. 1** Experimental setup

(30 min), Ra and VB are measured. Ra is measured using a profilometer. The level of flank surface wear is measured by a toolmakers microscope as shown in Fig. 2.

### 3 Result and Discussion

#### 3.1 Tool Flank Wear

Flank wear is one of the criteria to judge the cutting ability of the tool during machining at various cutting parameters. Figure 3 represents the graph of flank wear for both dry and machining with coolant conditions considering different cutting velocities. As shown in Fig. 3, VB rises with a rise in cutting velocity for both tools. However, when coolant is applied, a reduction in flank wear rate is noticed. A reduction of flank wear of 30%, 28.57%, 25%, and 9.17% is observed for 25, 35, 40, 51 m/min cutting velocity, respectively, when coolant is supplied than that of dry cutting conditions. The higher VB for dry machining might be due to elevated

**Fig. 2** Tool maker's microscope

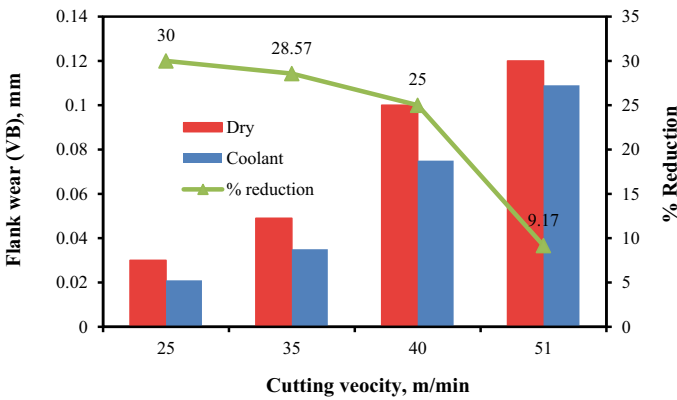
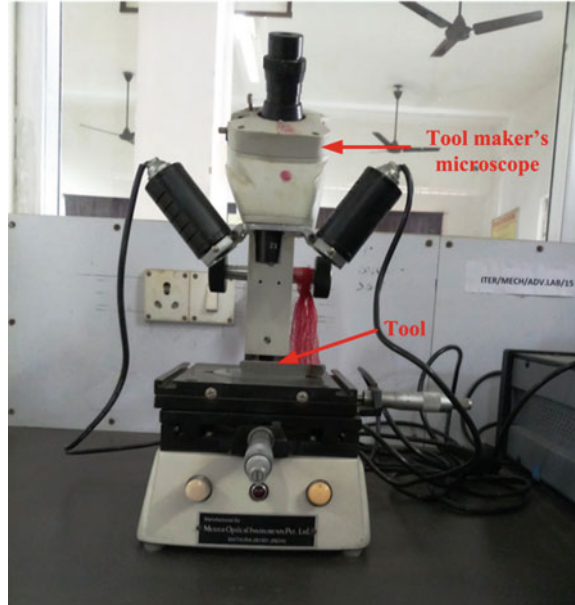


**Fig. 3** Cutting velocity versus flank wear at different cutting environments

temperature at the cutting zone due to the absence of coolants [7]. The continuous flow of coolants reduces the cutting zone temperature, thus, preventing the wear rate [7]. In addition to that as the coolant is supplied over the rake surface, breaking of the continuous chip encountered further reducing the intensity of VB. It is known that the chip carries away the maximum percentage of heat. The flow of continuous chip over the rake surface increases the cutting zone temperature deteriorating the tool properties resulting in higher tool wear as noticed for dry cutting conditions.

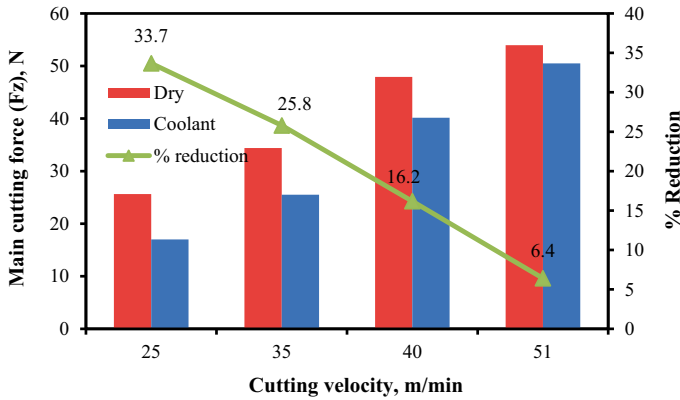


Fig. 4 Cutting velocity versus main cutting force at the different cutting environment

### 3.2 Cutting Force

Figure 4 represents the averaged main cutting force ( $F_z$ ) for both dry and machining with coolant cutting conditions at different cutting velocities. It is observed that an increase in cutting velocity continuously raises the  $F_z$  value for both with and without coolant cutting conditions from 25 to 51 m/min. However, when coolant is supplied, the  $F_z$  value is observed lower than that of dry cutting condition. This is because dry cutting increases the friction and temperature due to the absence of cooling and lubrication [6]. It is known that flank wear and crater wear have a profound impact on cutting forces [8]. An increase in flank wear changes the tool geometry altering the  $F_z$  values as observed in Fig. 4. During dry cutting, when the cutting velocity increases, a rise in cutting zone temperature is encountered. The increased cutting zone temperature softens the workpiece material and the cutting force required to cut a unit volume of material decreases [9]. With the increase in cutting velocity, mechanical wear dominates the workpiece softening, thus, raising the cutting force. At 51 m/min, the  $F_z$  value observed is very close for both dry and coolant conditions. This indicates cooling does not show any significant impact at higher cutting velocities.

### 3.3 Surface Roughness

Figure 5 represents the machined workpiece surface roughness for both dry and machining with coolant cutting conditions after 30 min of cutting operations. When cutting velocity increased, a decrease in  $R_a$  value is encountered for both conditions, and also a very interesting observation is noticed that the percentage of variation of surface roughness at dry machining and machining with coolant increases from 25 to

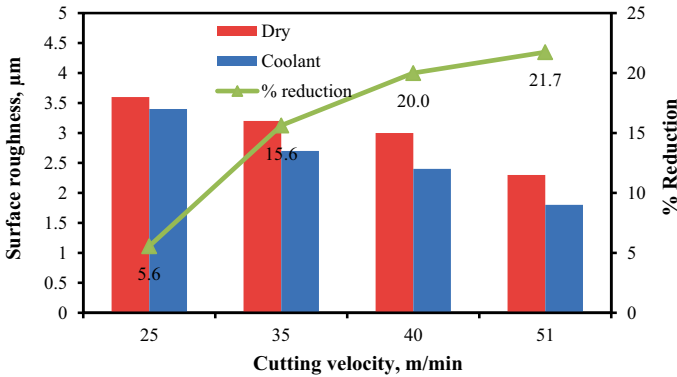


**Fig. 5** Cutting velocity versus surface roughness at the different cutting environment

51 m/min. This could be due to a decrease in the chip tool contact length with the rise in cutting velocity [10], thus, concentrating the heat towards the tool tip. This softens the workpiece and reduces the Ra value. In addition to this, an increase in cutting speed reduces the tensile stress acting on the tool and workpiece, thus, increasing the product surface quality [11]. Application of coolants on the cutting zone reduces the cutting zone temperature, thus, improving the surface finish of the workpiece. The direct contact of coolants at tool-chip and tool-workpiece interfaces helps in reducing the surface roughness compared to dry cutting [7]. The flow of coolant helps in chip breaking, thus, reduces the chances of the flow of chip over the rake surface for a longer time. According to Gajrani et al. [6], reducing chip tool contact length and adhesion of work material on tool surface helps in reducing the surface roughness.

## 4 Conclusion

Turning of mild steel workpiece under both coolant application and dry cutting environments were examined. A centrifugal cast single point cutting tool was used for the purpose. The comparison was made on the basis of tool flank wear, main cutting force, and workpiece surface roughness after 30 min of cutting operation. The following conclusions were drawn:

1. Under both the cutting conditions, the flank wear was seemed to rise with a rise in cutting velocity. However, when a coolant was used, the temperature of the cutting zone was also reduced with a concurrent reduction in the tool flank wear, compared to the dry cutting.
2. The percentage reduction of main cutting force for coolant cutting environment is highest at low cutting speed and gradually decreases with increasing cutting speed than that of dry cutting environment.

3. Surface roughness decreased with the use of coolant as compared with the situation under dry cutting conditions.

## References

1. Dhar NR, Islam MW, Islam S, Mithu MAH (2006) The influence of minimum quantity of lubrication (MQL) on cutting temperature, chip and dimensional accuracy in turning AISI-1040 steel. *J Mater Process Technol* 171:93–99
2. Dhar N, Kamruzzaman M (2007) Cutting temperature, tool wear, surface roughness and dimensional deviation in turning AISI-4037 steel under cryogenic condition. *Int J Mach Tools Manuf* 47:754–759
3. Attanasio A, Gelfi M, Giardini C, Remino C (2006) Minimal quantity lubrication in turning: effect on tool wear. *Wear* 260:333–338
4. Sarıkaya M, Güllü A (2014) Taguchi design and response surface methodology based analysis of machining parameters in CNC turning under MQL. *J Clean Prod* 65:604–616
5. Khan MA, Mia M, Dhar NR (2017) High-pressure coolant on flank and rake surfaces of tool in turning of Ti-6Al-4V: investigations on forces, temperature, and chips. *Int J Adv Manuf Technol* 90:1977–1991. <https://doi.org/10.1007/s00170-016-9511-6>
6. Gajrani KK, Suvin PS, Kailas SV, Sankar MR (2019) Hard machining performance of indigenously developed green cutting fluid using flood cooling and minimum quantity cutting fluid. *J Clean Prod* 206:108–123. <https://doi.org/10.1016/j.jclepro.2018.09.178>
7. Khanna N, Shah P, Chetan (2020) Comparative analysis of dry, flood, MQL and cryogenic CO<sub>2</sub> techniques during the machining of 15-5-PH SS alloy. *Tribol Int* 146:106196
8. Wang J, Huang CZ, Song WG (2003) The effect of tool flank wear on the orthogonal cutting process and its practical implications. *J Mater Process Technol* 142:338–346
9. Bai Y, Chaudhari A, Wang H (2020) Investigation on the microstructure and machinability of ASTM A131 steel manufactured by directed energy deposition. *J Mater Process Technol* 276:116410
10. Kıvak T, Sarıkaya M, Yıldırım ÇV, Şirin Ş (2020) Study on turning performance of PVD TiN coated Al<sub>2</sub>O<sub>3</sub>+TiCN ceramic tool under cutting fluid reinforced by nano-sized solid particles. *J Manuf Process* 56:522–539
11. Navas VG, Gonzalo O, Bengoetxea I (2012) Effect of cutting parameters in the surface residual stresses generated by turning in AISI 4340 steel. *Int J Mach Tools Manuf* 61:48–57



# Study and Analysis of Thermal Barrier Application of Lanthanum Oxide Coated SS-304 Steel



Sangita Sarangi, Santanu Mohapatra, and Ajit Kumar Mishra

**Abstract** For studying the thermal barrier application of the coated lanthanum oxide ( $\text{La}_2\text{O}_3$ ) on AISI SS-304, an experimental analysis was done. Plasma Arc Spray, a thermal spray process was used for coating of  $\text{La}_2\text{O}_3$  powder on SS-304 plate of 6 mm thickness in inert gas like argon environment by means of cross weaving technique. Due to properties like high melting point, low thermal conductivity and superior corrosion resistance  $\text{La}_2\text{O}_3$  can be used for temperature barrier applications. X-Ray Diffraction instrument was used to investigate the phase, SEM and Optical microscope was used to study the microstructure of the deposited metal. Both coated and uncoated sides of steel plate were subjected to heat. Infrared thermograph technique was used to measure the temperature of both coated and uncoated sides of steel plate. An effective decrease in temperature and heat was observed on  $\text{La}_2\text{O}_3$  coated side of AISI SS-304 plate.

**Keywords** Plasma spraying · Rare earth · Lanthanum oxide · Infrared thermograph technique · Thermal barrier

## 1 Introduction

Inorganic compound like lanthanum oxide ( $\text{La}_2\text{O}_3$ ) is the combination of oxygen and rare earth element lanthanum which is abundantly found in earth's crust. It is white in color, odorless, hexagonal in structure and solid form, thermally stable and insoluble in water. From different kinds of lanthanide due to the extraordinary properties  $\text{La}_2\text{O}_3$  has been widely used for experimental purpose [1, 2]. The study of details of thermodynamic behavior of  $\text{La}_2\text{O}_3$ – $\text{Y}_2\text{O}_3$  system was studied by Chen et al. [3]. Wang et al. studied the effect of  $\text{La}_2\text{O}_3$  on wear behavior of laser cladded iron-alloy coating on rail wheel and other rail accessories under lubricating condition [4]. The characteristic study of thin films of  $\text{La}_2\text{O}_3$  produced by spray pyrolysis method

---

S. Sarangi (✉) · S. Mohapatra · A. K. Mishra  
Department of Mechanical Engineering, Siksha 'O' Anusadhan Deemed to be University,  
Bhubaneswar 751030, India  
e-mail: [sangitasarangi@soa.ac.in](mailto:sangitasarangi@soa.ac.in)

has been done [5]. The consequence of annealed temperature on  $\text{La}_2\text{O}_3$  which was prepared by reflux method has been studied [6].

Zhang et al. [7] analyzed that the higher temperature requirement for drying the sol-gel coating caused in the formation of crack and thus reduced thermal barrier application of the coating. Addition of rare earth elements like lanthanum with the sol-gel coating improved the quality of the coating by minimizing the above problems. Liu et al. studied the morphology of thermal barrier coating (TBC) of YSZ with the addition of  $\text{La}_2\text{O}_3$  produced by plasma spraying and concluded that  $\text{La}_2\text{O}_3$  played a key role in reducing the grain growth in under higher temperature in TBC [8]. Xiaojie Guo et al. found that of lanthanum doped with YSZ (La-YSZ) TBC had better heat barrier capacity than simple YSZ TBC [9]. Plasma arc spray technique is one of the thermal spray technique used for coating purpose [10–13]. Wang et al. [14] developed lanthanum cerium oxide TBC by means plasma spray with higher segmentation and found that the previous coating had higher thermal resistance than the non-segmented one.

In this experiment,  $\text{La}_2\text{O}_3$  is used as coating material on steel substrate by means of plasma spray technique. Especially the suitability of  $\text{La}_2\text{O}_3$  for thermal barrier application was assessed.

## 2 Experimental Procedure

A sample size of dimension of 100 \* 60 \* 6 mm AISI SS-304 steel was considered for experimental purpose. Before coating of  $\text{La}_2\text{O}_3$  on steel substrate Nicraly (Ni-22 Cr-10 Alloy) in powder form was applied as bond coat between the top layer of coating of  $\text{La}_2\text{O}_3$  and the steel sample. Both Nicraly and  $\text{La}_2\text{O}_3$  powder were deposited on the sample through weaving process by means of Plasma Transferred Arc spray. In each pass around 30 micron of coating powder was sprayed on the substrate. Thickness of 120 micron of Nicraly was used as bond coat and 210 micron of thickness of  $\text{La}_2\text{O}_3$  powder was used as top layer of coating for conducting the experiment. For evaluation of microstructure and phase analysis two  $\text{La}_2\text{O}_3$  coated test samples of dimension of 10 \* 8 mm were considered. Optical microscope with SEM accompanied by proper application software was used to study the microstructure and X-Ray diffraction analysis was used to study the crystallinity and phase of the outer layer of coating. After coating the steel sample, heat was applied on both the uncoated and coated surface. Infrared thermo vision camera was used to measure the increment in temperature and to analyze the absorption of heat by the surface coated with  $\text{La}_2\text{O}_3$ .

### 3 Results and Discussion

#### 3.1 Microstructure Characterization

From the SEM image in Fig. 1, it is seen that the particles of  $\text{La}_2\text{O}_3$  powder are not of regular shape and size due to its preparation by calcinations process. It is observed the particle size of  $\text{La}_2\text{O}_3$  powder varies between 1 and 5  $\mu\text{m}$ .

The microphotograph of both the bond coated layer and top coated layer thickness is analyzed by optical microscope as shown in Fig. 2. The first layer is the steel substrate; second layer is the Nicraly which has been acting as bond coated material

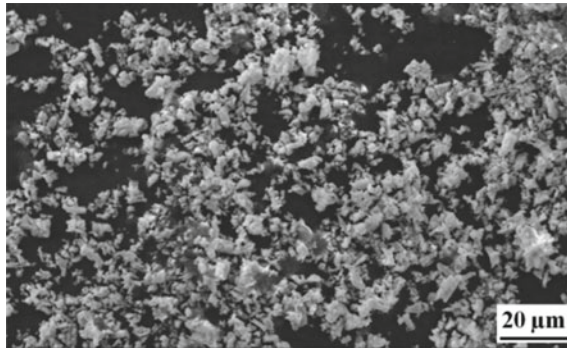


Fig. 1 SEM microstructure of  $\text{La}_2\text{O}_3$  powder

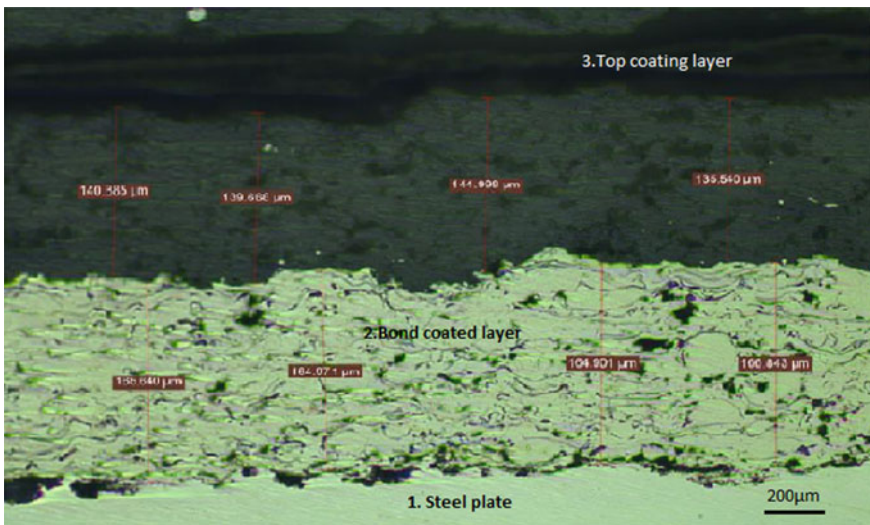


Fig. 2 Microphotograph of the coating thickness on the steel plate by optical microscope

between the steel plate and  $\text{La}_2\text{O}_3$ . Third layer of coating is of  $\text{La}_2\text{O}_3$ . Both Nicraly and  $\text{La}_2\text{O}_3$  powder are deposited by plasma transferred arc spray.

The variation in thickness between bond coated material and outer layer coating material ranges between 1.16 and 6.52%. From the above observation it is found that the bond coat material Nicraly as well as outer layer coating material  $\text{La}_2\text{O}_3$  powder are uniformly bonded with the steel sample.

### 3.2 Phase Structure Identification

In order to identify the phase and crystal structure of  $\text{La}_2\text{O}_3$  powder coating, the XRD analysis was performed on the top surface of the steel plate. The respective diffraction pattern is shown in Fig. 3. As can be seen the structure of  $\text{La}_2\text{O}_3$  is hexagonal type. Along the plane (1 0 1) maximum peak of  $\text{La}_2\text{O}_3$  occurred, and also at different planes different peaks are observed which shows the polycrystalline nature of  $\text{La}_2\text{O}_3$ .

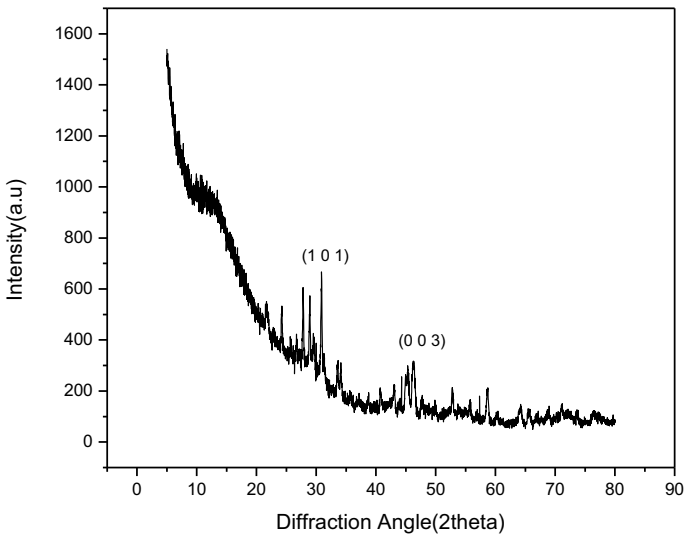


**Fig. 3** XRD pattern of lanthanum oxide coated on SS-304

**Table 1** Temperature reduction through  $\text{La}_2\text{O}_3$  coated surface

Serial no	Center point temperature	Temperature	Percentage reduction
1	353.3	406.5	13.08
2	385.97	428	9.82
3	513.7	529.8	3.03
4	630.7	642.2	1.7

### 3.3 Measurement of Heat Reduction and Thermal Barrier Application

Infrared thermograph technique was used to measure the reduction in heat on the  $\text{La}_2\text{O}_3$  coated side of steel plate and the range of temperature varies between  $-20$  and  $645$  °C. The ambient temperature was  $20$  °C.

Table 1 shows the reduction in temperature due to  $\text{La}_2\text{O}_3$  coating. When temperatures applied on uncoated side of the steel plate were  $406.5$ ,  $529.8$  and  $642.2$  °C, the center point temperature obtained on the coated side were  $353.3$ ,  $513.7$  and  $630.7$  °C respectively which was shown in Fig. 4a, b and c. Similarly when temperature  $428$  °C

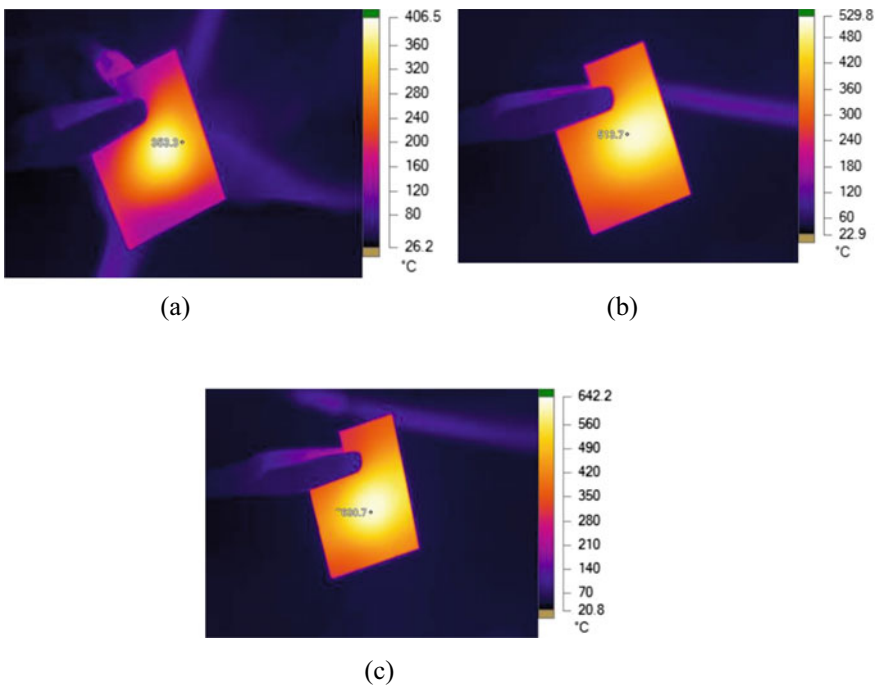


**Fig. 4** a First measurement heat by Infrared-thermography, b Second measurement heat by Infrared-thermography, c Third measurement heat by Infrared-thermography

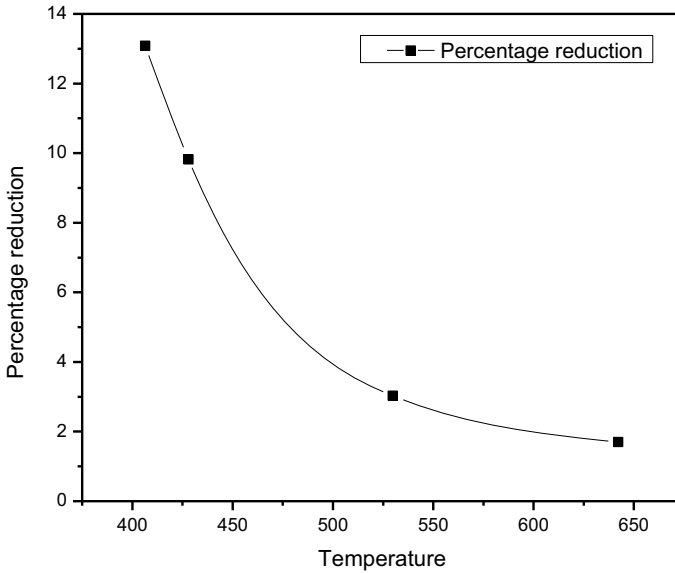


**Fig. 5** Percentage reduction in heat-temperature curve due to  $\text{La}_2\text{O}_3$  coating

had been applied on uncoated plate, the temperature obtained on the coated surface was  $385.97\text{ }^\circ\text{C}$ . So we found there were the reduction in percentage of temperature of 13.08, 3.03, 1.7 and 9.82 respectively. This is plotted in graphical form in Fig. 5. With increase in temperature there is gradual decrease in percentage reduction in heat. So  $\text{La}_2\text{O}_3$  coating can be used for thermal barrier application.

## 4 Conclusion

Application of  $\text{La}_2\text{O}_3$  powder as a coating material deposited on AISI 304 steel by means of plasma spray deposition for thermal barrier was investigated. Assessment of physical properties of the coated material, and the soundness of the coating was analyzed using optical microscope. Morphology of coated product was seen by using SEM and was obtained between 1 and  $5\text{ }\mu\text{m}$ . XRD analysis was done to know the crystal structure of the  $\text{La}_2\text{O}_3$  powder. Lanthanum Oxide is effective in reduction of surface temperature and can be utilized as a heat shield application. This material is very useful at lower temperature range. Though it can also be utilized as a heat shield for higher temperature up to  $700\text{ }^\circ\text{C}$ . Nevertheless it should be used to attenuate the surface temperature effectively up to  $500\text{ }^\circ\text{C}$  of operation.

## References

1. Lai BK, Johnson AC, Xiong H, Ramanathan S (2009) Ultra-thin nanocrystalline lanthanum strontium cobalt ferrite ( $\text{La}_{0.6}\text{Sr}_{0.4}\text{Co}_{0.8}\text{Fe}_{0.2}\text{O}_{3-\delta}$ ) films synthesis by RF-sputtering and temperature-dependent conductivity studies. *J Power Sources* 186(1):115–122
2. Sun J, Qiu XP, Wu F, Zhu WT (2005) H<sub>2</sub> from steam reforming of ethanol at low temperature over Ni/Y<sub>2</sub>O<sub>3</sub>, Ni/La<sub>2</sub>O<sub>3</sub> and Ni/Al<sub>2</sub>O<sub>3</sub> catalysts for fuel-cell application. *Int J Hydrogen Energy* 30(4):437–445
3. Chen M, Hallstedt B, Gauckler LJ (2005) CALPHAD modeling of the La<sub>2</sub>O<sub>3</sub>–Y<sub>2</sub>O<sub>3</sub> system. *Calphad* 29(2):103–113
4. Wang WJ, Fu ZK, Cao X, Guo J, Liu QY, Zhu MH (2016) The role of lanthanum oxide on wear and contact fatigue damage resistance of laser cladding Fe-based alloy coating under oil lubrication condition. *Tribol Int* 94:470–478
5. Kale SS, Jadhav KR, Patil PS, Gujar TP, Lokhande CD (2005) Characterizations of spray-deposited lanthanum oxide (La<sub>2</sub>O<sub>3</sub>) thin films. *Mater Lett* 59(24–25):3007–3009
6. Karthikeyan S, Selvapandian M Effect of annealing temperature on the properties of lanthanum oxide (La<sub>2</sub>O<sub>3</sub>) nanoplates by reflux routes. *Int J Eng Sci Res Technol*
7. Zhang SH, Kong G, Lu JT, Che CS, Liu LY (2014) Growth behavior of lanthanum conversion coating on hot-dip galvanized steel. *Surf Coat Technol* 259:654–659
8. Liu Y, Gao YF, Tao SY, Zhou XM, Li WD, Luo HJ, Ding CX (2008) Microstructure of plasma sprayed La<sub>2</sub>O<sub>3</sub>-modified YSZ coatings. *J Therm Spray Technol* 17(5):603–607
9. Guo X, Lin C, Zhang J, Liu Z, Jiang C, Zheng W, Zeng Y (2019) Effect of La<sub>2</sub>O<sub>3</sub> on microstructure and thermal conductivity of La<sub>2</sub>O<sub>3</sub>-doped YSZ coatings. *Materials* 12(18):2966
10. Delbos C, Fazilleau J, Rat V, Coudert JF, Fauchais P, Pateyron B (2006) Phenomena involved in suspension plasma spraying part 2: zirconia particle treatment and coating formation. *Plasma Chem Plasma Process* 26(4):393–414
11. Ananthapadmanabhan PV et al (2009) Plasma spheroidization and high temperature stability of lanthanum phosphate and its compatibility with molten uranium. *Mater Chem Phys* 113(1):417–421
12. Schlegel N, Ebert S, Mauer G, Vassen R (2015) Columnar-structured Mg-Al-spinel thermal barrier coatings (TBCs) by suspension plasma spraying (SPS). *J Therm Spray Technol* 24(1–2):144–151
13. Zhao Y, Wang L, Yang J, Li D, Zhong X, Zhao H, Shao F, Tao S (2015) Thermal aging behavior of axial suspension plasma-sprayed yttria-stabilized zirconia (YSZ) thermal barrier coatings. *J Therm Spray Technol* 24(3):338–347
14. Wang Y, Guo HB, Li ZY, Gong SK (2009) Segmented lanthanum cerium oxide thermal barrier coatings by atmospheric plasma spray. *Surf Eng* 25(7):555–558

# Effect of Casting Length on Solidification of Al-33 wt% Alloy in Twin-Roll Casting



Suvam Swayam Mohapatra and Seshadev Sahoo

**Abstract** Twin-roll casting is a combined process of casting and rolling to fabricate thin strips. It offers a little investment, and the casting parts are most probably refined microstructure, which attracts the interest of global casting industries. Therefore, it is necessary to study this process so that we can control the process. In the present study, steady-state modeling has been attempted for twin-roll strip casting with high casting speed by coupling the melt flow and solidification phenomena. With an increase in casting length, the cooling rate decreases, and solidified shell thickness increases as observed from the simulated results.

**Keywords** Twin-roll · Modeling · Solidification · Casting · Microstructure

## 1 Introduction

In today's world, the application of metal or alloy sheets has been grown up, and sheet metals can be found in airplane wings and fuselages, car bodies and medical tables, fan blades, etc. Since there is a vast application of metal or alloy sheet, every sheet manufacturing industry wants to make easier to produce sheet or strip from molten metal and wants to replace conventional operation procedures in their primary manufacturing processes. In the conventional sheet manufacturing process, quite an amount of time, energy, and capital are required to get a sheet from molten metal. So, in 1865, Sir Henry Bessemer made a breakthrough for sheet manufacturing industries; he invented the twin-roll casting process [1–3]. From this process, strips or sheets are directly produced from the melt by merging the casting and rolling process into a single step [4]. Mund et al. [5] did a simulation approach to observe that how solidification behavior gets affected by nozzle shape when twin-roll caster working at high speed. They observed that strips got prepared at nip position for circular shape nozzle, but for square, triangular, and elliptical shape, nozzle strip manufacturing

---

S. S. Mohapatra · S. Sahoo (✉)

Department of Mechanical Engineering, Institute of Technical Education and Research, Siksha O Anusandhan (Deemed to be University), Bhubaneswar, Odisha 751030, India  
e-mail: [seshadevsahoo@soa.ac.in](mailto:seshadevsahoo@soa.ac.in)



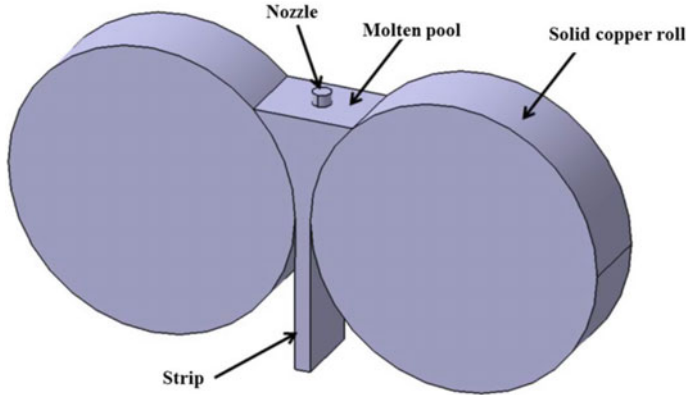


**Fig. 1** Schematic representation of twin-roll casting

was not accomplished at nip point. A simulation was done by coupling the turbulent flow and heat transfer in the wedge-shaped pool of a twin-roll strip casting process with a vertical slit entry and bifurcated slit entry nozzle-types were used [6]. Since rolls also have great significance in this casting, research has been done on rolls [7]. A two-dimensional numerical model was considered for thermal analysis of the roll in the strip casting process in which heat transfer and deformation analysis of the casting roll was coupled and to study the thermal stress and displacement [8]. The microstructure of the strip must be controlled because further, if we want to modify the microstructure of the strip, on which the mechanical property of the strip depends, it may not be possible. The microstructure relies on the rate at which it cools and solidification front speed at a different position in the strand which also depends on processing conditions. In the present research work, a steady-state model has been developed to study the influence of casting length on melt flow and solidification characteristics of Al-33 wt% Cu alloy in the twin-roll casting process. Figure 1 is the representation of the twin-roll caster.

## 2 Mathematical Model

By considering the process practically, the numerical simulation was carried out with the consideration of the following assumptions:

1. Thermo-properties will not change concerning time.
2. Molten metal is Newtonian and incompressible.
3. There is no relative velocity of the strip to roll.
4. The process is symmetric along the centerline.
5. Heat transfer coefficient is considered constant at the liquid–metal interface.

6. Shrinkage of the solidified shell at kiss point is extremely low.
7. Rolls are considered non-deformable.

A two-dimensional heat transfer equation was solved during the numerical simulation. Details of the mathematical model were given by Sahoo et al. [9, 10].

The continuity equation is

$$\frac{\partial u}{\partial x} + \frac{\partial v}{\partial y} = 0 \quad (1)$$

The momentum equation in the  $x$ -direction is

$$\frac{\partial p}{\partial x} + \frac{\partial(\rho uv)}{\partial x} = \frac{\partial}{\partial x} \left[ \mu \frac{\partial u}{\partial x} \right] + S_x \quad (2)$$

The momentum equation in the  $y$ -direction is

$$\frac{\partial p}{\partial y} + \frac{\partial(\rho uv)}{\partial y} = \frac{\partial}{\partial y} \left[ \mu \frac{\partial v}{\partial y} \right] + S_y \quad (3)$$

The energy equation is given by

$$\frac{\partial(\rho H)}{\partial t} + \nabla \cdot (\rho u H) = \nabla \cdot (K \nabla T) + S_h \quad (4)$$

where  $\rho$  is the density,  $H$  is the enthalpy, and  $S_h$  is the source term.

The model also considers the two-equation  $k$ - $\varepsilon$  model of turbulence which was given by Sahoo et al. [9, 10].

### Boundary conditions

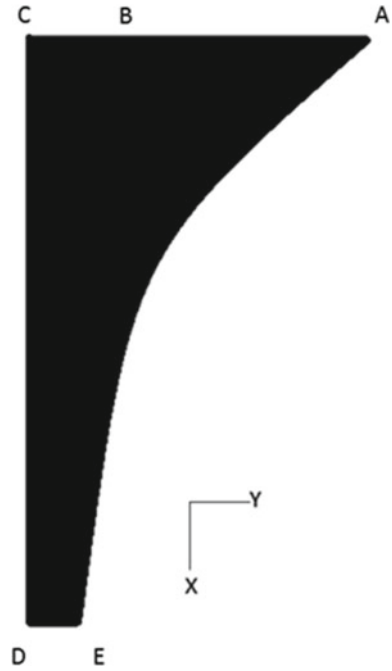
Figure 2 shows the computational domain used for numerical simulation.

- (i) At CB, the entry point of liquid metal,  $V_x = V_{in}$ ,  $V_y = 0$ ,  $k = 0.05(V_x^2 + V_y^2)$ ,  $\varepsilon = (C_\mu k^{1.5}/0.03) D_{in}$ ,  $T_{in} = 851$  K.
- (ii) At AB surface,  $\frac{\partial V_x}{\partial x} = \frac{\partial k}{\partial x} = \frac{\partial \varepsilon}{\partial x} = 0$ ,  $V_x = 0$ .
- (iii) At CD,  $\frac{\partial V_x}{\partial y} = \frac{\partial k}{\partial y} = \frac{\partial \varepsilon}{\partial y} = 0$ ,  $V_y = 0$ .
- (iv) At AE surface,  $V_x = V_{roll} \cos \theta$ ,  $V_y = V_{roll} \sin \theta$ , where  $V_{roll}$  is the speed at which roll is rotating, and  $\theta$  is the angular position of the node on the roll surface.
- (v) At DE,  $V_x = -V_{roll}$ ,  $V_y = 0$ .

## 3 Results and Discussions

In this research, numerical simulation of the casting of Al-33 wt% by varying casting length is carried out using ANSYS 19. A nozzle of 4 mm diameter is used to feed

**Fig. 2** Computational domain taken for model development



liquid metal, and liquid metal temperature is taken as 851 K. The casting parameters which are used for simulation are given in Table 1.

From the temperature profiles (Fig. 3), it is observed that the temperature decreases for the casting length which varies 0 and 5 mm below the nip point, but when the casting length increases more than 5 mm below the roll nip point, there is a slight increase in temperature. When metal is in contact with the roll surface, the heat transfer rate is high because of the cooling system which is present within both the rolls. The cooling system helps the molten metal to decrease its temperature and get solidify in shell form which will get merged and form a strip. But when metal crosses the nip point, there is no more contact with the roll surface. The solidified metal encountered the ambient air which has an extremely low heat transfer

**Table 1** Process parameters used for simulation

Parameters	Value
Roll diameter (m)	0.1524
Roll width (m)	0.0254
Speed at which casting is done (m/s)	0.7979
Liquid metal temperature (K)	851
Inlet diameter (m)	0.004
Casting length (mm)	0, 5, 10, 15

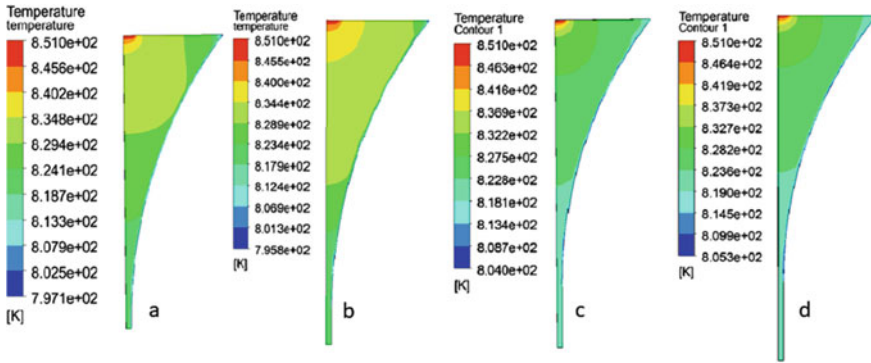


**Fig. 3** Temperature profile of the molten pool with varying casting length, **a** 0 mm, **b** 5 mm, **c** 10 mm, and **d** 15 mm

coefficient. Therefore, the heat transfer rate gets decreased, and some amount of heat accumulation within the shells. This will result in a slight increase in temperature.

From the simulation result (Fig. 4), it is observed that solidification does not occur at the nip point or just after the nip point. When the casting increases up to 5 mm, the shells are not merged to become a strip. Similarly, when casting length increases up to 10 and 15 mm after the nip point, it is found that shells are about to merge to form a strip. At a nip point, the thickness of the shell is 0.459 mm, and with an increase in casting length up to 15 mm, the thickness of the shell is 0.655 mm as seen in Fig. 5. The thickness of the shell is increasing because of the dissipation of the heat.

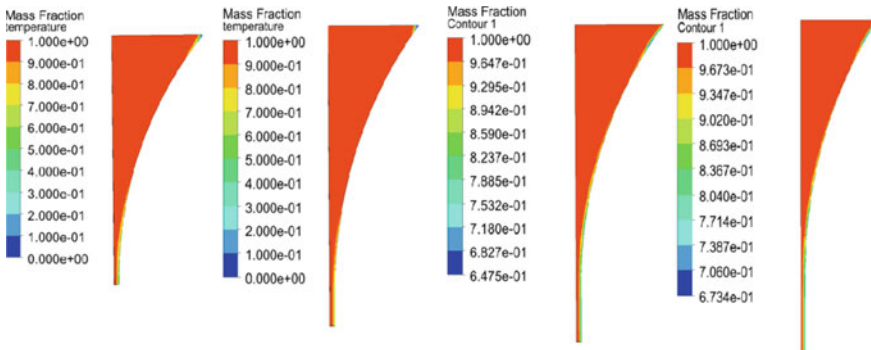
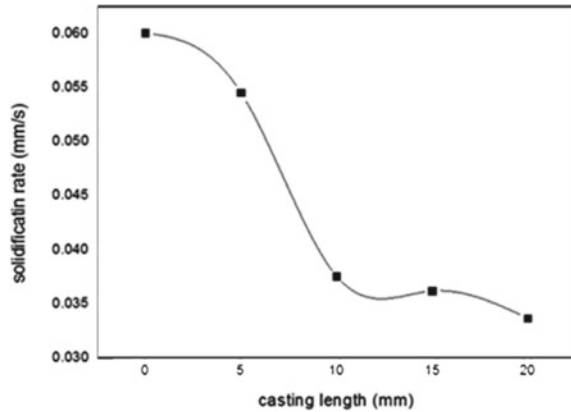


**Fig. 4** Solidification contour with varying casting length, **a** 0 mm, **b** 5 mm, **c** 10 mm, and **d** 15 mm

**Fig. 5** Change in solidification rate with casting length



## 4 Conclusions

Simulations were carried out using ANSYS 19 to investigate the solidification phenomena by changing casting length from 0 to 15 mm. From the analysis of the result, it is found that:

1. Solidified shells do not merge at the nip point or just after the nip point; instead of that, it merges much below the nip point; the shell thickness increases from 0.433 mm at the nip to 0.684 mm at 15 mm below the nip point.
2. With an increase in casting length, the temperature is slightly increased after the roll nip position due to the decrease in heat transfer rate.
3. The solidified shell thickness also decreases with an increase in casting length.

## References

1. Sahoo S (2016) Review on vertical twin-roll strip casting: a key technology for quality strips. *J Metall* 2016:1–13
2. Sahoo S, Kumar A, Dhindaw BK, Ghosh S (2012) Modeling and experimental validation of rapid cooling and solidification during high-speed twin-roll strip casting of Al-33 wt pct Cu. *Metall Mater Trans B* 43:915–924
3. Sahoo S, Ghosh S (2014) Heat transfer, solidification, and microstructure evolution in Al-33Cu alloy during the starting of twin-roll strip casting. *Steel Res Int* 85:207–218
4. Cook R, Grocock PG, Thomas PM, Edmonds DV, Hunt JD (1995) Development of the twin-roll casting processes. *J Mater Process Technol* 55:76–84
5. Mund C, Thatoi DN, Sahoo S (2017) Analysis of heat transfer and solidification characteristics in top side pouring high speed twin toll strip caster. *Heat Transf Res* 48:1693–1706
6. Santos CA, Spim JA Jr, Garcia A (2000) Modeling of solidification in twin-roll strip casting. *J Mater Process Technol* 102:33–39
7. Zhang XM, Jiang ZY, Yang LM, Liu XH, Wang GD, Tieu AK (2007) Modelling of coupling flow and temperature fields in molten pool during twin-roll strip casting process. *J Mater Process Technol* 187–188:339–343

8. Ren S, Fan J, Yu Y, Fang Y (2010) Physical and numerical simulation of flow and temperature in molten pool during strip casting process. *Mater Sci Forum* 654–656:1545–1548
9. Sahoo S (2015) Effect of process parameters on solidification of Al-33Cu strip in high speed twin roll strip casting-A numerical study. *IOP Conf Ser Mater Sci Eng* 75:1–9
10. Mund C, Thatoi DN, Sahoo S (2016) Effect of nozzle shape on solidification behaviour in high-speed twin-roll strip caster: a simulation approach. *Adv Mater Process Technol* 2:367–376

# Implementation of Industry 4.0 in Pharmaceutical Sector



Himanshu R. Mali, Praneet A. Chotalia, Shivangi Thakker,  
and Ajay K. Gangrade

**Abstract** Emerging technologies have brought a drastic change in the field of pharmaceutical development, as well as in manufacturing strategies. Pharma 4.0 is the revolution in the pharmaceutical sector dealing with automation and integration of the complete supply chain in an industry. Pharmaceutical manufacturing issues have the potential to cause significant influence on patient healthcare, as breaches in required quality can result in product recalls and patient injury. Moreover, product failures, facility, materials, or manufacturing issues are vital factors leading to disruptions in pharmaceutical supply chain. This research study makes an attempt to assess the barriers in implementation of Industry 4.0 in pharmaceutical industries using Interpretive Structural Modeling (ISM) and Analytic Hierarchy Process (AHP) methods. Solution for mitigating the barriers is proposed in the paper.

**Keywords** Pharma 4.0 · Interpretive structural modeling (ISM) · Analytic hierarchy process (AHP) · Industry 4.0

## 1 Introduction

Each industrial revolution has an objective to boost the productivity of the industry. The invention of steam power had increased productivity in the first industrial revolution. When electricity was employed to boost productivity, the second industrial revolution began. The third industrial revolution emerged when electronics and information technology were combined to boost production and efficiency [1]. Industry 4.0 is a new industrial field based on data collection and data exchange across the whole supply chain [2, 3]. On the other side, Industry 4.0 is a new means of integrating the digital and physical worlds. Industry 4.0, is defined as an “umbrella phrase for a new industrial paradigm” that includes the Internet of Things (IoT), Big Data, Cyber-physical Systems, and Robotics [4].

---

H. R. Mali (✉) · P. A. Chotalia · S. Thakker · A. K. Gangrade  
K J Somaiya College of Engineering, Somaiya Vidyavihar University, Mumbai, Maharashtra,  
India  
e-mail: [himanshu.mali@somaiya.edu](mailto:himanshu.mali@somaiya.edu)

## 2 Literature Review

Pharma 4.0 proposes a manufacturing system that aids businesses in adapting and iterating, integrating resources and personnel, delivering higher-quality goods with better patient outcomes. Pharma 4.0 adoption demands Technological engagement and proper allocation of resources to guarantee that necessary interconnections are formed and maintained, as well as to avoid any IT breakdowns that could result in costly production interruptions. Security issues are frequently identified as a road-block in fully accepting a new technology, so it is critical to guarantee that all databases are adequately secured. Pharmaceutical industries often use continuous process verification, which involves regularly assessing and testing all data generated during the manufacturing of a product against regulatory guidelines to ensure that it remains within the parameters established when the processes were validated [1]. The primary objective of the Pharma 4.0 movement is to make pharmaceutical operations more efficient and competitive. In the manufacturing process, emerging innovations are expected to improve efficiency and income while reducing human errors, physical pharma co-vigilance issues, and communication issues. A through literature survey was conducted for identification of barriers as per the methodology described in the next section.

## 3 Research Methodology

The objective of this study is to prioritize the challenges in implementation of Industry 4.0 in pharmaceutical industries. Initially, based on a comprehensive literature review, the barriers were identified. Integration of ISM and AHP MCDM methods was done to prioritize the barriers. ISM technique was used to show the interrelationship and construct the hierarchy among the nine challenges. AHP analysis was applied to prioritize the challenges based on the defined criteria aspects. This will help in deriving weights of each criteria aspect to get the final integrated diagram. Figure 1 shows the research methodology adopted for the paper.

## 4 Data Collection and Analysis

### 4.1 Data Collection

Through literature survey many barriers were identified out of which top 9 barriers were considered for study based on discussion with experts [5, 6]. These barriers and their description are given in Table 1.



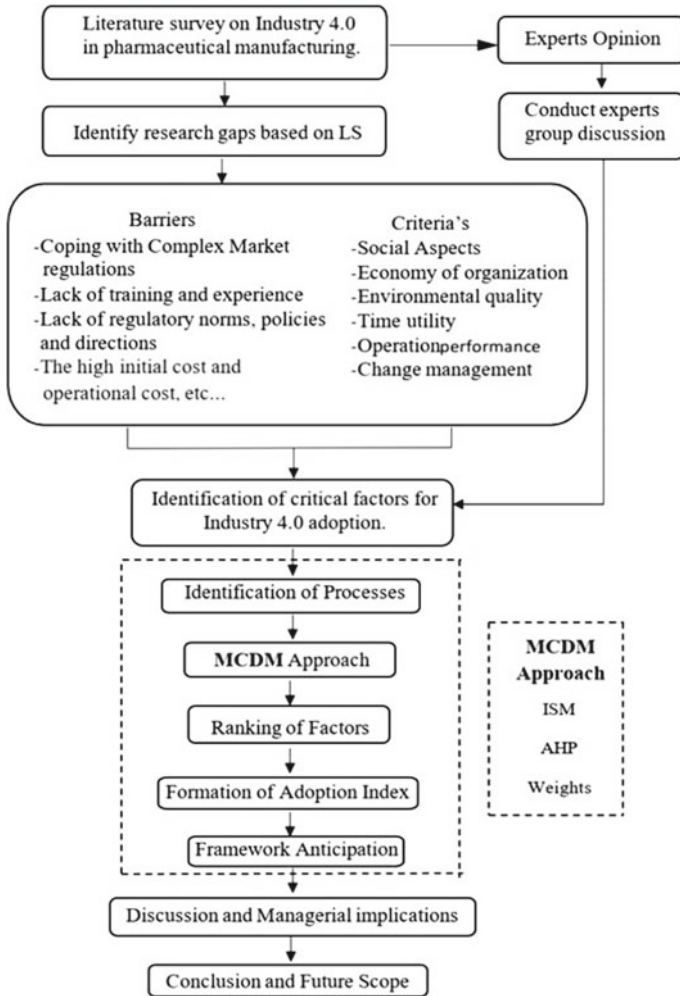


**Fig. 1** Research methodology flowchart

After collection of these barriers and criteria a matrix questionnaire was prepared for various aspects which are disrupted by these barriers. A Google form was initiated where the respondents working in pharmaceutical industries, market specialists and experts were asked to rate the impact of these barriers interlined to the different criteria's that were been analyzed through the literature review. Here barriers corresponding to their criteria were rated on a scale of 1–5 on basis of their impact. A total of 15 responses were collected. The total ratings of each disruption were found by adding the individual ratings given by each respondent. Profile of the respondents from various sectors is shown in Fig. 2.

**Table 1** Implementation barriers of Industry 4.0 in pharmaceutical sector

S. No.	Barriers [source]	Description
1	Coping with complex market regulations [1]	Implementation of new Industry 4.0 is generally by the Government and industry or labor bodies
2	Lack of training and experience [2, 3]	By implementing industry 4.0 there is a dynamic skill change requirement by the workforce. Industry requires thorough training for particular skill set
3	Lack of regulatory norms, policies and directions [2–4]	Implementation of Industry 4.0 leads to policy binding law of data protection and AI. Also, FDI norms are supposed to be adhered
4	The high initial cost and operational cost [1, 3, 7]	Industry 4.0 is heavily reliant on IoT networking technologies, and incorporating this heavy-duty system necessitates a significant investment in capital infrastructure
5	Lack of management support [1–3]	Management support for developing new like Industry 4.0 can hinder its implementation
6	Impact on population demography [2, 3, 7]	There could be disruptions caused in employment for this sector while implementing Industry 4.0
7	Lack of data management of smart product development [1, 2, 4, 8]	Infrastructure must be data leak compliant to insure safe data transfer or storage
8	Lack of IT technology for smart manufacturing [1, 3, 7, 9]	On hand industries which uses traditional methods could forfeit market due to lack of technology also others with low compatibility may be affected
9	Standardization of problem integration [2, 4, 10]	After implementation the consumer or the end user expectation should suffice. Hence for such issues standard frameworks needs to be established

## 4.2 Data Analysis

### A ISM

Interpretive Structural Modeling (ISM) is one of the popular strategies used for distinguishing relations shown by straightforward elements that identify an affair. ISM forms bits of knowledge to collect conclusions of the relations. This modeling starts with the recognition of all factors that are pertinent to a particular subject or affair [11].

The experts were asked to describe the contextual link between the challenges (*i* and *j*) and the way in which they will influence one another. The four symbols



**Table 3** Reachability matrix of barriers affecting implementation

Reachability matrix		F1	F2	F3	F4	F5	F6	F7	F8	F9	Driving power
	Factors										
1	Coping with complex market regulation	1	1	1	0	1	0	0	0	1	5
2	Lack of training and experience	0	1	0	0	0	0	0	1	0	2
3	Lack of regulatory norms, policies and directions	0	1	1	0	0	0	1	1	1	5
4	The high initial cost and operational cost	1	1	0	1	1	1	1	1	0	7
5	Lack of management support	0	1	1	0	1	0	1	1	1	6
6	Impact on population demography	0	1	0	0	0	1	1	1	1	5
7	Lack of data management of smart product development	0	1	0	0	0	0	1	1	0	3
8	Lack of IT technology for smart manufacturing	0	0	0	0	0	0	0	1	0	1
9	Standardization of problem integration	0	0	0	0	0	0	1	1	1	3
	Dependence	F1	F2	F3	F4	F5	F6	F7	F8	F9	
		2	7	3	1	3	2	6	8	5	

- For the X,  $(i, j)$  and  $(j, i)$  entries are replaced with 1.
- For the O, the entries  $(i, j)$  and  $(j, i)$  are replaced with 0 (Table 3).

From the reachability matrix, reachability sets, as well as antecedent sets, are created for all the barriers. The reachability set comprises the factor itself as well as factors that influence it, whereas the antecedent set contains the factor as well as other factors that influence it. Every factor’s intersection set includes regular variables from the reachability set and also antecedent variables. On the condition that reachability and intersection sets are equal, a factor is placed at a high level. Table 4 shows the level partition, using which the digraph was generated as displayed in Fig. 3.

**Table 4** Reachability set of barriers affecting implementation

	Reachability set	Antecedent sets	Intersection set	Level
F1	1,2,3,5,9	1,4	1	2
F2	2,8	1,2,3,4,5,6,7	2	2
F3	2,3,7,8,9	1,3,5	3	4
F4	1,2,4,5,6,7,8	4	4	1
F5	2,3,5,7,8,9	1,2,5	5	3
F6	2,6,7,8,9	4,6	6	2
F7	2,7,8	2,3,4,5,6,9	7	3
F8	8	2,3,4,5,6,7,8,9	8	1
F9	7,8,9	1,3,5,6,9	9	4

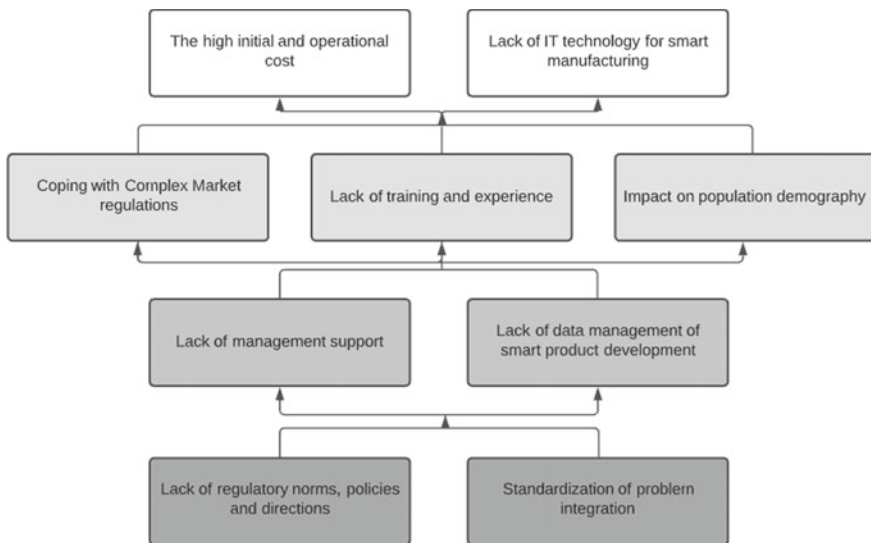


**Fig. 3** Digraph for the barriers in Industry 4.0

**B AHP**

In order to link the above ranking with the 6 criteria were analyzed using analytic hierarchy process. Weights of each criteria was normalized by following the procedure given below [7, 12].

15 experts were asked to rank each criteria on a scale of 1 to 5, with 1 signifying equal importance, 2 signifying moderate importance, 3 signifying strong, 4 signifying extremely strong, and 5 signifying extreme importance. For each of the ratings, a transpose reciprocal was taken on the other side of the diagonal. Then geometric mean was calculated for the sum of the ratings for each criterion, Table 5 shows the geometric mean of the criteria.

In order to get the criteria weights, each criterion is normalized pair wise by dividing each of the criteria with the sum total and added the same for every criterion and calculated its mean. The aspects then were ranked on basis of their weights as shown in Table 6.

**Table 5** Geometric mean of the criteria

	Criteria's	C1	C2	C3	C4	C5	C6
1	Social aspects	1	0.25	3	0.5	1	0.25
2	Economy of organization	4	1	5	2	3	1
3	Environmental quality	0.33	0.2	1	0.25	0.33	0.2
4	Time utility	2	0.50	4	1	1	0.33
5	Operation performance	1	0.33	3	1	1	0.33
6	Change management	4	1	5	3	3	1
	Sum	12.33	3.28	21.00	7.75	9.33	3.12

**Table 6** Weights of the criteria by AHP

Normalized pair wise matrix								
	Criteria	C1	C2	C3	C4	C5	C6	Criteria weights
6	Change management	0.3244	0.305	0.238	0.387	0.3215	0.3205	1.8965
2	Economy of organization	0.3244	0.305	0.238	0.258	0.3215	0.3205	1.7675
4	Time utility	0.1622	0.15	0.1904	0.129	0.1072	0.11	0.8469
5	Operation performance	0.0811	0.10	0.1428	0.129	0.1072	0.11	0.6701
1	Social aspects	0.0811	0.08	0.1428	0.065	0.1072	0.0801	0.5519
3	Environmental quality	0.03	0.0609	0.0476	0.032	0.04	0.0641	0.2668

From Table 6, we can depict that Change management has the most weight hence from digraph the most weight ranking for Change management it will have the highest impact on all the above-listed challenges and on contrast, it is least for environmental quality hence, this criteria will have the least impact on all the above-listed challenges.

## 5 Result

Nine barriers have been identified and analyzed which have caused hindrance in the implementation of Industry 4.0 in the pharmaceutical sector. Based on the level partitions obtained using the ISM modeling a digraph has been developed which has 4 levels representing the corresponding factors. The factors affecting the most (i.e., Level 1) are at listed at the top and the least (i.e., Level 4) at the bottom. To get the better of the above digraph 3 different channel outcomes are created from which we can resolve the above barriers listed as:

1. **Technology outcome:** Under Industry 4.0, technology is still at a critical stage. Cloud computing, machine learning, as well as the Internet of Things (IoT), are among the new digital technologies that are transforming the industrial landscape here. This helps us to suffice the above-listed barriers [8] Lack of IT technology for smart manufacturing and [13] Lack of data management in smart product development for businesses to achieve their Industry 4.0 goals, will need a high level of automation to overcome [4] the high initial cost and operational cost by increasing the ROI, pervasive connection for [1] Coping with Complex Market regulations, and the intelligent systems to overcome the above barriers.
2. **Process outcome:** The concept of process improvements has enlarged under Industry 4.0 to involve the integration of processes all-around a company's operations sufficing barrier [7] Lack of management support and [3] Lack of regulatory norms, policies, and directions, Supply Chain, and Product Lifecycle which is a specialization in terms to reduce the batches of products made with the same primary source. Hence from the ISM, the highest impacted barrier is resolved by knowing the product lifecycle well.
3. **Organization outcome:** Organization is Industry 4.0's third building element, companies have to change their organizational structures as well as processes to permit their staff to maintain with Industry 4.0 to be relevant in the face of increased competition. To make improvements, it must address Talent Readiness is a critical determinant for success will be the workforce's capacity to drive and implement Industry 4.0 activities resolving [2, 14] Lack of training and experience barriers and structure management will enable an organization to design and implement Industry 4.0 initiatives more successfully by making it more flexible, collaborative, and empowered.

## 6 Conclusion and Future Work

The implementation of Industry 4.0 for the pharmaceutical industry is influenced in numerous ways. ISM and AHP are integrated in this research for prioritizing the barriers. The ranking is useful for managers and practitioners in the pharmaceutical sector to develop the strategies for mitigating them. This paper also attempts to propose possible solutions for the identified disruptions. Change management was identified as the highest affected barrier which could be resolved by a strong organization structure.

The research is a roadmap for industries planning to implement Industry 4.0. Further research in this domain is possible by development of architecture for the pharmaceutical industry for implementing Industry 4.0. Nascent technologies like block chain and IoT may be explored for successful implementation of Industry 4.0 in pharma sector.

## References

1. Laínez JM, Schaefer E, Reklaitis GV (2019) Challenges and opportunities in enterprise-wide optimization in the pharmaceutical industry. Elsevier, pp 1359–6446
2. Masood T, Sonntag P (2020) Industry 4.0: adoption challenges and benefits for SMEs. Institute for Manufacturing, Department of Engineering, pp 0166–3615
3. Kumar R, Singh RK, Dwivedi YK (2020) Application of Industry 4.0 technologies in SMEs for ethical and sustainable operations: analysis of challenges. *J Cleaner Prod* 275:124063
4. Horvath D, Szabo R (2019) Driving forces and barriers of Industry 4.0. *Forecast Soc Change* 146:119–132. <https://doi.org/10.1016/j.techfore.2019.05.021>
5. Reinhardt IC, Oliveira J, Ring D (2020) Current perspectives on the development of Industry 4.0 in the pharmaceutical sector. *J Ind Inf Integr* 18:100131. <https://doi.org/10.1016/j.jii.2020.100131>
6. Kulkarni K, Bhattacharjee R, Narwane V (2020) Barriers to Industry 4.0 adoption: Indian scenario. *SSRN Electron J* <https://doi.org/10.2139/ssrn.3536802>
7. Zhou K, Liu T, Zhou L (2015) Industry 4.0: towards future industrial opportunities and challenges. In: 12th International conference on fuzzy systems and knowledge discovery (FSKD), pp 2147–2152
8. Masood T, Sonntag P (2020) Industry 4.0: adoption challenges and benefits for SMEs. *Comput Ind.* 121:103261. <https://doi.org/10.1016/j.compind.2020.103261>
9. Frank A, Dalenogare L, Ayala N (2019) Industry 4.0 technologies: implementation patterns in manufacturing companies. *Int J Prod Econ* 210. <https://doi.org/10.1016/j.ijpe.2019.01.004>
10. Stentoft J, Wickstrøm K, Philipsen K, Haug A (2020) Drivers and barriers for Industry 4.0 readiness and practice: empirical evidence from small and medium-sized manufacturers. *Prod Plann Control* 32:1–18. <https://doi.org/10.1080/09537287.2020.1768318>
11. Tripathy S, Sahu S, Ray PK (2013) Interpretive structural modelling for critical success factors of R& D performance in Indian manufacturing firms. *J Model Manag* 8(2):2140
12. Ghosh A, Mal P, Majumdar A (2019) Analytic hierarchy process. <https://doi.org/10.1201/9780429504419-2>
13. Machadoa CG, Winrotha M, Carlssonb D, Almströma P, Centerholtb V, Hallin M (2019) Industry 4.0 readiness in manufacturing companies: challenges and enablers towards increased digitalization. *Procedia CIRP* 81:1113–1118



14. Müller J (2019) Assessing the barriers to Industry 4.0 implementation from a workers' perspective. IFAC Proc 51–52. <https://doi.org/10.1016/j.ifacol.2019.11.530>
15. Arden N, Fisher A, Tyner K, Yu L, Lee S, Kopcha M (2021) Industry 4.0 for pharmaceutical manufacturing: preparing for the smart factories of the future. Int J Pharm. 602:120554. <https://doi.org/10.1016/j.ijpharm.2021.120554>

# Machining of Austenitic Stainless Steel Under Various Cooling-Lubrication Strategies



Smita Padhan, Ajay Kumar Behera, and Sudhansu Ranjan Das

**Abstract** This work highlights the performance analysis of four distinct cooling-lubrication techniques (dry, flood, minimum quantity lubricant MQL and compressed-air) in turning Nitronic 60 by using new generation SiAlON ceramic inserts. Several machinability parameters such as cutting force, cutting temperature, cutting tool wear, surface finish and cost estimation were analyzed for machining performance evaluation. It was observed that machining under MQL condition exhibit beneficial effects as compared to other three pre cited cooling and lubrication condition as the cutting fluid is applied in spray jet form to the cutting zone. Result shows that the tool life in machining under MQL are 138, 72 and 11% greater than dry, compressed air, flooded condition, respectively. The use of SiAlON ceramic tool results in more economically feasible under MQL environment as the total machining cost per component is lower (Rs. 19.79) in comparison to dry (Rs. 26.81), compressed air (Rs. 23.4), flooded (Rs. 21.76) machining conditions.

**Keywords** Machinability · Cost analysis · Cutting environment · SiAlON ceramic · Nitronic 60

## 1 Introduction

In present day, nickel-based alloys are commonly employed for various industrial applications because of its unique properties like weldability, formability, capability to retain its strength and toughness at elevated temperature, excellent resistance to creep, thermal and corrosion. Because of its outstanding physical and chemical properties, the use of nickel-based alloy is not only bound to aerospace industry but it

---

S. Padhan · S. R. Das (✉)

Department of Production Engineering, Veer Surendra Sai University of Technology, Burla  
768018, India

e-mail: [das.sudhansu83@gmail.com](mailto:das.sudhansu83@gmail.com)

A. K. Behera

Department of Mechanical Engineering, Siksha 'O' Anusandhan University, Bhubaneswar  
751030, India

© The Author(s), under exclusive license to Springer Nature Singapore Pte Ltd. 2023

435

P. Pradhan et al. (eds.), *Recent Advances in Mechanical Engineering*,

Lecture Notes in Mechanical Engineering,

[https://doi.org/10.1007/978-981-16-9057-0\\_46](https://doi.org/10.1007/978-981-16-9057-0_46)

also extensively used in nuclear power plant, oil and gas power industries, architecture building and construction, transport, food processing equipment, in various consumer products and medical applications.

Despite various advanced methods, machining is still considered to be one of the commonly used processes as the manufacturer can easily achieve the desired structural and the functional features on the component. However, the manufacturing engineer faces big challenges to machine nickel-based alloys as very high temperature and stress are developed during machining resulting work hardening of workpiece which primarily impacts on the tool life and surface quality of machined component. If the selection of cutting parameters and their ranges is not chosen properly with reference to the selected tool and work material combination, then it can lead to the degradation of workpiece quality and failure of the cutting tool by exceeding its tolerance limits. Therefore, to minimize the above pre-cited issues the use of an effective C/L environment is very essential which will be valuable from technological, economic and ecological prospective. The use of cutting fluids in machining process by using different C/L strategies remarkably increase the efficiency of the cutting operation by minimizing friction, controlling heat generation at the machining zone, improving chip removal rate and preventing corrosion. The cutting fluids effectively extract heat from machining area by continuously flowing through the cutting zone. It can also provide lubrication effect by forming a thin layer of oil film on cutting interface depending upon adhesive and cohesive nature of cutting fluid. Many researchers have been worked on different C/L strategies [1–4] to enhance the cutting performance [5, 6] and machinability [7, 8] of different hard-to-cut and difficult-to-cut workpiece materials during turning operation (EN-24, EN-31,42CrMo4, 17CrNiMo6, Haynes-25, Ti6Al4V, Inconel 825, 800, 718, AISI 202, AISI 316, AISI 420, AISI 1015, AISI 4140, AISI 4340, AISI 1045, AISI 1060, AISI 52,100, AISI D2). Based on considering previous research contribution, the primary purpose of the present study is (i) to evaluate cutting efficiency of modern generation SiAlON ceramic insert, (ii) to explore a comparative investigation toward machinability enhancement by using different cooling lubrication methods (i.e. MQL, flooded, compressed air-cooled, and dry) and (iii) to evaluate the overall machining cost per part during turning under various C/L environments.

## 2 Experimental Setup and Procedure

To achieve the objectives, the experiments were conducted by turning a cylindrical bar of Nitronic 60 austenitic stainless steel (diameter: 50 mm, length: 500 mm) as work material. The turning experiments were conducted on an HMT made high accuracy robust lathe having maximal power rating of 11 kW and highest speed limited to 2050 rpm. The cutting tool applied in the experiments is a KYS30 grade new generation SiAlON ceramic insert manufactured by Kenametal in the form of SNMG 120,412. During the turning operation, the ceramic insert is rigidly clamped to an ISO standard toolholder having description of PSBNR2020K12. Principal cutting

force ( $F_c$ ) is measured with the 9257B piezoelectric dynamometer manufactured by Kistler. A roughness tester (model: Surftest SJ-210, manufactured by Mitutoyo) is used to measure the roughness value ( $R_a$ ) of machined component after each experimental run. A high-resolution digital imaging microscope (model: Axiotech 100HD-3D) manufactured by Carl Zeiss was employed to measure tool wears on rake as well as flank surface of the tool insert after completion of each experimental trial. FLUKE made  $Ti_3_2$  infrared thermal imaging camera was employed to monitor the cutting temperature at the interface of workpiece and cutting edge of tool. A JSM-6084LV model scanning electron microscope (make: JOEL) was used to perform microstructural analysis of machined surface and worn-out tool after the turning experiment. Figure 1 depicts the experimental setup and work methodology followed by the present machinability investigation. The output responses considered in this study are surface quality, tool wear on both flank and rake face of insert, principal cutting force and machining zone temperature. The details of all input cutting factors and cutting condition taken in this study were summarized in Table 1.

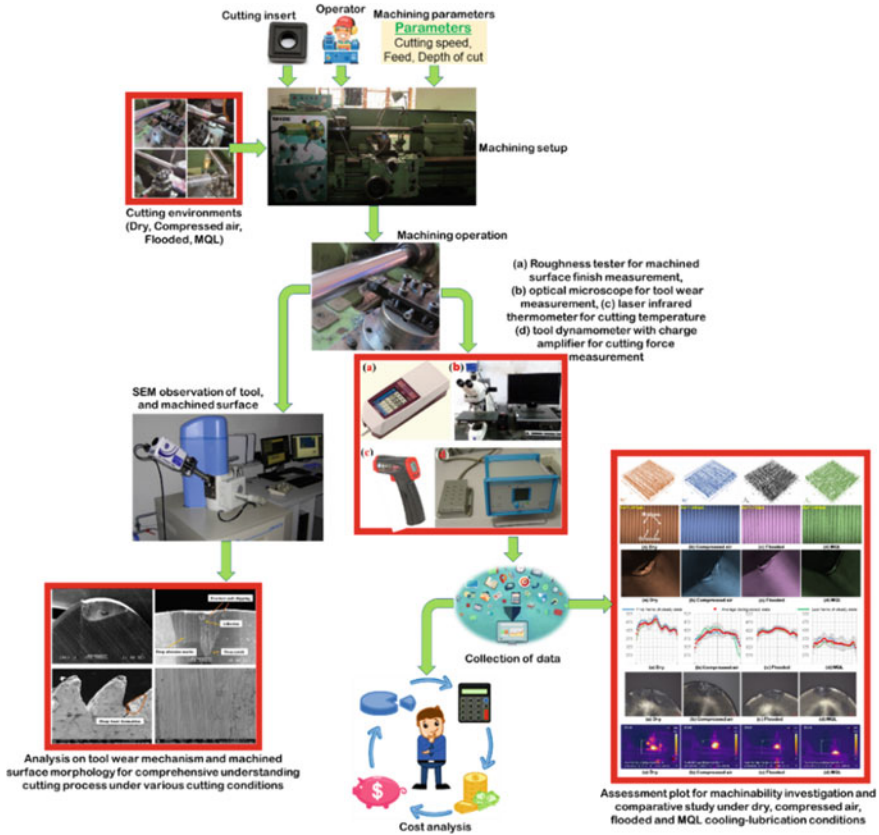


Fig. 1 Schematic representation of proposed methodology and experimental setup layout

**Table 1** Details of cutting process variable and their levels

Input parameters	Range
Axial feed (mm/rev)	0.12, 0.16, 0.20, 0.24
Machining speed (m/min)	51,67,87,111
Depth of cut (mm)	0.4
Cutting duration (s)	120
C/L strategy	MQL, flooded, compressed air-cooled, and dry

### 3 Discussion of Results

The optical images of crater wear under different machining environments (dry, compressed air, flooded, MQL) are shown in Fig. 2a. In dry as well as compressed air-cooled cutting conditions, due to the weak heat transfer capability of cooling medium, large amount of heat is generated at the interface of tool and workpiece, which is responsible for the development of thermal stress, which leads to the starting of cracking on rake face followed by edge chipping. However, due to the surplus availability of coolant at the cutting zone in flooded cooling condition, large amount of heat was taken out from the cutting zone, so it effectively minimizes the crater wear by reducing the generation of thermal stress on the tool rake surface. For MQL condition, as cutting fluid is applied in jet form to the cutting zone at high pressure, it effectively extracted heat from the cutting zone and resulting decrease in thermal stress build up in cutting tool. Thus, a very less chipping was observed on the tool insert in MQL condition compared to other C/L environment. Still some edge chipping was observed in MQL condition. Figure 2b shows flank wear on cutting insert in different C/L methods. Maximum flank wear was observed in dry cutting environment, whereas it was minimum in MQL cutting. Since, coolant is not applied in dry turning the heat generated during cutting is accumulated at cutting region causing rapid increase in cutting temperature. This high temperature promoted the formation of notch due to high thermal stress and adhesion of melted chip to the flank surface of the tool. Due to improper lubrication, chipping and abrasion type of wear are also seen on the flank face of cutting tool. However, in provision for MQL condition, due to its effective C/L capacity, slight edge chipping, negligible adhered material, compact notch, and very smooth abrasion marks were noticed, whereas compressed air-cooled condition gave better result in comparison to dry cutting condition. Figure 2c depicts IR thermography of cutting zone temperature in different cooling-lubrication methods using IR thermal imaging camera. Moreover, Fig. 2d shows the measurement signal images of the cutting temperature under the influence of various C/L environments. Maximum temperature was observed in dry cutting environment, whereas it was minimum in MQL condition. The use of coolant reduces the cutting temperature by providing highly effective heat extracting medium as well as lubrication. In addition, the reason of less heat generation in MQL condition is that, here the friction in between the tool-chip is decreased as the contact length

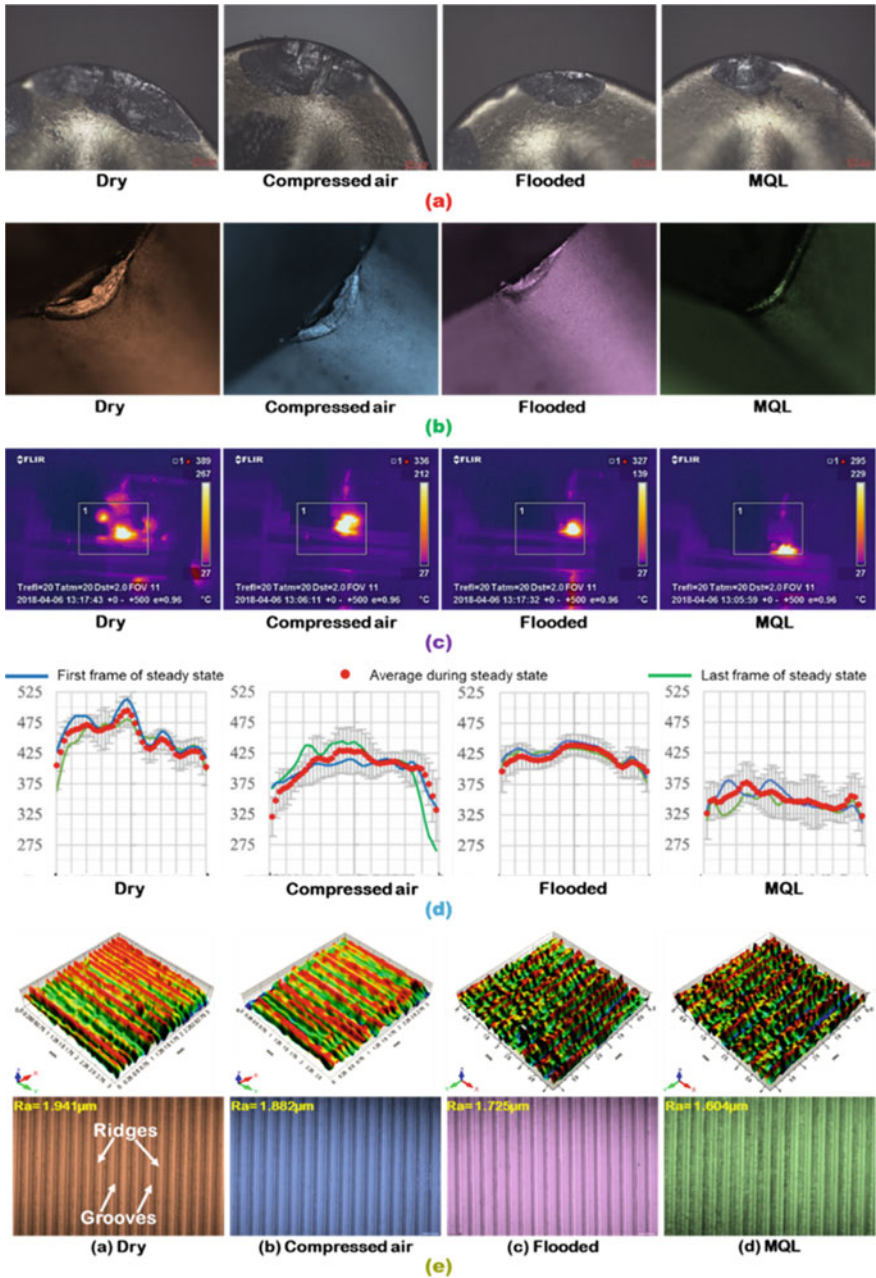


**Fig. 2** Machinability study under various turning environments at  $v = 111$  m/min,  $f = 0.24$  mm/rev,  $d = 0.4$  mm: **a** Crater wear, **b** Flank wear, **c** & **d** Cutting temperature, **e** Surface finish

between chip and tool is reduced. Figure 2e depicts the optical images and 3D images of machined surfaces in precited turning environments. Out of the four precited cutting conditions, the surface topography of machined surface (3D image profile) clearly reflects that turning with MQL presents a lower peak compared to other machining environments. Also, Fig. 2e shows reasonably low feed marks and feed mark area expansion to ridges under MQL. As the absence of cutting fluid in dry turning, high friction is generated at tool- work interface resulting wear at the cutting edge followed by increasing in cutting force. This increase in the principal cutting force consequently enhance the roughness value of the machined surface. In flooded condition, due to the presence of abundant cutting fluid which provide desired cooling and lubrication effect, which leads to reduction in cutting edge wear followed by improving surface quality. In case of MQL turning, as cutting fluid is supplied in spray form, due to aerosolization of cutting fluid effective cooling is obtained at the cutting zone. Thus, it subsequently protects the tool from the thermal stress and able to uphold the effectiveness of the cutting insert. In addition, cutting forces also increase comparatively less to other cooling methods.

By taking into consideration of control criterion of flank wear (i.e., VB till 0.3 mm), one more experiment was performed for each precited C/L condition by setting cutting speed and feed at their higher limit (i.e.,  $v = 111$  m/min and  $f = 0.24$  mm/rev) and doc at 0.4 mm for estimating tool life of SiAlON ceramic cutting insert. Effective cooling-lubrication capability by MQL technique results in improvement of tool life. Machining under above four precited C/L conditions experience the tool life of 34, 47, 73 and 81 min, respectively. These obtained results show that the tool life in turning in MQL are 138, 72 and 11% greater than dry, compressed air, flooded condition, respectively. To study the economic feasibility, Gilbert's approach was employed to estimate overall machining cost per component considering both direct and indirect cost associated with machining, as shown in Table 2. Results

**Table 2** Cost analysis in turning Nitronic 60 with SiAlON ceramic tool under various environments

Sl. no	Type of costs	Dry	Compressed air	Flooded	MQL
1	Machine and labor cost ( $\times$ ) per min	Rs. 5	Rs.5.17	Rs. 6	Rs. 5.42
2	Cutting cost per component ( $\times T_m$ )	Rs. 12.75	Rs. 13.18	Rs. 15.3	Rs. 13.82
3	Tool changing cost per component [ $\times T_d (T_m/T)$ ]	Rs. 1.87	Rs. 1.4	Rs. 1.05	Rs. 0.85
4	Cost of each tool	Rs. 650	Rs. 650	Rs. 650	Rs. 650
5	Average cost of each cutting tool edge ( $y$ )	Rs. 162.5	Rs. 162.5	Rs. 162.5	Rs. 162.5
6	Tooling cost per piece [ $y (T_m/T)$ ]	Rs. 12.19	Rs. 8.82	Rs. 5.68	Rs. 5.12
7	Overall cutting cost per piece, (2 + 3 + 6)	Rs. 26.81	Rs. 23.4	Rs. 21.76	Rs. 19.79

obtained from cost analysis reveals that the utilization of SiAlON ceramic tool is more economically feasible under MQL environment as the overall machining cost per component is lower (Rs. 19.79) as compared to dry (Rs. 26.81), compressed air (Rs. 23.4), flooded (Rs. 21.76) machining conditions. Thus, cost saving can be attained when using SiAlON ceramic tool in MQL condition.

## 4 Conclusions

Machining with MQL relatively performed well as compared to above three precited C/L condition and effectively removed heat and dewberries from the cutting zone and provided better cooling and lubrication effect. Implementation of MQL technique results in (i) minimizing cutting force by decreasing thermal stress. (ii) improve surface quality by providing better cooling and lubrication (iii) decrease cutting temperature by effectively removing heat from cutting zone and (iv) lower tool wear rate by decreasing thermal stress. During the investigation, the tool life of 81 min is recorded for MQL condition, whereas it was found to be 34, 47 and 73 in case of dry cutting, compressed air-cooled and flooded condition. Result shows that the tool life in machining under MQL are 138, 72 and 11% greater than dry, compressed air, flooded condition, respectively. The use of SiAlON ceramic tool results in more economically feasible under MQL environment as the total machining cost per component is lower (Rs. 19.79) in comparison to dry (Rs. 26.81), compressed air (Rs. 23.4), flooded (Rs. 21.76) machining conditions.

## References

1. Tamang SK, Chandrasekaran M, Sahoo AK (2018) Sustainable machining: an experimental investigation and optimization of machining Inconel 825 with dry and MQL approach. *J Braz Soc Mech Sci Eng* 40(8):1–13
2. Mia M, Gupta MK, Singh G, Królczyk G, Pimenov DY (2018) An approach to cleaner production for machining hardened steel using different cooling-lubrication conditions. *J Clean Prod* 187:1069–1081
3. Ukamanal M, Mishra PC, Sahoo AK (2020) Effects of spray cooling process parameters on machining performance AISI 316 steel: a novel experimental technique. *Exp Tech* 44(1):19–36
4. Gupta MK, Mia M, Pruncu CI, Kapłonek W, Nadolny K, Patra K, Sarikaya M, Sharma VS (2019) Parametric optimization and process capability analysis for machining of nickel-based superalloy. *Int J Adv Manuf Technol* 102(9–12):3995–4009
5. Mia M, Khan MA, Dhar NR (2017) Performance prediction of high-pressure coolant assisted turning of Ti-6Al-4V. *Int J Adv Manuf Technol* 90(5–8):1433–1445
6. Panday G, Ashraf MZI, Ibn Muneer K, Hossain KS, Ashik MFK, Kamruzzaman M (2018) Assessing near-dry lubrication (35 ml/h) performance in hard turning process of hardened (48 HRC) AISI 1060 carbon steel. *Int J Adv Manuf Technol* 99(5–8):2045–2057



7. Das A, Tirkey N, Patel SK, Das SR, Biswal BB (2019) A comparison of machinability in hard turning of EN-24 alloy steel under mist cooled and dry cutting environments with a coated cermet tool. *J Fail Anal Prev* 19(1):115–130
8. Panda A, Das SR, Dhupal D (2019) Machinability study of HSLA steel in hard turning with coated ceramic tool: assessment, modeling, optimization and economic aspect. *J Adv Manuf Syst* 18(4):625–655

# In Situ Synthesis of Cobalt Oxide and Carbon Nanocomposite



Rahul Kumar, Prasanta Kumar Sahoo, and Ankur Soam

**Abstract** The present work includes in situ synthesis of cobalt oxide and carbon nanocomposite by a solution-based approach. First, a slurry of sucrose and cobalt oxide nanoparticles in water was prepared, and then, it was dried in oven to obtain a dry powder. The powder sample was kept in tube furnace at high temperature in order to form carbon from sucrose and formation of nanocomposite of carbon and cobalt oxide. The composite was characterized by XRD to study the phase. Surface morphology of the synthesized nanocomposite was examined with scanning electron microscope. The results indicate that the cobalt oxide nanoparticles and sucrose derived carbon are distributed uniformly on the sample.

**Keywords** Cobalt oxide · Sucrose derived carbon · Nanocomposite · XRD

## 1 Introduction

Carbon and metal oxide-based nanocomposites have been considered as potential candidates for several application such as supercapacitor and battery systems [1–5]. Energy storage devices are becoming equally important as energy production systems. At present, batteries are being utilized in various application including electronic devices and electric vehicles. However, low life cycle and poor rate capability are main drawbacks associated with a battery. Supercapacitors or electrochemical capacitors have received a much attention as they have higher power density, lightweight, fast charging–discharging rate and long cycle life [6–12]. The electrochemical performance of a supercapacitor is governed by the morphology and microstructure of the electrode. A single material in supercapacitor does not meet the requirements of high energy and power density. Depending on the different charge storage mechanisms of electrode, supercapacitors are categorized into two kinds,

---

R. Kumar

Center for Energy Studies, Indian Institute of Technology Delhi, Delhi 110016, India

P. K. Sahoo · A. Soam (✉)

Department of Mechanical Engineering, Siksha ‘O’ Anusandhan University, Bhubaneswar, India

© The Author(s), under exclusive license to Springer Nature Singapore Pte Ltd. 2023

443

P. Pradhan et al. (eds.), *Recent Advances in Mechanical Engineering*,

Lecture Notes in Mechanical Engineering,

[https://doi.org/10.1007/978-981-16-9057-0\\_47](https://doi.org/10.1007/978-981-16-9057-0_47)

electrical double-layered capacitor (EDLC) and pseudocapacitor [13–15]. EDLC stores the charge electrostatically on the interface of electrode material and electrolyte. Carbon materials are typically examples of electrodes for EDLC. Reversible Faradaic reactions between electrode and electrolyte are responsible for pseudocapacitor to store the charge. Metal oxides, metal hydroxides and metal sulfides are some examples of electrode for pseudocapacitor.

Recent trends in supercapacitor research concentrate on the development of new electrode materials with desirable properties such as high surface area, high conductivity and good corrosion resistance to improve the supercapacitor performance [16–20]. Nanostructures materials are considered as promising electrodes for supercapacitor application because of their high surface area and excellent electronic conductivity [21–23]. Consequently, carbon nanostructures such as nanotubes and graphene nanosheets have widely been investigated for supercapacitor application in the past few years [20, 24–26]. However, carbon-based materials exhibit lower energy density and larger power density in supercapacitor. On the other hand, metal oxides are able to deliver larger energy density in supercapacitor but lower power density than carbon-based materials.

Therefore, metal oxides and carbon nanocomposites are being considered potential candidates for supercapacitor application [24, 27, 28]. The carbon in the composite improves the electrical conductivity and hence enhances performance of supercapacitor. Different metal oxides have been extensively studied in supercapacitor. Cobalt oxides have received much interest because of their larger value of specific capacitance, low cost and easy synthesis process [28, 29]. Moreover, cobalt oxides-based electrodes can be used in alkaline electrolyte with good electrochemical performance. The surface morphology and dimension which are importance in supercapacitor can easily be controlled during synthesis process. Therefore, in this work, we have selected cobalt oxide to make the nanocomposite with carbon. This structure may exhibit great performance in supercapacitor.

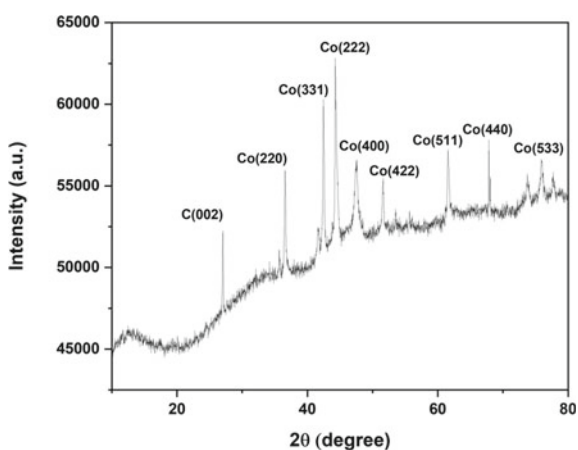
## 2 Experimental Details

Sucrose and cobalt oxide nanoparticles were used to fabricate the composite of cobalt oxide and carbon. Initially, PVA as a binder was dissolved in water. The solution was kept in glass beaker on a magnetic stirrer. After getting transparent solution, sucrose and cobalt oxide were added to the solution. The magnetic stirring was continued for 24 h. A homogeneous suspension of the mixture was obtained, and the suspension was kept in an oven to remove the water. The obtained mixture after drying process was annealed in flowing argon at 650 °C. A powder was obtained after annealing. This powder was used as composite of cobalt oxide and sucrose derived carbon.

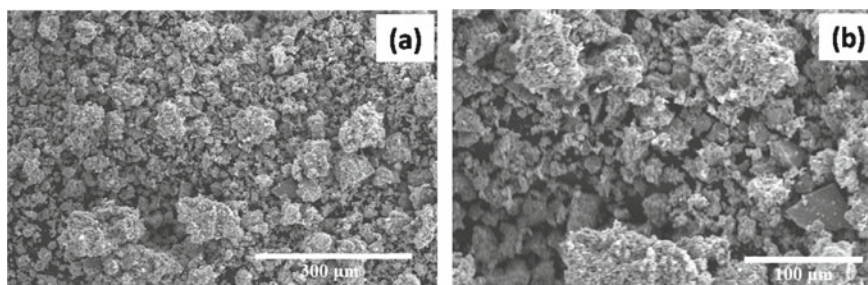
### 3 Results and Discussion

Figure 1 depicts the XRD pattern of the synthesized cobalt oxide and carbon nanocomposite. XRD was performed with an angle of  $10^\circ$  to  $80^\circ$  and using  $\text{Cu-K}\alpha$ :  $\lambda = 1.54 \text{ \AA}$ . The XRD shows the peaks from both cobalt oxide and carbon, which confirms the formation of cobalt oxide and carbon nanocomposite. Well-defined diffraction peaks are observed, which correspond to the (220), (311), (222), (400), (422), (511), (440) and (533) planes of cobalt oxide crystals ( $\text{Co}_3\text{O}_4$ ) [28]. The sharp peaks confirm the crystalline structure of  $\text{Co}_3\text{O}_4$  nanoparticles. A diffraction peak at about  $26.2^\circ$  can also be observed, which is from the (0 0 2) planes of hexagonal graphite structure [15]. No other peaks are seen in XRD indicating no impurity in the composite.

Further, the surface morphology of the composite was examined by SEM. The surface morphology is depicted in Fig. 2. These images are taken at two different



**Fig. 1** XRD pattern of cobalt oxide and sucrose derived carbon composite



**Fig. 2** SEM micrographs (a, b) of cobalt oxide and carbon nanocomposite at two different places and with different magnifications

places on the sample and with different magnifications to check the uniformity of the particles distribution. It is clear that the nanocomposite maintains the uniformity of distribution of particles. However, there is non-uniform size of the particles in the composite.

The non-uniform size is due to the presence of two different materials in the composite. The large particles (10–80  $\mu\text{m}$ ) are of sucrose derived carbon. The cobalt oxide is present on the sucrose derived carbon. Moreover, numerous pores are also observed in the composite, which are beneficial for supercapacitor application [30]. These pores increase the effective surface area of the samples and occupy large number of ions from electrolyte. Hence, the XRD and SEM results confirm the formation of cobalt oxide and carbon nanocomposite.

## 4 Summary

In summary, cobalt oxide and carbon nanocomposite was synthesized using sucrose as carbon source. The XRD confirmed the phases of cobalt oxide and carbon in the composite. Moreover, the sharp peaks in XRD reveal the crystalline nature of cobalt oxide. SEM results showed that the cobalt oxide and carbon particles are distributed uniformly in the composite. The synthesized composite may be utilized as electrode in supercapacitor application.

## References

1. Zhao D, Wang Y, Zhang Y (2011) High-performance Li-ion batteries and supercapacitors based on 1-D nanomaterials in prospect. *Nano-Micro Letters* 3(1). doi: <https://doi.org/10.5101/nml.v3i1.p62-71>
2. Hee S, Kim J, Soo Y (2004) Fabrication and characterization of a LiCoO<sub>2</sub> battery—supercapacitor combination for a high-pulse power system. *J Power Sources* 138:360–363. <https://doi.org/10.1016/j.jpowsour.2004.06.050>
3. Kumar R, Singh M, Soam A (2020) Study on electrochemical properties of silicon micro particles as electrode for supercapacitor application. *Surfaces and Interfaces* 19:100524. <https://doi.org/10.1016/j.surfin.2020.100524>
4. Kumar R, Soam A, Hussain R, Mansuri I, Sahajwalla V (2020) Carbon coated iron oxide (CC-IO) as high performance electrode material for supercapacitor applications. *J. Energy Storage* 32:101737. <https://doi.org/10.1016/j.est.2020.101737>
5. Kumar R, Soam A, Sahajwalla V (2020) Sucrose-derived carbon-coated nickel oxide (SDCC-NiO) as an electrode material for supercapacitor applications. *Mater Adv* 1(4):609–616. <https://doi.org/10.1039/d0ma00323a>
6. Pu B et al (2014) Flexible supercapacitors based on carbon nanomaterials. *J Mater Chem A Mater Energy Sustain* 3(1):22507–22541. <https://doi.org/10.1016/j.mattod.2015.01.002>
7. Huang M, Li F, Dong F, Zhang YX, Zhang LL (2015) MnO<sub>2</sub>-based nanostructures for high-performance supercapacitors. *J Mater Chem A* 3(43):21380–21423. <https://doi.org/10.1039/c5ta05523g>
8. Jeong GH, Baek S, Lee S, Kim SW (2016) Metal oxide/graphene composites for supercapacitive electrode materials. *Chem An Asian J* 11(7):949–964. <https://doi.org/10.1002/asia.201501072>

9. Beidaghi M, Gogotsi Y (2014) Capacitive energy storage in micro-scale devices: recent advances in design and fabrication of micro-supercapacitors. *Energy Environ Sci* 7(3):867–884. <https://doi.org/10.1039/c3ee43526a>
10. Soam A, Kumar R, Singh M (2020) Electrophoretically deposited bismuth iron oxide nanoparticles film for supercapacitor application. *Russ J Electrochem* 56(12):1037–1042. <https://doi.org/10.1134/S1023193520120241>
11. Soam A, Kumar R, Thatoi D, Singh M (2020) Electrochemical performance and working voltage optimization of nickel ferrite/graphene composite based supercapacitor. *J Inorg Organomet Polym Mater* 30(9):3325–3331. <https://doi.org/10.1007/s10904-020-01540-7>
12. Kumar R et al (2020) In situ carbon-supported titanium dioxide (ICS-TiO<sub>2</sub>) as an electrode material for high performance supercapacitors. *Nanoscale Adv* 2(6):2376–2386. <https://doi.org/10.1039/d0na00014k>
13. Maksoud MIAA et al (2021) Advanced materials and technologies for supercapacitors used in energy conversion and storage: a review. *Environ Chem Lett* 19(1):375–439. <https://doi.org/10.1007/s10311-020-01075-w>
14. Ko R, Carlen M (2000) Principles and applications of electrochemical capacitors. *Electrochim Acta* 45(15–16):2483–2498. [https://doi.org/10.1016/S0013-4686\(00\)00354-6](https://doi.org/10.1016/S0013-4686(00)00354-6)
15. Soam A, Mahender C, Kumar R, Singh M (2019) Power performance of BFO-graphene composite electrodes based supercapacitor. *Mater Res Express* 6(2):025054. <https://doi.org/10.1088/2053-1591/aaf125>
16. Raza W, Ali F, Raza N, Luo Y, Kim K, Yang J (2018) Recent advancements in supercapacitor technology nano energy recent advancements in supercapacitor technology. *Nano Energy* 52:441–473. <https://doi.org/10.1016/j.nanoen.2018.08.013>
17. Yan A, Wang X, Cheng J (2018) Research progress of NiMn layered double hydroxides for supercapacitors: a review. *Nanomaterials* (Basel) 8:747. <https://doi.org/10.3390/nano8100747>
18. Wang X, Wu D, Song X, Du W, Zhao X, Zhang D (2019) Review on carbon/polyaniline hybrids: design and synthesis for supercapacitor. *Molecules* 24(12):2263. <https://doi.org/10.3390/mol24122263>
19. Li J, Lu W, Yan Y, Chou TW (2017) High performance solid-state flexible supercapacitor based on Fe<sub>3</sub>O<sub>4</sub>/carbon nanotube/polyaniline ternary films. *J Mater Chem A* 5(22):11271–11277. <https://doi.org/10.1039/c7ta02008b>
20. Kumar N, Kumar A, Huang GM, Wu WW, Tseng TY (2018) Facile synthesis of mesoporous NiFe<sub>2</sub>O<sub>4</sub>/CNTs nanocomposite cathode material for high performance asymmetric pseudocapacitors. *Appl Surf Sci* 433:1100–1112. <https://doi.org/10.1016/j.apsusc.2017.10.095>
21. Part A (2010) Nanostructured materials for the construction of asymmetrical supercapacitors. *Journal of Power and Energy* 224(4):479–503. <https://doi.org/10.1243/09576509JPE861>
22. Yu G et al (2011) Solution-processed graphene/MnO<sub>2</sub> nanostructured textiles for high-performance electrochemical capacitors. *Nano Lett* 11(7):2905–2911. <https://doi.org/10.1021/nl2013828>
23. Iro ZS, Subramani C, Dash SS (2016) A brief review on electrode materials for supercapacitor. *Int J Electrochem Sci* 11(12):10628–10643. <https://doi.org/10.20964/2016.12.50>
24. Liu Y (2016) Fabrication of composite electrodes and supercapacitor devices. PhD Thesis, McMaster University, Materials Science Engineering <http://hdl.handle.net/11375/19108>
25. Frackowiak E, Béguin F (2001) Carbon materials for the electrochemical storage of energy in capacitors. *Carbon* 39(6):937–950. [https://doi.org/10.1016/S0008-6223\(00\)00183-4](https://doi.org/10.1016/S0008-6223(00)00183-4)
26. Wang W, Hao Q, Lei W, Xia X, Wang X (2014) Ternary nitrogen-doped graphene/nickel ferrite/polyaniline nanocomposites for high-performance supercapacitors. *J Power Sources* 269:250–259. <https://doi.org/10.1016/j.jpowsour.2014.07.010>
27. Lee SW, Kim KJ, Chen KS, Hammond PT, Shao-horn Y (2010) Carbon nanotube/manganese oxide ultrathin film electrodes for electrochemical capacitors. *ACS Nano* 4(7):3889–3896. <https://doi.org/10.1021/nn100681d>
28. Kumar R, Soam A, Sahajwalla V (2021) Carbon coated cobalt oxide (CC-CO<sub>3</sub>O<sub>4</sub>) as electrode material for supercapacitor applications. *Mater Adv* 2(9):2918–2923. <https://doi.org/10.1039/d1ma00120e>

29. Liao Q, Li N, Jin S, Yang G, Wang C (2015) All-solid-state symmetric supercapacitor based on Co<sub>3</sub>O<sub>4</sub> nanoparticles on vertically aligned graphene. *ACS Nano* 9(5):5310–5317. <https://doi.org/10.1021/acsnano.5b00821>
30. Yao X, Kong J, Zhou D, Zhao C, Zhou R, Lu X (2014) Mesoporous zinc ferrite/graphene composites: towards ultra-fast and stable anode for lithium-ion batteries. *Carbon* 79:493–499. <https://doi.org/10.1016/j.carbon.2014.08.007>

# Recovery of Iron Values from Blast Furnace Gas Cleaning Process Sludge by Medium Intensity Magnetic Separation Method



Malaya Kumar Jena , Jyotirmayee Mahanta,  
Manjula Manjari Mahapatra, Madhusmita Baliarsingh,  
and Subhadrata Mishra 

**Abstract** For a sustainable future, industries need to maximize productivity and minimize waste. Gas cleaning process sludge, a waste generated from steel plants contains a significant amount of iron and carbon value which can be recovered and reutilize. The present study focused on the magnetic separation of iron values from the gas cleaning process sludge at varying intensity (1000–4000 Gauss) and evaluated the grade and recovery. At 3000 Gauss and higher, the recovery and grade of the iron were significant. In addition to this, the highest grade was obtained at 3000 Gauss magnetic intensity, i.e., total Fe of 67.8% from a feed of 36.13% Fe. Also, the non-mag fraction can be used as a reductant due to the high carbon content which was already reported in the literature.

**Keywords** Magnetic separation · GCP sludge · Recovery · Waste re-utilization

## 1 Introduction

The growing demand for iron and steel has attracted many researchers to utilize low-grade iron ores along with the maximum recovery of iron value from the iron and steel processing downstream to minimize the loss. During the production of the iron and steelmaking process, a huge amount of solid wastes are generated in the form of slag, dust, slime, and sludge [1]. Nearly 2–4 t of wastes are generated to produce every single ton of steel [2]. These wastes are containing both metallic and non-metallic values such as iron oxides, carbon, silica, and alumina. Blast furnace gas cleaning process sludge is a metallurgical waste, which is a solid waste generated during the iron-making process [3, 4]. This gas cleaning process sludge (GCPS) is a combination of oxides whose major components are iron oxides and coke fines, in

---

M. K. Jena · J. Mahanta · M. Baliarsingh · S. Mishra (✉)  
CSIR-Institute of Minerals and Materials Technology, Bhubaneswar 751013, India  
e-mail: [subhadratomishra2010@gmail.com](mailto:subhadratomishra2010@gmail.com)

M. M. Mahapatra  
Parala Maharaja Engineering College, Berhampur 761003, India

© The Author(s), under exclusive license to Springer Nature Singapore Pte Ltd. 2023  
P. Pradhan et al. (eds.), *Recent Advances in Mechanical Engineering*,  
Lecture Notes in Mechanical Engineering,  
[https://doi.org/10.1007/978-981-16-9057-0\\_48](https://doi.org/10.1007/978-981-16-9057-0_48)



addition to other elemental compounds silicon, calcium, magnesium, and negligible heavy metals such as zinc, lead, and cadmium [5, 6]. Due to high carbon and iron contents in the blast furnace GCPS, it can be recovered [2]. The major mineral phases present in the blast furnace GCPS are iron in hematite ( $\text{Fe}_2\text{O}_3$ ) and carbon in the form of coke (C) along with fractions of magnetite ( $\text{Fe}_3\text{O}_4$ ), calcite ( $\text{CaCO}_3$ ), quartz ( $\text{SiO}_2$ ), dolomite ( $\text{CaMgCO}_3$ ), siderite ( $\text{FeCO}_3$ ) and clay minerals.

Additionally, a huge amount of GCPS is generated from blast furnace operation which is very difficult to dispose of due to environmental constraints. Direct disposal of GCPS can lead to serious environmental issues like air pollution and water pollution. To minimize the environmental impact and sustainable utilization of GCPS, many pieces of research are being carried out [2, 4, 7]. Also, different pyro metallurgical and hydrometallurgical processes have been developed to avoid this pollution many research works with the [8]. The modern steelmaking industry is focused to produce green steel with eco-friendly and zero waste to save our environment and further utilize the valuable minerals to maximize the economy [9]. With the losses of metals in industrial waste and difficulty in safe disposal, worldwide efforts are being made to effectively extract the metal content from the waste and generate the non-hazardous slag in a cementitious industry. The materials generated from the sludge and dust from the steelmaking route were recycled through sinter making process. Recycled waste has also some effect on sinter quality, strength, and productivity [2]. Most developing countries recycle this dust or sludge in sinter making plants, which have been generated through the gas cleaning process. The Institute of Gas Technology has developed a method fluidized-bed process for recovering direct reduced iron from blast furnace fuel dust and this technique reduced up to 90% iron element. The best economic countries Canada and USA used blast furnace dust and finer mill scale was essentially recycled in sinter plant [10]. A complete characterization and beneficiation process was conducted at IMMT, Bhubaneswar by Das et al. [10] to recovery the valuable particle from solid waste generated from the steel plant. This study on blast furnace dust from steel plant was summarized to recovery the carbon value with 80% by column flotation technique and further ferruginous phase magnetite can be removed by low-intensity magnetic separation technique. Another research work was done by a proper characterization study of blast furnace sludge from SSAB Europe Oy, Raahе, Finland and was examined that the sludge contains a high amount of iron and carbon, while negligible contents of zinc were available. SEM–EDX analysis indicates that hematite and zinc ferrite are a very fine fraction ( $< 20 \mu\text{m}$ ). The physical separation method was not possible to recover valuable minerals due to fine particle size; also hydrometallurgical process is not possible to recover zinc from blast furnace sludge due to its size fraction. In another sense briquettes, preparation is an appropriate method for handling this sludge and can be recycled again as feed material to blast furnace [11]. Furthermore, Jena et al. [12] utilized GCPS as a reductant for the reduction roasting of low-grade manganese ore. The study had reported that utilization of GCPS as a reductant to perform reduction roasting has a significant effect on phase transformation and resulted in good recovery of both iron (Fe) and manganese (Mn). Due to the presence of carbon in the GCPS, it serves as a reductant and stimulates the reduction roasting process.

**Table 1** Chemical analysis of GCPS sample

Assay value %				
Fe(T)	SiO <sub>2</sub>	Al <sub>2</sub> O <sub>3</sub>	MnO	LOI
36.13	7.95	5.25	0.15	35.04

**Table 2** Proximate analysis of GCPS sample

Fixed carbon (FC) %	Moisture %	Volatile matter (VM) %	Ash %	G.C.V (cal/g)
38.13	2.36	6.08	53.43	3181.7

This work focus on a study to established the sample preparation, compositional analysis and morphological study of GCPS to identify the valuable metallic content; furthermore proximate and energy analysis was done to know the carbon and calorific values. Then a suitable separation process was established to recover the iron content by different magnetic field intensity in a box magnetic separator.

## 2 Materials and Methods

### 2.1 Sample Preparation

The GCPS sample was collected from a landfill of a local iron and steel industry in Odisha. The collected sample was subjected to mixing by coning and quartering method and then 50 kg of representative sample was dried at 110 °C to remove the surface moisture. The dried sample was then taken for chemical analysis and proximate analysis. The chemical analysis and proximate analysis is presented in Tables 1 and 2, respectively. The GCPS sample contained iron (Fe) and carbon (C) as major mineral along with significant amount of silica (SiO<sub>2</sub>) and alumina (Al<sub>2</sub>O<sub>3</sub>).

### 2.2 Experimental Methodology

The representative GCPS sample was collected from the 50 kg dried sample for experimental analysis. Initially, the chemical characterization of the feed sample was carried out by wet chemical analysis and proximate analysis. Then, the feed sample was grounded below 200 μm size and then subjected to wet magnetic separation using a Box magnet apparatus (Make: BOXMAG-Rapid Limited) at medium magnetic field intensity, i.e., medium intensity magnetic separation (MIMS). For the magnetic separation test, the magnetic field intensity was varied from 1000 to 4000 Gauss with a 500 G increment and 1000 gm of representative sample was taken for each separation test. After experimentation, the collected mag and non-mag products of

each test were dried and then subjected to wet chemical analysis to estimate the total iron value.

### 3 Materials and Methods

The composition of the feed sample was analyzed by chemical analysis and proximate analysis. The composition and mineralogy of the separated sample was analyzed using XRD, SEM and wet chemical analysis. The obtained results from these analyses were briefly discussed below in the subsections.

#### 3.1 Magnetic Separation Process

Magnetic separation technique is an established method to remove gangue minerals from ferrous minerals. MIMS was adopted for this separation study and the effect of magnetic intensity on the separation process was evaluated. Both mag and non-mag fractions were analyzed to estimate the Fe grade. The results revealed that with increase in magnetic field intensity there is an increase in the Fe grade of the mag concentrate. However, at higher magnetic intensity, i.e., above 3000 G, there is a decrease in the Fe grade of the mag concentrate and an increase in the non-mag fraction. From Fig. 1, it can be clearly observed that after 3000 G, increase in magnetic field intensity has less impact on the separation process.

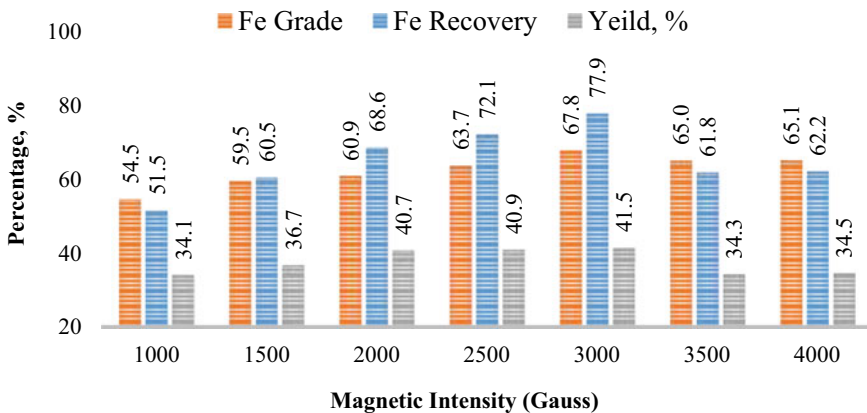


Fig. 1 Fe grade, recovery, and yield at various magnetic intensity

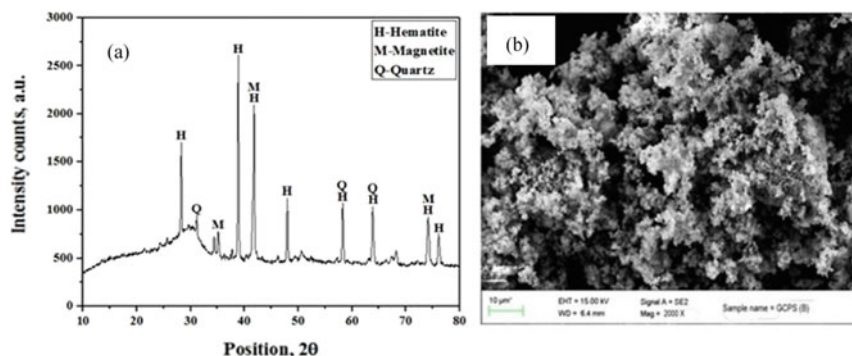


Fig. 2 a XRD plot and b photomicrograph of SEM-BSE image of mag fraction at 3000 G

### 3.2 Recovery and Yield of Iron Values

The recovery and yield was estimated after magnetic separation and chemical analysis of the samples at different magnetic intensity. The data were plotted and presented in Fig. 1. The increasing magnetic field intensity has significant effect on grade, recovery, and yield of iron values which can be understood from Fig. 1. However, the increase in magnetic intensity decreases the yield. It can be comprehended that due to higher magnetic intensity, silica and alumina contain increases in the mag fraction as they attached with the iron particles. The optimum recovery and yield was reported at 3000 G, i.e., 67.8% recovery with 41.5% yield.

### 3.3 Mineralogy of the Product Sample

The XRD pattern of the mag sample is shown in Fig. 2a, indicating that hematite and magnetite were the dominating mineral phases in the sample, with quartz phases present due to some secondary iron coated quartz. Figure 2b shows the SEM-BSE (Scanning Electron Microscope-Back Scattered Electron) image of the mag sample, which shows hematite with a snowball texture and some euhedral Hematite-Martite crystals with holes filled with gangue minerals.

## 4 Conclusion

This study investigated the separation and recovery of iron values from the GCP sludge by adopting medium intensity magnetic separation method. The grade, recovery, and yield were evaluated based on the chemical analysis of the separated samples. A 67.8% TFe was obtained from a feed of 36.13% TFe at 3000 G magnetic

intensity with recovery and yield of 77.9% and 41.5%, respectively. XRD study of mag fraction confirms that both hematite ( $\text{Fe}_2\text{O}_3$ ) and magnetite ( $\text{Fe}_3\text{O}_4$ ) are present in the concentrate along with silica ( $\text{SiO}_2$ ).

**Acknowledgements** The authors are thankful to the Director, CSIR-IMMT Bhubaneswar for the experimental facilities.

**Conflict of Interest** The authors declare no conflict of interest regarding this research with any organization or individuals.

## References

1. Yehia A, El-Rahiem FH (2005) Recovery and utilization of iron and carbon values from blast furnace flue dust. *Trans Inst Min Metall Sect C Miner Process Extr Metall* [Internet]. Available from: <https://doi.org/10.1179/037195505X28519>. Cited 11 Jan 2021
2. Das B, Prakash S, Reddy PSR, Misra VN (2007) An overview of utilization of slag and sludge from steel industries. *Resour Conserv Recycl* 50
3. Machado JGMS, Brehm FA, Moraes CAM, dos Santos CA, Vilela ACF, da Cunha JBM (2006) Chemical, physical, structural and morphological characterization of the electric arc furnace dust. *J Hazard Mater* 136
4. Mansfeldt T, Dohrmann R (2004) Chemical and mineralogical characterization of blast-furnace sludge from an abandoned landfill. *Environ Sci Technol* 38
5. Trung ZH, Kukurugya F, Takacova Z, Orac D, Laubertova M, Miskufova A et al (2011) Acidic leaching both of zinc and iron from basic oxygen furnace sludge. *J Hazard Mater* 192
6. Van Herck P, Vandecasteele C, Swennen R, Mortier R (2000) Zinc and lead removal from blast furnace sludge with a hydrometallurgical process. *Environ Sci Technol* 34
7. Kretzschmar R, Mansfeldt T, Mandaliev PN, Barmettler K, Marcus MA, Voegelin A (2012) Speciation of Zn in blast furnace sludge from former sedimentation ponds using synchrotron X-ray diffraction, fluorescence, and absorption spectroscopy. *Environ Sci Technol* 46
8. Zunkel AD (2000) Recovering zinc and lead from electric arc furnace dust: a technology status report [Internet]. *Recycl Met Eng Mater* 227–236. Available from: <https://doi.org/10.1002/9781118788073.ch21>
9. Baba Srinivas A, Kumar Sar S, Singh S, Yadav S (2017) Solid waste management from steel melting shop. *J Appl Adv Res* 2
10. Das B, Prakash S, Biswal SK, Reddy PSR, Mohapatra BK, Tripathy HK. Utilization of solid waste materials generated at steel plants by physical beneficiation technique: report submitted to Ministry of Steel. Govt. of India Regional Research, Bhubaneswar, India
11. Omran M, Fabritius T, Paananen T (2017) Effect of blast furnace sludge (BFS) characteristics on suitable recycling process determining. *J Miner Mater Charact Eng* 05
12. Jena MK, Mishra S, Das SK, Mustakim SM, Adesina A (2021) Sustainable utilization of GCP sludge as a reductant in the reduction roasting of low-grade manganese ore to recover Mn and Fe values. *Min Metall Explor* [Internet]. Available from: <https://doi.org/10.1007/s42461-021-00380-4>

# Fatigue Analysis of Rectangular Plate with a Circular Cut-Out



S. Siva Priya and P. K. Sahoo

**Abstract** The usage of the rectangular plate with a circular cut-out is common in aircraft structures. The stress rises, and stress concentrations occur around the cut-out boundary of structural components due to the change in geometry. It is essential to accurately evaluate the stress concentration factor (SCF) of the structural elements to predict fatigue life and fatigue damage. In this study, fatigue analysis of an aluminium alloy 2024-T3 panel with a circular cut-out of various diameter to width ratios such as 0.1 and 0.3 is carried out to predict the fatigue life and fatigue damage under constant amplitude loading. First, the static stress concentration factor ( $K_t$ ) of the aluminium panel with a cut-out under axial tensile stresses was determined using finite element and analytical approaches. Ansys (FEA) software is used for carrying out the FEA, and empirical Roark's analytical model is used for the analytical work. Second, the fatigue stress concentration factor ( $K_f$ ) is evaluated analytically. The convergence studies of finite element mesh are performed by comparing  $K_t$  values using three different meshes of varying the number of elements for 3-dimensional models. The comparison of static stress concentration factors obtained from FEA and the analytical (Roark's) model shows that both the results are in good agreement and  $K_f$  is less than the  $K_t$ . The equivalent stress plot shows that the stress concentration factor is more around the cut-out boundary. Third, fatigue analysis of the panel is carried out, and the fatigue life and fatigue damage are estimated.

**Keywords** Rectangular plate with a hole · SCF · Fatigue analysis

---

S. S. Priya

Department of Aerospace Engineering, Periyar Maniammai Institute of Science and Technology (Deemed to be University), Thanjavur 613403, India

P. K. Sahoo (✉)

Structural Technological Division, CSIR-National Aerospace Laboratories, Bangalore 560017, India

e-mail: [pks@nal.res.in](mailto:pks@nal.res.in)

## 1 Introduction

The problem of the plate with a circular cut-out is generally analysed using 2-dimensional approximated model since the load is applied on the plane of the plate and the thickness of the plate is very small compared to the overall dimension of the plate. The changes or deviations in stresses depend on plate dimensions, hole diameter, number of holes, and forces applied axially. Dhanjal and Arora [1] discussed that the stress distribution is caused by elements made by machining. Mekalke et al. [2] discussed that the rectangular plate with a central hole subjected to axial force produces structural damage of the material across the cut-out region. Various solutions were available to analyse and reduce stress concentration factors, including relief notches and holes. Shivlingesh et al. [3] studied that the SCFs vary according to dimension ratio, which is defined as the  $d/w$  ratio of beam. In both materials, at the edges of holes, the maximum stresses always occur. Brahmabhatt et al. [4] examined the rectangular plate using Ansys along a central elliptical hole. Shaik and Mirzana [5] have found that the finite width plate with a central cut-out under static loading having the stress concentration, which always takes place at hole edges.

Mallikarjun et al. [6] concluded that there is a rise in the angle of obliquity with the rise in maximum stress ratio. Kishore et al. [7] investigated that the maximum stress occurs at a border of the circular cut-out in both materials. Also, the thickness to depth ratio increases whenever there is a decrease in deformation and von Mises stresses for both materials. Endigeri and Mannur [8] showed that the composite rectangular plate with uniaxial loading gives high stress at the corners of holes, which may cause fracture of the material. So, auxiliary holes were used to reduce stresses. Ozkan and Toktas [9] used five models to find out the stress concentration factor in a plate with circular cut-out under uniaxial tensile stress. They concluded that the results obtained using REGA and ANN models are more accurate than analytical and FEA models.

## 2 Motivation and Literature Gap

Literature shows that much work has been done in fatigue life estimation of a rectangular plate with a circular cut-out under fluctuating load using the conventional S–N approach for high cycle fatigue (HCF). However, it is necessary to investigate a similar problem for identifying the best geometrical shapes and the geometrical sensitivity with respect to  $d/w$  ratios for optimising fatigue life and fatigue damage index. Fatigue life prediction depends on the accurate estimation of static and fatigue SCF. This study is very important for aircraft structures that consist of several rectangular panels with centrally placed cut-outs. This investigation is essential for structural integrity evaluation of airframes under fatigue load to avoid catastrophic accidents. The present work is a small contribution towards fulfilling the above gap.

### 3 Problem Definition

In the present work, a rectangular plate with a circular cut-out made of aluminium alloy 2024-T3 has been considered to calculate stress concentration factors (SCF) numerically and analytically under applied tensile load. The applied load varies from a maximum of 10 kN to a minimum of 1 kN. Two diameters to width ratios ( $d/w$ ) such as 0.1 and 0.3 have been considered in the analysis. Using SCF solutions, fatigue stress concentration factors are obtained. Subsequently, the fatigue life and fatigue damage index was calculated.

### 4 Material and Modelling

The dimensions of a rectangular plate with circular cut-out are given in Fig. 1. The material considered for the plate is Aluminium 2024-T3 alloy. Where, the diameter  $d = 5\text{ mm}$  and  $15\text{ mm}$ .

#### 4.1 Finite Element Model

The finite element model of the rectangular plate with a circular cut-out is generated using Ansys workbench finite element analysis software. The finite element model showing mesh and boundary conditions are shown in Fig. 2. The number of elements and nodes are respectively 398,839 and 1,777,649. The plate is subjected to tensile stress at one end, and another end is fixed.

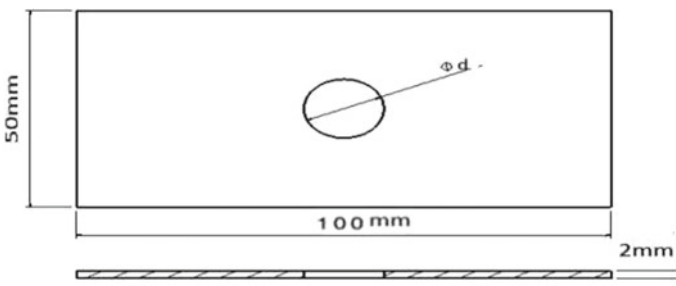


Fig. 1 Dimensions of a rectangular plate with circular cut-out



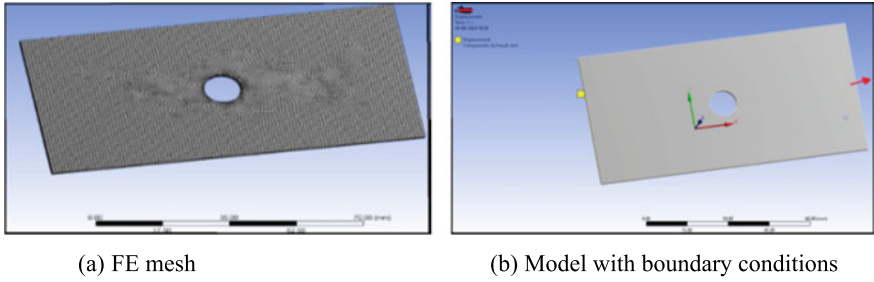


Fig. 2 Finite element models

### 4.2 The Analytical Model/Theoretical Calculation of $K_t$

The analytical model of SIF,  $K_t$  for the finite width with a circular hole at the centre as proposed by Roark cited in Ref. [9] is given in the following Eq. (1).

$$K_t = 3 - 3.14(d/w) + 3.667(d/w)^2 - 1.527(d/w)^3 \tag{1}$$

### 4.3 Stress Concentration Factor Calculation (Peterson’s Formula [9]) by FEA ( $K_t$ )

The equation for the stress concentration factor of a finite width rectangular plate with the central circular hole is given in the following Eqs. (2) and (3). The length of the plate is 100 mm, the thickness of the plate  $t = 2$  mm, width of the plate  $W = 50$  mm, with a hole having different diameters such as  $d = 5$  mm and 15 mm. Then uniform stress of 100 MPa is applied to one end and fixed support at other side.

$$\sigma_{\max} = K_t \sigma_{\text{nom}} \tag{2}$$

$$\sigma_{\text{nom}} = \frac{F}{(W - d)t} \tag{3}$$

where

- $\sigma_{\max}$  Maximum stress.
- $\sigma_{\text{nom}}$  Nominal stress.
- $F$  Load applied at one end.
- $W$  Width of the rectangular plate.
- $t$  Thickness of rectangular plate.

The SCF values for various  $d/w$  are evaluated and shown in Table 1.

**Table 1** SCF for different  $d/w$  ratios

<p><i>Case (i):</i>(<math>d/w = 0.1</math>)                  By Eq. (1), <math>K_t = 2.72</math>                  By Eq. (3),  <math>\sigma_{nom} = 111.11 \text{ N/mm}^2</math>                  By Eq. (2)  <math>\sigma_{max} = K_t * \sigma_{nom} = 302 \text{ N/mm}^2</math></p>	<p><i>Case (ii):</i>(<math>d/w = 0.3</math>)                  By Eq. (1), <math>K_t = 2.346</math>                  By Eq. (3)  <math>\sigma_{nom} = 142.85 \text{ N/mm}^2</math>                  By Eq. (2)  <math>\sigma_{max} = K_t * \sigma_{nom} = 335 \text{ N/mm}^2</math></p>
---	--

**Fatigue Stress Concentration Factor ( $K_f$ ).** The notch sensitivity equation is given by Eq. (4). The fatigue stress concentration factors for two different  $d/w$  ratios are found by using the Neuber Eq. (5).

$$Q = \frac{1}{1 + \frac{\sqrt{a}}{\sqrt{r}}} \tag{4}$$

The fatigue stress concentration factor  $K_f$  can be found by using Neuber Eq. (5).

$$K_f = 1 + \frac{K_t - 1}{1 + \frac{\sqrt{a}}{\sqrt{r}}} \tag{5}$$

$$K_f = 1 + q (K_t - 1) \tag{6}$$

$$\sqrt{a} = 0.246 - 3.08(10^{-3})S_{ut} + 1.51(10^{-5})S_{ut}^2 - 2.67(10^{-8})S_{ut}^3 \tag{7}$$

The Notch sensitivity ( $q$ ) and fatigue stress concentration factor ( $K_f$ ) for various notch radius are given in Table 2.

**Determination of Fatigue Limit.** The Basquin’s equation for fatigue limit of the material is given in Eq. (8).

$$S_f = aN^b \tag{8}$$

where

- $a$   $(fS_{ut})^2/S_e$ .
- $b$   $(-1/3) \log (fS_{ut})/S_e$ .

Ultimate strength of aluminium alloy 2024-T3,  $S_{ut} = 70\text{kpsi}$  (482.63 MPa).

**Table 2** Notch sensitivity ( $q$ ) and fatigue stress concentration factor ( $K_f$ ) for various notch radius

Notch radius	Aluminium alloy	
	$S_{ut} = 70 \text{ kpsi} = 482 \text{ MPa}$ ( $\sqrt{a} = 0.655$ )	
$r = 2.5 \text{ mm}$	$q = 0.707$	$K_f = 2.216$
$r = 7.5 \text{ mm}$	$q = 0.806$	$K_f = 2.086$

**Table 3** Fatigue results for various ( $d/w$ ) ratios

( $d/w$ ) ratios	Stress amplitude ( $\sigma_a$ )	Mean stress ( $\sigma_m$ )	Stress reversible ( $\sigma_{rev}$ )	Fatigue life ( $N$ ) cycles	Fatigue damage ( $D$ )
0.1	136	166	207	$5.69 * 10^5$	0.175
0.3	151	184	244	$1.39 * 10^5$	0.719

- To be conservative, for  $S_{ut} < 70\text{kpsi}$ , let  $f = 0.9$ .

( $f$ = Fatigue strength fraction)

- $S_e = 0.4 S_{ut}$  (For aluminium alloy)

Then,

$$a = 977.32.$$

$$b = - 0.117.$$

If a completely reversed stress  $\sigma_{rev}$  is given, setting  $S_f = \sigma_{rev}$ , the number of cycles to failure can be expressed as (Goodman’s equation) Eq. (9).

$$\sigma_{rev} = \sigma_a / (1 - \sigma_m / S_{ut}) \tag{9}$$

Using Eq. (8), number of cycles to failure can be obtained using the Eq. (10).

$$N = \left( \frac{\sigma_{rev}}{a} \right)^{1/b} \tag{10}$$

**Determination of Fatigue Damage Index.** The fatigue damage index is obtained using Palmgren–Miner’s Eq. (11).

$$D = n_i / N_i \tag{11}$$

The fatigue results for various ( $d/w$ ) ratios is shown in Table 3.

## 5 Results and Discussion

### 5.1 Equivalent Stress of Rectangular Plate with Circular Cut-Outs of Various ( $d/w$ ) Ratios

The equivalent stress for various diameter to width ratios ( $d/w$ ) such as 0.1 and 0.3 are shown in Fig. 3.

Figure 3 shows the equivalent (von Mises) stresses obtained from FEA for various  $d/w$  ratios. The maximum stress values are 332 MPa and 354 MPa for  $d/w$  ratios 0.1

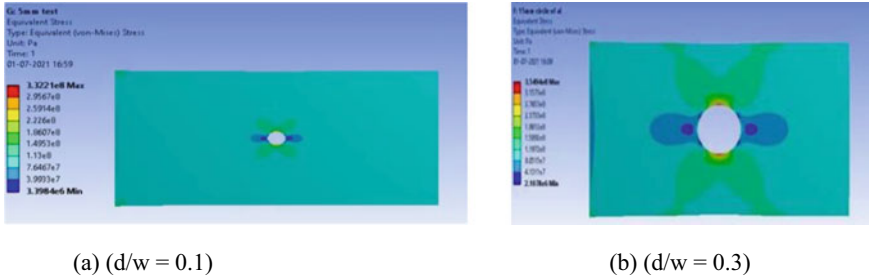


**Fig. 3** Equivalent stress of rectangular plate with circular cut-outs of various ( $d/w$ ) ratios

and 0.3, respectively. It is observed that the stresses at the corners of the holes increase with the increase in cut-out diameter. This trend indicates that the strength of the plate decreases with an increase in cut-out diameter.

### 5.2 Comparison of SCF for FEA and Analytical Model

The comparison of stress concentration factors various  $d/w$  ratios obtained from the analytical and FEA solutions are shown in Table 4 and Fig. 4.

**Table 4** Comparison of SCF for FEA and analytical model

$(d/w)$ ratio	Stress concentration factor ( $K_t$ ) (FEA)	Stress concentration factor ( $K_t$ ) (analytical model)	Error percent
0.1	2.99	2.72	0.09
0.3	2.47	2.346	0.05

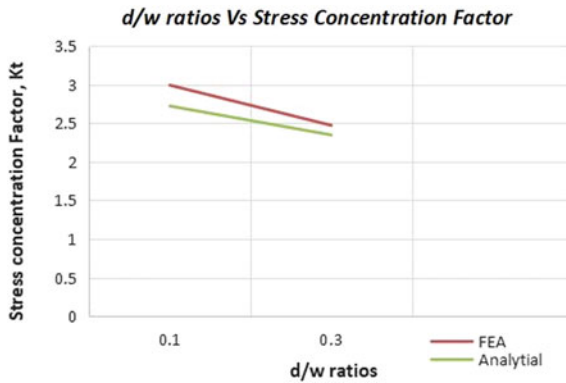


**Fig. 4**  $d/w$  ratios versus stress concentration factor

The stress concentration factors obtained using FEA and the analytical methods for various  $d/w$  ratios shows a good correlation. This stress concentration factor decreases with an increase in  $d/w$  ratio. The fatigue stress concentration factor (Table 3) is less than the static stress concentration factor.

### 5.3 Fatigue Life and Fatigue Damage Estimation of Various ( $d/w$ ) Ratios

The fatigue lives of a rectangular plate with cut-outs for various  $d/w$  ratios such as 0.1 and 0.3, as shown in Table 3, are respectively,  $5.69 \times 10^5$  and  $1.39 \times 10^5$ . The fatigue damage indices are 0.179 and 0.719. It is observed that fatigue life decreases with the increase in  $d/w$  ratio, and fatigue damage increases with an increase in  $d/w$  ratio. This trend is acceptable as the increased stress level around the cut-outs decreases fatigue, thereby increasing the damage index.

## 6 Conclusion

For all the  $d/w$  ratios of the rectangular plate with cut-outs, the maximum stress occurs at the cut-out region. The increase in hole size causes an increase in deformation because it is sensitive to the ( $d/w$ ) ratio. The stress concentration factor values obtained using FEA and the analytical approach shows a good comparison with a lesser error percentage between the two values. An increase in diameter to width ratio gives a decrease in theoretical stress concentration factor based on net-section area. The von Mises stress increases with the increase in the  $d/w$  ratio. The static stress concentration factor values of rectangular plates with cut-outs are more than fatigue stress concentration factors. The fatigue life increases with the decrease in the  $d/w$  ratio.

**Acknowledgements** The authors wish to acknowledge CSIR-Summer Research Training Program (CSIR-SRTP) 2020, under which this project work was carried out.

## References

1. Dhanjal S, Arora R (2015) Stress analysis of a rectangular plate with circular hole using three dimensional finite element model. *IJEBEA* 12(1):77–80
2. Mekalke GC, Kavade MV, Deshpande SS (2012) Analysis of a plate with a circular hole by FEM. *Journal of Mechanical and Civil Engineering* 25–30
3. Shivlingesh SB, Kivade B, Mallikarjun (2016) FEA analysis of stresses for cantilever beam with hole subjected to different mode of loading systems. *International Journal of Advanced Engineering Technology and Management Applied Sciences* 3(1):116–126

4. Brahmhatt D, Brahmhatt K, Patel D (2015) Stress concentration factor converts into stress intensity factor using ANSYS. *European J Adv Eng Technol* 2(1):4649
5. Shaik AS, Mirzana IM (2016) Stress concentration of rectangular plate with a hole made with composite material using finite element analysis. *IOSR-JMCE* 13(4):01–05
6. Mallikarjun B, Dinesh P, Parashivamurthy KI (2012) Finite element analysis of elastic stresses around holes in plate subjected to uniform tensile loading. *BIJIEMS* 2(4):136–142
7. Kishore MP, Reddy DR, Reddy MS (2018) Material effect on stress behavioural characteristics of composite rectangular plate. In: *IOP conference series: materials science and engineering*, vol 455(1). IOP Publishing, Bristol, p 012009
8. Endigeri BR, Mannur DV (2014) FEM for stress reduction by optimal auxiliary holes in a uniaxially loaded composite plate. In: *Proceedings of international conference on research in electrical, electronics and mechanical engineering*, Dehradun
9. Ozkan MT, Toktas I (2016) Determination of the stress concentration factor ( $K_t$ ) in a rectangular plate with a hole under tensile stress using different methods. *Materials Testing* 58(10):839–847

# To Study the Implementation of Kaizen in Northern Indian Manufacturing Industries



Nitesh Verma, Simranjit Singh Sidhu, Jagjeet Singh Chatha,  
and Santosh Bali

**Abstract** *Purpose* In a competitive environment, lean manufacturing is one of the important factors in every industry. This lean manufacturing system is known as the Toyota production system. Kaizen is one of the lean manufacturing techniques which means “continuous improvement”. This technique can be used at any place like home, industry, etc. Its small improvements which lead us to get maximum output (Bellgran et al. in Cost driven Green Kaizen in pharmaceutical production—creating positive engagement for environmental improvements, pp 1219–1214, 2019). It is a zero investment or minimum investment tool. The approach of the research includes a literature review about lean manufacturing techniques specially kaizen. This tool can be used in various manufacturing industries. *Design methodology* In this study, a qualitative survey of 38 North Indian manufacturing industries is collected and analysed using Cronbach, co-variance, correlation, regression, and t-test are conducted for developing relationships between input and output parameters. *Findings* The outcome of this study indicates that the implementation of kaizen is useful in eliminating MURA, 3M-MUDA, and MURI which means inconsistency, inconvenience, and wastage (Kumar in Int J Math Eng Manag Sci 4:452–459, 2019). There are some hardware and software enablers for kaizen. Hardware enablers include policies, essential rules, and institutional management. Software enablers include training, incentives, etc. Proper implementation of kaizen can improve quality reduce complaints, etc. The industries implemented kaizen more than 2 years gets the best outcomes with better productivity, waste elimination, cost reduction, better quality. *Research limitation* The chosen approach for this research study was limited to only the manufacturing organizations in North India. *Practical implications* This study will help the manufacturers to enhance the performance of their particular firms using kaizen implementation, especially in the countries which are developing. From the findings of study, academicians and practitioners would easily focus on the various issues related to continuous improvement of firm apart from operational measures.

---

N. Verma · S. S. Sidhu · J. S. Chatha (✉)  
Department of Mechanical Engineering, Punjabi University, Patiala, Punjab, India  
e-mail: [jagjeet\\_me@pbi.ac.in](mailto:jagjeet_me@pbi.ac.in)

S. Bali  
RIMT University, Mandi Gobindgarh, Punjab, India

**Keywords** Lean manufacturing system · Kaizen · Functions of kaizen · PDCA and SDCA kaizen · Innovation

## 1 Need for Study

Kaizen is a continuous improvement technique or tool which is used by many manufacturing industries in India and as well as across the world. With the increase in competitiveness in market, most of the organizations are continuously working and making efforts to bring changes in their business [3]. This competitive market demands superiority. It is very hard for industries or organizations to identify and also fulfil the required needs of customers. In such type of situations, kaizen is the most suitable tool for continuous improvement and for survival of the business world. Customer satisfaction is the prior factor according to the most of the surveys. However, there is a scarcity or lack of studies which understand the approach and its benefits adopted by north Indian manufacturing industries in region of Punjab, Haryana, Himachal Pradesh, Uttar Pradesh, and Rajasthan. Many industries from the states are unable to satisfy customers. Therefore, the present study is an attempt in finding out kaizen effect on performance of north Indian manufacturing industries.

## 2 Methodology

For achieving the objectives of the study, following methodology has been followed:

1. To discover the significance, kaizen literature review has been carried out in detail.
2. Survey of few manufacturing units have been finished through a questionnaire for understanding and surveying the present circumstances.
3. Appropriate subjective and quantitative systems have utilized to connect Kaizen and execution.

A rating scale that is used to measure opinions or attitudes is known as Likert scale. Respondents are asked to rate items on a level of agreement with the help of this scale. The rating of the Likert scale for the input parameters is (a) Not at all, (b) To some extent, (c) To a large Extent, (d) To full extent and for output parameters is (i) nominal gain (<10%), (ii) reasonable gain (11–30%), (iii) high gain (31–50%), (iv) extremely high gain (>50%).

The complete kaizen questionnaire was sent to around 85 organizations in northern region of India through the various communication means which have implemented this technique. More than 75 calls were made to interact with the staff (HR Department) of the organizations. The responses were received in the form of google forms also. The responses thus received have been analysed and compiled to evaluate the business performance of the north Indian industries regarding effectiveness of kaizen. Among these 85 industries around 50 industries helped us to fill the questionnaires



and among these 50 questionnaires only 38 were considered to be valid for the research. Sample size of this research is 38 industries.

In this research, sampling technique used here is random sampling. Random sampling is one of the techniques which is used to select a number of objects or bodies on random basis. The data collection method for this research is primary method. Primary data is the type of data which collected a fresh. This data is collected for the first time for research purpose. This data can be in the form of questionnaires, interview methods, through schedules, content analysis, observation method, etc.

### 3 Data Analysis and Results

Various statistical and analysis tools used are Cronbach alpha, multiple regression analysis, co-variance, co-relation, and *t*-test, respectively. These tools are used in SPSS statistical V26 software. On the basis of the objective of research study, analysis was performed and are classified below.

First of all, the data has been collected from various manufacturing organizations regarding various inputs for kaizen implementation (XA, XB, XC, XD, XE, XF, XG, XH) and outputs or performance parameters (YA, YB, YC, YD, YE, YF, YG). Variables have tested statistically through Cronbach alpha in order to validate or check the reliability of obtained data through kaizen questionnaire. Tables 1 and 2 describe or portray the detailed assessment of each input and performance parameters are considered for the research. The Cronbach alpha value have been observed mostly to be greater than 0.8, which validates the reliability of data obtained from the different organizations [4].

**Table 1** Cronbach alpha values for inputs of kaizen implementation

	Input parameters	Cronbach alpha value
XA	Management policies and commitment	0.878
XB	Training and involvement of employees	0.901
XC	Working environment issues	0.945
XD	Enablers effect on kaizen	0.927
XE	Skilled labour and latest machinery issues	0.903
XF	Role of innovation issues	0.950
XG	Role of supplier development issue	0.933
XH	Customer relationship issues	0.963

**Table 2** Cronbach alpha values for performance parameters leading to business excellence

	Performance parameters	Cronbach alpha value
YA	Overall business performance	0.921
YB	Waste elimination	0.939
YC	Quality	0.916
YD	Cost	0.881
YE	Flexibility and delivery	0.850
YF	Overall equipment effectiveness	0.885
YG	Safety and morale	0.910

Table 3 shows the inter-item co-variance matrix which tells or describes the co-variance for all the kaizen inputs and performance parameters. The data reveals that the co-variance value within a group is greater than the co-variance outside the group, which is recommended to be accepted.

Correlation analysis is performed to identify the relationship between each statement of input and output parameters. The correlation used is Karl Pearson correlation with significance level 0.05 [5]. The main purpose of Karl Pearson correlation matrix is to find and establish the relationship between parameters of the organizations. The correlation values in Table 4 indicate that there is a strong correlation of overall business performance YA with customer relationship XH (0.908\*\*), waste elimination YB with customer relationship XH (0.912\*\*), quality YC with role of innovation issues XF (0.734\*\*), cost YD with skilled labour and latest machinery XE (0.740\*\*), flexibility and delivery YE with role of supplier development XG (0.769\*\*), overall equipment effectiveness YF with role of innovation issues XF (0.779\*\*), safety and morale YG with role of innovation issues XF (0.721\*\*).

The technique used in this section is multiple regression analysis. This technique is used to develop mathematical models in between various dependent variables (all outputs) and independent variables (all the parameters of manufacturing or all inputs) [6].

The significant factors with  $(\beta)$  with level of significance, values of multiple regression coefficients  $(r)$ ,  $(r)^2$  and  $f$  for each performance indicator are given in Table 5. The results show that various success factors of kaizen implementation have significant contribution with respect to manufacturing performance parameters/factors. The table reveals that XA-management policies and commitment was found to be significant with YF-overall equipment effectiveness ( $t$ -value = 2.032). Similarly, XB-training and involvement of employees is significant with YA-overall business performance ( $t$ -value = 2.450), XC-working environment issues is significant with YA-overall business effectiveness ( $t$ -value = -2.165), YC-quality ( $t$ -value = -3.165), YD-cost ( $t$ -value = -2.274), YF-overall equipment effectiveness ( $t$ -value = -2.938), and YG-safety and morale ( $t$ -value = -1.684). The XD-enablers effect of kaizen is found significant with YE-flexibility and delivery ( $t$ -value =

**Table 3** Inter-item co-variance matrix

	XA	XB	XC	XD	XE	XF	XG	XH	YA	YB	YC	YD	YE	YF	YG
XA	0.335	0.312	0.298	0.224	0.269	0.312	0.278	0.322	0.304	0.356	0.227	0.218	0.218	0.241	0.223
XB	0.312	0.378	0.321	0.259	0.281	0.325	0.284	0.337	0.334	0.358	0.180	0.164	0.177	0.192	0.175
XC	0.298	0.321	0.630	0.372	0.466	0.528	0.490	0.556	0.456	0.540	0.268	0.302	0.334	0.314	0.326
XD	0.224	0.259	0.372	0.596	0.426	0.482	0.435	0.504	0.426	0.490	0.280	0.284	0.277	0.304	0.322
XE	0.269	0.281	0.466	0.426	0.650	0.597	0.547	0.641	0.551	0.631	0.393	0.430	0.413	0.436	0.446
XF	0.312	0.325	0.528	0.482	0.597	0.843	0.670	0.821	0.707	0.837	0.512	0.476	0.513	0.558	0.571
XG	0.278	0.284	0.490	0.435	0.547	0.670	0.718	0.714	0.619	0.711	0.436	0.445	0.456	0.478	0.490
XH	0.322	0.337	0.556	0.504	0.641	0.821	0.714	0.885	0.745	0.854	0.529	0.534	0.542	0.575	0.584
YA	0.304	0.334	0.465	0.426	0.551	0.707	0.619	0.745	0.832	0.810	0.528	0.532	0.526	0.545	0.605
YB	0.356	0.358	0.540	0.490	0.631	0.837	0.711	0.854	0.810	0.990	0.654	0.633	0.643	0.672	0.691
YC	0.227	0.180	0.268	0.280	0.393	0.512	0.436	0.529	0.528	0.654	0.662	0.488	0.488	0.518	0.533
YD	0.218	0.164	0.302	0.284	0.430	0.476	0.445	0.534	0.532	0.633	0.488	0.641	0.492	0.552	0.582
YE	0.218	0.177	0.334	0.277	0.413	0.513	0.456	0.542	0.526	0.643	0.488	0.492	0.661	0.475	0.497
YF	0.241	0.192	0.314	0.304	0.436	0.558	0.478	0.575	0.545	0.672	0.518	0.552	0.475	0.673	0.585
YG	0.223	0.175	0.326	0.322	0.446	0.571	0.490	0.584	0.605	0.691	0.533	0.582	0.497	0.585	0.760

**Table 4** Karl Pearson correlation matrix of input and output factors

Issues/variables	Management policies and commitment XA	Training and involvement of employees XB	Working environment XC	Enablers effect on kaizen XD	Skilled labour and latest machinery XE	Role of innovation XF	Role of supplier development XG	Customer relationship XH
Overall business performance YA	0.602**	0.622**	0.732**	0.776**	0.856**	0.892**	0.896**	0.908**
Waste elimination YB	0.618**	0.586**	0.745**	0.782**	0.860**	0.927**	0.902**	0.912**
Quality YC	0.510**	0.381*	0.478**	0.578**	0.693**	0.734**	0.715**	0.731**
Cost YD	0.479**	0.338*	0.527**	0.573**	0.740**	0.666**	0.713**	0.721**
Flexibility and delivery YE	0.504**	0.385*	0.613**	0.588**	0.747**	0.754**	0.769**	0.231
Overall equipment effectiveness YF	0.527**	0.395*	0.547**	0.612**	0.750**	0.779**	0.765**	0.774**
Safety and morale YG	0.441**	0.327*	0.514**	0.588**	0.694**	0.721**	0.710**	0.713**

\*\* Correlation is significant at the 0.01 level (2-tailed)

\* Correlation is significant at the 0.05 level (2-tailed)

**Table 5** Multiple regression among kaizen implementation input factors and output factors

Performance parameters	Significance <i>i/p</i> factor	Beta value $\beta$	<i>t</i> -value	Significance ( <i>p</i> -value)	<i>R/R</i> <sup>2</sup> -value	<i>F</i> -value
YA	XB	0.222	2.450	0.21	0.937/0.878	26.00
	XC	-0.337	-2.165	0.039		
YB	XF	0.684	2.910	0.007	0.944/0.891	29.564
YC	XC	-0.749	-3.165	0.004	0.847/0.717	9.172
	XE	0.796	1.999	0.055		
YD	XC	-0.532	-2.274	0.031	0.850/0.723	9.474
	XE	1.270	3.228	0.003		
YE	XD	-0.636	-2.226	0.034	0.843/0.711	8.931
	XE	0.815	2.028	0.052		
YF	XA	0.399	2.032	0.051	0.880/0.775	12.496
	XC	-0.619	-2.938	0.006		
	XD	-0.530	-2.101	0.044		
	XE	0.939	2.649	0.013		
YG	XC	-0.457	-1.684	0.103	0.793/0.628	6.123

-2.266) and YF-overall equipment effectiveness (*t*-value = -2.101). Similarly, XE-skilled labour and latest machinery issues is significant with YC-quality (*t*-value = 1.996), - cost (*t*-value = 3.228), YE-flexibility and delivery (*t*-value = 2.028), and YF-overall equipment effectiveness (*t*-value = 2.649). The factor XF-role of innovation issues is found significant with YB-waste elimination (*t*-value = 2.910).

This study includes the two tailed *T*-test analysis to analyse the three phases made on the time period. Basically, three phases of time are examined or evaluated to find the short, medium and long-term effects of kaizen implementation on performance parameters in organization [7]. Three phases are made on the basis of their experiences with Kaizen initiatives. The justification for each of these time periods or phases is explained below in detail [8].

**Period of transition** (less than 2 years of kaizen implementation): Period of transition is the time period or phase in which implementation of kaizen is at initial stages. The organizations are making efforts to overcome losses and some changes in efforts, policies, and working culture is done. The period of transition phase normally goes for less than 2 years from the beginning of kaizen implementation. As per the collected data, it was observed that there were a total number of 11 organizations in this period.

**Period of stability** (more than 2 years but up to 6 years of kaizen implementation): Period of stability is the period during which the improvement drives are stabilized and the organization starts getting benefit of kaizen implementation. The time period for this phase is considered to be more than 2 years but up to 6 years of implementation. As per the collected data, it was observed that there were a total number of 16 organization in this period.

**Period of maturity** (more than 6 years of kaizen implementation): Period of maturity is the period when the organization is habitual to the benefits and improvements made after implementing kaizen. It was observed that the organizations which implemented kaizen gets various benefits in term of competitive and strategic edge of performance, cost, quality, waste elimination, and flexible deliveries in comparison to the organizations who are at initial stages of implementing kaizen. As per the collected data, it was observed that there were a total number of 11 organizations.

The results for two tailed t-test for three phases shown in Tables 6, 7, and 8 reveals that t-values for phase t (II/III) for performance parameters YA (1.620), YB (1.553), YC (1.820), YD (1.307), YE (1.622), YF (5.940), YG (4.707) are found to be much better than the values for *t* (I/II) and *t* (I/III). Basically, these groups are based on the no. of years for the implementation of kaizen as well as on the basis of the mean obtained from their replies. The results clearly indicate that the organizations implementing kaizen from more than 2 years are getting best results in their outputs. The organizations implementing kaizen from more than 6 years are at their peaks in getting best results.

**Table 6** T-test analysis of phase-I and phase-III

Performance indicators	Phase-I		Phase-III		<i>t</i>
	Mean	SD	Mean	SD	
YA	1.8939	0.46710	3.5758	0.23995	10.622
YB	1.6818	0.34524	3.6061	0.17115	16.562
YC	2.0909	0.42239	3.4318	0.29772	8.606
YD	2.0909	0.44149	3.5091	0.20715	9.645
YE	2.1455	0.58713	3.4909	0.31450	6.700
YF	1.9545	0.26968	3.8409	0.20226	18.559
YG	1.9818	0.47711	3.9636	0.08090	13.583

**Table 7** T-test analysis of phase-I and phase-II

Performance indicators	Phase-I		Phase-II		<i>t</i>
	Mean	SD	Mean	SD	
YA	1.8939	0.46710	3.2083	0.72137	5.309
YB	1.6818	0.34524	3.1771	0.89952	5.228
YC	2.090	0.42239	3.2500	0.68920	4.957
YD	2.0909	0.44149	3.2125	0.72835	4.549
YE	2.1455	0.58713	3.1750	0.58822	4.472
YF	1.9545	0.26968	3.1875	0.32275	10.401
YG	1.9818	0.47711	3.5250	0.30000	10.345

**Table 8** *T*-test analysis of phase-II and phase-III

Performance indicators	Phase-II		Phase-III		<i>t</i>
	Mean	SD	Mean	SD	
YA	3.2083	0.72137	3.5758	0.23995	1.620
YB	3.1771	0.89952	3.6061	0.17115	1.553
YC	3.2500	0.68920	3.4318	0.29772	1.820
YD	3.2125	0.72835	3.5091	0.20715	1.307
YE	3.1750	0.58822	3.4909	0.31450	1.622
YF	3.1875	0.32275	3.8409	0.20226	5.940
YG	3.5250	0.30000	3.9636	0.08090	4.707

## 4 Conclusion

The conclusion is given below:

- The Cronbach Alpha indicates that all values are greater than 0.8, which indicates the high reliability of the questionnaire and also every input, output is acceptable.
- The data reveals that the co-variance value with in a group is greater than the co-variance outside the group, which is recommended to be accepted.
- The correlation analysis shows that there is a strong correlation of customer relationship, role of innovation issues, skilled labour and latest machinery, role of supplier development.
- It was obtained that management policies and commitment, working environment issues, enablers effect on kaizen, skilled labour and latest machinery issues, and role of innovation issues are the critical success factors of the study.
- The results for two tailed *t*-test for three phases reveals that *t*-values for phase *t*(ii/iii) for performance parameters are found to be much better than the values for *t*(i/ii) and *t*(i/iii).
- Kaizen is beneficial in any kind of workplace.

## References

1. Bellgran M, Kurdve M, Hanna R (2019) Cost driven Green Kaizen in pharmaceutical production—creating positive engagement for environmental improvements. In: 52nd CIRP conference on manufacturing systems, pp 1219–1214
2. Kumar R (2019) Kaizen a tool for continuous quality improvement in Indian manufacturing organization. *Int J Math Eng Manag Sci* 4:452–459
3. Saini S, Singh D (2019) Impact of lean implementation on firm performance: a study of northern Indian SME's. *Int J Lean Six Sigma*
4. Dave Y, Sohani N (2019) Improving productivity through Lean practices in central India based manufacturing industries. *Int J Lean Six Sigma* 10:601–621

5. Singh J, Singh H, Singh G (2018) Productivity improvement using lean manufacturing in manufacturing industry of Northern India: a case study. *Int J Prod Perform Manag* 67:1394–1415
6. Sahoo S, Yadav S (2018) Lean implementation in small- and medium-sized enterprises: an empirical study of Indian manufacturing firms. *Benchmarking: Int J* 25:1121–1147
7. Srinivasan G, Shah N (2018) Kaizen and lean implementation in pharmaceutical industries: a review. *Asian J Pharm Clin Res* 11:58–63
8. Kumar S, AK Dhingra, Singh B (2018) Kaizen selection for continuous improvement through VSM-FUZZY-TOPSIS in small-scale enterprises: an Indian case study. *Adv Fuzzy Syst* 1–10



# Protection of Vital Facilities from the Threat of External Explosion Using D3o Material



Mostafa Dada, Bahaa Eddin Ghrewati, and Manas Ranjan Das

**Abstract** In this research, an unconventional method has been used to absorb and redistribute blast loads to protect the external walls of structures by pasting the D3o layer, which is a mixture of Non-Newtonian Fluid and Polymers. The explosion is a violent chemical reaction involving solids, dust, and gas, with rapid release of energy and hot gases. This phenomenon takes only a few milliseconds and results in intense pressures and temperatures (Karlos and Solomos in Calculation of blast loads for application to structural components, Publications Office of the European Union, Luxembourg, 2013). Because of the special characteristics of the D3o material, it receives shock energy, absorbs it, and converts it to heat within fractions of a second. Adding the D3o layer can be considered a practical method of covering and protecting pre-existing or under-progress facilities. Abaqus software was used to simulate reinforced concrete wall ( $5000 \times 4000$ ) mm and D3o material (20) mm. A pressure of  $P_r = 0.25$  MPa was applied to the external wall alone first. Then D3o material was pasted on the front face of the reinforced concrete wall and the same pressure was applied again. Two cases were compared. Adding a layer of D3o (20 mm thick) to the reinforced concrete wall reduced deformation by 24.62% and max stress by 43.85%.

**Keywords** Explosion · D3o · Non-newtonian fluid · Polymers · Abacus software

## 1 Introduction

In recent decades, attention to the behavior of structures under blast loading has increased due to the escalation of terrorist attacks around the world targeting vital structures that remain a growing problem in modern societies. However, the traditional method of designing structures against terrorist attacks is generally based on increasing the rigidity of the structural elements and raising the structure's bearing capacity to receive the loads resulting from the explosion, leading to an increase in

---

M. Dada · B. E. Ghrewati · M. R. Das (✉)  
Siksha O Anusandhan Deemed to be University, Bhubaneswar, Odisha, India  
e-mail: [manasdas@soa.ac.in](mailto:manasdas@soa.ac.in)

© The Author(s), under exclusive license to Springer Nature Singapore Pte Ltd. 2023  
P. Pradhan et al. (eds.), *Recent Advances in Mechanical Engineering*,  
Lecture Notes in Mechanical Engineering,  
[https://doi.org/10.1007/978-981-16-9057-0\\_51](https://doi.org/10.1007/978-981-16-9057-0_51)

475

the structure’s weight or the threatened element. This again means that it is difficult to secure a pre-existing facility. Therefore, researchers are seeking a practical and quick technique to modify or secure pre-existing facilities, especially in the military community. Similar methods or techniques are proposed by adding a protective layer to the outer walls. In 2016, Ashish Tiwary [2] simulated several types of reinforced concrete walls: single, L, and U under air-blast and surface-blast using “ANSYS AUTODYN” software. Adding a thin steel plate (5 mm) as a cover to protect the exterior face of concrete walls reduces the pressure by 20% that reaches the concrete surface in a single reinforced concrete wall case. In 2020, Arief N. Pratomo [3] conducted a field experiment on reinforced concrete walls with an aluminum foam sandwich (100 mm) as cover exposed to an 8 kg TNT blast load with and without cover. The aluminum foam sandwich absorbed more than 98.3% of the energy from the impact.

## 2 Review of Literature on D3o

In 2017, Miao Tang [4] conducted several tests regarding (Internal Cell Structural Parameters, Rheological Properties, Mechanical Properties), which was the premier reference for this work Figs. 1, 2, 3, 4 and 5.

Storage modulus  $G'$ , loss modulus  $G''$  expresses the viscoelastic behavior. The loss  $\tan \delta$  expresses the material’s ability to dissipate energy. The compressive Stress–Strain curve represents the elastic and plastic behavior of D3o material and those parameters that have been used as input in Abaqus software.

**Fig. 1** Storage modulus  $G'$  and loss modulus  $G''$  changes versus angular frequency  $\omega$  [4]

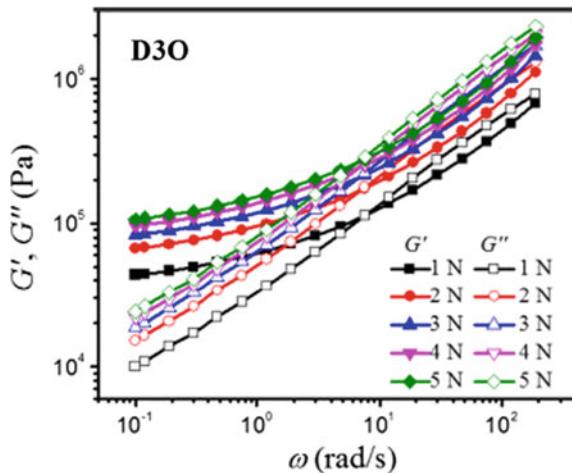


**Fig. 2** Changes in the normalized storage modulus  $G'$  and loss modulus  $G''$  by the moduli at 0.1 rad/s versus angular frequency  $\omega$  [4]

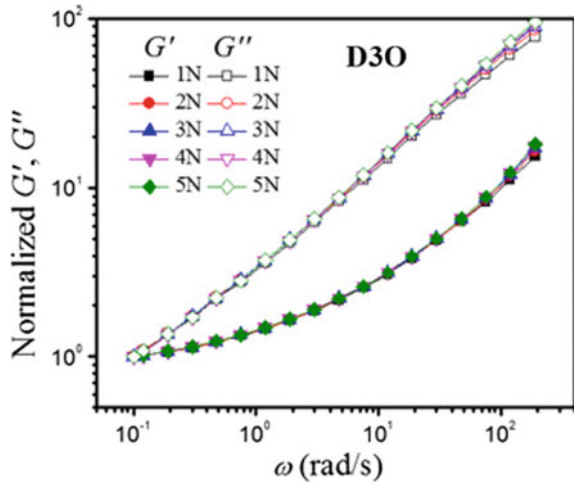
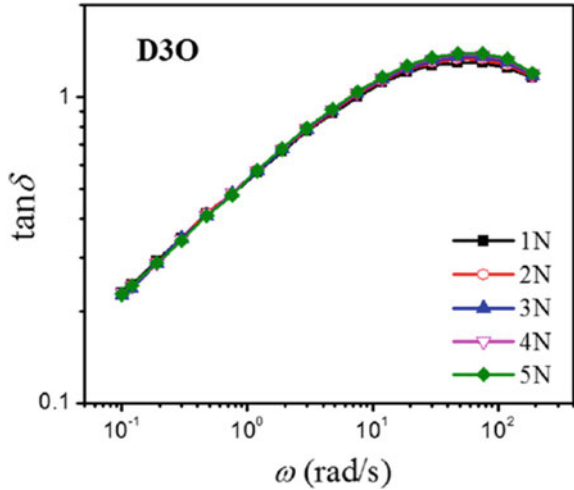


**Fig. 3** Changes in  $\tan \delta$  versus angular



### 3 Design Parameters

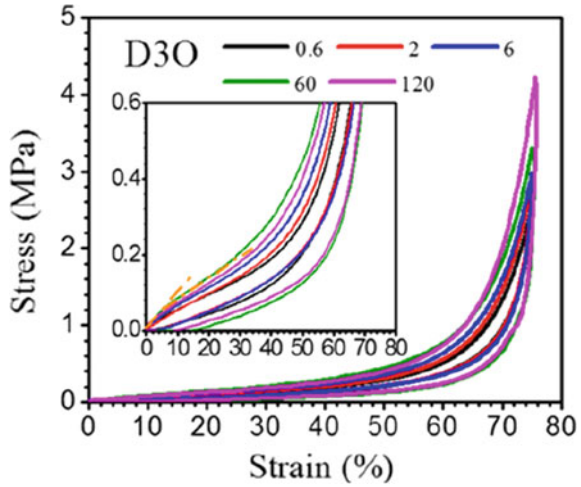
We have several variables we need to put fixed to find design parameters ( $W$ ,  $R$ ), and based on the Hopkinson–Cranz equation of  $Z = \frac{R}{\sqrt[3]{W}}$  (Scale law) [1], and Kingery-Bulmash Curves [5]:

Input parameters (fixed):

$$P_r = 2.5 \text{ MPa}, t_0 = 10 \text{ MS.}$$

$$P_r = 2.5 \text{ MPa}; Z = \frac{R}{\sqrt[3]{W}} = 1.58.$$

**Fig. 4** Stress–strain curves [4]



$Z = 1.58, t_0 = 10 \text{ MS}; \frac{t_0}{\sqrt[3]{W}} = 2; W = 125 \text{ kg of TNT.}$   
 $Z = \frac{R}{\sqrt[3]{W}} = 1.58; R = 7900 \text{ mm.}$

### 4 Methodology

Abaqus software was used to simulate a reinforced concrete wall of dimension (5000 × 4000) mm, D3o material (20 mm thick). Two models have been created. The first one was a reinforced concrete wall standing alone against  $P_r = 2.5 \text{ MPa}$  reflected pressure. Then, in the second model, we pasted (20 mm thick) D3o to the exterior face of the reinforced concrete wall under the same  $P_r = 2.5 \text{ MPa}$  reflected pressure. Shape deformation as the stop point and the standard concerning the reflected pressure is assumed in simulating a wall undergoing an explosion. According to ACI 318-08 [7], the permissible deformation can be calculated by Eq. (1). In the end, a comparison between the models was performed (Table 1).

$$L_{pr} = \frac{L}{360} = 138.88 \text{ mm (Permissible deformation)} \tag{1}$$

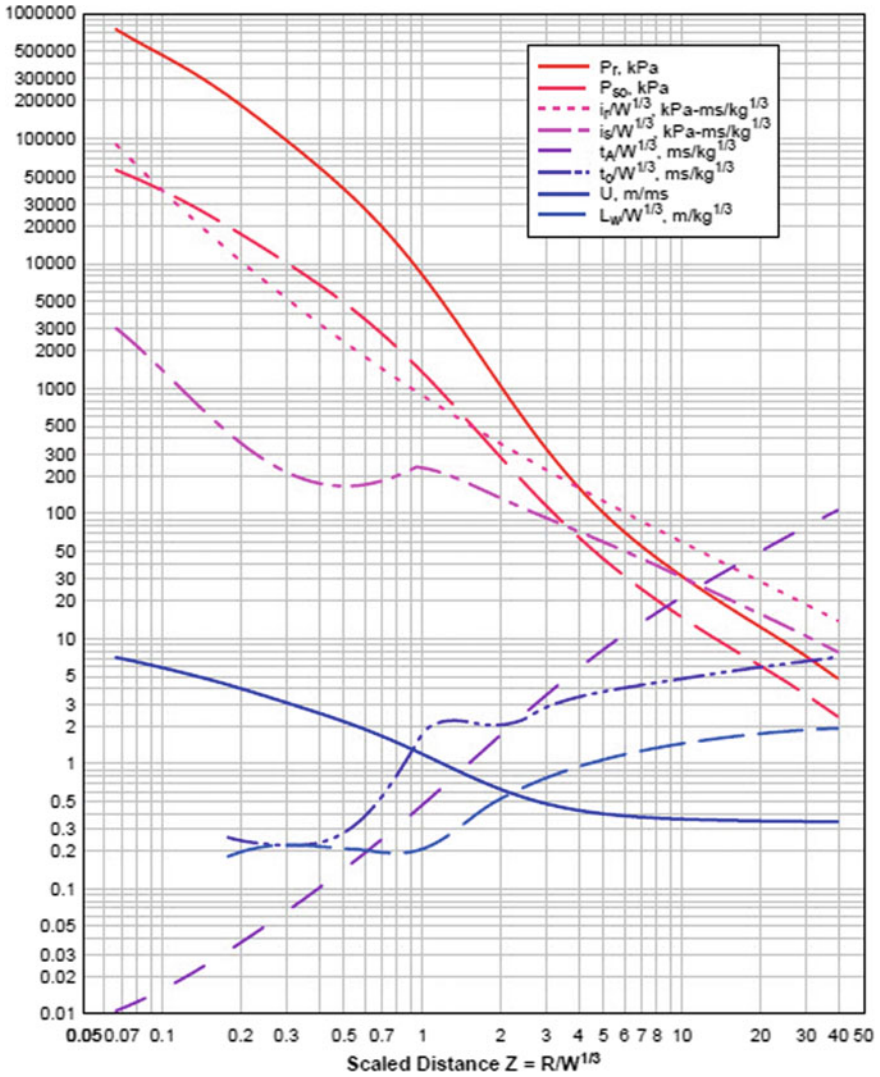


Fig. 5 Kingery–Bulmash curve for the surface-blast condition during the positive phase [5]

Table 1 Design parameters

Model	$t_0$ ms	$P_r$ mpa	$Z$	$W$ (TNT Kg)	$R$ (mm)
RC wall	10	2.5	1.58	125	7900
RC wall + D3o	10	2.5	1.58	125	7900

## 5 Results and Discussion

### 5.1 RC Model

In the first model, we had the reinforced concrete wall standing alone against the blast wave, and the max displacement  $U_z$  (130.7 mm) was observed in the middle part, as shown in Fig. 6 in red.

And the maximum Von Mises stress was observed on the front face of the reinforced concrete wall was  $p$  (17.88) MPa, as shown in Fig. 7 in red, which makes sense because the reinforced concrete wall is fixed against the movement of  $X$ ,  $Y$ , and  $Z$  from the sides.

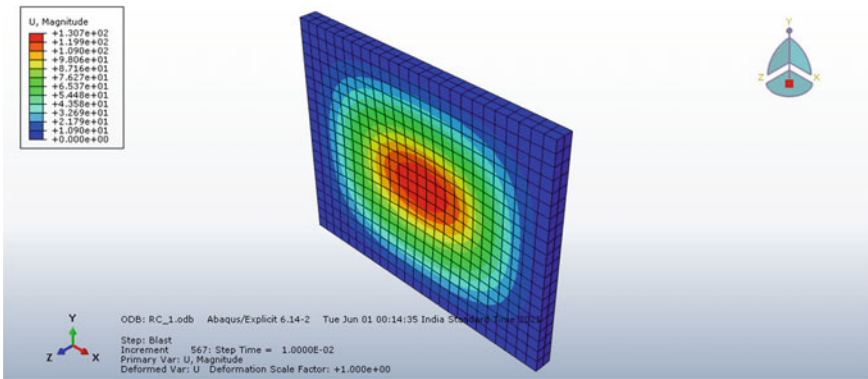


Fig. 6 RC/ $U_z$  displacement

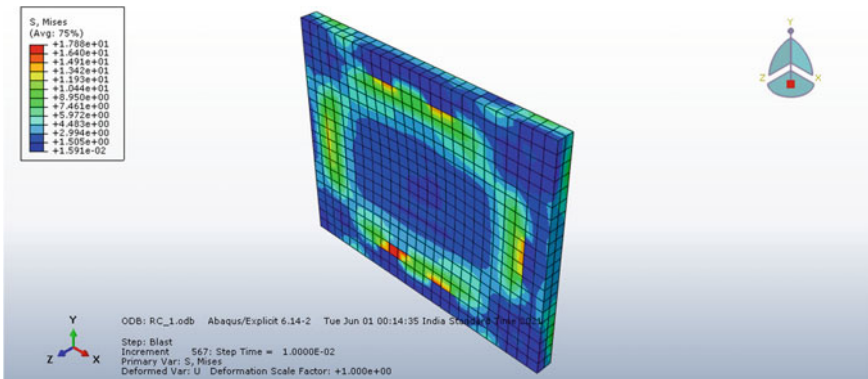


Fig. 7 RC/ $p$  von mises stresses RC wall front face

### 5.2 RC + D3o Model

In the second model, when we pasted the D3o layer to the front surface of the reinforced concrete wall, the max displacement  $U_z$  (98.10) mm was observed in the middle, as shown in Fig. 8 in red, so the D3o layer helped in reducing the max displacement from  $U_z$  (130.7) mm to  $U_z$  (98.10) mm.

During the blast incident, D3o began to absorb energy and convert it to heat up to a certain point, and its hardness increased at the same time. At this point, the D3o material starts to transfer more residual pressure to the reinforced concrete wall, and stresses start to be observed on the D3o layer as well. The maximum Von Mises stress was observed on the D3o front face  $p$  (3.93) MPa in red in Fig. 9.

The residual pressure that reaches the front face of the reinforced concrete wall from the D3o layer and the maximum Von Mises stress  $p$  (10.4) MPa in red is barely noticed as shown in Fig. 10 as compared to  $p$  (17.88) MPa without D3o. This is

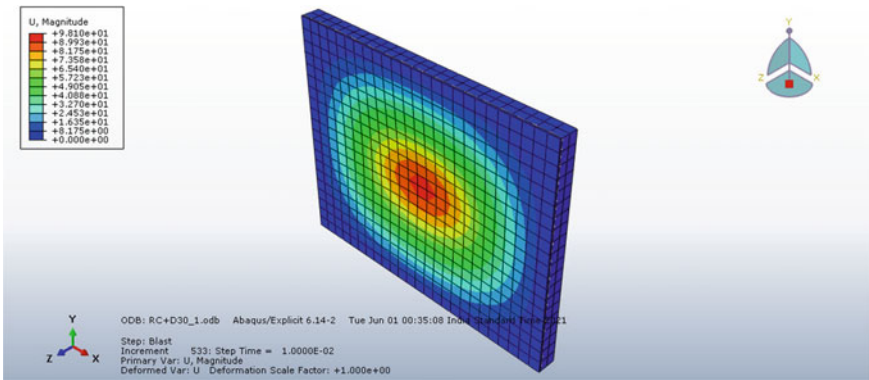


Fig. 8 RC + D3o/ $U_z$  displacement

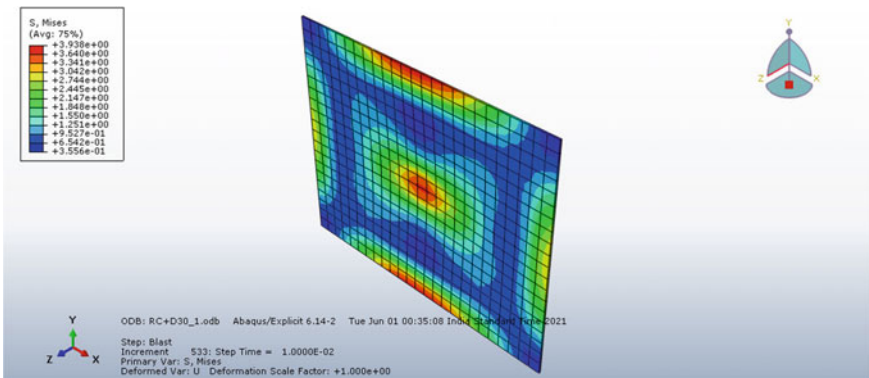


Fig. 9 RC + D3o/ $p$  von mises stresses D3o front face

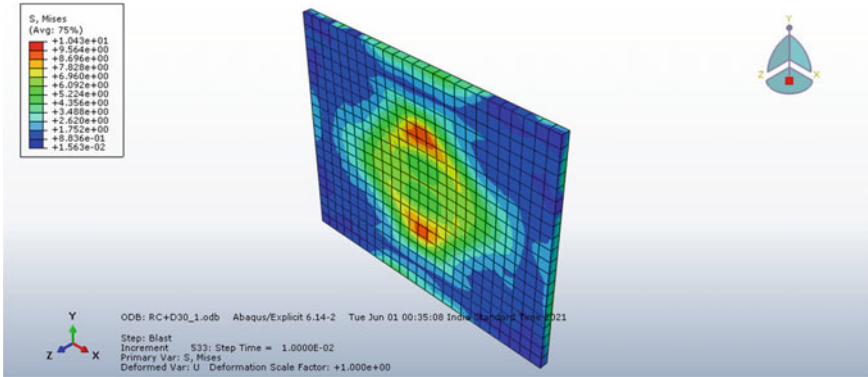


Fig. 10 RC + D30/p von mises stresses RC front face

because the D30 layer absorbed part of the pressure and redistributed the residual pressure over the front face of the reinforced concrete wall.

## 6 Conclusions

- Based on the Abaqus software simulation, adding a 20 mm thick layer of D30 to the reinforced concrete wall reduced the deformation by 24.62% and the max stress by 43.85%.
- D30 absorbed blast wave energy and converted it into heat through the polymer-diluted fluid transformation from flexible to solid (rapid-impact pressure state).
- Because of D30’s unique properties, the particles (polymer-chain) velocity movement distributed in the dilution fluid is less than the impact velocity of the air particles, thus reducing the residual pressure impact velocity that will affect the reinforced concrete wall.
- This method can be considered as a practical technique for covering and protecting pre-existing or under-progress facilities with conservative respect to the increase in temperature.

## References

1. Karlos V, Solomos G (2013) Calculation of blast loads for application to structural components. Publications Office of the European Union, Luxembourg
2. Tiwari AK, Tiwary AK, Dhiman A (2016) Analysis of concrete wall under blast loading. Int J Comput Appl 975:8887



3. Pratomo AN, Santosa SP, Gunawan L, Widagdo D, Putra IS (2020) Numerical study and experimental validation of blastworthy structure using aluminum foam sandwich subjected to fragmented 8 kg TNT blast loading. *Int J Impact Eng* 146:103699
4. Tang M, Huang G, Zhang H, Liu Y, Chang H, Song H, Xu D, Wang Z (2017) Dependences of rheological and compression mechanical properties on cellular structures for impact-protective materials. *ACS Omega* 2(5):2214–2223
5. Kingery CN, Bulmash G (1984) Airblast parameters from TNT spherical air burst and hemispherical surface burst, ARBRLTR-02555. MD: US Army Ballistic Research Laboratory, Aberdeen Proving Ground
6. D3o company. [www.D3o.com](http://www.D3o.com)
7. ACI Committee (2008) Building code requirements for structural concrete (ACI 318–08) and commentary. American Concrete Institute

# Investigation on Coefficient of Heat Transfer Through Impact of Engine Vibration



Ashwini Kumar, Aruna Kumar Behura, Gaurav Dwivedi, and D. N. Thatoi

**Abstract** Vibration plays an important role for enhancement of rate of heat transfer in any moving parts or device. Number of heat transfer equipment which works under vibrating conditions to influence the heat transfer rate to a great extent, such as motor car radiators, cooling of machine tools, and refrigerant condensers of household refrigerators. Proper vibration intensity might be more effective for heat transfer in such cases. The present work represents that the effect of vibration on convection heat transfer coefficient for flow of air in a pipe. The term vibration covers the cases in which a movement back and forth in a regular rhythm is induced either over the outside part or the means of doing something or the both by the fact of external forces. Also, a comparison of enhanced heat transfer rate for both with and without vibrational effect has been shown and has found that for varying values of Reynolds number, heat transfer decreases after a certain value of vibrational intensity, and for a particular value of dimensionless number,  $a/D$ , the relative increase in heat transfer is the maximum.

**Keywords** Nusselt number · Reynolds number · Vibration · Heat transfer coefficient · Frequency · Amplitude

---

A. Kumar

Department of Mechanical Engineering, SGT University, Gurugram, India

A. K. Behura (✉)

School of Mechanical Engineering, Vellore Institute of Technology, Vellore, India

e-mail: [akbehura.nit@gmail.com](mailto:akbehura.nit@gmail.com)

G. Dwivedi

Energy Centre, Maulana Azad National Institute of Technology, Bhopal, India

D. N. Thatoi

Department of Mechanical Engineering, ITER, S'O'A University, Bhubaneswar, India

© The Author(s), under exclusive license to Springer Nature Singapore Pte Ltd. 2023

P. Pradhan et al. (eds.), *Recent Advances in Mechanical Engineering*,

Lecture Notes in Mechanical Engineering,

[https://doi.org/10.1007/978-981-16-9057-0\\_52](https://doi.org/10.1007/978-981-16-9057-0_52)

## 1 Introduction

The vibrational influence on convective heat transfer rate has been investigated not to a great extent. However, it has been observed that an appreciable influence could only be obtained if the fluctuation is of enough intensity to change the central attribute of the boundary layer in the vicinity of the surface of the heat transfer, otherwise negligible. The influence of  $y$ -direction vibration on the transfer of heat rate from an  $x$ -direction tube inserted in a water tank was investigated [1] vibration, transfer of heat was reported to enhance. The work of Lemlich [2] is for horizontal heated wires to air in imposed of flow in parallel direction. The study [3] represented that enhancement in transfer of heat was influenced through the vibrational mean velocity to the air stream velocity. Tusi [4] found 25% enhancement in coefficient of transfer of heat for transverse vibration in an instance of  $y$ -direction heated plane surface. The works [5, 6] showed that transfer of heat was not affected till a specific crucial vibrational intensity (described as the product of frequency and amplitude) was induced. Transfer of heat to water for fully developed flow of turbulent in pipes was reported by Harison et al. [7].

The influence of  $y$ -direction vibration in natural convection from  $x$ -direction cylinder has been reported [8], whereas the influence of vibration in transverse direction in free convection has been reported [9]. Introduction of vibrational Reynolds number has been made to represent the results in such cases. Most of the heat transfer phenomena are associated with air or gas flow through pipes, which require more efficient heat transfer. Utilization of roughness artificially of number of geometries has been extensively investigated to increase the rate of transfer of heat in pipes and ducts. The recent works of Ashwini et al. [10] and [11–21] described for three side's artificial roughened air heater have been investigated for such enhancement in coefficient of transfer of heat. And many more investigations have been conducted to show the increment of coefficient of transfer of heat [22–25], by utilizing various methodology (computational fluid dynamics, use of booster mirror, using transverse wires as roughness element, wire screen, and reviews on methodology for such enhancement of coefficient of transfer of heat). Although, the influence of vibrational effect on transfer of heat, which also enhances rate of transfer of heat needs, is a step forward in this area in which coefficient of transfer of heat for air flow in a pipe has been investigated. Also, a comparison of enhanced heat transfer rate for both with and without vibrational effect has been shown and has found that for varying values of Reynolds number, heat transfer decreases after a certain value of vibrational intensity, and for a particular value of dimensionless number,  $a/D$ , the relative enhance in transfer of heat is the maximum.



**Fig. 1** Experimental set-up

## 2 Experimental Setup and Procedures

To see the impact of vibration on coefficient of move of warmth in constrained convection, a test study was made. The test area was encircled by nichrome wire warmer and mounted on a mechanical shaker, which comprises an engine. Change inside the engine speed brought about vibration of recurrence and plenty-fullness of the vibration at various paces. A vibration eat up mounted on the test line and associated with the vibration meter estimated the recurrence and abundance of vibration. A shaft oscilloscope was wont to show the vibration. Temperature estimating thermocouples were taken care of to the computerized temperature marker, while pace of wind current chose through an opening meter with Prandtl manometer. Recurrence ran up to 140 c/s and adequacy to 2.5 mm, while the warming force went from 60 to 80.

The vibrational Reynolds number has been considered to take into account the vibration of frequency and amplitude. Data were collected in forced convection with and without vibration.

Figures 1 and 2 show the setup for experimentation and the portion for test analysis with the thermocouples arrangement, respectively.

## 3 Results and Discussions

Tables 1 and 2 represent the typical data collected and worked out values of results, viz. Reynolds number, Nusselt number, and coefficient of transfer of heat for the two case (with and without vibrational influence). Figure 3 typically represents the results

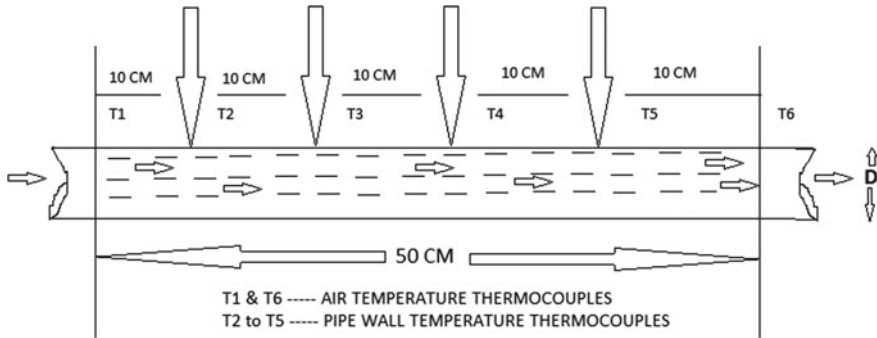


Fig. 2 Test section

Table 1 Without vibration

Temperature (°C)	Manometer (m)	Watt (W)	Frequency (Hz)	Amplitude (mm)	Re	h (W/mK)	Nu
314.3	0.11	80	0	0	14,938	41.8	42.9
316.3	0.12	80	0	0	15,473	43.6	44.4
315.9	0.13	80	0	0	16,129	45.2	46.1
315.5	0.14	80	0	0	16,772	46.6	47.7
315.1	0.15	80	0	0	17,391	47.6	48.7

Table 2 With vibration

Temperature (°C)	Manometer (m)	Watt (W)	Frequency (Hz)	Amplitude (mm)	Re	h (W/mK)	Nu
314.5	0.11	80	100	1	14,931	44.2	45.3
316.0	0.12	80	100	1	15,495	46.1	47.0
315.5	0.13	80	100	1	16,093	47.4	48.3
316.5	0.14	80	100	1	16,701	48.6	49.5
315.3	0.15	80	100	1	17,376	50.5	51.6

in between the coefficient of transfer of heat (Nusselt number) and flow Reynolds number for the vibrational and non-vibrational cases.

The curves represent that transfer of heat enhances with enhancing values of Reynolds number. Also, it is quite clear that for higher values of vibrational intensities, heat transfer is higher for the equal value of Reynolds number. Figure 4 typically represents the order of heat transfer increment for varying values of fluid flow pressure drop and vibrational intensity. It could be seen that for every value of flow pressure drop (Reynolds number), heat transfer decreases after a certain value of vibrational intensity (estimated in between  $a_f = 0.5$  to  $0.20$ ), i.e., a particular value of vibrational intensity ( $a_f$ ) might respond to the maximum heat transfer. Figure 5 typically

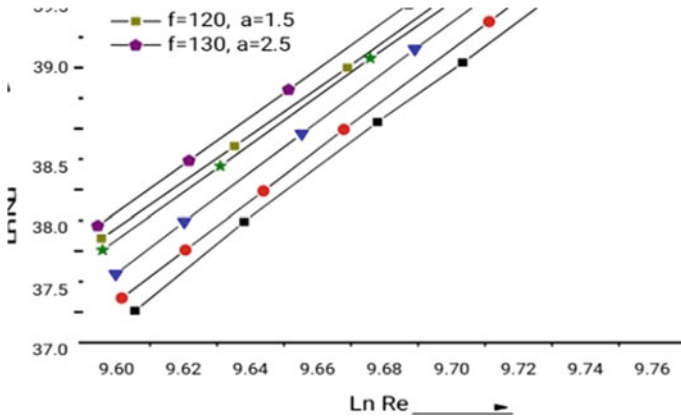


Fig. 3 Results between Re and Nu

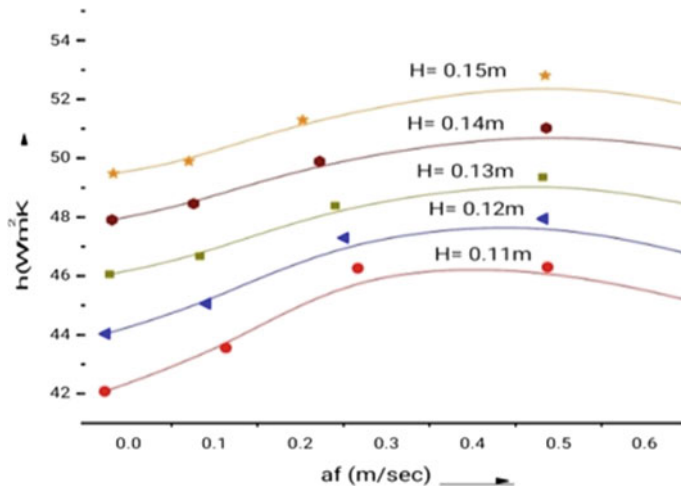


Fig. 4 Heat transfer enhancement for varying pressure drop and intensity

represents enhancement of transfer of heat because of vibration as compared to that of non-vibrational case as a function of dimensionless parameter  $a/D$ . It could be seen that the value of a particular  $a/D$  (estimated to be equal to 0.060); the relative increase in heat transfer is the maximum.

Correlations of the following form have been tried to work out for the value of relative increase in coefficient of transfer of heat with the help of the curves within the range of the values of parameters investigated:

$$h_v/h_0 = 0.99 + 1.72(a/D) \tag{1}$$

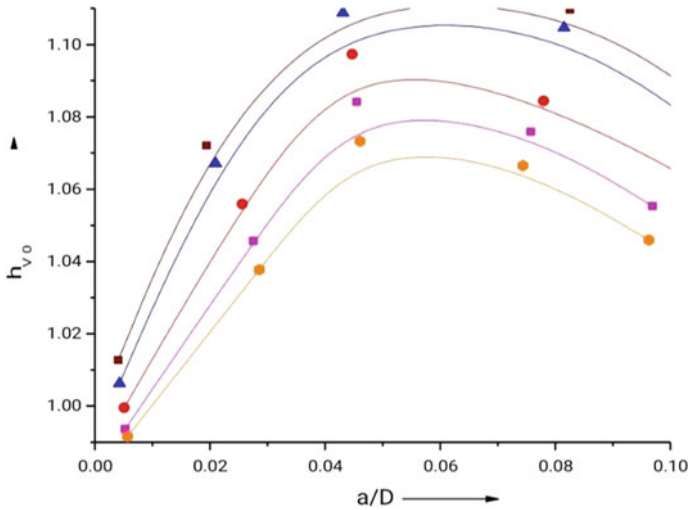


Fig. 5 Heat transfer versus non-vibrational function

for  $0 < a/D < 0.054$

$$h_v/h_0 = 1.135 + 0.83(a/D) \tag{2}$$

for  $a/D > 0.60$

The relation of heat transfer augmentation behind any heat transfer augmentation technique is due to induced turbulences in laminar boundary layer or more precisely in the laminar sub-layer, invariably associated with enhance in pressure drop. In the case of vibration, it could be attributed that both the flow Reynolds number and vibration influence turbulence together in the laminar sub-layer resulting in increase of transfer of heat, as could be seen from results. From Figs. 4 and 5, the possibility of the maximum heat transfer could be explored at a particular values of vibrational intensity for every values of flow Reynolds number, which might be a very important and desirable requirement for designing the heat transfer equipment acting under vibrational conditions to optimize for critical vibration to give the higher value of transfer of heat and lower value of pressure drop, and it needs a more and deep inside into the subject.

With the help of the results worked out within the available data, an attempt has been made to find correlations of the form as under for the vibrational case:

$$Nu = A_1 Re'' Pr''' (1 + A_2 Re''''') \tag{3}$$

Putting the value of  $A_1$  in Macadam's equation in simple case (i.e., without vibration) written asi:

$$\text{Nu} = 0.023 \text{Re}^{0.8} \text{Pr}^{0.4} \quad (4)$$

Equation (3) could be replaced as:

$$\text{Nu} = 0.023 \text{Re}'' \text{Pr}''' (1 + A_2 \text{Re}'''' ) \quad (5)$$

From the results available within the range of parameters studied, the values of  $n'$ ,  $n''$ , and  $A_2$  have been estimated to be 0.77, 0.4, and 284.85, respectively, such that Eq. (5) could be written as:

$$\text{Nu} = 0.023 \text{Re}^{0.77} \text{Pr}^{0.4} (1 + 284.85 \text{Re}'''' ) \quad (6)$$

The values of  $n'''$  in Eq. (6) for different vibrational intensities could be expressed as Eq. (7–10):

$$N''' = 0.030, \quad \text{for } 0 < a_f < 100 \quad (7)$$

$$N'' = 0.031, \quad \text{for } 100 < a_f < 180 \quad (8)$$

$$N''' = 0.029, \quad \text{for } 180 < a_f < 260 \quad (9)$$

$$N'''' = 0.028, \quad \text{for } 260 < a_f < 350 \quad (10)$$

## 4 Conclusions

On the foundations of above ideas and discussions, following measure conclusions have been found:

1. With enhancement in vibrational intensity, Nusselt number increases and hence the heat transfer coefficient.
2. Enhancement in heat transfer coefficient is up to a certain value of vibrational intensity, beyond which it seems to decrease.
3. It has been found that for varying values of Reynolds number, heat transfer decreases after a certain value of vibrational intensity.
4. It has been found that for a particular value of dimensionless number,  $a/D$ , the relative enhance in heat transfer is the maximum.
5. It needs a more extensive investigation to establish the behavior of vibration on heat transfer coefficient for different fluids under various vibrating situations.



## References

1. Martinelli RC, Boeiter LMK (1938) The effect of vibration upon the free convection from a horizontal tube. In: Proceedings of 5th international congress of applied mechanics, p 578
2. Lemlich R (1955) Effect of vibration on natural convection heat transfer. *Ind Eng Chem* 47(6):1175–1180
3. Anatanarayanan R, Ramchandran A (1958) Effect of vibration on heat transfer from a wire to air in parallel flow. *Trans ASME* 80:1426
4. Tusi Y (1953) The effect of vibration on heat transfer coefficient. PhD Thesis, Ohio State University
5. Shine A (1957) The effect of transverse vibration on the heat transfer rate from a heated vertical plate. M.S. Thesis, Ohio
6. Deaver AJ, Penny WR, Jefferson TB (1962) Heat transfer from an oscillating horizontal wire to water. *J Heat Transfer* 84C:251–256
7. Harison WB, Boleter WC, Jackson TW, Low A, Thomas FA (1972) Heat transfer to vibrating air columns. Final report, Project No. A-183, NACA N-49857
8. Lemlich R, Rao MA (1965) The effect of transverse vibration on free convection from a horizontal cylinder. *Int J Heat Mass Transfer* 8:27–33
9. Dawood AS, Manocha BL, Ali SMJ (1981) The effect of vertical vibration on natural convection heat transfer from a horizontal cylinder. *Int J Heat Mass Transfer* 24(1):491
10. Prasad BN, Kumar A, Singh KDP (2015) Optimization of thermo hydraulic performance in three sides artificially roughened solar air heaters. *Sol Energy* 111:313–319
11. Abuşka M (2018) Energy and exergy analysis of solar air heater having new design absorber plate with conical surface. *Appl Therm Eng* 131:115–124
12. Ansari M, Bazargan M (2018) Optimization of flat plate solar air heaters with ribbed surfaces. *Appl Therm Eng* 136:356–363
13. Kumar A, Prasad BN, Singh KDP (2016) Performance characteristics of three sides glass covered smooth solar air heaters. *Transylvanian Review* 24(11):3247–3256
14. Kumar A, Alam M (2016) A review on comparative study of thermal performance of artificially roughened solar air heaters. *Int Res J Adv Eng Sci* 01(2):4–12
15. Bachlaus M, Pandey MK, Mahajan C, Shankar R, Tiwari MK (2008) Designing an integrated multi-echelon agile supply chain network: a hybrid Taguchi-particle swarm optimization approach. *J Intell Manuf* 19:747–761
16. Bakri B, Eleuch O, Ketata A, Driss S, Driss Z, Benguesmia H (2018) Study of the turbulent flow in a newly solar air heater test bench with natural and forced convection modes. *Energy* 161:1028–1041
17. Belmecheri F, Prins C, Yalaoui F, Amodeo L (2013) Particle swarm optimization algorithm for a vehicle routing problem with heterogeneous fleet, mixed backhauls, and time windows. *J Intell Manuf* 24:775–789
18. Behura AK, Rout SK, Pandya H, Kumar A (2017) Thermal analysis of three sides artificially roughened solar air heaters. *Energy Procedia* 109:279–285
19. Bliss RW (1959) The derivation of several plate efficiency factor useful in the design of flat plate solar heat collectors. *Sol Energy* 3:55–64
20. Chamoli S, Chauhan R, Thakur NS, Saini JS (2012) A review of the performance of double pass solar air heater. *International Journal of Renewable and Sustainable Energy Reviews* 16:481–492
21. Chabane F, Moumimi N, Benramache S (2014) Experimental study of heat transfer and thermal performance with longitudinal fins of solar air heater. *Journal of Advance Research* 5:183–192
22. Coello CA, Pulido GT, Lechuga MS (2004) Handling multiple objectives with particle swarm optimization. *IEEE Trans Evol Computat* 8:256–279
23. Kumar A, Mahato A, Behura AK (2017) CFD analysis of solar air heater having corrugated absorber plate. *International Journal of Emerging Technology and Advanced Engineering* 7(9):575–5587

24. Dalle Donne M, Meyer L (1977) Turbulent convective heat transfer from rough surfaces with two-dimensional rectangular ribs. *Int J Heat Mass Trans* 20:582–620
25. Duffie JA, Beckman WA (2006) *Solar engineering of thermal processes*, 3rd edn. Wiley Interscience, New York

# Measurement of Local Spray Impingement Density by Using a Novel Patternator



Santosh Kumar Nayak, Siba Prasad Behera, Purna Chandra Mishra, and Achinta Sarkar

**Abstract** The current investigation confronts the measurement of the local impingement density of fluid spray which plays crucial role in ultra-fast cooling of heated metal surfaces in steel industry, electronic chip cooling, automobile industry for fuel injection, aviation, etc. An experimental setup was designed and fabricated to explore the influence of several controlling variables to enhance the spray density of a mechanical patternator. The flow behavior of the air atomizing nozzle was investigated at various parametric combinations and conditions. The working fluid used in this study was normal water-assisted with a range of air pressure from 2 to 4 bar. The amount of water was accumulated by the tubes attached to the patternator, and impingement density was calculated at the designated locations of the tubes. The effect of the controlling variables such as nozzle height, air, and water pressure upon the mass impingement density was analyzed. The experimental results revealed that the spray density was oval-shaped which is highly influence by nozzle height, air, and water pressure.

**Keywords** Impingement density · Patternator · Nozzle height · Spray cooling · Air and water

## 1 Introduction

The symmetrical and uniform nature of spray is describing by the term patternator which is employed to quantify as well as visualize the pattern of the spray emitted from a sprayer. Patteration is the distribution from any type of nozzle. A nozzle displaying “good patteration” desirable for the nozzle’s application such as metal quenching, combustion atomization, manufacturing quality control for research and development. Spray patteration has significant usage in various engineering and industrial purposes such as internal combustion engines, coatings, drying, agriculture, and consumer products. The droplet intensity has a strong clout on the spray heat

---

S. K. Nayak (✉) · S. P. Behera · P. C. Mishra · A. Sarkar  
School of Mechanical Engineering, KIIT University, Bhubaneswar, Odisha 751024, India  
e-mail: [sknayakfme@kiit.ac.in](mailto:sknayakfme@kiit.ac.in)

© The Author(s), under exclusive license to Springer Nature Singapore Pte Ltd. 2023  
P. Pradhan et al. (eds.), *Recent Advances in Mechanical Engineering*,  
Lecture Notes in Mechanical Engineering,  
[https://doi.org/10.1007/978-981-16-9057-0\\_53](https://doi.org/10.1007/978-981-16-9057-0_53)

transfer [1]. The study of droplet behavior during its motion through air has significance in several applications such as metal industry, agriculture, medical diagnosis, and various processes in automobile industry [2]. An early example of a patternator used for evaluating liquid rocket injectors is the one used by Rupe [3]. The spray peculiarities during metal quenching can be determined by using a mechanical patternator in association with a PDPA [4]. In automotive fuel injectors, the pulsed spray characteristics analyzed by a mechanical patternator [5]. The aftermath of uninterrupted and pulsed jets in crossflow was compared by using particle image velocimetry [6]. The mass flux as well as particle size distribution was measured by using a phase Doppler anemometer [7]. A correlation was developed for velocity concentration of passive scalar by using conventional imaging methods, i.e., PIV and planer laser-induced fluorescence (PLIF) [8]. The integral value method (IVM) and PDA are used for mass flux measurement [9]. The pattern of spray cross section measured by optical tomography [10]. The fuel sprays during combustion process were described by patternator having optimum resolution [11]. An optical patternator is employed to measure the spray patternation as well as spatial mass variation with the help of a light sheet produced by a laser diode and parallel lens [12].

The objective of the present investigation is to carry out a comprehensive analysis of the various controlling parameters which can enhance the mass impingement density (MID). The effects of various sequences of air and liquid pressure and target distance upon the mass impingement density were investigated. For designing persuasive spray cooling systems, it is highly imperative to compassionate the impact of MID and characteristics of spray parameters on cooling accomplishment.

## 2 Experimental Setup

The experimental structure in the current investigation dwells of the two main parts which are associated to form a design of system which is used to carry out the study of performance of the spray nozzle for measurement of local mass impingement density. The two main parts of the experimental setup are spray generator and a patternator. An air atomizing industry-oriented spray nozzle (1/4 J internal mix) supplied by Spraying System Company, Bangalore, India, was used in the current investigation. The spray generator consists of a centrifugal pump which boosts pressure of the supply water for spray formation. The two pressure regulators as well as a flow meter were used in the investigations to control and measure the flow rate of the water and air. A twin-cylinder reciprocating air compressor supplies high pressure air which is required for the atomization of the water particle. A patternator was designed and developed for the measurement of local MID. The schematic of the experimental setup was represented in Fig. 1.

Patternator was designed especially for analysis of the mass impingement density on spray cooling performance to enhance the cooling rate. The patternator contained arrays of 100 numbers of the graduated glass tubes having outer diameter ( $d_o$ ) 10 mm and inner diameter ( $d_i$ ) of 8 mm which is fixed on the hard plastic sheet of 4 mm

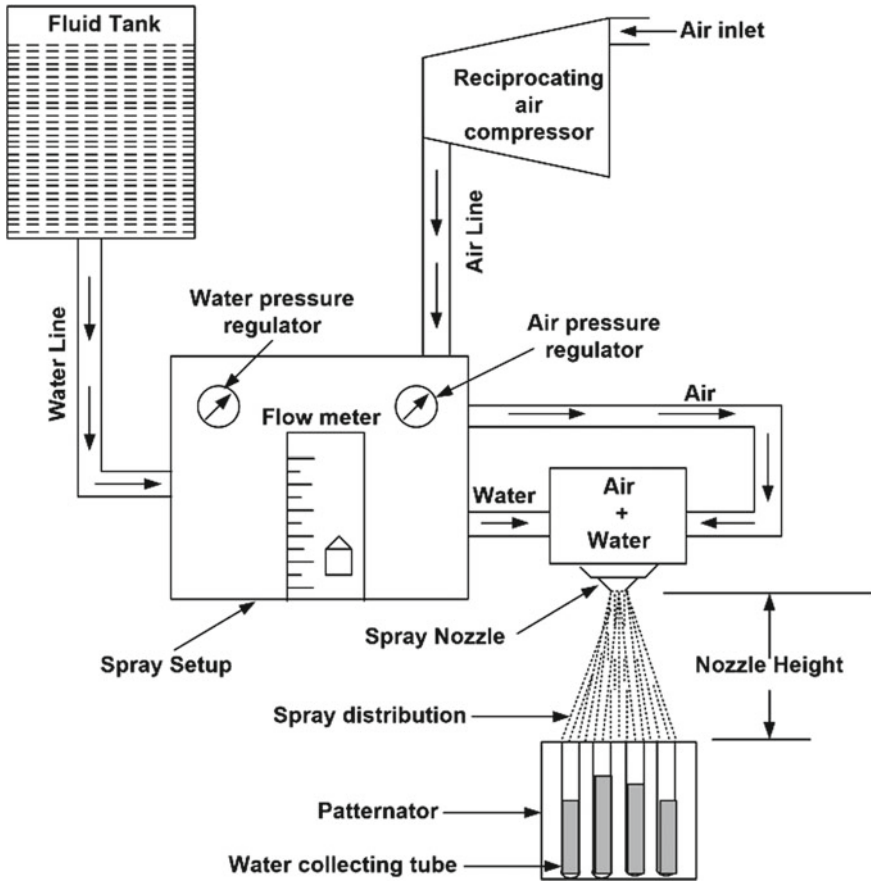
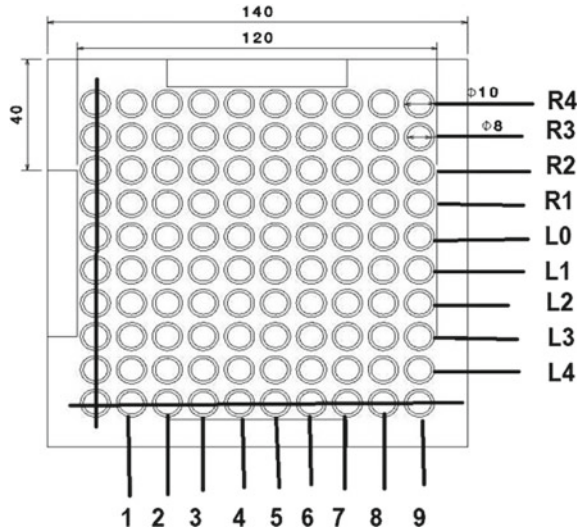


Fig. 1 Experimental setup

thickness having dimensions of 120 mm × 120 mm. The test tubes attached with are the measure of the mass impingement density of the air-assisted water sprays which are sprayed over the pattern sheet. The information regarding the tube position and tube number was proclaimed in Fig. 2. The liquid was collected separately in each tube during spray for a fixed time period  $\Delta t$ . For each nozzle height, air and water pressures were varied and spray was allowed to fall on the patternator surface. The local MID was calculated by knowing the volume of water collected by using Eq. (1).

$$\dot{m}_s = \frac{m_w}{(A \times \Delta t)} \times 3600 \tag{1}$$

**Fig. 2** Tube positioning and tube numbering in a spray patternator



where

$A$  Area of cross section of the container =  $(\pi/4) \times d_i^2 \text{ m}^2$ .

$d_i$  0.008 m.

$\Delta t$  Duration of spray = 10 s.

### 3 Results and Discussion

#### 3.1 Uncertainty Measurement

The uncertainty of measured parameters in the experimentation is recorded with repeated tests according to ASME test code [13]. Before conducting experiments, the instruments employed for measurement were calibrated to minimize the systematic errors so as to achieve accuracy in experiments. The maximum observed errors for the calculated variables have been professed in Table 1. Experiments were repeated for particular parametric condition, and the computed deviation from the average value was  $\pm 1.16\%$ .

#### 3.2 Effect of Air and Water Pressure on Flow Rate

The flow rate of water was calculated by collecting the water coming out of the spray nozzle at a particular duration for various air and liquid pressure combination. The air pressure plays vital role for controlling the amount of liquid required during

**Table 1** Measured experimental uncertainty

Significant parameters	Error
Collecting tubes (height, and diameter)	$B = \pm 0.05\%, \pm 0.05\%$
Nozzle height	$B = \pm 1.100\%$
Liquid flow rate	$B = \pm 1.20\%$
Air flow rate	$B = \pm 1.30\%$
Mass of water collected	$B = \pm 1.40\%$
Mass impingement density	$S = \pm 1.16\%$

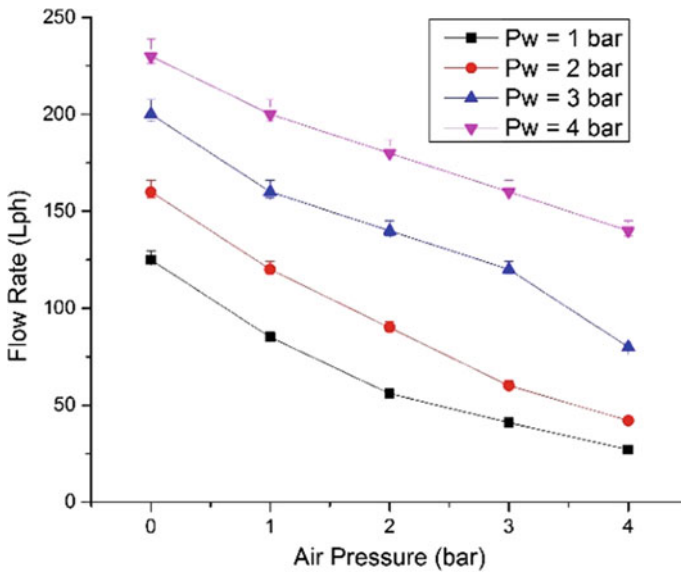


**Fig. 3** Consequence of air pressure upon flow rate at fixed water pressure

quenching process of steel as represented in Fig. 3. For a particular liquid pressure, the fluid flow rate drastically reduced due to increase in air pressure.

### 3.3 Effect of Air and Water Pressure on Local MID

The ramifications of the controlling variables such as air and liquid pressure and nozzle height upon the local MID were analyzed. The impact of each parameter on the MID was depicted in Fig. 4.

It is evident that the variation of MID with variation of air pressure is less significant than water pressure. The highest value of MID in this condition is accomplished

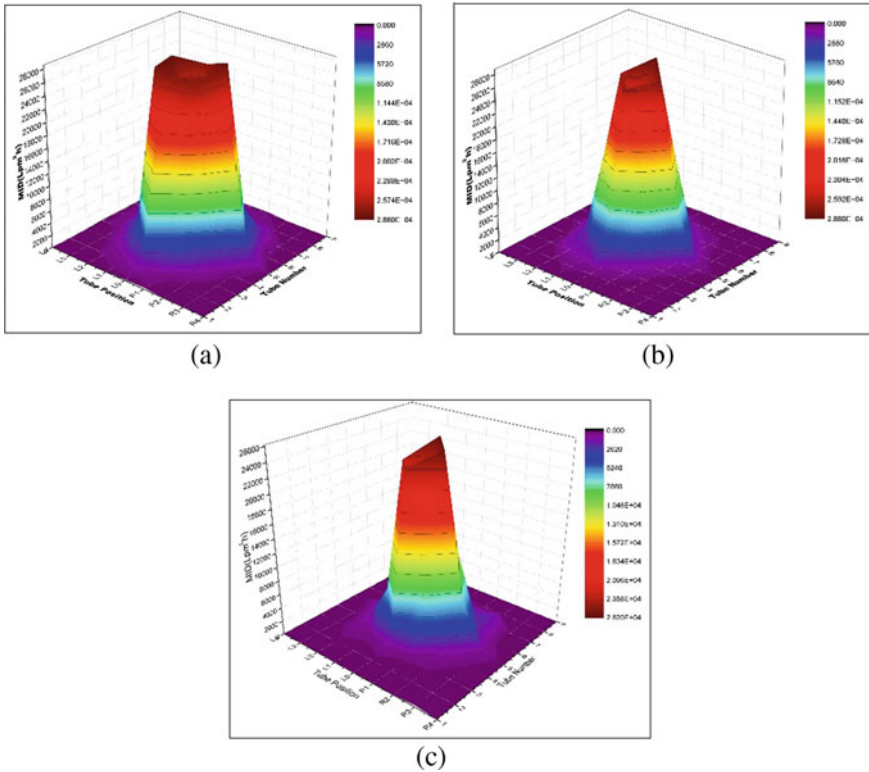


**Fig. 4** Distribution of local MID over the patternator surface at the time of spray at 4 bar liquid pressure, 120 mm target height and various air pressure (a) 2 bar, (b) 3 bar, and (c) 4 bar

at minimum value of air pressure and maximum level of liquid pressure and vice-versa. This is because of when the air pressure is more, there is more effective atomization of the water particle and maximum blown up of the water vapor which reduces the mass flux. The spray density was increased by escalation in water pressure and reduction in air pressure and hence enhance the mass flux.

### 3.4 Effect of Nozzle Height on Local MID

The impact of nozzle height on the MID was depicted in Fig. 5. With increase in spray distance, the impingement density drastically decreases. This is because the more is the distance, the more is the water-spread angle, and hence, a less amount of water was collected in the targeted space. Most of the water droplets fall outside the collected area.



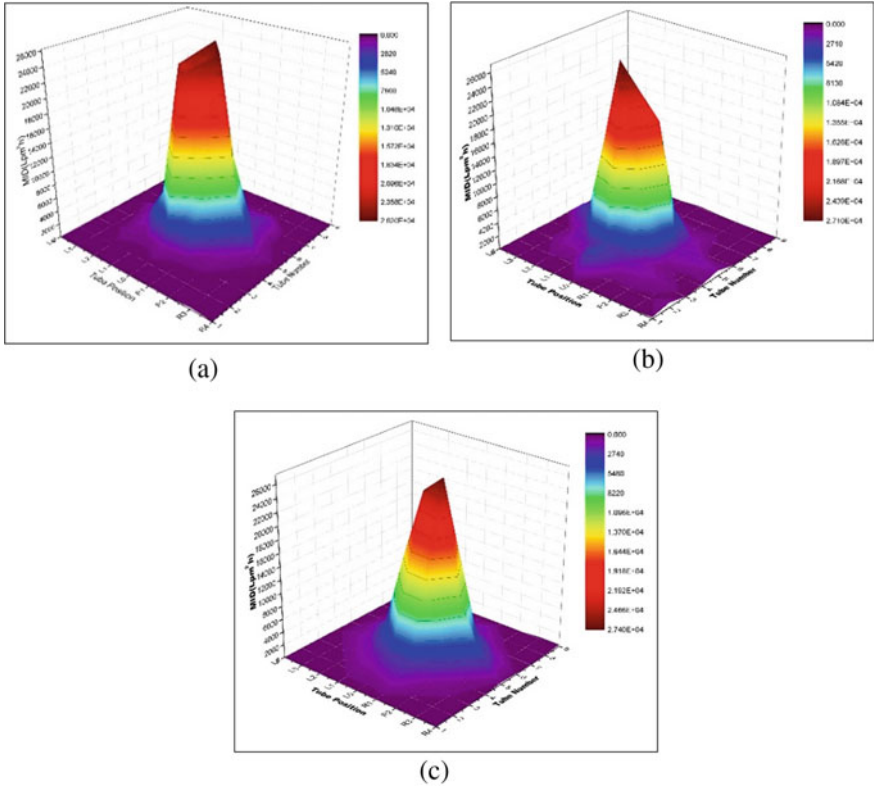


**Fig. 5** Distribution of local MID over the patternator surface at the time spray at 4 bar air and liquid pressure for target height of (a) 120 mm, (b) 180 mm, and (c) 240 mm

### 4 Conclusions

The patternator has been designed and fabricated to provide the maximum flexibility for specialized function to detect the position of the maximum cooling rate and mass impingement density. An elementary mechanical spray patternator was designed and developed to assess the provincial spray density at different locations of the targeted surface at numerous sets of air and liquid pressure.

- The magnitude of local MID is maximum at the center of the targeted area of the patternator for a fixed value of nozzle to target distance.
- The magnitude of local MID decreases with rising air pressure for fixed water flow
- The local MID reduces with increasing in nozzle to target distance.

## References

1. Issa RJ (2009) Multiphase spray cooling technology in industry. In: *Advanced technologies*. IntechOpen
2. Bayvel L, Orzechowski Z (1993) *Liquid atomization*. Taylor and Francis, Washington DC
3. Rupe JH (1953) The liquid phase mixing of a pair of impinging streams. In: *Progress Report 20-195*. Jet Propulsion Laboratory, Pasadena, CA
4. Puschmann F, Specht E, Schmidt J (2001) Measurement of spray cooling heat transfer using an infrared-technique in combination with the Phase-Doppler technique and a patternator. *Int J Heat Technol* 19:51–56
5. Hoffman JA, Martin JK, Coates SW (1997) A technique for obtaining spatial and temporal mass flux measurements of a pulsed spray: a description of the hardware and methodology. *Rev Sci Instrum* 68(11):4247–4252
6. Gordon M, Soria J (2002) PIV measurements of a zero-net-mass-flux jet in cross flow. *Exp Fluids* 33(6):863–872
7. Qiu HH, Sommerfeld M (1992) A reliable method for determining the measurement volume size and particle mass fluxes using Phase-Doppler anemometry. *Exp Fluids* 13(6):393–404
8. Simoens S, Ayrault M (1994) Concentration flux measurements of a scalar quantity in turbulent flows. *Exp Fluids* 16(3):273–281
9. Sommerfeld M, Qiu HH (1995) Particle concentration measurements by Phase-Doppler anemometry in complex dispersed two-phase flows. *Exp Fluids* 18(3):187–198
10. Cho S, Park G, Yoon Y (2013) Dense spray patternation using optical tomography. *Int J Aeronau Space Sci* 14(4):398–407
11. McVey JB, Russell S, Kennedy JB (1987) High-resolution patternator for the characterization of fuel sprays. *J Propul Power* 3(3):202–209
12. Ullom MJ, Sojka PE (2001) A simple optical patternator for evaluating spray symmetry. *Rev Sci Instrum* 72(5):2472–2477
13. Abernethy RB, Benedict RP, Dowdell RB (1985) ASME measurement uncertainty

# Performance of Chemical Route-Synthesized SnO<sub>2</sub> Nanoparticles



Harapriya Nayak, Usharani Panda, and Sushanta Kumar Kamilla

**Abstract** This paper focuses on the principle motto of the formation of SnO<sub>2</sub> nanoparticles and further its characterizations were created by the method of chemical precipitation method. The mode of analysis and evaluation was based on the methodology assisted with X-ray diffraction (XRD), scanning electron microscope (SEM), UV–visible absorption. By understanding the outcomes from the undertaken methods, powder form of SnO<sub>2</sub> with tetragonal rutile crystalline structures has been obtained with the dimension of crystallite size in the range of 31 nm. On arranging the histogram plot of SEM, the SEM examination on the same SnO<sub>2</sub> tends to present the average particle size to be 35 nm. The value of the optical band gap was found to be 3.7 eV, and the obtained value was compared with a defined value on bulk tin oxide with the retained properties by optical absorption estimation. This prepared sample can be used as very good electrochemical sensor material.

**Keywords** SnO<sub>2</sub> nanoparticles · X-ray diffraction (XRD) · Morphology (SEM) · Optical properties (UV–visible)

## 1 Introduction

A lot of consideration goes in favor of nano-sized materials as they carry unique extraordinary electrical, physical, synthetic, and attractive properties in contrast to mass semiconductors. With the diminishing of molecule size, the semiconductor's band structure deviates; the energy gap rises, and the edges convert to distinct-energy stages. This happens to impact the supposed quantum size [1–5]. These quantum size impacts have led to both an essential and connected investigation.

Tin oxide (SnO<sub>2</sub>) is one of the most interesting materials to be explored today; this is because it is a notable n-type semiconductor (SC) having a bandgap of 3.6–3.8 eV

---

H. Nayak · U. Panda · S. K. Kamilla (✉)

Department of Physics, Faculty of Engineering and Technology (ITER), Siksha 'O' Anusandhan Deemed to be University, Bhubaneswar, Odisha 751030, India  
e-mail: [sushantakamilla@soa.ac.in](mailto:sushantakamilla@soa.ac.in)

[6–13] and for its huge application in conduction of anode for gas sensors appliances devices in fluid precious stone arrangement, lithium-particle batteries, etc. [14–21].

SnO<sub>2</sub>, an n-type semiconductor with a wide bandgap (3.62 eV), is one of the most popular materials which have been used in sensing applications from health and safety to energy efficiency and emission control [22]. In accumulation, SnO<sub>2</sub> has a huge sensitivity to the presence of surrounding gas which makes it to be applied as gas sensors [23]. SnO<sub>2</sub> is one of the most important n-type semiconductors oxide which has been used in solar cells [24], gas sensors [25, 26].

For having a wide band gap (3.6 eV), SnO<sub>2</sub> has a special attention among the metal oxides. It contains also high carrier density, optical transparency, high stability, and thermal and chemical stabilities. On a comparison between bulk materials and nanomaterials, SnO<sub>2</sub> has many advantages on nanometer scale. It involves various technological applications, such as solid-state sensors, catalysts for oxidation of organic compounds, ceramics, transparent conductors, biomedicine, electronics, and optoelectronics [27].

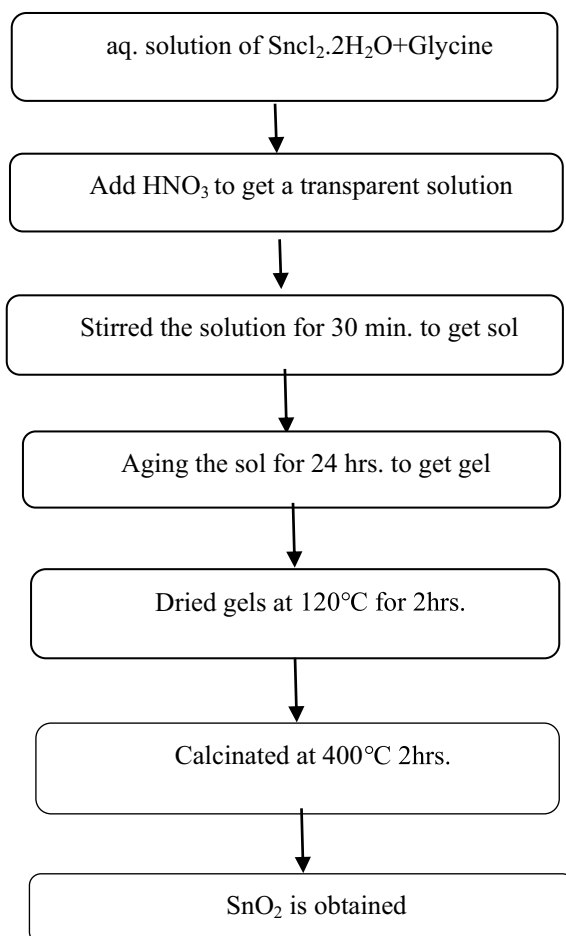
For the preparation of SnO<sub>2</sub> nanostructures, numerous procedures have been created, e.g., spin coating [28], rheotaxial growth and thermal oxidation (RGTO) [29], shower pyrolysis [30], aqueous techniques, chemical precipitation method [31], synthetic vapor affidavit, the warm vanishing of oxide powders, sol–gel approach, and auto-combustion method. We have also fabricated SnO<sub>2</sub>/Al electrode by this auto-combustion method, which has displayed a good sensitivity and better performance [32], chemical vapor deposition (CVD) [33], DC and RF sputtering [34], chemical bath deposition [35].

In this work, the production and interpretation of crystalline SnO<sub>2</sub> nanoparticles powder were inspected by synthetic precipitation technique which can be used as an electrochemical sensor material for further investigation [32].

## 2 Experimental Methodology

The formation of the SnO<sub>2</sub>-powdered nanocrystals was created by the consideration of the sol–gel method. This process was based on the dissolution of 2 g (0.1 M) of stannous chloride dehydrate (SnCl<sub>2</sub>·2H<sub>2</sub>O) with glycine. Upon reaching the stage, when the stannous chloride dehydrate has been dissolved completely, a defined amount of nitric acid in the form of the solution was added to the before-mentioned solution of stannous chloride dehydrate. The addition method was cleanly maintained with the addition to be by the dropwise under stirring for gaining apt results. The dehydration of the resultant gels took place on controlled conditions provided that the temperature of the surroundings be fixed at 80 °C for a time of 24 h. The resultant of the chemical addition tended to create a resulting gel, which was further filtered and dried. After the dehydration of the resultant gel, then the sample is calcinated at 400 °C for 2 h, and the tin oxide powdered nanocrystals are formed (Fig. 1).

The samples of the powered nanocrystals of generated tin oxide were analyzed with the preferred method of X-ray powdered diffraction (XRD) by considering the

**Fig. 1** Chemical process flowchart

device (RIGAKU Ultima IV). The X-beam diffractometer investigates crystalline states under typical barometrical conditions. This strategy is non-dangerous. X-beams concentrated on an example fixed on the hub of the spectrometer (goniometer) are diffracted by the example. The adjustments in the diffracted X-beam forces are estimated, recorded, and plotted against the pivot edges of the example. The outcome is alluded to as the X-beam diffraction example of the example. PC investigation of the pinnacle positions and forces related to this example empowers subjective examination, cross-section consistent assurance, or potentially stress assurance of the example. Subjective investigation might be directed based on pinnacle stature or pinnacle region. The pinnacle points and profiles might be utilized to decide molecule measurements and level of crystallization, and help direct exact X-beam auxiliary investigation.

For surface morphology, a specially designed scanning electron microscope has been implemented to produce effective results. It gives information about samples surface morphology, topography, composition, and crystal orientation. In SEM, an electron beam is used as a radiation source to get the greatest resolution. By scanning the electrons on the surface of the sample, we can get an image of the surface of the sample. Initially, an electron source is focused on the sample surface and is reflected from the sample in the form of the secondary electron, back-scattered electrons, and emitted X-rays; then, all are collected and give the image of the surface of the sample in 3D and black–white pattern.

The remaining parameter for providing an effective result for the analysis was optical absorption spectra of the samples of the generated tin oxide, and the optical absorption spectra were gathered from the utilization of OPTIMA SP-3000 UV–VIS spectrometer.

### 3 Characterization of the Created SnO<sub>2</sub> Powder

#### 3.1 XRD Analysis of SnO<sub>2</sub>

The under-laying figure, i.e., Fig. 2, represents the X-ray diffraction (XRD) pattern with showing the maximum of  $2\theta$  values of 26.5°, 33.8°, 37.9°, 51.8°, and 62.8° is

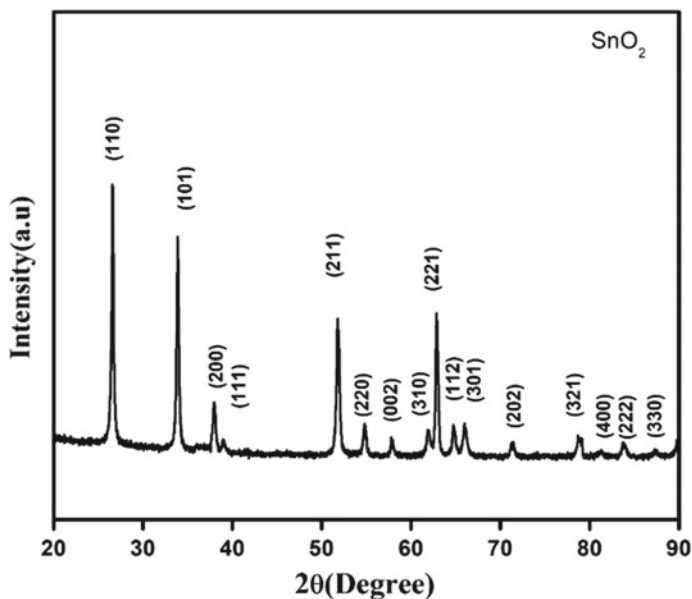


Fig. 2 Pattern for SnO<sub>2</sub> nanoparticles in XRD

generally labeled with (110), (101), (200), (211), and (221), respectively. The created tin oxide upon characterization tends to present a tetragonal structure having lattice parameters  $c = 3.1868 \text{ \AA}$  and  $a = 4.7344 \text{ \AA}$  with  $c/a = 0.6731 \text{ \AA}$ . The average crystallite or dimension size ( $D$ ) of the particle of tin oxide was determined by using Scherrer's equation:

$$D = \frac{k\lambda}{\beta \cos \theta}$$

In the above-presented equation which is Scherer's equation, the " $D$ " tends to represent the size of the crystals; " $K$ " represents as the shape factor that being defined to be 0.9 as constant; " $\lambda$ " represents the XRD wavelength; " $\beta$ " denotes the full width at half maximum (FWHM) value of the XRD peaks, and " $\theta$ " stands for the Bragg's diffraction angle. From the calculation, the considered value of the mean dimensional size of the SnO<sub>2</sub> nanoparticle was constructed in a range of 31 nm.

### 3.2 Morphology of SnO<sub>2</sub> Nanoparticles

Figure 3 displays the morphology details of SnO<sub>2</sub> using the scanning electron microscope. The particles are spherical. At some places of the micrograph, particle agglomeration is observed. The estimated average particle size is around 35 nm from the histogram plot of SEM of SnO<sub>2</sub> as shown in Fig. 4, which is consistent with XRD results. The image also shows that a large number of voids are present which is an

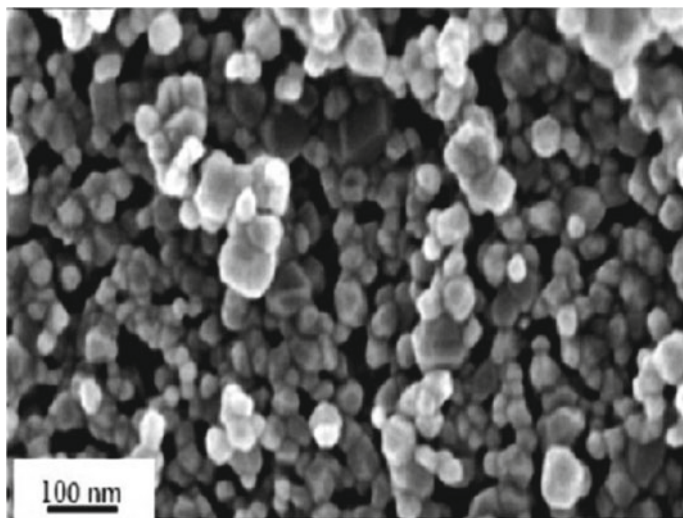


**Fig. 3** Morphology of SnO<sub>2</sub>

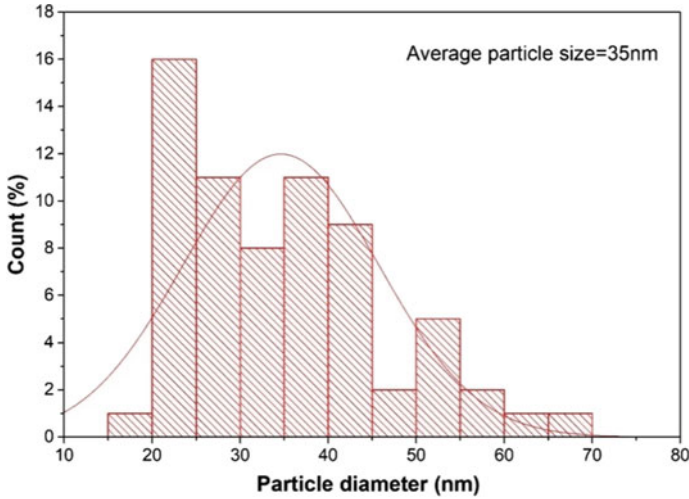


Fig. 4 Histogram plot of SnO<sub>2</sub>

important characteristic of sensors since the presence of voids increases the sensitivity of the sensor [36].

### 3.3 Optical Properties

Figure 5 represents the absorption spectrum of SnO<sub>2</sub> that has been deposited over a transparent medium preferably glass. The figure focuses upon representing the absorption coefficient in the prevailing ultra-violet region, whereas it is translucent in the visible region.

The optical bandgap ( $E_g$ ) of the semiconductor is decided by operating Tauc conception. The graph between  $(\alpha h\nu)^2$  and  $h\nu$  indicates the band-gap energy by extrapolating the direct part, can be found the  $E_g$  value when meeting with  $h\nu$  horizontal as shown in Fig. 6. The  $E_g$  resultant was observed to about 3.7 eV; the over two assets might be recognized with the preparation of nanostructures of SnO<sub>2</sub>; these qualities develop a satisfactory agreement rather than different specialists. The optical bandgap of SnO<sub>2</sub> nanoparticles is found to be 3.7 eV which is a little higher than the theoretical value, i.e., 3.6 eV. This is happening due to the nanostructure form of SnO<sub>2</sub>, as reported [37].



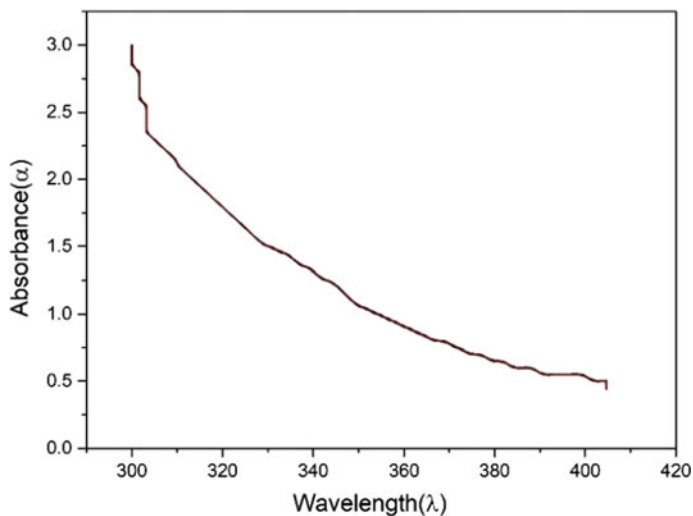


Fig. 5 SnO<sub>2</sub>'s absorption spectrum

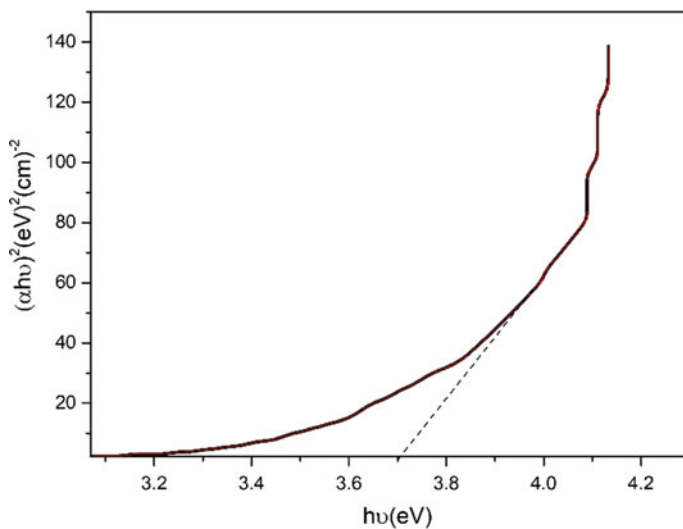


Fig. 6  $(\alpha h\nu)^2$  versus photon energy ( $h\nu$ ) of SnO<sub>2</sub>

## 4 Conclusion

SnO<sub>2</sub> nanoparticles powder was synthesized at 400 °C by substance precipitation method. We have carried out the structural, optical, and morphological properties of SnO<sub>2</sub> by XRD analysis, UV–visible absorption, and SEM, respectively. The prepared

sample was seemed to have been a tetragonal structure of SnO<sub>2</sub> by the XRD analysis. The particle size of the SnO<sub>2</sub> was found to be 35 nm estimated by plotting the histogram plot of SEM. The optical bandgap of SnO<sub>2</sub> nanoparticles is found to be 3.7 eV, which is slightly different from the theoretical value with retained properties of bulk tin oxide. This prepared sample can be used as very good electrochemical sensor material.

## References

1. Abou El-Nour KMM, Eftaiha A, Al-Warthan A, Ammar RAA (2010) Synthesis and applications of silver nanoparticles. Arab J Chem
2. Chiu HC, Yeh CS (2007) Hydrothermal synthesis of SnO<sub>2</sub> nanoparticles and their gas-sensing of alcohol. J Phys Chem
3. Kim SW et al (2003) Synthesis of monodisperse palladium nanoparticles. Nano Lett
4. Ristić M, Ivanda M, Popović S, Musić S (2002) Dependence of nanocrystalline SnO<sub>2</sub> particle size on synthesis route. J Non Cryst Solids
5. Pang G, Chen S, Kolytyn Y, Zaban A, Feng S, Gedanken A (2001) Controlling the particle size of calcined SnO<sub>2</sub> nanocrystals. Nano Lett
6. Köse H, Aydın AO, Akbulut H (2014) The effect of temperature on grain size of SnO<sub>2</sub> nanoparticles synthesized by Sol-Gel Method. Acta Physica Polonica A125(2):345–347
7. Nuțescu Duduman C, Barrena Pérez MI, Gómez De Salazar Y, Caso De Los Cobos JM, Carcea I, Chicet DL, Palamarciuc I (2016) Synthesis of SnO<sub>2</sub> by Sol-Gel method. Solid State Phenomena 254:200–206
8. Zamand N, Nakhaei Pour A, Housaindokht MR, Izadyar M (2014) Size-controlled synthesis of SnO<sub>2</sub> nanoparticles using reverse microemulsion method. Solid State Sci 33:6–11
9. Gu F, Wang SF, Lü MK, Zhou GJ, Xu D, Yuan DR (2004) Photoluminescence properties of SnO<sub>2</sub> nanoparticles synthesized by sol-gel method. J Phys Chem B108(24):8119–8123
10. Zhu X, Geis-Gerstorf J (2003) Sol-gel-derived Sb-doped SnO<sub>2</sub> nanoparticles controlled in size by Nb<sub>2</sub>O<sub>5</sub>. Chem Eng Technol 26(10):1084–1087
11. Li Y, Lim SH, White T (2004) Controlled synthesis and characterization of TiO<sub>2</sub> nanoparticles via a sol-gel method. Int J Nanosci 3(6):749–755
12. Zhang J, Gao L (2003) Synthesis of SnO<sub>2</sub> nanoparticles by the sol-gel method from granulated tin. Chem Lett 32(5):458–459
13. Shiomi H, Kakimoto C, Nakahira A, Takeda S (2000) Preparation of SnO<sub>2</sub> monolithic gel by sol-gel method. J Sol-Gel Sci Technol 19(1–3):759–763
14. Liu X, Han Y, Zeng J, Yang H, Zhou K, Pan D (2018) Hydrothermal synthesis of nano-SnO<sub>2</sub>@SiO<sub>2</sub> composites for lithium-ion battery anodes. J Mater Sci Mater Electron 29(7):5710–5717
15. Guler MO, Cevher O, Cetinkaya T, Tocoglu U, Akbulut H (2014) Nanocomposite anodes for lithium-ion batteries based on SnO<sub>2</sub> on multiwalled carbon nanotubes. Int J Energy Res 38(4):487–498
16. Li S, Xie W, Wang S, Jiang X, Peng S, He D (2014) Facile synthesis of rGO/SnO<sub>2</sub> composite anodes for lithium ion batteries. J Mater Chem A2(40):17139–17145
17. Yuan L, Konstantinov K, Wang GX, HK Liu, Dou SX (2005) Nano-structured SnO<sub>2</sub>-carbon composites obtained by in situ spray pyrolysis method as anodes in lithium batteries. J Power Sour 146(1–2):180–184
18. Tian H, Tan X, Xin F, Wang C, Han W (2015) Micro-sized nano-porous Si/C anodes for lithium ion batteries. Nano Energy 11:490–499
19. Lin J et al (2013) Graphene nanoribbon and nanostructured SnO<sub>2</sub> composite anodes for lithium ion batteries. ACS 7(7):6001–6006

20. Li H et al (2018) Fabrication of MoS<sub>2</sub>@SnO<sub>2</sub>-SnS<sub>2</sub> composites and their applications as anodes for lithium ion batteries. *Mater Res Bull* 108:106–112
21. Li H et al (2018) Porous SnO<sub>2</sub> hollow microspheres as anodes for high-performance lithium ion battery. *Mater Lett* 217:276–280
22. Miller DR, Akbar SA, Morris PA (2014) Sensors actuators. *B Chem* 204:250
23. Batzill M, Diebol U (2005) The surface and materials science of tin oxide progress. *Surf Sci* 79:47–154
24. Maddu, Akhiruddin, Hasiholan, Tua R, Kurniati M (2009) The growth of Nanocrystal SnO<sub>2</sub> film with chemical bath deposition method (CBD). *J Nanosci Nanotechnol*. ISSN:1979–0880
25. Xu GG, Zhang XY, Cui HZ, Chen ZW, Ding JX, Zhan XY (2016) Preparation of mesoporous SnO<sub>2</sub> by solvothermal method using *Stahlia* involucre leaves and application to n-butanol sensor. *Powder Technol* 302:283–287
26. Xie X, Wang XZ, Tian J, Song XJ, Wei N, Cui HZ (2017) Growth of porous ZnO single crystal hierarchical architectures with ultrahigh sensing performances to ethanol and acetone gases. *Ceram Int* 43:1121–1128
27. Al-Saadi TM, Hussein BH, Hasan AB, Shehab AA (2019) Study the structural and optical properties of Cr doped SnO<sub>2</sub> nanoparticles synthesized by sol-gel method. *Energy Procedia* 157:457–465
28. Gu F, Wang SF, Lü MK, Cheng XF, Liu SW, Zhou GJ, Xu D, Yuan DR (2004) Luminescence of SnO<sub>2</sub> thin films prepared by spin-coating method. *J Crystal Growth* 262(1–4):182–185
29. Sberveglieri G (1992) Classical and novel techniques for the preparation of SnO<sub>2</sub> thin-film gas sensors. *Sens Actuators B Chem* 6(1–3):239–247
30. Bader AB, Khalaph Muhammad S, Mohammed Jabbar A, Haneen Abass K, Salman Chiad S, Fadhil Habubi N (2020) Synthesis and characterization of Indium-doped CdO nanostructured thin films: a study on optical, morphological, and structural properties. *J Nanostruct* 10(4):744–750
31. Naje AN, Norry AS, Suhail AM (2013) Preparation and characterization of SnO<sub>2</sub> nanoparticles. *Int J Innov Res Sci Eng Technol* 2:7068–7072
32. Panda U, Kamilla SK, Mishra DK, Pattanaik P (in press) Performance of SnO<sub>2</sub>/Al working electrode as a sensor. *Int J Mater Eng Innov (IJMATEI)*
33. Jin J, Seung Pyung C, Kwang Joon H (2006) Structural and optical properties of SnO<sub>2</sub> thin films deposited by using CVD techniques. *J Korean Phys Soc* 48(5):960–963
34. Bo X, Ren X-G, Gu G-R, Lan L-L, Wu B-J (2016) Structural and optical properties of Zn-doped SnO<sub>2</sub> films prepared by DC and RF magnetron co-sputtering. *Superlatt Microstruct* 89:34–42
35. Maddu, Akhiruddin, Hasiholan, Tua R, Kurniati M (2009) The growth of nanocrystal SnO<sub>2</sub> film with chemical bath deposition method (CBD). *J Nanosci Nanotechnol*. ISSN 1979-0880
36. Thakare MG, Dighavkar CG, Borhade AV, Aher JS (2016) *Int J Recent Trends Eng Res* 2:114
37. Gnanam S, Rajendran V (2010) Luminescence properties of EG-assisted SnO<sub>2</sub> nanoparticles by sol-gel process. *Dig J Nanomater Biostruct* 5(3):699–704

# Mechanical Behaviors of Aluminum Matrix Composite Synthesized by Stir Casting Technique



Jayashree Pati, Supriya Priyadarshinee, Pragyan Mohanty, Ranjita Mahapatra, and S. K. Kamila

**Abstract** Due to light weight, the aluminum based metal matrix composite plays a major role in fabricating engine and body components of aerospace and automobile industry. This enhancement of mechanical behavior like strength, hardness, stiffness, fatigue strength and wear resistance of host aluminum composite is possible only by adding various ceramic compounds with aluminum matrix. In this work,  $TiB_2$  dispersed Al metal matrix ( $Al/TiB_2$ ) composite was synthesized by simple and low cost indigenously designed and developed programmable stir casting technique. This technique is based on principle of modification of programmable motor with mechanical stirrer from the top to mix reinforcement in the matrix material. Different weight fraction 2, 4, 6% of  $TiB_2$  was reinforced in Al356 alloy and the synthesized metal matrix composites were subjected for micro structural and mechanical property studies. Transmission electron micrograph (TEM) shows an even distribution of  $TiB_2$  ceramic particles in host Al metal. Vicker's micro hardness measurement indicates the increased values of hardness of the composite with higher weight fraction of  $TiB_2$  reinforcement.

**Keywords** Metal matrix composites ·  $TiB_2$  · Stir casting · TEM · Microhardness

## 1 Introduction

Metal matrix composites (MMCs) are formed by dispersing mainly ceramic particles in metal base like Al, Mg, Cu, Zn etc. Among these, aluminum is cost effective and carries versatile properties [1–8]. So, it is used as a prime matrix material. Low density, light weight, high damping capacity, high corrosion resistance etc. have made aluminum an attractive matrix component which can fulfill high need in automobile, aircraft, defence and many more. The metal matrix composite can be formed by dispersion of  $Al_2O_3$ , SiC, TiC,  $B_4C$ , BN, MgO, AlN,  $TiO_2$ ,  $SiO_2$ ,

---

J. Pati · S. Priyadarshinee · P. Mohanty · R. Mahapatra · S. K. Kamila (✉)  
Department of Physics, Faculty of Engineering and Technology (ITER), Siksha 'O' Anusandhan  
Deemed to be University, Bhubaneswar, Odisha 751030, India  
e-mail: [sushantakamilla@soa.ac.in](mailto:sushantakamilla@soa.ac.in)

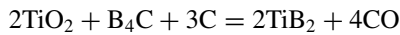
TiB<sub>2</sub>, graphite, fly ash, cow dung, red mud etc. Aluminum metal matrix composite is very much popular because it possesses good specific strength, high elastic modulus, high abrasion, good stiffness, promising wear resistance, high thermal conductivity, high hardness, thermal coefficient of expansion with low value, high temperature resistance, high strength to weight ratio etc. [1–9].

The MMCs can be synthesized by various processing ways like vortex method, spray deposition, chemical vapor deposition, powder metallurgy, squeeze casting, pressure infiltration, ultrasonic cavitation and stir casting method. Among these, stir casting route is the most common method in addition to effective, quick and economic in nature [9–13]. It is reported that Jin–feng NIE et al. fabricated (Al/TiB<sub>2</sub>)/TiC hybrid composite by in-situ reaction resulting 140 and 35% increase in ultimate tensile strength and microhardness respectively than that of aluminum alloy [11]. The spatial distribution of ceramic particles, its size, bonding, weight to volume ratio put a great impact to-ward properties of aluminum metal matrix composite. Fine grain size of matrix, strong bondage between matrix and dispersant, even distribution of ceramic particulates in the host metal can enhance the microstructural and mechanical behavior of the MMCs. Agglomeration and clustering of reinforced particles in the composite is a drawback not to result superior mechanical properties [14–20]. Padhi et al. [14] designed ultrasonic cavitation noncontact method to form aluminum metal matrix nanocomposite which is a fruitful process to increase these properties. According to D. Vishnuvardhan Reddy and his team, 90% Al7075 + 6%SiC + 4%TiC hybrid metal matrix composite prepared by stir casting method increased 7.4% in tensile strength compared to matrix alloy and it was observed that composites containing 6% of wt. TiC and 4% of wt. SiC exhibited excellent hardness properties (40% more compared to Al7075 alloy) [23]. Bujari et al. [25] had obtained that wear resistance of Al-Cu-2%B<sub>4</sub>C and 4%B<sub>4</sub>C composites were better than unreinforced alloy. Sahoo et al. [24] observed increase in wear resistance and hardness value with increase of wt% Si in Al-Si-TiB<sub>2</sub> composite synthesized by stir casting method. High value of Vicker's hardness as high as 485.9 +/- 16.9 in Al-TiB<sub>2</sub> nanocomposite with uniform dispersion of reinforcement in Al matrix was confirmed by Abdolreza Javadi [19] and his group. Sangaravadivel et al. [22] had resulted gradual increase of hardness for volume fraction addition of WS<sub>2</sub> reinforcement in AA7075 alloy. Mallireddy et al. [20] studied the AA7010-TiB<sub>2</sub>-in-situ metal matrix composite and obtained better mechanical and corrosion resistance of 10% TiB<sub>2</sub> than that of lower % addition to matrix.

Looking into the advantages of the stir casting techniques and also the importance of Al based metal matrix nano composites, Al/TiB<sub>2</sub> composite was fabricated by this method. The above process has been adopted to have even reinforcement of nano particles in the metal matrix with improved hardness property.

## 2 Experimental Technique

Following commercial aluminum 356 alloy was used for casting of Al metal matrix composite. Along with Aluminum, there are 0.95% Fe, 0.45% Mg and 0.26% Si present in the alloy. Around a temperature of 760 °C, aluminum metal of 420 g was subjected for melting putting inside of a graphite crucible. Different weight fractions 2, 4 and 6% of TiB<sub>2</sub> were synthesized in aluminum metal matrix to form the composite by simple and low cost indigenously designed and developed programmable stir casting technique. As TiB<sub>2</sub> does not occur in natural form, this ceramic compound was prepared by carbothermal reduction process by the chemical reaction of TiO<sub>2</sub> and B<sub>4</sub>C above 1050 °C. The following reaction is described for the various weight fraction of formation of TiB<sub>2</sub> powder.



The schematic diagram of stirring technique is shown in Fig. 1. The furnace along with graphite crucible was preheated upto a temperature of 800 °C and then aluminum metal matrix was subjected for melting within furnace. TiB<sub>2</sub> powder was preheated upto temperature of 400 °C in order to make moisture and impurities free. Various weight fraction of TiB<sub>2</sub> was added step by step to the molten Al metal and stirring process was carried out by means of a programmable electric motor vibrator under the stirring speed of 300 rpm. The graphite rod was used as the stirrer to continue the stirring process to nearly about 10–15 min. After this, the composite

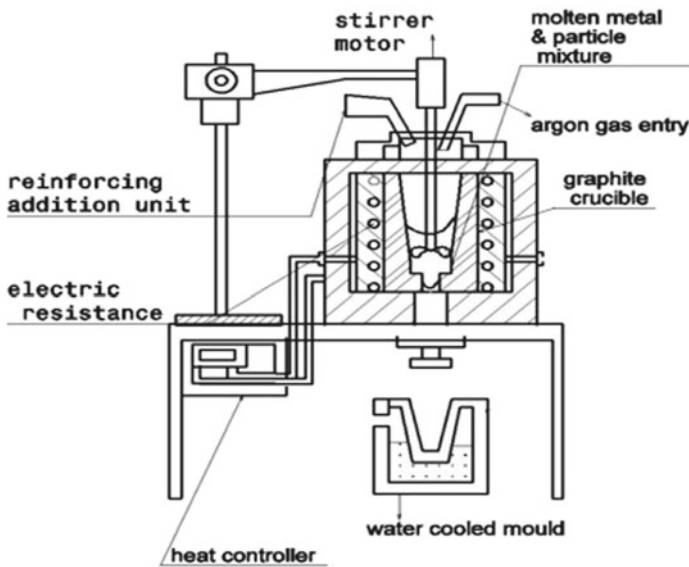
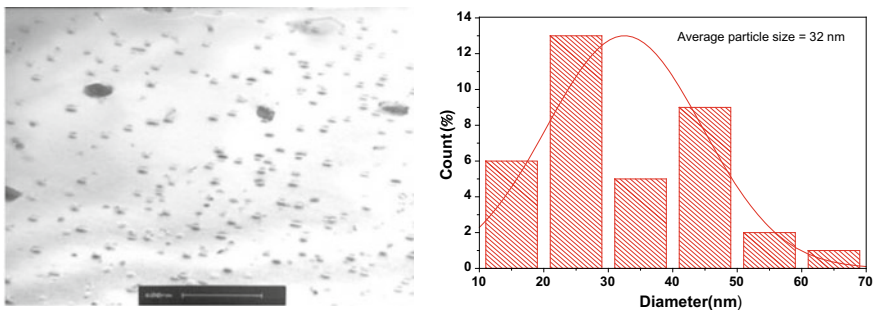


Fig. 1 Schematic diagram of Stirring technique

was solidified in mold and got furnace cooled. Now the specimen was made ready for microstructural and hardness test. For study of the microstructure, low speed abrasive cutter was used for cutting the sample. The specimen surface was polished by using 200, 400 and 600 grits of emery paper followed by cleaning in the solution of alcohol. After undergoing diamond polishing, the specimen surface was again cleaned with acetone. Then, specimen surface was etched with Keller's reagent for about 30–40 s. By using ultrasonic vibrator and dry hot air, etched material was cleaned in acetone. Uniform flatness of sample surface was achieved by subjecting to cold mounting. Then specimen was reduced to thin slices cutting by low speed diamond cutter of thickness around 92  $\mu\text{m}$  with the help of a dimpling grinder (Gaton Model-656), the middle portion of slices were made thin upto 20  $\mu\text{m}$ . Then it was kept under an ion milling vacuum chamber of 10–6 Torr (Gaton Precision polishing system model 691) and an electron beam energy of 5 keV was applied on the specimen thinned previously. By using the TEM (JEOL, JEM-2100) microstructural study was performed operating under an accelerating voltage of 200 kV. By measuring the permanent depth of the indentation, the hardness of the sample was measured. Smaller the indentation, harder is the material. Vicker's microhardness (Leica VMHT Auto digital) of the different samples was measured by putting the indenter at various locations.

### 3 Result and Discussion

Transmission electron micrographs (TEM) of 2%, 4%, 6%  $\text{TiB}_2$  of different weight fractions in Al MMCs have been shown in Figs. 2a, 3a and 4a respectively. The micrographs clearly reflect that  $\text{TiB}_2$  ceramic particulates are nearly dispersed evenly in aluminum metal matrix. In the micrographs, white spots are aluminum matrix and black spots are  $\text{TiB}_2$ . Al/ $\text{TiB}_2$  (2 wt.%) micrograph shows that titanium boride is mostly distributed throughout the matrix surface with uniformity. The black shaded holes formed in 4–6%  $\text{TiB}_2/\text{Al}$  TEM shows that there may be some voids or pores



**Fig. 2** a Transmission electron micrograph b histogram showing particle size distributions of 2%  $\text{TiB}_2$  dispersed in Al matrix

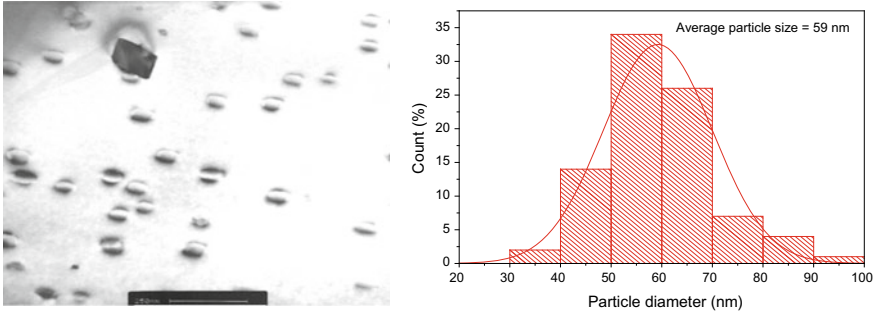


**Fig. 3** a Transmission electron micrograph b histogram showing particle size distributions of 4% TiB<sub>2</sub> dispersed in Al matrix

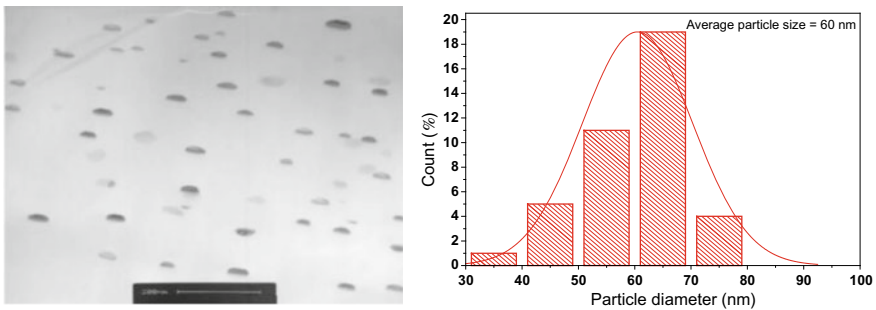


**Fig. 4** a Transmission electron micrograph b histogram showing particle size distributions of 6% TiB<sub>2</sub> dispersed in Al matrix

where dispersion might have not occurred properly. During stirring process, some air might have been trapped in molten form of metal with ceramic particles. The black colored TiB<sub>2</sub> have been found in cluster form for 4–6% Al/TiB<sub>2</sub> composites. Still, TEM images show that ceramic nanoparticles were almost evenly distributed in aluminum matrix. From histogram analysis of all three composition samples it was found that the particle size increases with increasing TiB<sub>2</sub> weight percentage in Al matrix which have been shown in Figs. 2b, 3b and 4b respectively.

The following formula was used to measure the Vickers hardness factor

$$Hv = \frac{2F \sin(136^\circ/2)}{d^2} \cong 1.854 \frac{F}{d^2}$$

where, Hv = Vickers hardness (kgf mm<sup>-2</sup>).

F = the load applied in kilogram-force.

d = the average length of two diagonals, d1 and d2 in millimeter.



**Table 1** Hardness distribution of different wt.% of TiB<sub>2</sub> dispersed Al metal matrix measured by Vickers microhardness indentation tester

Sample nos	Average Vicker's microhardness in Hv
As cast Al matrix	60
2% TiB <sub>2</sub> dispersed in Al matrix	66
4% TiB <sub>2</sub> dispersed in Al matrix	73
6% TiB <sub>2</sub> dispersed in Al matrix	84

A diamond indenter of the given shape was penetrated into the flat polished surface of the sample. By measuring the diagonal length of the indentation had resulted in the Vickers hardness factor. In the current investigation a square-base pyramid type diamond geometry was used with face angles of 136°. Under a 5 kg force applied load subjected for 10 s dwell time, the test was carried out. The varying values in the micro-hardness determined for a specific specimen was  $\pm 6$  Hv and the average was taken into consideration. The average Vickers microhardness values measured at different locations of the sample for different weight percentage has been shown in Table 1. It has been reported that Vickers microhardness of Al356 alloy is around of 60, whereas from the given Table 1, it was observed that the Aluminum/Titanium Boride composite with different wt.% have resulted higher hardness values than the bulk aluminum alloy. This implies the hardness factor has been increased significantly due to addition of TiB<sub>2</sub> powder in Al metal matrix.

From the literature it is also found that the hardness of a material is appreciably affected by its micro structure. The more evenly the particles dispersed in the matrix, more is its hardness. The given TEM micrographs also ensures higher hardness because of maximum extent of uniform reinforcement of TiB<sub>2</sub> dispersants in Aluminum matrix.

## 4 Conclusion

The following conclusions were drawn from this present work.

Al-TiB<sub>2</sub> composite was successfully fabricated by stir casting method. The TEM micrographs of the composite for various percentage doped TiB<sub>2</sub> (2, 4, 6%) in Aluminum revealed almost uniform distribution of the reinforcement in metal matrix. It was also observed from the TEM histograms that particle size increased with percentage increase of TiB<sub>2</sub> in weight dispersed in Aluminum molten metal. The addition of TiB<sub>2</sub> particles in Al matrix was able to improve the hardness of the composite significantly than that of Aluminum alloy. It was found that by increasing the wt.% of TiB<sub>2</sub> in Aluminum started increasing the hardness value. From this investigation, the superior hardness value was obtained for 6 wt.% of TiB<sub>2</sub> than that of 4%, 2% of weight TiB<sub>2</sub> in metal matrix composite. So, we have concluded that as wt.% of reinforcement will be more and more in the matrix having with even distribution of ceramic particles in metal, the mechanical strength of the composite

will be enhanced which is very much required in the field of automobile, aircrafts etc.

## References

1. Sharma R, Jha S, Kakkar K, Kamboj K, Sharma P (2017) A review of aluminum metal matrix composite and its properties. *Int Res J Eng Technol* 4(2): 832–840
2. Surappa MK (2003) Aluminium matrix composites: challenges and opportunities. *Sadhana* 28(1):319–334
3. Kakkar K, Jha SS, Sharma R, Kamboji K (2016) Study of properties of different aluminum metal matrix composites-a review. In: *Proceedings of 3rd international conference on manufacturing manfex*, 80–86
4. Hashim J, Looney L, Hashmi MSJ (1999) Metal matrix composites: production by the stir casting method. *J Mater Process Technol* 92:1–7
5. Sharma P, Chauhan G, Sharma N (2013) Production of AMC by stir casting. *Overv Int J Contemp Pract* 2:23–46
6. Wessley GJJ, Srinivas S, Ali MDA (2019) Preparation and characterization of an aluminum 6061 alloy based metal matrix composite. *Int J Eng Adv Technol* 8(3):113–116
7. Suresh S, Shenbag N, Moorthi NSV (2012) Aluminium-titanium diboride (Al-TiB<sub>2</sub>) metal matrix composites challenges and opportunities. *Procedia Eng* 38:89–97
8. Lawrence CA, Prabhu PS (2014) Production and characterization of Al 6061-TiB<sub>2</sub> In-situ metal matrix composite. *Int Adv Res J Sci Eng Technol* 1(3):156–158
9. Chen Z, Kang H, Zhao Y, Zheng Y, Wang T (2016) The role of TiB<sub>2</sub> in strengthening TiB<sub>2</sub> reinforced aluminium casting composites. *IOP Conf Ser Mater Sci Eng* 117:1–8
10. Nie JF, Wang F, Li Y, Fangliu Y, Liu X, Zhao YO (2017) Microstructure and mechanical properties of Al-TiB<sub>2</sub>/TiC in situ composites improved via hot rolling. *Trans Non-Ferrous Metals Soc China* 27(12):2548–2554
11. Chandana A, Lawrence ID, Jayabal S (2018) Retracted: characterization of particulate-reinforced aluminium 7075/TiB<sub>2</sub> composites. *Mater Today Proc* 5(6):14317–14326
12. Singh H, Haq MIU, Raina A (2019) Dry sliding friction and wear behaviour of AA6082-TiB<sub>2</sub> in situ composites. *SILICON*. <https://doi.org/10.1007/s12633-019-0037-/springerNatureB.V>
13. Poria S, Sahoo P, Sutradhar G (2016) Tribological characterization of stir-cast aluminium-TiB<sub>2</sub> metal matrix composites 8(4):591–599
14. Mohanty P, Mishra DK, Verma S, Mishra K, Padhi P (2016) Influence of ultrasonic cavitation on microstructure and mechanical response of an aluminum/alumina nanocomposite. *Sci Eng Compos Mater* 23(5):481–487
15. Pradeep P, Samuel PS, Kumar R, Lawrence DI, Jayabal S (2017) Characterization of particulate reinforced aluminium 7075/ TiB<sub>2</sub> composites. *Int J Civil Eng Technol* 8(9):178–190
16. Rane K, Dhokey N (2018) On the formation and distribution of in situ synthesized TiB<sub>2</sub> reinforcements in cast aluminium matrix composites. *J Compos Sci* 2:1–11
17. Tee KL, Lu L, Lai MO (2001) In situ stir cast Al- TiB<sub>2</sub> composite: processing and mechanical properties. *Mater Sci Technol* 17(2):201–206
18. Pramod SL, Rao AP, Murty BS, Bakshi SR (2015) Effect of Sc addition on microstructure and wear properties of A 356 alloy and A356-TiB<sub>2</sub> in situ composite. *Mater Des* 78:85–94
19. Javadi A, XiaochunLi SP (2018) Fabrication of high strength Al nanocomposites with populous TiB<sub>2</sub> nanoparticles. *Procedia Manuf* 26:629–632
20. Mallireddy N, Siva K (2020) Investigation of microstructural, mechanical and corrosion properties of AA7010-TiB<sub>2</sub> in-situ metal matrix composite. *Sci Eng Compos Mater*. <https://doi.org/10.1515/secm-2020-0010>
21. Shyn CS, Rajesh R, Dev Anand M (202) Review of aluminium 6061 metal matrix composites fabricated using stircasting method and applications. *AIP Conf Proc* 45:7959–7964. <https://doi.org/10.1063/5.0036169>

22. Sangaravadivel P, Sudarvannan V, Gukan R, Pradeep AD (2021) Investigation of mechanical properties on AA7075 matrix composites reinforced with tungsten di-sulfide particles. *Mater Today Proc* 45:7975–7964. <https://doi.org/10.1063/5.0036169>
23. Reddy DVV, Sravani PS, Deepthi N, Thirupathaiah C (2019) The Investigation of mechanical and metallurgical properties on Al7075-TiC-SiC reinforced hybrid composites by stir casting. *Int J Mech Prod Eng Res Dev (IJMPERD)* ISSN (P): 09(02):769–776; ISSN (E), pp 2249–800
24. Sahoo SK, Majhi J, Patnaik SC, Behera A, Sahoo JK, Sahoo BP (2017) Characterisation of Al-Si-TiB<sub>2</sub> in-situ composite synthesised by stir casting method. *Mater Sci Elixir Mater Sci* 113:49066–49069
25. Bujari SS, Kurahatti RV (2017) Microstructure and wear behavior of B4C particulates reinforced Al-4.5%Cu alloy composites. *IOSR J Mech Civil Eng (IOSR-JMCE)*e-ISSN 14(01) 04–09.2278–1684

# The Effect of Dedicated Newly Designed Dual-Axis Solar Tracking System and Cooling System on the Performance of a Commercial PV Panel



Achinta Sarkar, Pragyan Borthakur, Avijit Kumar, Aiman Adhikari, Aditya Paul, Siba Prasad Behera, and Santosh Kumar Nayak

**Abstract** Huge potentiality in the nature and being eco-friendly, the efficient utilization of the sources of renewable energy is the primary concern of the researchers throughout the world. Among all sources of renewable energy, solar energy plays an important role as a primary source of energy. It is the most promising form of renewable energy in the present century. In this study, a prototype of a high-efficiency dual-axis solar tracking system using Arduino nano and light sensing detectors (LDRS) in associate with a cooling system has been designed, fabricated, and tested. The main purpose of the present study is to gain the maximum amount of energy output and increase in efficiency of energy conversion. It is to be noted that the efficiency of photovoltaic cells is significantly reduced due to the solar panel surface overheating, which results in decrease of charge carrier motilities. Therefore, a cooling system is used to maintain the surface temperature of the solar panel. Experimental results revealed that there is a significant gain in energy (on an average 31.38%) with the tracking system, and the extra gain of 5% is noticed with the cooling system as compared to the static panel without cooling system, respectively.

**Keywords** Solar energy · Solar trackers · Cooling system · Temperature · Efficiency

## 1 Introduction

The world has been pursuing at its highest devastating states due to pandemic situation prevails because of COVID-19, global warming due to using of fossil fuels in energy and transportation sectors, faster depletion of the reserves of the fossil fuels, exponential hiking of the fossil oil prizes internationally, and the environmental degradation [1–3]. Therefore, the world is in need of an alternative clean renewable energy resource for power generation other than the existing conventional sources

---

A. Sarkar (✉) · P. Borthakur · A. Kumar · A. Adhikari · A. Paul · S. P. Behera · S. K. Nayak  
School of Mechanical Engineering, Kalinga Institute of Industrial Technology, University,  
Bhubaneswar, India  
e-mail: [achinta.sarkar1@gmail.com](mailto:achinta.sarkar1@gmail.com)

like fossil fuels. Moreover, fossil fuels will be depleted within next few decades. Available renewable energy sources are solar, wind, geothermal, wave, etc. Among these sources of energy, solar is the most promising one. Nevertheless, the energy production from hydropower plants depends on annual rainfall, while wind power depends on change in climate [4]. The burning of fossil fuels for energy is a normal practice. We tend to ignore the harmful aftermath of this. According to a survey by UNEP (2015), global-averaged mole fractions of carbon dioxide (CO<sub>2</sub>) in the air have already surpassed 410 parts per million (ppm), and if the CO<sub>2</sub> concentration follows the same trend as previous years, it may hit or exceed 414 ppm in 2021 [5].

Solar energy, which is renewable widely available and clean, provides enough energy to meet the worlds annual consumption needs. A photovoltaic solar panel converts directly solar energy into useful electrical energy through the process of photovoltaic. The output of photovoltaic cell directly depends on the intensity of light, and Sun's positions change continuously in a day. Nevertheless, a dual-axis solar tracker fabricated with the panel can track the radiations coming from the Sun to achieve the maximum solar energy conversion. The electrical efficiency of the cells decreases with the increase in temperature. It is to be noted that there is the irreversible damage occurs at some operating limit of cell surface temperature. Thus, surface cooling can improve the electrical energy production of a standard PV module as well as can enhance the working life of a PV panel.

By conducting a thorough literature survey, we found out the following:

- The single-axis solar tracker gives about 8–13% increase in efficiency as compared to that of a fixed mounted solar panel [5, 6].
- The dual-axis solar tracker gives above 24–38% increase in efficiency depending on the latitude of the location where the panel has been installed [7–11].
- Cooling systems help to increase the efficiency. Phase-changing materials (PCMs) integrated on PV cells can reduce peak temperature of the cell up to 30 °C during peak sunshine hours which enhances the efficiency of PV cell up to 10% [12, 13].

This study is based on the implementation of both the technologies, i.e., dual-axis tracking and cooling system. The PV panel is mounted on a stand that can move in both axes. A water-based cooling system is used to control the solar PV panel surface temperature.

## 2 Objective

The main objective of the present study is to increase the efficiency of solar panels and to make it more economical and versatile. Thus, it can be used and handled by ordinary people. The increase in efficiency can make it widely useful for domestic use which will reduce the dependence on the non-renewable energy to a reliable renewable energy.

### 3 Experimental Setup

**Dual-Axis Solar Tracker Setup:** The dual-axis solar tracker (Fig. 1) can move in east to west and north to south directions as well as it can be tilted relative to the horizontal plane with the help of a DC motor of speed 10 rpm each. Two pairs of sensor unit are placed in the setup, which detects the variation in Sun intensity and the exact position and sends the signal to Arduino Nano microcontroller. Then, the intensity is compared and analyzed to convey the signal to rotate the motor in a correct direction to achieve maximum intensity of light. Bevel gears are installed which is used for changing the direction of panel also to transmit power at 90° right angle. A limiting switch is used which controls the rotation of panel.

**Cooling System Setup:** The main task of the cooling system is to maintain the surface temperature of the solar panel. The cooling system setup mainly consists of a heat-exchanging pipe attached below the panel (Fig. 2). Water flows through this pipe which absorbs the heat from the panel surface and helps in maintaining the

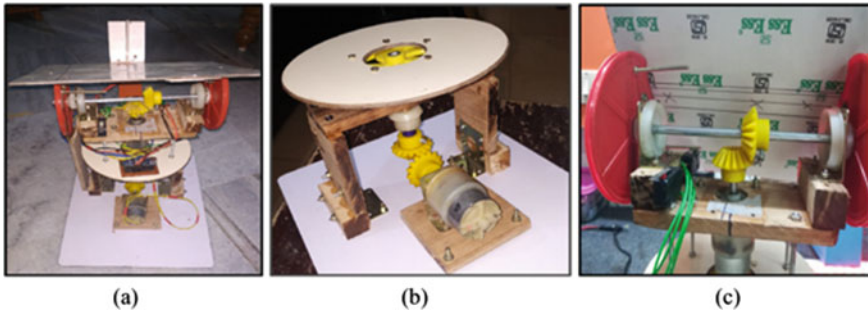


Fig. 1 a Dual-axis tracking setup, b Horizontal axis motor, and c Vertical axis motor

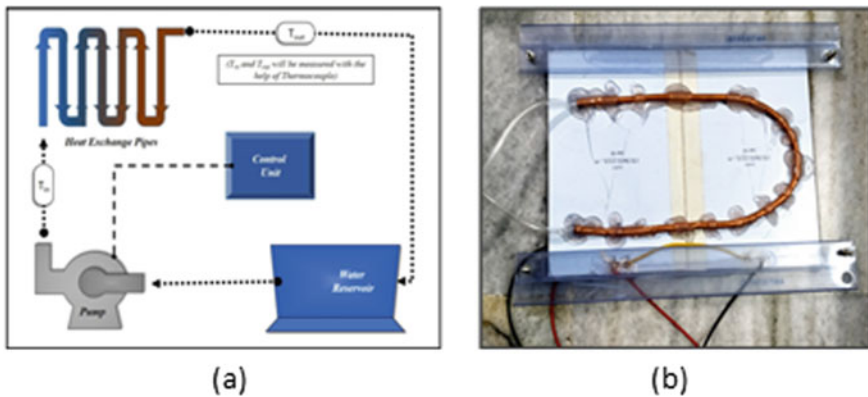


Fig. 2 Cooling a system setup b copper tube attached beneath of the panel surface

surface temperature. The setup also requires a water pump and a water reservoir. The flow of the water and operation of the pump is controlled by temperature module (W1209).

## 4 Methodology

In order to develop the dual-axis tracking system in the present study, light-dependent resistor (LDR), whose resistance decreases with the increase in incident light intensity, is used as the sensor for detecting the variation of intensity of light. Two 12-V full-g geared motors are used to rotate the solar panel in horizontal and vertical axes. To track the Sun movement accurately, dual-axis tracking system is necessary. Dual-axis tracker accurately moves the panel surface through the feedback system toward the Sun in such a way that the radiation is perpendicular to the plane of the panel. Thus, it gives the highest efficiency. The main objective of this experimental investigation is to improve the power gain by accurate tracking of the Sun. The daily motion causes the Sun to appear in east to west direction over the earth, whereas the annual motion causes the Sun to tilt at an angle of  $23.5^\circ$  while moving along east–west direction. Due to this reason, maximum efficiency of the solar panel is not achieved by single-axis tracking system. Two pairs of light-dependent resistors (LDRs) are used as sensors to track the Sun's exact position. One pair senses the position of the Sun in vertical axis, i.e., east and west side and other pair in the horizontal axis, i.e., north and south side. For this study, Arduino Nano microcontroller is used. The design of the light sensor is based on the use of the shadow that generates in the direction of the movement of the Sun at the edge of the panel. If the PV panel is not perpendicular to the sunlight, the shadow of the quadrant wall will cover one or two LDRs, and this causes different light intensity to be received by the sensing device. The output from the LDR comes to the input of the microcontroller, which then compares the intensity and determines the correct direction of rotation of the motors to orient the panel perpendicular to the sunlight. For the cooling system, copper tube is attached beneath the panel, which acts as the heat-exchanging pipe. The water flows through this pipe, which absorbs the heat from the surface of the panel to help maintain its temperature. The water is stored in a water reservoir, which is pumped through a 6 V water pump. The entire cooling system is controlled by a temperature module, which switches on when it reaches at the set temperature.

## 5 Results and Discussion

In the present study, experiments are conducted on a solar PV panel at static and with tracking system. The experiments are conducted from 7:30 to 16:30 h with one-hour interval. A comparative analysis on the generation of current, voltage, and gain in power has been conducted with tracking system as compared to the static condition

**Table 1** The effect of cooling on power generation of the solar PV panel

Days	Time (hour)	Initial voltage (when panel was not heated) (V)	Voltage (After 15 min, the panel temperature increased) (V)	Voltage (After 15 min of cooling, the panel temperature decreased) (V)
Day-1	12:30	11.9	11.4	11.8
	14:00	11.7	11.2	11.9
Day-2	12:30	11.8	11.5	11.8
	14:00	11.9	11.1	11.7

of the solar PV panel. In all aspects, the solar PV panel with tracking system produces highest output and gain in power in comparison to the panel at static condition as shown in Fig.

In the early morning, a very high amount of gain in energy (77.48%) with tracking system is estimated as compared to panel at static condition. On an average, 31.38% power has been gained throughout the day. Table 1 shows the comparison in the voltage output when cooling system is used for the afternoon hours of the day when the temperature is at peak. The testing was carried for two days between 12:30 pm and 2:00 pm.

## 6 Conclusion and Future Scope

The present study achieved a significant gain in energy with the use of solar tracking as well as cooling systems. The analysis of the results led us to believe that this research work (prototype) may contribute in the development of full solar tracking system to generate the higher energy and can be used for the domestic purposes. It is a simple and cost-effective control implementation as compared to the solar thermal energy reservoir. It has the ability to move the two axes simultaneously within their respective ranges, and increase the output voltage by maintaining the surface temperature (Fig. 3).

With the advancements of technology, the present study has a bright scope in providing higher efficiency in commercial PV panel. As India is a developing nation and heavily dependence on imported fossil fuels, hence, harnessing of solar energy has the potential to turn it into an energy-rich country with abundant resources. In the very near future, traditional energy would not be adequate to satisfy the demand, which necessitating the use of non-conventional energy sources.



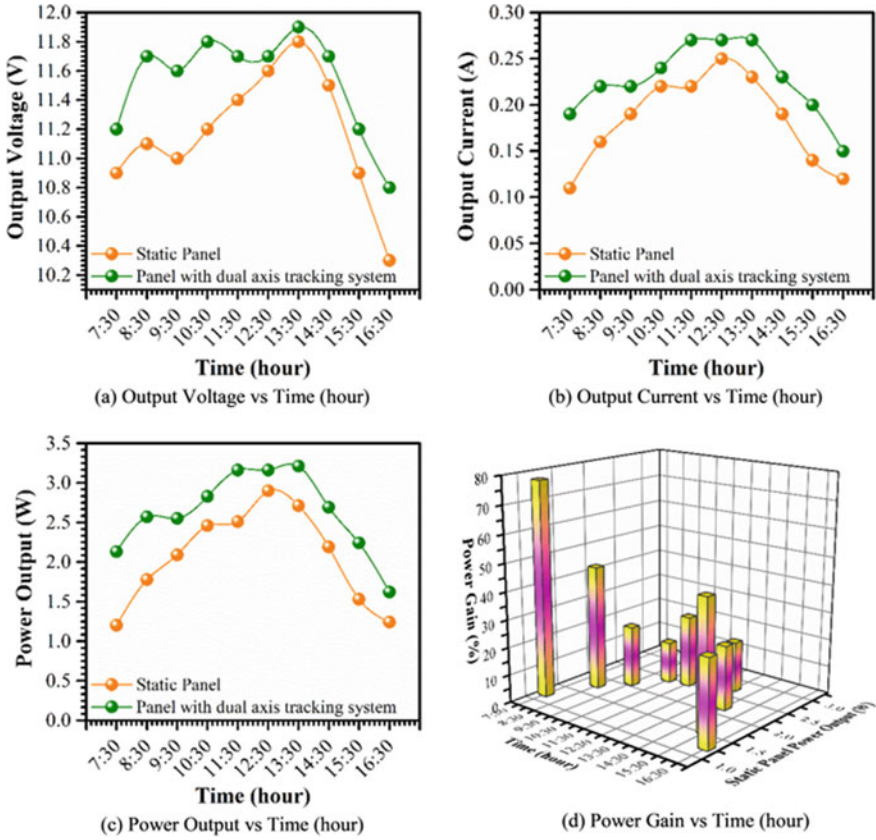


Fig. 3 Comparison of a output voltage, b output current, c power output, and d percentage gain in output power as compared to power generation with static panel with respect to time (hour)

### References

1. Carballo JA, Bonilla J, Roca L, Berenguel M (2018) New low-cost solar tracking system based on open source hardware for educational purposes. *Solar Energy* 174:826–836. <https://doi.org/10.1016/j.solener.2018.09.064>
2. Awasthi A, Shukla AK, Manohar SRM, Dondariya C, Shukla KN, Porwal D, Richhariya G (2020) Review on sun tracking technology in solar PV system. *Energy Rep* 6:392–405. <https://doi.org/10.1016/j.egy.2020.02.004>
3. Das M, Akpinar EK (2021) Investigation of the effects of solar tracking system on performance of the solar air dryer. *Renew Energy* 167:907–916. <https://doi.org/10.1016/j.renene.2020.12.010>
4. Climate change indicators and impacts worsened in 2020 (<https://public.wmo.int/en/media/press-release/climate-change-indicators-and-impacts-worsened-2020>)
5. Iqbal MK, Islam T, Chowdhury M, Imteaj A (2015) Construction of single axis automatic solar tracking system. *Int J u e-Service Sci Technol* 8(1):389–400

6. Dhanabal R, Bharathi V, Ranjitha R, Ponni A, Deepthi S, Mageshkannan P (2013) Comparison of efficiencies of solar tracker systems with static panel single-axis tracking system and dual-axis tracking system with fixed mount. *Int J Eng Technol* 5(2):1925–1933
7. Jaouhari EZ, Zaz Y, Moughyt S, Kadmiri EO, Kadmiri EZ (2019) Dual-axis solar tracker design based on a digital hemispherical imager. *J Sol Energy Eng* 141(1):2019
8. Laseinde T, Ramere D (2019) Low-cost automatic multi-axis solar tracking system for performance improvement in vertical support solar panels using Arduino board. *Int J Low-Carbon Technol* 14(1):76–82
9. Ferreira LA, Loschi HJ, Rodriguez AA, Iano Y, do Nascimento DA (2018) A solar tracking system based on local solar time integrated to photovoltaic systems. *J Solar Energy Eng* 140(2):021010-1-9. <https://doi.org/10.1115/1.4039094>
10. Yazidi A, Betin F, Notton G, Capolino GA (2006) Low cost two-axis solar tracker with high precision positioning. In: 2006 first international symposium on environment identities and Mediterranean area, pp 211–216
11. Kumar VSS, Suryanarayana S (2014) Automatic dual axis sun tracking system using LDR Sensor. *Int J Curr Eng Technol* 4:3214–3217
12. Tiwari AK, Sontake VC, Kalamkar VR (2020) Enhancing the performance of solar photovoltaic water pumping system by water cooling over and below the photovoltaic array. *J Solar Energy Eng* 142(2):021005-1-9. <https://doi.org/10.1115/1.4044978>
13. Waqas A, Jie J (2018) Effectiveness of phase change material for cooling of photovoltaic panel for hot climate. *J Solar Energy Eng* 140(4):041006-1-10. <https://doi.org/10.1115/1.4039550>

# Study of Electrical Behaviors of PVDF/BiGdO<sub>3</sub> Polymer Composite



Minakshi Padhy, Laxmidhar Sahoo, Ananya Rath,  
and P. Ganga Raju Achary

**Abstract** In this communication, Polyvinylidene fluoride or polyvinylidene difluoride (PVDF) polymer matrix and 10 wt% Bismuth Gadolinium Oxide (BiGdO<sub>3</sub>) as the inorganic phase based polymer-inorganic composite is fabricated. The structural, electrical modulus, dielectric and impedance behaviors were analyzed for the PVDF/BiGdO<sub>3</sub> polymer composite. The PVDF/BiGdO<sub>3</sub> polymer composite exhibited attractive dielectric and impedance behaviors with very low tangent loss. The effect of Maxwell–Wagner–Sillars polarization arises because of the accumulation of charges at the phase boundaries and the lower conductive capacity in the polymer phase. The Nyquist plot is fitted with an equivalent circuit model {(CQR)(CR)}, for (CQR):  $C$  = bulk capacitance ( $C_b$ ),  $Q$  = constant phase element,  $R$  = bulk resistance ( $R_b$ ); whereas for (CR):  $C$  = grain boundary capacitance ( $C_{gb}$ ),  $R$  = grain boundary resistance ( $R_{gb}$ ). The value of  $R_b$  decreased from  $8.985 \times 10^4 \Omega \text{ cm}^2$  to  $5.158 \times 10^4 \Omega \text{ cm}^2$  with rising temperature. From the Nyquist plot, the negative temperature coefficient of resistance (NTCR) behavior of the composite was predicted.

**Keywords** PVDF · BiGdO · Polymer composites · Relaxation time · Nyquist plot

## 1 Introduction

Polymer composites are one of the type of organic–inorganic composite materials, which leads high thermal stability and flexibility. Polyvinylidene fluoride or polyvinylidene difluoride (PVDF) as a matrix plays an important role due to its good breakdown strength, flexibility and good electrical properties. More over PVDF polymer is more compatible with electro ceramic (inorganic) fillers and also enhances the electronic and thermal behavior [1]. From literature it can be studied

---

M. Padhy · A. Rath · P. G. R. Achary (✉)

Department of Chemistry, Siksha ‘O’ Anusandhan (Deemed to be University), Khandagiri,  
Bhubaneswar 751030, India  
e-mail: [pgrachary@soa.ac.in](mailto:pgrachary@soa.ac.in)

L. Sahoo

K.B.D.A.V. College, Nirakarpur, Khordha, India

that the ceramic-polymer (PVDF) composites have very good ferroelectric, dielectric and piezoelectric properties [2]. It has been noticed that PVDF is taken as polymer or co-polymer matrix with different electroceramics like BaTiO<sub>3</sub> [3], MgTiO<sub>3</sub> [4], Pb(Zr<sub>x</sub>Ti<sub>1-x</sub>)O<sub>3</sub> (PZT) [5] etc. PVDF has better flexibility, breakdown strength with an overall dielectric constant of ~10. It has also comparatively better energy density (discharged, the energy density of 2.8 J/cm<sup>3</sup> at 2400 kV/cm) than other polymers [1]. On the other hand BiGdO<sub>3</sub> material has antiferroelectric and good dielectric behavior as well as unique luminous, electrical and electromagnetic properties [6, 7]. Due to the excellent breakdown electric field and flexibility of polymer materials, these are used widely in energy storage applications, but these have a lower dielectric constant. To enhance the dielectric permittivity and breakdown-strength, these are blended with the inorganic fillers as well as surface-modified inorganic fillers to obtain polymer/ceramic composites by managing the dispersion stability of fillers in polymers [8, 9]. Rare-earth ions (Gd<sup>3+</sup>, Er<sup>3+</sup>, Sm<sup>3+</sup>, etc.) have very interesting chemical characteristics, with a comparatively larger size, low ability for making covalent bonds, and high electrostatic influence with (-)vely charged-ligands. Sometimes higher ceramic fillers i.e. 30 wt% or above shows more dielectric permittivity, that frequently worsen the mechanical behavior of the composite [10] and very low percentage of filler loading may not reach the expectation.

In this study, Polyvinylidene fluoride or polyvinylidene difluoride (PVDF) polymer matrix and 10 wt% Bismuth Gadolinium Oxide (BiGdO<sub>3</sub>) as the inorganic phase based polymer-inorganic composite is fabricated. The structural, electrical modulus, dielectric and impedance behaviors were evaluated for the above PVDF/BiGdO<sub>3</sub> polymer composite.

## 2 Preparation of PVDF/BiGdO<sub>3</sub> Composite Films

The ceramic BiGdO<sub>3</sub> was synthesized by taking highly pure oxides of Bi and Gd and processed by using the solid-state reaction method. These oxides are mixed homogeneously by both dry and wet (in methanol medium) method with the help of Agate Mortar and Pestle (for 4 h). After that the powder was calcined at 850 °C. To know the formation of the material XRD analysis was done. By taking 10 weight% (wt% or phr) of BiGdO<sub>3</sub> in PVDF the polymer solution is prepared by utilizing the DMF as a solvent and followed 2 h sonication for homogeneous dispersion of BiGdO<sub>3</sub>. The obtained thick solution was used to make a thin sheet by using Petri dish and dried for 24 h without disturbing and collected from the Petri-dishes for further observations. For electrical analysis, the electroding was prepared at two opposed sides of the thin film (1 cm<sup>2</sup>) by painting a thin layer of high quality conducting silver paint (Alfa Aesar). The dielectric behavior was verified by LCR and Phase-Sensitive-Meter (model N4L, PSM-1735).

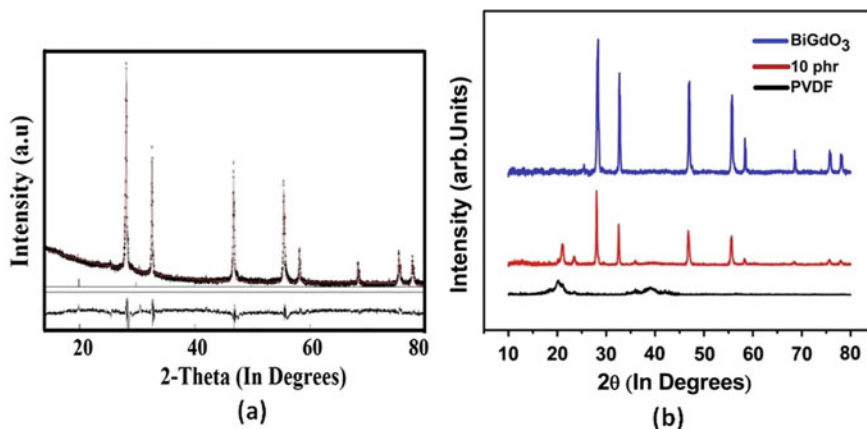


**Fig. 1** **a** The Rietveld refinement of the XRD patterns of BiGdO<sub>3</sub>. **b** XRD patterns of PVDF/BiGdO<sub>3</sub> composite with 10 phr filler

### 3 Results and Discussion

#### 3.1 XRD Analysis

The XRD pattern by means of the Rigaku diffractometer (Cu K $\alpha$  radiation;  $\lambda = 1.54056 \text{ \AA}$ ) in the range of  $2\theta$  ( $10^\circ$ – $80^\circ$ ) of BiGdO<sub>3</sub> and the 10 phr PVDF/BiGdO<sub>3</sub> composite film are represented in Fig. 1a, b. The Rietveld refinement of the XRD patterns of BiGdO<sub>3</sub> is accomplished by using MAUD software (Fig. 1a) and the reference material Bismuth Gadolinium Oxide (1004122.cif). From the refinement the synthesized BiGdO<sub>3</sub> material structure is found to be cubic-I2<sub>1</sub>3 with lattice parameter  $a = b = c = 10.946$ . From Fig. 1b, it can be analyzed that the XRD patterns of PVDF/BiGdO<sub>3</sub> composite have both the peaks of PVDF and BiGdO<sub>3</sub>. Here it is noticed that with the incorporation of BiGdO<sub>3</sub> in the PVDF, the intensity of the peaks of PVDF is reduced. This occurs because of the breaking up the orderly arrangement of the molecular structure of the PVDF.

#### 3.2 Dielectric Study

Both the dielectric permittivity ( $\epsilon_r$ ) and tangent loss ( $\tan \delta$ ) can be measured from the capacitance. Capacitance in between two parallel plate capacitors directly depends on the value of  $\epsilon_r$  of the material. When a dielectric-material is located in the gap of two parallel capacitors, the value of capacitance increases according to the material. The  $\epsilon_r$  can be defined as:  $\epsilon_r = C_p/C_0$ ;  $C_0 = \epsilon_0 A/d$  where,  $A$  and  $d$  is an area and

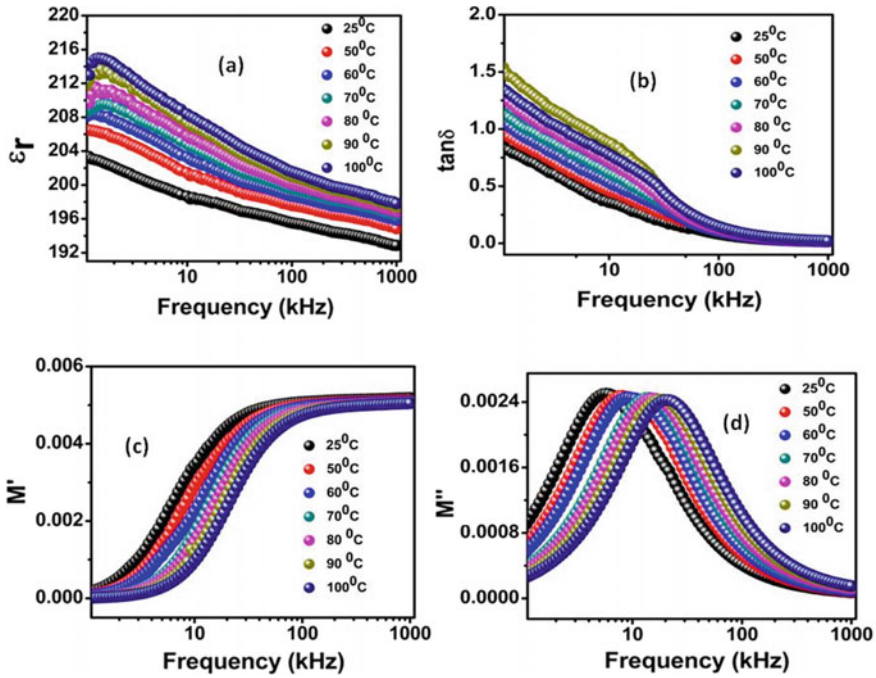


**Fig. 2** The frequency dependence of **a**  $\epsilon_r$ , **b**  $\tan \delta$ , **c**  $M'$  and **d**  $M''$  for PVDF/BiGdO<sub>3</sub> polymer composite

thickness of the material respectively.  $C_p$  is the capacitance of the material to be studied and  $C_0$  is the capacitance of the vacuum.

Figure 2a, b shows the variation of dielectric permittivity ( $\epsilon_r$ ) and  $\tan \delta$  with frequency respectively at various temperatures for the studied PVDF/BiGdO<sub>3</sub> polymer composite. The decrease in  $\epsilon_r$  and  $\tan \delta$  value is observed with rise in frequency. This type of properties is because of the interfacial-polarization (Maxwell–Wagner–Sillars polarization) [11]. From the figure it is noticed that the  $\tan \delta$  value is very low at room temperature and slowly increases with a rise in temperature. The reduction of the dielectric parameters ( $\epsilon_r$  and  $\tan \delta$ ) with an increase in frequency is also a common quality of dielectric materials. The dielectric relaxation mechanism can be better described by analyzing electric modulus of the material. The description of modulus is very important to know the way of interfacial polarization in a material. Moreover the electric-modulus mechanism is a very important factor to prevent the signal-intensity that occurs due to the electrode polarization. The complex electrical modulus is determined as  $M^* = M' + JM''$  and  $M^* = \frac{1}{\epsilon^*}$ ;  $M^* = \frac{\epsilon'}{\epsilon'^2 + \epsilon''^2} + j \frac{\epsilon''}{\epsilon'^2 + \epsilon''^2}$ , where  $M^*$ ,  $M'$ ,  $M''$  are complex electrical modulus, real parts of electrical modulus and imaginary parts of electrical modulus respectively. Further,  $\epsilon^*$ ,  $\epsilon'$  and  $\epsilon''$ . The effect of Maxwell–Wagner–Sillars polarization arises because of the accumulation of charges at the phase boundaries and the lower conductive

capacity in the polymer phase. Both the polymer and filler are responsible for the electrical relaxation behavior in this type of polymer composites. Figure 2c represents the frequency-dependent  $M'$  for PVDF/BiGdO<sub>3</sub> polymer composites at various temperature. The increment of the  $M'$  values with the rise in frequency forms the S-shaped dispersion of  $M'$  that indicates the ionic nature of PVDF/BiGdO<sub>3</sub> composite [12]. Due to segmental transition of PVDF the  $M'$  value reduces at lower frequencies and higher temperatures and remains constant at higher frequencies that describes the absence of orientation of dipoles [13, 14]. Figure 2d represents the variation of  $M''$  with frequency for PVDF/BiGdO<sub>3</sub> polymer composites at various temperatures. The shifting of relaxation peaks in the direction of high frequencies with a rise in temperature is because of the thermal activation of charge carriers. So, they possess a rapid movement and the decrease in the relaxation time, as well as increase in the relaxation frequency.

### 3.3 Impedance Study

Figure 3a represents a Nyquist plot (complex impedance spectrum) for 10 wt% PVDF/BiGdO<sub>3</sub> composite at various temperatures in a broad range of frequencies with inset of {(CQR)(CR)} circuit model. The Nyquist plot is fitted by using ZSIMP-WIN (version 2), from which it is observed the Nyquist plot demonstrates the outstanding resistive or capacitive behaviors of the grains and grain boundaries.

An equivalent circuit {(CQR)(CR)} is suggested to calculate the respective resistive and capacitive components ( $R$ ,  $C$ , and  $Q$ ). Table 1 shows calculated capacitance and the resistance value of grain and grain boundary. The value of  $n$  generally locates among '0' and '1',  $n = 0$  and  $n = 1$  for an ideal resistor and capacitor respectively [15]. The value of both  $R_b$  and  $R_{gb}$  is decreased with rising temperature, which recommends the NTCR behavior of the composite.

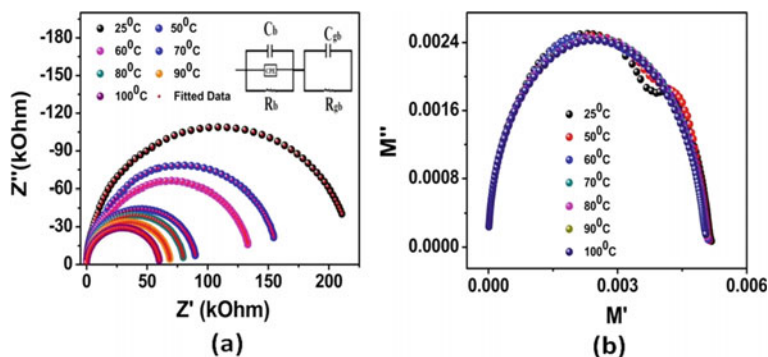


**Fig. 3** a Nyquist plot with inset of {(CQR)(CR)} circuit model and b Cole–Cole plot for PVDF/BiGdO<sub>3</sub> polymer composite

**Table 1** Grain and grain boundary resistance and parameters (fitted) of equivalent circuit: at various temperatures

Temp (°C)	$C_b$ (Fcm <sup>-2</sup> )	$Q$ (S s <sup>5</sup> cm <sup>-2</sup> )	$R_b$ ( $\Omega$ cm <sup>2</sup> )	$C_{gb}$ (Fcm <sup>-2</sup> )	$R_{gb}$ ( $\Omega$ cm <sup>2</sup> )	Frequency power ( $n$ )
25	$1.389 \times 10^{-14}$	$1.349 \times 10^{-9}$	$8.985 \times 10^4$	$1.412 \times 10^{-10}$	$2.086 \times 10^5$	0.978
50	$1.021 \times 10^{-12}$	$2.567 \times 10^{-9}$	$8.607 \times 10^4$	$1.469 \times 10^{-10}$	$1.901 \times 10^5$	0.985
60	$1.004 \times 10^{-10}$	$6.367 \times 10^{-10}$	$8.145 \times 10^4$	$1.590 \times 10^{-10}$	$1.217 \times 10^5$	0.994
70	$1.377 \times 10^{-10}$	$6.308 \times 10^{-11}$	$7.652 \times 10^4$	$1.153 \times 10^{-9}$	$1.389 \times 10^4$	0.829
80	$1.410 \times 10^{-10}$	$6.446 \times 10^{-11}$	$6.604 \times 10^4$	$9.783 \times 10^{-10}$	$1.435 \times 10^4$	0.821
90	$1.319 \times 10^{-10}$	$9.085 \times 10^{-11}$	$6.268 \times 10^4$	$2.054 \times 10^{-9}$	$6.512 \times 10^3$	0.782
100	$1.411 \times 10^{-9}$	$2.491 \times 10^{-10}$	$5.158 \times 10^4$	$1.119 \times 10^{-9}$	$5.708 \times 10^3$	0.715

$M''$  versus  $M'$  (Cole–Cole) plot can be used as a preference tool instead of the Nyquist plot to discriminate the outcomes of relaxation from conducting-sections (grain) and resistive-plates (grain boundary) in addition to resolve and understand the dynamical attributes of electrical-transport system i.e. rate of hopping (carrier/ion) and conductivity-relaxation time [16]. The observed successive semi-circular trends reveal the contribution of grain-boundaries/interfacial-behavior (1st semicircle) and the grain/bulk-behavior (2nd semicircle).

## 4 Conclusion

The PVDF with BiGdO<sub>3</sub> fillers with 10 wt% polymer composite film was prepared by using the solution casting method. The polymer composite film displayed better dielectric permittivity, low tangent loss and enhanced resistivity and capacitive properties. There was a decrease in grain boundary relaxation of the studied polymer composite with an increase in temperature, which was calculated from the cole–cole plot. From the Nyquist plot, the NTCR behavior of the composite was also predicted. The temperature and frequency dependent dielectric, modulus and impedance analysis contribute good ideas for the device application.

**Acknowledgements** The present work is funded by the UGC-DAE-CSR, Mumbai (CRS-M-297)



## References

1. Prateek TVK, Gupta RK (2016) Recent progress on ferroelectric polymer-based nanocomposites for high energy density capacitors: synthesis, dielectric properties, and future aspects. *Chem Rev* 116(7):4260–4317. <https://doi.org/10.1021/acs.chemrev.5b00495>
2. El-Sayed S, Abdel-Baset TA, Hassen A (2014) Dielectric properties of PVDF thin films doped with 3 wt.% of  $R\text{Cl}_3$  ( $R = \text{Gd}$  or  $\text{Er}$ ). *AIP Adv* 4(3):037114. <https://doi.org/10.1063/1.4869093>
3. Qu B, Hongliang D, Yang Z (2016) Lead free relaxor ferroelectric ceramics with high optical transparency and energy storage ability. *J Mater Chem C* 4. <https://doi.org/10.1039/C5TC04005A>
4. Wang J, Li Y, Sun N, Zhang Q, Zhang L, Hao X, Chou X (2017) Effects of Fe 3+ doping on electrical properties and energy-storage performances of the (Na 0.85 K 0.15) 0.5 Bi 0.5 TiO 3 thick films prepared by sol-gel method. *J Alloys Comp* 727:596–602. <https://doi.org/10.1016/j.jallcom.2017.08.169>
5. Yu G et al (2007) A glycosylated complex of gadolinium, a new potential contrast agent for magnetic resonance angiography? *Bioorg Med Chem Lett* 17(8):2246–2249. <https://doi.org/10.1016/j.bmcl.2007.01.067>
6. Jana R et al (2020) Anomalous structural behavior and antiferroelectricity in BiGdO<sub>3</sub> Detailed temperature and high pressure stud. *cond-mat.mtrl-sci*. [arXiv:2002.09332v1](https://arxiv.org/abs/2002.09332v1)
7. Saha S et al (2014) Dielectric relaxation and anti-ferromagnetic coupling of BiEuO<sub>3</sub> and BiGdO<sub>3</sub>. *J Magnet Magnet Mater* 360:80–86. <https://doi.org/10.1016/j.jmmm.2014.01.075>
8. Yao L et al (2018) High-energy-density with polymer nanocomposites containing of SrTiO<sub>3</sub> nanofibers for capacitor application. *Comp Part A Appl Sci Manuf* 109:48–54. <https://doi.org/10.1016/j.compositesa.2018.02.040>
9. Ponraj B, Bhimireddi R, Varma KBR (2016) Effect of nano- and micron-sized K<sub>0.5</sub>Na<sub>0.5</sub>NbO<sub>3</sub> fillers on the dielectric and piezoelectric properties of PVDF composites. *J Adv Cer* 5(4):308–320. <https://doi.org/10.1007/s40145-016-0204-2>
10. Guo Q et al (2016) Excellent dielectric properties of PVDF-based composites filled with carbonized PAN/PEG copolymer fibers. *Comp Part A Appl Sci Manuf* 87:46–53. <https://doi.org/10.1016/j.compositesa.2016.04.008>
11. Padhy M et al (2020) Structural, impedance and electrical evaluation of complex perovskite: Ca(Mn<sub>1/3</sub>Ni<sub>1/3</sub>W<sub>1/3</sub>)O<sub>3</sub>. *Bull Mater Sci* 43:258. <https://doi.org/10.1007/s12034-020-02229-w>
12. Padhy M et al (2020) Structural, dielectric, thermal and electrical characteristics of lead-free double perovskite: BiHoZnCeO<sub>6</sub>. *Appl Phys A* 126. <https://doi.org/10.1007/s00339-020-03852-4>
13. Saji J, Khare A, Mahapatra SP (2015) Impedance and dielectric spectroscopy of nano-graphite reinforced silicon elastomer nanocomposites. *Fib Polym* 16:883–893. <https://doi.org/10.1007/s12221-015-0883-2>
14. Padhy M, Khatua D, Choudhary RNP, Achary PGR (2021) Synthesis and characterization of single perovskite Ba(Ni<sub>1/3</sub>Mn<sub>1/3</sub>W<sub>1/3</sub>)O<sub>3</sub>. *Ferroelectrics* 572:135–146. <https://doi.org/10.1080/00150193.2020.1868878>
15. Padhy M, Choudhary RNP, Achary PGR (2021) Dielectric, ferroelectric and impedance study of Bi<sub>0.5</sub>Ba<sub>0.5</sub>Gd<sub>0.5</sub>Ti<sub>0.5</sub>O<sub>3</sub>. *J Mater Sci Mater Electron* 32:20625–20639. <https://doi.org/10.1007/s10854-021-06572-4>
16. Padhy M, Choudhary RNP, Achary PGR (2021) Impedance and electrical evaluation of Rare earth based perovskite: BiYbO<sub>3</sub>. *SPIN* 2150019. <https://doi.org/10.1142/S2010324721500193>

# Performance Characteristics Optimization of Castor Oil Biodiesel-Powered Compression Ignition Engine Using RSM-Whale Optimization Algorithm



**Bibhuti Bhusan Sahoo, Prasanta Kumar Sahoo, Abhishek Barua ,  
Dilip Kumar Bagal , Siddharth Jeet , Laxmi Narayan Rout,  
and Arati Rath**

**Abstract** This article discusses response surface methodology (RSM) modeling, followed by optimization of various castor biodiesel and fossil diesel blends, engine loading, and fuel injection pressure of a diesel engine powered by castor oil biodiesel blends. Based on the response surface methodology, the Box-Behnken technique was utilized for experimental design, and three output responses were evaluated: brake thermal efficiency (BTE), lowest brake-specific fuel consumption (BSFC), and exhaust gas temperature (EGT). The whale optimization method, in conjunction with the RSM design of experiment, was used to optimize engine operating parameters. The optimization method resulted in the creation of non-dominated optimum points, which provided insight into the engine's ideal operating circumstances. It was determined that the B15 mix of castor oil biodiesel provided the best BTE and BSFC, while the B25 blend provided the best EGT. In addition, the predictions provided by the whale optimization algorithm were more exact than those given by RSM. Finally, experimental confirmation was performed to determine the efficacy of the suggested technique.

**Keywords** ANOVA · Castor biodiesel · Compression ignition engine · Response surface methodology · Whale optimization algorithm

---

B. B. Sahoo · P. K. Sahoo (✉)  
Siksha 'O' Anusandhan University, Bhubaneswar, Odisha, India  
e-mail: [prasantakumarsahoo@soa.ac.in](mailto:prasantakumarsahoo@soa.ac.in)

A. Barua · S. Jeet  
Centre for Advanced Post Graduate Studies, BPUT, Rourkela, Odisha, India

D. K. Bagal · L. N. Rout  
Government College of Engineering, Kalahandi, Bhawanipatna, Odisha, India

A. Rath  
Kalinga Institute of Industrial Technology, Bhubaneswar, Odisha, India

## 1 Introduction

Nowadays, biodiesel is made from various organic compounds and used for powering compression ignition engine. They have shown to be a superior alternative to petroleum diesel fuel; although, it requires engine modification or quality enhancement. Biofuels can give a viable answer to the issue for the world's poorest countries. Alcohol, vegetable oils, biomass, and biogas are examples of bio-origin fuels. Some of these fuels may be used directly, while others must be manufactured to have characteristics similar to conventional fuels. The electricity consumed in agriculture and transportation is mostly dependent on diesel fuels; thus, alternatives to diesel fuels must be developed [1–5]. For the reason that of its renewability and lower gas emissions after burning, biodiesel has grown in popularity. Biodiesel such as *Jatropha*, soybean, Karanja, Mahua, castor oil, sunflower, neem and others are widely used as petroleum diesel replacements. Biodiesel derived from these substances is eco-friendly and biodegradable which can be used in either pure or in blended form with petroleum diesel [6–11].

Different researchers have tried to attain optimal way for the production of different blend of castor oil biodiesel, but very less attention has been given in optimizing the operation parameter and attaining a single blend which can be optimal in providing better performance of diesel engine power using castor oil biodiesel blend. Based on these findings, the goal of this research is to enhance diesel engine operating parameters in order to enhance the performance of a compression ignition engine fueled by a blend of castor biodiesel and petroleum diesel. As input operational parameters with varying levels, various castor biodiesel-fossil diesel mixes, fuel injection pressure, and engine load were investigated. Based on the response surface methodology, the Box-Behnken technique was employed for experimental design, and three output responses were evaluated: brake thermal efficiency, exhaust gas temperature along with brake-specific fuel consumption and optimized by employing whale optimization method. Following the forecast of the best operating parameters, confirmation experiments were carried out to validate the proposed model.

## 2 Biodiesel Preparation

Castor oil, like other less expensive vegetable oils available today, may be utilized as a feedstock in the manufacture of biodiesel. Because of its very low cloud and pour characteristics, the resultant fuel is ideal for cold winters. The transesterification process is used to produce biodiesel from castor oil. This procedure can be completed in three phases. Initially, 1000 cc of castor oil was heated at 110 °C for 60–80 min using a magnetic stirrer heating plate to eliminate moisture content. After heating, the oil is cooled to a temperature of around 60 °C. 300 cc of methanol was mixed with 1 to 1.5% weight of para-toluene sulphonic acid. After preparing the solution, it was progressively added to boiling oil and cooked for 60–90 min. The following

**Table 1** Different operational constraints with different levels

Code	Parameters	L-1	L-2	L-3
A	Biodiesel blend	15%	20%	25%
B	Injector nozzle pressure	160 bar	190 bar	220 bar
C	Engine load	20%	60%	100%

process is known as transesterification. 300 cc of methanol was combined with 1 percent weight of potassium hydroxide. This solution was boiled for 1 h and then allowed to cool in a separating flask for 14–16 h. Glycerol is separated from oil using this method (glycerol have more density). The next step is to wash the oil with water to remove any leftover glycerol and solution contaminants. To begin, heat the water to 60–65 °C, then combine it with the oil in a 1:4 ratio and shake vigorously for 2 min. The solution was let to stand for 15 min to allow the contaminants in the water to settle. This procedure is repeated 4–5 times. After the water treatment was done, the oil was heated to 110 °C for 60–90 min.

### 3 Experimental Arrangement

Investigations were conducted on a diesel engine linked to an eddy current dynamometer for the testing. Using a gasoline flowmeter, the rate of fuel consumption was measured. It was possible to adjust fuel injection pressure simply by tightening or loosening the injector unit's screw. This gauge was used to monitor and measure the exhaust gas's temperature. Table 4 provides the engine specifications, while Table 1 gives the various operating characteristics at various levels.

### 4 Whale Optimization Algorithm

Whale optimization algorithm is a novel metaheuristic algorithm that resembles humpback whale hunting [12]. Humpback whales hunt schools of shrimp or tiny fish near the surface by swimming around them in a diminishing circle and producing unique bubbles along a circle or '9'-shaped route. The first phase of the algorithm represents encircling prey and spiral bubble-net assaulting approach; exploited phase, the later phases where seek arbitrarily for a predator.

## 5 Results and Discussion

The experimental runs were conducted according to RSM Box-Behnken design and outcomes for exhaust gas temperature (EGT), brake thermal efficiency (BTE), and brake-specific fuel consumption (BSFC) were calculated and recorded in Table 2.

Figures 1, 2, and 3 show the plot of mean effect for BTE, EGT, and BSFC, respectively. In Fig. 1, the combination of A1, B1, and C2 represents the greatest value of the main impact plot for components A, B, and C, respectively, where BTE maximization is needed. As a result, the best diesel engine operating parameter combination is A1 B1 C2, i.e., B15 mix of castor oil biodiesel, fuel injector pressure of 160 bar, and engine load of 60%. In Fig. 2, the combination of A3, B2, and C2 represents the least value of the main effect plot for components A, B, and C, respectively, when EGT reduction is necessary. As a result, the best diesel engine operating parameter combination is A3 B2 C2, i.e., B25 mix of castor oil biodiesel, fuel injector pressure of 190 bar, and engine load of 60%. In Fig. 3, the combination of A1, B1, and C2 indicates the smallest value of the main effect plot for factors A, B, and C, respectively, where minimization of BSFC is required. Therefore, A1 B1 C2, i.e., B15 blend of castor oil biodiesel, fuel injector pressure of 160 bar, and engine load of 60% is the optimum diesel engine operating parameter combination. Table 3, 4, and 5 give the ANOVA results for BTE, EGT, and BSFC, respectively. In all three tables, it can be seen that the biodiesel blend is the most significant and contributing parameter for maximizing BTE and minimizing both EGT and BSFC while injector pressure is the second-most contributing factor in all three tables.

**Table 2** RSM based Box-Behnken design for experimental runs and output responses

Run No.	A	B	C	BTE (%)	EGT(K)	BSFC (kg/kWh)
1	15	160	60	34.88	534	0.25
2	25	160	60	29.5	466	0.29
3	15	220	60	34.39	522	0.25
4	25	220	60	30.67	496	0.29
5	15	190	20	33.17	514	0.26
6	25	190	20	28.77	473	0.29
7	15	190	100	34.11	521	0.26
8	25	190	100	28.97	467	0.30
9	20	160	20	31.22	501	0.31
10	20	220	20	30.86	505	0.30
11	20	160	100	29.91	497	0.30
12	20	220	100	29.23	511	0.30
13	20	190	60	29.33	481	0.31
14	20	190	60	28.99	477	0.30
15	20	190	60	29.56	489	0.32

**Fig. 1** Main effect plot for BTE

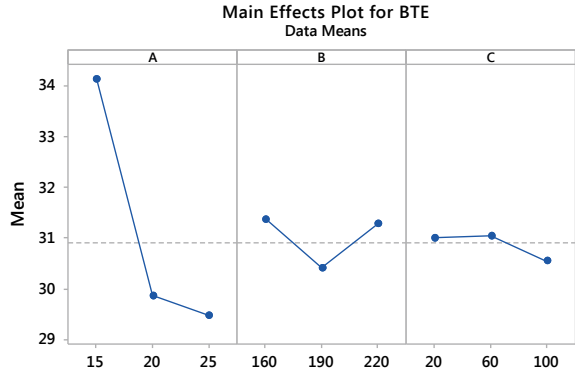


**Fig. 2** Main effect plot for EGT

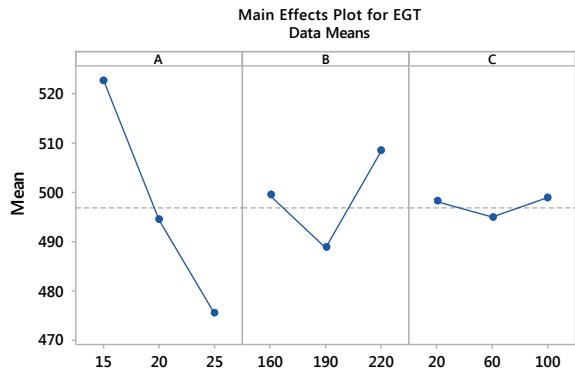
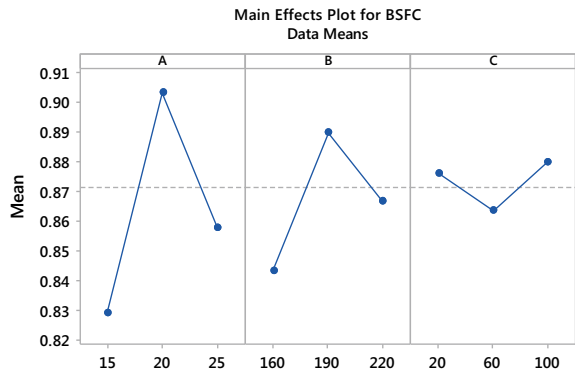


**Fig. 3** Main effect plot for BSFC



Regression equation was spawned after performing response surface methodology optimization, for serving for whale optimization algorithm.

Maximize

**Table 3** Analysis of variance of BTE

Source	DF	Adj SS	Adj MS	F-value	P-value	% influence
Model	9	62.8943	6.9883	13.24	0.005	95.97
Linear	3	43.8524	14.6175	27.69	0.002	66.92
A	1	43.4312	43.4312	82.28	0.000	66.27
B	1	0.0162	0.0162	0.03	0.868	0.02
C	1	0.4050	0.4050	0.77	0.421	0.62
Square	3	18.1905	6.0635	11.49	0.011	27.76
A * A	1	14.8926	14.8926	28.21	0.003	22.73
B * B	1	4.1356	4.1356	7.83	0.038	6.31
C * C	1	0.0080	0.0080	0.02	0.907	0.01
2-Way interaction	3	0.8514	0.2838	0.54	0.677	1.30
A * B	1	0.6889	0.6889	1.31	0.305	1.05
A * C	1	0.1369	0.1369	0.26	0.632	0.21
B * C	1	0.0256	0.0256	0.05	0.834	0.04
Error	5	2.6393	0.5279			4.03
Lack-of-fit	3	2.4748	0.8249	10.03	0.092	3.78
Pure error	2	0.1645	0.0822			0.25
Total	14	65.5336				

**Table 4** Analysis of variance of EGT

Source	DF	Adj SS	Adj MS	F-value	P-value	% influence
Model	9	6218.02	690.89	46.11	0.000	98.81
Linear	3	4628.25	1542.75	102.96	0.000	73.55
A	1	4465.12	4465.12	298.01	0.000	70.95
B	1	162.00	162.00	10.81	0.022	2.57
C	1	1.13	1.13	0.08	0.795	0.02
Square	3	1081.52	360.51	24.06	0.002	17.19
A * A	1	142.31	142.31	9.50	0.027	2.26
B * B	1	940.31	940.31	62.76	0.001	14.94
C * C	1	100.16	100.16	6.68	0.049	1.59
2-Way interaction	3	508.25	169.42	11.31	0.011	8.08
A * B	1	441.00	441.00	29.43	0.003	7.01
A * C	1	42.25	42.25	2.82	0.154	0.67
B * C	1	25.00	25.00	1.67	0.253	0.40
Error	5	74.92	14.98			1.19
Lack-of-fit	3	0.25	0.08	0.00	1.000	0.00
Pure error	2	74.67	37.33			1.19
Total	14	6292.93				

**Table 5** Analysis of variance of BSFC

Source	DF	Adj SS	Adj MS	F-Value	P-Value	% influence
Model	9	0.006898	0.000766	13.94	0.005	96.17
Linear	3	0.002825	0.000942	17.12	0.005	39.38
A	1	0.002813	0.002813	51.14	0.001	39.22
B	1	0.000012	0.000012	0.23	0.654	0.17
C	1	0.000000	0.000000	0.00	1.000	0.00
Square	3	0.004023	0.001341	24.38	0.002	56.09
A * A	1	0.003900	0.003900	70.91	0.000	54.37
B * B	1	0.000208	0.000208	3.78	0.110	2.90
C * C	1	0.000000	0.000000	0.00	1.000	0.00
2-Way interaction	3	0.000050	0.000017	0.30	0.823	0.70
A * B	1	0.000000	0.000000	0.00	1.000	0.00
A * C	1	0.000025	0.000025	0.45	0.530	0.35
B * C	1	0.000025	0.000025	0.45	0.530	0.35
Error	5	0.000275	0.000055			3.83
Lack-of-fit	3	0.000075	0.000025	0.25	0.858	1.05
Pure error	2	0.000200	0.000100			2.79
Total	14	0.007173				

$$\begin{aligned}
 \text{BTE} = & 122.4 - 4.150x_1 - 0.500x_2 + 0.0290x_3 + 0.0803x_1x_1 \\
 & + 0.001176x_2x_2 - 0.000029x_3x_3 + 0.00277x_1x_2 \\
 & - 0.00092x_1x_3 - 0.000067x_2x_3
 \end{aligned} \tag{1}$$

Minimize

$$\begin{aligned}
 \text{EGT} = & 1569 - 26.98x_1 - 8.113x_2 - 0.452x_3 + 0.2483x_1x_1 \\
 & + 0.01773x_2x_2 + 0.00326x_3x_3 + 0.0700x_1x_2 \\
 & - 0.01625x_1x_3 + 0.00208x_2x_3
 \end{aligned} \tag{2}$$

$$\begin{aligned}
 \text{BSFC} = & -0.539 + 0.05500x_1 + 0.00300x_2 - 0.000646x_3 \\
 & - 0.001300x_1x_1 - 0.000008x_2x_2 + 0.000000x_3x_3 \\
 & + 0.000000x_1x_2 + 0.000012x_1x_3 + 0.000002x_2x_3
 \end{aligned} \tag{3}$$

Subjected to constraints:

$$15 \leq a \leq 25; \quad 160 \leq b \leq 220; \quad 20 \leq c \leq 100$$



In the whale optimization algorithm, the total whale population size of 30 was taken with a range casing the complete array of values for  $x_1$   $x_2$   $x_3$  and maximum iteration of 100. Figures 4, 5, and 6 depict the fitness value obtained for BTE, EGT, and BSFC, respectively, and tabulated in Table 6.

Confirmatory experiments were carried out to determine the importance of projected values derived from the optimization method [12], which would aid in the development of optimal operating conditions for diesel engines. A fascinating observation is that the results generated by the whale optimization method are more exact than those obtained by the RSM. Using the whale optimization method, Table 6 shows that experimental findings of BTE, EGT, and BSFC are virtually identical to anticipated values, since maximizing of BTE coupled with reduction of EGT and BSFC is required for optimal functioning of a diesel engine. Compared to earlier research [11, 12], the results were quite similar.

**Fig. 4** Best fitness plot for BTE

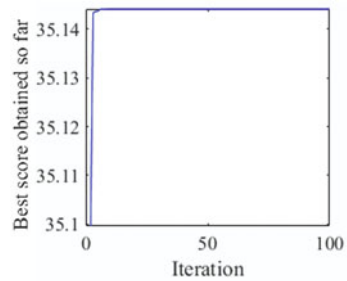


**Fig. 5** Best fitness plot for EGT

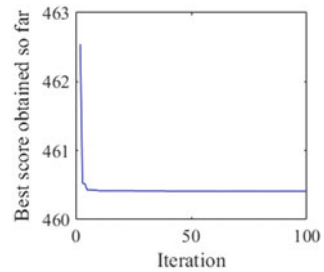


**Fig. 6** Best fitness plot for BSFC

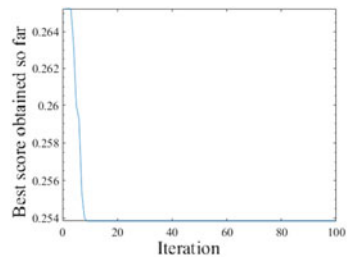


**Table 6** Optimal factor settings

Output responses	Algorithm	Biodiesel blend	Injector nozzle pressure (bar)	Engine load (%)	Predicted value	Experimental value
Brake thermal efficiency	Response surface methodology	15% or B15	160	60	35.15%	34.88%
	Whale optimization algorithm	15% or B15	160	60	35.14%	34.88%
Exhaust gas temperature	Response surface methodology	25% or B25	190	60	464.91 °C	460.11 °C
	Whale optimization algorithm	25% or B25	160	60	460.41 °C	460.11 °C
Brake-specific fuel consumption	Response surface methodology	15% or B15	220	60	0.3 kg/kWh	0.27 kg/kWh
	Whale optimization algorithm	15% or B15	160	100	0.2541 kg/kWh	0.253 kg/kWh

## 6 Conclusion

The examination of performance characteristics covers three distinct functioning constraints of a diesel engine, namely three blends of castor oil biodiesel and fossil diesel, fuel injection pressure, and engine load. For evaluation of enactment features of the diesel engine, whale optimization algorithm was employed for optimization of brake thermal efficiency, exhaust gas temperature, and brake-specific fuel consumption. It was found that B15 blend is optimal for improving BTE and minimizing BSFC, while B25 is optimal for minimizing EGT. According to ANOVA, if maximization of BTE was combined with minimization of EGT and BSFC, the blend of castor oil biodiesel and fossil diesel was the most influential parameter for managing the operation of the diesel engine while injector nozzle was the second-most contributing factor. It can be also seen that optimal response value for BTE and EGT was obtained in 60% load on engine, while BSFC was better in 100% loading condition. These operational parameter predictions will allow researchers to improve the performance of castor oil biodiesel fired diesel engines.

## References

1. Bagal DK, Patra, AK, Jeet S, Barua A, Pattanaik AK, Patnaik D (2021) MCDM optimization of Karanja biodiesel powered CI engine to improve performance characteristics using super hybrid Taguchi-Coupled WASPAS-GA, SA, PSO method. In: Next generation materials and processing technologies. Springer, Singapore, pp 491–503
2. Sharma A, Singh Y, Gupta SK, Singh NK (2021) Application of response surface methodology to optimize diesel engine parameters fuelled with pongamia biodiesel/diesel blends. *Energy Sour Part A Recovery Utilization Environ Effects* 43(2):133–144
3. Sharma A, Singh Y, Singh NK, Singla A (2019) Sustainability of jojoba biodiesel/ diesel blends for DI diesel engine applications-Taguchi and response surface methodology concept. *Ind Crops Prod* 139:111587
4. Pandian M, Sivapirakasam SP, Udayakumar M (2011) Investigation on the effect of injection system parameters on performance and emission characteristics of a twin cylinder compression ignition direct injection engine fuelled with pongamia biodiesel–diesel blend using response surface methodology. *Appl Energy* 88(8):2663–2676
5. Sivaramakrishnan K, Ravikumar P (2014) Optimization of operational parameters on performance and emissions of a diesel engine using biodiesel. *Int J Environ Sci Technol* 11(4):949–958
6. Vadlamudi S, Goud RNK, Krishnaiah T (2019) Performance of diesel engine using bio-fuel from sesame oil. *Int J Innov Technol Exploring Eng* 8(10):1554–1558
7. Bahar D, Kirti G, Mounika R, Rajesham S (2018) Study of performance and emission characteristics of a compression ignition engine using tamarind biodiesel. *Int J Adv Technol Eng Explor* 5(43):134–139
8. Kumar MV, Babu AV, Kumar PR, Reddy SS (2018) Experimental investigation of the combustion characteristics of Mahua oil biodiesel-diesel blend using a DI diesel engine modified with EGR and nozzle hole orifice diameter. *Biofuel Res J* 5(3):863
9. Vinay SB, Yadav AK (2020) Optimisation of performance and emission characteristics of CI engine fuelled with Mahua oil methyl ester–diesel blend using response surface methodology. *Int J Ambient Energy* 41(6):674–685
10. Ganapathy T, Murugesan KA, Gakkhar RP (2009) Performance optimization of Jatropha biodiesel engine model using Taguchi approach. *Appl Energy* 86(11):2476–2486
11. Karnwal A, Hasan MM, Kumar N, Siddiquee AN, Khan ZA (2011) Multi-response optimization of diesel engine performance parameters using thumba biodiesel-diesel blends by applying the Taguchi method and grey relational analysis. *Int J Automot Technol* 12(4):599–610
12. Mohanty, A., Nag, K. S., Bagal, D. K., Barua, A., Jeet, S., Mahapatra, S. S., & Cherkia, H. (2021). Parametric optimization of parameters affecting dimension precision of FDM printed part using hybrid Taguchi-MARCOS-nature inspired heuristic optimization technique. *Materials Today: Proceedings*.

# Stability Analysis of Rainfall Induced Unsaturated Slope by Reliability Based Optimization Using Solver



Abhipsa Kar and Manas Ranjan Das

**Abstract** Unsaturated soil slopes induced by rainfall is characterized by downward progression of a wetting front which causes reduction in soil suction near surface leading to instability. In this case slip surface forms at a depth equal to that of wetting front parallel to the slope surface. Due to uncertainties associated with soil properties as well as failure of these slopes, probabilistic approach using reliability based optimization is preferred over conventional factor of safety based deterministic approach for their stability analysis. Present work is an attempt in this direction. MS Excel-based SOLVER has been used for computation of Hasofer-Lind Reliability Index. Total cohesion ( $C_t$ ), wetting front depth ( $h$ ), angle of internal friction ( $\phi$ ) and unit weight of soil ( $\gamma_b$ ) have been considered as correlated normal random variables. A sensitivity analysis has also been performed. Results prove the simplicity, rationality and robustness of reliability based stability analysis of rainfall induced soil slopes. Influence of various parameters on probability of failure of these slopes has also been examined.

**Keywords** SOLVER · Reliability based optimization · Rainfall induced slope

## 1 Introduction

Slope refers to an unsupported and inclined mass of soil. Infinite slopes are natural slopes which represent a semi-infinite soil mass, whereas finite slopes are mostly man-made slopes. There may be natural or anthropogenic causes which lead to failure of slopes. One of the major natural causes of slope failure is intensive or prolonged rainfall. Rainfall induced slope failure is a common phenomenon occurring in the tropical and sub-tropical regions of the world which causes loss in economy and human lives. The stability of slope in unsaturated soils increases when there is an increase in suction stress in dry conditions [1]. Infiltration of water due to prolonged or heavy rainfall decreases the suction stress drastically which ultimately reduces

---

A. Kar (✉) · M. R. Das

Siksha 'O' Anusandhan (Deemed to be University), Jagamara, Khandagiri, Bhubaneswar, India  
e-mail: [abhpsakar@soa.ac.in](mailto:abhpsakar@soa.ac.in)

the stability of unsaturated slopes. Coupled hydro-mechanical constitutive model of unsaturated soil developed using ABACUS UMAT can effectively analyze the seepage and displacement changes of rainfall induced slopes [2]. Study on instrumented model slopes which were subjected to artificial rainfall proves the failure susceptibility of the slope with increase in slope angle [3]. Because of the wide range of uncertainties involved in determination of soil properties, reliability based optimization procedures have been developed for estimation of slope stability in rainfall induced unsaturated soils [4–7]. A range of values for wetting front depths were considered for modeling infiltration response of the slope. Analysis of failed slope near Seattle, Washington using reliability based design optimization and analysis of a multi-layered coastal-embankment slope using Monte Carlo technique and modified Morgenstern-Price method confirms the negative influence of rainfall infiltration on the stability of the unsaturated slope [1]. It has been amply demonstrated through several examples that Microsoft Excel-based Solver is a practical and transparent ellipsoidal perspective for efficiently performing reliability analysis [8–10]. Its advantages lie on finding different combinations of design values without depending on fixed values of safety factors.

In this context, a model has been developed in the present study for stability analysis of rainfall induced slope by reliability based optimization considering the selected soil parameters as correlated normal random variables. A spreadsheet-based optimization tool has been used for computation of reliability index and the values of the variables at design point [11].

## 2 Stability Analysis of Rainfall Induced Slope

### 2.1 Planar Slip Surface and Limit Equilibrium

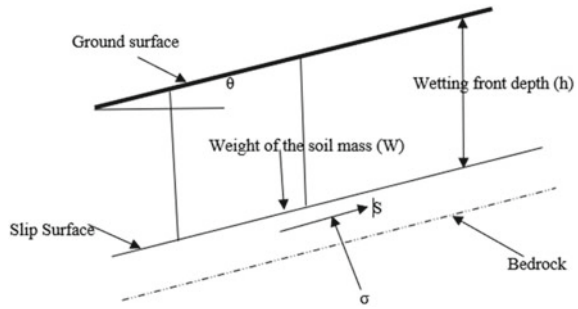
The failure surface lies parallel to the soil slope in majority of the infinite slope failures. Infiltration of rainwater into unsaturated soil slopes is responsible for the formation of a wetting front. The wetting front moves downward leading to the formation of failure surface. Factor of safety of a slope is the ratio of shear strength of soil to the shear stress acting mobilized along soil slope. The factor of safety (FOS) of a planar infinite slope is given by [6]

$$\text{FOS} = \frac{C_t + \gamma_b h \cos^2 \theta \tan \phi}{\gamma_b h \cos \theta \sin \theta} \quad (1)$$

where  $\gamma_b$  = unit weight of soil;  $C_t$  = total cohesion of the soil including the effect of matric suction;  $\theta$  = slope angle;  $h$  = depth of the wetting front.

The expanded Mohr–Coulomb model after incorporation of matric suction effects is given by

**Fig. 1** Failure surface of the slope



$$S = c' + (\sigma_z - u_a) \tan \phi' + (u_a - u_w) \tan \phi^h = C_t + ((\sigma_z - u_a) \tan \phi' \quad (2)$$

where  $S$  = shear strength of soil;  $\phi'$  = angle of internal friction;  $\phi^h$  = angle of rate of increase in shear strength with respect to matric suction;  $\sigma_z$  = total normal stress on the slope;  $u_w$  = pore water pressure;  $u_a$  = pore air pressure;  $c'$  = effective cohesion (Fig. 1).

## 2.2 Reliability Model

### Basic variables

The varying parameters  $\phi'$ ,  $h$ ,  $C_t$  and  $\Upsilon_b$  have been considered as basic variables in the present study. The value of  $\beta < 2.5$  is not much sensitive toward the distribution of the variables. The standard deviation of the variables is also small [6]. Therefore, a normal distribution of the variables is assumed for the present study. The statistics of the variables is mentioned in Table 1.

### Limit state function/Performance function

In the reliability approach, original space ( $S$ ) of random variables may be divided into safety and failure regions. The safety region,  $S_s$  can be defined as  $S_s = \{X|g(X) > 0\}$  and the failure region  $S_f$ , by  $S_f = \{X|g(X) \leq 0\}$ ; where  $g(X)$  represents the performance function. The boundary between safety and failure regions is represented by  $g(X) =$

**Table 1** Basic variables and their statistics

Random variable	Statistics			
	Mean	COV	Standard deviation	Distribution
$\phi'$	40°	0.035	0.035	Normal
$H$	0.2 m	0.05	0.05	Normal
$C_t$	2.93 kPa	0.39	0.39	Normal
$\Upsilon_b$	20.2 kN/m <sup>3</sup>	0.05	0.05	Normal

0 and is called the limit state surface. The value of factor of safety at limit state is 1. The performance function is given by

$$g(X) = C_t + \Upsilon_b h \cos^2 \theta \tan \phi - \Upsilon_b h \cos \theta \sin \theta \quad (3)$$

### Reliability Index

The most important step in a reliability analysis is the determination of reliability index or probability of failure of a system or a structure. For rehabilitation studies of geotechnical structures, reliability index is a significant parameter which measures the ability of a structure to function satisfactorily. It is not an absolute measure of probability. Implementation of reliability analysis will help in ensuring the maintenance of safety at a justifiable acceptable level. Transformation into standard normal variables for computation of reliability index as proposed by Hasofer and Lind [1] is given by

$$\bar{X} = \frac{Xi - E[Xi]}{\sigma[Xi]} \quad (i = 1, 2, \dots, n) \quad (4)$$

where  $\bar{X}$  represent the vector of design variables.

The Hasofer-Lind reliability index can be expressed as the minimum distance of the design point from the limit state surface and is given by [6]

$$\beta = \min \left( \bar{X}' \bar{X} \right)^{1/2} \quad (5)$$

The performance function in terms of reduced variables is given by

$$g(\bar{X}) = g(\bar{X}_1, \bar{X}_2, \dots, \bar{X}_n) \quad (6)$$

### Probability of failure

The probability of failure is evaluated using the following equation

$$P_f = P[g(x) < 0] \quad (7)$$

The relationship between reliability index and probability of failure is

$$\begin{aligned} P_f &= P[g(x) < 0] = \varphi(-\beta) \\ &= \text{Cumulative Distribution Function evaluated on } -\beta \end{aligned} \quad (8)$$

### Correlation Matrix

The correlation among the four design variables has been reflected in the correlation matrix. Correlated normal distribution of all the chosen variables is assumed in the

present study. The correlation matrix is duly checked to be positive definite as per requirement. For a symmetric matrix to be positive definite, all its Eigen values must be positive [9]. The correlation matrix is better explained by the ellipsoid perspective. If the variables are non-correlated, then each axis of the ellipsoid remains parallel to the corresponding co-ordinate axis. The ellipsoid becomes tilted if any correlation exists among the variables. This perspective has been employed in spreadsheet in a transparent and intuitive manner. The main objective in constrained optimization is to find the minimum distance of the ellipsoid touching the failure surface [10].

### 3 Methodology

Defining the safety of rainfall induced unsaturated slopes by taking the uncertainties in soil parameters into account is a critical challenge. There is a requirement for proper design methods for achieving consistent measures of reliability. In the present study Solver, a spreadsheet-based tool has been used for calculation of Hasofer-Lind reliability index for a rainfall induced unsaturated slope. Microsoft Excel, Windows 10 version has been used for developing the code. Gavin and Xue [6] determined the reliability index of a rainfall induced unsaturated slope using GASSA, FOSM approach and a Monte Carlo simulation. The data from a problem solved by Gavin and Xue [6] have been considered in the present study for a comparison. The screen shot showing computation procedure of reliability index using Solver is given in Fig. 2.

The values of design variables that are mentioned in  $x^*$  column are initially set to mean values. The correlation matrix is also entered in appropriate location. Boxed cells contain formula. The cell location for the reliability index ( $\beta$ ) contains the formula:  $SQRT(MMULT(TRANSPPOSE(nx),MMULT(MINVERSE(crmatrix),nx))))$ . This formula is transformed into a single variable by pressing the keys Ctrl + Shift + Enter simultaneously [5, 11]. Then Solver is invoked and reliability index ( $\beta$ )

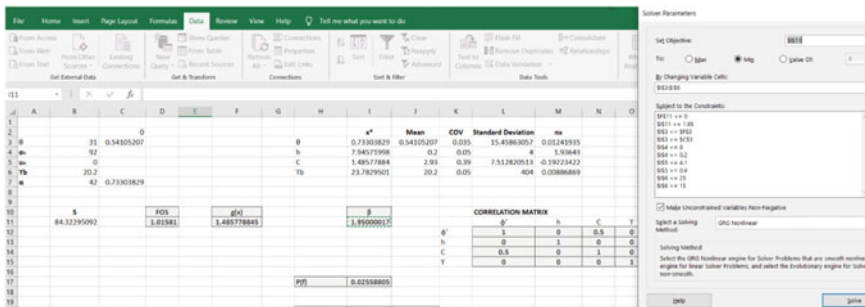


Fig. 2 Spreadsheet for the given example



is obtained by minimizing the above formula. The constraints in this constrained non-linear optimization problem are chosen as:  $g(x) \leq 0$ ;  $31^\circ \leq \phi \leq 42^\circ$ ;  $0.2 \leq h \leq 1$ ;  $0.9 \leq c \leq 4.1$ ;  $15 \leq \gamma \leq 25$ .

Solver is run many times to obtain a series of values for reliability index ( $\beta$ ). A database is created taking sets of data where each set comprises a reliability index value and associated values of variables at design point, FOS,  $P(f)$  and slope angle. Selective groups of data were considered for analysis as per requirement and results have been discussed in the next section.

### 4 Results and Discussion

Present study focuses on projecting reliability index as a measure of slope stability against failure. The relationship between  $\beta$  and corresponding expected performance level is considered as per USACE (1999) which is given in Table 2.

Table 3 shows 12 numbers of data sets taken from the database. Reliability Index ( $\beta$ ) is observed to increase from 1.94 to 2.45 as wetting front depth ( $h$ ) increases from 6.286 to 7.929 m. This may be attributed to the fact that in case of large wetting front depth (>6 m), saturation may be increasing the weight which adds to stability. This matches the observation of Gavin and Xue [6]. One interesting fact may be observed that FOS remains unchanged whereas  $\beta$  increases with increase in wetting front depth value and decrease in total cohesion indicating improvement in stability of the slope. This fact proves that reliability index is a better measure of stability of the slope as compared to FOS and thus strongly argues for use of reliability based analysis. It is also observed from the table that value of  $\beta$  increases with a decrease in the value of total cohesion. This may be attributed to the fact that a reduction in cohesion value may lead to an increase in hydraulic conductivity of soil which in turn enhances stability. But overall stability performance level of the slope is found to be below average to poor.

Figure 3 illustrates that reliability of the slope in terms of stability is influenced by wetting front depth and total cohesion of the soil. Moreover, as total cohesion

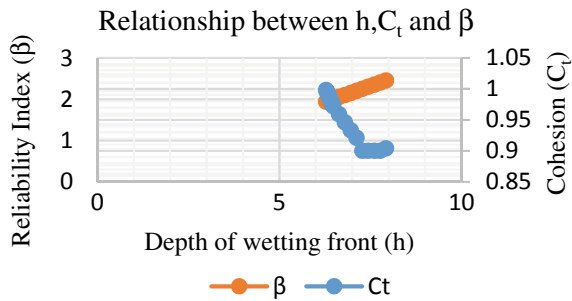
**Table 2** Reliability indices and corresponding expected performance level (U.S. Army Corps of Engineers 1999) [4]

Reliability index ( $\beta$ )	Probability of failure $P(f)$	Expected performance level
5	$2.87 \times 10^{-7}$	High
4	$3.17 \times 10^{-5}$	Good
3	0.00135	Above average
2.5	0.0062	Below average
2	0.0027	Poor
1.5	0.0668	Unsatisfactory
1	0.159	Hazardous

**Table 3** Variation of  $\beta$  with  $h$  and  $C_t$

$\phi'$	$\gamma_b$	$h$	$C_t$	$\beta$	FOS
55	15	6.286	0.998	1.94	0.867
55	15	6.318	0.994	1.95	0.867
55	15	6.35	0.99	1.96	0.867
55	15	6.382	0.985	1.97	0.867
55	15	6.414	0.981	1.98	0.867
55	15	6.446	0.976	1.99	0.867
55	15	6.478	0.972	2	0.867
55	15	6.8	0.946	2.1	0.867
55	15	7.12	0.921	2.2	0.867
55	15	7.44	0.9	2.3	0.867
55	15	7.767	0.9	2.4	0.867
55	15	7.929	0.904	2.45	0.867

**Fig. 3** Variation of  $\beta$  with  $h$  and  $C_t$



decreases, then wetting front depth increases leading to an increase in the reliability of the slope in terms of stability. This may be due to the fact that the total cohesion which includes the effect due to matric suction in the unsaturated soil may be responsible for inhibiting the wetting front depth leading to reduction in stability of the slope. This finding supports the observations made by Gavin and Xue [6].

From Fig. 4a, b, it is evident that reliability of the slope in terms of stability is least influenced by angle of internal friction and unit weight of soil. This indicates that presence of granular fraction in the soil hardly supports the stability of unsaturated infinite slope. From Fig. 4c it can be seen that soils having higher values of cohesion (soft clays) show a peculiar relationship. For high cohesive soils having cohesion values approximately greater than 1 kPa, the reliability of slope in terms of stability is insignificant though the wetting front depth ( $h$ ) increases up to cohesion value of 3 kPa. This may be due to the fact that high cohesive soils possess less permeability. Figure 4d shows influence of slope angle on factor of safety and reliability index. For higher ranges of slope angle, i.e.,  $40^\circ$ – $60^\circ$ , the FOS reduces below 1 which signifies instability although the influence of slope angle on reliability is insignificant as it

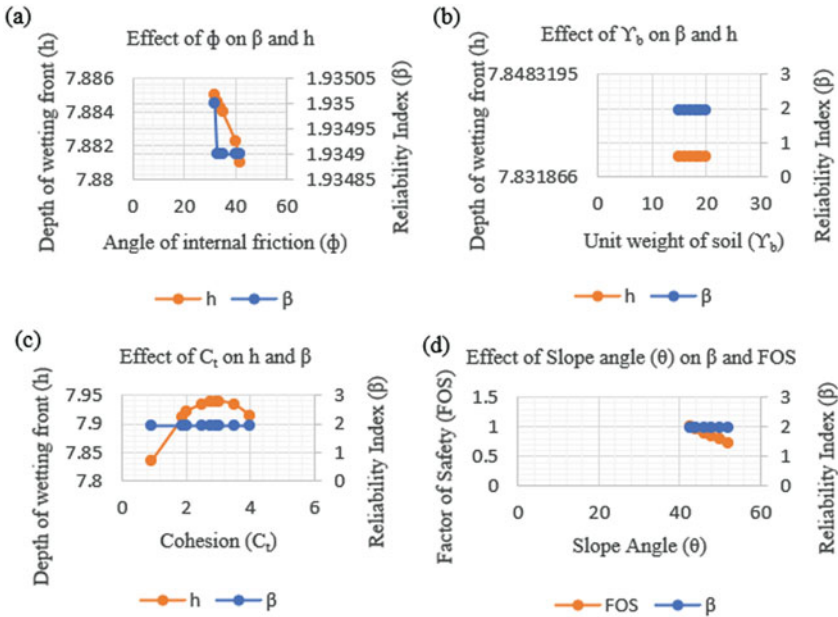


**Fig. 4** a Effect of  $\phi$  on  $\beta$  and  $h$ ; b Effect of  $\gamma$  on  $\beta$  and  $h$ ; c Effect of  $C_t$  on  $\beta$  and  $h$ ; d Effect of slope angle ( $\theta$ ) on  $\beta$  and FOS

is already unstable. This shows reliability based approaches are more rational as compared to deterministic approaches.

### 5 Conclusion

The novelty of the present study is amply demonstrated by the finding that instead of FOS-based traditional approaches, reliability based approach may be used for assessing stability of slopes. In the present work, spreadsheet-based optimization based on reduced gradient search method has been employed to determine the reliability index which is more simple, rational and robust as compared to deterministic approaches.

It has been found that stability of rainfall induced unsaturated slope is highly influenced by depth of wetting front and cohesion. The influence of angle of internal friction and unit weight of soil on slope stability is found to be insignificant. For higher range of slope angle, FOS is found to be governing criteria though a value of FOS less than 1 already points toward an unstable slope. This finding may help the policy planners more efficiently during landslides.

## References

1. Zhu JF, Chen CF, Zhao HY (2019) An approach to assess the stability of unsaturated multi-layered coastal-embankment slope during rainfall infiltration. *J Marine Sci Eng* 7:165. <https://doi.org/10.3390/jmse7060165>
2. Cai G, Li M, Han B, Di K, Liu Q, Li J (2020) Numerical analysis of unsaturated soil slopes under rainfall infiltration based on the modified glasgow coupled model. Hindawi, *Advances in Civil Engineering* Volume 2020, Article ID 8865179, 13p. <https://doi.org/10.1155/2020/8865179>
3. Gallage C, Abeykoon T, Uchimura T (2021) Instrumented model slopes to investigate the effects of slope inclination on rainfall-induced landslides. *Soils Found* 61(1):160–174
4. U.S. Army Corps of Engineers (1999) Risk-based analysis in geotechnical engineering for support of planning studies, engineering and design. Rep. No. 20314–1000, Department of Army, Washington, D.C.
5. Low BK (2005) Reliability-based design applied to retaining walls. *Geotechnique* 55(1):63–75
6. Gavin K, Xue J (2009) Use of a genetic algorithm to perform reliability analysis of unsaturated soil slopes, *Geotechnique* 59(6):545–549. <https://doi.org/10.1680/geot.8.T.004>
7. Raghuram ASS, Basha BM (2017) Reliability analysis of rainfall induced slope failure at near Seattle area. In: *Indian Geotechnical Conference 2017 (GeoNEst 2017)*, Washington
8. Hasofer AM, Lind NC (1974) Exact and invariant second-moment code format. *J Eng Mech Div* 1974(100):111–121
9. Ditlevsen O (1981) *Uncertainty modelling: With applications to multi-dimensional civil engineering systems*. McGraw-Hill, New York
10. Low BK, Tang WH (1997) Efficient reliability evaluation using spreadsheet. *J Eng Mech*
11. Low BK, The C, Tang WH (2001) Efficient reliability-based design using spreadsheet optimization. In: Corotis et al (eds) *Structural safety and reliability*. Swets & Zeitlinger. ISBN 90 5809 197 X

# Electrical Modulus and Conductivity Study of Styrene-Butadiene Rubber/Barium Hexaferrite Flexible Polymer Dielectrics



Deeptimayee Khatua, Laxmidhar Sahoo, R. N. P. Choudhary,  
and P. Ganga Raju Achary

**Abstract** Polymer composites films of Styrene-butadiene rubber (SBR)/Barium hexaferrite (BHF) of various weight percentages have been synthesized by solution casting technique. BHF nanoparticle, the inorganic filler was synthesized by sol-gel auto combustion strategy by utilizing ethylene glycol and urea. The structural analysis and phase quantification of BHF nanoparticle was carried out through the Rietveld refinement of the XRD through GSAS-II software code. After the confirmation of the BHF structure, the polymer composites of Styrene-butadiene rubber / Barium hexaferrite with 0.2.5, 5.0 and 10 parts per hundred ('phr') were fabricated. It is ensured that all the above composite films were completely dry and of uniform size by utilizing various methods. The effect of BHF nanoparticles, frequency (1 kHz to 1 MHz), and temperature (25–100 °C) on the electrical modulus and AC conductivity of these novel polymer dielectric systems were studied.

**Keywords** Barium hexaferrite · Rietveld refinement · Electric modulus · Styrene-butadiene rubber

## 1 Introduction

Over the most recent couple of years, researchers have demonstrated a developing interest in polymer composites because of their great mechanical, electrical, and thermal properties [1]. Polymers, for example, (polyvinylidene fluoride (PVDF), styrene-butadiene rubber (SBR), Ethylene-propylene-dieneterpolymer

---

D. Khatua · P. G. R. Achary (✉)

Department of Chemistry, Siksha 'O' Anusandhan, Deemed to be University, Khandagiri Square, Bhubaneswar 751030, India  
e-mail: [pgrachary@soa.ac.in](mailto:pgrachary@soa.ac.in)

L. Sahoo

Department of Chemistry, K.B.D.A.V. College, Nirakarpur, Kordha, India

R. N. P. Choudhary

Department of Physics, Deemed To Be University, Siksha O Anusandhan, Khandagiri Square, Bhubaneswar 751030, India

(EPDM), ethylene propylene elastic (EPR), Ethylene vinyl acetic acid derivation (EVA), natural elastic (NR) are utilized as matrix phase and various ceramics like, carbon black, graphene and so on utilized as filler or as reinforcement material. Other elastic composites have a significant part also in designing material because of their different application. Styrene-butadiene rubber which is well known as SBR, is manufactured elastic and it is synthesized by the copolymerization of styrene and butadiene. It has great scraped spot opposition and great maturing strength when ensured by added substances. It has flexible applications like the arrangement of heels and soles of shoe, and gaskets, biting gum and fastener in lithium particle battery. Be that as it may, this polymer matrix has low strength, poor versatility, poor tear strength, and poor tack [2]. The inconveniences or limitations of the polymer can be improved by incorporating the filler particles. Ceramics, nanoparticles, and ferroelectric materials can be utilized as filler materials. In this correspondence BHF ( $\text{BaFe}_{12}\text{O}_{19}$ ) was used as filler material. This filler can be utilized in magnetic recording media, permanent magnet, and micro device [3] because of its high coercivity, great chemical resistance and corrosion resistance. The electrical and dielectric properties of Ethylene vinyl acetic acid polymer framework improves through use of the inorganic filler BHF, which has just been introduced in our past paper [4]. Renukappa et al. reports the impact of carbon black on the tensile properties, for example, tensile strength and tensile modulus of SBR polymer matrix [5]. Jasan et al. [6] was explored the mechanical and electrical behavior of SBR/Manganous tungstate composite. Thermal and electrical behavior of SBR/metal composite was accounted for by Gwaily et al. [7]. The structural and mechanical property of SBR/nano copper polymer composites were explored by Hadizadeh Harandi et al. [8]. Multiple associations of covalent bond cation- $\pi$  collaboration and hydrogen connection among elastic and silica were accounted for by Qien et al. [9]. The polymer nanocomposite layer can be promising insulator candidate and can find their application in the future development of portable-displays, conformable-sensors, and other flexible-electronics application.

The work is done to investigate the effect of  $\text{BaFe}_{12}\text{O}_{19}$  filler loading on electrical modulus and conductivity of SBR polymer in the frequency range of 1 kHz to 1 MHz and at different temperatures.

## 2 Experimental

### 2.1 Synthesis of BHF Nanoparticles

Barium hexaferrite (BHF) nanoparticles were synthesized by utilizing Barium nitrate [ $\text{Ba}(\text{NO}_3)_2$ ], Iron nitrate [ $\text{Fe}(\text{NO}_3)_3 \cdot 9\text{H}_2\text{O}$ ], Urea [ $\text{CH}_4\text{N}_2\text{O}$ ], ethylene glycol [ $\text{C}_2\text{H}_6\text{O}_2$ ] as starting materials where ethylene glycol was taken as a gelling agent. Appropriate measures of Barium nitrate and Iron nitrate were dissolved in distilled water. Then  $\text{CH}_4\text{N}_2\text{O}$  was introduced in the arrangement with 1:1 ratio to metal nitrate. The solution mixture was heated on a hot plate with consistent stirring at

70 °C till a clear arrangement was obtained. A limited quantity of ammonia was added to the solution for changing the pH of the arrangement. Then the excess amount of water was eliminated by warming the arrangement at 70–80 °C on the hot plate. At that point, a fixed measure of  $C_2H_6O_2$  was added to it. By slow dissipation of water, a gooey gel was shaped. On consistent warming of the gel at 150–160 °C, the gel was burnt naturally and porous Barium hexaferrite was obtained. At that point, the material is moved to a crucible and calcined at 950–1000 °C for 4 h to get the desired fine BHF particles.

## 2.2 Fabrication of SBR/ BHF Polymer Films

After the synthesis of Barium hexaferrite nanoparticles, the composite films of SBR/BHF were fabricated by solution casting method where cyclohexane was taken as solvent. The fitting measures of BHF (0 phr, 2.5 phr, 5 phr, and 10 phr: ‘parts per hundred’) were added to the arrangement followed by 1 h sonication. The prepared viscous solution was taken in a Petridis and dried in an oven till the solvent dissipated. After the evaporation of the solvent the films were stripped out and were made ready to carry out the characterization.

## 3 Result and Discussion

### 3.1 Structural Study

Figure 1a describes the XRD pattern of BHF particles which was recorded by using Rigaku diffractometer where  $CuK_{\alpha}$  radiation,  $\lambda = 1.540 \text{ \AA}$  and the  $2\theta$  points lies in

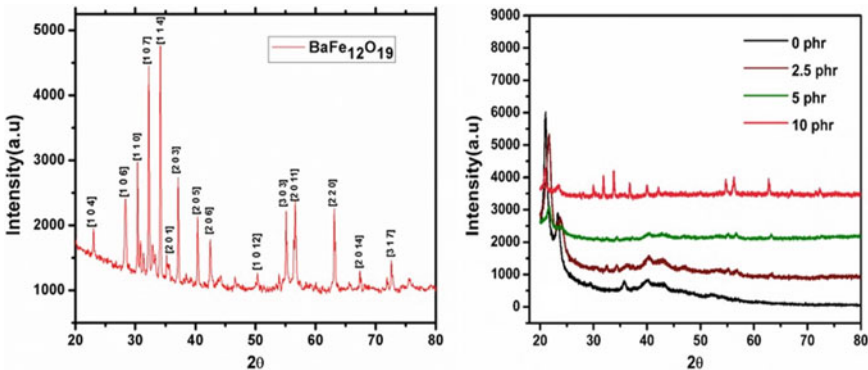


**Fig. 1** a XRD pattern of the filler BHF, b XRD pattern of composite films at different filler loading

between  $10^\circ$  and  $80^\circ$ . The sharp peaks show that the BHF is formed. The average crystallite size ( $D_{hkl}$ ) of the material is resolved from the full width at half maximum (FWHM) of most intense reflections (Fig. 1a) utilizing Debye–Scherrer connection,  $D_{hkl} = K\lambda/\beta_{0.5}\cos\theta$ ; where  $K = \text{constant} = 0.89$ ,  $\lambda = 1.5418 \text{ \AA}$ , and  $\beta_{0.5}$  is FWHM. The average crystalline size BHF particles are discovered to be 60.97 nm. The Rietveld refinement of the BHF particle has been performed by GSAS-II programming. Barium hexaferrite with space group P63/mmc is taken as a reference BHF material from the crystallography open database (COD). The introductory estimations of cell boundaries are  $a = 5.893 \text{ \AA}$ ,  $c = 23.194 \text{ \AA}$ , and cell volume =  $697.556 \text{ \AA}^3$ . The intensities of the peaks of the samples are totally matched with the reference BHF material. The Rietveld refinement design affirms the hexagonal structure with P63/mmc space group of the sample and the refined underlying boundaries are discovered to be  $a = 5.884 \text{ \AA}$ ,  $c = 23.1666 \text{ \AA}$ , and cell volume =  $694.629 \text{ \AA}^3$  with  $R_w$  esteem 5.156%. The XRD pattern of the composite films at various phr of the filler loading shows in Fig. 1b. At  $2\theta = 20.93^\circ$  a wide peak is acquired because of the amorphous nature of the SBR. If there should arise an occurrence of higher BHF loading the broadness of the peak diminishes slowly of SBR at higher filler content.

### 3.2 Electrical Modulus

The dielectric relaxation of the composite film was measured by the electrical modulus study the composite which is represented as the reciprocal of dielectric constant  $M = 1/\epsilon_r$  which can also be written as,

$$M^*(\omega) = M' + iM''$$

where  $M'$  and  $M''$  real and imaginary modulus of the film, respectively.  $M'$  and  $M''$  are  $\epsilon'/(\epsilon'^2 + \epsilon''^2)$  and  $\epsilon''/(\epsilon'^2 + \epsilon''^2)$ , respectively [10]. Figure 2a shows the change of real electrical modulus ( $M'$ ) with frequency 25–100 kHz. The value of  $M'$  of composite films increases with frequency and it decreases with increase in filler loading up to 5 phr BHF loading. At higher filler concentration exhibit higher value. Figure 2b depicts the variation imaginary part of electrical modulus with frequency change on the figure indicates that the value of imaginary modulus decreases with rise in frequency.

### 3.3 AC Conductivity

AC conductivity of the SBR/BHF composites were tested by using ‘Phase sensitive LCR/ impedance (PSM 1735) analyzer’. The electrical conductivity of a material can be determined by using the formalism  $\sigma_{ac} = \omega\epsilon_0\epsilon_r \tan \delta$ , where  $\omega$  refers to the angular frequency,  $\epsilon_0$  is the dielectric constant of vacuum [11]. It depends upon



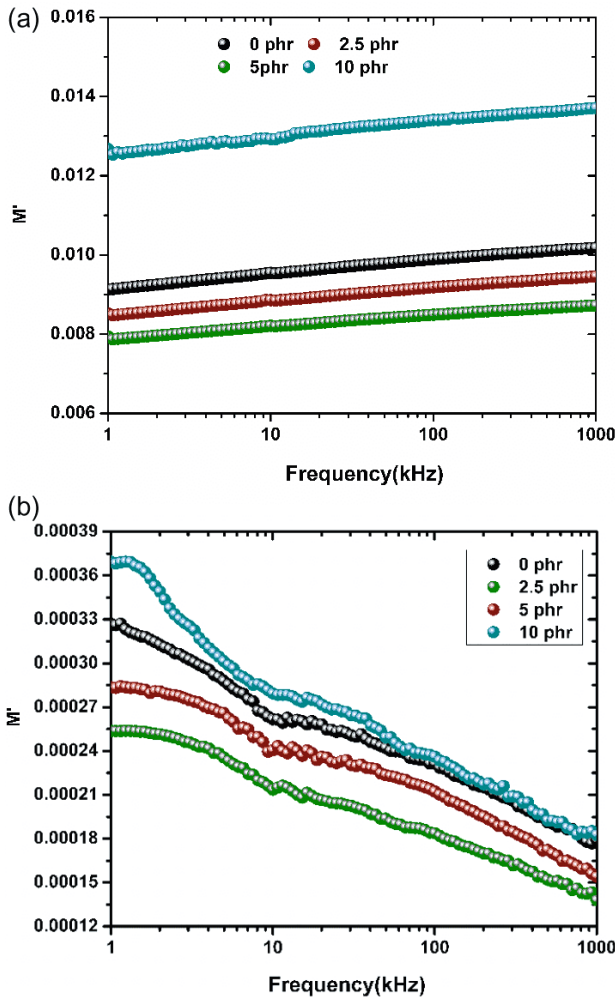


**Fig. 2** **a** Effect of frequency on real modulus at 25 °C. **b** Effect of frequency on imaginary modulus at 25 °C

the size, shape, concentration, distribution and surface tension of the matrix and the filler material. Figure 3a. depicts the response of  $\sigma_{ac}$  as the logarithmic function of frequency at 25 °C. The magnitude of AC conductivity of the composite increases with increase in frequency. Since the fibrous filler has more inter particle contact with polymer matrix it gives a percolation threshold at lower loading. But the BHF filler is spherical in nature hence there is no such change in AC conductivity is observed. The portability of charge transporters which is responsible for hopping can clarified the impact of temperature on the AC conductivity of a composite. When the mobility of hopping ions increases the conductivity of the system also increases. The influence of

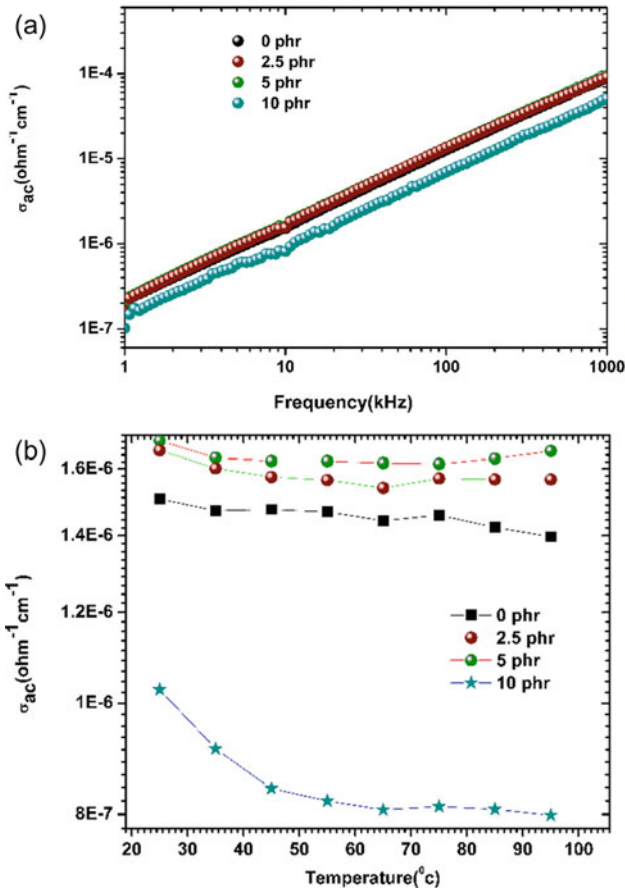


**Fig. 3** a Effect of frequency on AC conductive at 25 °C. b Effect of AC conductivity with temperature of different BHFF/SBR composites

temperature on conductivity is shown in the Fig. 3b. It can be observed that magnitude of conductivity slightly increases with increase in BHFF content up to 5 phr then it decreases at higher filler loading. Because at higher concentration the attraction between the filler particles rises which generate pores in polymer composites. And with increase in temperature there is no such tremendous change in AC conductivity value is observed which shows the stability of the material.

### 4 Conclusion

In summary, SBR polymer with barium hexaferrite based polymer nanocomposite with different phr were successfully fabricated at moderate temperature. The uniform

distribution of the filler barium hexaferrite in the SBR matrix is very important to show better property. These reported composites has been investigated in the wide frequency range from 1 kHz to 1 MHz and temperature in the range of 25–100 °C. The XRD examination showed the homogeneous scattering of fillers (BHF) particles in the polymer matrix (SBR). The AC conductivity of the composite showed marginally increments with BHF loading up to 5 phr. The present polymer nanocomposites can be promising insulator candidate and can find their application in the future development of portable-displays, conformable-sensors, and other flexible-electronics application.

**Acknowledgements** The present work is funded by the UGC-DAE-CSR, Mumbai (CRS-M-297).

## References

1. Meng C, Liu C, Chen L, Hu C, Fan S (2010) Highly flexible and all-solid-state paperlike polymer supercapacitors. *Nano Lett* 10(10):4025–4031
2. Latex SBR, Nanocomposites BSbrlatex based nanocomposites 5.1. 145–178
3. Dimri MC, Kashyap SC, Dube DC (2004) Electrical and magnetic properties of barium hexaferrite nanoparticles prepared by citrate precursor method. *Ceram Int* 30(7):1623–1626
4. Khatua D, Choudhary RNP, Achary PGR (2018) Electrical relaxation dynamics in EVA/BaFe 12 O 19 copolymer composites. *J Mater Sci: Mater Electron* 29(22):19425–19434
5. Renukappa NM, Samuel RS, Rajan JS, Lee JH (2009) Dielectric properties of carbon black: SBR composites. *J Mater Sci: Mater Electron* 20(7):648–656
6. Jasna VC, Ramesan MT (2017) Studies on the mechanical, electrical properties and interaction of petroleum fuels with SBR/manganous tungstate nanocomposites. *J Inorg Organomet Polym Mater* 27(4):968–978
7. Gwaily SE, Nasr GM, Badawy MM (2001) Thermal and electrical properties of irradiated styrene butadiene rubber-metal composites. *Egypt J Sol* 24(2):193–205
8. Harandi MH, Alimoradi F, Rowshan G, Faghihi M, Keivani M, Abadyan M (2017) Morphological and mechanical properties of styrene butadiene rubber/nano copper nanocomposites. *Results Phys* 7:338–344
9. Qian Z, Peng Z (2019) Reinforcing styrene-butadiene rubber composites by constructing multiple interaction between rubber and silica. *Polym Compos* 40(5):1740–1747
10. Rondinone AJ, Samia AC, Zhang ZJ (1999) Superparamagnetic relaxation and magnetic anisotropy energy distribution in CoFe<sub>2</sub>O<sub>4</sub> spinel ferrite nanocrystallites. *J Phys Chem B* 103(33):6876–6880
11. Yu S, Hing P, Hu X (2000) Dielectric properties of polystyrene–aluminum-nitride composites. *J Appl Phys* 88(1):398–404

# Effect of Alkaline and Acrylic Acid Treatment on Improving Tensile Strength of Rattan Fibers



Dolly Tiwari, Layatitdev Das, and J. R. Mohanty

**Abstract** The use of synthetic fibers such as glass, aramid, and carbon fiber as reinforcement for composite materials is driven by their better strength and better stiffness. However, synthetic fibers have serious drawbacks in terms of their recyclability, biodegradability, energy consumption, and implying health hazards. The strive for more sustainable options has shifted the focus from synthetic fibers to recyclable and biodegradable lignocellulosic fibers like date palm, banana, sisal, areca, bamboo. However, shortcomings like lower tensile strength, poor interfacial adhesion, poor resistance to water absorption make them a less attractive option. It is expected that chemical pre-treatment can remove the cementing materials like lignin, hemicellulose sticking around the fibers and subsequently enhance their tensile strength. In the present study, rattan fibers were subjected to alkaline and acrylic acid treatment. Untreated fibers were used as control. Acrylic acid-treated fibers were found to improve tensile strength of lignocellulosic fibers by 26% as compared to the control. The results indicate that alkaline and acrylic pre-treatments could improve compatibility between the polar hydrophilic fibers and the non-polar hydrophobic matrix material and increase wetting of the fibers in the matrix.

**Keywords** Rattan fiber · Alkaline treatment · Acrylic acid treatment · Tensile strength

---

D. Tiwari (✉) · L. Das · J. R. Mohanty  
Department of Mechanical Engineering, Veer Surendra Sai University of Technology, Burla,  
Odisha 768018, India  
e-mail: [dollytiwari29@gmail.com](mailto:dollytiwari29@gmail.com)

© The Author(s), under exclusive license to Springer Nature Singapore Pte Ltd. 2023  
P. Pradhan et al. (eds.), *Recent Advances in Mechanical Engineering*,  
Lecture Notes in Mechanical Engineering,  
[https://doi.org/10.1007/978-981-16-9057-0\\_61](https://doi.org/10.1007/978-981-16-9057-0_61)

565

## 1 Introduction

A composite material can be fabricated by combining two or more materials of notably different physical and chemical properties. The composite materials are lighter as well as stronger with great strength and stiffness. The component retains their individuality in the composite; that is, they do not diffuse or otherwise merge completely into each other, although they act in concert (Fig. 1). The composite materials are now gaining more acceptance in industries, medical applications, aerospace, rocket ships, sports, mainly due to the way in which it improves the properties of its base materials unlike the traditional materials. For example, carbon fibers when compared with 1020 grade of steel are five times stronger than the steel at the same time it is one-fifth of the weight of the steel [1]. Composite materials are known to possess flexibility, versatility, and durability, which allow wide range of possibility in designing from a simple tennis ball of clay-polymer composite to complex air crafts made of metal matrix composite [2]. In addition, their low coefficient of thermal expansion which makes them suitable to be used in making some of the parts of space shuttle and enhances functionality in harsh environmental condition. In addition, they have lower embedded energy in comparison with other structural metallic materials like steel, aluminum [3].

In order to comprehend the details of the composite material, it is required to describe the characteristics and properties of its components, types of reinforcing materials, and their polymer matrix. Due to their high stiffness and strength, the fibers like carbon fiber, glass fiber, aramid fibers are widely being used as reinforcement in polymer-based composite materials. However, in terms of recyclability and biodegradability, they pose serious threat to the environment and can also contribute to the carbon sink resulting in global warming [4]. In this scenario, natural fiber is an attractive alternative to these synthetic fibers. Some of the merits include recyclability, biodegradability, CO<sub>2</sub> consumption, low specific weight, comparable strength with glass fiber, reduced wear of tooling, low initial processing cost, low-energy consumption [5]. Natural fibers can be both plants derived as for example jute, coconut coir, areca, date palm, bamboo, banana, etc., and also can be animal derived as wool and silk. The natural fiber derived from plants is lignocellulosic and comprises of cellulose, hemicellulose, pectin, and waxy substances as the cementing material around the fibers. The cellulose structure generally contains three hydroxyl group out of which two are intramolecular and the other is intermolecular [6]. These hydroxyl groups

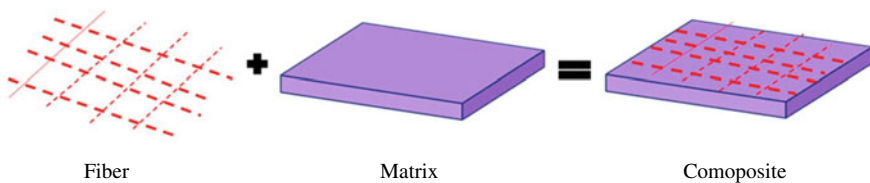


**Fig. 1** Structure of composite material

are hydrophilic in nature and are responsible for the moisture absorption. The fiber-matrix interface is a diffusion or reaction zone where they are either chemically or mechanically combined. In this zone, interfacial adhesion has a predominate function in characterizing the properties of the resulting composite material. A poor interfacial adhesion at the phase boundary will lead to poor dispersion of forces resulting in a weak composite structure. The main problem arises when compatibility between the polar hydrophilic fiber and non-polar hydrophobic matrix material is considered. The cellulosic hydroxyl group being hydrophilic in nature when comes in contact with the water it forms new hydrogen bond with the water molecule. The incorporation of such fibers into polymeric matrix composite results into absorption of moisture leading to swelling of the composite, formation of crack, crack propagation, poor dimensional stability, and eventually early failure, i.e., low life span of the composite material [7]. Moreover, the lignin, hemicellulose, and waxy substances present around the fiber act as a cementing material preventing the exposure of reactive functional group present on the surface of the fiber to the matrix material. Due to poor wetting of fiber in the matrix materials, the composite formed has low mechanical properties [8]. To address the above problems, the natural fibers of the composites are chemically modified so that it will be resistant to water absorption enhance interlocking at the interface and thermochemical modifications to make them thermostable so that they will not lose their functionality in varied range of temperature. Chemical treatment methods include alkaline, acrylic acid, malleated coupling agents, oleoyl chloride, potassium permanganate, sodium chlorite, silane, acetylation, isocyanate, benzoylation, stearic acid, peroxide, and fungal treatments [9].

## 2 Materials and Method

The raw material for the recent work is rattan stems. It was collected from Talcher, a city of Odisha, India. The chemicals used for this work such as sodium hydroxide and sodium chloride, acrylic acid, benzene, and distilled water have been purchased from the local market of Sambalpur, Odisha, India and used as such.

### 2.1 *Extraction of Fibers*

The rattan stems collected were first cleaned properly using tap water to eliminate the impurities. After cleaning of these stems, they were then sliced into desired pieces between two consecutive nodes of the stem and then dried in an oven for 15 min at 80 °C to remove excessive moisture. Then, these small rattan pieces were treated with 1% aqueous solution of sodium hydroxide (NaOH) for one hour at a temperature of 80 °C. Then, cooling of these sliced pieces was done to room temperature followed by washing in running tap water in order to separate any trace of NaOH solution clinging on the exterior of these pieces. Then, the pieces were sun dried, and then

finally, the fibers were extracted by slowly hammering the pieces with the help of a wooden hammer. These were the step followed for the first set of tensile strength analysis of fibers treated with NaOH and acrylic acid. For the second set of analysis, the fibers were extracted by water retting technique. In this technique, the stems were collected from rattan plant and were dipped in water for an interval of three to four days. Then, the water was changed and the same process was followed for around 15 days. During this interval, the stem absorbed water and swell due to which now fibers can be exacted with less difficulty.

## 2.2 Acrylic Acid Treatment

In acrylic acid treatment, the fibers pre-treated with NaOH were used. The pre-treated fibers with alkaline medium were then dipped in a solution containing water and benzene (9:1 cm<sup>3</sup>). This process was carried out for 15 min and at temperature 80 °C. Then, acrylic acid with 0.3 M treatment of the fibers was carried out. The treated fibers were soaked first in 1 g/L alkaline solution of NaOH for the next 15 min, and then further, it was dipped for 15 min in 6 g/L of NaCl and finally rinsed with distilled water.

## 2.3 Preparation of Test Specimen

To prepare the specimen as per ASTM C1309-97 and to conduct its single fiber pullout test, the untreated and chemically-treated single filaments of rattan fibers were taken. These filaments were hold by thick sheet of paper tab at its both ends in order to avoid slipping during machining. The specimen gage length was taken 40 mm. The rattan fiber was then glued using suitable adhesive at both end position of the slot that present in the paper tab (Fig. 2).

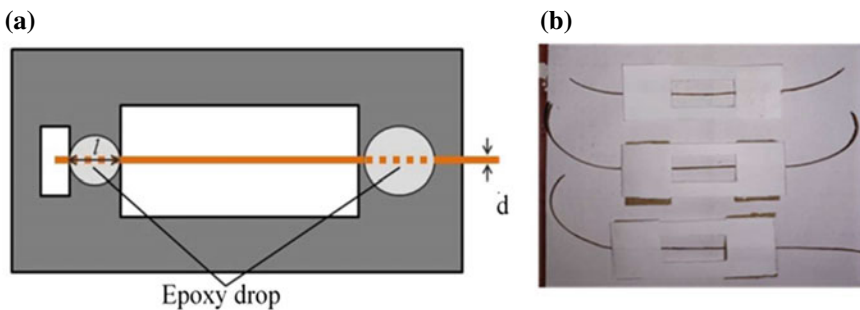


**Fig. 2** a Specimen setup, b rattan fiber fixed in paper tab

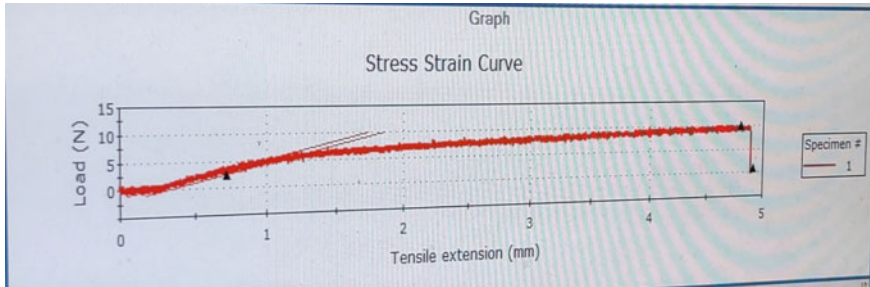


Fig. 3 Tensile test graph of untreated rattan fiber

## 2.4 Tensile Strength

The specimens to be investigated were board on INSTRON 3382 machine with a maximum load of 0.01 kN. Precautionary measures were taken to ensure that stress is uniformly distributed over the cross section of the specimen while the tensile test was performed, and results were not significantly influenced. This was achieved by adjusting the alignment of the specimen in-line with the cross-head axis. The test parameters in course of the tensile test were cross-head speed = 0.5 mm/min. Cut was incorporated on both sides of the tab at the mid gage during the test without disrupting the whole setup. The specimen was subjected to full-scale load till it triggered failure as shown in Fig. 3. A total of 5 strands per each chemical treatment were tested one after another, and the averages of the readings were recorded.

## 3 Results and Discussion

It was observed that the fibers treated with 5% NaOH recorded a tensile strength which is 22% higher than the untreated fibers. This could be due to the mercerization of rattan fibers resulting in fibrillation, increase in aspect ratio, and rough topography of the rattan fibers after alkaline treatment. The highest value was recorded by the fibers treated with acrylic acid (457 MPa), i.e., about 26% higher than the untreated rattan fibers and the lowest by the fibers treated with acrylic acid pre-treated with 5% NaOH (328 MPa). This may be due to the elimination of cementing materials like wax, gums, pectin, lignin, etc., steering to an elevation in the quantity of cellulose content responsible for enhancing the mechanical and physical properties of the rattan fibers. The acrylic acid-treated fibers possess high tensile strength as well as high stiffness due to cellulosic fiber esterification. Esterification leads to increase in surface roughness of fibers exposing more functional reactive sites of the fibers to the matrix for better interfacial bonding. The trend followed in water retaining capacity is alkaline > untreated > acrylic acid. The alkaline-treated fiber absorbed around 30% more than the control. However, the acrylic acid-treated fiber absorbed



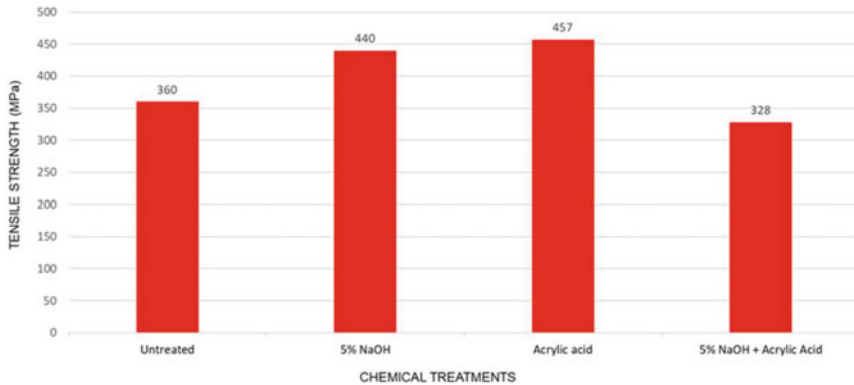


**Fig. 4** Effect of chemical treatments on tensile strength of rattan fibers

24% less water as compared to the control. This confirms that acrylic acid treatment effectively removed the hydroxyl group responsible for hydrophilic nature of rattan fibers and hence decrease its moisture absorption capacity effectively. However, the alkali-treated fiber absorbed more moisture as compared to untreated because of their hygroscopic nature (Fig. 4).

## 4 Conclusion

The importance of considering rattan fibers as a reinforcing element in polymer matrix-based composite depends on the characteristics at the interface between the fiber and the matrix and an excellent compatibility between the hydrophilic fibers and hydrophobic matrix. This can be accomplished by allowing suitable surface modification of natural fibers with different chemical pre-treatments and to specify their effects. In order to achieve the above desirable properties, trials were conducted on rattan fibers using alkaline and acrylic acid treatments. It was noticed that the strength of the fibers was found to be in order acrylic acid > alkaline > untreated. The highest valued was observed with acrylic acid (457 MPa). The trend followed in water retaining capacity is alkaline > untreated > acrylic acid. This confirms that acrylic acid treatment effectively removed the hydroxyl group responsible for hydrophilic nature of rattan fibers and hence decrease its moisture absorption capacity. The alkali-treated fiber being hygroscopic in nature does not effectively decrease the water retaining capacity of the fibers, however due to fibrillation of the fibers increases the aspect ratio and strength as compared to the untreated rattan fibers. The acrylic

acid treatment yielded better result in enhancing the strength and reducing the water absorption capacity of the fibers.

### Future Scope

The sky-rocketing demand for eco-friendly and biodegradable substitute posing minimal health threat to the humans paved the path for utilizing natural fibers as a best alternative to the synthetic fibers as reinforcement in composite materials. The fibers corresponding to best suited chemical treatments can be opted for making polymer-based composite and industrial feasibility can be studied by investigating the morphology of the composites.

### References

1. Srinivasulu NV, Tejaswi V (2012) Mechanical properties of polymer composite materials. *Int J Res Eng Technol* 1(1):78–81
2. Mattox DM (2001) Atomistic film growth and resulting film properties: residual film stress. *Vac Technol Coat* 22–23
3. Herrera JA, Grande JO, Migo VP, Arocena RE, Manalo RD (2021) Fabrication and characterization of electrospun copper oxide-cellulose acetate microfiber composite. *Philippine J Sci* 150(5):939–950
4. Ahmad Z, Yahaya I, Tajuddin M (2017) Morphological and thermal analysis of refitted rattan waste fibers. In: *AMCT 2017, Malaysisa*, p 403
5. Gurunathan T, Mohanty S, Nayak SK (2015) A review of the recent developments in biocomposites based on natural fibres and their application perspectives. *Compos A Appl Sci Manuf* 77:1–25
6. Santulli C (2019) Natural fiber-reinforced composites: recent developments and prospective utilization in railway industries for sleeper manufacturing. *Biomass, Biopolymer-Based Mater Bioenergy* 225–238
7. Mohammed L, Ansari MN, Pua G, Jawaid M, Islam MS (2015) A review on natural fiber reinforced polymer composite and its applications. *Int J Polym Sci*
8. Rajak DK, Pagar DD, Menezes PL, Linul E (2019) Fiber-reinforced polymer composites: manufacturing, properties, and applications. *Polymers* 11(10):1667
9. Rong MZ, Zhang MQ, Liu Y, Yang GC, Zeng HM (2001) The effect of fiber treatment on the mechanical properties of unidirectional sisal-reinforced epoxy composites. *Compos Sci Technol* 61(10):1437–1447
10. Sahoo SK, Mohanty JR, Nanda BK, Nayak S, Khuntia SK, Panda KR, Sahu R (2021) Fabrication and characterization of acrylic acid treated rattan fiber reinforced polyethylene terephthalate composites for packaging industries. *J Nat Fibers* 1–14

# A Study on Thermal Conductivity Characteristics of Waste Marble Powder/Epoxy Composites Using Different Models



Subhrajit Ray, Suvam Swain, and Binayak Pattanayak

**Abstract** A large amount of waste marble powder (WMP) is generated during the processing of marble stone. Nowadays, proper management of these solid wastes to develop useful material is a challenging issue. This paper reports the utilization of WMP as a filler material in epoxy-based composites to improve the thermal conductivity. Thermal conductivity of WMP-filled epoxy composites is evaluated following theoretical, experimental, and computational model. Thermal conductivity of the composites is determined using a thermal analyzer according to ASTM-E1530 procedure. Computational thermal conductivity of the sample was calculated using ANSYS software. Theoretical thermal conductivities are calculated based on rule of mixture and Maxwell's method. Thermal conductivity of the composites is found to be increased by the addition of WMP in epoxy composites. Overall, experimental and computational results show a considerable agreement.

**Keywords** WMP · Composite · FEA · Thermal conductivity

## 1 Introduction

Lightweight and heat conductivity are the two major issues while selecting the engineering material for microelectronic applications. Conventional metallic powder-filled composites in these sectors are limited due to their high cost. This opens up a new avenue to utilize the micro-industrial waste a filler material in polymer matrix composites (PMCs). At the same time, it is vital to explore various waste materials, and a synergetic research is required to meet the demand. Out of different properties,

---

S. Ray (✉)

Department of Mechanical and Electrical Engineering, CAET, OUAT, Bhubaneswar, India  
e-mail: [subhrajitmech@gmail.com](mailto:subhrajitmech@gmail.com)

S. Swain · B. Pattanayak

Department of Mechanical Engineering, ITER, SOA Deemed to be University, Bhubaneswar, India

thermal conductivity is found as one of the important characteristics of the material while selected for heat exposed areas. A good number of research reports are available regarding the heat conductivity of the composites.

Jung-il et al. [1] have investigated the positive temperature coefficient (PTC) characteristics of carbon black and nickel powder-reinforced PMC by irradiating with gamma rays at different levels. PTC found be dependent on melting point of matrix. Addition of filler improved the electrical conductivity and reduced the negative temperature coefficient of the specimen. Nikkeshi et al. [2] studied the dynamic viscoelastic characteristics of nickel powder-added epoxy composites at 30–300 °C range of temperature. The thermal conductivity of samples is improved up to seven orders magnitude as compared with neat epoxy resin. Thermal stability of composites is influenced by the roughness and size of nickel particle at elevated temperature. Sudarshan and Surappa [3] characterized the A356 Al-fly ash composites with two different ranges of particle sizes. They concluded that increase in elastic modulus, hardness, and proof stress by incorporation of fly ash and they also reported that greater mechanical properties were obtained with small-size range fly ash particle as compared to larger fly ash particles. Incorporation of fly ash increased the damping ability of Al alloy composite at elevated temperature. Kumlutas and Tavman [4] have studied the thermal conductivity of tin particle-filled PMC using experimental and numerical approach. Three dimensional model having cube lattice array and spheres is used to analyze the model based on finite element analysis. Experimental study was carried out using hot wire method at various filler concentrations. The heat conductivities of the specimen are improved by the filler addition, and all the models are found suitable up to 10% of filler concentration. Tsekmes et al. [5] investigated the thermal conductivity behavior of micro/nanoparticle-reinforced PMC. For low and moderate particles concentration, the thermal characteristics seem to be significant, and at high aspect ratio, the composite carries better thermal conductivity in the heat flow direction. Later on, the experimental results are compared with a 3D Comsol model and found the result in line of the experimental values. Rong et. al [6] observed the heat conductivity of specimen using 2D pictures and CNNs. 2D CNNs are found to be more convenient to estimate the conductivity of the specimen as compared with 2D images considered in normal or parallel direction of filler loading. Parallel direction image are found to be more than perpendicular cross-section image along heat flow direction. Addition of cenosphere reduced the weight and thermal conductivity of cementitious composites due to their hollow structure [7]. Analytical homogenization is conducted to forecast the heat conductivity of cementitious composites and to validate the date with experimental values. Image analysis confirmed the cenosphere distribution in the composites. Lee et al. [8] found the thermal conductivity of composites using micromechanics-based homogenization model. Eshelby tensor method or Mori–Tanaka method matched the thermal conductivity value found from FEA approach. Kim et al. [9] conducted 3D X-ray CT analysis to measure the thermal conductivity of graphene nanoparticle-added PMC. Addition of larger sized particle improved the thermal conductivity of samples. The conductivity was increased up to 121% by 20 wt% filler addition. Noh et al. [10] investigated the bulk and in-plane thermal conductivity of PMC reinforced with six types of carbon particles.

The carbon particles were seen to be uniformly dispersed irrespective of their shape and size. The thermal conductivity of samples increased linearly due to effective heat transfer network with minimizing the interface among filler and matrix.

The previous literature supports the thermal conductivity characteristics of different particle-added composites. However, the studies on industrial waste like WMP-reinforced PMC have still remained as less exposed area of research. In this context, the present work aims to find the experimental, theoretical, and numerical thermal conductivity of different PMCs and to compare the values.

### 1.1 Theoretical Modeling

For two phase composites, the heat flow depends on structure of conduction model. For parallel structured conduction model:

$$k_c = (1 - \Phi)k_e + \Phi k_m \tag{1}$$

where  $k_c$ ,  $k_e$ , and  $k_m$  are the thermal conductivities of the composite, epoxy, and WMP, respectively, and  $\Phi$  stands for the volume fraction of WMP.

For series structured conduction model:

$$\frac{1}{k_c} = \frac{1 - \Phi}{k_e} + \frac{\Phi}{k_m} \tag{2}$$

The above equations are found using rules of mixture (ROM).

Agari and Uno [11] predicted a conduction structure for particle-filled PMC. According to this model, the expression becomes:

$$\log k_c = \Phi C_2 \log k_m + (1 - \Phi) \log(c_1 k_e) \tag{3}$$

where  $C_1$  and  $C_2$  are the model constants found from test condition.  $C_1$  indicates structure of matrix, and  $C_2$  stands for effect of filler to form conductive chain.

Later on, Agari and Uno [12] modified the equation based on shape of filler.

For randomly dispersed filler, thermal conductivity equation can be stated as:

$$\frac{k}{k_e} = 1 + \frac{3\Phi}{\left(\frac{k_m + 2k_e}{k_m - k_e}\right) - \Phi} \tag{4}$$

This is known as Maxwell equation [13] for particle-reinforced PMC.

## 2 Experimental Details

In the present study, a mixture (10:1) of epoxy (Lapox, L-12) and hardener (K-6) is used as matrix material. Epoxy possesses thermal conductivity of 0.363 W/m K, density of 1.10 gm/cc, and modulus of 3.42 Gpa. The matrix materials are collected from Tirupati Sales, Kolkata, India. Waste marble powder (WMP) is used as filler material in this study. WMP holds a density of 2.68 gm/cc and thermal conductivity 2.070 W/m K. The WMP is collected from local construction sites. Matrix and fillers are mixed thoroughly using a mechanical stirrer as per the composition. The solution is poured in the mold of glass tube of dimension  $\Phi 30 \times 80$  mm. The internal part of the tube is sprayed with a mold release silicon spray. The composites are fabricated using simple liquid casting approach. The material after pouring in the tube was kept for 24 h for solidification. After solidification, the glass tube was broken and the samples are cut for the thermal characterization. The details of the composition of the samples are presented in Table 1.

### 2.1 Thermal conductivity Test

Untherm™ 2022 model is used to measure the thermal conductivity of PMC in accordance with ASTM-E1530 standards. The specimen was kept between two conductive plates, and the conductivity was measured from the temperature difference by the help of sensor mounted in it. Thermal conductivity between two surfaces can be presented in Eq. (5):

$$Q = K A \left( \frac{T_1 - T_2}{x} \right) \quad (5)$$

where  $Q$  stands for thermal flux (W),  $K$  is the thermal conductivity (W/m K),  $A$  is exposed area of sample ( $m^2$ ),  $T_1 - T_2$  is the temperature difference (K), and  $x$  is the width of composite (m). The heat resistance of composite can be calculated as follows:

**Table 1** Nomenclature of composites with their weight proportions

Symbol of composites	Composition	
	Epoxy (wt%)	WMP (wt%)
EM0	100	0
EM1	98.5	1.5
EM2	96.5	3.5
EM3	93.5	6.5

$$R = \frac{T_1 - T_2}{Q/A} \quad (6)$$

where  $R$  denotes as resistance offered by the composite ( $m^2\text{-K/W}$ ). The above two equations may be simplified as the following equation:

$$K = \frac{x}{R} \quad (7)$$

## 2.2 Finite Element Method (FEM) and ANSYS

FEM divides the system into multiple sub-systems to estimate the solution of problems using weighted residual method. The FEM can be used to solve fluid flow, stress developed, and heat transfer analysis under both linear and complex algorithm using ANSYS software.

## 3 Result and Analysis

### 3.1 Numerical Study

The effective thermal conductivities of (0–6.5 wt%) marble-filled PMCs are numerically estimated using ANSYS based on cubic model (3D).

### 3.2 Determination of the Problem

A 3D model (ABCD) is formulated having boundary conditions assuming as  $T_1 = 27^\circ\text{C}$  (ambient temperature) and  $T_2 = 100^\circ\text{C}$  with thermal conductivity of medium as  $2.5\text{ W/m}^2\text{ K}$  shown in Fig. 1. The outer surface parallel heat flow direction is considered as adiabatic wall. Temperature profiles of various samples using ANSYS are shown in Figs. 2a–d.

The theoretical conductivities of PMCs are calculated; numerical values are estimated using ANSYS and compared with the experimental data as shown in Table 2.

Thermal conductivities of different samples found from different models are validated with reference to experimental values. The percentage errors found from different models are given in Table 3. Percentage of error with reference to experimental data lies in the range of 1.83–3.44% for FEM model, 2.36–6.42%. Maxwell's model and 4.72–12.5% for ROM model.

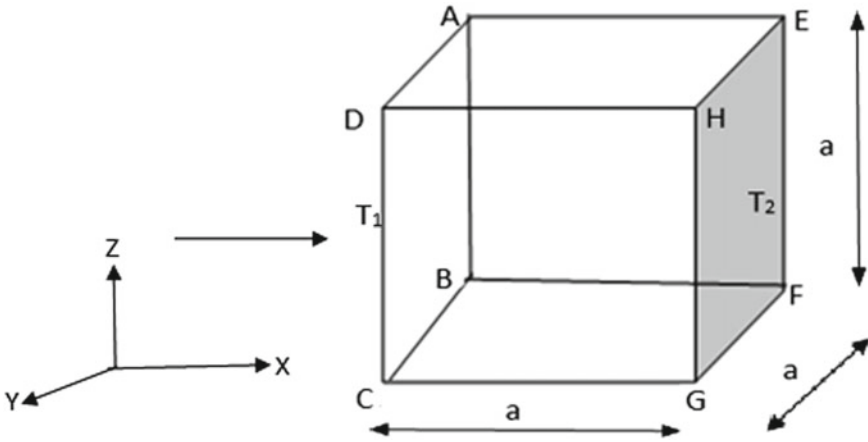


Fig. 1 3D model with heat flow direction

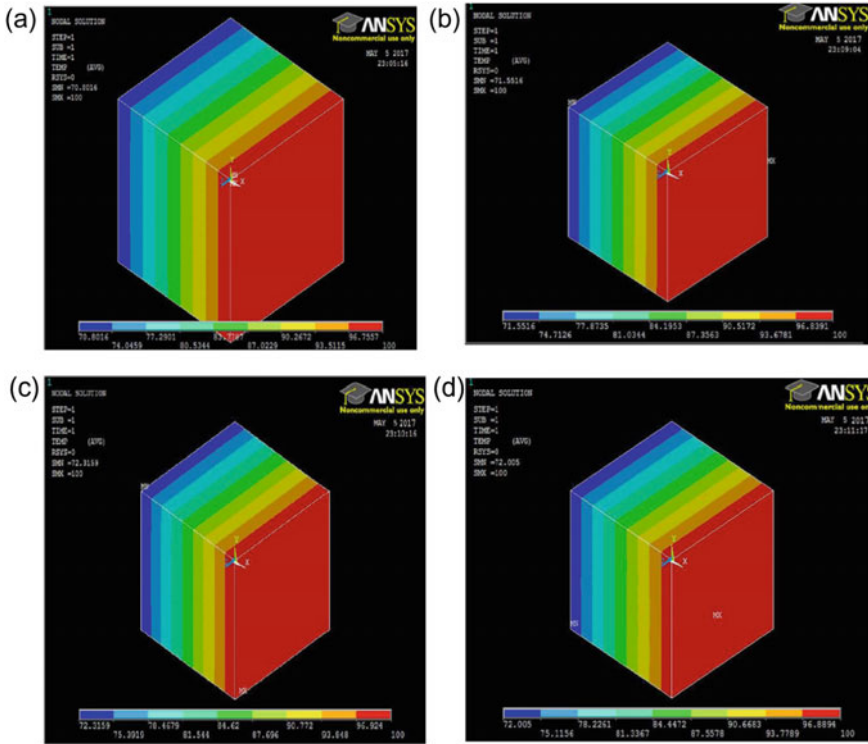


Fig. 2 a Temperature profile of EM0. b Temperature profile of EM1. C Temperature profile of EM2. D Temperature profile of EM3



**Table 2** Thermal conductivities of PMCs obtained under various models

Thermal conductivity (W/m K)	Composites			
	EM0	EM1	EM2	EM3
Rule of mixture (ROM) model	0.363	0.367	0.373	0.383
Maxwell’s model	0.363	0.372	0.386	0.408
FEM model	0.363	0.374	0.389	0.421
Experimental value	0.363	0.381	0.401	0.436

**Table 3** Error percentage compared with experimental data

Samples	Error percentage compared with experimental data		
	ROM model	Maxwell’s model	FEM model
EM1	4.72	2.36	1.83
EM2	6.98	3.74	2.99
EM3	12.5	6.42	3.44

## 4 Conclusion

The above studies lead to the following conclusions:

PMCs can be successfully fabricated using WMP and epoxy using simple liquid casting technique. FEM model can be used to determine the thermal conductivities of different PMCs. FEM model found more suitable for predicting thermal conductivities composites than ROM and Maxwell’s model. Thermal conductivity of PMC is improved up to 16.74% by the addition of 6.5 vol. % WMP. These PMCs can be used for making printed circuit boards, die chip, aeronautic motor flange, electronic cover, switch cover, air-conditioning unit, motor engine casing, etc.

## References

1. Il J, Kang PH, Nho YC (2004) Positive temperature coefficient behavior of polymer composites having a high melting temperature. *J Appl Polymer Sci* 92:394–401
2. Nikkeshi S, Kudo M, Masuko T (1998) Dynamic visco-elastic properties and thermal properties of powder-epoxy resin composites. *J Appl Polym Sci* 69:2593–2598
3. Surappa MK (2008) Synthesis of fly ash particle reinforced A356 Al composites and their characterization. *Mater Sci Eng A* 480(1–2):117–124
4. Kumlutas D, Tavman IH (2006) A numerical and experimental study on thermal conductivity of particle filled polymer composites. *J Thermoplast Compos Mater* 19(4):441–455
5. Tsekmes IA, Kochetov R, Morshuis PHF, Smit JJ (2014) Modeling the thermal conductivity of polymeric composites based on experimental observations. *IEEE Trans Dielectr Electr Insul* 21(2):412–423
6. Rong Q, Wei H, Huang X, Bao H (2019) Predicting the effective thermal conductivity of composites from cross sections images using deep learning methods. *Composites Sci Technol* 184:107861

7. Rheinheimer V, Yunpeng W, Tao W, Kemal C, Junyan W, Laura LD, Peter W, Min-Hong Z, Monteiro PJM (2017) Multi-scale studies of high-strength low-thermal-conductivity cement composites containing cenospheres. *Cement Concrete Composites* 80:91–103
8. Lee S, Lee J, Ryu B, Ryu. S.: A micromechanics-based analytical solution for the effective thermal conductivity of composites with orthotropic matrices and interfacial thermal resistance. *Scientific reports* 8(1),1–11,(2018).
9. Kim HS, Bae HS, Yu J, Kim SY (2016) Thermal conductivity of polymer composites with the geometrical characteristics of graphene nano platelets. *Sci Rep* 6(1):1–9
10. Noh YJ, Kim HS, Ku BC, Khil MS, Kim SY (2016) Thermal conductivity of polymer composites with geometric characteristics of carbon allotropes. *Adv Eng Mater* 18(7):1127–1132
11. Agari Y, Uno T (1986) Estimation on thermal conductivities of filled polymers. *J Appl Polymer Sci* 32(7):5705–5712
12. Agari Y, Ueda A, Nagai S (1991) Thermal conductivities of composites in several types of dispersion systems. *J Appl Polym Sci* 42(6):1665–1669
13. Maxwell JC (1873) *A treatise on electricity and magnetism*, vol. 1. Clarendon Press

# Structural, Dielectric, and Phase Shifting Characteristics of [(Pb<sub>0.5</sub>Bi<sub>0.25</sub>La<sub>0.25</sub>)(Fe<sub>0.5</sub>Ti<sub>0.5</sub>)O<sub>3</sub>] Electronic System



S. K. Pradhan, S. N. Das, D. Chauhan, S. Bhuyan, and R. N. P. Chaudhary

**Abstract** The present work describes the structural, dielectric, and phase shifting characteristics of lanthanum-modified BFO-PT electronic system. The electronic material [(Pb<sub>0.5</sub>Bi<sub>0.25</sub>La<sub>0.25</sub>)(Fe<sub>0.5</sub>Ti<sub>0.5</sub>)O<sub>3</sub>] has been fabricated using general solid-state grinding technique with exact stoichiometric proportion of corresponding raw powder. The XRD and SEM description shows the structural study of solid-state material. From X-ray diffraction (XRD) analysis, the material shows tetragonal single-phase structure. The uniform non-coarse grain with very small voids present on the surface of the material conforms the material strength which studied from scanning electron microscope (SEM). The tiny volume of rare earth material lanthanum is doped with BiFeO<sub>3</sub>–PbTiO<sub>3</sub> binary electronic system however increases dielectric value and decreases dielectric loss. The above conclusion is drawn by analyzing the electrical parameters with respect to temperature and frequency. Due to the high dielectric constant, less electrical loss and strengthen structural figure of the newly fabricated electronic material may be act as a strong competent in device design for lots of electronic application. The fabricated material also acts as good phase shifter by changing the value of externally connected inductances.

**Keywords** Dielectric loss · La-doped BFO-PT electronic material · Phase shifting

## 1 Introduction

The perovskite structure with ferroelectric and antiferromagnetic properties of BFO at high temperature region makes it as a noble and quality material for various electronic applications [1–3]. It may have more ferroelectric properties with potential application, but the great disadvantages are it offers less impedance to current which makes the material not suitable for certain applications [4–8]. In order to increase the resistivity, some perovskites like SrTiO<sub>3</sub>, BaTiO<sub>3</sub>, and PbTiO<sub>3</sub> may be added

---

S. K. Pradhan · S. N. Das (✉) · D. Chauhan · S. Bhuyan · R. N. P. Chaudhary  
Department of Electronics and Communication Engineering, Siksha 'O' Anusandhan Deemed to be University, Bhubaneswar 751030, India  
e-mail: [satyaprakashdas@soa.ac.in](mailto:satyaprakashdas@soa.ac.in)

chemically for further improvement. The reason behind the high conductivity nature of BFO is the oxygen vacancies inside the material. The vacancies are generated due to charge compensation in iron ion, i.e., reduction of  $\text{Fe}^{3+}$  to  $\text{Fe}^{2+}$  species [9, 10]. Now, the binary system BFO-PT appeared with stable structure and enhances properties still cons is impedance value not increases as expected. The rare earth material gives the solution for strengthen the resistivity as well as decrease the leakage current. So, in this effort, we debilitated rare earth material as lanthanum to iron site in BFO-PT solution in order to get stabilized structure, enhance resistance with less leakage current [11]. The work is focused on lanthanum-modified BFO-PT structure, morphology with electrical parameters analysis.

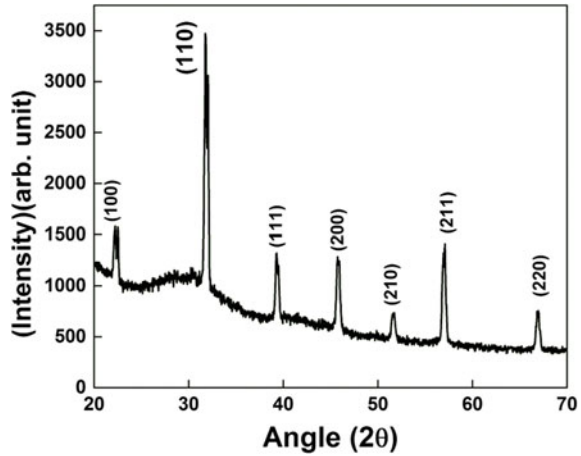
## 2 Experimental Procedure

The novel compound  $[(\text{Pb}_{0.5}\text{Bi}_{0.25}\text{La}_{0.25})(\text{Fe}_{0.5}\text{Ti}_{0.5})\text{O}_3]$  is formed by taking 99.9% pure oxides dry powder such as: titanium oxides, iron oxides, lead oxides, bismuth oxides, and lanthanum oxides as raw materials. First, the raw powders are weighted through weighing balance machine for their stoichiometric contributions in gram to form the intended material. Then, the weighted oxides are grinded for 3 h to make a homogenous fine mixer. An appropriate amount of methanol alcohol is added to above mixer and again steered for 4 h until getting solid powder form. The powder now calcined in a high-heat-controlled furnace up to a temperature  $900\text{ }^\circ\text{C}$ . From the calcined powder, the structure of the made material is studied by the help of XRD at angles from  $20^\circ$  to  $70^\circ$ . By the help of hydraulic pressure, the powder is now converted to disk-shaped form (adding poly vinyl alcohol acts as an adhesive) and again heated up to  $950\text{ }^\circ\text{C}$  in the furnace for making material (sintered form) further electrical measurement and SEM study. Before going for dielectric study through phase-sensitive meter of the material, the disk-shaped pellet is coated with silver painting for making conduction medium. The supply frequency ( $1V_{p-p}$ ) is 1 kHz to 1 MHz to phase-sensitive meter, and the material is kept in a temperature variation ( $25\text{--}500\text{ }^\circ\text{C}$ ) for material parameter measurement. The specimen is poled through polling machine for few hours in high voltage environment before going for phase shifting analysis.

## 3 Results and Discussion

The structural conformation through XRD of the electronic system  $[(\text{Pb}_{0.5}\text{Bi}_{0.25}\text{La}_{0.25})(\text{Fe}_{0.5}\text{Ti}_{0.5})\text{O}_3]$  is shown in Fig. 1. The XRD pattern consists of number of sharp peak with prominent elevation which is similar to perovskite and dissimilar to their parent constituents. So, it affirms the new crystalline structure of tetragonal phase. All the sharp peaks are indexed by help of POWD software [12].

**Fig. 1** Room temperature XRD pattern

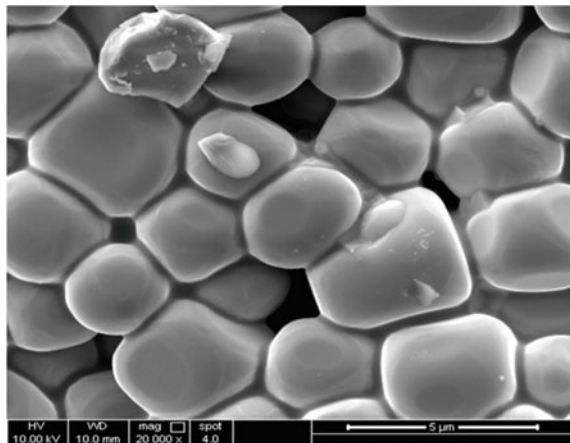


From the first principle study, the tetragonal phase of  $ABO_3$  is conformed. Here, the A–O long-range bond balances the B–O short-range bond inside the material [13].

The grain scattering study in the surface of the fabricated material  $[(Pb_{0.5}Bi_{0.25}La_{0.25})(Fe_{0.5}Ti_{0.5})O_3]$  is describe in Fig. 2 with help of SEM. It has seen that all the grains are uniformly and tightly packed with little voids which make the material good enough for electrical parameters measurement. The size of the grain found to be  $1.5 \mu m$  using scaling technique. The grain size of the fabricated material is comparatively small than that of parental material due to incorporation of rare earth material (lanthanum) to BFO-PT which is act as a squeezing agent for grain growth.

The description of relative dielectric constant as well as tangent loss with temperature for particular selected frequency is illustrated in Fig. 3. It is observed that the

**Fig. 2** Room temperature SEM micrograph



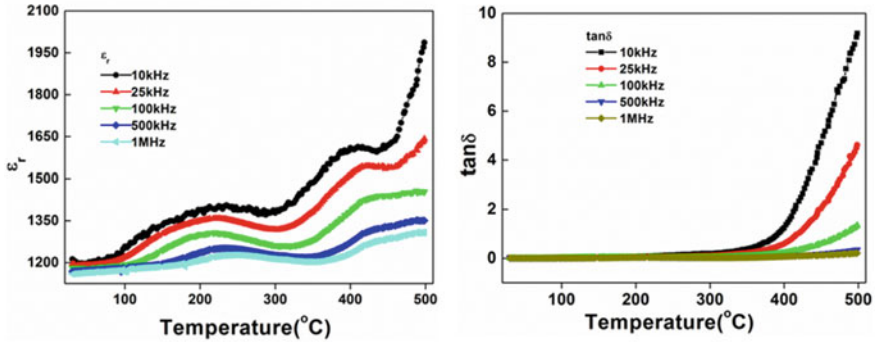


Fig. 3 Temperature dependent of dielectric constant and tangent loss at selected frequencies

dielectric constant sharply increases at higher temperature as compared to lower region which shows the typical behavior of ferroelectric material. Around 200 and 400 °C, the curve-shaped peak formed due to magnetic spiral spin of BFO and also due to revolution in dipole ordering of antiferromagnetic properties in the fabricated material [14]. In same fashion, the dielectric loss value suddenly rises at high temperature region, whereas at lower region, it shows very small value. This happens because of inadequate heated bulging carrier particles, i.e., carriers scattering inside the material.

The dielectric constant and the loss component of dielectric response to frequency at selected temperature are illustrated in Fig. 4. The two graphs prove that the synthesized material shows dielectric behavior as both the dielectric parameters value decreases with risen of frequency, independent of temperature which is a normal characteristic of dielectric material. This happens due to the degeneration of charge carriers at the boundary line of the surface of the material. Further, at low frequency area, the dielectric constant value shows higher value (selected high temperature); the

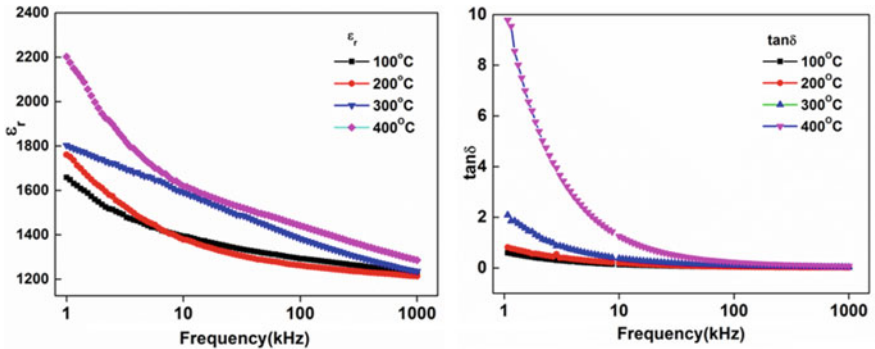
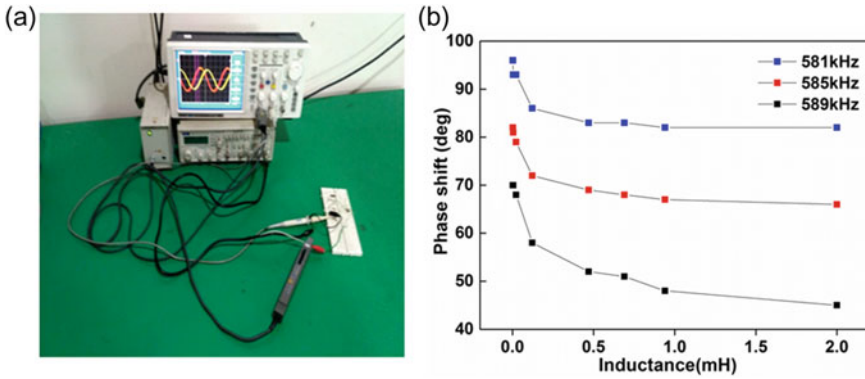


Fig.4 Frequency dependent of dielectric constant and tangent loss at selected temperatures



**Fig. 5** **a** Prototype setup for phase shifting characteristics, **b** phase shifting characteristics of the fabricated component

reason is the recurrent polarization of charge carriers and also due to accumulation of charge carriers inside the material [15].

The phase shifting capability of the material with appropriate arrangement (demonstration) is shown in Fig. 5a shows the practical circuitry for implementation of material as a phase shifting component with external inductances and power supply with dual trace CRO. The phase shift characteristic with respect to variation of the control inductance ( $L$ ) is shown in Fig. 5b. At 581 kHz, the phase shift changes from  $98^\circ$  to about  $85^\circ$  as  $L$  value increases from 0.002 mH to about 2 mH. While at 585 kHz, the phase shift changes from 93 to  $65^\circ$  as  $L$  value increases from 0.002 mH to about 2 mH. From equation, it is known that  $\Delta L$  increases with increasing the control inductance  $Lx$ , and the increase of  $\Delta L$  causes the increase of  $L$ . Also, from equation:

$$\Delta\phi = \angle V_o - \angle V_{in} = \arctan\left(\frac{1/\omega C' - \omega L'}{R'}\right) + \phi_o$$

It is known with the increase in  $L'$  value, the  $\phi$  value decreases. Therefore, the phase difference between  $V_o$  and  $V_{in}$  declines with increasing  $L$  [15]. So, the experiment proves that the fabricated material can act as a good component for phase shifting material.

### 4 Conclusion

The electronic material  $[(Pb_{0.5}Bi_{0.25}La_{0.25})(Fe_{0.5}Ti_{0.5})O_3]$  has been made by using solid-state grinding technique with proper heat process and the essential material parameters like structural behavior, grain orientation, electrical aspect like dielectric constant and loss are nicely analyzed. The XRD shows tetragonal phase of the

material structure with uniformly spread grain gives well support for electrical parameters measurement. The small doping of lanthanum on BFO-PT changes the value of dielectric parameters with respect to temperature as well as frequency which makes the fabricated solid-state electronic material as strong competent in device design for lots of electronic application.

## References

1. Das SN, Pattanaik A, Kadambini S, Pradhan S, Bhuyan S, Choudhary RNP (2016) Dielectric and impedance spectroscopy of Ni doped BiFeO<sub>3</sub>-BaTiO<sub>3</sub> electronic system. *J Mater Sci: Mater Electron* 27:10099
2. Dulkan E, Roth M, Janolin PE, Dkhil B (2006) Acoustic emission study of phase transitions and polar nanoregions in relaxor-based systems: Application to the Pb Zr<sub>1/3</sub>Nb<sub>2/3</sub>O<sub>3</sub> family of single crystals. *Phys Rev B* 73:12102
3. Das SN (2020) Relaxor (Pb<sub>0.7</sub>Bi<sub>0.3</sub>)(Mg<sub>0.231</sub>Nb<sub>0.462</sub>Fe<sub>0.3</sub>)O<sub>3</sub> electronic compound for magnetoelectric field sensor applications. *J Appl Phys* 128:114101
4. Kutnjak Z, Petzelt J, Blinc R (2006) The giant electromechanical response in ferroelectric relaxors as a critical phenomenon. *Nature* 441:956
5. Pradhan SK, Das SN, Bhuyan S, Behera C, Choudhary RNP (2017) Structural and electrical properties of lead reduced lanthanum modified BiFeO<sub>3</sub>-PbTiO<sub>3</sub> solid solution. *J Mater Sci: Mater Electron* 28:1186
6. Yan S, Mao C, Wang G, Yao C, Cao F, Dong X, Meng X (2016) The novel dielectric relaxation behavior around the Curie point of (Ba<sub>0.7</sub> Sr<sub>0.3</sub>)<sub>0.96</sub>Y<sub>0.04</sub>TiO<sub>3</sub> ceramics with giant effective permittivity. *Mater Res Express* 3:105035
7. Wang L, Zhu C, Luo H, Yuan S (2015) Studies on room temperature multiferroic properties of xBi<sub>0.5</sub>Na<sub>0.5</sub>TiO<sub>3</sub>-(1-x)NiFe<sub>2</sub>O<sub>4</sub> ceramics. *J Electroceramics* 35:59
8. Mazumder R, Sen A (2009) Effect of Pb-doping on dielectric properties of BiFeO<sub>3</sub> ceramics. *J Alloys Compd* 475:577–580
9. Palkar VR, John J, Pinto R (2002) Observation of saturated polarization and dielectric anomaly in magnetoelectric BiFeO<sub>3</sub> thin films. *Appl Phys Lett* 80:1628
10. Pradhan SK, Das SN, Bhuyan S, Sahoo S, Choudhary RNP (2020) Temperature and frequency dependent multiferroic features of gadolinium doped BiFeO<sub>3</sub>-PbTiO<sub>3</sub> electronic system. *Trans Electr Electron Mater* 21:175
11. Pradhan SK, Das SN, Bhuyan S, Haldar S, Choudhary RNP (2017) Dielectric dispersion and impedance spectroscopy of yttrium doped BiFeO<sub>3</sub>-PbTiO<sub>3</sub> electronic system. *J Mater Sci: Mater Electron* 28:9627
12. Wu E (1989) POWD, an interactive program for powder diffraction data interpretation and indexing. *J Appl Cryst* 22:506
13. Hill NA, Filippetti A (2002) Why are there any magnetic ferroelectrics?. *J Magn Magn Mater* 242:976
14. Das SN, Pradhan S, Bhuyan S, Choudhary RNP, Das P (2017) Modification of relaxor and impedance spectroscopy properties of lead magnesium niobate by bismuth ferrite. *J Electron Mater* 46:1637
15. Pradhan SK, Das SN, Bhuyan S, Behera C, Padhee R, Choudhary RNP (2016) Structural, dielectric and impedance characteristics of lanthanum-modified BiFeO<sub>3</sub>-PbTiO<sub>3</sub> electronic system. *Appl Phys A* 122:604
16. Du J, Hu J, Chen SK, Goh CS, Tseng KJ (2006) A tunable low-frequency piezoelectric phase shifter. *Sens Actuators A: Phys* 128:25



# Study on Physical and Mechanical Behavior of Bauhinia Vahlia Fiber Filled Glass–Epoxy Hybrid Composites



Rashmi Ray , Sankar Narayan Das, and Abhipreet Mohapatra

**Abstract** Epoxy is well-suited for a number of industrial applications because of its versatility and its diversity. In many high-performance fields however, the overall use of epoxy limited its employment due to delamination, intrinsic fragility, low impact resistance and hardness to fractures. Epoxy's limitations can be overcome through inclusion and modification prior to industrial use. The present research describes the development of hybrid composites made of epoxy reinforced with glass fiber and filled with Bauhinia Vahlia fiber. Bauhinia Vahlia (BV) found to be most promising natural fiber for manufacturing composites for its superior mechanical as well as thermal properties. In this study, the incorporation of BV fiber on physical and mechanical behavior of glass–epoxy composites was investigated. Various composite compositions with three distinct natural BV fiber percentages (4, 8, 12%) were fabricated using a hand layup technique. The results showed that increasing the percentage of natural fiber concentration improves mechanical qualities, however at larger BV fiber loading, the strength reduces due to presence of more voids which signifies poor bonding.

**Keywords** Bauhinia Vahlia · Natural fiber · Glass fiber · Epoxy · Composite

## 1 Introduction

Composite materials have a number of advantages over traditional materials, including mechanical (tensile, flexural and impact) and tribological (wear resistance) advantages (wear, corrosion and fatigue). Composites found an outsized range of

---

R. Ray · S. N. Das (✉)

Department of Mechanical Engineering, ITER, SOA University, Bhubaneswar, India  
e-mail: [sankardas@soa.ac.in](mailto:sankardas@soa.ac.in)

A. Mohapatra

Department of Mechanical Engineering, NIT Surathkal, Surathkal, India

© The Author(s), under exclusive license to Springer Nature Singapore Pte Ltd. 2023  
P. Pradhan et al. (eds.), *Recent Advances in Mechanical Engineering*,  
Lecture Notes in Mechanical Engineering,  
[https://doi.org/10.1007/978-981-16-9057-0\\_64](https://doi.org/10.1007/978-981-16-9057-0_64)

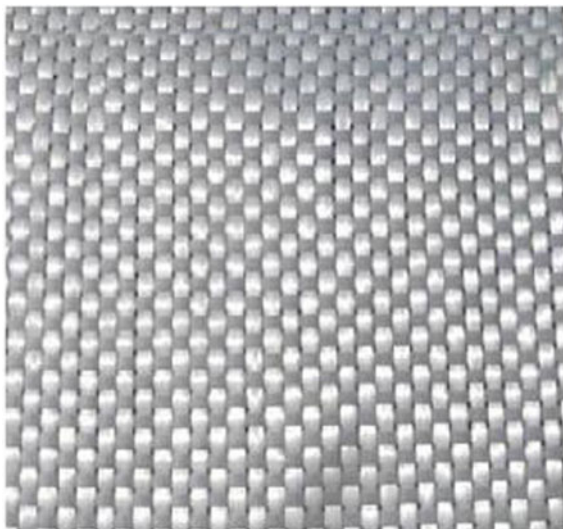
587

applications in the aerospace industry, applications in the field of mechanical engineering which includes machine components, automobiles, tanks, drive shafts, pressure vessels, electronic packaging and thermal management, aircraft structures and train coaches, etc. [1]. The genesis of the interest is that higher density fiber that is used in hybrid form is a more cost-effective utilization. A hybrid structure may also offer a more appealing combination of mechanical qualities, such as tensile, flexural and impact, than a single fiber reinforced composite [2]. Bio-composites are the combination of natural fibers with polymer matrices that may be thermosetting, thermoplastic or natural polymer. Thermoplastics polymers are recyclable, tough, easy to process [3]. Examples include polyvinyl alcohol, polyvinyl pyrrolidone, polyethylene, polypropylene, polystyrene, nylons and so on. Thermoset has low resin viscosity, good fiber wetting, excellent thermal stability and chemically resistant. But these are brittle and nonrecyclable [4]. Typical examples are epoxies, polyesters, phenolics, ureas, melamine, silicone and polyimides. A variety of thermoplastic or thermosetting polymers has been used with natural fibers to fabricate bio-composites for many applications [5–7]. Bio-composites are now used in a variety of industries, including automotive, medicinal, energy, toys, sports and so on. The advancement of new bio-composite materials with added functional properties in dynamic and smart packaging has made further scope for extension of materials innovation [8, 9]. In accordance with the current research, the objective of this project is to fabricate epoxy composite reinforced with laminated glass fibers and *Bauhinia Vahlia* fibers (chopped) randomly oriented to examine the influence of BV fiber percentage on physical and mechanical behavior of composites.

## 2 Materials and Methods

The BV stems used in this investigation were found in rural Odisha. The epoxy resin and hardener used was Araldite LY556 (320.816 g/mol) and HN951 (Molecular weight: 181.61), respectively. The laminated glass fibers and chemical sodium hydroxide is bought locally. Figures 1 and 2 illustrate laminated glass fiber and chopped BV fibers.

The BV stem fibers were made by removing the outer bark strips and cutting the inside bark into little bits of 3–4 mm long and 1 mm wide. 5% NaOH solution was used to treat the fibers for 1 h. The fibers were dried for 24 h at 60°C in an oven. Then, the fabrication of composite is done using the conventional hand layup method [10]. The epoxy resin is mixed with hardener at a 10:1 weight ratio. To make glass fiber reinforced epoxy composite sheets, the laminated glass fiber is inserted between layers of epoxy resin. This was followed by a middle layer of laminated glass fiber and a top layer of epoxy and BV fiber mixture. The composite cast is cured for 24 h under a 50 kg weight. Lastly, suitable dimensions specimens for characterization and testing are cut with a hack saw. The details of composite composition are shown in Table 1.

**Fig. 1** Laminated glass fiber**Fig. 2** Chopped BV fibers

## ***2.1 Morphological Analysis of BV Fiber***

A Leo Supra 35VP scanning electron microscope (SEM) was used to capture the surface of BV fiber. The surfaces of alkali treated and untreated BV fibers were examined using a 20 kV microscope. A 10 nm coating of gold was applied to the sample surfaces.

**Table 1** Details of composite composition

Composite designation	Composition
Composite 1 (C1)	Epoxy (80%) + Glass fiber (20%) + BV fiber (0%)
Composite 2 (C2)	Epoxy (76%) + Glass fiber (20%) + BV fiber (4%)
Composite 3 (C3)	Epoxy (72%) + Glass fiber (20%) + BV fiber (8%)
Composite 4 (C4)	Epoxy (68%) + Glass fiber (20%) + BV fiber (12%)

## 2.2 Physical Characterization of Composite

The formula for calculating the theoretical density ( $\rho_{ct}$ ) of composite material is [10]

$$\rho_{ct} = \frac{1}{\left[ \frac{W_{bvf}}{\rho_{bvf}} + \frac{W_{gf}}{\rho_{gf}} + \frac{W_m}{\rho_m} \right]} \quad (1)$$

where the weight fraction and density are represented by  $w$  and  $\rho$ , respectively. BV fiber, glass fiber, matrix and composite material are denoted by the suffix bvf, gf, m and ct, respectively. Using a simple water immersion procedure, the actual density ( $\rho_{ca}$ ) can be estimated experimentally. The following equation is used to compute the volume fraction of the voids ( $V_v$ ) in the composite

$$V_v = \frac{(\rho_{ct} - \rho_{ca})}{\rho_{ct}} \quad (2)$$

## 2.3 Mechanical Characterization of Composite

A Universal Testing Machine (UTM) was used to measure the composite's tensile properties (INSTRON 3382) at 10 mm/min crosshead speed [10]. The ASTM D638 test standard is used to conduct tensile tests on composite samples. Again, the three-point bending method was used to test the composite's flexural strength and flexural modulus in a Universal Testing Machine at a crosshead speed of 10 mm/min. Similarly, using a pendulum type Izod Impact testing machine, the ASTM D 256 standard was applied to determine the impact strengths of composites. Like a cantilever beam, specimens were vertically fastened and struck by a single pendulum swing released at a specified distance from the clamp. 3.45 m/s and 0.905 kg, respectively, were the hammer velocity and weight. The hardness of the composites sample was measured according to ASTM D785-98 standard in a Rockwell Hardness Testing Machine.

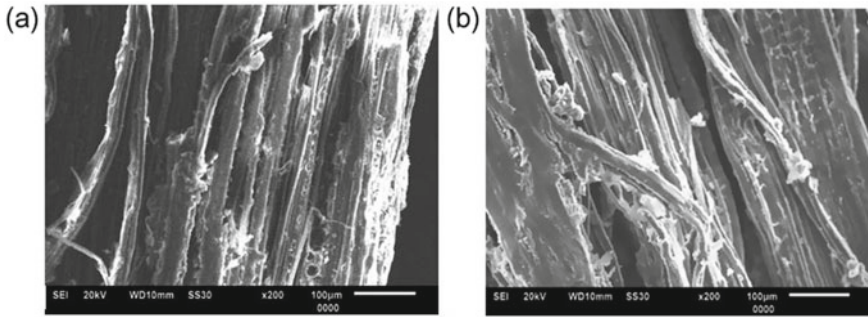
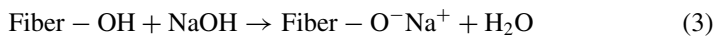


**Fig. 3** Scanning electron microscope of **a** untreated BV fiber, **b** NaOH treated BV fiber

### 3 Results and Discussion

#### 3.1 Scanning Electron Microscope (SEM)

Figure 3a displays scanning electron micrograph of untreated fiber that reveals porosity and non-uniform cellular features. The fiber surface is bounded by lignin and hemicellulose. Whereas, the alkali treated BV fibers in Fig. 3b shows more uniform and compressed cellular structures. The NaOH treatment re-energizes the hydroxyl groups present in cellulose and lignin. When natural fibers are exposed to NaOH solution, the hydroxyl group ionizes to alkoxide as follows:



#### 3.2 Void Fraction

The inclusion of voids in the composite accounts for the difference between theoretical and experimental densities as obtained from Eq. (1) and presented in Table 2. As the fiber loading increases from 0 to 12 wt% BV fiber, the void percentage in the composites increases. Maximum void found in 12% BV fiber loaded composites 4 obtained from Eq. (2). The presence of voids has a substantial impact on several mechanical properties, as well as the performance of composites in the workplace. An excellent composite should, without a doubt, have fewer voids.

**Table 2** Void fraction of composite

Composites	Theoretical data (g/cc)	Experimental data (g/cc)	Volume fraction of voids (%)
Composite 1 (C1)	1.776	1.750	1.46
Composite 2 (C2)	1.571	1.520	3.24
Composite 3 (C3)	1.493	1.400	6.22
Composite 4 (C4)	1.385	1.276	7.87

### 3.3 Mechanical Characterization

#### Tensile properties

Figure 4a depicts the tensile strength of the composite sample. The tensile strength of the composites increases when the natural fiber loading is increased to a certain percentage. In comparison to 0 and 4 wt% BV fiber, the composite sample with 8 wt% BV fiber reinforced composite had the maximum tensile strength. However, due to fiber agglomerations, epoxy and BV fiber bonding are weak at 12 wt% fiber loading. Consequently, the strength is decreasing. Also, formation of void between fiber and matrix is greatly affecting the mechanical properties [11]. This suggests that the increased tensile strength of the BV fiber reinforced composite up to 8 wt% could be attributable to improved adhesion between natural fiber and epoxy resin. The tensile modulus of composites, on the other hand, increased as the BV fiber loading increased, as seen in Fig. 4b. This could be attributed to higher brittleness of the composite as well as the degree of resistance, due to higher BV fiber weight percent and eventually resulting in greater stiffness of the composite.

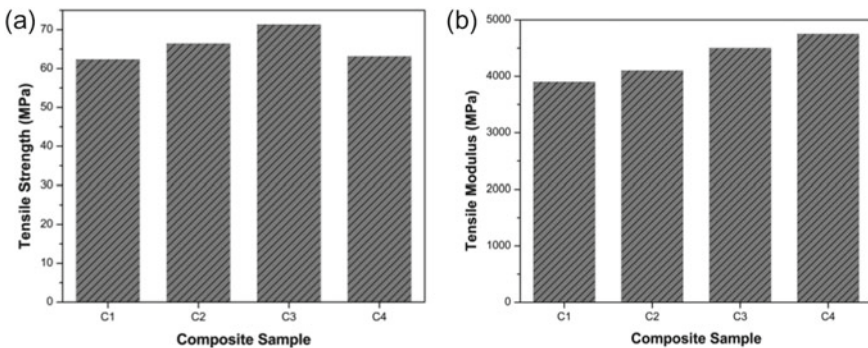


**Fig. 4 a** Tensile strength and **b** tensile modulus of composite sample

**Flexural properties**

When it comes to flexural characteristics, Fig. 5(a) shows that BV fiber loading raises the composite’s flexural strength and modulus by up to 8%. This is due to a good stress distribution between the epoxy and the BV fiber. However, at higher BV fiber loading (12 wt%), fiber–fiber contact is discouraged, and the fibers are poorly distributed within the matrices. Figure 5b shows the same behavior in the case of flexural modulus. With the inclusion of natural fiber, the flexural modulus increases by up to 8% by weight, then drops as more fiber is added.

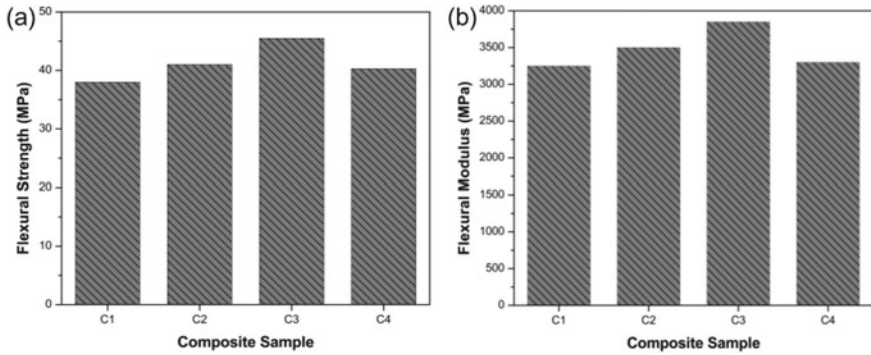


**Fig. 5** a Flexural strength and b flexural modulus of composite sample

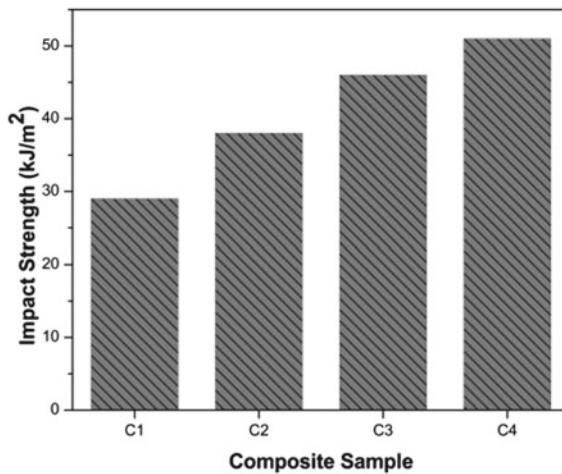
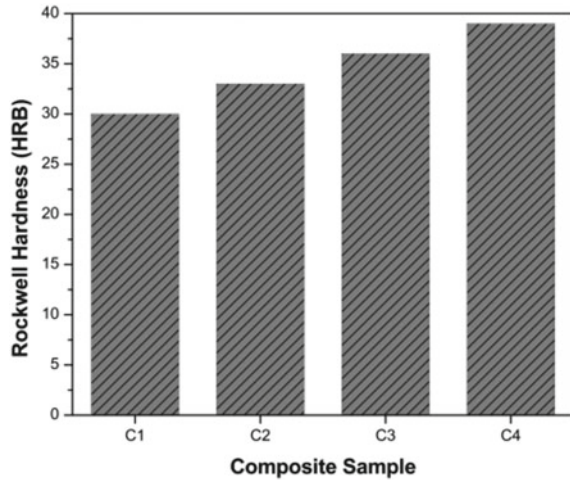


**Fig. 6** Impact strength of composite sample



**Fig. 7** Hardness of composite sample



### Impact strength

The impact strength of composite samples is shown in Fig. 6. In contrast to tensile and flexural strength, the impact strength increases with increased BV fiber weight percentage. This implies that due to addition of BV fiber loading, the energy absorbing capability of the composite increases and makes the composite material more ductile.

### Hardness

It has been discovered that when fiber loading increases, the Rockwell hardness values increase dramatically as shown in Fig. 7. The presence of BV fiber in epoxy causes the composites' stiffness to improve. As rigidity depends on fiber volume and modulus, this is the case. The outcomes show that the hardness value of the composites improves progressively as the BV fiber content increases, maximum at 12 wt%.

## 4 Conclusion

The present paper addresses a potential opportunity to build epoxy-based Bauhinia Vahlia/glass fiber hybrid composites that are made with varying percentages of BV fiber keeping a constant weight of glass fiber. The composite's tensile and flexural qualities were enhanced by the addition of appropriate quantities of BV fiber. However, the tensile and flexural strength decreases at 12 wt% Bauhinia Vahlia fiber, because to the larger volume fraction of voids. The addition of natural fiber leads to an improvement in impact strength and hardness of the composite material.



## References

1. Reddy PV, Reddy RS, Rajendra Prasad P, Mohana Krishnudu D, Reddy RM, Rao HR (2020) Evaluation of mechanical and wear performances of natural fiber reinforced epoxy composites. *J Nat Fibers* 1–14
2. Erdoğan YE, Korkmaz EE, Temiz Ş (2021) Effect of graphene nanoplatelet filling on mechanical properties of natural fiber reinforced polymer composites. *Materi Test* 63(4):322–328
3. Sathishkumar GK, Ibrahim M, Mohamed Akheel M, Rajkumar G, Gopinath B, Karpagam R, Karthik P, Martin Charles M, Gautham G, Gowri Shankar G (2020) Synthesis and mechanical properties of natural fiber reinforced epoxy/polyester/polypropylene composites: a review. *J Nat Fibers* 1–24
4. Kausar A (2021) Long fiber—reinforced epoxy composites. In: *Epoxy composites: fabrication, characterization and applications*, pp 83–96
5. Prabhu L, Krishnaraj V, Sathish S, GokulKumar S, Karthi N (2020) Study of mechanical and morphological properties of jute-tea leaf fiber reinforced hybrid composites: effect of glass fiber hybridization. *Mater Today: Proc* 27:2372–2375
6. Fernandes Medeiros de Queiroz H, Banea MD, Kioshi Kawasaki Cavalcanti D, de Souza e Silva Neto J (2021) The effect of multiscale hybridization on the mechanical properties of natural fiber-reinforced composites. *J Appl Polymer Sci* 51213
7. Ramasubbu R, Madasamy S (2020) Fabrication of automobile component using hybrid natural fiber reinforced polymer composite. *J Nat Fibers* 1–11
8. Sajith S, Arumugam V, Dhakal HN (2017) Comparison on mechanical properties of lignocellulosic flour epoxy composites prepared by using coconut shell, rice husk and teakwood as fillers. *Polym Test* 58:60–69
9. Saba N, Jawaid M, Alothman OY, Paridah MT, Hassan A (2016) Recent advances in epoxy resin, natural fiber-reinforced epoxy composites and their applications. *J Reinf Plast Compos* 35(6):447–470
10. Swain PTR, Das SN, Jena SP (2018) Manufacturing and study of thermo-mechanical behaviour of surface modified date palm leaf/glass fiber reinforced hybrid composite. *Mater Today Proc* 5(9):18332–18341
11. Arthanarieswaran VP, Kumaravel A, Kathirselvam M (2014) Evaluation of mechanical properties of banana and sisal fiber reinforced epoxy composites: Influence of glass fiber hybridization. *Mater Des* 64:194–202

# A Comparative Analysis on Physical and Mechanical Properties of Aluminum Composites with Al<sub>2</sub>O<sub>3</sub> and WS<sub>2</sub> Reinforcement



Sweta Rani Biswal and Seshadev Sahoo

**Abstract** Comparative investigation of aluminum-based metal matrix composite and aluminum-based hybrid metal matrix composite was represented here in this paper. This paper also aims to establish substantial results for the application of hybrid composites in place of metal matrix composites. This paper provides the importance of hybrid reinforcement such as tungsten disulfide WS<sub>2</sub> impact on the Al metal powder-based composites' physical and mechanical behavior. For this study, two different compositions were fabricated through powder metallurgy at 600 °C and 560 MPa, such as Al + 5 wt% Al<sub>2</sub>O<sub>3</sub> and Al + 5 wt% Al<sub>2</sub>O<sub>3</sub> + 5 wt% WS<sub>2</sub>. The analysis results on physical and mechanical properties reveal the potential impact of Al<sub>2</sub>O<sub>3</sub> and WS<sub>2</sub> reinforcement. The properties are significantly improved. This paper suggests selecting hybrid composites adding solid lubricant WS<sub>2</sub> in Al matrix which provides the best results.

**Keywords** Hybrid composite · Metal matrix composite · Hardness · Automotive

## 1 Introduction

Looking into the present scenario, scarcity in natural resources creates a big problem for automotive sector. To fulfil the customer demands for automotive parts from last two decades, researchers have focused on the inventions of new age materials such as Al metal matrix composites (Al MMCs) by considering the environmental safety and fuel efficiency. As per their inventions [1, 2], Al MMCs not only enhances the fuel economy requirements but also produces lightweight, high strength and eco-friendly materials with higher wear resistance. They have also suggested that Al MMCs provide remarkable performance with ceramic reinforcements such as SiC, Al<sub>2</sub>O<sub>3</sub> and B<sub>4</sub>C. [3]. Some of the researchers have also reported that Al MMCs have some major concerns with fabrication cost and low ductility and toughness.

---

S. R. Biswal (✉) · S. Sahoo

Department of Mechanical Engineering, ITER, Siksha 'O' Anusandhan (Deemed to be University), Bhubaneswar, India

e-mail: [swetaranibiswal@soa.ac.in](mailto:swetaranibiswal@soa.ac.in)

To resolve these issues, they have suggested that the addition of more than one reinforcement into matrix will not only enhance its property but also it will be more cost effective and have balance as per mechanical and tribological properties are concerned. This also creates the opportunity for tailor made material named as hybrid composites as per different applications [4]. These hybrid materials can be used for the fabrication of pistons, cylinder liners, bearings and flywheels like automotive parts where friction loss is a major concern [5–7]. Though there is a lot of research going on hybrid composites, where attempts are made on the fabrication techniques to reduce the fabrication cost and its properties by analyzing different processing parameters but still a huge gap is yet to be fulfilled. As per the review by Alaneme et al. [8] Comparative analysis is required between Al MMCs and Al hybrid metal matrix composites (Al HMMCs). As per the study, two types of reinforcements are used for Al HMMCs [9] such as hard particle addition with elastic modulus greater than 30 GPa such as silicon carbide (SiC), alumina ( $\text{Al}_2\text{O}_3$ ), boron carbide ( $\text{B}_4\text{C}$ ), titanium carbide (TiC) and silica (SiC) and soft reinforcements having elastic modulus lower than 2 GPa such as Gr,  $\text{MoS}_2$  and  $\text{TiO}_2$  particles. The addition of hard with soft reinforcement not only improves its hardness, but also greatly influences wear resistance by adding self-lubricating nature and thermal characteristics with addition of self-healing nature [10, 11].

As per reports, composites with varying combinations of hard and soft particle addition are yet to be discovered such as addition of tungsten disulfide ( $\text{WS}_2$ ) solid lubricant for development of HAMCs through cost effective fabrication route for some specific applications [12]. In this paper, we have attempted to do the comparative study on the physical and mechanical behavior between Al– $\text{Al}_2\text{O}_3$  (Al MMC) and Al– $\text{Al}_2\text{O}_3$ – $\text{WS}_2$  (Al HMMC). Fabrication methods which is used for this study is powder metallurgy. This paper intended to find out the impact of solid lubricant  $\text{WS}_2$  addition in the Al and  $\text{Al}_2\text{O}_3$  MMC.

## 2 Methodology

Aluminum MMC reinforced with  $\text{Al}_2\text{O}_3$  powder and aluminum HMMC reinforced with alumina and tungsten disulfide were manufactured using solid state processing technique, i.e., powder metallurgy (PM). Sample composition for the study is described in Table 1. Average size of pure Al powder,  $\text{Al}_2\text{O}_3$  powder and  $\text{WS}_2$

**Table 1** Material composition for MMC and HMMC

Composition	Weight % of Al matrix	Weight % of $\text{Al}_2\text{O}_3$ primary reinforcement	Weight % of $\text{WS}_2$ secondary reinforcement
Composition 1 (C1)	95	5	0
Composition 2 (C2)	90	5	5

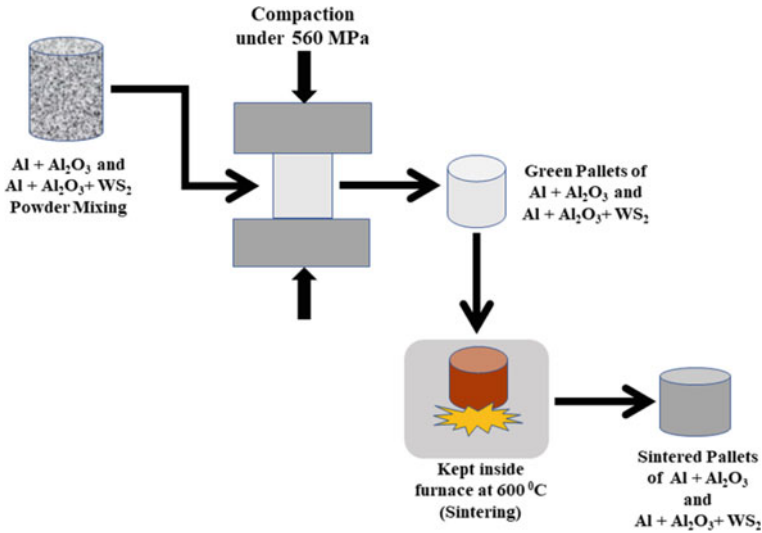


Fig. 1 Powder metallurgy fabrication method

powder were used 80 μm, 40 μm and 10 μm, respectively, for sample preparation. The process of fabrication is schematically represented in Fig. 1.

Hybrid composite as specified in Table 1 fabricated through powder metallurgy process using three steps such as powder mixing, compaction to form green pallets at pressure 620 MPa, and sintering to produced final sintered pallets at temperature 600 °C inside furnace and finally air cooled [13]. Mechanical stirring process has been adopted for powder mixing to distribute the reinforcements uniformly into matrix to avoid agglomeration [14]. The pallets formed after processing through powder metallurgy steps used for different characterizations such as density, porosity, XRD, micro structural study and hardness test.

### 3 Comparative Analysis of Result

The sample pallets for both composition 1 and composition 2 are made of diameter size 10 mm and thickness of 10 mm height and finally been tested for physical and mechanical properties study. For the study of physical and mechanical behavior study of composites, parameters like green density, theoretical density, porosity and hardness are calculated and tabulated in Table 2. For the calculation of theoretical density ( $\rho_{th}$ ), we have used the rules of mixture [15]. The equation is as follows:

$$\frac{1}{\rho_{th}} = \frac{Mm}{\rho_m} + \frac{Mr1}{\rho_{r1}} + \frac{Mr2}{\rho_{r2}} \tag{1}$$

**Table 2** Performance parameters of Al MMCs and Al HMMCs

Composition	Sample No.	Green density (g/cm <sup>3</sup> )	Sintered density (g/cm <sup>3</sup> )	Theoretical density (g/cm <sup>3</sup> )	Porosity in percentage (%)	Hardness (HVN)
C1	1	2.574	2.6984	2.753	1.98	35.07
	2	2.563	2.6968	2.753	2.04	38.087
	3	2.53	2.6977	2.753	2.01	32.05
	4	2.63	2.6953	2.753	2.1	33.71
	5	2.605	2.6961	2.753	2.08	34.671
	Average	2.5804	2.6968	2.753	2.07	34.7176
C2	1	2.73	2.82	2.851	1.081	50.86
	2	2.756	2.819	2.851	1.095	49.62
	3	2.717	2.822	2.851	1.01	45.89
	4	2.802	2.821	2.851	1.04	48.59
	5	2.789	2.818	2.851	1.14	51.08
	Average	2.7588	2.82	2.851	1.075	49.208

$Mm$ —Al weight fraction,  $\rho m$ —density of Al in gm/cm<sup>3</sup>

$Mr1$ —Al<sub>2</sub>O<sub>3</sub> weight fraction,  $\rho r1$ —density of Al<sub>2</sub>O<sub>3</sub> in gm/cm<sup>3</sup>

$Mr2$ —WS<sub>2</sub> weight fraction,  $\rho r2$ —density of WS<sub>2</sub> in gm/cm<sup>3</sup>

The density of Al, Al<sub>2</sub>O<sub>3</sub> and WS<sub>2</sub> are 2.71 gm/cm<sup>3</sup>, 3.95 gm/cm<sup>3</sup> and 7.5 gm/cm<sup>3</sup>, respectively. XRD results after sintering for both compositions are represented here in Fig. 2a. From the results we can observe that the presence of Al, Al<sub>2</sub>O<sub>3</sub> and

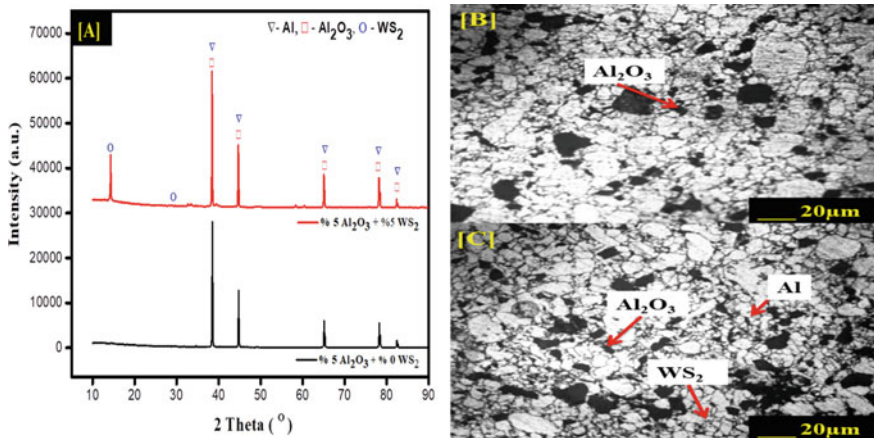


**Fig. 2** After sintering **a** XRD pattern of Al–Al<sub>2</sub>O<sub>3</sub> and Al–Al<sub>2</sub>O<sub>3</sub>–WS<sub>2</sub> hybrid composite, **b** optical micrograph of Al–Al<sub>2</sub>O<sub>3</sub> and **c** Optical micrograph of Al–Al<sub>2</sub>O<sub>3</sub>–WS<sub>2</sub> hybrid composite

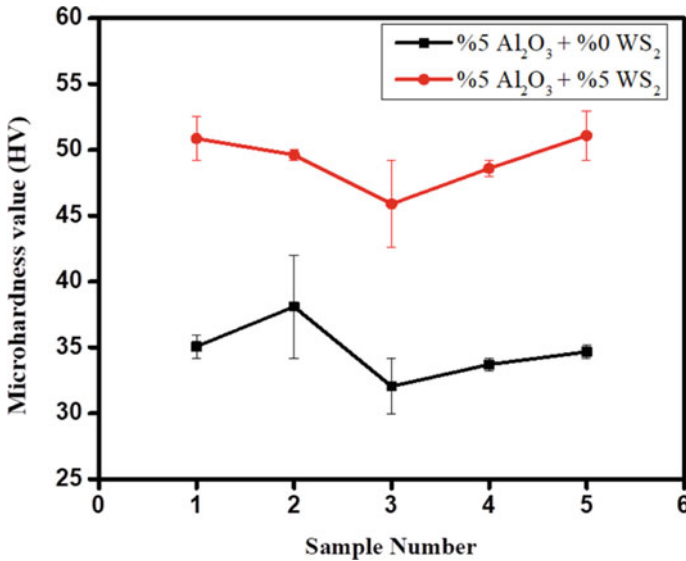


**Fig. 3** Hardness comparison graph of Al–Al<sub>2</sub>O<sub>3</sub> and Al–Al<sub>2</sub>O<sub>3</sub>–WS<sub>2</sub> hybrid composite

WS<sub>2</sub>. Figure 2b, c represents the optical micrographs of both the composition after sintering where the presence of Al, Al<sub>2</sub>O<sub>3</sub> and WS<sub>2</sub> clearly depicted. Here, samples were taken by the help of optical microscope at 200× magnification. We also can observe that WS<sub>2</sub> distribution in Fig. 2c is uniform and in some place it occupies the space of pores. The results represented in Table 2 have also indicated that the composition 2 is comparatively denser than composition 1 with an average porosity of 1.075.

By comparing the hardness value of both the composition in Table 2, we can come to the inference that with the addition of 5 wt% WS<sub>2</sub>, hardness value gets enhanced by 43.98%. For all the samples the hardness value of composition 2 is better than composition 1 as we can see in Fig. 3. Finally, we observed that the presence of 5 wt% WS<sub>2</sub> not only reduces the pore by 48% but also make the composite denser by 3.56% and harder by 43.98%.

## 4 Conclusion

In this paper, we have tried to establish the importance of aluminum hybrid composites in place of aluminum matrix composites. Aluminum with hybrid reinforcements is yet to be explored despite of providing excellent mechanical properties. Here in this paper, we have fabricated two types of aluminum-based composite, i.e., aluminum with alumina and aluminum with alumina and tungsten disulfide. Furthermore, comparative study had been made to analyze the influence of hybrid addition

with the single reinforcement with aim of determining how much improvement or decrement occurred. From the comparative study of physical properties, i.e., porosity, density and mechanical property, i.e., hardness we came to these inferences.

1. The density gets enhanced by 3.56% and porosity gets reduced by 48% by the addition of WS<sub>2</sub> in Al–Al<sub>2</sub>O<sub>3</sub> composite. That means physical property of hybrid composite is having better results as per single reinforced MMCs.
2. Comparative result of Al MMCs and Al HMMCs shows that there is an increment of 43.98% in hardness value.

The results of this research demonstrate the potential for the use of HMMCs in place of MMCs. Further work can be done to validate its consistency in results for different hybrid combination through proper fabrication technique to exhibit best properties. This may cause the limitation in application of this type of composite.

## References

1. Macke A, Schultz BF, Rohatgi P (2012) Metal matrix composites offer the automotive industry an opportunity to reduce vehicle weight, improve performance. *Adv Mater Process* 170:19–23
2. Miracle DB (2005) Metal matrix composites—from science to technological significance. *Compos Sci Technol* 65:526–540
3. Rohatgi P, Schultz B (2007) Light weight metal matrix composites- stretching the boundaries of metals. *Mater Matters* 2:16–19
4. Ravindran S, Mani N, Balaji S, Abhijith M, Surendaran K (2019) Mechanical behaviour of aluminium hybrid metal matrix composites—a review. *Mater Today: Proc* 16:1020–1033
5. Verma V, Khvan A (2019) A short review on Al MMC with reinforcement addition effect on their mechanical and wear behaviour. In: *Advances in composite materials development*. Intech Open
6. Culliton D, Betts AJ, Kennedy D (2013) Impact of intermetallic precipitates on the tribological and/or corrosion performance of cast aluminium alloys: a short review. *Int J Cast Met Res* 26(2):65–71
7. Sahoo S (2021) Self-lubricating composites with 2D materials as reinforcement: a new perspective. *Reinf Plast* 65(2):101–103
8. Bodunrin MO, Alaneme KK, Chown LH (2015) Aluminium matrix hybrid composites: a review of reinforcement philosophies; mechanical, corrosion and tribological characteristics. *J Market Res* 4(4):434–445
9. Rooy EL (1988) Aluminum and aluminum alloys, metals handbook, vol 15. ASM International, Russell Township, pp 743–770
10. Moghadam AD, Schultz BF, Ferguson JB, Omrani E, Rohatgi PK, Gupta N (2014) Functional metal matrix composites: self-lubricating, self-healing, and nanocomposites—an outlook. *JOM* 66(6):872–881
11. Sahoo S, Samal S, Bhoi B (2020) Fabrication and characterization of novel Al–SiC–hBN self-lubricating hybrid composites. *Mater Today Commun* 25:101402
12. Singh J, Chauhan A (2019) A review of microstructure, mechanical properties and wear behavior of hybrid aluminium matrix composites fabricated via stir casting route. *Sādhanā* 44(1):1–18
13. Biswal SR, Sahoo S (2020) Fabrication of WS<sub>2</sub> dispersed Al-based hybrid composites processed by powder metallurgy: effect of compaction pressure and sintering temperature. *J Inorgan Organometallic Polymers Mater* 1–8

14. Biswal SR, Sahoo T, Sahoo S (2021) Prediction of grain boundary of a composite microstructure using digital image processing: a comparative study. *Mater Today: Proc* 41:357–362
15. Chawla KK (2012) *Composite materials: science and engineering*. Springer, New York



# Abrasive Jet Machining of Quartz Plates with Hot Silica Abrasives



S. P. Behera, B. K. Nanda, Santosh Ku Nayak, B. C. Routara, and D. Dhupal

**Abstract** Quartz is a multifaceted lighter and high strength material having many engineering applications. It is hard-to-machine in conventional process to achieve the proper surface integrity with precision. This experimental machining work is conducted on quartz pieces with the indigenously fabricated fluidized bed abrasive jet machining (FB-AJM) set up using hot silica abrasives of different sizes. The effects of three machining input process parameters such as bed pressure ( $P$ ), temperature ( $T$ ), and grain size ( $G$ ) are considered on two outputs, namely material removal rate (MRR) and surface roughness ( $R_a$ ). Box–Behnken design of response surface methodology (RSM) is applied to obtain the experimental design matrix. The SEM micrograph analysis of the machined surface has been performed to reveal the plastic deformations for initiation and propagation of crack.

**Keywords** FB-AJM · Quartz · RSM · Hot abrasives · SEM

## 1 Introduction

Abrasive jet machining (AJM) is an important and efficient non-conventional process for machining operations, namely surface etching, polishing, finishing, drilling, and deburring on brittle or hard materials like sapphire, quartz, glass, ceramics, and semiconductor materials. The mechanism in AJM is associated with the impingement of very high velocity fine grain particles on the surface of target material causing micro-cracks, and the following high-speed air takes off the eroded particles. The machinability is affected by jet velocity, jet pressure, and tip distance of nozzle, grain size, and hardness of both abrasive and workpiece. Quartz material is a versatile material for its various uses in engineering applications, but the difficulty arises in

---

S. P. Behera · B. K. Nanda (✉) · S. K. Nayak · B. C. Routara  
School of Mechanical Engineering, KIIT University, Bhubaneswar, Odisha 751024, India  
e-mail: [banandafme@kiit.ac.in](mailto:banandafme@kiit.ac.in)

D. Dhupal  
Department of Production Engineering, VSSUT, Burla, Sambalpur, Odisha 768018, India

© The Author(s), under exclusive license to Springer Nature Singapore Pte Ltd. 2023  
P. Pradhan et al. (eds.), *Recent Advances in Mechanical Engineering*,  
Lecture Notes in Mechanical Engineering,  
[https://doi.org/10.1007/978-981-16-9057-0\\_66](https://doi.org/10.1007/978-981-16-9057-0_66)

605

its economic and accurate machining. The homogenous mixture of the hot abrasives and air is prepared inside the modified mixing chamber of AJM known as fluidized bed hot abrasive jet machining (FB-HAJM) system [1, 2]. Most of the literatures of AJM explain about the effect of the jet velocity, nozzle tip distance, sizes and types of abrasives, mixing ratio, nozzle material, and shape upon the machining responses, namely material removal rate, surface quality, over cut, and kerf design. Some other papers give the importance of numerical models for machining and optimize the process parameters by statistical approaches considering suitable design of experiments (DoE). Balasubramaniam et al. [3, 4] conducted experimental investigations to identify the abrasive jet deburring process factors and optimized the responses by Taguchi orthogonal array method. AJM process on alumina ceramics with aluminum oxide, silicon carbide, and synthetic diamond abrasives was suitably attempted [5] to reveal that aluminum oxide caused roughening of the surface where silicon carbide generated smooth surface, and synthetic diamond produced large-scale fragmentation. Getu et al. [6, 7] observed the consequence of embedding of angular and spherical abrasive particles during abrasive jet micro-machining of polymers that shielded the surface from subsequent impacts causing reduction in erosion rate and determined the conditions of embedment of particles. Ghobeity et al. [8] predicted the numerical model and experimental data related to the  $\mu$ -AJM of both masked and unmasked in glass workpiece. An economic mask fabrication technique is based on  $\mu$ -stereo lithography technology for  $\mu$ -AJM by Lee et al. [9]. Barletta et al. [1, 10] developed the new hybrid technique of fluidized bed-assisted abrasive jet machining (FB-AJM) to perform experiments on internal polishing of circular tubes. The roughness reduction of a reference unmasked channel in borosilicate glass was a function of post-blasting particle size and impact angle [11] as investigated by Jafar et al. [11]. Zhang et al. [12] introduced another concept of  $\mu$ -abrasive intermittent jet machining method small holes to solve the problem of colliding accumulation of abrasives at the bottom of the hole. The magnetorheological abrasive was developed [13] to make the flow for finishing process on stainless steel workpieces at different magnetic field strength. Jagannatha et al. [2] carried out a novel experiment on abrasive hot air jet machining and studied the effect of air temperature on the material removal rate of glass material along with the roughness. Efforts are being continuously made to achieve an effective AJM process for proper distribution of abrasives with air so as to make proper incident on the target material. Nanda et al. [14, 15] modified the mixing chamber as fluidized bed abrasive jet machining (FB-AJM) that supplied uniform mixture for drilling holes in ceramic glass fiber-reinforced polymer.

The present experimental work represents further development of FB-AJM setup where a hot abrasive chamber is attached for drilling of quartz material with hot silica particles. Experiments are conducted with the response surface method (RSM) of design of experiment (DoE).

## 2 Experimentation

The hot abrasive chamber in the FB-AJM setup with different fixtures is designed and fabricated as given in Figs. 1, 2, and 3. A reciprocating type air compressor is used to supply the required high pressure after passing through a dehumidifier (FRL unit) that removes some solid pollutants and atmospheric moisture. This clean, dry, and compressed air prevents the blocking of fine grains inside the flow paths. The nozzle is fabricated with the hard and wear-resistant D-2 steel material. An electric heating coil of 1.5 kW is wrapped inside the conical-shaped chamber with a thermocouple to maintain the desired temperature. The main flow line is then connected to the bottom of the heating chamber for continuous supply of hot homogeneous air abrasive mixture.

### 2.1 Details of Work Piece and Silica Particle

The quartz work pieces of dimensions  $2.5 \times 2.5 \times 0.2 \text{ cm}^3$  (Fig. 4a, b) are taken for drilling purpose in FB-HAJM setup. Generally, abrasives are selected depending on the physical properties of the work piece and surface finish. Hence, silica grits with 3

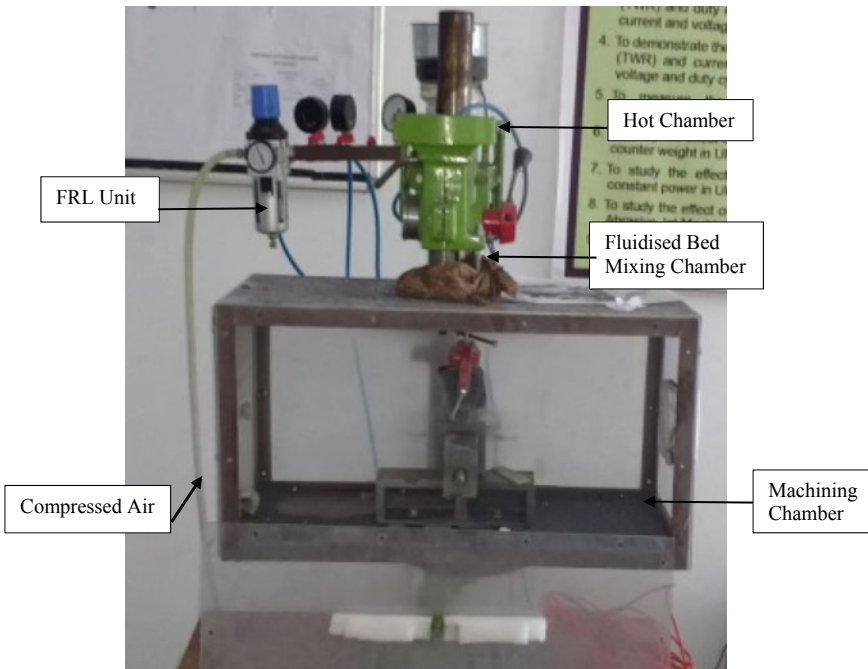
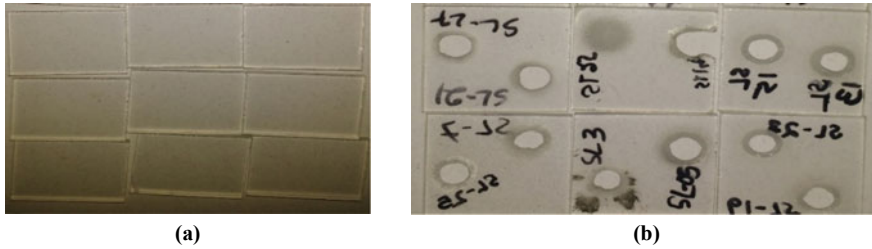


Fig. 1 FB-HAJM setup

**Fig. 2** Heating coil wrapped with glass wool



**Fig. 3** Abrasive heating chamber



**Fig. 4** **a** Quartz work piece before machining. **b** Work pieces after machining

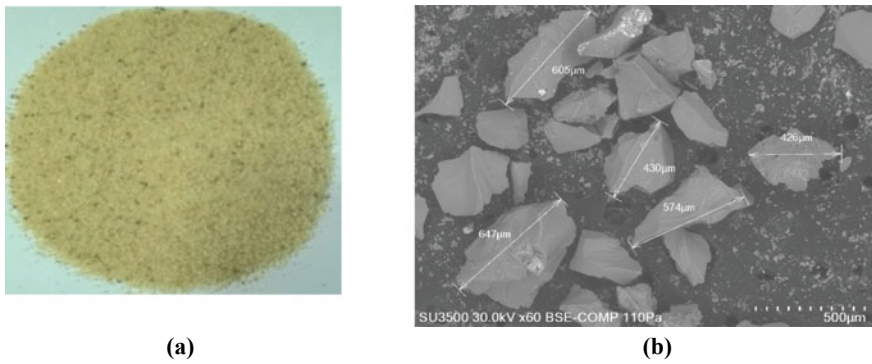


**Fig. 5** **a** Silica abrasives. **b** SEM of abrasives

sizes, 270, 350, and 560  $\mu\text{m}$  are chosen (Fig. 5a). The uneven sizes of silica particle with multiple cutting sides are properly visible in SEM micrograph (Fig. 5b). Their average sizes are considered here as the grain size ( $G$ ).

**2.2 Input Variables and Output Results**

The three input machining variables are as follows: pressure ( $P$ ), temperature ( $T$ ), grain size ( $G$ ), and the two outputs areas follows: material removal rate (MRR) and  $R_a$  (surface finish).

**2.3 Measurement of Removal Rate and Surface Quality**

Repeated bombardment of the high momenta abrasives on the quartz surface dislodged materials, and it is expressed on volume basis as:  $MRR = \rho(w_1 - w_2)/\Delta t$ , where  $(w_1 - w_2)$  is the weight loss in time  $\Delta t$ , and  $\rho$  is the density.

MITUTOYO-400 surface tester measures the surface quality at three-different positions of the slightly etched quartz surface to find the average value of Ra.

### 3 Design of Experiment (DoE) and Observation

#### 3.1 Design of Experiment (DoE)

Box–Behnken type response surface methodology (RSM) is utilized as the design of experiment (DoE) to find the 15 number of experimental runs with three parameters ( $P$ ,  $T$ ,  $G$ ), and three-levels from Design Expert software as in Table 1 and the observations are in Table 2.

The two responses MRR and Ra are measured for the 15 experimental runs conducted on the above fabricated setup, and the values are entered in Design Expert software for further statistical analysis and surface plots.

**Table 1** Input parameters

S. No.	Input parameter	Min level (−1)	Mid-level (0)	Max level (+1)
1	Pressure ( $P$ ), bar	4	5	6
2	Temperature ( $T$ ), °C	40	50	60
3	Grain size ( $G$ ), $\mu\text{m}$	270	350	560

**Table 2** Experimental table

Run	$P$ (bar)	$T$ (°C)	$G$ ( $\mu\text{m}$ )	MRR (cc/min)	Ra ( $\mu\text{m}$ )
1	5	40	270	0.012929	9.5264
2	6	50	270	0.008658	6.7673
3	5	50	350	0.010692	3.9993
4	5	60	560	0.01291	6.7511
5	5	50	350	0.010052	6.1172
6	4	60	350	0.010672	3.7972
7	6	50	560	0.012056	7.2383
8	5	40	560	0.012033	8.8525
9	4	50	270	0.01032	6.4647
10	4	50	560	0.011276	4.2743
11	6	60	350	0.008234	8.8617
12	6	40	350	0.01165	6.6758
13	4	40	350	0.009017	8.4945
14	5	60	270	0.011289	6.4018
15	5	50	350	0.010692	3.7993

### 3.2 Analysis of Variance (ANOVA)

#### ANOVA of Material Removal Rate

Model  $F$ -value is 5.87;  $p$ -value 0.0328 ( $<0.05$ ), “Lack of Fit  $F$ -value” of 5.32( $>0.05$ ) with  $R^2$  value 0.9136 indicate the significance of the model.

#### ANOVA of Surface Roughness

Model  $F$ -value is 5.28;  $p$ -value 0.0407 ( $<0.05$ ), “Lack of Fit  $F$ -value” of 0.8201( $>0.05$ ) with  $R^2$  value 90.49% indicate the significance of the model.

#### Response Surface Analysis and Discussion

The effect of the three input parameters on MRR are shown in Fig. 6a. It is found MRR initially increases with increase in  $P$  little beyond the mid-value, and after that it decreases slightly toward the end. MRR initially decreases with  $T$  and  $G$ , but later it increases.

Similarly, the three surface plots of  $R_a$  in Fig. 6b reveal that initially  $R_a$  decreases with  $T$  giving more finished surface, and after that it increases. Again,  $R_a$  increases with  $P$  and  $G$ .

#### SEM Micrograph Analysis and Discussion

The SEM micrograph analysis of the quartz surfaces is performed, and one of them is given in Fig. 7, where the propagation of crater lines due to plastic deformation is clearly visible. Some embedded grits are also seen that adheres to the machined surface.

#### Surface Plots

See Figs. 6 and 7.

## 4 Conclusions

The above experimental research work reveals following results:

- (a) The principle of induction heating is applied for the modification of the mixing chamber that effectively increases the kinetic energy of the silica grains giving less deterioration of cutting edges.
- (b) This FB-HAJM setup is very economic to create the necessary dynamic characteristic of silica abrasives.
- (c) From the various analysis of this experimental work of quartz with FB-HAJM, it is seen from the surface plots that MRR increases with increase in pressure,  $T$  and  $G$  with little fluctuations, and  $R_a$  initially decreases with  $T$  giving more finished surface but increases with  $P$  and  $G$ .
- (d) The SEM analysis clearly indicates the initiation and propagation of fracture lines with embedded silica particles.



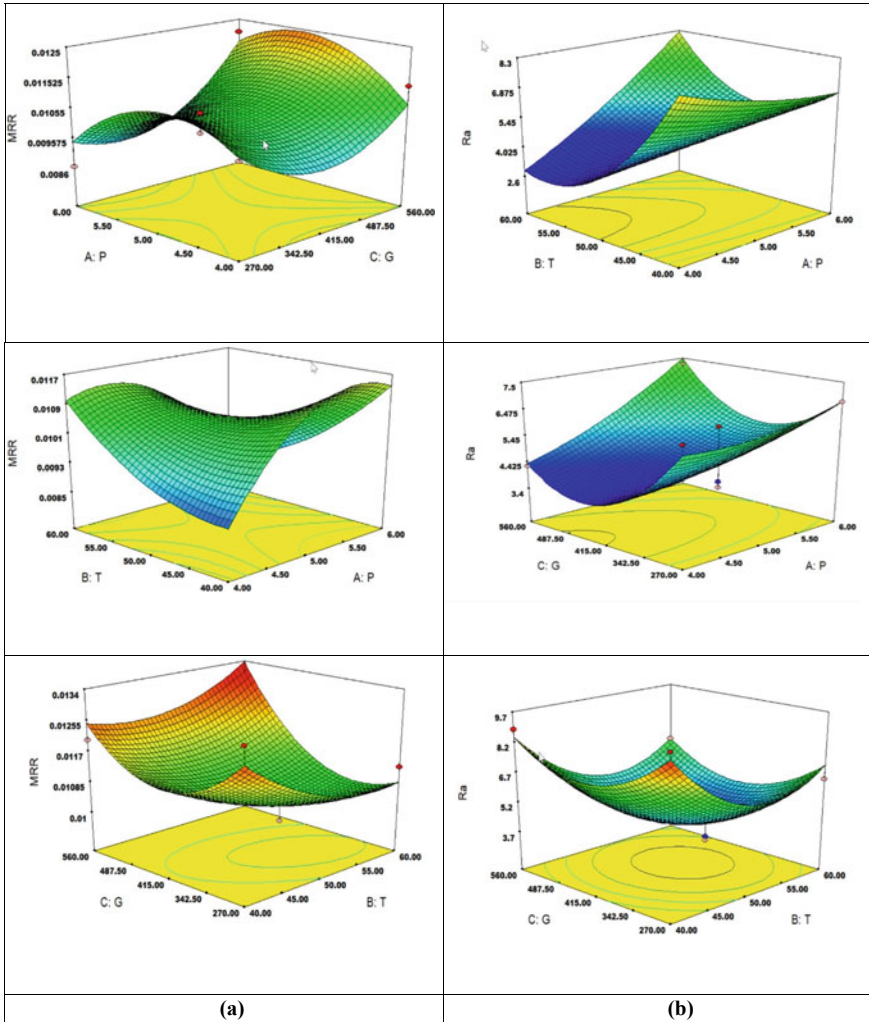
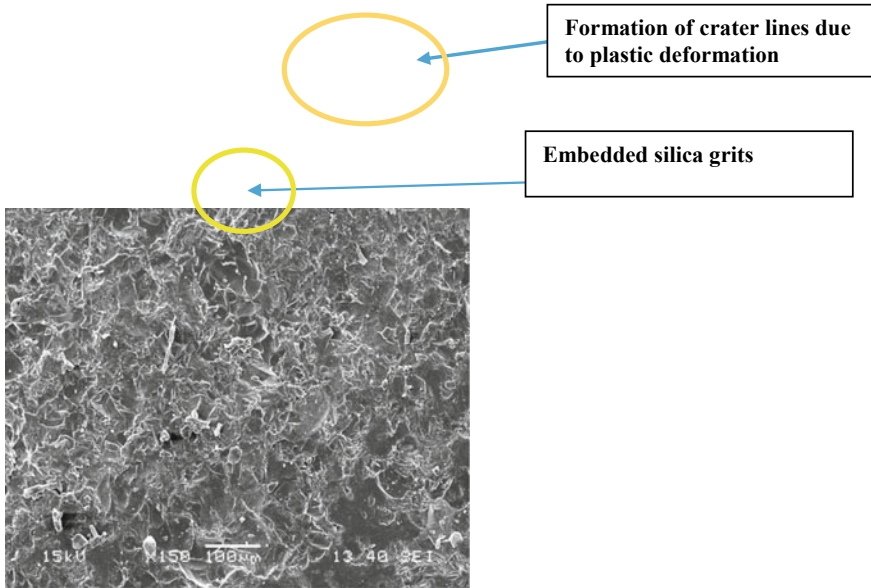


Fig. 6 a Surface plots of MRR. b Surface plots of Ra

- (e) Use of hot abrasives causes increase of MRR with better surface finish which is the innovation of this work. Hence, this work of FB-HAJM on quartz pieces can be extended to modern manufacturing and fabrication process of precious brittle materials.





**Fig. 7** SEM of machined quartz surface of Experiment No. 1

## References

1. Barletta M, Guarino S, Rubino G, Tagliaferri V (2007) Progress in fluidized bed assisted abrasive jet machining (FB-AJM): internal polishing of aluminium tubes. *Int J Mac Tools Manuf* 47(3-4):483–495
2. Jagannatha N, Hiremath SS, Sadashivappa K (2012) Analysis and parametric optimization of abrasive hot air jet machining for glass using Taguchi method and utility concept. *Int J Mech Mater Eng* 7(1):9–15
3. Balasubramaniam R, Krishnan J, Ramakrishnan N (1998) Investigation of AJM for deburring. *J Mater Process Technol* 79(1–3):52–58
4. Balasubramaniam R, Krishnan J, Ramakrishnan N (2000) An empirical study on the generation of an edge radius in abrasive jet external deburring (AJED). *J Mater Process Technol* 99(1–3):49–53
5. Wakuda M, Yamauchi Y, Kanzaki S (2003) Material response to particle impact during abrasive jet machining of alumina ceramics. *J Mater Process Technol* 132(1–3):177–183
6. Getu H, Spelt JK, Papini M (2012) Conditions leading to the embedding of angular and spherical particles during the solid particle erosion of polymers. *Wear* 292:159–168
7. Getu H, Spelt JK, Papini M (2008) Cryogenically assisted abrasive jet micromachining of polymers. *J Micromech Microeng* 18(11):115010
8. Ghobeity A, Krajac T, Burzynski T, Papini M, Spelt JK (2008) Surface evolution models in abrasive jet micromachining. *Wear* 264(3–4):185–198
9. Lee SP, Kang HW, Lee SJ, Lee IH, Ko TJ, Cho DW (2008) Development of rapid mask fabrication technology for micro-abrasive jet machining. *J Mech Sci Technol* 22(11):2190–2196
10. Barletta M (2006) A new technology in surface finishing: fluidized bed machining (FBM) of aluminium alloys. *J Mater Process Technol* 173(2):157–165
11. Jafar RHM, Papini M, Spelt JK (2013) Simulation of erosive smoothing in the abrasive jet micro-machining of glass. *J Mater Process Technol* 213(12):2254–2261

12. Zhang L, Kuriyagawa T, Yasutomi Y, Zhao J (2005) Investigation into micro abrasive intermittent jet machining. *Int J Mach Tools Manuf* 45(7–8):873–879
13. Jha S, Jain VK (2004) Design and development of the magnetorheological abrasive flow finishing (MRAFF) process. *Int J Mach Tools Manuf* 44(10):1019–1029
14. Nanda BK, Mishra A, Dhupal D (2017) Fluidized bed abrasive jet machining (FB-AJM) of K-99 alumina ceramic using SiC abrasives. *Int J Adv Manufact Technol* 90(9):3655–3672
15. Nanda BK, Mishra A, Das SR, Dhupal D (2020) Fluidized bed hot abrasive jet machining (FB-HAJM) of K-60 alumina ceramic. In: *Advances in unconventional machining and composites*. Springer, Singapore, pp 641–650

# Darcy-Forchheimer Flow Over a Stretching Sheet with Heat Source Effect: A Numerical Study



S. Sahu, D. N. Thatoi, and K. Swain

**Abstract** Due to numerous industrial and manufacturing processes such as polymer extrusion and cooling of electronic devices by fans, MHD boundary layer flow over a stretching sheet has sparked significant interest. The article examines the Darcy-Forchheimer flow of viscous fluid over a vertical stretching sheet embedded in a permeable matrix with internal heat source. Similarity transformations convert the governing partial differential equations (PDEs) into nonlinear ordinary differential equations (ODEs). The system of ODEs is solved by shooting technique using MATLAB software. The consequences of operational parameters on velocity, temperature, force coefficient, as well as Nusselt number are presented through graphs and tables. It is found that the local inertia parameter is discovered to have opposing impacts on velocity and temperature profiles. The Nusselt number increases with increase in magnetic parameter and heat source parameter.

**Keywords** Darcy-forchheimer flow · Heat transfer · Stretching sheet · Shooting technique

## 1 Introduction

Study over a stretching sheet is significant due to its wide applications in industry. Crane [1] studied the flow caused by stretched sheet. The flow and heat transfer through a permeable media have received a lot of consideration in recent years because of its different pragmatic applications in geothermal and oil repository. Further, Mahapatra and Gupta [2] extended the work of [1] with stagnation point flow. Moreover, number of works [3–6] related to this field were recorded in the literature. To control the heat transmission practice in industry, thermal radiation plays

---

S. Sahu · D. N. Thatoi  
Department of Mechanical Engineering, SOA University, Bhubaneswar 751030, India

K. Swain (✉)  
Department of Mathematics, Gandhi Institute for Technology, Bhubaneswar 752054, India  
e-mail: [kharabela1983@gmail.com](mailto:kharabela1983@gmail.com)

a substantial role as the quality of ultimate product depends on the heating/cooling factors. Makinde [7] and Golafshan and Rahimi [8] studied the flow of nanofluid past a vertical elongating sheet considering radiation effect. Several authors [9–13] have recently contributed to deformable surfaces through various flow models.

In this article, our objective is to study the Darcy-Forchheimer flow of viscous fluid past a vertical extended sheet embedded in a permeable matrix subject to magnetic field and internal heat source. The significance of nonlinear Darcy-Forchheimer is to take care of fast flow through porous media unlike linear Darcy model which is suitable for slow flow. The governing PDEs are transformed to system of nonlinear ODEs using similarity transformations. These systems of ODEs are solved numerically using shooting technique by the help of MATLAB software. The significances of physical parameters such as magnetic parameter ( $M$ ), porosity parameter ( $Kp$ ), inertia parameter ( $Fr$ ), heat source parameter ( $Q$ ), Prandtl number ( $Pr$ ), and Biot number ( $Bi$ ) on velocity, temperature, skin factor, and Nusselt number are conveyed through graphs and tables.

## 2 Mathematical Formulation

A steady, laminar, incompressible, and 2D flow of electrically conducting viscous fluid over a vertical stretching sheet with internal heat source are considered. A constant transverse magnetic field strength ( $B_0$ ) is applied to the flow. The magnetic Reynolds number is assumed to be small so that the induced magnetic field can be neglected in comparison with the applied magnetic field. Further, Darcy-Forchheimer flow model characterizes the flow through porous medium. The plate is placed along  $x$ -axis and  $y$ -axis is perpendicular to it as shown in Fig. 1. The flow is induced due to the stretching of the sheet in its own plane with the surface velocity  $u_w(x) = ax$ . The temperature of the sheet is the result of a convective heating process through conduction which is characterized by a temperature  $T_w$  and a heat transfer coefficient  $h$ .

Under the above assumptions, the mathematical equations with boundary conditions following Bakar et al. [14] are given by

$$u_x + v_y = 0 \tag{1}$$

$$uu_x + vv_y = vu_{yy} - \left( \frac{\sigma B_0^2}{\rho} + \frac{v}{Kp^*} \right) u - \frac{c_b}{\sqrt{Kp^*}} u^2 \tag{2}$$

$$uT_x + vT_y = \frac{k}{\rho c_p} T_{yy} + \frac{Q^*}{\rho c_p} (T - T_\infty) \tag{3}$$

$$\left. \begin{aligned} u = ax, v = 0, -kT_y = h(T_w - T_\infty) \text{ as } y = 0 \\ u = 0, T \rightarrow T_\infty \text{ as } y \rightarrow \infty \end{aligned} \right\} \tag{4}$$

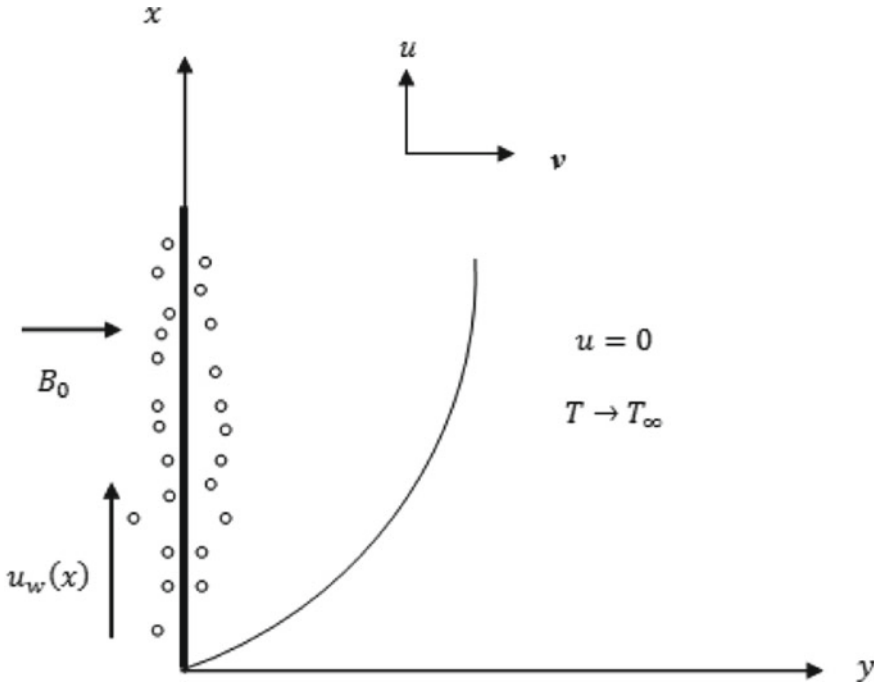


Fig. 1 Flow model and coordinate system

where  $u$  and  $v$  are the velocities, respectively, along  $x$  and  $y$  directions,  $B_0$  is the magnetic field strength,  $\nu, \rho, \sigma, k, T,$  and  $T_\infty$  are correspondingly viscosity, density, electrical and thermal conductivities, temperature, and ambient temperature of the fluid,  $c_p,$  specific heat,  $c_b,$  drag coefficient,  $Q^*,$  heat source/sink coefficient,  $Kp^*,$  porousness of the medium,  $a(> 0),$  constant and  $h,$  heat transmission factor.

The similarity conversions are conveyed as

$$u = axf'(\eta), v = -(va)^{1/2}f(\eta), \theta = \frac{T - T_\infty}{T_w - T_\infty}, \eta = y(a/\nu)^{1/2}$$

The renovated ODEs are

$$f''' = (1 + Fr)f'^2 - f''f + (M + Kp)f' \tag{5}$$

$$\theta'' = -Pr(f\theta' + Q\theta) \tag{6}$$

$$\left. \begin{aligned} f(0) = 0, f'(0) = 1, \theta(0) = 1 + \frac{1}{Bi}\theta'(0) \\ f'(\infty) \rightarrow 0, \theta(\infty) \rightarrow 0 \end{aligned} \right\} \tag{7}$$

where  $M = \frac{\sigma B_0^2}{a\rho}$ ,  $Kp = \frac{aKp^*}{v}$ ,  $Fr = \frac{c_b}{x\sqrt{Kp^*}}$ ,  $Pr = \frac{\mu c_p}{k}$ ,  $Q = \frac{Q^*}{a\rho c_p}$ , and  $Bi = \frac{h}{k}\sqrt{\frac{v}{a}}$  are, respectively, magnetic parameter, porosity parameter, local inertia parameter, Prandtl number, heat source parameter, and Biot number.

The local Nusselt number  $Nu_x = \frac{xq_w}{k(T-T_\infty)} \Rightarrow \frac{Nu_x}{\sqrt{Re_x}} = -\theta'(0)$  and skin friction  $C_f = \frac{2\tau_w}{\rho u_w^2} \Rightarrow C_f\sqrt{Re_x} = -f''(0)$  where  $q_w = -k\left(\frac{\partial T}{\partial y}\right)_{y=0}$ ,  $\tau_w = \mu\left(\frac{\partial u}{\partial y}\right)_{y=0}$  and  $Re_x = \frac{ax^2}{v}$  (local Reynolds number).

### 3 Results and Discussion

The nonlinear ODEs (5) and (6) subject to boundary conditions (7) are solved numerically using the shooting procedure in MATLAB software with the step length  $\Delta\eta = 0.01$  and error tolerance of  $10^{-5}$  appropriately. We compare the obtained results corresponding to the Nusselt number  $\theta'(0)$  with Wang [15] in Table 1 to validate the correctness of the ongoing analysis, and those are found to be in excellent agreement.

From Fig. 2, it is observed that  $f'(\eta)$  is the decreasing function of  $M$  and  $\theta(\eta)$  is an increasing function of  $M$ . The physical interpretation runs as the resistive force Lorentz force the outcome of interaction of the applied magnetic field with electric current opposes the motion of the fluid to slow down the flow. The resistance offered by the force enhances the internal thermal energy to step up temperature distribution in the flow domain. From Fig. 3, the similar explanation may be attributed to inertia factor, which reduces the momentum transport causing the slow flow and hike in temperature which is due to resistance offered by the porous matrix attributing permeability of the medium with the help of Darcy-Forchheimer term in governing equation. The asymptotic fall of velocity and temperature in the flow domain shows the laminarity in the flow domain. Figure 4 shows the effects of heat source/sink parameter ( $Q$ ) on temperature profiles  $\theta(\eta)$  for both the cases. The temperature profiles enhance with higher values of heat source parameter ( $Q > 0$ ) and decline with heat sink parameter ( $Q < 0$ ).

**Table 1** Comparison of  $\theta'(0)$  for several values of Pr with  $M = Fr = Kp = 0$  and  $Bi \rightarrow \infty$

Pr	Wang [15]	Present study
0.07	-0.0656	-0.0649
0.2	-0.1691	-0.1694
0.7	-0.4539	-0.4516
2	-0.9114	-0.91072
7	-1.8954	-1.89492
20	-3.3539	-3.35351
70	-6.4622	-6.46182

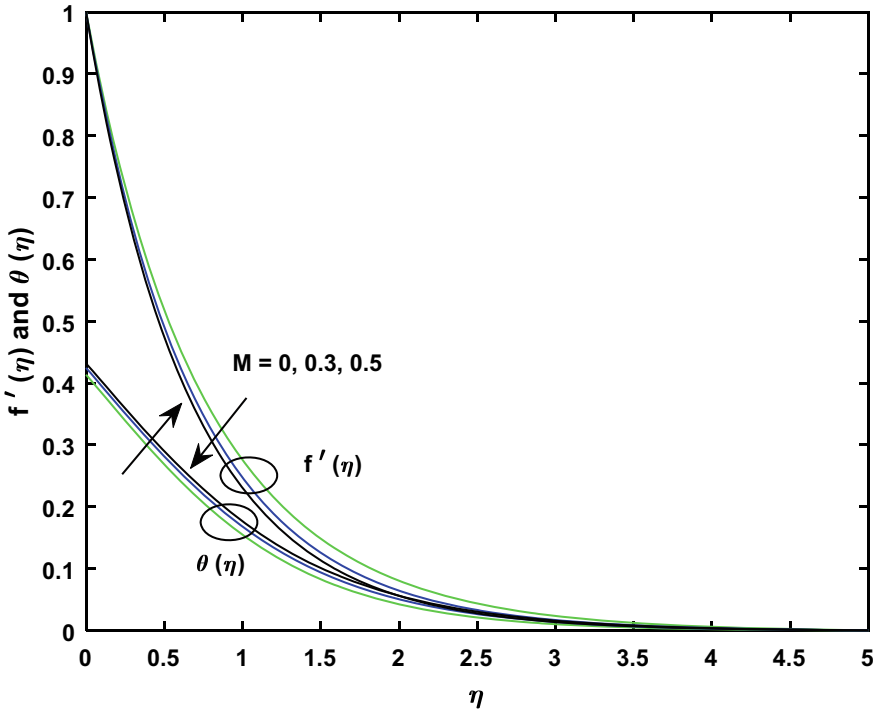


Fig. 2  $f'(\eta)$  and  $\theta(\eta)$  versus  $M$

Table 2 shows that  $f''(0)$  is an increasing function of  $M$  and  $Fr$  whereas slightly reduces with  $Q$ . Further,  $Nu_x$  is increases with  $M$  and  $Bi$  and decreases with  $Fr$  and  $Q$ . These results are well supported by Seth et al. [16]. The Biot number characterizes the heat conductivity between solid bounding surface and the fluid with the help of heat transfer coefficient and thermal conductivity. From the Eq. (7), it is evident that an increase in  $Bi$  reduces the temperature gradient in the flow domain leading to a constant temperature at the bounding surface ( $Bi \rightarrow \infty, \theta(0) \rightarrow 1$ ). Thus, for high Biot number, the present analysis reduces to problem of constant temperature at the plate. It is also interesting to note that for very small  $Bi$  ( $Bi \rightarrow 0$ ), the temperature at the plate assumes incredible high temperature. The high temperature of the bounding surface may lead to thermal instability of the flow domain.

### 4 Concluding Remarks

The MHD boundary layer flow and heat transfer of viscous fluid over a stretched sheet embedded in the porous medium by the influence of magnetic field and heat

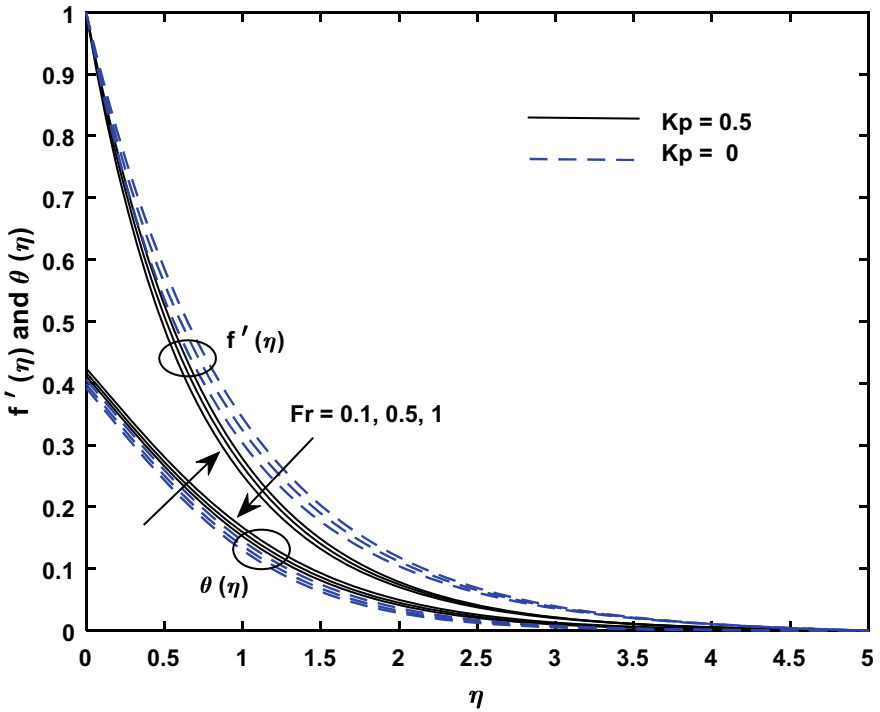


Fig. 3  $f'(\eta)$  and  $\theta(\eta)$  versus  $Fr$

source/sink are examined numerically. The following are some of the findings of the present study:

- Role of external magnetic field and internal heat source is to reduce and enhance the momentum transport and thermal transport, respectively, resulting reduce in velocity and rise in temperature.
- The role of Biot number is quite interesting and care should be taken to regulate the Biot number and inertia factor for assuming flow and heat transfer laminarity.



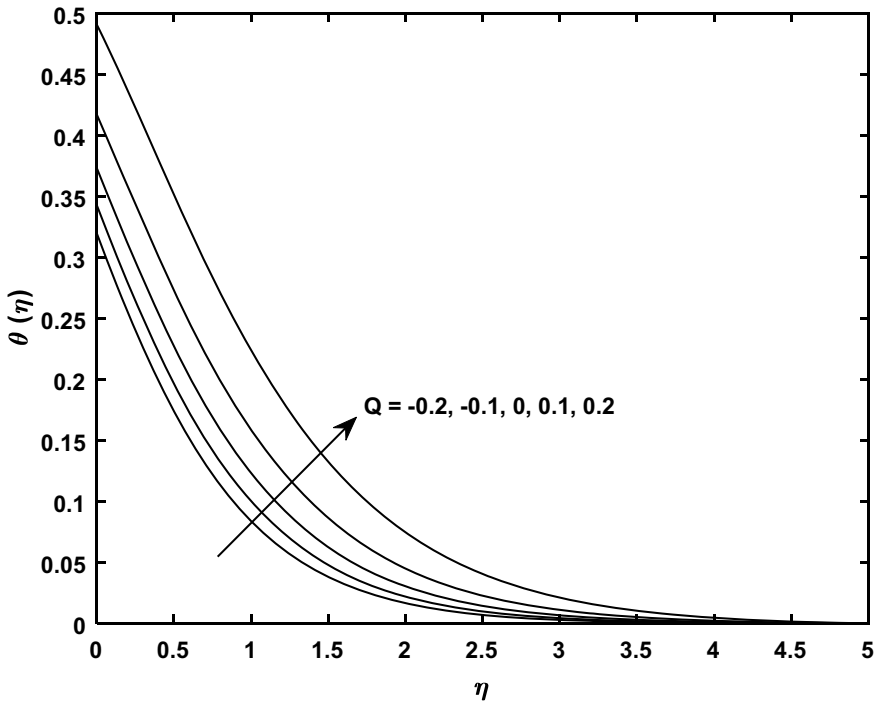


Fig. 4  $\theta(\eta)$  versus  $Q$

Table 2 Calculation of  $f''(0)$  and  $-\theta'(0)$  when  $Kp = 0.5$  and  $Pr = 2$

$M$	$Fr$	$Bi$	$Q$	$f''(0)$	$-\theta'(0)$
0.1	0.1	0.1	0.1	-1.290355	0.087724
0.5				-1.620293	0.095979
1.0				-1.735964	0.096853
	0.5			-1.780571	0.094248
	1.0			-1.928377	0.093136
		0.3		-1.928348	0.272901
		0.5		-1.928347	0.367355
			0.3	-1.919284	0.343609
			0.5	-1.901410	0.308226

### References

1. Crane L (1970) Flow past a stretching plate. *Z Angew Math Phys* 21(4):645-647
2. Mahapatra TR, Gupta A (2002) Heat transfer in stagnation-point flow towards a stretching sheet. *Heat Mass Transf* 38(6):517-521

3. Nayak MK, Dash GC, Singh LP (2016) Heat and mass transfer effects on MHD viscoelastic fluid over a stretching sheet through porous medium in presence of chemical reaction. *Propul Power Res* 5(1):70–80
4. Dessie H, Kishan N (2014) MHD effects on heat transfer over stretching sheet embedded in porous medium with variable viscosity, viscous dissipation and heat source/sink. *Ain Shams Eng J* 5:967–977
5. Swain K, Parida SK, Dash GC (2017) MHD heat and mass transfer on stretching sheet with variable fluid properties in porous medium. *Model Meas Contr B* 86(4):864–884
6. Mahdy A, Chamkha AJ (2010) Chemical reaction and viscous dissipation effects on Darcy-Forchheimer mixed convection in a fluid saturated porous media. *Int J Numer Meth Heat Fluid Flow* 20(8):924–940
7. Makinde OD (2005) Free convection flow with thermal radiation and mass transfer past a moving vertical porous plate. *Int Commun Heat Mass Transfer* 32:1411–1419
8. Golafshan B, Rahimi AB (2019) Effects of radiation on mixed convection stagnation-point flow of MHD third-grade nanofluid over a vertical stretching sheet. *J Therm Anal Calorim* 135:533–549
9. Swain K, Parida SK, Dash GC (2019) Higher order chemical reaction on MHD nanofluid flow with slip boundary conditions: a numerical approach. *Math Model Eng Probl* 6(2):293–299
10. Hayat T, Haider F, Muhammad T, Alsaedi A (2017) Darcy-Forchheimer flow with Cattaneo-Christov heat flux and homogeneous-heterogeneous reactions. *PLoS One* 12(4):e0174938
11. Panigrahi L, Panda JP, Swain K, Dash GC (2020) Heat and mass transfer of MHD Casson nanofluid flow through a porous medium past a stretching sheet with Newtonian heating and chemical reaction. *Karbala Int J Mod Sci* 6(3):322–331
12. Uddin I, Akhtar R, Zhiyu Z, Islam S, Shoaib M, Raja MAZ (2019) Numerical treatment for Darcy-Forchheimer Flow of Sisko nanomaterial with nonlinear thermal radiation by Lobatto IIIA technique. *Math Probl Eng* 15. Article ID 8974572
13. Rasool G, Shafiq A, Khaliq CM, Zhang T (2019) Magneto-hydrodynamic Darcy-Forchheimer nanofluid flow over nonlinear stretching sheet. *Physica* 94(10):1–25
14. Bakar SA, Arifin NM, Nazar R, Ali FM, Pop I (2016) Forced convection boundary layer stagnation-point flow in Darcy-Forchheimer porous medium past a shrinking sheet. *Front Heat Mass Transfer (FHMT)* 7:38
15. Wang CY (1989) Free convection on a vertical stretching surface. *J Appl Math Mech (ZAMM)* 69:418–420
16. Seth GS, Thipathi R, Mishra MK (2017) Hydromagnetic thin film flow of Casson fluid in non-Darcy porous medium with Joule dissipation and Navier's partial slip. *Appl Math Mech* 38:1613–1626

# Slurry Erosion Behaviour of HVOF-Sprayed NiAl Composite Coating



Pragyan Senapati, Harekrushna Sutar, Rabiranjana Murmu, and Shubham Gupta

**Abstract** Nickel-aluminium coating was deposited on AISI 304 stainless steel by HVOF process. The coating was characterised by scanning electron microscope and optical microscope. The surface hardness, surface roughness, thickness and fracture toughness value of the coating was determined. Slurry erosion testes were carried out on both the coated and uncoated samples by varying the impact angles at 30°, 60° and 90°, and their slurry erosion behaviour was studied. The coated samples exhibited 3.5 times, 1.9 and 1.04 times more resistance to slurry erosion at 30°, 60° and 90° impact angle, respectively, than the uncoated bare steel.

**Keywords** HVOF · Slurry erosion · NiAl

## 1 Introduction

The HVOF coatings are characterised by wear, corrosion and abrasion resistance along with protection of the substrate at high temperature. This coating process is carried out at a temperature of about 3000 °C and velocity of 1000 m/s. HVOF technique uses wide variety of coating powders: metals, ceramics, metal alloys and cermets. Coating powders of size ranging from 4 to 45 μm can be coated, and coating thickness of few millimetres can be obtained by this process. The advantages of HVOF coatings over other thermal coating processes are mostly related to its high coating quality such as high density, low porosity, retention of the powder chemistry, low in-flight exposure time leading to lower oxide content, smoother and thicker coatings due to high impact velocity and low residual stresses, respectively [1–3]. There are certain disadvantages of HVOF coatings such as complexity in the properties and microstructure of the coatings due various coating parameters,

---

P. Senapati · S. Gupta

Department of Mechanical Engineering, ITER, Siksha ‘O’ Anusandhan Deemed to be University, Bhubaneswar, India

H. Sutar (✉) · R. Murmu

Department of Chemical Engineering, Indira Gandhi Institute of Technology, Sarang, India  
e-mail: [h.k.sutar@gmail.com](mailto:h.k.sutar@gmail.com)

© The Author(s), under exclusive license to Springer Nature Singapore Pte Ltd. 2023

623

P. Pradhan et al. (eds.), *Recent Advances in Mechanical Engineering*,

Lecture Notes in Mechanical Engineering,

[https://doi.org/10.1007/978-981-16-9057-0\\_68](https://doi.org/10.1007/978-981-16-9057-0_68)

restriction in the powder size (5–60  $\mu\text{m}$ ), high investment in equipment and requirement of experienced and qualified workers for smooth operation of the equipment. NiAl has been widely used in recent years because of its high corrosion resistance. Karaoglanli et al. [4] produced CoNiCrAlY coatings by four different techniques such as cold gas dynamic spraying (CGDS), supersonic atmospheric plasma spraying (SSAPS), detonation gun (D-gun), Atmospheric plasma spraying (APS) and High velocity oxygen fuel (HVOF) on Inconel718 superalloy. They reported that CGDS and HVOF techniques showed better reliability in terms of thermally grown oxide than other coating techniques, and CGDS technique coatings were more oxidation resistance than other techniques. In another research done by Karaoglanli et al. [5], they deposited CoNiCrAlY powder on Ni-based superalloys by adopting techniques like APS, HVOF and CGDS to study the abrasion wear and microstructural properties of the coatings. The CGDS method-coated samples displayed higher values of roughness and hardness and lower value of volume loss in comparison to the other two methods of coating. Khanna and Rathod [6] adopted HVOF and CGDS techniques to deposit CoNiCrAlY powder on the substrate 316L SS. CGDS coatings showed superior oxidation resistance, low wear rate and good friction behaviour. Lui et al. [7] compared the abrasive wear, microstructure and mechanical properties of alumina-titania coatings deposited by two different methods such as HVOF and plasma spray (PS). The abrasive resistance of the HVOF-coated samples was 2–3 folds higher than the plasma-sprayed coatings, and the former coated samples exhibited higher values of hardness and toughness than the latter samples. A comparative study was carried out on Ni, NiCr and NiAl coatings deposited by HVAF, HVOF and APS techniques by Sadeghimeresht et al. [8] for comparing the corrosion resistance of the different coatings. The HVAF-sprayed coatings exhibited better coating characteristics and corrosion resistance behaviour than the other two coatings. Pores and micro-cracks were prominently visible in APS coatings, less visible on HVOF coatings and not detected in HVAF coatings. Lima et al. [9] deposited the nanostructured and conventional  $\text{TiO}_2$  powders by adopting two different methods such as HVOF and APS. The nanostructured  $\text{TiO}_2$  powders sprayed by HVOF process exhibited abrasion and crack propagation resistance along with higher bond strength when compared with conventional  $\text{TiO}_2$  powders deposited by HVOF and APS processes. Kaushal et al. [10] compared the high temperature corrosion behaviours of Ni/20Cr coatings developed by HVOF, detonation gun and cold spray methods. The coatings were deposited on T22 boiler steel, and it was found that coatings developed by detonation gun method showed better corrosion resistance due to formation protective phases of  $\text{Cr}_2\text{O}_3$  and  $\text{NiCr}_2\text{O}_4$  in comparison to other two methods.

In the present research work, a comparative study is done on the slurry erosion behaviour of NiAl-coated samples and AISI304 stainless steel. The parameter like impact angle has been varied to analyse the erosion of the coated and uncoated samples.

**Table 1** Salient parameters of HVOF coating process

Factors	Title/magnitude
Pressure	Oxygen: 1 MPa
	Air: 0.5–0.6 MPa
	Fuel LPG: 0.7 MPa
Flow rate	Oxygen: 0.0042–0.0045 m <sup>3</sup> /s
	Air: 0.01 m <sup>3</sup> /s
	Fuel LPG: 0.001–0.0011 m <sup>3</sup> /s
	Nitrogen: 0.0014–0.0016 m <sup>3</sup> /s
Carrier gas	Nitrogen
Gun	MEC Hipo jet 2700
Nozzle to substrate distance	0.18 m

## 2 Experimentation

### 2.1 Coating Material and Substrate

NiAl powder with 95 wt% Ni and 5 wt% Al with grain size 45/22  $\mu\text{m}$  was used as coating powders. The nominal chemical composition (wt%) of NiAl powder was Ni (min 93.5), Al (4–5.5), B (max 0.15) and impurities (max 1.0). SS304 used as substrate has nominal chemical composition (wt%): C (0.07), Cr (17.5), Mn (2.0), Si (1.00), P (0.045), S (0.015), Ni (10.5), N (0.1) and Fe (balance).

### 2.2 Coating Procedure

The substrate AISI304 stainless steel was coated by HVOF technique in a closed chamber. The sample of size 100 mm  $\times$  100 mm  $\times$  10 mm was grit blasted with alumina before coating, to obtain a better interlocking between the coating powder and the substrate. Immediately after the grit blasting, the coating procedure took place so that the nascent surface does not develop oxidised layer so as to avoid poor quality coating. The coating parameters are listed in Table 1.

### 2.3 Slurry Jet Erosion Tester

The slurry jet erosion tester produces a jet of stream comprising of water and erodent that repetitively strikes the surface of the coated and uncoated sample. The slurry jet erosion tester conforms to ASTM G 73 international standard test method. The samples were cut into 25 mm  $\times$  25 mm  $\times$  10 mm in a wire EDM before erosion. The

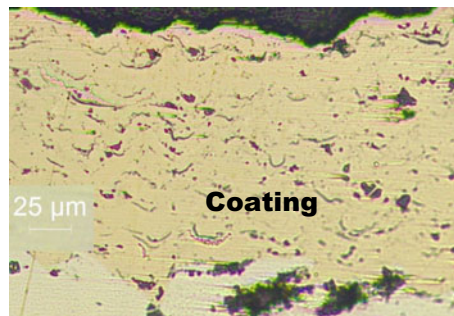
**Table 2** Test parameters for slurry jet erosion

Water	400 L soft water (tap water)
Erodent	Silica sand
Erodent size	200 $\mu\text{m}$
Velocity of the jet stream	20 m/s
Impact angles	30°, 60° and 90°
Erodent discharge rate	400 cc/min
Test duration	30 min
Stand-off distance	50 mm
Water temperature	Ambient
Nozzle diameter	$\Phi$ 4 mm

test parameters are listed in Table 2. A nozzle is used to direct slurry with velocity on to the specimen. A positive displacement vane pump delivers uninterrupted flow of water, by operating the pump at different speeds. The specimen for test is placed at a distance of 50 mm from the tip of the nozzle. The specimen holder can be placed at three different angles of 30°, 60° and 90°.

### 3 Results and Discussion

The porosity and thickness of the coatings were determined from the optical microscopic image of the coating. The porosity per cent was determined by calculating the area of the pores and voids present in the coating. Figure 1 shows the optical microscopic image of the NiAl coating. The surface roughness value of the coating was determined by taking a sample length of 6 mm and a cut off distance of 0.25 mm in a surface roughness measuring apparatus. A diamond indenter was used to determine the micro-hardness and fracture values of the coating. Table 3 gives the porosity, thickness, roughness, hardness and fracture toughness values of the coatings.

**Fig. 1** Optical microscopy image of NiAl coating

**Table 3** Different properties of NiAl-coated sample and AISI304ss

S. No.	Sample	Porosity values (%)	Thickness ( $\mu\text{m}$ ) $\pm$ SD	Surface roughness, Ra value ( $\mu\text{m}$ )	Surface hardness (HV0.3) $\pm$ SD	Fracture toughness ( $\text{MPa } \sqrt{\text{m}}$ ) $\pm$ SD
1	NiAl-coated sample	3–5	234 $\pm$ 9	5.0–5.7	204 $\pm$ 15	2.05 $\pm$ 0.7
2	AISI304	–	–	3.0–5.2	129 $\pm$ 22	1.82 $\pm$ 1.2

### 3.1 Effect of Impact Angle on Erosion Rate

The experimental parameters considered are impact angle (30°, 60° and 90°), impact velocity of 20 m/s, and erodent size of 200  $\mu\text{m}$ . The graph represents that the erosion at all angles in case of coated samples is less in comparison to the AISI 304 stainless steel. The uncoated steel presented the ductile nature where the maximum erosion has taken place at low impact angle of 30° and 60°, and minimum erosion has taken place at high impact angle of 90° due to work hardening. In case of coated samples at lower impact angles of 30° and 60°, the silt particles slide the surface causing micro-cutting and ploughing action with less removal of coating material, whereas at 90° impact angle, pitting action would have been the major cause of more material removal. The graphical presentation of erosion rate with impact angles of the coated and uncoated samples is given in Fig. 2.

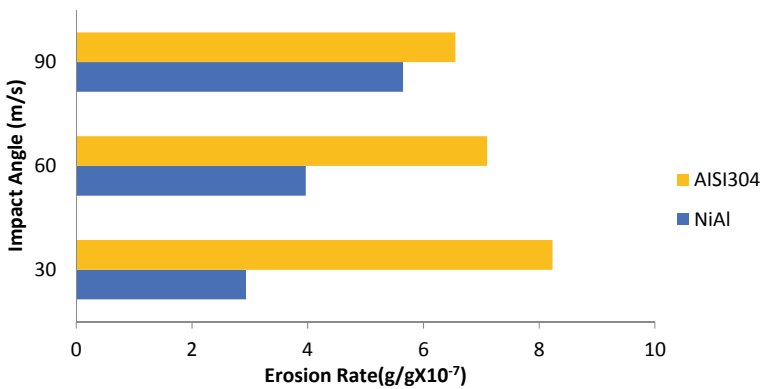


**Fig. 2** Variation of erosion rate versus impact angles with AISI304 and NiAl-coated samples after slurry jet erosion

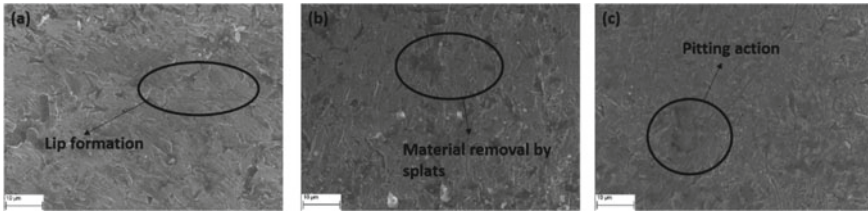


**Fig. 3** SEM photographs of NiAl-coated samples at **a** 30°, **b** 60° and **c** 90° impact angle

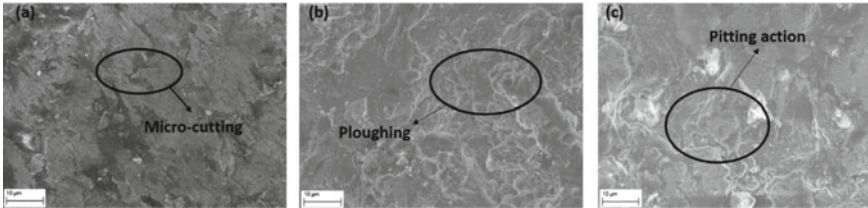


**Fig. 4** SEM photographs of uncoated samples at **a** 30°, **b** 60°, and **c** 90° impact angle

### 3.2 SEM Mechanism

The scanning electron microscopic images of the coatings were obtained, and the mechanisms of erosion were determined (Figs. 3 and 4). In case of coated samples, the erosion mechanism mostly found was material removal by lip formation, splats, and pitting action, whereas in case of uncoated samples, the erosion mechanism involved was pitting action and micro-cutting.

## 4 Conclusion

The following conclusions were drawn based on the experimental results:

- (a) The NiAl coating was successfully obtained on AISI 304 steel by using HVOF process.
- (b) The coated samples showed 3.5 times, 1.9 and 1.04 times more resistance to slurry erosion at 30°, 60° and 90° impact angle, respectively, than the uncoated bare steel.
- (c) The coated samples exhibited higher values of micro-hardness and fracture toughness than the uncoated samples.
- (d) The major erosion mechanism in both coated and uncoated samples was pitting action and micro-cutting.



## References

1. Senapati P, Sutar H (2020) Surface erosion behaviour over NiCrBSi-Al<sub>2</sub>O<sub>3</sub> composite coatings. *Mater Res Exp* 7:076512. <https://doi.org/10.1088/2053-1591/aba396>
2. Senapati P, Sutar H, Murmu R, Bajpai S (2021) Experimental design of solid particle wear behavior of Ni-based composite coatings. *J Compos Sci* 5(5):133. <https://doi.org/10.3390/jcs5050133>
3. Senapati P, Padhy M, Sahu T (2017) Coating materials and methodologies for the protection of hydro turbine runner. *Int J Mech Eng Technol (IJMET)* 8(7):524–536
4. Karaoglanli AC, Ozgurluk Y, Doleker KM (2020) Comparison of microstructure and oxidation behavior of CoNiCrAlY coatings produced by APS, SSAPS, D-gun, HVOF and CGDS techniques. *Vacuum*, 109609. <https://doi.org/10.1016/j.vacuum.2020.109609>
5. Karaoglanli AC, Caliskan H, Gok MS, Erdogan A, Turk A (2014) A comparative study of the microabrasion wear behavior of CoNiCrAlY coatings fabricated by APS, HVOF, and CGDS techniques. *Tribol Trans* 57(1):11–17. <https://doi.org/10.1080/10402004.2013.820372>
6. Khanna AS, Rathod WS (2015) Development of CoNiCrAlY oxidation resistant hard coatings using high velocity oxy fuel and cold spray techniques. *Int J Refract Metal Hard Mater* 49:374–382. <https://doi.org/10.1016/j.ijrmhm.2014.08.010>
7. Liu Y, Fischer TE, Dent A (2003) Comparison of HVOF and plasma-sprayed alumina/titania coatings—microstructure, mechanical properties and abrasion behavior. *Surf Coat Technol* 167(1):68–76. [https://doi.org/10.1016/s0257-8972\(02\)00890-3](https://doi.org/10.1016/s0257-8972(02)00890-3)
8. Sadeghimeresht E, Markocsan N, Nylén P (2016) A comparative study on Ni-based coatings prepared by HVAF, HVOF, and APS methods for corrosion protection applications. *J Therm Spray Tech* 25:1604–1616. <https://doi.org/10.1007/s11666-016-0474-9>
9. Lima RS, Marple BR (2006) From APS to HVOF spraying of conventional and nanostructured titania feedstock powders: a study on the enhancement of the mechanical properties. *Surf Coat Technol* 200(11):3428–3437. <https://doi.org/10.1016/j.surfcoat.2004.10.137>
10. Kaushal G, Bala N, Kaur N et al (2014) Comparative high-temperature corrosion behavior of Ni-20Cr coatings on T22 boiler steel produced by HVOF, D-Gun, and cold spraying. *Metall Mater Trans A* 45:395–410. <https://doi.org/10.1007/s11661-013-1984-4>

# Performance Analysis of DICI-VCR Engine Fueled with Cottonseed Biodiesel and Diesel Blends



Shubham Pangavkar, Siraj Sayyed, and Kishor Kulkarni

**Abstract** The research paper focuses on performance and emission analysis of cottonseed biodiesel and diesel blends on DICI-VCR engine. The blends of cottonseed biodiesel and diesel were prepared in proportions of 10:90, 20:80, 30:70, and 50:50. The experimentation was performed at full throttle condition by using different compression ratios of 16:1, 17:1, and 18:1. The suitability and quality of blends were tested at the preliminary stage and further experimentation conducted to assess the characteristics of DICI-VCR engine. The physiochemical properties of blends were found within the permissible limits as prescribed by ASTM standards. Results showed that highest 33.05% BTE for B30 at 16:1 CR, mechanical efficiency 73.13% at 18:1 CR for B20 blend, volumetric efficiency 76.69% observed at 16:1 CR, AFR 79.36 observed for B20 blend at 18:1 CR, and BSFC 0.84 kg/kWh observed for multiple blends in all compression ratios. Overall blend 20:80 showed optimum results at 18:1 compression ratio. The percentage errors with their permissible ASTM limits were provided.

**Keywords** Diesel · Blends · Cottonseed biodiesel · Engine performance · VCR engine

## Abbreviations

AFR	Air-fuel ratio, (ratio)
ASTM	American society for testing and material
BP	Brake power
BSFC	Brake specific fuel consumption, (kg/kWh)
BTE	Brake thermal efficiency, (%)
CO	Carbon monoxide

---

S. Pangavkar · S. Sayyed · K. Kulkarni (✉)  
Department of Mechanical Engineering, Marathwada Institute of Technology, Aurangabad, MS  
431010, India  
e-mail: [kkenergy@gmail.com](mailto:kkenergy@gmail.com)

CR	Compression ratio, (ratio)
CSO	Cottonseed oil
CSOB or CSB	Cottonseed oil biodiesel
CSOME or COME	Cottonseed oil methyl ester
D or D2	Neat diesel
GHG	Greenhouse gas
NOx	Oxides of nitrogen
VCR	Variable compression ratio

## 1 Introduction

Diesel engines are widely used in various applications such as transportations, industries, gensets, and agricultures for their low specific fuel consumptions (SFC) and efficiency [1]. Fossil fuels contribute more than 80% of the world energy needs [2]. Ever increasing prices of fossil fuels in underdevelopment country India increase the outflow of foreign currencies to search a suitable alternate fuel for fossil diesel [3]. Renewable biodiesel is easily available, environment friendly, and GHG emission reduction fuel produced from long chains of fatty acids of edible/non-edible oils and animal fats [4]. Several methods are available to produce biodiesel from crude oils, but transesterification is a most common among all. Biodiesel possesses few of the properties similar to neat diesel (D2) [5]. There are several feedstocks available in India for production of biodiesel such as *Jatropha Carcus*, *Pongamia Pinnata*, *Madhuca Indica*, and *Azadirachta Indica*. Oils from edible category are not suitable for biodiesel production due to food security, so non-edible oils are utilized [1]. Many researchers have performed experimentation to assess the characteristics of CI engine using blends of non-edible oils such as cottonseed oil (CSO) and biodiesel (CSOB). Chattopadhyay et al. [6] studied the production of cottonseed oil biodiesel (CSOB) through transesterification by using pancreatic lipase as a catalyst and concludes that 80% yield obtained with molar ratio 1:15 after 4 h at 37 °C and physiochemical properties for the blend 20:80 observed very close to petroleum diesel. Jamshaid et al. [7] optimized the tribological characteristics such as lubricity, friction coefficient, and scar diameter of wear of CSOME through response surface methodology. The study revealed that 6:1 molar ratio, 0.97% catalyst (w/w) at a temperature of 63.8 °C gave 98.3% yield. It has been concluded that CSOME 100 have lower coefficient of friction than that of other blends under considerations.

Numerous authors have assessed the performance, combustion, and emission characteristics by using blends of cottonseed oil biodiesel (CSOB) and diesel. Nabi et al. [8] performed an experimentation on diesel engine using CSO biodiesel and concluded that 77% yield obtained at 20% methanol and 0.5% NAOH. Reduction in CO, PM, and smoke emissions with the slight increase in NOx was observed. Similarly, Aydin and Bayindir [9] were tested diesel engine on various blends of CSOME and D2 diesel at full loading condition and variable speeds. The study revealed that

blend B5 and B20 showed similar results whereas increase of biodiesel in the blends reduces the emission levels. Kale and Prayagi [10] concluded that an improvement in brake and indicated thermal efficiencies was observed when engine fueled with CSO biodiesel. Dwivedi et al. [11] proved that viscosity of biodiesel was improved by using pyrogallol as an anti-oxidant and aluminum as a metal contaminants. The performance characteristics such as BTE and BSFC was increased when use of metal contaminants. Authors further extends their study by utilizing preheating, dual biodiesel/diesel mixtures, and ternary blends. Hosoz et al. [12] performed experimentation at full load condition of diesel engine fueled with preheated COME. The preheating of biodiesel utilized to lower the viscosity at various temperatures of 30, 60, 90, and 120 °C. Preheating up to 90 °C showed favorable results in BTE, BP, and CO on expense of NOx. BP decreases at 120 °C due to very low viscosity and excessive fuel supply. Sharma et al. [13] compared the performance of diesel engine fueled with the blends of mixed jatropha and cottonseed biodiesel with diesel. Vijendla et al. [14] assessed the performance characteristics of Pongamia and CSOME dual biodiesel blended CI engine and the study revealed that B10 blend showed better results as compared to neat diesel. Further study performed by using numerical analysis for BTE and BSFC. The correlations were developed by using regression analysis among BTE and BSFC versus engine torque and speed [15].

Gopal et al. [16] performed an experimentation on CSOB-ethanol blended CI engine using preheating of air. The study showed reduction in CO and HC observed with increase in NOx and the preheating also improves the ignition delay and vaporization characteristics. Agbulut et al. [17] investigate the characteristics of diesel engine on the blends of diesel-biodiesel-alcohol. The experimentation was performed at constant load and variable speeds ranging from 1750 to 3250 and concluded that the blend D90E10 showed reduction in CO and HC by 42% and 40%, respectively. NOx and CO<sub>2</sub> vary between 2 and 7%. Recently, Ninawe and Tariq [18] have performed experimental analysis on carbon nanotubes (CNT) blended CSB/diesel. The blends B10, B15, and B20 with 50 ppm CNT tested on CI engine at full throttle condition and variable loadings. The study showed that the blend B15 improves the BTE, BSFC, and reduction in CO, HC was observed as compared to blends under consideration. Recently, Siraj et al. [19] studied the performance, combustion, and emission characteristics multiple biodiesels and blends restricted to 10% biodiesels with 90% diesel and results showed that highest (46.91%) reduction in CO by D90+JB5+NB5 blend.

The present research work focuses on blends of cottonseed oil biodiesel (CSOB) to analyze the performance characteristics of DICl-VCR engine. Total five blends are considered for the experimentation by using three compression ratios (CR) 16:1, 17:1, and 18:1 at full throttle condition with varying loads ranging from 0 to 100% in a step of 25%. The comparative performance characteristics graphs are plotted against the loads for blends under considerations at different CR.

## 2 Experimental Program

The blends of cottonseed biodiesel and diesel are prepared on the basis of volume % basis and designated as 10:90 (CSOB10% and D90%) for cottonseed biodiesel 10% and diesel 90%, similarly 20:80 (CSOB20% and D80%), 30:70 (CSOB30% and D70%), and 50:50 (CSOB50% and D50%), respectively. Table 1 shows the blends of CSOB and diesel.

The physical and chemical properties are measured as per the ASTM standards. Density of biodiesel and diesel blends is measured by hydrometer as per ASTM D941 standard and similarly kinematic viscosity, flash point, cetane number, and higher heating value of blends under considerations measured by viscometer bath tub (Fenoke tube), Pensky marten closed cup apparatus, ignition quality tester, and bomb calorimeter as per ASTM D445, ASTM D93, ASTM D613, and ASTM D240 standards. Table 2 shows the characterization of cottonseed oil biodiesel (CSOB) and diesel blends.

The experimentation has been performed on single cylinder direct injection variable compression (DICI-VCR) engine test rig. At the preliminary level, the suitability and quality of CSOB and diesel blends were tested and found within the permissible limits as prescribed by ASTM standard. Further experimentation on blends under consideration is performed at variable loading conditions from 0 to 100% with a step of 25% at full throttle condition by using variable compression ratio as 16:1, 17:1, and 18:1. The test rig is computerized and the engine coupled with data acquisition

**Table 1** Blends of cottonseed biodiesel (CSOB) and diesel

Blend name	Designation	Cottonseed biodiesel (vol. %)	Diesel (vol. %)
B0	Neat Diesel	0	100
B10	10:90	10	90
B20	20:80	20	80
B30	30:70	30	70
B50	50:50	50	50

**Table 2** Characterization of CSOB blends

Physiochemical Property	Blends					Limits as per ASTM D 6751	% Errors
	B0	B10	B20	B30	B50		
Density (kg/m <sup>3</sup> )	838	843	849	854	863	–	0.5
Kinematic viscosity (mm/s <sup>2</sup> )	2.55	2.76	2.85	2.91	3.05	1.9–6.0	0.5
Flash point (°C)	51	57	66	71	82	130 min	1.0
Cetane number (No.)	50	51	52	54	57	47 min	1.0
Higher heating value (MJ/kg)	42.5	41.78	41.49	41.11	40.87	–	1.0

**Table 3** Specification of DICl-VCR engine test rig

Particulars	Specifications
Make	Kirloskar oil engines limited
Model No	TV-1
Type/ No. of strokes	Four-stroke
Aspiration	Natural
Cooling	Water-cooled
Bore: Stroke (mm)	87.5: 110
Displacement (cc)	661
Injection pressure (bar)	200
Rated power (kW)	5.2 or 7 hp
Dynamometer	Eddy current type (water cooled)
Compression ratio (CR)	12–18
Engine speed (rpm)	1500

system, computer, temperature sensors, eddy-current dynamometer, etc. The data pertaining to engine performance and combustion is recorded by the computer with the help of test rig software. The specifications of the DICl-VCR engine test rig are given in the Table 3.

### 3 Results and Discussion

Figure 1 illustrates the relation between load and brake thermal efficiency of CSOB blends at different CR. From the figure, it has been observed that BTE increases with increase in load for all the blends under considerations. This can be attributed due to

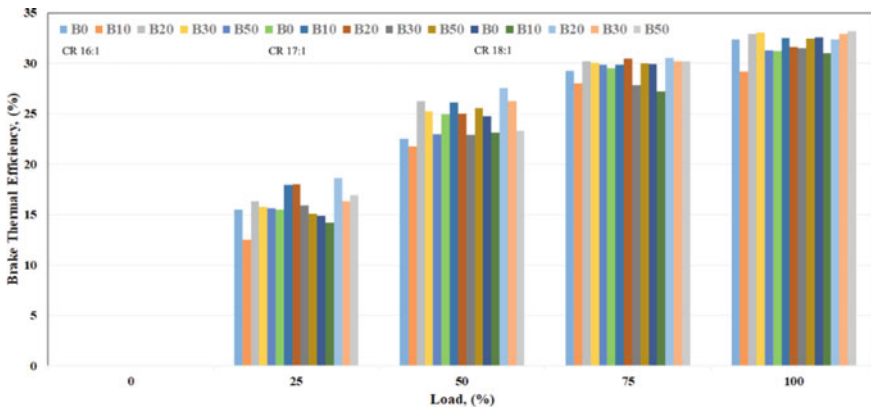


**Fig. 1** Load versus brake thermal efficiency of CSOB blends at different CR

reduction in heat loss and increase in power. The highest 33.05% and lowest 12.5% BTE observed for B30 and B10 blend at 16:1 CR in comparison with others. Overall improved results are observed for the blend B20 at 18:1 CR as compared to other blends.

Figure 2 illustrates the load versus mechanical efficiency at different CR. Mechanical efficiency is increases with increasing the load and vice-versa. This can be attributed due to rise and fall of compression ratio. Highest 73.13% and the lowest 63.74% mechanical efficiency at full throttle condition with 100% load observed for B20 and B10 blends at 18:1 CR and 16:1 CR. Mechanical efficiency varies with the range of 0 to 73.13% for all the blends under consideration.

Figure 3 illustrates the load versus air-fuel ratio (AFR) for CSOB blends at different CR. AFR decreases with increasing the load. It has been observed from the figure at 17:1 and 18:1 CR, AFR is higher as compared to 16:1 CR for all the

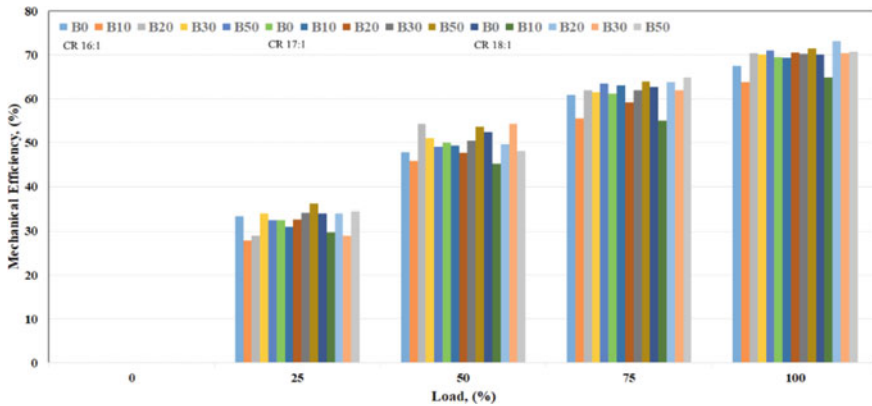


Fig. 2 Load versus mechanical efficiency of CSOB blends at different CR

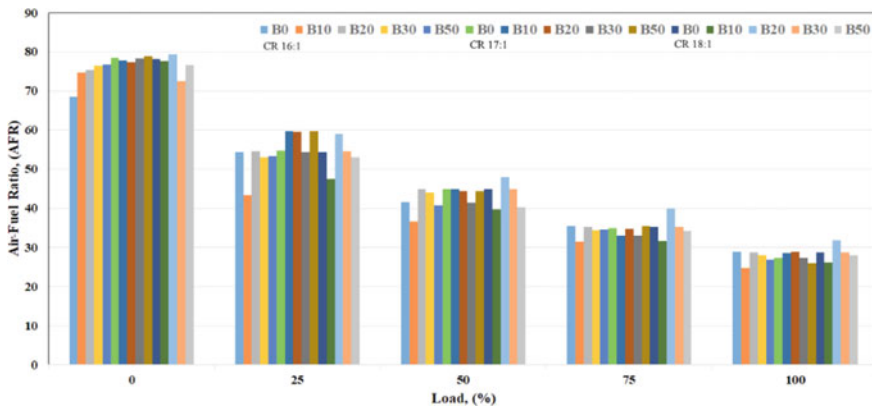


Fig. 3 Load versus air-fuel ratio of CSOB blends at different CR

blends under consideration. Highest 79.36 and the lowest 24.84 AFR observed for B20 and B10 blend at full load condition for 18:1 CR and 16:1 CR, respectively.

Figure 4 illustrates the load versus volumetric efficiency of CSOB blends at different CR. Volumetric efficiency decreases with increase in load for all the blends under consideration. In all the loading condition volumetric efficiency is slightly higher for neat diesel (B0) blend as compared to others. Highest 76.69% and the lowest 73.24% efficiency seen for the blend B0 and B10 at no load and full load conditions with 16:1 CR.

Figure 5 illustrates the load versus brake specific fuel consumption (BSFC). BSFC decreases with increase in load. This is attributed due to higher % increase in brake power with loadings as compared to BSFC. Marginal variations in BSFC observed for all the blends under conversations at different CR. Highest 0.84 kg/kWh observed

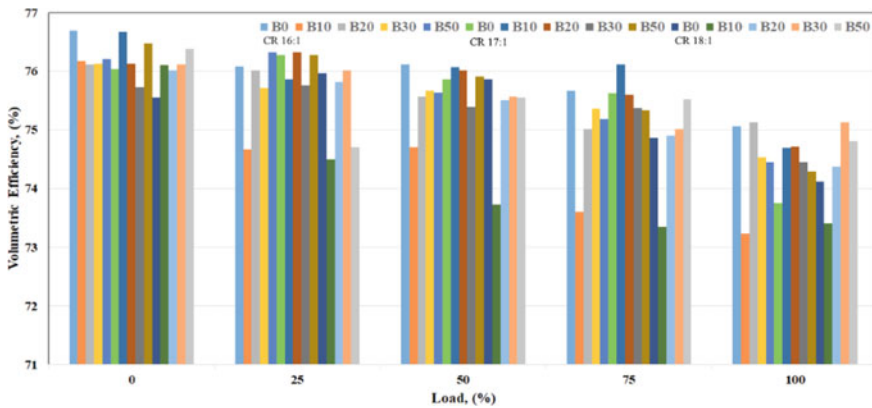


Fig. 4 Load versus volumetric efficiency of CSOB blends at different CR

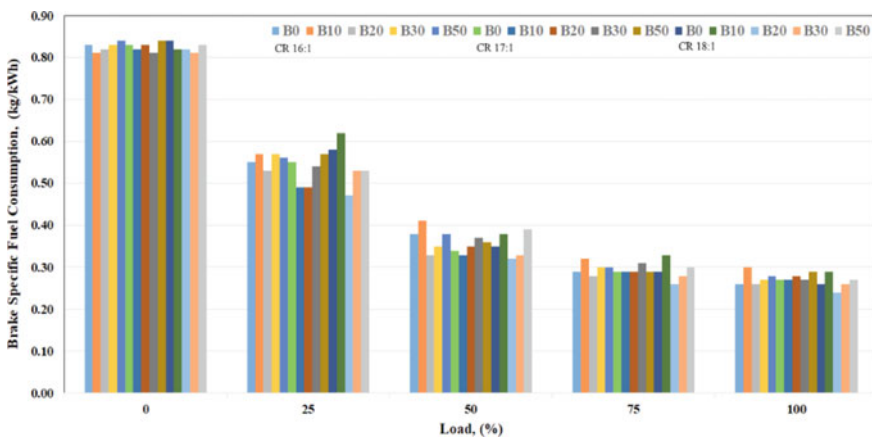


Fig. 5 Load versus brake specific fuel consumption of CSOB blends at different CR



for multiple blends in all considered CR and lowest 0.24 kg/kWh BSFC observed for B20 blend at 18:1 CR at full loading condition.

## 4 Conclusion

The experimentation on the blends of cottonseed biodiesel and diesel was performed on five different blends ranges from B0 to B50 at full throttle condition and varying loads from 0 to 100% in a step of 25%. At the preliminary stage, physiochemical properties were characterized and found with the permissible limits as prescribed by ASTM and further experimentation on DICI-VCR engine test rig perform and CI engine performance characteristics were evaluated. Overall improved results for B20 blends observed at 18:1 CR.

## References

1. Sayyed S, Das RK, Kulkarni K (2019) Experimental investigation and development of correlations for pongamia pinnata biodiesel. MATEC Web Conf 272:01009. <https://doi.org/10.1051/mateconf/201927201009>
2. Huang D, Zhou H, Lin L (2011) Biodiesel: An alternative to conventional fuel. Energy Procedia 16(PART C):1874–1885. <https://doi.org/10.1016/j.egypro.2012.01.287>
3. Tyagi SK, Kothari R, Tyagi VV (2019) Recent advances in biofuels in India. Biofuels 10(1):1–2. <https://doi.org/10.1080/17597269.2018.1532732>
4. Moser BR (2009) Biodiesel production, properties, and feedstocks. 229–266. <https://doi.org/10.1007/s11627-009-9204-z>
5. Siraj S (2017) Effects of thermal, physical, and chemical properties of biodiesel and diesel blends. Am J Mech Ind Eng 2(1):24. <https://doi.org/10.11648/j.ajmie.20170201.14>
6. Chattopadhyay S, Karemore A, Das S, Deysarkar A, Sen R (2011) Biocatalytic production of biodiesel from cottonseed oil: standardization of process parameters and comparison of fuel characteristics. Appl Energy 88(4):1251–1256. <https://doi.org/10.1016/j.apenergy.2010.10.007>
7. Jamshaid M et al (2019) Production optimization and tribological characteristics of cottonseed oil methyl ester. J Clean Prod 209:62–73. <https://doi.org/10.1016/j.jclepro.2018.10.126>
8. Nabi N, Rahman M, Akhter S (2009) Biodiesel from cotton seed oil and its effect on engine performance and exhaust emissions. Appl Therm Eng 29(11–12):2265–2270. <https://doi.org/10.1016/j.applthermaleng.2008.11.009>
9. Aydin H, Bayindir H (2010) Performance and emission analysis of cottonseed oil methyl ester in a diesel engine. Renew Energy 35(3):588–592. <https://doi.org/10.1016/j.renene.2009.08.009>
10. Kale BN, Prayagi SV (2012) Performance analysis of cottonseed oil methyl ester for compression ignition engines. 2(8):117–120
11. Puniyani K, Malik R, Kumar H, Dwivedi G (2019) Optimization of fuel properties of cottonseed biodiesel and its impact on engine performance and emission. SN Appl Sci 1(11). <https://doi.org/10.1007/s42452-019-1348-9>
12. Karabektas M, Ergen G, Hosoz M (2008) The effects of preheated cottonseed oil methyl ester on the performance and exhaust emissions of a diesel engine. Appl Therm Eng 28(17–18):2136–2143. <https://doi.org/10.1016/j.applthermaleng.2007.12.016>
13. Sharma L, Grover NK, Bhardwaj M, Kaushal I (2012) Comparison of engine performance of mixed Jatropa and cottonseed derived biodiesel blends with conventional diesel. 3(1):29–32

14. Prasad SB, Vejjendla V, Nageswara Rao, Sugumar R, Prasad KA, Ramana Murty Naidu SCV (2019) Performance analysis of dual biodiesels of pongamia and cotton seed oils and numerical analysis of BTE and BSFC. *Int J Eng Adv Technol* 8(3):672–683
15. Vejjendla SBP, Kishore KL, SNCHDV, Rao VN (2019) Experimental investigations on performance of dual biodiesels blended with diesel on VCR diesel engine experimental investigations on performance of dual biodiesels blended with diesel on VCR diesel engine. May 2016
16. Gopal KN et al (2017) Performance analysis and emissions profile of cottonseed oil biodiesel—ethanol blends in a CI engine performance analysis and emissions profile of engine. *Biofuels* 1–8. <https://doi.org/10.1080/17597269.2017.1306679>
17. Ağbulut Ü, Sarıdemir S, Albayrak S (2019) Experimental investigation of combustion, performance and emission characteristics of a diesel engine fuelled with diesel–biodiesel–alcohol blends. *J Brazilian Soc Mech Sci Eng* 41(9). <https://doi.org/10.1007/s40430-019-1891-8>
18. Ninawe G, Tariq M (2020) Impact of carbon nanotubes as additives with cotton seed biodiesel blended with diesel in Ci engine—an experimental analysis. *Nat Environ Pollut Technol* 19(1):211–219
19. Sayyed S, Das RK, Kulkarni K (2021) Experimental investigation for evaluating the performance and emission characteristics of DICl engine fuelled with dual biodiesel-diesel blends of *Jatropha*, *Karanja*, *Mahua*, and *Neem*, *Energy* 121787. <https://doi.org/10.1016/j.energy.2021.121787>

# Fuzzy Logic Investigations on Wear Analysis of P/M-Produced Aluminum Composite Through Non-lubricated Mode



Rajesh Kumar Behera, Aezeden Mohamed, Birajendu Prasad Samal, Isham Panigrahi, and Sasanka Choudhury

**Abstract** The metal matrix composites (MMCs) are most suitable replacements not only in the steel materials but also in the aluminum alloys in various automobile and aerospace systems and components. The present research fabricated novel aluminum-based MMCs which has undergone with dry sliding or non-lubricated tests to verify the wear characteristics of the composite. The study reveals the non-lubricated wear behavior of the composites at the sliding speed of 1.5 m/s and the loads of (15, 25, 35, and 45) N under normal ambient condition by using a pin-on-disk tribometer. The results shown the wear rate of the composite is much lower than that of the matrix alloy and also decreases with increasing of SiC content. Further, the experimental values have applied to fuzzy model with percentages of SiC where the applied loads were taken as inputs and the wear rate as the output. The output of the developed fuzzy model was compared with experimentally obtained results, and the deviation is declared to be within 3.0%.

---

R. K. Behera  
Biju Patnaik University of Technology, Rourkela, Odisha, India

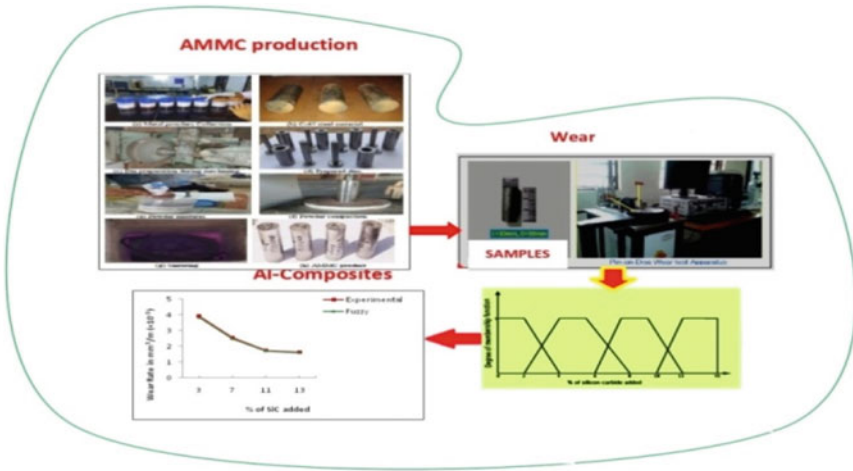
A. Mohamed  
Department of Mechanical Engineering, Papua New Guinea University of Technology, Lae, Morobe Province PMB 411, Papua New Guinea

B. P. Samal  
Department of Mechanical Engineering, Orissa Engineering College, Bhubaneswar, India

I. Panigrahi  
Programme Head Automobile Engineering, KIIT University Bhubaneswar, Bhubaneswar, Odisha, India

S. Choudhury (✉)  
Department of Mechanical Engineering, SOA Deemed to be University, Bhubaneswar 751030, India  
e-mail: [sasankachoudhury@soa.ac.in](mailto:sasankachoudhury@soa.ac.in)

### Graphic abstract



**Keywords** Aluminum-based MMC · Powder metallurgy (P/M) · Dies · Wear · Reinforcement · Fuzzy logy

## 1 Introduction

The silicon carbide (SiC) ceramics have better chemical, physical, and mechanical properties like high hardness, mechanical stability at high temperatures, excellent thermal conductivity, high resistance to heat and low coefficient of thermal expansion. This low-density ceramic is an abrasive material that has many applications including wide band gap semiconductors in high-power electronics, structural ceramics in the automotive, and aerospace industries. SiC is most widely used approach to powder synthesis called as the adhesion process. Combustion synthesis provides energy conservation methods for the production of silicon carbide powders.

Ideally, the existing structural materials should completely replace with a high-yielding material, perhaps including reinforcement. Adopting lightweight and high-performance metal matrix composites (MMCs) for the aerospace, automotive and consumer industries are difficult due to the high cost of manufacturing and its complex forms. Although there are many technical issues, powder metallurgy can be the key for solving this problem. One of the problems that directly affect the quality and properties of the composite materials is uniform distribution of reinforcement in the matrix material. Continuously, reinforced aluminum metal matrix composites are a range of materials with desirable properties such as high specific hardness, low density, high specified strength, control coefficient of thermal expansion, increased fatigue resistance, and excellent degree of stability at high temperatures [1–4]. The commonly used metal matrix composite system will consist of an aluminum alloy

which is reinforced with solid-carbide particles, such as silicon carbide (SiC) [5, 6]. These composite materials have many reinforcement mechanisms as compared to conventional or continuous-reinforced composite materials [7–10]. Numerous experimental and analytical studies have been carried out to understand the mechanical behavior and wear resistance of the composites. We are dealing with an innovative technique for analyzing the wear behavior of aluminum metal matrix composite (AMMC) products. The resulted fuzzy logic values are compared with the experimental values to calculate the wear loss [11–16]. The pin-on-disk tribometer was used to perform experiments with different loads and sliding speeds for a given time and remote design to analyze performance measurements of wear loss using this method to obtain low wears [17].

Several fuzzy rules were formulated [18–20] using experimental data and the input parameters. The fuzzy rules using input trapezoidal membership functions were mapped to obtain fuzzy results as an output function. The results show that the specific wear rate decreases with increasing loads.

## 2 Experimental Methods

In the current study, powder metallurgy (P/M) technique was adopted for production of AMMC samples. In this process, the main raw material is an aluminum matrix, which is reinforced with Si, Mg, Cu, and SiC. Composites are made using different metal powders (see Fig. 1) using different steps such as weighing, mixing/mixing, compacting, and sintering. The AMMC has been extended its strength by adding 1, 2, 5, 6, 8, 10, 12, 14, and 15% by weight of silicon carbide in the matrix element, respectively. Silicon (Si) with powder particle size 325 mesh, magnesium (Mg) with powder particle size 100 mesh, copper (Cu) with powder particle size 325 mesh, and silicon carbide (SiC) with powder particle size 325 mesh are mixed with aluminum powder with a 325 mesh particle size.

**Fig. 1** Metal powders



**Fig. 2** C-45 steel dies

The powders of the mixture were poured into a metal die (C-45 steel) as illustrated in Fig. 2 and compacted with a digital compression testing machine. The compacted green composite was recovered from the die cavity and was sintered inside a muffle-type furnace. The sintering temperature was maintained at about 620 °C, and the green samples were annealed for 24 h.

### ***2.1 Specimen Sample Preparation for the Wear Test***

The cylindrical pin samples shown in Fig. 3 are sliced to a size of 10 mm in diameter and 30 mm in length. The tests are executed for various axial loads of 15, 25, 35, and 45 N and placed the PIN (specimen) on a specific track diameter. During inspection by the experiment, the pin remains stationary, and the disk is rotated. The loads are applied by the self-loading system to press the pin against the disk. The rotational speed of motor or disk can be changed by the system controller, and the wear-test readings are recorded.

**Fig. 3** Wear test sample

## 2.2 Wear Tests

The non-lubricated or dry-sliding wear tests were carried out with a pin-on-disk tribometer (make: DUCOM) for AMMC samples. The system allows the minute identification of the wear characteristics between two components. Before an experimental test, the surfaces of spindle and disk surfaces finely polished with sand-papers with different grades so that the contact surface will smooth. All wear tests were performed with respect to ASTM G-99 standards under non-lubricated conditions at normal ambient temperature (35 °C) and 75% relative humidity. During testing, a certain area of debris usually settles on the pin. We cleaned the pin after each iteration to make sure the pin is still in direct contact with the disk. The sample weight loss after each test was calculated by calculating the sample weight in both (before and after) individual test with an electronic weighing device. Preventive measures were considered to establish that the test specimens were continuously cleaned in order to remove retaining residual wear during the experimental procedure.

## 3 Results and Discussion

The fuzzy wear behavior expert system uses a fuzzy if-then rule consists a set of initiative fuzzy rules that interpret input data and produce a crisp output. In this study, the output is significantly influenced by the input variables, which are as follows: sliding speed, sliding distance, and loads.

From Table 1, experiments with different samples of reinforced SiC were performed at constant speed and sliding distance with varying loads and obtained the above results. The variability of the wear rate with the change of the percentage of SiC content is presented in the diagram and illustrated in Fig. 4. It can be shown

**Table 1** For sliding speed of 1.5 m/s, load of 15, 25, 35, and 45 N, and sliding distance of 500 m

Exp. No.	SiC percentage, %	Wear rate, mm <sup>3</sup> /m (×10 <sup>-3</sup> )			
		Load, 15 N	Load, 25 N	Load, 35 N	Load, 45 N
1	1	5.7432	8.1356	9.3622	10.4438
2	2	4.6243	6.4612	7.5132	8.2632
3	5	3.3165	4.6278	5.4994	6.2653
4	6	2.9863	4.1618	5.0426	5.7904
5	8	2.4942	3.4124	4.0972	4.8866
6	10	2.1448	2.8621	3.4916	4.1192
7	12	1.7962	2.4323	3.0244	3.5314
8	14	1.6694	2.2427	2.7144	3.2619
9	15	1.5948	2.1792	2.6432	3.1167

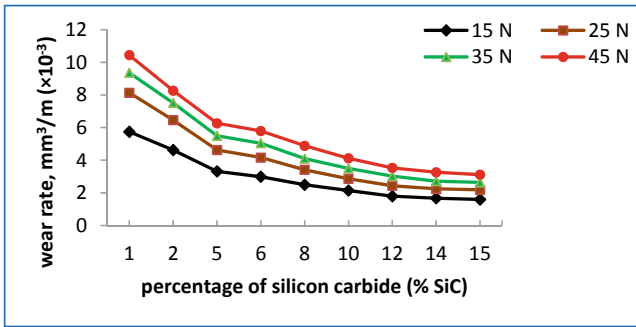


**Fig. 4** Graphical representation of experimental data representing variation of wear rate (y-axis) with the percentage of SiC (x-axis)

that the wear rate increases with reduction in percentage of SiC for any given load for a constant sliding speed of 1.5 m/s and sliding distance at 500 m.

### 3.1 Applications of Fuzzy Logic Approach to Evaluate Wear Rate of the Composites

A fuzzy approach is one of the elements of artificial intelligence, i.e., gaining popularity and is used in control systems and experimental recognition. It is based on the observation obtained from experiments on the basis of imprecise and numerical information. These models are capable of recognizing, representing, manipulating, interfering, and using data and information that are unclear and uncertain. Percentage of silicon carbide is varied at a given loads is considered as input parameters for a constant sliding speed at 1.5 m/s and of sliding distance 500 m which is to calculate the intensity of wear as output parameter in the proposed fuzzy model. The fuzzy inference system changes the crisp input data into sets of fuzzy input using trapezoidal input membership function. Fuzzification is done by mapping input data with the sets of if and then fuzzy rules to create a set of fuzzy output data. The defuzzification process is done using output trapezoidal membership function (see Fig. 5). The defuzzification process converts a set of fuzzy output into crisps values, i.e., wear rates as output parameter. Table 2 shows ‘if-then rules’ based upon experimental results.

Fuzzy logic is used to assess the wear behavior of an aluminum matrix composite. The below table shows a logical approach to the experimental results which is used to assess the wear rate. The fuzzy inference engine map shows in Fig. 6 that each element of the input fuzzy set to each rule base rule to produce the output fuzzy set. The optimization of the input parameters of the wear test on the pin-on-disk tribometer from the gray relational analysis can be used to obtain a better quality minimizing the loss of wear and the frictional force. The concept of fuzzy logic is



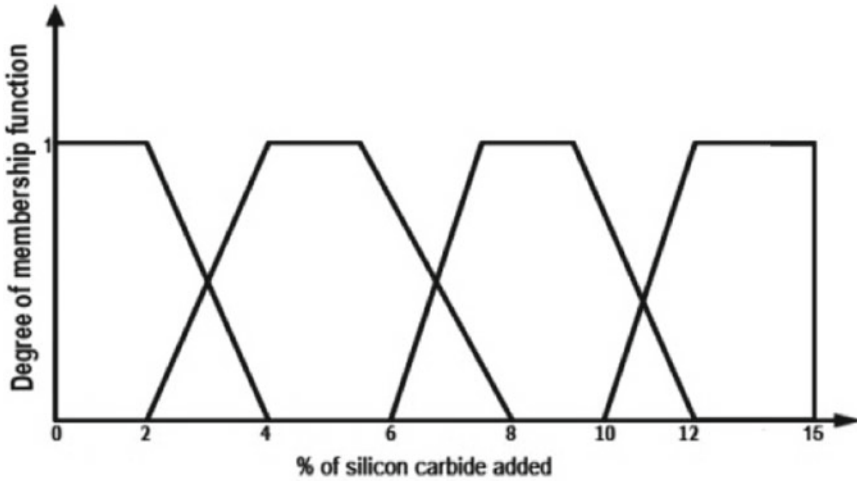


Fig. 5 Trapezoidal membership functions with input as percentage of SiC

then incorporated into this multivariate system to obtain an improved fuzzy gray score. The fuzzy inference system includes a triangular membership function, and the if-then rules have been formulated to scramble the gray relational coefficient for each note.

The major benefit of the fuzzy logic-based approach is a high quality interpretability of ‘Fuzzy If-Then’ rules. Tables 3, 4, 5 and 6 represent the percentage deviation of fuzzy results from the experimental results at different variables where the specific wear rate of the composite sample is decreasing by increasing the load from 15 to 45 N at constant sliding speed 1.5 m/s, while at a constant sliding speed, when the SiC reinforcement is increasing, specific wear rate is increasing at dry conditions.

The results of the above tables shows that when the input data are uncertain or fuzzy, the wear rate changes. When the difference between the maximum and minimum values is large, the wear rate increases or decreases considerably. It increases or decreases depending on the nature of the bevel. If the input is biased toward the maximum, wear is likely to increase, but if the input is biased toward the minimum side, it has the opposite effect. It can be seen that the proposed method can show that the wear rate will be an increased or decreased value depending on the sliding speed and the load on the axis. It can be seen that with 0% or a crisp number of fuzzy input data, the proposed method approaches the optimal value more quickly. The proposed method is very competitive in terms of the quality of the solution, minimizing the wear rate of the composite.

**Table 2** Fuzzy rules

S. No.	Rule box				
1	If, SiC = 0	V = 1.5	SD = 500	L = 15	Then, 5.7 < WR < 5.8
2				L = 25	Then, 8.1 < WR < 8.2
3				L = 35	Then, 9.3 < WR < 9.4
4				L = 45	Then, 10.4 < WR < 10.5
5	If, SiC = 2	V = 1.5	SD = 500	L = 15	Then, 4.6 < WR < 4.7
6				L = 25	Then, 6.4 < WR < 6.5
7				L = 35	Then, 7.5 < WR < 7.6
8				L = 45	Then, 8.2 < WR < 8.3
9	If, SiC = 5	V = 1.5	SD = 500	L = 15	Then, 3.3 < WR < 3.4
10				L = 25	Then, 4.6 < WR < 4.7
11				L = 35	Then, 5.4 < WR < 5.5
12				L = 45	Then, 6.2 < WR < 6.3
13	If, SiC = 6	V = 1.5	SD = 500	L = 15	Then, 2.9 < WR < 3.0
14				L = 25	Then, 4.1 < WR < 4.2
15				L = 35	Then, 5.0 < WR < 5.1
16				L = 45	Then, 5.7 < WR < 5.8
17	If, SiC = 8	V = 1.5	SD = 500	L = 15	Then, 2.4 < WR < 2.5
18				L = 25	Then, 3.4 < WR < 3.5
19				L = 35	Then, 4.0 < WR < 4.1
20				L = 45	Then, 4.8 < WR < 4.9
21	If, SiC = 10	V = 1.5	SD = 500	L = 15	Then, 2.1 < WR < 2.2
22				L = 25	Then, 2.8 < WR < 2.9
23				L = 35	Then, 3.4 < WR < 3.5
24				L = 45	Then, 4.1 < WR < 4.2
25	If, SiC = 12	V = 1.5	SD = 500	L = 15	Then, 1.7 < WR < 1.8
26				L = 25	Then, 2.4 < WR < 2.5
27				L = 35	Then, 3.0 < WR < 3.1
28				L = 45	Then, 3.5 < WR < 3.6
29	If, SiC = 14	V = 1.5	SD = 500	L = 15	Then, 1.6 < WR < 1.7
30				L = 25	Then, 2.2 < WR < 2.3
31				L = 35	Then, 2.7 < WR < 2.8
32				L = 45	Then, 3.2 < WR < 3.3
33	If, SiC = 15	V = 1.5	SD = 500	L = 15	Then, 1.5 < WR < 1.6
34				L = 25	Then, 2.1 < WR < 2.2
35				L = 35	Then, 2.6 < WR < 2.7

(continued)

**Table 2** (continued)

S. No.	Rule box				
36				$L = 45$	Then, $3.1 < WR < 3.3$

SiC (SiC reinforcement in '%'),  $V$  (speed in 'm/s'),  $L$  (load in 'N'),  $SD$  (sliding distance in 'm'),  $WR$  (wear rate in 'mm<sup>3</sup>/m' ( $\times 10^{-3}$ ))

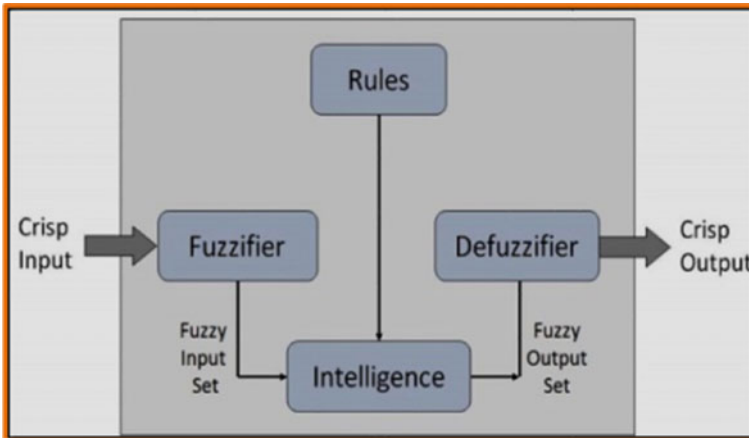


**Fig. 6** Fuzzy inference system

**Table 3** Percentage deviation of fuzzy results from the experimental results at load of 15 N, speed of 1.5 m/s, and sliding distance of 500 m

No. of trials	SiC-added percentage	Wear rates ( $\times 10^{-3}$ mm <sup>3</sup> /m)		% deviation of fuzzy output from experimental outputs
		$E$ (experimental)	$F$ (fuzzy)	$\Delta = \frac{E-F}{E} \times 100$
1	3	3.9257	3.8315	2.99
2	7	2.5328	2.4742	2.31
3	11	1.7426	1.6981	2.55
4	13	1.6122	1.5714	2.53

## 4 Conclusions

The estimated analysis of the dry-sliding wear rate of AMMC has been investigated, and the following conclusions have been drawn.

1. For a given sliding speed and sliding distance, higher the percentage of SiC higher will be the wear resistance in a metal matrix composite.
2. The fuzzy result has been compared with experimental results, and the percentage deviation does not exceed 3.0%.

**Table 4** Percentage deviation of fuzzy results from the experimental results at load of 25 N, speed of 1.5 m/s, and sliding distance of 500 m

No. of trials	SiC-added percentage	Wear rates ( $\times 10^{-3}$ mm <sup>3</sup> /m)		% deviation of fuzzy output from experimental outputs
		<i>E</i> (experimental)	<i>F</i> (fuzzy)	$\Delta = \frac{E-F}{E} \times 100$
1	3	5.6824	5.5576	2.19
2	7	3.7918	3.7131	2.07
3	11	2.5214	2.4511	2.78
4	13	1.6122	1.5713	2.53

**Table 5** Percentage deviation of fuzzy results from the experimental results at load of 35 N, speed of 1.5 m/s, and sliding distance of 500 m

No. of trials	SiC-added percentage	Wear rates ( $\times 10^{-3}$ mm <sup>3</sup> /m)		% deviation of fuzzy output from experimental outputs
		<i>E</i> (experimental)	<i>F</i> (fuzzy)	$\Delta = \frac{E-F}{E} \times 100$
1	3	6.5814	6.4707	1.68
2	7	4.1126	4.0123	2.43
3	11	3.0826	3.0044	2.53
4	13	2.7682	2.7035	2.33

**Table 6** Percentage deviation of fuzzy results from the experimental results at load of 45 N, speed of 1.5 m/s, and sliding distance of 500 m

No. of trials	SiC-added percentage	Wear rates ( $\times 10^{-3}$ mm <sup>3</sup> /m)		% deviation of fuzzy output from experimental outputs
		<i>E</i> (experimental)	<i>F</i> (fuzzy)	$\Delta = \frac{E-F}{E} \times 100$
1	3	7.3154	7.1582	2.14
2	7	5.1123	5.0111	1.97
3	11	3.8611	3.7818	2.05
4	13	3.2923	3.2086	2.54

3. The application of fuzzy rule on the matrix metal composite is found to be best suited in the application of wear analysis.
4. The proposed method is very competitive in terms of standard fuzzy solution, which minimizing the rate of wear of the new developed aluminum composite.

## References

1. Behera RK, Samal BP, Panigrahi SC et al (2020) Microstructural and mechanical analysis of sintered powdered aluminium composites. *Adv Mater Sci Eng* 2020(1893475):1–7
2. Behera RK, Samal BP, Panigrahi SC (2019) Manufacture of die and their designing parameters for sintered AMC product. *Matér Tech* 107(1–7):605
3. Behera RK, Samal BP, Panigrahi SC et al (2019) Mechanical properties and micro-structural study of sintered aluminium metal matrix composites by P/M technique. *J Mod Manuf Syst Technol* 3:089–097
4. Mazahery A, Shabani MO (2012) Study on microstructure and abrasive wear behavior of sintered Al matrix composites. *Ceram Int* 38(5):4263–4269
5. Garcla-Cordovilla C, Narciso J, Louis E (1996) Abrasive wear resistance of aluminium alloy/ceramic particulate composites. *Wear* 192(1–2):170–177
6. Ghosh S, Sahoo P, Sutradhar G (2011) Wear behaviour of Al-SiCp metal matrix composites and optimization using Taguchi method and grey relational analysis. *J Miner Mater Charact Eng* 11:1085–1094
7. Uzkut M (2013) Abrasive wear behaviour of SiCp-reinforced 2011 Al-alloy composites. *Mater Technol* 47:635–638
8. Narayan M, Surappa MK, Pramila Bai BN (1995) Dry sliding wear of Al alloy 2024-Al<sub>2</sub>O<sub>3</sub> particle metal matrix composites. *Wear* 181–183:563–567
9. Park BG, Crosky AG, Hellier AK (2001) Material characterization and mechanical properties of Al<sub>2</sub>O<sub>3</sub>-Al metal matrix composites. *J Mater Sci* 36:2417–2426
10. Prasad BK (2007) Investigation into sliding wear performance of zinc-based alloy reinforced with SiC particles in dry and lubricated conditions. *Wear* 262(3–4):262–273
11. Salguero J, Manuel J, Martinez SV, Batista ID (2018) Application of pin-on-disc techniques for the study of tribological interferences in the dry machining of A92024-T3 (Al–Cu) alloys. *Materials* 11(7):1236(1–11)
12. Zhang H, Zhang Z, Friedrich K (2007) Effect of fiber length on the wear resistance of short carbon fiber reinforced epoxy composites. *Compos Sci Technol* 67(2):222–230
13. Aruri D, Adepu K, Adepu KS et al (2013) Wear and mechanical properties of 6061-T6 aluminum alloy surface hybrid composites [(SiC + Gr) and (SiC + Al<sub>2</sub>O<sub>3</sub>)] fabricated by friction stir processing. *J Mater Res Technol* 2(4):362–369
14. Alrobei H (2020) Effect of different parameters and aging time on wear resistance and hardness of SiC-B4C reinforced AA6061 alloy. *J Mech Sci Technol* 34(5):2027–2034
15. Pradhan S, Ghosh S, Barman TK et al (2017) Tribological behavior of Al-SiC metal matrix composite under dry, aqueous and alkaline medium. *SILICON* 9(6):923–931
16. Kori SA, Chandrashekharaia TM (2007) Studies on the dry sliding wear behaviour of hypoeutectic and eutectic Al–Si alloys. *Wear* 263(1–6):745–755
17. Abdel-Kader MG (2001) Evaluating investments in advanced manufacturing technology: a fuzzy set theory approach. *Br Count Rev* 33:455–489
18. Yadav OP, Singh N, Chinnam RB, Goel PS (2003) A fuzzy logic based approach to reliability improvement estimation during product development. *Reliab Eng Syst Saf* 80:63–74
19. Daws KM, AL-Dawood ZI, AL-Kabi SH (2008) Selection of metal casting processes: a fuzzy approach. *Jordan J Mech Ind Eng* 2:45–52
20. Kannan CR, Padmanabhan P (2016) Analysis of the tool condition monitoring system using fuzzy logic and signal processing. *Circ Syst* 7:2689–2701

# Numerical Study on Hydrodynamics Analysis of Geldart B Group of Particles in a 2D Fluidized Bed Drier



Vasujeet Singh, Pruthiviraj Nemalipuri, Vivek Vitankar,  
Harish Chandra Das, Malay Kumar Pradhan, and Swaroop Jena

**Abstract** Bubbling fluidized bed boilers are the most extensive fluidized bed application in chemical industries—the CFD simulation of non-reactive two-dimensional fluidized bed drier has been carried out using the Eulerian–Eulerian two-fluid method with Geldart B group of particles, using Fluent 2020R2 software. A comparative study at three different sizes of particles (0.180, 0.280 and 0.380 mm) using Syamlal O’Brien drag models for a wide range of velocity (0.1–1 m/s) has been performed.  $k - \epsilon$  turbulence model has been used to model the turbulence and mixing inside the system. CFD. The model is validated with the existing experimental data and shows good agreement. Numerical results show that fluidized bed pressure drops increased as particle diameter increased, and further, the value of bed pressure drop increases as the superficial gas velocity increases up to the minimum fluidization velocity (0.184 m/s), beyond which there is no additional rise in bed pressure drop as the superficial gas velocity increases. It has also been noticed that disperse phase particles form clusters near the riser’s wall due to its shear effects.

**Keywords** CFD · CFBC · Boiler · Bed material

---

V. Singh · P. Nemalipuri (✉) · H. C. Das  
Department of Mechanical Engineering, National Institute of Technology Meghalaya, Shillong,  
India  
e-mail: [pruthiviraj@nitm.ac.in](mailto:pruthiviraj@nitm.ac.in)

V. Vitankar  
FluiDimensions, Pune, India

M. K. Pradhan  
Government of Odisha, OSDMA, Bhubaneswar, India

S. Jena  
Factories and Boilers, Government of Odisha, Bhubaneswar, India

## Abbreviations

$\alpha_l$	Fluid Phase Volume Fraction
$\rho_l$	Density of Fluid
$v_l$	Velocity of Fluid
$\alpha_s$	Dispersed Phase Volume Fraction
$\rho_s$	Density of Dispersed Phase
$v_s$	Velocity of Dispersed Phase
$\theta_s$	Granular Temperature
$e_{ss}$	Restitution Coefficient
$\varepsilon_s$	Bulk Viscosity
$T_s$	Particle Relaxation Time
$Re_s$	Reynolds Number
$\gamma_{\theta_s}$	Collisional Dissipation
$\rho_{sus}$	Suspension Density
$g_o$	Radial Particle Distribution Function
$P_s$	Solid Pressure
$\emptyset$	Internal Frictional Angle
$I_{2D}$	Second Invariant of Deviatorial Stress Tensor
$\theta_s$	Granular Temperature
$e_{ss}$	Restitution Coefficient
$\tau_l$	Stress Tensor for Fluid Phase
$\tau_s$	Stress Tensor for Dispersed Phase
$K_{sl}$	Fluid–Solid Exchange Coefficient
$C_d$	Drag Coefficient
$k_{\theta_s}$	Diffusion Coefficient
$\Delta h$	Difference in Water Column

## 1 Introduction

Fluidized bed driers are most widely used in the pharmaceutical and agriculture industries. Fluidization is used for the process to obtain quality grains from the paddy with minimum damage to pests [1, 2]. A comprehensive simulation study on different internment heat pump drying for moisture diffusion, energy consumption and drying time on Chinese cabbage seeds was carried out by Ebert et al. [3]. The results indicate that in intermediate drying percentage of energy-saving was 48.1% over continuous drying. The hydrodynamics and heat transfer characteristics at four different % (2.5%, 7.5%, 12.5% and 20%) mixing of biomass and sand in a pressurized circulating fluidized bed have been investigated by Kalita et al. [4, 5] at a superficial gas velocity of 6, 7, 8 m/s and system pressure of 1, 3 and 5 bar. They reported that higher pressure and higher superficial gas velocity are found favourable

for achieving a higher heat transfer coefficient. Biomass blending of 12.5% and a pressure of 5 bar are optimum to achieve a maximum wall to bed heat transfer coefficient and uniform circulation rate. Another industrial application of fluidization is fluidized bed boiler which comes into the picture in 1960s. In only two decades, it becomes the workhorse of 40–50% of power production industries due to its numerous advantages over conventional furnaces [6, 7]. In chemical industries, most of the problems are multiphase and multiphysics. More than one physical phenomenon is intermingling together, so the mathematical modelling of such problems is not straightforward [8, 9]. Two distinct approaches (Eulerian–Eulerian and Eulerian–Lagrangian) have been used to solve the multiphase flow problems. In the Eulerian–Eulerian approach, both the phases (fluid phase and dispersed particle phase) are considered as an interpenetrating continuum. In this approach, both fluid and dispersed particulate phases are being solved using a separate set of conservation equations. From the experimentation, it has been concluded that the Eulerian–Eulerian approach is suitable for high dispersed phase volume fraction (>20%) [10–12]. The second approach is Eulerian–Lagrangian approach. The fluid phase is solved using conservation equations, and the dispersed particulate phase is solved using Newtonian mechanics [13, 14]. Experiments suggest that this approach is more accurate as compared to the Eulerian–Eulerian approach and suitable for low dispersed phase volume fraction (<20%) [15]. Fluidized bed boilers have a high (<40%) solid volume fraction, so the current research problem also has been solved using the Eulerian–Eulerian approach. Kinetic theory of granular flow also has been incorporated to solve the dispersed phase collisions. Bubble formation, variation in the flow patterns, bed voidage and other hydrodynamics parameters are investigated for three different particle diameters at different gas velocity. In this current research hydrodynamic study of a 2D fluidized bed, riser has been carried out. The effect of superficial gas velocity on bed pressure drop, void fraction and solid volume fraction has been analysed for three different particle diameters (0.180, 0.280, 0.380 mm).

## 2 Computational Modelling and Boundary Conditions

CFD Simulations were performed to understand hydrodynamics in a CFB drier. The Eulerian–Eulerian multiphase model was applied to solve the multiphase flow physics of gas and granular phase. The Eulerian–Eulerian theory states that gas and dispersed phases are mathematically interpenetrating continua with each other. The kinetic theory of granular flow, which conserves the energy associated with random particle fluctuation, has been used to close solid stress terms in multiphase flow equations. The standard  $k - \epsilon$  turbulence model is used to simulate the mixing and turbulence generated inside the system. Unsteady-state simulation with a time step size of 0.001 s and 50 iterations per time step is done on a two-dimensional computational domain discretized into square cells. The governing equations are solved using the SIMPLE algorithm with a second-order discretization scheme (Table 1; Fig. 1).



**Table 1** Mathematical modelling parameters

S. No.	Modelling parameters	Value
1	Riser height	1000 mm
2	Riser width	280 mm
3	Mean particle diameter	180 $\mu\text{m}$ , 280 $\mu\text{m}$ , 380 $\mu\text{m}$
4	Particle density	4200 $\text{kg/m}^3$
5	Gas density	1.225 $\text{kg/m}^3$
6	Gas viscosity	$1.8 \times 10^{-5}$ $\text{kg/m-s}$
7	Static bed height	300 mm
8	Minimum fluidization velocity	0.1179 m/s
9	Superficial gas velocity	0.1–1 m/s
1	Restitution coefficient	0.9
2	Solid volume fraction	0.55
3	X mesh spacing	5 mm
4	Y mesh spacing	5 mm
5	Number of elements	8960
6	Number of nodes	9177
7	Multiphase model	Eulerian–Eulerian
8	Drag model	Syamlal O'brien
9	Time step size	0.001 s
10	Number of time step	8000
11	Maximum iteration per time step	50

### 3 Conservation of Mass Equations for Fluid and Dispersed Phase

$$\frac{\partial(\alpha_l \rho_l)}{\partial t} + \nabla(\alpha_l \rho_l v_l) = 0 \quad (1)$$

$$\frac{\partial(\alpha_s \rho_s)}{\partial t} + \nabla(\alpha_s \rho_s v_s) = 0 \quad (2)$$

The following is the Navier–Stokes equation for the gas phase and the particulate phase:

$$\frac{\partial(\alpha_l \rho_l v_l)}{\partial t} + \nabla(\alpha_l \rho_l v_l v_l) = -\alpha_l \nabla P + \nabla \tau_l + \alpha_l \rho_l \vec{g} + F_{\text{ext}} \quad (3)$$

$$\frac{\partial(\alpha_s \rho_s v_s)}{\partial t} + \Delta(\alpha_s \rho_s v_s v_s) = -\alpha_s \Delta P - \nabla P_s + \Delta \vec{\tau}_s + \alpha_s \rho_s \vec{g} + F_{\text{ext}} \quad (4)$$

In the Eulerian–Eulerian model, solid pressure is given below,

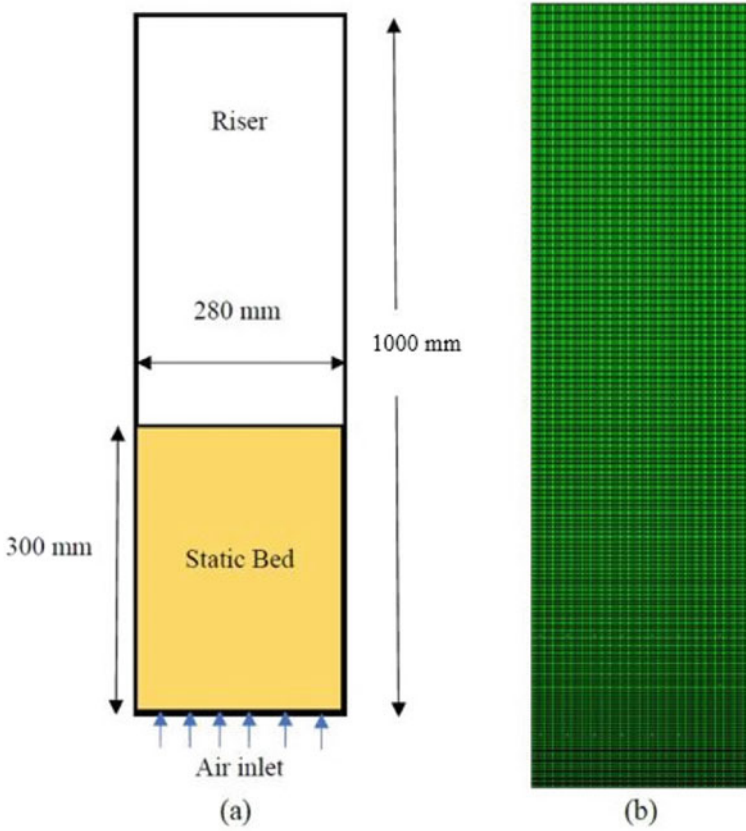


Fig. 1 a Dimension of setup. b Quadrilateral mesh used for simulation

$$P_s = \alpha_s \rho_s \theta_s + 2\rho_s(1 + e_{ss})\alpha_s^2 g_o \theta_s \tag{5}$$

$$g_o = \left[ 1 - \left( \frac{\alpha_s}{\alpha_{s_{max}}} \right)^{1/3} \right]^{-1} \tag{6}$$

Solid viscosity is defined as the sum of viscosity due to collision with other particles, viscosity due to the fluctuation in kinetic energy and viscosity due to friction.

$$\mu_{Solid} = \mu_{Collisional} + \mu_{kin} + \mu_{friction} \tag{7}$$

#### 4 Collisional Viscosity

$$\mu_{\text{Col}} = \frac{4}{5} \alpha_s \rho_s d_s g_o (1 + e_{ss}) \left( \frac{\theta_s}{\pi} \right)^{1/2} \quad (8)$$

#### 5 Viscosity Due to Fluctuation in Kinetic Energy

$$\mu_{\text{kin}} = \frac{\alpha_s d_s \rho_s \sqrt{\theta_s \pi}}{6(3 - e_{ss})} \left[ 1 + \frac{2}{5} (1 + e_{ss}) (3e_{ss} - 1) \alpha_s g_o \right] \quad (9)$$

#### 6 Frictional Viscosity

$$\mu_f = \frac{P_s \sin \emptyset}{2\sqrt{I_{2D}}} \quad (10)$$

In Navier–Stokes equation,  $\tau_l$  and  $\tau_s$  represent the stress tensor for the gas phase and the solid phase, respectively.

$$\tau_l = \alpha_l \mu_l (\nabla \vec{v}_l + \nabla \vec{v}_l^t) - \frac{2}{3} \alpha_l \mu_l (\nabla \cdot \vec{v}_l) \bar{I}_l \quad (11)$$

$$\tau_s = \alpha_s \mu_s (\nabla \vec{v}_s + \nabla \vec{v}_s^t) - \alpha_s \left( \varepsilon_s - \frac{2}{3} \mu_s \right) \cdot \vec{v}_s \quad (12)$$

In Eq. (10),  $\varepsilon_s$  is the bulk viscosity and it uses to calculate the expansion and depression resistance of the particles given by Lun et al.

$$\varepsilon_s = \frac{4}{3} \alpha_s d_s \rho_s g_o (1 + e) \left( \frac{\theta_s}{\pi} \right)^{1/2} \quad (13)$$

Syamlal O'Brien drag model has been used to simulate the drag force over the particles, Fluid–solid exchange coefficient ( $K_{sl}$ ) can be written in the following general form.

$$K_{sl} = \frac{\alpha_s \rho_s f}{T_s} \quad (14)$$

Fluid–solid exchange coefficients define by various researchers differently for different types of flow conditions. Drag factor, according to the Syamlal O'Brien drag model, is defined as:

$$f = \frac{C_d Re_s \alpha_l}{24 v_{rs}^2} \tag{15}$$

where  $C_d$  is the drag coefficient,

$$C_d = \left( 0.63 + \frac{4.8}{\sqrt{Re_s/v_{rs}}} \right)^2 \tag{16}$$

By putting the value of drag factor and the particle relaxation time,  $K_{sl}$  has the following form,

$$K_{sl} = \frac{3\alpha_s \alpha_l \rho_l}{4v_{rs}^2 d_s} C_d \left( \frac{Re_s}{v_{rs}} \right) (v_s - v_f) \tag{17}$$

$V_{rs}$  stands for relative settling velocity, which is defined as the ratio of the particle’s terminal settling velocity to the sphere’s terminal settling velocity.

Where  $V_{rs}$  is the terminal velocity,

$$v_{rs} = 0.5 \left( A - 0.06 Re_s + \sqrt{(0.06 Re_s)^2 + 0.12 Re_s (2B - A) + A^2} \right) \tag{18}$$

$$A = \alpha_l^{4.14}$$

$$B = 0.8 \alpha_l^{1.28} \text{ for } \alpha_l < 0.85$$

$$B = \alpha_l^{2.65} \text{ for } \alpha_l > 0.85.$$

## 7 Result and Discussions

To validate the mathematical model, results of bed pressure drop and bed density have been capered with the existing results of Zhao et al. [16]. Simulation results are in good agreement with the results of Zhao et al. [16] as depicted in Figs. 2, 3 and 4.

**Fig. 2** Variation of bed pressure drop with superficial gas velocity

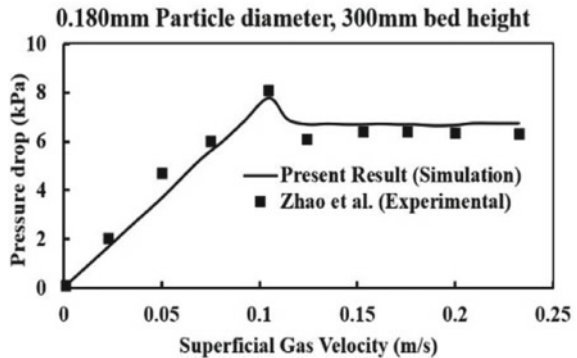


**Fig. 3** Variation of bed pressure drop with time

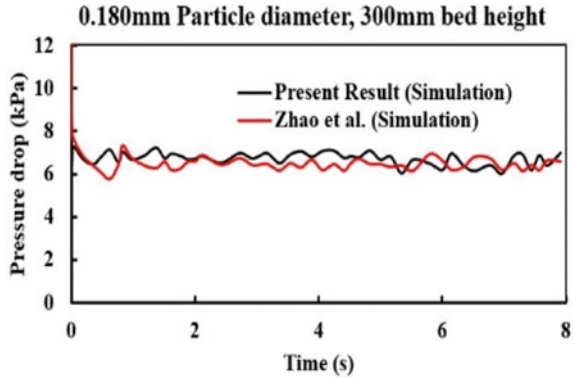
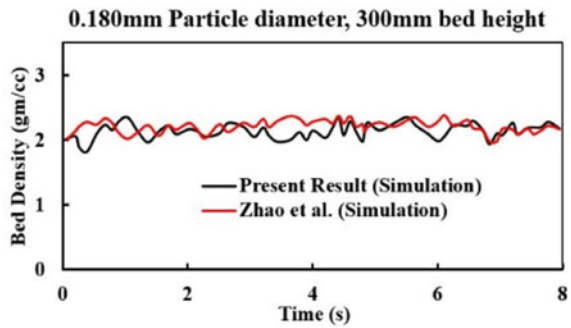


**Fig. 4** Variation of bed density with time



Bed pressure drop has been measured at three different locations (100 mm, 350 mm and 600 mm) along with the height of the riser above the distributor plate. These points have been marked as P1, P2 and P3, respectively. By measuring the pressure drop at three different locations, this method helps in comparison with the lower and upper regions of bed pressure drop. Figure 5 shows the variation of bed pressure drop (P1–P3) with simulation time on the X-axis for three different sizes

**Fig. 5** Pressure drops (P1–P3) for different sizes of particles

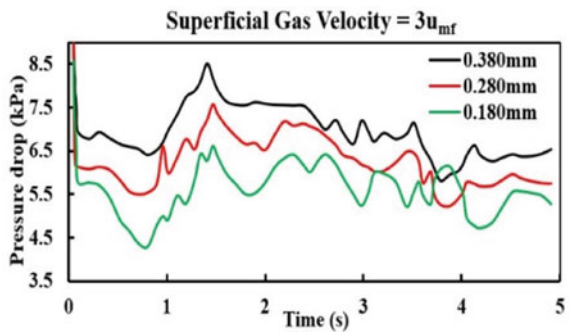
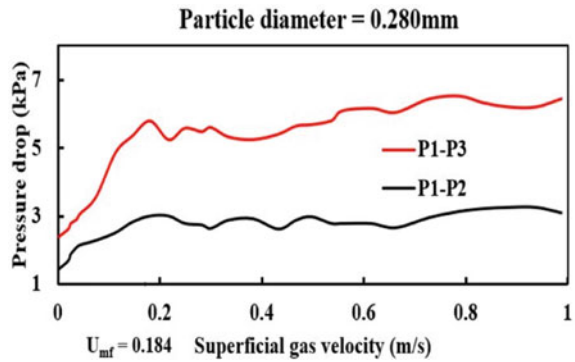


**Fig. 6** Variation of pressure drop with superficial gas velocity



of particles (0.180, 0.280 and 0.380 mm). It can be concluded from Fig. 5 that more fluctuation in bed pressure drop has been observed up to 4 s of simulation time. This is because of the mixing of intermixing of the dispersed and continuous phase, formulation of bubbles, and movement of the bubbles in an upward direction. After the 4 s, when the flow stabilizes and starts repeating a definite particulate pattern, then the curve of bed pressure drop becomes flatter. It also has been noticed for higher particle diameter.

Variation of bed pressure drop (P1–P3 and P1–P2) for a range of superficial gas velocity (0–1 m/s) at a particular size of particles (0.280 mm) has been depicted in Fig. 6. It can be noticed from Fig. 6 that the value of bed pressure drop increases up to superficial gas velocity (0.184 m/s) and, after that, attain a constant value. This is because solid particles are in contact with each other at the initial stage of fluidization and have more cohesive force between the particles, so more pressure drag is required to break this interparticle cohesive force. Once the interparticle force breaks, there is no further increment in the bed pressure drop with an increase in the superficial gas velocity. It also has been concluded that with the increase in the superficial gas velocity, the pressure drop in the upper half of the bed increases more rapidly compared to the lower half of the bed. This is because there will be a more solid volume fraction at a higher velocity at the upper half of the bed than the lower half, so there will be more pressure drop. Variation of void fraction along the height of the riser for three different diameters of the particles (0.180, 0.280 and 0.380 mm) at a constant superficial gas velocity ( $3U_{mf}$ ) has been depicted in Fig. 7. It can be observed from the graph that the void fraction curve shows an up and down trend up to a particular height inside the riser. This is due to the bubble formation and intermixing of the phases at the lower section of the riser. After that void fraction rises and attains a constant value of 1, which indicates that there are no solid particles above that height inside the riser section, by comparing the void fraction graph for different diameters of particles (0.180, 0.280 and 0.380 mm) conclusion can be made that for smaller diameter of particles there is more void fraction has been observed in the lower section of the riser. Figure 8 shows the variation of void fraction along with the height of the riser for different superficial gas velocities ( $3U_{mf}$ ,  $4U_{mf}$  and  $5U_{mf}$ )

**Fig. 7** Variation of void fraction along the height of riser for different particles size

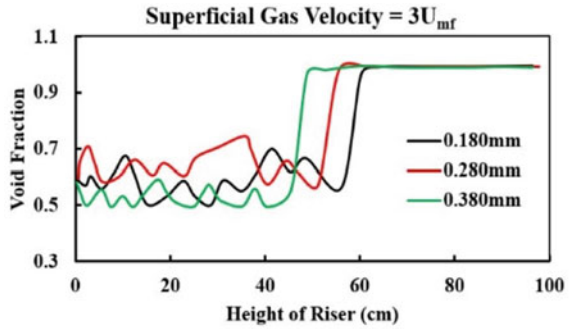
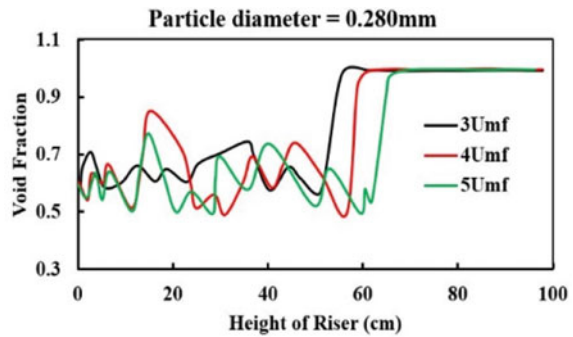
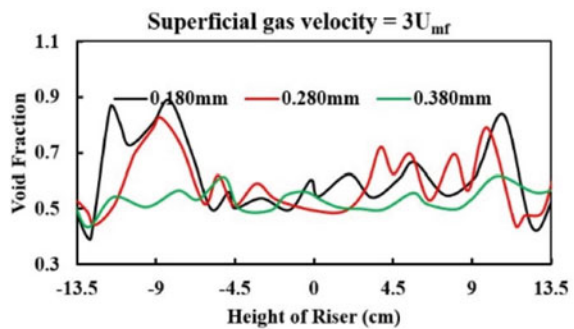


**Fig. 8** Variation of void fraction along with the height of riser for different superficial gas velocity



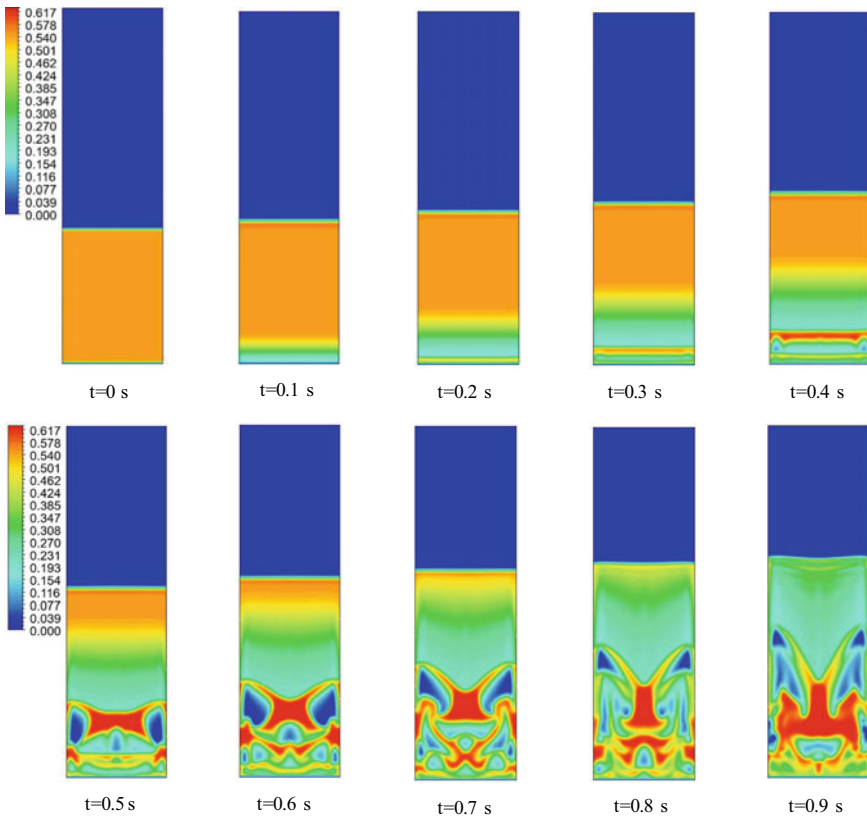
at a constant (0.280 mm) diameter of particles. From the graph, it can be noticed that void fraction curves show the up and down jump in the bottom section of the riser. This is due to the fact of intermixing and high turbulence inside the system. It can also be concluded that at higher superficial gas velocity, the void fraction curve reaches a value at a higher height. This is because dispersed phase particles get lifted to a higher height at a high superficial gas velocity. Figure 9 shows the variation of void fraction for three different diameters of particles (0.180, 0.280 and 0.380 mm) at 3U<sub>mf</sub> superficial gas velocity along the width of the riser.

**Fig. 9** Variation of void fraction along the width of riser for different particles size



### 8 Solid Volume Fraction Contours

Contours of volume fraction for dispersed phase at different time intervals are shown in figure below. At time  $t = 0$  s, all solid particles are at rest at the base of the riser; as air enters with the proceeding of time inside the riser section through the distributor plate, it applies the drag force over the particles. As a result of drag force, the bunch of particles start lifting inside the riser, lift to 0.4 s and then fall towards the base plate. Upon this, air bubble formation starts inside the riser and creates high turbulence by mixing the phases. These bubbles form at various locations in the riser, and as time proceeds, at the top surface of the fluidized bed, these bubbles blend and expand in size and rapture. The same phenomenon of lifting a bunch of particles, bubble formation and intermixing of the particles has also been observed in sawdust simulation.





## 9 Conclusions

To better design of fluidized bed boiler, a detailed hydrodynamics study is required. This hydrodynamic study will guide us for better gasification and combustion inside the fluidized bed boiler. The outcome from the detailed study is presented below:

- Using the Eulerian–Eulerian two-fluid process, hydrodynamics analysis of three distinct Geldart B groups of particles (0.180, 0.280 and 0.380 mm) was conducted within a 2D riser.
- Fluidized bed pressure drops increased as particle diameter increased; a maximum value of 7 kPa was observed with particle diameter 0.380 mm, and a minimum value of 5.5 kPa was observed with a particle diameter of 0.180 mm. With a particle diameter of 0.280 mm, a pressure drop of 6 kPa was observed.
- Based on the simulation results, the value of bed pressure drop increases as the superficial gas velocity increases up to the minimum fluidization velocity (0.184 m/s), beyond which there is no additional rise in bed pressure drop as the superficial gas velocity increases.
- By examining the void fraction curve along with the riser's height, it can be inferred that bubble forming and high phase intermixing occurred in the lower portion of the riser, which is beneficial for heat and mass transfer within the fluidized bed riser. The fluidized bed's height rises as particle diameter decreases. With 0.180 mm particle diameter, the fluidized bed height increased to 60 cm, while with 0.380 mm particle diameter, the fluidized bed height decreased to 45 cm.
- Furthermore, it has been observed that as the superficial gas velocity increases, the fluidized bed height increases. At 0.280 mm particle diameter, the highest fluidized bed height (65 cm) was observed at five times minimum fluidization velocity ( $5U_{mf}$ ). In contrast, the lowest fluidized bed height (50 cm) was observed at three times minimum fluidization velocity ( $3U_{mf}$ ).

## References

1. Hai Z, Xiuqing X (2004) Particulate concentration enrichment of primary air in pulverized coal boilers. *China Particuol* 2:230–233
2. Weinstein W, Graff RA, Meller M, Shao MJ (1983) The effect of the imposed pressure drop across a fast fluidized bed. In: Kunii D, Toei R (eds) *Fluidization, engineering foundation*. United Engineering Trustees, Inc., New York, pp 299–306
3. Ebert TA, Glicksman LR, Lints M (1993) Determination of particle and gas convective heat transfer component in circulating fluidized bed. *Chem Eng Sci* 48:2179–2188
4. Mahapatro A, Kalita P, Mahanta M, Saha UK, Mallick SS (2014) Numerical simulation of gas-solid flow in a pressurized circulating fluidized bed riser. In: *Proceedings of the 11th international conference on fluidized bed technology*, vol 11, pp 323–328
5. Kalita P, Saha UK, Mahanta P (2013) Parametric study on the hydrodynamics and heat transfer along the riser of a pressurized circulating fluidized bed unit. *Exp Thermal Fluid Sci* 44:620–630

6. Tymoteusz S, Renata K, Anna B, Wojciech M, Tomasz C, Aleksander P (2020) Advanced approach to modelling of pulverized coal boilers for SNCR process optimization-review and recommendations. *Int J Thermofluid* 224: 472–478
7. Rezwani K, Jamal N (2017) Numerical modelling of solid biomass combustion: difficulties in initiating the fixed bed combustion. *Energy Proc* 110:390–395
8. Kunii D, Levenspiel O (1991) *Fluidization engineering*, 2nd edn. Butterworth-Heinemann, Boston, MA, USA
9. Souza-Santos ML (2004) *Solid fuels combustion and gasification*. CRC Press, pp 1–431. ISBN-13: 978-1420047493
10. Ergun S, Orning AA (1949) Fluid flow through randomly packed columns and fluidized beds. *Ind Eng Chem* 41(6):1179–1184
11. Gupta AVSSKS, Nag PK (2002) Bed-to-wall heat transfer behaviour in a pressurized circulating fluidized bed. *Int J Heat Mass Transf* 45(16):3429–3436
12. Casleton DK, Shadle LJ, Ross AA (2010) Measuring the voidage of a CFB through image analysis. *Powder Technol* 203(1):12–22
13. Mahmoudi S, Baeyens J, Seville J (2011) The solids flow in the CFB-riser quantified by single radioactive particle tracking. *Powder Technol* 211(1):135–143
14. Sagegh S, Peter T, Edward J, Robin W, Ping L (2018) Scale up challenges and opportunities for carbon capture by oxy-fuel circulating fluidized beds. *Appl Energy* 232:527–542
15. Ravelli S, Perdichizzi A, Barigozzi G (2008) Description application and numerical modelling of bubbling fluidized bed combustion in waste to energy plant. *Prog Energy Combust Sci* 34:224–253
16. Zhao Y, Tang L, Luo Z, Liang C, Xing H, Wu W, Duan C (2010) Experimental and numerical simulation studies of the fluidization characteristics of a separating gas–solid fluidized bed. *Fuel Process Technol* 91:1819–1825

# Simulation of Natural Gas Combustor Using CFD



Ankur Kumar, Pruthiviraj Nimalipuri, Vasujeet Singh, Vivek Vitankar, Harish Chandra Das, Malay Kumar Pradhan, and Manoj Kumar Panda

**Abstract** The combustors are the direct-fired heaters or burners where the fuel burns in stoichiometric composition and evolves an enormous amount of heat for process heating. The natural gas combustor utilizes natural gas as fuel for the combustion process. Several designs of natural gas combustors are available for the above-said process; based on the application, the design of the combustor is determined. The current research is motivated towards the CFD simulation of natural gas combustor using Species Transport model along with different Turbulence models (Standard  $k - \epsilon$ , Realizable  $k - \epsilon$ , RNG  $k - \epsilon$ , Standard  $k - \omega$  and SST  $k - \omega$ ) and Radiation models (Discrete Ordinate (DO), P1 and Rosseland) in two different simulation tools (Ansys Fluent and Star CCM+). The flow, thermal and combustion analysis of natural gas combustor is performed with the above-mentioned combustion, radiation and turbulence models in Ansys Fluent. The results obtained from the simulation using Ansys Fluent are compared with the available experimental results of Sayre et al. (Scaling Characteristics of Aerodynamics and Low-NO<sub>x</sub> Properties of Industrial Natural Gas Burners, The SCALING 400 Study, Part IV: The 300 kW BERL Test Results. International Flame Research Foundation, The Netherlands, 1994, [1]) to validate the adopted methodology. The best-predicted turbulence and radiation model, along with the Species Transport model, is used in Star CCM+. The simulated results in both the software are compared with the experimental results and are in close agreement.

---

A. Kumar · P. Nimalipuri (✉) · V. Singh · H. C. Das  
Department of Mechanical Engineering, National Institute of Technology Meghalaya, Shillong, India  
e-mail: [pruthiviraj@nitm.ac.in](mailto:pruthiviraj@nitm.ac.in)

V. Vitankar  
FluiDimensions, Pune, India

M. K. Pradhan  
OSDMA, Government of Odisha, Bhubaneswar, India

M. K. Panda  
Factories and Boilers, Government of Odisha, Bhubaneswar, India

**Keywords** CFD · Natural gas combustor · Ansys fluent · Star CCM+

## Nomenclature and Abbreviations

$\rho$	Mass density
$P$	Pressure
$\tau$	Shear stress
$R_i$	Net production of species $i$
$G_k$	Turbulence kinetic energy generation due to mean velocity
$S_i$	Rate of creation
$\mu_t$	Turbulent viscosity
$d_t$	Turbulent diffusivity
$G_b$	Turbulence kinetic energy generation due to buoyancy
$\alpha_\varepsilon$	Inverse effective Prandtl numbers
$Sc_t$	Turbulent Schmidt number
$J_i$	Diffusion flux of species $i$
CFD	Computational fluid dynamics
DO	Discrete ordinate
RNG	Re normalized group
SST	Shear stress transport
RKE	RKEturbulence model
BERL	Burner engineering research laboratory

## 1 Introduction

A generic swirl-stabilized natural gas burner is designed on the basis of previous studies on fluid mechanics of swirling flows and flames. The natural gas burner is vertically-fired consisting of a plate at the base, octagonal “spool” sections, and a furnace hood of conical shape with an exhaust duct of cylindrical shape.

Simulations were carried out on the combustor on which the series of experiments were conducted in Burner Engineering Research Laboratory (BERL) located at Sandia National Laboratory, USA [2]. The experiments presented by Sayre et al. [1] is a part of a large project on the scaling of natural gas flames (SCALING 400 Study). It is reported that natural gas will gradually take the place of coal as essential fuel for power generation [3] and many natural gas burners have been designed [4].

Tonggnotti et al. [5] adopted an evolution of the models has been given by comparing the measurements with the temperature of the CFD field and the  $NO_x$  predictions. Chen et al. [6] focused on the Non-staged natural gas flame of a 300 kW burner. Results predict that the finite rate/eddy dissipation model produces the closest agreement with experimental data. Gomes et al. [7] found that increasing heat flux

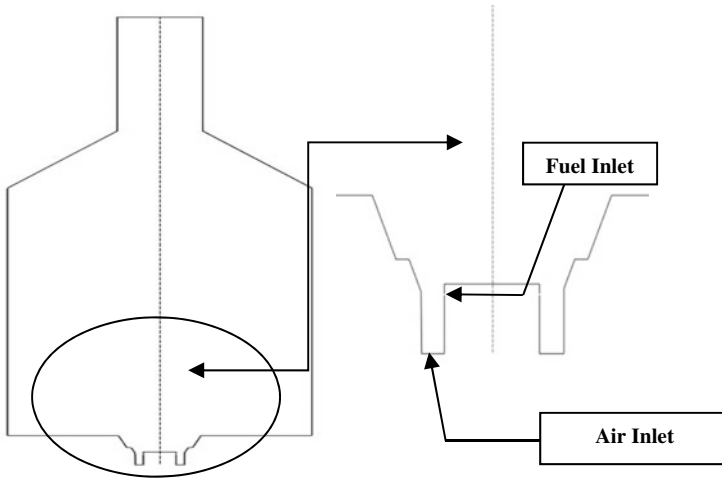


**Fig. 1** Schematic of 2D BERL combustor

and wall temperatures on the aluminium surface caused the damage due to too intense flames are obtained by the combustion process.

This research mainly focuses on analysing natural gas combustor using different turbulence models and radiation models with Eddy Dissipation Combustion Model (Fig. 1).

## 2 Mathematical Modelling and Numerical Simulation of Natural Gas Combustor (BERL)

### 2.1 Mathematical Modelling

In this current research, the two-equation turbulence are used for the analysis of the natural gas combustor.

Mass conservation equation is given by:

$$\frac{\partial \rho}{\partial t} + \nabla(\rho \vec{U}) = 0$$

Momentum conservation equation in all principal directions is given by:

$$\frac{\partial(\rho u)}{\partial t} + \nabla(\rho u \vec{u}) = -\frac{\partial \mathbb{P}}{\partial x} + \frac{\partial \tau_{xx}}{\partial x} + \frac{\partial \tau_{yx}}{\partial y} + \frac{\partial \tau_{zx}}{\partial z} + \rho f_x$$

$$\frac{\partial(\rho v)}{\partial t} + \nabla(\rho v \vec{v}) = -\frac{\partial \mathbb{P}}{\partial y} + \frac{\partial \tau_{xy}}{\partial x} + \frac{\partial \tau_{yy}}{\partial y} + \frac{\partial \tau_{zy}}{\partial z} + \rho f_y$$

$$\frac{\partial(\rho w)}{\partial t} + \nabla(\rho w \vec{w}) = -\frac{\partial \mathbb{P}}{\partial z} + \frac{\partial \tau_{xz}}{\partial x} + \frac{\partial \tau_{yz}}{\partial y} + \frac{\partial \tau_{zz}}{\partial z} + \rho f_z$$

Species Transport Equation is given by:

$$\frac{\partial}{\partial t}(\rho Y_i) + \nabla(\rho \vec{u} Y_i) = -\nabla \vec{J}_i + \underline{R}_i + S_i$$

The diffusion flux  $\vec{J}_i$  can be given as:

$$\vec{J}_i = -\left(\rho D_{i,m} + \frac{\mu_t}{Sc_t}\right) \nabla Y_i - d_{T,i} \frac{\nabla T}{T}$$

The RNG  $k - \epsilon$  model has a similar form to the standard  $k - \epsilon$  model and is given by:

$$\frac{\partial}{\partial t}(\rho k) + \frac{\partial}{\partial x_i}(\rho k u_i) = \frac{\partial}{\partial x_j} \left( \alpha_k \mu_{eff} \frac{\partial k}{\partial x_j} \right) + g_k + g_b - \rho \epsilon - Y_M + S_k$$

$$\frac{\partial}{\partial t}(\rho \epsilon) + \frac{\partial}{\partial x_i}(\rho \epsilon u_i) = \frac{\partial}{\partial x_j} \left( \alpha_\epsilon \mu_{eff} \frac{\partial \epsilon}{\partial x_j} \right) + C_{1\epsilon} \frac{\epsilon}{k} (g_k + C_{3\epsilon} g_b) - C_{2\epsilon} \rho \frac{\epsilon^2}{k} - R_\epsilon + S_\epsilon$$

## 2.2 Numerical Simulation

Numerical simulation was performed on the natural gas combustor using two CFD tools, namely, Ansys Fluent and Star CCM+. For that a step by step procedure is followed and explained below.

### A. Preprocessing

#### a. Geometry Creation

In the present work geometry is created using Ansys design modeller. Figure 2 shows the detailed geometry created in the design modeller.



**Fig. 2** Computational domain

**b. Creation of Mesh**

For the present study total of four meshes were considered for the grid-independent solution. The details of all these meshes are listed in Table 1 (Fig. 3).

**Table 1** Detail of all meshes

	Number of nodes	Number of elements	Average quality	Average skewness	Average aspect ratio
Mesh-a	37,256	35,958	0.9156	0.1056	1.1537
Mesh-b	60,481	58,698	0.9279	0.1686	1.1759
Mesh-c	81,142	79,351	0.9320	0.1261	1.1586
Mesh-d	117,499	115,159	0.9526	0.1425	1.1624

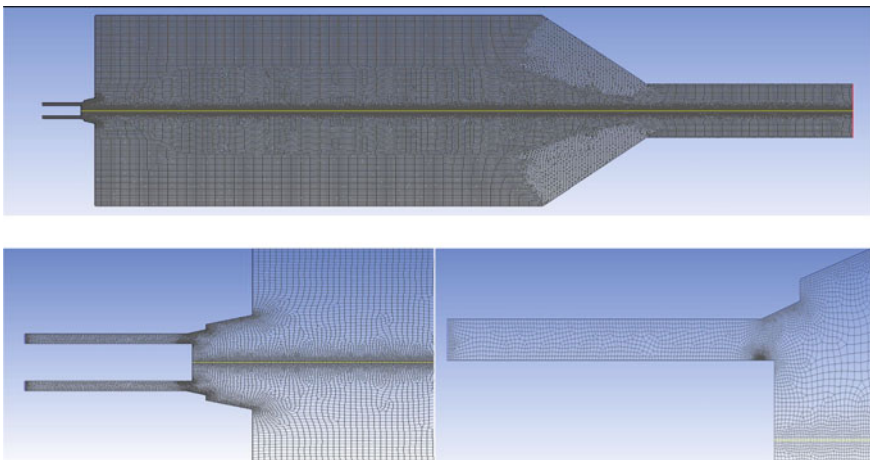


**Fig. 3** Pictorial representation of mesh-a

**Table 2** Boundary conditions at different locations

Fuel composition		Wall thermal conditions	
Species	Mole fraction	Temperature (K)	Emissivity
CH <sub>4</sub>	0.965	312	0.5
C <sub>2</sub> H <sub>6</sub>	0.017	1173	0.5
C <sub>3</sub> H <sub>8</sub>	0.001	1173	0.5
C <sub>4</sub> H <sub>10</sub>	0.001	1273	0.5
CO <sub>2</sub>	0.003	1100	0.5
N <sub>2</sub>	0.013	Profile	0.5
H <sub>2</sub> O	0.000	1305	0.5
O <sub>2</sub>	0.000	1370	0.5
Flow boundary conditions		Air inlet	Fuel inlet
V <sub>axial</sub> (m/s)		Profile	0
V <sub>Radial</sub> (m/s)		0	157.25
V <sub>Tang</sub> (m/s)		Profile	0
Temperature (K)		312	308
Turbulence intensity (%)		17	5
Hydraulic diameter (m)		0.029	0.0018

### B. Setup and Solution

For the present study, energy equation, eddy dissipation combustion model, five different turbulence models and three different radiation models were used. In Table 2, detailed information of boundary conditions is described.

### C. Post Processing

Plots and contours were generated in the CFD post. First of all a radial line is generated at the location 0.027 m from the burner throat. Then X–Y plot of different variables were generated on that line, then exported that data to an excel file and compared the results with the experimental value.

## 3 Results and Discussion

After completion of all sets of simulation, the comparison plot for temperature in the radial direction at location 0.027 m from burner throat is plotted using different turbulence and radiation models.



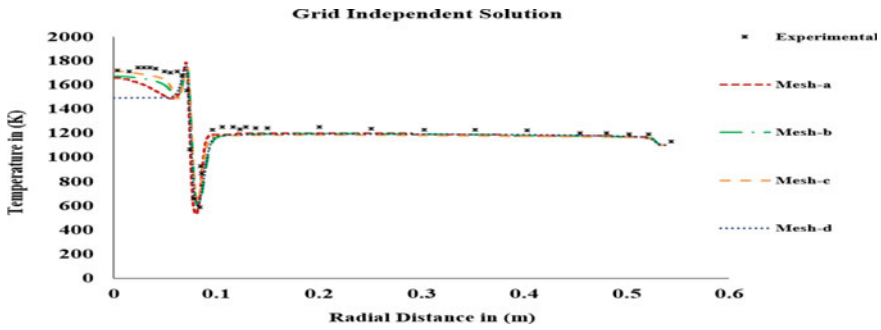


Fig. 4 Temperature variation at 0.027 m from burner throat using different meshes

### 3.1 Grid Independent Solution

From the graph plotted below, it is seen that mesh-c of yellow colour is predicting good in high temperature zone, but mesh-a of red colour is predicting more accurate to experimental data. So from Fig. 4 it is concluded that mesh-a is the best mesh for the current study; from here next all simulations were performed using the mesh-a discretized domain.

### 3.2 Comparison of Results for Different Turbulence and Radiation Models

The present study conducts a comparative analysis of five different turbulence models, three radiation models, and one combustion model with experimental data. The objective is to predict the best suitable combination of models for the simulation of natural gas combustors. Figures 5, 6, 7, 8 and 9 depicts the comparative analysis by fixing combustion and turbulence models, varying radiation models.

Figure 5 shows the temperature at 0.027 m from burner throat for the RKE turbulence model by varying three different radiation models. From the comparison, we conclude that the DO radiation model predicts closely with the experimental results. Similarly, Figs. 6, 7, 8 and 9 describes the analysis for different turbulence models by varying radiation models. By comparing all results, it is seen that the combination of RNG  $k - \epsilon$  and DO radiation model along with Specie Transport combustion model predicts well with experimental results.

Figure 10 shows the variation of temperature at 0.027 m from burner throat using DO radiation model and RNG  $k - \epsilon$  turbulence model.

Figure 11 shows the variation in axial velocity at 0.027 m from burner throat using DO radiation model and RNG  $k - \epsilon$  turbulence model and it is in good agreement with experimental results.

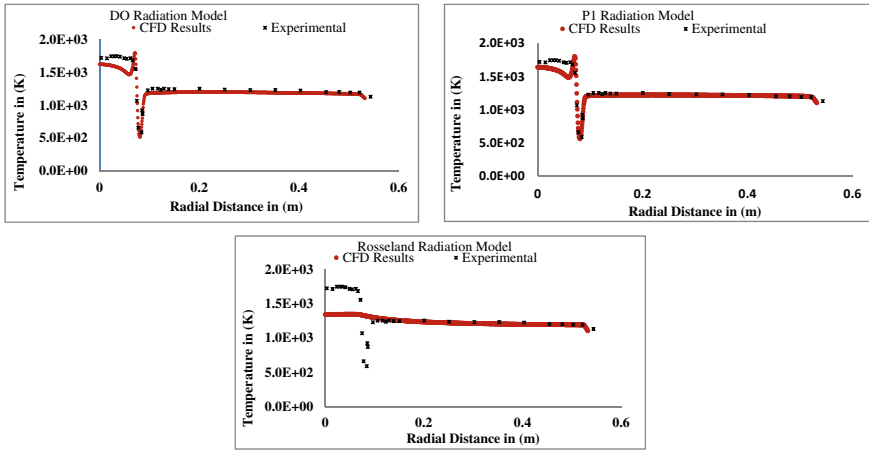


Fig. 5 Variation in temperature at 0.027 m burner throat using Realizable  $k - \epsilon$  turbulence model

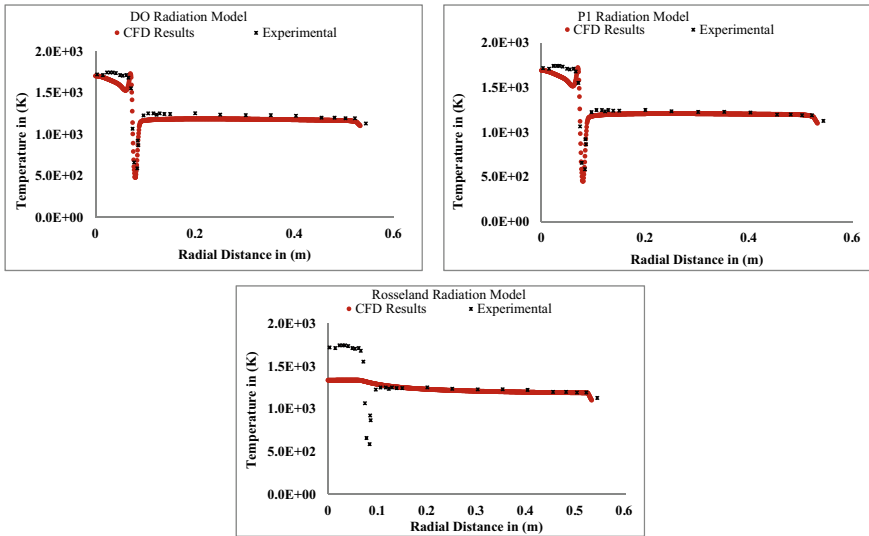


Fig. 6 Variation in temperature at 0.027 m burner throat using RNG  $k - \epsilon$  turbulence model

Figure 12 describes the variation in tangential velocity at 0.027 m from burner throat using DO radiation model and RNG  $k - \epsilon$  turbulence model and at major locations, it is in good agreement with experimental results.

Above Fig. 13 shows the temperature contour at centre plane for RNG  $k - \epsilon$  turbulence model with DOs radiation model. From above figure one can say that the flame is spreading in the direction of flow.

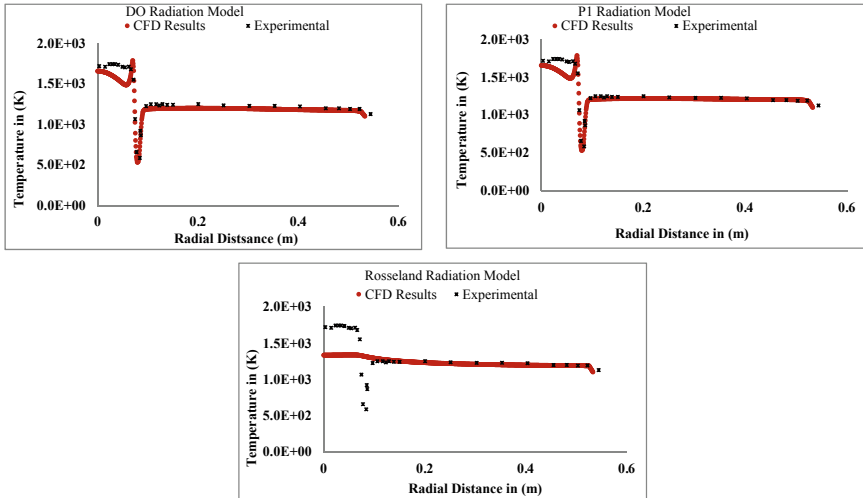


Fig. 7 Variation in temperature at 0.027 m burner throat using Standard  $k - \epsilon$  turbulence model

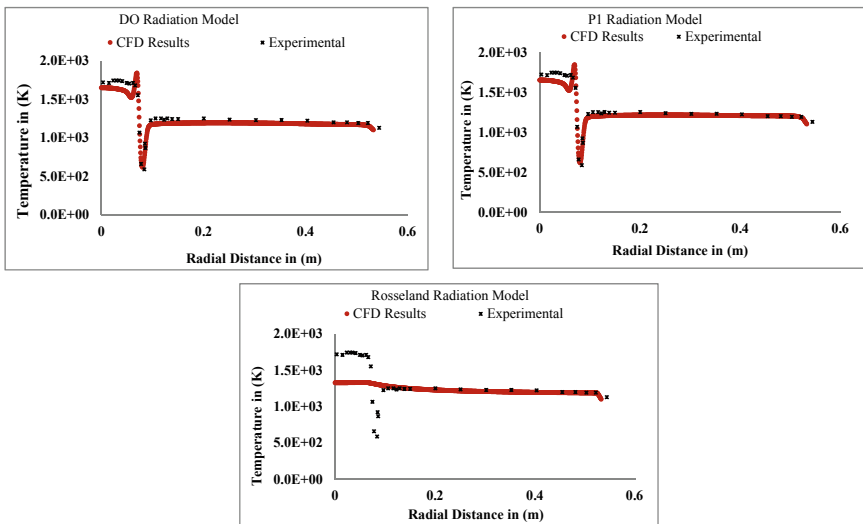


Fig. 8 Variation in temperature at 0.027 m burner throat using Standard  $k - \omega$  turbulence model

Above Fig. 14 shows the velocity contour at the centre plane using RNG  $k - \epsilon$  turbulence model with DOs radiation model. From the above figure, it is observed that the velocity is spreading in the direction of flow.

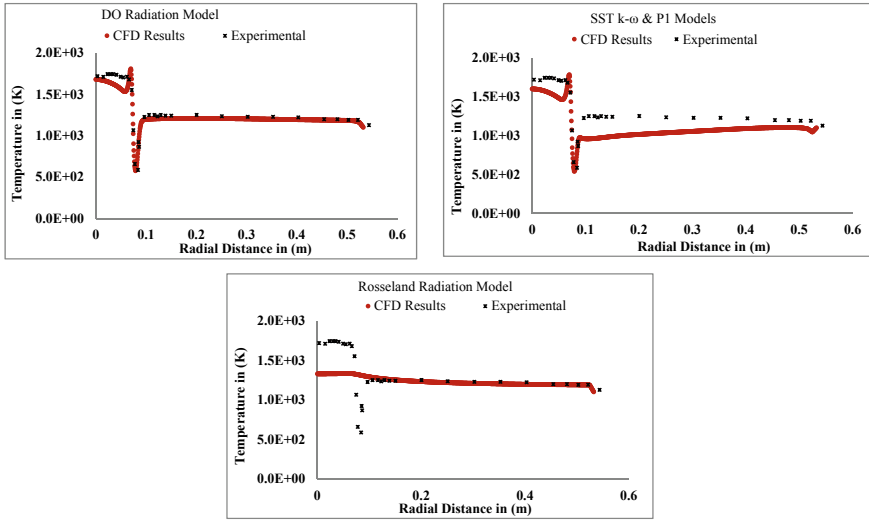


Fig. 9 Variation in temperature at 0.027 m burner throat using SST  $k - \omega$  turbulence model

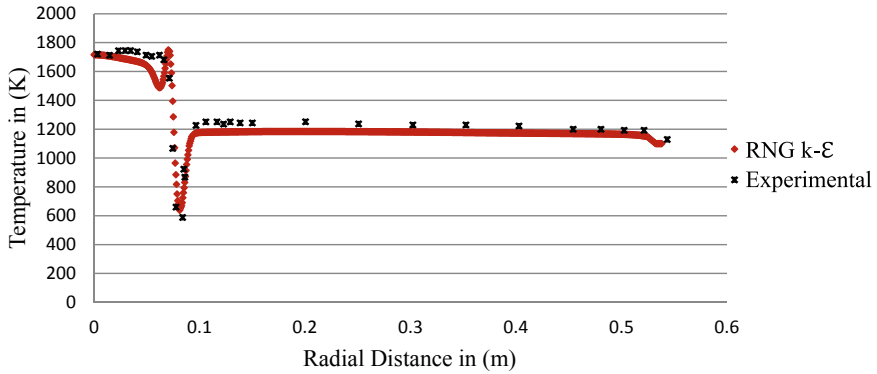
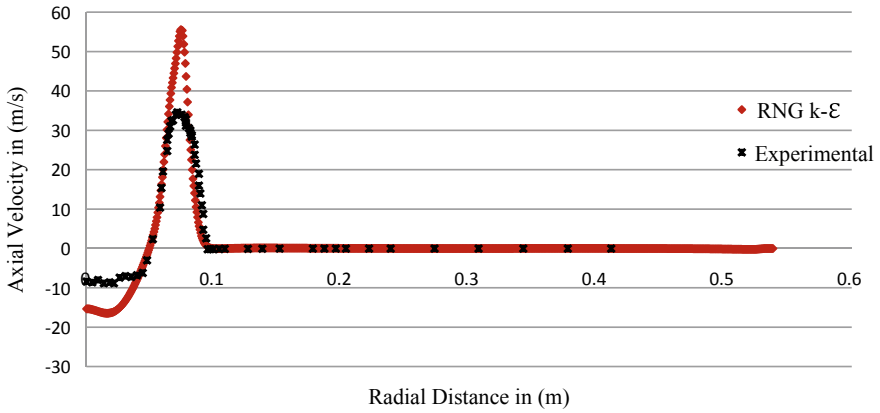


Fig. 10 Variation in temperature at 0.027 m burner throat using RNG  $k - \epsilon$  turbulence model

### 4 Star CCM+

Simcentre STAR CCM+ is a multi-physics package for the simulation of products and designs operating under real-world conditions. Uniquely, Simcentre STAR CCM+ brings automated design exploration and optimization to the simulation toolkit of every engineer, allowing us to efficiently explore the entire design space instead of focusing on single-point design scenarios.

Figure 15 shows the variation in temperature at 0.027 m from burner throat in the radial direction using Star CCM+ (Figs. 16 and 17).



**Fig. 11** Variation in axial velocity at 0.027 m burner throat using RNG  $k - \epsilon$  turbulence model

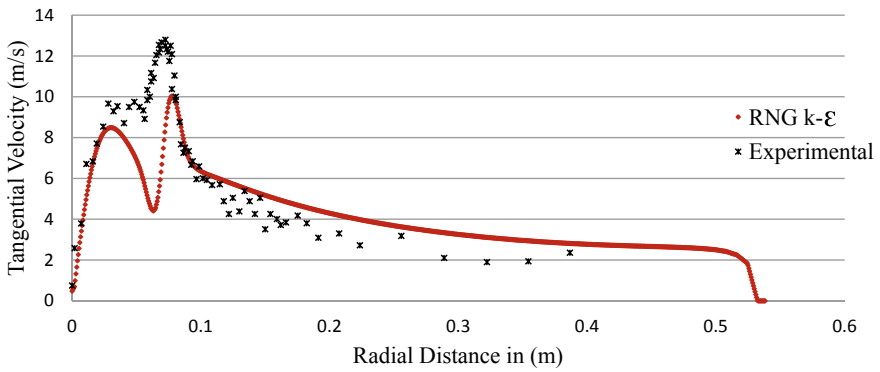


**Fig. 12** Variation in tangential velocity at 0.027 m burner throat using RNG  $k - \epsilon$  turbulence model

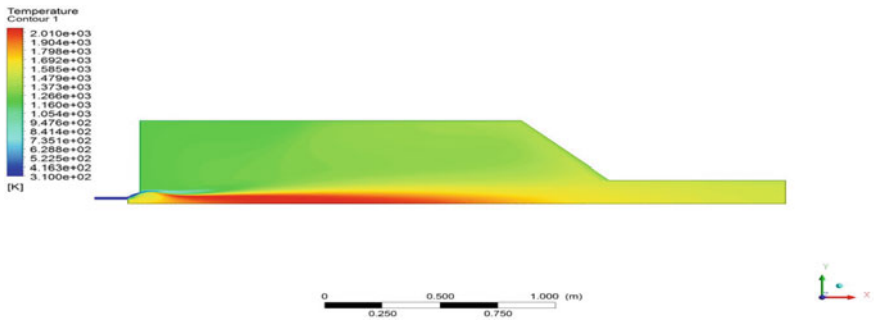


**Fig. 13** Temperature contour for RNG  $k - \epsilon$  turbulence model



Fig. 14 Velocity contour for RNG  $k - \epsilon$  turbulence model

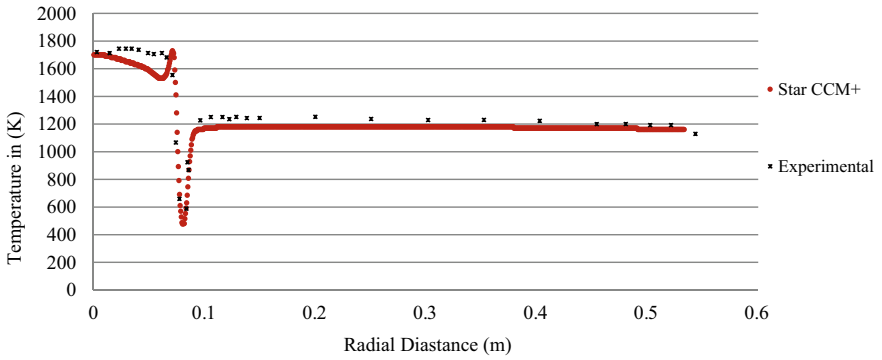


Fig. 15 Variation in temperature at 0.027 m burner throat using Star CCM+

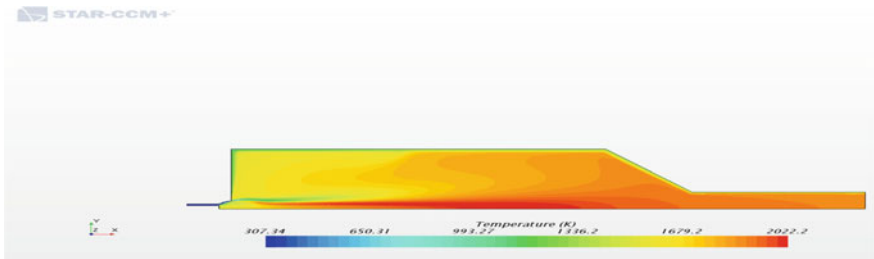


Fig. 16 Temperature contour using Star CCM+

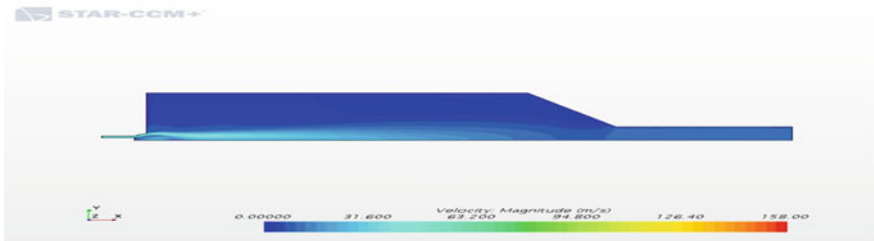


Fig. 17 Velocity contour using Star CCM+

From the above figures, it is observed that the flame is spreading in the direction of flow.

## 5 Conclusion and Future Scope

From the above results and discussion, the following conclusions are drawn:

- Species Transport combustion model is investigated with five turbulent models and three radiation models separately. The RNG  $k - \epsilon$  model with DO radiation model excellently predicts the results compared to the experimental data.
- For velocity prediction, the RNG  $k - \epsilon$  turbulence model is more suitable with Eddy Dissipation Model. But in case of axial velocity, the maximum value is showing more from experimental value and tangential velocity is showing some less from the experimental values.
- Eddy Dissipation model with DO radiation model predicts the better results in both the CFD tools and are predicting closely with experimental data.
- The predicted temperature of natural gas flame through the simulation with Ansys Fluent and STAR CCM+ is very much closer to the experimental result.

## References

1. Sayre A, Lallemand N, Dugué J, Weber R (1994) Scaling characteristics of aerodynamics and low- $\text{NO}_x$  properties of industrial natural gas burners, the SCALING 400 study, part IV: the 300 kW BERL test results. IFRP Doc No F40/y/11. International Flame Research Foundation, The Netherlands
2. Kaufman KC, Fiveland WA, Peters AAF, Weber R (1994) The BERL 300 kW un-staged natural gas flames with a swirl-stabilized burner. Case-I: hot wall conditions. GRI contract no. 5093-260-2729. Gas Research Institute
3. Pember RB, Colella P, Howell LH, Almgrea AS, Bell JB, Crutchfield WY, Beckner VE, Kufman KC, Fiveland WA, Jessee JP (1996) The modeling of a laboratory natural gas fired with a high order projection method for unsteady combustion. In: 26th international symposium on combustion University Federico II, Nables, Italy, 28th July–2 Aug 1996
4. Mason CF, Wilmot NA (2014) Jump processes in natural gas markets. *Energ Econ* 46:S69–S79
5. Tognotti L, Falcitelli M, Pasini S (2002) Modeling partial combustion systems and predicting  $\text{NO}_x$  emissions with an integrated CFD based approach. *Comput Chem Eng* 26:1171–1181
6. Chen X, Lorra M, Yeats D, Jian C (2007) A simulation study of the BERL combustor. In: 5th joint ASME/JSME fluids engineering conference, 30th July–2nd Aug 2007
7. Angela PG, Nieckele O, Naccache MF, Sebastiao M (2011) Combustion performance of an aluminium melting furnace operating with natural gas and liquid fuel. *Appl Therm Eng* 31:841–851

# Simulation of AlSi10Mg Powder for Temperature Profile by DMLS Method



Ashok Kumar Sahoo, Seshadev Sahoo, and Virendra Patel

**Abstract** In today's modern era, DMLS for additive manufacturing is advance technology to manufacture components directly from powders. It has vast advantages over conventional process like minimization of loss of material and cost-effective. The quality of the product depends on temperature profile, which is govern by laser diameter, scanning seed, laser power, hatching distance, and scanning pattern. Here, temperature profile and molten pool dimensions were investigated for ALSi10Mg in COMSOL 5.4 platform where all parameters are kept constant, while scanning speed is varied. From the investigation, it is found out that peak temperature and molten pool depth decrease as scanning speed increases.

**Keywords** Laser sintering · AlSi10Mg · Simulation · Thermal profile · DMLS

## 1 Introduction

In recent scenario, additive manufacturing plays vital role in manufacturing and production industries, which is used to manufacture complex and intricated components as per our requirement [1]. Highly accurate and precise dimensions with complex geometry can be easily produced. In DMLS, component is formed layer-by-layer manner where melting and remelting present to produce metallic and non-metallic products [2]. Here, laser with high energy source fuses the powder bed to produce good quality components in layer form [3]. The quality of the components depends on process parameter like laser diameter, laser power, hatching space, scanning speed, and layer thickness which have impact on temperature profile and molten pool dimensions [4].

Samantray et al. [1] a 3D transient thermal model of AlSi10Mg powder bed was developed in DMLS process and studied in ANSYS 17.0 to examine the effect of layer thickness and laser spot of the laser size on molten zone temperature in order to

---

A. K. Sahoo · S. Sahoo (✉) · V. Patel

Department of Mechanical Engineering, ITER Siksha 'O' Anusandhan (Deemed to be University), Bhubaneswar 751030, India

e-mail: [seshadevsahoo@soa.ac.in](mailto:seshadevsahoo@soa.ac.in)



develop a good quality product. They have found out that the molten pool temperature decreases with varying laser spot size and layer thickness. Quanquan et al. [5] the overhanging structure of AlSi10Mg was produced by changing the diameter from 5 to 30 mm and thickness of the wall by 5 mm in software. Here, part support and base support provide support to inner circle and the base part. Study was made to investigate the influence of overhang structure on product quality like distortion, roughness, and thermo-mechanical properties. Sahoo [6] a 3D numerical model is developed by finite volume method for the DMLS process for the investigation of temperature profile and molten pool variation with varying energy input and porosity percentage. It has been out that with varying above properties, the temperature profile changes that leads to product quality. Nazami et al. [2] author has developed thermo-mechanical model using ANSYS 2019 platform to study the stress produced with varying laser spot overlapping percentage for a 1D layer AlSi10Mg powder bed. It has been found out that with increase in overlapping percentage, the residual stress and principal stress in the built-in parts increase, but it is not same for the 10% overlapping. Sahoo [7] a 3D thermal model was developed and analyzed by ANSYS 2019 for a single pass and single layer. In this model, the variation in thermal stress and thermal strain has predicted with varying hatching spacing. As hatching space increases, the principal stress in product part decreases. Nandy et al. [3] studied the sintering mechanism for different sizes of AlSi10Mg powders in DMLS method using molecular dynamics. The parameters like neck growth, radius of gyration, ratio of shrinkage, and MSD with respect to time were studied. Samantaray et al. [4] a transient thermo-mechanical model of AlSi10Mg alloy was prepared by ANSYS 17.0. Here, author has studied thermal profile to find out sintering depth at varying process parameters. It is found out that with increase in laser power, the sintering depth increases. Liu et al. [8] a 3D FEM was developed to study the effect of scan speed on thermal properties in multi-layering SLM process by using ANSYS. As the laser moves from first to second layer, the pool depth and temperature increase gradually. Without multi-layer remelting, there is variation in temperature distribution and molten pool depth.

## 2 Model Description

COMSOL 5.4 is a multi-physics software which has been used to develop the thermo-mechanical model of AlSi10Mg in DMLS process. Heat transfers by finite element method (FEM) to find out the temperature profile and molten zone dimensions for the model.

Assumption taken for the FEM model is as follows:

1. The bed of AlSi10Mg powder is homogenous.
2. The laser flux is taken as Gaussian heat distribution.
3. The convective coefficient is constant.
4. The  $c$ ,  $\rho$ , and  $k$  of AlSi10Mg is temperature depended only.

The dimension of the physical model is  $10 \times 10 \times 5$  mm. The laser scans the powder bed in the  $X$ -axis direction as shown in Fig. 1; the  $Z$ -axis is the depth of the model, and  $Y$ -axis is the width of the model (Fig. 2).

The meshing of the model is broking down into two parts, the part which is in contact with the laser and plays major role in thermal cycle is very finely meshed to get accurate result, while the other part which is away from the contact is fine meshed to balance between the simulation time and result. The parameters of the meshing are given below:

1. Maximum size of the element is  $5.5 \times 10^{-5}$
2. Minimum size of the element is  $2 \times 10^{-6}$

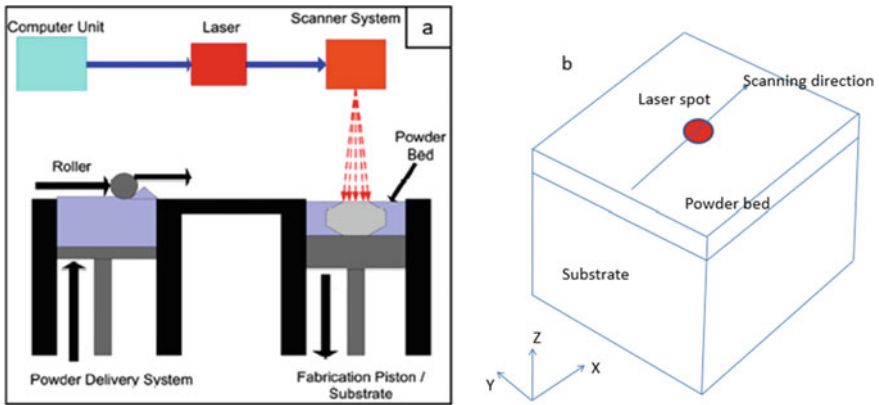


Fig. 1 a DMLS process description. b Substrate and powder in laser sintering

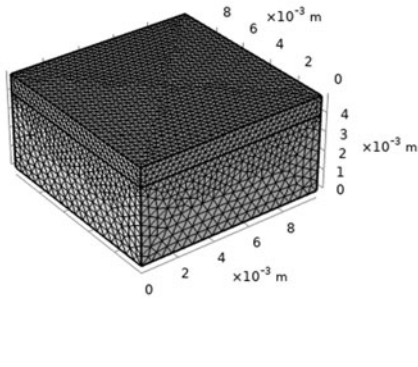
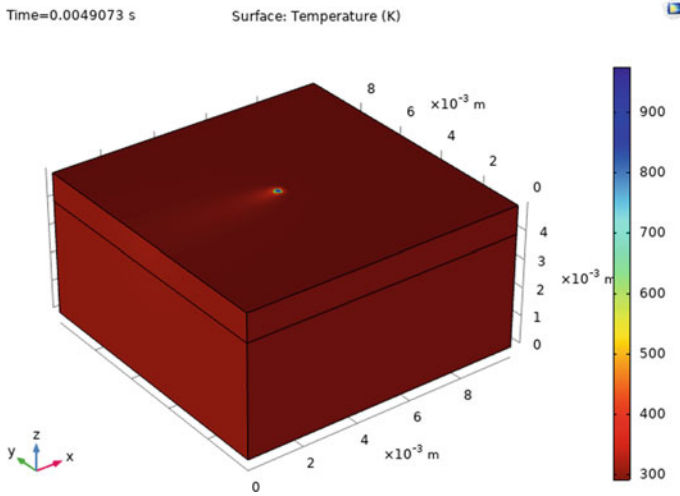


Fig. 2 Meshing of the model



**Fig. 3** Simulation progress of AlSi10Mg

3. Maximum growth of the element is 1.4
4. Curvature factor is 0.4
5. Resolution of the narrow region is 0.7 (Fig. 3).

### 2.1 Heat Profile Model

In DMLS method, the powder in the bed and the surrounding are adiabatic and closed system; the energy equation for temperature distribution as a function of time and space is given by

$$\rho c \frac{\partial T}{\partial x} = k_p \left( \frac{\partial^2 T}{\partial x^2} + \frac{\partial^2 T}{\partial y^2} + \frac{\partial^2 T}{\partial z^2} \right) + Q(x, y, z \in D)$$

where  $\rho$  (density in  $\text{Kg/m}^3$ ),  $c$  (specific heat capacity in  $\text{J/Kg } ^\circ\text{C}$ ),  $T$  (temperature in  $^\circ\text{C}$ ),  $k_p$  (thermal conductivity of the powder in  $\text{W/m } ^\circ\text{C}$ ),  $Q$  (heat generated in  $\text{J/m}^3$ ).

Before the process, the initial temperature condition of the powder and substrate is  $25\text{ }^\circ\text{C}$  and  $75\text{ }^\circ\text{C}$ , respectively, and is given by

$$T_o = T(x, y, z, t)|_{t=0},$$

The boundary conditions for the conduction, surface convection, and radiation can be written as;

$$k_p \frac{dT}{dn} = Q + Q_c + Q_r$$

where  $S$  (surface which is for heat conduction, radiation, and convection),  $n$  (normal vector of the surface),  $Q$  (input laser heat),  $Q_c$  (heat due to convection), and  $Q_r$  (heat due to radiation).

### Heat Source Model

The DMLS process of the powder, the heat flux intensity is nearly Gaussian distribution and is given by;

$$Q_s = A_1 \frac{P_w}{\pi r^2} e^{-\frac{((x-x_0-vt)^2 + (y-y_0)^2)}{r^2}}$$

where  $A_1$  (absorptivity of the powder),  $Q_s$  (Gaussian heat flux),  $P_w$  (laser power),  $x, y$  (coordinates,  $x_0, y_0$  are initial coordinates of the laser center),  $v$  (scan speed of the laser),  $t$  (time),  $r$  (radius of the laser beam).

In DMLS process, change in phase plays a vital role in thermal analysis of the model in which the enthalpy  $H$  ( $\text{J/m}^3$ ) is given by;

$$H = \int_{T_{\text{ref}}}^T \rho c \partial T$$

## 3 Result and Discussion

The thermo-mechanical model was prepared for the study of temperature profile along the scanning and depth direction. Also, the molten pool dimensions have been identified from the model in DMLS process using COMSOL 5.4. The parameters of the laser for the finite element model simulation were taken as follows:

1. Laser diameter = 0.08 mm
2. Laser power = 295 W
3. Scanning speed = 1000, 1250, 1500 mm/s.

The laser's scanning speed is varied and the effect of it seen temperature distribution in the model, and molten pool depth has effect of it (Table 1).

### 3.1 Effect of Scanning Speed

Figure 4 shows the variation of temperature with respect to time for scanning speed of 1500 mm/s. Here, it can be seen that at different point having coordinates (3, 5), (5, 5, 5), (7, 5, 5) in mm are the laser position on the surface of the model at  $Z$

**Table 1** Thermophysical properties of AlSi10Mg [1]

Temperature (°C)	20	100	200	300	400
Thermal conductivity $k$ (W/mK)	147	155	159	159	155
Specific heat capacity $c$ (J/Kg K)	739	755	797	838	922
Heat transfer coefficient $h$ (J/m <sup>2</sup> K)	80				
Density $\rho$ (Kg/m <sup>3</sup> )	2.65				
Emissivity $\epsilon$	0.3				

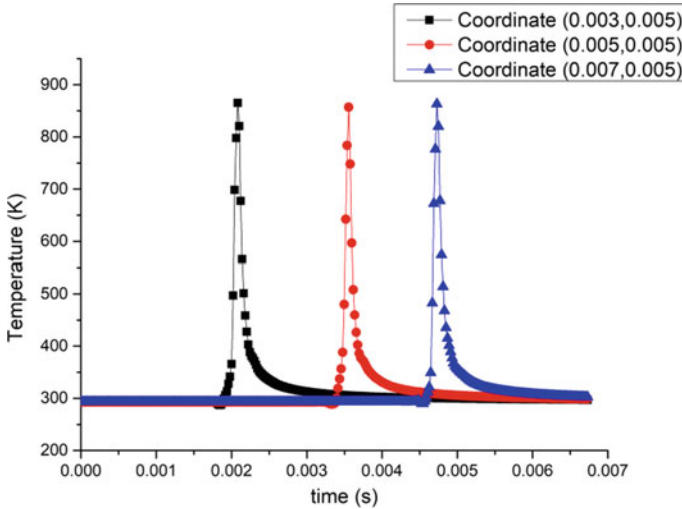


**Fig. 4** Variation of temperature with time at different points for scanning speed of 1500 mm/s

coordinate 5 mm and temperature profile at that point. The maximum temperature attained by every point is same as the heat input is uniform.

Figure 5 shows variation of temperature for different scanning speed along  $Y$ -axis. The surface of the model at coordinate (5, 5) in mm is taken as center, and the variation of temperature toward right and left of the  $Y$ -axis is shown. The temperature is maximum at the center of the laser and decreases along the  $Y$ -axis toward left and right. The maximum temperature decreases as the scanning speed increases because the heat flux input decreases which is the function of time. Also, the weld pool decreases as the scanning speed increases which depends on temperature profile.

Figure 6 shows the variation of temperature along  $Z$ -axis, i.e., depth. The peak temperature decreases as the scanning speed increases; up to 0.2 mm depth, the temperature decreases rapidly, and after that rate of decrease slows, and finally, below 0.3 mm, it becomes constant. The depth of the weld pool also decreases as the scanning speed increases due the decrease in heat flux which depends on time of contact between the laser and the surface at that time.

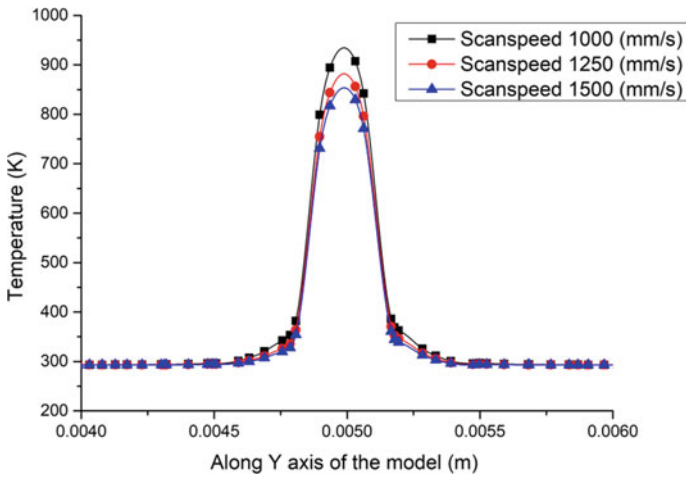


Fig. 5 Variation of temperature with surface along Y-axis for different scanning speed

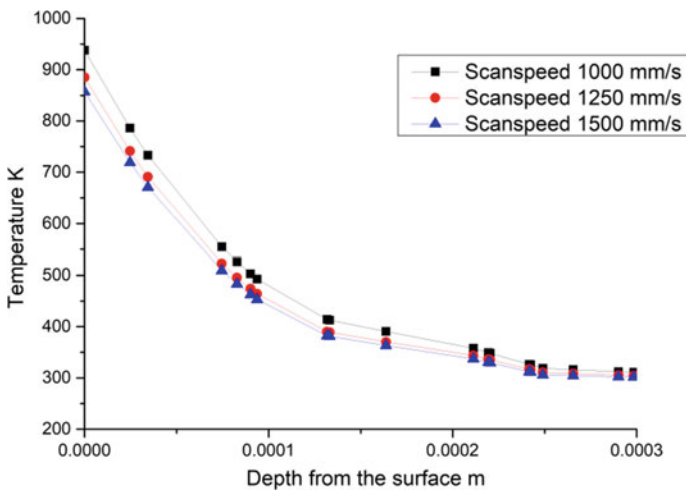


Fig. 6 Variation of temperature with depth along the Z-axis

## 4 Conclusion

The thermo-mechanical model prepared by COMSOL 5.4 for AlSi10Mg powder is studied, and temperature profile is plotted along X- and Y-axis. The temperature profile gives the dimensions of the weld pool which is linked with the quality of the product. The thermal stress depends on temperature profile and cooling rate. The following conclusions are deduced:

1. The peak temperature of the model decreases with increases in laser's scanning speed.
2. The weld pool depth and width along *Y*- and *Z*-axis decrease with the increase in laser's scanning speed.

## References

1. Samantaray M, Thatoi DN, Sahoo S (2020) Finite element simulation of heat transfer in laser additive manufacturing of AlSi10Mg powders. *Mater Today Proc* 22:3001–3008
2. Nazami GR, Panda BK, Sahoo S (2021) Finite element simulation of residual stress in direct metal laser sintering of AlSi10Mg built part: effect of laser spot overlapping. *Mater Today Proc* 41:445–450
3. Nandy J, Yedla N, Gupta P, Sarangi H, Sahoo S (2019) Sintering of AlSi10Mg particles in direct metal laser sintering process: a molecular dynamics simulation study. *Mater Chem Phys* 236:121803
4. Samantaray M, Thatoi DN, Sahoo S (2021) Modeling and optimization of process parameters for laser powder bed fusion of AlSi10Mg Alloy. *Lasers Manuf Mater Process* 6(6):1–18
5. Han Q et al (2018) Manufacturability of AlSi10Mg overhang structures fabricated by laser powder bed fusion. *Mater Des* 160:1080–1095
6. Sahoo S (2021) Direct metal laser sintering of AlSi10Mg alloy parts: modeling of temperature profile. *Mater Today Proc* 35:118–123
7. Sahoo S (2021) Prediction of residual stress and deformation of build part with variation of hatch spacing in direct metal laser sintering of AlSi10Mg built part: thermo-mechanical modelling. *J Laser Appl* 33:032011
8. Liu B, Li B-Q, Li Z, Bai P, Wang Y, Kuai Z (2019) Numerical investigation on heat transfer of multi-laser processing during selective laser melting of AlSi10Mg. *Res Phys* 12:454–459

# Multi-objective Optimization of EDM and Powder Mixed EDM for H-11 Steel



S. Tripathy  and Deba Kumar Tripathy

**Abstract** Electrical discharge machining (EDM) is a benchmark method for material removal from workpiece in aerospace, automotive, dies and mold making industries, etc. To enhance the process performance of EDM, powder mixed electrical discharge machining (PMEDM) is being expansively put to use by practitioners for improving the performance of the process while maximizing the efficiency and enhancing the quality of the surface. The present study aims at investigating the influence of “concentration of powder ( $C_p$ ), peak current ( $I_p$ ), on time of spark ( $T_{on}$ ), duty cycle (DC), and gap voltage ( $V_g$ ) on responses like rate of material removal (MRR), rate of tool wear (TWR), wear ratio of the electrode (EWR), and roughness of the surface (SR)” for EDM and PMEDM of H-11. Taguchi’s experimental design technique is used along with technique for order of preference by similarity to ideal solution (TOPSIS) followed by gray relational analysis (GRA) to estimate the performance of the process. Graphite powder of size less than  $53\ \mu\text{m}$  has been used as the additive for experiments conducted with  $L_{27}$  orthogonal array. Electrolytic copper has been taken as the tool electrode for conducting the experiments. An improvement of 0.115631 and 0.14211 in preference value is observed while conducting the confirmatory experiments with the use of TOPSIS and GRA. The optimal set of input parameters from TOPSIS is achieved at  $C_p = 6\ \text{g/l}$ ,  $I_p = 3\ \text{A}$ ,  $T_{on} = 200\ \mu\text{s}$ , DC = 80%, and  $V_g = 50\ \text{V}$  and from GRA as  $C_p = 6\ \text{g/l}$ ,  $I_p = 3\ \text{A}$ ,  $T_{on} = 150\ \mu\text{s}$ , DC = 80%, and  $V_g = 30\ \text{V}$ .

**Keywords** Electric discharge machining · PMEDM · Gray relational analysis · TOPSIS

---

S. Tripathy (✉)

Department of Mechanical Engineering, ITER, Siksha ‘O’ Anusandhan (Deemed to be University), Bhubaneswar, India

e-mail: [sasmeetatripathy@soa.ac.in](mailto:sasmeetatripathy@soa.ac.in)

D. K. Tripathy

Ex-Professor Emeritus, IIT, Kharagpur, India

© The Author(s), under exclusive license to Springer Nature Singapore Pte Ltd. 2023

P. Pradhan et al. (eds.), *Recent Advances in Mechanical Engineering*,

Lecture Notes in Mechanical Engineering,

[https://doi.org/10.1007/978-981-16-9057-0\\_74](https://doi.org/10.1007/978-981-16-9057-0_74)



## 1 Introduction

Electrical discharge machining (EDM) is used for material removal in the form of debris by the generation of high-controlled pulses in the dielectric fluid. This thermo-electric process removes material by formation of short interval discharges due to dielectric ionization with a minimal separation between electrodes. There a series of bombardment between electrons and ions which in turn increases the temperature to about 8000–12,000 °C, thus creating plasma channel in the discharge gap. PMEDM is another development to the EDM process which produces superior surfaces and homogenized white layer. Adding powders to the electrolyte decreases its insulation capacity and increases the gap between the electrodes resulting in uniform removal.

Pecas and Henriques [1] investigated on PMEDM to increase the process performance. Kansal et al. [2, 3] used Taguchi technique and response surface methods, utility concept and optimization of multiple parameters to improve process performance. Singh and Yeh [4] optimized the process parameters using gray relational analysis for aluminum matrix composites machined with SiC powder. Singh et al. [5] used aluminum powder mixed dielectric and copper tool for machining H-11 and investigated the surface roughness. Reverse polarity improves the surface quality. Talla et al. [6] and Tripathy and Tripathy [7] optimized multiple process parameters using various techniques like PCA and GRA. Senthil et al. [8] focused on multiple output responses while machining Al-CuTiB<sub>2</sub> using TOPSIS for optimization of process parameters. Sidhu et al. [9] performed tests to rank the severity of surface defects while improving the process performance.

Present investigation focuses on understanding the effect on response parameters with the variation of input parameters during PMEDM of H-11 and identifying the optimum set of parameters using GRA and TOPSIS. The study will also establish a comparison between EDM and PMEDM for achieving maximized MRR while minimizing TWR, EWR, and SR with graphite powder added to the electrolyte in varying concentrations. GRA and TOPSIS have been used to compare between the enhancements in the preference values obtained using the multi-objective optimization.

## 2 Experimental Technique

Taguchi technique has been used for the experiments in die sinking Electronica Smart ZNC EDM machine. Machining tank of 20 l capacity used is shown in Fig. 1. A pump with a stirring arrangement was mounted in the newly designed system.

Weight difference of workpiece and tool was measured prior to and after the operation to calculate the MRR and TWR. The ratio of weight of wearing out of the tool and the workpiece expressed in percentage gives the electrode wear ratio (EWR). H-11 workpiece, electrolytic copper tool, and graphite powder of less than 53 μm added to the dielectric were used for the experimental studies.

**Fig. 1** PMEDM setup



### 2.1 Experimental Design

Machining parameters and their ranges were chosen based on the pilot experiments while using Taguchi’s  $L_{27}$  orthogonal array for conducting the tests. The levels of the input parameters are taken to be powder concentration of 0, 3, and 6 gm/l, peak current at 3, 6, and 9 A, on time of pulse at 100, 150, and 200  $\mu$ s, duty cycle of 7, 8, 9 and gap voltage of 30, 40, and 50 V.

### 2.2 Multi-objective Optimization

#### 2.2.1 Topsis

TOPSIS is used to identify the most appropriate alternative. The selected criteria must be closest to the best positive solution and furthest from the best negative solution. The optimal solution is nearest to ideal solution given by the following:

Step-1 Decision matrix can be represented as

$$D_m = \begin{bmatrix} f_{11} & f_{12} & f_{13} & \cdots & f_{1n} \\ f_{21} & f_{22} & f_{23} & \cdots & f_{2n} \\ f_{31} & f_{32} & f_{33} & \cdots & f_{3n} \\ \vdots & \vdots & \vdots & \ddots & \vdots \\ \vdots & \vdots & \vdots & \ddots & \vdots \\ f_{m1} & f_{m2} & f_{m3} & \cdots & f_{mn} \end{bmatrix} \tag{1}$$

where  $f_{ij}$  is the performance of  $i$ th alternative.

Step-2 The expression to get the normalized matrix is as follows:

$$r_{ij} = \frac{f_{ij}}{\sqrt{\sum_{i=1}^m f_{ij}^2}} \quad j = 1, 2, \dots, n. \tag{2}$$

Step-3 Normalized decision matrix using weightages is given by  $K = [k_{ij}]$ :

$$K = w_j r_{ij} \tag{3}$$

where

$$\sum_{j=1}^n w_j = 1.$$

Step-4 To find the ideal solution, the following step is used:

$$K^+ = \left\{ \left( \sum_i^{\max} k_{ij} | j \in J \right), \left( \sum_i^{\min} | j \in J | i = 1, 2, \dots, m \right) \right\} \\ = \{k_1^+, k_2^+, k_3^+, \dots, k_n^+\} \tag{4}$$

$$K^- = \left\{ \left( \sum_i^{\min} k_{ij} | j \in J \right), \left( \sum_i^{\max} | j \in J | i = 1, 2, \dots, m \right) \right\} \\ = \{k_1^-, k_2^-, k_3^-, \dots, k_n^-\} \tag{5}$$

Step-5 The positive and negative separation between alternatives may be found using:

$$P_i^+ = \sqrt{\sum_{j=1}^n (k_{ij} - k_j^+)^2}, \quad i = 1, 2, \dots, m \tag{6}$$

$$P_i^- = \sqrt{\sum_{j=1}^n (k_{ij} - k_j^-)^2}, \quad i = 1, 2, \dots, m \tag{7}$$

Step-6: The closeness of the positive ideal solution to the nearest alternative is calculated by

$$s_i = \frac{P_i^-}{P_i^+ + P_i^-}, \quad i = 1, 2, \dots, m \tag{8}$$

Step-7 Alternatives with most and least preferred solutions were calculated and ranked.

### 2.2.2 Gray Relational Technique:

The performance of the process is evaluated by gray relational grade (GRG) where the maximum value represents the optimal condition [10]. The criterion followed by MRR is “higher the better:”

$$x_i(p) = \frac{y_i(p) - \min y_i(p)}{\max y_i(p) - \min y_i(p)} \quad (9)$$

TWR, EWR, and SR follow “lower the better” criteria:

$$x_i(p) = \frac{\max y_i - y_i(p)}{\max y_i(p) - \min y_i(p)} \quad (10)$$

where  $x_i(p) = \text{GRG}$ ,  $\min y_i(p) = \text{least value of } y_i(p)$ , and  $\max y_i(p) = \text{maximum value where } p = 1, 2, 3, 4$ . The GRC is calculated as

$$\xi_i(p) = \frac{\Delta_{\min} + \psi \Delta_{\max}}{\Delta_{0i}(p) + \psi \Delta_{\max}} \quad (11)$$

where “ $\Delta_{0i}(p) = |x_0(p) - x_i(p)|$ ”,  $\psi$  is the distinctive coefficient lying between  $0 \leq \psi \leq 1$ ,  $\Delta_{\min}$  is the least value for  $\Delta_{0i}$  and  $\Delta_{\max}$  is the highest value for  $\Delta_{0i}$ .” GRG is given by

$$\gamma_i = \frac{1}{n} \sum_{q=1}^n \xi_i(p) \quad (12)$$

where  $n$  is the number of response parameter.

## 3 Results and Discussion

### 3.1 Effect of Adding Powder on MRR and TWR

Adding graphite powder in 3gm/l increases the MRR and reduces the TWR. With further increase in powder concentration to 6 gm/l, the MRR increases further with less TWR and improved surfaces. The variation of MRR and TWR with powder concentration is shown in Figs. 2 and 3. The variations of output responses like

**Fig. 2**  $C_p$  versus MRR

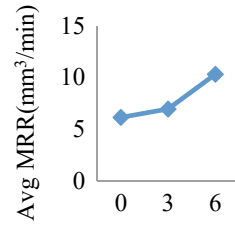
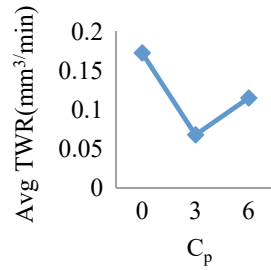


**Fig. 3**  $C_p$  versus TWR

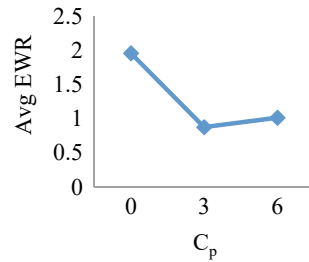


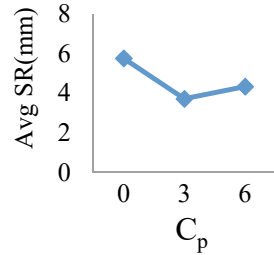
MRR and TWR with  $C_p$  indicate that as  $C_p$  rises, MRR also shows an increase and TWR decreases, but increases further with  $C_p$ .

### 3.2 *Electrode Wear Ratio*

As  $I_p$  and  $T_{on}$  increase, EWR also increases in the absence of conductive powder in the dielectric. As powder concentration increases, the EWR reduces and the variation is shown in Fig. 4.

**Fig. 4**  $C_p$  versus EWR



**Fig. 5**  $C_p$  versus SR

### 3.3 Roughness of the Machined Surface

In the absence of powder, the surface roughness increases. Additives improve the surface quality while reducing the SR as shown in Fig. 5. As the  $T_{on}$  increases, pulse intensity decreases and plasma channel diameter increases creating smoother surfaces. With the increase in pulse current, the SR increases as the large dispersive energy causes violent sparks and impulsive forces which result in the formation of well-built craters leading to the increase of SR. During flushing, the SR increases due to improper flushing. On suspending powder to the dielectric, the surface quality improves as a consequence to the reduction of SR.

### 3.4 Topsis

Equations (1)–(7) give the preference value. The preference value of the alternative has been calculated using Eq. (8). Considering the performance parameters equally important, equal weights were assigned. The maximum preference value is obtained at run #21 which is thus the optimum set followed by #20 and #19. Optimum arrangement of input parameters is found to be  $C_{p3}I_{p1}T_{on3}DC_2V_{g3}$ .

#### 3.4.1 TOPSIS Confirmatory Test

After finding the optimum arrangement of parameters, the confirmatory test is performed as shown in Table 1.

### 3.5 Gray Relational Technique

Equations (9) and (10) were used for normalization of process parameters. GRC calculated by Eq. (11) was used to calculate GRG using Eq. (12). The total mean GRG is found to be 0.6778.

**Table 1** Findings of confirmation test:

Initial set of factors		Optimum factor setting
Level	$C_{p1}I_{p1}T_{on1}DC_1V_{g1}$	$C_{p3}I_{p1}T_{on3}DC_2V_{g3}$
MRR	2.5641	8.0432
TWR	0.017228	0.0267
EWR	0.6718	0.331957
SR	3.8	3.08
Value of preferred solution	0.733579	0.84921
Ideal solution preference value = 0.115631		

### 3.5.1 Confirmation Testing

The estimated GRG,  $\hat{\gamma}$ , is calculated as

$$\hat{\gamma} = \gamma_m + \sum_{i=1}^p (\bar{\gamma} - \gamma_m) \tag{13}$$

where  $\gamma_m$  = total mean GRG,  $\gamma_i$  = mean GRG at the optimum level,  $p$  = key parameters influencing the process performance. The agreement of optimal machining parameters and assessed parameters is presented in Table 2 which agrees well with each other.

From Table 2, it can be observed that the MRR varies within 7.18–9.21 mm<sup>3</sup>/min. TWR decreases from 0.0418 to 0.0221 mm<sup>3</sup>/min. The EWR and SR subsequently vary within 0.5821% to 0.2399% and 3.32 μm to 1.99 μm, respectively. An enhancement of 0.14211 is prominent in GRG after justification. Table 3 gives the confirmation test results using TOPSIS and GRA along with the improvement.

**Table 2** Confirmation test findings

Initial set of factors		Optimum factor setting	
		Predicted	Experimental
Level	$C_{p2}I_{p2}T_{on2}DC_2V_{g2}$	$C_{p3}I_{p1}T_{on2}DC_2V_{g1}$	$C_{p3}I_{p1}T_{on2}DC_2V_{g1}$
MRR	7.18		9.21
TWR	0.0418		0.0221
EWR	0.5821		0.2399
SR	3.32		1.99
Gray relational grade	0.749087		0.884
Improvement of GRG = 0.14211			

**Table 3** Significant process parameters at their optimized level and relative error estimation

Technique	Set of optimum parameters	Enhancement in preferred grades
TOPSIS	$C_{p3}I_{p1}T_{on3}DC_2V_{g3}$	0.115631
Gray relational analysis	$C_{p3}I_{p1}T_{on2}DC_2V_{g1}$	0.14211

## 4 Conclusion

The machining of H-11 workpiece using graphite powder added dielectric and copper tool has been performed. The major conclusions from the study are

1. Addition of conductive powders improves the surface quality and causes uniform material removal while producing fewer cracks.
2. The optimal process parameter set is found to be  $C_p = 6 \text{ g/l}$ ,  $I_p = 3 \text{ A}$ ,  $T_{on} = 200 \text{ } \mu\text{s}$ ,  $DC = 80\%$ , and  $V_g = 50 \text{ V}$  from TOPSIS and  $C_p = 6 \text{ g/l}$ ,  $I_p = 3 \text{ A}$ ,  $T_{on} = 150 \text{ } \mu\text{s}$ ,  $DC = 80\%$ , and  $V_g = 30 \text{ V}$  from GRA.
3. Improvement in the preferred values is 0.115631 and 0.14211 obtained from confirmatory tests with TOPSIS and GRA.
4. SR increases with increase in other parameters without powder added dielectric.

## References

1. Pecas P, Henriques E (2008) Electrical discharge machining using simple and powder mixed dielectric: the effect of the electrode area on the surface roughness and topography. *J Mater Process Technol* 200:250–258
2. Kansal HK, Singh S, Kumar P (2005) Parametric optimization of powder mixed electrical discharge machining by response surface methodology. *J Mater Process Technol* 169:427–436
3. Kansal HK, Singh S, Kumar P (2006) Performance parameters optimization (multi-characteristics) of powder mixed electric discharge machining (PMEDM) through Taguchi's method and utility concept. *Indian J Eng Mater Sci* 13:209–216
4. Singh S, Yeh MF (2012) Optimization of abrasive powder mixed EDM of aluminium matrix composites with multiple responses using gray relational analysis. *J Mater Eng Perform* 21(4):481–491
5. Singh B, Singh P, Tejpal G, Singh G (2012) An experimental study of surface roughness of H-11 in EDM process using copper tool electrode. *Int J Adv Eng Technol* 3(4):30–33
6. Talla G, Sahoo DK, Gangopadhyay S, Biswas CK (2015) Modeling and multi-objective optimization of powder mixed electric discharge machining process of aluminium /alumina metal matrix composite. *Eng Sci Technol Int J* 1–5
7. Tripathy S, Tripathy DK (2016) Multi-attribute optimization of machining process parameters in powder mixed electro-discharge machining using TOPSIS and grey relational analysis. *Eng Sci Technol Int J* 19(1):62–70
8. Senthil P, Vinodh S, Singh AK (2014) Parametric optimisation of EDM on Al-Cu/TiB2 in-situ metal matrix composites using TOPSIS method. *Int J Mach Mach Mater* 16(1):80–94
9. Sidhu SS, Batish A, Kumar S (2014) ED machining of particulate reinforced MMC's. *Int J Mech Aerosp Ind Mech Manufact Eng* 8(3):503–509



10. Datta S, Bandyopadhyay A, Pal PK (2008) Solving multi-criteria optimization problem in submerged arc welding consuming a mixture of fresh flux and fused slag. *Int J Adv Manuf Technol* 35:935–942

# Production Optimization for a Biofuel Prepared from a High Acid Value Fuel like Nahar Oil, Its Properties and Feasibility to Use in a Four-Stroke DI Diesel Engine



Animesh Das, Manjula Das Ghatak, and Pinakeswar Mahanta

**Abstract** The increase in demand for diesel leads to investigate the identification of a new alternate fuel for diesel. Additionally, the use of fossil fuel results in the emission of unburnt hydrocarbon, carbon monoxide, particulate matters which pollute the environment. This paper shows the production procedure, composition of acid contains, and properties of biodiesel from Nahar oil which contains very high amount of free fatty acid and evaluation of performance parameters in a non-modified compression ignition (CI) engine through direct injection (DI) system powered with biodiesel mixed in different proportion with petroleum diesel.

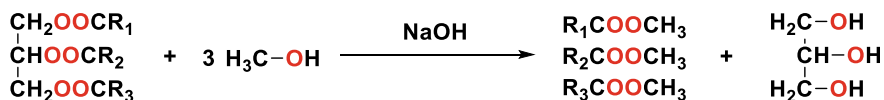
**Keywords** Transesterification · FFA · Acid No. · NOME · BTHE · BSFC · BP · HC · DICI

## 1 Introduction

Fossil fuels are produced from the anaerobic decomposition of buried dead organism, and thus, millions of years are required for the production of fossil fuels [1]. So, it is very important to develop some ecofriendly and convenient way for the future to some extent. In the environmental concerns and the reduction of fossil fuels have stimulated to discover substitute of mineral diesel, which could play a vital role in industrial and transportation segment [2]. It has already been established that these vegetable oil-derived fuels emit comparatively less destructive emissions of greenhouse gas than fossil fuels [3]. The most common procedure to make biodiesel from any crude oil is known as transesterification reaction [4]. Transesterification is the reaction where a long-chain hydrocarbons shortens its chain length and reduces the viscosity of fuel considerable. In this reaction, crude oils which contains long-chain hydrocarbons reacted with alcohol in presence with a catalyst may be base or acid to reduce the reaction time and produced biodiesel and glycerol [5].

---

A. Das (✉) · M. D. Ghatak · P. Mahanta  
Department of Mechanical Engineering, NIT Arunachal Pradesh, Yupia, Arunachal Pradesh, India  
e-mail: [animeshdas990@gmail.com](mailto:animeshdas990@gmail.com); [animesh.phd@nitap.ac.in](mailto:animesh.phd@nitap.ac.in)



But, this transesterification is not always conceivable, especially for the oils contain high free unsaturated fatty acid or free fatty acid [6]. More than a certain percentage (nearly 5–6%), free fatty acid measures in the natural oils turns out to be undeniably challenging to deliver biodiesel by transesterification measure [7]. The cycle rather prompts saponification [2]. Development of soap makes it truly challenging to isolate the deposit of glycerol from biodiesel [8]. Present investigation contains production of biodiesel from Nahar oil, and engine performance parameters testing of different prepared biodiesel blends and comparison of performance characteristics with conventional diesel [9–11].

## 2 Materials and Method

Animal fat and vegetable oils consist of fatty acid and glycerol. The basic type of fat, triacylglycerol is composed of two different things—these are glycerol and fatty acid. Triacylglycerol is the combination of three fatty acids and one glycerol [12]. Fat contains a lot of hydrocarbon chains [10]. So, if the fatty acid chains are broken down, it will develop some hydrocarbon rich fuel which is nothing but the biodiesel. The main idea of producing the biodiesel is the separation of glycerol backbone from the fatty acid chain which process is called transesterification.

### 2.1 Characterization of Nahar Seed Oil

The biodiesel extraction and their properties from fresh Nahar oil were well characterized to define fatty acid value and different physico-chemical belongings. Conformations of fatty acid content extracted from Nahar oil are summarized in Table 1 [9].

The fatty acid content from Nahar oil was found 31.83 mg KOH/g, and the respective FFA content was isolated in 16.1%. From GC analysis, it was found that oleic acid (45.55%) is the major component in fatty acid extracted from Nahar oil with linoleic acid (22.08%), palmitic acid (16.09%), and stearic acid (8.08%), which are mainly accountable for pour point and high cloud.

**Table 1** Fatty acid compositions in Nahar oil

Name of fatty acids	Formulation	Composition
Palmitic acid	C16:0	16.09
Myristic acid	C14:0	2.29
Oleic acid	C18:1n9c	45.5.5
Tricosanoic acid	C23:0	0.12
Linoleic acid	C18:2n6c	22.08
Stearic acid	C18:0	8.08
Cis-11 eicosenoic acid	C20:1	1.02
Alpha-linolenic acid	C20:3n6	0.013
Behenic acid	C22:0	0.51
Arachidonic acid	C20:4n6	0.46
Cis-13,16 docosadienoic acid	C22:2	0.23

## 2.2 Production of Biodiesel

The reaction conditions mainly amount of base for transesterification process, temperature, and reaction time were optimized to produce maximize of oil content from Nahar seeds. Due to high fatty acid value of Nahar oil, various efforts were unsuccessful through base-treated transesterification reactions by generating soap and water, which regrets the rate of reaction. Here, we have developed an acid–base two-step transesterification procedure to minimize the higher amount of free fatty acid contents in crude Nahar oil in initial esterification.

**First Stage Acid Esterification.** Initially, the FFA content of Nahar oil was transformed into methyl ester of fatty acid. Various optimization reactions were performed to evaluate the methanol quantity present in the oil as well as amount of hydrochloric acid (HCl) required for esterification, reaction temperature, addition rate also reaction time to complete the conversion. As we can see from Fig. 1 that 6:1 molar ratio of methanol and crude Nahar oil by using 0.1 N of hydrochloric acid, the acid rate decreased to 24 mg KOH/g was observed after 30 min of the reaction at 60 °C. When 0.5% (v/v) of hydrochloric acid was employed, the transformation rate was rapidly accelerated, and acid value decreased to 2.9 mg KOH/g within 70 min of the reaction. The transformation rate was quicker for initial 45 min as compared to the completion reaction time. Moreover, further addition of hydrochloric acid, the reaction mixture color was changed unexpectedly; this may be due to the charring preheated triglyceride in presence of high content of hydrochloric acid. Sequential adding of 0.50% (vol/vol) hydrochloric acid afterward 30 min of the reaction offered superior transformation within short time compared to one-time addition of 1.20% (vol/vol) hydrochloric acid in methanol and oil reaction blend. Acid no. of Nahar oil was decreased to 2.4 mg KOH/g at a time from 34 mg KOH/g within 105 min, where other parameters like temperature (60 °C), rate of mixing (500 rpm), and amount of

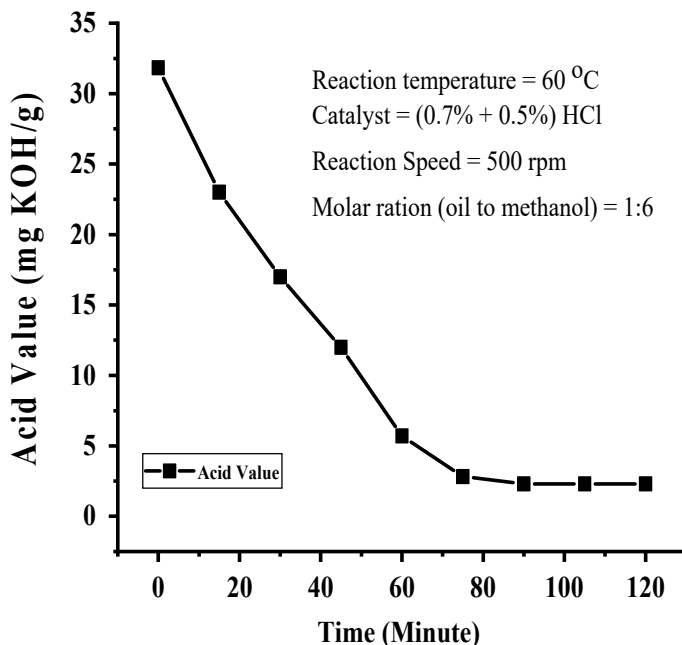


**Fig. 1** Reduction of acid value with time

used hydrochloric acid (0.7 + 0.5)% (v/v) were keeping unchanged. Only, the by-product in the esterification was water, which was removed through a work-up using hexane. Hexane layer was extracted, and aqueous layer was removed from separating funnel. Hexane layer was further passes through anhydrous sodium sulfate ( $\text{Na}_2\text{SO}_4$ ) to remove excess water. After that the produced esterified oil was immediately transferred into the transesterification process employing calcium oxide (NaOH) as an efficient reagent.

**Second Stage Alkali Catalyzed Transesterification.** Here, we have established the integrative influence of molar proportion of alcohol to oil (4:1 to 12:1) and the catalyst loaded amount (0.5–3.00 wt%). In this study, other constraints, for example, reaction time, temperature of the reaction, and mixing speed, were unchanged to get the optimum reaction condition. As we can observed from Fig. 2 that the increasing loading catalyst amount from 0.5 to 1.5 wt%, the formation of biodiesel was also increased. When the catalyst-loading amount was augmented from 3 to 4 wt%, extreme yield of biodiesel has been isolated at molar proportion of 1:6 to 1:8. Maximum transesterified product 74% was isolated by using 2 wt% of NaOH catalyst for both molar proportion of 1:8 and 1:10. Molar proportion of 1:8 was offered maximum isolated biodiesel product (82%), when 2.5 wt% of NaOH was used as a catalyst. From several set of optimized reaction conditions, it was established that molar proportion of 1:8 and 2.4 wt% of catalyst charging amount offered the highest

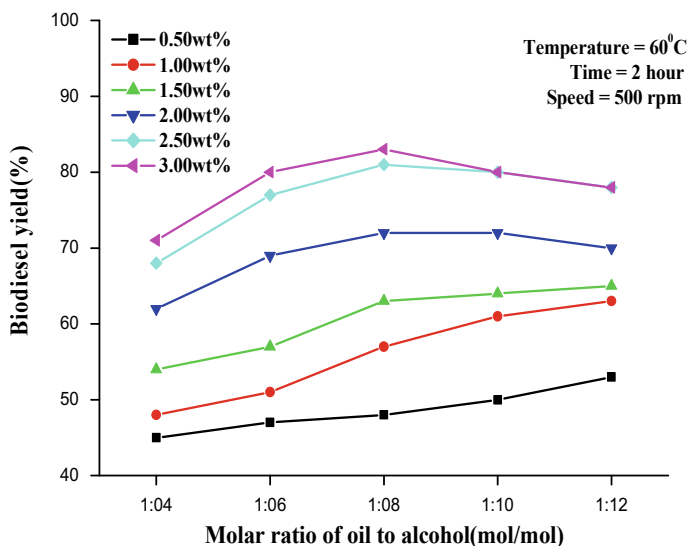


**Fig. 2** Change in yield % with molar ratio of oil

amount transesterified product. Other reaction conditions were also optimized to get additional improved biodiesel product. We have studied various reaction temperatures wide ranging from 50 to 80 °C to establish the outcome of temperature upon the reaction to improve the reaction time as well as the isolated yield of biodiesel product. It was observed from Fig. 3 that when temperature were raised to 65 °C from 60 °C, only, 2% of increment yield was isolated, where 70 °C was showing negative effect on the isolated biodiesel yield.

This negative effect was observed probably because of the higher temperature than boiling point methanol. It was established that at 65 °C maximum 84% yield of biodiesel was observed within 2.5 h of reaction time. When the mixing rate was increased from 500 to 600 rpm, 88% yield of biodiesel product was isolated; further, increment of mixing rate was not offered any fruitful result in respect of yield or reaction time (Fig. 4).

### 3 Results and Discussion

#### 3.1 Fuel Properties

Before conducting engine performance test of Nahar oil methyl ester (NOME) significant properties like calorific value, viscosity, flash point, and pour point for all three blends of biodiesel (B10, B20, and B30) along with pure diesel and pure biodiesel (B100) are determined which is shown in Table 2 [13]. Property table clearly indi-

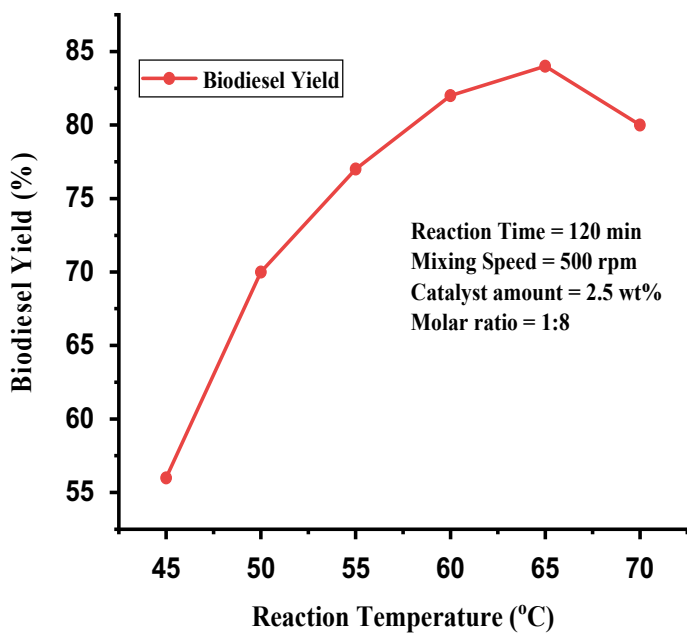


Fig. 3 Change in yield % with reaction temp

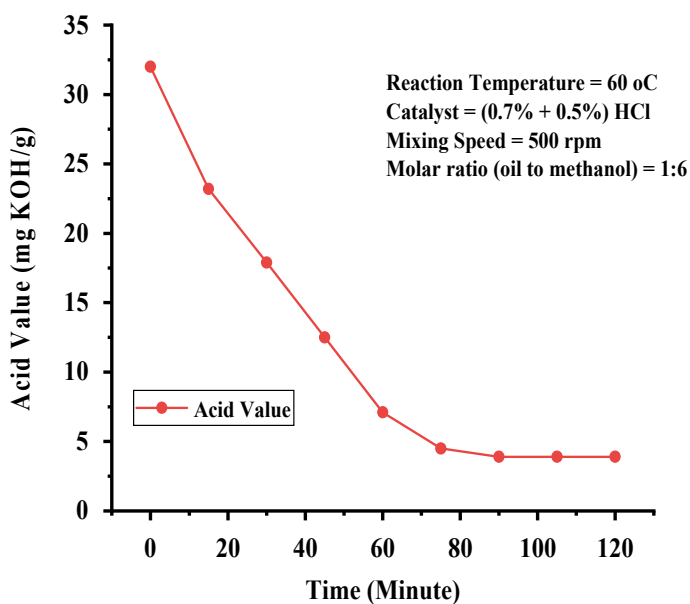


Fig. 4 Change in yield % with time

**Table 2** Properties of pure diesel and different blends with Nahar oil

Properties	Pure diesel	B10	B20	B30	B 100
Density (kg/m <sup>3</sup> )	837.8	840.4	846.8	852.7	876.05
Viscosity (cSt@40 °C)	1.81	2.04	2.56	2.96	3.65
Calorific value (kJ/kg)	43,347	43,056	42,710	42,070	39,767
Flash point (°C)	53	64	75	83	160
Fire point (°C)	58	73	82	93	164
Pour point (°C)	-8.7	-7.1	-6.3	-5.3	3.2

cates that viscosity of pure NOME is much higher than pure diesel, and calorific value is meaningfully lesser than diesel which is same for all blends also. The flash point and fire point are also higher for 100% NOME and its blends and similar kind of nature for pour point also.

### 3.2 Engine Performance Test

The experiment is carried in a four-stroke CI engine having four cylinder. The parameters to measure engine performance like brake thermal efficiency, specific fuel consumption are obtained by testing fuels in a multi-cylinder test rig. Normally, this engine is run by pure diesel. In this experiment, biofuel blend is required to run through the engine. Biodiesel blend is prepared manually by mixing 100% biodiesel (B100) and pure diesel in different proportion to prepare B10, B20, B30 blends, respectively, and poured through the engine fuel tank. The calorific value and the density of B10, B20, and B30 blends are obtained from the characterization. The load can be applied by varying the torque. Loads of approximately 5, 10, 15, and 20 kg were selected. These loads represent 25%, 50%, 75%, and 100% of the total load, respectively, where 0% load is called as no load, and 100% load is called as full load. After the engine begin running on the biofuel, the engine is allowed to stabilize for some time at no load, and then, 5 kg load is applied with the help of a dynamometer.

**Engine Specification.** Before starting the engine, it is ensured that there is sufficient water flow. The water flow to the cooling tank is kept at a level of 300 lph (liquid per hour), and the water flow to the calorimeter is kept at 70 lph. First, water flow is sufficiently ensured so that the engine does not heat up during the course of its running. During the engine testing, the compression ratio is maintained at 18. The load was changed by using a dynamometer, and the dynamometer was of eddy current type.

**Variation in Brake-Specific Fuel Consumption.** It clearly shows that pure diesel consumes least than any other blends of fuels almost for all loads except very high range of loads. From Fig. 5, it is clearly vibrant that for higher range of loads consump-



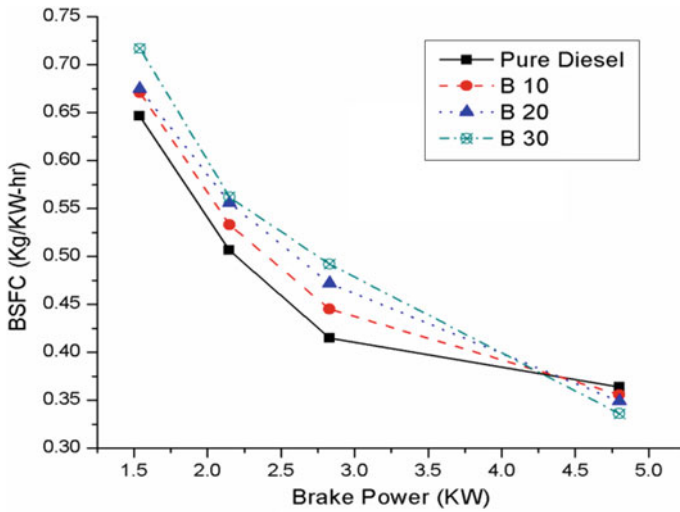


Fig. 5 Variation in brake-specific fuel consumption with brake power

tion of biofuel is slightly less than pure diesel and that is true for all biodiesel blends which indicates that for higher loads biodiesel from Nahar oil burns completely and becomes more efficient than petroleum fuel.

**Variation in Brake Thermal Efficiency.** Figure 6 shows that initially in case of lower loads brake thermal efficiency of pure diesel is higher than any other blends

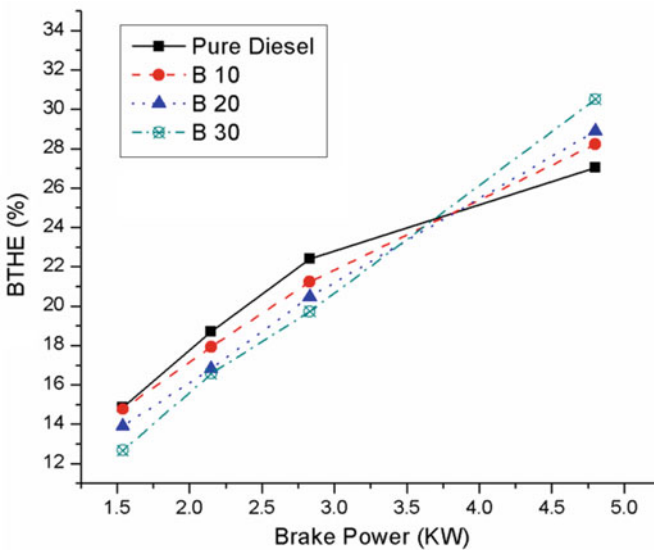


Fig. 6 Variation in brake thermal efficiency with brake power

of n biodiesel which gradually increases its difference with all proportioned blends up to a certain limit of loads. In higher loads, thermal efficiency of pure diesel then gets almost saturated after a certain limit, whereas biodiesel blends continue its increment in same rate. So, in higher load condition, the thermal efficiency of B30 is significantly higher pure diesel as well as all other different blends. It concludes that combustion of higher proportioned blend of biodiesel from Nahar oil produces much energy than fossil fuel, especially for higher loads.

## 4 Conclusion

The creation of fuel-quality biodiesel from high FFA feed stocks is researched in the current investigation. It is tracked down that the FFAs couldn't be transesterified with the basic impetus transesterification measure. The impacts of alcohol to oil molar proportion, energy entirety of catalyst, temperature during reaction, and time taken to complete reaction are investigated in each progression. This two-step esterification technique decreases the general creation cost of the biodiesel, as it utilizes minimal expense crude non-consumable oils. The current investigation uncovers that biodiesel from crude Nahar oil is very appropriate as an option in contrast to diesel. Though the efficiency of all biodiesel blends is less than pure diesel but not much discrepancy from pure diesel and can be a very worthy replacement of diesel in near future.

## References

1. Mohiddin MN, Saleh AA, Reddy ANR, Hamdan S (2018) A study on chicken fat as an alternative feedstock: biodiesel production, fuel characterisation, and diesel engine performance analysis. *Int J Automot Mech Eng* 15:5535–5546
2. Naik M, Meher LC, Naik SN, Das LM (2008) Production of biodiesel from high free fatty acid Karanja (*Pongamia pinnata*) oil. *Biomass Bioenergy* 32:354–357
3. Huzayyin AS, Bawady AH, Rady MA, Dawood A (2004) Experimental evaluation of diesel engine performance and emission using blends of jojoba oil and diesel fuel. *Energy Convers Manag* 45:2093–2112
4. Das A, Ghatak MD (2018) An experimental study on performance of CI engine fuelled with waste cooking oil. *IOP Conf Ser Mater Sci Eng* 377
5. Puhan S, Vedaraman N, Ram BVB, Sankamarayanan G, Jeychandran K (2005) Mahua oil (*Madhuca Indica* seed oil) methyl ester as biodiesel-preparation and emission characteristics. *Biomass Bioenergy* 28:87–93
6. Ramadhas AS, Jayaraj S, Muraleedharan C (2005) Biodiesel production from high FFA rubber seed oil. *Fuel* 84:335–340
7. Dhar A, Kevin R, Agarwal AK (2012) Production of biodiesel from high-FFA neem oil and its performance, emission and combustion characterization in a single cylinder DIC engine. *Fuel Process Technol* 97:118–129
8. Cardoso A, Neves S, Da Silva M (2008) Esterification of oleic acid for biodiesel production catalyzed by  $\text{SnCl}_2$ : a kinetic investigation. *Energies* 1:79–92

9. Dash SK, Lingfa P, Chavan SB (2018) An experimental investigation on the application potential of heterogeneous catalyzed Nahar biodiesel and its diesel blends as diesel engine fuels. *Energy Sources Part A Recover Util Environ Eff* 40:2923–2932
10. Mahanta P, Sarmah JK, Kalita P, Shrivastava A (2008) Parametric study on transesterification process for biodiesel production from *Pongamia pinnata* and *Jatropha curcus* oil. *Int Energy J* 9:41–46
11. Banapurmath NR, Tewari PG, Hosmath RS (2008) Performance and emission characteristics of a DI compression ignition engine operated on Honge, *Jatropha* and sesame oil methyl esters. *Renew Energy* 33:1982–1988
12. Demirbaş A (2003) Biodiesel fuels from vegetable oils via catalytic and non-catalytic supercritical alcohol transesterifications and other methods: a survey. *Energy Convers Manag* 44:2093–2109
13. Das A, Ghatak MD (2021) An investigative study on engine performance and combustion products of a manual diesel engine fueled with an oil produced from locally available Nahar seeds. *Pollut Res* 40:1502–1510

# Optimization of Power Consumption and Cost Analysis in Hard Turning Under NFMQL Condition



Lalatendu Dash, Ajay Kumar Behera, and Sudhansu Ranjan Das

**Abstract** This work addresses on predictive optimization of power consumption in hard turning using response surface methodology. Machining trials are performed under nanofluid assisted minimum quantity lubrication (NFMQL) with varied cutting conditions (speed, depth of cut, axial feed) obtained by  $L_9$  orthogonal array design. Afterwards, cost analysis is executed for economic machining. With the tool life of 34 min, Gilbert's machining economic model calculated the overall machining cost per part of Rs. 51.50 in hard turning of AISI D3 steel employing TiCN/Al<sub>2</sub>O<sub>3</sub>/TiN coated carbide tool. Results clearly established that machining under NFMQL condition provides environment friendliness, technologically viable and economically feasible to progress sustainability.

**Keywords** Turning · AISI D3 steel · Power consumption · RSM · Cost analysis

## 1 Introduction

Day-by-day, heat-treated hardened die steels have considerable need for industries like bearing, mold and die production in order to achieve excellent performance. Hardened AISI grade D3 steel (above 45 HRC) is classified as category of hard-to-cut material owing to its specific attributes [1] and thereby machining of hardened steel experienced high energy consumption and heat generation caused by severe friction and temperature at friction interfaces. Due to wide spread of green sustainable machining, the industries are efforting their center of attention toward a motivational practice “Go Green—Think Green—Act Green” as it reduces negative environmental impact as well as energy consumption because of low carbon dioxide

---

L. Dash · S. R. Das (✉)

Department of Production Engineering, Veer Surendra Sai University of Technology, Burla  
768018, India  
e-mail: [das.sudhansu83@gmail.com](mailto:das.sudhansu83@gmail.com)

A. K. Behera

Department of Mechanical Engineering, Siksha 'O' Anusandhan University, Bhubaneswar  
751030, India

emission during product manufacturing. Therefore, execution of hard machining with rightly chosen machining parameters and efficient cooling-lubrication strategy ensures environmental friendliness [2], technologically viable and economically feasible approach toward safer and cleaner production. For this reason, researchers have employed various optimization techniques [3–12] to control and minimize the power consumption without compromising the product quality.

Though, literatures related to application of response surface methodology for predictive optimization in hard turning are available in large numbers, unfortunately there has been no systematic study. In perspective to fill the research gap as stated above, this work focused on predictive optimization of power consumption in hard turning under NFMQL employing response surface methodology. Moreover, investigation attend to cost estimation study in hard turning under NFMQL condition is still a matter of concern from economical point-of-view.

## 2 Experimental Setup and Procedure

A heat-treated AISI D3 steel cylindrical bar (size: 200 mm long and 45 mm diameter) having hardness of 51HRC is chosen as work material to perform machining trials on a heavy duty and high precision lathe (Mihir 250X). The cutting tool is multilayer (TiCN/Al<sub>2</sub>O<sub>3</sub>/TiN) coated carbide tool having ISO designation CNMG 120412MT TT8115 (make: Taguttech) which is clamped into a PCLNL2020K12 toolholder. During experimental trials at each parameter settings, a 3 $\phi$ -energy meter (make: Visiontek, model: 37TM) was employed for measurement of power consumption.

The number of machining trial was designated by  $L_9$  orthogonal array, based on Taguchi method which is associated with three control factors each of having three levels namely axial feed (0.07, 0.14, 0.21 mm/rev), cutting speed (55, 95, 135 m/min) and depth of cut (0.1, 0.2, 0.3 mm). Experimental layouts results consisting of nine runs are presented in Table 1. Figure 1, pictorially represents the schematic layout of procedure followed for machining setup and experimental investigations.

## 3 Discussion of Results

### 3.1 Optimization of Power Consumption Using Response Surface Methodology

To accomplish best solution of optimization problem, the present study employed a reliable technique known as desirability function approach of RSM that assigns a score to the response and chooses the factor settings to minimize the power consumption. Such task for predicting optimal solution to the response,  $P_c$  was obtained using standard statistical software package Design Expert 11. The desirability function is

**Table 1** Experimental results

Trial no	Machining parameters			Machining response
	$v$ (m/min)	$f$ (mm/rev)	$d$ (mm)	$P_c$ (W)
1	55	0.07	0.1	650
2	55	0.14	0.2	605
3	55	0.21	0.3	790
4	95	0.07	0.2	930
5	95	0.14	0.3	1115
6	95	0.21	0.1	1210
7	135	0.07	0.3	1330
8	135	0.14	0.1	1195
9	135	0.21	0.2	1150



**Fig. 1** Schematic of machining setup and procedure for experimental investigation

capable to transform each response to a desirability level in the range zero-one (i.e., from least to most desirable). Essentially, this approach translates the desirability function to a common scale (0–1) and then combines it using the geometric mean and optimize a series of results. The main target of optimization procedure is to synchronize correct set of conditions that will be capable to get a desirability value of one. With a set of 29 solutions, the highest desirability values (close to 1) were sorted out shown on ramp function graph, Fig. 2a. The optimal values are indicated as points on each ramp graph which results in maximum desirability value. A bar plot is shown in Fig. 2b that presents the overall desirability value of 0.93. As observed from this figure, the optimum cutting solution was preferred at cutting speed ( $v$ ) of 55 m/min, doc ( $d$ ) of 0.1 mm, axial feed ( $f$ ) of 0.07 mm/rev. The power consumption ( $P_c$ ) was found as 655 W at the optimum parametric machining conditions.

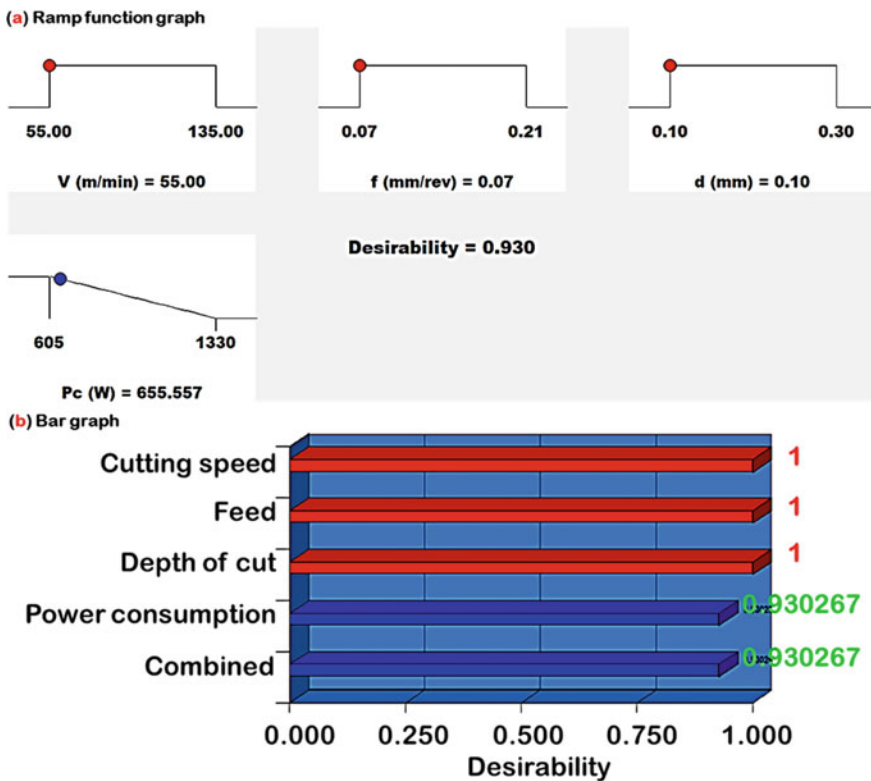


Fig. 2 Optimization results using RSM

### 3.2 Cost Analysis

In machining operation, economic activity plays a vital role in improving production rate as well as product quality. Innovation, exploration, planning and the use of resources are still being attempted to ensure the machining process more effectively, efficiently, commercially sustainable and environmentally safe. This involves knowledge or consciousness of the factors which control or influence machining economy and how. For example, enhancement of both MRR and surface finish requires machining at high cutting speed but it raises the possibility of frequent of cutting tools (edges) due to rapid tool wear caused by increased cutting temperatures, are substantially controlled by proper cutting fluid application. However, cutting fluid not only favorably reduces cutting temperature, friction and tool wear in machining but also causes severe environmental pollution and health hazards, which is a tremendous social problem in addition to other technical and financial problems. Therefore, both economy and environment friendliness need to be explored while planning and carrying out the machining operation.

For this reason, one more experimental trial was carried out under NFMQL condition coupled with similar machining settings for to evaluate the tool life of coated carbide cutting insert. The estimation of life is considered according to control criterion of tool wear (particularly flank wear, VB upto 0.3 mm). Figure 3 shows the growth of flank wear with machining duration upto the tool life of coated carbide tools in turning of hardened AISI D<sub>3</sub> alloy die steel, performed at  $d = 0.1$  mm,  $v = 55$  m/min,  $f = 0.07$  mm/rev (i.e. at optimum parametric settings according to desirability function approach of RSM). It is to be noted that the depth of flank wear progression is steady with cutting time and experience the life of 34 min. With the measured tool life, a cost analysis is executed according to Gilbert's machining economic model [1] in order to estimate total cost per component machined by coated carbide tool. Table 2 shows a detailed economic analysis in dry hard turning operation using coated carbide tool. Results reveal that the application of coated carbide insert in hard turning is more economically viable under NFMQL environment as the overall machining cost per component is less (Rs. 51.50). In brief, the TiCN + Al<sub>2</sub>O<sub>3</sub> + TiN coated carbide tool holds considerable economic advantages as the production cost is reduced.

## 4 Conclusions

Using desirability function analysis of RSM, the suitable cutting solution was preferred at cutting speed ( $v$ ) of 55 m/min, doc ( $d$ ) of 0.1 mm, and axial feed ( $f$ ) of 0.07 mm/rev. The estimated power consumption ( $P_c$ ) was found as 655 W. Under the flank wear criterion of hard turning according to ISO 3685, the satisfactory performance of TiCN + Al<sub>2</sub>O<sub>3</sub> + TiN coated carbide insert ends at tool life of 34 min at the optimum parametric machining settings. With the measured tool life,



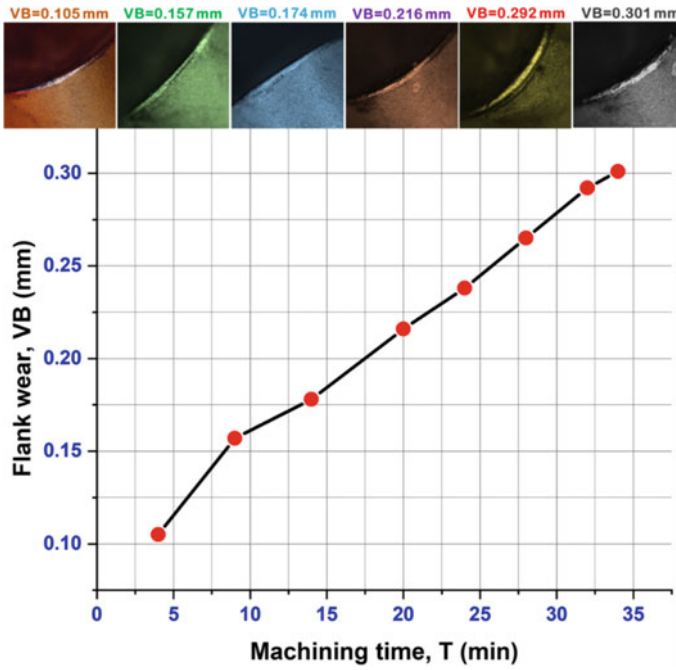


**Fig. 3** Development of flank wear with time at cutting conditions:  $d = 0.1$  mm,  $v = 55$  m/min,  $f = 0.07$  mm/rev

**Table 2** Machining economic assessment of coated carbide tools in finish hard turning

Production costs and times	TiCN + Al <sub>2</sub> O <sub>3</sub> + TiN coated carbide insert
Machine and operator rate ( $x$ )	Rs. 8/min
Machining time per component ( $T_c$ )	4.15 min
Direct labor and machining cost per component, ( $xT_c$ )	Rs. 33.20
Machine downtime to replace a tool ( $T_d$ )	4 min
Tool life per cutting edge ( $T$ )	34 min
Tool replacement cost per component, ( $xT_d \left(\frac{T_c}{T}\right)$ )	Rs. 3.90
Cost of cutting insert	Rs. 472
Mean cost of single cutting edge ( $y$ )	Rs. 118
Tool cost per component, ( $y \left(\frac{T_c}{T}\right)$ )	Rs. 14.40
Overall machining cost expenditure per component, ( $xT_c + xT_d \left(\frac{T_c}{T}\right) + y \left(\frac{T_c}{T}\right)$ )	Rs. 51.50

Work diameter ( $d$ ) = 45 mm, axial length of cut ( $l$ ) = 300 mm, machining time per component ( $T_c = \frac{\pi dl}{1000vf} = 4.15$  min

Gilbert's machining economic model calculated the overall machining cost per part of Rs. 51.50, which is economically viable under NFMQL environment. Hard turning under optimum parametric conditions with NFMQL strategy undertakes worthwhile reduction in machining power consumption, that seeks environment friendliness, technologically viable and economically feasible to improve sustainability.

## References

1. Dash L, Padhan S, Das SR (2020) Experimental investigations on surface integrity and chip morphology in hard turning of AISI D3 steel under sustainable nanofluid-based minimum quantity lubrication. *J Braz Soc Mech Sci Eng* 42(10)
2. Padhan S, Das A, Santoshwar A, Dharmendrabhai TR, Das SR (2021) Sustainability assessment and machinability investigation of austenitic stainless steel in finish turning with advanced ultra-hard SiAlON ceramic tool under different cutting environments. *Silicon* 13:119–147
3. Kant G, Sangwan KS (2014) Prediction and optimization of machining parameters for minimizing power consumption and surface roughness in machining. *J Clean Prod* 83:151–164
4. Varma KR, Kaladhar M (2016) Multiple performance characteristics optimization of hard turning operations using utility based-Taguchi approach. *J Mech Eng* 45(2):73–80
5. Bilga PS, Singh S, Kumar R (2016) Optimization of energy consumption response parameters for turning operation using Taguchi method. *J Clean Prod* 137:1406–1417
6. Zerti O, Yaltese MA, Khettabi R, Chaoui K, Mabrouki T (2016) Design optimization for minimum technological parameters when dry turning of AISI D3 steel using Taguchi method. *Int J Adv Manuf Technol* 89(5–8):1915–1934
7. Bagaber SA, Yusoff AR (2017) Multi-objective optimization of cutting parameters to minimize power consumption in dry turning of stainless steel 316. *J Clean Prod* 157:30–46
8. Zerti A, Yaltese MA, Meddour I, Belhadi S, Haddad A, Mabrouki T (2019) Modeling and multi-objective optimization for minimizing surface roughness, cutting force, and power, and maximizing productivity for tempered stainless steel AISI 420 in turning operations. *Int J Adv Manuf Technol* 102:135–157
9. Padhan S, Dash L, Behera SK et al (2020) Modeling and optimization of power consumption for economic analysis, energy-saving carbon footprint analysis, and sustainability assessment in finish hard turning under Graphene nanoparticle-assisted minimum quantity lubrication. *Process Integr Optimization Sustain* 4:445–463
10. Karaaslan F, Şahinoğlu A (2020) Determination of ideal cutting conditions for maximum surface quality and minimum power consumption during hard turning of AISI 4140 steel using TOPSIS method based on fuzzy distance. *Arab J Sci Eng* 45:9145–9157
11. Dash L, Padhan S, Das A, Das SR (2021) Machinability investigation and sustainability assessment in hard turning of AISI D3 steel with coated carbide tool under nanofluid minimum quantity lubrication-cooling condition. *Proceedings of the institution of mechanical engineers, Part C. J Mech Eng Sci.* <https://doi.org/10.1177/0954406221993844>
12. Nur R, Yusof NM, Sudin I, Nor FM, Kurniawan D (2021) Determination of energy consumption during turning of hardened stainless steel using resultant cutting force. *Metals* 11(4):565

# Analysis of Parametric Study on Weld Properties in TIG Welding



Shailesh Dewangan , Pavitra Singh, Manoj Kumar Agrawal, and S. Deepak Kumar

**Abstract** Quality of joint play a vital role in the production of any industry. Nowadays, it is due to the very rigid and sharp economic market conditions in the manufacturing industry. The main objective of the industries is to reveal the production of better-quality products at a minimum cost and increase productivity. Tungsten Inert Gas (TIG) welding is the most vital and common operation for joining similar or dissimilar materials by heating, applying pressure, or using the filler material. TIG welding gives a better response for the company's main goal in terms of good quality and higher productivity with less time at a lower cost. In this research project, finding the impact of the parametric study on weld properties in TIG welding. The selected machining parameters are welding current, speed, and gas flow rate, which influence receptive responses such as unnotched tensile strength and notch tensile strength using an optimization viewpoint. Determination of the ideal processing parameters and their impact on better welding quality and higher productivity is investigated.

**Keywords** Optimization · Response surface methodology · Notch tensile strength · TIG welding · Unnotched tensile strength

## 1 Introduction

TIG arc welding is now widely employed in many industries. Because Coalescence is generated by heating the workpiece with an electrical arc struck between the tungsten electrode and the job. It is simple to utilize. Esme et al. [1] has experimentally examined the overall quality characteristics of the weld metal is to be improved and

---

S. Dewangan (✉) · S. D. Kumar  
Department of Mechanical Engineering, Chouksey Engineering College, Bilaspur, India  
e-mail: [shaileshdewangan123@gmail.com](mailto:shaileshdewangan123@gmail.com)

P. Singh  
School of Energy Science and Engineering, IIT Guwahati, Guwahati, Assam, India

M. K. Agrawal  
IET, GLA University, Mathura, Uttar Pradesh, India

also estimated ANOVA techniques in TIG welding. Process parametric optimization is used for the geometry of the welded joints in TIG welding using Taguchi-based gray relation analysis and verified optimal results in confirmation experiments. TIG welding process is used for metal and used in titanium and titanium alloys [2]. Titanium is a reactive metal that can be embrittled by different gas like hydrogen, oxygen, and nitrogen, at high temperatures. This can be useful in the TIG welding process.

If welding pure titanium material in the TIG welding process directly affects microhardness. Because during the process of welding, the heat-affected zone temperature variation. This type of material (pure titanium material grade-2) in TIG welding using with tine plate by Krishnanunni et al. [3]. On the pool's surface, the temperature gradient is lessened when welding speed or electrode gap is increased, and inward Marangoni convection is diminished, resulting in a lower value is obtained in weld depth/width ratio [4]. Li et al. [5] looked at the effects of two different types of weld pools: wide-shallow and narrow-deep. Heat flux is relocated from the margins of the weld pool to the center via inward Marangoni convection, resulting in a deep and narrow weld pool shape of stainless-steel material [6]. TIG welding is not only used for joining the part as well as using prediction method, but regression analysis is also used such as neural network, genetic neural, and backpropagation neural network [7]. Today various types of a joint using the TIG welding and another process [8, 9]. Now a days using friction stir welding is mostly used in today's industries [10].

According to the researchers, most of the TIG welding process is done, but TIG in different material welding characteristics is rarely used. So, the major goal of this research is to determine the impact of TIG welding parameters such as gas flow, welding current, and speed on receptive output parameters, known as unnotched tensile strength and notch tensile strength. Experiment using design of experiment technique for response surface methodology using design expert software and finding the optimum results.

## 2 Experimentation

Through a comprehensive literature review and previous studies, the most influential elements that mechanical properties of TIG welded connections and how they affect the form of the weld pool have been determined with machining parameters. Machining parameters and their different levels are represented in Table 1.

### 2.1 Selection of Workpiece Material

Two materials are selected for the welding process. The first material is stainless-steel, a variation of 16%, chromium 7%, and nickel austenitic alloy, the most familiar and frequently used in the stainless-steel family. And the second one is mild steel

**Table 1** Welding input parameters and their range

S. No.	Input parameters	Unit	Levels of input parameters		
			Low	Medium	High
1	Gas flow rate	l/min	5	8	11
2	Welding current	A	100	137.5	175
3	Welding speed	cm/min	10	15	20

is this material one of the most used for construction. Composition of mild steel material is carbon 0.18%, magnesium 0.71%, silicon 0.41%, sulfur 0.04%, and rest iron. The welding joint of the different workpiece materials is shown in Fig. 1.

In this experiment using three factors such as gas flow rates, welding current and welding speed each parameter are divided into three categories lower, medium, and high, all value is showing in Table 2. A total of 17 experiments have conducted the design of the experiment by box Behnken RSM method using design expert software.

For statistical software analysis, two types of tensile specimens have been created from the experimentally first notched tensile specimens and second unnotched tensile specimens. The Instron UTM (Model 8801) is used to measure NTS and UTS of base metal and TIG welded joints at a strain value of 0.001/s. The design table and calculated responses value are represented in Table 2.

**Fig. 1** Tensile specimen of different workpiece material after TIG welding



**Table 2** Design matrix and observed responses

S. No.	Welding current (A)	Welding speed (cm/min)	Gas flow rate (l/min)	NTS (MPa)	UTS (MPa)
1	175.0	10	8	787.22	612.13
2	175.0	15	5	771.54	612.91
3	100.0	15	5	703.87	620.26
4	137.5	20	11	721.65	635.88
5	137.5	15	8	770.63	639.42
6	100.0	15	11	690.24	640.61
7	100.0	20	8	685.69	618.48
8	137.5	10	5	765.68	624.15
9	175.0	20	8	726.75	631.37
10	100.0	10	8	728.42	633.42
11	137.5	10	11	737.25	632.42
12	137.5	15	8	775.23	639.67
13	137.5	20	5	709.94	616.24
14	137.5	15	8	783.27	642.64
15	175.0	15	11	782.32	645.69
16	137.5	15	8	773.27	612.32
17	137.5	15	8	763.27	622.64

### 3 Results and Discussion

#### 3.1 Influence of Machining Parameters Notched Tensile Strength (NTS)

In process of TIG welding to analyzing the notched tensile strength, welding current is most influencing parameters. Welding speed is also giving the significant response for analyzed NTS. According to the 3-D (showing Figs. 2, 3 and 4) surface plots of NTS is clearly assessment of welding current and welding speed is given significant response and gas flow rate is not affect significantly, this is also confirming by analysis of variance that is shown in Table 3.

Based on the data input, an equation is commonly recommended in response surface methodology. The regression equation (second-order polynomial) of NTS is found using RSM methods shown in Eq. (1). Where  $A$  is welding current,  $B$  is welding speed, and  $C$  is the gas flow rate.

$$\begin{aligned} \text{NTS} = & 745.66 + 32.45 \times A - 21.82 \times B - 2.45 \times C - 4.44 \times AB \\ & + 6.10 \times AC + 10.0 \times BC \end{aligned} \quad (1)$$

Design-Expert® Software

NTS

787.22

685.69

X1 = B: Welding Speed  
X2 = C: CGas Flow Rate

Actual Factor  
A: Welding Current = 137.50

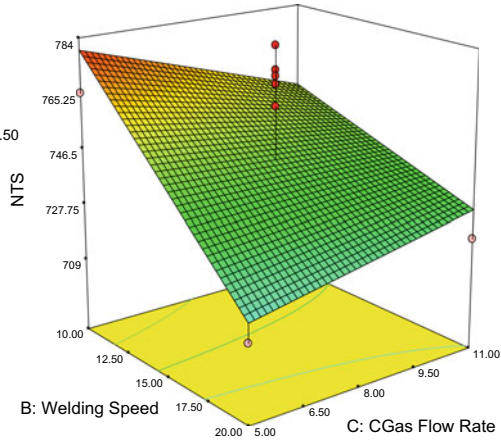


Fig. 2 3-D surface plot welding speed and gas flow rate versus NTS

Design-Expert® Software

NTS

787.22

685.69

X1 = A: Welding Current  
X2 = C: CGas Flow Rate

Actual Factor  
B: Welding Speed = 15.00

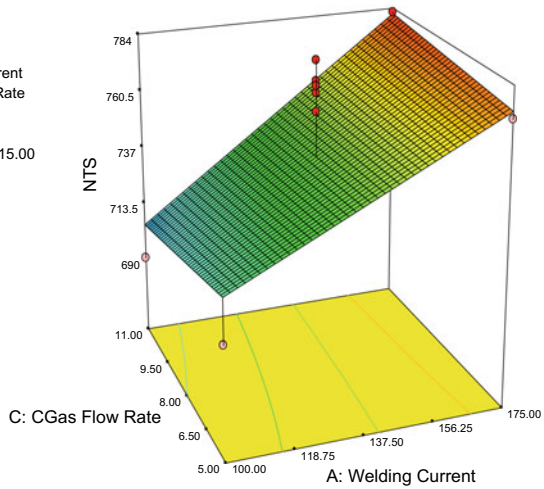


Fig. 3 3-D surface plot welding current and gas flow rate versus NTS

Design-Expert/E Software



X1 = A: Welding Current  
X2 = B: Welding Speed

Actual Factor  
C: CGas Flow Rate = 8.00

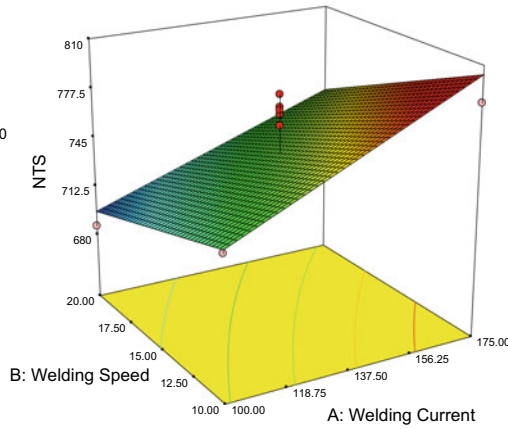


Fig. 4 3-D surface plot welding current and welding speed versus NTS

Table 3 ANOVA for notched tensile strength

Source	Sum of squares	DF	Mean square	F-value	p-value
Model	12,911.01	6	2151.84	3.47	0.0405
A-welding current	8424.67	1	8424.67	13.57	0.0042
B-welding speed	3808.03	1	3808.03	6.13	0.0327
C-gas flow rate	47.87	1	47.87	0.077	0.7869
AB	78.68	1	78.68	0.13	0.7292
AC	148.96	1	148.96	0.24	0.6348
BC	402.8	1	402.8	0.65	0.4392
Residual	6207.69	10	620.77		
Lack of fit	5996.97	6	999.49	18.97	0.0066
Pure error	210.72	4	52.68		
Total	19,118.7	16			

The *F*-value of 3.47 for the model indicates that it is significant. Due to noise, there is only a 4.05% chance that a “Model *F*-value” this large will occur. Model terms are significant when “Prob > *F*” is less than 0.0500. *A* and *B* are important model terms in this scenario. The model terms are not important if the value is bigger than 0.1000. Model reduction may improve your model if there are many inconsequential model terms.



### 3.2 Influence of Machining Parameters of Unnotched Tensile Strength (UTS)

In the analysis of unnotched tensile strength in TIG welding gas flow rate is most important factor then welding current and welding speed. According to the 3-D surface plot (Figs. 5, 6 and 7) of when gas flow rate is increasing the UTS is also

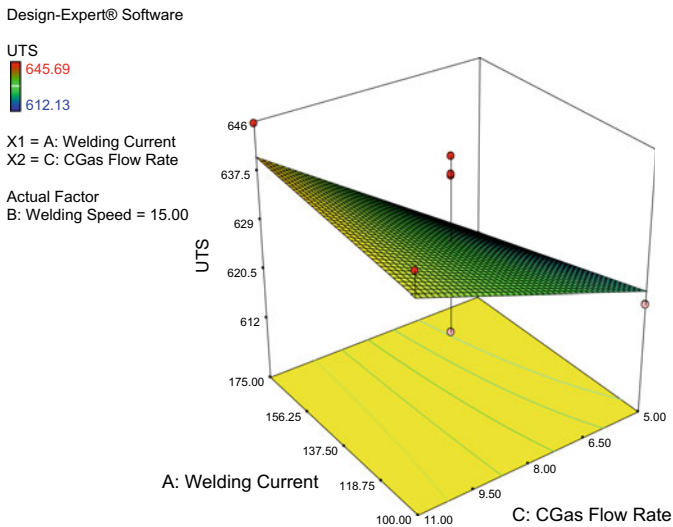


Fig. 5 3-D surface plot welding current and welding speed versus UTS

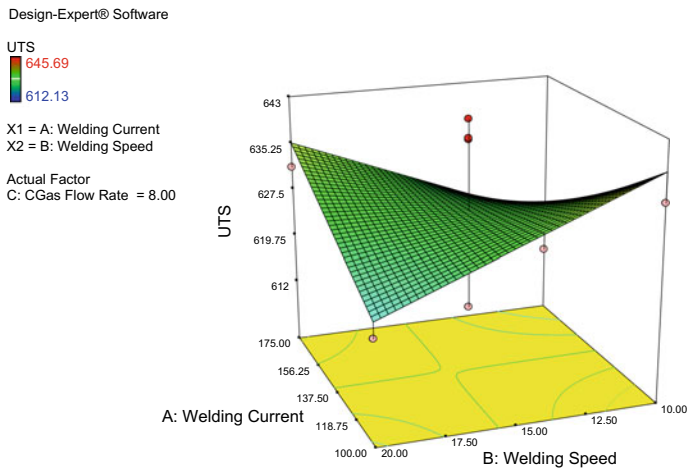


Fig. 6 3-D surface plot welding current and gas flow rate versus UTS

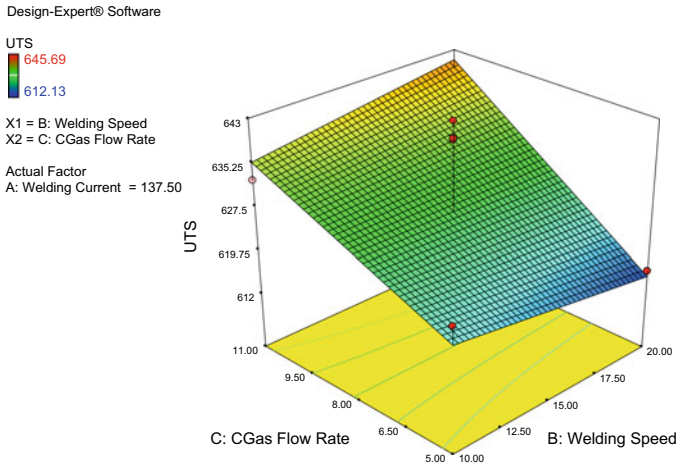


Fig. 7 3-D surface plot gas flow rate and welding speed versus UTS

increase similar type of study is presented by Moi et al. [11]. In this analysis prediction of UTS using a second-order polynomial regression equation is showing in Eq. (2).

$$\begin{aligned}
 \text{UTS} = & 628.25 - 1.33 \times A - 0.019 \times B + 10.13 \times C + 8.54 \times AB \\
 & + 3.11 \times AC + 2.84 \times BC
 \end{aligned}
 \tag{2}$$

In Table 4, the analysis of variances for unnotched tensile strength clearly defines that the *p*-value of gas flow rate is 0.014 is the most significant factor. After that welding current and welding speed, respectively. In this analysis, welding, current and speed is not showing a significant effect on UTD.

Table 4 ANOVA for unnotched tensile strength

Source	Sum of squares	DF	Mean square	F-value	p-value
Model	1198.18267	6	199.6971	2.1385	0.138
A-welding current	14.2311125	1	14.2311	0.1524	0.704
B-welding speed	0.0028125	1	0.0028	0.0000	0.996
C-gas flow rate	820.9352	1	820.9352	8.7912	0.014
AB	292.0681	1	292.0681	3.1277	0.107
AC	38.626225	1	38.6262	0.4136	0.535
BC	32.319225	1	32.3192	0.3461	0.569
Residual	933.817125	10	93.3817		
Lack of fit	234.001445	6	39.0002	0.2229	0.949
Pure error	699.81568	4	174.9539		
Total	2131.9998	16			

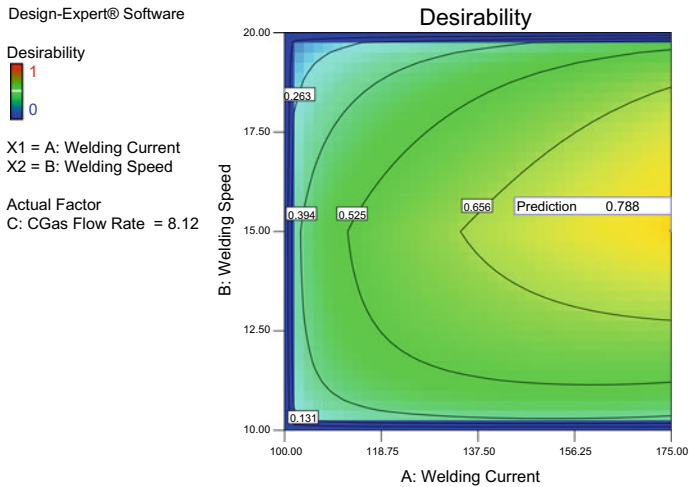


Fig. 8 Optimum results of NTS and UTS

Table 5 Optimum process parameters results

Welding current (A)	Welding speed (cm/min)	Gas flow rate (l/min)	NTS (MPa)	UTS (MPa)	Desirability
175	15	8.12	751.459	627.427	0.788

### 3.3 Numerical Optimization

This research aims to find the best parametric settings for achieving maximum tensile strength for both NTS and UTS of welded specimens at the same time, which is critical for optimal welded joint quality. The best parametric setting for achieving maximal NTS and UTS of welded specimens was determined using the desirability approach. According to the illustration in Fig. 8. Optimum parameters setting for is to be achieved (Welding Current is target = 175.00, Welding Speed is target = 15.00, Gas Flow Rate is target = 8.12) for the max value of NTS and UTS is also presented in Table 5.

## 4 Conclusion

- In the analysis of notched tensile strength, welding current is the most influencing factor; after that welding speed and gas flow rate, respectively. And with the unnotched tensile strength, the gas flow rate is the most affecting parameter, followed by welding current and welding speed.

- The notched tensile strength (NTS) for all welded joints is observed larger than unity, indicating that TIG welded joints are rather immune to notches or geometric gaps.
- Optimum parameters setting for is to be achieved for welding current is 175.00 A, welding speed is 15.00 cm/min, gas flow rate is 8.12 l/min. For the max value of NTS (751.459 MPa) and UTS (627.427 MPa).

## References

1. Esme U, Bayramoglu M, Kazancoglu Y, Ozgun S (2009) Optimization of weld bead geometry in TIG welding process using grey relation analysis and Taguchi method. *Mater Tehnol* 43(3):143–149
2. Patil HS, Patel DC, Patil CS (2019) Characterizations of TIG welded joints of unalloyed commercially pure titanium Gr-2 for weld process parameters. *Frat Integrita Strutt* 13(48):377–384
3. Krishnanunni S, Paul DJ, Unni V (2013) Effect of welding conditions on hardness of commercially pure titanium. *Akgec Int J Technol* 3(2):19–24
4. Dong W, Lu S, Li D, Li Y (2011) GTAW liquid pool convections and the weld shape variations under helium gas shielding. *Int J Heat Mass Transf* 54(7):1420–1431
5. Li D, Lu S, Dong W, Li D, Li Y (2012) Study of the law between the weld pool shape variations with the welding parameters under two TIG processes. *J Mater Process Technol* 212(1):128–136
6. Gopinath V, Manojkumar T, Sirajudeen I, Yogeshwaran S, Chandran V (2015) Optimization of process parameters in TIG welding of AISI 202 stainless steel using response surface methodology. *Int J Appl Eng Res* 10(13):11053–11057
7. Dutta P, Pratihari DK (2007) Modeling of TIG welding process using conventional regression analysis and neural network-based approaches. *J Mater Process Technol* 184(1):560–568
8. Dewangan S, Kumar SD, Jha SK, Prakash A (2021) Prediction of formability of MIG and TIG welded joints by Erichsen cupping test and fuzzy-logic technique. *Int J Mater Eng Innov* 12(3):246–258
9. Dewangan S, Kumar SD, Jha SK, Biswas CK (2020) Optimization of micro-EDM drilling parameters of Ti-6Al-4V alloy. *Mater Today Proc* 33:5481–5485
10. Giri P, Tiwari S, Shrivastava SP (2020) Parameters affecting strength of friction stir welding joint on aluminium alloy: a review. *J Sci Res Allied Sci* 6(2455):118–127
11. Moi SC, Pal PK, Bandyopadhyay A, Rudrapati R (2018) Determination of tungsten inert gas welding input parameters to attain maximum tensile strength of 316L austenitic stainless steel. *J Mech Eng Stroj Cas* 68(3):231–248

# Mechanical and Thermal Properties of Rice/Wheat Straw Fiber Reinforced Epoxy Composites: A Comparative Study



Prabir Kumar Jena , Pradeep Bhoi, and Rabindra Behera

**Abstract** The novelty of the present work is to choose the best alternative composite material with suitable mechanical and thermal properties which can be preferentially used as building material. To achieve the desired objective, a comparative study of rice and wheat straw fiber reinforced epoxy composite has been made in the present work to recommend the most suitable one from the application point of view. The composite material has been prepared with straw content varying from 5 to 20% by weight percentage employing the hand lay-up technique. The tensile, compressive and thermal properties of the prepared test specimen are obtained experimentally. The experimental results thus obtained reported that the tensile strength of wheat straw fiber reaches a maximum value of 6.18 MPa while reaching 4.18 MPa in case of rice straw fiber. While comparing the results for compressive strength it is found that the rice straw fiber attains a maximum value of 14.25 MPa against 10.78 MPa in case of wheat straw fiber. The thermal conductivity value of both wheat and rice straw fiber reinforced composite decrease with increase in fiber loading.

**Keywords** Composites · Epoxy resin · Rice straw · Wheat straw · Mechanical properties · Thermal conductivity

## 1 Introduction

The rapid growth in global waste over the preceding years has increased environmental consciousness and brought apprehension over environmental sustainability. Both, the academic researchers and the scientific community have given their best effort in resolving the aforementioned issue by developing biodegradable and environmental friendly composites with superior mechanical and thermal properties. The

---

P. K. Jena (✉) · P. Bhoi

Department of Mechanical Engineering, VSS University of Technology, Burla, India

e-mail: [pkjena\\_me@vssut.ac.in](mailto:pkjena_me@vssut.ac.in)

R. Behera

Central Workshop, VSS University of Technology, Burla, India

© The Author(s), under exclusive license to Springer Nature Singapore Pte Ltd. 2023

P. Pradhan et al. (eds.), *Recent Advances in Mechanical Engineering*,

Lecture Notes in Mechanical Engineering,

[https://doi.org/10.1007/978-981-16-9057-0\\_78](https://doi.org/10.1007/978-981-16-9057-0_78)

recent time has seen numerous applications of natural fiber reinforced composites as building materials. Rice straw can be one among the existing fiber and has the potential to be used as building material. Rice crop is considered as one of the most consumable ones in all developing countries. Production of rice crop secures second rank in the world. The residuals obtained from rice crop has been increased with an increase in its production rate [1]. The residual may be in the form of rice straw and rice husk. The burning of residuals may be one of the causes for environmental pollution. Therefore, there is a need for proper utilization of this residual in a certain form. From application point of view, rice straw fiber can be seen as one of the most promising reinforcing filler because of the following properties such as: low cost, light weight and exhibit superior mechanical and thermal properties in terms of thermal insulation [2]. Buzarovska et al. [3] investigated the tensile strength of rice straw as filler material with PHBV as matrix material for a different filler volume fraction. The results obtained revealed that the tensile strength decreases with increase in volume fraction. The possible cause is the improper distribution of rice straw. Improvement in results can be obtained by treating the surface before mixing with the matrix material that develops better adhesion between the filler and matrix. Grozdanov et al. [4] investigated the effect of rice straw fiber content as reinforcement in poly propylene. They followed two step methodology such as extrusion and compression molding to prepare the composite. They reached at the same result as Oksman and Lindberg [5]. The results obtained pointed out that the increase in rice straw fiber content resulted in reduced tensile strength. One of the reasons may be a poor interfacial bond that exists between the rice straw fiber and poly propylene at higher fiber loadings. Yang et al. [6] also revealed that the tensile strength of the composites decreases with increase in fiber loading. Their findings suggest that the irregular shape reinforcements have the inability to support load transfer from the polymer matrix, thus, reduces the strength of the composites. Ranjan et al. [7] investigated the mechanical properties of both the untreated and NaOH treated rice straw fiber at different fiber loading. The outcome of their findings shows that the NaOH treated fiber has more tensile strength compared to the untreated one. The increase in mechanical strength of composites mostly depends on strong bonding between the hydrophilic natural fibers and the hydrophobic polymer matrix as pointed out by Lee et al. [8]. Halvarsson et al. [9] investigated the mechanical and water absorption coefficient properties of wheat straw fiber reinforced in different matrix. They reported that the increase in melamine content brought improvement in the results of water absorption and tensile strength. Pan et al. [10] investigated the effect of fiber content and size on the mechanical properties of wheat straw fiber reinforced polypropylene composite. Avella et al. [11] studied the mechanical and thermal characteristics of wheat straw fiber as reinforcement and polyester as matrix. The wheat straw fiber is treated with steam at high temperature, which make the fiber to exhibit more cellulose content and more reactive. The authors conveyed that the treated fiber retains a higher value of Young modulus compared to polyester. From thermal analysis the authors reported that the rate of polycrystallization increases with the presence of wheat straw fiber. Mittal and Sinha [12] investigated the influence of fiber loading on mechanical and water absorption properties of wheat straw fiber reinforced epoxy composites. The authors

also compared the mechanical strength of untreated fiber with fiber treated with alkali of different concentrations. The results obtained reported that the tensile strength of wheat straw fiber treated with 3% of NaOH is more compared to the untreated one. Tong et al. [13] investigated the transmittance, mechanical and thermal properties of wheat straw fiber reinforced with polymethyl methacrylate (PMMA). The authors observed that the wheat straw fiber has a good binding characteristics with PMMA. The results obtained describe that the composite has superior mechanical properties and thermal insulation characteristics. Other characteristics of the rice straw fiber is that it can be employed for thermal insulation purposes. Wahyuni et al. [14] carried out their investigation on thermal conductivity of rice straw fiber with polypropylene as the matrix material. They pointed out that the thermal conductivity decreases with increase in the fiber volume fraction. Composite with fine straw size possesses maximum tensile strength and lower thermal conductivity as compared to coarse fiber. Tao et al. [15] have carried out their investigation on both compressive strength and thermal conductivity of rice straw fiber. The results obtained showed that both the compressive strength and thermal conductivity decrease with increase in fiber loading.

The above described literature pointed out research findings on mechanical and thermal properties of individual rice and wheat straw fiber reinforced composite in different environments. There is a need to have a comparison between the two in the same environment. The current work mainly focused on the comparative analysis of the composite made of these above two fibers in the same environment to propose the most suitable one from application point of view. Both mechanical and thermal properties of the composites are experimentally carried out to highlight the suitable one in terms of strength and thermal insulation type.

## 2 Materials and Method

### 2.1 *Untreated Rice and Wheat Straw Fiber Reinforced Composite Preparation*

In the current work, chopped rice and wheat straw fiber are used as reinforcement material for fabrication of polymer composite. Rice straw and wheat straw used in the present investigation are collected from Sundargarh, Odisha. Cleaning of fiber is then made and kept for more than 24 h to dry. The fiber is then cut into small pieces of size about (3–5 mm). The wooden mold of dimension (180 × 160 × 5) mm<sup>3</sup> has been designed to prepare the test specimens as per ASTM standards. The present work uses Lapox L-12 epoxy resin and the corresponding hardener Lapox K-6 which are procured from HARIPA INDIA pvt. Ltd. The resin and hardener are taken in the ratio of 10:1. The fiber made of required size and the required weight percentage calculated based on the matrix material, which is thoroughly mixed with epoxy resin and then poured into the mold cavity. Silicon spray is sprinkled over the



**Fig. 1** Short rice and wheat straw fiber reinforcement

mold prior to pour the mixture for easy removal of a sample after curing. Samples of composite are prepared with fiber loading varied from 5 to 20% by weight for conducting different tests. One of the rectangular samples prepared employing hand lay-up technique is shown in Fig. 1.

## 2.2 *Experimental Tests on Mechanical Properties*

The mechanical properties include the determination of tensile and compressive strength of untreated rice and wheat straw fiber reinforced composites.

**Tensile strength.** The tensile strength of the specimen is obtained using Universal Testing Machine (INSTRON 3382). The specimen of size 165 mm × 20 mm × 5 mm is used to carry out the tensile strength. The specimen is rigidly fixed in the clamps as shown in Fig. 2 and the load is increased slightly till the fracture to occur. During the test, for better result to obtain the cross head speed is maintained as 2 mm/min and

**Fig. 2** Tensile test arrangement in INSTRON 3382





the results thus obtained for tensile strength are recorded for different fiber weight percentage.

**Compressive strength.** The uniaxial compression test is carried out on cylindrical specimens using the same UTM INSTRON 3382. The required dimension of both the rice and wheat straw fiber specimen is as diameter equals to 20 mm and the length measures 40 mm. The crosshead speed is maintained as 1 mm/min while conducting the experiment. The compression of the specimen is continued till failure occurs. Figures 3 and 4 represent the specimen and the experimental setup arrangement for the compression test.

**Experimental determination of thermal conductivity.** The effective thermal conductivity of both the wheat and rice straw fiber is experimentally measured using TEMPOS, the thermal properties analyzer instrument which is procured from METER group, USA. The experimental setup to perform the experiment is shown in Fig. 5. To carry out the experiment, a hole of diameter 2.4 mm, is made over the specimen to fit the TR3 sensor needle in the hole. To ensure good thermal contact

**Fig. 3** Cylindrical specimen for compression test



**Fig. 4** Compression test arrangement in INSTRON 3382



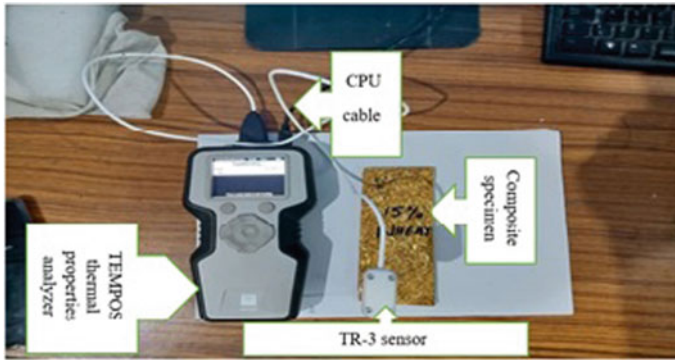


**Fig. 5** Thermal conductivity measurement set up

between the sensor and the specimen glycerin is applied in the hole prior to insert the sensor needle. The constant power supply of  $3.58 \text{ W/m}$  is applied to the specimen from the 5A power source batteries. The temperature measurement mode was operational for five minutes during which the sensor gets heated for half the time and cooled for another half time to obtain the temperature of the test samples.

### 3 Results and Discussion

The experimental results obtained for mechanical and thermal properties are highlighted for fair comparison.

#### 3.1 Mechanical Properties

In the mechanical properties, experimental tests are carried out to find the tensile strength, compressive strength of the rice and wheat straw fiber reinforced epoxy composite. The comparison of results obtained for tensile strength is presented in Fig. 6 for different rice and wheat straw fiber (weight %). It is evident from Fig. 6 that the tensile strength first increases and then decreases with increase in fiber loading. The decrease of tensile strength is due to the poor interfacial bond that exists between the reinforcement and matrix at higher fiber loadings. The tensile strength of rice straw fiber reaches a maximum value of  $4.19 \text{ MPa}$  while reaching a maximum of  $6.18 \text{ MPa}$  for wheat straw fiber at 10% weight fraction.

The comparison of compressive strength obtained from different straw content (weight %) is presented in Fig. 7. It is evident from Fig. 7 that the compressive strength for both the fiber first increases and then decreases with increase in fiber loading. Both the fiber reaches their respective maximum value of compressive strength of

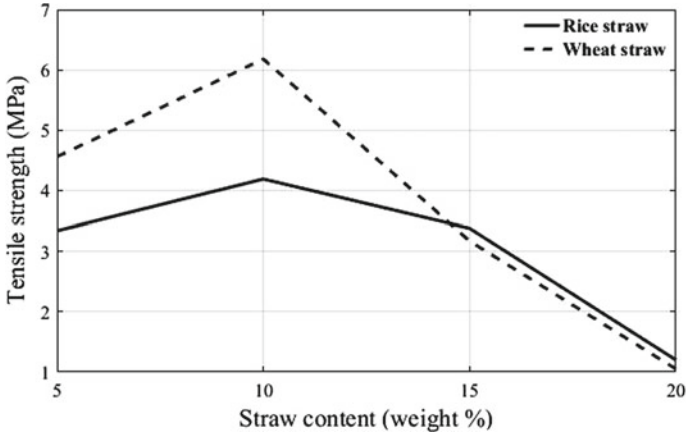


Fig. 6 Tensile strength versus straw fiber content (weight %)

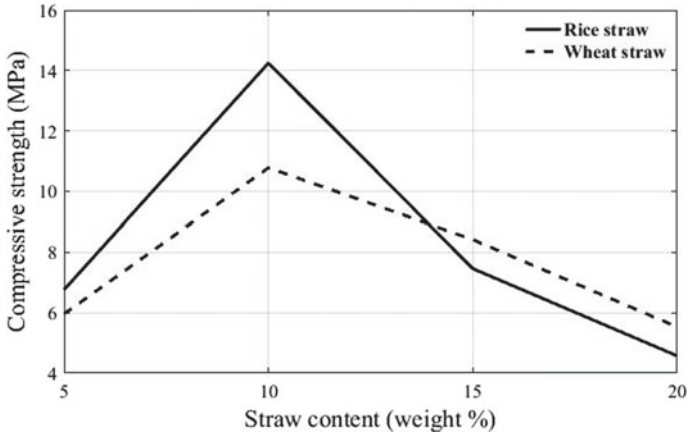
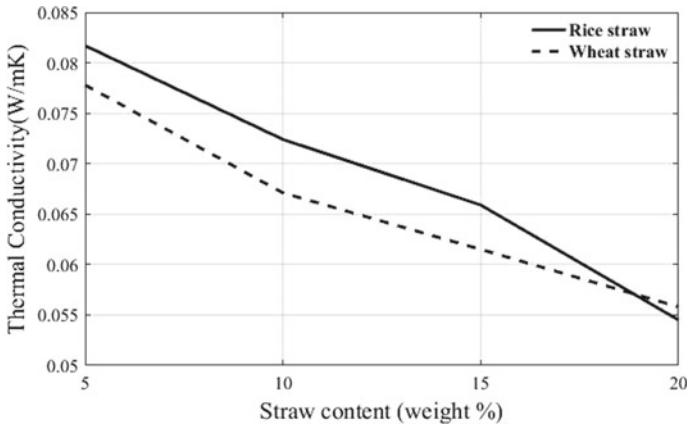


Fig. 7 Compressive strength versus straw fiber content (weight %)

straw content (10% weight). The possible cause for the decrease of compressive strength may be due to irregular shape and uneven distribution of reinforcements that have the inability to transfer load from the matrix at higher fiber loading. It is also observed that rice straw fiber reaches a maximum value of 14.25 MPa while reaching a value of 10.78 MPa in case of wheat straw fiber at 10% weight fraction. But with increase in fiber loading the rice straw fiber attains less value of compressive strength compared to wheat straw fiber.



**Fig. 8** Thermal conductivity versus straw fiber content (weight %)

### 3.2 Thermal Conductivity

The temperature of the test specimen obtained from the experimental setup is recorded and presented in Fig. 8 for fair comparison. It is observed from Fig. 8 that the thermal conductivity of composite made of wheat straw and rice straw decreases with increase in fiber loading. Both the rice and wheat straw fiber have porous structure. The thermal conductivity value of fibers, mostly depends on the size of pore, length of the fiber and distribution of the fiber in the composite. The increase in fiber loading results in increase of surface area and pore size, thus reduces the effective thermal conductivity. Figure 8 confirms that the wheat straw fiber has less thermal conductivity compared to rice straw.

## 4 Conclusion

A comparative analysis of mechanical and thermal properties has been made between rice and wheat straw fiber reinforced composite to select the best one which can be subsequently utilized as building material. The experimental results reveal that the wheat straw fiber reinforced composite retains a higher value of tensile strength in comparison to rice straw fiber reinforced composite. However, the composite made of rice straw holds a good value of compressive strength compared to wheat straw fiber-based composite. From the study of thermal conductivity, it is found that the wheat straw fiber reinforced composite has less thermal conductivity value compared to rice straw fiber at different fiber loading. The outcome of all the results suggests that wheat straw fiber can be recommended as a building material.

## References

1. Ozioko FU (2011) Effect of carbonization temperature on wear rate behavior of rice husk ash reinforced epoxy composites. *Leonardo Electr J Pract Technol* 19:172–182
2. Petchwattana N, Chanakul SCS (2012) Mechanical properties, thermal degradation and natural weathering of high density polyethylene/rice hull composites compatibilized with maleic anhydride grafted polyethylene. *J Polym Res* 19(7):1–9
3. Buzarovska A, Bogoeva-Gaceva G, Grozdanov A, Avella M, Gentile G, Errico M (2008) Potential use of rice straw as filler in eco-composite materials. *Aust J Crop Sci* 1(2):37–42
4. Grozdanov A, Buzarovska A, Bogoeva-Gaceva G, Avella M, Errico ME, Gentile G (2006) Rice straw as an alternative reinforcement in polypropylene composites. *Agron Sustain Dev* 26(4):251–255
5. Oksman K, Lindberg H (1998) Influence of thermoplastic elastomers on adhesion in polyethylene wood flour composites. *J Appl Polym Sci* 68(11):1845–1855
6. Yang HS, Kim DJ, Lee YK, Kim HJ (2003) Rice straw-wood particle composite for sound absorbing wooden construction material. *Bioresour Technol* 86(2):117–121
7. Ranjan C, Ahmed Z, Kumar SR, Kumar A, Kumar A, Kumar K (2021) Fabrication and strength analysis of rice straw fibers reinforced epoxy biodegradable composite. *Mater Today: Proc* 46(1):331–335
8. Lee HS, Cho D, Han SO (2008) Effect of natural fiber surface treatments on the interfacial and mechanical properties of henequen/polypropylene biocomposites. *Macromol Res* 16(5):411–417
9. Halvarsson S, Edlund H, Norgren M (2009) Manufacture of non-resin wheat straw fibreboards. *Ind Crops Prod* 29(2–3):437–445
10. Pan M, Zhou D, Bousmina M, Zhang SY (2009) Effects of wheat straw fiber content and characteristics, and coupling agent concentration on the mechanical properties of wheat straw fiber-polypropylene composites. *J Appl Polym Sci* 113(2):1000–1007
11. Avella M, Rota GL, Martuscelli E, Raimo M (2000) Poly(3-hydroxybutyrate-co-3-hydroxyvalerate) and wheat straw fibre composites: thermal, mechanical properties and biodegradation behaviour. *J Mater Sci* 35(4):829–836
12. Mittal V, Sinha S (2017) Study the effect of fiber loading and alkali treatment on the mechanical and water absorption properties of wheat straw fiber-reinforced epoxy composites. *Sci Eng Compos Mater* 24(5):731–738
13. Tong J, Wang X, Kuai B, Gao J, Zhang Y, Huang Z, Cai L (2021) Development of transparent composites using wheat straw fibers for light-transmitting building applications. *Ind Crops Prod* 170
14. Wahyuni NLE, Soeswanto B, Aulia H, Fadhilah RA (2019) The effects of rice straw weight fraction and particle size on thermal conductivity and mechanical properties of polypropylene composite. *J Phys: Conf Ser* 1295(1):012067
15. Tao Y, Li P, Cai L (2016) Effect of fiber content on sound absorption, thermal conductivity, and compression strength of straw fiber-filled rigid polyurethane foams. *BioResources* 11(2):4159–4167

# Islanding Detection of Multi-DG-Based Microgrid Using Support Vector Machine



Anasuya Roy Choudhury, Ranjan Kumar Mallick, Ramachandra Agrawal, Sairam Mishra, Pravati Nayak, and Subashish Samal

**Abstract** In the proposed study, a signal processing method known as empirical mode decomposition (EMD) and a machine learning technique called support vector machine (SVM) are combined to recognize islanding situations in a distribution generation (DG) integrated microgrid system. At first, EMD is retrieving the insight features of the voltage signal through its most informative intrinsic mode component. These feature data are collected under three different conditions, namely islanding, load switching and capacitor switching. Further, SVM classifier is trained and then utilized to segregate the class of event as islanding or non-islanding. A microgrid system is simulated in MATLAB environment, and a classification capability of more than 94% is achieved under noise-free conditions, whereas an accuracy of 91% is accomplished under 30 dB signal-to-noise ratio (SNR).

**Keywords** SVM · DG · Microgrid · Perceptron · Islanding detection

## 1 Introduction

During the last decades, several methods have been proposed for islanding detection; one of them is support vector machine. Islanding is a critical condition in which the microgrid is disconnected from the main grid, consisting of loads and DG and still carry on power distribution by the distribution generations to which network is connected [1]. Islanding causes many problems such as safety concerns, damage to customer's appliances, and inverter damage. It allows a maximum of 2 s of delay for detection of unintentional islanding [2]. A common method used in islanding detection of MGs is both over/under voltage relay and over/under frequency relay

---

A. R. Choudhury · R. Agrawal · S. Mishra · P. Nayak  
Department of Electrical Engineering, Siksha 'O' Anusandhan Deemed to be University,  
Bhubaneswar, India  
e-mail: [anasuyaroy339@gmail.com](mailto:anasuyaroy339@gmail.com)

R. K. Mallick (✉) · S. Samal  
Department of Electrical and Electronics Engineering, Siksha 'O' Anusandhan Deemed to be  
University, Bhubaneswar, India

(or ROCOF) [3]. Islanding is defined as the lack of any monitoring signal at any given moment [4].

The signal is derived at the point of common coupling and is then compared with the set of predicted values in the passive method, meanwhile the active method detects by introducing signals at point of common coupling that is usually not considered because of the issues of power quality [5, 6]. If the algorithm gets detected by the parameters stated above in the area of separation, it determines islanding to have occurred. Scada system is monitored by switch state monitoring system, and the circuit breaker's operating status can be monitored using a SCADA system [7].

## 2 Support Vector Machine (SVM)

Support vector machines (SVMs) are utilized to solve problems of regression and classification, and the theory is applied in several fields of science. Classical support vector machines are based on binary classification, an approach that results in the development of the artificial neural network. The support vector machines deal with separable linear data using soft margin and kernels functions with the non-separable data [8]. Apart from hyperplane, two other lines are drawn parallel to the hyperplane, and the distance between the two parallel planes is known as marginal distance, and that type of hyperplane has to be chosen where there is the maximum marginal distance among the two parallel lines [9]. The datasets which are passing through the marginal lines which are drawn parallel to the hyperplane are known as the support vectors kernels and are used to convert low dimension to high dimension [10].

$$x_i \in R^N \quad \text{and} \quad y_i \in \quad (1)$$

The main objective is to search for an optimal hyperplane  $h : y = W^T x - b = 0$  which has the maximum distance to the nearest training pattern to force the learning generalization of the machine.

$$\min_{wb} \frac{1}{2} (w^T w) \quad (2)$$

$$\text{Subjected to: } y_i (w^T x_i + b) \geq 1, \forall i$$

Subject to the previous approach was reformulated to solve the common problem by considering relaxing optimization for defining which is so-called as the soft margin [11]. The presented problem is now written as,

$$\min_{wb} \frac{1}{2} (w^T w) + C \sum_{i=1}^n \varepsilon_i \quad (3)$$

### 3 System Under Study

The parameters are tabulated in Table 1. The proposed system investigated consists of a utility grid rated 120 kV, 50 Hz. The utility grid is configured to 25 kV bus bar and the PCC by 2 transforms-1 and 2 as shown in Ref. [12] (Fig. 1).

In Fig. 2, the line diagram of multi-DG-based microgrid is shown.

**Table 1** System parameter specification

Distribution components	Specifications
Utility grid	120 kV, 50 Hz
Doubly fed induction generators	9 MW, 575 V, 50 Hz/each
Distributed line parameters	50 Hz, 10 km, 3 phase pi section $R1 = 0.1153 (\Omega/\text{km})$ , $R0 = 0.413 (\Omega/\text{km})$ $L1 = 1.05 \times 10^{-3} (\text{H}/\text{km})$ , $L0 = 3.32 \times 10^{-3} (\text{H}/\text{km})$ $C1 = 11.33 \times 10^{-9} (\text{F}/\text{km})$
Transformer-1	Side1: star grounded; Side2: delta connected 50 MVA, 120 kV/25 kV, $R1 = R2 = 0.08/30 \text{ p.u.}$ , $Rm = Lm = 500 \text{ p.u.}$ , $L1 = L2 = 0.08 \text{ p.u.}$
Transformer-2 and 3	Side1: delta connected, Side2: star grounded 12 MVA, 25 kV/575 V $R1 = R2 = 0.025/30 \text{ p.u.}$ , $Rm = 500 \text{ p.u.}$ $L1 = L2 = 0.025 \text{ p.u.}$ $Lm = \text{Inf}$

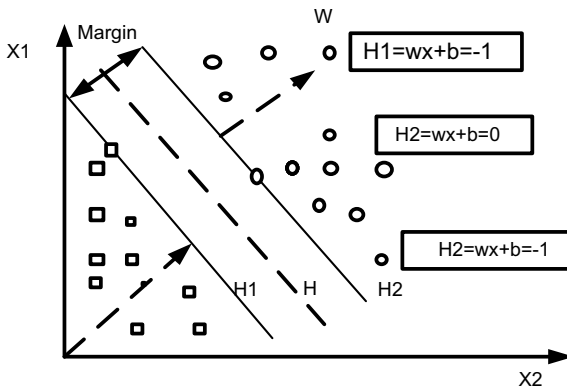


**Fig. 1** Classification process of SVM



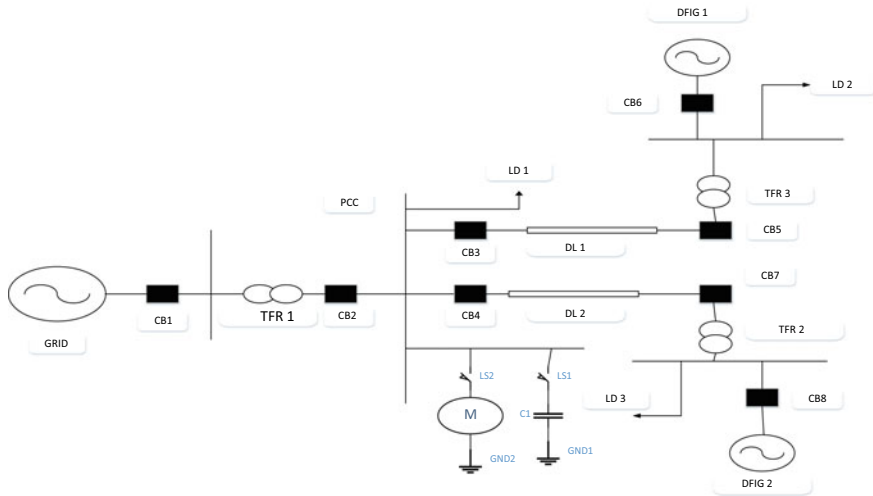


Fig. 2 Multi-DG-based microgrid

### 4 Empirical Mode Decomposition (EMD)

EMD is a signal processing method that empirically decomposes a time series data-based signal while preserving the time domain. In the process decomposition, the input signal is split into intrinsic mode functions (IMFs) of different bands of frequencies [13]. Any function can be decomposed into IMFs should have with: (1) there can only be one optimum between two consecutive zero crossings and at, (2) At every data point the mean of every upper and lower optimum envelopes must be zero [14] (Fig. 2).

Initially, the local extremums which are indicated by  $x_L(t)$  and  $x_U(t)$ , respectively. The mean can be determined using the equation given below:

$$m(t) = \frac{x_L(t) + x_U(t)}{2} \tag{4}$$

After then, a succession of mean elimination process will be carried out till the final IMF is obtained.

$$I_1(t) = x_i(t) - m_i(t) \tag{5}$$

$I_1(t)$  denotes the first IMF. The signal component after  $i$ th shifting is  $x_i(t)$  and the  $i$ th mean is  $m_i(t)$ .

$$r_1(t) = x(t) - m_i(t) \tag{6}$$

With the replacement of  $x(t)$  by  $r_1(t)$ , the same process is repeated to evolve the subsequent IMFs ( $I_2(t), I_3(t), I_4(t) \dots$  etc.).

$$x_R(t) = \sum_{n=1}^{N-1} I_n(t) + r_N(t) \tag{7}$$

### 5 Simulation and Results

The model under examination will proceed as per the flow diagram in Fig. 4 so as to recognize the two events as islanding or non-islanding (load or capacitor switching). The collection of the voltage signal took place from the point of common coupling (PCC) as displayed in Fig. 3. As we are not considering any fault cases, hence, data collected from any of the three phases will result in obtaining the same information. For instant, the phase-A data is empirically decomposed and represented within a timeframe of 0.68–0.78 s in Fig. 3 after imposing intentional islanding in the microgrid at 0.7 s. The EMD of the voltage signal results in two different IMFs. It can be noted that the IMF-1 obtained has higher frequencies and IMF-2 as of fundamental frequency.

As IMF-2 is displaying a promising correlation with the original signal, thus, it is identified as the most informative IMF and chosen for data collection purposes. A total of 1080 datasets have been stored in a database with 4 predictor variables with 540 data samples of islanding and 270 each from load switching and capacitor switching are collected, respectively, as of Table 2. Further, the machine learning classification learner will train the SVM classifier with 60% training data.

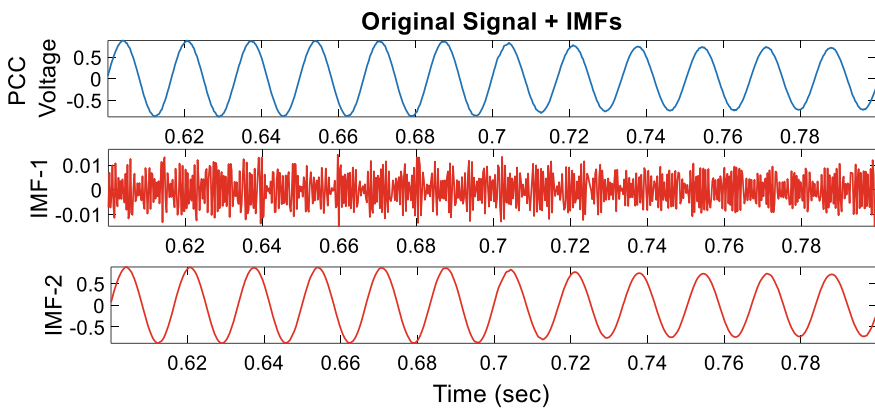


Fig. 3 Decomposed waveforms of PCC retrieved voltage signal

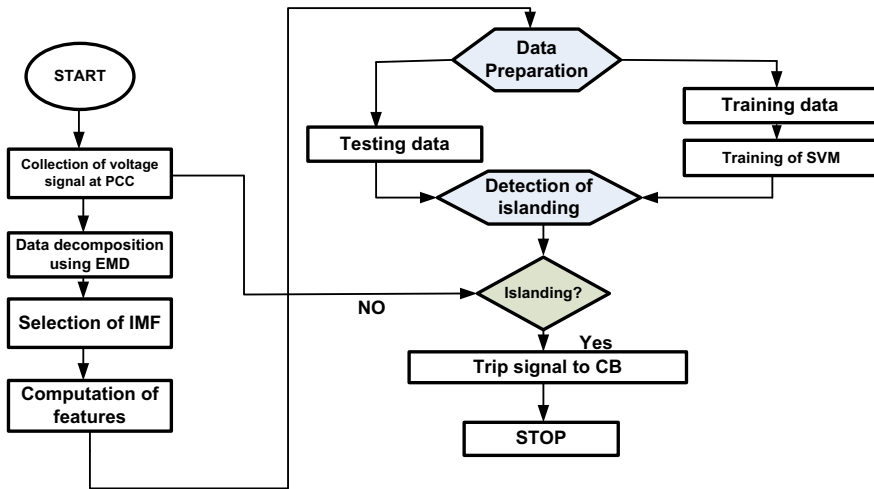


Fig. 4 Flowchart of the proposed detection method

Table 2 Samples collected from different class of events

S. No.	Event class	Collected events	Notation
1	Islanding	540	ISLAND
2	Switching of load	270	L/CSWC
3	Switching of capacitor	270	

This process is called testing. One of such performance indices is classification accuracy. The overall and individual accuracy formulae are presented in Eqs. (8) and (9), respectively.

$$AC_{OVR} = \frac{\sum \text{True Predictions}}{\text{Total Number of Events}} \tag{8}$$

$$AC_{IND} = \frac{\text{Truly Predicted Event of an Individual Class}}{\text{Total Number of Events of the Individual Class}} \tag{9}$$

But it is very important to determine a confusion matrix of any machine learning model to evaluate its performance indices. In simple terms, confusion matrix is a tabular representation of events predicted by the trained model which says the statistics of events truly predicted as one class and falsely predicted as another. Noise-free condition is generally an ideal condition where the power system is supposed to be dissociated from any external hindrances. A confusion matrix under such scenario can be seen in Table 3 which obtains an overall accuracy of  $528 + 484/1080 = 0.937$ , i.e., 93.7% where the individual accuracies are as follows,

**Table 3** Noiseless condition confusion matrix

	Predicted ISLAND	Predicted L/CSWC
Truly ISLAND	528	12
Truly L/CSWC	56	484

$$AC_{ISLAND} = \frac{528}{540} = 0.977 = 97.7\%, \quad AC_{L/CSWC} = \frac{484}{540} = 0.896 = 89.6\%$$

Whereas, in the real world, there is a mere possibility for non-existence external hindrance. Electromagnetic interference, communication line presence are the main causes of obtaining polluted signals in the power line. So as to realize such a scenario in a virtual environment like Simulink additive, white Gaussian noise (AWGN) can be added to the collected signal. Mathematically, these are represented in terms of signal-to-noise ratio [12] as given in Eq. (10)

$$SNR(\text{indB}) = 10 \log \frac{\text{Sig}_p}{\text{Noe}_p} \tag{10}$$

where  $\text{Sig}_p$  is the power of signal and  $\text{Noe}_p$  is the power of noise.

Here, a SNR of 30 dB is taken into consideration, and the respective confusion matrix is shown in Table 4. The overall accuracy is drastically got down to 88.7%, in this case, and the individual accuracies can be found as,

$$AC_{ISLAND} = \frac{506}{540} = 0.937 = 93.7\%, \quad AC_{L/CSWC} = \frac{484}{540} = 0.852 = 85.2\%$$

Moreover, the data extracted from the EMD decomposed signal is providing more accurate results to that of some published research in the field of islanding detection using SVM. A comparative analysis of the same is expressed in Table 5.

**Table 4** Noisy condition confusion matrix

	Predicted ISLAND	Predicted L/CSWC
Truly ISLAND	506	34
Truly L/CSWC	80	460

**Table 5** Comparison with pre-published articles

S. No.	Published article	Accuracy (in %)
1	Pattern recognition [15]	94%
2	Probabilistic NN + SVM [16]	97%
3	Proposed	97.7%

## 6 Conclusion

The paper proposes an EMD-based support vector machine classifier to identify the islanding condition in a multi-DG-based microgrid test system. The three basic conditions such as islanding, load switching, and capacitor switching cases simulated at various power mismatch conditions. An efficient database is prepared considering the features and cases. The capability of SVM can be enhanced by optimizing the parameters in the future study.

## References

1. Thukaram D, Khincha HP, Vijaynarasimha HP (2005) Artificial neural network and support vector machine approach for locating faults in radial distribution systems. *IEEE Trans Power Delivery* 20(2):710–721
2. Dhumal RK, Rajendra KVY, Mehrotra SC (2013) Classification of crops from remotely sensed images: an overview. *Int J Eng Res Appl (IJERA)* 3(3):758–761
3. Baghaee HR et al (2017) Eigenvalue, robustness and time delay analysis of hierarchical control scheme in multi-DER microgrid to enhance small/large-signal stability using complementary loop and fuzzy logic controller. *J Circ Syst Comput* 26(06):1750099
4. Steigerwald RL, Ferraro A, Turnbull FG (1983) Application of power transistors to residential and intermediate rating photovoltaic array power conditioners. *IEEE Trans Ind Appl* 2:254–267
5. Olivares DE et al (2014) Trends in microgrid control. *IEEE Trans Smart Grid* 5(4):1905–1919
6. Dehkordi NM et al (2018) Distributed noise-resilient secondary voltage and frequency control for islanded microgrids. *IEEE Trans Smart Grid* 10(4):3780–3790
7. Moutis P, Hatziaargyriou ND (2014) Decision trees-aided active power reduction of a virtual power plant for power system over-frequency mitigation. *IEEE Trans Industr Inf* 11(1):251–261
8. Zhang PY, Shu S, Zhou MC (2018) An online fault detection model and strategies based on SVM-grid in clouds. *IEEE/CAA J Automat Sin* 5(2):445–456
9. Baghaee HR et al (2019) Support vector machine-based islanding and grid fault detection in active distribution networks. *IEEE J Emerg Sel Top Power Electron* 8(3):2385–2403
10. Cervantes J et al (2020) A comprehensive survey on support vector machine classification: applications, challenges and trends. *Neurocomputing* 408:189–215
11. Pérez Hernández L, Flórez JM, Cebayos JB (2009) A linear approach to determining an SVM-based fault locator's optimal parameter. *Ing Invest* 29(1):76–81
12. Uyar M, Yildirim S, Gencoglu MT (2008) An effective wavelet-based feature extraction method for classification of power quality disturbance signals. *Electr Power Syst Res* 78(10):1747–1755
13. Wei Y et al (2018) A hybrid approach for weak fault feature extraction of gearbox. *IEEE Access* 7:16616–16625
14. IEEE Std (2018) Photovoltaics, distributed generation, and energy storage. In: *IEEE standard for interconnection and interoperability of distributed energy resources with associated electric power systems interfaces*, pp 1547–2018
15. Mohanty SR et al (2013) Classification of disturbances in hybrid DG system using modular PNN and SVM. *Int J Electr Power Energy Syst* 44(1):764–777
16. Faqhruldin ON, El-Saadany EF, Zeineldin HH (2014) A universal islanding detection technique for distributed generation using pattern recognition. *IEEE Trans Smart Grid* 5(4):1985–1992